1998

Solid-State Sensors, Actuators, and Microsystems Workshop

www.hh1998.org

Sponsored by the
Transducer Research Foundation, Inc.
Additional support provided:
Defense Advanced Research Projects Agency

Hilton Head Workshop
June 8 - 11, 1998 • Hilton Head, South Carolina
Editors: Luc Bousse & Antonio J. Ricco

TRF Catalog Number: 98TRF-0001
Library of Congress Control Number: 98-60214
ISBN Number: 0-9640024-2-6
ISSN 1539-2058 (Print) • ISSN: 1539-204X (Electronic)
DOI 10.31438/trf.hh1998.0

1998

Solid-State Sensors, Actuators, and Microsystems Workshop

Hilton Head Island, South Carolina • June 8 - 11, 1998

TRF Catalog Number: 98TRF-0001
Library of Congress Control Number: 98-60214
ISBN Number: 0-9640024-2-6
ISSN 1539-2058 (Print) • ISSN: 1539-204X (Electronic)
DOI 10.31438/trf.hh1998.0

If you have questions regarding the installation, please contact:

The Printing House
Phone: +1-608-873-4500
Hours: Monday through Friday, 8 am - 5 pm CST
E-mail: graphics@printinghouseinc.com

Greetings from the General Chairman

On behalf of the Organizing and Technical Program Committees, it is my pleasure to welcome you to Hilton Head Island! The 1998 Solid-State Sensor and Actuator Workshop, eighth in the biannual series, offers an outstanding technical program and many opportunities for stimulating discussion. We hope you will benefit personally and professionally from this meeting, sharing in the enthusiasm that make it an ongoing success: the number of applicants has increased by 40%, and the number of abstracts submitted by nearly 60%, relative to our very successful 1996 meeting!

The Hilton Head Workshop is one of the regional sensor, actuator, and microsystems meetings held in North America, Europe, and Asia in even-numbered years, alternating with the international Transducers conferences in odd-numbered years. Our workshop format provides a highly interactive forum for engineers and scientists from the Americas to present and discuss in detail recent advances in emerging technologies for sensing and actuating microdevices, along with miniaturized systems for physical, chemical and biological analysis. The single-session format allots ample time for discussion of each oral presentation, with three poster sessions providing for detailed one-on-one discussions of results and ideas.

Work on the technical program began in earnest last Fall as four invited speakers were selected and the call for papers broadcast. In January, over 200 technical abstracts were received, and the Technical Program Committee undertook the challenge of selecting just 85 of these for presentation. Supplementing these papers are the Late News Poster Session, for the presentation of very recent results, as well as the Open Poster Session, providing an additional forum for in-depth discussion.

The Rump Session will provide an opportunity for very informal, frank discussion of a topic of current interest and controversy. Likewise, we hope the opening reception, the banquet, the leisurely lunches provided each day, the breaks, and all of the poster sessions will provide many further opportunities for personal contacts and conversations. We encourage you to take advantage of the unscheduled time on Tuesday afternoon to explore and enjoy the beautiful environs on Hilton Head!

This Workshop is made possible only through the diligence and support of key individuals and organizations. The non-profit Transducers Research Foundation sponsors and underwrites this meeting, providing business infrastructure. Thanks are due to the Defense Advanced Research Projects Agency, Dr. Albert P. Pisano, and the National Science Foundation, Dr. Rajinder P. Khosla, for financial support of graduate student presenting authors — students have been an integral part of this Workshop since its inception — and to Professors Mehran Mehregany and Richard Muller for securing and distributing this support. Bernadette Fulton of Sandia National Labs is our capable Workshop Secretary, and Patrick Riehl of the Berkeley Sensor & Actuator Center has kept us communicating via our world-wide web site.

I want to thank in particular the Technical Program Committee, chaired by Luc Bousse, for arranging an excellent technical program. The myriad local arrangements here on Hilton Head have been ably handled by Mark Allen; Dave Eddy and Luc Bousse guided the production of the Technical Digest and CD-ROM; and Joe Giachino has kept a careful watch on financial matters. Finally, my thanks to all the authors for the technical contributions that are the heart of this meeting, and to all the participants who will keep our discussions lively!

Enjoy your workshop!

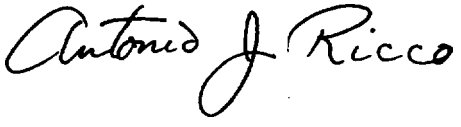

Antonio J. Ricco
General Chairman

1998 Solid-State Sensor & Actuator Workshop

Organizing Committee

General Chairman	Antonio J. Ricco Sandia National Laboratories
Technical Program Chairman	Luc J. Bousse Caliper Technologies
Treasurer	Joseph M. Giachino Ford Motor Company
Publications	David S. Eddy General Motors Corporation
Local Arrangements	Mark G. Allen Georgia Institute of Technology
Program Meeting Arrangements	Robert J. Huber University of Utah
Student Travel Grants	Richard S. Muller University of California at Berkeley
	Mehran Mehregany Case Western Reserve University

Technical Program Committee

Debborah Charych
Lawrence Berkeley National Laboratory

Jiri Janata
Georgia Institute of Technology

Gregory T. A. Kovacs
Stanford University

Mehran Mehregany
Case Western Reserve University

Martin A. Schmidt
Massachusetts Institute of Technology

Philip Congdon
Texas Instruments

Hal Jerman
Quinta Corporation

Marc Madou
Ohio State University

David J. Monk
Motorola, Inc.

Yang Zhao
Analog Devices, Inc.

Solid-State Sensor and Actuator Workshop
June 8 – 11, 1998
Crowne Plaza Resort
Hilton Head Island, South Carolina

Program and Table of Contents

Sunday, June 7

3:00 to 7:00 pm	Registration
7:00 to 9:00 pm	Welcome Reception

Monday, June 8

Tuesday, June 9

Thursday, June 11

Contributed Posters (Monday June 8)

Contributed Posters (continued)

Contributed Posters (continued)

Contributed Posters (continued)

TECHNICAL PAPERS

Solid-State Sensors, Actuators, and Microsystems
Workshop

1998
Hilton Head Island, South Carolina
June 8 - 11

A Microanalytical Device for the Assessment of Coagulation Parameters in Whole Blood

Celine Bisson, John Campbell, Rhonda Cheadle, Marianne Chomiak, John Lee, Cary Miller, Catherine Milley, Peter Pialis, Sandra Shaw, Wenda Weiss, Cindra Widrig

i-STAT Canada Ltd.

Kanata, Ontario K2L 1T9

ABSTRACT

The following describes the development of a disposable cartridge for use at the patient side to perform traditional coagulation assays on fresh whole blood samples. The cartridge provides a means by which a blood sample can be metered and quantitatively mixed with reagents which activate the coagulation cascade. Clot formation is subsequently detected using a microfabricated sensor also housed within the cartridge. The functional features of the cartridge and sensor are described and clinical results are presented.

INTRODUCTION

i-STAT Corporation manufactures a system for patient-side testing comprised of disposable test cartridges and a hand held or patient-monitor-contained analyzer. The cartridge is assembled from molded components and houses the necessary calibrants and sensors to perform a variety of clinical chemistry tests. Currently i-STAT produces cartridges containing various combinations of electrochemical sensors which have been miniaturized through microfabrication techniques. Thin-film photolithographic processes and nanoliter partial-drop dispensing technology are utilized to produce potentiometric (Na^+, K^-, Cl^-, urea, Ca^{+2}, pH, and CO_2), amperometric (glucose, creatinine, oxygen), and conductometric (hematocrit) sensors. i-STAT manufactures 10 products containing various combinations of these 11 tests. The sensors are packaged so that single cartridges accommodate the most common testing patterns.

A typical cartridge is shown in Figure 1. Conduits and valves used for calibrant and sample delivery are indicated. The biosensors reside on the chips at the top of the cartridge. The reagents needed to carry out the signal generating reaction on each sensor are contained within layers at the sensor's surface. This eliminates chemical cross-talk and allows the tests to be performed in a single conduit. No accurate fluid positioning is required.

Our R&D plan intends the addition of several new classes of tests to the currently available battery so that complete patient-side testing is available in a single instrument. To perform these tests, new functionality will be added to the cartridge and features within the present analyzer that are not yet employed in current product will be put to use. Future tests will be run on today's platform, however, and future cartridges will be manufactured with modifications of current processes.

Under development at present is a series of new cartridges designed to perform coagulation assays in existing i-STAT instruments. These tests are used to assess the function of an individual's hemostatic system. In an assay, the enzymes responsible for coagulation are activated by the addition of specific reagents and the elapsed time to clot formation is measured.

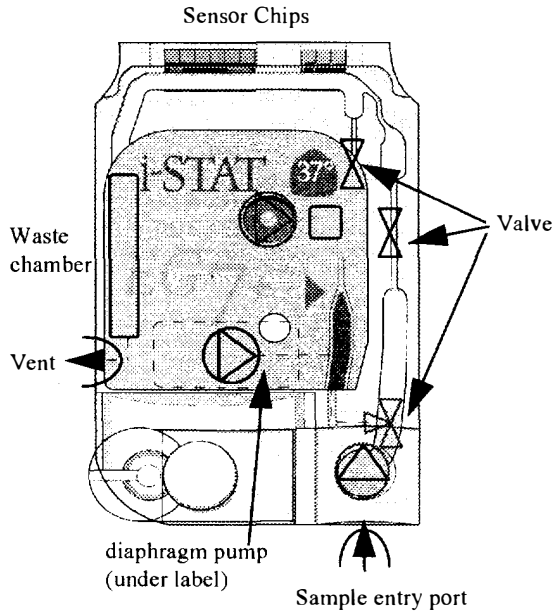

Figure 1. i-STAT cartridge for electrolyte and blood gas testing. Valves and pumps are schematically indicated.

BACKGROUND

Coagulation in blood or plasma occurs when fibrinogen is enzymatically converted to fibrin. In this conversion, small peptide fragments are cut from the fibrinogen molecule to produce individual fibrin strands. The strands then form a hydrogen-bonded network that serves to gel the sample. The enzyme responsible for liberation of the fibrinopeptides is the protease thrombin. It is generated in its active form as the penultimate step in the "coagulation cascade" -- a series of sequential protease activations involving nine plasma proteins. This cascade is depicted in Figure 2.

The most common coagulation tests are performed in platelet free plasma that is taken from centrifuged whole blood. During collection, trisodium citrate is added to the blood to temporarily remove ionized calcium, a required cofactor for a number of the protease reactions. This prevents clotting during transport and handling of the sample. A test is performed by adding an activator to the plasma, incubating the mixture to allow complete activation of the first enzyme in the cascade, and finally adding calcium chloride in excess of the citrate

0-9640024-2-6/hh1998/$20©1998TRF
DOI 10.31438/trf.hh1998.1

Solid-State Sensors, Actuators, and Microsystems Workshop
Hilton Head Island, South Carolina, June 8-11, 1998

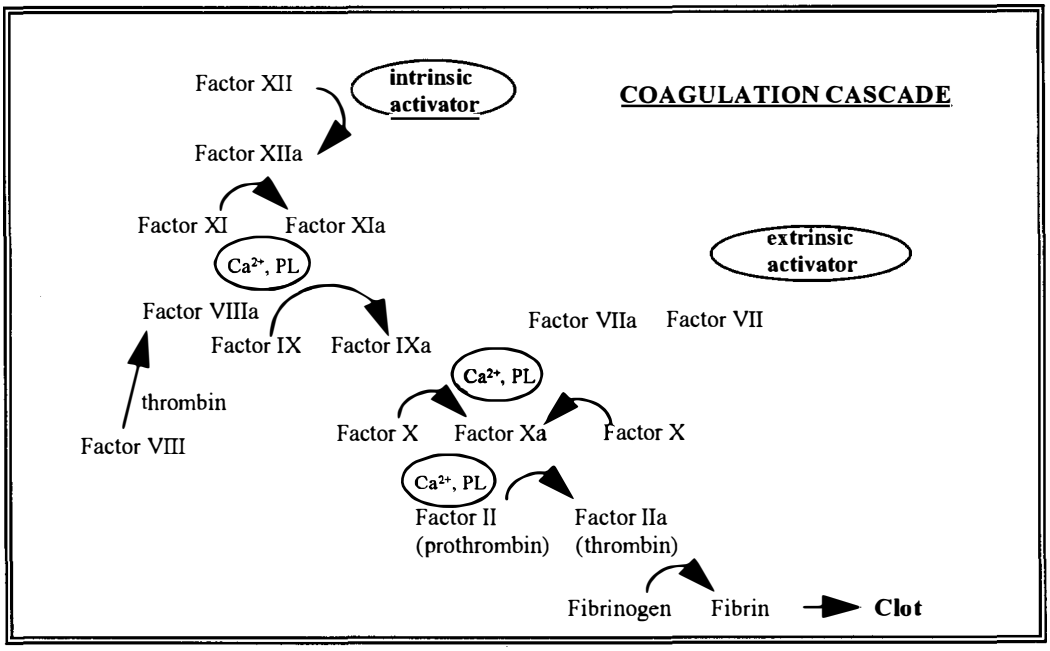

Figure 2. Enzymatic steps occurring in the coagulation cascade. Each factor shown is present in plasma as an inactive protease. During coagulation, the enzymes are sequentially converted to their active forms, denoted by the appended "a". The arrows indicate the sequence of activations required for clot formation. As indicated, many of the reactions also require the presence of free calcium ions and phospholipids (PL). Coagulation can be initiated through the activation of the intrinsic (activation of Factor XII) or extrinsic pathway (activation of FactorVII).

concentration to allow coagulation to proceed. The endpoint is reached when clot formation is detected either optically (as the plasma becomes turbid) or mechanically (as the plasma viscosity increases) [1]. A Prothrombin Time test (PT) adds an extrinsic activator and measures the time for clot formation via activation of Factors VII, X, and II. An activated Partial Thromboplastin Time test (aPTT) initiates coagulation with an intrinsic activator and is used to assess the function of Factors XII, XI, IX, VIII, X, and II. It is also sensitive to inhibitors of these enzymes.

The functions which must therefore be incorporated within the cartridge are a means by which reagent may be quantitatively mixed into a blood sample and a method for detecting a clot. These two aspects of the cartridge design are discussed below.

ADDITION OF REAGENT TO A METERED BLOOD SEGMENT

To initiate coagulation, reagent must be rapidly and quantitatively mixed into a test sample. In a benchtop instrument, this is accomplished by injecting an aqueous solution containing the reagents into a measured aliquot of plasma. Although it is possible to engineer similar "stop-flow" mixing into a cartridge, it has been found that the simpler dissolution of dry reagent provides adequate speed and reproducibility of homogenization.

Current single test devices which do not have convective mixing capability typically employ a high surface-area-to-volume ratio reaction vessel in which the walls of the cell are coated with dry reagent. Diffusion provides sufficiently rapid homogenization. As the required dissolution time in the coagulation tests is on the order of seconds, the upper limit of such a chamber's shortest dimension is approximately 25 microns. Such geometries, however, do not easily lend themselves to a multi-assay format or to the integration of non-coagulation tests. Because it is intended that the mixing strategies devised here be generally applicable to future cartridges types, larger bore conduits allowing serial testing and fluid wash-out are preferred. With larger diameter channels, convection is required to provide rapid mixing.

In the coagulation cartridge, the clot reaction is initiated in a specific region of the flow channel over the sensor chips. A length of the wall within the channel is coated with reagent, as indicated in Figure 3. In other applications, reagent may be added in the pre-sensor channel or sample holding chamber. Convection is induced by oscillating a segment of blood in the region of the flow channel containing the reagent. The motion is controlled so that the trailing edge of the blood segment continually moves on and off of the reagent coating, as depicted in Figure 4. This mixing profile confines the dissolving reagent to a defined region of the blood. The remainder of the segment is available for the addition of other reagents or testing with other sensors.

The oscillation is maintained with feedback from the fluid sensor coincident with the reagent coating. This sensor comprises the two parallel bars on the chip shown in Figure 5. These bars lie perpendicular to the length of the flow channel and the electrical resistance between them can be used to monitor the relative position of the fluid front. Feedback from this sensor is used to control the motor direction and speed so that the center, amplitude, and frequency of the oscillation can be maintained. With such control it is possible to obtain

reproducible mixing profiles in varying hematocrit (and therefore viscosity) samples.

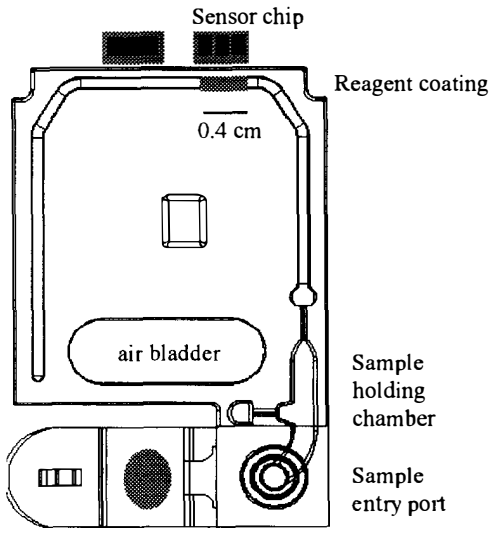

Figure 3. Coagulation Cartridge with air bladder and reagent coating shown. Sample holding chamber is approximately 25 microliters. The forward 10 microliters of sample is moved into the sensor channel for the coagulation assay. The upper right portion of the sensor channel is coated with a reagent layer. The sensor chip coincident with this segment contains the endpoint sensor and the fluid positioning sensor. It is the chip shown in Figure 5.

Figure 6 shows the resulting concentration gradient along the channel. The sample used here is whole blood. In this experiment, an aqueous solution containing an electroactive marker was deposited in the region of the flow channel indicated above and dried. Complete dissolution of the reagent into a 0.4 cm section of blood would lead to a concentration in that segment of 80 μM. The graph indicates the oxidation current after mixing. It also shows the current expected in un-adulterated blood and that containing 80 μM of the marker. The individual points represent the current at an electrode in the position indicated by the x axis. Across the 2 mm of solution at the edge of the sample, the concentration varies by approximately 10%.

Once mixing has been completed, the segment of the blood containing the reagent must be held above the sensing electrode. This is also accomplished using the signal from the conductometric sensor to maintain a specified resistance typical of the fluid front resting between the two electrodes. In this manner the fluid position along the channel can be controlled to within 0.1 mm.

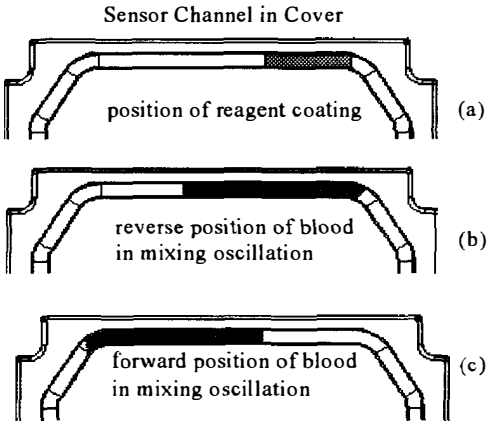

Figure 4. Position of blood during oscillation for dissolution of reagent coating the flow channel as depicted in (a).

CLOT DETECTION

The preferred detection methodology at i-STAT is that which results in the lowest cost for integration of multiple tests into a single platform. This has lead to the development of electrochemical sensors, of which there are several options available for coagulation testing. Below are examples of viscometric and electrogenic endpoint detection schemes which may be used.

Viscometric Endpoint Detection. The relative viscosity of a sample can be assessed by monitoring the velocity of a column of that fluid as a function of the pressure differential across the length of the segment. For a constant pressure profile, increasing viscosity will be manifested as a slowing in the fluid. To make an electrochemical viscometric detector in this cartridge, a means of imparting a pressure gradient and an electrochemical detector of the fluid speed are required.

The former is achieved by oscillating the fluid via the air bladder as described above. This produces a roughly sinusoidal variation in the pressure gradient with an amplitude and frequency determined by the plunger motion. The fluid speed can be monitored using amperometric, conductometric, or potentiometric sensors. For example, if there is an electroactive species in the oscillating fluid, the current for its reduction (or oxidation) at a disc electrode will also oscillate. It increases as the stagnant layer at the electrode surface thins during acceleration and decreases as the depletion layer grows when the fluid stops to turn around. The AC and DC components of this signal can be tailored by adjusting the electrode geometry and fluid motion profile.

Once the blood begins to clot, the increased viscosity lessens the response to the pressurization. Both the amplitude of the AC signal and the DC offset decrease. A clot curve is shown in Figure 7. Events within the curve, such as a shift in the phase angle of the AC current relative to plunger motion, may be used to indicate the coagulation endpoint.

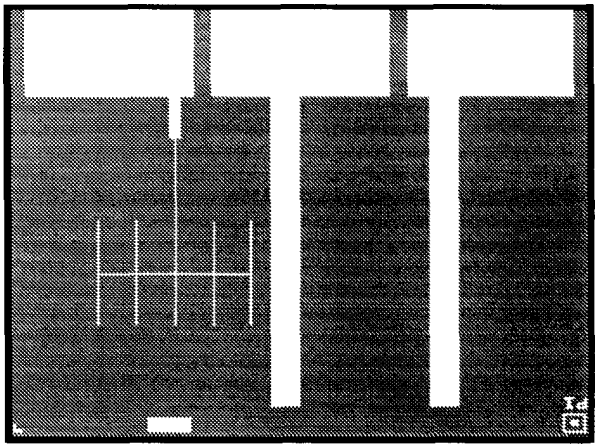

Figure 5. Sensors for fluid positioning and amperometric detection. The two bars on the right together make up the conductometric sensor. Their output is a measure of the local channel resistance. They are used to monitor the position of the fluid edge during mixing and to maintain the position of this edge throughout testing. The sensor to the left is an that used endpoint detection. For reference, the contact pads shown at the top of the chip are 1 mm wide.

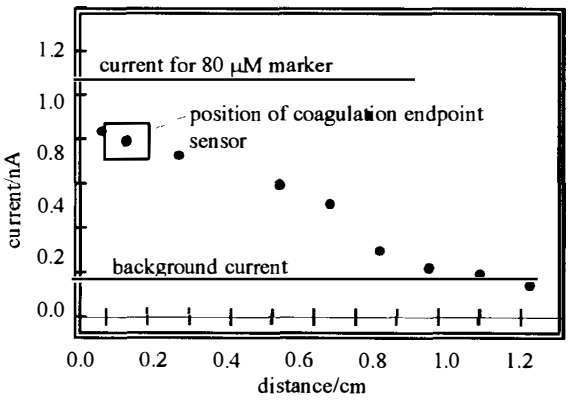

Figure 6. Resulting current for the described dissolution of a typical electroactive marker in blood. The measurements were made with sensors downstream of the conductometric sensor by the distance on the x axis. If dissolved completely in 0.4 cm of the channel, the quantity of the marker present would result in an 80μM solution.

The sensing electrode used in this assay merits note. The specification is that it must provide a means for direct oxidation or reduction of a species dissolved in whole blood. It also must remain stable for up to 15 minutes, the longest a clot test will run. This means that the surface of the electrode must be protected against fouling from blood components yet remain accessible for direct electron transfer by the redox species. Thick semi-permeable protective coatings are not satisfactory, however, as they would not provide the necessary sensitivity to fluid motion. To meet these criteria, electrode coatings deposited using molecular self-assembly and/or plasma processing techniques have been developed.

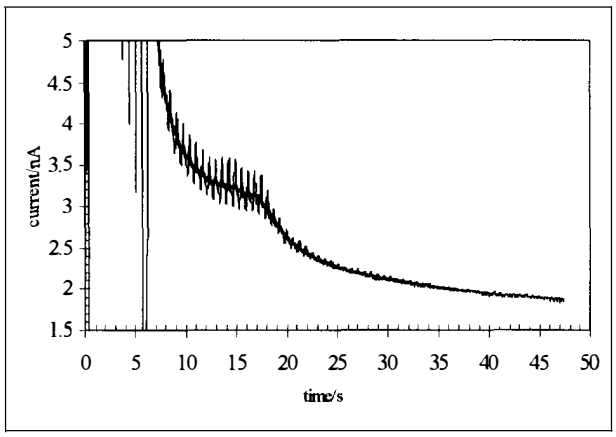

Figure 7. Electrochemical viscometric clot detection in a PT test. Shown is the current for the oxidation of an electroactive marker used as an indicator of clot formation. the marker is mixed into the blood along with activators of the intrinisic coagulation pathway. The high current from 0 to 5 seconds occurs as a result of the relatively rapid fluid motion during mixing. The oscillating current between approximately 8 and 17 seconds is as expected for the low amplitude oscillation of un-clotted blood. As the viscosity increases due to clotting, the AC level and DC offset of the signal both decrease.

Electrogenic Endpoint Detection. Fibrinogen is cleaved by activated thrombin. The time at which this enzyme is produced in the active form consequently correlates to the time for physical clot formation. The ability to detect thrombin therefore offers an alternative method of endpoint detection.

Thrombin is a protease that hydrolyzes peptides at the carboxyl terminal of arginine. Its presence can therefore be determined by the addition of an arginine containing substrate which, upon conversion, generates a colored, fluorescent, or electroactive species. A number of such substrates have been described in the literature[2] and chromogenic endpoint detection has been used to determine clot times in plasma samples[3].

An electrode like the one described above can be used to amperometrically detect the liberated electrophore directly. Alternatively, the signal may be carried to the sensing electrode via mediators which have chemically oxidized or reduced the generated marker. The latter strategy offers several advantages. For example, it removes the need for an electrophore with rapid heterogeneous electron transfer kinetics. It also allows the use of "thick" electrode coatings which will diminish noise induced by incidental fluid motion. Furthermore, a mediator couple may also be detected potentiometrically. The latter point is particularly relevant for design flexibility of multiple-test cartridges. Both amperometric and potentiometric sensors for endpoint detection have been developed. Clot curves resulting from the conversion a substrate are shown in Figure 8. Again, a number of features from these curves may be used to indicate the endpoint.

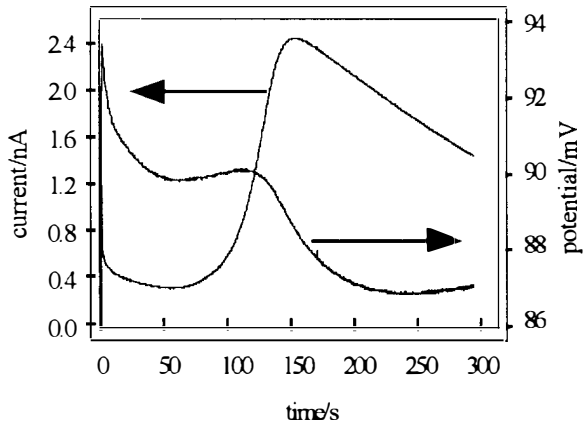

Figure 8. Electrogenic Clot Curve. The electrogenic substrate along with activators of the intrinsic pathway are mixed into a blood sample prior to the time marked as 0. The signals shown are the amperometric (left axis) and potentiometric (right axis) detection of the electroactive marker liberated by thrombin. The current increases (potential decreases) when thrombin is generated and plateaus once the substrate is completely hydrolyzed.

Combination Method. In that the most common clot detection methods rely on the formation of a physical clot, these tests are sensitive to deficiencies in any of the coagulation proenzymes as well as deficiencies in fibrinogen. Because the electrogenic method determines only the time for the activation of thrombin, however, it will not be prolonged in the event of a low fibrinogen sample. To make an electrogenic endpoint "match" a viscometric test one therefore needs an estimate of the sample fibrinogen to correct the thrombin time when necessary.

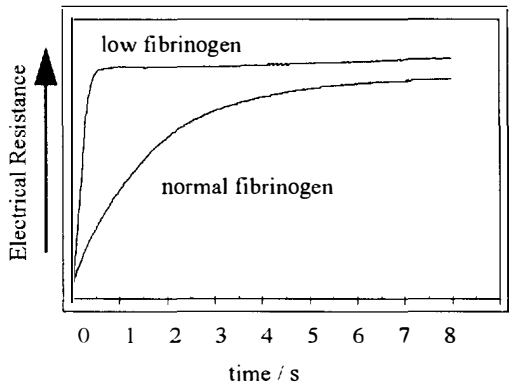

Figure 9. Viscometric assessment of the clotted sample. At t=0 the air bladder is compressed to induce movement in the clotted blood. As the fluid is pushed off of the conductometric sensor, the measured electrical resistance between its electrodes increases. The rate of change of the resistance is indicative of the speed of the moving fluid and therefore the fibrin content of the clot.

Because the flow resistance of a clotted sample increases with increasing fibrin concentration, a measurement of this resistance can be made to assess the concentration of fibrinogen originally present in the sample. This determination is made by gently pushing the clotted sample and measuring the time transient for the resulting fluid motion. Again the conductometric sensor is used to monitor the fluid response. Electrical resistance transients for samples with low and normal fibrinogen concentrations are shown.

TEST RESULTS

To be accepted, this test must have the same anticoagulant and factor sensitivities as the commonly used methods. It also must be similarly precise. The former is demonstrated in method comparison studies while the latter is ascertained through the use of commercially available control plasmas. Some results are presented below.

Precision. Precision is most easily assessed using commercially available control plasmas. Table 1 shows the clot time, within sample precision, sample to sample precision, and total precision for i-STAT aPTT cartridges as well as the reference benchtop instrument. The samples were prepared by re-hydrating lyophilized control plasmas with de-ionized water as per the manufacturer's instructions and re-calcifying to normal levels with 25 mM $CaCl_2$. The total precision of the new and reference tests is comparable.

Table 1

Precision data for normal level control plasmas in

Parameter	i-STAT aPTT Cartridges	MLA 700 w/ Pacific Hemostasis Kontact Reagent
result	28.6 seconds	27.4 seconds
number of test events	15	22
samples per test event	2	2
within run precision	0.73 seconds	0.91 seconds
run to run precision	0.71 seconds	0.83 seconds
total precision	1.02 seconds	1.23 seconds

Anticoagulant sensitivity. The Activated Clot Time (ACT) test is the standard test used to determine the adequacy of anticoagulation during cardiovascular surgery and renal dialysis. It is traditionally a whole blood test in which an activator of the intrinsic pathway is added to the samples and the time to physical clot formation, measured viscometrically, is determined. It is used to monitor heparin, an anticoagulant, at high doses. Figure 10 shows the correlation of the i-STAT cartridge to measurements made on an Array Medical Actalyke reference instrument. Samples were prepared by spiking freshly drawn whole blood with sodium heparin to create concentrations from 1 to 5 U/ml plasma.

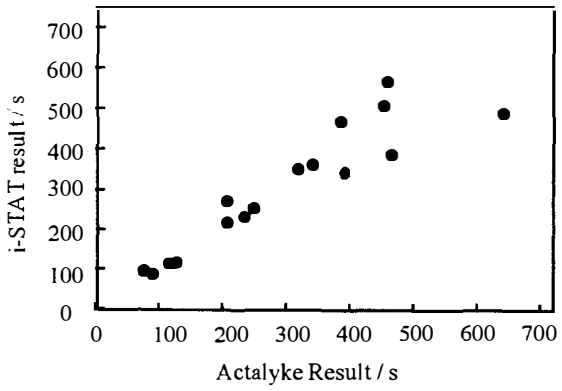

Figure 10. Coagulation times in an Activated Clot Time test (ACT) vs. a reference instrument.

Factor Sensitivity. Factor deficient citrated plasma samples were mixed in varying proportions with normal plasma to produce samples with partial factor deficiencies. The plasma was then mixed with washed red blood cells and re-calcified to produce factor deficient whole blood samples. The blood samples were run in test cartridges and the plasma samples were tested on a benchtop plasma instrument (MLA 700 using Pacific Hemostasis Kontact Reagent). The results are shown in Table 1. The values given are quotients of the clot times for the abnormal and normal samples. Table 1 also shows similar data obtained using a reference whole blood instrument.

Table 2

Factor sensitivity of the aPTT test

Sample	% Factor Present	Plasma aPTT ratio for i-STAT	Plasma aPTT ratio for MLA*	Plasma ratio for Coagu-Check Plus cartridge**
Normal	100	1.00	1.00	1.00
Factor VIII	50	1.12	1.15	1.55
	25	1.19	1.05	
	10	1.41	1.35	2.52
	5	1.63	1.47	
Factor IX	50	1.12	1.12	1.16
	25	1.23	1.27	
	10	1.35	1.44	1.76
	5	1.57	1.59	
Factor X	50	1.12	1.23	
	25	1.14	1.3	
	10	1.3	1.43	
	5	1.42	1.64	
Factor XI	50	1.04	0.97	1.45
	25	1.69	1.52	
	10	1.02	1.69	2.38
	5	2.24	2.23	
Factor XII	50	1.46	1.18	
	25	1.72	1.21	1.13
	10	1.94	1.32	
	5	2.34	1.45	1.85

* In-house results using citrates plasma ** Results taken from CoaguCheck Plus package insert

CONCLUSION

Cartridges for performing coagulation assays using the i-STAT platform has been developed. The cartridge performance equivalent to that of the benchtop plasma instruments and other point-of-care whole blood analyzers.

[1] Machin, S.J.; Mackie, I.J.; Chitolie, A.; Lawrie, A.S. *Clin. Lab. Haem.*, 1996, **18**, 1-6

[2] Claeson, *Blood Coagulation and Fibrinolysis*, 1994, **5**, 411.: Peuriot,M.; (b) Nigretto, J-M.; Jozefowicz, M. *Thrombosis Research*, 1981, **22**, 303.

[3] Walenga, J.; Fareed, ZJ. Bermes, E.W., *Seminars in Thrombosis and Hemostasis*, 1983, **9**, 172. (b) Becker, U., Bartl, K.; Lill, H.; Wahlefeld, W., *Thrombosis Research*, 1985, **40**, 721.

GENETIC ANALYSIS SYSTEMS: IMPROVEMENTS AND METHODS

Rolfe C. Anderson, Gregory J. Bogdan, Alex Puski, Xing Su
Affymetrix, Inc., 3380 Central Expressway, Santa Clara, CA 95051

ABSTRACT

We have developed integrated genetic analysis systems employing improved structures and methods for manipulating fluids and temperatures, new enzymatic reactions, and increased process density. Enhanced mixing, rapid thermal cycling, and fluidic reliability have been demonstrated. Experiments have revealed a new meniscus-driven mixing phenomenon generally characteristic to liquid-plug flow systems. The integrated fluid and thermal control methods developed in this work can be generally applied to other systems for chemical and biochemical analysis and may be amenable to further miniaturization.

INTRODUCTION

Analytical processes benefit from improved reproducibility and reduced operator intervention as entire sample-preparation processes and analytical steps are combined on a single device. Miniaturization and integration can provide device portability, multiplicity, and potentially low cost. Integration of genetic analysis are particularly valuable because complex multistep assays on multiple samples are often desired.

Reports on the development of miniaturized analysis systems have typically been limited to single reactions followed by analysis [**1**, **2**], or have described single operations such as cell lysis [**3**, **4**]. We previously reported on a device that performs a multistep virus mutation assay, first extracting genetic material from a blood sample, then performing a series of enzymatic reactions, and finally carrying out a hybridization reaction with a polynucleotide array [**5**].

Polynucleotide GeneChip® arrays enable the rapid parallel monitoring of genetic information through the selective hybridization of nucleic acids. After a prepared sample reacts with the array, regions of binding are detected using fluorescence imaging [**6**]. GeneChip arrays are fabricated using a photo-directed synthesis technique, where tens of thousands of regions with different polynucleotide probes are created on a glass surface. GeneChip applications include HIV virus polymorphisms [**7**], gene expression [**8**], cystic fibrosis [**9**], cancer-related mutations [**10**], and other sequence analysis assays. These assays generally include the preparation of a labeled and fragmented polynucleic acids at an appropriate concentration. The required series of bench-top processes include extraction and purification of nucleic acid from a sample, enzymatic amplification of the region of interest (e.g. PCR), followed by fragmentation, and labeling reactions. An automated system incorporating these processes offers the advantages of reduced sample volumes, contamination and operator handling, and better reproducibility.

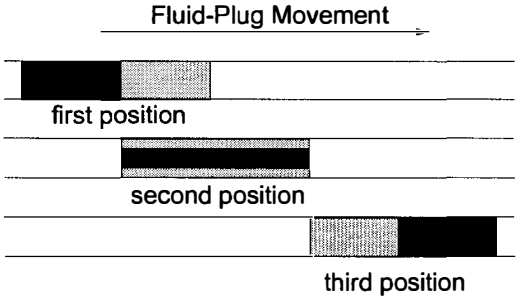

***Figure 1**. Observed meniscus recirculation mixing. Idealized sketch of dye positions as liquid plug is moved through a channel.*

We previously reported on an entire HIV assay from nucleic acid extraction through hybridization using new methods for positioning, metering, and debubbling microliter-volume fluids without the use of sensors. In this work: a) the ability to manipulate fluids has been greatly enhanced by the development of structures and methods for reliable fluid linking, positioning, and mixing, b) an improved thermal control scheme has been demonstrated with faster cycling and scaleability, c) new enzymatic reactions with applications to other genetic assays such as a cytochrome P450 mutation assay have been demonstrated, and d) cartridges for this assay with multiple sample handling for higher throughput have been designed, fabricated and tested.

MENISCUS RECIRCULATION MIXING

Homogeneous mixing in reaction systems is generally desirable and has been widely discussed for microfluidics [**11**] but the hydrodynamics of fluid plugs separated by air has not been represented. In these systems fluid movement at the meniscus can dominate mixing. Flow visualization experiments have revealed a circulation phenomenon that is specific to systems with a moving meniscus. In the experiment, a liquid plug dyed with two different colors is introduced into the channel. As illustrated in Figure 1, moving the fluid plug through a channel causes the dye at the trailing end of a fluid to first penetrate the center of the channel and then encompass the leading end of the fluid plug [**12**]. As a

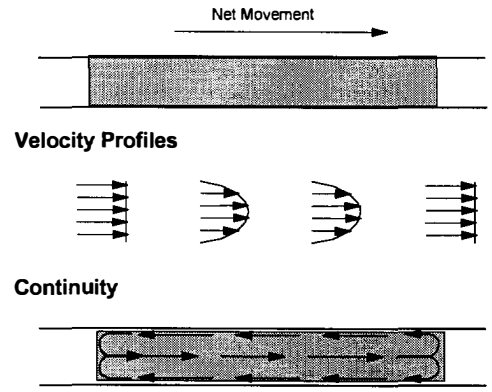

***Figure 2.** Circulation flow induced by moving liquid plug through a channel. A uniform (plug flow) velocity profile is imposed by the movement of the leading and trailing menisci. Towards the midpoint of the plug, parabolic flow is approached. The requirement of fluid continuity causes the radial inward and outward velocities drawn at the trailing and leading edges, respectively. (Note: last sketch is drawn in Eulerian reference frame).*

0-9640024-2-6/hh1998/$20©1998TRF
DOI 10.31438/trf.hh1998.2

Solid-State Sensors, Actuators, and Microsystems Workshop
Hilton Head Island, South Carolina, June 8-11, 1998

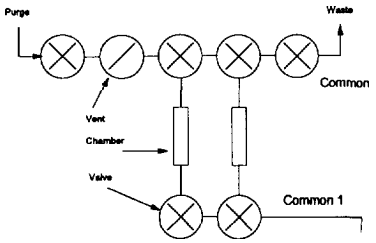

Figure 3. *Sensorless fluid positioning in reaction chambers terminated with valves using vent in secondary common channel. This arrangement has improved reliability and eliminated evaporation during high-temperature operations.*

result, leading and trailing fluid colors are seen to switch positions repeatedly as the fluid plug progresses through the channel. We found that after traveling five fluid-plug lengths the water appears homogeneous, apparently due to a combination of diffusion and circulation mixing. As depicted in Figure 2, this circulation effect can be explained by superimposing velocity profiles with continuity requirements. We include fluid-plug movement in our systems to exploit this effect when mixing is required. A more detailed mechanistic understanding of the observed hydrodynamics, scaling and dependence on fluid properties will be useful in future designs.

RELIABLE FLUIDIC MANIPULATION

We previously described polymeric structures for positioning, metering, and linking fluids that employ diaphragm valves and porous hydrophobic vents. We found these structures to be generally reliable for many reagent mixtures in molecular biology. Also, rounded channel cross sections have been found to produce more reliable fluid movement than square ones, particularly in the presence of surfactants.

Reagents with surfactants (such as Taq-Gold) can cause reversible blockage of the hydrophobic vents, apparently by creating a surface hydrophilic layer [**13**]. After such exposure the vents exhibit state-dependent behavior: they permit the free passage of gas in both directions only after gas has been forced through the membrane from the dry side. This vent-clearing step must be repeated after any subsequent contact with liquid.

Fluid positioning and linking structures with improved reliability were developed to take advantage of this behavior. For example, by terminating each chamber with a valve instead of a vent, and positioning liquids using a vent in a secondary common, evaporation has been reduced and reliability has been improved, Figure 3. This arrangement allows greater freedom in clearing the vent during fluid movement.

An improved fluid linking structure (the "T-Linker") is shown in Figure 4. The purge step (ii) provides the vent clearing necessary for reliable operation with surfactants. Hundreds of linking processes have been carried out sequentially using test solutions with as much as five times the normal amount of surfactant, with no failures.

TEMPERATURE-CONTROLLED REACTION CHAMBERS

Researchers have demonstrated that rapid thermal cycling can improve the performance of PCR reactions [**14**]. A system with two temperature zones using thermoelectric coolers was reported previously. Ideally, an integrated analytical system should be

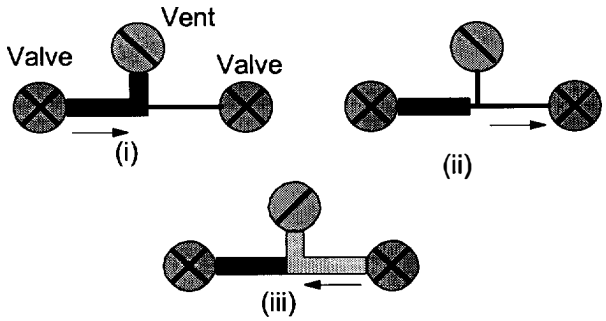

Figure 4. *Improved linking structure (T-linker) with improved reliability. Operation sequence is (i) load first reagent through left valve, (ii) purge vent through right valve, and (iii) load second reagent through right valve.*

scaleable to a number of independently controlled thermal zones that can be cycled rapidly. One thermal-control method with improved ramp rate and scaleability is shown in Figure 5. Arrays of resistive heating elements with sensors are sandwiched between the reactor cartridge and a thermal insulating layer. The insulating layer is in contact with a constant cooling source (e.g. a thermoelectric cooler).

The steady state heat loss Q through the thermal insulator is given by

$$Q = (k A / x) (T - T_{cooler})$$

where k and x are the thermal conductivity and thickness of the thermal insulator, A is the heater area, T is the heater temperature, and T_{cooler} is the surface temperature of the thermoelectric cooler. If we assume the thermal mass of the cartridge and reaction chamber contents are small, the time constant τ for cooling is given by

$$\tau = (x^2 C \rho) / k$$

where C and ρ are the heat capacity and density of the thermal insulator, respectively. These equations are graphed in Figure 7 along with experimental results, assuming the thermal insulator has the properties of phenolic resin from CRC handbook: k = 0.2 W / M K, C = 1.6 J / g K, ρ = 1.3 g / cm^2 , and data using the cooling time from 100°C to 50°C as t, while T_{cooler} = 0°C, without the used of fitting parameters [**15**]. Arrays of these thin-film elements have been fabricated and PCR reactions have been successfully performed using these structures. A cooling rate exceeding 10°C/sec after reaching steady state was demonstrated,

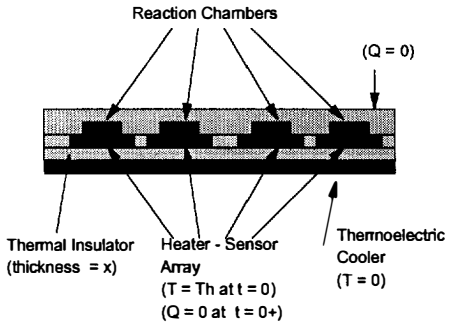

Figure 5*. Thermal element array for rapid temperature cycling. Cross section schematic showing thermal elements/sensors, thermal insulator, and cooler. Boundary conditions used in simple model are in parenthesis.*

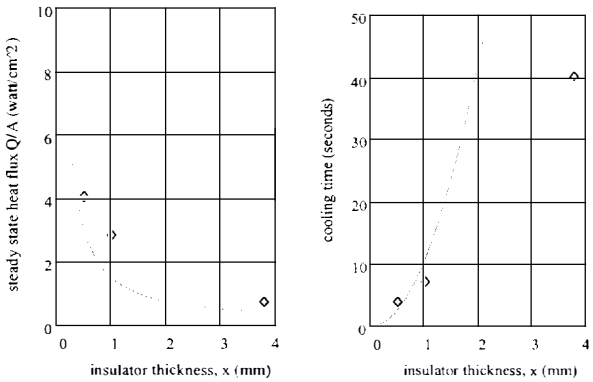

Figure 7. ***(a)*** *Steady state heat flux as a function of thermal insulator thickness: theory and experiment.* ***(b)*** *Transient cooling versus thermal insulator thickness: theory and experiment. (Cooling through the top of the structure may explain the faster than expected rate of the 4 mm insulator data.)*

significantly faster than other reports.

CYTOCHROME P450 SYSTEM

A multisample microfluidic system aimed at cytochrome P450 genotyping has been designed, fabricated, and demonstrated. The GeneChip CYP450 assay enables the rapid detection of mutations in enzymes related to drug metabolism [**16**]. This microfluidic system carries out a series of enzymatic reactions to prepare four separate samples for GeneChip hybridization. After isolating genomic DNA, a series of three enzymatic reactions are carried out: multiplex PCR, fragmentation and dephosphorylation (using nuclease and alkaline phosphatase), and fluorescent labeling using terminal transferase, Figure 6 [**17**].

The microfluidic cartridge carries out the steps shown within the dotted box in Figure 6. Four samples are prepared simultaneously in the design shown in Figure 8 for the P450 assay in a polycarbonate cartridge measuring 7 by 3.8 by 0.7 cm [**18**].

At the beginning of the procedure, the user loads the reagent cocktails for the fragmentation and labeling reactions into storage chambers, and loads the PCR reaction mixture into the reaction

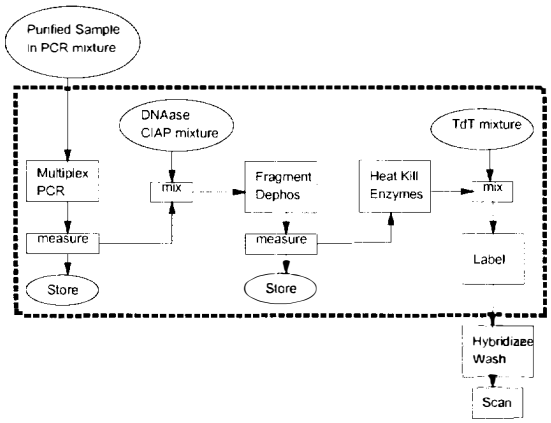

Figure 6. *GeneChip CYP450 assay for mutations in the cytochrome P450 genes. The steps within the dotted box are carried out by the microfluidic system.*

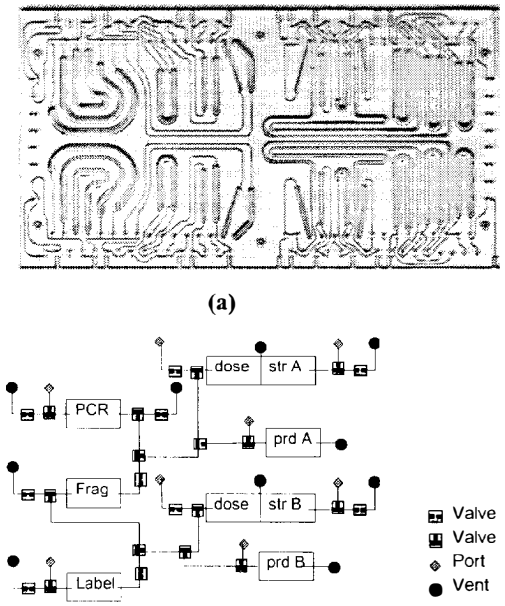

Figure 8. ***(a)*** *Image of 7 by 3.8 by 0.7 cm polycarbonate cartridge that prepares four independent samples simultaneously (two different designs) for a GeneChip-based cytochrome P450 assay. A series of three enzymatic reactions is carried out on each sample.* ***(b)*** *Schematic of one sample reaction pathway.*

chamber. PCR is carried out automatically, measured and mixed with the fragmentation cocktail mixture and the unused portion stored for quality control, Figure 6. After incubation in the fragmentation reaction chamber, the temperature is raised to inactivate the nuclease and alkaline phosphatase enzymes. This reaction product is measured and mixed with the labeling cocktail and the unused portion is stored for quality control. This mixture is transferred to the final reaction chamber and incubated. After the reaction is complete, the user removes the product and stored samples. Two different fluidic designs are incorporated in the cartridge; a schematic of one of these is shown in Figure 8.

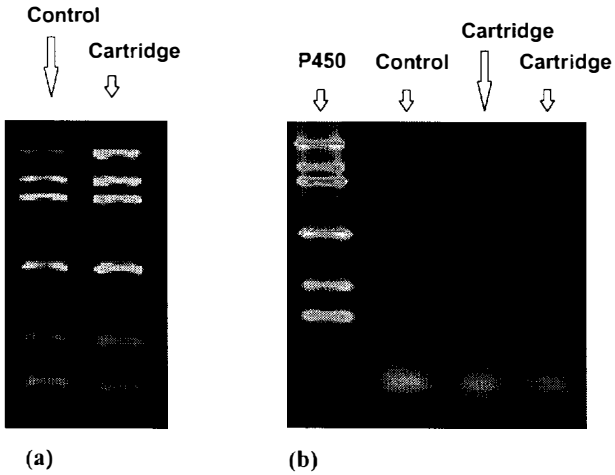

Figure 9. *Agarose gel images of product from reactions carried out in test cartridges compared with control reactions carried out on a bench top. (a) Cytochrome P450 multiplex PCR. (b) DNAase fragmentation.*

Fluidic operation of this design was verified first with water, then mock reagents containing the appropriate surfactants and salts, and finally with actual samples. Thermal performance was confirmed using arrays of thermocouples mounted within the reaction chambers **[19]**. Each of the CYP450-assay reactions were carried out in a test cartridge, Figure 9. Sequence analysis performed using hybridization to the GeneChip array was comparable to that found using the standard bench-top sample-preparation assay.

CONCLUSIONS

We have demonstrated several enhancements to the miniaturized genetic-analysis system reported previously, including structures for improved reliability in handling fluids and scaleable thermal control. Additional enzymatic reactions have been successfully demonstrated in the cartridge-based systems, including multiplex PCR for cytochrome P450, DNAase fragmentation, and a terminal deoxy-transferase reaction. We have also introduced a unique mixing phenomenon that can be generally exploited in microfluidic systems. Automated systems to perform other multistep biochemical and chemical processes could be developed using the devices and structures described in this work.

ACKNOWLEDGEMENTS

The advice and assistance of scientists at Affymetrix were invaluable in performing these experiments. The authors would like to particularly thank Tom Ryder, Clotilde Teiling, and Weiwei Liu for validating the CYP450 results. This work was supported by NIST cooperative agreement 70NANB5H031.

REFERENCES

1 A.T. Wooley, D. Hadley, P. Landre, A.J. deMello, R.A. Mathies. M.A. Northrup, "Functional Integration of PCR Amplification and Capillary Electrophoresis in a Microfabricated DNA Analysis Device," *Analytical Chemistry*, 1996 68(23):4081-4086.

2 D.J. Harrison and N. Chiem, "Immunoassay Systems on Chip," *Technical Digest of 1996 Solid-State Sensor and Actuator Workshop*, Hilton Head Island, South Carolina, (1996), p. 5.

3 P.C. Li , D.J. Harrison, "Transport, Manipulation, and Reaction of Biological Cells On-chip using Electrokinetic Effects," *Analytical Chemistry*, 1997, 69(8):1564-1568.

4 P. Andersson, P. Li, Y. Ning, D. Harrison, *Technical Digest of Transducers '97, International Conference on Solid-State Sensors and Actuators*, Chicago (1997), p. 1311-1314.

5 R.C. Anderson, G.J. Bogdan, Z. Barniv, T.D. Dawes, J. Winkler, K. Roy, "Microfluidic Biochemical Analysis System," *Technical Digest of Transducers '97, International Conference on Solid-State Sensors and Actuators*, Chicago (1997), p. 477-480, and

R. C. Anderson, G. J. Bogdan, and R. J. Lipshutz, "Miniaturized Genetic-Analysis System," *Technical Digest of 1996 Solid-State Sensor and Actuator Workshop*, Hilton Head Island, South Carolina, (1996), pp. 258-261.

6 GeneChip is a registered trademark of Affymetrix Inc.

7 M.J. Kozal, N. Shah, N. Shen, , R. Yang, R. Fucini, T. Merigan, D. Richman, D. Morris, E. Hubbell, M.S. Chee, T.G. Gingeras, *Nature Medicine*, 1996, 2:7:753-759.

8 D.J. Lockhart, H. Dong, M.C. Byrne, M.T. Follettie, M.V. Gallo, M.S. Chee, M. Mittmann, C. Wang, M. Kobayashi, H. Horton, E.L. Brown, *Nature Biotechnology*, 14:13:1675-1680, December 1996.

9 M.T. Cronin, R.V. Ficini, S.M. Kim, R.S. Masino, R.M. Wespi, C.G. Miyada, *Human Mutation*, 1966, 7:244-255.

10 J.G. Hacia, L.C. Brody, M.S. Chee, S.P.A. Fodor, and F.S. Collins, *Nature Genetics*, 14:441-447, December 14, 1996.

11 U.D. Larsen, J. Branebjerg, G. Blenkenstein, "Fast Mixing by Parallel Multilayer Lamination," *Proceedings of the 2nd International Symposium on Miniaturized Total Analysis Systems μTAS96, Basel* (1996) 228, and

R. Miyake, T.S.J. Lammerink, M. Elwenspoek, J.H.J. Fluitman, "Micro Mixer with Fast Diffusion," *MEMS 1993*, 143.

12 Water dyed with food coloring was moved through 0.7 by 0.7 mm channels in polycarbonate. This effect was also observed when moving the same fluid through 1.6 mm id tubing.

13 Taq-gold from Perkin Elmer contains 0.5 w/% Tween20. For example, when a Durapel (Millipore) membrane is placed in contact with a 0.5 w/% Tween20 solution for 3 seconds, the originally hydrophobic surface becomes hydrophillic.

14 C.T. Wittwer, D.J. Garling, "Rapid Cycle DNA Amplification: Time and Temperature Optimization," *BioTechniques*, vol. 10, 1:76-83, 1991.

15 Cooling through the top of the structure may explain the faster than expected rate of the 4 mm insulator data.

16 C. Sachse, et al. "Cytochrome P450 2D6 variants in a Caucasian Population: Allele Frequencies and Phenotypic Consequences," Am J Hum Genet 60: 284-295, 1997.

17 Some details and modifications are described below. A full description of the reaction protocols are described in the Affymetrix product brochure "GeneChip® CYP450 Assay"

PCR Reaction 15 ul mixture includes 2 units of TaqGold polymerase and 2.5 mM $MgCl_2$. Thermal program includes: (1) an initial denature at 95°C for 5 minutes, (2) a denature at 95.5 °C for 20 seconds, (3) an anneal at 64°C for 20 seconds, (4) an extend at 72°C for 60 seconds, (5) steps 2 through 4 repeated 35 times total.

Fragmentation Reaction 15 ul mixture includes 0.6 units DNAase, 1.5 units CIAP, and 1ug DNA. Thermal program consists of 20 minute incubation at 25°C followed by 10 minute termination at 95°C.

Labeling Reaction 20 ul mixture includes 10 units terminal transferase, 1X TdTase buffer and 25 uM FITC-ddATP.

18 Channels are 250 um deep with a 125 um radius and chambers are 0.7 mm deep with a 0.6 mm radius. Reaction chambers have 20 ul volume.

19 It was necessary to use thermocouples with 50 um diameter wires to minimize conductive heat loss along these wires.

DISPOSABLE MICRODEVICES FOR DNA ANALYSIS AND CELL SORTING

Hou-pu Chou, Charles Spence, Anne Fu, Axel Scherer and Stephen Quake*
Dept of Applied Physics, California Institute of Technology
Pasadena, CA 91125

ABSTRACT

We have developed microfabricated devices to size and sort microscopic objects, based on measurement of fluorescent properties. With these devices, we have demonstrated sizing and sorting on various biological entities, ranging from *E. Coli* cells to single molecules of DNA. The microfabricated devices have several advantages over macroscopic systems, including size, cost and sensitivity. For example, the detection volume for our devices is 375 femtoliters, more than an order of magnitude smaller than what has been achieved with flow cytometry.

INTRODUCTION

Traditionally, biologists have measured the size of molecules indirectly - they first measure mobility with gel electrophoresis, and then infer the size from the mobility. This method is powerful, yet has some drawbacks. For medium to large DNA molecules the resolution is limited to approximately 10%. Gel electrophoresis is time consuming; it generally takes at least an hour to run the gel, not including the set up time to cast the gel. Furthermore, for large molecules the procedure fails. This has been alleviated to some extent by the development of pulsed field gel electrophoresis, but running times can be days.

With the development of high affinity intercalating DNA stains, it has become possible to directly measure the length of single molecules by quantitating fluorescence. This in principle allows the measurement of extremely long DNA molecules; in fact, the longer the molecule, the better the signal. Other groups have used this technique with traditional methods in flow cytometry to measure length distributions of DNA molecules.[1][2]

We have developed microfabricated devices to size and sort microscopic objects based on their fluorescent properties. The devices are fabricated out of silicone elastomer, using a replica method. Negative master devices are fabricated from silicon wafers using standard processing techniques. Liquid elastomer is poured on the wafer and cured in an oven. The resulting device can be peeled off of the wafer and will bond hermetically to glass. This is a simple and cheap process, allowing the devices to be disposable while the master wafers are recycled indefinitely. This fabrication technique was first suggested by Austin's group at Princeton [3], building on work by the Whitesides group at Harvard. [4]

Previously, we have shown that these devices could be used to size a homogenous solution of 48kbp DNA with 10% resolution.[5] We have now extended those results to demonstrate sizing of DNA molecules ranging in length from 2kbp to 200kbp with a typical resolution of 10%. The DNA is fluorescently stained with the dye YOYO-1, at a stoichiometry of one dye molecule per 7.5 base pairs. The fluorescent signal is imaged onto an avalanche photodiode detector with a high numerical aperture objective. The signal is strong enough that photon counting detection is not required, an advantage over traditional flow cytometric measurements.

By designing a junction in the channel, molecules and cells can be sorted. After measuring the length of the molecule, a servo can decide to "keep" or "discard" the cell. We have demonstrated sorting of fluorescent beads and *E. Coli* cells in our devices. Manipulation was accomplished with electro-osmotic flow. Electrodes were inserted at the ends of the three channels, and a potential of up to 60V was used to manipulate the cells and beads. We were able to move cells at speeds of 100 microns/sec, and have demonstrated switching times of ~75 milliseconds.

DEVICE FABRICATION AND MOUNTING

Negative master devices were fabricated in silicon, and used as molds for the silicone elastomer. Standard contact photolithography techniques were used to pattern the oxide surface of a silicon wafer, which was then etched by reactive ion etch with a C_2F_6/CHF_3 gas mixture. A 3 minute O_2 RIE was used to remove carbon residue on the silicon surface. The oxide was then used as a mask for the silicon underneath, which was etched with KOH. The silicone elastomer (General Electric RTV 615) components were mixed together, and pumped in an evacuated chamber for 30 minutes to remove dissolved oxygen. The liquid elastomer was then poured on the mold (spin coating was used in cases where the device thickneess needed to be well controlled) and cured in an oven at 95 degrees for two hours. After this, the devices could be peeled from the silicon master and would bond hermetically to glass.

The devices were patterned as shown in figure 1. The large channels had lateral dimensions of 100 microns, which narrowed down to 5 microns at the T junction. The depth of the channels ranged from 2.5 to 20 microns. In early prototypes, we found that due to the large aspect ratio (100 microns in width by 2 microns in depth), some of the elastomer channels would bow and and block themselves by sealing directly to the glass. This was remedied in later versions by adding support pillars to the mask that would prop up the large channels and prevent bowing (see figure 1).

The elastomer is naturally hydrophobic, preventing aqueous solution from entering the channels. We modified the surface of the devices by soaking it in dilute HCl (0.02% in water) for 40 minutes at 43 C. After this treatment, the devices were hydrophilic and aqueous solution would easily enter by capillary

0-9640024-2-6/hh1998/$20©1998TRF
DOI 10.31438/trf.hh1998.3

Solid-State Sensors, Actuators, and Microsystems Workshop
Hilton Head Island, South Carolina, June 8-11, 1998

action. The devices could be cleaned and reused several times if desired.

Devices were mounted in one of two ways. For the DNA sizing devices, sample wells were created during the fabrication process by gluing small aluminum cylinders to the silicon wafer molds. The final RTV devices were attached to a cover slip in such a way that the sample wells were only partially covered. This allowed access with a pipette tip for introduction of the sample. The flow rate was determined by capillary action within the channels.

For the cell sorting devices, an inverted method was used. Holes were cut in the devices with a razor blade at the input and output portions, forming sample wells. The device was placed on a cover slip or microscope slide, and used in an inverted microscope. Then the aqueous samples were introduced via capillary action, and controlled with electro-osmotic forces. Tin plated copper electrodes were inserted into sample wells for this purpose.

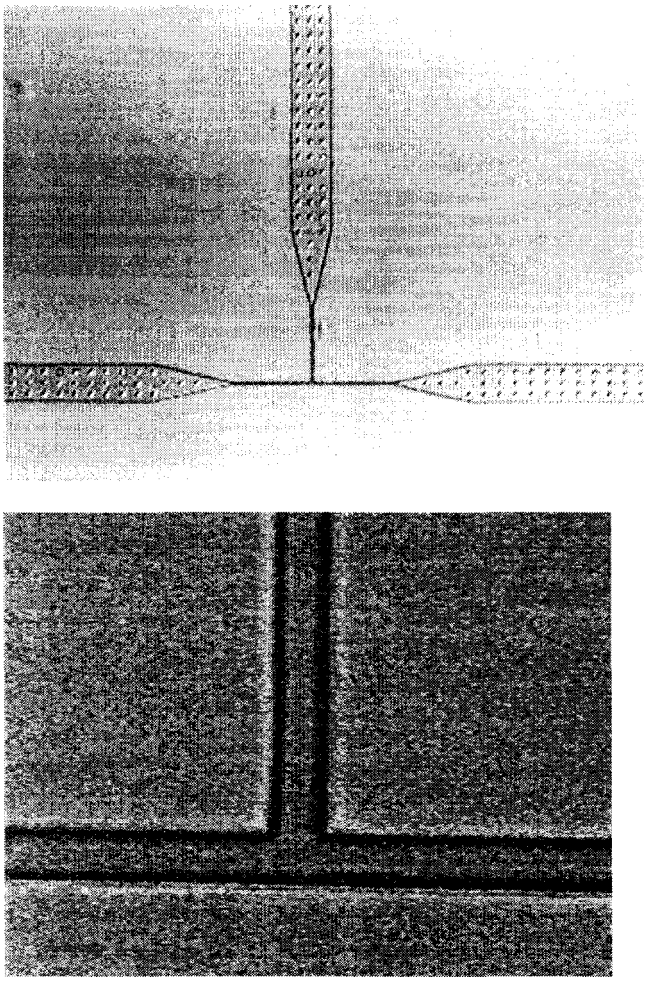

Figure 1. Top: Optical micrograph of an elastomer device. The large channels are 100 microns wide; the channels narrow down to a width of 5 microns at the T-junction. The depth of the channels is 3 microns. The large channels extend approximately 1 cm in length (not shown) for making macroscopic fluidic contacts. Bottom: Higher magnification image of the T-junction. The channels here are 5 microns wide. Note the high fidelity of the replica fabrication process for the straight lines and corners of the channels.

EXPERIMENTAL SETUP

For the DNA sorting devices, an upright optical microscope (Olympus) was used. A 3 mW air cooled argon ion laser (Uniphase) emitting at 488nm was used for fluorescent excitation. The laser was focused through a 60x 1.4NA oil immersion objective, which was also used to collect the emitted fluorescence. Auxiliary lenses were used to adjust the size of the focused spot to approximately 30 microns. The large spot size was chosen to give uniform excitation across the width of the channel. The quality and uniformity of the spot was evaluated by imaging a thin layer of fluorescein in solution with a CCD camera. The image was digitized and evaluated for symmetry and gaussian shape. Dielectric filters were used to filter laser tube fluorescence (CVI 488 nm line filter) and to reduce background and scattered light from the emitted fluorescence (Chroma D535/50M). A dichroic filter was used to introduce the laser light into the optical train (Chroma 500 DCLP).

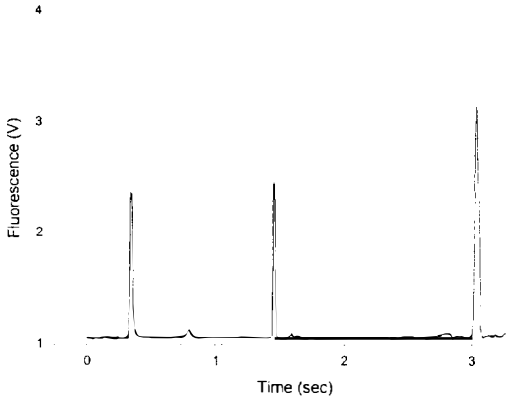

Figure 2: Pulses from single molecules of fluorescently stained DNA as they flow through the device.

Fluorescence was imaged onto a 5 mm avalanche photodiode detector (Advanced Photonics). The detector was cooled to -40 degrees with a two stage thermoelectric cooler (ITI 6320/157/040C), which reduced the dark current of the detector from 50 nA to 90 pA. The detector was biased at 2400 V, giving an estimated gain of 500-1000. The photocurrent was converted to a voltage by a Burr Brown OP128 ultra low noise op amp operating at a gain of 100 mV/nA. A second stage amplifier provided additional voltage gain of 10. The signal was low pass filtered at 1.6 kHz, and digitized at 5 kHz by a National Intruments Lab PC1200 board on a PC running Labview. Analysis of the noise level as a function of laser power indicates that the background fluctuations are shot noise limited.

The depth of focus of the microscope was checked by centering a 1 micron fluorescent bead in the laser beam. The detector output as a function of focal distance shows that the signal is essentially flat over a depth of 5 microns. This was then used to design the microfabricated devices; the depth was chosen so that the DNA molecules always remained in the plane of focus of the microscope.

Lambda phage DNA (Gibco) was either digested with HindIII or ligated, then was diluted in buffer (TE with 10 mM NaCl) and stained with the intercalating dye YOYO-1 (Molecular Probes) at a stoichiometry of approximately one dye molecule per 7.5 base pairs. Single molecules of DNA gave measurable pulses whose height corresponded to the length of the molecule. Pulses were collected in large batches and then analyzed off line with home written software for peak detection.

The total interaction region imaged on the detector is approximately 375 femtoliters, smaller than is achievable with standard methods of flow cytometry. This volume is largely determined by the size of the laser spot, and can be reduced further by the use of cylindrical optics.

The cell sorting devices were mounted on an inverted microscope (Zeiss). Electrodes were attached as described above, and a switching box was built to manipulate a potential of 60 Volts between the three channels. Each channel could be independently set for either 60 V, ground, or float. *E. Coli* cells expressing green fluorescent protein were introduced into the devices by capillary action and observed with fluorescence microscopy. Fluorescence was excited with a mercury lamp, and recorded on videotape with a CCD camera (Hamamatsu). The video images were later digitized and the position of the cells as a function of time was measured.

RESULTS

Data was taken from two heterogenous solutions of DNA. In the first, a λ/HindIII digest, fragments of length 2kbp-23kbp were identified. The typical resolution was 10% per molecule. A histogram of the peak heights is shown in figure 3. By locating the center of the peaks in the histogram, the cumulative precision is higher. 977 molecules were analyzed. The smallest resolved molecule is on the order of of 2 kilobase pairs. This is not an intrinsic limit of the method, and we believe that with further improvements to the electronics and analysis we can improve the sensitivity to 1 kilobase pair. We intend to continue improving the fluidic portion of the device to increase the throughput.

It is worth pointing out the extremely small amount of material used for such an analysis. A total of 977 molecules were analyzed, i.e. on the order of a zeptomole. The analysis was performed in a total reagent volume of tens of nanoliters. Again, these are not intrinsic limits of the system and we believe that with further improvements, the reaction volumes can be reduced substantially.

The second DNA sample we analyzed was a λ ladder; peaks ranging from 50kbp to 200kbp were identified. 1761 molecules were identified in 25 minutes of running time. The resolution per molecule is about 5%. There is a clear trend over the data sets showing improving resolution with increasing molecule length. This particular length range of DNA molecules is impossible to separate with ordinary gel electrophoresis; one must resort to pulsed field gels.

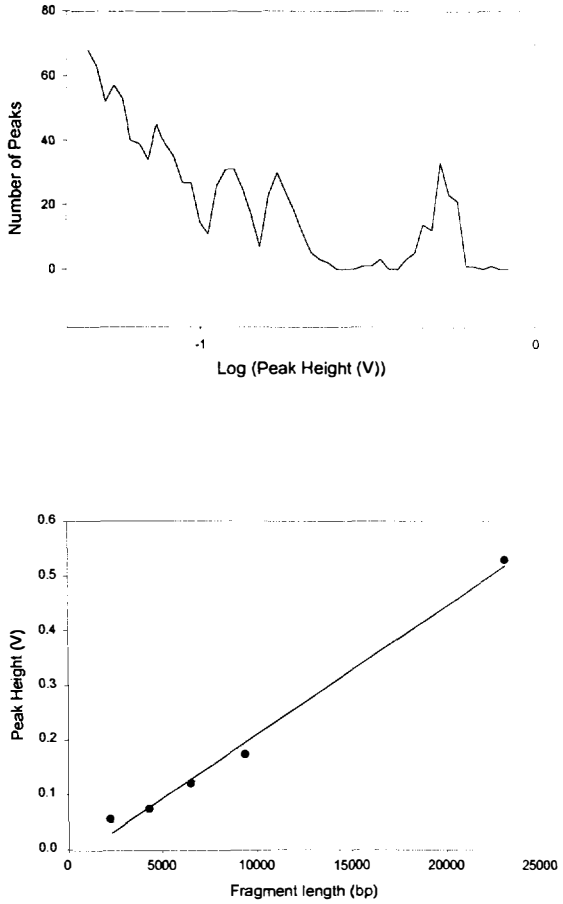

Figure 3: Top: A histogram of pulse heights from the λ/HindIII digest. The heights were measured by taking the maximum value of the peaks; no fitting was done. Fragments of length 2kbp, 4kbp, 6 kbp, 9kbp and 23 kbp were identified. Bottom: The sizes of the fragments are known independently of this measurement, and can be used to test the precision of the method. The peak height versus length is plotted, showing good linear agreement.

We have also demonstrated the principle of cell sorting with electro-osmotic manipulation in our devices. *E. Coli* cells were manipulated with electric fields, and switched between one of two possible output channels. A graph of the position versus time of a single *E. Coli* cell as the field is repeatedly reversed is shown in figure 5. The estimated switching time is 50-100 milliseconds, leading to a maximum cell sorting rate of 10-20 Hz. We believe with higher potentials and some device design improvements, we could reach a single channel switching time of 1 millisecond. Then with 100 channels switching in parallel, the overall throughput of the device would be 100 kHz.

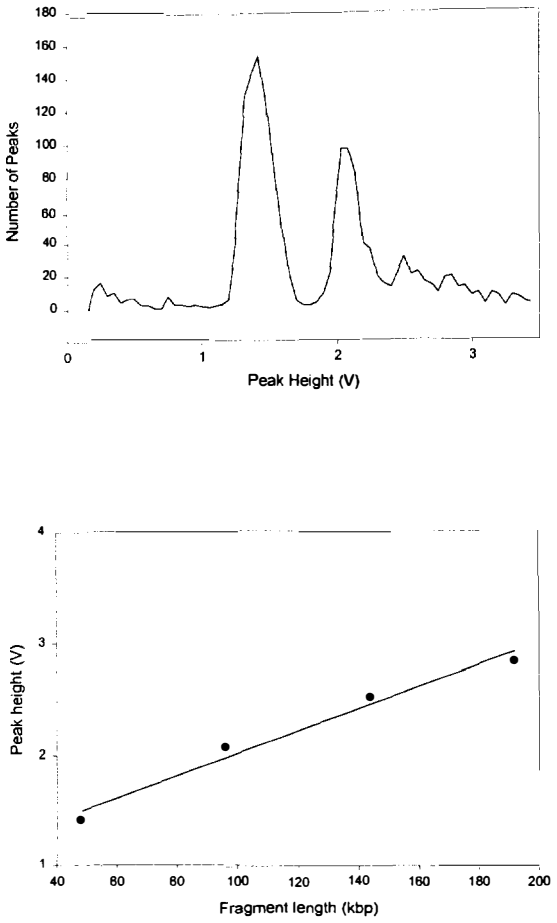

Figure 4: Top: A histogram of pulse heights from the λ ladder. The first through third multimers can clearly be seen, while the fourth multimer is barely resolved. Bottom: Graph of known fragment length versus peak position.

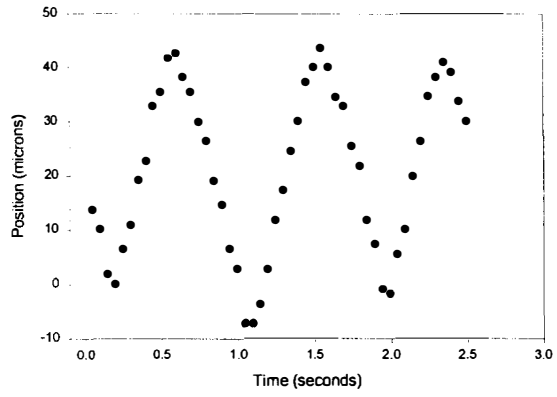

Figure 5: E Coli position versus time as a 60V potential is repeatedly reversed.

One concern is whether the high electric fields in the device would damage or kill the bacteria. To test this, we drove bacteria through the devices and collected them at the output port with a micropipette. The bacteria were then grown up an agar plates, showing that they could indeed survive the sorting process.

CONCLUSION

We have successfully demonstrated DNA sizing and cell sorting in microfabricated devices. With further improvements, we believe that this method will be competitive with the current state of the art in gel electrophoresis, and will find specialized applications in cell sorting, such as lab on a chip. These devices are extremely easy to fabricate from a silicon master, reducing production costs and rendering the devices truly disposable. This is advantageous for cell sorting applications in which contamination is a concern.

There are numerous possible applications for such technology. We anticipate that the DNA analytical system will be used for many routine biological assays, due to its speed and low material requirement. One possible application is DNA fingerprinting. A portable system could be brought to the scene of a crime for direct analysis on small blood samples. Since the system does not require PCR, the chance of false signals is reduced. Furthermore, the chance of laboratory error due to contamination and handling will be reduced.

We envision both technologies demonstrated in this paper as stepping stones to building gene cloning "lab on a chip" devices. Small amounts of DNA can be recovered from restriction and ligation reactions, and separated according to size. Performing transfection on the chip allows very small (nanoliter) reaction volumes, so only small amounts of DNA are necessary. The properly transfected cells can then be separated via fluorescent or colorimetric assays in the cell sorting device. Single cells can then be grown into macroscopic amounts necessary for clone libraries, etc.

REFERENCES

[1] A. Castro, F.R. Fairfield and E.B. Schera, *Anal. Chem.* **65**, 849 (1993).
[2] Z Huang *et al*, *Nucleic Acids Res.* **24**, 4202 (1996).
[3] R.H. Carlson *et al*, *Phys. Rev. Lett.* **79**, 2149 (1997).
[4] R.J. Jackson, J.L. Wilbur and G.M. Whitesides, *Science* **269**, 664 (1995).
[5] H.P. Chou, C. Spence, A. Scherer and S. Quake, to appear in *Proceedings of the SPIE* (1998).

* To whom correspondence should be addressed. Email quake@cco.caltech.edu, fax (626) 793 8675

ACKNOWLEDGEMENTS

We thank Frances Arnold for the generous loan of equipment used in the cell sorting device.

AN ACTIVE THREE-DIMENSIONAL MICROELECTRODE ARRAY FOR INTRACORTICAL RECORDING

Qing Bai, Marcus D. Gingerich, and Kensall D. Wise
Center for Integrated Sensors and Circuits
Department of Electrical Engineering and Computer Science
The University of Michigan, Ann Arbor, MI 48109-2122

ABSTRACT

This paper reports a three-dimensional (3D) microelectrode array with on-chip circuitry for use in the central nervous system (CNS). The active 3D array is created by microassembling 2D active probes and uses right-angle gold beams as lead transfers between the probes and a mounting platform. In order to improve fabrication yields and ensure successful 3D microassemblies, new bulk micromachining and encapsulation techniques have been developed to protect the on-chip circuitry from the probe release etch and from the body electrolytes. Since an external clock must be used in active 3D arrays to synchronize the readouts from several multiplexed probes, clock suppression to 10ppm or better must be obtained in order to resolve 50μV neural signals. The CMOS probes reported here achieve this performance and have successfully recorded single-unit neural activity *in vivo*.

INTRODUCTION

Improved understanding of the central nervous system and the successful realization of auditory and visual prostheses to aid the handicapped are important goals for the neurosciences, but progress in both of these areas depends strongly on the development of improved microelectrode arrays for electrical recording and stimulation at the cellular level. Various micromachining technologies [1-5] have been developed over the years to create one-, two- and three-dimensional passive arrays for acute and chronic use. Multichannel 2D active probes (containing on-chip electronics) have also been reported for recording [6,7] and stimulation [8,9] in the CNS. However, there is a continuing need to develop still higher-performance arrays suitable for accessing large neuronal populations in 3D volumes of tissue using very few external leads. Such active 3D arrays can be realized by assembling 2D probes using a high-yield process reported recently [10].

The fabrication of active probes requires that a CMOS IC process be merged with the boron-etch-stop process used to define the probe shanks and electrode sites while encapsulating the entire structure to shield it from the probe release etch and from body electrolytes. Although a fabrication process for 2D active probes has been reported [7, 11], further improvements were needed to achieve high yield and meet the challenges of the 3D structure. New bulk micromachining and encapsulation techniques have been developed to ensure full compatibility between the probe structure and on-chip circuitry.

With a growing demand for multi-site recording arrays and large 3D structures, it is becoming critically important to develop active probes so that multiplexing can be used to reduce external lead counts and electronically select sites that are close to active neurons. Active 3D multiprobe arrays also require that an external clock be supplied to all probes in the array to permit synchronization among the various outputs. Because the neural signals of interest extend down to amplitudes well under 50μV, the potential noise problems associated with multiplexing such low-level signal channels pose a significant challenge, both in designing the on-chip circuitry as well as in the external demultiplexing system. This paper demonstrates bulk-micromachined CMOS active probes with externally-clocked multiplexing that maintain low noise performance and achieve high yield.

FABRICATION OF ACTIVE 3D PROBES

CMOS active probes are fabricated using a combination of the deep boron etch-stop technology used to fabricate passive probes and a 3-μm p-well CMOS process. The process has 16 masking steps and consists of three main phases: 1) definition of the probe substrate, including deep and shallow boron diffusions; 2) a self-contained CMOS process sequence; and 3) formation of the iridium electrode sites and gold bonding pads, circuit encapsulation, and release of the probe from the host substrate. Although most of this process had been successfully developed previously, providing adequate encapsulation for the on-chip circuitry and achieving high yield during the probe release etch remained important issues as this work began.

Figure 1 shows the structure of an active probe for use in a 3D microassembly. The probe substrate has mounting "wings" containing slots for alignment spacers that hold the probes parallel and orthogonal to the mounting platform; electroplated gold beams form lead transfers between the probes and this platform. The probe release etch is more challenging for 3D active probes than for 2D probes because there is no etch-stop below the circuit area and the lightly doped silicon there must be retained while the probe shanks and wings are thinned to the 15μm-deep etch-stop layer. This need to preserve silicon in

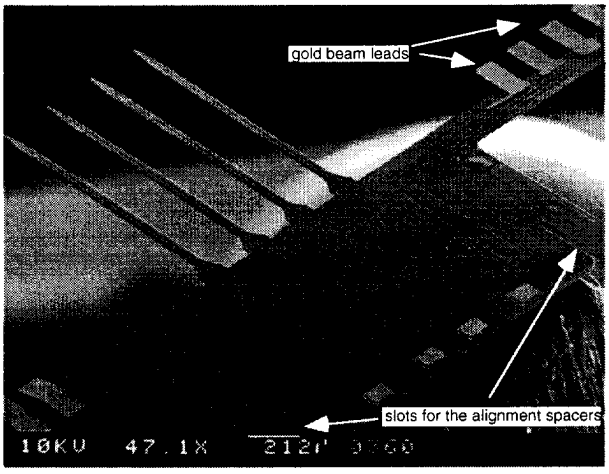

Figure 1: SEM of an active probe that has gold-plated beams for orthogonal lead transfers and slots for the alignment spacers associated with 3D microassembly.

0-9640024-2-6/hh1998/$20©1998TRF
DOI 10.31438/trf.hh1998.4

Solid-State Sensors, Actuators, and Microsystems Workshop
Hilton Head Island, South Carolina, June 8-11, 1998

some areas while removing it in others has made it difficult to maintain a sufficiently broad process window to ensure high yield in the past. However, satisfactory margins have now been achieved using deep RIE and dielectric corner compensation as shown in Fig. 2.

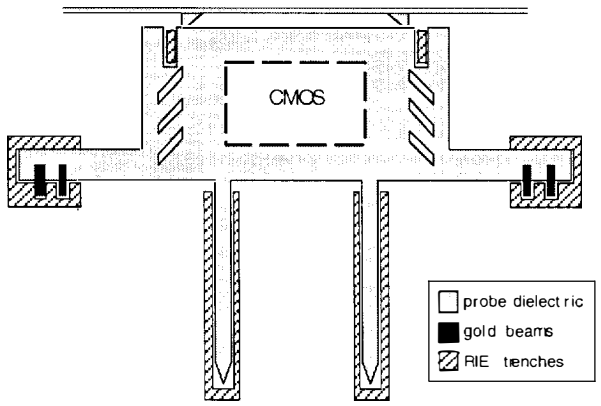

Figure 2: Diagram of an active probe that has deep RIE etched trenches around the wings and shanks to facilitate early release of those areas and corner compensation dielectric bridges to protect rear circuit area from corner undercutting during EDP.

Corner undercutting has sometimes been an important source of yield loss in active probe fabrication in spite of leaving a wide boron-doped silicon rim around the active areas. This can occur when crystallographic planes such as the {331} are accessible to the front-side etch at outside (convex) pattern corners as shown in Fig. 3, where an unprotected corner was attacked by EDP to undercut the masking oxide. A simple way to avoid this problem is to include dielectric masking bridges at such corners (Figs. 2 and 3), preventing the {331} planes from being exposed. These corner compensation bridges provide protection until either the {111} planes meet to undercut the bridges from the front or the front- and back-side etch planes meet each other, allowing attack of the circuit areas from below. The corner-compensation dielectric bridges break off when the probes are released from the wafer.

The mounting wings and probe shanks must be thinned to their etch-stop thickness to ensure high dimensional precision. This needs to occur from the front since the back etch would result in very thin silicon under the circuit areas and an inadequate process window. Normally, since the shanks are aligned with the <110> directions and are only slightly tapered, any undercut from the front must work backward from the shank tips and convex corners. This process is slow and can allow the circuit areas to be attacked from the back, destroying the circuitry. To increase the process etch window, deep-etched trenches can be formed around the wings and shanks so that the front undercut etch proceeds laterally in the <110> directions, as illustrated in Fig. 4. For 50µm-wide probe shanks, 70µm-deep slots have been etched around the probes using deep RIE, facilitating their release from the front. This leaves a thick silicon layer under the circuitry, ensuring a wide process window.

Encapsulation of the active probes is another important processing issue. Stress-compensated LPCVD oxide and nitride layers are used under the electrode interconnects, while LTO and PECVD nitride form the top passivation layers. A polymer film may be used to offer additional protection against the biological environment. In order to prevent junction spiking and aluminum hillocking during deposition of the top dielectrics, 100nm-thick titanium plugs are used with multiple titanium/aluminum layers for circuit metalization. This fabrication process has resulted in a high yield of 2D and 3D active probes. Figure 5 shows optical and SEM views of completed active 3D arrays.

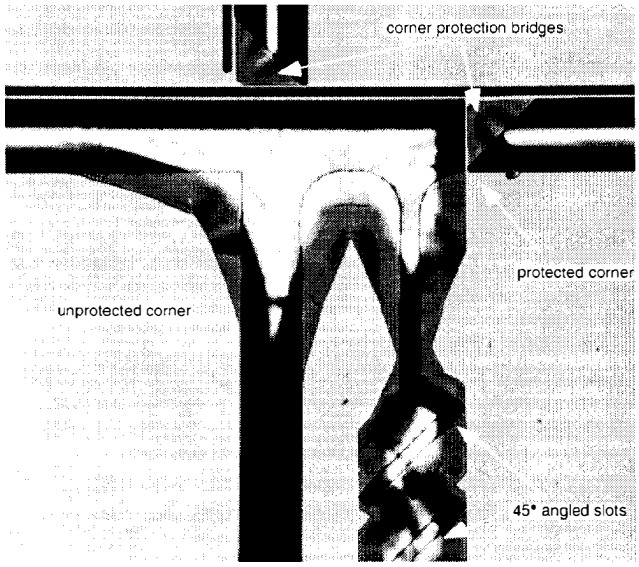

Figure 3: A testing device structure with dielectric mask after 40 min. EDP etch. It shows that circuit areas can be well-protected from corner undercutting in EDP by using corner compensation dielectric bridges. The 45° angled slot openings also help to clear the wing area for the alignment spacers.

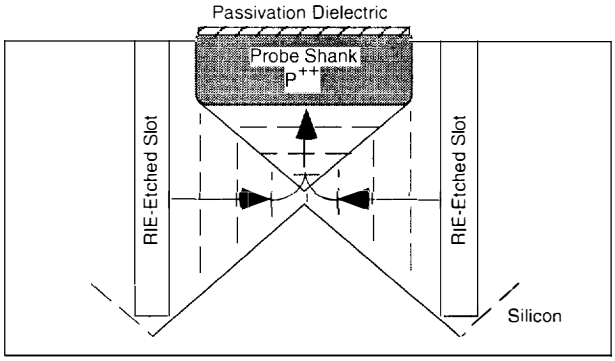

Figure 4: Cross-section of a probe shank with slots along its sides. These slots allow lateral etching to undercut the shank from the front in EDP, well before the etch front from the backside of the wafer reaches them. Thus, thick silicon can be preserved over the circuit area while the shanks and wings are released from the front.

EXPERIMENTAL RESULTS

Several active probes have been developed to test different amplifier/multiplexer designs and shielding concepts. The probes contain four shanks with multiple sites per shank and outputs that are buffered, unbuffered, multiplexed, or nonmultiplexed. The on-chip signal processing circuits on

these probes reduce the output impedance levels, provide signal amplification, and multiplex the recorded signals to reduce the number of required external leads. However, this circuitry can also add noise to the recording channels. The measured noise from the input devices in this circuitry is typically less than 15 μV-rms over the frequency range of interest (100Hz-10kHz). This is less than the thermal noise from a typical recording site and does not degrade the overall signal-to-noise ratio (SNR). Recent experiments using one of the buffered probes have shown this. On this probe, a passive site was located adjacent to every buffered/active one, with a site-separation of 24μm center-to-center and a site area of 81μm^2. The voltage buffer in this case was a simple source follower with an output impedance of 3kΩ and a gain factor between 0.85 to 0.9. Figure 6 shows *in vivo* recordings obtained using this probe. The on-chip buffers clearly do not degrade the overall noise performance of the recording system.

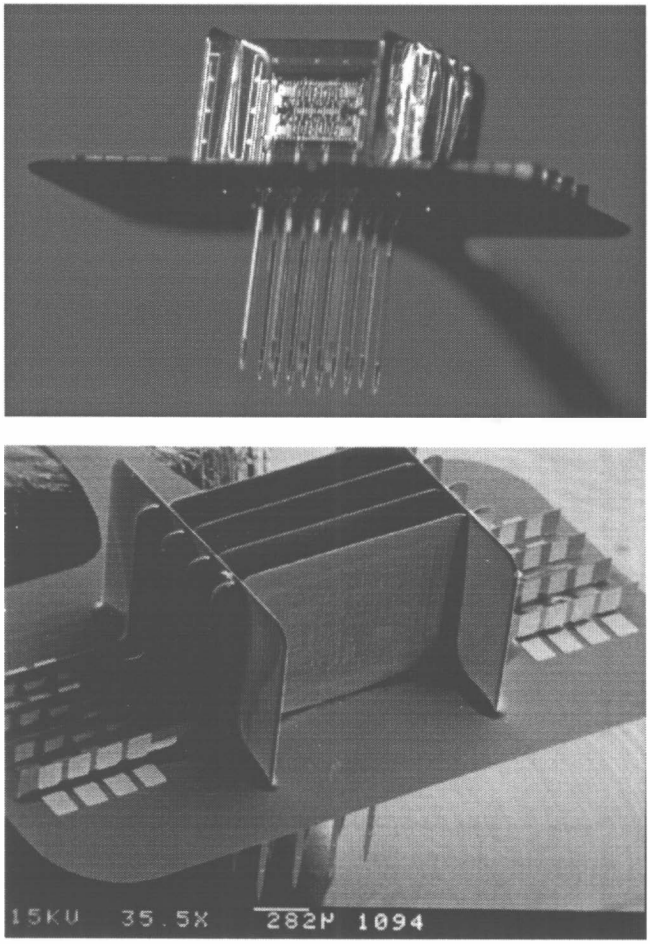

Figure 5: Optical (top) and SEM (bottom) views of the completed active 3D microelectrode arrays.

In multi-probe 3D arrays, an off-chip clock is required to allow synchronization of the different probe outputs. However, this poses a potential noise problem and requires suppression of the 5V clock signal to 10ppm or better. Achieving this performance, in turn, requires an understanding of all possible coupling mechanisms, both between leads and on the chip itself. Figure 7 shows the system diagram for one simple multiplexed probe and its external demultiplexing circuitry. This probe, the simplest design of four multiplexed probes that have been developed, consists of voltage buffers, a two-bit counter, and CMOS switches. The probe was carefully laid out to minimize noise coupling. The external demultiplexing system contains three stages: a first amplification stage, a demultiplexing stage, and a second amplification/filtering stage. A 200kHz non-symmetrical (20% duty cycle) clock is used with a 2μs delay and a 2μs sampling duration to avoid switching noise. The demultiplexing system itself has a total gain of 5000 and an equivalent input noise of less than 5μV. Neural signals recorded with one of these probes are shown in Fig. 8. The noise level of the recovered demultiplexed signals is low but still higher than that of the same nonmultiplexed (clock-off) signals (about 40μV compared with 20μV, respectively). The main source of this clock noise is coupling between the external clock lead and the multiplexed 10kΩ data-output line. For closed-loop buffer designs having output impedances of 1kΩ or less, the clock noise is expected to be significantly reduced (<15μV). Coupling on the probe substrate itself is very small since the substrate forms a ground plane below the interconnect lines and the extracellular fluid forms a ground plane above them in most recording situations.

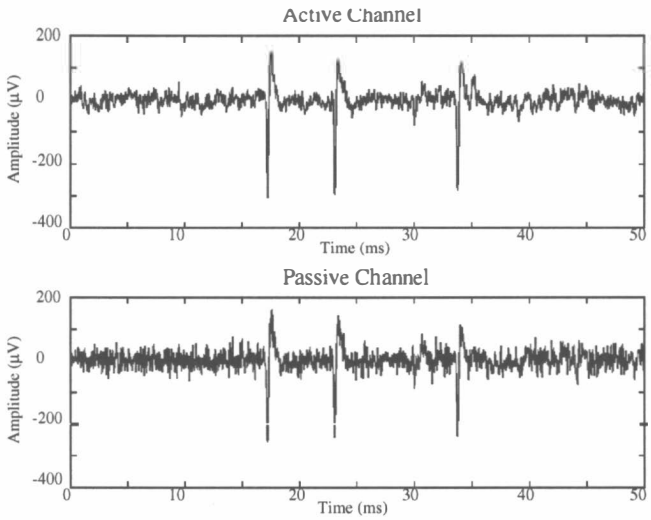

Figure 6: Spontaneous neural activity recorded through a buffered/active channel (above) and an unbuffered/passive channel (below), which are only 24μm apart.

CONCLUSIONS

An active 3D microelectrode recording array has been fabricated and tested. It was created by microassembling 2D active silicon probes using a right-angle beam-lead-transfer technique. A process that combines deep RIE and dielectric corner compensation has been developed to protect the on-chip circuitry from undercutting during the probe-release etch. Single-unit neural responses have been successfully recorded *in vivo* using these probes with an off-chip demultiplexing system, Even the simplest of these probes has exhibited clock suppression to better than 10ppm, and probes having output resistances less than 1kΩ are expected to show noise levels well below the thermal noise floor of the recording sites themselves. The test results with these active probes are forming the basis for a much larger 1024-site 3D array now in development.

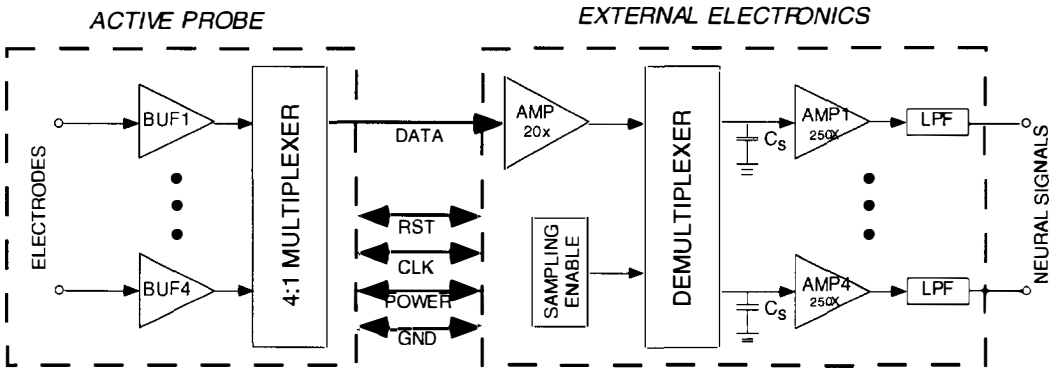

Figure 7: Block diagram of the overall on-chip multiplexing and off-chip demultiplexing system.

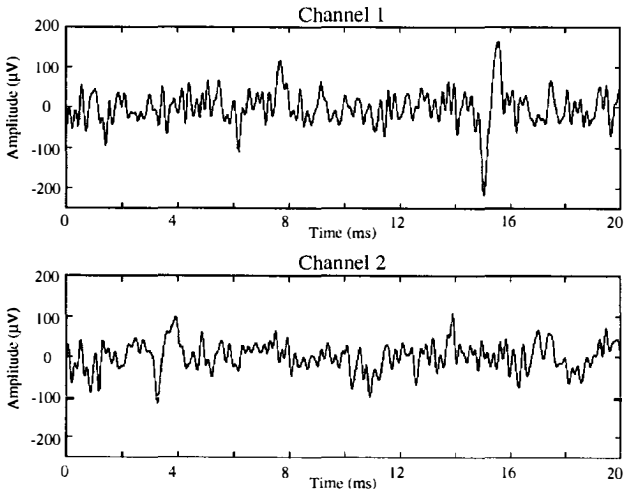

Figure 8:) Simultaneous neural signals recorded in guinea pig auditory cortex by the multiplexer-demultiplexer active probe system. The responses are driven by white noise bursts, and the two channels are 200μm apart.

ACKNOWLEDGMENTS

The authors would like to thank Drs. F. T. Hambrecht and W. Heetderks of the Neural Prosthesis Program, National Institute of Neurological Disorders and Stroke, for their encouragement and support of this work. The assistance of Mr. J. Wiler and Mrs. J. Hetke in the animal testing were also very much appreciated.

REFERENCES

1. K. Najafi, K. D. Wise, and T. Mochizuki, "A High-Yield IC-Compatible Multichannel Recording Array," *IEEE Trans. Electron Devices*, *32*, pp. 1206-1211, July 1985.

2. J. F. Hetke, J. L. Lund, K. Najafi, K. D. Wise, and D. J. Anderson, "Silicon Ribbon Cables for Chronically-Implantable Microelectrode Arrays," *IEEE Trans. Biomed. Engr.*, *41*, pp. 314-321, April 1994.

3. A. C. Hoogerwerf and K. D. Wise, "A Three-Dimensional Microelectrode Array for Chronic Neural Recording," *IEEE Trans. Biomed. Engr.*, *41*, pp. 1136-1146, December 1994.

4. P. K. Campbell, K. E. Jones, R. J. Huber, K. W. Horch, and R. A. Normann, "A Silicon-Based Three-Dimensional Neural Interface: Manufacturing Processes for an Intracortical Electrode Array," *IEEE Trans. Biomed. Engr.*, *38*, pp. 758-767, August 1991.

5. D. Kewley, M. Hills, D. Borkholder, I. Opris, N. Maluf, C. Storment, J. Bower, and G. Kovacs, "Plasma-Etched Neural Probes," *Sensors and Actuators A, 58*, pp. 27-35, 1997.

6. K. Najafi and K. D. Wise, "An Implantable Multielectrode Recording Array with On-Chip Signal Processing," *IEEE J. Solid-State Circuits*, *21*, pp. 1035-1044, December 1986.

7. J. Ji and K. D. Wise, "An Implantable CMOS Circuit Interface for Multiplexed Microelectrode Recording Arrays," *IEEE J. Solid-State Circuits*, *27*, pp. 433-443, March 1992.

8. S. J. Tanghe and K. D. Wise, "A 16-Channel CMOS Neural Stimulating Array," *IEEE Journal of Solid-State Circuits*, *27*, pp. 1819-1825, December 1992.

9. C. Kim and K. D. Wise, "A 64-Site Multishank CMOS Low-Profile Neural Stimulating Probe," *IEEE J. Solid-State Circuits*, *31*, pp. 1230-1238, September 1996.

10. Q. Bai and K. D. Wise, "A High-Yield Process for Three-Dimensional Microelectrode Arrays," *Digest Solid-State Sensor and Actuator Workshop*, Hilton Head, S.C., pp. 262-265, June 1996.

11. J. L. Lund and K. D. Wise, "Chip-Level Encapsulation of Implantable CMOS Microelectrode Arrays," *Digest Solid-State Sensor and Actuator Workshop*, Hilton Head, S.C., pp. 29-32, June 1994.

A MICRO FLUXGATE MAGNETIC SENSOR USING MICROMACHINED 3-DIMENSIONAL PLANAR COILS

Trifon M. Liakopoulos, Ming Xu and Chong H. Ahn

University of Cincinnati
Center for Microelectronic Sensors and MEMS (CMSM)
Department of Electrical and Computer Engineering and Computer Science
P.O. Box 210030, Cincinnati, OH 45221-0030, USA

ABSTRACT

A new micro fluxgate magnetic sensor using micromachined 3-dimensional solenoid coils has been designed, fabricated, and characterized in this work. The fluxgate sensor adopts a ring-type shape and second-harmonic principle, and is composed of exciting coils, a ring core, and sensing coils. Using a newly developed UV lithography-based thick photoresist process and electroplating techniques, planar three-dimensional magnetic fluxgate sensors were fabricated on a silicon wafer. The measured sensor output shows excellent linear characteristics over the range of ±500 μT with a resolution of approximately 60 nT, achieving the sensitivity of 8360 VT^{-1}. Furthermore, this sensor also shows a wide sensing range of ±1.5 mT. Using this highly sensitive, on-chip fluxgate sensor, various applications are expected from space research to portable navigation systems.

INTRODUCTION

A wide range of sensing applications requires the detection of magnetic field. Different magnetic sensors and techniques have been developed and are capable of measuring a wide range of DC magnetic fields from 10^{-10} to 10^{-3} T.

The fluxgate magnetic sensor [1] is known as one of the most sensitive magnetic sensors. In terms of the range and resolution, the fluxgate sensor stands higher than low sensitivity solid-state devices such as Hall effect and magnetostrictive magnetic sensors, and is comparable to ultrahigh sensitive but very expensive quantum-effect SQUIDs [2].

Since first developed in the 1930s and 1940s for submarine detection, the fluxgate sensors have been used for geophysical prospecting, airborne field mapping, and space applications [3]. They also can serve as orientation sensors for virtual reality applications or as ferromagnetic object detectors. Fluxgate compasses extensively have been part of aircraft and miniaturized ultra sensitive navigation systems.

Recently there has been a large demand for the realization of on-chip fluxgate magnetic sensors, with exciting and sensing control IC circuits. Fabrication of a micro-fluxgate sensor utilizing Si process technology is driven by advantages such as the small size, light weight, low cost, higher resolution and integration of the supporting electronic circuitry [4-7]. However, when the dimensions of the device decrease, the sensitivity and operation range can have some drawbacks. Some of these can be compensated by increasing the operational frequency, which requires more complex electronic circuits for its signal processing. Micromachined on-chip magnetic sensors can be an applicable solution to address the drawbacks.

In this work we present a micro-fluxgate sensor, with planar three-dimensional solenoid-type coils as excitation and sensing elements. A new planar, UV lithography-based thick photoresist process was developed for the fabrication of the planar solenoid coils [8]. The explored fluxgate sensor is a ring core/second harmonic-type sensor and has a size of 5 mm x 2.5 mm x 100 μm. The exciting and sensing elements are composed of magnetic cores and solenoid conductor coils, where electroplated Cu conductors are wound around the electroplated Ni/Fe permaloy core. An innovative micro fluxgate magnetic sensor with micromachined planar solenoid-type coils has been designed, fabricated and characterized in this work.

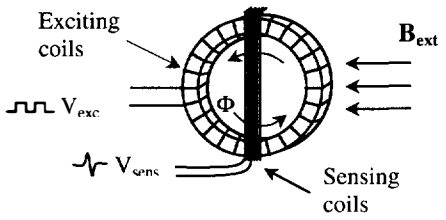

Figure 1. *Illustration of a ring core/second harmonic fluxgate magnetometer configuration.*

THEORY AND DEVICE DESIGN

One basic configuration of a fluxgate sensor consists of a magnetic ring core, an excitation coil wound around it, and at least one pickup coil. A schematic illustration of such configuration is shown in Figure 1. A square wave pulse current can be applied to the excitation coils to drive the ring core through its B-H curve. The amplitude of the excitation current is so adjusted that the excitation field oscillates periodically between the positive and negative saturation region. The sensing coils are wound around the whole body of the ring core. The output signal will be proportional to the change of the magnetic flux that flows through the face area of the sensing coils.

Faraday's law describes the induced output voltage at the sensing winding as

$$V_{emf} = -N A \mu_0 \mu_r \left(\frac{dH}{dt} \right), \qquad (1)$$

where V_{emf} is the induced electromotive force, N is the number of turns, A is the cross section area of the magnetic core, μ_0 and μ_r are the magnetic permeabilities of air and magnetic core respectively, and H is the magnetic filed.

If there is no external magnetic field, the closed path of the flux of the excitation field in the core results in zero net flux through the sensing winding. In this case, no output signal in the sensing winding is produced. Whereas, if the core is oscillating,

0-9640024-2-6/hh1998/$20©1998TRF
DOI 10.31438/trf.hh1998.5

Solid-State Sensors, Actuators, and Microsystems Workshop
Hilton Head Island, South Carolina, June 8-11, 1998

with the presence of an external magnetic field B_{ext}, from zero magnetization to saturation and backwards (i.e., twice each excitation period), the flux through the sensing winding changes from a maximum value to zero. The produced output signal will be proportional to the change of the magnetic field flux with time as it is indicated in Equation 1. Since this change is occurring four times for each excitation period, the output pulse has the double frequency with respect to the exciting input signal. Thus, these types of fluxgate sensors are called second harmonic fluxgate magnetometers. Since a square wave input signal produces an abrupt change on the magnetization of the core, a strong output signal can be generated at the sensing coils. Of course, the use of a triangular excitation wave is being adopted in several applications. In the triangular wave case, the output signal will be linearly depended on the excitation frequency, and therefore the sensor is usually driven at higher frequencies to get a high sensitivity.

Based on the configuration described above, we designed a ring-type second harmonic fluxgate sensor as shown in Figure 2. The sensor has a size of 5 mm x 2.5 mm x 100 μm, where the width of the conductors is 50 μm and the spacing between them is 30 μm. The excitation and pick-up windings are fabricated using electroplated copper. The excitation winding has 41 turns around the magnetic core. The pick up winding has 14 turns around both paths of the magnetic core. As shown in Figure 2(a), the wrapping of the excitation coil around the core is interrupted in the middle of the core, so the pick up coil can be placed in the center. We choose this simple configuration over some more complicated interleaved formation. With this configuration, the pick up winding is more "tight" wound around the core so we can minimize the external noise or coupling interference of the two windings.

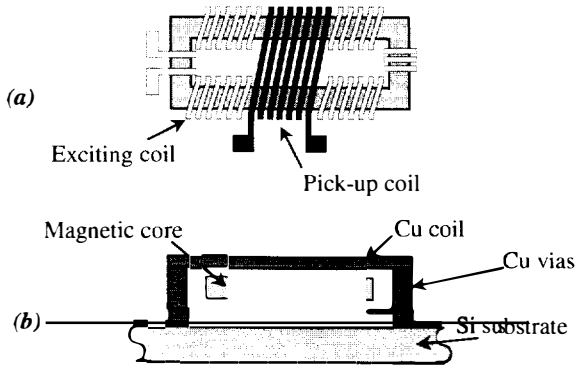

Figure 2. *Schematic illustration of a ring type microfabricated magnetic sensor: (a) top view and (b) cut view.*

FABRICATION

The fabrication of the device was based on a newly developed UV lithography based thick photoresist process. The fabrication steps are summarized in Figure 3. We started with a Silicon oxidized wafer on the top of which was deposited Ti/Cu seed layer. Using thick photoresist (AZ-4000 series) and conventional UV-lithography, we prepared the molds in the photoresist where the bottom Cu conductors were to be electroplated. The thickness of the photoresist defines the thickness of the electroplated Cu conductors. Using electroplating techniques, 25 μm thick Cu was electroplated. The seed layer was then removed and a new photoresist layer was spun to the wafer.

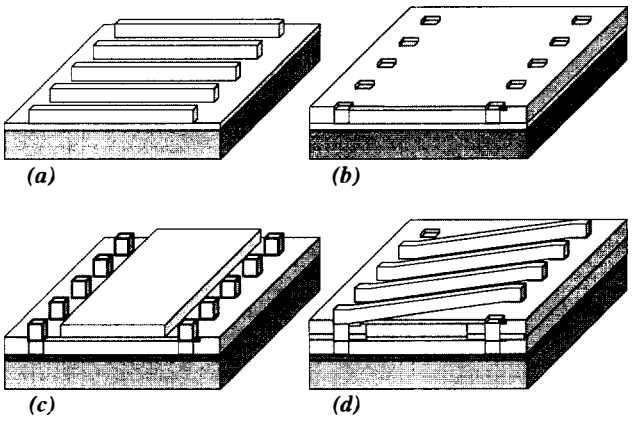

Figure 3. *UV-lithography and electroplated based fabrication steps: (a) on top of SiO_2 wafer, electroplate Cu conductors; (b) open via connections in hard cured photoresist; (c) electroplate vias and magnetic core; and (d) hard cure the second layer of photoresist and electroplate the top conductors.*

After the conductor vias were patterned, a hard curing step was necessary to electrically insulate and support the next layers.

Spinning the photoresist on the top of electroplated Cu conductors usually gives a non-uniform surface. This can cause problems with the photolithography for the following layers. This problem was solved with a hard curing step. By hard curing at 220 ^{o}C, we achieved a re-flow of the photoresist and a very smooth surface to continue the fabrication of the next layers. On the top of the hard cured photoresist, we deposited another seed layer, and we patterned and electroplated the vias and then the magnetic core. The conductor vias have a cross section of 50 μm x 50 μm and a thickness of 25 μm.

The magnetic core is formed from electroplated Ni/Fe (80%/20%) permalloy. Permalloy is often used as a core material for fluxgate sensors due to its high permeability and fast frequency response. The higher the permeability of the core, the easier saturation can be reached with low excitation current. This is desirable especially when the sensor needs to be integrated with CMOS. The thickness of the electroplated core is very critical in defining the characteristics of the fluxgate sensor. Since the induced output voltage is proportional to the face area of the pickup winding (i.e., total cross-sectional area of the core), the increase of the magnetic core will proportionally improve the sensitivity of the sensor. The advantage of electroplated magnetic core over sputtered one is that the thickness and pattern can be

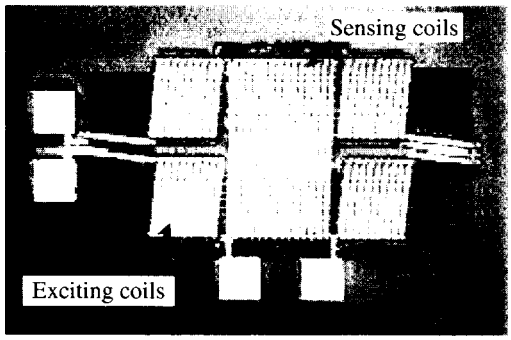

Figure 4. *Microphotograph of the fabricated micro-fluxgate sensor with dimensions 5 mm x 2.5 mm x 100 μm.*

easily controlled to a desirable dimension and shape, so the sensitivity and the operational range of the sensor can also easily be tailored. The devices in this work were fabricated with a 15 μm thick magnetic core.

When the vias and magnetic core were in place, we removed the seed layer and we performed another hard curing process. Finally, the last step was followed to pattern and electroplate the 25 μm top conductor lines. A microphotograph of the fabricated fluxgate sensor is shown in Figure 4.

EXPERIMENTS

In order to characterize the fabricated devices, very simple excitation and sensing (input/output) circuits were built. Considering the number of turns of the exciting winding, the geometry of the core, and the saturation magnetization of the electroplated Ni/Fe permalloy (e.g., 0.8 T for the permalloy electroplated in this work), the current that was required to saturate the magnetic core was approximately 220 mA. Figure 5 shows the measurement system of the fluxgate sensor. The driving circuit shown in Figure 5 is able to provide an oscillating current of 300 mA to ensure saturation of the core. The input of this circuit was connected to a function generator which can provide square or triangular waveforms. A square wave pulse-signal of 3 Vpp was used for these experiments.

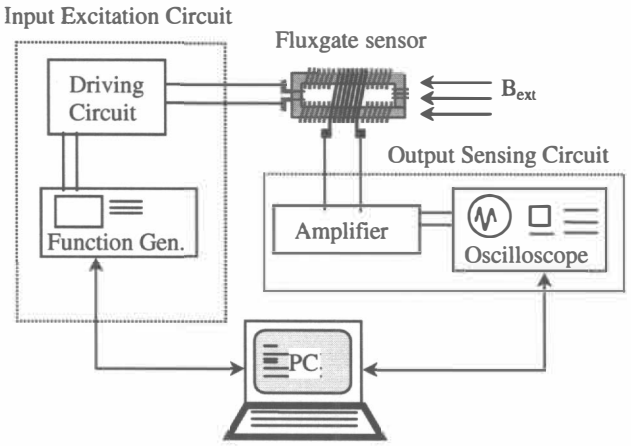

Figure 5. *Measurement system of fluxgate sensor*

The measured resistance of the exciting coil was 1.2 Ohms over the operating frequencies of 1-200 kHz. This low resistance limits the power consumption to approximately 100 mW in this sensor.

The output signal from the fluxgate sensor needs to be amplified. A commercially available op-amp was used to amplify the output signal approximately 20 times.

The magnetic field to be measured was produced from a solenoid, whose dimensions and electrical and magnetic characteristics are precisely known. In order to measure a wide range of magnetic fields, two different solenoids were used with different number of turns. By precisely controlling the current in the solenoids, we could produce external magnetic fields in the range of 0 – 1.5 mT. The fluxgate sensor was placed in the center of the solenoid, where the magnetic field was assumed homogeneous and constant. A photograph of the fluxgate probe with the electronic circuitry is shown in Figure 6. The measurements were performed in a magnetically shielded box to

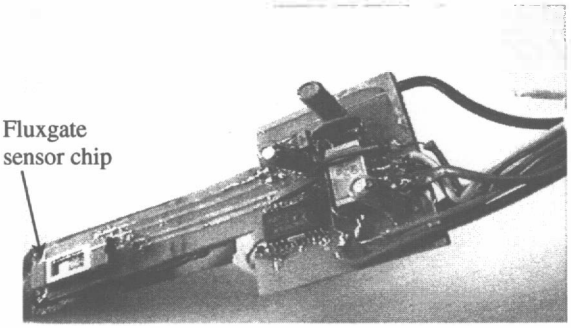

Figure 6. *Fluxgate probe with the supporting electronics.*

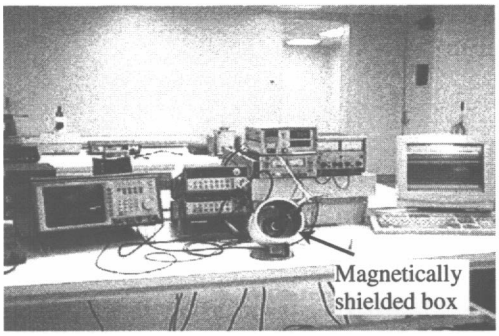

Figure 7. *Experimental setup with a magnetically shielded box.*

minimize external noises as shown in Figure 7, and the output voltage was measured with a digital oscilloscope.

Since the fabrication process of this sensor can be compatible with CMOS, the supporting driving and sensing electronic circuits can be integrated with the sensor in one chip, adopting a post-fabrication process of the fluxgate sensor.

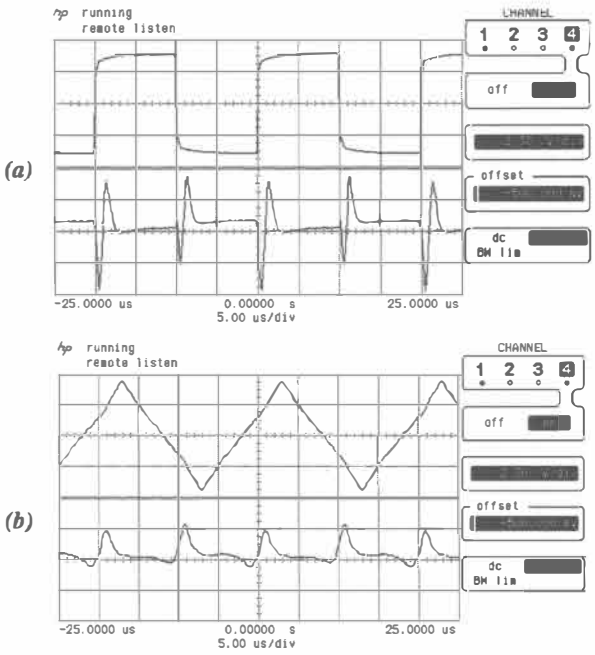

Figure 8. *Measured waveform of 3 Vpp input (upper) and output (lower) signal at 50 kHz: (a) square wave and (b) triangular wave.*

RESULTS AND DISCUSSION

In these experiments, we used a square wave input current of 300 mA to drive the exciting winding. Figure 8 shows the input and output signals of the sensors at a frequency of 50 kHz for the square and triangular input signal, respectively.

The sensitivity of the fluxgate sensor does not have significant dependence on the excitation frequencies when a square wave is used. From Equation 1, the amplitude of the output voltage depends on the change of the magnetic field over time, and thus the square wave is related to the rising and falling time of the pulse. When, a triangular waveform is used, there is a linear dependence of the sensitivity with the excitation frequency. In order to improve the sensitivity, it is preferable to drive the fluxgate sensor at high excitation frequencies with triangular waveforms, but more complicated electronic circuits will be required in this case. In this work however, the thick magnetic core (~15 μm) allow us to get fairly high sensitivity at low excitation frequencies with the square wave excitation pulse.

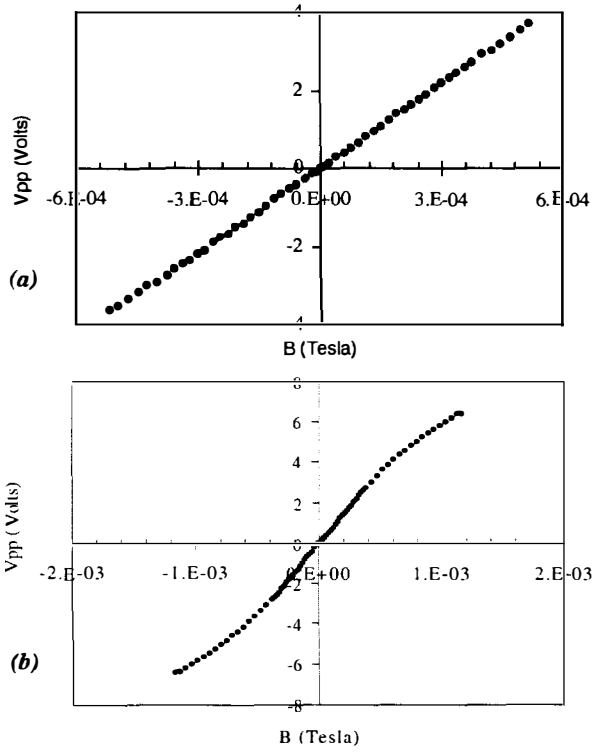

Figure 9. *Output signals versus external magnetic field: (a) linear dependence of the amplitude Vpp of the output signal over the external magnetic field (±500 μT) and (b) wide range external magnetic field measurements (±1.3 mT).*

Measured output signals versus external magnetic fields are plotted in Figure 9. The sensor shows a very linear sensitivity from –500 μT to +500 μT as shown in Figure 9(a). The measured resolution of the sensor is approximately 60 nT. The measured sensitivity of the fluxgate sensor cell without any amplification is 360 VT^{-1} for 1 kHz and 418 VT^{-1} for 100 kHz. However, the sensitivity of the whole sensor system with amplifiers is approximately 8360 VT^{-1} at 100 kHz. To demonstrate a wide sensing range of this sensor, measurements are performed in the range of -1.3 mT to +1.3 mT and the results are presented in Figure 9(b). As shown in Figure 9(b), the linearity of the curve begins to break at the magnetic fields over approximately ±500 μT. From the plots shown in Figure 9, no hysteresis was observed when the measurements were performed in both directions.

The geometry and magnetic of the magnetic core is considered as very important factors to shape the performance of the fluxgate sensor. By an optimized thickness of the core, the operational range of the sensor and its sensitivity can be flexibly controlled in this device.

Furthermore, to enhance the sensitivity of the sensor with a high frequency excitation, measurements are under development while the frequencies of the triangular excitation pulse are varied.

CONCLUSION

In this work, a micro fluxgate magnetic sensor has been designed, fabricated and functionally characterized. Micromachining techniques were used to fabricate the fluxgate sensor cell, which is composed of a magnetic core and the 3-dimensional planar solenoid coils for the excitation and sensing elements. The sensor cell sensitivity of approximately 400 VT^{-1} without amplification, was achieved over the frequency range of 1 kHz – 100 kHz, but the achieved sensitivity of the whole sensor system was 8360 VT^{-1} at 100 kHz. A linear dependence of the output Vpp signal was shown for the range of –500 μT to +500 μT with a resolution of approximately 60 nT. The power consumption was ~100 mW. Using the highly sensitive, on-chip fluxgate sensor, realized in this work, numerous applications are expected from space research and submarine detection to potable navigation systems and biomedical image systems.

AKNOWLEDGMENTS

This work was partially supported by a DARPA grant under contract number AF F30602-97-2-0102. The authors thank Hoechst-Celanese company for the AZ-photoresist donation. We would also like to thank Nihat Okulan, Srinivasan Iyengar, Hyoung-Jin Cho and Dan Sadler, for useful discussions and suggestions.

REFERENCES

[1] F. Primdahl, "The fluxgate magnetometer", J. Phys. E: Sci. Instrum. Vol. 12, pp. 241-253, 1979.

[2] R. S. Popovic, et al, "The future of magnetic sensors", Sensors and Actuators, A56, pp. 39-55, 1996.

[3] R. Ripka, "Review of fluxgate sensors", Sensors and Actuators, A33, pp. 129-141, 1992.

[4] S.O. Choi, S. Kawahito, et al, "An integrated micro fluxgate magnetic sensor", Sensors and Actuators, A55, pp. 121-126, 1996.

[5] S. Kawahito, H. Satoh, et al, "High resolution micro-fluxgate sensing elements using closely coupled coil structures", Sensors and Actuators, A54, pp. 612-617, 1996.

[6] R. Gottfried-Gottfried, et al., "A miniaturized magnetic-field sensor system consisting of planar fluxgate sensor and a CMOS readout", Sensors and Actuators, A54, pp. 443-447, 1996.

[7] T. Seitz, "Fluxgate Sensor in Planar Microtechnology", Sensors and Actuators, A21-A23, pp. 799-802, 1996.

[8] T. M. Liakopoulos et all, "A bio-magnetic bead separator on glass chip using semi-encapsulated spiral electromagnets", proc., 1997 International conference on Solid-State Sensors and Actuators, vol.1, pp. 485–488, 1997.

A WAFER-BONDED, SILICON-NITRIDE MEMBRANE MICROPHONE WITH DIELECTRICALLY-ISOLATED, SINGLE-CRYSTAL SILICON PIEZORESISTORS

Mark Sheplak, **Kenneth S. Breuer**, and **Martin A. Schmidt**
Microsystems Technology Laboratories, Massachusetts Institute of Technology
77 Massachusetts Ave., Cambridge MA 02139 USA

ABSTRACT

This paper presents the design, fabrication, and testing of a piezoresistive microphone for wind-tunnel acoustic measurements. The microphone was fabricated by an aggressively scaled process which produces a 1500 Å-thick silicon-nitride membrane that supports 850 Å-thick, dielectrically-isolated, single-crystal silicon piezoresistors. Measured results include a linear response up to 155 dB, a sensitivity of -93 dB ($22.4\mu V/Pa$), and a bandwidth of at least 6 kHz.

INTRODUCTION

Compliance with the FAR 36-Stage 3 community noise standard is one of the major factors determining the commercial viability of the High-Speed Civil Transport [**1**]. Experimental acoustic data from forward-flight, jet-noise experiments plays an important role in verifying noise suppression techniques. Unfortunately, existing microphone technology is insufficient for this application because the signal-to-noise ratio is limited by the flow noise generated by the interaction of the microphone package (*e.g.*, the nose cone) and the wind-tunnel flow. A miniature microphone, flush-mounted to the surface of a laminar-flow airfoil offers the potential to reduce wind noise to acceptable levels. Surface mounting requires that the side length of the microphone be much smaller (≤ 1.0 mm) than the local curvature of the airfoil. In addition, the airfoil thickness places size limitations on the microphone package. These spatial requirements preclude the use of conventional condenser microphones, but are potentially achievable by a microfabricated transducer. Most existing silicon microphones [**2,3**] were designed for audio applications such as hearing aids [**4**] and lack the dynamic range and bandwidth requirements for wind-tunnel measurements (Table 1). Specifically, the wind-tunnel environment requires a larger maximum sound-pressure level (SPL), finer spatial resolution, and a larger bandwidth than the hearing aid application.

	wind tunnel	hearing aid[**4**]
dynamic range	60–160 dB	27–120 dB
f_{res}	> 50 kHz	≈ 5.0 kHz
temperature range	-7 55 C	-
relative humidity range	10 - 95 %	10 95 %
diaphragm size	< 0.5 mm	≈ 3.0 mm

Table 1: Comparative microphone specifications for wind tunnel and hearing aid applications (0 $dB = 20$ μPa).

A microphone is an electro-mechanical-acoustic transducer that transforms acoustical energy into electrical energy. Although many different transduction principles have been employed [**2**], all are based on the detection of a pressure-induced structural deflection. Although most silicon microphones employ capacitive sensing schemes, concerns about about narrow-gap condensation, as well as indications of favorable scaling advantages [**5**] lead to the selection of a piezoresistive sensing scheme over a capacitive scheme for this study. Piezoresistive microphones incorporating various combinations of materials and construction techniques have been fabricated for both acoustics [**6,7**] and fluid mechanics [**8,9**] measurement applications. These microphones are not appropriate for forward-flight aeroacoustic measurements because they either lack the proper spatial and temporal resolution [**6,7**] or possess unacceptably low sensitivities [**8,9**]. Our microphone design incorporates the transduction advantages of single-crystal silicon piezoresistors [**7,9**] with the spatial and temporal resolution advantages of thin-film diaphragms [**8**]. The device structure consists of ultra-thin, dielectrically isolated piezoresistors on top of a silicon-rich, silicon-nitride diaphragm. Several types of pressure-sensors designs have employed single-crystal silicon piezoresistors on silicon-nitride diaphragms by utilizing silicon-under-insulator technology [**10**] and the BE-SOI technique [**11**]. The wafer-bond/thin-back process presented in this article is a significant improvement over these processes in terms of diaphragm geometry and piezoresistor placement tolerances and it produces silicon-dioxide encapsulated piezoresistors.

SENSOR DESIGN

A piezoresistive microphone transforms acoustic energy into electrical energy by transducing the strain on the top surface of a deflected membrane, which is deformed by the acoustic pressure, into a corresponding

[1]Mark Sheplak is presently affiliated with the Department of Aerospace Engineering, Mechanics, & Engineering Science, University of Florida, PO Box 116250, Gainesville, FL 32611-6250.

0-9640024-2-6/hh1998/$20©1998TRF
DOI 10.31438/trf.hh1998.6

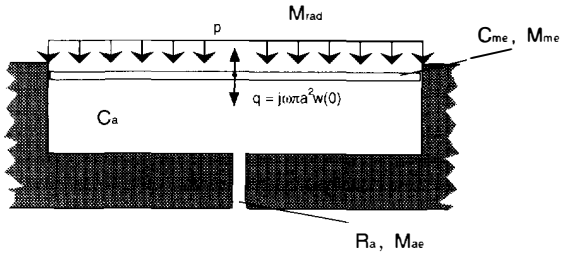

Figure 1: A schematic of the lumped acoustic model. Note that the microphone vent is exposed to the same pressure fluctuations as the diaphragm.

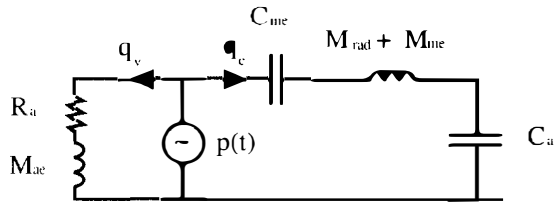

Figure 2: The equivalent circuit of the lumped acoustic model shown in Figure 1.

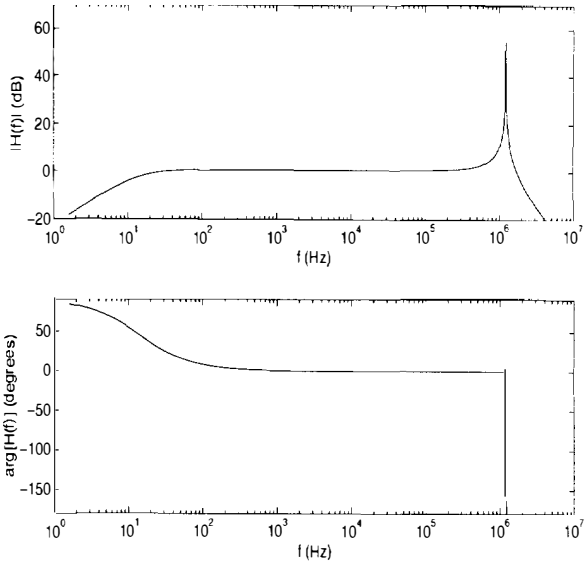

Figure 3: Theoretical Bode diagrams of dynamic response, $H(\omega) = q_c(\omega)/j\omega p(\omega)$ (0 dB = acoustic sensitivity at 1 kHz).

change in resistance. Therefore, the behavior of the stress or strain field as a function of loading is of particular importance. The exact characterization of the load displacement field behavior for a micromachined diaphragm is complicated by the presence of large in-plane forces due to processing, thermal expansion, and packaging. For our application, the piezoresistor placement and diaphragm geometry were determined by employing a fundamental structural model [**12**]. We found that a 1500 Å-thick, 210 μm-diameter silicon-nitride membrane meets the required performance specifications for wind-tunnel testing. The cavity and vent were sized by coupling the structural model into a lumped-element model (Figure 1). In this model, the distributed deflection of the diaphragm is lumped into a rectilinear piston possessing an effective mass (M_{me}) and compliance (C_{me}). In addition, this model incorporates the acoustic impedance due to the cavity compliance (C_a), vent mass (M_{ae}) and dissipation (R_a), and diaphragm radiation mass (M_{rad}). The equivalent circuit for this model is shown in Figure 2. In this electro-acoustic analogy, voltage is replaced by pressure, $p(t)$, and current by volume velocity, $q(t)$. The acoustic sensitivity is $q_c(\omega)/j\omega p(\omega)$. This model predicts a flat, minimum-phase response from 100 Hz–300 kHz with a resonant frequency greater than 1 MHz (Figure 3).

SENSOR FABRICATION

The microphone device structure consists of 850 Å-thick, silicon-dioxide encapsulated (150 Å-thick), single-crystal silicon piezoresistors on top of a 1500 Å-thick, 210 μm-diameter silicon-nitride membrane. Figure 4 is a SEM of a the top view of the microphone and Figure 5 is the corresponding cross-sectional schematic. Pressure equilibration is achieved by a 10 $\mu m \times 10\ \mu m \times 2.25\ mm$-long, channel which is vented to the surface. The U-shaped aspects of the vent intensify the viscous losses per unit length. This winding vent design conserves chip real estate while achieving the desired acoustic resistance. The arc-shaped and tapered resistor design results in piezoresistors that possess equal mean resistance, but respond with an equal and opposite change in resistance for a given deflection. This permits the use of both constant-current and constant-voltage excitation for fully-active and half-active Wheatstone bridges to maximize sensitivity and minimize thermal drift. Advantages over previous piezoresistive microphone designs include: superior gauge factors and reduced $1/f$ noise of single-crystal silicon compared to polycrystalline silicon [**6,8**], and no temperature-dependent leakage currents compared to diffused piezoresistors [**7**]. The microphones were fabricated using a silicon-nitride/silicon fusion-bond and thin-back process outlined in Figure **6**. To begin the process, a 150 Å-thick passivating oxide is grown on a SIMOX handle wafer. The membrane material, 1500 Å of silicon-rich silicon nitride, is deposited and polished in preparation for bonding **(A)**. The cavity and vent are etched into the handle wafer using a DRIE and 7000 Å of thermal oxide is grown as a bonding layer **(B)**. The wafers are bonded in a 20% O_2 / 80% N_2 ambient and annealed at 1100 C for one hour **(C)**. The bonded pair are first ground back to eliminate most of the substrate and then etched back to the buried oxide on the device wafer using a 20% KOH solution at 90 C. The piezoresistors are ion-implanted

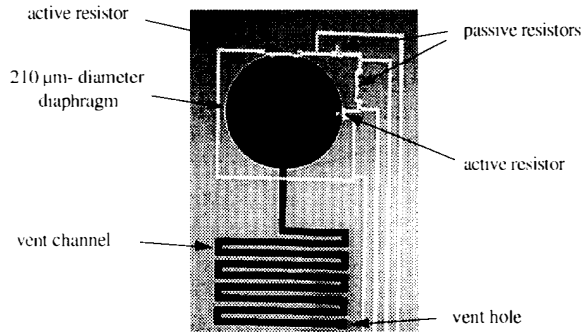

Figure 4: A SEM of a half-active, full-bridge microphone.

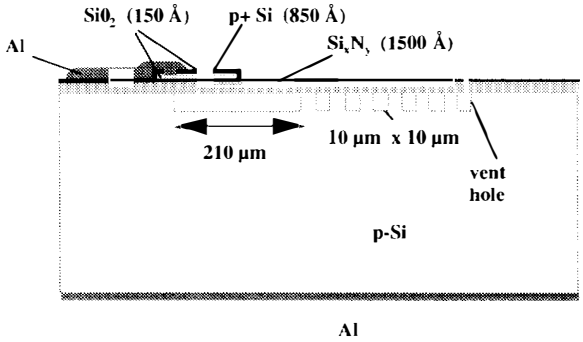

Figure 5: A cross-sectional schematic of the microphone device structure (not drawn to scale).

with boron ($2E18/cm^3$) and the buried oxide is stripped using a 7:1 BOE. The piezoresistors are patterned using a plasma etch and a 150 Å-thick top passivation oxide is grown **(D)**. Contact cuts are made, followed by metalization, venting, and die separation **(E)**.

This process yielded oxide-encapsulated single-crystal piezoresistors on top of a silicon-rich, silicon-nitride diaphragm using standard step and repeat projection lithography. Process features include strict diaphragm geometry tolerances (±3%) and 0.25 μm piezoresistor alignment (Figure 7). The process also eliminates one packaging function by compactly integrating the cavity and vent on chip.

RESULTS AND DISCUSSION

The acoustic sensitivity and linearity was determined by testing the microphone with a reference microphone (B&K 4138) in a plane-wave tube. The test setup permits the independent variation of both SPL (50 Pa- 1100 Pa) and frequency (200 Hz 6000 Hz). Figure 8 demonstrates a linear response up to 155 dB at 1 kHz. The measured sensitivity is -93 $dB \pm 3$ dB (0 dB = 1 V/Pa) for a 10 V excitation and 0.7 mW power consumption (Figure 9). This represents over a five-fold increase in sensitivity and a two-order-of-magnitude decrease in power con-

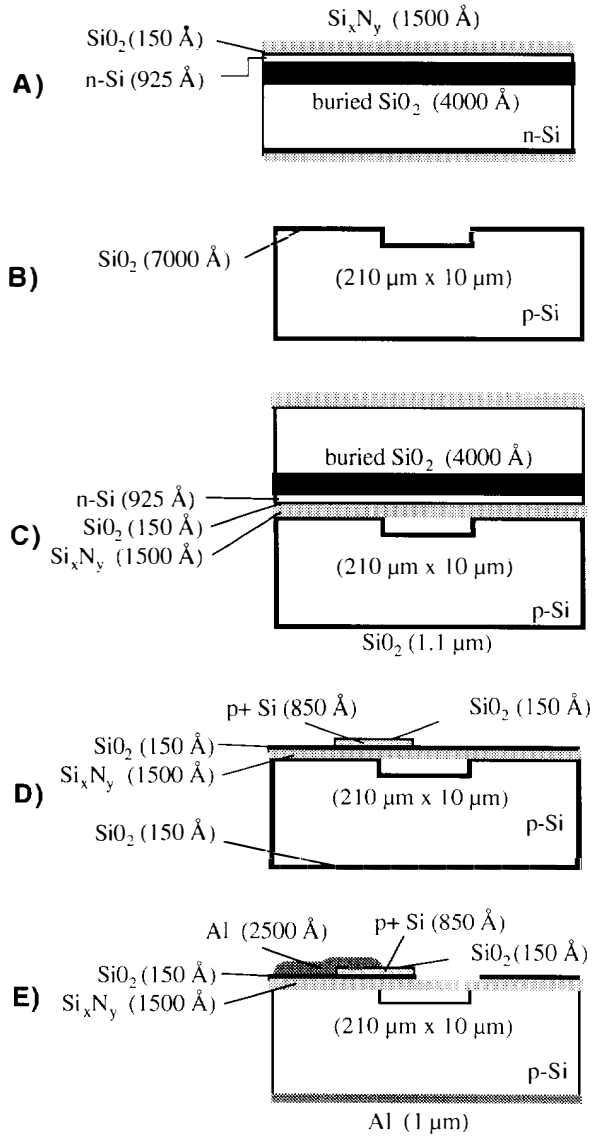

Figure 6: A schematic of the microphone fabrication sequence. Note that for simplicity the winding vent was not drawn.

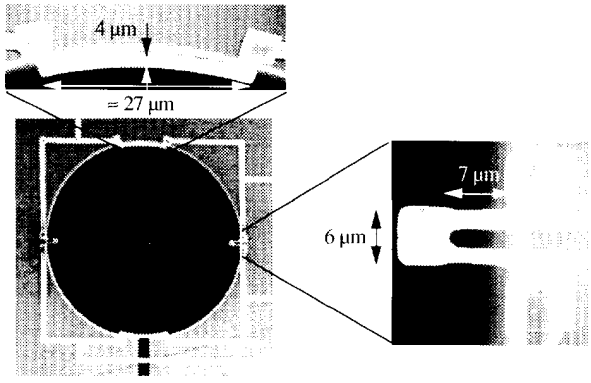

Figure 7: A SEM of the diaphragm region of a fully-active, full-bridge microphone.

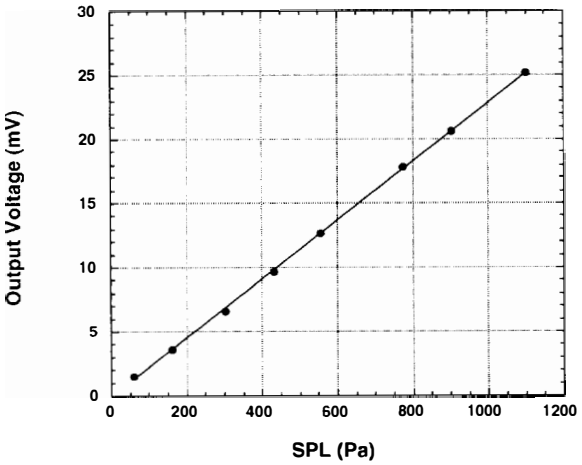

Figure 8: The output voltage of a fully-active, full bridge microphone as a function of SPL at 1 kHz for an excitation voltage of 10 V.

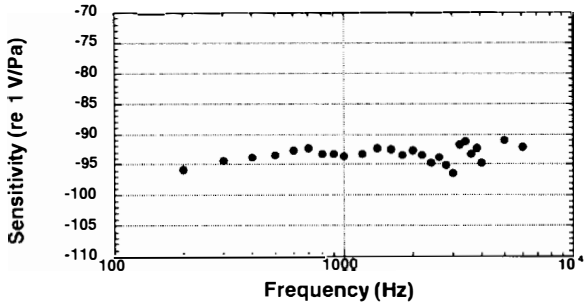

Figure 9: The acoustic sensitivity of a fully-active, full bridge microphone as a function of frequency for an excitation voltage of 10 V. The response is flat to within the calibration of the plane-wave tube.

sumption over commercially available devices [**9**]. The measured and predicted sensitivity agree to within 3 dB. The predicted noise floor of this device due to Johnson noise is 63 dB. Acoustic sensitivity testing at NASA-Langley Research Center's Jet Noise Laboratory confirms our sensitivity results while noise measurements indicate a noise floor of 92 dB. We believe that this high level is mainly due to noise pick-up via the package and cabling.

CONCLUSIONS

A piezoresistive microphone for wind-tunnel measurements has been developed. The devices were fabricated using a novel wafer-bonding process that permits the fabrication of sub-micron thick, silicon-dioxide encapsulated, single-crystal silicon piezoresistors on a silicon-nitride membrane. The microphone was designed by using coupling a fundamental structural model and a lumped-element dynamic model. This device has been tested at both MIT and NASA-Langley. The measured acoustic sensitivity is in good agreement with predicted values, but the noise floor is higher than expected. Currently, detailed sensitivity and noise testing are ongoing at NASA-Langley and the University of Florida.

ACKNOWLEDGMENTS

Support for this work was provided by NASA-Langley Research Center (Contract #: NAG-1-1785 monitored by Dr. J.M. Seiner). Samples were fabricated in the Microsystems Technology Laboratories (MTL) and the staff of the MTL are thanked for their assistance.

REFERENCES

1. A.W. Wilhite and R.J. Shaw, "HSCT Research Picks Up Speed", *Aerospace America*, August, 1997, 24-29.
2. P.R. Scheeper *et al.,* "A Review of Silicon Microphones", *Sensors and Actuators A*, 1-11 (1994, Vol. 44).
3. J.J. Bernstein and J.T. Borenstein, "A Micromachined Silicon Condenser Microphone with On-Chip Amplifier", *1996 Hilton Head Tech. Dig.* 239-243.
4. Knowles Electronics Co., EM Series specification sheet.
5. R.R. Spencer *et al.,* "A Theoretical Study of Transducer Noise in Piezoresistive and Capacitive Silicon Pressure Sensors", *IEEE Trans. of Electron Dev.*, 1289-1298 (1988, Vol. ED-35).
6. R. Schellin and G. Hess, "A Silicon Subminiature Microphone Based on Piezoresistive Polysilicon Strain Gauges", *Sensors and Actuators A*, 555-559, (1992, Vol. 32).
7. R. Schellin *et al.,* "Low Pressure Acoustic Sensors for Airborne Sound With Piezoresistive Monocrystalline Silicon and Electrochemically Etched Diaphragms", *Sensors and Actuators A*, 156-160 (1995, Vol. 46-47).
8. E. Kälvesten *et al.,* "A Small-Size Silicon Microphone for Measurements in Turbulent Gas Flows", *Sensors and Actuators A*, 103-108, (1994, Vol. 45).
9. Kulite Semiconductor Products, Inc. MIC-093 specification sheet.
10. B. Folkmer *et al.,* "A Pressure Sensor Based on a Nitride Membrane Using Single Crystalline Piezoresistors", *Transducers '95 Tech. Dig.*, 574-577.
11. C.A. Desmond *et al.,* "Fabrication of a High-Sensitivity Pressure Sensor with Nitride Membranes and Single Crystal Piezoresistors using Wafer Bond and Etch Back", *Volume 95-1, Spring Meeting of The Electrochemical Society, Inc.*, 1995, 645-646.
12. M. Sheplak and J. Dugundji, "Large Deflections of Clamped Circular Plates Under Tension and Transitions to Membrane Behavior," *J. Applied. Mech.*, in press, March 1998.

MICROMACHINED CONDENSER MICROPHONE FOR HEARING AID USE

David Schafer, Steven Shoaf and Peter Loeppert
Knowles Electronics IC Group
Rolling Meadows, IL 60008

ABSTRACT

An integrated-circuit/micromachining process, mechanical design and acoustic package have been developed which yield a condenser microphone occupying less than half the volume of earlier hearing-aid microphones. Fabrication combines a low-voltage CMOS process with surface and bulk micromachining to produce a single-chip device incorporating diaphragm, backplate, buffer amplifier and backplate bias supply, all operating from a 1.3 V supply (single hearing aid battery). Nominal characteristics of parts being fabricated currently are: sensitivity -40 to -37 dBV/Pa at 1 KHz, low-frequency rolloff 150 Hz or below, first resonance (peak in sensitivity) at 15 to 17 KHz and A-weighted input-referred noise 28 to 32 dB SPL. A lumped-element equivalent circuit model accounts for sensitivity, frequency response and thermal-mechanical noise sources in the device.

INTRODUCTION

Micromachining technology is both technologically and economically attractive for manufacture of further-miniaturized hearing-aid microphones for use in new systems such as completely in the canal (CIC) instruments. However, due to the high performance standards applied to hearing-aid microphones, careful optimization of design and materials is needed in order to achieve a micromachined device acceptable for this use. In this paper we describe a particular choice of materials, process and design, based on integrated circuit and micromachining technology, which for the first time to our knowledge has largely achieved this goal. The external appearance of the device is shown in Figure 1. The volume of this part is approximately half that of earlier hearing-aid microphones.

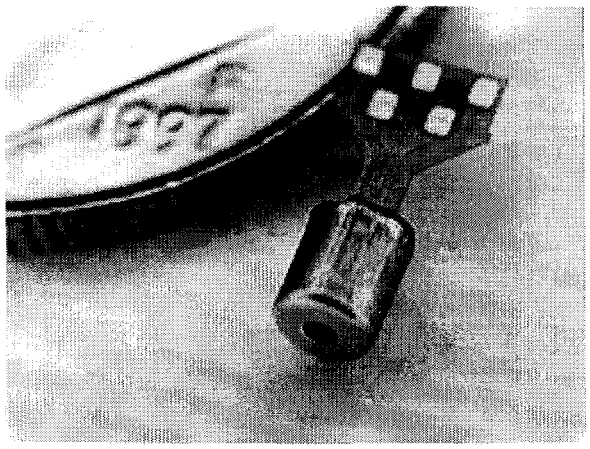

Figure 1. *Assembled microphone. The coin is a dime.*

The major characteristics of interest are sensitivity, input-referred noise (most simply quoted as an A-weighted rms value to correspond to the frequency range of human hearing) and frequency response. The open circuit sensitivity (volts per unit pressure) of a condenser microphone is given by

$$sensitivity = (\frac{V_b}{C_m})(\frac{dC_m}{dp})$$

where V_b is the voltage applied across the diaphragm / backplate, C_m is the capacitance of the diaphragm / backplate (which we refer to as the "motor"), and p is the acoustic pressure. If for purposes of discussing scaling issues we temporarily treat the diaphragm as a piston, spaced a distance s from the backplate, this expression becomes

$$sensitivity = (\frac{V_b}{s})(\frac{ds}{dp})$$

Electret hearing-aid microphones use stored charge to provide backplate voltages of several hundred volts. If an active circuit method is instead used to generate V_b, bias values are limited to 10-20 V due to the low value of the supply voltage (1.3 V).

In order to achieve comparable sensitivity, a non-electret microphone must have a value of *(1/s)(ds/dp)* roughly ten times higher than that of an electret microphone. As shown in published examples of micromachined devices **[1-6]**, this requirement tends to drive designs toward thin diaphragms (a few microns) and/or small motor air gap dimensions (also a few microns). For a diaphragm diameter less than 1 mm as discussed here, the diaphragm thickness must be near 1 micron for adequate compliance. This is compatible with integrated circuit and micromachining processes, although residual membrane stress in the finished diaphragm must be kept very low (typically 1 MPa or less) to preserve the compliance gained. Also, the need for control of the motor air gap means that any distortion of the diaphragm due to residual stress or stress gradients must be small compared to a few microns.

Once micron-sized motor air gaps are adopted, squeeze-film damping of the diaphragm motion due to viscosity of the air in the gap becomes significant **[1,2,7,8]**, first of all because of its contribution to the thermal-mechanical noise of the device **[9]** and secondarily because of its effect on frequency response.

DESIGN

In the device described here, high compliance is achieved in a small space by arranging the diaphragm structure in a "mushroom" form, specifically a disc which is anchored at the center and free to bend at the edges. Due to the mechanical boundary conditions set up in this arrangement, this structure has approximately five times the linear compliance of an edge-supported diaphragm of the same diameter. For the diaphragm material used here (0.75 micron PECVD nitride), the compliance is higher than necessary. Corrugations are added to the diaphragm to bring it to the desired compliance.

0-9640024-2-6/hh1998/$20©1998TRF
DOI 10.31438/trf.hh1998.7

Solid-State Sensors, Actuators, and Microsystems Workshop
Hilton Head Island, South Carolina, June 8-11, 1998

In the mushroom configuration, as-deposited stress in the diaphragm material is relieved except for the area around the anchor. Finite element simulation studies indicate that this area of unrelieved stress has very little impact on the diaphragm position.

Since the greatest compliance in this structure occurs at the diaphragm edge, the working area of the motor is located there. As shown in Figure 2, the backplate is a tensioned thin film of 1.1 micron PECVD/LPCVD silicon nitride which is largely cut away in regions near the center of the device. The working area is an annular region at the diaphragm edge, of width equal to about one-fourth of the diaphragm radius. In this working area, the backplate is further perforated to form a web-like structure of low acoustic resistance.

A portion of the diaphragm edge, of minimal width and airgap, overlaps the backplate to form a controlled-resistance pressure relief path.

The source capacitance of the motor is about 0.2 pf. The on-chip amplifier is an MOS follower circuit with an input capacitance of 0.2 pf and an A-weighted output noise level of approximately -108 dBV. 12 V bias is provided to the backplate by an on-chip ring oscillator and charge pump.

FABRICATION PROCESS

The device is fabricated using a low-voltage CMOS process sequence followed by additional process steps which build up the transducer structure. The PECVD silicon nitride passivation layer of the CMOS process, tensioned with an LPCVD nitride layer preserved from a LOCOS step of the CMOS process, is used to form the backplate web. The net tensile stress of this two-layer film stiffens the web to the point that its compliance is negligible compared to that of the diaphragm. The backplate is metallized with chrome.

Two sacrificial layers are deposited and patterned next. The first, 3 microns thick, is used to form corrugated relief in the surface which is eventually replicated in the diaphragm. The second, 1 micron thick, is a blanket layer which defines the regions where the diaphragm is to be anchored. In the motor working area the air gap is 4 microns, while at the diaphragm edge (pressure relief path) the gap is 1 micron.

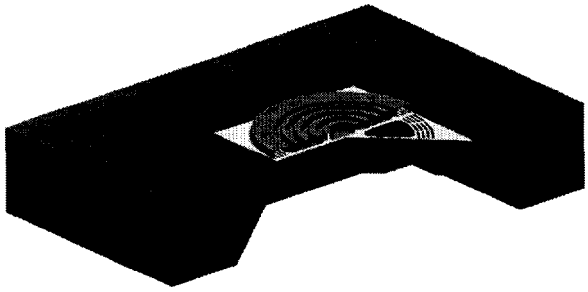

Figure 2. *Finished micromachined die, cut away to reveal the configuration of the thin-film diaphragm and backplate, as well the front and back holes.*

A second layer of PECVD nitride (0.75 micron thick) is deposited and patterned for use as the diaphragm. The diaphragm is also metallized with chrome. Finally TiW/Au is deposited and patterned for use in leadout and bond pads.

The finished wafers are micromachined in KOH. Etching occurs on both the front and back surfaces, creating holes which meet halfway through the wafer. The layout of the passivation web on the front causes four individual holes to be formed on the front side of the wafer, with "ribs" of unetched silicon between them. A cutaway view of the resulting structure is shown in Figure 2.

A plan view of a microphone die, 2 x 2 mm in size, is shown in Figure 3. The diaphragm is 0.8 mm in diameter. There is considerable unused silicon area, which allows more circuitry to be added or the die size to be reduced.

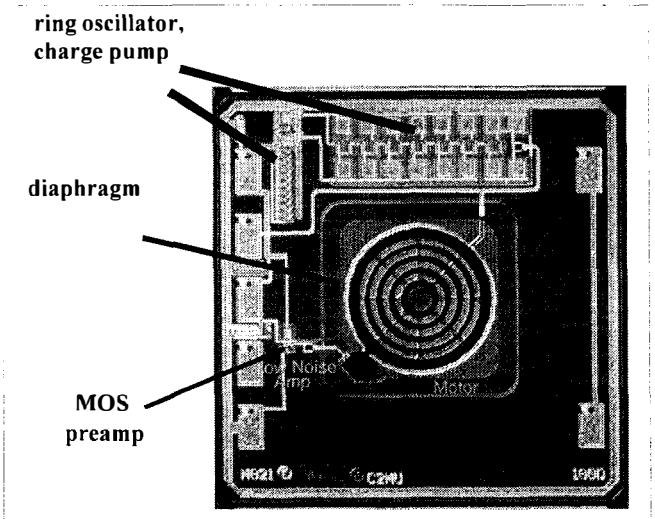

Figure 3. *Plan view of microphone die.*

PACKAGING

The device is assembled into a cylindrical package, shown in Figure 4. The micromachined die is first TAB bonded to a copper/polyimide flexible lead set, then mounted in an injection-molded plastic "cradle", next held in place in the stainless steel case using a second plastic insert, and finally sealed in place with heat-curing encapsulant. The cradle incorporates the acoustic back cavity required for the diaphragm, and the acoustic path formed by both plastic parts creates a light-blocking port. The case diameter is 0.090" and the case length 0.105".

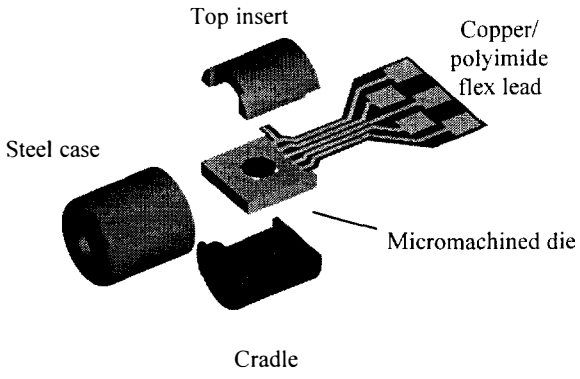

Figure 4. *Exploded view of packaging arrangement*

DEVICE PERFORMANCE

Nominal performance characteristics of parts being fabricated currently are: sensitivity -37 to -40 dBV/Pa at 1 KHz, low-frequency rolloff 150 Hz or less, first resonance (peak in sensitivity) at 15 to 17 KHz, and A-weighted input-referred noise 28 to 32 dB SPL. The frequency response is shown in Figure 5. In an alternate design, with a smaller, more highly damped motor and lower-inertance port, usable response extends out to 30 KHz which makes the device useful for ultrasonic sensing applications.

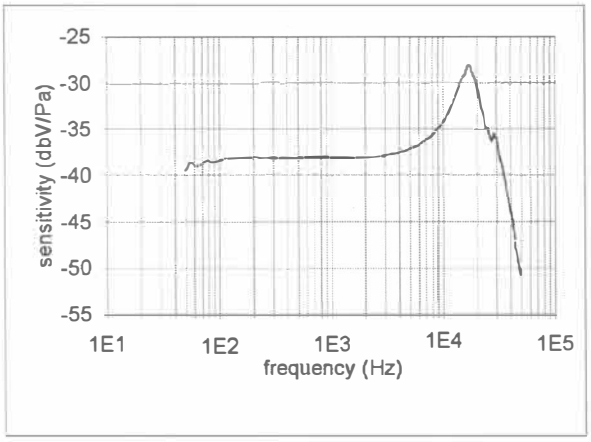

Figure 5. Frequency response

DEVICE MODELING

A lumped-element electrical-acoustical equivalent circuit model of the device, shown in Figure 6, is useful for accounting for sensitivity, frequency response and noise. In the left half of the equivalent circuit, current represents volume displacement rate u and electric potential represents acoustic pressure p. The port, front volume, back cavity, motor inertance and motor damping are represented using two-terminal passive elements.

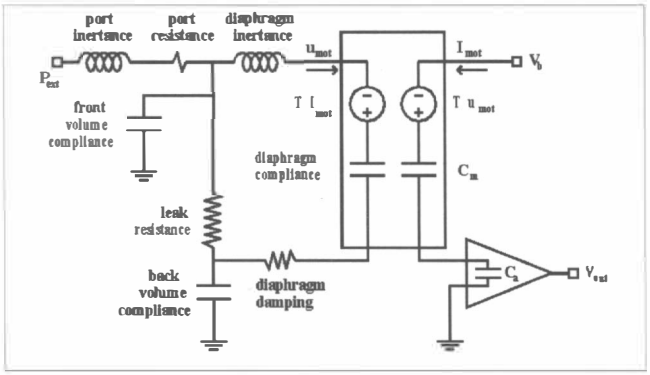

Figure 6. Lumped-element equivalent circuit model of microphone

The transducer characteristics of the motor at angular frequency ω are represented as a four-terminal element with two passive elements (volume compliance, electrical capacitance of the motor) and two dependent sources which represent the effect of the motor volume displacement rate u on the net motor voltage v, and the effect of the motor current i on the net diaphragm pressure load p:

$$v = T \times u \;;\; p = T \times i \;;\; T = \left(\frac{i}{\omega}\right)\left(\frac{V_b}{C_m}\right)\left(\frac{dC_m}{d(volume)}\right)$$

The buffer amplifier and its input capacitance C_a are represented in the right half of the figure.

The values of several elements in the equivalent circuit model may be obtained from an ac measurement in which a small ac drive signal v_b is applied to the backplate terminal (overriding the output of the on-chip charge pump which has very little current capacity) and measuring the amplitude and phase of the ac gain v_{out}/v_b where v_{out} is the output signal. The ac gain depends on the ratio of the net electrical impedance of the motor to the capacitive input impedance of the buffer amplifier. At zero dc backplate bias the transducer is inactive and the ac gain depends just on C_m/C_a. Since C_a is known from other wafer-level measurements then the value of C_m for the model can be determined and consistency with the nominal air gap and motor area checked. At non-zero dc backplate bias (T not zero), the ac gain measurement couples to the mechanical side of the system. By sweeping the drive frequency through the appropriate range, we can identify mechanical resonances of the device from the corresponding frequency dependence in the ac gain.

To study the dynamics of the motor alone, we have done ac gain measurements on micromachined, unpackaged die as shown in Figure 7. In this case the diaphragm is the only compliance present.

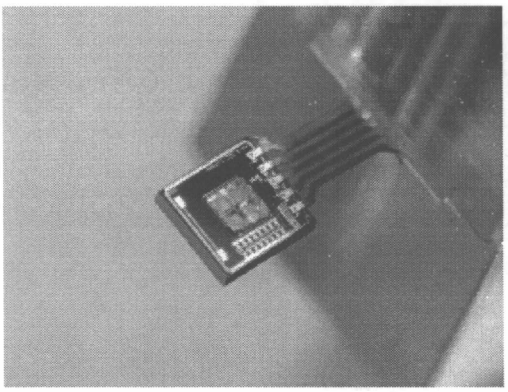

Figure 7. ac gain measurement on a micromachined, unpackaged die, used to study motor dynamics.

As the frequency is swept through the diaphragm resonance, the real part of the ac gain shows a relatively small shift (only a few percent), but the imaginary part shows a dip whose center frequency and width can easily be measured.

Figure 8 shows the out-of-phase component (quadrature signal from a lockin amplifier) of the ac gain signal vs. frequency for a particular part (#1597) under different ambient conditions. Each plotted curve is the result of subtracting a zero-backplate-bias (baseline) sweep from a second sweep at 12 V bias.

Vacuum measurement of the resonance provides the clearest indication of the diaphragm characteristics alone since the inertance and damping effects of air are then removed. Under these conditions the resonance is relatively narrow. The resonant frequency at 29.4 KHz under rough vacuum in Figure 8 agrees with the frequency of a "piston-like" vibrational mode of the diaphragm seen at 28.9 KHz in finite-element analysis simulations. This tends to confirm the accuracy of the finite-element analysis for other calculations such as the quasi-static compliance of the diaphragm.

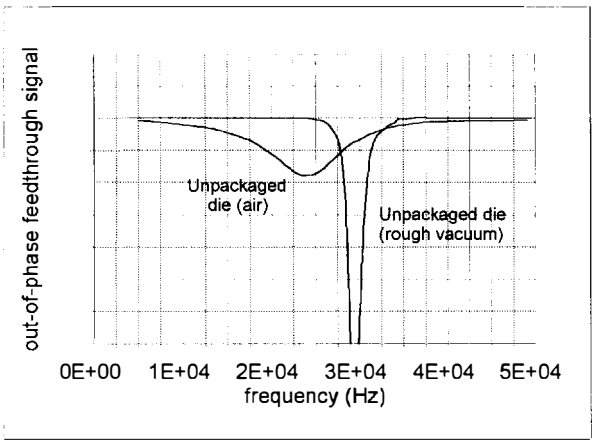

Figure 8. *Mechanical resonances seen in ac gain spectrum.*

When the ac gain spectrum is re-measured in air the resonance shifts downward to 24.4 KHz and the width increases to 9.7 KHz. The resonance width change is accounted for to within about 25% by a manual estimate of the damping effects of air viscosity in the motor gap assuming laminar flow with a parabolic velocity profile. Thus the damping seen in the unpackaged die as appears to be internal to the motor and thus able to be carried over without modification to the model of the packaged device. The estimated inertance of air in the motor gap, on the other hand, does not account for the observed frequency shift, which appears to come from the mass loading effects of ambient air and the inertance of the holes in the die.

When the part of Figure 8 is mounted on a variable-volume test cavity set at 2 mm^3 (equivalent to the package "cradle"), the resonance moves back up to about 26 KHz. In fully packaged parts the resonance finally moves back down to 15 to 17 KHz as seen as the peak in the sensitivity (Figure 5). Reproducing these successive shifts in the ac gain of the equivalent circuit determines the port inertance and back volume compliance values of the model.

NOISE ANALYSIS

The output voltage noise spectrum of the part discussed above (#1597) is shown in Figure 9. The part is still on the test cavity, now set at 2.9 mm^3 volume to bring the resonance down somewhat.

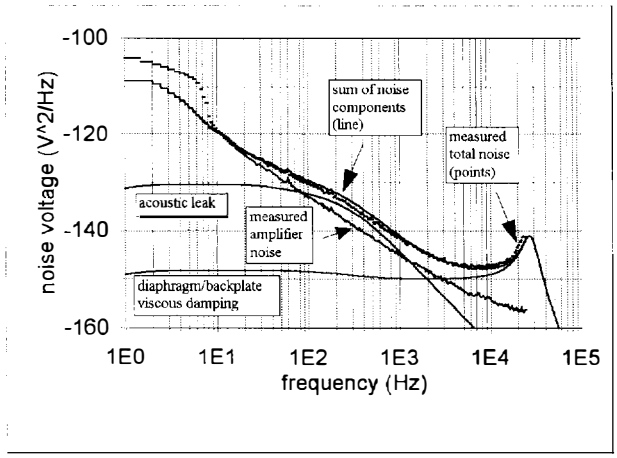

Figure 9. *Noise spectrum of the part shown in Fig. 8, mounted on the test cavity, set at 2.9 mm^3 volume.*

Noise spectra at $V_b = 0$ and $V_b = 12$ V are shown. At $V_b = 0$ the transducer is inactive and only electronic noise sources appear, mainly the 1/f noise of the amplifier. At $V_b = 12$ V, two additional features appear: a 3-4 dB increase over a broad range from 100 Hz to 5 KHz and a sharp rise above 10 KHz.

Thermal noise of the acoustic resistances in the equivalent circuit model account for these added noise features quite well. Two additional curves in Figure 9 show the model-predicted contributions to the output voltage noise from the motor damping resistance and the leak resistance, each taken as a pressure noise source of spectral density $P^2 = 4kTR$, where R is the respective acoustic resistance. Added to the amplifier noise, the total is accounted for to within 1 or 2 dB. On an A-weighted basis, the buffer amplifier, relief path resistance and diaphragm damping each contribute about one-third to the total input-referred noise, which is 32 dB SPL in this example.

ACKNOWLEDGEMENTS

The authors would like to acknowledge the contributions of the IC fabrication group at KEICG, Jay Cech, Engineering Manager, and Ian Arnott, Director. We would also like to acknowledge Karen Crow, Irene Gomez and Debora Nicholson for implementation of the assembly process and for acoustic and electrical measurements.

REFERENCES

1. J. Berqvist, F. Rudolf, J. Maisano, F. Parodi and M. Rossi, "A Silicon Condenser Microphone with a Highly Perforated Backplate", *Technical Digest of the 6th International Conference on Solid-State Sensors and Actuators (Transducers '91)*, San Francisco, CA, USA, 6/24-28/91, pp.266-269.

2. J. Bernstein, "A Micromachined Silicon Condenser Microphone with On-Chip Amplifier", *Technical Digest of the 1996 Solid-State Sensor and Actuator Workshop*, Hilton Head Isl., SC, 6/3-6/96, Transducer Research Foundation, Cleveland (1996), pp. 239 - 243.

3. P. Scheeper, W. Olthuis and P. Bergveld, "Improvement of the Performance of Microphones with a Silicon Nitride Diaphragm and Backplate", *Sensors and Actuators **A**, 40*, 179-186 (1994).

4. Y. Ning, A. Mitchell and R. Tait, "Fabrication of a Silicon Micromachined Capacitive Microphone Using a Dry-Etch Process", *Sensors and Actuators **A**, 53*, 237-242 (1996).

5. Q. Zou, Z. Li and L. Liu, "Design and Fabrication of Silicon Condenser Microphone Using Corrugated Diaphragm Technique", *Journal of Microelectromechanical Systems, 5*, 94 (1996).

6. M. Pedersen, W. Olthuis and P. Bergveld, "A Silicon Condenser Microphone with Polyimide Diaphragm and Backplate", *Sensors and Actuators **A**, 63*, 97-104 (1997).

7. Z. Skvor, "On the Acoustical Resistance Due to Viscous Losses in the Air Gap of Electrostatic Transducers", *Acustica, 19*, 295-299 (1967/68).

8. G. Plantier and M. Bruneau, "Heat Conduction Effects on the Acoustic Response of a Membrane Separated by a Very Thin Air Film from a Backing Electrode", *J. Acoustique, 3*, 243-250 (1990).

9. T. Gabrielson, "Mechanical-Thermal Noise in Micromachined Acoustic and Vibration Sensors", *IEEE Trans. Elect. Devices, 40*, 903-909 (1993).

FABRICATION AND TESTING OF MICROMACHINED SILICON CARBIDE AND NICKEL FUEL ATOMIZERS FOR GAS TURBINE ENGINES

N. Rajan, M. Mehregany, C. A. Zorman, and T. P. Kicher*
Microfabrication Laboratory
Dept. of Electrical Engineering and Applied Physics
*Dept. of Mechanical and Aerospace Engineering
Case Western Reserve University
Cleveland, OH 44106

ABSTRACT

Bulk micromachining of high-temperature materials is an enabling technology for the application of MEMS devices in high-temperature environments. This paper presents a novel molding method for fabricating silicon carbide (SiC) fuel atomizers for gas turbine engines. The devices are compared to similar nickel (Ni) atomizers fabricated using the LIGA process. Performance and erosion tests demonstrate that both types of atomizers are able to perform well at pressures in excess of 2500 kPa, with the SiC devices exhibiting a higher erosion resistance. The results demonstrate a significant improvement over similar silicon (Si) devices, which are limited in operation to pressures below 1400 kPa and are comparatively not resistant to erosive wear.

INTRODUCTION

The fabrication of micromachined fuel atomizers from high-temperature materials is a follow-on to our earlier research on Si micromachined atomizers. The Si devices afforded a high level of dimensional precision, which is lacking in both conventionally-machined and macrolaminate atomizers **[1,2]**. However, under extremely erosive operational conditions, the Si atomizers suffered significant wear. While the development of hard coatings for these Si devices provided a solution for improving the wear resistance **[1]**, there remains a need for fabricating the complete atomizer from a material with high-temperature stability.

The fabrication of MEMS devices from high-temperature materials has been hampered by the lack of processing technologies to micromachine high-performance ceramics, like SiC. While RIE techniques have been developed to fabricate surface micromachined structures from SiC thin films **[3]**, more complex three dimensional structures have not yet been realized. SiC's excellent chemical stability/inertness significantly limits pattern delineation, depth and accuracy when utilizing etch processes. Processes like LIGA provide the opportunity to fabricate micromachined devices from Ni, harnessing a material already used in the aerospace industry for its high-temperature characteristics and wear resistance in alloyed form. However, LIGA is not widely available and is often costly, driving the search for viable fabrication alternatives.

A novel processing approach is introduced in this paper to fabricate bulk micromachined MEMS devices, such as the atomizer, from materials other than Si. The approach uses Si molds fabricated by deep reactive ion etching (DRIE) and provides for controlled depth variations in the thickness direction. SiC atomizers are fabricated by high-rate deposition of SiC into these molds. While fabrication of Ni atomizers using this molding approach is currently in progress, Ni atomizers were also fabricated in two layers using the LIGA process, with the two layers of the device being assembled after release. The performance of the SiC and Ni (LIGA) atomizers are compared with one another and with Si atomizers.

FABRICATION

The Si molds were fabricated out of a 500 μm-thick (100) Si substrate using DRIE. The process flow is shown in Fig. 1. The novelty of the process lies in the patterning of both the first and second etch step masks before any DRIE etching, overcoming the problem of patterning a substrate for a second etch after the first bulk etch is completed.

The two mask materials used to fabricate the mold were thermal oxide and thick photoresist (Shipley AZ 4620). The process begins with a 1 μm growth of silicon dioxide on the substrate. The oxide was patterned using a standard lithographic process for the first etch. This pattern defined the etch mask for the deepest parts of the mold. The next step required the patterning of the thick photoresist on top of the patterned oxide layer. Notice from the process flow that the resist necessarily exposes more of the underlying substrate than the oxide. This allowed the exposed surfaces during the first etch to continue being etched during the second etch step.

The first etch was then performed to a depth of 275 μm, defining the depth of the annulus, inlet slots, and swirl chamber. After the first etch was completed, the oxide layer was removed using buffered HF, exposing the areas for the second etch defined by the thick photoresist. The second etch was then performed to remove an additional 125 μm of Si, resulting in a maximum mold depth of 400 μm, and a minimum mold depth of 125 μm, with the unetched center

0-9640024-2-6/hh1998/$20©1998TRF
DOI 10.31438/trf.hh1998.8

Solid-State Sensors, Actuators, and Microsystems Workshop
Hilton Head Island, South Carolina, June 8-11, 1998

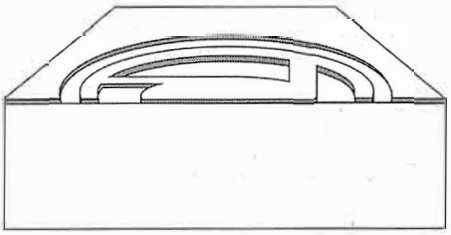

Step 1: Grow oxide and pattern

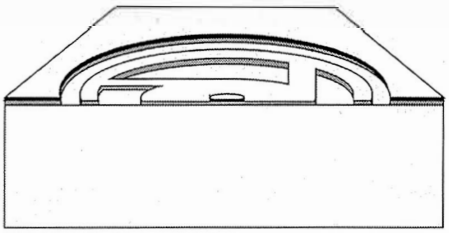

Step 2: Spin on thick resist and pattern

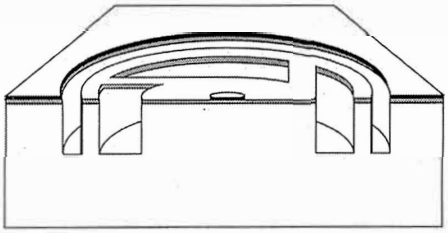

Step 3: First 275 μm deep DRIE etch

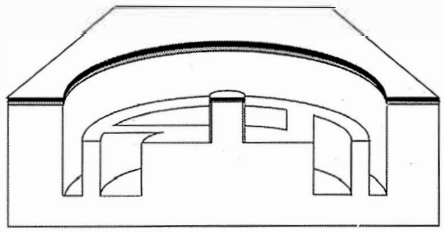

Step 4: Remove oxide and second DRIE etch for an additional 125 μm

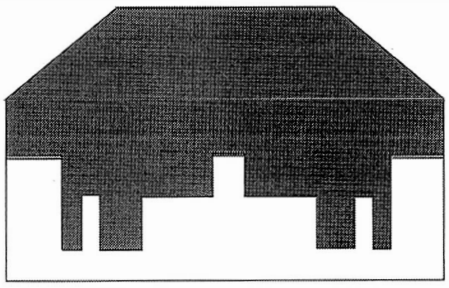

Step 5: Deposit 400μm of SiC

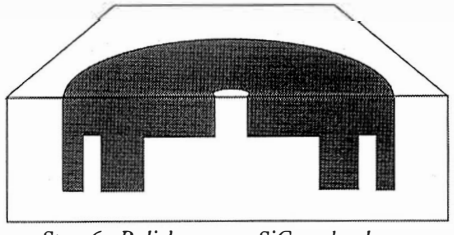

Step 6: Polish excess SiC and release

Fig 1: Process flow for SiC atomizer microfabrication.

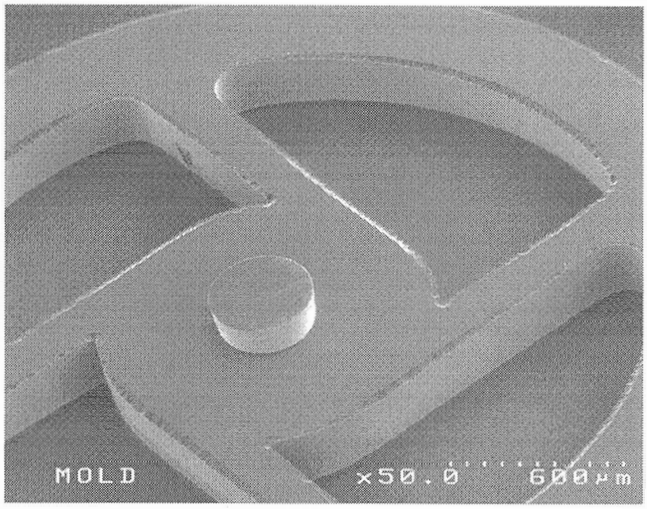

Fig. 2: SEM photo of the Si mold prior to SiC deposition.

post providing the molding for the exit orifice through hole. The final step for the mold preparation was the removal of the resist using piranha. An SEM micrograph of the mold is shown in Fig. 2.

The SiC mold filler was deposited in a high-rate SiC CVD reactor to a thickness of 400 μm using methyltrichlorosilane (MTS) at a temperature of 1200°C. As the deposition occurred both in the mold and on the field areas, mechanical polishing was required to remove the excess SiC. This was achieved using a two step process. The first step was a lapping phase for the rapid removal of SiC using a 15 μm polycrystalline diamond suspension on a cast iron polishing plate. The second step utilized a 1 μm polycrystalline diamond suspension to slow the removal of the SiC, as well as to reduce its surface roughness. Once the SiC was completely removed from the field area, the device was released using a KOH solution at 55°C. It should be noted that the mold filler can be any material that can sustain high deposition rates on a Si substrate, and work is currently under way to fabricate Ni (i.e. in alloyed form) atomizers using the Si molds and electroless plating.

The LIGA devices were fabricated using the MCNC LIGAMUMPs thick nickel (200 μm) process. For this process, the atomizer was designed in two halves, with the first containing the channel, annulus, and swirl chamber floors, as well as the exit orifice, and the second containing the structures used to define the channel, annulus, and swirl chamber walls. The mold was made from PMMA and Ni electroplating was used to deposit the atomizer structures.

EXPERIMENTAL PROCEDURE

The micromolded atomizers were tested for standard performance characteristics and erosion resistance. The tests were performed at the Parker Hannifin Gas Turbine Fuel Systems Division laboratory (Mentor, OH) using an evaluation format established at Parker for the testing of prototype atomizers. The performance measurements were

accomplished using a Parker A-3000 test stand. The spray quality was qualitatively evaluated and the fuel flow in lbs/hr (PPH) was measured for both SiC and Ni atomizers. The erosion test was designed to exaggerate real-world operating conditions by flowing an erosive mixture several orders of magnitude more aggressive than jet fuel. The erosive mixture was composed of variously sized black and red iron oxide particles, Arizona road dust, and salt water in MIL-C-7024 Type II test fluid. The contaminated fluid was fed through the atomizers at a pressure of 2660 kPa for a duration of 4.5 hours.

RESULTS AND DISCUSSION

The Ni atomizers were successfully fabricated in two parts using the MCNC LIGAMUMPs process. SEM micrographs of the two parts of the Ni devices are shown in Fig. 3. The SiC devices were also successfully fabricated using the Si micromolding process. An SEM micrograph of the SiC device is shown in Fig. 4. Examination of the SiC atomizer surfaces reveals SiC protrusions from the exit orifice and at various locations in the swirl chamber. These outgrowths are generated during the SiC CVD process, not during mold fabrication. The SEM micrograph in Fig. 2 shows the surfaces of a typical Si mold to be smooth and featureless. It has been observed that depositing SiC using MTS as the deposition gas results in void formation on the Si substrate at low deposition rates [4]. It is hypothesized that the irregular SiC device morphology is a consequence of this phenomenon.

The flow performance of the SiC and Ni atomizers were compared to Si micromachined atomizers of like design [1]. The Si micromachined atomizers were used as a reference for evaluating the SiC and Ni devices. Despite the morphological differences in the flow surfaces, the results showed that all devices had comparable flow numbers and comparable spray angles, with the Ni atomizers having slightly lower flow rates. The average flow rate for the SiC atomizers was 9 PPH, and the Ni atomizers 7 PPH, at an operating pressure of 660 kPa. Similar Si atomizers averaged 10 PPH at the same pressure. In addition, both the SiC and Ni devices could be operated continuously at much higher pressures than the Si devices, spraying consistently at pressures in excess of 2000 kPa, even though the SiC atomizer swirl chamber floor was generally half the thickness of comparable Si devices.

The erosion tests showed that the SiC devices performed better than the Ni devices, and both were superior to the Si atomizers in [1]. This is demonstrated clearly by the SEM photos of Figs. 5 and 6. Figure 5 is a set of pre- and post-erosion SEM micrographs of the Ni atomizers, with the inlay providing a close-up of the exit orifice edge. It was determined that this was the area most susceptible to erosive wear [1]. Figure 5 shows that the relative softness of Ni compared to SiC has led to heavy gouge patterns at the orifice edge, with significant scouring on the swirl chamber floor close to the exit orifice. This is attributed to the relatively high purity of the Ni in the electroplated form. In contrast, the SiC atomizers (Fig. 6) show no discernible evidence of wear.

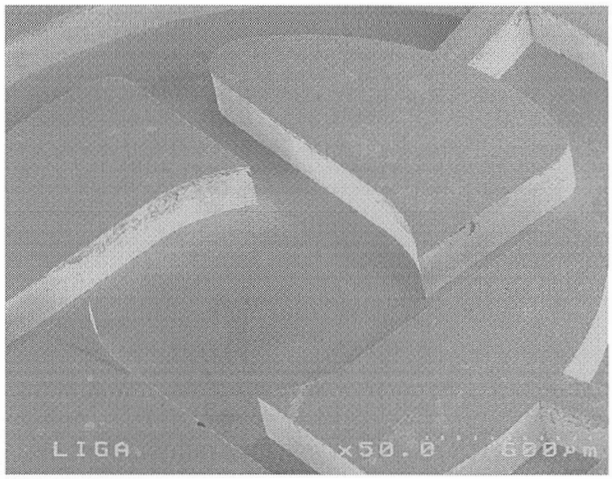

(a)

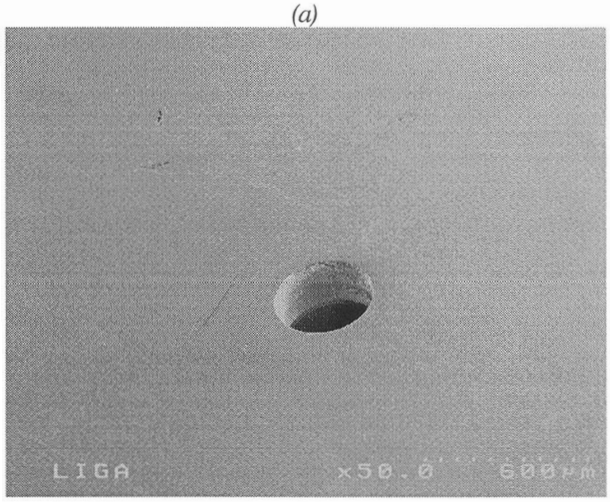

(b)

Fig. 3: SEM photos of the two parts of a Ni atomizer: (a) One half defining the annulus, inlet slot, and swirl chamber walls; and (b) the other half containing the exit orifice (SEM scales identical to that in Fig. 4).

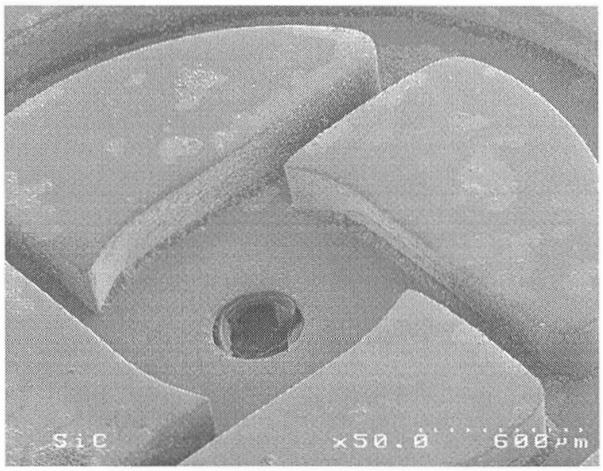

Fig. 4: SEM photo of a SiC atomizer.

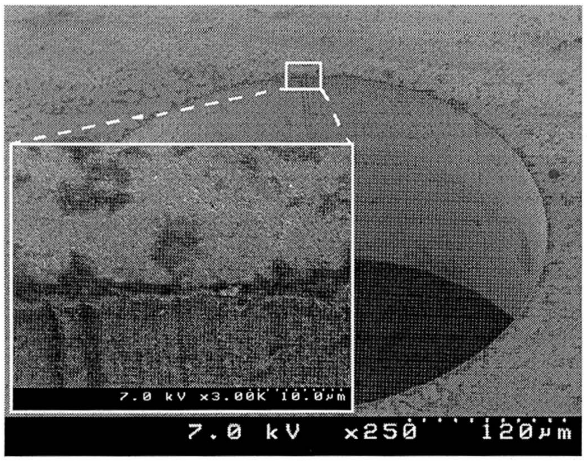

(a)

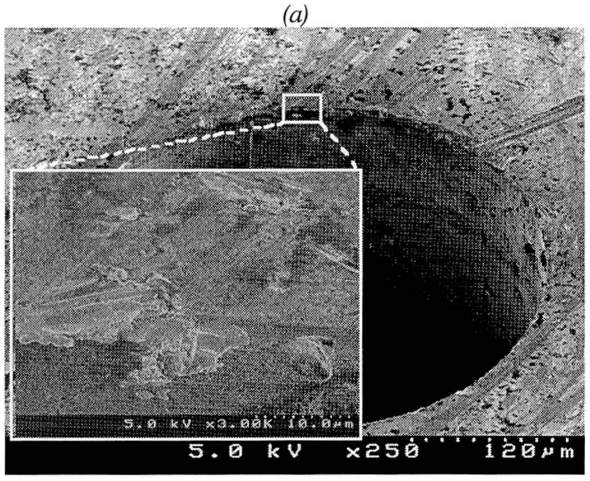

(b)

Fig. 5: SEM photos of the Ni atomizer exit orifice edge with close-up inlays: (a) Before the erosion test; and (b) after the erosion test.

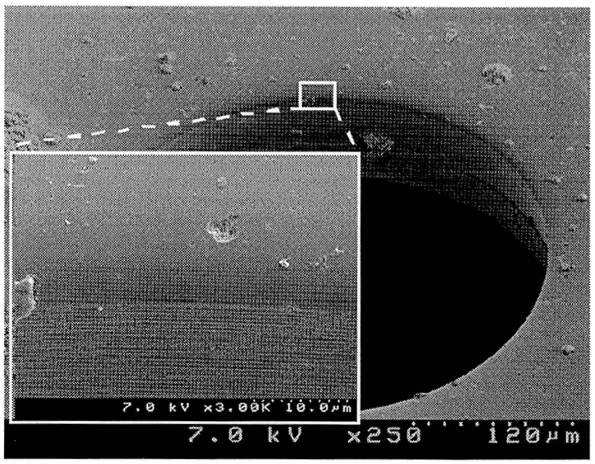

(a)

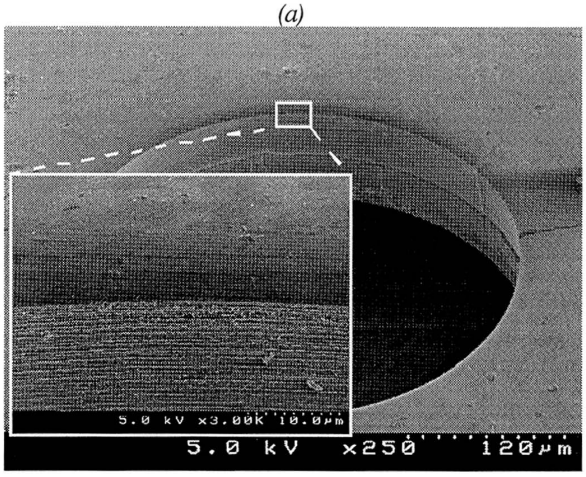

(b)

Fig. 6: SEM photos of the SiC atomizer exit orifice edge with close-up inlays: (a) Before the erosion test; and (b) after the erosion test.

CONCLUSIONS

SiC atomizers were successfully fabricated using a novel Si molding process and were compared with Ni atomizers fabricated using the MCNC LIGAMUMPs process. Both types of atomizers performed well at high pressures with the SiC devices exhibiting superior erosive wear resistance to Ni, and both materials outperforming Si. Performance tests demonstrated that both SiC and Ni atomizers exhibited similar flow performance to Si devices, with average flow rates of 9 and 7 PPH respectively at 660 kPa, compared to 10 PPH for the Si atomizers.

ACKNOWLEDGMENTS

The authors would like to acknowledge collaboration through the Aerospace MEMS Consortium (in part supported by DARPA), in particular Parker Hannifin Corporation for the use of their test facilities, and Dr. K. Stark at Advanced Micromachines Incorporated for the DRIE etching. The CWRU work was supported by a Multidisciplinary University Research Initiative from ARO (Contract Number DAAH04-10097).

REFERENCES

1. N. Rajan, C.A. Zorman, M. Mehregany, R. DeAnna, and R.J. Harvey, "Effect of MEMS-Compatible Thin-Film Hard Coatings on the Erosion Resistance of Silicon Micromachined Fuel Atomizers", *Int'l Conf. on Metallurgical Coatings and Thin Films,* San Diego, CA, (April 1998).

2. R. J. Harvey, "Progress on Comparison Study of the Erosion of Conventionally Machined and Macrolaminated Pressure-Swirl Atomizers", *Int'l Gas Turbine and Aeroengine Congress and Exhibition*, (1997).

3. A. Fleischman, S. Roy, C.A. Zorman, M. Mehregany, and L.G. Matus, "Polycrystalline Silicon Carbide for Surface Micromachining", *9th Annual Workshop on Microelectromechanical Systems,* San Diego, CA, (Feb. 1996).

4. C.C. Chiu, S. B. Desu, G. Vhen, C.Y. Tsai, and W.T. Reynolds, Jr., "Deposition of Epitaxial β-SiC Films on Porous (100) from MTS in a Hot Wall LPCVD Reactor", *J. Mater. Res., 10,* 1099, (1995).

DEVELOPMENT OF A HYDROGEN COMBUSTOR FOR A MICROFABRICATED GAS TURBINE ENGINE

A. Mehra, I. A. Waitz
Gas Turbine Laboratory, Department of Aeronautics and Astronautics
Massachusetts Institute of Technology
Cambridge, MA 02139

ABSTRACT

As part of an effort to develop a new generation of micro heat engines, a program is underway to fabricate a gas turbine engine capable of producing 50W of electrical power in a package less than one cubic centimeter in volume. This paper focuses on the combustor for such an engine, specifically describing the design, fabrication and testing of a first-ever hydrogen combustor micromachined from silicon. Complete with a fuel manifold and injector holes, the combustion chamber measuring less than 0.07 cm^3 in volume has been successfully demonstrated to provide exit temperatures up to 1800K. The combustor efficiencies were found to be in the range of 40%-60% due to large heat loss to the test mount. The device has been experimentally tested at elevated temperatures for over fifteen hours, demonstrating the satisfactory performance of silicon in such environments. Combined with a materials study that shows that the performance of a silicon microcombustor will not be oxidation limited, these results are a significant step towards establishing the viability of building a micro gas turbine engine using silicon microfabrication techniques.

INTRODUCTION

Recent advances in the field of microfabrication have opened the possibility of building a micro gas turbine engine. By using the material properties of silicon and the precision obtainable from microfabrication technology, a micro gas turbine engine could produce tens of watts of power while weigh-ing only a few grams, and being a few millimeters in dimen-sion. Such a device would represent a significant advance in compact electrical power sources by providing over ten times the energy and power density of the best batteries available today. Besides power generation, microengines could become an enabling technology for numerous other applications such as boundary layer and circulation control, micro air vehicle propulsion, micro refrigeration, micro rocket engines, auto-motive fuel pumps, and mobile power units.

A feasibility study, preliminary design and performance estimates of a device requiring 7 grams of jet fuel per hour and producing 10-100 Watts of electrical power have been presented by Epstein *et al.* **(1)** and Groshenry **(2)**. This device is shown in Figure 1. Since several micro heat en-gine applications require the conversion of chemical energy into fluid and thermal power, it is necessary to develop combustion strategies suitable for use in these miniature devices. The challenges and preliminary design of such a combustor were described by Waitz *et al.* **(3)**, along with the results for premixed hydrogen combustion in a macro-fabricated steel rig measuring 130 mm^3 in volume. This paper extends these results. Non-premixed hydrogen-air combustion is demonstrated in a first-of its-kind combustor that is micromachined from silicon, and has an integral fuel manifold and injector holes. The results of a materials study are also presented to establish the viability of silicon as a suitable material for a micro gas turbine engine.

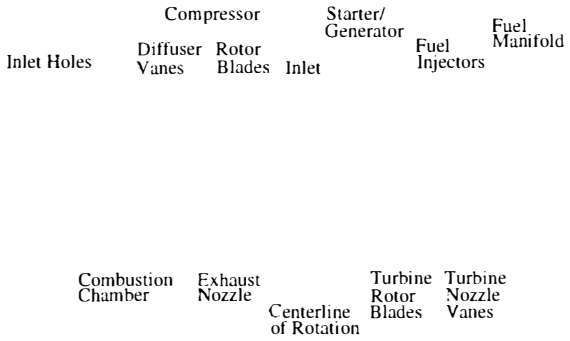

Figure 1: Baseline design of the MIT micro gas turbine engine and electrical generator.

HYDROGEN-AIR MICROCOMBUSTORS

Before describing the fabrication and testing of the microcombustor, we briefly review the primary challenges and the proposed combustion strategies.

Overview of Microcombustion Technology

The design and operation of a combustor at the micro scale is primarily limited by the following:

1. *Shorter residence time for mixing and combustion:* Since combustor residence time approximately scales with combustor volume and compressor pressure ratio **(4)**, the residence time in a low pressure, low volume, geometrically scaled down microcombustor may be a tenth to a hundredth of that in a conventional large scale gas turbine combustor. This imposes constraints on the time available for fuel mixing and chemical reactions[1].
2. *High heat loss at the micro scale:* The surface area-to-volume ratio of the microcombustor is 500 m^{-1}, compared to 3-5 m^{-1} for a large scale combustor. Thus, high heat transfer losses may prevent the attainment of typical large scale combustor efficiencies which are in excess of 99.9%, and may also affect fuel flammability limits due to flame quenching.

[1]Compared to a conventional sized gas turbine with pressure ratios in excess of 30:1, the pressure ratio for the baseline microengine is only 4:1.

0-9640024-2-6/hh1998/$20©1998TRF
DOI 10.31438/trf.hh1998.9

Solid-State Sensors, Actuators, and Microsystems Workshop
Hilton Head Island, South Carolina, June 8-11, 1998

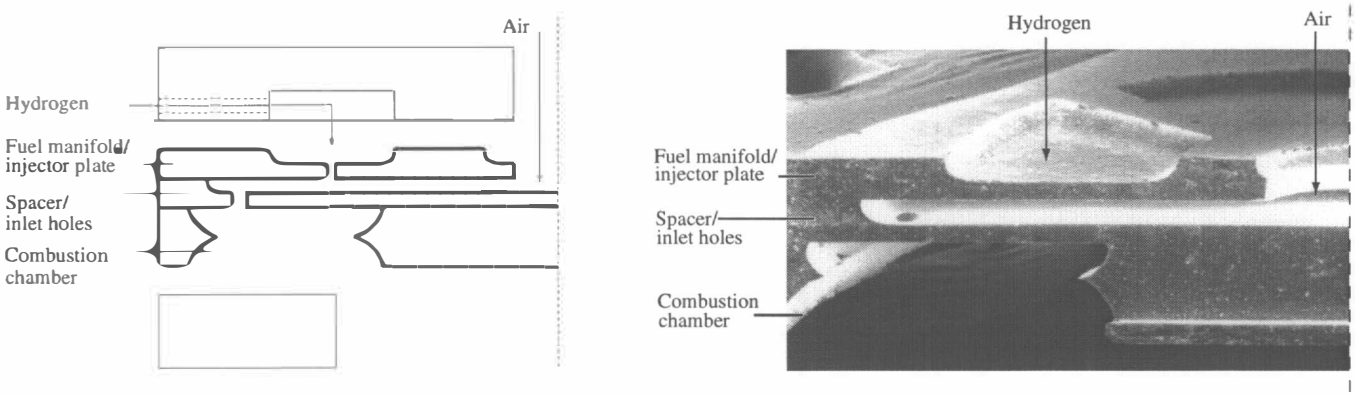

Figure 2: Schematic and SEM cross-section of half of the combustor, showing the fuel manifold, injectors, and air flow path.

In response to these challenges, the design of the microcombustor is based on the following strategies:

1. Relative to the size of the engine, the size of the combustor was increased by a factor of 40 to increase the flow residence time.
2. The fuel was introduced at approximately 50 injector-hole diameters upstream of the combustor inlet holes to facilitate fuel-air mixing.
3. Hydrogen was chosen as a fuel since it has wider flammability limits, and an order of magnitude lower chemical reaction time than hydrocarbon fuels[2].

In keeping with these concepts, the design, fabrication and testing of a micromachined silicon combustor has been completed. This is presented in the following sections.

Design of the Microcombustor

The schematic of the microcombustor assembly is shown in Figure 2. The microfabricated portion consists of a stack of three silicon wafers housing the fuel manifold and injectors, the combustor inlet holes, and the combustion chamber. The chamber is an annular region 1 mm in height, with a volume of 66 mm^3, and an inner and outer diameter of 5 mm and 10 mm respectively. The axial length of the combustor was chosen in accordance with the computational fluid dynamics (CFD) predictions for the minimum volume necessary for complete combustion at atmospheric pressure. It also facilitates the fabrication of the entire combustion chamber from a single 1 mm thick wafer.

The fuel injector size and spacing was based on semi-empirical models for normal jet injection and mixing to satisfy lateral spreading and penetration requirements. The final device consists of a total of 76 30μm diameter injector holes equally spaced at a radius of 3 mm.

The overall combustor dimensions were set by the preliminary design studies completed by Epstein *et al.* (1). The size and number of combustor inlet holes was chosen to eliminate the upstream propagation of a flame into the compressor exit flow path.

[2]While initial efforts have primarily concentrated on the use of hydrogen, a program for the use of hydrocarbon-air combustion is also currently underway (3).

Fabrication Process

The three stack fusion-bonded assembly required a total of five masks and six deep etches. The fabrication process for each of the wafers involved the following steps:

1. Photolithography: A 10μm coating of resist was used to pattern the top surface of the wafer with the appropriate fuel manifold, spacer plate or combustion chamber geometry.
2. Isotropic Deep Reactive-Ion Etching (DRIE), (5): Dry chemistry employing an SF_6 plasma was used to etch the 200μm fuel manifold and spacer plate. Half of the 1000μm deep combustion chamber was also isotropically etched, the double-sided etching technique being employed to minimize the run-out in the side walls of the combustor[3].
3. Patterning bottom side: After coating 10μm of resist, infra-red alignment was used to expose the bottom side of the three wafers to pattern the corresponding fuel injectors, combustor inlet holes, or combustion chamber geometry.
4. Anisotropic DRIE: Finally, a time multiplexed inductively coupled plasma of SF_6 and C_4F_8 was used to anisotropically etch the 200μm deep fuel injectors and combustor inlet holes in the top two wafers of the stack. (The other side of the combustion chamber wafer was isotropically etched.)

Following the completion of the processing on the three individual wafers, the wafers were RCA cleaned, and aligned bonded using a Electronic Visions aligner. The bonding was completed in two steps - the first and second wafers were bonded first; the stack was then annealed, RCA cleaned, and finally bonded to the third wafer. Post-bond annealing was carried out in an inert ambient for one hour at 1100°C. The 1.8 mm thick wafer-stack was finally die-sawed to obtain thirteen out of the possible sixteen die on the 100 mm wafer.

A cross section of the completed stack showing the fuel manifold, injector holes and fluid flow paths is shown in Figure 2. Individual scanning electron micrographs of each of the wafers are shown in Figures 3-5.

[3]Since none of the features required parallel side walls, isotropic etching was chosen to minimize process time.

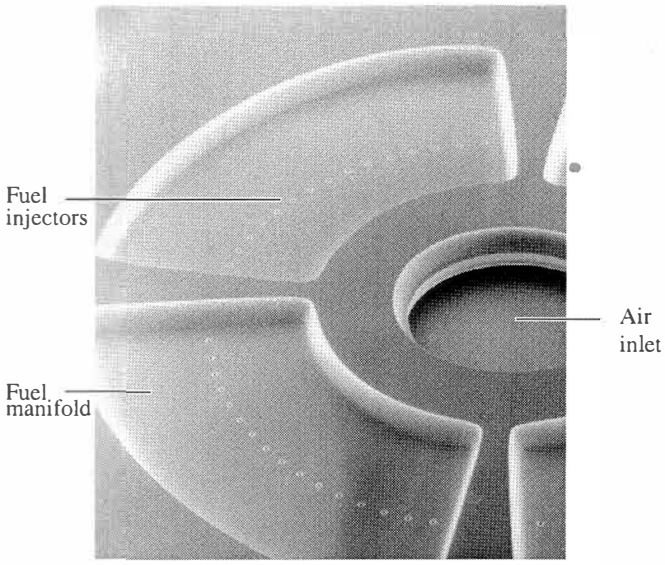

Figure 3: SEM of the fuel manifold, showing the ring of 76 30μm fuel injector holes.

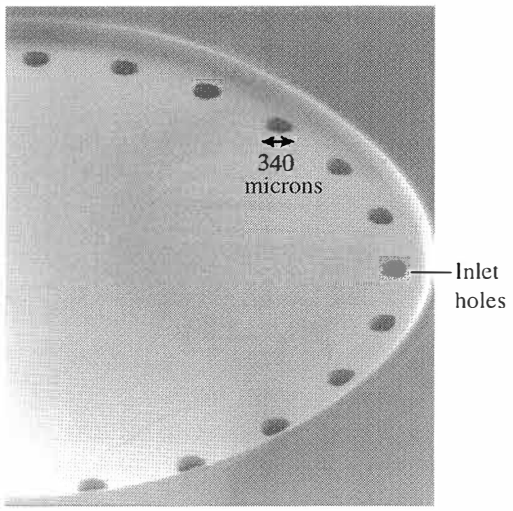

Figure 4: Isotropically etched spacer plate, showing the 24 340μm combustor inlet holes at r=4.5 mm.

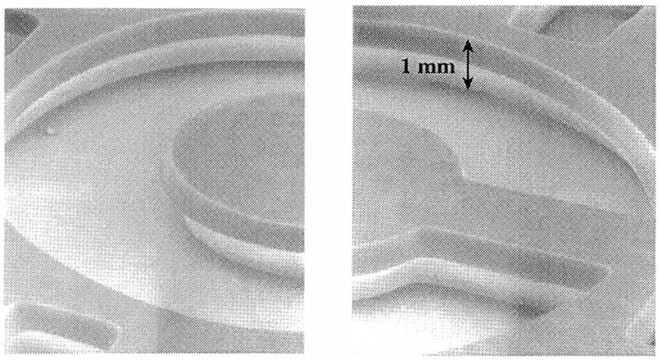

Figure 5: Isotropically etched, 1 mm high annular combustion chamber, with an inner and outer diameter of 5 mm and 10 mm respectively.

Experimental Tests

Apparatus

A schematic of the experimental test rig is shown in Figure 6. The microfabricated structure was clamped between invar plates whose thermal expansion coefficients were chosen to match that of silicon. The invar plates also housed the macro-fluidic connections for the air and hydrogen feeds, along with inlet and exit thermocouples. Type K thermocouples were employed for temperature measurements. However, because of large temperature gradients along the length of the wire, an error analysis for the thermal conductivity, radiative emissivity and calibration drifts predicted that the uncertainty in temperature measurements would be up to ±120K (**6**). While these uncertainty bounds were considered acceptable to establish the onset of combustion, efforts are currently underway to incorporate non-intrusive optical techniques to improve temperature diagnostics.

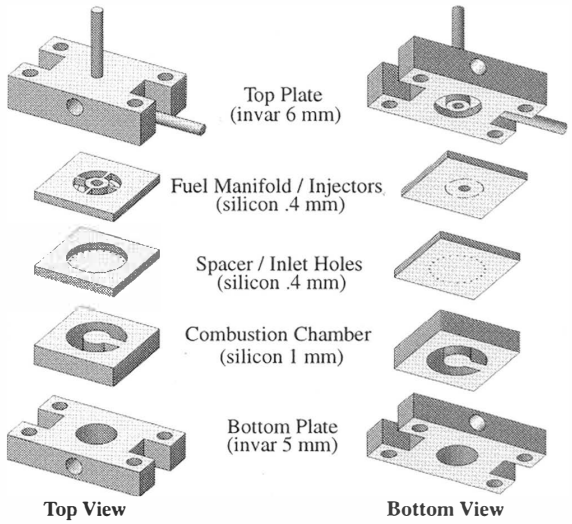

Figure 6: A schematic of the microcombustor test rig (Wafer thicknesses are exaggerated for illustrative effect).

Results

Atmospheric test results were obtained for premixed and non-premixed hydrogen-air combustion over most of the flammability range. The combustor operating parameters under stoichiometric conditions are shown in Table 1. The

Air mass flow $\dot{m}_a$ (g/sec)	.045
Fuel mass flow $\dot{m}_f$ (g/sec)	1.3×10^{-3}
Flow residence time (sec)	1.7×10^{-3}
Average wall temperature (K)	900
Exit temperature (K)	1800
Fluid power (Watts)	70
Combustor efficiency	44%
Space heating rate ($MW/m^3/atm$)	~ 1000

Table 1: Microcombustor operating parameters for stoichiometric hydrogen combustion at 1 atm. (premixed).

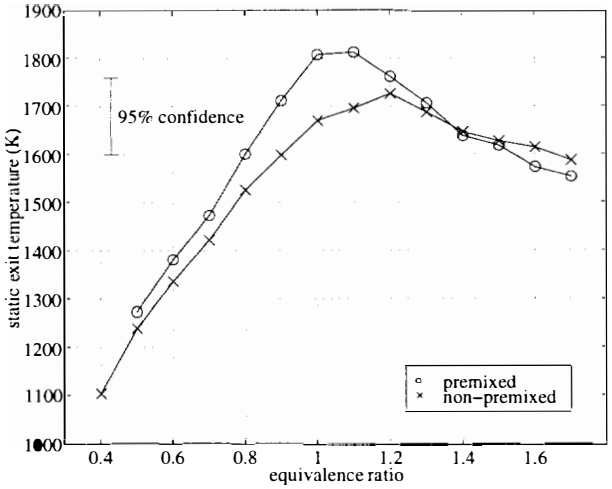

Figure 7: Microcombustor test results, showing exit temperatures up to 1800K.

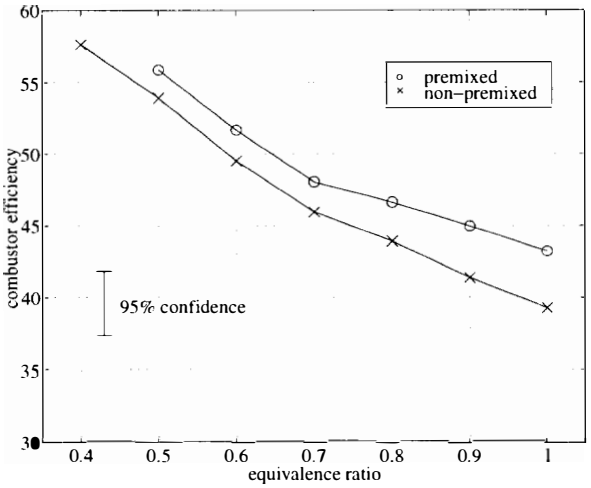

Figure 8: Efficiency measurements for the microcombustor.

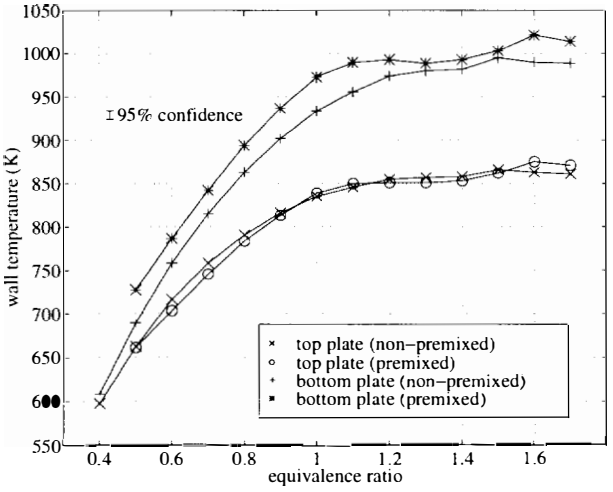

Figure 9: Microcombustor test results, showing wall temperatures well below the melting point of silicon.

corrected results for the exit temperatures are also shown in Figure 7, indicating satisfactory attainment of exit temperatures up to 1800K. As expected, the peak exit temperatures occurred slightly beyond stoichiometric conditions. For the premixed case however, the exit temperatures were approximately 100K higher, suggesting incomplete fuel-air mixing upstream of the combustor. This is attributed to a slight mis-alignment of the wafers during bonding, which effectively reduced the fuel mixing length on one side of the combustor.

Even though desired turbine inlet temperatures were obtained, poor thermal isolation of the rig resulted in excessive heat loss. As defined in Eq. (1), and shown in Figure 8, the combustor efficiency was found to be in the range of 40%-60%.

$$\eta_{comb} = \frac{(\dot{m}_a + \dot{m}_f)C_pT_{exit} - \dot{m}_aC_pT_{inlet}}{\dot{m}_f h_f} \quad (1)$$

The losses correlated well with a simple heat transfer model for the heat loss through top and bottom invar plates, suggesting that incomplete combustion was not the source of the inefficiency. Thus, the *combustion* efficiency is predicted to have been close to unity, even though the combustor efficiency was significantly lower. Currently, efforts are underway to improve the thermal insulation of the rig, and increase the combustor efficiency into a more desirable range.

As shown in Figure 9, the walls of the combustor were found to be relatively cooler than the combustion gases. This is attributed to the excessive heat loss out of the combustor, which allows the structure to operate below the melting point of silicon even as the combustor gas temperature is in excess of 2000K. While improved thermal insulation is expected to raise the wall temperature, the reduced equivalence ratios required to achieve desired turbine inlet temperatures would also correspondingly lower the chamber temperature. This suggests that the combustor walls shall continue to operate at relatively cooler temperatures, even if thermal insulation and combustor efficiency are further increased.

Overall, while high pressure testing and improved temperature diagnostics still need to be employed, the combustor has been successfully tested to provide turbine inlet temperatures of up to 1800K for over fifteen hours. As shown in Figure 10, the structure maintains its structural integrity, and shows no visible damage. These results demonstrate the satisfactory performance of a micromachined silicon combustor for applications in a micro heat engine.

OXIDATION, MATERIALS STUDY

As shown in Figure 10, post-combustion examination of the silicon microcombustor indicated oxidation patterns around the structure and the combustion inlet holes. A materials study was consequently undertaken to further quantify the effects of silicon oxidation in a combustion environment.

Oxidation Tests

As part of an oxidation study, a combustor plate consisting of "finger-like" structures with sizes between $20\mu m \times 500\mu m \times 450\mu m$ and $1600\mu m \times 2000\mu m \times 450\mu m$ was fabricated and tested inside the combustor. Shown in Figure 11, the plate was fabricated by anisotropically etching through a single $450\mu m$ silicon wafer.

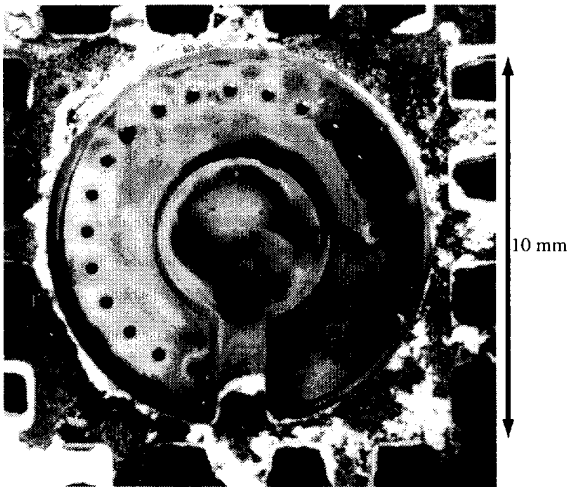

Figure 10: Post-combustion appearance of the rig after 15 hours of testing at T_{exit} ~1800K. While the oxidation patterns are apparent, the structure shows no visible damage.

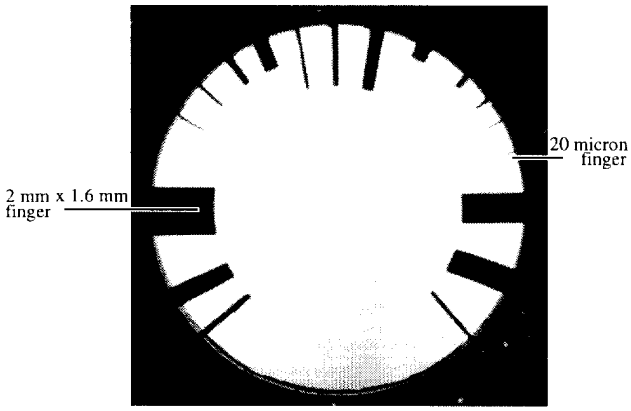

Figure 11: Photograph of the silicon combustor plate with "finger-like" structures (sizes range between 20μm × 500μm × 450μm and 1600μm × 2000μm × 450μm).

The structure was exposed to a combustion environment for over 8 hours at atmospheric pressures and flow temperatures in excess of 2000K[4]. Depending on the size and aspect ratio of the fingers, and hence the temperature at which they equilibrated, the fingers grew between 1μm and 10μm of amorphous oxide. This suggests that the "active-oxidation" of silicon is not an overriding concern for this particular application, the oxide thickness being the same order of magnitude as that predicted by the Deal-Grove passive oxidation model **(7)**.

The thinnest of the fingers however, measuring 20μm × 500μm × 450μm, grew crystalline oxide. This is shown in Figure 12. While the thinnest finger is expected to have experienced the highest tip and surface temperatures, the specific criteria causing the growth of crystalline versus amorphous oxide on the walls of the microcombustor have not yet been established.

Although atmospheric pressure testing failed to reveal any limiting failure mechanisms, elevated pressure testing of the fingered combustor plate identified creep to be the failure mechanism for silicon in microcombustion environments. As shown in Figure 13, at fluid temperatures in excess of 2200K, and at higher stress levels resulting from pressures of approximately 3 atm., several of the fingers were found to creep. The location of the point where the different fingers began to be bend correlated well with a two-dimensional heat transfer model for the temperature distributions along the length of the fingers. This suggests that creep failure of the fingers followed the brittle-to-plastic transition of silicon, occurring at approximately 900K.

[4]The overall wall temperature was once again in the range of a 1000K.

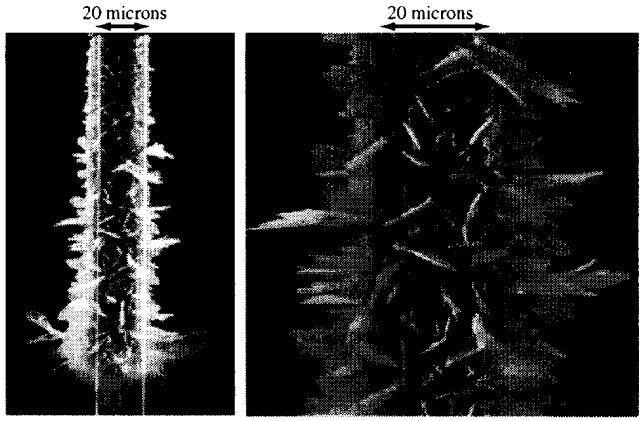

Figure 12: Crystalline oxide growth on the 20μm × 500μm × 450μm finger.

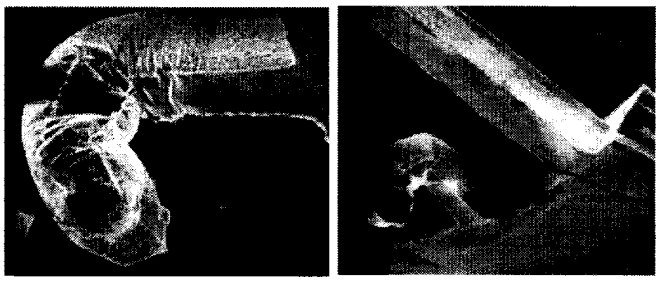

Figure 13: SEM of a 200μm × 450μm × 2000μm structure after combustion, showing creep limited performance of silicon.

Turbine Vane Tests

Although atmospheric tests showed that oxidation was not a limiting factor in the operation of a silicon microcombustor, the impact of higher Mach number (~ 1) and associated higher heat transfer rates in a typical turbine flow environment is unknown. While the effects on the critically stressed rotor cannot be assessed in the absence of a spinning structure, a set of 150μm high turbine nozzle guide vanes was exposed to the combustor exhaust in order to examine the effects of oxidation in a highly erosive, high temperature and pressure, supersonic flow environment. Figure 14 shows before and after pictures of a turbine stator vane following a five hour exposure to combustion exhaust at 1800K and 2.5 atm., and at a mass flow of 0.1 g/sec. While "pitting" and erosion is visible on the blade surface,

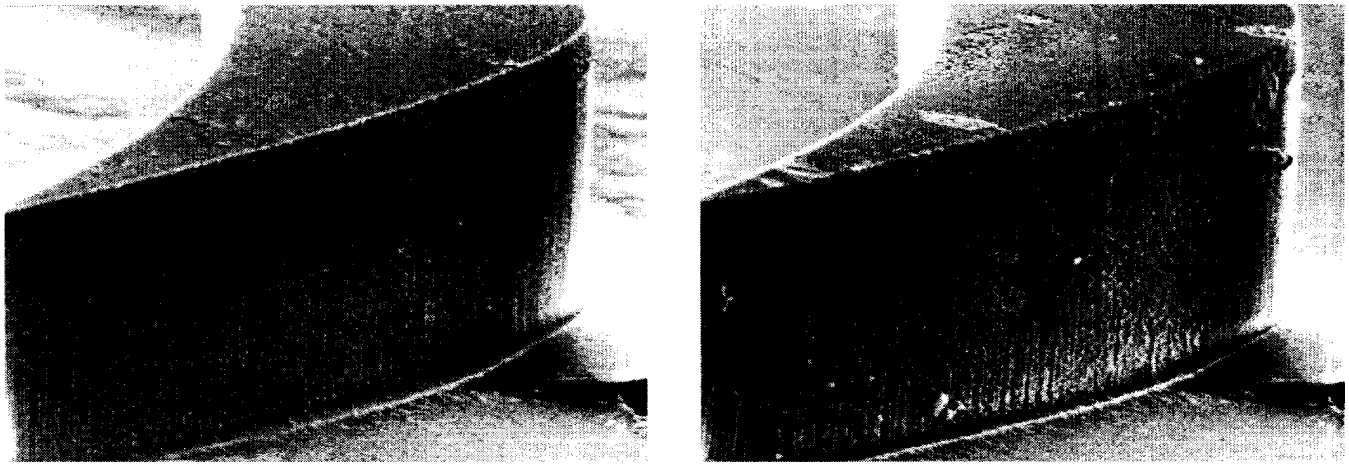

Figure 14: Before and after pictures of the vanes following a 5 hour exposure to combustion exhaust gases at 1800K, Mach number ~ 1. Although the blades exhibit minor erosion and "pitting", they maintain their structural integrity. (The blades are 150μm high).

the vanes appeared to be minimally damaged; the increase in throat area resulting in no more than a 2% change in mass flow. This establishes the survivability of a static vane structure in a high pressure and temperature, and high Mach number flow environment.

SUMMARY AND CONCLUSIONS

As part of an effort to develop a micro gas turbine engine using silicon microfabrication technologies, the design, fabrication and testing of a first-ever hydrogen combustor micromachined from silicon has been reported. Complete with a fuel manifold and injector holes, the combustion chamber measuring less than 0.07 cm^3 in volume has been successfully demonstrated to sustain premixed and non-premixed hydrogen combustion, providing exit temperatures of up to 1800K. While the performance of silicon was found to be creep limited at elevated pressures and temperatures in excess of 2200K, the combustor has been experimentally tested at elevated temperatures for over fifteen hours, thereby demonstrating the satisfactory performance of silicon in such harsh environments. Combined with the results of an oxidation study which showed that the performance of a silicon microcombustor will not be oxidation limited, these results are an important step towards establishing the viability of building a new generation of micro heat engines using silicon microfabrication technology.

ACKNOWLEDGMENTS

We would first like to recognize and thank Professor Alan H. Epstein for his conception and pursuit of the MIT microengine project, and for being a constant source of encouragement and inspiration. We acknowledge the support of the fabrication team comprising Professor Martin A. Schmidt, Professor Stephen D. Senturia, Dr. Arturo A. Ayon, Dr. Reza Ghodissi, and C. C. Lin, for training and provision of etch recipes. We are also grateful to all the other members of the MIT microengine team for support during various stages of this research, especially Dr. Gautam Gauba and Yang-Sheng Tzeng for their research on temperature diagnostics for microcombustion phenomenon. Finally, special thanks to Diana Park for all the help with the graphics.

This work was largely supported by the Army Research Office through Grant DAAHO4-95-1-0093, with Dr. Richard Paur as program manager. All devices were fabricated at the MIT Microsystems Technological Laboratories.

Nomenclature

T	Temperature (K)
C_p	Specific heat at constant pressure (kJ/kg-K)
h_f	Fuel heating value (kJ/kg)
$\dot{m}_a$	Mass flow rate of air (kg/sec)
$\dot{m}_f$	Mass flow rate of fuel (kg/sec)
η_{comb}	Combustor efficiency

References

[1] Epstein *et al.*, *"Micro-Heat Engines, Gas Turbines, and Rocket Engines"*, presented at the 28^{th} AIAA Fluid Dynamics Conference, 1997.

[2] Groshenry, C., *"Preliminary Study of a Micro-Gas Turbine Engine"*, S.M. Thesis, Massachusetts Institute of Technology, 1995.

[3] Waitz, I. A., Gauba, G., Tzeng, Y-S., *"Combustors for Micro-Gas Turbine Engines"*, Proceedings of the ASME Aerospace Division, AD-Vol. 52, 1996.

[4] Kerrebrock, J. L., *"Aircraft Engines and Gas Turbines"*, 2nd ed., MIT Press, 1992.

[5] Ayon *et al.*, *"Characterization of a Time Multiplexed Inductively Coupled Plasma Etcher, Part 1"*, submitted to the Journal of Vacuum Science and Technology, 1997.

[6] Tzeng., Y-S., *"An Investigation of Microcombustion Thermal Phenomenon"*, S.M. Thesis, Massachusetts Institute of Technology, 1997.

[7] Deal, B. E., Grove, A. S., *"General Relationship for the Thermal Oxidation of Silicon"*, Journal of Applied Physics, Vol. 36., p. 3770., 1965.

Etching Characteristics and Profile Control in a Time Multiplexed Inductively Coupled Plasma Etcher

A. A. Ayón, C. C. Lin, R. A. Braff, and M. A. Schmidt
Department of Electrical Engineering and Computer Science (EECS)

R. Bayt
Department of Aeronautics and Astronautics

H. H. Sawin
Department of Chemical Engineering & EECS

Microsystems Technology Laboratories
Massachusetts Institute of Technology

ABSTRACT

This paper reports on a complete designed experiment of a deep reactive ion etch process in which matrices of 8 and 4 variables were explored in order to optimize uniformity, anisotropy, Aspect Ratio Dependent Etching (ARDE), photoresist and silicon etching rate. A database results from these experiments which permits customization of operating conditions to obtain desired etch characteristics.

INTRODUCTION

Until the advent of high density plasma etchers, the options for fabricating High Aspect Ratio Structures (HARS) in silicon, such as reactive ion etching (RIE) and electron cyclotron resonance (ECR), had limited success in fulfilling the requirements of high etch rate, good selectivity to masking material, anisotropy and compatibility with other processes. A recent alternative that is satisfying the need of such processes is the time multiplexed deep etcher (TMDE) patented by Robert Bosch Gmbh **[1]**. This approach utilizes an etching cycle flowing only SF_6 (figure 1), and then switches to a sidewall passivating cycle using only C_4F_8.

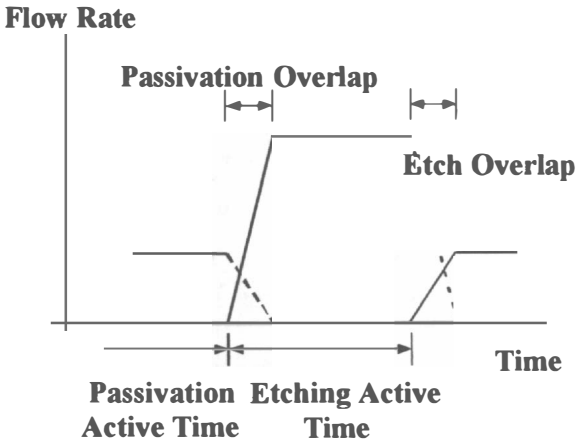

Figure 1. Graph showing the gas flow cycles during plasma etching. Note the overlaps caused by the finite time response of the flow controllers.

During the subsequent etching cycle, the passivating film is preferentially removed from the bottom of the trenches due to ion bombardment, while preventing etch of the sidewalls. The final result is anisotropic sidewalls that exhibit scalloping (figure 2), with peak to valley amplitudes as low as 50 nm. Higher electrode power to pressure ratios and shorter etching cycles reduce this effect.

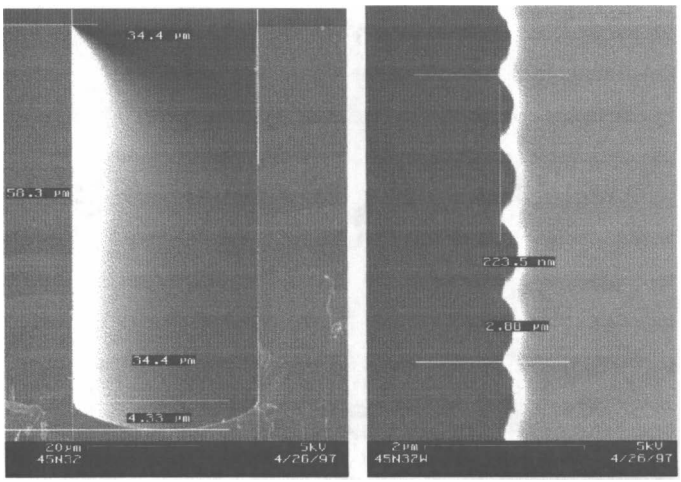

Figure 2. Micrograph view of an anisotropic etch (left) and the scalloping observed on the walls due to the periodic etch/deposition.

The success of Bosch's TMDE scheme, hinges upon the deposition of the inhibiting films. These films prevent the etching of the sidewalls by SF_6 discharges that contain large concentrations of atomic fluorine that spontaneously etches silicon. SF_6 discharges lack polymer forming species to block spontaneous etching **[2]**.

By supressing the time multiplexing, the equipment can be run with continuous flows of SF_6 or C_4F_8. With SF_6 it is possible to achieve isotropic etch rates as high as 1380 Å/sec. Using C_4F_8, teflon-like films can be deposited for use as anti-stiction films.

EXPERIMENTAL DETAILS

This work was performed using a Surface Technology Systems Multiplex ICP. The equipment includes two independent 13.56 MHz RF power sources: a 1000 W supply for a single-turn inductive coupling coil around the etching chamber to create the plasma, and a 300 W supply connected to the wafer electrode to vary the RF bias

0-9640024-2-6/hh1998/$20©1998TRF
DOI 10.31438/trf.hh1998.10

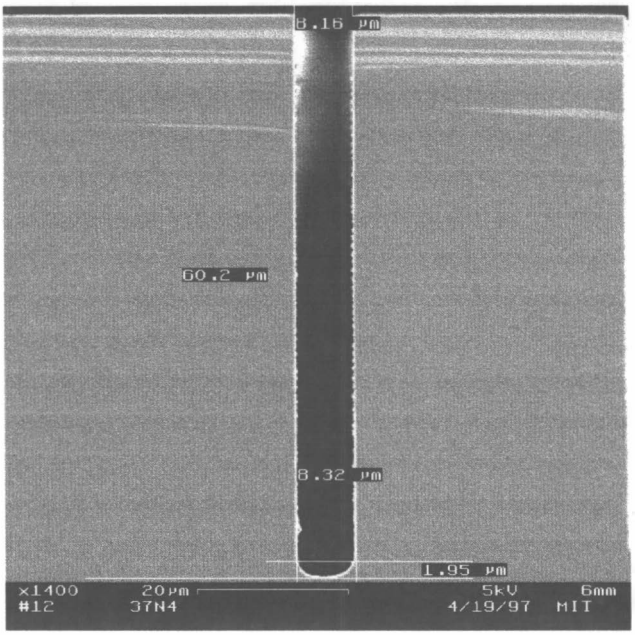

(a)

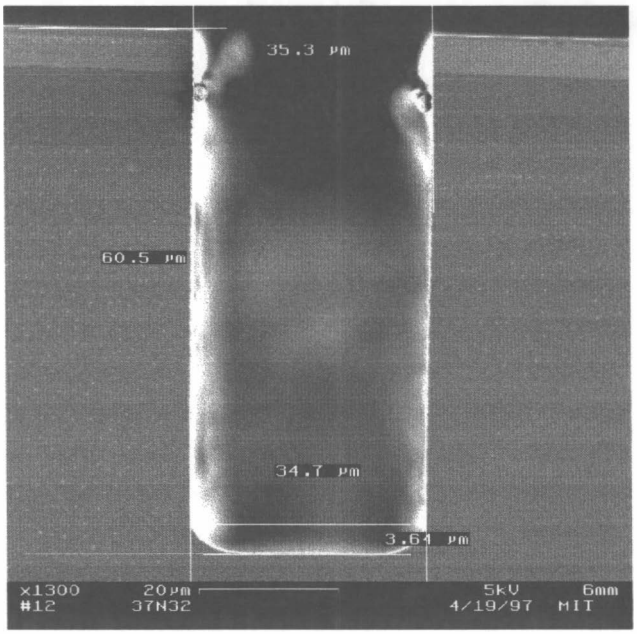

(b)

Figure 5. Trenches of width 8.32 μm in (a) and 35.3 μm in (b). Their measured depth differs by only 0.3 μm.

Uniformity values were obtained by comparing the depth of trenches of nominal width of 64 μm in the middle of the wafer, with trenches located 3 cm away. This variable is important because of its influence in determining the overetch time needed to completely clear features throughout the wafer. In the low electrode power region (~8 W), this variable benefits from lower SF_6 flow rate, while in the mid to high applied electrode power regions (~12 W), it is necessary to increase the SF_6 flow rate. In general, lower operating pressure settings are benefitial for this response because the diffusivity varies inversely with the pressure.

Anisotropy is of importance in every application, and the ability to tailor the slope of trench walls is one characteristic of this deep silicon etching tool. As expected, anisotropy has a well defined dependence on applied electrode power and chamber pressure [9]. Anisotropy increases as the applied RF-bias electrode power is increased.

With pressure the behavior of this response is different. Initially, anisotropy increases with pressure increases, as thicker polymer films are deposited protecting the sidewalls. However, as the pressure is increased even further, the reduction in the average ion energy as well as the increase in the ion angle of incidence combine to produce deleterious effects on anisotropy.

It was also observed the relevance of SF_6 flow rate in tailoring the anisotropy. In general, higher SF_6 flow rates decrease the anisotropy and promote surface roughening (figure 6).

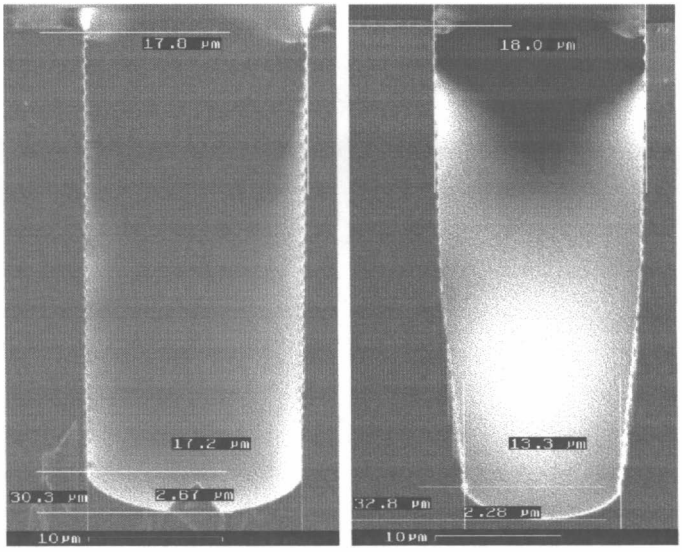

Figure 6. Micrographs of trenches etched in 10 minutes with an SF_6 flow rate of 85 sccm (left) and 125 sccm (right) respectively.

Among the applications of the obtained information is the etching of deep narrow trenches like the one shown in figure 7. In that figure, the trench presented has an average width of 12 μm and a measured depth of 404 μm. Narrower trenches and submicron thin walls are also possible and this is shown in figure 8.

Other applications include the utilization of the passivation films to control the notching effect when etching SOI wafers. This is accomplished by depositing a thicker polymer film when approaching the buried dielectric layer (figures 9).

CONCLUSIONS

The observed behavior presented in this report is an important tool to locate and optimize operating conditions to etch high aspect ratio structures. The performance of this deep reactive ion etcher allows the tailoring of etch rates of 4+ μm/min with anisotropic profiles, nonuniformities of less than 4 % across the wafer, and ARDE control with a depth variation of less than 1 μm for trenches of dissimilar width.

potential of the wafer with respect to the plasma. This arrangement permits the independent control of the energy of the ions reaching the substrate as well as the ion flux **[3]**.

Backside helium pressurization is used to provide good heat transfer between the wafer and the electrode to maintain a constant wafer temperature. Low temperatures reduce the etching rate of the photoresist, thereby allowing its use as a mask for etching silicon. The photoresist can also be used as a bonding material for mounting the device wafer to a handle wafer during processes requiring etching through a wafer **[4]**. This mounting is required to prevent helium leaks into the chamber. Device wafers can also be mounted on quartz wafers for visual verification of the etch completion.

It is possible to operate with a predetermined common pressure for both etching and passivating active cycles, or with a fixed angular position for the opening of the automatic pressure control valve (APC). In the first case the position of the throttle valve (or APC valve) varies as the gas flow changes during each cycle. In the latter case, the position of the throttle valve is fixed and the pressure is determined by the gas flow rate. The results presented in this report used this latter approach. Higher values of the APC valve position in degrees correspond to higher pressures. However, the trip pressure is fixed at 90 mT creating an upper pressure limit in these experiments.

For the eight-variable experiment the samples were prepared in the following fashion: 4" single crystal silicon <100> wafers were coated with photoresist AZ4620 (Hoechst Celanese, Sunnyvale, CA) spun at 3000 rpm (thickness ≈6 μm) and baked in a convection oven at 90°C for 30 minutes. The samples were then exposed in a contact aligner with a wavelength of 320 nm and power density of 6 mW/cm^2, developed with AZ440 (Hoechst Celanese, Sunnyvale, CA), and baked again at 90°C for 30 minutes. We used an SEM to study each etched sample. The etching time for these samples was fixed at 30 minutes each.

In order to obtain information on the influence of coil power during etching, an additional four-variable experiment was also performed. This matrix consisted of samples prepared in the following fashion: 4" single crystal silicon <100> wafers were coated with photoresist OCG 825 (Shipley, Marlboro, MA), with viscosity 20 cs, baked and exposed in the same fashion but developed with OCG 934 (1:1). In this case the expected photomasking material thicknes is approximately 1 μm. We used an optical interferometer to measure the thickness of the photoresist layer before and immediately after etching each sample, and a profilometer to measure the depth of the etched trenches. All etches had a duration of 3 minutes.

These sets of experiments are adequate to fit a quadratic model and were analyzed using commercial software. The systematic investigation produced response surfaces **[5]** that enable us to predict appropriate operating conditions for different processing requirements.

MEASURED PERFORMANCE

The etching rate of silicon has a predominant dependence on applied coil power (figure 3), because this input determines the degree of ionization and dissociation of the glow discharge. Although not seen in figure 3, this response also benefits from higher SF_6 flow rates as well as higher applied electrode power settings. Increasing electrode power during the etching cycle increases primarily the ion bombardment energy and secondarily the ionization and dissociation of the discharge, all of which increase the etching rate. For low SF_6 flows, power increases only have a marginal effect on etching rate. At low flows the concentrations of products (SiF_4) that dissociate and redeposit increases **[6]**.

The etching rate dependence on trench width, also known as ARDE **[7, 8]**, varies with operating conditions (figure 4) and, therefore, it is also feasible to control this effect. ARDE benefits with high SF_6 flow rates because of the reduction of product species in the discharge that contribute to redeposition. An example that exhibits small ARDE is shown in figure 5. This was accomplished by using an SF_6 flow rate of 140 sccm.

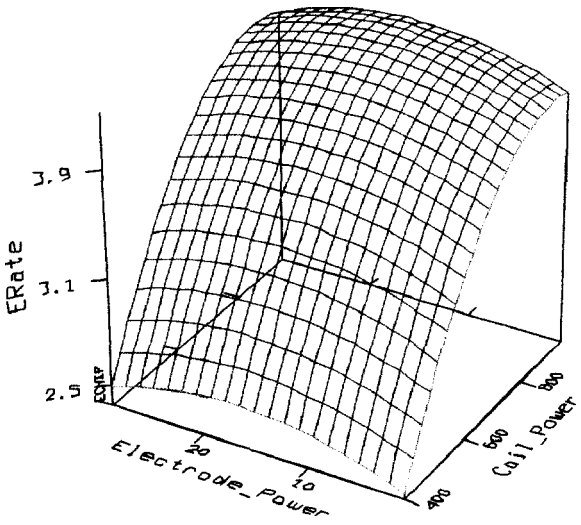

Figure 3. Silicon etching rate (μm/min) dependence on applied RF-bias electrode power (W) and RF-inductive coil power (W).

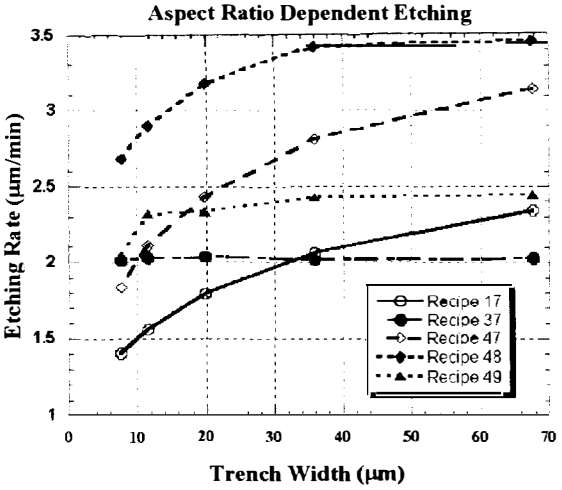

Figure 4. Aspect Ratio dependent Etching variation with trench width for different operating conditions.

Low photoresist etching rate is necessary for robust operation. This response is strongly influenced by the applied electrode power, because this variable determines the ion bombardment energy. Lower electrode power settings are always favorable for achieving high selectivities. Furthermore, higher pressure settings also benefit this response.

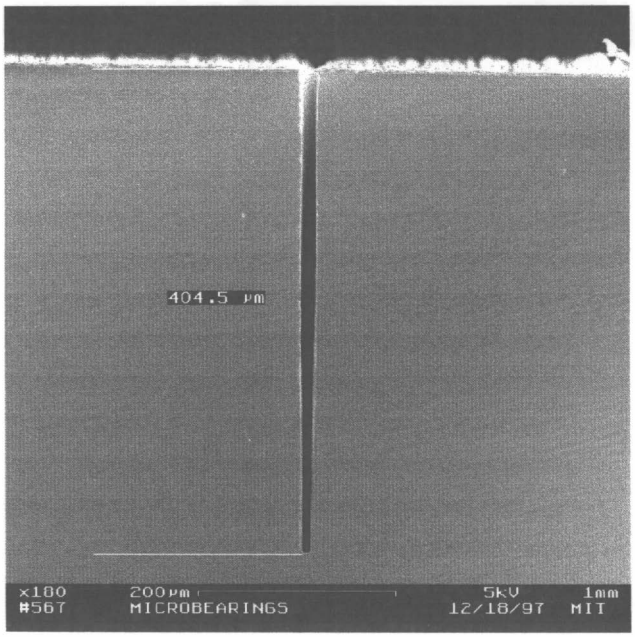

Figure 7. Micrograph of a trench etched applying 600 W during the passivation cycle and 750 W during the etching cycle.

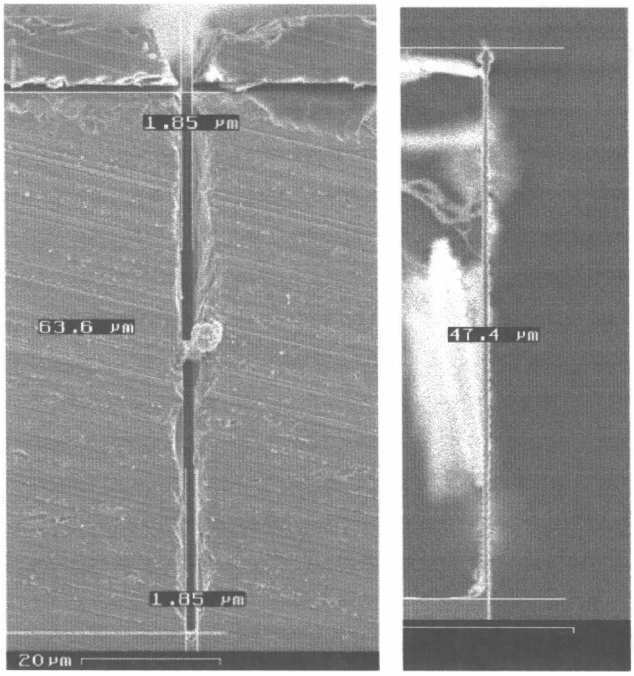

Figure 8. Micrograph of a trench 1.85 µm wide and 63.6 µm deep on the left, and a wall 0.8 µm thick and 47.4 µm tall on the right.

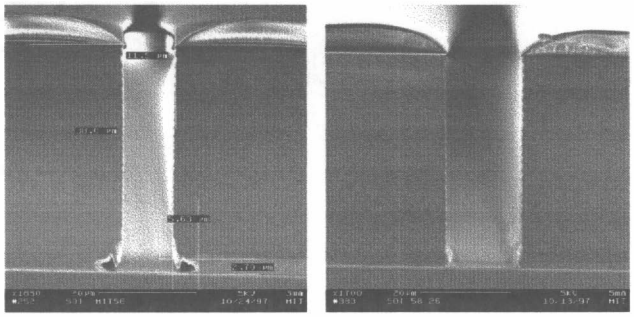

Figure 9. The footing effect appears when the etch stops on a buried oxide layer. It is clearly seen in the left micrograph. This effect can be suppressed controlling the passivation films as shown in the right micrograph.

ACKNOWLEDGMENTS

We thank Dr. R. Paur, U.S. Army Research Office, and Dr. R. Nowak, DARPA, for support of this project, and a NSF Fellowship (R.A.B). The cooperation of the staff of the Microsystems Technology Laboratories at MIT is also appreciated.

REFERENCES.

1. Robert Bosch Gmbh, patents 4855017 and 4784720 (USA), and 4241045C1 (Germany).
2. A. J. Roosmalen, J. A. G. Baggerman and S. J. H. Brader, "Dry Etching for VLSI", p. 113, Plenum Press (1991).
3. M. A. Lieberman and A. J. Lichtenberg, "Principles of Plasma Discharges and Materials Processing", p. 387, John Wiley, 1994.
4. R. Bayt, A. A. Ayón and K. Breuer, "A Performance Evaluation of MEMS-based Micronozzles", 33rd AIAA/ASME/SAE/ASEE Joint Propulsion Conference & Exhibit, Seattle (1997).
5. I. Tepermeister, N. Blayo, F. P. Klemens, D. E. Ibbotson, R. A. Gottscho, J. T. C. Lee and H. H. Sawin, "Comparison of Advanced Plasma Sources for Etching Applications. I. Etching rate, Unifomity, and Profile Control in a Helicon and a Multiple Electron Cyclotron Resonance Source", J. Vac. Sci. Technol., B12, 2310 (1994).
6. D. C. Gray, I. Tepermeister and H. H. Sawin, "Phenomenological Modeling of ion-enhanced surface kinetics in fluorine-based plasma etching", J. Vac. Sci. Technol., B11, 1243 (1993).
7. R. A. Gottscho, C. W. Jurgensen and D. J. Vitkavage, "Microscopic uniformity in plasma etching", J. Vac. Sci. Technol. B10, 2133 (1992).
8. J. Logan, K. Petersen, E. H. Klaassen, M. Noworolski, N. Maluf and W. McCulley, Proceedings of the third International Symposium on Semiconductor Wafer Bonding: Physics and Applications, Vol. 95-7, pp. 489-496, 1995.
9. C. B. Zarowin, "Relation between the RF discharge parameters and plasma etch rates, selctivity and anisotropy", J. Vac. Sci. Technol., 2A, 1537 (1984).

Multiple Depth, Single Crystal Silicon MicroActuators For Large Displacement Fabricated by Deep Reactive Ion Etching

Chris Seung-Bok Lee, Sejin Han* and Noel C. MacDonald

School of Electrical Engineering and The Cornell Nanofabrication Facility
Cornell University, Phillips Hall, Ithaca, NY 14853
* School of Mechanical and Aerospace Engineering, Cornell University

ABSTRACT

The design, fabrication and testing results of a Single-Crystal-Silicon (SCS) comb-drive actuator fabricated at two depth levels by Deep Reactive Ion Etching (DRIE) are presented in this paper. Prior work on deep microactuators has focused on DRIE or LIGA where the height of the spring is the same as the height of the comb fingers. In this paper, we present a DRIE fabricated comb drive actuator where the height of the spring is significantly less than the height the comb fingers. This gives the benefit of a compliant spring with a large displacement per unit of actuator force. A single mask, multiple depth fabrication allows the spring depth to be controlled independent of the depth of comb fingers, utilizing the loading effect of the Bosch silicon etching process and the masking of released beams using PECVD oxide.

A displacement of 130 μm at 37 volts is achieved on a 4 mm by 4 mm comb-drive actuator, where the comb fingers are 100 μm deep and the depth of folded flexure springs is 22 μm. A resonant frequency of 220 Hz is measured in air. Different suspension systems are evaluated using ABAQUS simulation, and the experimental results of the actuator are shown to be in a good agreement with the simulation.

INTRODUCTION

Bosch silicon etching process [1] is a newly developed deep silicon dry etching technique at room temperature involving a cycle of silicon sidewall passivation and an aggressive SF_6 etch. A typical silicon etch rate is 3.5 μm/min with a selectivity of 100:1 on oxide and 50:1 on photoresist. The PlasmaTherm SLR-770 (Shuttle Locked Reactor) runs the Bosch process using an inductively coupled plasma source at 2 MHz and an industry standard 13.56 MHz RF source to generate a high density plasma. By controlling more than 15 process parameters during the etch step and the passivation step, we have recently fabricated a wide range of complex 3-D structures that are often impossible to construct using a conventional RIE technology [2].

Bosch silicon etching is ideally suitable for fabricating a large displacement, high force actuator because of its ability to produce straight and deep high aspect ratio fingers. A single mask, multiple depth process allows the spring depth to be controlled independent of the depth of comb fingers, utilizing the loading effect of Bosch silicon etching process and the masking of released beams using PECVD oxide.

In this paper, we fabricated a deep etched comb drive actuator where the depth of the spring is 22 μm and the depth of the comb fingers is 100 μm. It results in a spring stiffness small enough to achieve a significant increase in the displacement per unit of actuator force. A displacement of 130 μm at 37 volts is measured on a 4 mm by 4 mm comb-drive actuator. This device has a resonant frequency of 220 Hz in air. The resonant frequency is expected to increase to approximately 500 Hz with a modified layout in future work.

Such a large linear displacement at a low operating voltage is attractive in x-y microstage applications [3], data storage technology [4-5], and applications that require positioning various nanotools [6].

The two level depth process can easily be scaled for the fabrication of multiple depths of high-aspect-ratio single crystal silicon structures on a single wafer, as will be discussed in the fabrication section. The fabrication of self-aligned, two-level structures is also demonstrated using the same two level depth process flow. This allows the benefit of a compliant spring system coupled to a large capacitance and a high proof mass structure.

DESIGN CONSIDERATIONS

Spring design

To achieve large displacements at low operating voltages, a suspension system must be compliant in the direction of displacement. Stiffness in the orthogonal directions must be high in order to prevent side instability. To design an optimum suspension system, ABAQUS was used to simulate the displacement as a function of the actuator force for three different spring systems: fixed-fixed, crab legs, and folded flexure. In the simulation, three dimensional beam element were used. Materials were assumed to deform elastically. The nonlinear geometry option was used to calculate the large deflection behavior of the beam. Boundary conditions were defined such that the spring was assumed to be clamped at the pad.

At a given spring dimension, the ABAQUS simulation showed that the folded flexure design has the largest deflection per unit of force and the largest linear deflection range, as shown in Figure 1. This result is in a good agreement with a previous work on the evaluation of various suspension systems for large displacement purposes [7].

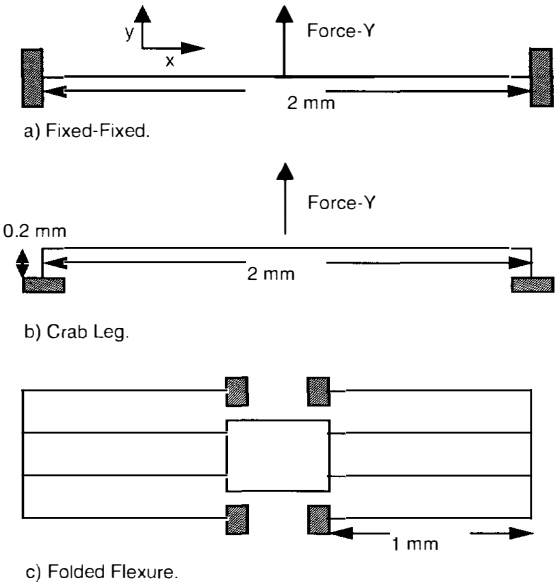

Figure 1. (a)- (c) Three different spring structures for the simulation.

0-9640024-2-6/hh1998/$20©1998TRF
DOI 10.31438/trf.hh1998.11

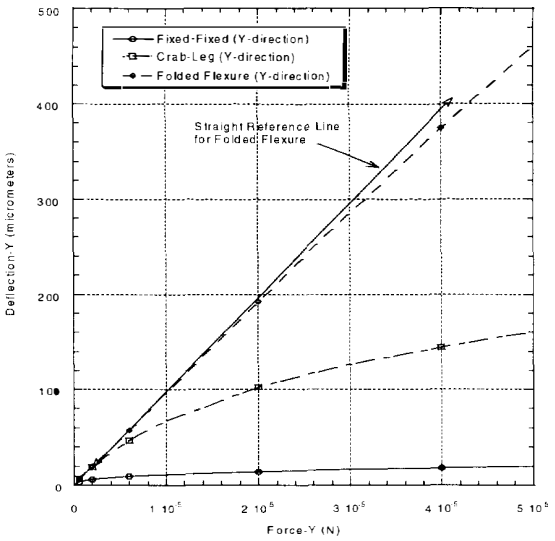

(d)

Fig 1. (d) ABAQUS simulation results for maximum deflection versus applied force. Three different spring systems are simulated and compared. The simulated beam depth, width and equivalent modulus are 20 μm, 3.05 μm and 92.3 Gpa, respectively. The linear deflection range of folded flexure is shown.

Stability and Design Parameters

The movable fingers of the comb drive are centered between the fixed fingers. This gives a zero resultant force along the direction perpendicular to the stroke avoiding a failure mode of movable fingers touching the fixed fingers. Any deviations from the perfect symmetry will cause the movable fingers to move perpendicular to the stroke direction. Side stability has been investigated previously **[7-8]**. Actuation stability is a function of several design parameters and can be summed up by the following expression, where a deflection greater than $Y_{critical}$ will cause side instability:

$$Y_{critical} = g\sqrt{\frac{k_x}{2k_y}} - \frac{y_0}{2} \qquad (1)$$

where g is the finger gap, y_o is the initial comb finger overlap, and the direction of actuation is in the y direction. The equation (1) indicates that actuators with smaller finger gaps become unstable at smaller displacements than those with the larger gaps, side instability is proportional to the overlap length and increases with applied voltage because the spring constant of folded flexure in the x-direction decreases with increasing beam displacement in the y-direction. For folded flexure system, spring constants in x and y directions are given by:

$$k_x = k_{x1}k_{x2} / (k_{x1} + k_{x2}) \qquad (2)$$

$$k_y = \frac{2 \cdot 2Ehb^3}{L^3} \qquad (3)$$

where h is the height of springs, L is the length of springs, b is the spring width, k_{x1} is the axial spring constant at zero-deflection, and k_{x2} accounts for the reduced axial spring constant as the lateral deflection increases,

$$k_{x1} = \frac{2 \cdot 2Ehb}{L} \qquad (4)$$

$$k_{x2} = \frac{2 \cdot 200EI}{3L\delta_y^2} \qquad (5)$$

A factor of 2 is included in each equation since there is a folded flexure spring at both ends of the backbone. At the stability limit, k_x is approximately equal to k_{x2}, and deflection in beam segment δ_y is approximately equal to $Y_{critical}$. By substituting (2) and (3) into (1), we obtain:

$$(Y_{critical})^2 + \frac{y_0}{2}(Y_{critical}) - gL\sqrt{\frac{25}{18}} = 0 \qquad (6)$$

Figure 2 shows a plot of $Y_{critical}$ as a function of folded flexure spring length, comb finger gap, and initial finger overlap. The graph shows a design space of these three parameters that satisfies the stability criteria given in equation (6). For a given value of desired displacement, various combinations of finger gap, spring length and overlap length can be selected. Actuators with smaller gaps become unstable at smaller displacements compare to actuators with larger gaps. Consequently, actuators with smaller gaps require a large value of L, increasing the ratio of k_x/k_y, to compensate for the effect of small g, as shown in equation (1).

In practice, two physical limitations restrict the length of springs and the size of finger gaps. As in a conventional RIE, Bosch etching is limited to an aspect ratio of about 30:1. Consequently, a limited range of finger gap sizes is available for a desired displacement based on the aspect ratio requirement. Secondly, thin PECVD oxide and Al films on a released silicon spring structure creates an intrinsic stress. As the length of the released springs increase, the displacement due to the intrinsic stress becomes greater, and a better design is needed to keep the spring planar **[9]**. Therefore, possible ranges of finger gaps and spring lengths are limited by the fabrication and physical constraints.

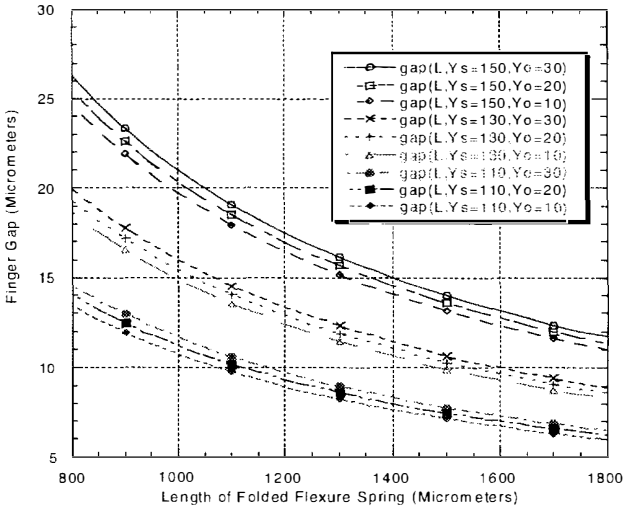

Figure 2. $Y_{critical}$ as a function of the folded flexure spring length, initial finger overlap, and the comb finger gap. Units are in micrometers. Y_s is the critical deflection, L is the length of spring, and Y_o is the initial finger overlap.

Design Parameters

In our initial design, we selected the folded flexure spring system based on comparisons in the previous sections. The comb actuators are attached to two folded flexure springs at each end of the backbone. We specified the depth of the comb fingers and the depth

of the backbone to be 100 μm. The silicon spring width and depth are 2 μm and 22 μm respectively. The initial finger overlap is 30 μm and the targeted displacement is 130 μm. As shown in Figure 2, the necessary finger gap is 14.5 μm for a spring length of 1100 μm to achieve $Y_{critical}$ of 130 μm. The fabricated actuator is shown in Figure 3.

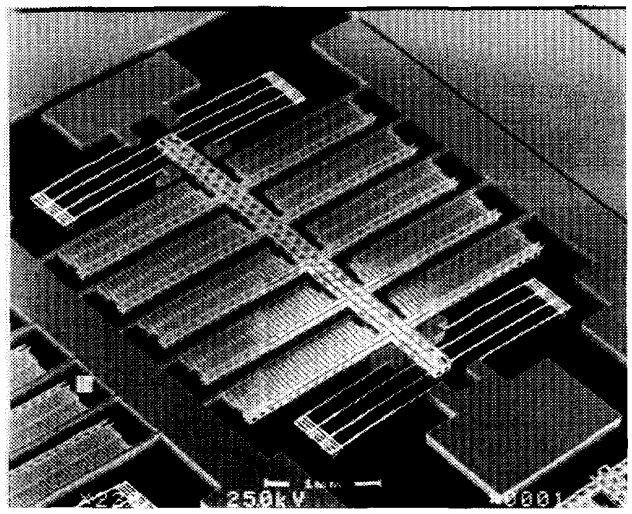

Figure 3. SEM of the deep etched microactuator

FABRICATION

The fabrication sequence for a large motion in-plane actuator is illustrated in Figure 4. A 2 μm thick PECVD oxide layer is deposited on a (100) P-type silicon wafer. This oxide thickness is needed since the typical selectivity of silicon to oxide in DRIE is 100:1. An additional 1 μm of oxide is conservatively added to protect silicon structures during the isotropic silicon etch for release. The oxide is patterned using OCG 897-21i resist on GCA 6300 i-line stepper, and the pattern is transferred to the SiO_2 film using CHF_3 plasma in a Magnetron RIE etcher as shown in Figure 4b.

A first deep silicon etch is performed using the PlasmaTherm SLR-770 for the first 22 μm. The patterned silicon structure is conformally passivated with PECVD oxide [Figure 4c]. After clearing the floor oxide using another CHF_3 plasma etch, a second deep silicon etch is carried out for an additional 30 μm, making the height of silicon structures thus far 50 μm [Figure 4d]. A time-controlled SF_6 plasma selectively releases the spring system since the width of silicon springs is 2.0 μm, whereas the silicon width of the remaining beams of the actuator is 4 μm. Only silicon beams with previously deposited PECVD oxide are protected during this step. Thus the springs are limited to a height of 22 μm [Figure 4e].

Once the springs are released, a third silicon etch step continues an additional 50 μm, making the comb fingers 100 μm tall [Figure 4f]. In order to release the movable fingers and the backbone, another layer of PECVD oxide is deposited. After the floor oxide etch, a 30 μm silicon etch is performed to facilitate the release of silicon structures using the isotropic SF_6 etch. Finally, aluminum is conformally sputtered for metallization [Figure 4g]. The electrical isolation is provided by a PECVD oxide overhang, where a portion of inner silicon core is etched out during the release process. This overhang isolates metal from the silicon substrate **[10]**.

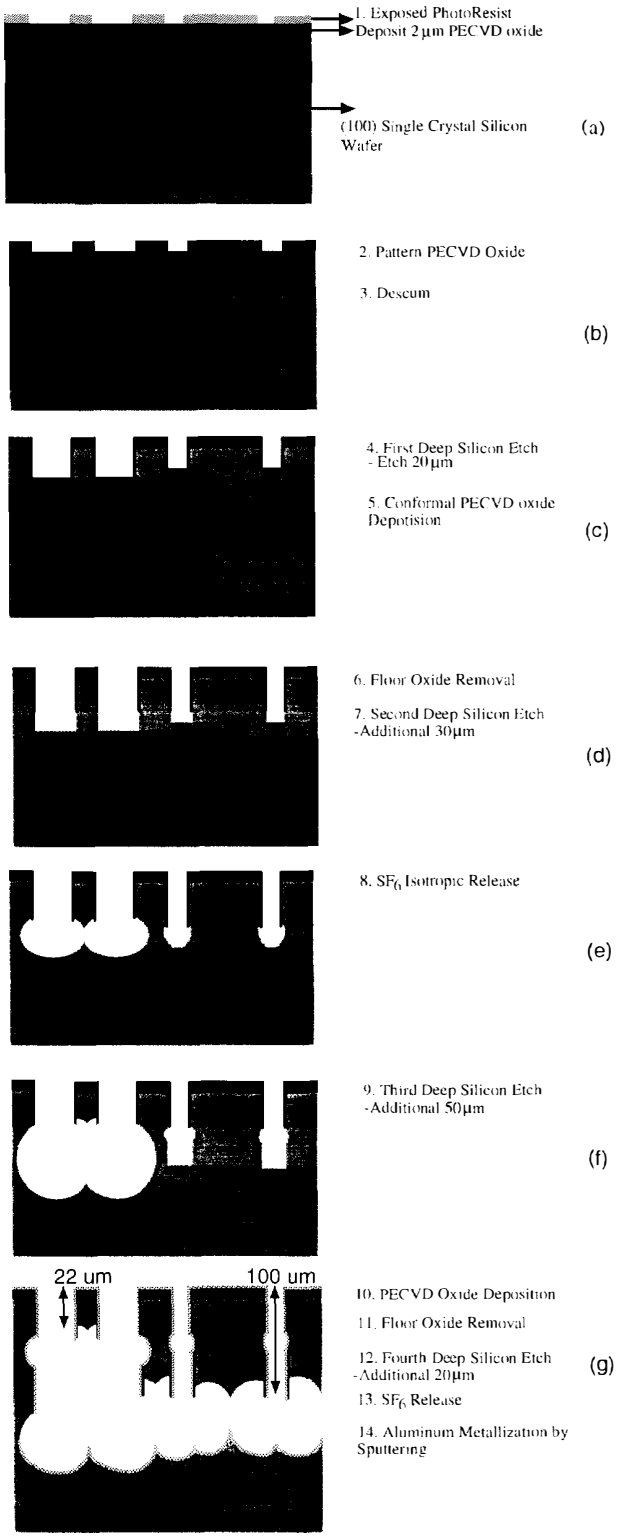

Figure 4. A schematic summary of process flow for two level depth large displacement microactuator.

The first isotropic SF_6 etch step produces a notch on wider beams that are not released. This may prevent a continuous metallization on the sidewalls. Therefore, it is important to minimize the first SF_6

etch time. There are three ways to ensure the minimal undercut. Taking advantage of the loading effect inherent in the Bosch process, the undercutting effects are minimized by the geometrical condition that the comb fingers are placed in a more confined area than the springs. Secondly, a time-controlled SF_6 etch is characterized so that the etch time is enough to release only the springs. By using a re-entrant profile, the width is reduced, requiring a shorter release time. These factors contribute to reducing the notching on the sidewall of deeper structures and permit a continuous metal film on the sidewall. The re-entrant profile of comb fingers in conjunction with the effects of the first two factors is shown in Figure 5.

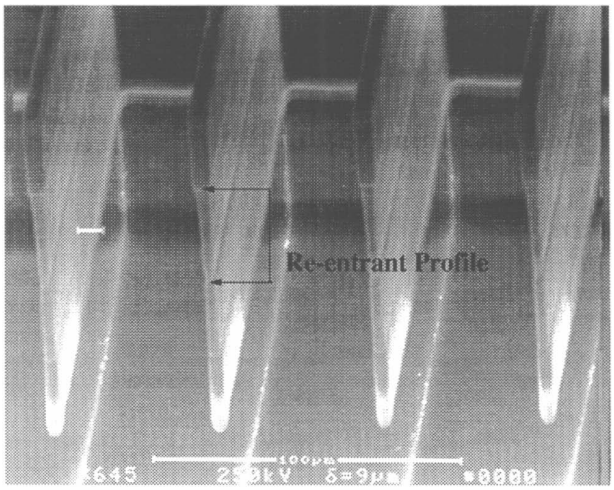

Figure 5. Re-entrant profile of comb fingers to minimize the first SF_6 etch time.

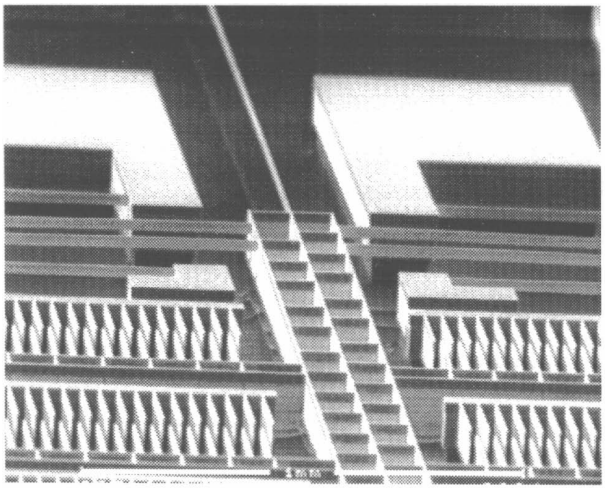

Figure 6(a). A 22 μm deep spring is attached to a 100 μm deep actuator.

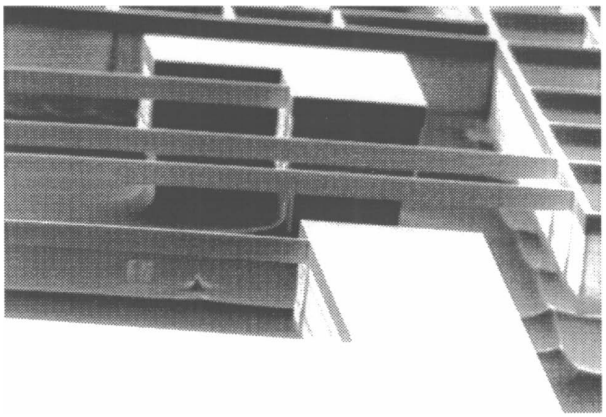

Figure 6(b). A closer view of 6(a)

Fabrication of SCS structures on a single wafer can easily be scaled from the two level depth process into multiple levels. In the two level fabrication, a smaller depth structure is made possible by selecting a narrow silicon beam width in an open space whereas the deeper structures are designed with a larger silicon beam width in a more confined space. For the case of a three level process, the deepest structure is fabricated by designing the silicon width to be more than the width of the less deep structures in a confined space.

In conjunction with the multiple depth fabrication, it is possible to fabricate multiple level structures [11] using the same process flow shown in Figure 4. For example, a released spring from 4(e) can serve as a mask for a shadow mask for producing an underlying structure. Since the Bosch Silicon etching is not based on a high degree of anisotropic bombardment of ions as in the standard RIE, the distance between the end of the released mask and the beginning of the substrate with respect to its open space must be optimized. If this distance is too large and/or its surrounding spacing is not confined enough, the substrate is exposed to the Bosch etching and the silicon underneath the masking silicon structure will be etched away. Self-aligned, two-level comb fingers are shown in Figure 7.

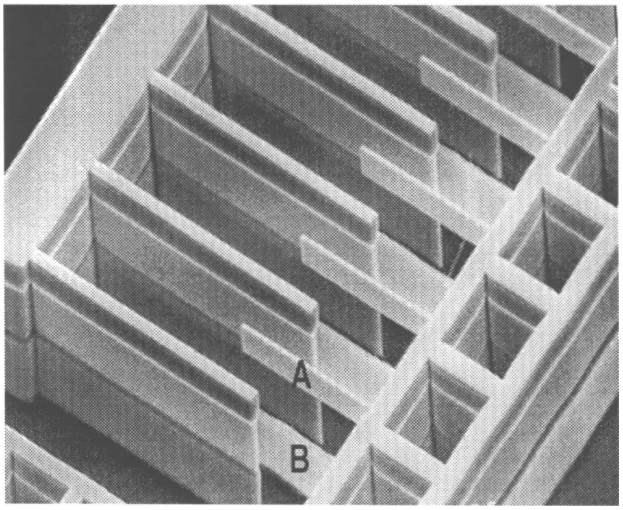

(a)

Figure 7. (a) SEM picture of self-aligned two level comb fingers fabricated by the two level process.

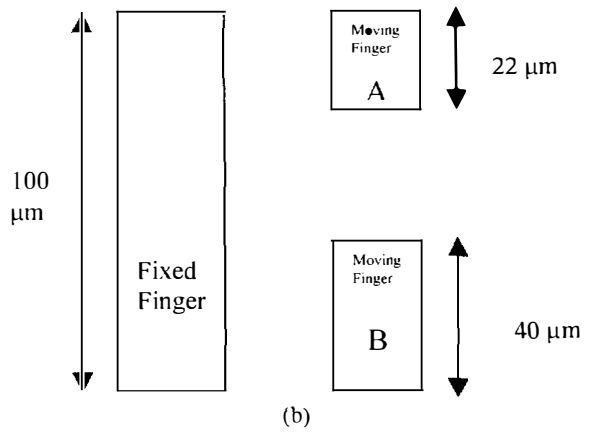

(b)

Figure 7. (b) Schematic cross-section of the device

RESULTS AND DISCUSSIONS

For a dc driving voltage, the displacement is given by:

$$d = \frac{nh}{2gK_y}V^2 \tag{7}$$

where n is the number of fingers, h is the height of comb fingers, g is the gap between comb fingers, k_y is the spring constant in the direction of displacement and V is the applied voltage. For this tested large displacement comb drive, there are 310 comb fingers and each finger is 100 μm tall with 15 μm gap spacing. The folded flexure spring is a composite material wherein the silicon core is surrounded by a layer of PECVD oxide and a layer of aluminum, as shown in Figure 8. For the calculation of k_y, a composite modulus needs to be approximated using the following equation **[12]**.

$$E_{eq} = \Sigma \frac{E_i(h_i^3 - h_{bi}^3)}{h_T^3} \tag{8}$$

where, h_i is a lateral distance from the center of the beam to the end of i layer, h_{bi} is a lateral distance from the center of the beam to the beginning of i layer and h_T is a half of total width of the beam. The equivalent modulus of 92.3 GPa is calculated for an effective spring width of 3.05 μm.

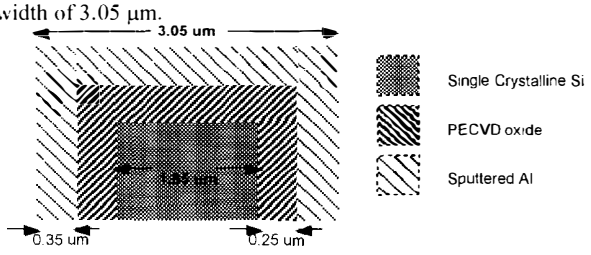

Figure 8. Cross-section of beam at the end of process.

A displacement of 130 μm is measured at 37 volts. Motion of the comb fingers under an optical microscope is shown in Figure 9. ABAQUS simulated values are shown to be in good agreement with the experimental results as indicated in Figure 10. The comparison of calculated and measured displacement shows that the small deflection theory is valid for displacements up to roughly 90 μm, which is approximately 8% of the spring length. This range of linearity for a folded spring structure is reasonably consistent with the work done by Legtenberg et al [7].

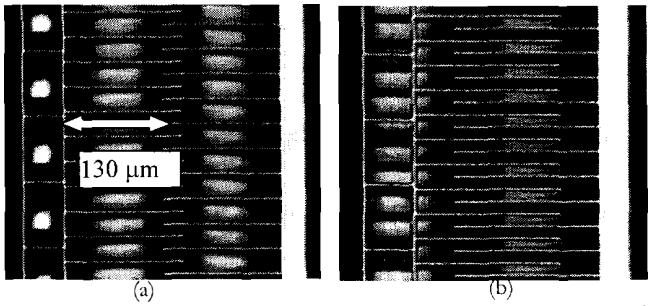

Figure 9. Optical microscope pictures. (a) The initial position of comb finger. (b) Displacement of 83 μm at 28 volts

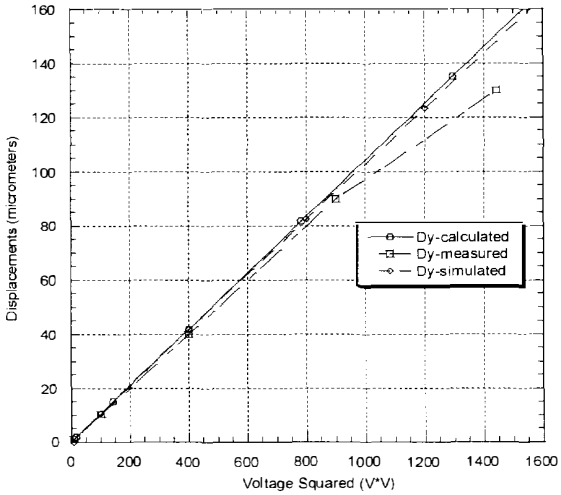

(a)

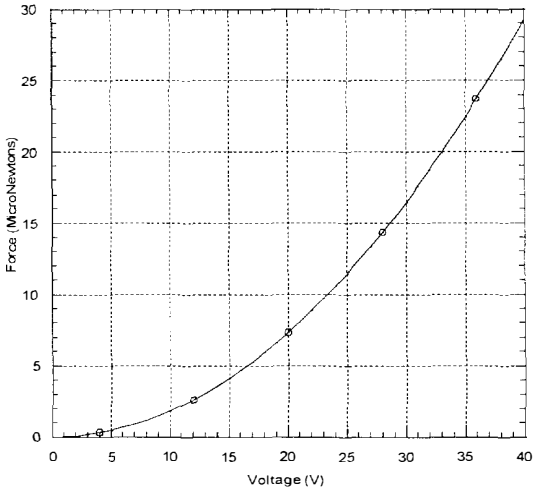

(b)

Figure 10. (a) Comparison of measured, simulated and calculated displacement as a function of voltage squared. (b) Actuator force as a function of applied voltage. There are 310 comb fingers, each with 15 μm finger gap, 30 μm initial finger overlap and 100 μm depth. The length of folded flexure spring is 1100 μm. They are 22 μm deep and the effective width is 3.05 μm.

Resonant frequency is expressed by:

$$f_r = \sqrt{\frac{k_{sus}}{m_{moving}}} \quad (9)$$

where m_{moving} is the mass of the moving structure and k_{sus} is the spring constant of suspension. The calculated value of resonant frequency is 198 Hz which is in reasonable agreement with the experimental measurement of 220 Hz. The discrepancy is most likely due to inaccurate measurements of the width of composite layers. A perfect rectangular cross section of deeper silicon structures is not possible due to the release of shorter beams as discussed above. Also, the etch profile tends to get slightly tapered as the aspect ratio increases. All these factors contribute to the difficulty of estimating the accurate mass of moving structures. For an accurate estimation of k_{sus}, the effect of small out-of-plane curvature on the spring needs to be accounted for, as the spring is not perfectly planar. A higher resonant frequency is possible by minimizing the dimensions of the actuator.

Future Work

Currently, we are working on the design of a large linear displacement x-y stage with a low operational voltage that can move more than a 100 μm in both x and y directions. The x-y stage is driven by four large displacement actuators. A mechanical coupling of suspension systems and the decoupling of x and y directions are carefully being investigated for stable operation.

Webb et al. have demonstrated isolated released silicon segments, allowing the use of the silicon core as a conductor and eliminating the aluminum layer [**13**]. Work is being done on implementing this approach for a two level depth actuator design.

Fabrication of a Z-motion actuator has been carried out. A multilevel depth fabrication enables the use of shorter springs as well as fabrication of movable fingers at a different height than the fixed fingers. As in the case of a spring system, this can easily be done by designing the width of a shorter finger to be less than the width of the taller one. Thus, narrower beams will be released before the wider beams. This vertical asymmetry in the comb finger design has a vertically asymmetric electric field acting on the movable fingers. Consequently, there will be a net vertical force creating a static displacement or a vibrational excitation of the comb fingers [**14**].

CONCLUSION

We have demonstrated the fabrication and operation of a two level deep etched microactuator. The single crystal microactuator has 22 μm deep folded flexure springs and 100 μm deep comb fingers. A displacement of 130 μm at 37 volts was achieved. A resonant frequency of 220 HZ was measured. The experimental data matches well with the ABAQUS simulation.

The two level depth process can easily be scaled for the fabrication of several depths of high-aspect-ratio single crystal silicon structures on a single wafer. The fabrication of self-aligned, two-level structures is also demonstrated using the same two level depth process flow.

ACKNOWLEDGEMENT

This work is supported by DARPA. All the fabrication was performed at the Cornell Nanofabrication Facility (CNF) which is supported by the NSF, Cornell University, and Industrial affiliates. The authors would like to thank fellow graduate students: Michael Wolfson, John Chong, Russ Webb and Trent Huang for their useful inputs and technical support. Also thanks to Dr. H. Neves from Cornell University and Professor M.T. Saif from University of Illinois at Urbana-Champaign for review of the manuscript.

REFERENCE

1. US Patent #5501893: Method of Anisotropically Etching Silicon

2. P. Hartwell et al. "Deep Silicon RIE with Profile Control", 44th national meeting of the American Vacuum Society, Oct. 97, San Jose, CA. On Line at http://mems.ee.cornell.edu/macd/

3. V.P. Jaecklin, C. Linder and N.F. de Rooij, "Comb actuators for xy-microstages", Sensors and Actuators, A-32, pp. 83-88.

4. Y.Xu, S.A. Miller, and N.C. MacDonald, "MicroElectroMechanical scanning tunneling microscope", Proc. 8th Int. Conf. Solid-State Sensors and Actuators, Trasducers 95 . Stockholm, Sweden, pp. 640-647.

5. C.Morehouse, "A Vision of Ultra-High Density Memory", 1996 Int'l NonVolatile Memory Technology Conference, pp. 30-33.

6. C.J. Kim, A.P. Pisano and R.S. Muller, "Overhung electrostatic micro gripper", J. Microelectromech. Syst. 1, pp. 31-36

7. R Legtenberg, A.W. Groeneveld and M. Elwenspoek, "Comb-drive actuators for large displacements", J. Micromech. Microeng., 6, pp. 320-329.

8. T. Hirano, T. Furuhata, K.J. Gabriel and H. Fujita, "Design, Fabrication, and Operation of Submicron Gap Comb-Drive Microactuators", J. Microelectromech. Syst. 1, pp. 52-58.

9. M.T.A Saif and N.C. MacDonald, "Planarity of Large MEMS", J. Microelectromech. Syst. 5, pp. 79-97.

10. K.A. Shaw, Z.L. Zhang, and N.C. MacDonald, "SCREAM I: A single mask, single-crystal silicon, reactive etching process for microelectromechanical structures", Sensors and Actuators, A-40, pp. 63-70.

11. W. Hofmann and N.C. MacDonald, "Fabrication of multiple-level electrically isolated high-aspect ratio single crystalline silicon microstructures", the tenth annual international workshops on Micro Electro Mechanical Systems, pp. 460-464, Nagoya, Japan, 1997.

12. E.P. Popov, Mechanics of Materials, Prentice Hall, 1976

13. R. Webb, S. Adams, B. Reed, C.S.B. Lee, and N.C. MacDonald, "Suspended Thermal Oxide Isolation for SCS MEMS with Embedded Electronics", To Be Published, On Line at http://mems.ee.cornell.edu/macd

14. S.A. Miller, K. Turner, and N.C. MacDonald, "Microelectromechanical scanning probe instruments for array architectures", Rev. Sci. Instrum., 68 (11), pp. 4155-4162.

A PATH TO LOW COST GYROSCOPY

John A Geen
Analog Devices Inc., Micromachined Products Division
Cambridge, MA 02139-3556

ABSTRACT

The theoretical framework for low cost, micromachined gyros and their commercial attractiveness have both been established for over a decade. However, they are still not manufactured by the millions, as had been expected. This paper illustrates some of the practical issues by tracing the development of a commercial gyro.

INTRODUCTION

Micromachining, as a means of making low cost gyroscopes, has inspired engineering imaginations for over a decade. Yet, it is only in the last year that such gyros have approached mass production. That is, with a capacity of millions of pieces each year. Their commercial attractiveness has been widely recognized **[1,2,3]**. Also many companies and universities have published plausible designs **[3,4,5,6,7,8]** but reduction to practice continues to be difficult.

This paper outlines the path taken by Analog Devices Inc. (ADI) over the past few years in pursuit of a gyro and, of course, the associated dollars. The starting position was very good. ADI was already producing micromachined accelerometers at a multi-million per year rate so that many of the process issues were understood. Further there was a deep conviction that integration with the electronics would, eventually, yield the lowest cost instrument. This provided the perseverance necessary for the undertaking.

There is generally more than one route to an objective and usually no uniquely best one. During the development ADI found it necessary to change paths in response to commercial pressures. The objective here is to share the two approaches and give an overview of their relative merits, sketching the technical issues along the way.

GYROSCOPES

These instruments measure rotation with respect to an inertial frame, an abstraction inaccessible for mechanical attachment or direct observation. This detachment is the source of their usefulness and of their difficulty in manufacture. They cannot exploit the first order effects measured in physically referenced rotation measuring devices, such as synchros or optical shaft encoders. Instead they must extract tiny, second order signals from a plethora of interfering effects.

There are at least two physical phenomena which have been demonstrated plausible for a micromachined inertial rotation sensor **[9]**. The rapid development in integrated optics may, one day, make it economical to use Sagnac interferometry. This is the basis of laser and fiber-optic gyros which reliably guide modern aircraft. In the meantime, Coriolis accelerometry forms the basis of the mechanical gyros which dominate the low cost market. One can regard mechanical gyros as vibrating accelerometers. Spinning gyros can even be squeezed into this definition by decomposing their spin into a pair of orthogonal vibrations. Thus, the commercial dominance of piezoelectric gyros makes sense in the light of the long established position of piezoelectric accelerometers **[10]**. Similarly, the aspiration to make the lowest cost gyro by micromachining is reinforced by the spectacular success of micromachined accelerometers **[11]**.

However, the Coriolis acceleration in a micromachine is indeed tiny. For example, take a reasonable vibration in the region of 10 microns amplitude at 16kHz giving an excitation velocity of the order 1m/s and acceleration 100km/s^2 . Then, the Coriolis acceleration corresponding to an angular rate resolution of 1^o/s would be 35mm/s^2., about 4milligee. In absolute terms, this does not seem too difficult for a mass produced part. There are examples of much better, low cost, micromachined accelerometers **[12]**. The difficulty lies in that signal being about a third of a part per million of the excitation. The problem of mechanical cross coupling is formidable.

Fortunately, the mechanically coupled acceleration is 90^o phase displaced with respect to the velocity induced, Coriolis acceleration and can be rejected by a synchronous demodulator to the extent of its phase accuracy **[13,14]**. This rejection is limited. So, the quality of the mechanical design is measured by the size of the interfering 90^o, or "quadrature" signal it produces from manufacturing tolerances. High aspect ratio flexures can be very valuable in improving those tolerances and give quadrature as low as 125ppm **[15]**. Also, control of the flexure sidewall angles was recognized as critically important even in the bulk etched devices with very large aspect ratios **[16]**.

A "CONVENTIONAL" APPROACH

ADI started in 1994 with tightly coupled accelerometers vibrating in vacuo, an approach which had enough previous history in discrete form **[17]** and micromachined **[4,5]** together with enough variants over the past few years **[1,3,8,15,20]** to call "conventional".

The integrated surface micromachining process gives a sub millimetric sensor size, restricted mostly by the curvature of the structural film. Also, for a given planar geometry and taking electrical collapse into account, the Coriolis signal varies roughly as the sixth power of the linear dimensions of the sensor. Thus, a vacuum is needed to give the vibration a high Q. That produces the most motion and, therefore, signal from the very limited electric drive available in a fully integrated structure. Even so, the differential capacitance for a given gyro input is only a millionth of that available in the preceding bulk micromachined instruments. Further, with that very small signal, the vacuum is necessary to reduce Brownian noise to an acceptable level.

The tight coupling between the devices, forcing them into perfect antiphase, enhances Q in the manner of a tuning fork, helps with the phase accuracy for quadrature rejection and helps with the rejection of external disturbances at the vibration frequency. Resonance tuning of the accelerometer was avoided because of the bandwidth conflict **[13]** stability difficulties and beat frequency noise.

0-9640024-2-6/hh1998/$20©1998TRF
DOI 10.31438/trf.hh1998.12

Solid-State Sensors, Actuators, and Microsystems Workshop
Hilton Head Island, South Carolina, June 8-11, 1998

Three very different structures were fabricated. none taking more than 1mm by 1mm. One of the more interesting is shown in figures 1 and 2.

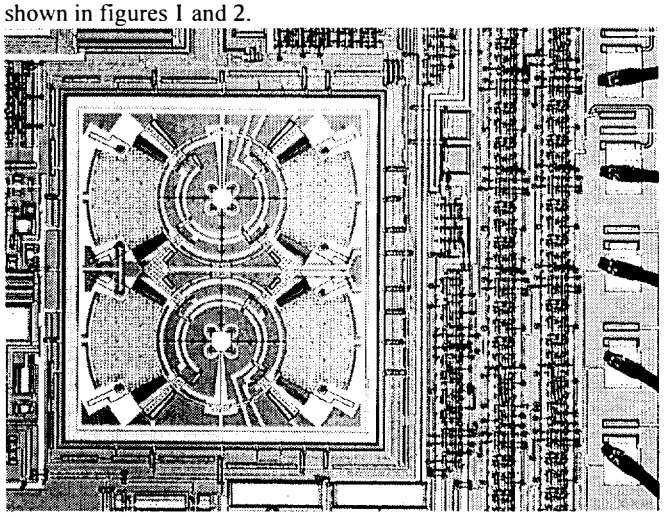

Figure 1. Part of Gyro Die Showing Sensor

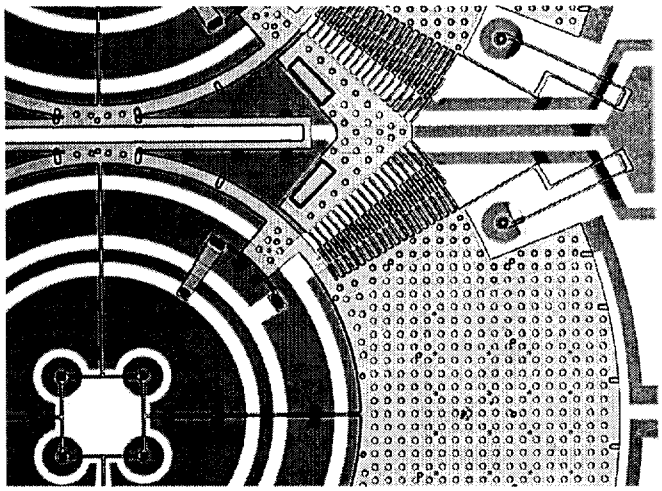

Figure 2. Detail of Sensor Showing Coupling, Drive and Flexures

The two rings vibrate rotationally in antiphase. The drive is similar to that of Howe and Tang [**18**] and four plates capacitively sense the Coriolis motion perpendicular to the plane of the substrate. The antiphase coupling between the opposite plates on a ring is intrinsically perfect while the fork coupling between the two rings has a stiffness ratio about 200 between antiphase and phase. The sensing capacitors are connected analogously to the "cross quad" or "common centroid" method for reducing the errors in the input transistors of operational amplifiers. This reduces the sensitivity to manufacturing process and temperature gradients. The high order of symmetry also helps with quadrature motion from tether sidewall mismatch and from drive levitation [**19**].

INTEGRATED ELECTRONICS

Accepting the limitations of the conventional sensor design and conservative mechanical design rules looked to ADI's strengths in precision electronics to provide good overall performance. The electronics is outlined in figure 3 and is dominated by the need to accommodate a quadrature signal of several hundred parts per million from worst-case manufacturing tolerances. A phase accuracy requirement of a milliradian follows. together with the need to accommodate many times full scale of interfering signal.

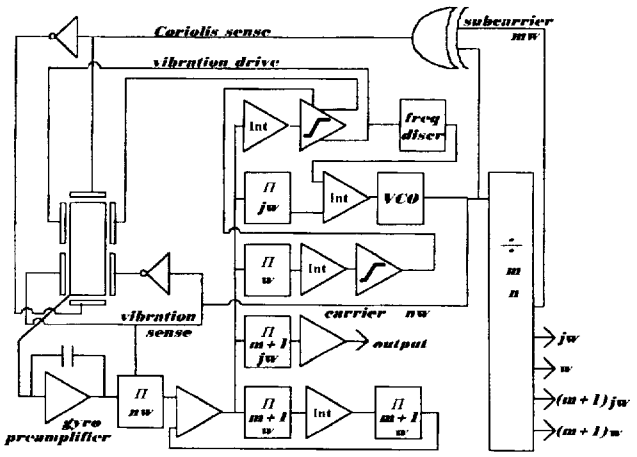

Figure 3. Vacuum Gyro Electronics Functions

Sensitivity to the very small differential capacitances was achieved with a high frequency carrier, and a subcarrier was used to differentiate Coriolis from vibration signals. In this way, a common high frequency preamplifier and demodulator of poorly defined gain and phase could be used for both the angular rate signal and a velocity stabilizing servo, resulting in a gyro scale factor essentially insensitive to electronics gain. The carrier and subcarrier were phaselocked to the vibration frequency to avoid the large, unmodelable null errors that result from temperature variation of harmonic beat frequencies.

Headroom in the amplifiers and demodulators was eased by nulling quadrature using a purely electronic servo. Nulling by electromechanical feedback would have complicated the servo compensation circuits without tangible benefit. It is worth noting that, unlike open loop trimming, closed loop quadrature nulling does not improve the angular rate null. The same phase errors which would give rate offset in the Coriolis demodulator give an exactly corresponding Coriolis-phased error signal to a quadrature nulling servo.

The resulting architecture has four, similar, digital phase sensitive demodulators, one for the Coriolis signal, one for the quadrature servo, one for the velocity servo and one for the phase lock loop. In practice, there is also a frequency discriminator to ensure initial capture. The total chip area taken by the sensor and this, rather complex electronics is 5mm by 5mm.

PACKAGING

It was assumed that a package similar to a standard IC would be used to minimize production costs. It took nearly a man-year of intense effort to yield a reliable vacuum package with this constraint. A prerequisite was the development of a simple means of measuring, on thousands of parts, leaks far smaller than those detectable by standard equipment. This was provided by measuring the resonance Q of the ADXL05 micromachined accelerometer. It is both a sensitive and a rapid technique for the pressures of interest, around 50millitorr. Eventually, in 1995, many consecutive batches were produced which had no perceptible leaks after severe thermal cycling of the glass-sealed ceramic.

RESULTS

The resulting gyros worked to the target specification of 0.5deg/s accuracy. A typical error plot is shown in figure 4.

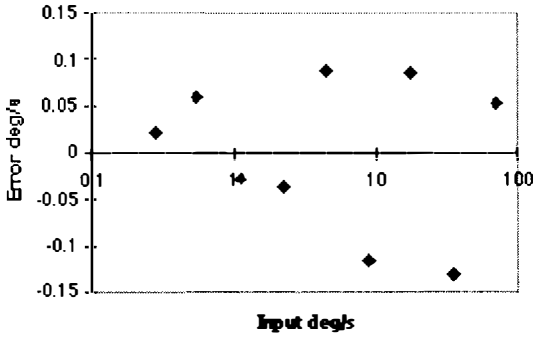

Figure 4. Vacuum Gyro Angular Rate Error vs. Input

THE REAL WORLD INTERVENES

During the 18 months needed for the prototype gyro development the rest of the world moved on. It had been projected that gyros with the target specification could be sold for about $30 at which our product was nicely profitable. However, advances in piezoelectric gyros dropped the million quantity prices to about $15 for automotive navigation grade and $5 for camera grade. It was clear that in order to compete with this trend we had to reduce both chip size and packaging cost.

Further, it came as an unpleasant surprise to find that surface micromachined devices were not robust in vacuo. The structures shown in figure 1 can, at atmospheric pressure, be hard mounted in ceramic packages, shock tested until the packages shatter, and be recovered undamaged. However, at 50millitorr they can be destroyed by the shock of packages striking each other in normal IC test equipment. This implied that either soft mounting or a non-standard package would be needed. Each of these options seemed an unacceptable expense.

Late in 1995 a solution to these cost problems was evolved and a new sensor was put into fab. One which did not need a vacuum or the complex electronics support. Then, in 1996, commercial reality asserted itself. There was a world shortage of semiconductors. The limited fab capacity had become precious. The micromachining division could not meet the exploding demand for accelerometers in a shared facility so a dedicated micromachining fab was set up in Cambridge. All hands were needed to get the new facility to the point where it could satisfy the orders, which are about a million pieces each month in 1998. The gyro project was shut down for a year while the infrastructure needed for its manufacture was reestablished.

A "NEW" APPROACH

Faced with the economic necessity of a die shrink and the elimination of the vacuum package, it was necessary to reexamine the basic assumptions of an electronics solution. The old sensors occupied only 4% of the die area. In search of smaller die it seemed reasonable to shift some complexity from electronics to mechanics. It was apparent that by increasing the drive and accelerometer fingers the signal size limitation by air damping could be overcome. The penalty, of course, would be a larger sensor but also a temperature sensitivity of both signal size and quadrature. While the viscosity of air is very temperature dependent, it is also very consistent so that a damping dominated gyro scale factor can be accurately compensated with minimal electronics. More significantly, signal phasing would be poorly defined, spoiling quadrature rejection. On the other hand, if the sensor itself has a few degrees of phase error then the complexities of precision phase electronics can be eliminated. Thus, both the electronics complexity and vacuum problems are soluble by a low quadrature. This can be achieved at the expense of sensor structural complexity.

The basic low-quadrature principle is to anchor an accelerometer structure to the substrate by a flexure which allows the Coriolis motion but is very stiff to both the exciting vibration and the cross-coupling angular motions. Then, the vibrating mass is suspended from the accelerometer by a flexure which is very stiff to Coriolis motion and angular motion but allows the vibration at high amplitude without stress stiffening. Coupling caused by imbalance of the flexures or drive is suppressed by stiffness. Coupling out of plane must propagate through two sets of misalignments, mostly sidewall errors, so that the already small coefficient is squared. The result is quadrature coupling significantly less than one part per million whereas the Coriolis effect is only attenuated by the vibrator to total inertia ratio.

It is still advantageous to use an antiphase pair of structures to double the signal without exceeding curvature limitations, to reject linear acceleration and to locally conserve momentum. The last increases the Q somewhat and desensitizes the system to mounting conditions. However the Q is low enough for the two vibrators to match adequately without a special coupling.

Needless to say, patents have filed and it should be noted that this is quite different from the designs of Geiger and the team at HSG-IMIT **[20]**. There, the vibrator is anchored to substrate and the accelerometer suspended from it so that the accelerometer moves with the vibration.

The sensor is in figure 5. It is 2microns thick, has nearly 5000 fingers and has a Q of 20 at 10kHz. It vibrates with an amplitude of 9microns at that frequency. The observed resonant frequency does not shift noticeably with amplitude and the response decays graciously above the resonant peak giving experimental verification of the stress relief mechanism. The quadrature is so small that stray electrical coupling from vibration drive to accelerometer electronics is the dominant gyro error source. This is apparent from a linear dependency on the drive voltage. Quadrature errors have a quadratic dependence.

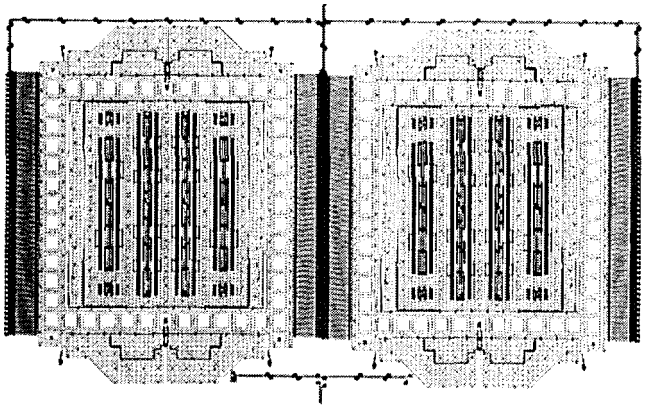

Figure 5. A Gyro Structure with Less than 1 ppm Quadrature

The electronics does not have any servo loops, resulting in a dramatic reduction in die size despite retaining a thermometer output and adding a digital output option to the rescaleable analog output. The die, with complete electronics, is 3mm by 3mm and the package is an IC "cerpak" 10mm by 10mm by 3mm. It takes about 2.5mA from a single ended 5V supply.

The change in approach seems to be yielding the needed results. Still, there is much work to be done for the transition of prototype into production. Amongst other things, we must run about 120,000 die through fab for qualification before releasing them.

ACKNOWLEDGMENTS

At this point it is appropriate to acknowledge the efforts of Joe Kung who broke new ground in CAD to layout the old sensors, Don Carow for his endless patience in FEA, John Chang for his test work and meticulously minimizing the digital electronics, Steve Lewis for optimizing the high frequency amplifier, Yang Zhao for developing the vacuum measurement, Dipak Sengupta for developing the vacuum package, Steve Sherman for designing the "new" electronics, Joe Catalano for laying out that chip. Barbara Berthold for SEMs, Bill Riedel with Jeff Swift for comments on the draft paper and Craig Core with the manufacturing team at Cambridge for making the necessary process enhancements.

Thanks are due to ADI for permission to publish the work. Also, grateful thanks are offered for the partial funding received from the DARPA TRP.

REFERENCES

1. Cimoo Song, *Commercial Version of Silicon Based Inertial Sensors*, Transducers '97 p.839.
2. Brand & Connelly, *Micromachined Silicon Inertial Sensors, a Defense Conversion Technology*, 1994 Joint Service Data Exchange, Scottsdale, AZ.
3. Brand & Connelly, *Advances in Michromechanical Systems for Guidance Navigation and Control*, 1997 American Institute of Aeronautics and Astronautics.
4. Hulsing, US Patents 5,241,861 & 5,341,682.
5. O'Brien, Burns & Geen, US Patent 5,392,650.
6. Geen, US Patents 5,635,638 & 5,635,640.
7. Putty & Najafi, *A Micromachined Vibrating Ring Gyroscope*, p.213, S.S.S.A.W, 1994, Hilton Head.
8. Clark, Howe & Horowitz, *A Surface Micromachined Z-Axis Vibrating Rate Gyro*, p.283, S.S.S.A.W, 1996, Hilton Head.
9. Lawrence, *Modern Inertial Technology*, Springer, 1993, ISBN 0-387-97868-2.
10. Toshihiko Ichinose & Jiro Terada, *Angular Rate Sensor for Automotive Application* p.49, 1995 SAE International, 950535, ISSN 0148-7191.
11. Sherman, Samuels & Riedel, *A Low Cost Dual Axis Accelerometer*, p.1, 1997 SAE International, 970607, ISSN 0148-7191.
12. ADXL105 data sheet, www.analog.com/iMEMS
13. Hunt & Hobbs, *Development of an Accurate Tuning Fork Gyro*, 1964, Proc. IME, Vol.179, Pt.3E, p.129.
14. Blanco & Geen, *Inertial Sensor Micromachining at Northrop*, 49th Institute of Navigation, 1993
15. Lutz et al., *A precision Yaw Rate Sensor in Silicon Micromachining*, p.847, Transducers '97.
16. Zavracky et al., *Fabrication of Vertical Sidewalls by Anisotropic Etching of Silicon (100) Wafers*, J. Electrochem. Soc., Vol.141, No.11, Nov.1994.
17. Peters, US Patent 4,510,802, 1983 filing.
18. Howe & Tang, US Patent 5,025,346
19. Tang, Lim & Howe, *Electrostatic Comb Drive Levitation and Control Method*, J of MEMS, Vol.1, No.4, Dec.1992.
20. Geiger et al., *New Designs of Micromachined Vibrating Rate Gyros with Decoupled Oscillation Modes*, Transducers '97.

Low-Noise MEMS Vibration Sensor for Geophysical Applications

J. Bernstein, R. Miller, W. Kelley and P. Ward
The Charles Stark Draper Laboratory
Cambridge, MA 02139-3563

ABSTRACT

The need exists for high sensitivity, low noise vibration sensors for various applications such as geophysical data collection, tracking vehicles, intrusion detectors, and underwater pressure gradient detection. In general, these sensors differ from classical accelerometers in that they require no DC response, but must have a very low noise floor over a required bandwidth. Theory indicates a capacitive micromachined silicon vibration sensor can have a noise floor on the order of $0.1\mu g/\sqrt{Hz}$ over 1 kHz bandwidth while reducing size and weight 10-fold compared to existing magnetic geophones. With early prototypes we have demonstrated Brownian-limited noise floor at 1.5 $\mu g/\sqrt{Hz}$, orders of magnitude more sensitive than surface micromachined devices such as the industry standard ADXL05.

INTRODUCTION

A vibration sensor can be thought of as a very high sensitivity accelerometer with no DC output requirement. With no drift or bias stability spec., the design can be optimized to give the lowest noise floor. Applications for these devices include geophysical sensing, machinery vibration and failure prediction, tracking and identification of vehicles or personnel, and underwater pressure gradient sensing.

Traditional vibration sensors using permanent magnets and fine wire coils are called geophones **[1]**, and measure *velocity* above the fundamental resonance. This is in contrast to capacitive accelerometers which measure *acceleration* below their fundamental resonance. Piezoelectric and ferroelectric accelerometers are also used for these applications. Micromachined sensors can offer size and weight advantages over traditional sensors.

Previous efforts to make micromachined high resolution vibration sensors or accelerometers have included capacitive **[2-4]**, tunneling **[5]**, piezoresistive, optical and piezoelectric sensors. Capacitive sensors have the advantage of no exotic materials, low noise and compatibility with CMOS readout electronics. Tunneling sensors have a low noise floor, but due to the small dynamic range at the tip require a very stiff feedback loop which reduces the useful bandwidth and dynamic range.

THEORY

The sensor is modeled as a spring-mass-damper system with capacitive pickoff. Because no DC output is required, it was decided for initial tests to build a single-capacitor sensor rather than a differential capacitor design. Noise sources modeled include Brownian mechanical noise from air damping and electronic noise from the readout circuit **[6]**.

The Brownian force is $F_B = \sqrt{4kTD}$ (N/$\sqrt{Hz}$), which causes Brownian motion of the proof mass x_B

$$x_B = \frac{\sqrt{4kTD}}{k_{sp} + j\omega D - \omega^2 M} \qquad (\mathrm{m}/\sqrt{Hz}) \qquad (1)$$

where D is the damping coefficient of the proof mass M supported by spring constant k_{sp}. Solving for the acceleration which generates the same motion, and substituting $Q = \omega_0 M / D$, $\omega_0 = \sqrt{k_{sp}/M}$, and g = 9.8 m/s^2, gives for Brownian equivalent acceleration noise in g/$\sqrt{Hz}$:

$$g_{n,B} = \frac{\sqrt{4kTD}}{Mg} = \frac{1}{g}\sqrt{\frac{4kT\omega_0}{MQ}} \qquad (\mathrm{g}/\sqrt{Hz}) \qquad (2)$$

From Eq. 2 we see that a large mass and high Q (low damping) are helpful to achieve a low noise floor. In order to use a sensor with a high Q, it must be force rebalanced to prevent ringing at the resonant frequency. In the work presented here, the sensors are over-damped, with a Q of about 0.3.

The sensitivity of the device is calculated for the simple case of a DC bias voltage with a high input impedance buffer amplifier. A bias voltage of ½ the snap-down voltage (V_{SD}) is assumed. The sensitivity at low frequency is the V/m in the sense gap times the m/g of the proof mass below resonance:

$$M_0 = \frac{V_{SD}}{2x_0}\frac{Mg}{k_{sp}} = \frac{V_{SD}}{2x_0}\frac{g}{\omega_0^2} \qquad (\mathrm{V/g}) \qquad (3)$$

The snap-down voltage is $V_{SD} = \sqrt{\frac{8k_{sp}x_0^3}{27\varepsilon_0 A}}$. Substituting for the mass M and V_{SD} gives for sensitivity M_0:

$$M_0 = \frac{g}{\omega_0}\sqrt{\frac{2t\rho_{Si}x_0}{27\varepsilon_0}} \qquad (\mathrm{V/g}) \qquad (4)$$

where t is the proof mass thickness, and ρ_{Si} is the density of silicon. From this we see that sensitivity is inversely proportional to the fundamental resonant frequency.

We consider also an electronic readout noise component, which has in general both equivalent input current noise and voltage noise components. The total equivalent front-end noise is called $v_{n,e}$. This voltage noise can be converted to an equivalent g-noise by dividing by the transducer sensitivity in V/g:

$$g_{n,e} = \frac{v_{n,e}}{M_0} \qquad (\mathrm{g}/\sqrt{Hz}) \qquad (5)$$

The total noise is the r.m.s. combination of electrical and Brownian contributions.

$$g_{n,T} = \sqrt{g_{n,B}^2 + g_{n,e}^2} \qquad (\mathrm{g}/\sqrt{Hz}) \qquad (6)$$

0-9640024-2-6/hh1998/$20©1998TRF
DOI 10.31438/trf.hh1998.13

Voltage noise for a low-noise CMOS front end is typically in the 5 to 20 nV/$\sqrt{Hz}$ range above the 1/f corner. Lower noise can be obtained but at the cost of increased current consumption.

To achieve a noise level of 10 ng, a vacuum package must be used to reduce Brownian motion noise.

Fig. 1 is a contour map of combined g-equivalent noise as a function of electrical noise (1nV to 100 nV/$\sqrt{Hz}$) and Q (1 to 10^4). To achieve a noise level of 10 ng/$\sqrt{Hz}$ requires a Q of 3000 and a front end equivalent noise of under 2 nV/$\sqrt{Hz}$. For this calculation, the silicon proof mass is assumed to be 4 mm X 4 mm X 0.38 mm with a 3 μm sense gap, a resonant frequency of 1 kHz, and sensitivity of 0.233 V/g.

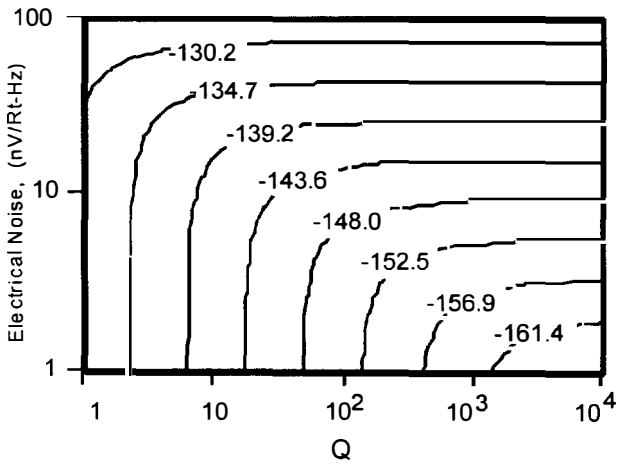

Fig. 1. Total noise in dB // 1g/$\sqrt{Hz}$, as a function of Q and front-end electrical noise.

Table 1. Design Specification for Vibration Sensor

Resonant Frequency	Units	500 Hz Sensor	1 kHz Sensor	10 kHz Sensor
Self Noise Floor * (Combined Brownian and electronic)	ng/$\sqrt{Hz}$	25	43	338
Sensitivity with unity gain buffer	V/g	0.49	0.245	0.025
Maximum g-level (open loop)	g's	0.3	1.2	120
Displacement per g	m	10^{-6}	2.5 X 10^{-7}	2.5 X 10^{-9}

* Assumes 8 nV/$\sqrt{Hz}$ electrical noise, Q = 100

ELECTRONICS DESIGN

To evaluate the vibration sensor prototypes two types of electronics were used: an open-gate JFET source follower, and a custom CMOS ASIC. The JFET buffer allowed quick, reasonably low noise measurements to be made with a very compact circuit (inside the sensor package) although 1/f and current noise are high at low frequencies. The ASIC uses a carrier to reduce 1/f noise, resulting in better low frequency performance. Fig. 2 shows the open-gate JFET buffer circuit used. This circuit has a DC input impedance of several TΩ , which combined with a typical sensor capacitance of 50 pF gives an RC time constant of minutes. It was sometimes necessary to shine light in the package to allow the JFET to reach bias equilibrium (photonic reset).

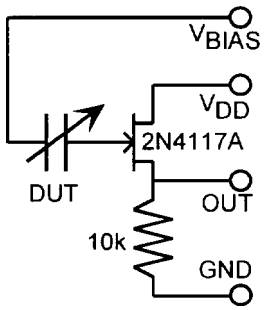

Fig. 2. Open-gate JFET buffer circuit.

A custom CMOS mixed signal ASIC was designed in-house and fabricated at Orbit Semiconductor. The design implements synchronous modulation / demodulation using square waves and a novel RF rebalance technique. The block diagram of the system is shown in Fig. 3. The circuit rebalances the proof-mass below the frequency range of interest, while allowing higher frequency vibration signals to pass through open-loop.

The ASIC applies equal and opposite 100kHz square waves to the sensor and a reference capacitor. Vibrations cause a mismatch between the fixed capacitor and the time varying sensor. The charge amplifier converts the capacitance mismatch into an output voltage which is then amplified by the AC gain stage.

The vibration signal is modulated on a 100KHz carrier . The amplifier stages process this signal at 100KHz to avoid 1/f noise in the CMOS transistors. The signal is demodulated after AC amplification to recover the vibration signal.

Application of RF voltage to the sensor applies a force proportional to the square of the applied voltage amplitude. The integral rebalance controller adjusts the carrier amplitude and tunes the time average sensor capacitance to match the fixed reference capacitor. Open loop maximum g's are set by proof mass motion of about 10% of the sense gap. Closed-loop maximum g's are determined by the available rebalance voltage.

The bandwidth of the rebalance loop is designed to be low (<1Hz). The rebalance loop nulls DC and sub 1 Hertz accelerations maintaining signal null with changes in temperature and sensor orientation. This allows high gain in dynamic range limited CMOS (5V) electronics. Vibration above 1Hz are not rebalanced and are sensed open-loop.

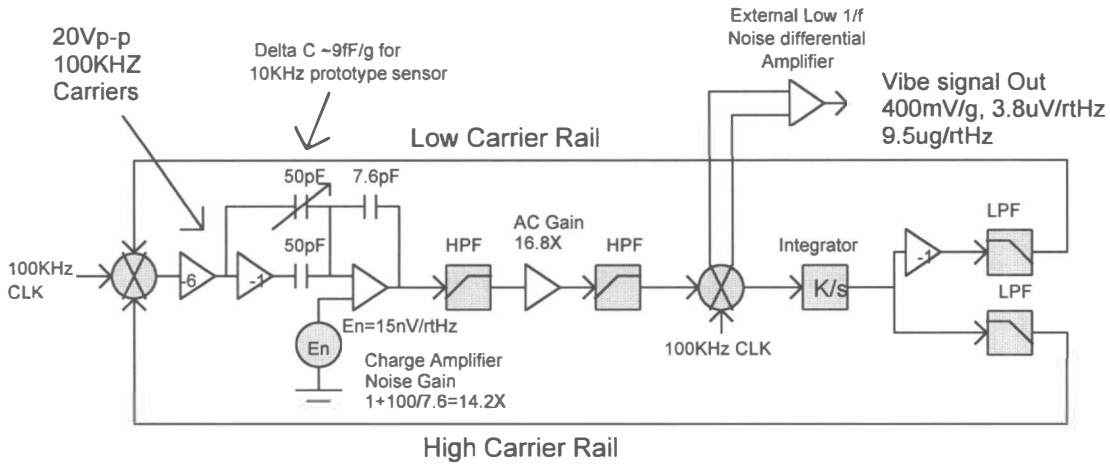

Fig. 3 CMOS ASIC Block Diagram

SENSOR FABRICATION

The sensors are fabricated on 0.38 mm thick double-side polished wafers using the Bosch process in an STS etcher. A recess 3 μm deep is etched into the wafer to define anchors and create the sense gap. 30 μm deep damping-relief trenches are then etched to reduce squeeze-film damping. A 10 μm thick boron diffusion is used to create an etch stop layer on both faces of the wafer. After electrostatic bonding to a glass wafer with readout electrodes, the STS etcher is used to trench through the wafer. A brief anisotropic etch in EDP (Ethylene-Diamine-Pyrocatechol-Water) then undercuts the springs.

Figs. 4 and 5 show a sensor chip after the deep ICP (Inductively Coupled Plasma) etch and before the anisotropic etch. A central proof mass is supported by springs attached to 4 anchors on a glass substrate. Damping-relief trenches are visible in Fig. 5 facing the glass substrate. Fig. 6 shows a completed prototype sensor.

Devices were fabricated with 3 proof mass sizes ((3 mm)^2, (4 mm)^2, and (5 mm^2)) and 3 resonant frequencies (500 Hz, 1kHz, and 10 kHz) to cover various applications. Kovar flat-packs were used to house the sensors.

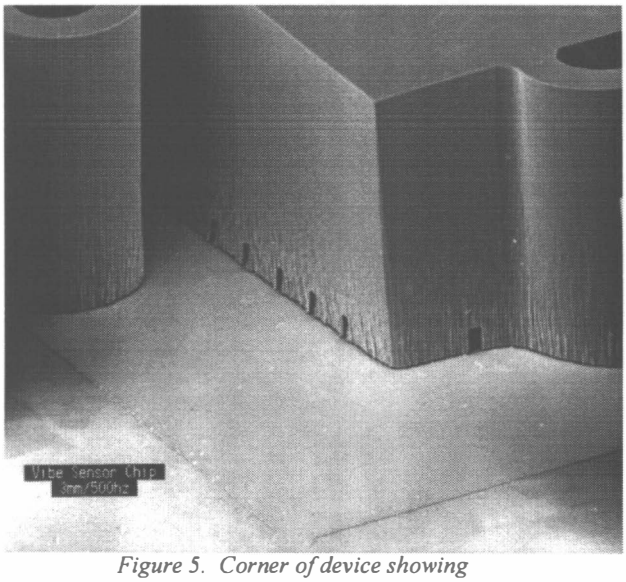

Figure 5. Corner of device showing electrodes and damping-reduction trenches.

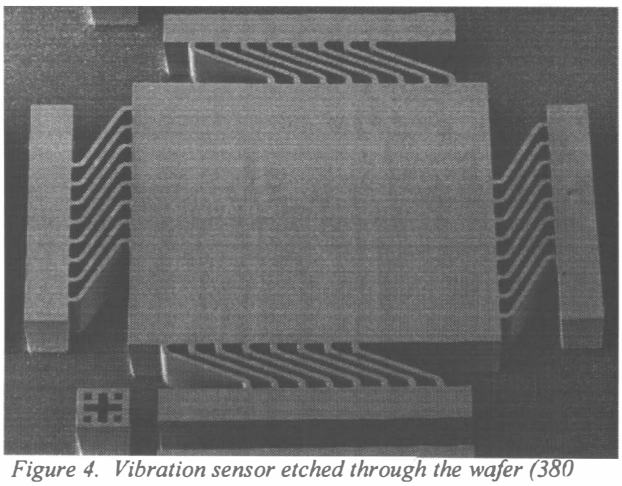

Figure 4. Vibration sensor etched through the wafer (380 μm), before anisotropic etch. Proof mass is 3 mm X 3 mm.

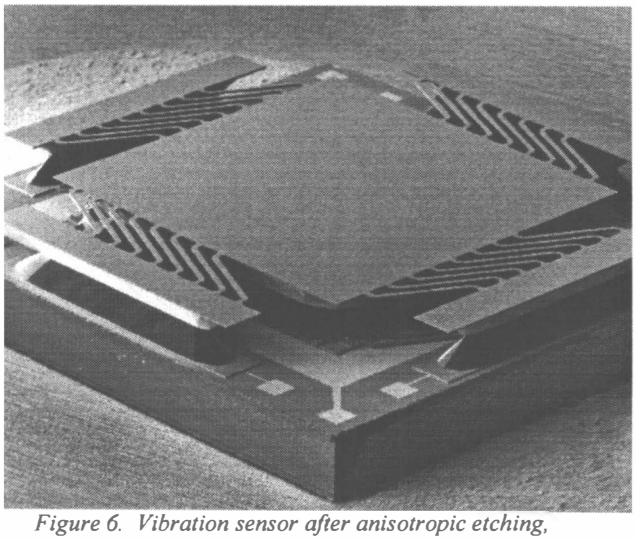

Figure 6. Vibration sensor after anisotropic etching, leaving thin flexures supporting large proof mass.

TEST RESULTS AND DISCUSSION

Chip level testing includes capacitance-voltage curves and current - voltage curves to measure leakage resistance (typically greater than 1 TΩ). Frequency response with a commercial JFET buffer is shown in Fig. 7. A sensitivity of 72 mV/g was obtained at a bias voltage of 22 V. The noise floor (measured on a vibration isolated platform) was as low as 1.5 $\mu g/\sqrt{Hz}$ which is the Brownian limit for this device (Fig. 8). A battery powered low noise pre-amp using OP 37 op-amps was used to raise the signal level above the noise floor of the dynamic signal analyzer (HP 3563A).

Fig. 9 shows the advantage of the RF carrier readout chip over a baseband CMOS readout. Orders of magnitude reduction in 1/f noise are achieved using the ASIC.

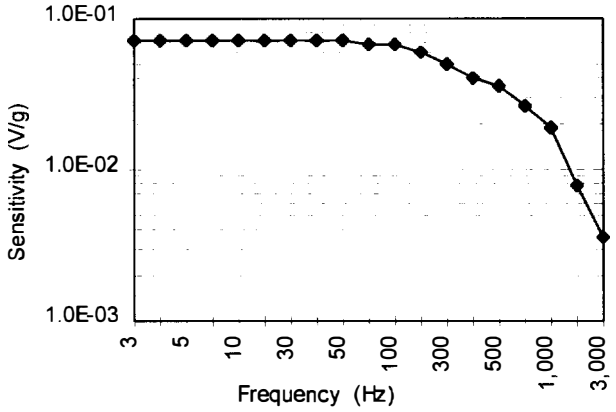

Fig. 7. Frequency Response of 3mm X 3 mm device, design resonance at 1 kHz, Q = 0.3.

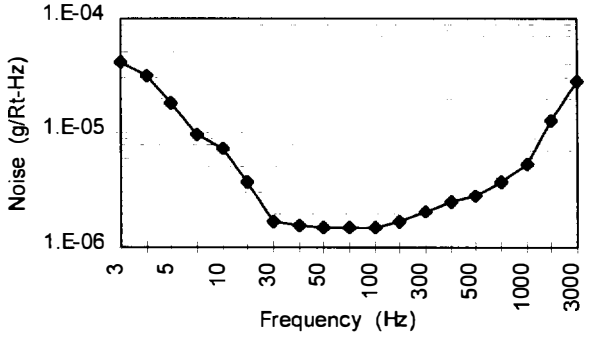

Fig. 8. Plot of acceleration noise in $g/\sqrt{Hz}$ using source-follower buffer circuit. Device is same as Fig. 8.

CONCLUSIONS

A bulk micromachined vibration sensor has been fabricated and tested with a novel, custom CMOS ASIC which removes 1/f noise while requiring only a single sense capacitor and one dummy capacitor. Vibration noise at the Brownian noise limit (1.5 $\mu g/\sqrt{Hz}$) was achieved using an overdamped sensor with 1kHz fundamental resonance. Theory indicates that orders of magnitude improvements can be made over existing MEMS sensors in both bandwidth and noise floor by the use of wafer-thick bulk micromachining technology with optimized low noise electronics. These sensors should be useful for geophysical work, underwater sensing, machinery monitoring, and sensing of vehicles and people.

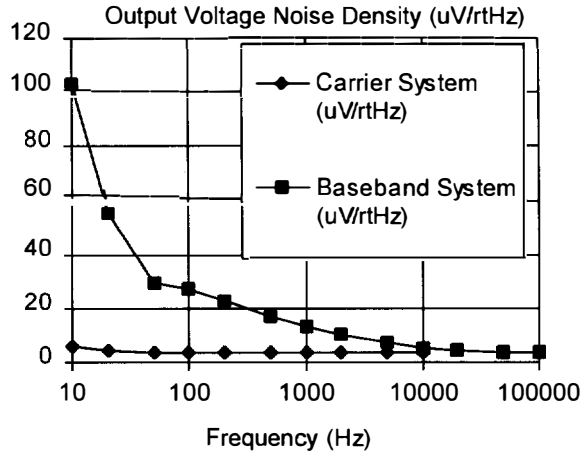

Fig. 9. Baseband vs. synchronous modulation / demodulation noise with Orbit CMOS ASIC readout chip.

REFERENCES

1. Geospace Inc, GS-14 geophone, 7334 N. Gessner Road, Houston TX 77040, USA.
2. W. Henrion, L. DiSanza, M. Ip, S. Terry, and H. Jerman, "Wide Dynamic Range Direct Digital Accelerometer", Technical Digest of the 1990 Solid-State Sensor and Actuator Workshop, Hilton Head Isl., SC, 6/4-6/7, pp. 153-157.
3. K. Bult, A. Burstein, D. Chang, "Wireless Integrated Microsensors" Proceedings of the 1996 Hilton Head Solid State Sensor and Actuator Conference, Transducer Research Foundation, Hilton Head Isl., SC, pp. 205-210.
4. M. Lemkin et. al., "A 3-axis force balanced accelerometer using a single proof mass," The 9th International Conference on Solid-State Sensors and Actuators - Transducers 97, Chicago Illinois, pp. 1185-88, June 1977.
5. C.H. Liu, J.D. Grade, A.M. Barzilai, K.K. Reynolds, A. Partridge, J.K. Rockstad, and T.W. Kenney, "Characterization of a highly sensitive tunneling accelerometer", The 9th International Conference on Solid-State Sensors and Actuators - Transducers 97, Chicago Illinois, Technical Digest, pp 471-472.
6. T.B. Gabrielson, "Mechanical-thermal noise in micromachined acoustic and vibration sensors," IEEE Transactions on Electronic Devices, vol. 40, #5, pp. 903-909.

A HIGH PERFORMANCE PLANAR PIEZORESISTIVE ACCELEROMETER

Aaron Partridge, J. Kurth Reynolds, Benjamin W. Chui, Eugene M. Chow, Alissa M. Fitzgerald, Lian Zhang, Susan R. Cooper, Thomas W. Kenny
Departments of Electrical and Mechanical Engineering,
Stanford University, CA 94305-4021

Nadim I. Maluf
Lucas NovaSensor,
Fremont, CA 94539

ABSTRACT

There is great interest in the use of Deep Reactive Ion Etching (DRIE) to build micromechanical devices. In previous work, we have demonstrated a technique for forming piezoresistive strain gauges on the sidewalls of DRIE high-aspect ratio flexures. In this paper, we report on the development of a planar piezoresistive accelerometer which combines the advantages of simple and inexpensive piezoresistive sensing with the design flexibility offered by DRIE processing of micromechanical structures. The design, fabrication, and experimental testing of these devices is described. The resulting accelerometers offer excellent performance within a technology that should be manufacturable at very low cost. This work also illustrates the potential importance of piezoresistive sensing in DRIE microstructures.

INTRODUCTION

The academic MEMS community has developed a large assortment of accelerometers in the last 20 years, using almost every possible combination of the available transduction mechanisms, materials, and fabrication technologies. Meanwhile, the industrial MEMS community has primarily delivered bulk-micromachined silicon piezoresistive accelerometers. Initially described almost 20 years ago, this simple sensor has proven useful in many applications, is manufacturable at low cost, and does not require sophisticated integration of preamplification circuitry **[1]**. Commercially successful accelerometers of this sort can be found packaged as hybrids with off-the-shelf instrumentation amplifiers and laser-trimmed thick-film circuits from many companies.

The sensitivity of a piezoresistive accelerometer can be increased by focusing the inertially-induced strain into a very small region. Unfortunately, this strategy reduces the dynamic range of the accelerometer, because there is a maximum strain the silicon flexure can be subjected to before breakage. The anisotropic etching of silicon used to manufacture these parts worsens this problem, because the flexure is always bounded by crystallographic planes. The corners at these intersections cause non-uniformities in the stress, leading to an allowed average strain in the piezoresistor which is well below the maximum that could be tolerated. Rounding of these corners would allow larger values of average strain, and higher sensitivity.

In the last 2 years, many researchers in this community have used Deep Reactive Ion Etching (DRIE) to fabricate high aspect ratio silicon microstructures **[2]**. This technology allows fabrication of high-aspect ratio planar flexures from single crystal silicon of arbitrary 2-dimensional shape. This is important because it is the first technique suitable for volume fabrication of silicon flexures that is not constrained by the crystal planes. One example application of this technology is the development of planar capacitive accelerometers with crystalline silicon flexures **[3]**.

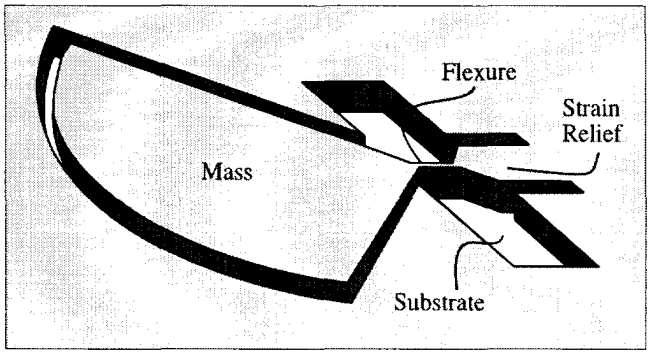

Figure 1 This drawing illustrates the mechanical design of the planar piezoresistive accelerometer. A "pie-shaped" mass is supported from a single high aspect-ratio flexure, which is doped to form a piezoresistive sensor on a vertical surface. The strain relief isolates the strain-sensiive elements of the accelerometer from package-induced stress, and the lateral motion of the mass is caged by the surrounding silicon.

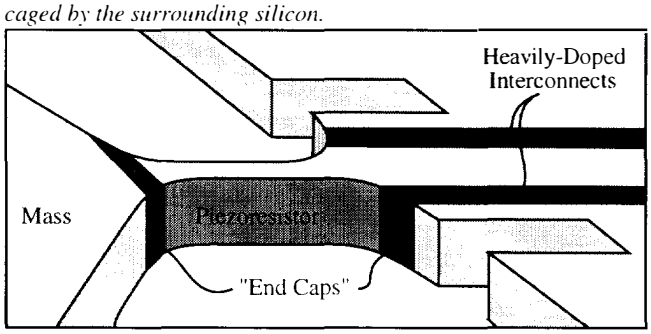

Figure 2. This drawing illustrates a close-up of the flexure, showing the location of the heavily and lightly-doped regions. The electrical circuit path is along the top surface, down the sidewall at the base of the flexure, along one surface of the flexure, back up onto the top of the mass, and back down the backside of the flexure.

In the last year, our group has developed a technique for fabrication of piezoresistive sensors on the vertical surfaces of a DRIE-fabricated planar flexures **[4]**. This technique uses an oblique ion implantation to form the doped silicon piezoresistors, and opens the door for inexpensive piezoresistive sensing to be used with DRIE-released planar flexures for many applications.

Whenever a flexure and a displacement transducer are combined, the result is an accelerometer. Therefore, it is now relatively easy for researchers with access to ion implantation and DRIE etching to make accelerometers. We set out to demonstrate an inexpensive accelerometer with resolution better than 0.5 mg/$\sqrt{\text{Hz}}$, and comparable bandwidth, dynamic range, drift, etc. to the Analog Devices ADXL05, a high-performance, low-cost accelerometer **[5]**.

0-9640024-2-6/hh1998/$20©1998TRF
DOI 10.31438/trf.hh1998.14

Solid-State Sensors, Actuators, and Microsystems Workshop
Hilton Head Island, South Carolina, June 8-11, 1998

DESIGN

In a piezoresistive sensor, all of the signal-induced strain should be focused into the piezoresistive region, maximizing the resistance change. To achieve this, piezoresistive sensor designers use bosses and other structural elements to concentrate the strain. Building long flexures, as is common in capacitive accelerometer designs, would be detrimental to a piezoresistive accelerometer. Long flexures would decrease the sensors resonant frequency and hence the bandwidth, while spreading the strain over a large volume. For example, the common quad-supported capacitive accelerometer topology is ill-suited to piezoresistive devices because the strain from acceleration is divided over the four legs, each bending sigmoidally, which quarters, then halves the sensor strain. Building piezoresistors on each leg does not win it back; the strain concentration is lost. Therefore, an optimal planar piezoresistive accelerometer should not look anything like a planar capacitive accelerometer. In fact, it really ought to look somewhat like bulk piezoresistive accelerometers, which consist of a mass suspended from one edge by a small flexure.

Guided by this rationale, we have designed and built singly supported proof masses with small piezoresistors on one side of their support flexures as shown in Figs. 1 and 2.

Assuming that the mass is rigid, the flexure is massless, displacements are small, tangential strain dominates shear strain in the flexure, and the silicon has a simple Young's modulus, we can derive this expression for the strain in the flexure :

$$\varepsilon = \frac{4\rho R^2 \sin(\theta)}{Ew^2} A \qquad (1)$$

Here, ρ is the density of silicon, R is the length of the proof mass, θ is the included angle of the proof mass, E is Young's Modulus, the w is the width of the flexure, and A is the acceleration. Some important conclusions from the equation for strain are that it scales with the cube of the length of the mass, is inversely proportional to the square of the flexure width and is linear with the acceleration. Note that the sensitivity is neither a function of the silicon thickness nor the flexure length.

The sensor bandwidth is limited by the resonant frequency of the proof mass. From the listed assumptions we have a simple spring–mass system with a lateral resonance given by:

$$f = \frac{1}{2\pi}\sqrt{\frac{Ew^3}{3\rho l R^4 (1+\nu)(2\theta + \sin(2\theta))}} \qquad (2)$$

where ω is the resonance frequency, ν is Poisson's ratio, and l is the flexure length. The lateral resonant frequency is inversely proportional to the square of the proof mass length, to the 3/2 power of the flexure width, and is inversely proportional to the square root of the flexure length. The lateral resonant frequency is not a function of the silicon thickness.

The vertical and torsional resonances are given by:

$$f_{out} = \frac{1}{2\pi}\sqrt{\frac{Ewt^2}{3\rho l R^4 (1+\nu)(2\theta + \sin(2\theta))}} \qquad (3)$$

$$f_{tor} = \frac{1}{2\pi}\sqrt{\frac{Ew(t^2+w^2)}{3\rho l R^4 (1+\nu)(2\theta - \sin(2\theta))}}$$

where t is the thickness of the mass and flexure. The out-of-plane resonance is higher than the in-plane resonance by the aspect ratio of the flexure. Simply,

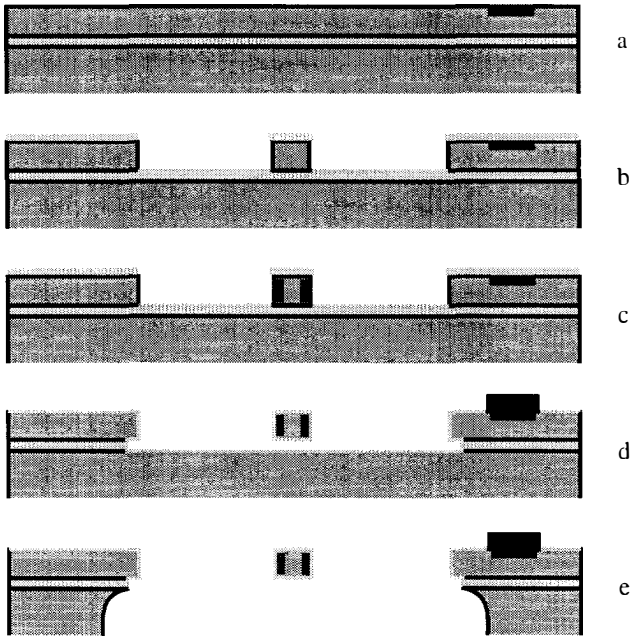

Figure 4. Fabrication procedure. (a) Top-surface implants form p+ conductive paths and n+ substrate contacts. (b) Oxides are deposited and the top layer of silicon is etched to define sensors. (c) Oblique implants dope the sensor and return paths on etched sidewalls. (d) Sensors are partially undercut, passivated and bondpads defined. (e) Resist is applied to the topside for protection during release. Backside silicon is plasma etched, and resist is plasma etched, releasing devices.

$$\frac{f_{out}}{f} = \frac{t}{w} \qquad (4)$$

and there is a similar result for the torsional resonance. From this analysis we can see that we should minimize the flexure width, and maximize the mass length. The narrowest flexure that can be reliably defined in our lithography is about 2.4 μm. We also built sensors with flexure width of 4.4 μm. We choose a thickness of 30 microns because of limitations on DRIE undercut control. Sensors were built with length of 0.2mm, 0.5mm, 1.0mm, and 2.0mm to study the variations of yield and performance.

FABRICATION

We begin with moderately doped n–type wafers, oxidize, bond and grind back to build our BESOI substrate. We next implant and anneal a top surface p+ traces which connect our bondpads to the piezoresistors, and an n+ substrate contact.

Next, we deposit and pattern LTO, and define the structure with a 30μm deep anisotropic silicon etch. After the etch, we implant the sidewalls of the flexure to form the sensor and a return current path. The sensor is moderately p–doped while the opposite side of the flexure is heavily p–doped. This implant is patterned to avoid creating current paths other than through the piezoresistor.

The oxide is etched in HF to undercut the flexure only, and the implants are annealed and passivated with thermal oxide. Then, bond pads are metallized, and the topside is covered in thick resist. The backside is etched in the DRIE to release the parts [6], and the resist is removed in an oxygen plasma.

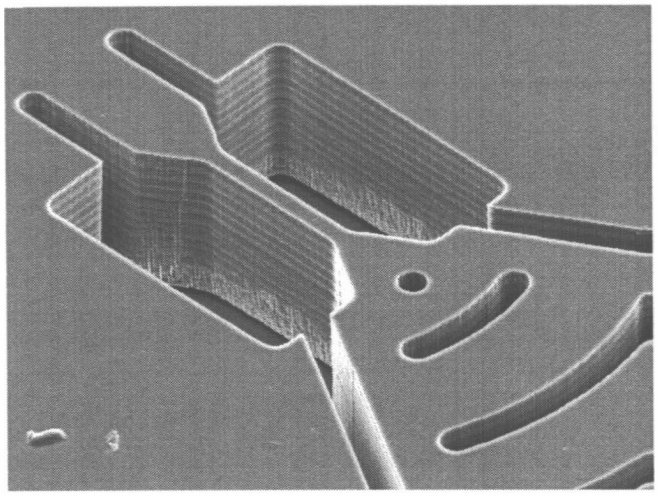

Figure 5 shows an SEM micrograph of the flexure supporting the mass in our accelerometer. This flexure is 30um long and 4.4u wide. The piezoresistors and return current conductors are formed by implanting at approximately 30° from vertical [4]. The piezoresistor is implanted with medium dose while the return path is implanted with a heavy dose, generating a return conductor. (SEM Phot courtesy of R. Lawton and H. Rockstad, JPL)

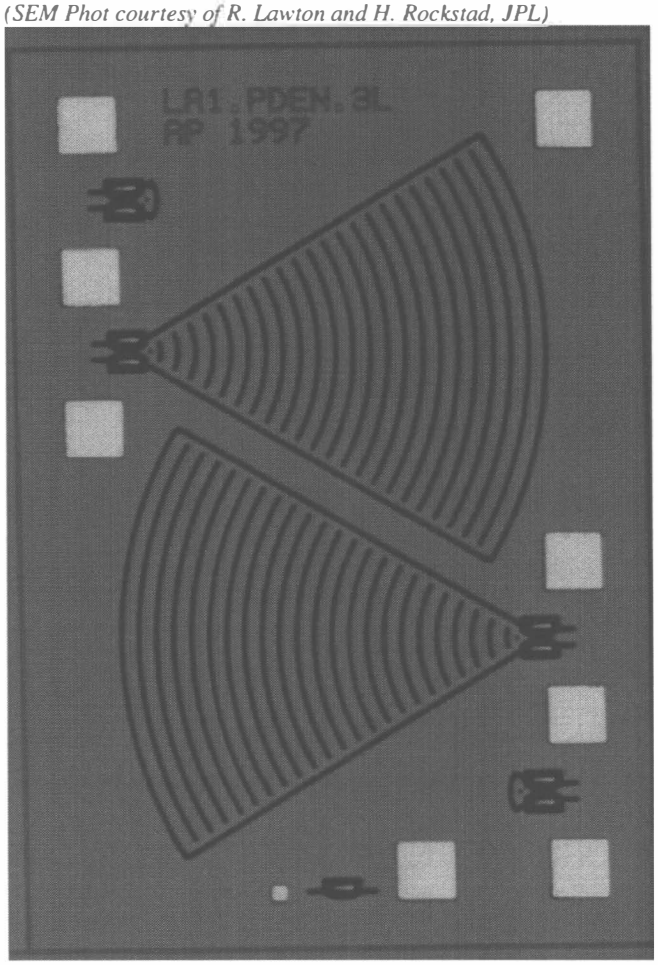

Figure 6 shows an optical micrograph of a complete, full-bridge sensor. The two pie-shaped areas are released proof masses, each joined by a flexure from the tip of the pie to the substrate. Three smaller devices with identical piezoresistors and flexures provide matched bridge resistors and a thermal calibration resistor.

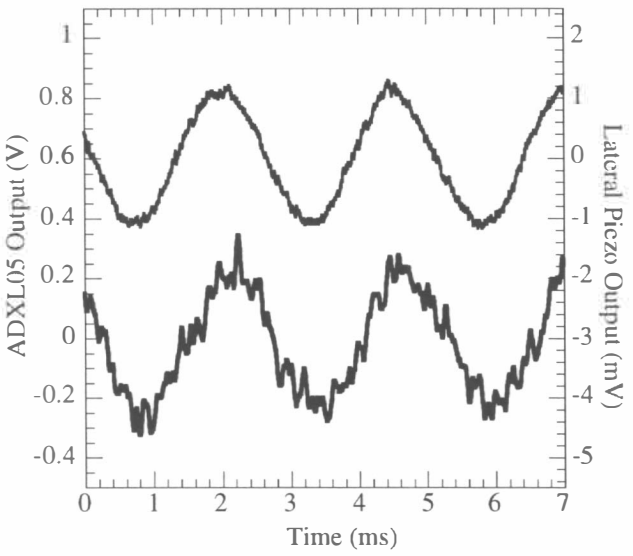

Figure 7. This plot shows the sigle-sweep output signal of a 1mm lateral piezoresistive accelerometer (upper curve) and the ADXL05 (lower curve) to the same 0.2 g, 400Hz acceleration signal. The signal/noise ratio for the lateral piezoresistor is about 5x better within the full 100 kHz bandwidth of the circuitry used to acquire both signals.

After processing, the devices are mounted in DIPs, and lids are bonded after heating at 150C for 2 hours. The sensors are sealed with air at atmospheric pressure. We believe that this sealing procedure allows some humidity into the package which probably contibutes to surface leakage and adds noise. Experiments on professionally sealed sensors are planned.

EXPERIMENTAL RESULTS

We have built accelerometers with four proof mass lengths (0.2mm, 0.5mm, 1.0mm, and 2.0mm) and two hinge thicknesses (2.4u and 4.4u). We have evaluated these accelerometers for sensitivity, linearity, bandwidth, and noise.

Figure 7 shows the time-domain acceleration response of a 1mm lateral piezoresistive accelerometer compared to the response of an ADXL05 accelerometer subjected to the same 0.2g acceleration. Both sensors feature mechanical cutoff frequencies near 1 kHz, and both are operated with amplification circuits that offer bandwidth in excess of 100 kHz. We can see from this data that the lateral piezoresistive accelerometer has a somewhat better signal/noise ratio than the ADXL05 at this frequency.

Measurements of the frequency response of representative lateral piezoresistive accelerometers are shown in Fig. 8. The sensors with the longest masses offer the largest sensitivity, as well as the lowest resonant frequencies. The trends in these parameters with mass length are roughly consistent with expectations from the equations presented earlier. These sensors are damped only by the ambient pressure sealed within the package. There are squeeze-film effects at the ends of the accelerometer motion which can be adjusted by changing the size of the gaps surrounding the mass, or by changing the pressure or viscosity of the gas used to seal these sensors.

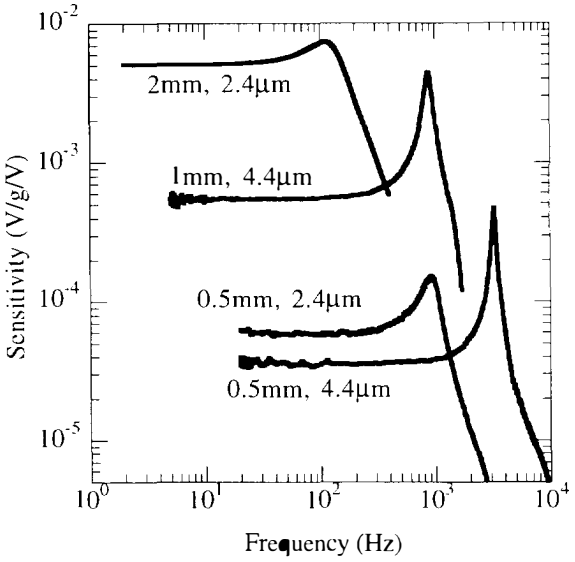

Figure 8. This plot shows the sensitivity of 4 lateral piezoresistive accelerometers as a function of frequency. Each curve is labeled with the length of the proof mass and the width of the flexure.

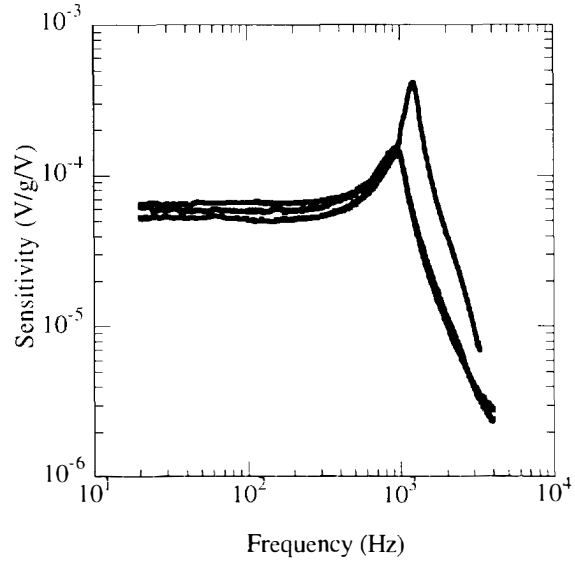

Figure 9. This graph shows the sensitivity of 3 nominally identical 0.5mm, 2.4μm accelerometers to illustrate the uniformity that has been achieved in this process. The sensitivity of these sensors below resonance is within 5% for this group.

Three different accelerometers with 0.5mm flexures were characterized to illustrate the variations in process parameters. Figure 9 shows the measured frequency response of these 3 accelerometers. The variations in sensitivity among these sensors are within 5% of the mean at all frequencies below the resonance. demonstrating the uniformity possible with the fabrication procedure described above. The sensor with the more pronounced peak was packaged at elevated temperatures in an effort to limit trapped humidity, and is probably at a reduced pressure after cooling. This reduced pressure could explain the increased sensitivity of this device on resonance.

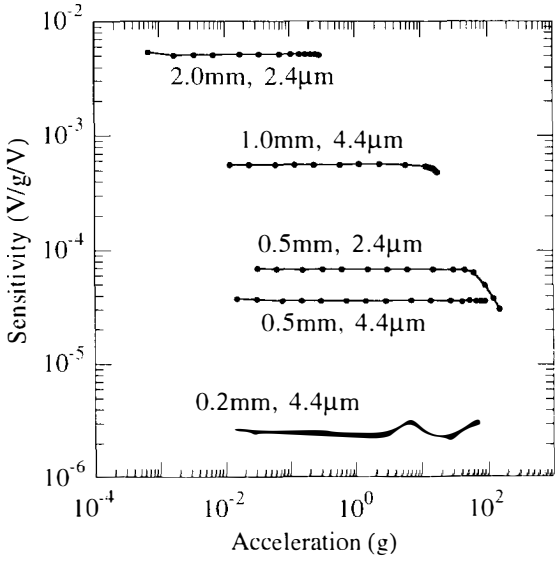

Figure 10. This graph shows the sensitivity of a representative set of accelerometers as a function of applied acceleration signal. In almost every case, the sensors display linearity within 5% for signals up to the level where the mass begins to undergo collisions with the endstops

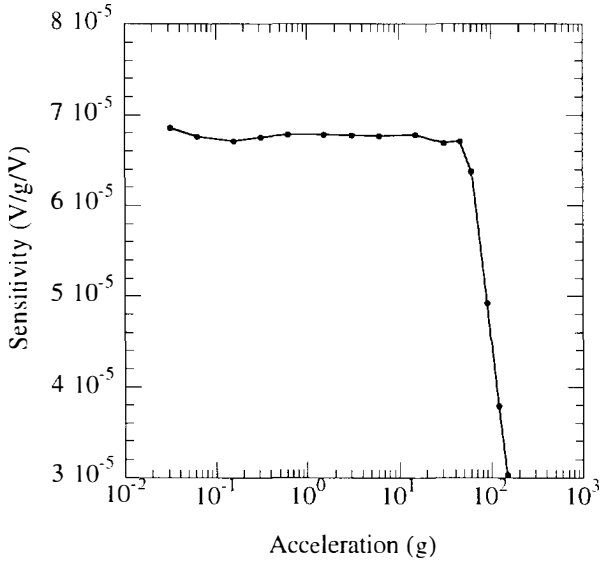

Figure 11. This graph shows the linearity data for the accelerometer with the 0.5mm long, 2.4μm wide flexure. The sensor output signal was calibrated against a laser interferometer in this measurement. At signal levels below the collisions with the endstops, the sensitivity was measured to be within 2% of the mean value.

The linearity of these sensors was measured, and is plotted in Fig. 10. The large 2mm sensors are of course the most sensitive but they hit their endstops at the smallest accelerations. The smaller devices have lower sensitivity but greater range. Figure 11 shows the linearity of a typical 0.5 mm flexure on an expanded vertical scale. This sensor has sensitivity within 2% of the mean for accelerations measured from 30mg to 50g. In all cases, the

sensors encounter the endstops before significant nonlinearity arises from other sources. These endstops have successfully protected all mounted sensors from breakage without evidence of stiction, but extensive shock testing must be carried out to fully evaluate their performance.

The design of these accelerometers includes a capability for self-test. Electrical contacts can be added to the silicon structures which form the endstops, and a test voltage can be applied to that electrode causing the mass to deflect a known amount. Figure 12 shows a micrograph of an electrode formed at one of the stops which is suitable for this application.

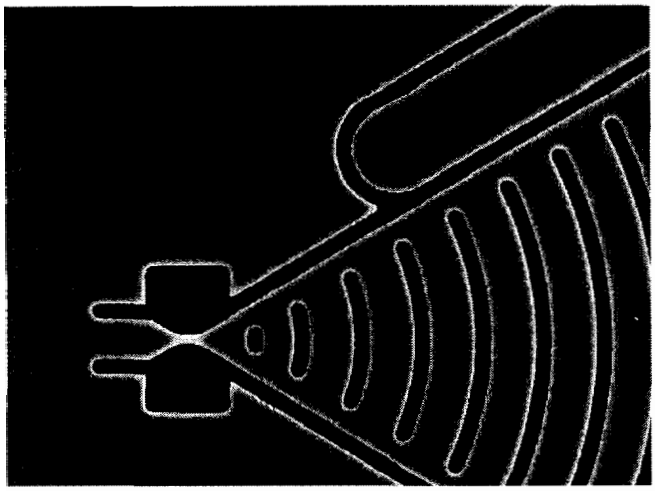

Figure 12. This SEM micrograph shows an image of a lateral piezoresitive accelerometer with additional electrodes for self-test. Voltages may be applied to the element on the upper left of the figure, causing a lateral force on the mass, and producing a suitable acceleration test signal.

Noise in piezoresistive sensors is generally attributed to Johnson noise, amplifier noise, temperature coefficients, and other sources of drift. Most of the real work in improving the performance of commercial piezoresistive sensors is associated with use of temperature compensation and with strain-relieved mounting. Preliminary temperature compensation is achieved by building full Wheatstone bridges using resistive elements with the same temperature coefficients as the sense elements. Strain relief is achieved by "soft die attach" techniques which use compliant materials for mechanical attachment, such as silicone, and minimizing transmission of package stress to the sense elements. We have implemented a full Wheatstone bridge of identical sense elements, as shown in Fig. 6. Strain relief is achieved by attaching the flexure to a mechanical support which is cantilevered off of the substrate, and thereby isolating the strain-sensing elements from substrate stress, as shown in Figs. 1, 2 and 5.

Figure 13 shows measurements of the noise spectra of current "best" and "worst" accelerometers, along with a noise measurement taken from a lateral piezoresistive test structure built in a similar process. In addition, the voltage noise of a commercial piezoresistive sensor is plotted. There are several conclusions to be drawn from this data. First and foremost, the "best" and "worst" accelerometers both exhibit significant noise in excess of the noise measured from a test structure and from the commercial piezoresistive sensor. The source of this excess noise is not precisely known at this time, but it is very likely due to current leakage along the surfaces of the piezoresistor or through the flexure. Work is underway to identify and eliminate this noise source, and there is every reason to believe that the noise can be brought into line with the lowest curves in Fig. 13. Also, the noise from the test structure and the commercial piezoresistive sensor are at about the same level, indicating that the lowest noise curve is a reasonable target for our devices.

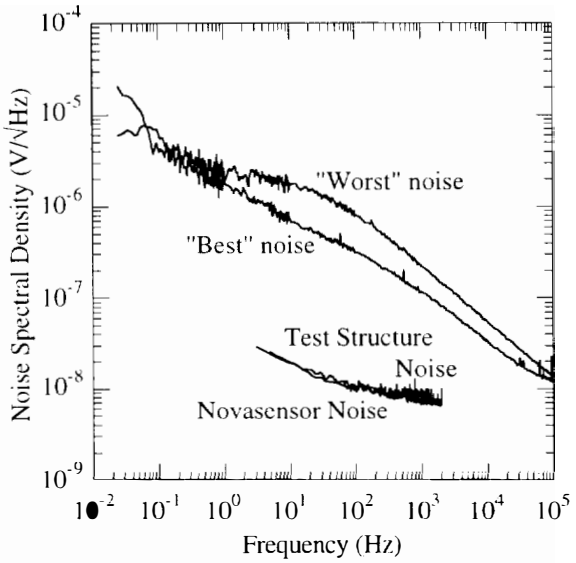

Figure 13. This graph shows the Noise Spectral Density of the lateral piezoresistive accelerometers. The noise is not dependent on size or shape of sensor, but is found to vary between the two upper curves for most sensors in the current generation. For comparison, we also plot the noise of a commercial piezoresistive pressure sensor, and a lateral piezoresistive test structure made in a process very similar to the accelerometer process ***[4]****.*

Given the sensitivity curves shown in Fig. 8 and the noise curves in Fig. 13, we can plot the resolution of our lateral piezoresistive accelerometers, as shown in Fig. 14. This data shows that the current performance of these sensors is already competitive with the ADXL05. It is important to note that the performance of these sensors should improve significantly if the noise can be lowered to the levels that have been measured for lateral piezoresistive test structures.

The performance of these accelerometers is summarized in Table 1. This table compares the 1mm lateral piezoresistive accelerometer to the commercial specifications for the ADXL05, and indicates that the current performance of this device is already very impressive.

Parameter	ADXL05	1mm Lateral Piezoresistor
Sensitivity	200 mV/g	0.7 mV/g
Bandwidth	1.5 kHz	1 kHz
Range	5g	10g
Linearity	0.2%	<2%
Noise	0.1g RMS	0.03g RMS
Resolution	0.5 mg/√Hz	2mg/√Hz - 0.04mg/√Hz

Table 1 Comparison between ADXL05 and present performance for 1mm lateral piezoresistive sensor.

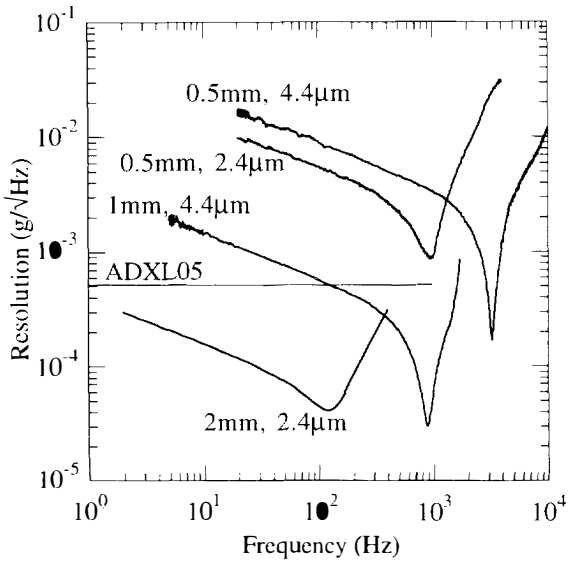

Figure 14. This graph shows the resolution of several lateral piezoresistive accelerometers. The resolution of the ADXL05 is shown for reference

DISCUSSION

Piezoresistive sensing offers many important advantages for low-cost sensors. Probably the most significant advantage is that the resistance measuring circuitry can be implemented as low-cost hybrids with laser-trimmed thick-film circuit elements for offset compensation. Many companies have manufactured small, moderate, or large quantities of such sensors while maintaining profit margins in low-cost applications. Clearly, any measurement technology which can capitalize on this infrastructure and improve performance should find broad applications.

The piezoresistive sensors described here can be inserted directly into such a production environment. The fabrication process used for these sensors was developed in close coordination with Lucas NovaSensor, and is specifically compatible with existing low-cost sensor fabrication procedures in use in their facility. Reliable cost models also exist at Novasensor for sensors manufactured using these techniques, and these models indicate that the sensors described in this manuscript can be manufactured in moderate quantities for a few dollars/unit.

The current performance of these sensors is comparable with ADXL05 performance levels. The limitation to this performance is currently due to excess noise related to surface or internal leakage currents in the sensor. We have good reason to believe that this noise source can be eliminated, because it has been eliminated in test structures fabricated using the same approach. If this noise can be brought into agreement with the noise seen on test structures, the resolution of this sensor will improve to as much as 2-3 orders of magnitude below that of the ADXL05, which would enable use of this sensor in a much broader range of applications.

Generally, the academic MEMS community has not shown much recent interest in piezoresistive sensing methods. The well-known problems with temperature coefficients and limited sensitivity have probably contributed to this lack of interest. Nevertheless, industrial manufacturers of piezoresistive sensors have managed to handle these problems with careful packaging and bridge circuits. Given the higher cost of other sensing technologies, perhaps piezoresistors deserve some re-examination. The combination of piezoresistive sensing and DRIE-etching of planar flexures may have many applications beyond acceleration sensing, such as gyroscopes, flow sensors, magnetic field sensors, and so on.

CONCLUSIONS

We have designed and built a high-performance piezoresistive accelerometer using DRIE etching and oblique ion implantation. The resulting prototype accelerometers offer performance parameters consistent with the best inexpensive commercial accelerometer, the ADXL05, and there is good reason to expect significant performance improvements very soon. Finally, this general technology may find broad use in other sensing applications.

ACKNOWLEDGEMENTS

The authors thank Dan Rugar of IBM Almaden for advice and assistance on critical point drying, Pauline Prather of Stanford for assistance with device packaging, and Howard Rockstad of JPL for support and patience. This work is supported by JPL/NASA, NSF CAREER (ECS-9502046), NSF Instrumentation for Materials Research (DMR-9504099), and the Terman Fellowship.

REFERENCES

1. L.M. Roylance and J.B. Angell, "A Batch Fabricated Silicon Accelerometer", *IEEE Transactions on Electron Devices*, ED-26, 1911 (1979).

2. For examples, see E.H. Klaassen et.al, "Silicon Fusion Bonding and Deep Reactive Ion Etching: A New Technology for Microstructures", *1995 International Conference on Solid-State Sensors and Actuators*, (Transducers '95) 556 (1995).

3. B.P. van Drieënhuizen, N.I. Maluf, I.E. Opris, G.T.A. Kovacs, "Force-Balanced Accelerometer with mG Resolution, Fabricated using Silicon Fusion Bonding and Deep Reactive Ion Etching" *1997 International Conference on Solid-State Sensors and Actuators*, (Transducers '97), 1229-30, 1997.

4. B.W. Chui, T.W. Kenny, H.J. Mamin, B.D. Terris, and D. Rugar, "Independent Detection of Vertical and Lateral Forces with a Sidewall-Implanted Dual-Axis Piezoresistive Cantilever", *Appl. Phys. Lett.* 72, 1388 (1998). and B.W. Chui, H.J. Mamin, B.D. Terris, D. Rugar, T.W. Kenny, "Sidewall-Implanted Dual-Axis Piezoresistive Cantilever for AFM Data Storage Readback and Tracking.", *Proceedings of IEEE International Workshop on MEMS. Heidelberg, pp. 12 (1998).*

5. F. Goodenough, "Airbags Boom when IC Accelerometer Sees 50g", *Electronic Design* 39 (1991). and Analog Devices ADXL05 Data Sheet, Analog Devices, Norwood CT.

6. E.M. Chow et al, "Fabrication of High-Density Cantilever Arrays and Through-Wafer Interconnects", Proceedings, 1998 Solid State Sensor and Actuator Workshop, Hilton Head, this digest (1998).

A STUDY OF MICROCANTILEVER QUALITY FACTOR

Kevin Y. Yasumura[a], **Timothy D. Stowe, Eugene M. Chow, Timothy Pfafman, Thomas W. Kenny**
Departments of Applied Physics, Electrical Engineering, and Mechanical Engineering, Stanford University, Stanford California 94305-4021

Daniel Rugar
IBM Research Division, Almaden Research Center, San Jose, California 95120-6099

ABSTRACT

Micromechanical cantilevers are commonly used for detection of small forces in MEMS sensors (accelerometers) and in scientific instruments (atomic force microscopes). A fundamental limit to the measurement of small forces is imposed by the mechanical analog of Johnson noise, thermomechanical noise, which is governed by dissipation of mechanical energy in the force measuring cantilever. In this paper we report on measurements of the mechanical quality factor, Q, for arrays of silicon nitride, polysilicon, and single crystal silicon cantilevers. By studying the dependence of the mechanical energy dissipation on the cantilever material, geometry, and surface treatments, we hope to identify the dissipation mechanisms, and offer guidelines for the design of cantilevers for measurements of small forces. Preliminary results show that Q decreases with cantilever thickness indicating surface loss mechanisms. Significant improvement of the Q is obtained after annealing in either N_2 or forming gas.

INTRODUCTION

The majority of MEMS sensors measure forces applied to micromechanical flexures. Examples include pressure sensors which measure force on a diaphragm, and accelerometers and gyroscopes which measure inertial force on a proof mass. Because of the cost advantages associated with miniaturization, many sensors are required to measure surprisingly small forces. For example, the Analog Devices ADXL05 accelerometer features a proof mass with a mass of approximately 10^{-10} kg and is capable of detecting an acceleration as small as 5×10^{-4} g in a 1 Hz bandwidth. This acceleration represents a force of 0.5 pN applied to the mass.

Ordinarily, sensor performance is improved by reducing the noise of the preamplifier used to convert the physical signals to electrical signals, and by controlling other error sources such as uncompensated thermal drift. There eventually comes a point, however, where thermodynamics imposes a barrier to further sensor improvement. For the case of microcantilevers optimized for use in force detection, thermomechanical noise sets a limit to the ultimate force resolution **[1]**.

Thermomechanical noise is a consequence of the cantilever being in thermal equilibrium with its environment (i.e., a heat bath with many microscopic degrees of freedom). Energy dissipation in the cantilever causes the stored mechanical energy to leak away and be converted to heat. The stronger the coupling between the cantilever and the heat bath, the faster the decay of cantilever motion towards thermal equilibrium and the lower the mechanical quality factor, Q, of the oscillating mode. Conversely, the coupling to the heat bath has the consequence that the cantilever will be subjected to constant random excitation by its interaction with the many microscopic degrees of freedom in the heat bath. This relationship between the energy dissipation and random excitation is embodied in the "fluctuation-dissipation theorem" of statistical mechanics, which applies to mechanical systems just as it applies to the Johnson noise across an electrical resistor. The net result is that the lower the mechanical Q of the system, the larger the force noise.

The equipartition theorem gives a measure of how much thermal energy is in each mode of a microcantilever. The mean square vibration amplitude associated with a mode of oscillation is given by

$$\frac{1}{2}k_BT = \frac{1}{2}k\langle x^2\rangle. \qquad (1)$$

We can calculate the equivalent force noise associated with mechanical dissipation by imposing the requirement that random thermal excitations must produce the mean square vibration amplitude given by Eq. 1. The mean square vibration amplitude is the integral over all frequencies of the force noise spectral density multiplied by the mechanical transfer function

$$\langle x^2\rangle = \int_0^\infty |G(f)|^2 S_F df, \qquad (2)$$

where the transfer function is

$$G(f) = \frac{f_0^2/k}{(f_0^2 - f^2) + i(ff_0/Q)}. \qquad (3)$$

This results in a force noise spectral density of $S_F = 4kk_BT/\omega_0 Q$. This spectral density results in a noise force in a bandwidth B of

$$F_{min} = \sqrt{\frac{4kk_BTB}{\omega_0 Q}}. \qquad (4)$$

This minimum detectable force can also be expressed in terms of the cantilever dimensions: w is the cantilever width, l is the cantilever length, and t is the cantilever thickness.

$$F_{min} = \left(\frac{wt^2}{lQ}\right)^{1/2}(k_BTB)^{1/2}(E\rho)^{1/4}, \qquad (5)$$

where E is the modulus of elasticity and ρ is the mass density of the cantilever material. From this equation for the minimum detectable force a strategy can be found to design ultrasensitive cantilevers: make them narrow, thin, and long. This strategy is effective only if high mechanical Q is maintained. Unfortunately, relatively little is understood about the mechanisms responsible for intrinsic energy dissipation in micron and submicron thick microstructures.

[a] Department mail: Department of Applied Physics, Stanford University, Stanford, CA, 94305-4021; Electronic mail: yasumura@leland.stanford.edu

0-9640024-2-6/hh1998/$20©1998TRF
DOI 10.31438/trf.hh1998.15

Solid-State Sensors, Actuators, and Microsystems Workshop
Hilton Head Island, South Carolina, June 8-11, 1998

For a beam oscillating in a flexural mode, the stored energy is proportional to the square of the peak strain integrated over the volume of the beam. If the primary source of dissipation is due to bulk internal losses (i.e., internal friction due to lattice dislocations, impurities, two level systems, etc.) and if the dissipation is proportional to the square of the strain, as is usually the case, then the energy lost per cycle will also be proportional to the square of the peak strain integrated over the volume of the beam. Since the stored energy and the dissipation involve the same volume integrals of strain squared, their ratio, and hence Q, will be independent of cantilever geometry.

On the other hand, if the dissipation is not due to bulk internal losses, but rather due to surface losses **[2]**, then the dissipation will be proportional to the square of the peak strain integrated over the *surface* area of the beam. After evaluation of the appropriate integrals, one finds that the Q for a cantilever oscillating in its lowest order flexural mode will be proportional to thickness, t. This dependence on thickness would be expected for micromechanical systems with large surface-to-volume ratios.

Based on this reasoning, we have set out to study the relationship between dissipation and controllable cantilever properties such as material, geometry, and surface treatment. We have fabricated arrays of silicon nitride, polysilicon, and single crystal silicon cantilevers and performed measurements of the Q of these cantilevers. In this paper we present the preliminary results from this ongoing study.

CANTILEVER FABRICATION

Three materials have been used to fabricate our cantilevers—silicon nitride, polysilicon, and single crystal silicon. The first, silicon nitride, was chosen because of its durability, ease of fabrication, and general use as a processing material. The second material, polysilicon, was chosen because of its wide use in the MEMS community as a sensor material. A number of fabrication processes rely on a top polysilicon layer from which a sensor or device is fabricated, making a study of dissipation in polysilicon resonators of wide interest. The last material, single crystal silicon, was chosen because of its expected low internal friction as exhibited by larger bulk oscillators **[3,4]** and low internal stress allowing for the fabrication of ultrathin cantilevers with little or no curling **[5].**

Silicon nitride cantilevers, as shown in Fig. 1, were fabricated from LPCVD low stress silicon nitride grown on ⟨100⟩ silicon wafers. After film deposition, the cantilevers were patterned and then defined using an SF_6 dry etch. A TMAH etch was then used to etch away the exposed silicon and undercut the cantilevers. Finally, critical point drying was used to release the thin cantilever structures **[6].**

Polysilicon cantilevers were fabricated from polysilicon-on-insulator wafers. Starting with a ⟨100⟩ silicon wafer, a 4000 Å-thick layer of thermal oxide was grown. Next a polysilicon layer of the desired cantilever thickness was deposited. The cantilevers were then patterned using a mask pattern similar those in Fig. 1 and protective layers of low temperature oxide and silicon nitride were deposited to protect the cantilevers during backside patterning and a TMAH etch. Lastly, the topside silicon nitride layer was removed and a BOE etch was used to free the oxide encased cantilever structures. Finally, a critical point drying step was performed.

Single crystal silicon cantilevers start with ⟨100⟩ SOI wafers. A thermal oxidation was performed to thin down the top silicon layer to the desired cantilever thickness. A BOE etch was then used to remove the top oxide layer exposing the top silicon layer for cantilever patterning. As in the polysilicon process, low temperature oxidation and silicon nitride deposition was then used for frontside protection and as a backside masking layer during the backside TMAH etch. The cantilevers were then released with a BOE etch followed by critical point drying to prevent cantilever stiction and curling. Fig. 2 shows a photograph of a 600 Å-thick single crystal silicon cantilever. Further details of the fabrication process can be found in the work of Stowe, *et al.* **[5]**.

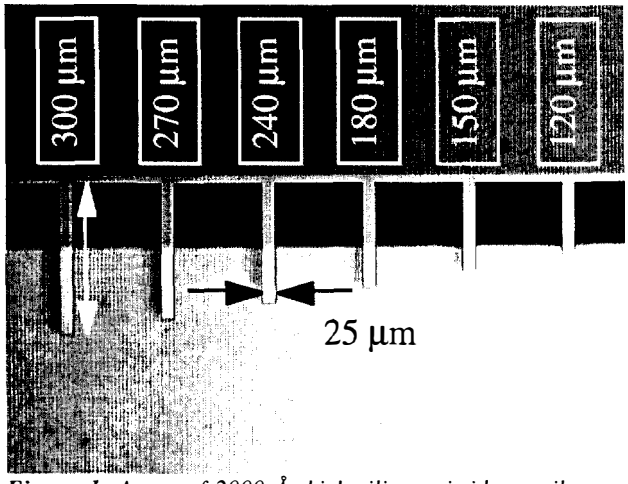

***Figure 1**. Array of 2000 Å-thick silicon nitride cantilevers. Shown is part of an array of w = 25 µm cantilevers of length varying from 120 to 300 µm. Cantilever arrays made from silicon nitride and polysilicon use this array pattern.*

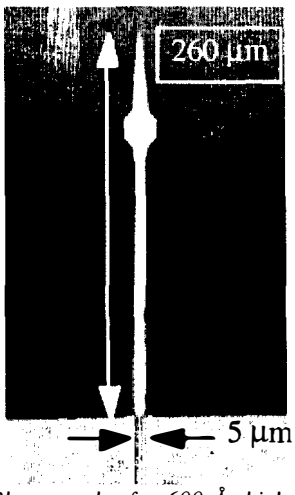

***Figure 2**. Photograph of a 600 Å-thick single crystal silicon cantilever. Arrays of such cantilevers consist of cantilevers of varying length. Shown is a cantilever with a neck width of 5 µm and length of 260 µm.*

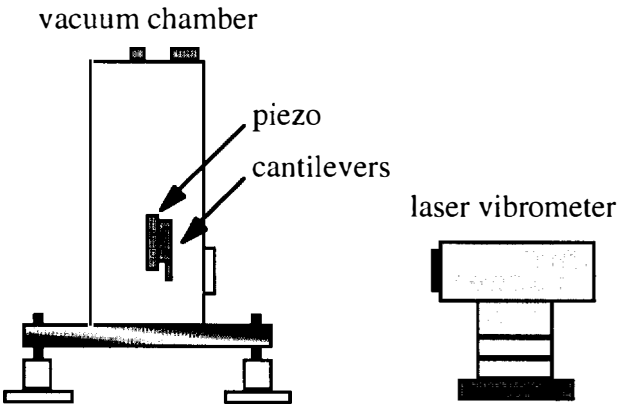

***Figure 3**. Diagram of the Q measurement system. Shown are the vacuum chamber, piezoelectric disk stack, cantilever die, and laser doppler vibrometer.*

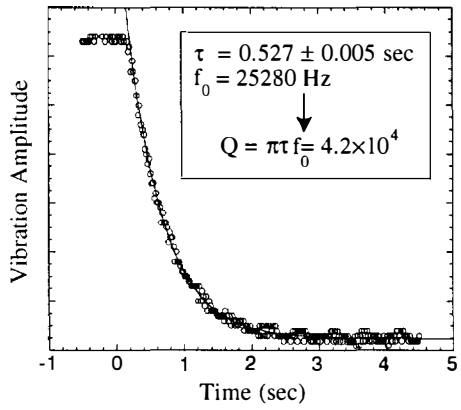

***Figure 4**. Sample cantilever ring-down and exponential curve fit. Cantilever is polysilicon t = 2.3 μm, w = 25 μm, l = 210 μm.*

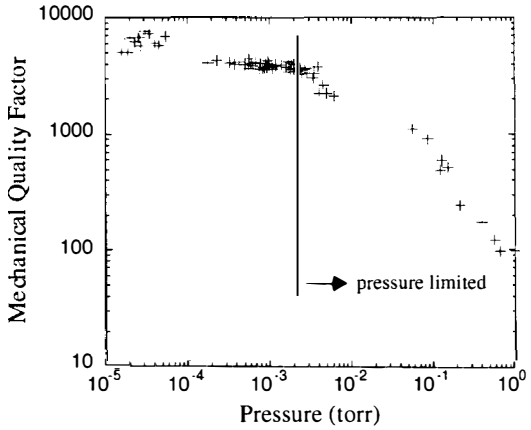

***Figure 5**. Q vs. pressure for a 5100 Å-thick silicon nitride cantilever.*

Q MEASUREMENTS

A diagram of the experimental system is shown in Fig. 3. The cantilevers were placed in a vacuum chamber on a stack of piezoelectric disks. A viewport on the side of the dewar allows the use of an external laser doppler vibrometer (LDV) to measure the cantilever motion. The LDV is a commercially available system which measures the velocity dependent doppler shift of the reflected laser radiation [7].

A "free ring-down" technique was used to measure cantilever Q. The cantilevers were first driven on-resonance to a steady state amplitude. The drive excitation was produced by applying an oscillating voltage to the piezoelectric disks on which the cantilever die has been mounted. The drive was stopped abruptly and the cantilever motion was measured as the amplitude decayed. Figure 4 shows a typical ring-down for a polysilicon cantilever. The ring-down was then curve fit to an exponential function. From the fit, the time constant of the ring-down, τ, was obtained. The decay time constant, with the cantilever resonance frequency for the first mode, allows calculation of the cantilever $Q = \pi\tau f_0$. The exponential decay curve fit allows us to be sure of the accuracy of each Q measurement. Data presented in this paper are averages of multiple ring-down measurements for each cantilever. As shown in Fig. 4, the error for each individual cantilever ring-down measurement is on the order of a few percent.

One important source of energy dissipation in micromechanical oscillators is air damping. Figure 5 shows a measurement of the mechanical Q as a function of air pressure for silicon nitride cantilevers 5100 Å thick. At atmospheric pressure, the Q of this cantilever was significantly suppressed by air damping. We can see that at pressures of 1 mtorr and below, the dissipation associated with air damping becomes negligible compared to intrinsic loss mechanisms. The work described in this paper was performed under vacuum at a pressure of 10^{-6} torr. The measurements were performed at room temperature.

For the cantilever used in Fig. 4, the repeatability and long term stability of the cantilever Q was measured over a period of two hours. The results are plotted in Fig. 6. Over this two hour time span the Q had a standard deviation of 1% demonstrating excellent measurement reproducibility. On the other hand, retesting of cantilevers after they have been exposed to laboratory air for several days can show much larger Q variability.

Measurements of Q for arrays of silicon nitride cantilevers were carried out for thicknesses of 2000 Å, 5100 Å, and 7000 Å, lengths from 120 to 300 μm, and widths of 10 and 25 μm. Fig. 7 shows data for three arrays of silicon nitride cantilevers of thicknesses 2000 Å, 5100 Å, and 7000 Å. All of the cantilevers in Fig. 7 had a width of 10 μm. Each of the points in Fig. 7 are the result of the averaging of multiple ring-down measurements for each cantilever. Several trends are clear from this data. First, the Q is roughly independent of the cantilever length. Both bulk (volume) and surface dependent dissipative processes are expected to produce length independent Q's. However, there is an increase in the mechanical Q as the thickness of the cantilever increases. This behavior is most clearly seen in

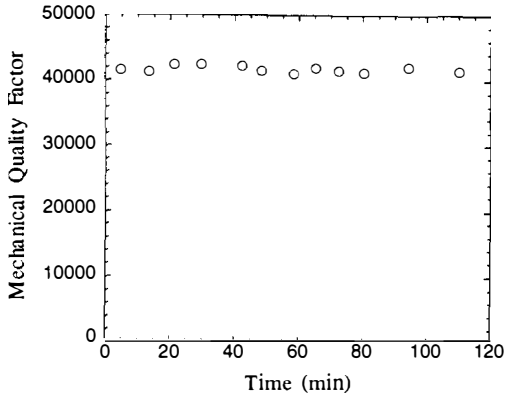

Figure 6. *Mechanical Q vs. Time for a polysilicon cantilever (t = 2.3 μm, w = 25 μm, l = 210 μm) showing a 1% standard deviation in the mechanical Q over a two hour time span.*

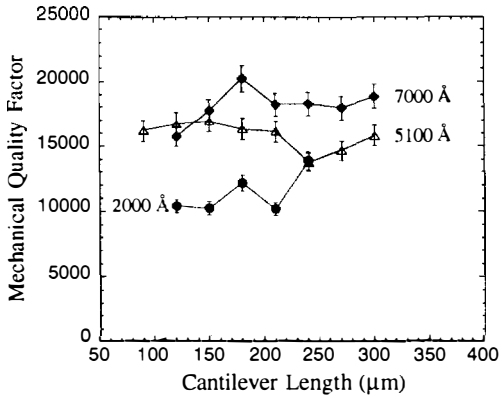

Figure 7. *Mechanical quality factor vs. cantilever length for silicon nitride cantilevers of thicknesses 2000 Å, 5100 Å, and 7000 Å. Cantilever width is 10 μm for all three thicknesses.*

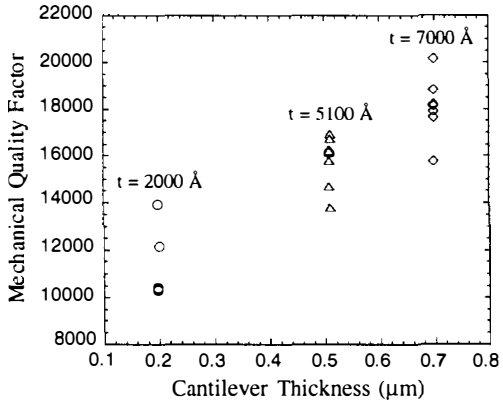

Figure 8. *Mechanical quality factor vs. cantilever thickness for three silicon nitride cantilever thicknesses (2000 Å, 5100 Å, 7000 Å).*

Fig. 8, where we have replotted the data as a function of cantilever thickness. The strong thickness dependence is indicative of surface loss mechanisms, as discussed earlier.

Figure 9 shows data for silicon nitride cantilevers of thickness 5100 Å and two widths of 10 and 25 μm. The Q's of these cantilevers are independent of the cantilever width. Just as the cantilever Q is expected to be length independent for both volume and surface dissipative processes, the cantilever Q should also be independent of cantilever width.

Single crystal silicon cantilevers show geometrical dependence similar to the nitride devices. Figure 10 shows data for single crystal silicon cantilevers of thicknesses 600 Å and 1700 Å. Consistent with the data in Figs. 7 and 8, we see that the Q is roughly independent of cantilever length and proportional to thickness.

Figure 11 shows a compilation of data from our work and from the literature for single crystal silicon oscillators of varying thickness at T = 4K. As in the case of silicon nitride cantilevers, the Q of single crystal silicon oscillators is highly dependent on the oscillator thickness, suggesting surface dominated loss mechanisms. Because this plot has data for different kinds of oscillators it should not be over interpreted, but the general trend is evident—an increase in the mechanical Q as the oscillator dimensions increase. Included in Fig. 11 is data for ultrathin silicon cantilevers **[5,9]**, doubly supported high frequency silicon resonators **[8]**, commercially available silicon cantilevers **[10]**, double torsional oscillators **[11]**, and suspended bulk silicon crystals **[12]**. Shown in Fig. 11 is a line fit to the four thinnest oscillators (t = 600 Å, 1700 Å, 3300 Å, and 1.5 μm). These micron- and submicron-scale cantilevers have a roughly linear Q vs. t dependence. The larger oscillators deviate from this linear dependence possibly because loss mechanisms other than surface mechanisms begin to dominate and limit the Q as the oscillator size increases.

In order to make quantitative comparisons of different cantilever geometries and materials, a parameter which we shall call the 'loss parameter' γ must be introduced. Recall from Eq. 5 that the strategy to make sensitive force sensing microcantilevers was to make them narrow, thin, and long (small k/ω_0) while maintaining high mechanical Q. This general strategy tells us that Q is not the best parameter to use when comparing different oscillators. Even though larger bulk silicon oscillators can obtain Q's of 600,000 at room temperature **[4]**, the large mass and high spring constant of these oscillators make them poor force detectors. In order to determine whether a cantilever, and more generally any oscillator, would be a sensitive force measurement device, all of the cantilever dependent terms in Eq. 4 must be taken into account. By using $\gamma \equiv k/\omega_0 Q$, we can compare cantilevers of different geometries and materials. Expressed in terms of the cantilever geometries and material properties, γ can be expressed as

$$\gamma = 0.246 \frac{wt^2}{lQ} (E\rho)^{1/2} \qquad (6)$$

for the first flextural mode of a simple beam cantilever. For more complicated structures, the correct spring constant and resonance frequencies for each mode of oscillation must be used. This analysis can therefore be extended to include torsional and double torsional oscillators as well as more complex systems where an effective spring constant and resonance frequency can be either calculated or measured directly. Figure 12 shows a

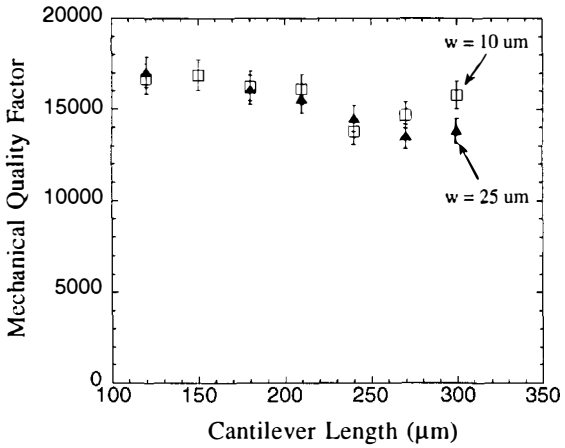

Figure 9. *Mechanical quality factor vs. cantilever length for silicon nitride cantilevers of thickness 5100 Å. Two cantilever widths are shown, 10 μm and 25 μm.*

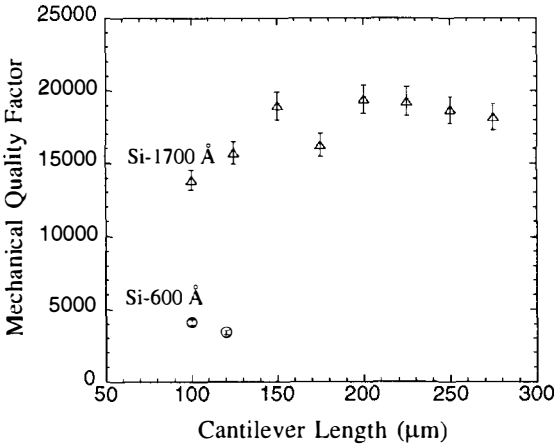

Figure 10. *Mechanical quality factor vs. cantilever length for single crystal silicon cantilevers of thickness 600 and 1700 Å.*

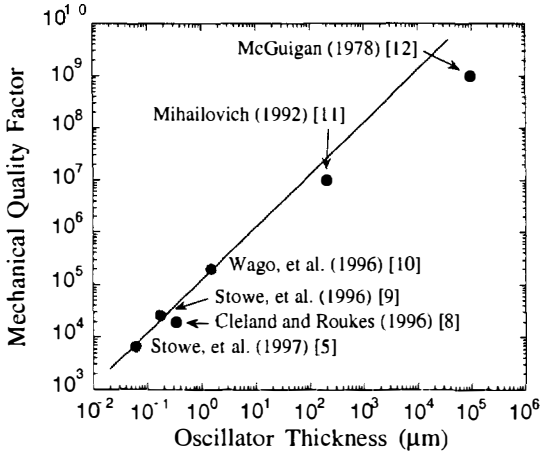

Figure 11. *Mechanical quality factor vs. oscillator thickness for single crystal silicon oscillators at T = 4K.*

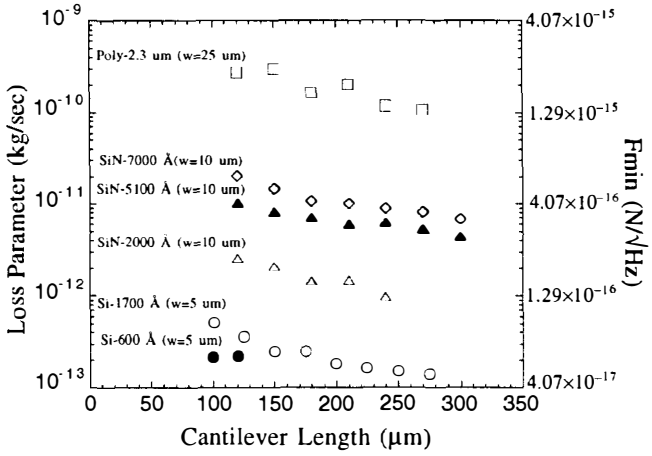

Figure 12. *Loss parameter $\gamma = k/\omega_0 Q$ vs. cantilever length comparison plot. Arrays of silicon nitride, polysilicon, and single crystal silicon cantilevers are shown with their thicknesses and widths. The equivalent minimum force detectable is shown on the right for cantilevers at room temperature.*

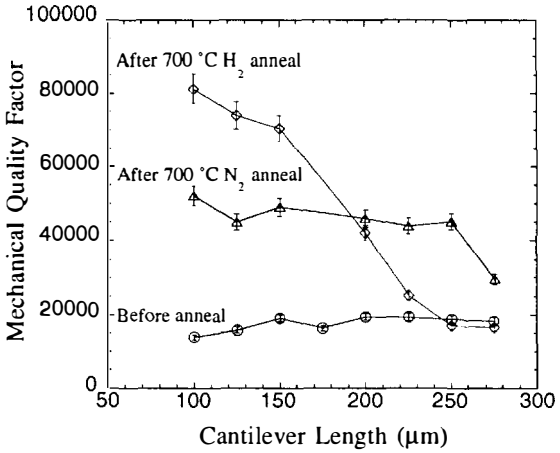

Figure 13. *Mechanical quality factor vs. cantilever length for a die of single crystal silicon cantilevers of thickness 1700 Å showing the effects of surface treatments.*

summary plot of the loss parameter γ for silicon nitride, polysilicon, and single crystal silicon cantilevers. The equivalent minimum force detectable at room temperature is also shown on Fig. 12 for comparison. A 1700 Å-thick single crystal silicon cantilever of length 275 μm, width 5 μm, and Q of 1.8×10^4 has a loss parameter $\gamma = 1.4\times10^{-13}$ kg/sec. This corresponds to a room temperature force noise of 4.8×10^{-17} N/√Hz or 48 aN/√Hz. Let us now compare this cantilever to a thicker nitride cantilever of approximately the same length. A 5100 Å-thick silicon nitride cantilever of length 270 μm, width 10 μm, and Q of 1.5×10^4 has a loss parameter $\gamma = 5.1\times10^{-11}$ kg/sec and a force sensitivity of 290 aN/√Hz. Thus the silicon cantilever has six times lower equivalent force noise than the thicker silicon nitride cantilever at room temperature. In Fig. 12 we can also see that the relationship between cantilever stiffness and length causes the longer cantilevers to have improved force resolution than the shorter cantilevers. This is expected because longer cantilevers have lower k/ω_0 yet have the same approximate Q.

SURFACE TREATMENTS

As seen in Figs. 8 and 11, the mechanical Q of both silicon nitride and single crystal silicon cantilevers are dependent on the cantilever thickness, suggesting surface dominated loss mechanisms. Possible sources of surface loss are adsorbates on the cantilever surface or surface defects created during the cantilever fabrication process. High temperature surface treatments of 1700 Å-thick single crystal silicon cantilevers are shown in Fig. 13. A 1 hour 700°C anneal in a nitrogen atmosphere increased the Q by a factor of two. Subsequent annealing of the same cantilever array in forming gas (Ar with 4.25% H_2) for 1 hour at 700°C caused additional increase in the Q for the shorter cantilevers—up to 80,000. The ability to influence the Q of these cantilevers so dramatically using surface treatments is promising.

CONCLUSIONS

The goal of this study is to understand the dissipation mechanisms in micromechanical oscillators. For all of the silicon nitride and single crystal silicon cantilevers studied, surface dissipation mechanisms appear to be the dominant source of energy dissipation. For both silicon nitride and single crystal silicon cantilevers a linear Q vs. cantilever thickness behavior has been observed. This behavior is consistent with surface-dominated energy dissipation. Further, preliminary experiments on 700°C surface treatments of silicon cantilevers indicates that surface contaminants or defects can be removed via such treatments allowing up to four fold Q increase.

It is clear that further experiments should be carried out. For example, performing experiments in ultra-high vacuum would allow better control over surface characteristics. Also, Q measurements over a broader set of cantilever thicknesses need to be performed to establish a quantitative thickness dependence of the Q. Finally, the role of other surface characteristics, such as deposited films, should be explored.

ACKNOWLEDGMENTS

This work has been supported by the National Science Foundation CAREER Award (ECS-9502046), the National Science Foundation GOALI Award (ECS-9422255), the National Science Foundation Instrumentation for Materials Research Program (DMR 9504099), and the Terman Fellowship.

REFERENCES

1. T.B. Gabrielson, "Mechanical-Thermal Noise in Micromachined Acoustic and Vibration Sensors", *IEEE Transactions of Electron Devices, 40*, 5, 903-9 (1993).

2. R.E. Mihailovich and N.C. MacDonald, "Dissipation measurements in vacuum-operated single-crystal silicon microresonators", *Sensors and Actuators A, 50*, 199-207 (1995).

3. V.B. Braginsky, "Systems with Small Dissipation" (The University of Chicago Press, Chicago, 1985).

4. R.A. Buser and N.F. De Rooij, "Very High Q-factor Resonators in Monocrystalline Silicon", *Sensors and Actuators, A21-A23*, 323-327 (1990).

5. T.D. Stowe, K. Yasumura, T.W. Kenny, D. Botkin, K. Wago, and D. Rugar, "Attonewton force detection using ultrathin silicon cantilevers", *Appl. Phys. Lett., 71*, 288-290 (1997).

6. G.T. Mulhern, D.S. Soane, and R.T. Howe, *1993 International Conference on Solid-State Sensors and Actuators: Transducers '93* (Yokohama, Japan, 1993).

7. Polytec P.I., 302 Sensor Head with OVF3001 Controller.

8. A.N. Cleland and M.L. Roukes, "Fabrication of high frequency nanometer scale mechanical resonators from bulk Si crystals", *Appl. Phys. Lett., 69*, 2653-5 (1996).

9. T.D. Stowe, K. Yasumura, T.W. Kenny, D. Botkin, K. Wago, and D. Rugar, "Ultrasensitive vertical force probe for magnetic resonance force microscopy", *Solid-State Sensor and Actuator Workshop, Hilton Head*, South Carolina (1996).

10. K. Wago, O. Züger, R. Kendrick, C.S. Yannoni, and D. Rugar, "Low temperature magnetic resonance force detection", *J. Vac. Sci. Technol. B, 14*, 2, 1197-201 (1996).

11. R.E. Mihailovich, "Low temperature properties of boron doped silicon", *Phys. Rev. Lett., 68*, 3052-5 (1992).

12. D.F. McGuigan, "Measurements of the mechanical Q of single-crystal silicon at low temperatures", *J. Low Temp. Phys., 30*, 621-9 (1978).

MEMS DEFORMABLE MIRRORS FOR ADAPTIVE OPTICS

Thomas Bifano, Raji Krishnamoorthy Mali
Dept. of Aerospace and Mechanical Engineering
Boston University, Boston, MA 02215.

Julie Perreault, Mark Horenstein
Dept. of Electrical and Computer Engineering
Boston University, Boston, MA 02215.

David Koester
MEMS Technology Applications Center, MCNC
3021 Cornwallis Road, RTP, NC 27709.

ABSTRACT

This paper describes the development of continuous and segmented deformable mirrors fabricated using surface-micromachining technology. Such mirrors have applications in adaptive optics imaging systems to correct phase aberrations in the optical path. Electrostatic actuators with 2 μm surface-normal stroke provide controlled deformation to the mirror surface. Results of electromechanical characterization of several deformable mirrors are presented. Real time correction of optical aberrations is demonstrated using a single mirror segment with closed-loop feedback control.

INTRODUCTION

MEMS based deformable mirrors have been investigated by several research groups as an inexpensive and high-performance alternative technology to more conventional piezoelectric deformable mirrors. Previous research has focused on continuous, bulk-micromachined modal mirrors **[1,2]** and surface-micromachined, piston-motion segmented mirrors **[3]**. Our research investigates the first continuous-membrane, zonal correctors to be fabricated using surface-micromachining techniques. We have also developed segmented mirrors (both piston and tip-tilt types) having fill factors of 95 to 98% which are much higher than previously demonstrated.

Figure 1 shows a schematic of three deformable mirror systems evaluated in our experiments. In each case, the mirror(s) are supported by multiple attachments to an underlying array of identical, fixed-fixed electrostatic actuators. These actuators provide precise control of the position of the mirror's attachment points in the surface-normal direction. The typical actuator is constructed from a 300 μm-square deformable membrane spaced at a 350 μm center-to-center distance from its nearest neighbors. Segmented mirrors capable of pure piston motion only have no inter-actuator coupling, allowing much simpler control algorithms in multi-actuator systems. However, they may exhibit undesirable diffraction due to the gaps between segments. Continuous mirrors offer the advantage of no diffraction, but a complicated control algorithm is required to address inter-actuator coupling. Segmented mirrors with tip-tilt motion are a hybrid design and permit matched optical phase at mirror segment edges.

Prototype actuators and mirror systems were first fabricated in a three-layer multi-user polysilicon foundry process offered by MCNC (MUMPS). **[4]**. A detailed study of

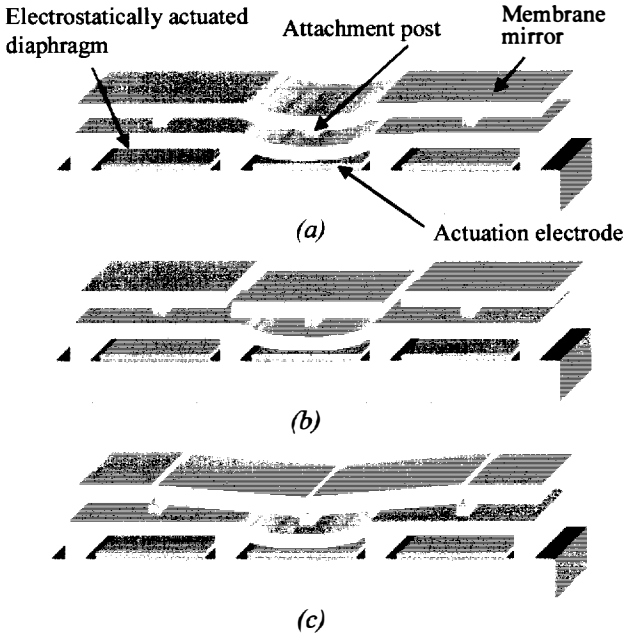

Figure 1. *Schematic of deformable mirror array sections with (a) continuous mirrors (b) segmented mirrors with piston motion (c) segmented mirrors with tip-tilt motion.*

electrostatic actuators fabricated in MUMPS reported previously **[5]**, indicated a device yield that was sufficiently high (~95%) to make large-scale mirror arrays feasible. Statistical analysis of an ensemble of ramp actuation tests on these actuators revealed a position repeatability of 10 nm for σ limits corresponding to 99% probability. A dynamic motion response study showed the actuators to have a mechanical response frequency bandwidth greater than 70 kHz. However, some electrostatic charging effects were observed, possibly due to the presence of surface leakage paths **[6]**.

Our early attempts to fabricate deformable mirrors using the MUMPS foundry process resulted in devices with excessive surface topography caused by patterning and etching of successive thin films. A novel planarization strategy based on setting a maximum line spacing for all patterned layers was developed and has enabled us to control surface topography to submicron levels. Restraining line spacing allows each deposited layer to fill in gaps as its conforms to the surface of the most recently deposited layer. Using this planarization strategy, we

0-9640024-2-6/hh1998/$20©1998TRF
DOI 10.31438/trf.hh1998.16

have been able to fabricate mirrors with 0.75 μm stroke capability. using the MUMPS foundry process. Experimental and modeling results for these mirrors have been previously reported [7].

The maximum line width planarization strategy also has been used to fabricate the mirrors described in this paper. Some print-through from underlying layers still occurs, but surface imperfections are limited to a fraction of a micron. In future designs, chemical mechanical polishing (CMP) of the final polysilicon layer will be added to eliminate this nanometer scale print-through.

FABRICATION AND TESTING OF MIRRORS

In our most recent set of experiments, prototype mirrors were fabricated using a custom, three-layer polysilicon surface micromachining process using polysilicon as the structural material, phospho-silicate glass (PSG) as the sacrificial material, and silicon nitride for electrical isolation of the actuators from the underlying substrate. Acid access for sacrificial release of the devices was provided by anisotropically etching holes in the substrate from the backside, thus avoiding holes in the mirror surface. Figure 2 shows the measured voltage-deflection curves for square actuators of various sizes. The usable range of deflection for these actuators before electrostatic pull-in occurs is 2 μm. Actuator motion was characterized using a single point displacement-measuring laser doppler interferometer.

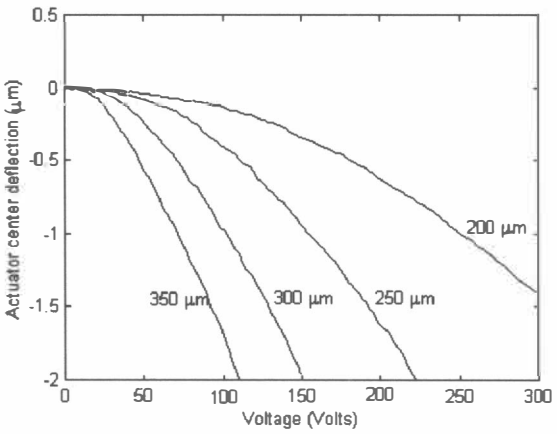

Figure 2. *Meaured deflection versus voltage for electrostatic fixed-fixed actuators.*

An interferometric surface-mapping microscope (Phase Shift Technology MicroXAM) was used to map the surfaces of the mirrors. Figures 3(a) and 3(b) show a surface map measurement and cross-sectional surface profile of a continuous mirror supported by a 3x3 actuator array before deflection of any actuators. Figures 3(c) and 3(d) show the same surface maps after the deflection of the center actuator. Figure 4 shows the deflection of the mirror center versus voltage in response to a voltage ramp applied to the central actuator. Larger mirror arrays incorporating 100 and 400 actuators have also been fabricated in our experiments. Figure 5, for example, is a scanning electron micrograph (SEM) of a continuous mirror supported by 100 actuators.

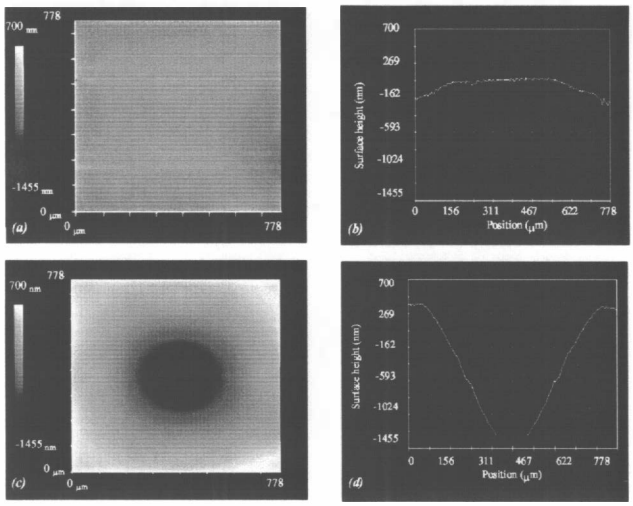

Figure 3. *(a) and (b) show the surface map and x-profile through the center of a nine-element continuous mirror. (c) and (d) show the surface of the mirror when pulled down by the center actuator energized to 155 V. These measurements were made using an interferometric microscope.*

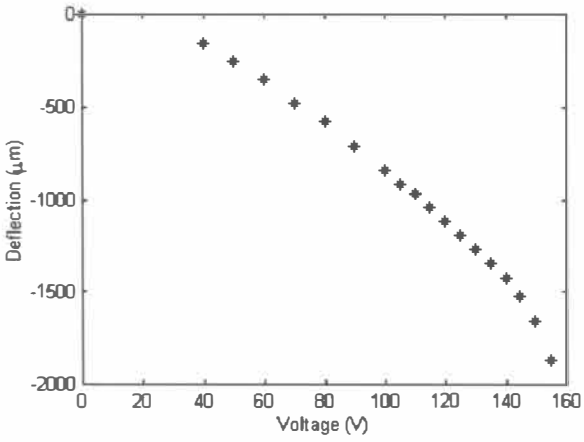

Figure 4. *Response of a 3x3 actuator array supporting a continuous mirror membrane. Vertical actuator stroke is 2μm.*

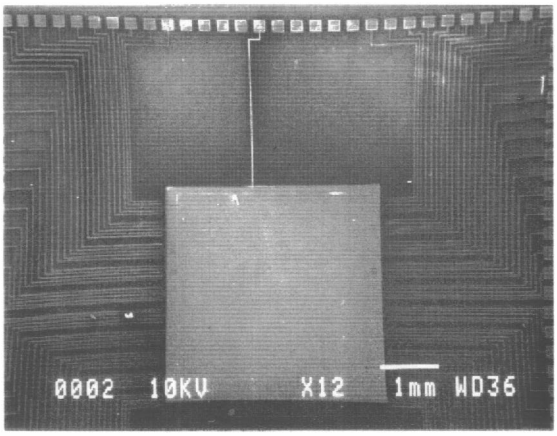

Figure 5. *SEM micrograph of a 10x10 actuator array supporting a continuous mirror membrane.*

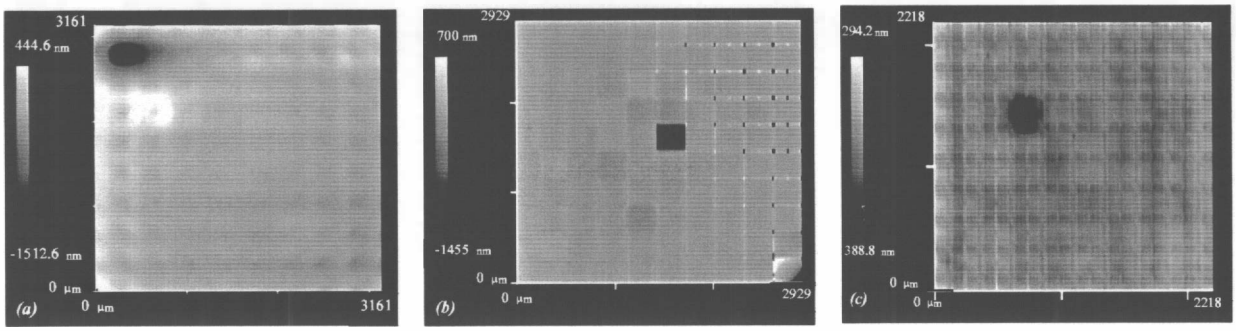

Figure 6. *Interferometric surface maps of 10x10 actuator arrays with (a) continuous mirror (b) segmented mirrors with piston motion (c) segmented mirrors with tip-tilt motion. In each case a single actuator has been deflected.*

Figure 6 shows interferometric surface maps of all three deformable mirror designs with local deflection caused by a single actuator. In these surface maps, darker color indicates that the surface has been pulled down. Note that significant coupling between actuators occurs in the continuous and hybrid tip-tilt mirrors because they are mechanically coupled through the mirror membrane. This coupling results in a smooth influence function in the neighborhood of the deflected actuator. In the case of the segmented piston mirror, no inter-actuator coupling occurs, resulting in sharp surface transitions at the boundaries of the actuated segment.

To evaluate the optical properties of the mirror, the local surface roughness of the polysilicon was measured using an atomic force microscope (Digital Instruments Dimension 3000). The peak-to-peak surface roughness was found to be 0.03λ, with an rms value of 0.007λ (λ=633 nm). Measurements also show post-release deformation of approximately λ/6 to λ/2 for various mirrors, depending on the size of the actuators used. This initial deformation is due to residual stresses and stress gradients in the thin film polysilicon, and is about 10% of the total available actuator stroke. The measured reflectivity of the polysilicon was approximately 50% at 633 nm. In future designs, a high reflective coating could be added to improve the reflectivity and optical efficiency of the mirrors.

ADAPTIVE OPTICS

In adaptive optics systems, deformable mirrors are used as active elements for phase aberration correction. Applications of AO systems include astronomy, medical imaging, and optical image correlation. The most common AO systems use nominally flat, deformable secondary mirrors whose shape is adjusted to compensate for aberrations in optical wavefronts. An aberrated incoming wave is sent to a wavefront sensor (e.g., a Hartmann sensor) which optically analyzes the wavefront for tilt and shape. The output of the wavefront sensor is used to produce "tilt" signals to control a tilt, or steering, mirror, and "shape" signals to control the surface of a deformable mirror. These control signals together generate a conjugate shape that corrects the aberration.

We have performed preliminary experiments to demonstrate the feasibility of using our MEMS deformable mirrors for optical wavefront correction. Figures 7 and 8 show the laboratory setup and results of an experiment in which a collimated beam of light was focused on a 3x3 actuator array supporting a continuous mirror membrane of the type shown in Fig. 1(a). The collimated beam, derived from a 1mW HeNe laser, was reflected off the MEMS deformable mirror and projected into a far field image plane through a beamsplitter. Figure 8 shows the far-field intensity distribution of the beam as reflected off the mirror. When the central actuator is energized, pulling the mirror into a concave shape, it causes the focal point to be pulled closer to the mirror plane. As a result, the projected image of the beam diverges in the far field.

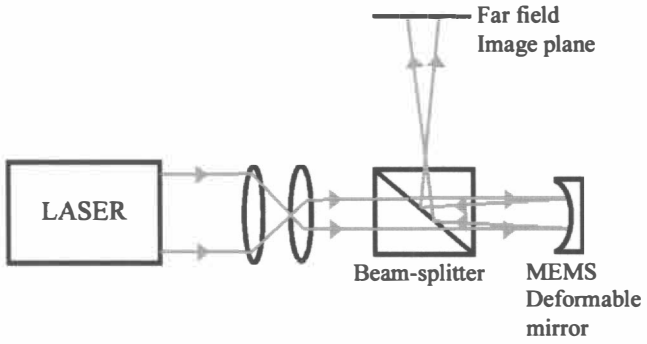

Figure 7. *Schematic of experimental setup using the nine element mirror to focus a collimated laser beam.*

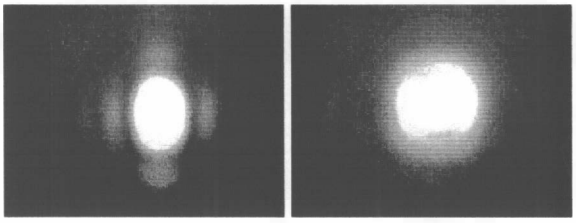

Figure 8. *Measured far-field intensity distribution for plane wave reflected off of an (a) undeflected MEMS deformable mirror and (b) deflected MEMS mirror.*

In a second experiment, we have implemented a real time closed loop controller capable of dynamically correcting aberrations in a laser beam. Figure 9 shows the experimental setup. A collimated 4 mW HeNe laser beam was focussed through a lens onto a single segment of a tip-tilt MEMS mirror array of the type depicted in Fig. 1(c). A dynamic aberration was introduced using warm air turbulence caused by a candle flame

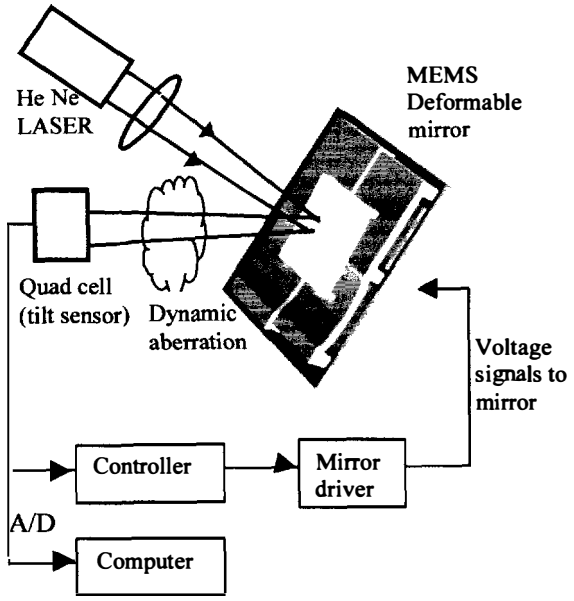

Figure 9. *Schematic of experimental setup for real time control of wavefront tilt aberration.*

near the beam. The wavelength of the aberration was much larger than the beam diameter, hence the effect of the aberration was to introduce a dynamic beam tilt. A *quad cell* photodetector was used to determine the centroid of the reflected beam along two orthogonal axes in the image plane. A quad cell contains four photodetectors, one in each quadrant, and integrates the energy in each quadrant to calculate the effective centroid of an incident beam. Two differential outputs from the quad cell (one for each axis) were fed into a closed-loop feedback circuit with proportional control. The control signals were amplified, added to an offset, and used to drive four actuators at the corners of a tip-tilt MEMS mirror segment. Because electrostatic actuators can only be pulled toward the substrate, an offset is required to permit both positive and negative tilt about an initial bias deflection.

Figure 10 shows measured wavefront tilt of the laser beam

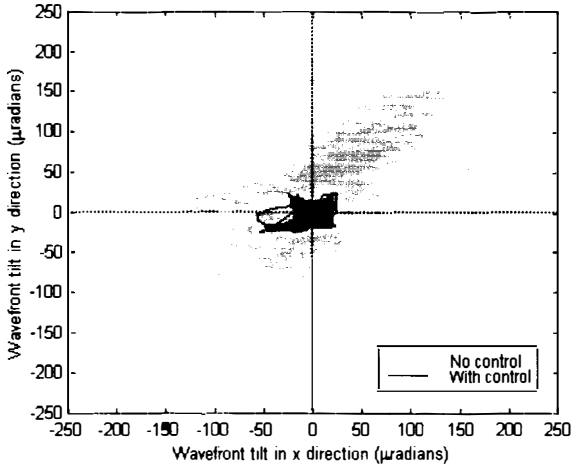

Figure 10. *Random variations in two axis wavefront tilt measured by a quad cell photodetector, demonstrating correction of beam tilt.*

along x and y axes (sampled at 2 kHz for 5 seconds). Grey corresponds to trajectories of beam tilt with the controller off, while the black corresponds to trajectories of beam tilt with the controller on. Significant reduction in beam tilt is evident the adaptive optics controller is activated.

DISCUSSION

Control of tilt using a single mirror segment demonstrates the fundamental operations needed to correct more complex wavefront aberrations. In an adaptive optics system based on a large array of MEMS actuators having many degrees of freedom, a Hartmann wavefont sensor, which is an array of lenslets, can be used to detect multiple wavefront aberrations. In such a system, local wavefront slopes translate into shifts in position of the individual focussed Hartmann spots. Detection of these spot shifts can be used to supply correction signals to the actuators of the mirror array.

ACKNOWLEDGMENTS

The authors would like to thank the Defense Advanced Research Projects Agency (DARPA) for funding this research project. Thanks are also due to Seth Pappas and Asaf Fishov for assistance with the control circuitry and Kendra Cermak for assistance with electromechanical characterization of actuators.

REFERENCES

1. G. Vdovin, P. Sarro, "Flexible mirror micromachined in silicon," *Appl. Optics*, 34 (1995), pp. 2968-2972,.

2. Miller, M. Argonin, R. Bartman, W. Kaiser, T. Kenny, R.Norton, E. Vote "Fabrication and characterization of a micromachined deformable mirror," *Proc. SPIE 1945* (1993), pp. 421-430.

3. M. Roggemann, V. Bright, B. Welsh, S. Hick, P. Roberts, W. Cowan, J. Comtois, "Use of micro-electro mechanical deformable mirrors to control aberrations in optical systems: theoretical and experimental results," *Optical Engineering*, Vol. 36 no.2 (May 1997), pp. 1327-1338.

4. D. Koester, R. Mahadevan, K.W. Markus, "MUMPs Introduction and Design Rules", MCNC Technology Applications Center, 3021 Cornwallis Road, Research Triangle Park, NC, Oct. 1994. (http://mems.mcnc.org/mumps.html)

5. R. Krishnamoorthy Mali, T. Bifano, M. Horenstein, N. Vandelli, "Development of microelectromechanical deformable mirrors for phase modulation of light," *Optical Engineering*, Vol. 36 no. 2 (Feb. 1997) , pp. 542-548.

6. M. Horenstein, T. Bifano, R. Krishnamoorthy Mali, N. Vandelli, " Electrostatic effects in micromachined actuators for adaptive optics," Journal of Electrostatics, 42(1-2), (Sep 1997).

7. T. Bifano, R. Krishnamoorthy Mali, J. Dorton, J. Perreault, N. Vandelli, M. Horenstein, D. Castañon, "Continuous membrane, surface micromachined, silicon deformable mirror," *Optical Engineering*, Vol. 36, no. 5, (May 1997), pp. 1354-1360.

HIGH-ASPECT-RATIO ROTARY POLYGON MICROMOTOR SCANNERS

A. A. Yasseen, J. N. Mitchell, D. A. Smith, and M. Mehregany
Microfabrication Laboratory
Department of Electrical Engineering and Applied Physics
Case Western Reserve University
Cleveland, Ohio 44106

ABSTRACT

This paper describes a polygon micromotor scanner fabricated from single crystal silicon by deep reactive ion etching (DRIE) for in-plane scanning applications. The scanner consists of an outer-rotor wobble micromotor with a 1.4 mm-diameter, 200 μm-thick rotor. The outer-rotor design circumvents optical beam interference with wires or probes that provide electrical excitation to the motor. A variety of rotor polygon types were designed and fabricated, including those with 3, 4, 6, and 8 facets. After fabrication of the components, the scanners were assembled and operated for extended periods in room air. Typical scanners were operated at 60V. The optical beam was reflected off the sidewall of the polygon rotor using external optics at a wavelength of 1310 nm. During dynamic optical measurements, 1.8 mm diameter gradient-index (GRIN) lenses were used as optical elements, and a repeatable signal was detected indicating less than 0.4° of misalignment of the reflective surface due to rotor wobble or tilt.

INTRODUCTION

MEMS technology has been demonstrated for the application of optical scanning utilizing a variety of approaches. A 20 μm-tall reflective nickel polygon, plated on the surface of a polysilicon micromotor for in-plane scanning, was demonstrated in **[1]**. This device suffered large optical beam loss due to the small reflecting surfaces and required critical optical alignment. Optical scanning was demonstrated using a beam diffracted by grating elements that were etched into the relatively large-area rotors of polysilicon micromotors **[2]**. The device required out-of-plane optical alignment. Flip-up, vibrating, hinged mirrors that used resonant comb drive actuation for bar-code reading were demonstrated in **[3]**. The devices had fast scan speed, but limited scan angle and complex fabrication.

With the advent of DRIE technology, three-dimensional complex microstructures can be designed and fabricated with tall (100's of microns) geometries out of single crystal (SC) silicon, providing a unique flexibility in developing micromachined devices **[4]**. The absence of residual stresses in SC silicon imposes no limitations on the device's lateral dimensions. Integration with electronics is feasible, where the electronics can be fabricated anywhere on the surface, including the moving parts themselves. Optimized DRIE etch can potentially result in smooth sidewalls that may be suitable for optical applications. DRIE-fabricated, micromachined devices were reported recently including those for optical applications. Vertical, 75 μm-tall mirrors actuated by electrostatic comb drive for fiber-optic switching were reported in **[5]**. Devices with a 200 μm-tall mirror mounted on top of a stepping salient-pole micromotor to deflect an optical beam in the plane of the device to realize a 1x8 optical switch were demonstrated in **[6]**.

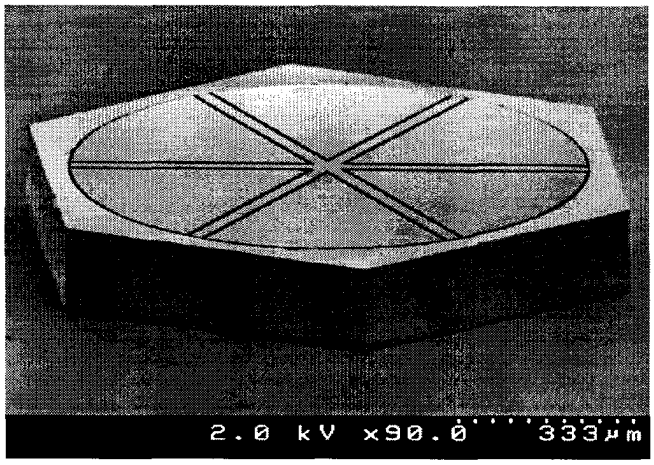

Figure 1. *SEM photo of a typical DRIE fabricated polygon scanner using a hexagonal rotor. The rotor is 1.4 mm in diameter, and the reflecting sidewalls are 200 μm-tall.*

MICROSCANNER DESIGN

The scanner micromotor design is based on the outer-rotor wobble motor in which the stator is folded inside the rotor, exposing the rotor outer radius sidewalls for optical coupling **[7]**. A means is required to prevent the rotor shorting to the stator during operation. The device presented here implements a hexagonal star-shaped bearing design between stator poles with protrusions that extend slightly beyond the stator (Fig. 1). These protrusions limit the rotor travel during its radial and angular motion to prevent it from shorting to the stator and define its points of role and slide (Fig. 2). The amount of bearing protrusion out of the stator determines the rotor/stator gap during operation. The difference between the bearing radius and the rotor's inner radius, when the rotor is centered on the stator axis, determines the bearing clearance. Note that in operation, the rotor/stator gap is approximately (g-d). The overall device

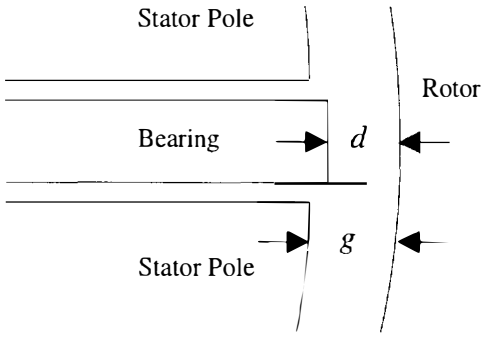

Figure 2. *Top-view schematic of an outer-rotor wobble micromotor. With the rotor at the center of the stator, d is the bearing clearance, and g is the rotor/stator separation.*

0-9640024-2-6/hh1998/$20©1998TRF
DOI 10.31438/trf.hh1998.17

Solid-State Sensors, Actuators, and Microsystems Workshop
Hilton Head Island, South Carolina, June 8-11, 1998

dimensions were kept relatively large (1.4 mm-diameter, 200 μm-thick) to facilitate assembly and to provide large optical reflecting surfaces. These larger surfaces reduce optical beam losses, while relaxing optical alignment requirements. The outer rotor design also prevents optical beam interference with wires or probes that provide electrical excitation to the motor. Furthermore, in comparison to the micromotors reported in **[6]**, rotor assembly to a corresponding stator is easier and was occasionally carried out manually without the need for a microscope or a probe station. The design resulted in relatively rugged motors, since it did not have fragile bearing posts at the center that are likely to break during assembly.

MICROSCANNER FABRICATION

The fabrication process is similar to that of the devices reported in **[6]** and will be described here briefly. Starting with a 200 μm-thick, silicon wafer that is fusion bonded to a 500 μm-thick, silicon substrate with 1.5 μm of thermally-grown silicon dioxide, the recess pattern was defined and etched followed by the bushing definition and delineation in the rotor dies (Fig. 3). The rotor stator pattern was then defined and etched using DRIE through the top wafer, endpointing on the underlying oxide of the substrate. After a short phosphorous doping from a solid source, the wafer was diced into rotor and stator dies. The sacrificial oxide was stripped off the field area of the stator dies by a short BHF etch, while the rotor dies were fully released in HF and rinsed in DI water. Individual rotors were then collected and assembled onto corresponding stators. Rotors to be tested optically were Al-coated for improved reflectivity.

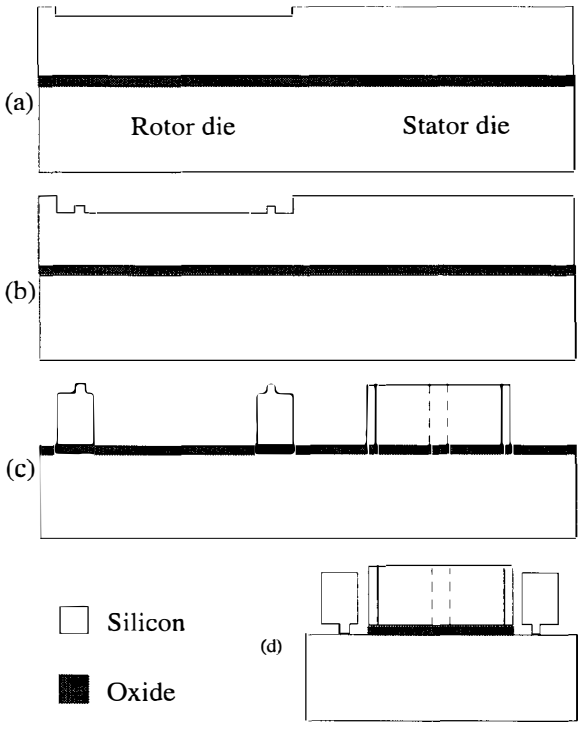

Figure 3. *Cross-sectional schematics describing the micromotor fabrication process: (a) after recess definition and patterning to a depth of 8 μm; (b) after bushing definition and patterning to a depth of 2 μm; (c) after rotor/stator definition and DRIE patterning through the top wafer; and (d) after rotor release and assembly onto the corresponding stator.*

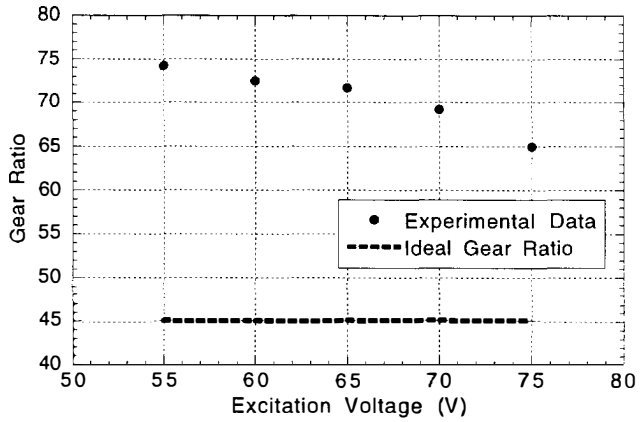

Figure 4. *Gear ratio versus excitation voltage for the octagonal rotor micromotor. The g and d parameters for this device are 13 and 11 μm, respectively. An excitation speed of 500 rpm was used. The rotor gear ratio was measured by dividing the excitation speed by the average steady-state rotor speed.*

MECHANICAL MEASUREMENTS

Upon assembling and testing the scanner actuation, it was verified that motor operation is highly DRIE etch dependent. The etch influences critical motor parameters such as rotor/stator gaps and bearing clearance. Great care is hence exercised to select rotor and stator patterns that are fully compatible given the initial design dimensions and their alteration due to the DRIE etch. It should be noted however that with a repeatable and reliable etch, these factors can be compensated for at the design stage. The inner rotor and bearing diameters of the device were 1005 μm and 983 μm, respectively. The diameter of the stator was 979 μm. With an assembled device, the rotor/stator separation was 13 μm, and the bearing clearance was 11 μm. After release and assembly, the scanners were operated smoothly and reproducibly, even after storage in room air for extended periods (e.g., several months). The minimum operating voltage of the device was 50V. It was noticed that at high voltages (e.g., >75V), the levitation force was strong enough to lift the rotor out of the plane of the substrate and result in poor device functionality. As a result, the operating voltage of the device was kept as low as possible, while maintaining the device operation. The micromotor gear ratio versus voltage is shown in Fig. 4. The higher experimental gear-ratio is due to the rotor slip, which increases with decreasing excitation voltage. Note that in this figure, the ideal gear ratio is defined as the bearing radius divided by the bearing clearance. Maximum operating speed when driven using a six-phase excitation to induce rotation was 58 rpm.

OPTICAL MEASUREMENTS

The scanner was tested dynamically using the experimental set up shown in Fig. 5. A 1310 nm laser source illuminated the scanner through a multi-mode fiber coupled to a gradient-index (GRIN) lens, which was positioned 10 mm from the rotor. The GRIN lens collimated the beam, preventing divergence and minimizing the beam diameter at the detector. Two germanium photo diode IR detectors, coupled to GRIN lenses through fiber, were placed in the plane of the scanner at fixed angles, separated by 30°, to receive the scanning beam. The GRIN lenses are highly sensitive to any angular misalignment in the beam, allowing the tilt in the device to be characterized. Electrical actuation of the device via the placement of probes, to contact the stator-poles, did not interfere with the optical

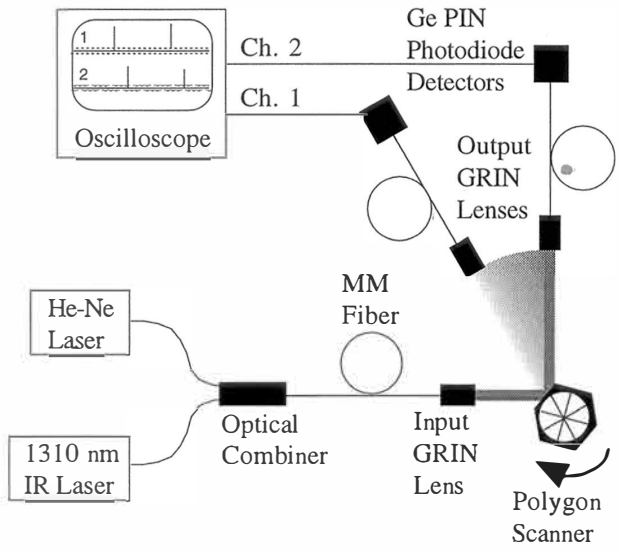

Figure 5. Schematic of the experimental setup used to perform optical testing on the scanner.

beam, since the stator is located inside the rotor.

For reflection off a given facet, the beam intensity remained high over large angles (Table 1). Of the light incident on the scanner, up to -10.8 dB of optical power was observed at the detector. Much of the loss is due to the partial reflectivity of the 400 μm-diameter beam by the 200 μm-tall sidewall and due to the surface roughness of the sidewalls. To improve the coupling efficiency, a laser diode objective lens replaced the GRIN lens, with the spot focused near the scanner surface. The spot size of 125 μm at the polygon surface was smaller than the height of the scanner surface, ensuring no losses due to partial beam reflection. The coupling efficiencies improved by about 5 dB and are shown in Table 1. The spot size was also measured in the scanning plane, 2 mm after the facet. This yielded the scanner resolution, which was found to be 318 dpi.

The center point of the input beam was positioned off axis to a point slightly more than halfway to the outer radius of the stator. This produces a larger scan angle than an on-axis beam would. However, it results in beam translation, as well as angular motion during scanning. Using this arrangement, the beam angular scan range for the hexagonal rotor was seen to be 110° with the parameters for the other facet numbers shown in Table 1. The detectors were placed within the scan arc and under electrical actuation. The beam was seen to scan repeatedly from detector 1 to 2 (Fig. 6) as the different facets reflected the beam.

Table 1. Experimentally determined relationship between number of facets and optical scanning parameters.

Number of facets	3	4	6	8
Theoretical scan angle	120°	90°	60°	45°
Scan line angular range	50°	80°	110°	95°
Optical efficiency at 90° reflection using GRIN lenses (dB)	-13.6	-10.8	-10.8	-13.7
Optical efficiency at 90° reflection using an objective lens (dB)	-9.2	-6.3	-5.6	-6.6

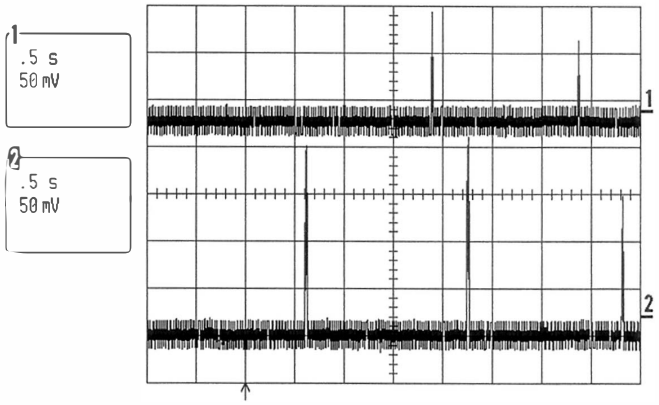

Figure 6. Oscilloscope trace of detected output optical power from the rotating hexagonal scanner. The detectors were at two fixed angles separated by 30°. Actuation signal speed was 500 rpm at 55V.

DISCUSSION

The results in Table 1 indicate that more facets generally results in a larger scan angular range. Fewer facets yields better transmission of the optical beam over greater angles due to the larger lateral facet size. However, more facets yield a greater number of scans per second. A device with 6 or 8 facets would seem best at balancing these effects.

Even with the small spot size and Al-coated surface, the coupling efficiencies in Table 1 are still fairly low. In order to coat the polygons, they were mounted vertically on their side. The Al-sputtering process only produced a uniform coating on exposed flat horizontal surfaces. Thus, any angled or vertical surfaces would have incomplete coating. For example, the top facet of a hexagon receives better coating than the adjacent two facets, and the remaining facets receive nearly no coating. The 3-facet polygon had no horizontal facets exposed to the sputtering and had a relatively poor coating. Nearly all of this remaining loss is due principally to the sidewall roughness resulting from the DRIE etch. A close-up SEM photo of the scanner sidewall is shown in Fig. 7. The sidewall is relatively smooth over the top 40% of the surface (i.e., assembly results in a flipped rotor in Fig. 7) with an rms surface roughness, as reported in **[5],** of 360Å. The roughness increases over the

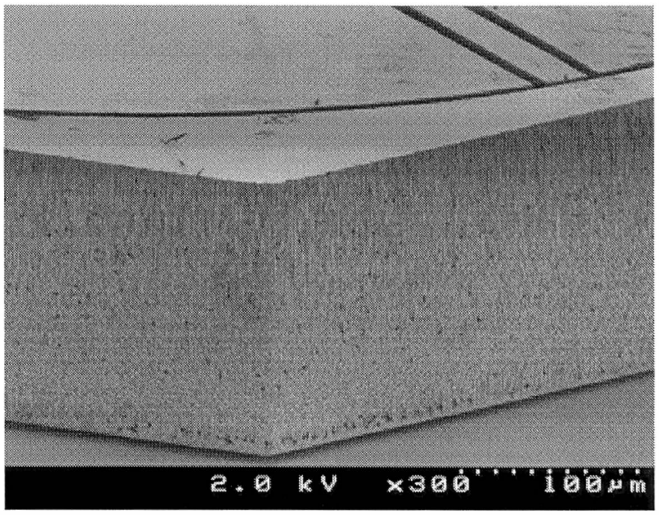

Figure 7. A close-up view of the etched polygon scanner sidewall from Fig. 1. Note that the rough area is on the top due to assembly.

remainder of the sidewall surface until vertical grooves of nearly 1 μm in depth and width are observed near the base. The amount of feature undercut was as much as 10 μm. This limits the optical reflectivity by producing a large amount of scattering.

The scanning traces of Fig. 6 show the device operation from start-up to continuous rotation. Since the Ch. 1 and 2 GRIN lens pickups were placed at 60° and 90° from the input, respectively, they show different peak intensities due to the off axis position of the input beam. Spacing between the peaks is fairly consistent, indicating reliable motor operation. Measurement of the spacing on the trace yields a rotational speed of 6.76 rpm ± 0.09. The mechanical measurements from Fig. 4 yield a rotational speed of 6.74 rpm ± 0.07 at 55V for the same actuation speed. Since not only were different rotors used for the mechanical and optical measurements, but also different stators, these results indicate good repeatability of performance (and etch) for different devices.

The use of GRIN lenses for output beam detection allows the amount of angular variation in the rotor during actuation to be determined. For instance, a beam angle offset of 1° corresponds to a loss of 12 dB for these GRIN lenses. In Fig. 6, the intensity varies by less than 35% giving a beam angle offset of less than 0.2°. Since the power readings were rarely less than 25% of the maximum value, this indicated a maximum angular offset of 0.8° in the optical beam. Thus, despite the wobbling of the device as it rotated, it showed good repeatability of alignment with an out-of-plane tilt of the polygon of less than 0.4°.

The relatively low rotational speed of the device could be improved by two methods. The excitation speed or the bearing clearance could be increased to reduce the gear ratio. The latter option may create excessive wobbling, however, which would be detrimental to optical alignment.

To facilitate assembly, a decrease in feature size is desirable to create a greater clearance between the rotor and stator patterns. However, from a device perspective, large clearances are not desirable as they create excessive wobbling during operation. To address both of these issues, we envision a wafer scale assembly scheme in which a rotor wafer is placed on top of a stator wafer (similar to the flip-chip technique), hence speeding the assembly process and rendering the devices more suitable for batch fabrication. An additional issue with the scanner is that the rotor may disassemble if the device is turned upside down or is exposed to large mechanical shocks. This could be prevented if a cap is incorporated into the design (e.g., via an additional wafer bonding step) that extends slightly beyond the stator edge over the top of the rotor.

CONCLUSIONS

We have demonstrated an optical scanner based on a micromotor implementation using a DRIE fabrication approach. The large optical reflecting surfaces reduced optical power loss, while facilitating optical alignment. However, the roughness of the etched sidewalls contributed to optical loss. A repeatable signal was detected during device operations indicating a less than 0.4° misalignment of the reflecting surface due to wobble or tilt.

ACKNOWLEDGMENTS

The authors would like to acknowledge STS Ltd., UK and AMMi Inc., Cleveland, OH for the DRIE etching, and R. Burla for help in the initial experiments. The work is supported in part by DARPA under Contract #: DABT63-95-C-0070.

REFERENCES

1. K. Deng, H. Miyajima, V. Dhuler, M. Mehregany, S. Smith, F. Merat, and S. Furukawa, "The Development of Polysilicon Micromotors For Optical Scanning Applications," in *Technical Digest, IEEE Solid-State Sensor and Actuator Workshop* (Hilton Head, SC, June 1994), p. 234.

2. A. Yasseen, S. Smith, M. Mehregany, and F. Merat, "Diffraction Grating Scanners Using Polysilicon Micromotors," in *Proceedings, IEEE Micro Electro Mechanical Systems Workshop* (Amsterdam, Netherlands, Jan. 1995), p. 175.

3. M. Kiang, O. Solgaard, R. Muller, and K. Lau, "Surface Micromachined Electrostatic-Comb Driven Scanning Micromirrors for Barcode Scanners," in *Proceedings, IEEE Micro Electro Mechanical Systems Workshop* (San Diego, CA, Jan. 1996), p. 192.

4. E. Klaassen, K. Petrerson, J. Noworolski, J. Logan, N. Maluf, J. Brown, C. Storment, W. McCulley, and G Kovacs, "Silicon Fusion Bonding and Deep Reactive Ion Etching: A New Technology For Microstructures," in *Sensors and Actuators A*, Vol. 52, p. 132, 1996.

5. C. Marxer, C. Thio, M. Gretillat, N. de Rooij, R. Battig, O. Anthamatten, B. Valk, and P. Vogel, "Vertical Mirrors Fabricated by Deep Reactive Ion Etching for Fiber-Optic Switching Applications," in *J. of Microelectromechanical Systems*, vol. 6, no. 3, p. 277, September 1997.

6. A. Yasseen, J. Mitchell, T. Streit, J. Klemic, D. Smith, and M. Mehregany, "A Rotary Electrostatic Micromotor 1x8 Optical Switch," in *Proceedings, IEEE Micro Electro Mechanical Systems Workshop* (Heidelberg, Germany, Jan. 1998), p. 116.

7. K. Deng, and M Mehregany, "Outer-rotor Polysilicon Wobble Micromotors," in *Proceedings, IEEE Micro Electro Mechanical Systems Workshop* (Oiso, Japan, Jan. 1994), p. 269.

8. Surface Technology Systems Ltd., Newport, UK, Available HTTP: http://www.stsystems.com.

LOW INSERTION LOSS PACKAGED AND FIBER-CONNECTORIZED SI SURFACE-MICROMACHINED REFLECTIVE OPTICAL SWITCH

V. Aksyuk, B. Barber, C.R. Giles, R. Ruel, L. Stulz, and D. Bishop
Bell Laboratories, Lucent Technologies, 700 Mountain Ave.
Murray Hill, NJ 07974

ABSTRACT

A Si surface micromachined single mode fiber optical switch is using a novel vertical actuator to interpose a gold coated self-assembling silicon vane in a fiber gap to achieve 0.81dB minimum insertion loss in the transmit state with 38-80dB transmission isolation and 2.15dB return loss in the reflection state, all in the 1550nm wavelength region. The minimum actuation voltage is 4V with virtually no power consumption. Rise and fall times as low as 50μs are obtained with 20V drive voltage.

INTRODUCTION

Conventional opto-mechanical fiberoptic switches have low insertion loss, high contrast ratio, wide optical bandwidth and low polarization dependence. However they are relatively bulky, expensive and slow. Micromachined switches combining the performance of bulk mechanical switches with small size, low cost and moderate speed are excellent candidates for a variety of applications, including reconfiguration switches in optical cross-connects and in WDM add/drop multiplexers. A number of devices have been reported utilizing bulk **[1]**, surface micromachining **[2,3]** and other fabrication techniques **[4]**. However, of those suitable for lightwave applications some require unique processes, others need complex manual assembly, while yet others have large actuation voltages or consume unacceptably high power.

We used a relatively simple commercially available Si surface micromachining process to build a set of MEMS optical switches featuring excellent optical performance, low actuation voltage, ultra-low power consumption, small size, moderate speed, no manual assembly of micromechanical structures and potentially low cost.

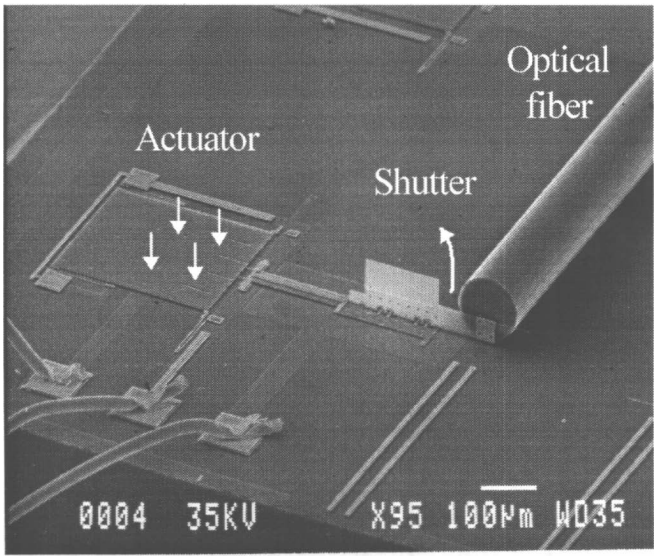

Figure 1. *MEMS optical switch. For clarity the second optical fiber is not shown.*

DESIGN AND FABRICATION

Fig.1 is an SEM micrograph of one of our switches. The three layer Si surface micromachining Multi-User MEMS Process (MUMPS) available through MCNC was used for fabrication **[5]**. Switches were built with one fixed and two structural polisilicon layers, 0.5, 2 and 1.5 μm thick. Si nitride was used to insulate the micromechanical structure from the wafer. Mirror surface was produced with Cr-gold metallization. Phosphosilicon glass sacrificial layers were removed by etching in HF during the final release step. Each 2.5x2.5 mm^2 die was then epoxied in a ceramic 16 pin dual-in-line package (DIP) and single-mode optical fibers suitable for 1550nm wavelength region were placed in microfabricated alignment rails with less then 20 μm gap between the fiber faces. No active alignment was required to achieve low insertion loss. The fibers were fixed to the chip and package with a UV curable adhesive.

All our devices are two-port reflective switches consisting of a movable shutter connected to a novel electrostatic out-of-plane actuator capable of inserting the shutter in the light path between two fibers. The shutter is a polysilicon plate with a reflective gold layer deposited on one of its sides forming a mirror. The plate is connected to the actuator lever by means of hinges **[6]** and has to be rotated 90 degrees to its operating vertical position upon the release. While in earlier versions of the switch this assembly had to be done manually, later versions (Fig.2) include a self-assembly mechanism to perform this step automatically upon release. The mechanism uses energy stored in high tensile residual stress metal layer to produce vertical motion, which is then used to rotate and lock the shutter in its final position.

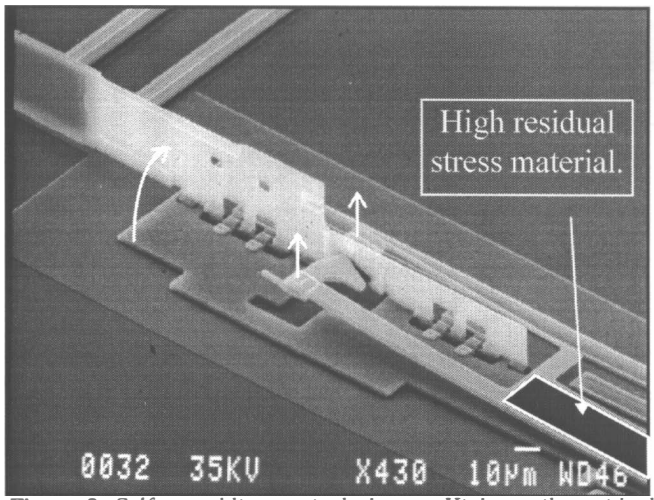

Figure 2. *Self-assembling optical shutter. High tensile residual stress metal is deposited on a polysilicon beam anchored at one end. Upon release the metal-poly sandwich structure deforms, moving the free end of the beam upward. The lifting structure engages the cut in the hinged-plate shutter causing it to rotate 90 degrees into its operating position.*

0-9640024-2-6/hh1998/$20©1998TRF
DOI 10.31438/trf.hh1998.18

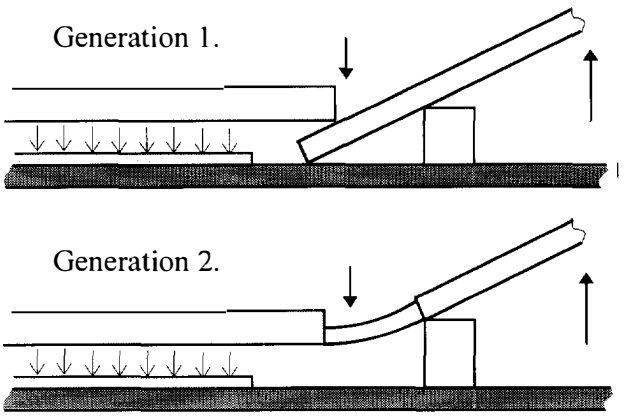

Figure 3. *Simplified actuator schematic. In reality, the actuator plate is not rigid, resulting in a complicated zip lock - like capacitor closing. The resting posts are also not shown.*

With zero volts applied to the actuator, the shutter edge is 5 to 10 μm below the centers the two fiber cores, and the light is transmitted from one fiber into the other. The fiber faces are antireflection coated (R ≈ 0.1%) to reduce unwanted back-reflection and Fabry-Perot resonances. When voltage is applied, the shutter is moved upward into the light path, blocking transmission and reflecting the light back into the input fiber. A relatively large shutter displacement (more than 15μm, determined by the 8 μm mode diameter of the single mode telecommunication fiber used) is required to make a low insertion loss, high contrast ratio switch.

The schematic of the actuator is shown in Fig.3. A downward force is generated by an electrostatic actuator consisting of two initially parallel plates. A lever mechanism is then used to produce a large vertical displacement of the shutter The capacitor dimensions are ranging from 220 x 170 to 300 x 350 μm^2 with a typical 0-volt gap between the plates of 2.75 μm. The bottom plate is fixed and the top plate is suspended on a flexible support. To prevent the top plate from touching the bottom plate and shorting the capacitor, an array of 0.75μm tall polysilicon posts (dimples) are protruding from the bottom surface of the top plate. Holes are made in the bottom plate corresponding to the posts such that the posts touch down not on the bottom plate but on the insulating silicon nitride layer beneath it. The lever mechanism includes a 500 to 575μm long polysilicon beam capable of rotation around a horizontal pivot axis, providing the necessary mechanical advantage. In one version of the switch (Generation 1) the beam is attached to the substrate by weak torsional springs and engaged under the edge of the movable capacitor plate. In the other (Generation 2) it is connected to the plate by means of 2 thin polysilicon flexures measuring typically 1.5 by 2 by 18 μm (Fig. 3). The size of the flexures is chosen to provide sufficient beam rotation angle for a given capacitor gap, while not requiring too high of a voltage to deform.

RESULTS AND DISCUSSION

In Fig.4 the lever angle and corresponding shutter displacement are plotted as a function of voltage applied to the actuator. Because the moving plate of the actuator is only 1.5 μm thick, and the mechanical stress is mostly concentrated at the point where the lever mechanism is connected to the plate, the deformation of the plate is significant and plays an important role during actuation. In fact, especially for stiff Generation 2 lever mechanisms, the actuator mostly works in a "zip-lock" mode as opposed to "parallel-plate" mode. As the voltage is increased, the part of the plate furthest from the lever moves down until the resting posts touch down. At this voltage the lever beam deflection is still small. As the voltage continues to increase, the plate is deforming, resting posts closer to the lever touch down and the lever edge of the plate moves down as well, acting on the lever and lifting the shutter up.

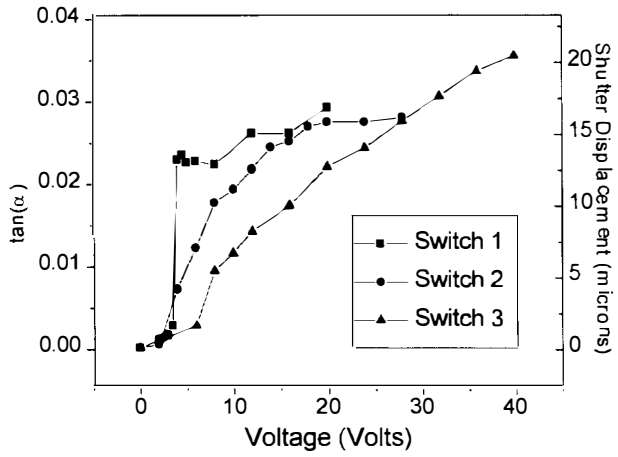

Figure 4. *Lever tilt angle and shutter displacement as a function of actuator voltage. Switch 1 has a first generation lever design, Switches 2 and 3 have second generation levers with different flexure stiffness. These curves are defined by the stiffness of the plate and lever suspensions, pivot and capacitor geometry and lever length.*

This zip-lock action was directly observed by looking at the movable plate shape with an interferometric profilometer. It also manifests itself in the displacement vs. voltage characteristic of the device: while for softer levers, (i.e. Switch 1) a snap-down voltage exists corresponding to the 1/3 instability of a parallel-plate actuator, for stiffer lever mechanisms, (Switches 2 and 3) displacement is a smooth function of voltage, corresponding to the continuous zip-lock action. This mode of operation may also be beneficial in lowering the actuation voltage.

Our switches had the following optical characteristics: insertion loss in the transmit state including loss of two FC-PC connectors ranged from 0.81 to 3.26 dB, return loss in the reflection state varied from 1.15 to 3.77 dB, including the loss of two connectors. These insertion losses are comparable to the ones achieved with conventional opto-mechanical switches. Transmission isolation ranged between 38 dB to greater then 80 dB while reflection return loss varied from 15 to 25 dB. The low return loss resulted from weak reflections in the fiber gap and might be improved by using angle-cleaved rather than antireflection-coated fibers. Less than 0.05 dB polarization-state induced variation of transmit-state insertion loss or reflect-state return loss was observed.

Fig.5 shows light transmission as a function of the applied voltage for three different switch designs. The smooth, continuous switching action for Switches 2 and 3 seen on Fig. 5 make them particularly good candidates for use as variable attenuators with almost 80 dB of dynamic range **[7]**.

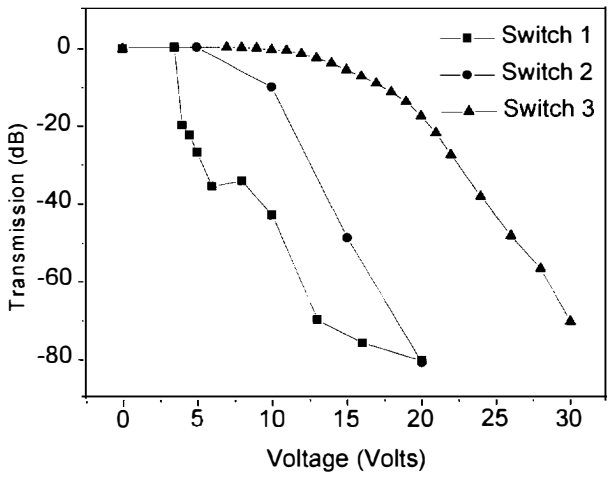

Figure 5. *Switch transmission as a function of actuator voltage. Switches 2 and 3 may also be used as variable attenuators with high dynamic range*

Fig.6 and 7 show transmission as a function of time for two different switches under various square-wave applied voltages. From these data, the rise and fall times can be extracted, as well as switching delay time, defined as the time between the voltage step and the start of the optical switching action.

Switch opening times corresponding to a voltage change from a finite value to 0 are determined by the spring constants of the flexures returning the shutter to its initial position, the shutter inertia as well as the position of the shutter in the closed state.

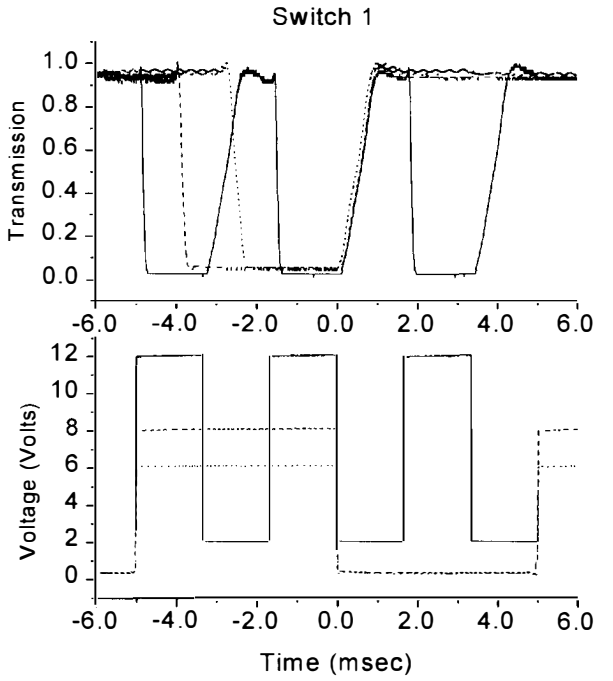

Figure 6. *First generation, low voltage switch operation with different actuator voltages. Shutter closing delay and fall times are voltage dependent while shutter opening delay and rise times are not.*

These values are less then 150 μsec delay and 890 μsec rise for Switch 1 (softer flexures) and 65 μsec delay and 45 μsec rise time for Switch 2 (stiffer flexures). The opening delay time is due to the shutter edge placed initially above the light beam, blocking the light, and having to travel a finite distance down before letting the light through. The rise times correspond to the speed of the shutter edge crossing the beam. For Switch 1 the shutter position in the closed state is defined by the lever mechanism geometry and is voltage independent, while for Switch 2 the shutter is higher for larger actuation voltage resulting in longer switch delay time and shorter rise time.

The closing delay and fall times correspond to the voltage step from 0 to a finite value and the shutter moving up. They are determined by the distance the shutter has to travel before it starts blocking the beam, the actuator force accelerating it and its mass.

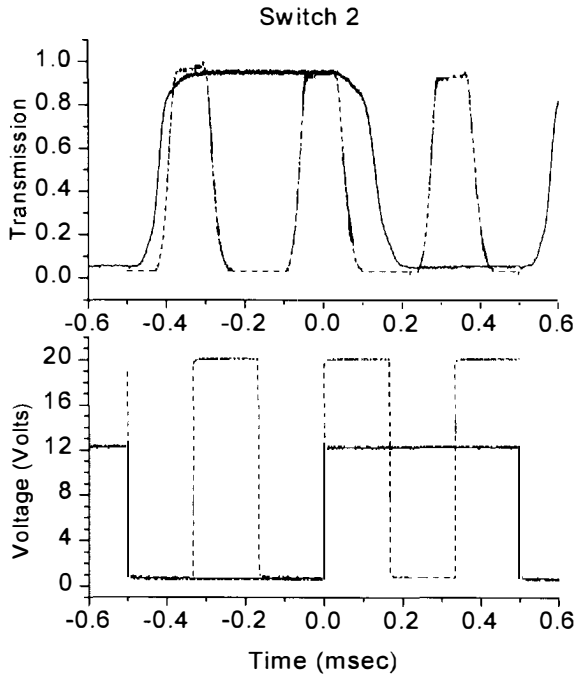

Figure 7. *Second generation, fast switch operation. 10 times faster operation relative to Switch 1 is achieved with twofold increase in actuation voltage.*

In Fig.8, closing times are shown to monotonously decrease with increasing voltage, as the shutter is driven up faster by the larger electrostatic force. At large drive voltages the speed of the device is limited by the opening time. It is either voltage independent or increasing slightly and then saturating, as the position of the shutter under bias becomes defined by the actuator geometry. In addition, a tradeoff exists between the maximum switching speed and the minimum actuation voltage – stiffer flexures make the switching action faster but require larger actuation forces and correspondingly larger voltages.

Currently the effort is being made to further optimize the switch performance for higher speeds and lower actuation voltages by decreasing the shutter mass and improving the actuator design. In particular, first tests have been successful on the next generation lever mechanism where the friction point has been eliminated. To lower the actuation voltage thinner, more compliant flexures are also being considered.

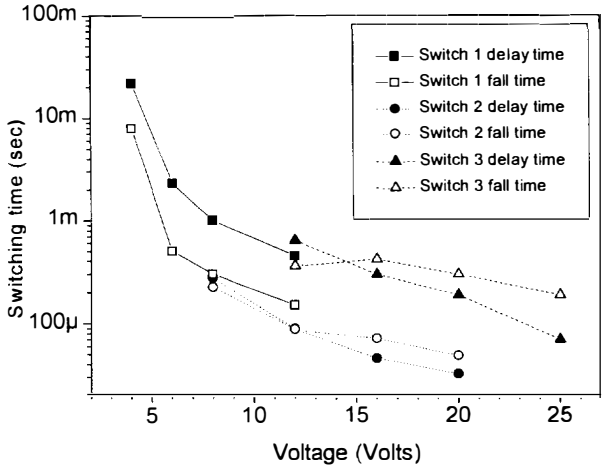

Figure 8. *Switch closing time as a function of actuator voltage. Solid symbols - switch delay time. Open symbols - fall time. Delay time results from the shutter having to accelerate and travel some distance before it starts blocking the beam.*

CONCLUSION

In summary, we have described a new Si-surface-micromachined reflective optical switch suitable for use in reconfigurable lightwave network components including protection switches, optical cross-connects and WDM add/drop multiplexers. Having a movable thin gold-coated silicon vane in the switch enabled close placement of optical fiber endfaces to achieve excellent optical characteristics without additional lenses or collimators. These switches had a minimum insertion loss of 0.8dB. exhibited ~2dB return loss and >80dB transmission isolation in the reflect-state. The minimum actuation voltage was 4V and with 20V they were able to switch in 50 µsec. Very compact packaging was shown and quiescent power consumption of the electrostatic actuator was negligible. Two actuator geometries were investigated here and new geometries are being developed to optimize the drive voltage and switching times. The actuator design is amenable to other switch configurations, including 2x2 optical switches with a single actuator, and larger fabrics using arrays of devices.

REFERENCES

1. H. Toshiyoshi and H. Fujita, "Electrostatic Micro Torsion Mirrors for an Optical Switch Matrix", *Journal of Microelectromechanical Systems,* vol. 5, no. 4, 231 (1996).

2. S.S. Lee, E. Motamedi and M.C. Wu, "Surface-Micromachined Free-Space Fiber Optic Switches With Integrated Microactuators for Optical Fiber Communication Systems", *Transducers'97 Technical Digest,* Vol. 1, p. 85.

3. E. Hashimoto, Y. Uenishi, K. Honoma and S. Nagaoka, *Transducers'97 Technical Digest*, Vol.1, p.331.

4. C. Marxer, C. Thio, M.-A. Gretillat, N. F. De Rooij, R. Bättig, O. Anthamatten, B. Valk, P. Vogel, "Vertical Mirrors Fabricated By Deep Reactive Ion Etching For Fiberoptic Switching Applications", *Journal of Microelectromechanical Systems*, vol. 6, no. 3, 277 (1997).

5. D. Koester, R. Majedevan, A.Shishkoff, and K. Marcus, *Multi-User MEMS Processes (MUMPS) Introduction and Design Rules,* rev. 4, 7/15/96, MCNC MEMS Technology Applications Center, Research Triangle Park, NC 27709

6. K. S. J. Pister, M. W. Judy, S. R. Burgett, and R. S. Fearing, "Microfabricated hinges", *Sensors and Actuators A,* vol. 33, no. 3, 249 (1992)

7. B. Barber et al., submitted to *Electronics Letters.*

LEVERAGED BENDING FOR FULL-GAP POSITIONING WITH ELECTROSTATIC ACTUATION

Elmer S. Hung and Stephen D. Senturia
Massachusetts Institute of Technology
Cambridge, MA 02139

ABSTRACT

The pull-in instability limits the travel distance of an elastically-suspended parallel-plate electrostatic actuator to about 1/3 of the gap. In this paper we report an electrostatic actuator design which can achieve complete gap travel without pull-in. The specific structure which has been fabricated and tested is designed for positioning mirrors in a tunable diffraction grating known as a polychromator; however, the actuation principle, which we call "leveraged bending," should be applicable to a wide range of devices.

INTRODUCTION

The use of electrostatic actuation for microelectromechanical systems (MEMS) is attractive because of the high energy densities and large forces available in microscale devices. In many electrostatic actuators, the positions of electrodes are controlled by a balance between an electrostatic attractive force and the action of a mechanical restoring force. A large range of motion for analog positioning can be extremely useful for a wide variety of tuning applications. Unfortunately, with electrostatic actuation, the interaction of a nonlinear electrostatic force with an elastic restoring force causes a "pull-in" phenomenon which prevents electrodes from being stably positioned over a large distance.

In this paper we report the use of a "leveraged bending" approach to design an electrostatic actuator which can achieve complete gap travel without pull-in. The actuator is used to position mirrors in an analog-tuned reflective phase grating known as a polychromator. Polychromator design and implementation are described as a case study example of the leveraged bending technique.

PULL-IN PROBLEM

The pull-in problem can be illustrated by a simple $1D$ model: Consider an ideal system (Fig. 1) consisting of two parallel conductive plates separated by gap z, with one plate fixed on the substrate and the other suspended by an elastic restoring force (a linear spring). If a voltage V is applied across the plates, the attractive force, neglecting fringing, is given by:

$$F_e = \frac{\epsilon_0 A V^2}{2z^2}$$

where A is the area of the movable plate and ϵ_0 is the permitivity of free space. The electrostatic force is nonlinear, since it depends on $1/z^2$, while the elastic restoring force, $F_m = k(g_0 - z)$, is linear with z, where k is the spring constant and g_0 is the unactuated gap.

The equilibrium position of the plate may be found by equating the electrostatic and mechanical force [1]. As

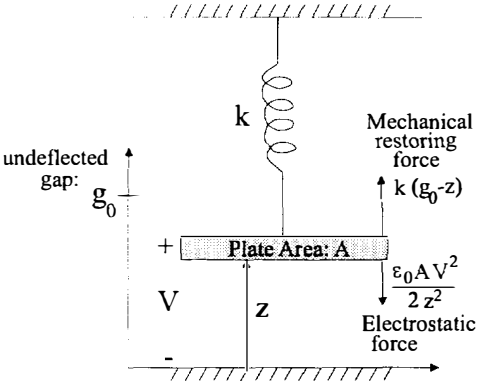

Figure 1. *Ideal $1D$ parallel plate electrostatic actuator with linear restoring force.*

V increases, the gap distance at first decreases gradually. However, at a critical voltage value called the pull-in voltage, $V_{PI} = \frac{8kg_0^3}{27\epsilon_0}$, a bifurcation occurs and the plate suddenly collapses. The maximum stable deflection of the plate before pull-in is 1/3 of the undeflected gap.

The positive feedback mechanism can be explained as follows: As the plate moves lower, more charge is drawn onto the plate to increase the electric field and keep the potential difference between the plates constant. The increase in charge and field in turn increases the electrostatic force, which pushes the plate lower again. This phenomenon is fundamental to many voltage-controlled electrostatic actuators.

There have been several previous efforts to increase the travel of electrostatic actuators without pull-in. Seeger and Crary [2] propose a stabilization technique using a matched MOS capacitor in series with an electrostatic actuator. Burns and Bright [3] use a multi-phase flexure to extend travel distance. Chu and Pister [4] report an algorithm for closed-loop voltage control of electrostatic actuators. Unlike the leveraged bending method, all three of these techniques require the fabrication of additional structures or electronics.

ACTUATION PRINCIPLE

The basic idea behind leveraged bending is to work around the pull-in instability by applying electrostatic force only on the portion of a structure, then using the rest of the structure as a "lever" to position specific parts of the structure through a large range of motion (see Fig. 2). The key is that the electrostatically-actuated portions of the structure do not have to deflect far enough to violate the pull-in limit.

Leveraged bending is best illustrated using the polychromator grating example. This application [5,6] requires a linear array of long, flat, closely-packed mirrors,

0-9640024-2-6/hh1998/$20©1998TRF
DOI 10.31438/trf.hh1998.19

Solid-State Sensors, Actuators, and Microsystems Workshop
Hilton Head Island, South Carolina, June 8-11, 1998

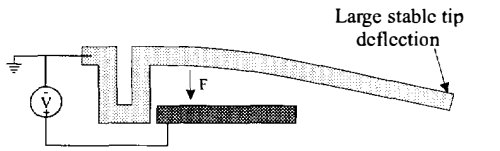

(a) Leveraged bending: cantilever

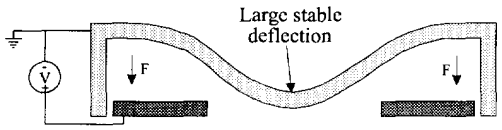

(b) Leveraged bending: Fixed-fixed beam (Low residual stress)

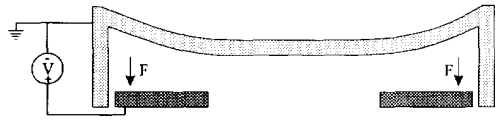

(c) Fixed-fixed beam (High tensile residual stress)

Figure 2. *Using leveraged bending to extend the stable travel range of an electrostatic actuator. Simple examples of leveraged bending applied to: (a) cantilevers and (b) doubly-clamped, fixed-fixed beams. (c) For fixed-fixed beams, tensile residual stress can limit the leveraged bending effect (see Eq. (4)).*

each of which is vertically positioned independently. The heights of the mirrors determine the optical path length of reflected light, thus effectively controlling the optical transfer function of the grating.

Each grating element consists of a conductive double-beam structure (Fig. 3), following the design of Bifano et al. [7], but with actuation electrodes only beneath a portion of the lower beam nearest the supports. Both beams are doubly-supported but the beams are staggered so that the flat mirror beam "rides" on top of the bottom beam, which bends under actuation (Fig. 3(b)). Voltage is applied to the actuation electrodes, and both beams are grounded. The voltage is controlled in an analog fashion to position the mirror beam vertically. A grounded landing pad between the actuation electrodes prevents welding if the beam touches down.

The bottom beam functions as a lever so that the middle of the beam moves further than the part of the beam over the actuation electrodes. It is possible to design the structure so that the middle of the beam travels the full gap before pull-in occurs.

Leveraged bending offers a number of distinct advantages for the polychromator grating design, at the cost of increased actuation voltage. First, for a given required analog travel distance, a smaller gap is needed. This is important in a surface micromachined process because thinner sacrificial layers mean shorter deposition times and less topography to complicate subsequent processing. The smaller gap distance also means less electrostatic crosstalk due to fringing fields from neighboring actuators. The dense mirror packing, large number of actuators, and fabrication process make other methods for full-gap travel difficult to implement. In addition, the design quite naturally provides for a grounded landing electrode which is important for eliminating stiction during operation.

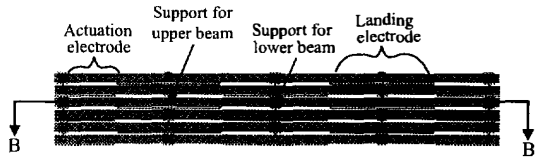

(a) Top view of grating (from layout)

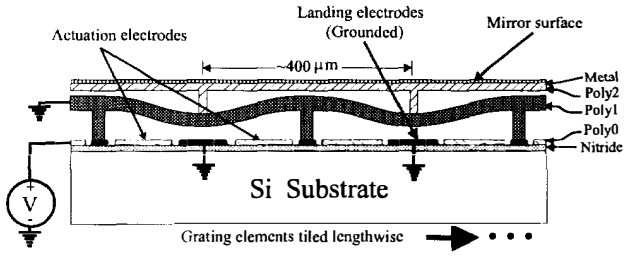

(b) Side view of grating (under actuation)

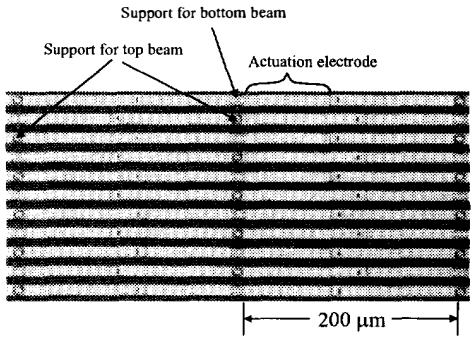

(c) Photograph of MUMPs grating

Figure 3. *Polychromator diffraction grating design. (a) Top view of grating design from layout. (b) Schematic side view of grating showing a cut along the length of a single grating element (cut B from (a)). The bottom beam is shown bent under actuation. The beam would be flat with no applied voltage. (c) Photograph of a MUMPs grating used for prototyping.*

Prototype gratings were fabricated using the MUMPs process from MCNC [8]. The design and analysis in this paper focus on the MUMPs polychromator grating example.

ACTUATOR MODELING

Accurate, efficient models are necessary to explore the design space of the actuator. Since the upper mirror beam does not affect actuation to first order, the grating element is modeled by considering just the lower beam. The $2D$ equilibrium equation for an elastic beam with electrostatic force is given by:

$$EI\frac{\partial^4 z}{\partial x^4} - S(z)\frac{\partial^2 z}{\partial x^2} = F_{elec} \qquad (1)$$

where x is the distance along the the beam, $z(x)$ is the gap height, E is the elastic modulus, $I = wh^3/12$ is the moment of inertia, w is the beam width, h is the beam thickness, $S(z)$ is the force in the beam due to stress

(see Eq. (3)), and F_{elec} is the electrostatic force per unit length. Neglecting fringing fields we approximate:

$$F_{elec} = -\frac{\epsilon_0 a(x) V^2}{2z^2} \tag{2}$$

where $a(x)$ represents the shape of the actuation electrode and V is the applied voltage. The $S(z)$ term contains two contributions, one from the residual stress left in the beam after processing, and one from a nonlinear "strain-stiffening" effect due to the stretching of the beam as it deforms. $S(z)$ is modeled as follows:

$$S(z) = hw\,[\sigma_0(1-\nu) + E\frac{\Delta L}{L}] \tag{3}$$

where σ_0 is the biaxial residual stress, ν is the Poisson ratio, ΔL is the elongation in the length of the beam due to deformation, and L is the length of the beam. Note that the nonlinear strain stiffening by itself increases the travel distance of electrostatic actuators beyond 1/3 of the gap. The ends of the beam are assumed to have perfectly clamped boundary conditions. The beam equation is simulated using a finite difference code.

DESIGN TRADEOFFS

The design space for the grating actuator involves three key parameters: the length of the beam L, the actuation electrode length, L_1, and the residual stress, σ_0, in the bottom beam.

The choice of beam length, L, is primarily determined by fabrication constraints, since actuation voltage decreases and travel distance increases with increasing L. For the MUMPs process, $L = 400\,\mu m$ was chosen for baseline design (a relatively long beam with good yield).

The choice of actuation electrode length, L_1, represents a trade-off of travel distance for actuation voltage. Shorter actuation electrodes increase the travel distance but also increase actuation voltage.

For example, assuming $L = 400\,\mu m$, suppose we would like to pick the length of the actuation electrode, L_1. Fig. 4 shows a simulation illustrating the tradeoff between actuation voltage and travel distance for varying actuation electrode length, L_1. Curves extending from the upper left to lower right show that pull-in voltage (left axis) is reduced for larger L_1. Curves extending from the lower left to upper right show that the beam deflects further at pull-in (right axis) for smaller L_1. The two different curves represent traces for different values of residual stress (for MUMPs, typical residual stress is about -10 MPa).

Based on Fig. 4, $L_1 = 80\,\mu m$ was chosen for the baseline actuation electrode length in order to get full-gap travel while minimizing actuation voltage. Full-gap actuation requires $108\,V$, about 6.1 times higher than the pull-in voltage of a similar beam with a full actuation electrode. Note, however, that the ratio between full-gap and full-electrode actuation voltage varies significantly depending on the specific structure involved.

Residual stress in the beam is also important for grating design, particularly if the stress is tensile. Although this is not an issue with the MUMPs process, it is worth noting that a tension-dominated beam acts like a rubber band. When force is applied at the ends of the beam, the middle of the beam remains flat, reducing the lever effect that increases travel (Fig. 2(c)). A rule of thumb for determining whether the actuator is tension-dominated can be obtained by comparing the analytical solutions [9] for Eq. (1) in the bending and tension-dominated cases, neglecting strain stiffening and assuming uniform load on the beam over the actuation electrodes. This analysis indicates that the residual stress, σ_0, for the fixed-fixed beam grating design must be roughly:

$$\sigma_0 < \frac{Eh^2}{2(1-\nu)L_1(L-L_1)} \tag{4}$$

for leveraged bending to be useful in the fixed-fixed beam design. Thus thicker, shorter beams and shorter actuation electrodes tend to increase the tensile residual stress that can be tolerated. For the beam dimensions of the

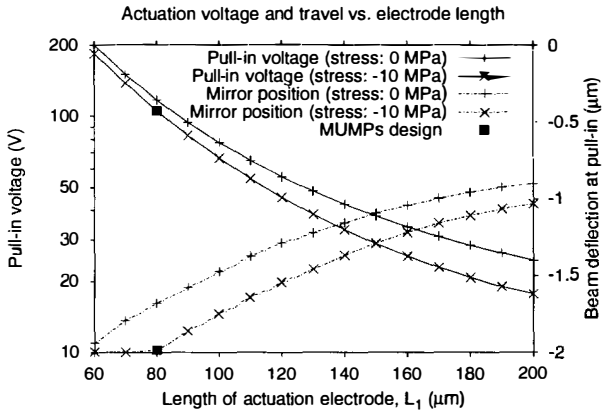

Figure 4. *Finite difference simulation of the tradeoff between actuation voltage and travel distance vs. L_1 (for $L = 400\,\mu m$, beam thickness and gap $= 2.0\,\mu m$). Curves extending from the upper left to lower right show that pull-in voltage (left axis) is reduced for larger L_1. Curves extending from the lower left to upper right show that the beam deflects further at pull-in (right axis) for smaller L_1.*

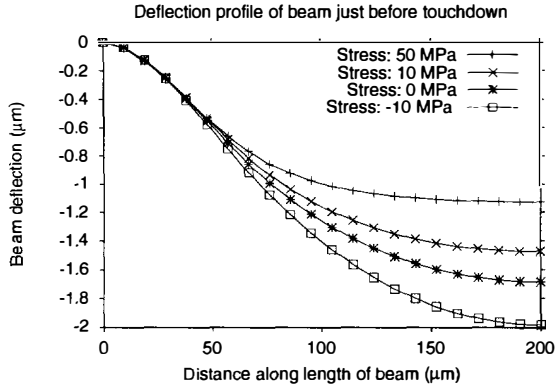

Figure 5. *Finite difference simulation of the deflection profile for an $L = 400\,\mu m$ long beam with an $L_1 = 80\,\mu m$ actuation electrode at the maximal deflection position before pull-in. For more tensile (positive stress) beams, travel is reduced because the middle of the beam stays flat when force is applied to the ends of the beam. For stress $= -10$ MPa (typical for MUMPs), full gap travel without pull-in is predicted.*

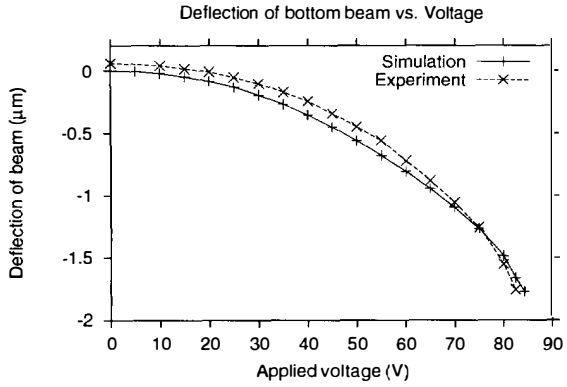

Figure 6. *Graph of bottom beam deflection vs. voltage for MUMPs grating elements without the top beam ($L = 400\,\mu m$ and $L_1 = 80\,\mu m$). More than $1.75\,\mu m$ of stable travel was measured out of a $2\,\mu m$ gap. Measurement compares well with finite difference simulation. Small discrepancies may be due to unmodeled compliant supports in the real structure. Position and film thickness measurements made using a WYKO interferometric profilometer.*

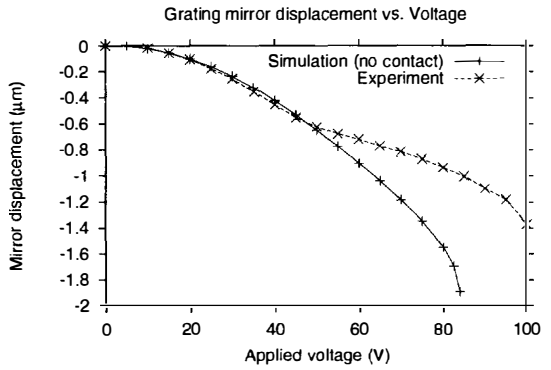

Figure 7. *Graph of measured mirror position vs. voltage for MUMPs grating element. After the mirror travels $0.67\,\mu m$, the top beam hits the post of the bottom beam, causing the structure to become stiffer. The simulation shows what would happen without this effect.*

MUMPs gratings, Eq. 4 yields $\sigma_0 < 13$ MPa. This is confirmed by Fig. 5 which shows the profile of the beam at pull-in for varying stress values, illustrating how maximum travel distance decreases with tensile residual stress for the fixed-fixed beam grating design.

EXPERIMENTAL RESULTS

Position and film thickness measurements were made using a WYKO interferometric profilometer. Measurements of MUMPs structures with the bottom grating beam only (no mirror beam) demonstrate that at least $1.75\,\mu m$ of travel is possible out of the $2\,\mu m$ gap (Fig. 6). Material property values were extracted using the thickness measurements and pull-in voltage measurements of test structures as described in [1]. The extracted material properties and thicknesses were used in the simulation plotted against the experimental data in Fig. 6.

With the MUMPs process, the nominal bottom gap is $2\,\mu m$, while the nominal upper gap is only $0.75\,\mu m$. Thus, in the full grating element, after the bottom beam deflects beyond about $0.75\,\mu m$, the top beam contacts the post of the bottom beam, making the structure stiffer (Fig. 7). Although not intentional, the effect is similar to the multi-phase flexures used by Burns, et al. [3]. The simulation matches the measured deflection before contact well, showing that the bottom beam model is an accurate predictor of grating element behavior. Gratings with a larger upper gap are currently being fabricated in a custom process at the Honeywell Technology Center.

CONCLUSIONS

This paper investigates the leveraged bending technique for extending the stable travel range of electrostatic actuators. As a case study example, the leveraged bending technique is used to design and implement the polychromator, a reflective phase grating with many mirrors, vertically positioned in an analog fashion.

The leveraged-bending approach offers a number of key advantages for the polychromator grating design, including ease of fabrication, less electrostatic crosstalk, and anti-stiction landing electrodes. The utility of the technique and the models on which it is based are verified with experimental measurements of deflection vs. voltage characteristics using prototype gratings.

ACKNOWLEDGMENTS

Support for this research was provided by the Defense Advanced Research Project Agency under contract N66001-97-C-8620. The authors wish to thank Bill Herb, Dave Burns, Aravind Padmanabhan, Ben Hocker, David Arch, Mike Butler, Mike Sinclair, Tony Ricco, and Erik Deutsch for useful discussions.

REFERENCES

[1] P. M. Osterberg and S. D. Senturia, "M-TEST: A test chip for MEMS material property measurement using electrostatically actuated test structures," *J. Microelectromech. Syst.*, **6** 2, 1997, pp. 107-118.

[2] J. I. Seeger and S. B. Crary, "Stabilization of electrostatically actuated mechanical devices," *Transducers '97*, pp 1133-1136.

[3] D. M. Burns and V. M. Bright, "Nonlinear flexures for stable deflection of an electrostatically actuated micromirror," *Proc. SPIE: Microelectronics Structures and MEMS for Optical Processing III*, Vol. 3226, Sept. 1997, pp. 125-135.

[4] P. B. Chu and K. S. J. Pister, "Analysis of closed-loop control of parallel plate electrostatic microgrippers," *Proc. IEEE Int. Conf. Robotics and Automation*, May 1994, pp. 820-825.

[5] M. B. Sinclair, M. A. Butler, A. J. Ricco, and S. D. Senturia, "Synthetic spectra: a tool for correlation spectroscopy," *Applied Optics*, **36** 15, 1997, pp 3342-3348.

[6] M. B. Sinclair, M. A. Butler, S. H. Kravitz, W. J. Zubrzycki, and A. J. Ricco,"Synthetic infrared spectra," *Optics Letters*, **22** 13, 1997, pp 1036-1038.

[7] T. G. Bifano, et al., "Continuous-membrane surface-micromachined silicon deformable mirror," *Optical Engineering*, **36** 5, May 1997, pp 1354-1360.

[8] D. A. Koester, R. Mahadevan, and K. W. Markus, *MUMPS Introduction and Design Rules*, MCNC MEMS Technology Applications Center, 1994.

[9] W. C. Young, *Roark's Formulas for Stress and Strain*, McGraw Hill, NY, 1989.

INTEGRATED CHEMICAL ANALYSIS ON PLASTIC MICROFLUIDIC DEVICES

Travis D. Boone, Herbert H. Hooper, and David S. Soane
Soane BioSciences, Inc., Hayward CA 94545-3716

ABSTRACT

Soane BioSciences is developing low-cost, mass-produced, plastic microfluidic devices for a variety of microfluidic applications including DNA analysis, clinical diagnostics, and drug discovery. Plastic substrates with complex patterns of 10-100μm-sized channels are reproducibly formed against mold tools fabricated by micromachining techniques. These substrates are used to produce plastic devices on which high-efficiency electrophoretic separations of DNA and other biomolecules have been achieved in 1-10 minutes. Plastic microfluidic devices offer several advantages over glass or silicon structures including lower processing temperatures, greater surface treatment options for electro-osmotic flow control, lower cost, and simpler extension to multi-layer device fabrication.

INTRODUCTION

The concept of microfabricating one or more components of analytical instruments dates at least to the work of Terry and coworkers, who described a microfabricated gas chromatograph almost 20 years ago [1]. The rationale for employing microfabrication technologies in analytical instrumentation are many: reducing instrument size and cost, reducing sample and reagent volumes, reducing analysis time, increasing analysis throughput, and integrating sample preparation and analysis functions. The specific objectives for a given program depend very much on the application and customer environment.

In the area of liquid-phase analysis, various methods have been explored for pumping and manipulating fluids in microstructures. A particularly promising approach is the use of electrokinetic phenomena, which avoids mechanical pumps and valves. Pace [2] and Kovacs [3] were the first to propose the concept of "chip-CE", wherein capillary electrophoresis separations are performed in microfabricated columns on planar substrates. Subsequently, groups at Ciba-Geigy [4-7], University of Alberta [8,9], Oak Ridge National Laboratory [10,11], University of California - Berkeley [12,13], and PerSeptive Biosystems [14] have demonstrated various implementations of electrically-driven separations on microfabricated chip devices. In addition to separations, several groups have explored "integrated" chip-CE, meaning the integration of various analytical protocols (e.g., mixing, reaction, separation) onto a single chip [15-17].

Most micro-scale electrophoretic devices have been fabricated from glass or silica. However, when single-use devices are desired, glass chips may not be cost-effective. As early as 1990, Soane [18] and Eckstrom [19] proposed the use of polymeric materials in chip-CE. Soane focused on thermoplastics such as polymethylmethacrylate (PMMA), while Eckstrom *et al.* investigated elastomeric polymers such as PDMS. More recently, the Novartis group [20] has demonstrated electrophoretic separations in PDMS microchannel devices.

We have been developing technology for the manufacture and use of polymeric devices in chip-CE applications, with the goal of producing single-use chips at an acceptable cost structure. We have reported results for chip-CE in PMMA microdevices [21] and in composite devices with a PMMA base enclosed by an elastomeric PDMS cover [22]. We have also explored and employed numerous other base and cover materials, and investigated the suitability of their optical, mechanical and surface properties in various applications. In this paper, we report on some of our observations and results.

EXPERIMENTAL DETAILS

Plastic Chip Fabrication

There are numerous methods for forming capillary size channels in polymeric substrates. However, several methods, such as direct machining or laser etching, can produce surfaces which are not sufficiently smooth for capillary electrophoresis. Replication methods, such as injection molding, compression molding, and casting tend to provide much smoother surfaces which we have found very suitable for capillary electrophoresis.

One general approach which we have employed involves two primary steps: (1) formation of microstructures in a base layer, and (2) sealing of the base layer with a cover layer. To form the base layer, microfluidic patterns are first micromachined on a glass or silicon master (see **Figure 1**) using common photolithographic and etching techniques. A metal mold is then formed via electroplating against the master. Such metal molds can be mounted on tooling for injection molding, as shown in **Figure 2**. Polymer substrates are then formed in large volumes by injection or compression molding (**Figure 3**). These replicates can be discrete chips, or may consist of multiple chip patterns which can be diced out of a composite part, as shown in **Figure 4**. Extremely smooth and precise channels of micrometer dimensions can be formed, as demonstrated by the actual 3-D profile of a molded plastic chip in **Figure 5**.

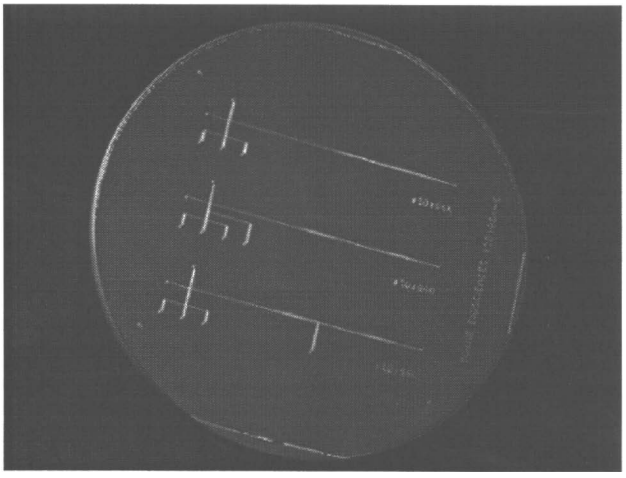

Figure 1. *4" silicon wafer with etched microfluidic patterns.*

0-9640024-2-6/hh1998/$20©1998TRF
DOI 10.31438/trf.hh1998.20

Solid-State Sensors, Actuators, and Microsystems Workshop
Hilton Head Island, South Carolina, June 8-11, 1998

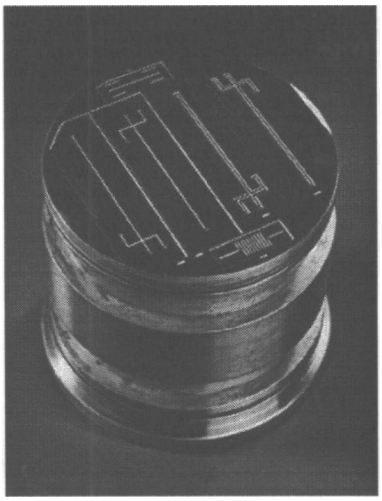

Figure 2. *Nickel electroform grown on a silicon master and mounted on an injection molding insert.*

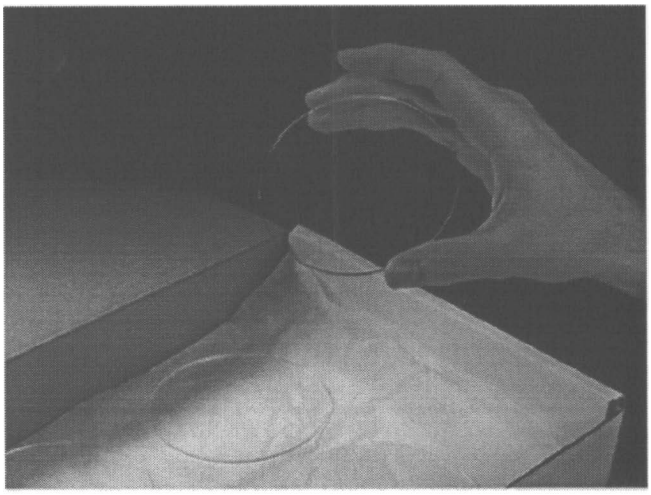

Figure 3. *Plastic microfluidic substrates can be mass produced at low cost.*

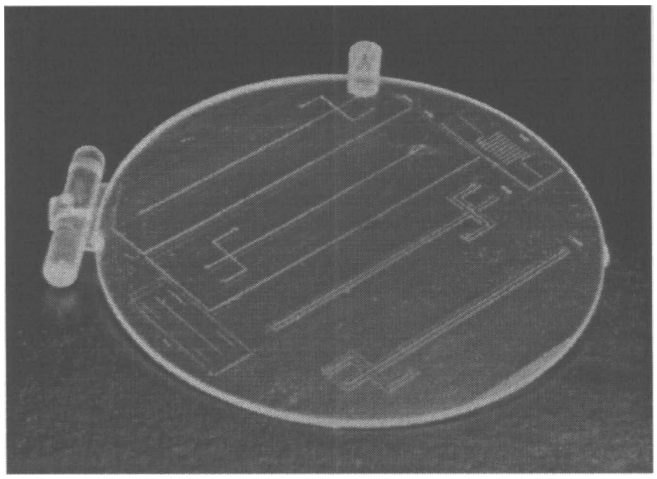

Figure 4. *An injection molded plastic microfluidic substrate formed from the mold tool shown in Figure 2.*

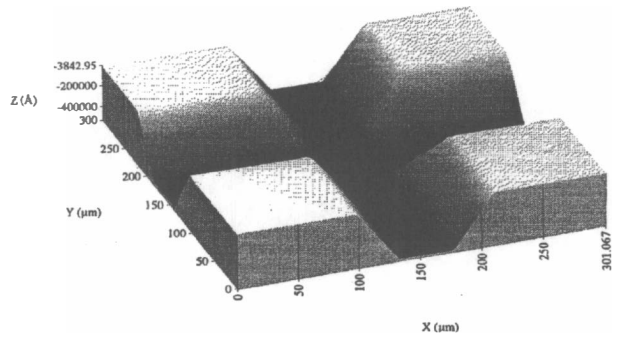

Figure 5. *Profilometry scan of an injection molded plastic microfluidic channel intersection. Measurement was performed on a Tencor P-10 system. The channels are approximately 100μm wide and 50μm deep.*

We have developed proprietary methods to form enclosed microchannels by sealing various polymer films to base substrates. **Figure 6** shows an example of a completed, sealed and functional plastic chip ready for use.

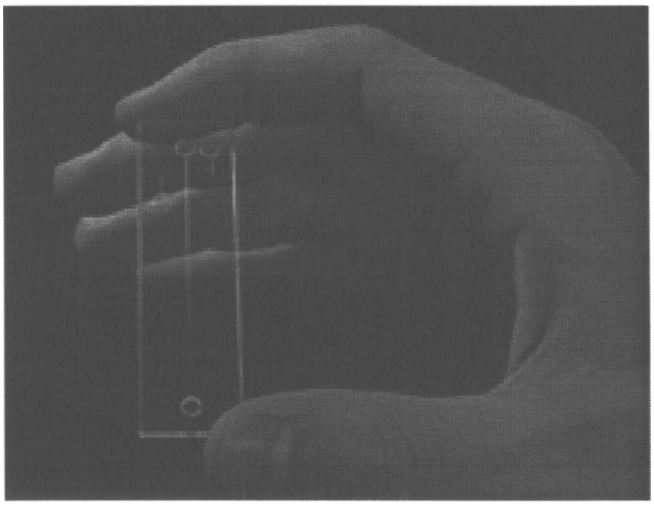

Figure 6. *A sealed, functional plastic microfluidic card with a cross channel for nanoliter injections and separations of sample. The channels of 100μm width x 50μm depth connect four reservoirs for samples and electrode contacts.*

In addition to rigid, injection molded chips (approximately 1mm in thickness), we have produced microfluidic structures in flexible film formats (~100μm thick). An example of a multiplexed microfluidic pattern on a film format is shown in **Figure 7**. Continuous films with formats which mate to standard microtiter well patterns can be employed to perform biological assays in high throughput.

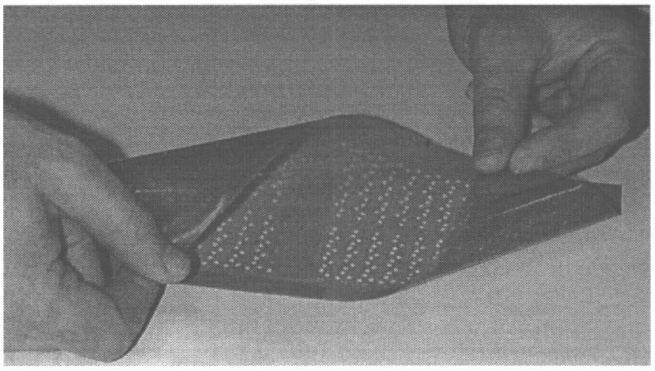

Figure 7. Multiplexed microfluidics in a continuous plastic film. Reagent micro-reservoirs mate with standard microtiter plate formats.

Surface Treatment and Fluid Manipulation

Electrokinetic flow involves both electrophoretic and electro-osmotic components. While one or the other may dominate in a given situation, both forces usually contribute to analyte or reagent movement, as most biomolecules carry a charge, and most surfaces have some degree of charge in aqueous buffers. A great deal is known regarding electro-osmotic flow (EOF) in fused silica capillaries, based on the long history of fused silica columns in capillary electrophoresis, and the numerous methods which have been developed to control EOF in these columns. This knowledge from fused silica columns is directly transferable to glass chips.

Comparatively little is known regarding EOF in plastic capillaries or channels. We have developed surface chemistries and treatment methods which enable us to achieve desired magnitudes of electro-osmotic flow in plastic microchannels. The level of electro-osmotic forces desired depends on the specific microfluidic manipulations to be performed. EOF should be low for high-resolution nucleic acid separations, moderate for stream contacting and mixing, and high for fluid transport and capillary electrochromatography. We have developed various surface treatment techniques to span this desired range of performance, as demonstrated in **Figure 8**. Lifetime studies indicate that these surface modifications can generate stable electro-osmotic flow rates over long periods and multiple runs.

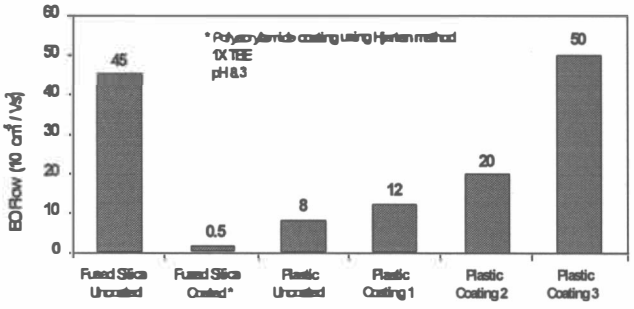

Figure 8. Effect of surface modifications on electro-osmotic flow for fused silica and plastic capillaries.

With controlled surface properties, electro-osmotic flow can be used to meter, dispense and mix fluid streams on plastic devices.

Figure 9 demonstrates our ability to mix two electrokinetically-driven streams at a T junction. The relative amounts of the two streams entering the downstream channel are precisely and independently controlled by the applied electric fields.

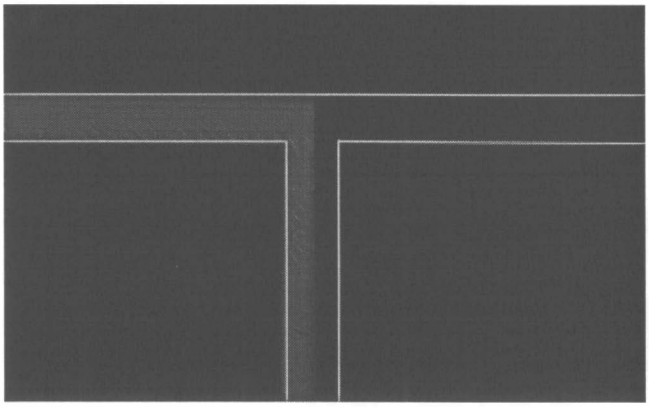

Figure 9. *Electrokinetically controlled mixing of a fluorescent and non-fluorescent fluid at a T intersection on a plastic chip. The incoming streams meet head on at the top of the figure, then flow toward the bottom where they mix by diffusion. The ratio of the two incoming flows can be electronically controlled. Channels: ~100μm width, ~35μm depth.*

Liquid measurement and dispensing is a ubiquitous operation in biology and analytical labs. In **Figure 10** a succession of images is presented showing on-chip liquid measurement and dispensing, wherein a nanoliter size plug is being dispensed into a channel. This capability is important not only for sample and reagent metering and dispensing, but also for sample introduction in on-chip separations.

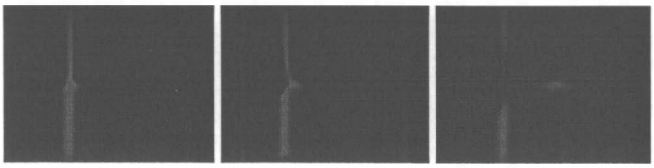

Figure 10. *Sub-nanoliter (0.5nl) injections at a cross injector on a plastic chip. A fluorescent dye has been added for visualization.*

In order to apply high electric fields for rapid, high-resolution electrophoretic separations, the chip must effectively conduct heat away from the fluid in channels. **Figure 11** compares an Ohm's law plot derived on the acrylic chip with a similar plot derived from a conventional fused silica capillary of length dimension identical to that of the acrylic chip channel (5.5 cm). The plots were derived from a channel or capillary filled with 0.5X TBE buffer; voltage across the channel/capillary was increased in 200-250 volt increments starting at 0 volts, and after a stabilization period of ~ 15 seconds, the current through the channel/capillary was recorded. For this experiment, a 75 mm ID polyimide-clad fused silica capillary was used to derive a comparative Ohm's law plot. **Figure 11** reveals that the trend of the plot for the acrylic channel is similar to the plot for the fused silica capillary, with both drawing ~ 20 mA current at 5000 Volts applied potential. This similarity implies that the cross-sectional area of the acrylic

channel and of the silica capillary are essentially identical. Finally, based on the close similarity of the two plots, the heat dissipation properties of the acrylic channel compares favorably to the heat dissipation from the silica capillary, at least at the low power conditions (~100 milliwatts) used here. The circumferential area for a non-circular chip channel is greater than for a circular capillary with equivalent cross-sectional area; thus, a larger circumferential surface area-to-volume ratio could yield enhanced heat dissipation in the chip and could compensate for the poorer thermal conductivity of the plastic chip. The field strength in these experiments intentionally was limited to ~1100 V/cm, though no problems were experienced with dielectric breakdown of the chip components at the maximum field strength.

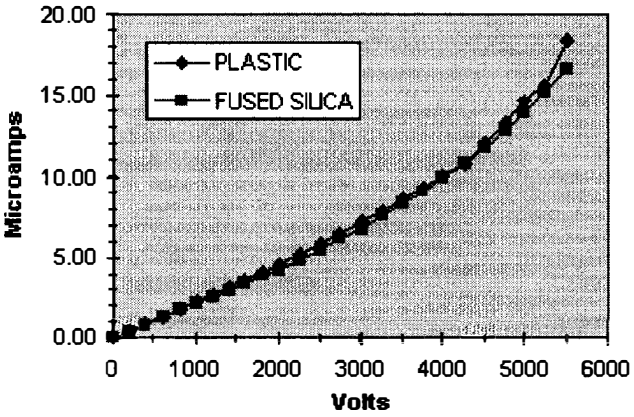

Figure 11. *Ohm's law plot comparing the heating behavior of silica capillaries and plastic channels. 5.5cm separation lengths were used with 0.5x TBE. Capillaries and chip channels had comparable cross-sectional areas of ~4400μm².*

Detection

Detection is accomplished with a confocal fluorescence approach similar to the work of Mathies *et al.* [23]. A basic schematic of the breadboard platform is shown in ***Figure 12***.

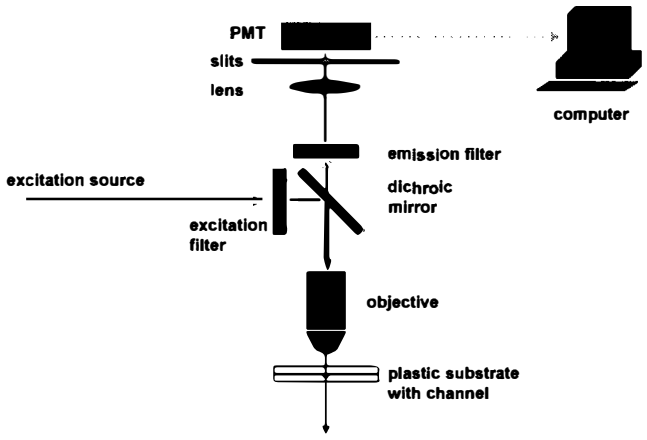

Figure 12. *Schematic diagram of confocal laser-induced fluorescence (LIF) detection.*

RESULTS

Rapid DNA Separations

We have demonstrated rapid, high-resolution separations of nucleic acids in plastic microfluidic devices. An example of a separation of a double-stranded DNA restriction digest is shown in **Figure 13**. This chip-CE separation is similar in speed and resolution to separations reported with glass devices [12], indicating that plastic devices can provide comparable performance to glass.

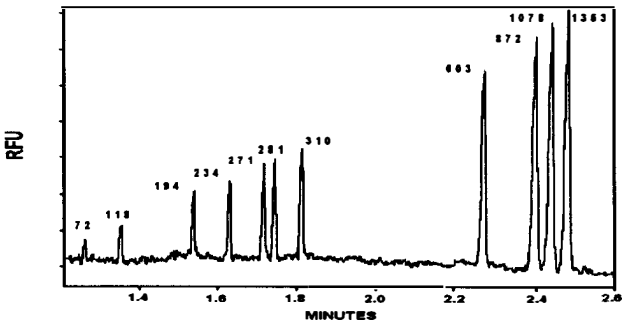

Figure 13. *Separation of Hae III φX174 on a plastic chip. Buffer: 0.5xTBE, 0.5% polymer gel, 2.5μg/ml EtBr. Conditions: 180V/cm, detection 4cm from injection, Ex: 488nm.*

Table 1 summarizes run-to-run and chip-to-chip reproducibility data for migration times for the 11 peaks in the Hae III digest of φX174 DNA on 7 chips randomly selected from an injection molding run of 500 chips. The relative standard deviation (%) is shown for six sequential runs on each chip as well as composite reproducibility for all data on each peak on all chips. The run-to-run migration time reproducibility is quite good, with RSD values below 1% for all peaks. No effort was made to control the chip temperature during the course of these runs and thus some variation in migration times due to changes in room temperature would be expected. Chip-to-chip reproducibility of migration times was somewhat higher than run-to-run reproducibility and ranged from 2.0 to 3.0 percent among the 7 chips used in this evaluation. This may be explained by slight variations in the effective field strengths and effective migration distances used in the evaluation among the 7 chips since a constant voltage was used for all chips and the total channel length varied by about 1.5%.

	Peak										
Chip	1	2	3	4	5	6	7	8	9	10	11
1	0.76	0.70	0.55	0.64	0.58	0.61	0.46	0.78	0.77	0.80	0.81
2	0.71	0.60	0.64	0.67	0.75	0.76	0.83	0.86	0.86	0.85	0.82
3	0.23	0.27	0.36	0.38	0.47	0.45	0.51	0.49	0.48	0.50	0.50
4	0.15	0.73	0.72	0.79	0.87	0.87	0.93	1.09	1.10	1.09	1.12
5	0.08	0.32	0.36	0.30	0.35	0.39	0.41	0.52	0.46	0.51	0.53
6	0.43	0.58	0.61	0.62	0.71	0.73	0.75	0.77	0.75	0.76	0.78
7	0.14	0.41	0.39	0.38	0.39	0.42	0.40	0.57	0.67	0.64	0.66
ALL	2.2	2.1	2.3	2.5	2.5	2.6	2.7	2.9	3.0	3.0	3.0

Table 1. *RSD % of the migration times of Hae III φX174 peaks from runs of the type shown in Figure 13.*

Separations of sequencing reactions have also been performed on plastic chips, as shown in **Figure 14**. Note that single base resolution is being approached for up to 350 bases in only 10 minutes.

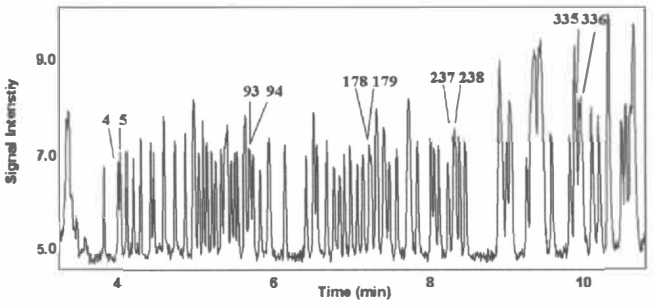

Figure 14. *Rapid, high-resolution separation of ssDNA in a plastic chip. M13mp18 T-terminated sequence/energy-transfer (FAM-TAMRA) primer, 5% uncrosslinked polymer, 7M Urea, 1X TBE, 200 V/cm, Ex: Ar laser at 488 nm, Em: 570-590 nm.*

We have also performed competitive immunoassays and enzyme inhibition assays in plastic microfluidic devices. Competitive binding assays with electrophoretic separation of bound and free human insulin have been performed with nanomolar sensitivity using fluorescence detection, as shown in **Figure 15**.

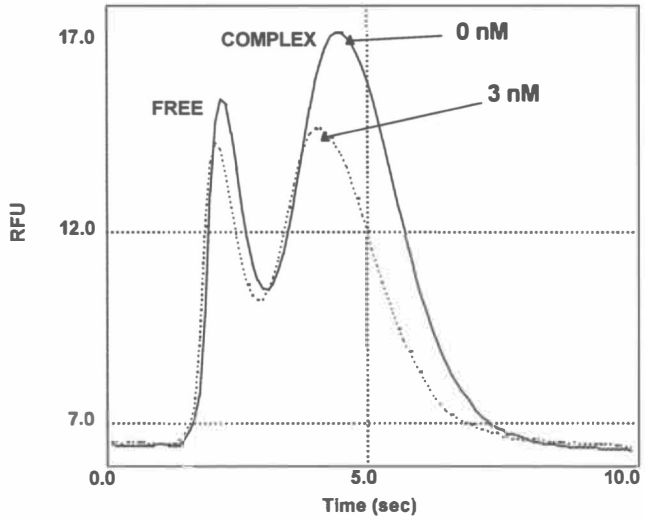

Figure 15. *Competitive immunoassay of human insulin standards on a plastic chip; Displacement of CY-5 insulin from complex by human insulin. Effective separation distance: 1.0 mm.*

In the case of enzyme assays, we have demonstrated electro-osmotic pumping of enzyme, inhibitor and substrate through plastic microchannels, on-chip enzymatic reaction, with no inhibition from the plastic, and separation of peptide substrate from product. Representative results from such an assay are shown in **Figure 16**.

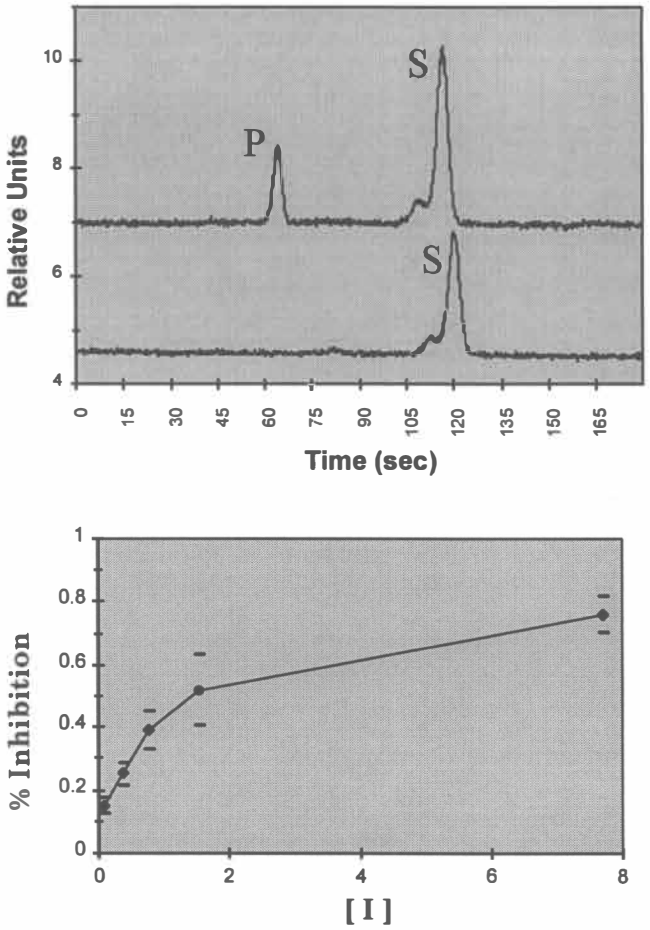

Figure 16. *Enzyme inhibition assay. Top: Separations of peptide substrate (S) and product (P) resulting from an enzymatic reaction. Bottom: An IC_{50} curve generated from running the enzymatic assay with varying levels of a test inhibitor.*

Microbead Manipulation

In addition to solution-phase assays, SBio has demonstrated the feasibility of manipulating paramagnetic particles in microfluidic devices by electrokinetic and magnetic forces. The particles provide a mobile, and spatially-definable solid phase for use in various assays. An injection of particles at a cross-channel is shown in **Figure 17**. Plugs of magnetic microbeads can be captured with a magnet in a well-defined zone downstream of the injection point, as shown in **Figure 18**. Beads can be released by subsequent removal of the magnetic field.

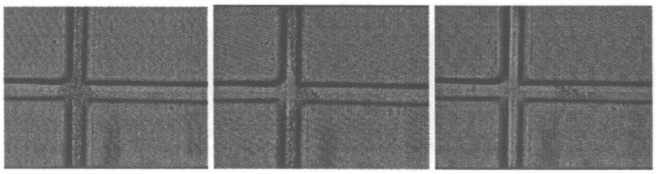

Figure 17. *Snapshots (taken at ~0.1 sec intervals) of an electrokinetically-injected plug of microbeads in buffer on a plastic chip. . Beads: 1μm diameter, in 0.1% suspension in 1 X TBE.*

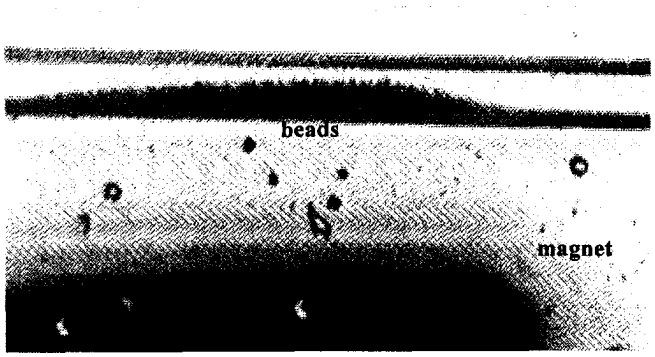

Figure 18. *Capture of magnetic beads in a flow field on a plastic chip microchannel of ~100μm width and ~35μm depth. The stream is flowing to the left at ~100μm/sec.*

CONCLUSIONS

We have developed high-volume fabrication methods, surface treatments, and assay protocols to perform rapid biochemical assays on disposable plastic chips. Plastic microfluidic devices offer several advantages over glass or silicon structures including lower processing temperatures, greater surface treatment variety for electro-osmotic flow control, lower cost, and simpler extension to multi-layer device fabrication. Mass-produced, disposable, microfluidic devices hold the promise of revolutionizing drug discovery and diagnostic markets.

REFERENCES

1. Terry, S.C.; Jerman, J.H.; Angell, J.B. *IEEE Trans. Electron. Devices*, ED-26, 1880-1886 (1979).
2. Pace, S.J. *U.S. Patent* 4,908,112, 1990.
3. Kovacs, G.T.A.; Holland, K.O. EP 0376611A2, 1990.
4. Harrison, D.J.; Manz, A.; Fan, Z.; Lüdi, H.; Widmer, H.M. *Anal. Chem.* **1992**, *64*, 1926-1932.
5. Effenhauser, C.S.; Manz, A.; Widmer, H.M. *Anal. Chem.* **1993**, *65*, 2637-2642.
6. Effenhauser, C.S.; Paulus, A.; Manz, A.; Widmer, H.M.. *Anal. Chem.* **1994**, *66*, 2949-2953.
7. Seiler, K.; Fan, Z.H.; Fluri, K.; Harrison, D.J. *Anal. Chem.* **1994**, *66*, 3485-3491.
8. Fan, Z.; Harrison, D.J. *Anal. Chem.* **66**, 177-184 (1994).
9. Chiem, N.; Harrison, D.J. *Anal. Chem.* **1997**, *69*, 373-378.
10. Jacobson, S.C.; Hergenröder, R.; Moore, Jr., A.W.; Ramsey, J.M. *Anal. Chem.* **1994**, *66*, 4127-4132.
11. Jacobson, S.C.; Ramsey, J.M. *Anal. Chem.* **1996**, *68*, 720-723.
12. Woolley, A.T.; Mathies, R.A. *Proc. Natl. Acad. Sci. USA* **1994**, 91, 11348-11352.
13. Woolley, A.T.; Mathies, R.A. *Anal. Chem.* **1995**, *67*, 3676-3680.
14. Koutny, L.B.; Schmalzing, D.; Taylor, T.A.; Fuchs, M. *Anal. Chem.* **1996**, *68*, 18-22.
15. Hadd, A.G.; Raymond, D.E.; Halliwell, J.W.; Jacobson, S.C.; Ramsey, J.M. *Anal. Chem.* **1997**, *69*, 3407-3412.
16. Li, P.C.H; Harrison, D.J. *Anal. Chem.* **69**, 1564-1568 (1997).
17. Effenhauser, C.S.; Briun, G.J.M; Paulus, A. *Electrophoresis* **1997**, *18*, 2203-2213.
18. Soane, D.S.; Soane, Z.M. US Patent 5,216,022 (1992).
19. Eckström, B.; Jacobson, G.; Ohman, O.; Sjodin, H. PCT Patent Application WO 91/16966 (1991).
20. Effenhauser, C.S.; Bruin, G.J.M.; Paulus, A.; Ehrat, M. *Anal. Chem.* **69**, 3451-3457 (1997).
21. McCormick, R.M.; Nelson, R.J.; Alonso-Amigo, M.G.; Benvegnu, D.J.; Hooper, H.H. *Anal Chem.* **1997**, *69*, 2626-2630.
22. Soane, D.S.; Soane, Z.M.; Hooper, H.H.; Alonso-Amigo, M.G.; PCT Patent Application WO 97/38300 (1997).
23. Huang, X.C.; Quesada, M.A.; Mathies, R.A. *Anal. Chem.* **1992**, *64*, 2149-2154.

ACKNOWLEDGEMENTS

We would like to thank the following researchers at Soane BioSciences for efforts on plastic chip fabrication, surface treatments, DNA separations, immunoassays, enzymatic assays, and microbead manipulation: Goretty Alonso-Amigo, Dominic Benvegnu, Tor Bjornson, Kejun Fan, Danny Hion, Thu Le, Randy McCormick, Alex Sassi, Larry Shea, Anne Wainright, and Qifeng Xue.

HIGH-SPEED MICROCHIP ELECTROPHORESIS: EXPLORING THE LIMITS

Stephen C. Jacobson, Christopher T. Culbertson, and J. Michael Ramsey

Oak Ridge National Laboratory
P.O. Box 2008
Oak Ridge, TN 37831-6142

ABSTRACT

Microchip electrophoresis was used to resolve a binary mixture in 0.8 ms using a separation field strength of 53 kV cm^{-1} and a separation length of 200 µm. The microchip design permitted an electric field strength of 6.1 V cm^{-1} in the separation channel per volt applied to the microchip. Concurrently, the spatial extent of the injection plug and the detector observation region were minimized to increase separation efficiency. Plate counts were generated at rates up to 260,000 plates s^{-1}.

INTRODUCTION

Microfabricated substrates are rapidly becoming a convenient platform with which to execute liquid phase analysis, and consequently, a variety of techniques have been implemented on microchips. Capillary electrophoresis [1, 2,3,4], synchronized cyclic electrophoresis [5], free-flow electrophoresis [6], and capillary gel electrophoresis [7,8] have been demonstrated for the separation of ions. Coupling of sample handling and reactions with separation techniques can provide complete chemical analysis, i.e., the Lab-on-a-Chip concept. Some simple monolithically integrated devices have appeared in the literature and include pre- [9,10] and postcolumn [11,12] chemical reactions in conjunction with electrophoretic separations. In other work, a hybridized device combined a microfabricated silicon thermal cycler for PCR amplification and a glass microchip for product analysis [13]. In addition, a monolithic glass device combined multiplexed PCR amplification and electrophoretic product sizing [14]. As more features are integrated into a planar format, performance optimization becomes essential, especially if pursuing high-speed analysis.

In this paper we describe instrumentation for sub-millisecond electrophoretic separations representing an ≈ 100-fold decrease in analysis time over previous methods. High-speed electrophoretic separations have been performed in capillaries using optical gating for sample introduction [15], and on microchips using a simple cross geometry [3]. Both approaches had analysis times on the order of 100 ms. Several issues must be addressed to enhance the separation performance in capillary electrophoresis. Most importantly, the separation field strength must be optimized to reduce the analysis time and minimize dispersion due to diffusion and thermal convection. In addition, the spatial extent of the injection plug and detector observation region must be minimized. The injection plug length can be minimized by fabricating narrow channel dimensions for the injection valve and confining the sample volume within the injection cross using electric fields. Similarly, the detector observation length can be minimized for fluorescence detection by having a small excitation volume or tight spatial filtering. The channel manifold can be designed to reduce the potential drop in areas not contributing to the separation so that high separation field strengths can be achieved with modest applied potentials. To achieve this design goal in a single etch step, narrow channels were fabricated for the injection valve and separation channel, and wide channels for all other sections of the channel manifold. This enabled separation field strengths of 6.1 V cm^{-1} per volt of applied potential.

EXPERIMENTAL SECTION

The microchips were fabricated using standard photolithographic, wet chemical etching and bonding techniques as described previously. Briefly, a photomask was fabricated by sputtering chrome (30 nm) and gold (100 nm) onto a glass slide, spinning a positive photoresist onto the gold film, and exposing the microchip design (Figure 1) into the photoresist using a CAD/CAM laser machining system (argon ion, 457 nm). Subsequently, the metal films were etched using KI/I_2 for Au and $K_3Fe(CN)_6/NaOH$ for Cr. The channel design was then transferred onto glass substrates using a positive photoresist and UV exposure. After developing the photoresist, the chrome film was etched, and then channels were etched into the substrate in a dilute, stirred HF/NH_4F bath. 3.5-mm access holes to the channels were drilled in the substrate followed by bonding of the cover plate to the substrate over the etched channels to form a closed network of channels. Cylindrical glass reservoirs were affixed on the substrate using epoxy.

Control of the high voltage at the four fluid reservoirs was performed using a single high voltage power supply (10A12-P4, Ultravolt) with voltage division in 5% increments. High voltage relays (K81C245, Kilovac) were used to toggle between the sample loading and separation modes. Input to the power supply and high voltage relays was computer controlled. An average delay of 500 µs was observed when switching from the sample loading mode to the separation mode. Platinum electrodes provided electrical contact from the high voltage leads to the solutions in the reservoirs. With this configuration, injection volume was controlled by applying potentials at each of the reservoirs during the injection and separation modes. The sample flowing through the injection valve from the sample to

0-9640024-2-6/hh1998/$20©1998TRF
DOI 10.31438/trf.hh1998.21

Solid-State Sensors, Actuators, and Microsystems Workshop
Hilton Head Island, South Carolina, June 8-11, 1998

sample-waste reservoir was spatially confined by electric fields in the buffer and separation channels. To execute the separation, the voltages are reconfigured with the primary flow from the buffer reservoir to the waste reservoir. The sample and sample-waste reservoirs are maintained at a fraction (50%) of the potential applied to the buffer reservoir in the separation mode to prevent leakage of sample into the separation channel from the sample and sample-waste channels. This scheme introduces small spatial extent sample plugs and provides high separation efficiency and volumetric reproducibility (< 0.3% relative standard deviation).

Microchip separations were monitored using on-microchip laser induced fluorescence detection.[10] An argon ion laser (514.5 nm, ≈ 10 mW; Coherent) was used for excitation and focused to an ≈ 25 μm spot onto the separation channel using a lens (200 mm focal length). The fluorescence signal was collected using a 100x (0.7 NA) objective lens (Mitutoyo), followed by spatial filtering (0.4 mm diameter pinhole) and spectral filtering (550 nm cut-on), and measured using a photomultiplier tube (PMT; Oriel 77340). The PMT response was amplified (Kiethley 428M) and recorded with an oscilloscope (Tektronix TDS350). The data on the oscilloscope was then transferred to a Macintosh computer using a GPIB interface and Labview 4.1 (National Instruments). The compounds used for the experiments were rhodamine B (RB; 8 μM; Exciton) and dichlorofluorescein (DCF; 4 μM). The buffer in all of the reservoirs was 1 mM sodium tetraborate and 5 mM N-[2-Hydroxyethyl]piperazine-N'-[2-ethanesulfonic acid] (HEPES).

RESULTS AND DISCUSSION

Estimates of the minimum efficiency, separation length, and separation field strength were needed to design a microchip for high-speed electrophoresis. The minimum number of plates required to resolve rhodamine B (RB) and dichlorofluorescein (DCF) can be calculated from equation 1 [16],

$$(1) \quad N = \left(\frac{4\ R\ \mu_{avg}}{\mu_{RB} - \mu_{DCF}} \right)^2$$

where N is the number of theoretical plates, R is the resolution, and μ_x are the electrokinetic mobilities for RB, DCF, and their average (avg). For a desired resolution of 1.5, and the electrokinetic mobilities for RB and DCF of 6.2 x 10^{-4} and 4.0 x 10^{-4} $cm^2V^{-1}s^{-1}$, respectively, 185 plates are required.

The separation length, L_{sep}, can then be calculated from equation 2,

$$(2) \quad L_{sep} = N\ H_{total}$$

where H_{total} is the total plate height with contributions from diffusion, injection plug length, l_{inj}, and detector observation length, l_{det}, respectively. H_{total} can be calculated from equation 3,

$$(3) \quad H_{total} = \frac{2\ D\ t_{DCF}}{L_{sep}} + \frac{l_{inj}^2}{16\ L_{sep}} + \frac{l_{det}^2}{12\ L_{sep}}$$

where D is the diffusion coefficient (3 x 10^{-6} cm^2s^{-1}), and t_{DCF} is the migration time of the slower component (1 ms). The sample plug injected onto the separation channel is assumed to be a Gaussian function, and for this calculation a baseline width (4σ) of 30 μm was used. The detector observation length was considered to be a rectangular function defined by the spatial filter and is 4 μm. Using these assumed values in equation 3 results in an estimated separation length of ≈ 100 μm. Lastly, the separation field strength, E_{sep}, required to resolve these components in under 1 ms can then be estimated by equation 4,

$$(4) \quad E_{sep} = \frac{L_{sep}}{t_{DCF}\ \mu_{DCF}}$$

yielding a value of 26 kV cm^{-1}.

Figure 1 shows a schematic of the microchip designed to meet these criteria. Wide channels were used to minimize the potential drop from the reservoirs to the injection valve and separation channel. Figure 2 shows a photograph of a microchip. The fabrication included a single etch step with constant channel depths of 7.0 μm. Consequently, the different resistivities per unit length result from different channel widths. The wide channels are 440 μm wide, and the narrow channels are 26 μm wide. The 26 μm linewidth was the narrowest, high quality line that could be produced with our in-house direct-write system. The relative resistivity between the narrow and wide channels is 16.9 per unit length, and consequently, the potential drop along the wide channel is

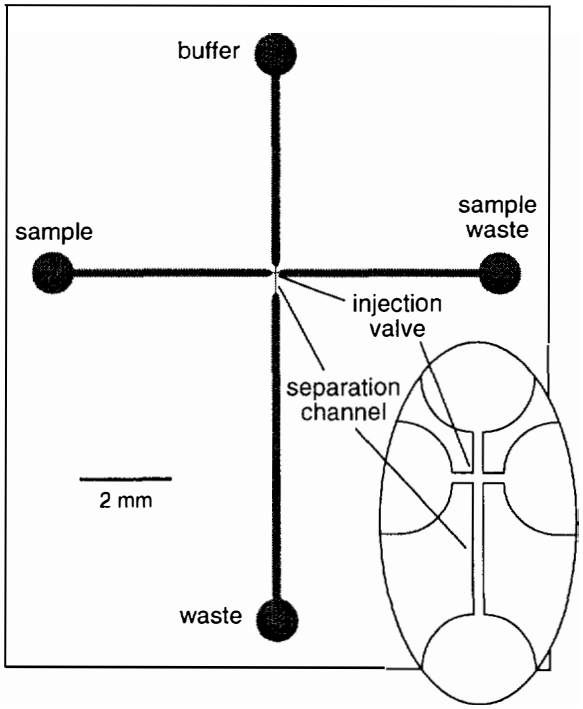

Figure 1. Schematic of microchip used for high-speed electrophoretic separations. Inset. Enlargement of the injection valve and separation channel.

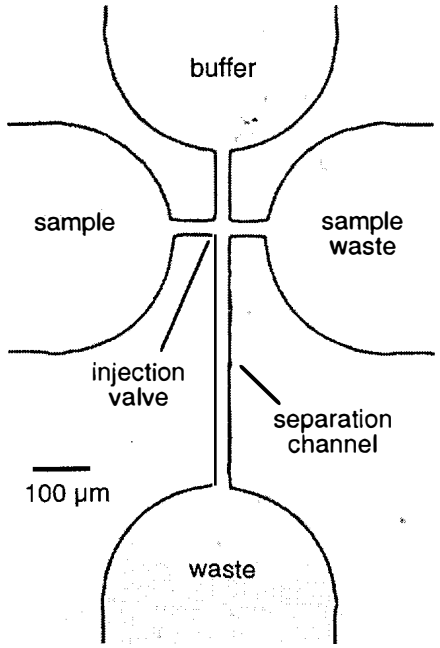

Figure 2. Photograph of microchip used for high-speed electrophoretic separations. The area of the photograph is 0.8 x 1.2 mm, and the injection valve and separation channel are shown. The wide channels are 440 µm wide, and the narrow channels are 26 µm wide.

16.9 times less than along the narrow channels for a given length. This design gives a separation field strength of 6.1 V cm^{-1} per volt of applied potential. If a microchip of similar dimension were fabricated with constant width channels, the applied potential would have to be over 8 times greater to achieve equivalent separation field strengths. For example, the highest separation field strength used in this work was 53 kV cm^{-1} which would require 71 kV of applied potential for a microchip with a uniform width channel design. Such high potentials are clearly not practical.

Figure 3 shows an electrophoretic separation from a single injection of the binary mixture of rhodamine B and dichlorofluorescein resolved in 0.8 ms using the microchip depicted in Figure 2. The separation was monitored 200 µm downstream from the injection valve, and a separation field strength of 53 kV cm^{-1} was used (8.6 kV applied to the microchip). The variation of sample velocity with the separation electric field strength is plotted in Figure 4. The solid lines are calculated from an average of the velocities at the two lowest field strengths (13 and 27 kV cm^{-1}) and extrapolated to higher separation field strengths to demonstrate the deviation from linear behavior at higher field strengths (40 and 53 kV cm^{-1}). This nonlinear behavior can be attributed to Joule heating of the buffer which lowers the buffer viscosity resulting in higher linear velocities. To lessen the Joule heating in the channels, 83% of the buffer composition was a zwitterionic organic buffer, HEPES. The heat dissipated in the separation channel for the 53 kV cm^{-1} separation field strength was estimated to be 172 W m^{-1} assuming a potential drop of 2.8 kV, a current of 32 µA, and a length of 520 µm. This value is considered to be exceedingly high for conventional capillary electrokinetic separations, but the separation efficiency was not adversely affected as discussed below. For the lower separation field strengths (13 and 27 kV cm^{-1}), the electroosmotic mobility of 6.21 x 10^{-4} cm^2 V^{-1} s^{-1} was estimated and coincided well with previously reported values [17] which indicated that the calculation of the electric field strength in the separation channel was

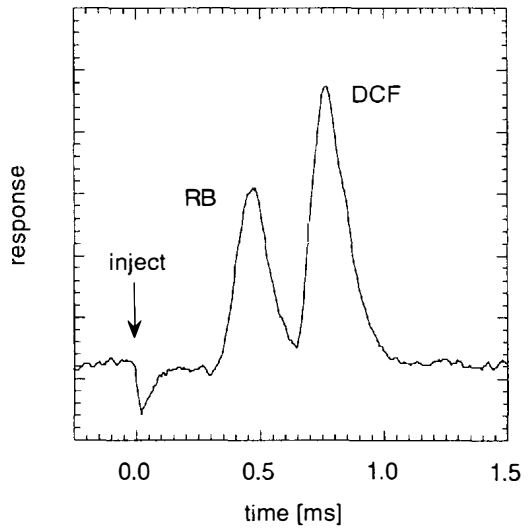

Figure 3. High-speed electropherogram of rhodamine B (RB) and dichlorofluorescein (DCF) resolved in 0.8 ms using a separation field strength of 53 kV cm^{-1} and a separation length of 200 µm. The start time is marked with an arrow at 0 ms.

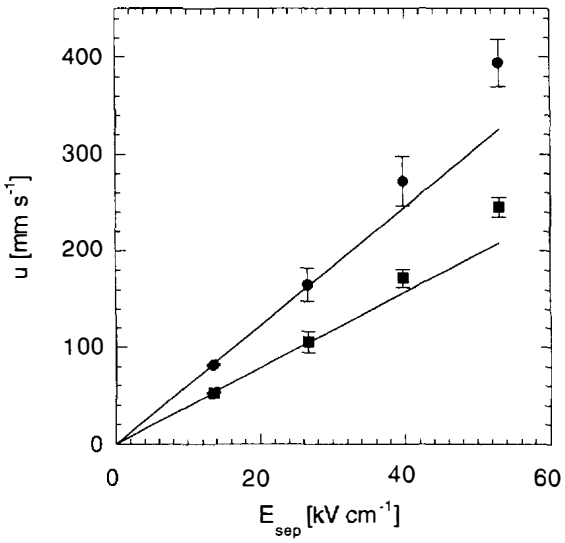

Figure 4. Variation of linear velocity (u) with separation field strength (E_{sep}) for rhodamine B (●) and dichlorofluorescein (■). Lines are calculated from the average mobilities measured at separation field strengths of 13 and 27 kV cm^{-1}. The errors bars are ± σ.

acceptable. Also, the ratio between the electrokinetic mobilities for rhodamine B and dichlorofluorescein remain nearly constant at 1.58 over the range of separation field strengths. Although the volumetric flow rate is normally considered to be minuscule in electrokinetically driven microchannel devices, the high linear velocities produced here result in a volumetric flow rate of over 4 $\mu L\ min^{-1}$, which is two orders of magnitude higher than most microchip assays.

In conclusion, the initial demonstration of sub-millisecond separations was extremely promising. Straightforward improvements in the separation efficiency and analysis time can be made by reducing the contributions of the injection plug width and Joule heating to the plate height. High-speed microchip electrophoresis could be a useful tool for ultra-high throughput drug discovery, monitoring millisecond time-scale kinetics for chemical and biochemical reactions, or as the final dimension to multi-dimensional separation systems.

ACKNOWLEDGEMENTS

This research is sponsored by the U.S. Department of Energy, Office of Research and Development. Oak Ridge National Laboratory (ORNL) is managed by Lockheed Martin Energy Research Corporation for the U.S. Department of Energy under contract DE-AC05-96OR22464. C.T.C. was supported through an appointment to the ORNL Postdoctoral Research Associates Program administered by ORISE and ORNL.

REFERENCES

1. D.J. Harrison, A. Manz, Z. Fan, H. Lüdi, H.M. Widmer, "Capillary Electrophoresis and Sample Injection Systems Integrated on a Planar Glass Chip," *Anal. Chem.*, *64*, 1926 (1992).

2. D.J. Harrison, K. Fluri, K. Seiler, Z. Fan, C.S. Effenhauser, A. Manz, "Micromachining a Miniaturized Capillary Electrophoresis-Based Chemical Analysis System on a Chip," *Science*, *261*, 895 (1993).

3. S.C. Jacobson, R. Hergenröder, L.B. Koutny, J.M. Ramsey, "High-Speed Separations on a Microchip," *Anal. Chem.*, *66*, 1114 (1994).

4. L.B. Koutny, D. Schmalzing, T.M. Taylor, M. Fuchs, "Microchip Electrophoretic Immunoassay for Serum Cortisol," *Anal. Chem.*, *68*, 18 (1996).

5. N. Burggraf, A. Manz, C.S. Effenhauser, E. Verpoorte, N.F. de Rooij, H.M. Widmer, "Synchronized Cyclic Capillary Electrophoresis - A Novel Approach to Ion Separations in Solution," *J. High Res. Chromatogr.*, *16*, 594 (1993).

6. D.E. Raymond, A. Manz, H.M. Widmer, "Continuous Sample Pretreatment Using a Free-Flow Electrophoresis Device Integrated onto a Silicon Chip," *Anal. Chem.*, *66*, 2858 (1994).

7. C.S. Effenhauser, A. Paulus, A. Manz, H.M. Widmer, "High-Speed Separation of Antisense Oligonucleotides on a Micromachined Capillary Electrophoresis Device," *Anal. Chem.*, *66*, 2949 (1994).

8. A.T. Woolley, R.A. Mathies, "Ultra-High-Speed DNA Sequencing Using Capillary Electrophoresis Chips," *Anal. Chem.*, *67*, 3676 (1995).

9. S.C. Jacobson, R. Hergenröder, A.W. Moore, J.M. Ramsey, "Precolumn Reactions with Electrophoretic Analysis Integrated on a Microchip," *Anal. Chem.*, *66*, 4127 (1994).

10. S.C. Jacobson, J.M. Ramsey, "Integrated Microdevice for DNA Restriction Fragment Analysis," *Anal. Chem.*, *68*, 720 (1996).

11. S.C. Jacobson, L.B. Koutny, R. Hergenröder, A.W. Moore, J.M. Ramsey, "Microchip Capillary Electrophoresis with an Integrated Postcolumn Reactor," *Anal. Chem.*, *66*, 3472 (1994).

12. K. Fluri, G. Fitzpatrick, N. Chiem, D.J. Harrison, *Anal. Chem.*, "Integrated Capillary Electrophoresis Devices with an Efficient Postcolumn Reactor in Planar Quartz and Glass Chips," *68*, 4285 (1996).

13. A.T. Woolley, D. Hadley, P. Landre, A.J. deMello, R.A. Mathies, M.A. Northrup, "Functional Integration of PCR Amplification and Capillary Electrophoresis in a Microfabricated DNA Analysis Device," *Anal. Chem.*, *68*, 4081 (1996).

14. L.C. Waters, S.C. Jacobson, N. Kroutchinina, J. Khandurina, R.S. Foote, J.M. Ramsey, "Microchip Device for Cell Lysis, Multiplex PCR Amplification, and Electrophoretic Sizing," *Anal. Chem.*, *70*, 158 (1998).

15. A.W. Moore Jr., J.W. Jorgenson, "Study of Zone Broadening in Optically Gated High-Speed Capillary Electrophoresis,"*Anal. Chem.*, *65*, 3550 (1993).

16. J.C. Giddings, *Unified Separation Science*, John Wiley & Sons, Inc., New York (1991).

17. For example, P.K. Dasgupta, S. Liu, "Electroosmosis: A Reliable Fluid Propulsion System for Flow Injection Analysis," *Anal. Chem.*, *66*, 1792 (1994).

OLIGONUCLEOTIDE LIGATION REACTIONS ON A CHIP USING MAGNETIC PARTICLES

Z. Hugh Fan; Rajan Kumar; Gregory Deffley;
Qianping Dong; Paul Stabile; Thomas Fare
Sarnoff Corporation,
CN 5300, Princeton, NJ 08543-5300
E-mail: hfan@sarnoff.com

Abstract

We report the incorporation of magnetic particles into microfluidics for DNA diagnostics and discuss its advantages. Magnetic particles are transported using electroosmotic pumping to locations where they are held by a magnetic field. Annealing, ligation, and denaturation of oligonucleotides have been demonstrated on magnetic beads in microfabricated devices. The successful execution of these steps indicates the feasibility of isothermal nucleic acid amplification schemes using fluid cycling rather than thermal cycling.

Introduction

Fluid pumping used in most microfabricated devices results in the displacement of one solution with another at a particular location. As a result, chemical reactions have to be implemented along the channel flow, as demonstrated in microsystems using electroosmosis **[1, 2]**. Using this scheme, multi-step reactions such as DNA amplification are very difficult to execute unless the channel is unreasonably long. In addition, multiple side channels used to supply reagents will disturb the fluid flow system. To overcome these problems, we have incorporated magnetic particles into microfluidic systems. Sequential chemical reactions can take place on the surface of particles while the particles are held stationary by a magnetic field. The product of each step can be separated from undesired reagents simply by washing prior to the subsequent reaction. Fluid pumping does not displace the components on beads and multi-step reactions can be implemented at one location in a microfabricated device.

Nucleic acid amplification technologies, e.g., polymerase chain reaction (PCR) and ligase chain reaction (LCR), have been demonstrated in microfabricated devices **[3-6]**. Work to date has consisted of miniaturizing macroscale tubes (~1 ml) into microscale chambers (~10 µl), hence most features of microfluidics have not been fully utilized. We have conceived of isothermal amplification approaches that take advantage of microfluidics. Unlike thermal cycling in the conventional amplification methods, fluid cycling can be used to execute denaturation, annealing, and ligation (LCR) or extension (PCR). These three steps in each cycle are carried out by introducing appropriate reagents rather than adjusting temperatures. The advantages of this approach include isothermal reactions, fast analysis, and other benefits enabled by miniaturization **[7]**. To show the feasibility, we have demonstrated individual, room-temperature reaction of each step, and the combination of oligonucleotide annealing and ligation reactions in a microfluidic system.

Experimental Section

Devices and Fabrication. Figure 1 shows the layout of the devices used for oligonucleotide ligation reactions. The channels are about 50 µm wide and 20 µm deep. The devices were made of two 54 x 54 x 0.5 mm glass plates. The channels were defined in one plate using photolithography. The holes at the channel ends were made in the second plate and they provide access to channels **[8]**. A glass plate with channels and a plate with holes were laminated together using a modified anodic bonding method described previously **[9]**. The device was then assembled with a Plexiglas fixture that is used for solution introductions and electrical connections.

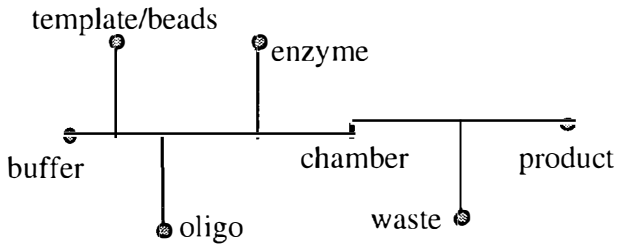

Figure 1. *The layout of a device used for oligonucleotide ligation reactions.*

Apparatus. An apparatus with voltage controls and a microscope system was assembled in-house. A Fluke high voltage power supply (Model 412B, Seattle, WA) was connected to a chip device via a control system. The system consists of relays and electronics that is able to simultaneously deliver ten different voltages for electroosmotic pumping. The voltages and the relays were controlled by a computer with a program written in C language. An inverted fluorescence microscope (Olympus IX70, Melville, NY) with a CCD color camera (Optronics, Goleta, CA) was used for monitoring transport of magnetic particles and fluorescence measurements. The images of

0-9640024-2-6/hh1998/$20©1998TRF
DOI 10.31438/trf.hh1998.22

beads and fluorescence were recorded on a VCR tape or acquired by an imaging software (MetaMorph, Universal Imaging, Hollis, NH).

Materials and Reagents. Corning 7740 (Pyrex) glass plates were purchased from Specialty Glass Products (Willow Grove, PA). Streptavidin-coated magnetic beads (Dynabeads® M-280) were procured from Dynal Inc. (Oslo, Norway) and T4 DNA ligase was from New England BioLabs (Beverly, MA). All oligonuleotides were obtained from Operon Technologies (Alameda, CA) and their sequences are listed in Table 1. The buffer used for ligation reactions consists of 50 mM tris-HCl at pH 7.8, 10 mM $MgCl_2$, 10 mM DTT, and 1 mM ATP. A buffer solution of pH 8.2 was prepared from 50 mM boric acid and 50 mM tris(hydroxymethyl) aminomethane (tris) (BioRad, Hercules, CA). All other chemicals are of reagent grade and all solutions were prepared in water from Milli-Qplus water system (Millipore, Bedford, MA). All solutions were filtered before use with a Millipore 0.22 μm membrane filter unit.

Table 1. *Sequences of oligonucleotides used in reactions.*

LCRA (24-mer)	5'-PTTGTGCCACGCGGTTGGGAATGT A-3'
LCRB (26-mer)	5'-AGCAACGAATGTTTGCCCGCCAGT TG-3'
LCRTEMP (60-mer)	5'-XCTGAATTACATTCCCAACCGCGT GGCACAACAACTGGCGGGCAAACAG TCGTTGCTGATT-3'
mActin-4 (30-mer)	5'-FTGTGGATCAGCAAGCAGGAGTAC GATGAGT-3'.
mActin-8 (30-mer)	5'-XACTCATCGTACTCCTGCTTGCTG ATCCACA-3'.

Note: P, X, and F stands for phosphate, biotin, and fluorescein groups, respectively.

Labeling and Gel Electrophoresis. The samples collected from the device were concentrated with seeDNA according to manufacturer's protocol (Amersham, Arlington Heights, IL). T4 kinase (New England BioLabs) and γ-P^{33}-ATP (DuPont NEN, Boston, MA) were used to radioactively label oligonucleotides. Samples were then analyzed on a 12%C polyacryamide slab gel. The gel electrophoresis was performed under denaturing conditions in 8 M urea. The gel was dried and scanned using a phosphor imaging system (Storm 840, Molecular Dynamics, Sunnyvale, CA).

Results and Discussions

Bead Manipulation. Magnetic particles have been extensively used for the preparation, separation, and detection of biological molecules such as DNA, mostly because of their efficiency, simplicity, and low cost. We have applied biomagnetic techniques in microfabricated devices to perform sample preparation for DNA diagnostics, including capture of *Escherichia coli* using affinity beads and lysis of bacterial cells to extract DNA onto beads **[10]**. The transportation, localization, and manipulation of magnetic particles have been reproducibly performed in chips.

Electroosmotic pumping was exploited to transport magnetic particles and a permanent magnet was used to hold them. Figure 2 shows magnetic beads that were electroosmotically pumped to the chamber where the beads were captured by a magnet. Various types of particles have been examined using a range of pumping buffers. Dynabeads® are very reliably pumped in 50 mM tris-borate buffer at pH 8.2.

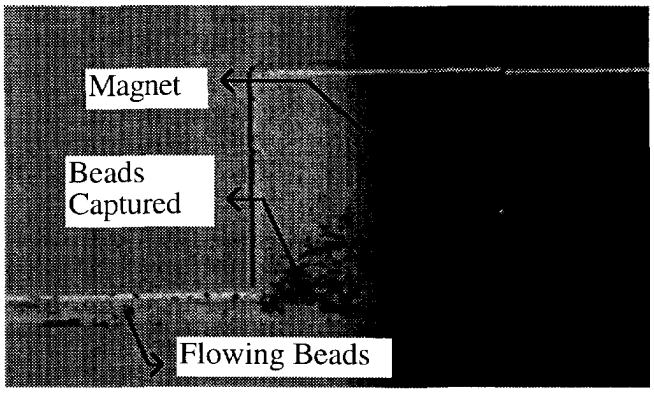

Figure 2. *Dynabeads® (2.8 μm diameter) were electroosmotically pumped through a 50 x 150 μm channel into the chamber and then captured by a magnet. The chamber is 1 mm square with the depth of 50 μm. 500 V was applied to the channel, with an end-to-end distance of 38 mm.*

Annealing. Oligonucleotide probes need to hybridize with the template in order to be ligated by ligase. The annealing step was first demonstrated in a chip device by mixing beads with reagents (data not shown). Briefly, beads attached with a template (mActin-8) were introduced into the device using electroosmotic pumping and a magnet was used to hold the beads near the reaction chamber. After the accumulation of a certain number of beads, a fluorescently-labelled probe (mActin-4) was pumped through these beads. The probe was expected to hybridize to the template because of their complementary sequences. After pumping a wash buffer through the beads, fluorescence on beads indicated the annealing of the probe on the template. The annealing between LCRTEMP and fluorescently labeled LCRA had also been confirmed in a chip before we pursued ligation reactions.

Ligation Reactions. Oligonucleotide ligation reactions were performed in the device shown in Figure 1. The reservoirs were filled with reagents as indicated. All steps involved in ligation reactions are schematically shown in Figure 3. Magnetic beads carrying a template (LCRTEMP) were pumped from the reservoir to the chamber by applying

a voltage between the bead reservoir and the waste well. These beads were localized and accumulated in the chamber by a magnet. Two oligonucleotide probes (LCRA and LCRB) with complementary sequences to the template were then introduced into the chamber and hybridized with the template on beads. T4 DNA ligase in the ligase buffer was then pumped into the chamber and the enzyme ligated two hybridized probes. After the completion of the ligation, tris-borate buffer was pumped to wash non-specifically adsorbed oligonucleotides to waste. The magnet was then released and beads with ligated probes were transported to the product well by pumping the buffer again. The collected samples were denatured and radioactively labeled off-chip, followed by the analysis using gel electrophoresis. The gel electrophoregram in Figure 4 shows the presence of ligation products on the beads. The ligation yield is approximately 25% based on the intensities of oligo and ligated probe bands.

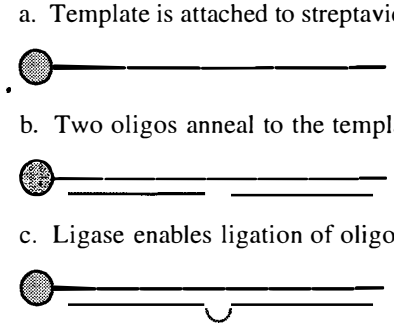

Figure 3. *The protocol of oligonucleotide ligation reactions using DNA T4 ligase.*

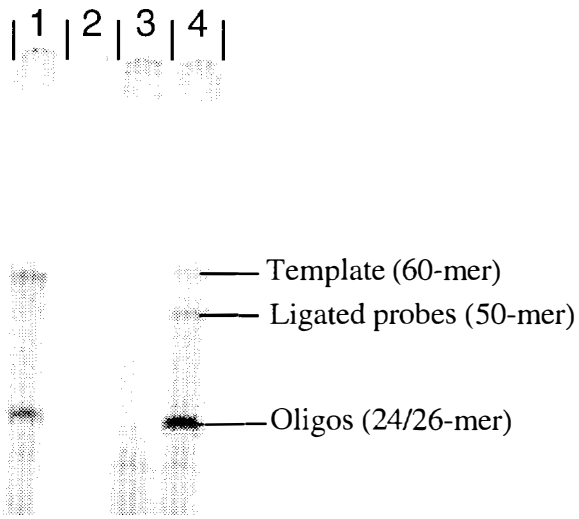

Figure 4. *Gel electrophoregram showing ligation products on the beads. Lane 1: standard (1 fmol LCRA and 1 fmol LCRTEMP); Lane 2: empty lane; Lane 3: waste well; Lane 4: product well.*

Denaturation. Denaturation of double-stranded DNA is the step to produce single-stranded DNA that can be used as a template for the hybridization of complementary oligonuleotide probes. The method used in conventional LCR (or PCR) is to heat the double-stranded DNA to a temperature near boiling. We employed 0.1 M NaOH rather than heating to denature DNA in the fluid cycling scheme. Electroosmotic pumping of NaOH was achieved by alternately transporting a plug of NaOH and a buffer **[11]**. Figure 5 shows the denaturation of an oligonucleotide probe (mActin-4) from a template (mActin-8) in a microfabricated device. The template was attached to beads via streptavidin-biotin conjugation. The fluorescently-labelled probe was annealed to the template in an Eppendorf tube. The beads with this double-stranded DNA were introduced into the device using electroosmotic pumping and a permanent magnet held the beads at a designated site. The top picture of Figure 5 shows a plug of fluorescent beads in the main channel of the device in Figure 1. After NaOH solution was electroosmotically pumped through the plug of beads, we observed the disappearance of fluorescence on beads, as shown in the bottom picture of Figure 5. This result indicates denaturation of DNA by NaOH.

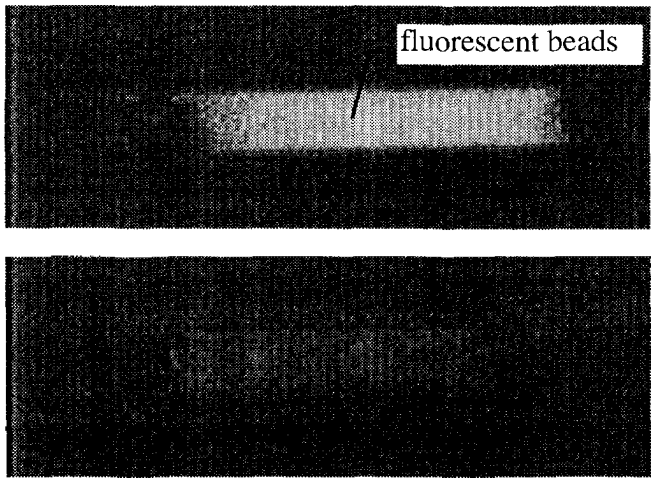

Figure 5. *The room temperature denaturation of oligonucleotides using 0.1 M NaOH in a microfabricated device. (top) A plug of beads carrying a template annealed with a fluorescently-labelled oligonucleotide was electro-osmotically pumped into the device and held in place by a magnet. (bottom) The same plug of beads shows little fluorescence after the denaturation step.*

Conclusion

The advantages of using magnetic particles in microfluidic systems and heterogeneous chemical reactions between solid and liquid phases have been demonstrated. Many existing biomagnetic applications could be transferred to microscale to take advantage of miniaturization **[12]**. The success of on-chip oligonucleotide annealing, ligation,

and denaturation reactions indicates the feasibility of microfluidics-enabled amplification schemes. However, many challenges, such as the reaction yield, remain to be addressed.

Although radioactive labeling and gel electrophoresis were used as an analytical method to verify our approach, multi-probe hybridization will be the detection method of choice in the final device.

References

1. S. Hossein; T. Tang; D. J. Harrison, "Electroosmotic Pumping of Organic Solvents and Reagents in Microfabricated Reactor Chips", *J. Am. Chem. Soc.*, **1997,** 119, 8716-8717.
2. A. G. Hadd; D. E. Raymond; J. H. Halliwell; S. Jacobson; J. M. Ramsey, "Microchip Devices for Performing Enzyme Assays", *Anal. Chem.*, **1997**, 69, 3407-3412.
3. M. A. Northrup; M. T. Ching; R. M. White; R. T. Watson, "DNA Amplification with a Microfabricated Reaction Chamber", *Transducers' 93*, **1993**, 924-926.
4. J. Cheng; M. A. Shoffner; K. R. Mitchelson; L. J. Kricka, P. Wilding; "Analysis of Ligase Chain Reaction Products Amplified in a Silicon-glass Chip Using Capillary Electrophoresis", *J. Chromatogr. A*, **1996**, 732, 151-158.
5. A. T. Woolley; D. Hadley; P. Landre; A. J. deMello; R. A. Mathies; M. A. Northrup, "Functional Integration of PCR Amplification and Capillary Electrophoresis in a Microfabricated DNA Analysis Device", *Anal. Chem.*, **1996**, 68, 4081-4086.
6. L. C. Waters; S. C. Jacobson; N. Kroutchinina; J. Khandurina; R. S. Foote; J. M. Ramsey, "Microchip Devices for Cell lysis, Multiplex PCR Amplification, and Electrophoretic Sizing", *Anal. Chem.*, **1998**, 70, 158-162.
7. A. Manz; N. Graber; H. M. Widmer, "Miniaturized Total Chemcial Analysis Systems: a Novel Concept for Chemcial Sensing", *Sensors & Actuators*, **1990**, B1, 244-248.
8. Z. H. Fan; D. J. Harrison, "Micromachining of Capillary Electrophoresis Injectors and Separators on Glass Chips and Evaluation of Flow at Capillary Intersections", *Anal. Chem.*, **1994**, 66, 177-184.
9. Z. H. Fan; P. York; S. Cherukuri, "Chip Fabrication for Combinatorial Chemistry", *Microstructures and Microfabricated Systems*, Edited by P. J. Hesketh; G. Barna; H. G. Hughes, The Electrochemical Society, **1997**, pp86-93.
10. Z. H. Fan; R. Kumar; P. Stabile, "On-Chip Cell Capture and Lysis Using Magnetic Particles", *11th Internationational Symposium on High Performance Capillary Electrophoresis*, Orlando, FL, Feb. 1-5, **1998**, pp109.
11. Z. H. Fan; T. Davis, G. Deffley, unpublished result.
12. L. G. Rashkovetsky; Y. V. Lyubarskaya; F. Foret; D. E. Hughes; B. L. Karger, "Automated Microanalysis Using Magnetic Beads with Commercial Capillary Electrophoretic Instrumentation", *J. Chromatogr. A*, **1997**, 781, 197-204.

Acknowledgment

This work is financially supported by the Microflumes program managed by Dr. R. Ritts at the Defense Advanced Research Projects Agency (DARPA) and administered by SPAWAR Systems Center at San Diego, CA. Support from Drs. S. Cherukuri, P. York, and J. Ladd at Sarnoff is greatly appreciated. We acknowledge technical assistance and discussions from S. Perna, D. Ludington, B. Hoghooghi, D. Fishman, T. Davis, B. Lal, D. Lo Iacono, D. Pancholy, S. Lipp, and M. Massaro at Sarnoff. We are grateful for support from Orchid Biocomputer Inc., which is a Sarnoff technical venture responsible for commercializing this technology.

INTEGRATING MICROFLUIDIC SYSTEMS AND NMR SPECTROSCOPY: PRELIMINARY RESULTS

Jonathan D. Trumbull, Ian K. Glasgow, David J. Beebe, and Richard L. Magin
Department of Electrical and Computer Engineering
Beckman Institute for Advanced Science and Technology
University of Illinois at Urbana-Champaign
405 North Mathews Avenue
Urbana, IL 61801

ABSTRACT

The philosophy of miniature total analysis systems (μ-TAS) hinges on the integration of multiple chemical processing steps and the means of analyzing their results on the same miniaturized system. We have investigated coupling chip-based capillary electrophoresis (CE) with nuclear magnetic resonance spectroscopy (NMR) bringing unprecedented structural analysis capability to μ-TAS systems. In this paper, we present our initial experimental results and conclusions which are applicable to a wide range of microfluidic systems. Linewidths of 1.4 Hz have been demonstrated using single turn planar NMR coils integrated with microfluidic channels.

INTRODUCTION

The use of chip-based capillary electrophoresis systems offer substantial advantages over more conventional implementations only if they allow either parallel operations to be performed, provide a needed size advantage, or integrate with subsequent processes. This paper is concerned with the integration of CE chips with NMR and the associated benefits and difficulties. A brief description of pulse NMR [1] will be given followed by details specific to volume limited samples. After this background information, we will describe the fabrication and testing of two fluidic-NMR devices. No description of the electrokinetic effects, electroosmotic flow (EOF) and electrophoresis, encountered in CE systems will be given since excellent references are available for both general information [2, 3] and details specific to on-chip CE [4-6].

BACKGROUND

NMR, although often described classically, is a quantum phenomenon. When a nucleus possessing a magnetic moment is placed in a static magnetic field, it exists in quantized orientations. For the ^{1}H nucleus, the alignment can be parallel or antiparallel to the static field with the antiparallel case having slightly higher energy. Because the energy difference is small compared to the average thermal energy of the system, a Boltzman distribution results with only a slight excess of protons being in the lower energy state (~10^{-5} of the entire sample at typical field strengths). Protons may be excited into the high energy state by the application of a short pulse from a RF coil. As the system decays to its equilibrium state, it produces an exponentially damped signal called the free induction decay (FID). The contribution to the FID from each part of the sample volume has a frequency that is linearly dependent upon the value of the static magnetic field at that location. Because the local field is influenced by the chemical environment the proton is in, the FID will be composed of different frequencies corresponding to the various functional groups on the compound. In 1-D NMR, this information is represented by its frequency spectrum with the contributions of different functional groups showing up as "lines". More sophisticated pulse sequences and analysis (2-D NMR) provide the researcher with the means to determine the structure of the molecule in question.

For NMR to become a useful tool for the analysis of volume limited samples, several obstacles must be overcome. First since the excess population of low energy protons is so small, the signal is very weak. Thus it is necessary to couple the sample strongly to the coil by filling as much of the coil's interrogation volume as possible (fill factor). Significant progress has been made towards understanding the scaling of coupling for microcoils [7, 8] and is summarized by Webb [9].

A conflicting constraint to maximizing the fill factor is the requirement that the coil not affect the homogeneity of the static field since the lines in the NMR spectrum would be broadened and the resolution decreased. To meet this requirement, the coil must be positioned away from the sample (which decreases the sensitivity) or made from a material whose magnetic properties match that of the surroundings. This can be done with relative ease by layering metals to provide a net zero magnetic susceptibility [10, 11]. The more obvious solution, creating an alloy of these materials, cannot be used because of the large decrease in conductivity in otherwise suitable metal combinations [12]. Another approach is to match the surroundings to the coil through a susceptibility matching fluid [7].

NMR has been combined successfully with high performance liquid chromatography (HPLC) [13-16] but faces serious problems as a detector in CE applications because of the lower sample volumes required to prevent Joule heating [2]. One of the first reported discrete CE-NMR systems required injection concentrations approaching 1 M for reasonable online detection times [17]. Given that the detection limits for laser induced fluorescence (LIF) extend to the 10^{-12} M range [18], this is clearly unacceptable. If the role of NMR were changed to solely that of an analyzer of accumulated fractions, much longer acquisition times would be tolerable and lower concentrations therefore permissible. Automated CE fraction collection has been previously accomplished using capillary tubes and external components [19], but a more elegant method is that of a microfabricated collection system [20]. Such a system would allow the separations to be performed using a conventional detection scheme (i.e. UV absorbance or fluorescence) while collecting selected fractions into sample reservoirs with integral NMR receiver coils. After a sufficient amount of the pure substances were obtained, the entire system could be placed into a superconducting magnet and the compound's spectra obtained.

FABRICATION

The first system, "Trident", was designed to be a proof of concept fluidic-NMR device to gauge the effectiveness of integrated, single-turn planar NMR coils. Although less sensitive than solenoidal coils, from a fabrication perspective they are easier to produce than solenoidal or saddle coils.

Referring to Figure 1, the channels consist of polyimide layers between a 50 x 75 mm glass microscope slide and a 45 x 70 mm x no. 1 thickness (0.15 mm) cover glass. The polyimide types used, Pyralin® PD PI-2721 and PI-2723 (Du Pont Electronics, Wilmington, DE), are negative tone photodefineable polyimide precursors. First, 2 mm holes were drilled through the slide, and the channel bottom was formed by spin coating a layer of PI-2723. The roughly 30 μm thick walls of the channels consisted of two

0-9640024-2-6/hh1998/$20©1998TRF
DOI 10.31438/trf.hh1998.23

Solid-State Sensors, Actuators, and Microsystems Workshop
Hilton Head Island, South Carolina, June 8-11, 1998

patterned PI-2721 layers. Next, PI-2723 was spin coated onto the cover glass and soft baked. To solvent bond this "top" layer to the patterned "walls" layer on the slide, a mixture of 4 parts by volume of Pyralin solvent T-9039 to 1 part PI-2723 was spin coated at 7000 rpm for 30 seconds onto the top layer. Immediately, this cover glass was pressed firmly onto the slide so that the solvent layer was now between the top and wall layers. Finally, the polyimide was cured in a tube furnace (Lindberg/Blue M, Asheville, NC).

A lift-off process was used to pattern the coil on the outer surface of the cover glass. The metal was formed from 3 evaporated layers: Cr/Cu/Cr with respective thicknesses of 150, 9700, and 150 Å. The resistance of the coil, pad to pad, was measured to be 5.9 ohms. Acrylic wells were then placed over the drilled holes and bonded with epoxy. The completed system is shown in Figure 2.

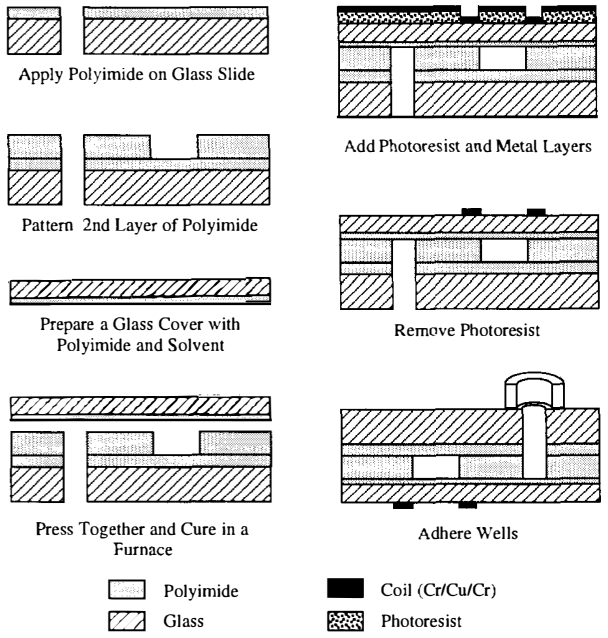

Figure 1: *Fabrication steps used to produce the polyimide device ("Trident").*

The second device type created (Figure 3), "SpinCollector" was made from etched glass capillaries using methods developed from [4, 5]. 1 mm thick, annealed Pyrex glass wafers were etched in HF and HNO_3 to a depth of 20 µm through a Cr/Au mask. Access holes were drilled ultrasonically and the mask was stripped. They were then cleaned in a 1% HF bath for 1 minute with ultrasonic agitation to remove any loose glass particles [21]. After thorough cleaning [5], the wafers were thermally bonded to unprocessed pieces forming closed channels. Initially 150 µm thick Pyrex was used as a cover piece, but repeated bonding problems due to a slight bending of the thin glass forced us to use standard 1 mm pieces. This bonding problem has since been solved by using a sodium silicate low temperature process [22] which pulls the two surfaces together quite nicely.

A coil was then formed through a lift-off process on the undrilled side over the disk-shaped reservoir, and glass wells were attached using epoxy.

Both "Trident" and "SpinCollector" designs were fitted to printed circuit board (PCB) bases containing tuning capacitors. Connections between the PCB and the coil were made with 24 AWG magnet wire and conductive epoxy (Epo-tek H20E, Billerica, MA).

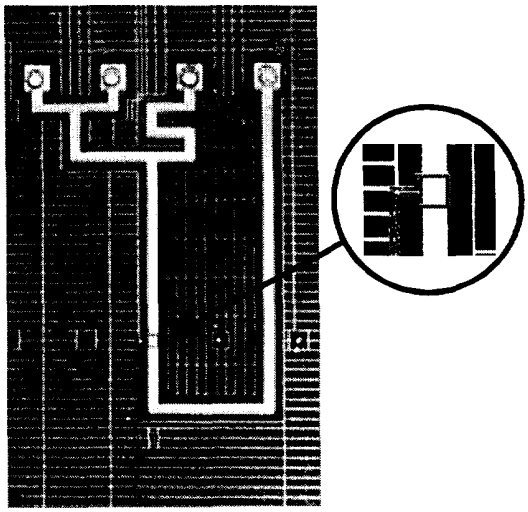

Figure 2: *Completed "Trident" polyimide structure with blowup of the NMR receiver coil which is 1mm on a side (inner) with a trace width of 200 µm. Assuming a channel depth of 30 µm, the coil encloses a sample volume of 30 nL. Note that the fluidic channels are the thicker lines connected to the access holes on the top. The other lines are for solvent venting during curing.*

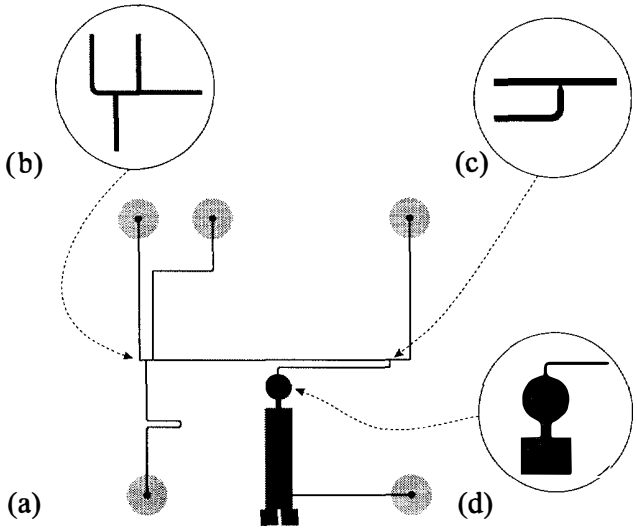

Figure 3: *Mask layout for "SpinCollector". (a) The complete device. The 5 wells are located on the periphery interconnected by the 200 µm wide, 20 µm deep channels in glass. Close up views of: (b) the "double-T" injector, (c) collection junction, and (d) the collection reservoir with integrated NMR coil.*

METHODS

To quantify the SNR and linewidth of both the "Trident" and "SpinCollector" designs, each was loaded with deionized water, matched to 50 Ω using a network analyzer, and inserted into the bore of a 5.9 Tesla (250 MHz) Oxford/89-mm superconducting magnet (Oxford Instruments, UK). The integrated planar coil was used for both the 90° transmit pulse and the received FID (bandlimited to 1000 Hz). 4096 time points were sampled and Fourier transformed. Signal to noise was determined by measuring the peak height and comparing it to the RMS noise. Linewidth was found by fitting the peak to a Lorentzian curve and finding the width at half height.

Fraction collection in the "SpinCollector" device was tested using two amino acids, arginine and alanine, at a pH of 9.0 where the difference in charge facilitates the separation. Tagging was accomplished using a standard fluorescein isothiocyanate (FITC; Molecular Probes, Eugene, OR) protocol [18]. 3.0 mM concentrations of the amino acids in 50 mM borate buffer were added to an equal amount of 3 mM FITC dissolved in acetone (0.1% pyridine). After reacting overnight in a light-tight box, the acetone was pulled off under vacuum and the borate run buffer was degassed using an ultrasonic bath. Both the run buffer and the sample were filtered to 0.2 μm (Millipore, Bedford, MA) and introduced to the wells.

The experimental setup used is depicted in Figure 4. High voltage power supplies (MJ15N100; Glassman, Whitehouse Station, NJ) switched by Kilovac (Santa Barbara, CA) K43C234 10 kV relays provided the potential needed to drive the injection, separation, and fraction collection. The control software was written in Visual Basic 5.0 (Microsoft, Redmond, WA) using ComponentWorks 1.1 and an AT-AO-6 control board both from National Instruments (Austin, TX). Visualization was provided by an Olympus BX60 epi-fluorescent microscope and a PentaMAX intensified CCD camera (Princeton Instruments, Trenton, NJ). Selected pictures taken with the camera are presented in Figure 6. No NMR spectra were taken of collected samples due to the low concentrations necessary for tagging (FITC precipitates in aqueous solutions at required concentrations).

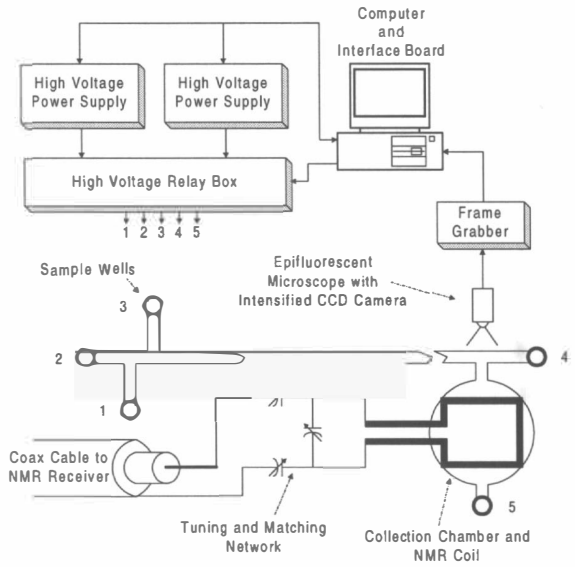

Figure 4: Setup for separation and fraction collection.

The conceptual sequence of events needed to collect one fraction is detailed in Figure 5 and is similar to that used in [20]. A 1 mm long (~2 nL) plug is defined in (a) by applying a voltage across the top and bottom left wells causing a net motion upward. By switching the voltage, the individual components move to the right (shown in (b)) at a velocity characteristic of their charge/mass ratios. After becoming distinguishable bands in (c), the front analyte is detoured to the reservoir in (d). The separation column is cleared in (e) to make way for the next run. A slight efflux is maintained while the second band passes by to prevent contamination of the collected sample. By running many such cycles, enough of the "unknown" could be accumulated for NMR analysis.

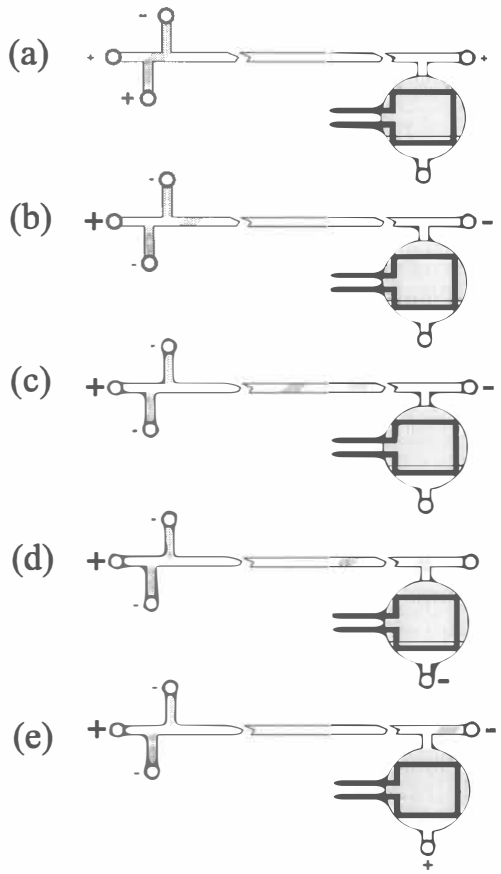

Figure 5: Schematic representation of (a) plug injection, (b) initial separation, (c) further separation, (d) collection of desired analyte, (e) clearing column. Note that the relative size of the "+" and "-" characters indicates the magnitude of the potential.

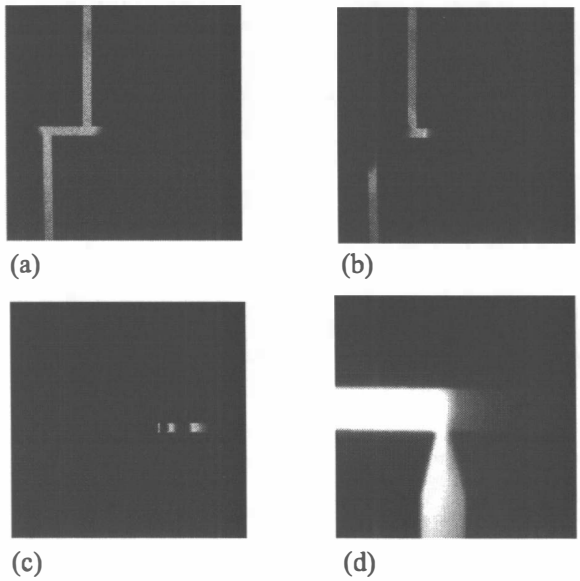

Figure 6: A selected iteration of the separation and collection sequence imaged with an intensified CCD and epi-fluorescent microscope: (a) plug is defined, (b) separation starts, (c) distinct bands formed (ARG, ALA, and unbound FITC), (d) selected plug is collected. This is repeated until substantial sample accumulates in the reservoir.

RESULTS

The SNR for the "Trident" polyimide system, shown in Figure 7(a), was 23.5/scan with a linewidth of 1.4 Hz that is the narrowest for any microfabricated planar coil to date including those using a susceptibility matching fluid [23]. It was apparent, however, that the SNR was significantly lower than required for the system to be used as an online detector of reasonable concentrations (water is 55 M).

Although the "SpinCollector" design held 393 nL of sample, the coil was significantly farther away (1 mm versus 150 μm) which resulted in only a slight increase in SNR to 41/scan with a linewidth of 3.1 Hz.

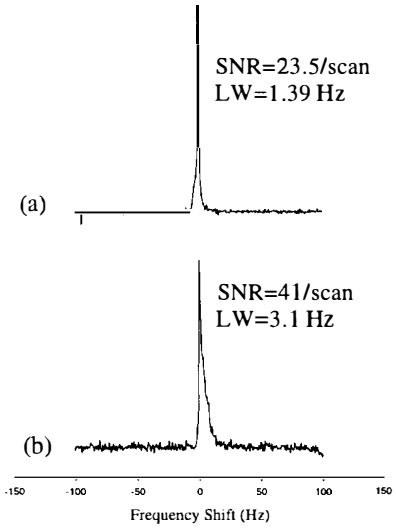

***Figure** 7: NMR spectra of H_2O for (a) "Trident" with 16 scans signal averaged giving a 23.5 SNR per scan and a linewidth of 1.39 Hz, (b) "SpinCollector" with a linewidth of 3.1 Hz and SNR of 41 for a single scan*

DISCUSSION

Trying to detect analytes would still prove difficult at these SNR. For example, identifying 100 mM arginine using "SpinCollector" would take approximately 6 hours. Note that the acquisition time increases as the square of the concentration decreases so the time required for the same volume of 100 μM amino acid would take almost 700 years (we will post the exact results at Hilton Head 2682 barring unforeseen circumstances)! Also, keep in mind that this does compare favorably with conventional 5 and 10 mm NMR saddle coils in terms of mass sensitivity [7].

The low SNR of the two tested devices is a direct result of their geometry. A square planar coil has a sensitive region that extends out over half its effective radius. While allowing a larger volume to be interrogated, it also means that our choice of a thin channel above the coil amounts to a sub-optimal filling factor. There are two possible solutions. First, change the sample volume from a slice to a dome shaped region fully contained within the "sweet-spot" of the coil. This would increase the total signal but with the added expense of needing additional sample. A more sophisticated method involves "pulling" the sensitive region in closer to the coil so that the SNR for a given unit volume increases. The simplest way of shaping the field with a rectangular geometry is to reduce the smallest dimension as shown in Figure 8.

For a thin sample directly above a 5 mm coil, the sensitivity per unit volume increases by a factor of 65 as the coil shrinks to 100 μm. What is needed is a surface coil configuration that approximates the field pattern of an array of these smaller coils without dramatically increasing the resistance. Given this 65 fold increase in sensitivity, the acquisition time would drop 65^2=4225 times!

Even having this hypothetical performance increase, the planar element cannot be compared to solenoidal coils in the same sample size regime [7, 9] whose limits of detection stretch to the low picomole arena given mere minutes of acquisition time. Planar coils do, however, provide a significant improvement over standard NMR mass detection limits for small volumes and are easily integrated into batch fabricated analytical devices. Discrete wound solenoids provide a drastic improvement in sensitivity, but are difficult to integrate with planar processes.

Regardless of the choice of planar versus solenoid, the ability to perform additional steps or mechanics are important for some applications.. For example, combinatorial chemistry is typically accomplished on small resin beads that serve as the solid support for tethered compounds present in quantities of 100's of picomoles. For a high resolution spectra to be obtained, the compounds must be cleaved from the beads, or the sample must be spun in the coil [24]. Cleaving is a "destructive" process and spinning at kHz range frequencies on a chip would prove challenging at best. If high concentrations of liquid phase analytes can be used (or if enrichment can be performed on chip [25]), planar NMR coils offer more than just easy integration with other processes. By shrinking the sample to the nanoliter range, the volume over which the magnetic field must be uniform decreases appropriately allowing either a smaller (much less expensive) magnet to be used, or multiple spectrums to be taken in parallel in a conventional magnet (multiplying throughput). With the large initial expenditure for a high-field superconducting magnet and the associated cost of ownership, these benefits are significant with volume limited samples.

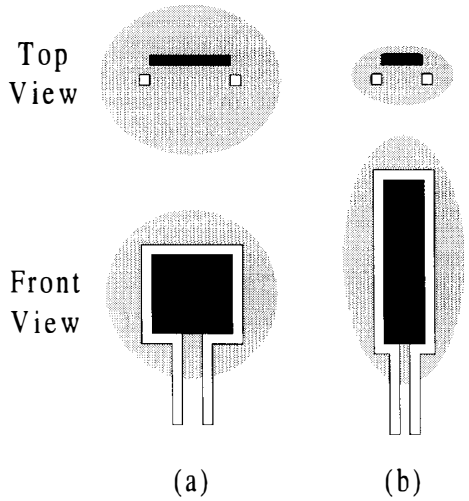

***Figure 8:** Increasing the sensitivity by altering the geometry of sample (black) and coil (white) to shrink the interrogation region (gray): (a) square planar coil, (b) rectangular planar coil with equivalent sample volume.*

CONCLUSIONS

It has been shown that the integration of NMR into μ-TAS is feasible from a fabrication standpoint. By extrapolating the current experimental results through simulation, improvements are planned that may allow small volumes (~100 nL) of high (~10 mM) concentration solutions to be analyzed in reasonable amounts of time (~hours). If the fabrication process can tolerate "pick and place" assembly, lower concentration spectra can be obtained using

hand wound or nontraditional solenoids [26-28].

ACKNOWLEDGEMENTS

We would like to thank Timothy L. Peck of the Magnetic Resonance Microsensors company for his valuable help with simulations, Andrew G. Webb, Jeffery E. Stocker, and Juan G. Santiago for their insightful suggestions, and Bruce Flachsbart for the use of "his" fabrication facilities.

REFERENCES

[1] A. E. Derome, *Modern NMR Techniques for Chemistry Research*, vol. 6. Oxford: Pergamon Press, (1987), pp. 1-96.

[2] J. Jorgenson and K. D. Lukacs, "Zone Electrophoresis in Open-Tubular Glass Capillaries", *Analytical Chemistry*, 53, 1298-1302, (1981).

[3] G. M. Janini, and Haleem J. Issaq, "The Buffer in Capillary Zone Electrophoresis," in *Capillary Electrophoresis*, N. A. Guzman, New York: Marcel Dekker, Inc., 1993, pp. 119-160.

[4] D. J. Harrison, A. Manz, Z. Fan, H. Ludi, and H. M. Widmer, "Capillary Electrophoresis and Sample Injection Systems Integrated on a Planar Glass Chip", *Analytical Chemistry*, 64, 1926-1932, (1992).

[5] N. Chiem and D. J. Harrison, "Microchip-Based Capillary Electrophoresis for Immunoassays: Analysis of Monoclonal Antibodies and Theophylline", *Analytical Chemistry*, 69, 373-378, (1997).

[6] S. C. Jacobson, R. Hergenröder, L. B. Koutny, R. J. Warmack, and M. J. Ramsey, "Effect of Injection Schemes and Column Geometry on the Performance of Microchip Electrophoresis Devices", *Analytical Chemistry*, 66, 1107-113, (1994).

[7] D. L. Olson, T. L. Peck, A. G. Webb, R. L. Magin, and J. V. Sweedler, "High-Resolution Microcoil ^{1}H-NMR for Mass-Limited, Nanoliter-Volume Samples", *Science*, 270, 1967-1970, (1995).

[8] T. L. Peck, R. L. Magin, and P. C. Lauterbur, "Design and Analysis of Microcoils for NMR Microscopy", *Journal of Magnetic Resonance*, 108, 114-124, (1995).

[9] A. G. Webb, "Radiofrequency Microcoils in Magnetic Resonance", *Progress in Nuclear Magnetic Resonance Spectroscopy*, 31, 1-42, (1997).

[10] F. O. Zelaya, S. Crozier, S. Dodd, R. McKenna, and D. M. Doddrell, "Measurement and Compensation of Field Inhomogeneities Caused by Differences in Magnetic Susceptibility", *Journal of Magnetic Resonance*, 115, 131-136, (1995).

[11] J. F. Schenck, "The Role of Magnetic Susceptibility in Magnetic Resonance Imaging: MRI Magnetic Compatibility of the First and Second Kinds", *Medical Physics*, 23, 815-850, (1996).

[12] M. B. Bever, "Encyclopedia of Material Science and Engineering", Cambridge: The MIT Press, (1986), pp. 848-850.

[13] G. Schlotterbeck, L. H. Tseng, H. Händel, U. Braumann, and K. Albert, "Direct On-Line Coupling of Capillary HPLC with ^{1}H NMR Spectroscopy in the Nanoliter Scale", *Analytical Chemistry*, 69, 1421-1425, (1997).

[14] S. A. Korhammer and A. Bernreuther, "Hyphenation of High-Performance Liquid Chromatography (HPLC) and other Chromatographic Techniques (SFC, GPC, GC, CE) with Nuclear Magnetic Resonance: A Review", *Fresenius' Journal of Analytical Chemistry*, 354, 131-135, (1996).

[15] B. Behnke, G. Schlotterbeck, U. Tallarek, S. Strohschein, L. H. Tseng, T. Keller, K. Albert, and E. Bayer, "Capillary HPLC-NMR Coupling: High-Resolution ^{1}H NMR Spectroscopy in the Nanoliter Scale", *Analytical Chemistry*, 68, 1110-1115, (1996).

[16] N. Wu, A. Webb, T. Peck, and J. Sweedler, "On-Line NMR Detection of Amino Acids and Peptides in Microbore LC", *Analytical Chemistry*, 67, 3101-3107, (1995).

[17] N. Wu, T. L. Peck, A. G. Webb, R. L. Magin, and J. V. Sweedler, "Nanoliter Volume Sample Cells for ^{1}H NMR: Application to On-Line Detection in Capillary Electrophoresis", *Journal of American Chemical Society*, 116, 7929-7930, (1994).

[18] J. V. Sweedler, J. B.7 Shear, H. A. Fishman, and R. N. Zare, "Fluorescence Detection in Capillary Zone Electrophoresis Using a Charge-Coupled Device with Time-Delayed Integration", *Analytical Chemistry*, 63, 496-502, (1991).

[19] D. J. Rose and J. Jorgenson, "Fraction Collector for Capillary Zone Electrophoresis", *Journal of Chromatography*, 438, 23-34, (1988).

[20] C. S. Effenhauser, A. Manz, and H. M. Widmer, "Manipulation of Sample Fractions on a Capillary Electrophoresis Chip", *Analytical Chemistry*, 67, 2284-2287, (1995).

[21] O. Diepold, "Smoothing of Ultrasonically Drilled Holes in Borosilicate Glass by Wet Chemical Etching", *Journal of Micromechanics and Microengineering : Structures, Devices, and Systems*, 6, 29-32, (1996).

[22] B. Quenzer, "Low-Temperature Silicon Wafer Bonding", *Sensors and Actuators A*, 32, 340-344, (1992).

[23] J. E. Stocker, T. L. Peck, A. G. Webb, M. Feng, and R. L. Magin, "Nanoliter Volume, High-Resolution NMR Microspectroscopy Using a 60-μm Planar Microcoil", *IEEE Transactions on Biomedical Engineering*, 44, 1122-1127, (1997).

[24] P. A. Keifer, L. Baltusis, D. M. Rice, A. A. Tymiak, and J. N. Shoolery, "A Comparison of NMR Spectra Obtained for Solid-Phase-Synthesis Resins Using Conventional High-Resolution, Magic-Angle-Spinning, and High-Resolution Magic-Angle-Spinning Probes", *Journal of Magnetic Resonance, Series A*, 119, 65-75, (1996).

[25] R. Zhang and S. Hjertén, "A Micromethod for Concentration and Desalting Utilizing a Hollow Fiber, with Special Reference to Capillary Electrophoresis", *Analytical Chemistry*, 69, 1585-1592, (1997).

[26] J. A. Rogers, R. J. Jackman, and G. M. Whitesides, "Constructing Single- and Multiple-Helical Microcoils and Characterizing Their Performance as Components of Microinductors and Microelectromagnets", *IEEE Journal of Microelectromechanical Systems*, 6, 184-191, (1997).

[27] J. A. Rogers, R. J. Jackman, G. M. Whitesides, D. L. Olson, and J. V. Sweedler, "Using Microcontact Printing to Fabricate Microcoils on Capillaries for High Resolution Proton Nuclear Magnetic Resonance on Nanoliter Volumes", *Applied Physics Letters*, 70, 2464-2466, (1997).

[28] A. D. Feinerman, R. E. Lajos, V. White, and D. D. Denton, "X-Ray Lathe: An X-Ray Lithographic Exposure Tool for Nonplanar Objects", *Journal of Microelectromechanical Systems*, 5, 250-255, (1996).

METROLOGY AND SIMULATION OF CHEMICAL TRANSPORT IN MICROCHANNELS

P. M. St. John*, T. Woudenberg, and C. Connell
PE Applied Biosystems
850 Lincoln Centre Drive
Foster City, CA 94404

M. Deshpande and J. R. Gilbert
Microcosm Technologies, Inc.
215 1st St
Cambridge, MA 02142

J. Molho, A. E. Herr, T. W. Kenny, M. G. Mungal
551 Terman
Stanford University
Stanford, CA 94305

M. Garguilo and P. Paul
Sandia National Laboratory
Livermore, CA

ABSTRACT

We are working towards building a CAD tool (NetFlow) for microfluidic systems. To support the development of this tool, diffusion and flow experiments are being performed in microchannels. In this paper, we describe the novel flow visualization approach developed for these experiments and report experimental results and corresponding simulations for fluid transport in microchannels. The experimental approach relies on the use of a caged, charged fluorescent dye which can be activated (uncaged) by a UV laser beam and tracked by fluorescence imaging [1]. In contrast to standard methods for inserting a dye plug in a microchannel, this is the only technique which allows definition of very precise regions at any place along the channel. Specifically, this allows a narrow definition of starting plugs and therefore an improved determination of the flow profile. We have used this technique to study diffusion, pressure-driven flow, and electrokinetic flow in various microchannel geometries.

INTRODUCTION

There is a wide interest in micron-scale integrated chemical/biochemical analysis or synthesis systems, also referred to as lab-on-a-chip. The microfluidic systems being explored today rely on both pressure [2] and electrokinetic effects [3,4] for controlling fluid transport. Complicated relationships between the shape and size of the microchannels and the behavior of multi-component fluids are not completely understood. Researchers are forced to use costly trial and error methods in the design of microfluidic systems.

Discrepancies between experimental measurements and simulations exist because the modeling equations may not fully capture the essential physics and because the experimental parameters used in the simulations are often approximate (e.g. calculation of diffusion constant and mobility in a microchannel). We are attempting to simulate simple flow in specific microchannel geometries and extract parameters which will enable us to predict flow in more complex structures and ultimately allow us to take an active role in the design of microfluidic structures. Flow predictions have direct applications in microcapillary electrophoresis systems where long channels are advantageous for resolved separation of DNA fragments out to several kilobases but device area must be minimized. Flow predictions are also useful for determining the geometries needed for chemical reactions in microchannels.

EXPERIMENTAL

Silicon microchannel structures were fabricated as "negative" masters using standard photolithography and an STS deep reactive ion etch (DRIE) was used to create raised rectangular structures with dimensions of 50 μm in width, 5 cm in length and 40 – 80 μm in height. An RTV silicone elastomer (Dow Corning) was used to form positive replicas of the silicon structures (Fig. 1) [5]. Scanning electron micrographs (SEMs) show the etched silicon sidewalls and the corresponding elastomer replica (Au sputtered) (Fig. 2). The striae located near the top of the silicon structure was a result of over-etching. The etched silicon region was smooth to an RMS roughness of ~ 7.26 nm, determined by atomic force microscopy. The elastomer SEM shows the reproduction of the features present in

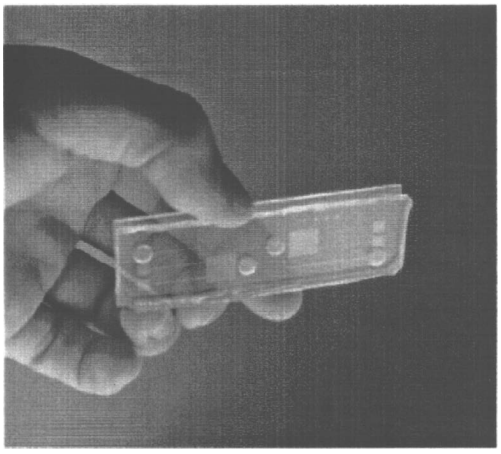

Figure 1. Photograph of the elastomer device with three test microchannels. The circles are the injection wells and the squares are used to study pressure driven flow in a sudden expansion.

0-9640024-2-6/hh1998/$20©1998TRF
DOI 10.31438/trf.hh1998.24

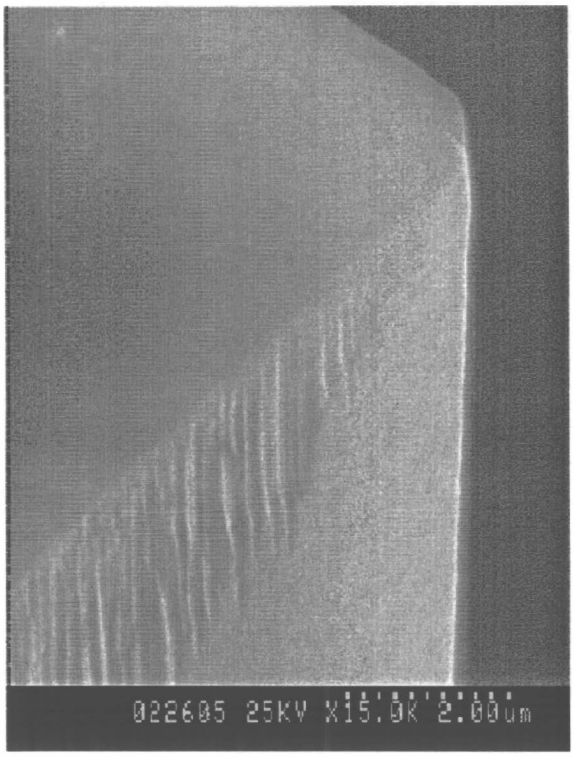

Figure 2a. SEM of the silicon mold

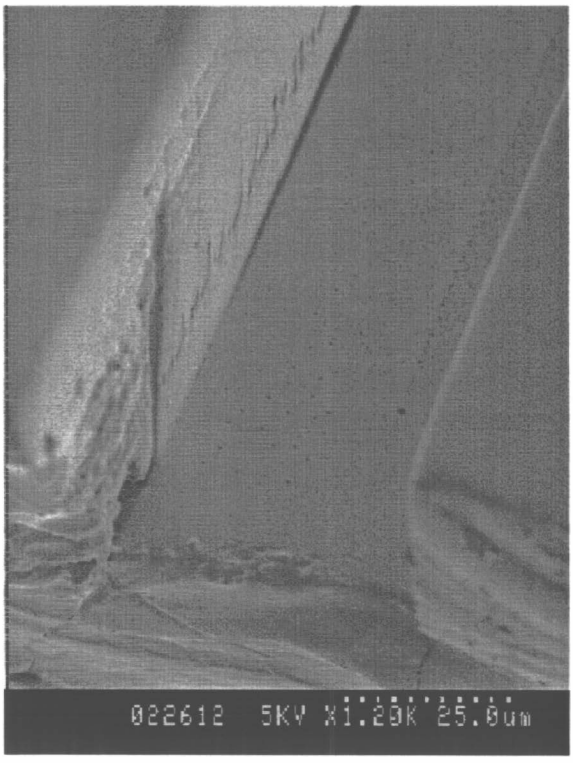

Figure 2b: SEM of the elastomer channel

the silicon. Note the striations which run the length of the channel on the lower portion of the channel wall. This corresponds to the rough overetched region of the silicon mold. The region of the elastomer which replicated the etched silicon surface had an RMS roughness of ~ 7 nm. The rough edge at the opening of the elastomer channel came from slicing the elastomer structure with a razor blade. The channel was not cleaned prior to metal sputtering and particulates can be seen on the channel floor. The elastomer channels were sealed with either glass microscope slides or elastomer coated glass microscope slides and wells were created in the elastomer using a mechanical hole punch (Figure 1).

Serpentine microchannels in borofloat glass (not shown) were fabricated by Alberta Microelectronics Centre (Alberta, Canada) using standard photolithography and an isotropic wet etch to yield a smooth hemispherical cross-section. A commercially available additive made from a polyacrylamide short chain polymer (ABI DNA Fragment Analysis Reagent 7% w/w) was used (0.1% v/v aqueous) to suppress electroosmotic flow (EOF) **[6]** in both glass and elastomer structures. Although EOF suppression was verified by observing ion travel under an applied field, the extent of suppression was not quantitated. In this paper, electrophoretic flow refers to negatively charged dye migration towards the positive electrode and electroosmotic flow refers to dye carried toward the negative electrode, despite charge.

The caged fluorophore (fluorescein) was purchased from Molecular Probes and used in micromolar quantities dissolved in either distilled water or Tris-EDTA buffer, pH = 7.4. The dye is negatively charged, both caged and uncaged (fluorescein, -2). When caged, the dye solution is non-fluorescent. Upon photo-activation of a UV light illuminated volume, the protecting group is cleaved and the dye fluoresces. Approximately 0.3 mW average power of 355 nm light from a pulsed Nd:YAG laser (Uniphase) was used for ~ 0.1 s to uncage the fluorophore in a 20 μm spot. In the electrokinetic experiments, the laser beam was focused using a UV microscope objective which defined a sharp start zone. A continuous wave Microblue diode pumped laser at 473 nm (Uniphase) was used for fluorescence excitation (Figure 3). The Microblue was positioned close to Brewster's angle for glass to minimize laser scatter into the microscope. Pressure driven flow was imaged at Sandia National Laboratories where the experimental setup is similar to that described above with the exceptions that the uncaged region is rectangular in shape and that the uncaging time is much less than one millisecond. Fluorescence images of the molecules diffusing and moving in the local flow were collected using a microscope objective (total magnification = 100 X) and a video rate, interlaced camera. Images were analyzed and flow parameters were extracted for simulations. The evolution of the fluorescent profiles under electrokinetic and pressure-driven flow are shown here by comparing a sequence of timed images to corresponding times from the simulations.

The numerical simulations were performed using the NetFlow module in Memcad **[7]**. It employs a three-dimensional finite element based tool to solve the Navier-Stokes equations. The electrokinetic effects can be broadly divided into two categories: electrophoresis, involving the transport of a charged species through a carrier due to a differential in the mobility, and electroosmosis, involving the pumping of the carrier fluid due to wall based effects. Electrokinetic effects were incorporated by coupling the Navier-Stokes equations with the Poisson equation for the electric field and with the Poisson-Boltzmann equation for the zeta potential in the electroosmotic cases **[8]**.

The equations are solved here under the assumption of a dilute solution i.e. the carried species does not affect the material properties of the carrier. This allows the equations to be solved in their incompressible form. The finite element meshes were chosen generally to allow for adequate resolution of the

boundary layer and accurate representation of all the experimentally observed fluid physics.

In the design of practical micro-devices, however, accurate coupling of the electrokinetic effects requires the knowledge of several material and physical parameters, such as the diffusivity and the mobility of the solute in the solvent and extent of surface charge on the inner walls of the microchannels. Additionally wall-based effects such as chemical binding sites might exist that affect the flow patterns. Our approach is to extract the required material parameters through quantitative comparison with experimental measurements in simple geometries and use the extracted parameters for simulations and comparisons in more complex geometries.

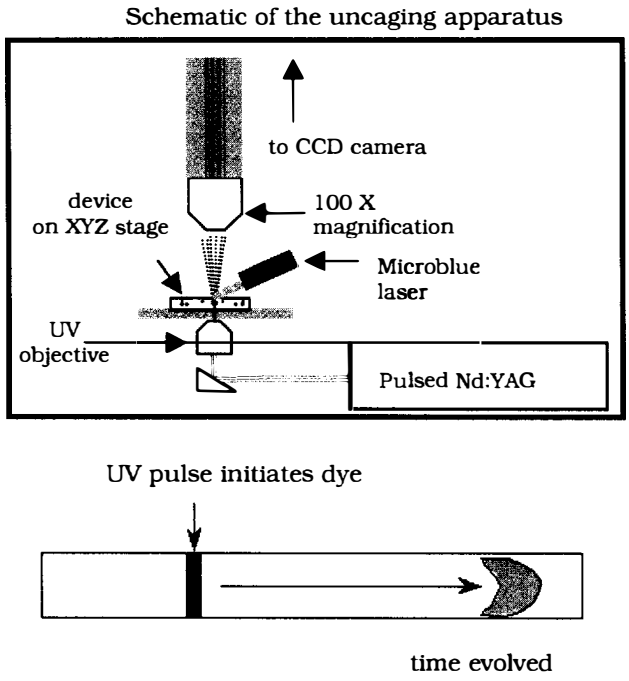

Figure 3. *Top: Schematic of the experiment. The Nd:YAG laser is used to uncage the dye and a Microblue 473 nm laser is used to excite the fluorescence. Bottom: Illustration of the uncaging process. The starting fluorescent fluid volume is defined by the uncaging laser (either as a spot or as a ribbon).*

RESULTS AND DISCUSSION

Figure 4 shows a timed series of pressure-driven flow in microchannels which expand into a large planar reservoir. This figure demonstrates that the simulation qualitatively reproduces the dye dispersion from laminar flow seen during the experiment. The channel width was 100 μm by 40 μm deep. The flow rate was approximately 15 μL/hr.

The Reynolds number, Re, in this experiment is typical for bioanalytical systems (Re = 0.05) although, it appears low when compared to typical numbers in micropumps (Re ~ 100). The images therefore differ from what on might expect to see at higher Reynolds number. The governing equations become linear and harmonic which results in the flow pattern appearing as if it evolved from a point source in Fig. 4. The experiments and simulations in the figure show good agreement which is to be expected for low Reynolds number flows. Similar experiments and stimulations were conducted on various other geometrical microchannel shapes and serve to verify the capabilities of our module in the simulation of pressure-driven flows.

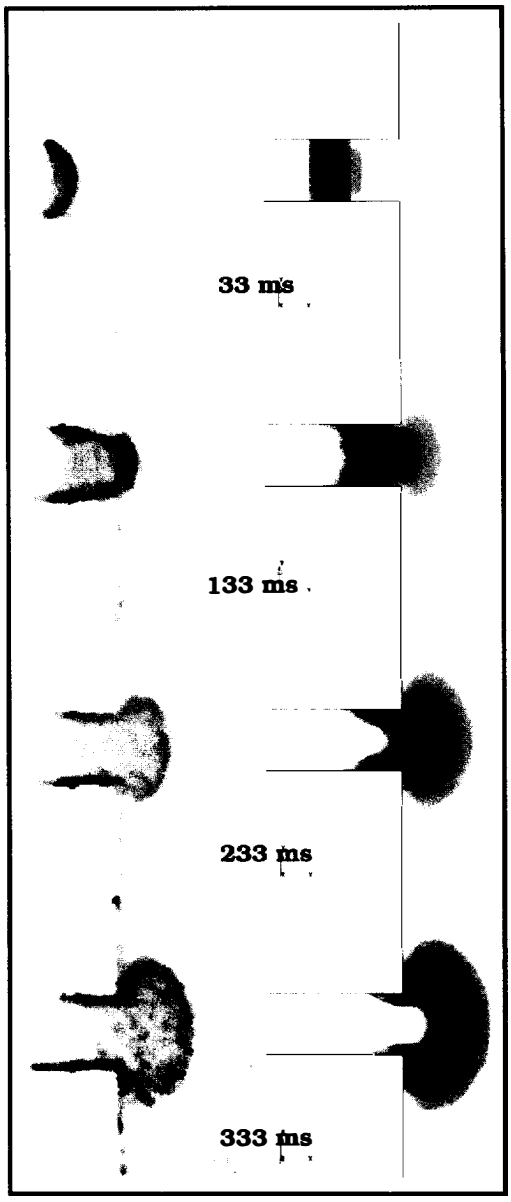

Figure 4. *Experimental and simulated pressure-driven flow entering a sudden expansion in an elastomer structure.*

Electrokinetic measurements using a range of applied fields and in a number of geometries were compared to simulations of electroosmotic and electrophoretic flow in both elastomer and glass microchannels. Figure 5 shows the simple case of a time-lapse experimental electrophoretic flow at a field strength (E) = 85.8 V/cm in a 50 μm straight elastomer channel with a 0.1% flowable and water soluble polymer added to the dye solution to suppress EOF **[6]**. For the case of electrophoretic flow where EOF is assumed negligible, the simulated and experimental band shape are similar. The simulated image (right) shows some of the features of the NetFlow software. This image is a 2-D histogram of the integrated experimental fluorescent profile for t = 0.99 s. The 2-D histograms provide crucial information regarding the surface forces acting on the flow. The simulation shows an intense

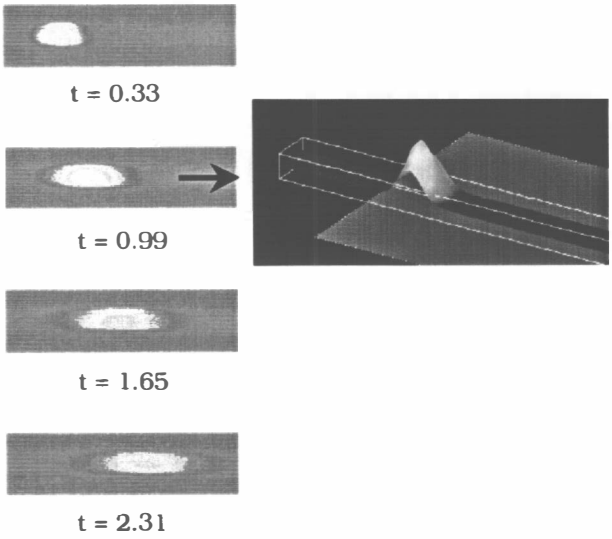

Figure 5. Left: Experimental electrophoretic flow in an elastomer channel, E = 85.8 V/cm. Right: Column integration tool from NetFlow used to form 2-D image/histogram corresponding to the fluorescence.

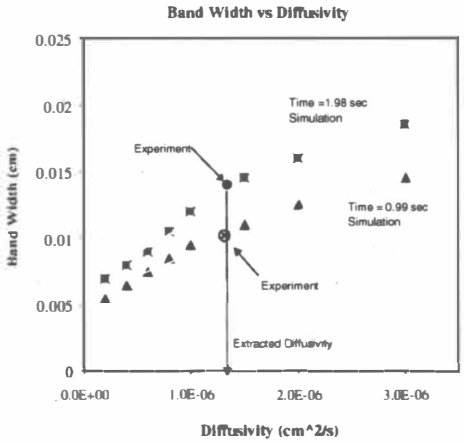

Figure 6. Graph of the simulated band width at two distinct times (squares and triangles) vs. a range of diffusivities. Experimental data (circles) were added to the plot to extract the diffusivity

center region (high mass fraction) and regions of very low intensity along the channel walls, implying that the fluorescent plug may be repelled in this region. The band broadening occurs rapidly because the low mass dye has a high diffusion constant, ~ 1.3 x 10^{-6} cm^2/s. The migration of the band is towards the positive electrode which is expected for electrophoretic flow of a negatively charged species with suppressed EOF.

The simulations can also be used to extract parameters from the experimental data. Figure 6 shows a graph of the simulated band width at two distinct times (t = 0.99 s, triangles, and t = 1.98 s, squares) as a function of predicted diffusivities. We were able to extract a diffusivity of the uncaged fluorophore in the microchannel, D = 1.3 x 10^{-6} cm^2/s, by comparing the experimental bandwidths (circles) at t = 1.98 s and t = 0.99 s with the calculated curves. This number seems reasonable considering other reported numbers for diffusivity, $D_{sucrose}$ = 5.21 x 10^{-5} cm^2/s (at 298 K) [9] (sucrose has 60% the mass of fluorescein) and $D_{fluorescein}$ was reported to be 3.3 x 10^{-6} cm^2/s by polarography (experimental conditions unknown) [4]. The velocity of the uncaged dye was extracted from the experimental data by plotting the distance versus time for a fluorescent plug moving in an applied field (extracted from experimental images like those shown in Fig. 5). A linear regression was used to obtain the slope or velocity of the line. Velocities at several voltages were obtained in this way and plotted versus the field strength. In the absence of electroosmotic flow, the slope of the line is equal to the electrophoretic mobility (μ). The mobility was estimated to be 2.3 x 10^{-4} cm^2/Vs, using the linear region of the graph (E > 60 V/cm). The plot shows a non-linear behavior between velocity and field strength for E < 60 V/cm. We suspect this is not an interaction between the dye molecules and the solvent because the dye is in such low concentration compared to the solvent. A more likely explanation might be the error associated with obtaining measurements at low field strengths when the diffusion velocity is approximately the same order of magnitude as the convective velocity. The extracted diffusivity and mobility from the elastomer straight channels was used successfully in modeling the plug profile in the glass u-shaped channels implying that these parameters can be used to predict flow in a variety of structures.

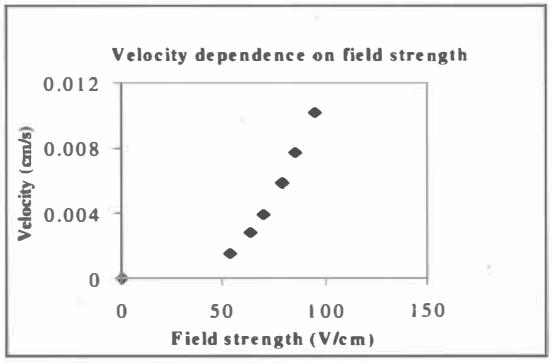

Figure 7. A plot of the velocity vs. field strength used to obtain the mobility of uncaged fluorescein.

Although the field strengths used here are typical for DNA electrophoresis (~100 V/cm), the diffusivity of the caged fluorophore in aqueous solution is much higher than that of DNA because of its lower molecular weight ($m.w._{caged\ fluorescein}$ = 827 d, $m.w._{DNA}$ ~ several hundred kd). Therefore, the band profile is dominated by diffusion at these field strengths. In order to predict the loss of resolution from diffusion in DNA separation, a lower diffusivity must be used. We have also examined the flow profile in more complex geometries. Figure 8 compares the experimental to simulated fluorescence profile under electrophoresis in a u-shaped glass microchannel at four different time steps. The images corresponds to E = 69.5 V/cm. The inset shows the current density in the same section of the microchannel. As the figure shows, the higher current density on the inner wall of the bend causes the inner region of the band to move faster than the outer region, resulting in an asymmetric profile and eventual band broadening. The greater distance traveled by the species along the outer wall further adds broadening and asymmetry to the band. As it travels past the u-shaped bend the band takes the shape of a parallelogram. In principle, this shape can be corrected by allowing the band to negotiate an equal and opposite turn downstream of this bend.

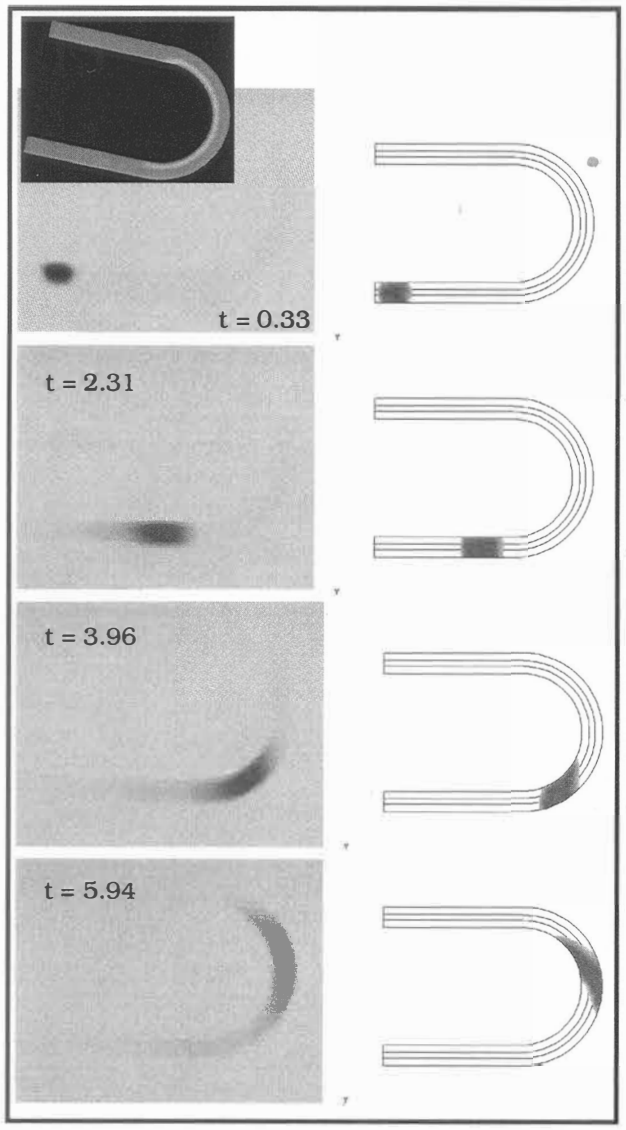

Figure 8. *Experimental (left) and simulated (right) electrophoretic flow in a 50 μm diameter glass microchannel (radius of curvature = 0.25 mm), E = 69.5 V/cm (inset: current density in channel, the lightest region corresponds to the highest current density).*

However, the broadening effects of the bend and the diffusion cannot be corrected.

The simulation at E = 69.5 V/cm in Fig. 8 closely matched the experiment. As the field strength was increased further the band was observed to take on a parabolic shape that grew increasingly well-defined with increasing field strength. This behavior is contrary to expectations and is not represented in the numerical models. Consequently, the agreement between experiment and simulations falls off at high voltages. Figure 9 shows the experimental band profile at 0.66 s after uncaging the fluorophore at a range of field strengths, E = 108 – 125 V/cm. As the field strength increases above E ~ 100 V/cm, the parabolic profile becomes more pronounced. The increasing parabolic profile with increasing field strength has also been observed in straight microchannels (data not shown) and straight capillaries **[10]** and is therefore not due to the asymmetry in the field. The simulations in this field range did not match the experimental data. There are several possible reasons for the observed parabolic shape at high voltages. One possibility is the variation in properties (diffusivity, viscosity, and mobility) across the channel due to joule heating which would cause a temperature gradient in the channel, that becomes more significant at higher voltages. Temperature gradients and their effects on the electrokinetic flow behavior in microchannels have been observed by other researchers **[11]**. A $1 - 2^0$ C rise in temperature in the channel can cause the mobility (and viscosity

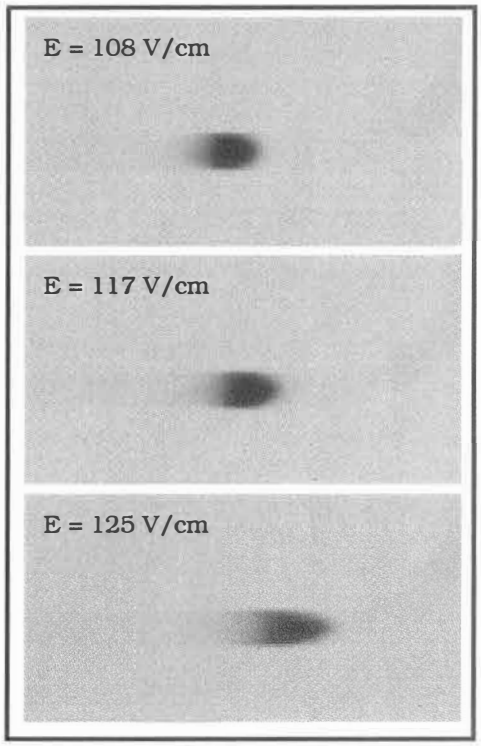

Figure 9. *A series of profiles at t = 0.66 s after the dye was uncaged at varying field strengths.*

of the carrier) to change by 2 – 3%. At higher voltages, where the temperature rise is significant, the change in these material properties may affect the overall flow pattern. A temperature rise may also effect the polymer additive **[6]**, resulting in an incomplete EOF suppression. If EOF is present, then non-uniformities in the zeta potential could induce a pressure gradient and a corresponding parabolic component of the flow. Finally, the parabolic shape may be present at all field strengths but masked by the more rapid decrease in fluorescence at lower field strengths due to diffusion. We are currently exploring these mechanisms to explain the observed deviations from plug-like flow, using both experimental and numerical techniques. An appropriate physical model can then be developed and incorporated into the electrokinetic terms to represent this behavior.

CONCLUSION

We have used a caged fluorophore to image electrokinetic and pressure-driven flow profiles in both glass and elastomer microchannels with varying geometries. Parameters such as diffusivity and mobility were extracted from the experimental data and used in the simulations. This imaging technique has already revealed some interesting and unexpected behavior in these relatively simple fluidic systems. We are looking forward

to using this method to study these behaviors and extract theoretical models or behavioral models suitable for insertion in modeling tools such as NetFlow.

ACKNOWLEDGEMENTS

This work was funded, in part, by DARPA (Grant no. F30602-96-2-0306). We would like to acknowledge EG&G IC Sensors for some of the silicon fabrication, Charles Evans & Associates for AFM data and the use of the Stanford Nanofabrication Facility.

REFERENCES

1. P. Paul, D. Rakestraw, and M. Garguilo, "Imaging of pressure- and electrokinetically –driven flow through open capilllaries", *Anal. Chem.*, accepted.

2. J. B. Gravesen, O. S. Jensen, "Microfluidics-a review", *J. Micromech. Microeng.* 3, 168 (1993) and references therein; J. P. Brody and P. Yager, "Low Reynolds number micro-fluidic devices", Solid State Sensors and Actuators Workshop, p. 105, Hilton Head, SC (1996); D. L. Hitt and M. L. Lowe, "Confocal imaging and numerical simulations of converging flows in artificial microvessels", *SPIE*, 2978, 145 (1997); O. Bakajin, J. Chou, S. S. Chan, J. Knight, L. L. Sohn, R. H. Austin, "Nanoscale structures and flows in biotechnology", SPIE, San Jose, CA (1998).

3. C. S. Effenhauser, A. Paulus, A. Manz, and H. M. Widmer, "High speed separation of antisense oligonucleotides on a micromachined capillary electrophoresis device", *Anal. Chem.*, 66, 2949 (1994); S. C. Jacobson, R. Hergenroder, L. B. Koutny, and J. M. Ramsey, "High-speed separations on a microchip", *Anal. Chem.*, 66, 1114 (1994); P. Wilding., J. Pfahler, H. Bau., J. N. Zemel, and L. J. Kricka, "Manipulation and Flow of Biological Fluids in Straight Channels Micromachined in Silicon", *Clinical Chemistry*, 40/1, 43 (1994).

4. A. H. Fan and D. J. Harrison, "Micromachining of capillary electrophoresis injectors and separations on glass chips and evaluation of flow at capillary intersections", *Anal. Chem.*, 66, 177 (1994)

5. C. S. Effenhauser, G. J. M. Bruin, A. Paulus, and M. Ehrat, "Integrated capillary electrophoresis on flexible silicone microdevices: Analysis of DNA restriction fragments and detection of single DNA molecules on microchips", *Anal. Chem.*, 69, 3451 (1997).

6. H. M. Wenz, J. Ziegle, D. M. Demorest, J. Stevens, P. M. Williams, and J. W. Efcavitch (unpublished results); H. M. Wenz, "Capillary electrophoresis as a technique to analyze sequence-induced anomalously migrating DNA fragments", *Nucleic Acids Res.*, 22, 4002 (1994).

7. MEMCAD v4.0, Microcosm Technologies, Inc. (www.memcad.com) (1998).

8. G. M. Mala, D. Li, J. D. Dale, "Heat transfer and fluid flow in microchannels", American Society for Mechanical Engineers, 59, 127 (1996); A. Manz, C. S. Effenhauser, N. Burggraf, D. J. Harrison, K. Seller, and K. Flurl, "Electroosmotic pumping and electrophoretic separations for miniaturized chemical analysis systems", *J. Micromech. Microeng.* 4, 257 (1994); X. C. Qui, L. Hu, J. H. Masliyah, and D. J. Harrison, "Understanding fluid mechanics within electrokinetically pumped microfluidic chips", *1997 International Conference on Solid-State Sensors and Actuators*, Chicago, IL (1997).

9. P. W. Atkins, "Physical Chemistry", Third Edition (W. H. Freeman and Company, New York 1986).

10. J. I. Molho, A. E. Herr, T. W. Kenny, M. G. Mungal, P.M. St. John, M. G. Garguilo, D. J. Rakestraw, P. H. Paul, M. Deshpande, and J. R. Gilbert, "Fluid transport mechanisms in microfluidic devices", ASME (1998), in preparation.

11. E. Grushka, R. M. McCormick, and J. J. Kirkland, "Effects of temperature gradients on the efficiency of capillary zone electrophoresis separations", *Anal. Chem.* 61, 241 (1989)

NOVEL INTERCONNECTION TECHNOLOGIES FOR INTEGRATED MICROFLUIDIC SYSTEMS

D. Jaeggi[1,2], B. L. Gray[2,3], N. J. Mourlas[1,2], B. P. van Drieënhuizen[2], K. R. Williams[2], N. I. Maluf[1,2], and G. T. A. Kovacs[1]

[1]Stanford University, Center for Integrated Systems, CISX 218, Stanford, CA 94305-4075
[2]Lucas NovaSensor, 1055 Mission Court, Fremont, CA 94539
[3]University of California, Micro Instruments and Systems Laboratory, Davis, CA 95616

ABSTRACT

A new approach to realize silicon based integrated microfluidic systems is presented. By using a combination of silicon fusion bonding (SFB) and deep reactive ion etching (DRIE) [**1**, **2**], multi-level fluidic "circuit boards" are fabricated and used to integrate microfluidic components into a hybrid system. As application examples, we demonstrate a multi-level laminating mixer and a multi-level manifold with multiple pressure sensors. To interface the microfluidic system to the macroscopic world, three types of DRIE-fabricated, tight-fitting fluidic couplers for standard capillary tubes are described. One type of coupler is designed for minimal dead space, while another type reduces the risk of blocking capillaries with adhesive. A third design demonstrates for the first time a silicon/plastic coupler combining the DRIE coupler technology with injection-molded press fittings.

INTRODUCTION

Integrated microfluidic systems have recently been gaining interest for many applications including chemical, medical, automotive, and industrial. A major reason is the need for accurate, reliable, and cost-effective liquid and gas handling systems with increasing complexity and reduced size. While a wide range of integrated fluidic devices such as valves, pumps, mixers, and flow sensors have been demonstrated [**3**], efficient interconnections between these devices and coupling to the macroscopic world are not yet available. However, it is primarily these and other packaging issues that will determine the success of microfluidic devices in commercial applications.

Interconnection schemes for microfluidic devices are analogous to printed circuit boards for electronic parts. A miniature hybrid fluid circuit board based on bonding of plastic has been demonstrated [**4**]. Microfluidic systems with a higher integration level have used epoxy printed circuit board technology [**5**] or gasketed stacked modules [**6**]. A further reduction in size can be obtained with fully monolithic systems. However, the integration complexity of these systems is usually limited by wet silicon etch processes for the definition of channels and vias. The new approach presented in this paper is to use DRIE technology to fabricate complex fluidic "circuit boards". DRIE offers many advantages over wet silicon etch processes, in particular, higher density of fluidic interconnects, precise via holes with uniform cross-sections through the wafer thickness, and the ability to fabricate vias and channels of arbitrary size and shape. The fabrication process includes a combination of DRIE, SFB, and anodic bonding to obtain multi-level fluidic substrates. These fluid circuit boards can be used to build arbitrarily shaped multi-level structures or can be combined with surface-mounted microfluidic devices.

Another major issue in integrated microfluidic systems is the coupling of the fluidic circuits to the macroscopic world. Fluidic couplers consisting of a capillary tube glued into an insertion channel which is iso- or anisotropically etched into a silicon substrate have been previously demonstrated [**7**, **8**]. These couplers do not have accurately fitted insertion channels resulting in difficult handling and increased dead space. Our approach is to use successive DRIE steps to fabricate accurately sized cross-sections for the connecting capillaries. To circumvent the necessity of gluing the capillaries, a new coupler combining DRIE with injection-molded press fittings has been developed allowing the capillaries to be exchanged.

FABRICATION

Figure 1 illustrates the fabrication process for multi-level fluidic circuit boards. The first deep etch, approximately 100 μm in depth,

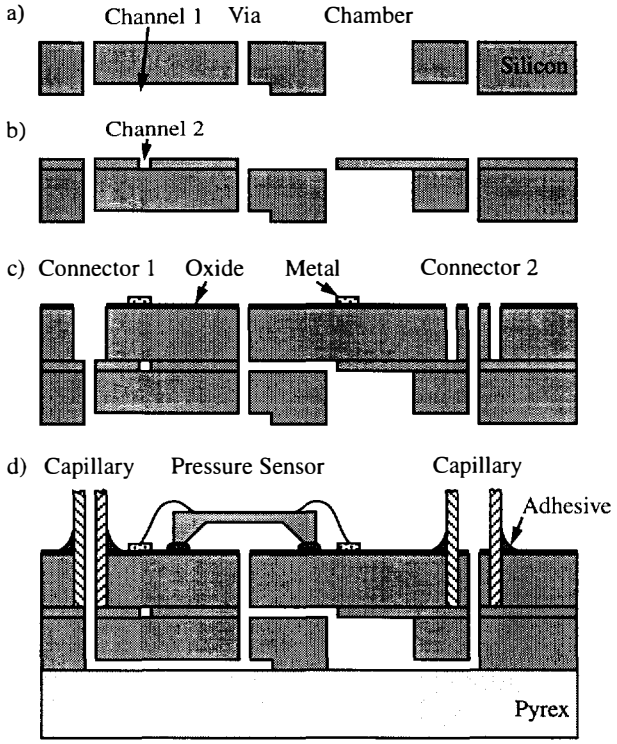

Figure 1. *Illustration of the fabrication process for silicon fluidic circuit boards: a) DRIE first channels, through-wafer vias, and chambers; b) SFB, grind back, and polish second wafer and DRIE second channels; c) SFB third wafer, define metal interconnects, and DRIE connectors as well as pressure sensor vias; d) anodically bond pyrex and attach capillaries and pressure sensors.*

0-9640024-2-6/hh1998/$20©1998TRF
DOI 10.31438/trf.hh1998.25

Solid-State Sensors, Actuators, and Microsystems Workshop
Hilton Head Island, South Carolina, June 8-11, 1998

is performed on a double-sided polished silicon wafer to define the first channels. This is followed by a second DRIE step from the opposite side of the wafer to form interconnection vias, 50 - 100 μm in diameter, all the way through the 390 μm thick wafer. All silicon etches are performed using a tool from Silicon Technology Systems (Abercarn, U.K.) at etch rates of 2 - 3.2 μm/min. A second silicon wafer is bonded to the first and polished down to 100 μm in thickness. Second level channels are then etched through the second wafer. A third SFB step caps the second level of channels with a third 390 μm thick wafer. Aluminum metallization (0.8 μm) is patterned on top of the three-wafer stack to provide electrical interconnects to the surface mounted components, e.g., pressure sensors or microvalves. It is isolated from the silicon by 0.3 - 0.6 μm of thermally grown silicon oxide. The final DRIE step etches entirely through the top wafer, defining couplers to capillary tubing and access holes for surface-mounted fluidic components. A transparent glass substrate that is anodically bonded to the bottom of the stack aids in flow visualization, but may be replaced by a silicon wafer to result in an all silicon stack.

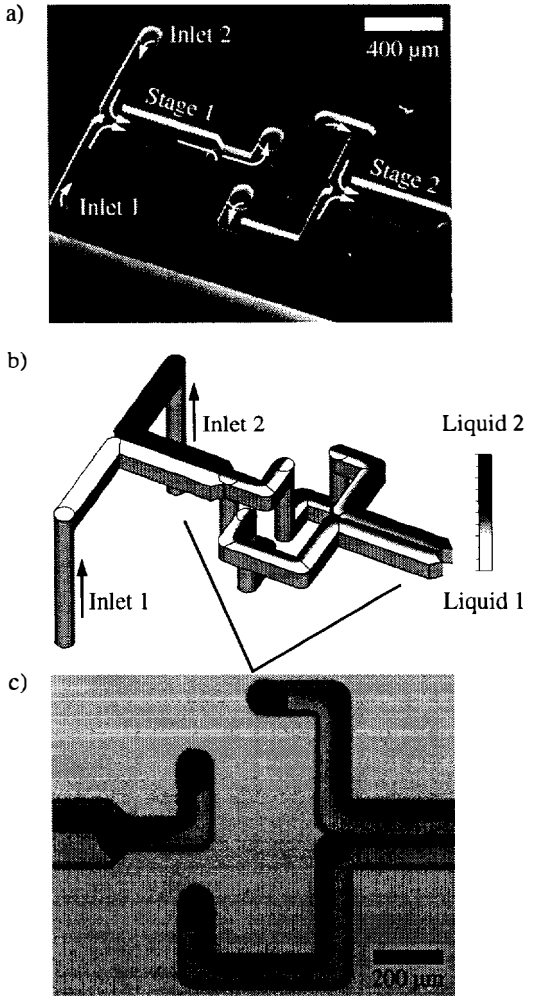

Figure 2. *Illustrations of a multi-level laminating mixer. Mixing occurs by successive separation and reuniting of fluid streams to increase the contact area between the two fluids, resulting in faster mixing by diffusion: a) SEM photograph of first channel level and vias of first two (of six) stages; b) CFD simulation result; c) Photograph of an actual mixer operating at 60 μl/min using water dyed with different colors.*

The result of the overall process is a four-wafer stack, with two interconnected channel levels that can be accessed by surface mount components and external capillaries through vias etched in the top wafer.

MULTI-LEVEL STRUCTURES

The process shown in Figure 1 can be used to fabricate structures that utilize three-dimensional flow patterns for operation. An example of such a structure is a multi-level laminating mixer [**9**]. Mixing of two fluids in a reasonable amount of time is fundamental to the creation of "on-chip" microfluidic processing systems. However, the channel sizes and flow rates associated with such processing systems usually imply low Reynolds numbers, precluding turbulence as a mixing mechanism. Mixing by diffusion can be very slow unless the two fluids are laminated to increase their contact area.

Figure 2a shows an SEM photograph of one level of channels and vias of the first two (of six) stages of a laminating mixer. The channels are 100 μm deep. Two fluids entering the inlet ports laminate at the first horizontal junction, producing two side-by-side fluid streams. Successive vertical separation and horizontal reuniting of fluid streams increases the number of laminates with each stage and, thus, the contact area between the two fluids [**9**]. After the second stage, four laminates exist, with each following stage doubling the number of laminates to 2^n, where n is the stage number. We performed computational fluid dynamics (CFD) simulations using the tools of CFD Research Corporation (Huntsville, AL) [**10**]. Figure 2b shows a simulation result of the first two stages of the mixer, where the differently dyed water at each inlet port has a flow rate of 30 μl/min. The Schmidt number used was 1200, evaluated from separate measurements. Figure 2c shows a close-up of the first vertical split and second reunification in a fabricated mixer with the same input conditions. We see the expected four laminates in the second stage, which is in qualitative agreement with simulation results.

HYBRID SYSTEMS

As a demonstration of an integrated hybrid microfluidic system, five pressure sensors were directly mounted on a silicon substrate

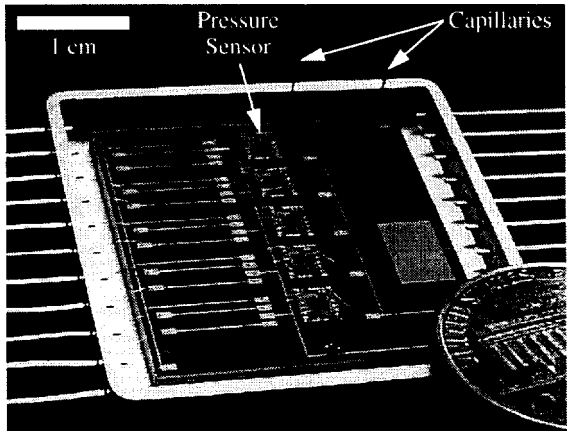

Figure 3. *Photograph of a fluidic circuit board demonstration system with five pressure sensors mounted on a substrate with an embedded microchannel. The five pressure sensors are mounted 4 mm apart over 100 μm diameter access holes to the buried 100-μm square channel.*

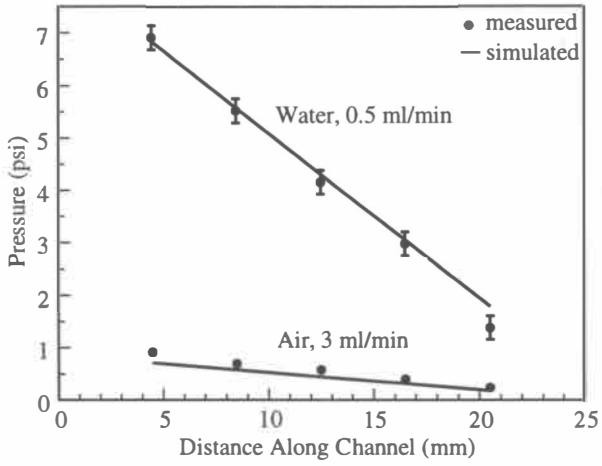

Figure 4. *Measured and simulated data for air and water showing pressure drop along the 100-μm square microchannel for the system shown in Figure 3. The simulation results were obtained using CFD simulations.*

with an embedded 100-μm square microchannel and pressure ports leading from the channel to the sensors (Figure 3). The commercially available piezoresistive pressure sensors (Lucas NovaSensor, Fremont, CA) have a pressure range of 0 - 30 psi. Sensitivities, calibrated after surface mounting using a dead-weight tester, measured 4.7 - 5 mV/psi. A syringe pump was used to provide constant flow rates. Pressure inside the channel was measured for water and air flowing at 500 μl/min and 3 ml/min, respectively (Figure 4). The worst case error between measured data and simulation results obtained using CFD modeling was 25%. The kinematic viscosities used in the models were 1×10^{-6} m^2/s and 1.51×10^{-5} m^2/s for water and air, respectively.

FLUIDIC COUPLERS

Fluidic couplers for standard capillary tubing are fabricated using the process sequence shown in Figure 1. The left coupler in Figure 1d illustrates the first design. DRIE is used to define circular holes matching the inside and outside diameter of the capillaries,

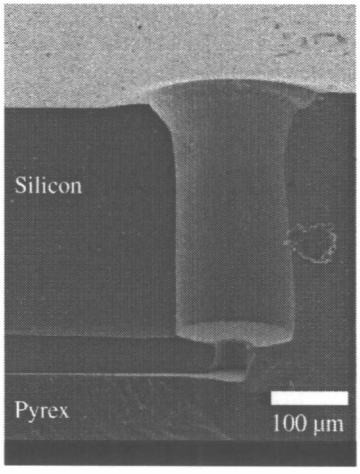

Figure 5. *SEM photograph of a minimum dead space fluidic coupler for capillaries with 150 μm and 50 μm outer and inner diameters, respectively.*

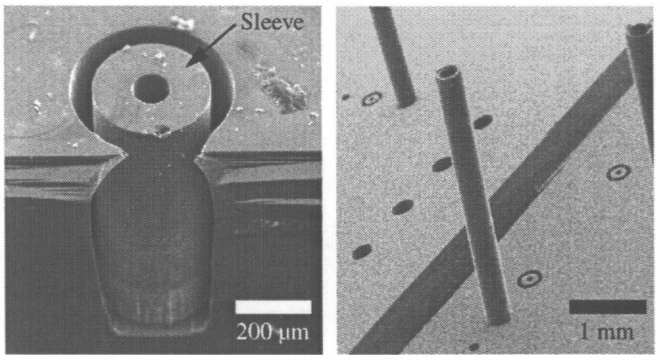

Figure 6. *a) SEM photograph of a fluidic coupler with a 110 μm thick sleeve around the bore to prevent blocking of capillaries with adhesive. The silicon is partially cleaved to show the sleeve; b) SEM photograph of capillaries inserted into the sleeve coupler.*

thus, eliminating any dead space. Figure 5 shows a SEM photograph of the minimum dead space coupler. The capillary is inserted into the opening and held with adhesive.

It was observed that improperly cleaved capillaries with a cusp at the end did not fit well into the insertion channel and allowed seeping of adhesive into the capillary/silicon interface. Therefore, the second type of coupler has a silicon "sleeve" around the etched bore, as illustrated in the right coupler in Figure 1d. Figure 6a shows a SEM photograph of a coupler with a 110 μm thick sleeve. The sleeve acts as barrier to adhesive and enhances the mechanical integrity of the coupling, but also introduces some dead volume. Figure 6b shows fused silica capillaries with 250 μm and 360 μm inner and outer diameters, respectively, inserted into the sleeve couplers. To quantify the dead volume introduced, CFD simulations were performed. A dead volume on the order of 2 nl at a flow rate of 100 μl/min was estimated for the structure shown in Figure 6a.

Figure 7 is an illustration of the third type of coupler which requires no gluing of capillaries. The plastic press fitting is fabricated using injection molding of polyoxymethylene (POM) plastic [**11**]. To align and hold the plastic part in place, the silicon stack and the pyrex have additional through holes for pegs fabricated by DRIE and ultrasonic drilling, respectively. The plastic pegs are

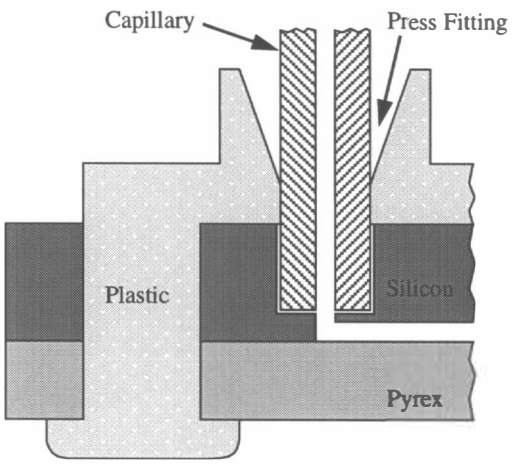

Figure 7. *Illustration of silicon/plastic coupler with press fitting. Heat-staked pegs are used to hold the injection molded plastic part against the silicon.*

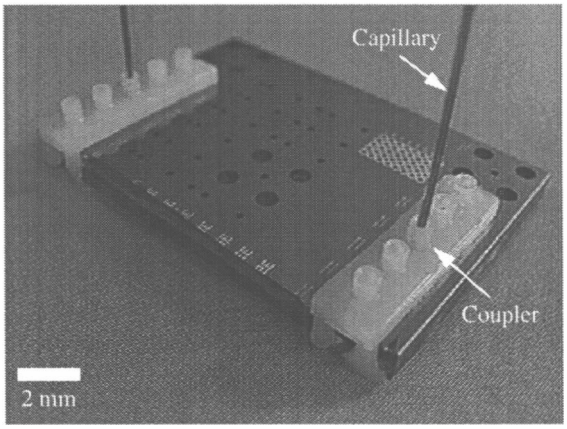

Figure 8. Photograph of two arrays of silicon/plastic couplers with inserted capillaries accessing a 50-μm square microchannel.

melted with a heat-staking tool at temperatures reaching 250 °C. The tool consists of an adapted soldering-iron with a copper block attached to it. Figure 8 shows two arrays of couplers with inserted capillaries that are connected through a microchannel in the substrate. Leakage tests of the new couplers were performed by pressurizing a blocked microchannel with water and measuring the pressure loss versus time. Figure 9 shows that the new silicon/plastic coupler alone is not leak proof at a pressure of 60 psi. By introducing a silicone gasket, cut from a 500 μm thick sheet, between the plastic and the silicon, we obtained a sealed fluidic coupler system for pressures up to a maximum of 60 psi. This compares to glued capillary connectors which are known to hold pressures up to approximately 2000 psi [8]. To quantify the mechanical integrity of the silicon/plastic couplers, pull-tests with a load cell were performed. We measured pull-out forces up to 2 N.

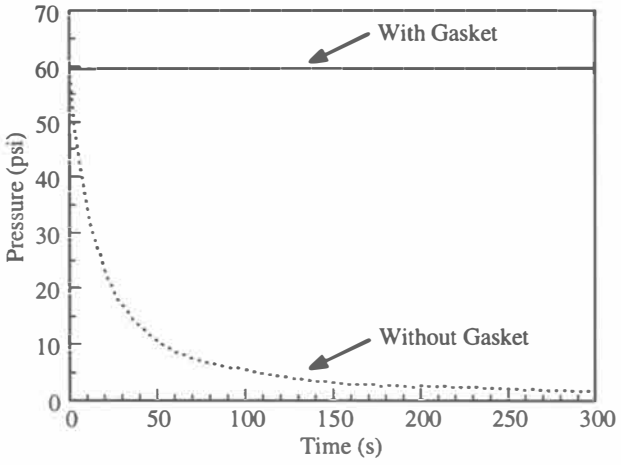

Figure 9. Measured water pressure loss in a blocked test channel indicating a sealed connection for a silicon/plastic coupler with a 500 μm thick silicone gasket.

CONCLUSIONS

We have presented a novel technology for the fabrication of fluidic circuit boards including couplers to standard capillary tubes. The circuit board can either be used to interconnect hybrid mounted fluidic devices such as pressure sensors or to obtain multi-level fluidic structures such as laminating mixers. A novel silicon/plastic press fitting coupler is user-connectable to capillary tubing and is leak proof for pressures below 60 psi. For higher pressures, adhesive-held capillaries may be necessary.

AKNOWLEDGEMENTS

Funding for this work was provided by the DARPA MicroFlumes Program (Contract Number: N66001-96-C-8631). The authors would like to thank R. Scimeca of Lucas NovasSensor, Fremont, CA, M. G. Giridharan of CFD Research Corporation, Huntsville, AL and T. Callenbach of H. Weidmann AG, Plastic-Technologies, Rapperswil, Switzerland for their help and technical discussion with processing, CFD modeling, and heat-staking, respectively. Load cell measurements by G. Cornella, Department of Materials Science and Engineering, Stanford University, CA are gratefully acknowledged.

REFERENCES

1. E. H. Klaassen, K. Petersen, J. M. Noworolski, J. Logan, N. I. Maluf, J. Brown, C. Storment, W. McCulley, and G. T. A. Kovacs, "Silicon Fusion Bonding and Deep Reactive Ion Etching; A new Technology for Microstructures," *Transducers '95 Digest of Technical Papers*, vol. 1, Stockholm, 1995, pp. 556-559.

2. B. P. van Drieënhuizen, N. I. Maluf, I. E. Opris, and G. T. A. Kovacs, "Forced-Balanced Accelerometer with mG Resolution, Fabricated using Silicon Fusion Bonding and Deep Reactive Ion Etching," *Transducers '97 Digest of Technical Papers*, vol. 2, Chicago, 1997, pp. 1229-1230.

3. P. Gravesen, J. Branebjerg, and O. S. Jensen, "Microfluidics - A Review," *J. Micromech. Microeng.*, vol. 3, 1993, pp. 168-182.

4. D. Verlee, A. Alcock, G. Clark, T. M. Huang, S. Kantor, T. Nemcek, J. Norlie, J. Pan, F. Walsworth, and S. T. Wong, "Fluid Circuit Technology: Integrated Interconnect Technology for Miniature Fluidic Devices," *Proc. of the Solid-State Sensor and Actuator Workshop 96*, Hilton Head, 1996, pp. 9-14.

5. T. S. J. Lammerink, V. L. Spiering, M. Elwenspoek, J. H. J. Fluitman, and A. van den Berg, "Modular Concept for Fluid Handling Systems: A Demonstrator Micro Analysis System," *Proc. MEMS '96*, San Diego, 1996, pp. 389-394.

6. W. K. Schomburg, B. Büstgens, J. Fahrenberg, and D. Maas, "Components for Microfluidic Handling Modules," *Micro Total Analysis Systems*, ed. by A. van den Berg and P. Bergveld, Kluwer Academic Publishers, Dordrecht, 1995, pp. 255-258.

7. R. J. Reay, R. Dadoo, C. W. Storment, R. N. Zare, and G. T. A. Kovacs, "Microfabricated Electrochemical Detector for Capillary Electrophoresis," *Proc. of the Solid-State Sensor and Actuator Workshop 94*, Hilton Head, 1994, pp. 61-64.

8. V. L. Spiering, J. N. van der Moolen, G.-J. Burger, and A. van den Berg, "Novel Microstructures and Technologies Applied in Chemical Analysis Techniques," *Transducers '97 Digest of Technical Papers*, vol. 1, Chicago, 1997, pp. 511-514.

9. H. Möbius, W. Ehrfeld, V. Hessel, T. Richter, "Sensor Controlled Processes in Chemical Microreactors," *Transducers '95 Digest of Technical Papers*, vol. 1, Stockholm, 1995, pp. 775-778.

10. CFD-GEOM, CFD-ACE, CFD-VIEW Manuals, CFD Research Corporation, Huntsville, 1997.

11. *Concise Encyclopedia of Polymer Science and Engineering*, ed. by J. I. Kroschwitz, John Wiley & Sons, New York, 1990.

Sizing, Fractionation and Mixing of Biological Objects Via Microfabricated Devices

Olgica Bakajin, R. Carlson, C.F. Chou, S.S. Chan,
C. Gabel, James Knight, Ted Cox and R.H. Austin
Departments of Physics and Biology
Princeton University, Princeton, NJ 08544

SUMMARY

One aspect of micro and nanofabrication that has not been exploited a great deal has been the ability to make structures to probe and separate complex mixtures using designed environments. We will give three brief examples of such second-generation uses of microfabrication, as opposed to simply shrinking the size of the vessels or tubes used in macroscopic lab environments. The three examples chosen are blood cell fractionation and cell sorting, asymmetric brownian motion fractionation and ultra-high speed fluid mixing.

INTRODUCTION

Silicon micromachining has opened up a new world of sub-micron spaces in which you can study biological objects on a scale commensurate with their size and operational environment. Since silicon micromachining is so highly sophisticated in terms of technology, it is possible to design and construct highly creative structures which can probe specific aspects of a biological object. Such structures can also be very practical and useful in applied areas such as biotechnology.

The manipulation and sorting of biological particles poses unique challenges to microfabrication because of the complex physical properties of biological particles. These properties range from size (DNA is an extremely long but thin polymer while the cell is a compact sphere) to adhesive properties (white blood cells are selectively extremely sticky while red blood cells are designed to be quite non-adhesive). An even more important issue is the fact that each biological particle, whether it be the sequence of a DNA fragment or a white blood cell, is unique. Often it is vital to ascertain the uniqueness of the particles, to sort them and find a very rare individual in a population of millions. Many biological sensors rely upon highly specific molecular interactions to sort out a heterogeneous population. We have taken a different approach, the fabrication of micron to nanometer structures which probe the physical properties of biological particles and separate them based on their interactions with physical obstacles.

A related issue to that of structure selection is surface properties. Biological objects, in particular proteins and cells, are notoriously adhesive, and in the microfabricated world surface is everything so the problems of sample loss are only compounded. The silicon dioxide surface of a silicon wafer, or the glass surface of a etched glass wafer, is not a good surface for biology since it can be quite adhesive and in our hands will stop every white blood cell in a drop of blood as it enters a micromachined volume. While one can devise lotions and potions consisting of complex proteins such as bovine serum albumin, the presence of another complex biological component can only serve to further confound the delicate analysis of a already complex object. Thus, we have expended a great deal of work to find very clean and simple surfaces which will not by themselves selective bind biological objects. The materials of choice, silicone elastomers, offer three attractive advantages: they can be used as replicas of negative image micromachined master wafers so that very inexpensive copies of the structures can be made, they self-seal hermetically to clean surfaces so many of the bonding problems in micromachining are removed, and there are ways to selectively modify the surface of silicones if so desired.

DEVICE FABRICATION AND MODIFICATION

Silicone replicas were made by pouring 5 grams of degassed silicone mixed 1/10 with catalyzing agent over a 3" wafer. The silicone was polymerized by putting the wafer in a 80 °C oven for 15 minutes. The silicone replica was peeled off the master wafer and placed for 2 minutes in an oxygen plasma vacuum chamber (Herrick Scientific). This is a crucial step which makes the silicone hydrophilic for approximately 1/2 hour. The hydrophilic silicone was placed against the desired window material and immediately wet with water. If the structure is to withstand positive hydrostatic pressures the silicone sealed structure was placed in a water bath at 80 °C for 24 hours to enhance adhesion top the mating surface. There are further details about this process which we would be glad to discuss.

EXPERIMENTAL RESULTS

Cell Sorting: Cells respond to their environments in a variety of ways. For the human leukocyte, this complex environment consists of the human circulatory system, the study of which is most often physiological in nature. Here we demonstrate, using physiological flow conditions and a

0-9640024-2-6/hh1998/$20©1998TRF
DOI 10.31438/trf.hh1998.26

Solid-State Sensors, Actuators, and Microsystems Workshop
Hilton Head Island, South Carolina, June 8-11, 1998

microfabricated array of channels with length scales similar to those of human capillaries (see Figure 1), a novel interaction of leukocytes with their physical environment [1]. Using vital chromosome stains and cell specific, fluorochrome labeled antibodies, we observe that the eventual adhesion of the leukocytes to the array does not occur in a manner consistent with a random process (Figure 2). Further, the distribution of cells in the arrays displays a strong dependence on cell type and nuclear morphology, with granulocytes penetrating a smaller distance than lymphocytes and interacting with the lymphocytes in a self-exclusionary manner. The physical distortion of the cells is the same as they experience in vivo, and we propose that this complex non-random behavior is due to a hydrodynamic shear and deformation activated change in the cells relevant to observed *in vivo* behavior. Because we use reversibly sealed arrays, in the near future we will be able to probe differences among individual stuck cells, either physically using techniques such laser tweezers or atomic force microscopy, or via blotting transfer techniques to explore the biochemical variations among cells.

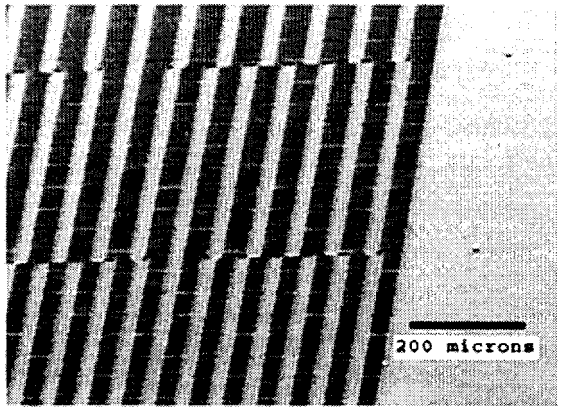

Figure 1. Multiple-length array for cell separation

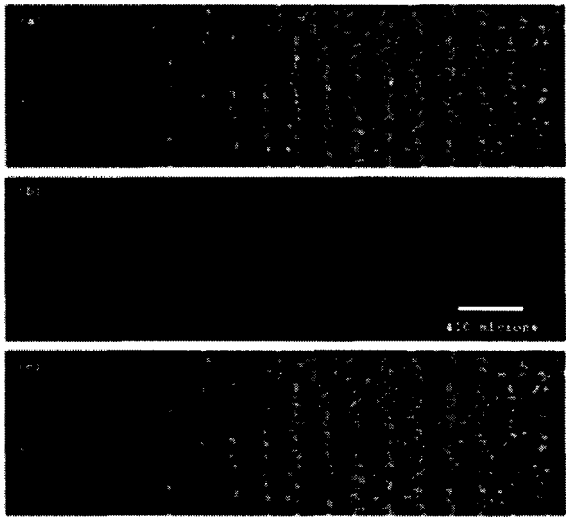

Figure 2. Anti-body fluorescence of labeled leukocytes. Top panel is the raw image, middle is the T-lymphocyte cells, bottom is granulocytes.

Brownian motion as a fractionating device: In a microfabricated world it is possible to design structures very difficult to realize in normal materials, here we discuss how asymmetry in structures gives rise to a rectified brownian motion. Tom Duke [2] and Deniz Ertas [3] realized independently that by making using a combination of asymmetric structures, flow and brownian motion it would be possible to construct devices which in a continuous injection manner could fractionate objects based upon their diffusion constants. The basic idea is fairly simple: one uses a wall and an opening which brings molecules down along the wall. Because the wall breaks left-right symmetry those molecules with a larger diffusion constant will move further from the wall on the average than molecules of small diffusion constants. If two exits exist at some distance down the wall the smaller molecules will be more likely to exit far from the wall than large molecules. The major advantage here is that the ejection is continuous and so is the extraction, so that you don't have to run as a single event. Ertas proposed a conceptually elegant but difficult to fabricate structure, while Duke and Austin proposed a very simple structure simply consisting of rectangles rotated at an angle to the applied field direction. Figure 3 shows the oriented block configuration of Duke and Austin, while Figure 4 shows how injected molecules would be expected to migrate at differing angles to the applied field direction.

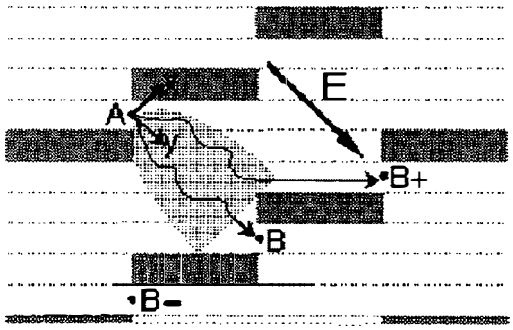

Figure 3. An asymmetric array of blocks. The electric field points 45^{o} to the lower right.

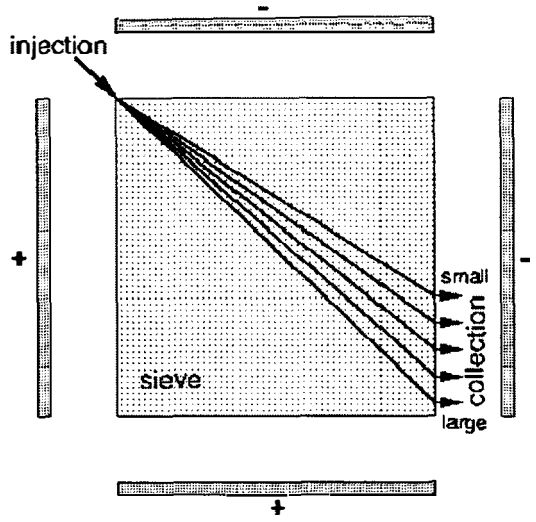

Figure 4. The deflection due to rectified brownian motion.

The performance of such devices will be governed by the dimensionless quantity D/va, where D is the diffusion constant of the object, v is its electrophoretic speed and a is the characteristic opening of the asymmetric pores determines resolution.. Intuitively, there is a "sweet spot" for the resolution of this device. If D is too large or va too small, blurring occurs because of too rapid diffusion. If D is too small or va too large, most objects go straight down through the center channels. Figure 5 shows how the normalized resolution of the channels shown in Figure 3 changes as a function of D/va.

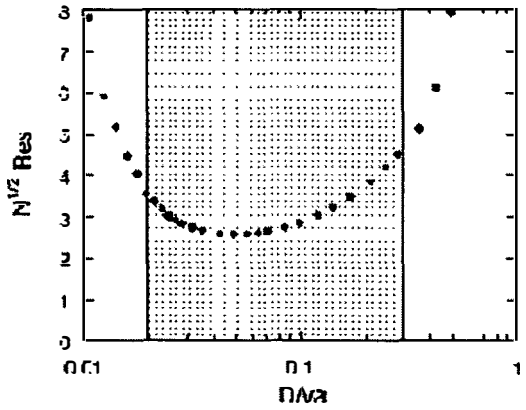

Figure 5. The normalized resolution of the array shown in Figure 3 as a function of D/va

This is very much work in progress. We should be able to show you at the meeting video of the actual fractionation occurring, or explain to you why it doesn't work as well as it should.

Micro/Nano Fluidics for Ultra-rapid Mixing: Mixing Nanoliters in Microseconds Mixing of fluids at the macroscopic scale normally occurs at high Reynolds numbers via turbulence (the cream in your coffee this morning). The Reynolds number R_e is a measure of the ratio of (a) the linear momentum/time transported past a fixed point in space carried by moving fluid of density ρ and speed v to (b) the rate at which the momentum is lost due to the shearing viscosity of the fluid η as it moves with characteristic shearing length L: $R_e = a/b = \rho vL/\eta$. In the micron world of microfabrication R_e is always well below the turbulent threshold of about 1000 even at 1 m/s fluid velocities.

Thus, in the microfabricated world mixing cannot occur via turbulence but rather only through brownian diffusion, a process we exploited in the last section to fractionate materials. The classic example involving how long it would take Caesar's flatulence to reach the rear of the Roman Senate us usually cited in freshman physics as an example of how slow diffusion is, since the characteristic τ to diffuse a distance x is given by: $\tau = x^2/2D$ where D is the diffusion constant of the object in the solvent. This doesn't necessarily doom mixing to long time scales however. If you make things REALLY small, like nanometers, you can achieve sub-microsecond "mixing" times via diffusion. Further, since the process is diffusive and not turbulent here is no "dead time" in a diffusive mixer but instead a calculable continuous process.

The next question is then: how can you possibly make fluid streams moving at meters/sec 100 nm wide? Via hydrodynamic focusing, a well understood in the conventional flow cell cytometer. We describe in this report a microfluidic, continuous-flow mixer capable of diffusive mixing times of less than ten microseconds. This is achieved without inducing turbulence and in an open architecture that reduces dead time by permitting observation of the entire mixing process. Figure 5 is an epifluorescence image of the microfabricated device: four rectangular channels, 10 microns deep and wide, intersect at the center. Fluorescent dye labels the flow from the inlet channel and appears bright, while nonfluorescent buffer flows from the side channels. The side flow squeezes, or 'hydrodynamically focuses', the inlet flow into a thin stream that exits the intersection sheathed in buffer fluid. The focusing width can be controlled by varying the relative pressures driving the side and inlet flows, and widths as small as 20 nanometers have been measured.

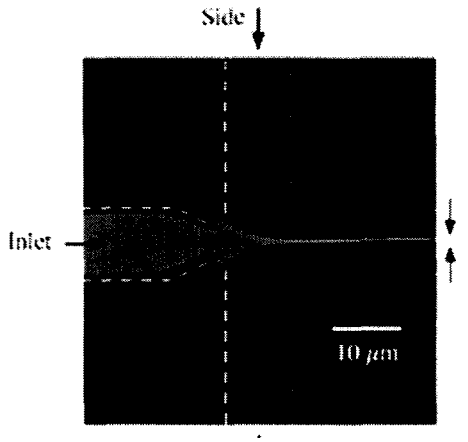

Figure 6. Epifluorescence image of a hydrodynamic jet forming a sub-micron wide jet. Dotted lines show outline.

At such small length scales, molecules from the side flow rapidly diffuse across the inlet stream, resulting in fast mixing. resolution better than a microsecond per micron. A further consequence of the focusing is the small sample volume consumed by the mixer. The volume flow rates of the focused reactant stream are typically on the scale of nanoliters per second, over three orders of magnitude less than the flows in comparable turbulent mixers (4). While this renders the technique undesirable for mixing coffee, it is ideal for use with expensive biochemical samples.

It is fairly simple under conditions of low Re to calculate the in/out fluid patterns, since there is a linear relation between the volume of fluid flow Q in liters/sec and the applied pressure drop ΔP, in other words, the fluid flow looks like current flow in a resistive circuit. The pressures P then become voltages V, and the jet that is formed now is the current injected from the center "wire". The critical parameter is the ratio of the side pressure P_S to the center pressure P_C, which we call α. Figure 7 shows a comparison of the calculated jet width using the resistive net shown in the insert to the measured jet width as determined from integrated jet intensity. Note that at pinch-off the jet width goes to approximately 20 nm width! The insert shows how the device can resolve shorter times as α approaches pinch-off.

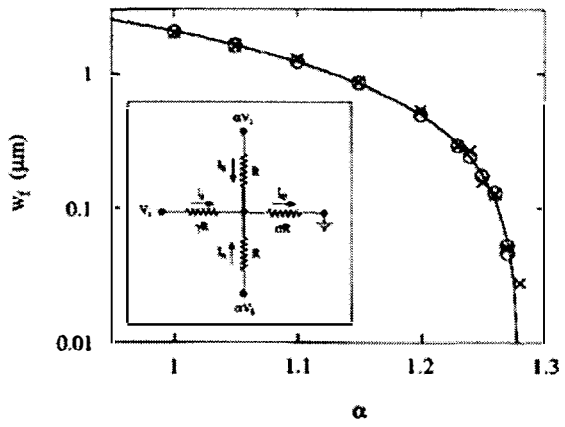

Figure 7. Measured vs. calculated jet width.

A jet width of 20 nanometers moving at 1 m/sec gives a time resolution for mixing yielding resolution better than a microsecond per micron. A further consequence of the focusing is the small sample volume consumed by the mixer. The volume flow rates of the focused reactant stream are typically on the scale of nanoliters per second, over three orders of magnitude slower than the rates in comparable turbulent mixers (4). While this device is rather undesirable for mixing coffee, it is ideal for use with expensive biochemical samples.

We have begun experiments utilizing this technology. Figure 8 shows the results of a fluorescence quenching experiment where iodine molecules in the side solution quench via overlap of electronic orbitals the emission of fluorescein molecules. Scanning along the jet with a digital stage on the microscope allows one to measure in a steady state way ultra-rapid mixing kinetics, in this case with a resolution of less than 10 microseconds.

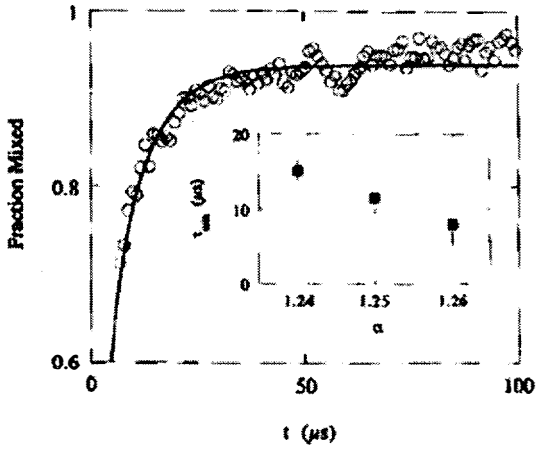

Figure 8. Quenching kinetics of fluorescein.

Now that this technology is well understood [5], we are proceeding with protein folding experiments both using fluorescence quenching, and through etched 400 micron deep channels time-resolved X-ray scattering at CHESS, the Cornell synchrotron light source in collaboration with Sol Gruner and Lois Pollack.

CONCLUSIONS

There are many exciting possibilities for microfabricated structures in biology that go beyond making the same things smaller. Our devices are actually quite simple to make, but we do hope show some of the potentials of the technology.

ACKNOWLEDGMENTS

The authors gratefully acknowledge financial support from ONR, NIH, Perkin Elmer, Hewlett Packard and Caliper Technologies.

REFERENCES

[1] R. H. Carlson, C. V. Gabel, S. Chan and R Austin, " Self-Sorting of White Blood Cells in a Lattice", *Phys. Rev. Lett.* 15 (1997) 2149-2152.

[2] T. A. J. Duke and R. H. Austin, "Microfabricated Sieve for the Continuous Sorting of Macromolecules", *Phys. Rev. Lett.* 16 (1998) 1552-1555.

[3] D. Ertas, "Lateral Separation of Macromolecules and Polyelectrolytes in Microlithographic Arrays", *Phys. Rev. Lett.* 16 (1998) 1548-1551

[4] H. Strehlow, Rapid Reactions in Solution (VCH Publishers, New York, 1992)

[5] J. Knight et al. In Press, *Phys. Rev. Lett.*

DESIGN AND FEEDBACK CONTROL OF ELECTROSTATIC ACTUATORS FOR MAGNETIC DISK DRIVES

David A. Horsley*, Naiyavudhi Wongkomet, Roberto Horowitz, and Albert P. Pisano
Berkeley Sensor and Actuator Center
497 Cory Hall, University of California at Berkeley, CA 94720

ABSTRACT

This paper presents a microfabricated actuator designed for high precision servo-positioning in a magnetic hard disk drive. The device is actuated using electrostatic force generated with parallel-plate capacitive electrodes. The displacement of these electrodes is measured using a dedicated capacitive sensing interface, allowing closed-loop control to be used to extend the servo bandwidth. Using the sensing electronics and a simple phase-lead compensator, a prototype device was used to actuate a 1.6 mg ceramic slider over a 1.2 kHz bandwidth.

INTRODUCTION

The magnetic hard disk drive continues to maintain a significantly lower cost per megabit in comparison to competing solid-state memory technology. One means of maintaining this advantage is by increasing the data storage density by reducing the size of each data bit, requiring increased accuracy in positioning the read/write heads over the disk. To this end, a dual-stage positioning mechanism has been proposed, using a conventional voice-coil motor (VCM) for coarse positioning and a high bandwidth secondary actuator for fine positioning [1]. In this paper we will describe a microfabricated secondary actuator which is only slightly larger than the ceramic block, referred to as the slider, which bears the magnetic read/write heads in a disk drive. This actuator is designed to carry the slider and will itself be mounted on the VCM-actuated arm upon which the slider is usually attached. The advantage to this approach over competing designs is that the actuators are batch-fabricated for low cost, but are not expected to significantly effect either the head or suspension fabrication processes. Electrostatic actuation has been selected for ease of fabrication, since the structural material need only be conductive, rather than ferromagnetic or piezoelectric. Previously, we described a rotational, microfabricated actuator for this purpose [2].

ACTUATOR DESIGN

The actuator, illustrated in Fig. 1, consists of a translating central shuttle which is anchored to fixed stator segments via a flexural suspension. Actuation is achieved by electrostatic force generated using capacitive electrodes which are mounted in opposing pairs between the shuttle and stators. The device is quad-symmetric, meaning that the upper stator segments are used to pull the shuttle in the $+x$ direction, while the lower segments are used to push the shuttle in the $-x$ direction. Because the disk-drive application requires high output force over a relatively small displacement range (±1 μm), parallel plate capacitors have been selected rather than interdigitated ("comb-finger") electrodes. The main drawback to this configuration is that the electrostatic attraction between parallel-plate capacitors is a nonlinear function of the separation between the plates. However, assuming a nominal capacitive gap of g_0 and an electrode length of l_p, the ratio of the parallel-plate force to the interdigitated force is l_p/g_0. Since typical electrode lengths are over ten times greater than the capacitive gap, the parallel plate configuration enjoys an order of magnitude greater output force than an interdigitated design with the same area and capacitive gap. It is well known that a voltage driven parallel plate has a stable actuation range of $\pm g_0/3$; at larger displacements the electrostatic force dominates over the restoring force from the suspension and the electrodes pull together. To ensure that the actuator will not exceed this range under normal operation, a nominal capacitive gap of 10 μm was selected, allowing a ± 3.3 μm stable actuation range. Furthermore, to prevent the electrodes from coming into contact due to a large external shock, fixed stoppers which are biased at the same potential as the shuttle are placed above and below the shuttle, limiting the displacement to a maximum range of ± 4 μm. Due to the fact that the actuator is composed of conductive, doped polysilicon, it is currently possible to implement only minimal electrical isolation between components, so each shuttle electrode is bordered by two stator electrodes, both biased at the same potential as illustrated in the top of Fig. 1. The effect of the parasitic capacitive gap, αg_0, is to diminish the electrostatic force generated from the primary capacitive gap, g_0. Increasing α results in a greater net force on each shuttle capacitor but reduces the total number of capacitors per unit length. As proposed in [3], an optimization was performed to maximize the total actuation force, resulting in a value of $\alpha = 2.2$.

FABRICATION PROCESS

Actuators were fabricated using a modified version of the HexSil process first described in [4]. The advantage of this process is that it produces high aspect-ratio structures with heights of up to 100-200 μm using a molded, 4 μm thick, CVD polysilicon film. Molds are fabricated by etching deep trenches into standard (100) silicon wafers using deep reactive ion etching (DRIE). Since the depth of these trenches determines the height of the finished actuators, the mold DRIE is a critical process. Prototype molds were limited to 50 μm depths, but future devices will have doubled thickness and output force. Following the mold fabrication, the mold is filled with in-situ phosphorous doped CVD polysilicon on top of a CVD SiO_2 sacrificial layer. To ensure conformality of the SiO2 film it is formed by thermally oxidizing a conformal CVD polysilicon layer. The surface polysilicon is then patterned and metallized using conventional surface micromachining techniques. A cross-sectional optical micrograph of the filled trenches is shown in Fig. 2. Note that there are bright bands visible in the sacrificial layer due to incomplete oxidation of the polysilicon. The completed structures are released from the mold wafer by an etch in hydrofluoric acid (HF), which removes the sacrificial layer. The actuators are then assembled onto copper interconnect on a target

* Present address: DiCon Fiberoptics, 1331 Eighth St., Berkeley, CA 94710

0-9640024-2-6/hh1998/$20©1998TRF
DOI 10.31438/trf.hh1998.27

Solid-State Sensors, Actuators, and Microsystems Workshop
Hilton Head Island, South Carolina, June 8-11, 1998

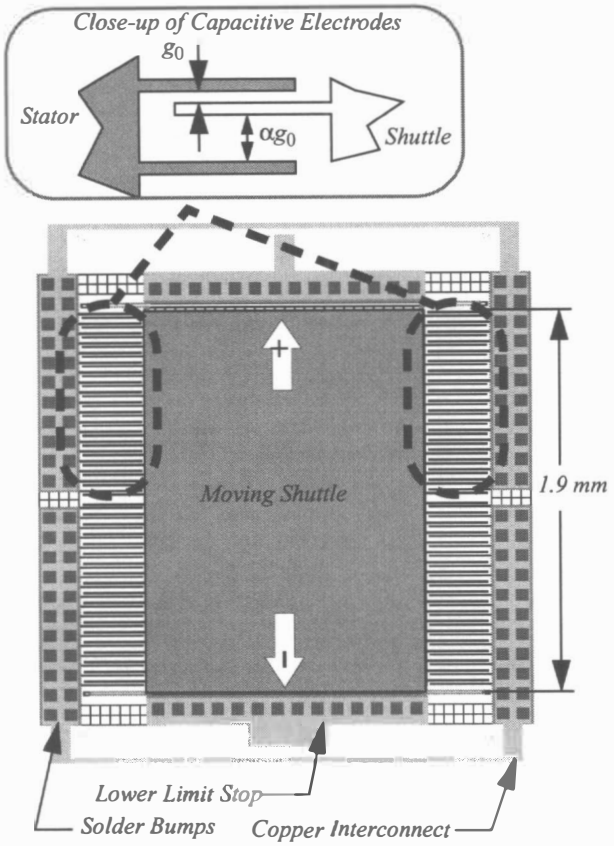

Figure 1. Actuator layout. The upper stator segments (circled) serve to pull the shuttle in the + x direction, while the symmetric lower stator electrodes push the shuttle in the - x direction.

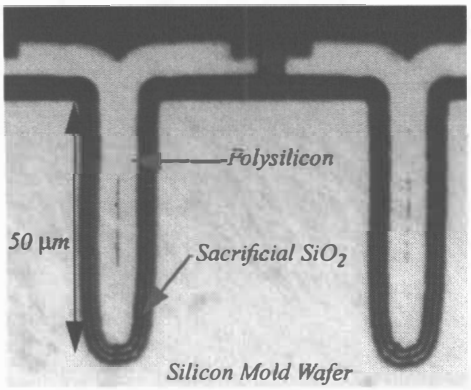

Figure 2. Optical micrograph of filled mold trenches. Note that slight bowing of the mold trenches has resulted in voids in the polysilicon beams. Also, bright bands in the sacrificial layer are observed due to incomplete oxidation.

substrate using a solder bump bonding process described in [5]. Due to the fact that the structural material is uniformly conductive, electrical isolation is achieved through the use of break-away or fusible beams as illustrated in Fig. 3.

ACTUATION DYNAMICS

For small deflections, $x(t)$, the mechanical behavior of the actuator in response to an applied electrostatic force, $F(x,v_1)$, may be described by a mass-spring-damper model,

$$m\ddot{x}(t) + b\dot{x}(t) + k_m x(t) = F(x, v_1) \tag{1}$$

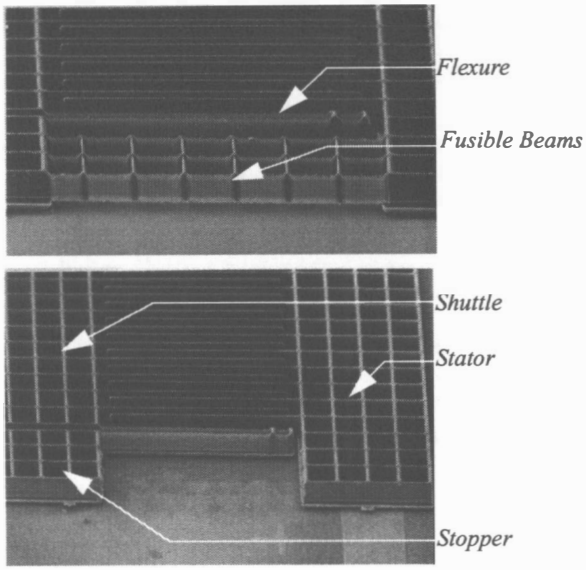

Figure 3. Electrical isolation of assembled actuators. Top: fusible beams connecting the stopper and stator segments. Bottom: the same region after the application of a brief pulse of current.

where m denotes the total mass of the slider and actuator, b denotes the damping coefficient, and k_m is the suspension spring constant. Although the electrostatic force, $F(x, v_1)$, is a nonlinear function of both the actuator displacement and the applied voltage, use of push-pull stator segments which are DC biased with a voltage V_0 and driven with a differential input voltage, v_1, allows small-signal linearization. A linear approximation for the force is then given by the first-order Taylor-series expansion:

$$F(x, v_1) \approx k_e(V_0)x + k_v(V_0)v_1 \tag{2}$$

Assuming the capacitor configuration illustrated in Fig. 1, with a nominal capacitive gap of g_0 and a parasitic capacitive gap of αg_0 (where $\alpha > 1$):

$$k_e(V_0) = \left.\frac{\partial F}{\partial x}\right|_{(0,\,V_0)} = \frac{2\varepsilon_0 A}{g_0^3}\left(1 + \frac{1}{\alpha^3}\right)V_0^2$$
$$k_v(V_0) = \left.\frac{\partial F}{\partial v_1}\right|_{(0,\,V_0)} = \frac{2\varepsilon_0 A}{g_0^2}\left(1 - \frac{1}{\alpha^2}\right)V_0 \tag{3}$$

where ε_0 is the permittivity of air and A is the total capacitive area of each stator (neglecting parasitics). Substituting the linearized electrostatic force from Eq. (2) into the actuator equation of motion from Eq. (1) yields a linear actuation model:

$$m\ddot{x}(t) + b\dot{x}(t) + (k_m - k_e(V_0))x(t) = k_v(V_0)v_1 \tag{4}$$

Note that k_v represents a voltage-to-force gain, while the effect of k_e is that of a negative, electrostatic spring. This electrostatic spring term reflects the tendency for the parallel plates to pull together for sufficiently high voltage, which occurs when $k_e(V_0) \geq k_m$.

For a fixed bias voltage, V_0, the Laplace transform of Eq. (4) is that of a simple second-order system,

$$\frac{X(s)}{V_1(s)} = \frac{k_v(V_0)}{ms^2 + bs + (k_m - k_e(V_0))} \tag{5}$$

Typical microfabricated actuators exhibit very lightly damped resonances, implying that if the resonant frequency is near the desired servo bandwidth, the settling performance will be poor. One approach is to design the actuator to have an extremely high resonance frequency so that the actuator dynamics will have negligible effect on the servo system performance. For this approach to succeed, the resonance frequency should be from five to ten times greater than the servo bandwidth. Alternatively, the actuator may be designed to have an open-loop resonant frequency which is well within the control bandwidth. Feedback is then used to provide the desired closed-loop resonant frequency and damping ratio. The advantage of the latter approach is quickly seen by noting that the DC gain of the actuator transfer function listed in Eq. (5) is:

$$A_0 = \left(\frac{m}{k_m - k_e(V_0)}\right)\left(\frac{k_v(V_0)}{m}\right) = \frac{1}{\omega_n^2}\left(\frac{k_v(V_0)}{m}\right) \qquad (6)$$

Thus, for a fixed mass and bias voltage, an actuator which has a resonance that is within the control bandwidth will require 100 × lower input voltage to achieve the same displacement as an actuator with a resonant frequency which is ten times higher.

CLOSED-LOOP ACTUATION

For a second-order system, the closed-loop DC gain and the resonant frequency are related to their open-loop values by:

$$A_{cl}\omega_{n,cl}^2 = A_0\omega_n^2 = \text{GBW} \qquad (7)$$

where GBW is a constant, analogous to the gain-bandwidth product used to describe first-order systems such as op-amps. Although slight increases in bandwidth may be obtained at the cost of diminished phase-margin, the actuation bandwidth is roughly proportional to the resonant frequency. Thus, feedback can be used to trade DC gain for bandwidth or vice-versa. However, Eq. (7) shows that in order to double the closed-loop bandwidth, the closed-loop DC gain must diminish by a factor of four. The control strategy is to choose the loop gain to achieve the desired closed-loop bandwidth, then use phase-lead compensation to yield a desired phase-margin. The block-diagram of the control system is illustrated in Fig. 4.

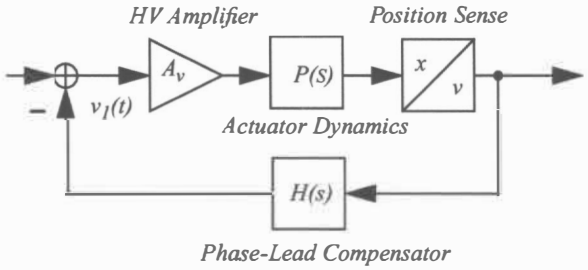

Figure 4. *Block-diagram of closed-loop control architecture.*

The actuator displacement is measured using a capacitive position sensing interface which is illustrated in Fig. 5. The custom sensing circuit utilizes a pseudo-differential switched-capacitor capacitive sensing scheme [5]. On-chip coupling capacitors shield the sensing electronics from the high-voltage drive signal, which is in the range of ±40 V. Correlated double sampling is used to eliminate amplifier offset, 1/f noise, switch charge injection, and kT/C noise. To minimize the coupling of the drive signal into the sensing channel, sensing and the driving signals are separated by both frequency division and time division techniques. Unfortunately, this coupling, referred to as feedthough, is not completely suppressed and the minimum detectable signal is limited to approximately 20 nm using these electronics.

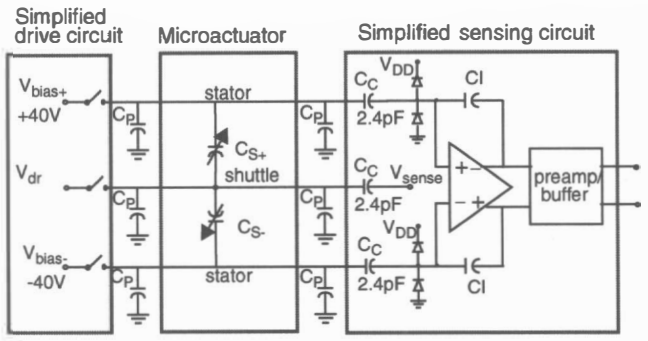

Figure 5. *Simplified circuit for capacitive sensing interface.*

EXPERIMENTAL RESULTS

The parameters of the open-loop actuation transfer function listed in Eq. (5) were identified by measuring the actuator frequency response using a laser-doppler vibrometer (LDV). A slider with a measured mass of 1.6 mg was bonded to an actuator, as shown in Fig. 6. Open-loop frequency response measurements taken before and after attaching the slider allowed the moving mass of the actuator to be estimated at 97 ± 10 μg. By measuring the resonant frequency and DC-gain at multiple bias voltages, as illustrated in Fig. 7, estimates for the suspension spring constant, k_m, as well as the electrostatic model parameters, k_v and k_e, were produced. The values estimated from experimental data are listed along with theoretically estimated values in Table 1. Two different actuator designs were fabricated which were identical except for the fact that one had a larger shuttle than the other. Good agreement is observed between the measured and theoretical values with the exception of the damping coefficient. This error is due to the fact that the theoretical damping model included only viscous gas damping and did not account for added damping due to series resistance between the input amplifier and the capacitive electrodes.

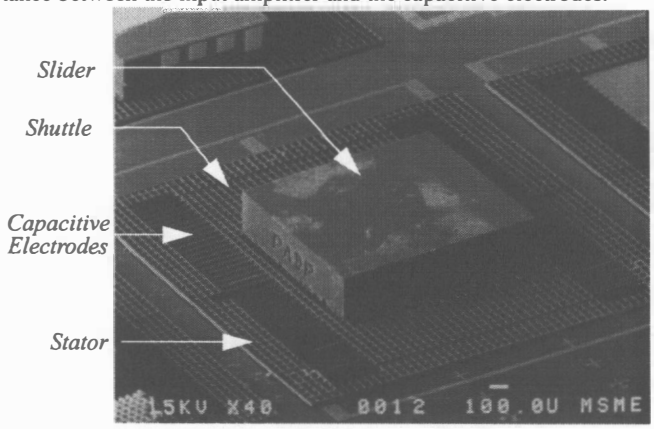

Figure 6. *Scanning electron micrograph of a 1.2 mm × 1.0 mm × 0.3 mm slider assembled onto the 2.2 mm × 2.0 mm × 0.5 mm actuator.*

Table 1: Actuation Model Parameters at V_0 = 40 V.[a]

parameter	*units*	*Design #1*	*Design #2*
m	μg	97 ± 10 (87)	44 ± 5 (46)

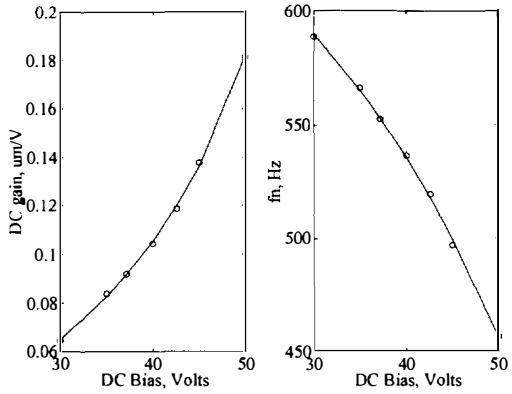

Figure 7. *Measured DC gain and resonance freq. vs. bias voltage.*

Table 1: Actuation Model Parameters at V_0 = 40 V.[a]

parameter	*units*	*Design #1*	*Design #2*
k_m	*N/m*	29 ± 2 (33)	29 ± 2 (33)
b	*μN-s/m*	78 ± 12 (41)	58 ± 14 (33.5)
k_e(40 V)	*N/m*	9.4 ± 0.6 (10.1)	9.4 ± 0.6 (10.1)
k_v(40 V)	*μN/V*	2.0 ± 0.1 (2.2)	2.0 ± 0.1 (2.2)

a. Theoretical values appear in parenthesis.

Following the open-loop system identification experiments, closed-loop control was implemented using both LDV measurements and capacitive position sensing. The measured open and closed-loop transfer functions from input voltage to output displacement are shown in Fig. 8, while the closed-loop response to a 100 Hz, ± 10 V square-wave, measured using capacitive sensing, is plotted in Fig. 9. Note that the higher bandwidth achieved using LDV measurements came at a cost of a four-fold reduction in DC gain, corresponding to a greatly reduced actuation range at ± 40 V. A summary of the closed-loop results is provided in Table 2.

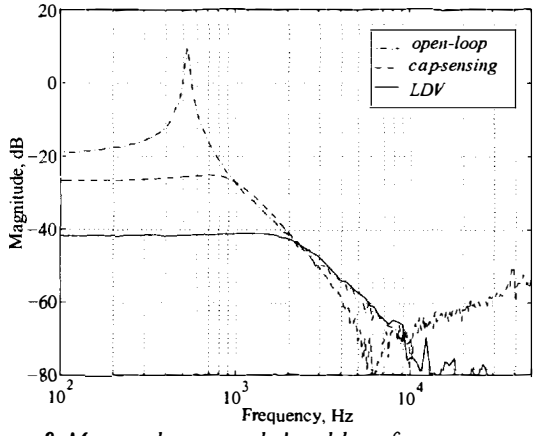

Figure 8. *Measured open- and closed-loop frequency response.*

CONCLUSIONS

Closed-loop position control of a disk-drive slider has been demonstrated using a microfabricated actuator. A dedicated capacitive sensing interface was utilized to demonstrate a closed-loop bandwidth of 1.1 kHz, although reducing the DC gain by a factor of four allowed a bandwidth of over 2.4 kHz to be achieved. Future devices which have a doubled thickness will allow a proportionate increase in DC gain and capacitive sensing resolution.

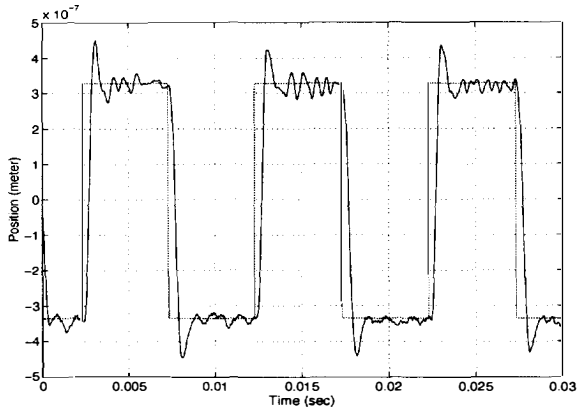

Figure 9. *Measured closed-loop response to a 100 Hz square-wave.*

Table 2: Summary of Closed-Loop Results

	DC gain, μm/V	*BW, Hz*	*Phase Margin, Deg.*	t_{settle} *msec.*
Open-Loop	*0.1*	*820*	NA	100
LDV	*0.01*	*2474*	45	0.5
Cap. Sensing	*0.035*	*1170*	38	2.0

ACKNOWLEDGMENTS

This research was funded by DARPA contract DABT 63-95-C-0028. The authors thank Chris Keller, Angad Singh, and Michael Cohn for their help with developing the actuator fabrication process, along with Stephen Williams of Quantum Corporation for providing the pico-sliders.

REFERENCES

1. L.-S. Fan, H.H. Ottesen, T.C. Reiley, R.W. Wood, "Magnetic Recording-Head Positioning at Very High Track Densities Using a Microactuator-Based, Two-Stage Servo System", *IEEE Trans. Ind. Electronics*, v 42, pp. 222-233, June 1995.
2. D.A. Horsley, A. Singh, R. Horowitz, A.P. Pisano, "Angular Micropositioner for Disk Drives," *Proc. 10th Int. Conf. on MEMS (MEMS '97),* Nagoya, Japan, pp. 454-459, 1997.
3. T. Imamura, T. Koshikawa, M. Katayama, "Transverse Mode Electrostatic Microactuator for MEMS-Based HDD Slider," *Proc. 9th Int. Conf. on MEMS (MEMS '96),* San Diego, CA, pp. 216-221, 1996.
4. C.G. Keller and M. Ferrari, "Milli-Scale Polysilicon Structures," *1994 Solid-State Sensor and Actuator Workshop*, Hilton Head, SC, pp.132-137.
5. A. Singh, D.A. Horsley, M.B. Cohn, A.P. Pisano, R.T. Howe, "Batch Transfer of Microstructures using Flip-Chip Solder Bump Bonding," *Transducers '97*, Chicago, IL, pp. 265-268.
6. N. Wongkomet, Ph.D. Dissertation, Department of Electrical Engineering and Computer Science, University of California at Berkeley, May 1998.

HIGH TUNING-RATIO MEMS-BASED TUNABLE CAPACITORS FOR RF COMMUNICATIONS APPLICATIONS

J. Jason Yao, SangTae Park, and Jeffrey DeNatale
Rockwell Science Center
1049 Camino Dos Rios, Thousand Oaks, CA 91360

ABSTRACT

We have designed, fabricated, and experimentally tested a high tuning-ratio MEMS-based tunable capacitor for RF communications applications. The tunable capacitor is made of single crystal silicon using anisotropic deep silicon etching techniques like the inductively coupled plasma (ICP). The capacitor structure is subsequently released and sputter coated with a metal thin film for improved electrical performances. As application-determined parameters, the nominal base capacitance (unbiased) is designed to be between 1 pf and 5 pf, and the tuning ratio has been demonstrated to be in excess of 300%.

INTRODUCTION

Tunable capacitors, or varactors, are widely used in RF communications applications for low-noise parametric amplifiers, harmonic frequency generators, and frequency controllers such as voltage controlled oscillators (VCO). Conventional solid-state varactors are made in either silicon or gallium arsenide using either p-n or Schottky-barrier junction structures. Several figures of merit used for tunable capacitors include unbiased base capacitance, tuning ratio, equivalent series resistance or quality factor Q, and associated inductance or electrical self-resonance. The value of unbiased base capacitance depends on the circuit requirements of a specific application and the frequency the tunable capacitor is used for. Typical values are on the order of 1 pf. As for the other figures of merit, solid-state components [1] suffer from a small tuning ratio (typically 30%), excessive resistive loss caused by large series resistance and thus a low Q (typically a few 10's), and a low electrical self-resonance due to large parasitics if made on silicon substrates. Drastic measures are often required for the solid-state components to improve on one single parameter, e.g., using light power to increase the tuning ratio [2].

Recent efforts within the MEMS field [3-4] have shown promising results in the realization of a MEMS-based high performance tunable capacitor. These devices were made of parallel metal plates, and the capacitance tuning functionality was achieved by adjusting the spacing between the parallel plates via electrostatic means. Some of the shortcomings of a solid-state varactor, such as large resistive losses, have been overcome with the parallel plate MEMS approach. The tuning range, 16% reported in [3] and 25% in [4], with a theoretical limit of 50%, however, requires further improvement for many RF applications.

The objective of the work presented here is to develop and demonstrate a MEMS silicon-based tunable capacitor that has a continuous tuning range of at least 300%, or a 3-to-1 tuning ratio. Other parametric requirements of the tunable capacitor include a high Q factor or a minimum equivalent series resistance, and a high electrical self-resonant frequency or a small inductance value. This paper will discuss in detail the design, modeling, fabrication, and experimental results obtained thus far. The combination of these MEMS performance advantages, along with others including smaller size, lower weight, lower manufacturing cost via batch fabrication techniques, improved linearity, and reduced parts count, should make the MEMS device a suitable and attractive replacement for solid-state varactors in a wide range of RF communications applications.

DEVICE DESIGN

The design of the MEMS tunable capacitor is tightly oriented around its objective to replace solid-state varactors in an existing military application. Although the concept of a MEMS tunable capacitor can be applied to many military and commercial applications, and consequently the device can be designed quite differently to meet the different needs of various applications, the work described in this paper has a focused set of parametric goals since its application is defined and specific. The theory behind the design is thus strictly application-driven, while the MEMS technology is both enabling and enhancing.

Table 1 lists a set of key device parameters. These parameters define the design-space for the tunable capacitor, which will be further illustrated through the detailed discussions in the following sub-sections.

Parameter	Performance
Tuning Ratio	3 to 1
Base Capacitance (unbiased)	1-5 pf
Tuning Voltage	< 15 V
Quality Factor Q	100 @ 400 MHz
Electrical Self-Resonance	5 GHz

Table 1: Key parameters for the tunable capacitor define the device's fundamental design-space.

Tuning Range

The electrostatic actuation scheme is predetermined as the preferred choice of actuation for its ultra low power-consumption characteristic. However, when electrostatic actuation is applied to a cantilevered parallel plate system, the equilibrium between the electrostatic attracting force and the spring back force of the cantilever holds only for a deflection smaller than or equal to one-third of the initial gap between the two parallel plates. Once that limit of one-third of the initial gap is surpassed, the electrostatic force becomes larger than the spring back force, and the cantilever system will snap shut, or become unstable. This limitation imposes a theoretical limit of 50% on the tuning range of any electrostatically actuated parallel plate system:

$$MTR = \frac{\frac{\varepsilon A}{\left(1 - \frac{1}{3}\right) \cdot x_0} - \frac{\varepsilon A}{x_0}}{\frac{\varepsilon A}{x_0}} = 50\% \qquad (1)$$

where MTR is the maximum tuning range, ε is the dielectric constant, A is the surface area, and x_0 is the initial gap between the two parallel plates.

Unlike the parallel plate system, the interdigitated "comb" structure does not have the 50% tuning-range limitation. Its movement relies on the electrostatic force generated by fringing fields at the ends of the "comb" structure, and thus is independent of and not limited by the gap spacing between the two electrodes. This configuration allows a large motion on the order of 10's μm with a relatively small actuation voltage, thus a large tuning range for the tunable capacitor, and is the preferred choice of design.

0-9640024-2-6/hh1998/$20©1998TRF
DOI 10.31438/trf.hh1998.28

Solid-State Sensors, Actuators, and Microsystems Workshop
Hilton Head Island, South Carolina, June 8-11, 1998

Base Capacitance

The base capacitance, or the unbiased capacitance, is the minimum capacitance when only a unidirectional drive is used for actuation and tuning. This capacitance needs to be between 1 pf and 5 pf, required by the specific application. To achieve this large capacitance, the capacitance density must be maintained as high as possible.

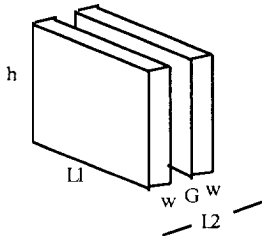

Figure 1: A schematic drawing illustrates a basic parallel plate capacitor structure.

Figure 1 illustrates a unit cell of a basic parallel-plate system, which is a convenient model for general capacitors. The total capacitance, C_0, is:

$$C_0 = [\varepsilon * h * L_1/G] * [L_2/(G+w)] \quad (2)$$

or, the capacitance per unit area is:

$$C_0/(L_1 * L_2) = \varepsilon * h/[G*(G+w)] \quad (3)$$

Equation 3 demonstrates conclusively that the aspect ratio (height, h, over lateral dimensions, G or w) must be kept large to maximize the overall capacitance per unit area. This conclusion suggests that the deep anisotropic silicon etch technique using inductively coupled plasma (ICP) is an excellent manufacturing technology for the tunable capacitor device.

Tuning Voltage and Microphonics

The tradeoff between the tuning voltage and microphonics is a key design issue for the tunable capacitor. With a predetermined capacitance, the required tuning voltage for a certain tuning range depends on the spring constant of the system. To reduce the tuning voltage, the spring constant needs to be kept small. However, an excessively small spring constant will result in unwanted microphonics related problems, and cause the device to be sensitive to environmental vibrations.

In this design work, the focus is on minimizing microphonics while maintaining the tuning voltage within an allowed range predetermined by the system employing the tunable capacitor. Once the tuning voltage is determined, the spring constant can also be determined thereafter. The effort is then focused on minimizing the device mass without compromising the overall capacitance. A mechanical resonant frequency of 20 kHz is determined to be sufficiently high for the tunable capacitor applications. Table 2 illustrates two possible but extreme scenarios where sufficient resolutions can still be maintained for a design where the maximum tuning range of 3 to 1 is achieved with a device movement of 10 μm. For the specific application the tunable capacitor is designed, a resolution of 9 bit is sufficient.

	Scenario 1	Scenario 2
Vibration	10 g	1 g
Resonant Freq.	20 kHz	20 kHz
Deflection	6 nm	0. 6 nm
Tuning Range	10 μm	10 μm
Resolution	10 bit	14 bit

Table 2: Microphonics presents minimal effects on the MEMS based tunable capacitor.

Equivalent Series Resistance and Quality Factor Q

The equivalent series resistance and quality factor, Q, are two interdependent parameters, used to partially describe the electrical performance of a capacitor. The quality factor is defined as the ratio between the imaginary term of a capacitor and its real term, or:

$$Q = (\omega CR)^{-1} \quad (4)$$

where R is the equivalent series resistance of a capacitor.

Single crystal silicon is a preferred mechanical material for the tunable capacitor for the reasons mentioned previously, including the high aspect ratio achievable with ICP and its other superior mechanical properties. However, silicon is not a good conductor to provide a low equivalent series resistance and a high Q. Highly doped silicon is especially cautioned because its conductivity, though higher, is still not high enough to be used as a good electrical conductor for the capacitor. In addition, the increased stress level in a heavily doped silicon material may present other challenges in manufacturing of a large MEMS structure. A preferred embodiment is to use silicon as the main mechanical material, and subsequently coat the silicon structure with a layer of metal thin film, such as aluminum, for its good electrical conductivity. Since the metal thin film is a small portion of the metal-silicon structure, the overall device behaves mechanically like single crystal silicon and electrically like aluminum, and thus combines the advantages of the two materials.

Inductance and Electrical Self-Resonance

The associated inductance within a capacitor and the capacitor's electrical self-resonance are two other interdependent parameters often used to describe the capacitor's RF performance. The electrical self-resonance, ω_0, is defined as:

$$\omega_0 = (LC)^{-1/2} \quad (5)$$

where L is the associated inductance within a capacitor, C. Since as the frequency increases, the impedance of a capacitor decreases while that of an associated inductor increases, the overall "capacitor" device becomes inductive when frequency is higher than the self-resonant frequency. Therefore, the self-resonant frequency of a capacitor determines the frequency range in which the capacitor can be used effectively.

To have a high electrical self-resonance, a capacitor must have its associated inductance as small as possible. This involves detailed design to address the tradeoffs between the issues in the mechanical domain and those in the electrical domain, and is beyond the scope of this presentation.

With the confinements of the parametric requirements listed above, the tunable capacitor design is graphically illustrated in Fig. 2. This design presents a two-terminal device solution, which can be schematically illustrated as in Fig. 3(a). The RF signal shares the same two terminals with the biasing or tuning voltage. This configuration resembles very much a solid-state varactor diode, in which biasing choke is needed to isolate the RF signal and the tuning voltage. A more integration-compatible solution that would eliminate the need of large biasing inductors is schematically represented in Fig. 3(b), where a separate tuning capacitor is used. This tuning capacitor can be made much larger than the RF capacitor for linearity purposes, and is mechanically joined with the RF capacitor at the shared ground terminal. Movements generated by the tuning capacitor will thus cause mechanical motion in the RF capacitor, and hence realize the tuning capability. Figure 4 shows a micrograph of such a three-terminal tunable capacitor device. Note that due to the complexity in biasing, solid-state varactors are normally used with one terminal grounded. Hence, the three-terminal configuration does not present any

additional constraints to its applications as a replacement to the solid-state varactors.

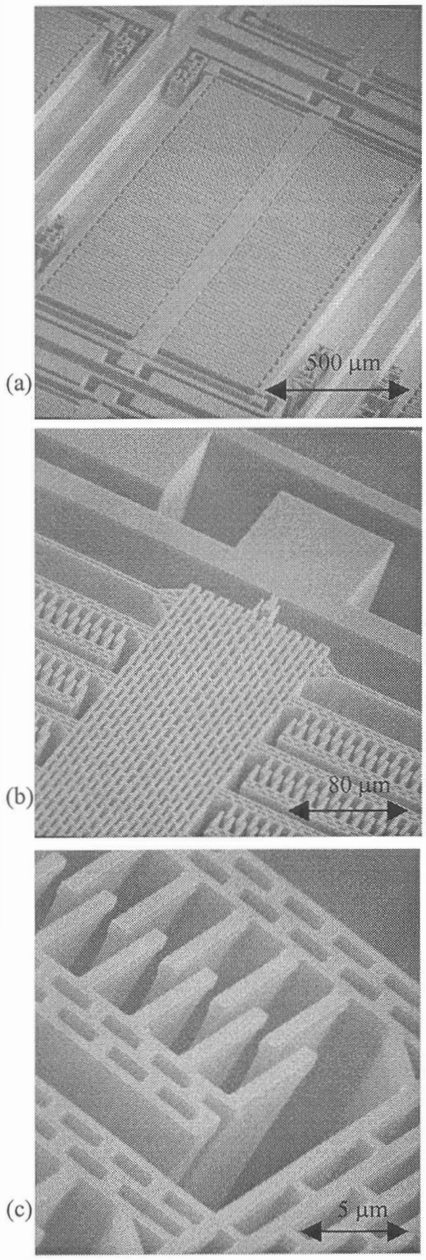

Figure 2: Scanning electron micrographs with three different magnifications showing perspective views of a MEMS-based tunable capacitor. The high aspect-ratio and the anisotropic side-wall profile provided by ICP are critical to the performance of the tunable capacitor.

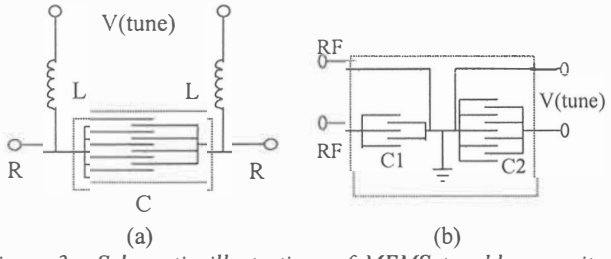

Figure 3: Schematic illustrations of MEMS tunable capacitors. The dashed boxes highlight the MEMS portion.

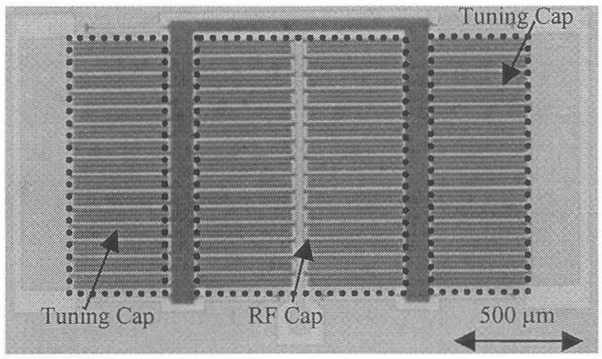

Figure 4: Top view micrograph of a three-terminal tunable capacitor that offers independent tuning and RF connections.

EXPERIMENT AND RESULTS

The tunable capacitor typically occupies an area of 1 mm^2, and is comprised of a large array of interdigitated "comb" or "finger" structures, which are 2-µm in width, 2-µm spaced, and nominally 30 µm in height, Fig. 2. By applying a tuning voltage between the "fingers", an electrostatic force is created to move the suspended structures relative to each other and to change the overlapping distance between the "fingers", and thus the total capacitance. The single crystal silicon device is created using anisotropic deep silicon etching techniques like the inductively coupled plasma (ICP). The starting material is a silicon on insulator (SOI) wafer, with the device silicon layer approximately 30 µm thick and a silicon dioxide interlayer of 2 µm. Figure 5 schematically illustrates the process sequence.

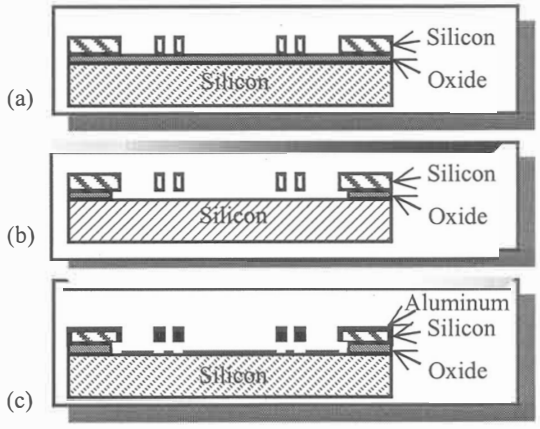

Figure 5: Schematic illustration of the 1-mask process sequence.

The structural pattern of the tunable capacitor design is first transferred to the device silicon layer using photolithography and ICP anisotropic etch, stopping on the underlying silicon dioxide layer, Fig. 5(a). Figure 6 is a scanning electron micrograph of a cross sectional view of the silicon lines and spacing created using such technique. The nominal line width and spacing are 2 µm, and the silicon height in this particular sample is 20 µm. The buried silicon dioxide layer is then selectively removed using hydrofluoric acid, and dried in a super critical carbon dioxide vessel, Fig. 5(b). A coat of aluminum is sputtered on after the structural release to reduce the equivalent series resistance of the tunable capacitor device. During the metal sputtering, the suspended structure naturally creates an electrical discontinuity between the electrodes within the capacitor and between the capacitor and the substrate. No further metal lithography or etching steps are needed. This results in a single-mask MEMS process that provides the structure, the isolation and the interconnect metallization.

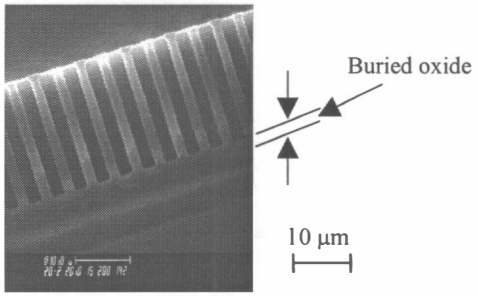

Figure 6: Cross sectional view of silicon structures, 2 μm line and spacing, on buried silicon dioxide layer, created using anisotropic deep silicon etch.

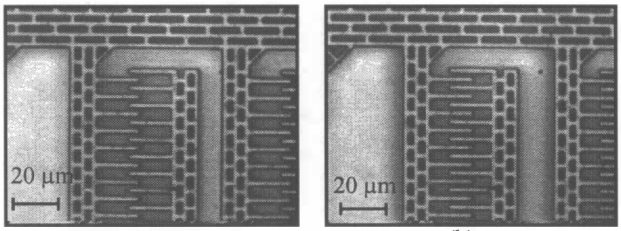

Figure 7: A portion of the tunable capacitor with (a) 0 V and (b) 15 V tuning voltage.

The device has been tested with a DC tuning voltage. Continuous tuning has been observed by varying the tuning voltage, and no resonant operational mode is required. Figure 7 shows a top view of a portion of the tunable capacitor device with the tuning voltage at (a) 0 V and (b) 15 V. The increase in the overlapping distance between the fingers indicates that a tuning ratio of 3 to 1 has been achieved. Alternatively, the capacitance tuning can be characterized by extracting the imaginary part of the Y-parameter out of the measured S-parameters. Figure 8 is a plot of the Y-parameter as a function of the sweeping signal frequency from 30 MHz to 400 MHz. A capacitance change from 3.28 pf with 0 V tuning voltage to 6.44 pf with 5 V tuning voltage has been observed - a tuning ratio of ~ 200% for this particular test.

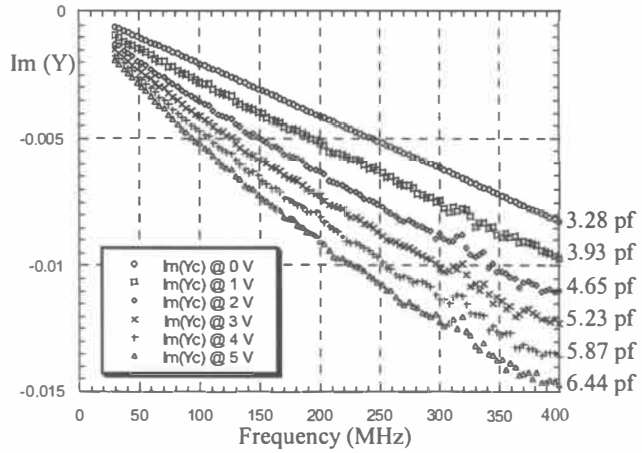

Figure 8: Imaginary part of the extracted Y-parameter from the measured S-parameters as a function of the sweeping signal frequency, showing capacitance tuning of about 200% with 5 V.

Due to the nature of this 1-mask process, the capacitor structure is only about 2 μm away from the underlying silicon substrate. This configuration presents a large parasitic effect in the RF performance of the tunable capacitor. Figure 9(a) illustrates this parasitic effect using S11 in a Smith chart, for a frequency sweep from 30 MHz to 2 GHz. The overall shape, along with the small, local resonant loops, is a clear indication of the unwanted parasitic effect. Based on this learning, we have decided to remove the portion of the silicon substrate directly underneath the tunable capacitor with a second masking step to minimize the parasitic effect. Dramatic improvements have been observed as shown in Fig. 9(b), which is a S11 plot for a frequency sweep from 30 MHz to 6 GHz. This improved tunable capacitor exhibits a near-ideal capacitive behavior with an electrical self-resonance as high as 5 GHz.

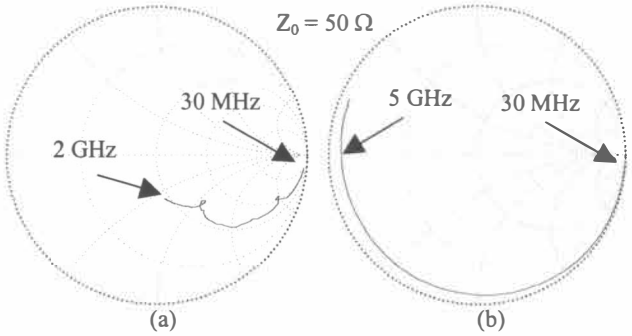

Figure 9: S11 plots showing (a) strong parasitic effects with silicon substrate intact, and (b) minimal parasitic effects with portions of the silicon substrate removed.

CONCLUSION

The MEMS tunable capacitor presented in this paper uses an interdigitated "comb" structure approach, and eliminates the 50% tuning limit in the parallel plate approach. In addition to the advantages demonstrated in the parallel-plate MEMS approach, we have experimentally demonstrated a large tuning ratio in excess of 300%. Minimal parasitic effects have been achieved by removing portions of the underlying silicon substrate. It should be noted that these tunable capacitors are tuned in a non-vacuum environment with a small tuning voltage less than 15 V of a frequency from DC up to the mechanical resonance of the structures, which is typically between 5 kHz and 10 kHz. The MEMS tunable capacitor presented here does not use resonant mode of tuning operation, which is not acceptable for most RF applications.

ACKNOWLEDGEMENTS

This work is supported by DARPA/ETO MEMS Program under BAA 96-19, Contract # F30602-97-C-0091. The authors also express their thanks to the RSC Clean Room Staff and Test Engineers for their help and support in the development of this project.

REFERENCES

[1] M. Soyuer, K. A. Jenkins, J. N. Burghartz, and M. D. Hulvey, "A 3V 4 GHz nMOS Voltage-Controlled Oscillator with Integrated Resonator," in Technical Digest – IEEE International Solid-State Circuit Conference, Feb. 1996, pp. 394-395

[2] D-W Kim and Y-S Kwon, "Photoresponse of Area-Variable Varactor Diode," Electronics Letters, v 32, n 5, Feb. 29, 1996, pp. 466-467

[3] D. J. Young and B. E. Boser, "A Micromachined Variable Capacitor for Monolithic Low-Noise VCOs," in Technical Digest – Solid State Sensor and Actuator Workshop, 1996, pp. 86-89

[4] A. Dec and K. Suyama, "Micromachined Varactor with Wide Tuning Range," Electronics Letters, v 33, n 11, May 22, 1997, pp. 922-924

A Low-Noise RF Voltage-Controlled Oscillator Using On-Chip High-Q Three-Dimensional Coil Inductor and Micromachined Variable Capacitor

Darrin J. Young, Vincent Malba*, Jia-Jiunn Ou, Anthony F. Bernhardt*, and Bernhard E. Boser
EECS Department, University of California, Berkeley, CA 94720
* Lawrence Livermore National Laboratory

ABSTRACT

A RF voltage-controlled oscillator (VCO) employs an on-chip, high-Q, three-dimensional (3-D) coil inductor and micromachined variable capacitor for frequency tuning. Unlike conventional spiral inductors, the 3-D inductor minimizes the substrate loss and achieves a record Q of 30 at 1 GHz. The micromachined variable capacitor achieves a 15% tuning range with a nominal 2pF capacitance and a Q value above 60 at 1 GHz. Both passive components are fabricated on silicon substrates and thus amenable to monolithic integration with standard IC processes. The prototype VCO exhibits a phase-noise of -136 dBc/Hz at 3 MHz offset frequency from the carrier, suitable for most wireless communication applications, in particular GSM [**1**]. The VCO is tunable from 855 MHz to 863 MHz under 3V, limited by the test setup.

INTRODUCTION

Increased demand for wireless communication motivates a growing interest in monolithic personal communication transceivers [**2**]. Current radio designs, however, depend on off-chip components to implement key building blocks such as the low-noise RF VCOs. The off-chip devices increase package complexity, final system area, and cost. Therefore, monolithic implementations are highly desirable.

The various cellular telephony standards require VCOs with frequencies in the low Gigahertz range and a tuning range less than 5% of the carrier frequency. Narrow channel spacing and large blocking signals call for an extremely low phase-noise from the oscillator. Phase-noise below -135 dBc/Hz at 3 MHz offset frequency, for example, is required for GSM [**1**].

Current VCO designs in personal communication transceivers employ an off-chip high-Q LC tank circuit to meet the low phase-noise requirement. Typical values are on the order of 5 nH with a Q of 30 for the inductor, and 2 pF with a Q of at least 50 for the varactor. Frequency tuning is achieved by modulating the depletion width of the varactor diode. A typical capacitance change of at least 10% is required to cover the tuning range. However, the off-chip components rely on processes and materials that differ substantially from standard IC fabrication and are consequently not compatible for monolithic integration.

On-chip silicon junction capacitors and spiral inductors have also been used to implement monolithic VCOs. However, this approach results in a poor phase-noise because of the low Q passive components [**3**, **4**]. The silicon junction diodes exhibit an excessive series loss resulting in a limited Q value below 10. The on-chip spiral inductors suffer from an even lower Q around 3 at 1 GHz [**5**]. Two issues contribute to this low quality factor: eddy currents in the substrate and metal resistive losses. The first problem can be addressed in part by removing the silicon substrate underneath the inductor, leading to a Q value around 5 [**6**]. Reference [**7**] reports a Q close to 10 at 1 GHz by using copper traces on sapphire substrate. While improving the Q value, sapphire substrates are incompatible with standard IC processes.

In this paper, we report a low phase-noise RF VCO using a silicon IC-compatible, high-Q, 3-D coil inductor [**8**] and micromachined variable capacitor [**9**]. The oscillator achieves a low phase-noise suitable for most wireless communication applications. To reduce the fabrication complexity of the prototype oscillator, the inductor, variable capacitor, and active electronics are realized on separate substrates and wire bonded to form the VCO. Because all the components are fabricated on silicon wafers, they are amenable to integration on the same substrate.

MONOLITHIC 3-D COIL INDUCTOR

The 3-D high-Q coil inductor, shown in Figure 1, is one of the key elements to achieve a low phase-noise in the VCO. The device consists of two turns of 5 μm-thick, 50 μm-wide copper traces electroplated around an alumina core. Compared to spiral inductors, this geometry minimizes the coil area in close proximity to the substrate and hence the eddy current loss, which is the dominant contributor to the limited Q value of spiral designs. The proposed device thus achieves a maximized Q and self-resonant frequency. Copper is selected as the interconnect metal for its low sheet resistance, critical for achieving a high Q. Alumina is used as the core material because of its negligible loss tangent at high frequencies, another key parameter to ensure a high Q value.

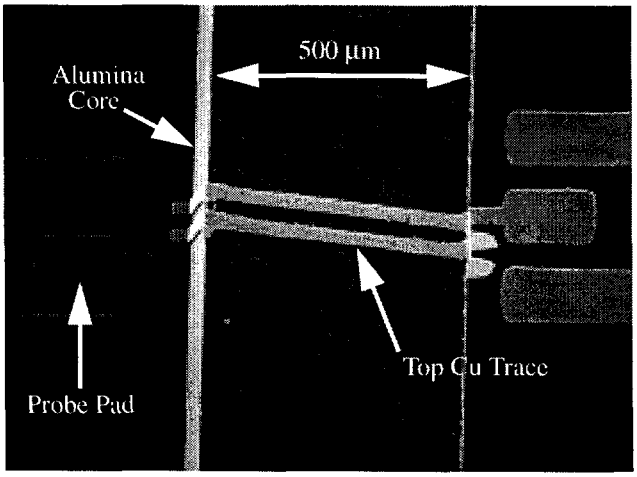

(1a) Top View

0-9640024-2-6/hh1998/$20©1998TRF
DOI 10.31438/trf.hh1998.29

Solid-State Sensors, Actuators, and Microsystems Workshop
Hilton Head Island, South Carolina, June 8-11, 1998

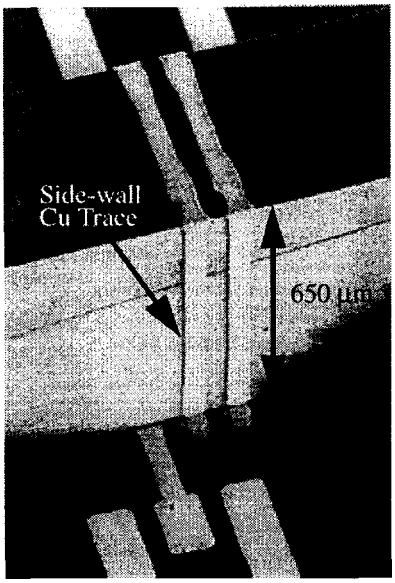

(1b) Side View

Figure 1. SEM of a Two-Turn 3-D Coil Inductor

The fabrication process is described in reference [8] in details. Figure 2 illustrates the simplified process flow. A 5 µm thick low-temperature oxide is deposited first to serve as an insulating layer (Fig. 2a). Electroplated copper with 5 µm thickness forms the inductor bottom metal traces (Fig. 2b-2c). The alumina core is then attached to the bottom traces with an adhesive film and covered by sputtered copper seed layer with electroplated photoresist on top (Fig. 2d). To fabricate the copper traces on the side-wall and the top of the core, the resist is exposed with a three-dimensional maskless direct-write laser lithography tool. After developing the resist, 5 µm thick copper traces are electroplated around the core to complete the inductor coil (Fig. 2e). Because of the low processing temperature (170 ^{o}C maximum), the inductors can be fabricated on top of wafers with completed electronics without affecting the characteristics of active devices. This is particularly crucial in RF applications where the availability of the most recent IC technology is a critical competitive advantage.

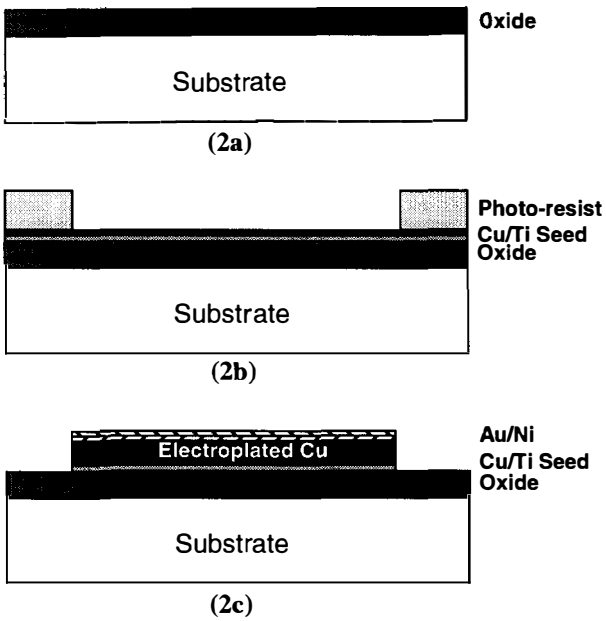

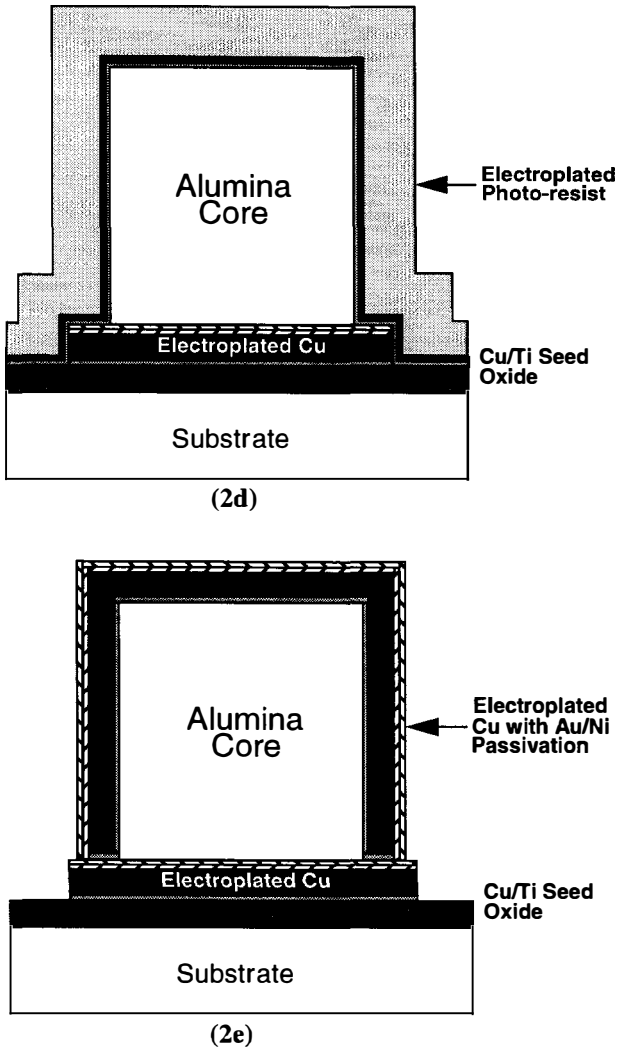

Figure 2. 3-D Inductor Fabrication Process Flow

The fabricated two-turn inductor achieves 8.2 nH inductance with a measured Q of 16 at 1 GHz, as shown in Figure 3.

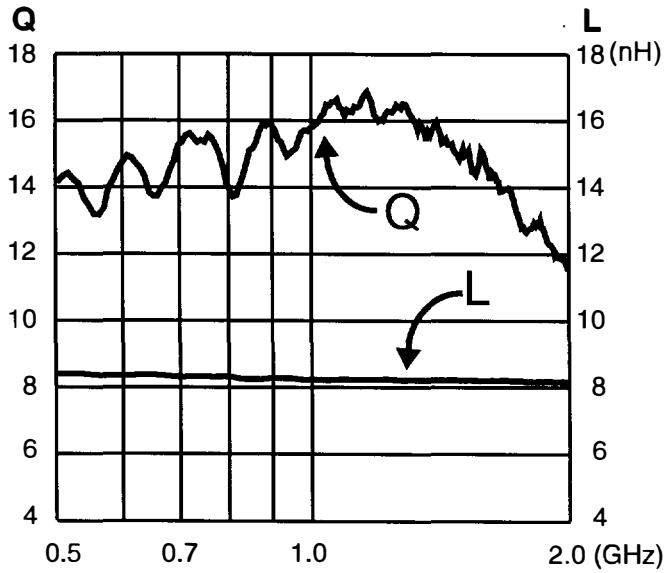

Figure 3. L and Q vs. Frequency for a Two-Turn Inductor

This performance is substantially superior to that of spiral inductors with typical Q values around 3. A one-turn inductor demonstrates a record Q of 30 measured at 1 GHz with 4.8 nH inductance, which matches the quality factor of discrete counterparts. The self-resonant frequencies for these devices are over 8 GHz, well above the frequency of interest.

MICROMACHINED VARIABLE CAPACITOR

The high-Q variable capacitor is another key element in the low phase-noise VCO. This is realized as a surface-micromachined all-aluminum microstructure [9]. Figure 4 presents an SEM of a fabricated single capacitor. It consists of a thin aluminum plate suspended in air nominally 1.5 μm above a bottom aluminum layer by four mechanical springs. Aluminum is selected as the structural material for its low sheet resistance, critical for achieving a high Q value.

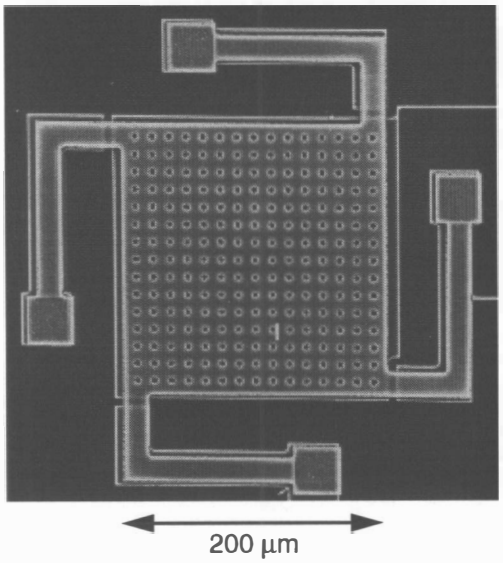

Figure 4. SEM of a Micromachined Variable Capacitor

A DC bias applied across the capacitor causes an electrostatic pull-down force and consequent reduction of the air gap, resulting in a capacitance increase. Figure 5 shows four such capacitors connected in parallel with 2.04pF at zero bias and 2.35pF at 3V, corresponding to a 15% capacitance increase. The variable capacitor achieves a measured Q over 60 at 1GHz. This matches or exceeds the quality factor of discrete varactor diodes, and is at least an order of magnitude better than that of a typical on-chip silicon junction capacitor.

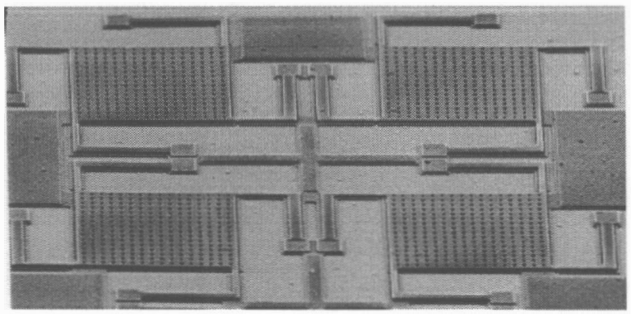

Figure 5. Four Parallel-Connected Micromachined Capacitors

The fabrication technology is fully compatible with standard IC processing [9], permitting the capacitor to be fabricated on top of wafers with completed electronics. Ultimately, the micromachined capacitors could be realized with copper, permitting co-fabrication with the inductors. It is expected that the low intrinsic stress of electroplated copper [10] would also reduce the warping, thus allowing a smaller air gap. This would result in a reduced area and tuning voltage.

PROTOTYPE VCO AND MEASUREMENTS

The high-Q passive components and a CMOS die containing active electronics are attached to a test board and wire bonded to form the VCO, as shown in Figure 6.

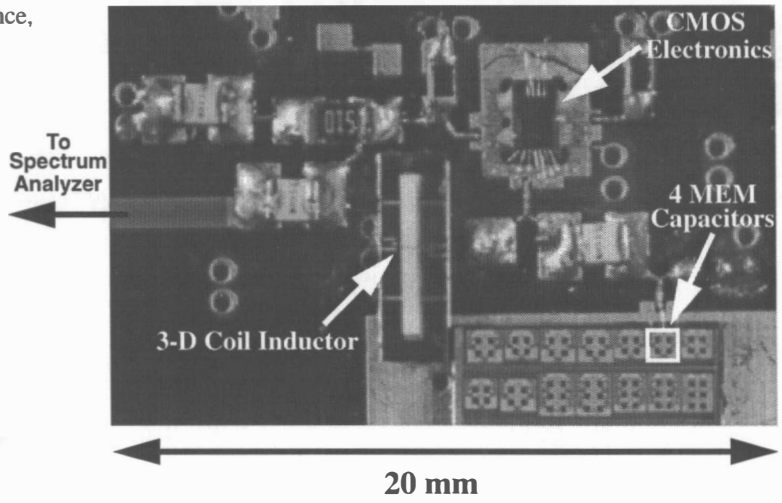

Figure 6. Prototype VCO Test Board

Figure7 illustrates the VCO configuration. The Colpitt's oscillator topology is chosen for its simplicity. The electronics are fabricated with HP's 0.8 μm CMOS process.

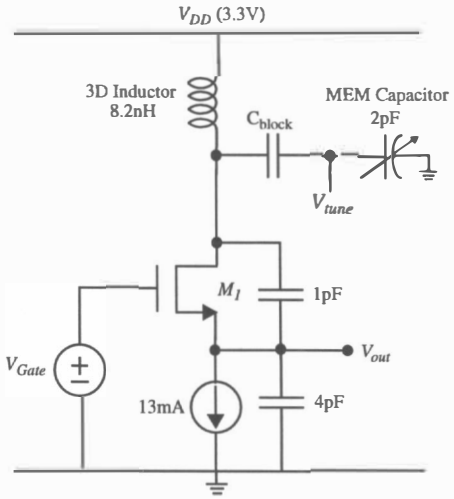

Figure 7. VCO architecture

Figure 8 shows the oscillator output power spectrum at 863MHz with a phase-noise of -136 dBc/Hz measured at 3 MHz offset frequency, as plotted in Figure 9.

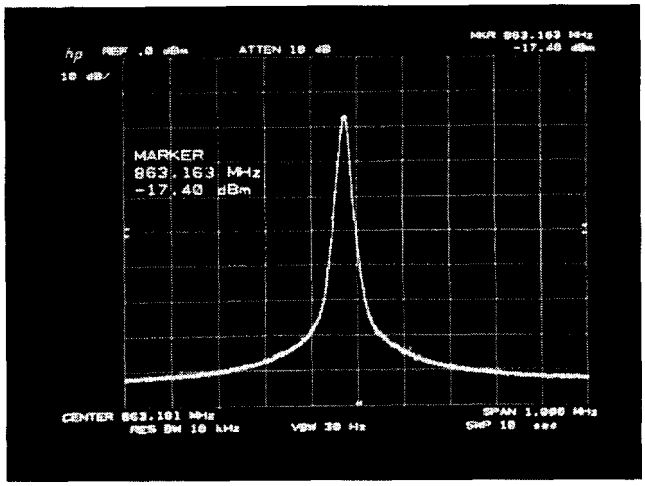

Figure 8. VCO Output Power Spectrum

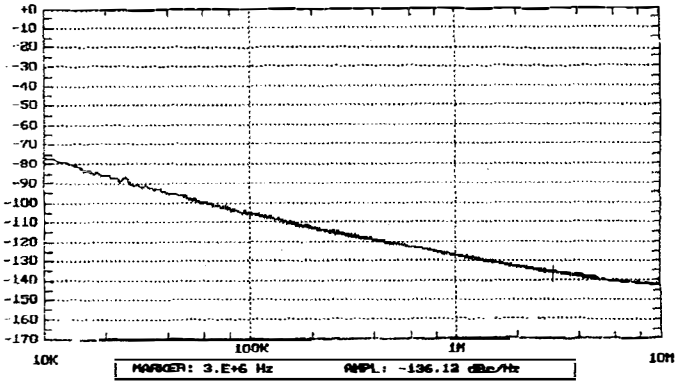

Figure 9. Measured Phase-Noise Plot

This performance is suitable for most wireless communication applications, in particular GSM. This level of performance has not been achieved by VCOs relying on on-chip spiral inductors and silicon junction capacitors. The prototype oscillator dissipates 43 mW from a 3.3 V supply, and is tunable from 855 MHz to 863 MHz over 3V limited by the parasitics of the test setup.

CONCLUSION

A prototype RF VCO has been built using an on-chip, IC-compatible, high-Q, 3-D coil inductor and micromachined variable capacitor. These passive components match or exceed the performance of discrete counterparts. They are also amenable to monolithic integration with standard IC processes. The oscillator meets the stringent GSM phase-noise requirement and demonstrates that a complete monolithic high-performance VCO can be achieved for cellular telephony applications.

ACKNOWLEDGMENTS

The authors wish to thank Christopher Harvey, Leland Evans, and Robert T. Graff from Lawrence Livermore National Laboratory for the processing assistance. Certain fabrication steps were carried out in the Berkeley Microfabrication Laboratory. Phase-noise testing was performed at Philips Semiconductors.

REFERENCES

[1] P. Davis, et al., "Silicon-on-Silicon Integration of a GSM Transceiver with VCO Resonator", *ISSCC Dig. Tech. Papers*, pp.248-249, February 1998.

[2] P. R. Gray, R. G. Meyer, "Future Direction in Silicon ICs for RF Personal Communications", *CICC Dig. Tech. Papers,* pp. 83-90, May 1995.

[3] B. Razavi, "A 1.8GHz CMOS Voltage-Controlled Oscillator", *ISSCC Dig. Tech. Papers*, pp. 388-389, February 1997.

[4] M. Zannoth, B. Kolb, J. Fenk, and R. Weigel, "A Fully Integrated VCO at 2GHz", *ISSCC Dig. Tech. Papers*, pp. 224-225, February 1998.

[5] J. N. Burghartz, et al., "Microwave Inductors and Capacitors in Standard Multilevel Interconnect Silicon Technology," *IEEE Transactions on Microwave Theory and Techniques.* vol. 44, no. 1, pp. 100-104, January 1996.

[6] J. Y-C. Chang, A. A. Abidi, and M. Gaitan, "Large Suspended Inductors on Silicon and Their Use in a 2-μm CMOS RF Amplifier," *IEEE Transactions on Electron Device Letters*, vol. 14, no. 5, pp. 246-248, May 1993.

[7] J. N. Burghartz, et al., "Monolithic Spiral Inductors Fabricated Using a VLSI Cu-Damascene Interconnect Technology and Low-Loss Substrate," *IEDM Dig. Tech. Papers*, pp. 96-99, December 1996.

[8] D. J. Young, V. Malba, J. J. Ou, A. F. Bernhardt, and B. E. Boser, "Monolithic High-Performance Three-Dimensional Coil Inductors for Wireless Communication Applications," *IEDM Dig. Tech. Papers*, pp. 67-70, December. 1997.

[9] D. J. Young and B. E. Boser, "A Micromachined Variable Capacitor For Monolithic Low-Noise VCOS," *Solid-State Sensor and Actuator Workshop, Dig. Tech. Papers*, pp. 86-89, June 1996.

[10] L. -S. Fan, S. J. Woodman, R. C. Moore, L. Crawforth, T. C. Reiley, and M. A. Moser, "Batch-Fabricated Area-Efficient Milli-Actuators," *Solid-State Sensor and Actuator Workshop, Dig. Tech. Papers*, pp. 38-42, June 1994.

Electrostatically Actuated Microswitches; Scaling Properties

N.E. McGruer, P.M. Zavracky, S. Majumder, and R. Morrison
Department of Electrical and Computer Engineering, Northeastern University
360 Huntington Ave., Boston, MA 02115

G.G. Adams
Department of Mechanical, Industrial, and Manufacturing Engineering, Northeastern University
360 Huntington Ave., Boston, MA 02115

ABSTRACT

The continuing need for small switches with very high ratios of off impedance to on impedance has sparked interest in microfabricated switching devices. By scaling the vertical dimensions of electrostatically-actuated, surface-micromachined, micromechanical switches, we have reduced the threshold voltage from approximately 130 V to 24 V, while maintaining the contact and separation forces constant. By increasing the number of contacts, the current handling capacity has been increased by an order of magnitude to 150 mA.

INTRODUCTION

Development of microfabricated switching devices is being stimulated by a continuing need for small switches with very large ratios of off impedance to on impedance. Low on-state resistances are achieved by bringing two conductors into physical contact; high off-state impedances are a result of using small contact areas to minimize capacitance. Examples of such microfabricated switching devices employing electrostatic [1,2,3,4,5,6,7,8,9,10], magnetic [11,12], and thermal [13,14] actuation have been reported. The ideal actuation method would operate both at low power levels and at low voltages. In contrast to magnetic or thermally actuated devices, electrostatically actuated switches inherently operate at very low power levels, and are relatively simple to fabricate. However, with the exception of some low-force devices prone to contact sticking, devices reported to date generally have had threshold voltages for contact closure of over 50 V.

In previous publications, we have described the design, fabrication, and preliminary electrical characteristics of electrostatically-actuated, surface-micromachined, micromechanical switches and relays. [1,15,16,17] An SEM micrograph of such a microswitch is shown in Figure 1. When a voltage is applied to the gate electrode the beam bends down and brings the contact tip under the beam into contact with the drain electrode. When the voltage is removed, the restoring force of the beam pulls the contact away from the drain, overcoming stiction forces. These devices typically had threshold voltages for contact closure of 50 to 200 V. In this work, we have reduced the threshold voltage of our devices by nearly an order of magnitude, to 21 Volts, while maintaining the same contact and separation forces. This threshold voltage reduction was guided by one of the simple scaling laws described in the next section. Lower contact force switches of the same design have operated at voltages as low as 6V. We have also increased the current handling capacity of the microswitches, to at least 150 mA, by increasing the number of contacts from 2 to 64, again maintaining the same force per contact. The devices discussed here have gold-gold contacts. Individual microswitch contacts typically have an initial resistance of 0.1-1Ω, and a current handling capability of over 15 mA with no visible contact damage after 10^8 cycles.

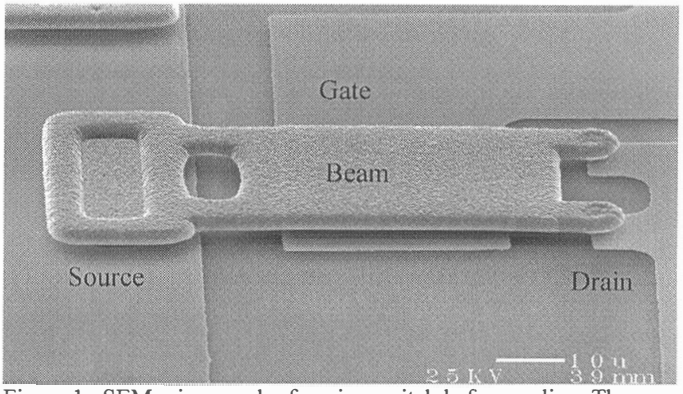

Figure 1. SEM micrograph of a microswitch before scaling. The indentations at the free end of the cantilever correspond to contact bumps underneath the beam.

SCALING LAWS

Scaling laws for electrostatically actuated switches, analogous to the well-known constant-field scaling law for MOS devices, can be derived using plate theory and the fact that the electrostatic force is proportional to the square of the electric field. These simple scaling laws are useful in rapidly transforming designs in force, actuation voltage, horizontal dimensions, vertical dimensions, and resonant frequency. To simplify this discussion, it will be limited to the scaling of a fixed *design*. In this context, a *design* means a given shape as viewed from above; the size may vary, but all the horizontal dimensions must vary proportionally such that the shape is unchanged. The concept of a *fixed design* is attractive practically as well as conceptually. If the lateral dimensions do not change the scaling can be performed without changing the photomasks used in the microfabrication. Even when the lateral dimensions are scaled proportionally, certain important properties remain constant. One of these is the overvoltage factor, which we define as the ratio V_m/V_t, where V_m is the maximum voltage that can be applied without bringing the beam into contact with the gate, and V_t is the threshold voltage of the device. A second conserved property is the ratio of the contact capacitance to the gate capacitance. One can therefore optimize a design for several important properties, and the design can subsequently be transformed to a more desirable operating voltage, force, or size, depending on the limitations of the fabrication process.

Three scaling laws are described in the following paragraphs, followed by a discussion of the limits of their applicability. The scaling laws describe how the operating voltage, the operating force, or the device size can be changed while

0-9640024-2-6/hh1998/$20©1998TRF
DOI 10.31438/trf.hh1998.30

Solid-State Sensors, Actuators, and Microsystems Workshop
Hilton Head Island, South Carolina, June 8-11, 1998

holding the other two parameters constant. These changes are achieved by adjusting the beam thickness and the separation between the beam and the gate, in addition to the horizontal size. The three scaling laws are summarized in Table 1.

Constant-Horizontal-Size, Constant-Force Scaling to Reduce Actuation Voltage

In this type of scaling the horizontal dimensions remain the same. The vertical dimensions are scaled to reduce the actuation voltage, while keeping the contact and separation forces constant. The three as-fabricated vertical dimensions of interest are shown in Figure 2. They are the gap between the beam and the underlying metallization (d), the tip height (t), and the thickness of the beam (h).

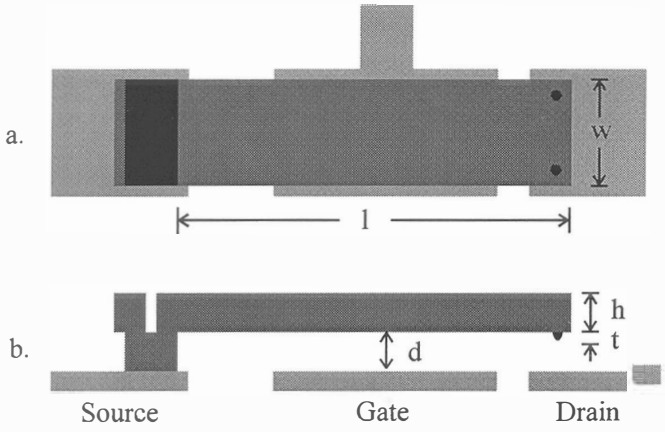

Figure 2. a. Top view of microswitch showing horizontal dimensions w and l. b. Side view of microswitch showing beam thickness (h), beam-gate gap (d), and tip height (t).

The electrostatic force per unit area at the conductor surfaces is given by $\frac{1}{2}\varepsilon E^2$, where ε is the permitivity of the dielectric and E is the electric field at the surface. Since the electrostatic force depends only on the electric field, the force pulling the beam down will remain the same if the electric field does not change with scaling. In the limit of nearly parallel electrodes, and ignoring fringing fields, the electric field will be the same if the vertical dimensions of the dielectric gap (d and t), the vertical deflection of the beam, and the actuating voltage are all multiplied by the same scaling factor, k_1 ($k_1<1$).

To complete the scaling, the restoring forces exerted by the scaled beam for the scaled deflection must be equal to the to the original restoring forces. The restoring forces are proportional to the deflection and to the stiffness of the beam. Since the deflection is scaled down by the factor k, the stiffness must be scaled up by the factor $1/k_1$. The stiffness is proportional to h^3, so this may be achieved by increasing the beam thickness by the factor $k_1^{-1/3}$.

Constant-Force, Constant-Voltage Scaling to Reduce Size

The object here is to reduce the horizontal dimensions of the device, keeping the actuation voltage and the contact and separation forces constant. All horizontal dimensions are reduced by a scaling factor k_2. For example, w and l, shown in Fig. 2, are both reduced. This leads to reduction of the actuator area by a factor k_2^2. To keep the total electrostatic force pulling the beam down constant, the electrostatic force/unit area must be increased by a factor $1/k_2^2$. The force is proportional to the square of the electric field, so the electric field must be increased by a factor $1/k_2$. This is achieved by decreasing the vertical dielectric gap by a factor k, and holding the actuation voltage constant.

Again, the restoring force must kept the same, considering both the reduced horizontal extent of the beam and the reduced deflection of the beam. The stiffness of the structure must be scaled up by a factor of $1/k_2$, since the deflection is scaled down by a factor of k_2. The stiffness is proportional to the width of the beam, w, and to the inverse cube of the beam length, l, and to the cube of the beam thickness (h). Therefore, to increase the stiffness by the factor $1/k_2$, with both horizontal dimensions scaled down by a factor k_2, the beam thickness, h, must be decreased by the factor $k_2^{1/3}$.

Constant-Voltage, Constant-Horizontal-Size Scaling to Increase Force

Here the horizontal size of the design and the actuation voltage remain constant, but the dielectric gap and the thickness of the beam are adjusted to give higher contact and separation forces. Following the earlier discussion, to increase the electrostatic force by a scaling factor $1/k_3$, the electric field must be increased by the factor $k_3^{-1/2}$. To do this at a constant actuation voltage, the gap must be decreased by the factor $k_3^{1/2}$.

The restoring force is adjusted by increasing the beam thickness. The goal here is to increase the restoring force by the factor $1/k_3$, to match the increase in the electrostatic force. This is done by increasing the beam thickness (h) by the factor $k^{-1/2}$, which increases the beam's stiffness by a factor of $k_3^{-3/2}$. Coupled with the factor of $k_3^{1/2}$ in deflection, the restoring force is increased by the desired factor of $1/k_3$.

	Actuation Voltage	Device Size	Contact Force	Dielectric Gap	Beam Thickness	Resonant Frequency
Reduce voltage	k_1	1	1	k_1	$k_1^{-1/3}$	$k_1^{-1/3}$
Reduce Size	1	k_2	1	k_2	$k_2^{1/3}$	$k_2^{-1.67}$
Increase Force	1	1	$1/k_3$	$k_3^{1/2}$	$k_3^{-1/2}$	$k_3^{-1/2}$

Table 1. Summary of the three scaling laws described in the text in terms of the scaling parameters k_1, k_2, k_3. Note that $k_1<1$, $k_2<1$, $k_3<1$ to reduce voltage, reduce size, or increase force, respectively.

Experimental Results

In this work, one scaling goal was to reduce the actuation voltage of the microswitches, without changing the photomasks, maintaining the same contact force. We chose the constant-horizontal-size, constant-force scaling law to reduce the actuation voltage. This scaling law dictates that the gap between the cantilever beam and the actuation electrode be multiplied by a factor k_1 ($k_1 < 1$) to achieve the same electric field, and consequently the same electrostatic force, at a lower voltage. The beam thickness is multiplied by $k_1^{-1/3}$ to increase its stiffness and maintain the original separation force with the smaller deflection.

The original 120V devices had gold beams, 2.8 μm thick, with a beam-electrode gap of 1.8 μm, similar to the device shown in Figure 1. The length of the device is 70 μm and the width is 30 μm. The contact tip is typically 1/2 of the gap in thickness. The 24 V devices had the gap scaled down by a factor of 8 to 0.23 μm, with a tip 0.11 μm high and a beam thickness of

6.4 μm. A scaled switch is shown in Figure 3. Figure 4 compares the threshold voltages predicted by the simple scaling law above with the measured threshold voltage of scaled switches. Preliminary results indicate that the electrical performance changes little over this range of scaling.

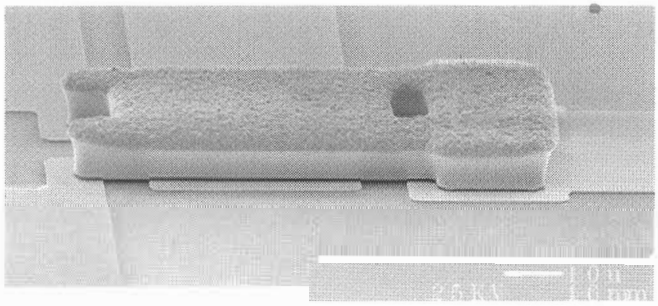

a.

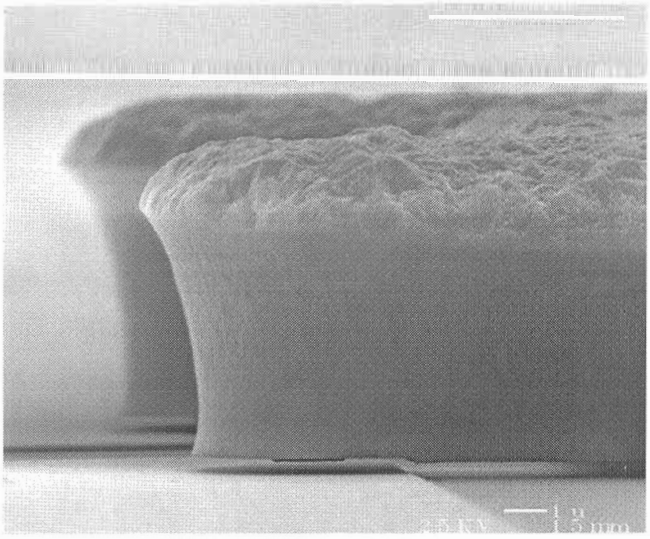

b.

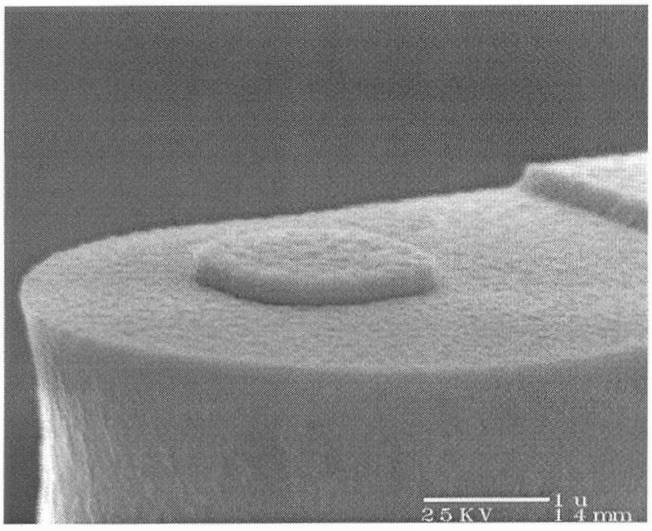

c.

Figure 3. SEM micrographs of scaled microswitch. a. - switch, b - contact end, c - tip detail. Beam thickness 5.8 μm, beam-gate gap 0.33 μm.

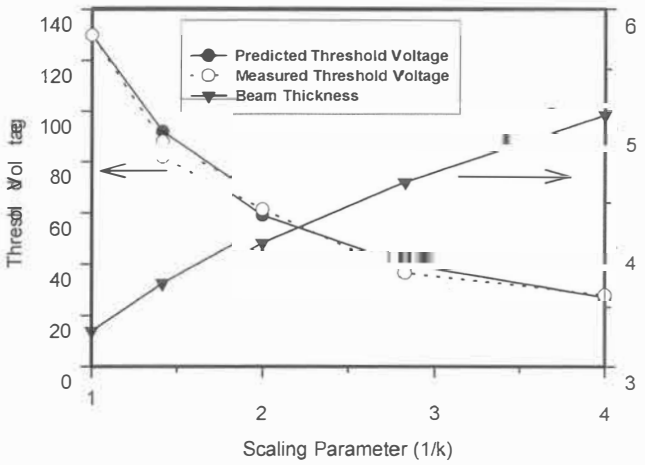

Figure 4. Threshold voltage predicted by the scaling law and measured. The increase in beam thickness with reduction in the beam-gate gap is also shown. The contact total force is approximately 80 μN for the two-contact switch.

A second type of scaling increased the number of contacts in a switch from 2 to 64, as shown in Figure 5. Figure 6 shows that the current handling capacity increases with the number of contacts.

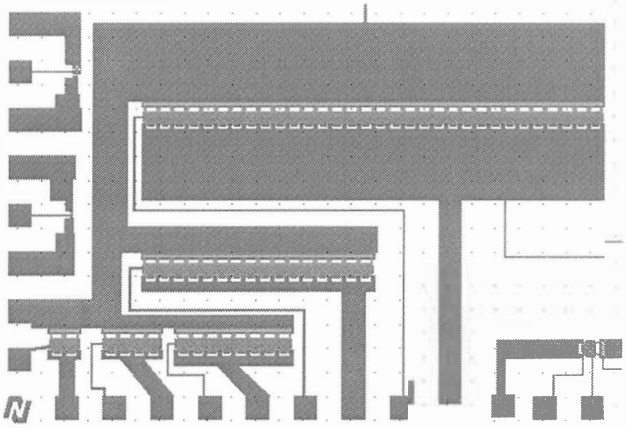

Figure 5. Layout Drawings of single beam multiple contact switches with 4, 8, 16, 32, and 64 contacts.

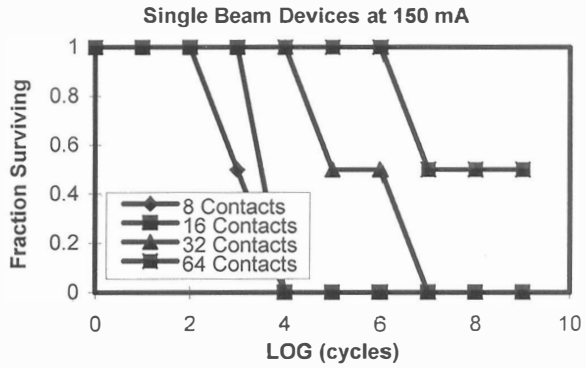

Figure 6. Data from eight devices, two of each number of contacts, showing the improvement in the lifetime with increasing number of contacts, for cold-switched currents. One of the 64 contact devices continued to survive after 10^9 cycles.

The contact resistance is expected to decrease inversely with the number of contacts. Since the contact resistance itself is not

directly accessible, the standard deviation of the contact resistance the first ten cycles is shown in Figure 7 below. The sequence of five switches increase in the number of contacts form 4 to 64 in factors of two. If the contacts were acting equally and in parallel, we would expect a decrease in the standard deviation of a factor of the square root of sixteen for an increase from 4 to 64 contacts, which is approximately what is observed.

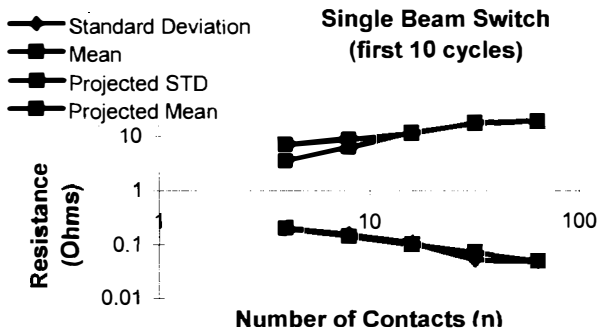

Figure 7. The graph shows plots of the Standard Deviation and the Mean of the total switch resistance as a function of the number of contacts. Two curves are also presented. The linear projection of the standard deviation is based on the value of the formula $Std(4)/\sqrt{n/4}$ where $Std(4)$ is the standard deviation of the resistance of the four contact switch and n is the number of contacts. The projected mean is derived from an estimate of the numbers of squares in the leads to each of the switches shown in Figure 5. The lead resistance of the 64 contact switch is divided by the number of squares for that switch and used as a measure of the sheet resistance for the leads (0.78 Ohms/sq). This is then used to calculate the lead resistance for the other switches and plotted as shown.

DISCUSSION

The scaling laws described above can be applied over a wide range of switch dimensions. However, certain limitations do exist. For example, due to the fabrication process the beams have a residual stress gradient, creating an initial downward curvature. If that stress gradient were constant through the beam thickness, then the downward deflection due to curvature would scale with the square of the beam length and would be independent of the beam thickness. Thus the scaling used in order to reduce the gap would be limited. Fortunately, however, the stress gradients are greatest in the bottom of the beam. Thus as the beam thickness is increased in order to reduce the gap, the effect of the stress gradients on the initial curvature decreases and the thicker beams have less initial curvature.

Another potential limitation is associated with the beam thickness-to-length ratio. For a cantilever beam, if that ratio is greater than 0.1, the correction factor due to shear deformation is less than 1%. However for a beam fixed at one end and pinned at the other end, the shear correction is about 10%. Prior to closing, the switch acts as a cantilever beam, whereas the deformation after closure may approach that of a fixed-pinned beam.

Small horizontal size and low actuation voltage are desirable properties in a microswitch. In addition, relatively large contact and separation forces are desirable to overcome stiction forces and lower the contact resistance.[1,15,18] The scaling laws predict that we can achieve all these goals simultaneously, provided that the gaps between the beam and the gate and between the upper and lower contacts can be reduced sufficiently. Alternatively, the voltage and force goals can be achieved at a larger gap if the horizontal dimensions of the device are increased.

REFERENCES

1. P.M. Zavracky, N.E. McGruer, and S. Majumder, *J. Microelectromech. Sys.*, vol. 6, pp. 3-9, 1997.
2. J.J. Yao and M.F. Chang, "A Surface Micromachined Miniature Switch for Telecommunications Applications with Signal Frequencies from DC up to 4 GHz," *Proc. Transducers '95, Stockholm Sweden*, vol. 2, pp384-387, 1995.
3. J. Simon, S. Saffer, and C.J. (CJ) Kim, *J. Microelectromech. Sys.*, vol. 6, pp. 208-216, 1997.
4. K. Petersen, "Dynamic Micromechanics on Silicon: Techniques and Devices," *IEEE Trans. On Electron Devices*, vol. ED-25, pp. 1241-1250, 1978.
5. J. Randall, C. Goldsmith, D. Denniston, and T-H. Lin, "Fabrication of Micromechanical Switches for Routing Radio Frequency Signals," *J. Vac. Sci. Technol. B*, vol. 14, p. 3692, 1996.
6. M.A. Gretillat, P. Thieubaud, C. Linder, and N.F. de Rooij, *J. Micromech. Microeng.*, vol 5, pp 156-160, 1995.
7. J. Drake, H. Jerman, B. Lutze and M. Stuber, "An electrostatically actuated micro-relay," *Transducers '95 Eurosensors IX*, Stockholm, Sweden (1995).
8. M. Sakata, "An electrostatic microactuator for electro-mechanical relay," *Proc IEEE MEMS Workshop '89 (Salt Lake City, UT)* 149-51 (1989).
9. S. Roy and M. Mehregany, "Fabrication of Electrostatic Nickel Microrelays by Nickel Surface Micromachining," *Proc. IEEE Microelectromechanical Systems Workshop*, Amsterdam, the Netherlands, pp. 353-357, 1995.
10. I. Schiele, J. Huber, C. Evers, B. Hillerich, and F. Kozlowski, "Micromechanical Relay with Electrostatic Actuation," *Proc. Transducers '97, p. 1165, (1997).*
11. H. Hosaka, H. Kuwano, and K. Yanagisawa, " Electromagnetic Microrelays: Concepts and Fundamental Characteristics," *Sensors and Actuators A*, vol. 40, p. 41, 1994.
12. W.P. Taylor, M.G. Allen, and C.R. Dauwalter, "A Fully Integrated Magnetically Actuated Micromachined Relay," *Proc. 1996 Solid State Sensor and Actuator Workshop, Hilton Head, pp. 231-234, 1996.*
13. E. Hashimoto, H. Tanaka, Y. Suzuki, Y. Uenishi, and A. Watabe, "Thermally Controlled Magnetization Actuator for Microrelays," *IEICE Trans. Electron.*, vol E80-C, p. 239, 1997.
14 J. Simon, S. Saffer, and Chang-Jin (CJ) Kim, "A Liquid-Filled Microrelay with a Moving Mercury Microdrop, *J. Microelectromechanical Sys.*, Vol 6, p 208, 1997.
15. S. Majumder, P.M. Zavracky, N.E. McGruer, "Electrostatically Actuated Micromechanical Switches," *J. Vac. Sci. Tech. A*, vol. 15, p. 1246, 1997.
16. S. Majumder, N.E. McGruer, P.M. Zavracky, G.G. Adams, R.H. Morrison, and J. Krim, "Measurement and Modeling of Surface Micromachined, Electrostatically Actuated, Microswitches," *International Conference on Solid-State Sensors and Actuators, Digest of Technical Papers*, Vol. 2, pp. 1145-1148, 1997.
17. S. Majumder, N.E. McGruer, P.M. Zavracky, R.H. Morrison, G.G. Adams, and J. Krim, "Contact Resistance Performance of Electrostatically Actuated Microswitches," *American Vacuum Society, 44th National Symposium* Abstracts, p. 161, 1997.
18. H. Ziad, K. Baert, and H.A.C. Tilmans, "Design Considerations of the Electrical Contacts in (Micro)relays," SPIE Vol. 2882, p. 210, 1996.

MULTI-REGIME INTEGRATED TRANSDUCER NETWORKS

S.C. Jacobsen, M. Olivier, B.J. Maclean, M.G. Mladejovsky and M.R. Whitaker
Sarcos Research Corporation, 360 Wakara Way, Salt Lake, UT 84108
Center for Engineering Design, University of Utah, Salt Lake UT 84112.

ABSTRACT

The approach described in this paper has been used to design and manufacture a variety of sensors and networks for the measurement of: strain, rotation, displacement, pressure, vibration, flow, multi-axis fluid shear, multi-axis strain, touch, multi-axis acceleration, and sound. This paper discusses four example systems.

System State Sensors
- UniAxial Strain Transducer (UAST)
- Rotational Displacement Transducer (RDT)

Fluid State Sensors
- Fluid Shear Transducer (FST)
- Pressure Transducer Network (PTN)

INTRODUCTION

Beginning in 1982, Sarcos Incorporated and the Center for Engineering Design at the University of Utah became involved in an increasing number of projects focused on the development of robots and other sensor-intensive machines. For example, one robotics project for Disney used thousands of high resolution rotation and strain sensors. A typical robot included 50 Degrees-of-Freedom (DOF) and required approximately 90 sensors and 50 actuators. Entertainment robotics projects alone have required over 4000 sensors and 2000 actuators. In these applications, sensors have accounted for up to 30 percent of system cost, and up to half of the system failures have occurred in the supporting wiring harnesses and connectors. Sensors and wiring assemblies have been primary drivers of cost and reliability in other similar applications such as undersea tele-robots, prosthetic limbs, and body motion capture systems (where wiring is routed across moving structures and sensors reside in harsh environments).

In the early 80's, Sarcos began investigating new approaches to sensor and network design [1-5]. Specifically required were robust systems with: high resolution, absolute digital multiplexed output, small size, and low cost. Of main interest were the multiplexed systems which could reduce the wire counts necessary to support interconnected groups of multi-regime sensors.

In 1986 a first proposal was submitted to DARPA entitled "Micro Electro Mechanical Systems" (MEMS). In that project, and others later funded by DARPA, NASA, NAVSEA, and commercial sponsors, a number of approaches were investigated. Sensors are emerging from those development efforts and are now a part of preliminary application efforts in aircraft (F18, F15, C141, C130), helicopters (AH-64 and UH-60), submarines (LSV, RCM), railroad operation monitoring systems, robots, automotive, and structural systems.

APPROACH

The sensors defined herein are composed of two basic subsystems - (1) a planar silicon base which contains an array of many field detectors along with supporting electronics, and (2) a companion array of electrostatic field emitters residing on the surface of an adjacent planar armature made of quartz, sapphire, or glass. Base and armature surfaces interact in close proximity and can, depending on the configuration of emitter and detector arrays, measure specified relative movements between the armature and base with high resolution. Figure 1 shows base and armature structures used in the RDT.

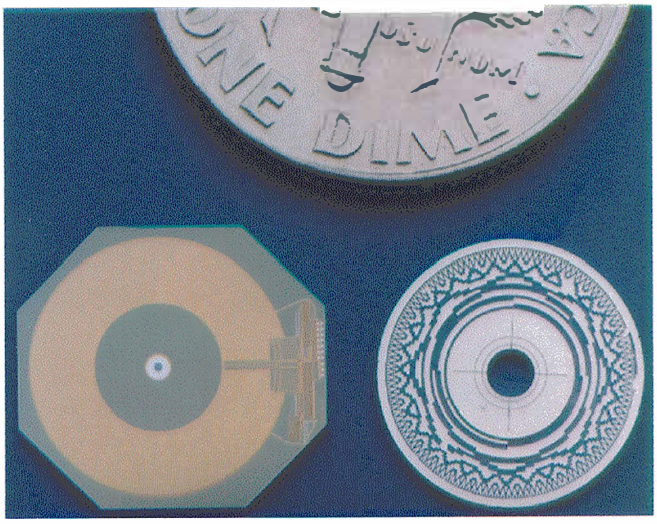

Figure 1. *Base and armature structures used in the Rotary Displacement Transducer (RDT).*

In operation, the gap between armature and base is small and is tightly maintained either by direct contact, between bearing surfaces created on the structures, or by a suspension system composed of adjacent bearings or flexures. In the four examples of this paper, relative movements are restricted to one or two DOF. In other cases relative movements can be up to six DOF.

Emitters and detectors which reside on armatures and bases are the fundamental measuring elements in each sensor. A detector (typically 20 to 150 by 50 to 150 μm) is a conductive region on the base which is connected to a local circuit that performs amplification and conversion functions. An emitter (typically 30 to 200 by 100 to 300 μm) is a conductive region on the armature which is driven either capacitively from the base, or by a connected source. The shape details of emitters and detectors are very different for various sensors.

Emitters and detectors are configured into arrays designed to be maximally sensitive to certain relative motions between base and armature, and minimally sensitive to other movements. On to the emitter array is impressed one or a group of signals which are then sensed by the detector array. Figure 2 schematically illustrates one simple arrangement of emitters, detectors, and circuits configured linearly with slightly different spacing to form a vernier arrangement. In the following section, a vernier array is discussed in more detail as the basis for the UniAxial Strain Transducer (UAST). In Figure 2, the top

0-9640024-2-6/hh1998/$20©1998TRF
DOI 10.31438/trf.hh1998.31

Solid-State Sensors, Actuators, and Microsystems Workshop
Hilton Head Island, South Carolina, June 8-11, 1998

line of cross-hatched rectangles represents emitters in the moving armature and the bottom rectangle represents a detector, connected to circuits in the base. Figure 3 illustrates the signals created by an array of detectors driven by two sets of interleaved emitters and identical inverted waveforms (180 degrees out of phase). Note the beats in the interference pattern created by the overlay of the emitter array on the detector array.

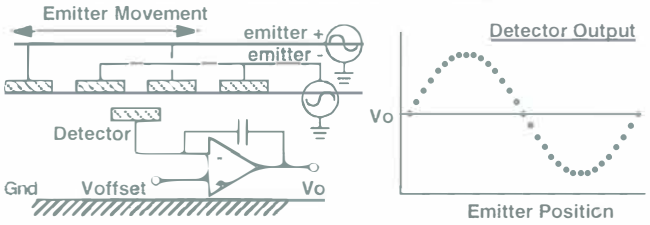

Figure 2. Schematic diagram showing emitters, single detector, and associated circuitry.

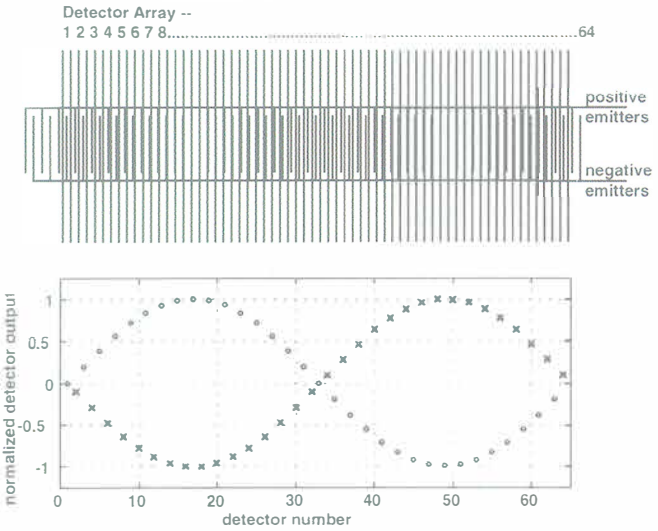

Figure 3. Schematic representation of signals from multiple detectors in a vernier array. The vernier arrangement of field emitter and field effect detectors produces a periodic waveform which phase depends on the relative position between the armature and the base.

In the case of Fig. 3, the waveform, defined by plotting detector output against its spatial position, appears similar to a sinusoid with its phase shifting when the emitter array is translated past the detector array. In general, signals from the detector array are combined by local circuitry and processed to produce a digital signal which represents the relative position of base and armature. Digital signals are created by circuits on the base which operate very uniformly from detector to detector, are drift-free, and can be multiplexed onto a minimal-wire bus using various architectures to be discussed later.

Each sensor uses a "front end" which interacts with the physical environment to transform a measured parameter, such as rotation, strain, shear, or pressure, into a micro-movement of the armature which is converted to a signal by the base chip. Sensors include packages with pass-through mechanisms, or ports, which allow sealed interaction with the environment through the front-end and into the armature. Packages also include sealed conduits to pass wiring between individual sensor nodes and central processing modules.

Challenges of this approach include: defining array architectures and signal processing schemes for each application, designing base chips with non-standard configurations of circuitry (non-orthogonal), creating suspension and/or on-chip bearing systems to maintain precise relationships between armatures and bases, defining multiplexing schemes which can be used successfully with existing systems, and designing packages with non-restrictive pass-throughs which are resistant to challenging environments.

UNI-AXIAL STRAIN TRANSDUCER (UAST)

UAST - Objectives

The UAST is part of a strain sensing network for applications such as: condition-based operation and maintenance, integrated load cells, large dynamic range scales, and others. Targeted characteristics include: (1) high resolution, (2) high strain operating range with high allowable overextension without damage (bangs), (3) refresh rates necessary for structural monitoring at lower frequency ranges (up to 1 kHz) and higher ranges for vibration monitoring (up to 20 kHz), (4) system architecture designed for use of up to 128 sensors on a digital network, (5) high vibration and impact tolerance for rugged applications, (6) shielding against electromagnetic fields, and (7) a package size and shape suitable for a broad range of uses.

UAST version 3 (UAST 3), shown in Fig. 4, was completed in 1997. Figures 5 and 6 show applications of UAST 3 on a half-scale F-18 scale model test apparatus, and on an AH-64 Apache Longbow helicopter rotor blade.

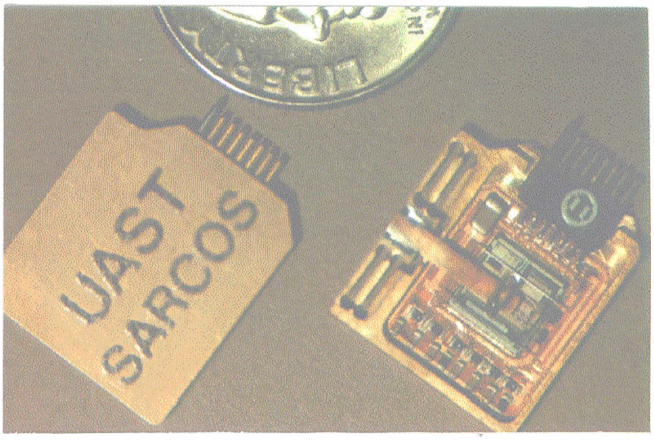

Figure 4. Photograph showing the UAST 3 package, base chip, quartz emitter, internal circuitry, and emitter drive flexure.

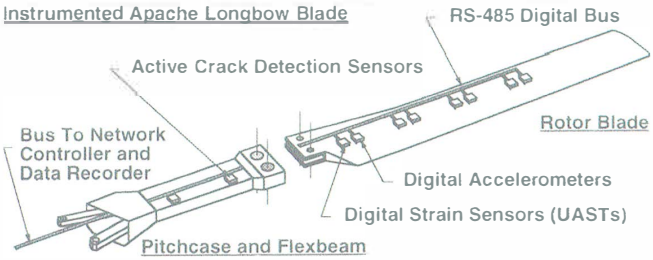

Figure 5. AH-64 Apache rotor blade equipped with UAST sensors used to monitor dynamic load cycles as well as crack growth.

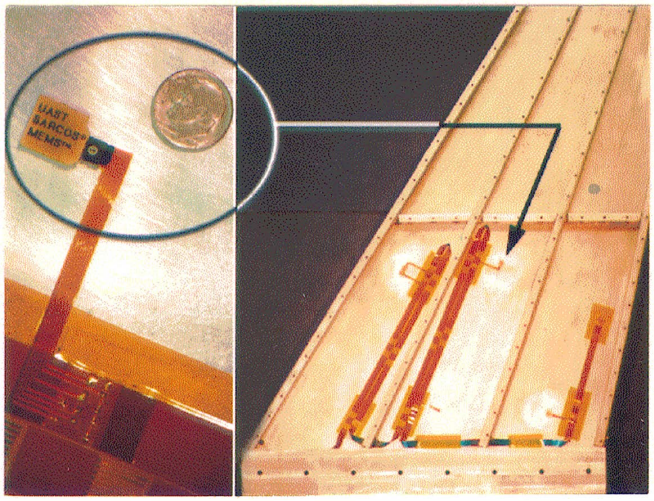

Figure 6. *Half-scale F-18 vertical tail torque box showing a network of UAST 3 sensors used for prognostics and health monitoring.*

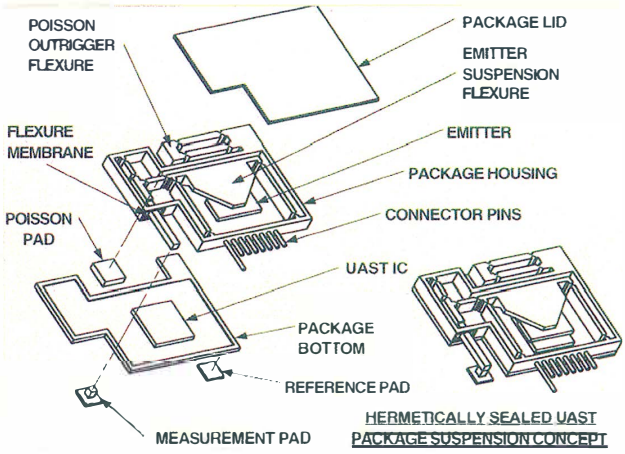

Figure 7. *UAST version 4 package - hermetically sealed.*

UAST - Configuration

Figure 4 shows the UAST 3 package with dimensions of 12 x 13.5 x 2.5 mm. The package material is beryllium-copper and the emitter support arm is assembled by a soldering process. The package includes three mounting pads on the housing bottom side. Two pads are static and one is movable via a double flexure suspension which is connected to a link which moves the armature over the base. The primary function of the package is to attach to the structure to be monitored, and pass strain displacements from the third attachment pad (the front end) to the armature which position is computed by the base. The package also contains four capacitors which provide the filtering required for the base chip operation.

The armature operates in direct contact with the base chip and is supported by a bearing surface which provides a clearance gap of approximately 2 to 5 μm between the emitter and detector arrays. Although contact friction causes some hysteresis, resolution is sufficient to monitor strains down to 0.35 micro-strain (3.5 nm at 10 mm gage length) with high bandwidth and dynamic range. Note here that the UAST is really a micro linear extensometer and not a strain gage since relative displacement, not material distortion, is used to generate an output.

UAST 3 as applied in the configuration shown in Fig. 4, is not hermetically. An upcoming system, UAST 4, will include a flexion-based, sealed package, similar to that illustrated in Fig. 7. UAST 4 is also mounted via two base pads and a moving pad. Observe that one of the base pads is suspended by a transverse flexure which isolates the measurement from Poisson-induced deflections. The moving pad is supported by a beam and flexure assembly which passes through a membrane flexure into the inside of the package. The internal link segment, together with certain flexures, supports the quartz armature which contains the emitter array. In this design the emitter element moves over the base chip without contact.

An emerging development, the IC chip for UAST 5, will be designed in 0.6 micron CMOS and will include both intrinsic and computation-based temperature compensation, load cycle counting, new strain computation algorithm, power saving auto-sleep modes, high sample rates, smaller foot print, and multiple communication protocols.

UAST - Armature & Base

Figure 8 shows the major functional blocks of the UAST 3 base chip. As indicated earlier, the strain information is obtained by measuring the relative displacement between the base and the armature. The vernier arrangement between the emitter fingers and the detector array results in a quasi-sinusoidal waveform of detector output (see Fig. 3) in which the magnitude of the strain is encoded in the phase of the waveform.

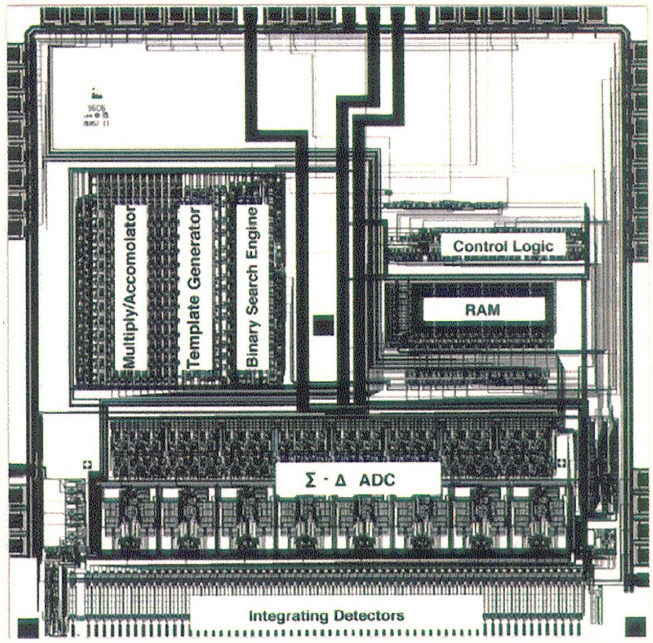

Figure 8. *Layout of the UAST 3 base chip showing the major functional blocks.*

The emitter array consists of two interleaved sets of conductive elements (lithographically patterned chromium film) driven with identical, reverse polarity, waveforms. The detector array elements, along with associated circuits, are fabricated in silicon using 1.2 micron CMOS design rules.

UAST 3's detector pads are 24 by 89 μm with a centerline spacing of 55.8 μm. Emitter pads are 24 by 200 μm with a centerline spacing of 57.6 μm (which corresponds to an interference spatial wavelength of 115.2 μm). Note that the

difference in spacing between emitter and detector array elements determines the interference-pattern wavelength as well as the sensitivity to phase translation of the waveform shown in Fig. 3.

To convert the output of 64 detectors into a single digital multiplexed output the following procedure is accomplished on the single chip shown in Fig. 8. First, a series of up to 16 strobe pulses are applied to the emitter fingers in order to record the waveform on the array of 64 charge-integrating amplifiers connected to the detectors. Next, the analog outputs of the detector array are fed to 8 parallel sigma-delta analog-to-digital converters (ADC) which share the task of digitizing the 64 detector values and placing the results in RAM. Each conversion requires $2^{(n+1)}$ clock pulses to create n-bits of detector resolution (supporting from 7 to 12 bits of conversion, depending on the UAST resolution mode selected). To start the strain computation algorithm, shown in Fig. 9, a 14-bit triangular waveform of 64 template values is generated with the same period as the detector data but with one of 2^{15} (32,768) phase positions. A convolution can then be performed by successively summing the products between the respective detector and template values at a given template position. When this is done for all 32,768 possible template locations, a periodic function is created whose phase corresponds to the relative position of the armature and base. For efficiency, the convolution is calculated only 15 times by executing a binary search to find the zero-axis crossing of the convolution waveform (this approach yields 15-bits of resolution between the armature and base when operating the ADCs with 12-bit conversions, i.e., 0.35 micro-strain for a 10 mm gage length). Note that all 64 detector values contribute to the final calculated strain (displacement) value, providing a robust form of spatial filtering which, incidentally, has no sensitivity to DC offsets in the detector waveform. This important attribute allows the UAST to calculate the same answer regardless of variations in the gap between the armature and base. Finally, the resulting digital strain number is multiplexed onto a common 5-wire bus (including power, ground, distributed 10 MHz clock, token, and data) using the token passing method diagrammed in Fig. 10 (other methods using random addressing of UASTs on bi-directional RS-485 busses have also been developed for health-monitoring applications on AH-64 and UH-60 helicopters).

UAST - Performance

Intrinsic to the operation of a UAST sensor network is the flexibility to trade sensor sample rate against UAST strain resolution, i.e., using fewer clock pulses to convert the detector values, speeds up the calculation of the strain value but with a corresponding decrease in strain resolution. The number of sensors on the network also impacts the sample rate since more sensors require more time to transmit their data which occurs at 2.5 Mbits/sec. For example, 128 sensors operated in 15-bit mode (resolution of 0.35 micro-strain, i.e., 3.5 nm) can be sampled at 131 Hz each, while 10-bit mode (11.25 micro-strain resolution) allows sampling at 786 Hz each. Likewise, a smaller number of 8 sensors can be operated in 15-bit and 10-bit modes while sampling at 148 Hz and 2452 Hz, respectively [1]. Note that in the UAST, sampling across the detector array is accomplished simultaneously, in a snap-shot fashion. Likewise, via use of the token line, data is acquired synchronously across the entire network.

Along with the many attributes of the UAST detection scheme come design issues associated with integrating the base and armature into a viable transducer package which provides ease of installation and robust operation in harsh environments (vibration, temperature, moisture, electrical interference, shock, etc.). The simple UAST packaging schemes used thus far on proof-of-concept hardware platforms are currently being redesigned to provide hermeticity, low profile for embedability in composites, lower fabrication costs, and other performance aspects associated with near-term real world applications.

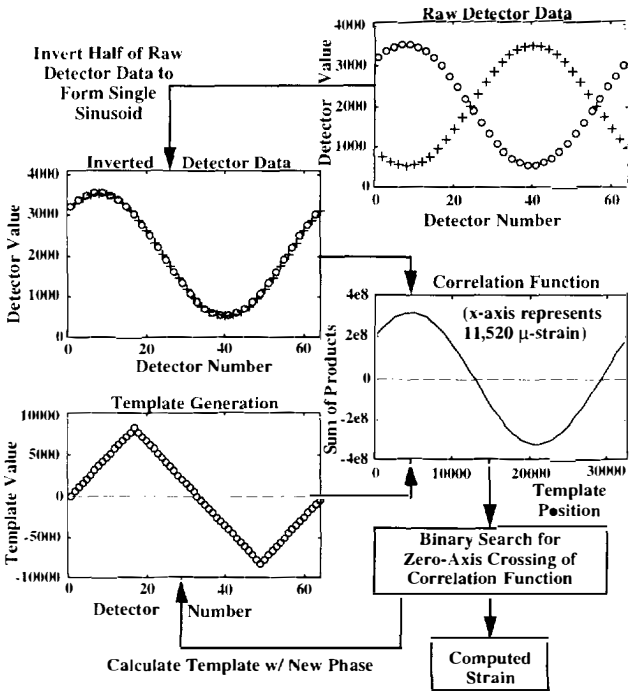

Figure 9. A binary search for the zero-axis crossing of a correlation function is formulated using the sum of products between the measured detector data and digitally synthesized template values.

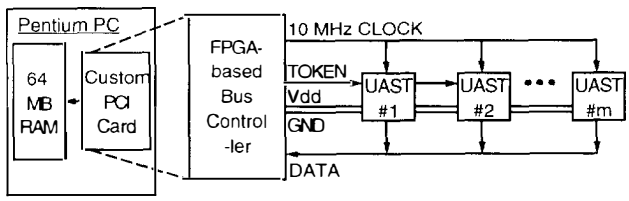

Figure 10. Multiplexing and token passing network scheme.

ROTARY DISPLACEMENT TRANSDUCER

RDT - Objectives

The RDT is a networked encoding systems for use in robotics and other applications where many DOF are monitored. Target characteristics include: (1) absolute encoding of angular position - to insure stability at startup; (2) resolution of 15 to 16 bits, upgradable to even higher resolutions - the present systems give 13 bits of resolution with prototypes already designed to achieve 15 bits resolution; (3) small size: 3 stacked dimes, (4) unshielded three-wire bus architecture capable of

supporting up to 128 sensors at a rate of 400 samples/sec per sensor (fast enough to do real time dynamic compensation in small, fast actuators and to allow accurate computation of rotational velocity from dynamic position measurements).

RDT - Configuration

RDT version 2 (RDT 2) was designed to achieve 13 bits of resolution and was completed in 1995, with only a few minor problems. The armature and base chip for RDT 2 were shown earlier in Fig. 1. The basic elements of the RDT 2 package are shown below in Fig. 11. The components include: (1) shaft, spring-disk, and armature - which are connected in the assembled device; (2) housing with bearing tube and electrical connectors; (3) base chip which gets bonded to the housing and contains a 1 mm diameter hole for shaft pass-through. It is important to note that all electronic elements required for the operation of the sensor are fabricated as part of the base chip.

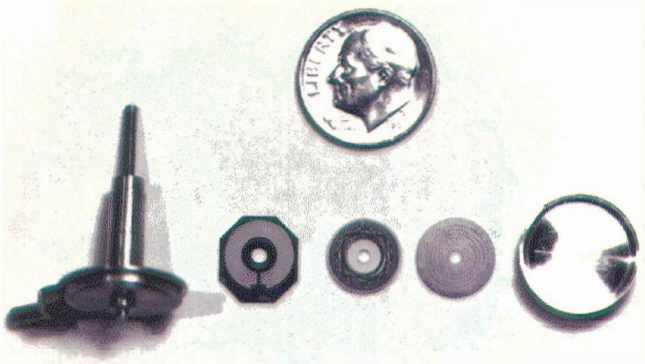

Figure 11. *RDT 2 package components, showing, from left to right, the rotor shaft and housing, the base IC chip, the armature (rotor disk), the disk spring, and the housing cover.*

The armature (rotor disk) and base IC chip are in direct contact at the center region of the base chip, where a through-hole has been drilled. A flat bearing surface at the center of the base is achieved by standard IC processing, and a hard passivation layer is used as the bearing surface. A small mesa, approximately 10 μm high, is micromachined on the sapphire armature and provides a well-controlled gap between the emitter and the detector planes. At assembly, the gap between the base and the armature is filled with silicone oil to provide lubrication and to increase electrostatic coupling. The spring-disk (Fig. 11) is designed to be soft in the axial and tilt directions and stiff in rotation. The axial stiffness and preload of the spring are sufficient to maintain contact between the rotor disk and the base IC for acceleration at high g-levels while running. Figure 12 shows an industrial ruggedized package which is sealed, and features a 4-wire pass-through.

The RDT is designed to allow multiplexing of up to 128 sensors on a three-wire bus. The first wire provides power and data, the second wire provides reset, address increment and data-clock, and the third wire is the ground return. Each RDT contains an address register determined by wirebonds on seven pads of the base chip shown in Fig. 1. A pulse train from the bus first resets the entire network and then counts the register until a comparison is achieve at each RDT. When the comparison register agrees with the sequential address, a 16-bit serial data stream is impressed on the data line. The network thus produces time-staggered data which may impact or limit the type of control approach used, e.g., matrix-based or serial control.

Reset and address-increment are encoded on the three state clock line as a full 5V amplitude pair of pulses or as a single pulse, respectively. Data bits are serially clocked out by an interleaved half amplitude clock pulse. The data bits are encoded on to the power line by modulating the current drawn by the sensor. An RS-232 interface has been implemented but various other interfaces to a digital controller can be easily developed.

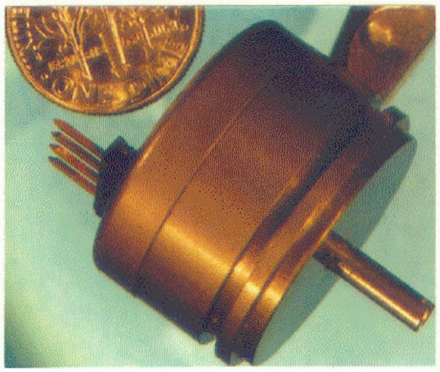

Figure 12. *Industrial package for RDT 2 and RDT 3.*

RDT - Armature & Base

The RDT 2 armature and base IC chip are shown in Fig. 1. The sapphire armature disk includes an electrically interconnected metallization pattern divided into a 10-bit Gray code uninterrupted around the entire 360 degrees. Each track of the Gray code has a complementary metallization pattern which provides the differential signal required for the detector pairs, meaning that there is a total of 20 tracks.

The base chip is fabricated using 2.0 micron, 2 metal, single poly-CMOS design rules. It contains two arrays of detectors, a radial and a circumferential array, along with circuits for encoding angular position into a 13-bit binary number and all of the circuitry for 3-wire multiplexing. Each detector reads the signals from a pair of complementary tracks on the armature disk. A ten detector pair radial array reads the 10 complementary tracks on the armature to produce the 10 most significant bits. The outer tracks of the armature and the circumferential detector array are arranged to form a vernier which provides the three least significant bits of the 13-bit value. Unlike UAST 3, which uses convolution to digitize the vernier output, RDT 2 uses a logic array and the output of 16 detector pairs to produce the 3 least significant bits. RDT 3, currently under development, is designed to provide increased resolution (up to 16 bits) and to decrease the required packaging precision.

RDT - Performance

In summary, an RDT capable of achieving 13 bits of resolution (RDT 2) has been demonstrated. A device capable of at least 16 bits resolution is under development. These devices provide absolute encoding of angular position over 360 degrees. The RDT is designed to allow multiplexing of up to 128 sensors on a three-wire bus with a sampling rate of at least 400 samples/sec per sensor.

Continuous rotation life tests have demonstrated operation in excess of 200,000,000 cycles at 2500 rpm. Cycling with 90 deg. oscillations and high acceleration at 1Hz showed continued operation after 1.2 million cycles. In all

cases the tests terminated before failure of the device. The maximum speed at which the devices have been operated is approximately 2500 rpm, but higher speeds should be possible.

FLUID SHEAR TRANSDUCER (FST)

FST - Objectives

Advanced submarine, ship, and aircraft configurations are routinely developed and evaluated using numerical techniques (computational fluid dynamic analyses) which often require experimental validation. Moreover, some of these configurations utilize conformal or adaptive surfaces to actively manage separation, turbulence, boundary layer development, and other features of flow. As such, distributed transducers are needed to detect and measure fluid-induced shear (as well as pressure), in two directions, over the surfaces of scale model and operational vehicles moving in fluid. For example, Fig. 13 illustrates a separated flow over an airfoil where each shear sensor in an array could be used to determine surface flow direction, collectively used to indicate separation, and unsteady flow.

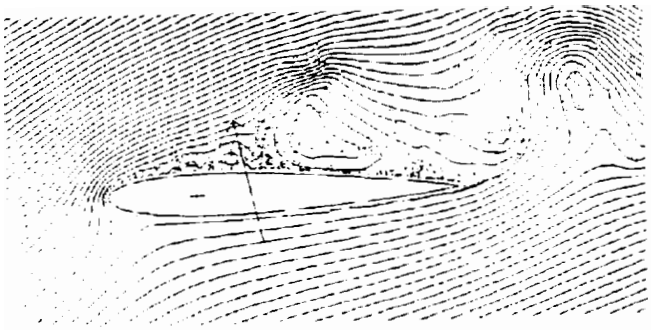

Figure 13. *Flow separates on a NACA 0012 airfoil above 16 degrees angle-of-attack for Re numbers above 10,000,000.*

FST - Configuration

Fluid shear transducers (FST), which are based on "direct force" measurements, are a natural extension of the CMOS sensing described in this paper. In order to minimize interaction between the fluid and sensor, as well as sensitivity to body loads such as gravity and vehicle accelerations, the sensing disk (see Fig. 14) must be supported on a stiff suspension which undergoes small translational movements and possesses high rotational stiffness for minimal cross-axis coupling. For example, using a viscous fluid-coupling between the flow and a 1.8 cm diameter suspended disk, to characterize flows with local Reynolds numbers above 10,000,000, a sensor must resolve transverse forces on the order of 50 μN (0.2 Pa of shear) with a dynamic range of 0.8 N (3 kPa) and be designed to survive substantial overloads. For a suspension with a lateral stiffness of 1,300 N/m, this corresponds to resolving dimensional deflections of less than 30 Angstroms over a range several times greater than 112 μm.

Many applications need high spatial and large bandwidth shear measurements which naturally leads to a requirement for multiplexing sensor outputs on to common busses. Also, the sensor networks will have to operate in water at great depths so sealed packages with pressure compensation are often necessary. In addition to solving these and the mechanical suspension and packaging design issues, a CMOS IC sensor is required which can make high resolution bi-axial measurements with a large dynamic range. The resulting bi-axial strain transducer (BiAST) IC chip, presently under development, will work for other applications as well, including measurements of bi-axial strain, acceleration, and others. Development of a three (orthogonal) axis CMOS IC sensing chip (TriAST) design is already underway.

Figure 14 shows the configuration of an individual shear sensor, including details of the viscous shear-coupled disk, sensor housing, suspension rods which allow controlled translation of the disk and armature with low vertical deflection, welded bellows to permit relative translational motion between the disk and housing (with high rotational stiffness to prevent cross-axis coupling) while maintaining a hermetic seal between the sensor interior and the fluid environment, armature and base chip at the bottom of the housing which measure armature translation in two dimensions, and sensor receptacle (sensor/receptacle size is 19 mm dia. and 18 mm in height). The suspension facilitates a controlled spacing between the base and armature of approximately 12 μm. The system is temperature-compensated by the suspension configuration and compatibility of materials.

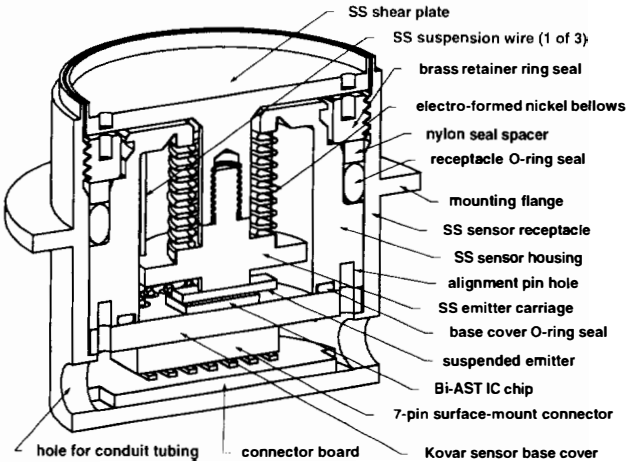

Figure 14. *Cutaway illustration of the FST sensor module and receptacle.*

Figure 15 shows a string of "vaulted" (sealed) sensors where mixed types of transducers (some are two-axis shear, others are pressure, and a thin film anemometer module is also shown). All sensors share a common sensor receptacle and network conduit interface. In addition to each sensor module being hermetically sealed, the conduit tubing and receptacles form a separate control volume which can be gas-filled and pressure compensated (via a bellows with sufficient starting volume to accommodate the anticipated increase in external water pressure) to prevent intrusion of water when operating the network at great pressures. The sensor modules utilize standardized connectors and O-ring seals to facilitate easy removal or to reconfigure the network with different combinations of sensor types for various applications.

FST - Armature & Base

At the heart of the two-axis surface shear stress sensor is the BiAST, which uses the CMOS IC chip layout shown in Fig. 16. Again, like the UAST, the BiAST is really a micro-extensometer, not a strain transducer (the sensor base or

armature are not distorted but, rather, sensor output is based on measured displacements between the base and armature). The BiAST base chip includes two orthogonal sets of 64-element detector arrays interacting with a suitably designed, driven set of orthogonal emitter arrays. Together these form two separate verniers which can be used to make measurements for the two in-plane axes. The detector and emitter element spacing are the same as those for the UAST 3 (55.8 and 57.6 μm, respectively) and the BiAST shares the eight analog-to-digital converters, template generator, and strain computation engine of the UAST 3 between the two arrays. As such, the BiAST first samples both detector arrays and then begins conversion of the X-axis detectors with subsequent calculation of the X-axis displacement. The Y-axis detector values are then converted with subsequent calculation of the Y-axis value. Thus, the BiAST can sample only half as fast as the UAST for the same level of output resolution. Otherwise, its performance is expected to be on par with that of the UAST 3.

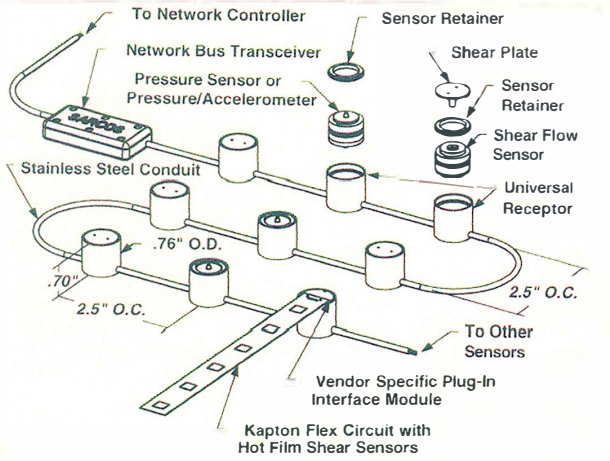

Figure 15. *Shown are a number of interconnected standard packages configured with different sensors. Included are: two-axis flush-mounted flow sensors, pressure sensors, and a hot film anemometer strip.*

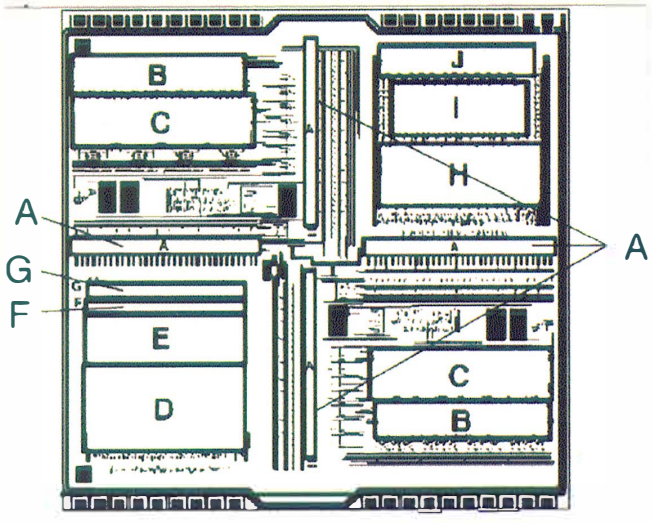

Figure 16. *Preliminary IC chip layout of the BiAST presently under development. A) 32 ea. integrating detectors; B) 4 ea. Delta-Sigma modulators; C) 4 ea. accumulators; D) multiplier-accumulator; E) template generator; F) binary search registers; G) binary search control; H) EEPROM + new functions; I) 64 x 12 RAM; and J) token interface + BiAST control.*

PRESSURE TRANSDUCER NETWORK (PTN)

PTN - Objectives

In addition to shear stress measurements, pressure distribution data with high spatial density and large sample rates are essential to characterize flow features around hydrodynamic surfaces, such as submarine control surfaces, propulsor and hull; aircraft foils and adaptive surfaces; turbine blades; and others. With this in mind, integrated networks of micro pressure transducers tailored for applications in demanding environments, such as aircraft, submarines, and other systems, have been developed.

For example, Fig. 17 shows a network of pressure and vibration sensors integrated on both faces of a prototype 1/4-scale propulsor blade section. This network consists of 72 sensors housed in 56 hermetic packages designed for use in different environments. More specifically, the network is divided into two major branches, installed on opposite faces of the blade and comprised of: (1) 8 nodes which perform analog-to-digital conversion and transmit data over a digital bus at a combined rate of 12 Mbits/sec; (2) 8 high-speed pressure sensors (sampled at 50 kHz); (3) 32 low speed-sensors (sampled at 5 kHz); and (4) 32 collocated pressure and vibration sensors (also sampled at 5 kHz). The CMOS base/armature concept outlined throughout this paper was readily combined with bulk silicon micro-machining techniques and better-than-hermetic bonding methods to fabricate the sensors used in this example.

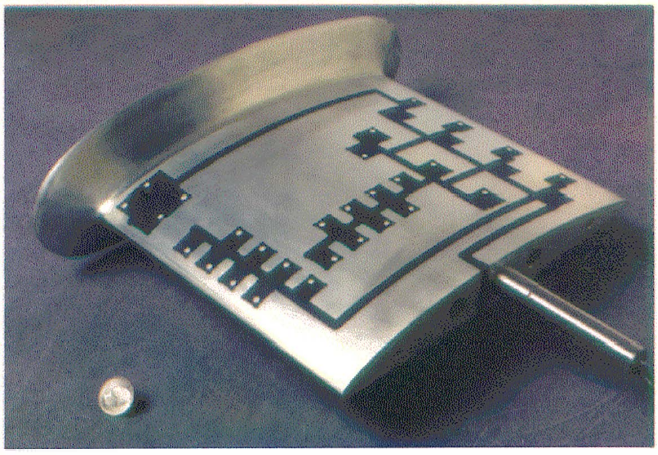

Figure 17. *Propulsor test blade showing the layout of the pressure and vibration sensor network.*

PTN - Configuration

Figure 18 illustrates a hermetically sealed, flat pressure sensor package in which the sensing diaphragm is placed in direct contact with the environment and where the electrical conduits are sealed in metallic tubes in a way that is similar to that used for the shear stress sensor network described in the previous section.

In the PTN sensor package, a silicon sensing diaphragm covered with a low stress silicon nitride film is eutectically bonded to a 1-to-2 mm thick Pyrex® plate, and the latter is then eutectically bonded to a plated Kovar case. Kovar tubes are brazed on the case and act as vaults for the network electrical conduits. Electrical connection between the IC chip and the network bus is provided by a flexible Kapton® conduit which is flip-chip bonded to the IC chip. Passive electronic components,

such as filter capacitors and bias resistors are mounted on the Kapton® flexible conduit and the latter, is then, attached to the lid. Electrical insulation and passivation of the diaphragm and housing are provided by low stress silicon nitride (deposited on the diaphragm) and by a 15 to 25 µm thick Parylene conformal coating over the entire package.

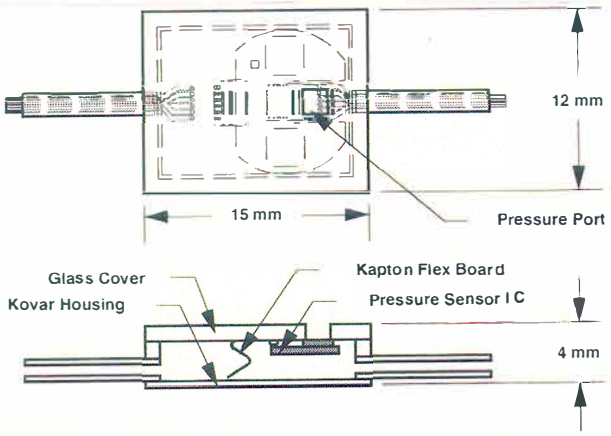

Figure 18. *Schematic representation of a new type of pressure and vibration sensors package.*

PTN - Armature & Base

Similar to the other sensors described throughout this paper, the pressure sensors exploit the field-based (base/armature) sensing technique [**1-5**] and a concept called the "block approach", where bulk micro-machined elements such as pressure-sensing diaphragms or proof masses are joined (in multiple layers if necessary) to conventionally fabricated VLSI CMOS IC chips to form complete transducers.

Figure 19 shows a micrograph of a typical pressure sensing CMOS IC chip (base) and pressure-sensing diaphragm (armature). Each base IC chip (2.2 x 4.4 x 0.5 mm) features: (1) a differential pair of field-based sensors, with one detector pad located toward the center of the diaphragm (maximum deflection area) and one located at a corner (reference sensor) to minimize temperature effects and variation in the assembly gap, (2) a contact and bonding aluminum frame to which the sensing diaphragm is attached, (3) a 5-pole Chebychev switched-capacitance low-pass filter, and (4) multiplexing and bus driver electronics. In principle, an array of detectors, located on the base, could be used to enhance resolution and, to respond to the mechanical dynamics of the membrane.

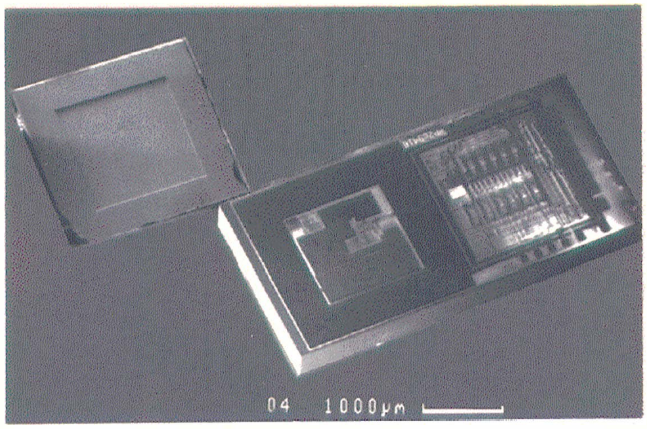

Figure 19. *Micrograph showing a typical pressure sensor CMOS IC base chip and a diaphragm.*

The pressure sensing diaphragm used as the armature in these devices consists of: (1) a contact and bonding outer frame (approx. 2350 x 2350 µm wide), and (2) a square diaphragm area (approx. 1500 x 1500 µm wide) of variable thickness. The diaphragms are RIE micro-machined out of 50 µm thick, n-type single crystal silicon membranes, metallized and then hermetically sealed, under vacuum, to the CMOS base chip.

PTN - Performance

Pressure sensors developed to date have been tailored to operate over the range from 0 to approximately 3 atm. and have a spectral noise density of approximately 1.5 $Pa/Hz^{1/2}$ (i.e., approx. 10 bits of dynamic range for the slow pressure sensor). Shock tube tests have demonstrated the capability of the devices to accurately monitor transient pressure variations with characteristic frequencies above 20,000 Hz. In practice, the diaphragm may be designed to adjust the dynamic range as dictated by the application. It is also anticipated that enhanced pressure resolution could be achieved by replacing the synchronously demodulated field-based sensor, used in the current device, by the charge-integrating amplifier developed for the UAST and the BiAST.

ACKNOWLEDGMENTS

The authors gratefully acknowledge the direct contributions from D.P. Marceau, D.L. Wells, F.L. Williams C.C. Davis, D.G. Petelenz, and D. Beutel. The authors also gratefully acknowledge support for this effort by Defense Advanced Research Projects Agency under contract numbers: F33615-87-C-5267, N00014-93-C-0112, N00014-96-C-0345, DAAH01-95-C-R144, DABT63-95-C-0033, N00014-93-C-0181, from NAVSEA under Newport News Shipbuilding (N00024-95-C-2102) as well as from DARPA and NASA funded projects through Martin Marietta, McDonnell Douglas and Boeing.

REFERENCES

1. B.J. Maclean, M.G. Mladejovsky, M.R. Whitaker, M. Olivier and S.C. Jacobsen, "A Digital MEMS-Based Strain Gage for Structural Health Monitoring", in Proceedings of Material Research Society Symposium, Boston, MA, Dec. 1-5 (1997).

2. S.C. Jacobsen, et. al., "Field-based Microsystems for Strain Measurement", *Proc. ASME Winter Annual Meeting*, November, Chicago, IL (1988).

3. S.C. Jacobsen, et. al. "Displacement Sensing by Direct Mechanical Modulation of Shaped Electro-Active Micro-Structures", *Proc. IEEE Micro-Electro Mechanical Systems Workshop*, Feb. 11-14, Napa Valley, CA (1990).

4. S.C. Jacobsen, et. al., "Field-Based State Sensing in Micro-Motion Systems", in *Integrated Micro-Motion Systems - Micromachining, Control, and Applications*, F. Harashima, Ed., Elsevier Science Publishers (1990).

5. S.C. Jacobsen, et. al., "Advanced Intelligent Mechanical Sensors (AIMS)", *Proc. IEEE Transducers '91*, June 24-28, San Francisco, CA (1991).

5-LEVEL POLYSILICON SURFACE MICROMACHINE TECHNOLOGY: APPLICATION TO COMPLEX MECHANICAL SYSTEMS

M. Steven Rodgers and Jeffry J. Sniegowski
Intelligent Micromachine Department Sandia National Laboratories
Albuquerque, New Mexico 87185-1080

ABSTRACT

We recently reported on the development of a 5-level polysilicon surface micromachine fabrication process consisting of four levels of mechanical poly plus an electrical interconnect layer **[1,2]**. We are now reporting on the first components designed for and fabricated in this process. These are demonstration systems, which definitively show that five levels of polysilicon provide greater performance, reliability, and significantly increased functionality. This new technology makes it possible to realize levels of system complexity that have so far only existed on paper, while simultaneously adding to the robustness of many of the individual subassemblies.

INTRODUCTION

Although MEMS is the acronym for MicroElectroMechanical Systems, the "systems" aspect is not often exhibited since limitations imposed by established technologies restrict design complexity and the interactions that can occur between components. A new 5-level polysilicon surface micromachine fabrication process now provides a base for designing sophisticated mechanical systems-on-a-chip. To demonstrate this, we combined totally redesigned versions of many previously demonstrated concepts: electrostatic actuators, microengines, transmissions, rack and pinion assemblies, self-positioning mirrors, and a pin-in-maze discriminator **[3,4,5]** into a single interconnected system. Also demonstrated for the first time are the fabrication of gears on moveable plates, shaft and bushing interconnect linkages, embedded hold-down pins in a linear rack, and guides with release mechanisms that keep mating sets of gears in proper alignment until engagement occurs. This is believed to be the most complex, fully actuated, surface micromachined mechanical system ever fabricated. The drawing set contains hundreds of thousands of entities on 17 drawing layers. These are combined to generate 14 photolithographic masks that are used during the 240-step fabrication sequence. Functionality of this system was demonstrated with components from the first production run confirming that performance, reliability, and complexity could all be simultaneously improved by this 5-level technology.

5-LEVEL POLYSILICON STACK

Figure 1 depicts the 5-level polysilicon / silicon dioxide stack that is the basis for this technology. Referred to as SUMMiT-V (Sandia Ultra-planar Multi-level Mems Technology V) **[6]**, four mechanical levels of polysilicon are fabricated above a thin poly0 electrical interconnect layer. Two microns of sacrificial oxide is typically sandwiched between each polysilicon level. The oxide between poly1 and poly2, however, is only 0.5 μm thick. This thin deposition defines the clearance in gear hubs and hinges. In areas surrounding the hubs and hinges, it is often etched away so that the 1.0-μm thick poly1 and the 1.5-μm thick poly2 form a single rigid composite layer. Poly3 and poly4 are 2.25-μm thick films that are deposited on chemically mechanically polished (CMP) layers of oxide **[7]**. This CMP planarization alleviates several photolithographic and film etch issues and frees the designer from constraints that would otherwise be imposed by the underlying topography.

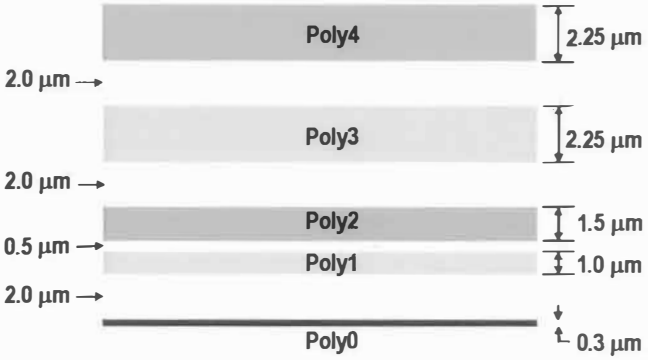

Figure 1. *Shaded regions represent the 5 levels of polysilicon, and the clear spaces between them represent layers of sacrifical oxide. This stack is built on a 6-inch single crystal silicon wafer with a dielectric foundation of 0.63 μm of oxide and 0.80 μm of nitride.*

GOAL OF WORK

Driving the development of this work was the goal of designing a research prototype that demonstrates the feasibility of building complex microelectromechanical systems for enhanced safety of weapons.

Requirements:

- System is to be fabricated using multi-level surface micromachining technology.
- Its function is to provide for directing an optical data signal to a target electronic assembly only after the correct electrical sequence is fed to a micromechanical discriminator (lock).
- System is to be fabricated in the disabled state.
- A predefined 24-bit code will be used to enable the system.

0-9640024-2-6/hh1998/$20©1998TRF
DOI 10.31438/trf.hh1998.32

Solid-State Sensors, Actuators, and Microsystems Workshop
Hilton Head Island, South Carolina, June 8-11, 1998

- The discriminator will be a single attempt device, with any incorrect code sequence permanently disabling the system.
- Optical access for the data signal is to be through holes cut from and through the backside of the fabrication substrate. Openings will be 400-500 microns in diameter to accommodate a Vertical Cavity Surface Emitting Laser (VCSEL) or a small fiber optic cable.
- Discriminator shall incorporate low power actuators that permit the enabling code to be optically entered.

Envisioned was a system of two positionable mirrors fabricated in close proximity to each other so that light entering through a hole in the substrate would strike one mirror, be deflected to the other mirror, and then back down through the second substrate opening and on to the target element (figure 2). These mirrors would be fabricated flat against the substrate and driven to the correct position by electrostatically controlled microengines [8]. To prevent operation prior to receiving the unlock sequence, a mechanism comprised of an incomplete gear train, which is to couple the power from microengines to the linear racks that drive the mirrors, would be employed. To enable the system, a set of power coupling gears must be inserted to complete the drive train. The gears that form these power coupling links would be mounted on moveable structures attached to linear pin-in-maze plates "cut" with the binary code. Upon completion of the correct code sequence, these gears would become fully engaged. The CAD drawing for the actual implementation of this system is shown in figure 3. Note that two of these assemblies are required for full beam routing.

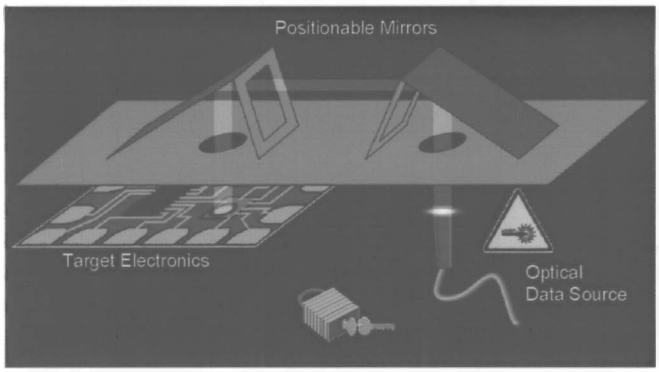

Figure 2. Dual-mirror-redirect safety concept. Mirrors are fabricated flat over these openings and cannot be driven to this operating position until the proper keys are inserted into their drive mechanisms.

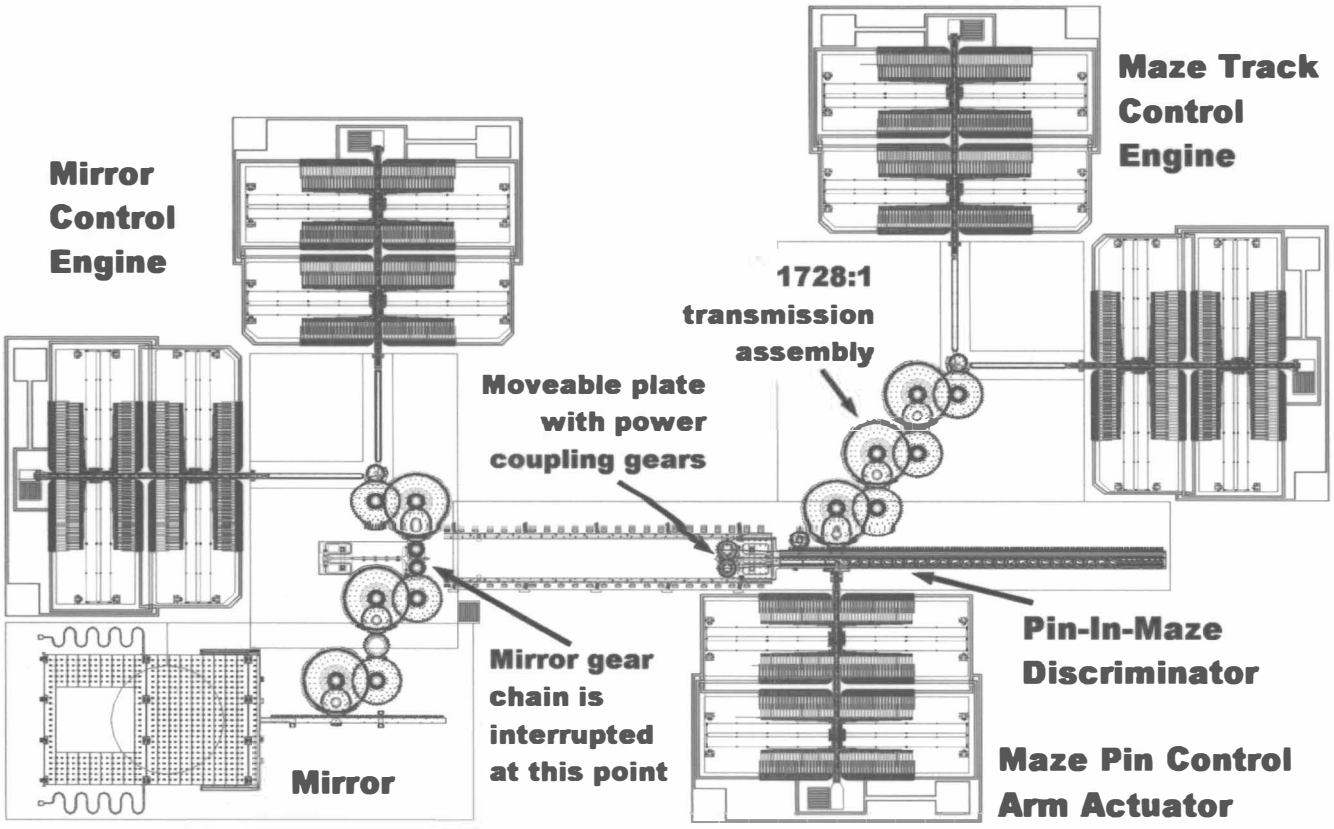

Figure 3. Enhanced versions of several previously demonstrated MEMS devices were redesigned in the 5-level technology so that they could be integrated into a single unified system. A total of 39 gears ranging in size from 72 to 288 μm in diameter are employed along with 5 electrostatic actuators, 2 rack and pinion assemblies, a linear maze track with 3 embedded hold down/guide pins, 1 set of guide rails, 2 autoreleasing gear alignment mechanisms, a pop-up mirror with 12 hinges and self-shadowing etch release hole covers, and a rotary anti reverse mechanism. Eleven electrical connections are required for system operation.

PERFORMANCE AND RELIABILITY

As system complexity increases, the yield and reliability of individual components must be very high in order to have appreciable yield of the entire system. This is especially true of actuation assemblies, which must provide enough force to reliably drive significant mechanical loads. To first order, using one level, the amount of force obtainable from an electrostatic actuator is proportional to its size [9]. Additional fabrication levels allow the structure to be built up vertically instead of laterally, significantly increasing the amount of force available per unit area. All of the mechanical levels available in the 5-level technology are layered together to form the actuators shown in figure 4. Even more important than the increased force performance, however, is the dramatically increased "z" axis stiffness that results from stacked levels in the actuator support springs (figure 5). The cubic relationship between thickness and stiffness makes these structures approximately 100 times as stiff as their first generation counterparts in the "z" direction. This increases robustness and helps tremendously in the final release process where the surface tension of the etchant acts to pull the moveable portion of the comb drive assembly down to the underlying substrate and leaves it adhered. These drives are far more reliable and generate several times the force of the original devices.

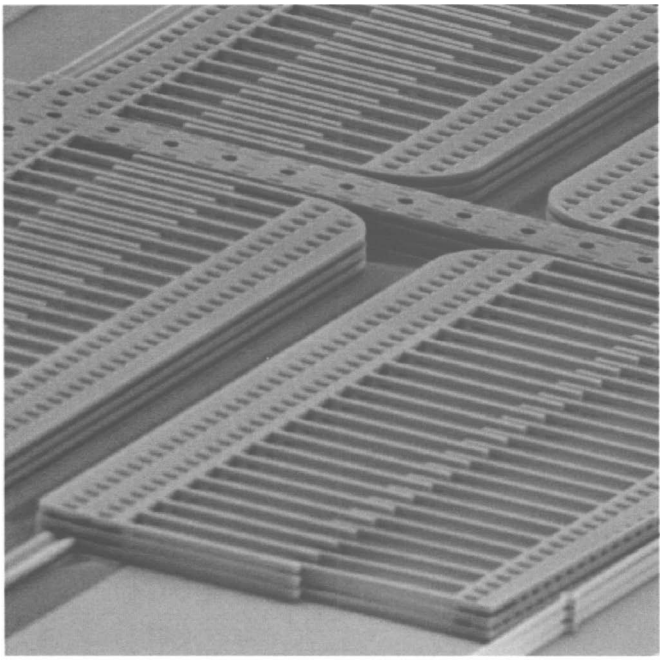

Figure 4. *All four mechanical layers of polysilicon are utilized to increase electrostatic actuator performance. In this region, the first two are laminated together to form a more rigid base layer.*

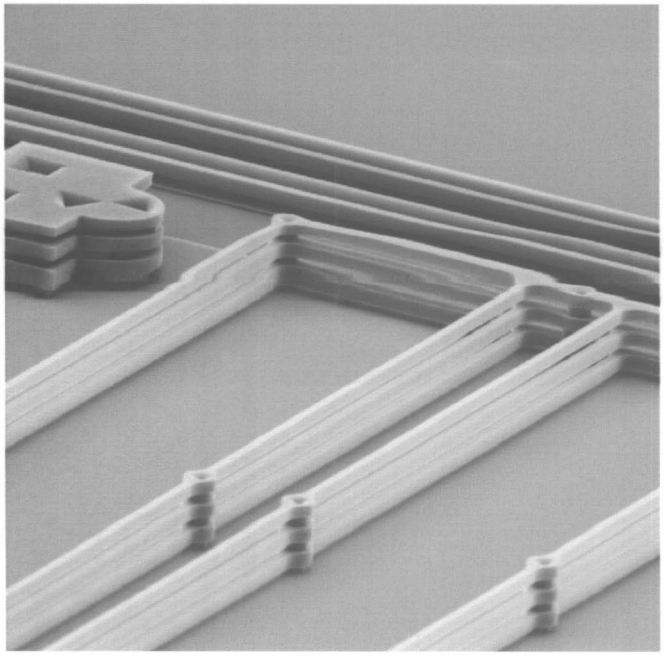

Figure 5. *Similar layering of the support springs generates a structure that is approximately 100 times stiffer than first generation devices in the "z" axis.*

This multi-level technology also promotes reliability by permitting the exploration of alternative linkages between the linear electrostatic actuators and drive gears that comprise each microengine. The shaft and bushing linkage shown in figure 6 pivots like earlier pin joints [8]. It does not, however, have the large inverted rivet head structure associated with pin joints that could come in contact with the underlying substrate and reduce reliability due to stiction. This type of linkage also generates less off axis torque on the comb drive than commonly used elastic links, thus reducing the possibility of lateral clamping between the electrostatic actuator fingers [4].

Drive force from the new high-output microengine is further increased through the use of the cascadable gear reduction unit shown in figure 7. Each unit provides a 12:1 gear reduction ratio with a corresponding increase in torque. Six of the units have been coupled together to provide a 3 million to 1 gear reduction assembly that has demonstrated the ability to shear gear teeth. The actual safety system uses three of the 12:1 gear reduction units to create a 1728:1 transmission that drives the linear rack containing the maze. This produces ample force to overcome friction and stiction effects [2,10] and provides 138 nanometer positional resolution of the rack per microengine revolution.

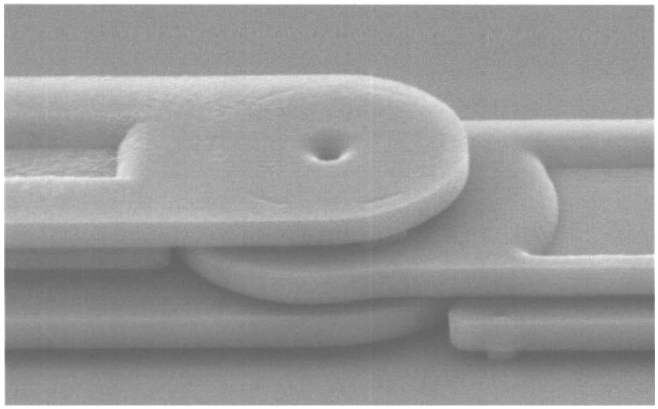

Figure 6. *Close-up of low stiction linkage assembly that interconnects one of the microengine linkage arms with its electrostatic actuator.*

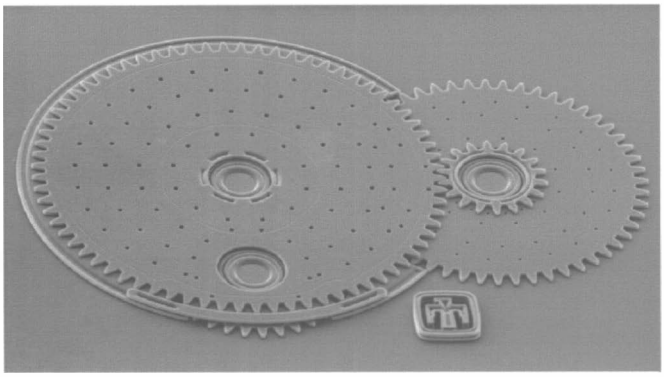

Figure 7. *Each cascadable gear reduction assembly increases drive torque by an order of magnitude.*

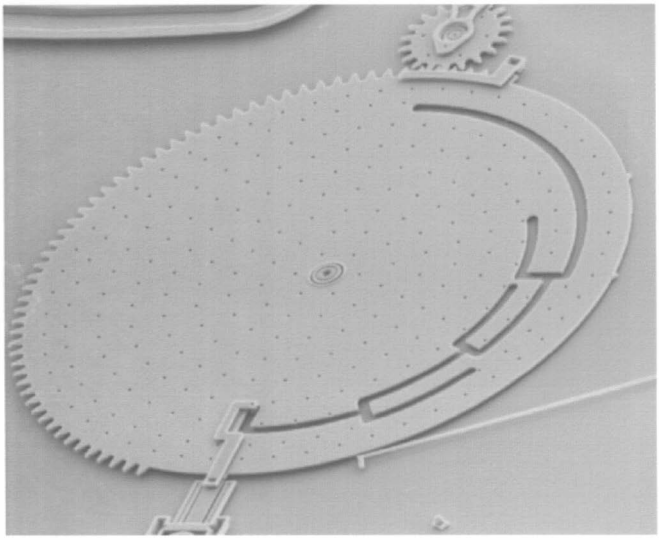

Figure 8. *This early rotary pin-in-maze discriminator was fabricated in a 4-level polysilicon process.*

ENHANCEMENTS AND NEW FUNCTIONALITY

We initially demonstrated that pin-in-maze discriminators could successfully be fabricated in a surface micromachine technology with the 3-decision point rotary device shown in figure 8 [5]. As the maze wheel rotates, the control arm must move a pin that rides inside the maze radially back and forth so that the pin never takes a dead end path. Once a dead-end path is taken, the lock is permanently disabled due to an anti-reverse mechanism that prevents retries. If all the correct paths are taken, the wheel will rotate until the pin comes to the very end of the maze, and at this point the device is considered to be unlocked [11]. Although useful for demonstration purposes, this design was not directly expandable to the desired 24-bit functionality, since the maze pattern actually cuts all the way through the maze wheel. The longer the maze pattern, the more the outside portion of the maze is severed from the main wheel. Thus a maze with 24 decision points would not be structurally sound.

The rotary maze was fabricated in a 4-level polysilicon technology, while an additional level of material is needed to support larger mazes. Figure 9 illustrates how this was accomplished with the 5-level process for the 24-bit linear pin-in-maze configuration. Essentially everything was moved up one level and a solid flat plate was defined under the maze to support each side of the structure. The additional level of structural material also allowed pins to be embedded within the structure of the rack to confine its movement both vertically and laterally. A representative cross section of the moveable portion of the maze track assembly is indicated with the light gray fill at the bottom of figure 9.

On one end of this rack is a plate with two power coupling gears that will be inserted into and complete the mirror drive train upon completion of the unlock sequence. These two sets of gears are pictured in figure 10. As the gears engage, their rotational alignment guides simultaneously disengage through release mechanisms fabricated in the top 2 levels of polysilicon. After this occurs (figure 11), the mirror control engine can be activated to drive the mirror into the correct operating position. Figure 12 shows the two opposing mirrors required for complete system implementation. The mirror on the right has been enabled and driven to the desired operating position, while the mirror on the left is in its fabricated state. The spring-like structures on the mirror sides apply pressure on the gears and hinges to facilitate precise positioning.

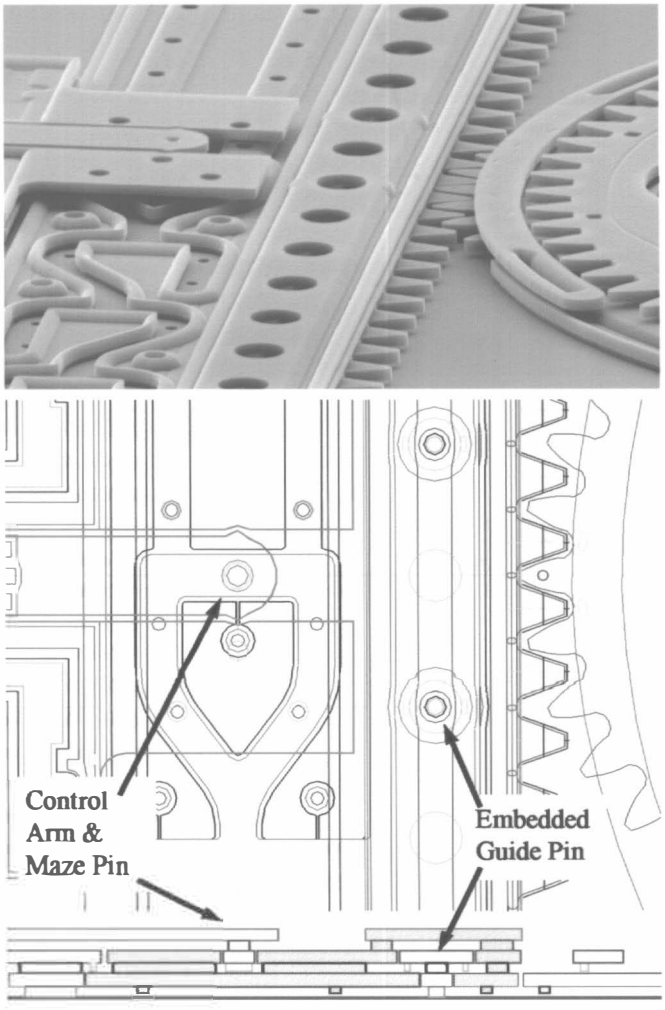

Figure 9. *Scanning electron micrograph and CAD layout of a section of the maze track assembly and control arm.*

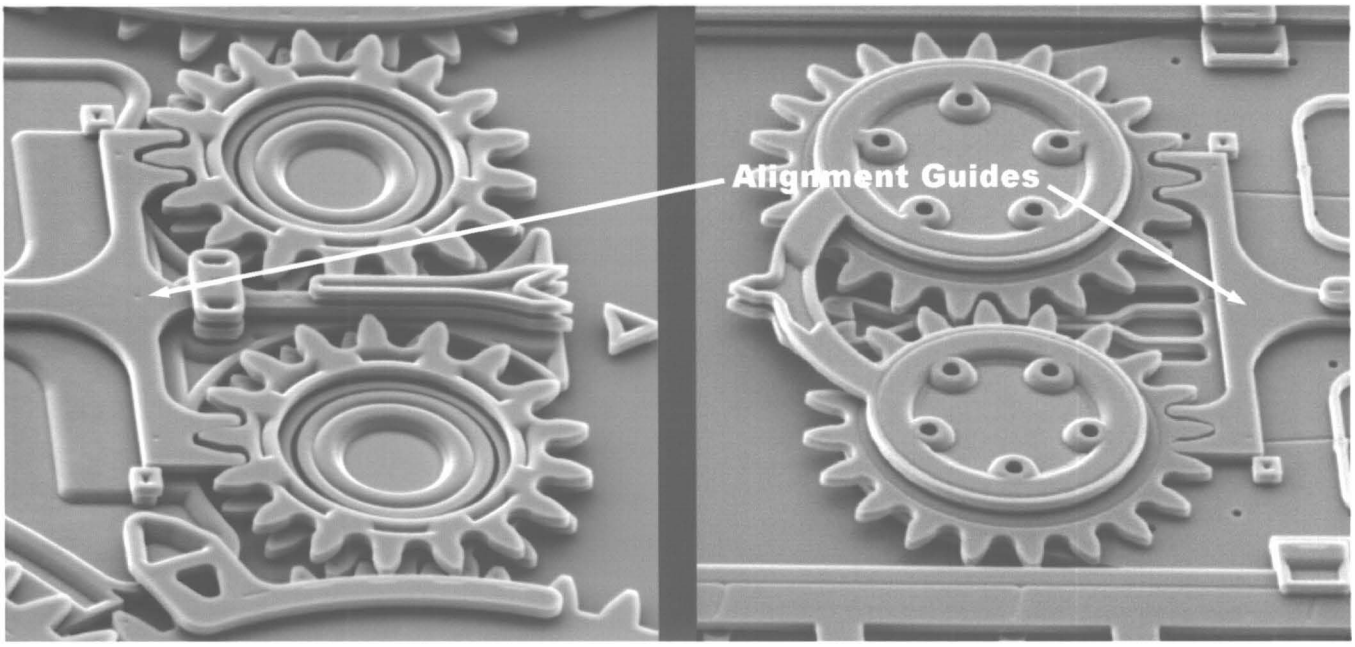

Figure 10. *As the linear pin-in-maze discriminator is operated, power coupling gears on the maze track plate (right) move towards the uncoupled gears in the mirror drive train (left) and complete mechanical coupling. Rotational alignment guides automatically release when gears engage, and a spring clip snaps in place to prevent plate disengagement.*

CONCLUSIONS

With a 2-level polysilicon technology, it is possible to make simple actuators; with 3 levels, gears with hubs; and with 4 levels, linkages that attach to the gears to provide continuous 360^0 rotation. The 5-level technology presented here now allows complex moveable components to be fabricated on translatable stages. This permits significant interactions to occur between various subassemblies, thereby allowing the mechanical "systems" aspect of MEMS to be much more realizable.

In addition, full utilization of these levels, even in structures that can be defined in a single mechanical layer, has been shown to have significant benefits on performance and reliability. Although data on a statistically significant number of components is not presently available, almost all of the first run devices were found to be functional. Hundreds of assemblies will

Figure 11. *After the successful negotiation of the maze, the coupling gears complete the mirror drive train. Note that the alignment guides are now pulled away from the gears.*

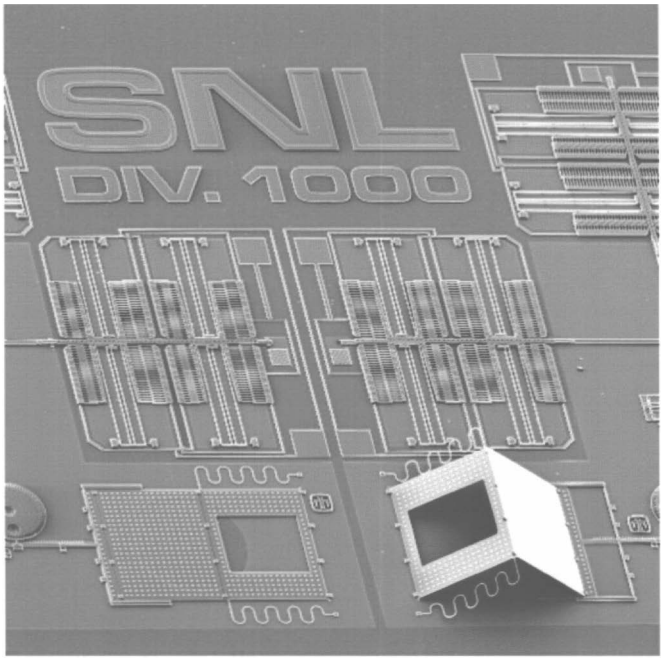

Figure 12. *With its gear train completed, the mirror on the right has been driven to its correct operating position. Operation of the second mirror will establish the optical data path.*

be subjected to extensive testing once baselining of this technology is complete.

ACKNOWLEDGEMENTS

The authors are grateful to Michael Callahan for funding this work, the personnel of the Microelectronics Development Laboratory at Sandia National Laboratories for fabricating the devices, and to Gary Zender for the SEM images.

Sandia is a multiprogram laboratory operated by Sandia Corporation, a Lockheed Martin Company, for the United States Department of Energy under contract DE-AC04-94AL85000.

REFERENCES

1. J. J. Sniegowski and M. S. Rodgers, "Multi-layer enhancement to polysilicon surface-micromachining technology", *IEDM97*, 12/7-10/97, Washington DC, (1997) pp. 903-906.

2. J. J. Sniegowski and M. S. Rodgers, "A Manufacturing Method For Multi-layer Polysilicon Surface-Micromaching Technology", *1998 Government Application Conference Digest of Papers, XXIII,* 3/16-19/98, Arlington, VA, (1998) pp. 87-90.

3. J. J. Sniegowski and E. J. Garcia, "Surface Micromachined Gear Trains Driven by an On-Chip Electrostatic Microengine", *IEEE Electron Device Letters, 17*, 366 (1996).

4. J. J. Sniegowski, S. L. Miller, G. LaVigne, M. S. Rodgers, and P. J. McWhorter, "Monolithic Geared Mechanisms Driven by a Polysilicon Surface Machined On-chip Electrostatic Engine", *Technical Digest of the 1996 Solid State Sensor and Actuator Workshop,* Hilton Head Island, SC, 6/3-6/96, Transducers Research Foundation, Cleveland (1996) pp.178-182.

5. M. S. Rodgers, J. J. Sniegowski, S. L. Miller, C. C. Barron, and P. J. McWhorter, "Advanced micromechanisms in a multi-level polysilicon technology", *Proc. of SPIE Micromachined Devices and Components III, 3224*, 9/29/97, Austin, TX, (1997) pp. 120-130.

6. More technical information can be found at the web site http://www.mdl.sandia.gov/Micromachine.

7. R. D. Nasby, J. J. Sniegowski, J. H. Smith, S. Montague, C. C. Barron, W. P. Eaton, P. J. McWhorter, D. L. Hetherington, C. A. Apblett, and J. G. Fleming, "Application of Chemical-Mechanical Polishing to Planarization of Surface Micromachined Devices", *Technical Digest of the 1996 Solid State Sensor and Actuator Workshop,* Hilton Head Island, SC, 6/3-6/96, Transducers Research Foundation, Cleveland (1996) pp.48-53.

8. E. J. Garcia and J. J. Sniegowski, "Surface Micromachined Microengine as the Driver for Micromechanical Gears", *Proc. of the 8th International Conf. on Solid-State Sensors and Actuators and Eurosensors IX,* 6/25-29/95, Stockholm, Sweden 1, (1995) pp. 365-368.

9. W. C. Tang, Ph.D. Thesis, University of California, Berkeley, CA. (1990).

10. S. L. Miller, J. J. Sniegowski, G. LaVigne, and P. J. McWhorter, "Friction in surface micromachined microengines", *Proc. SPIE Smart Electronics and MEMS, 2722*, 2/28-29/96, San Diego, CA, (1996) pp. 197-204.

11. G. L. Benavides, "Rotary Pin-In-Maze Discriminator", U. S. Patent 5626040, Sandia National Laboratories, May 6, 1997.

MULTIDIMENSIONAL MOTION ANALYSIS OF MEMS USING COMPUTER MICROVISION

Dennis M. Freeman freeman@mit.edu
Alexander J. Aranyosi aja@mit.edu
Michael J. Gordon mjgordon@mit.edu
Stanley S. Hong stanhong@mit.edu

Department of Electrical Engineering and Computer Science and Research Laboratory of Electronics
Massachusetts Institute of Technology, Cambridge, Massachusetts 02139

ABSTRACT

Tools for in situ motion analysis of microelectromechanical systems (MEMS) are primitive by comparison to those available for microfabricated electronic systems. A potentially powerful method, which we call computer microvision, results from analysis of video images from a light microscope with algorithms from machine vision. In this paper, we demonstrate two practical applications of computer microvision: to calibrate a MEMS fatigue testing device, and to obtain a modal decomposition of motions of a microfabricated gyroscope.

The fatigue test structure was provided by Failure Analysis Associates, Inc. A proof mass is rotated about its single point of attachment to the substrate under a variety of controlled stimulus and environmental conditions. Motions are induced by electrical stimulation of one comb drive and sensed by the capacitance change in a second comb. Computer microvision was used to measure full six-degree-of-freedom motion of the proof mass. Results provide a direct calibration of the sense signal.

The microfabricated gyroscope is a tuning fork gyroscope provided by The Charles Stark Draper Laboratory. Two proof masses move alternately toward and away from each other in a tuning fork fashion. Angular rotations of the substrate about the axis of symmetry between the proof masses induce out-of-plane motions that are sensed as the output. The gyroscope is structurally complex and supports many modes of motion. Motions of the proof masses were measured using computer microvision, and the results were decomposed into components representing in-plane modes. Measurements were repeated at different frequencies to characterize the frequency dependence of each mode of motion. Modes were well fit as second order resonances. The tuning-fork (difference mode) resonant frequency (in air) was 22.8 kHz with quality of tuning (Q) of 202. The hula (common mode) resonant frequency was 20.9 kHz with a Q of 162.

BACKGROUND

MEMS are fabricated using VLSI methods similar to those used to fabricate electronic devices. Unlike electronics, however, simple methods for testing and characterizing internal failure modes of micromechanical devices do not exist. This limitation has important consequences for designers and fabricators of MEMS. For the designer, it can result in large numbers of costly prototypes. For the fabricator, it means increased costs because defects go undetected until late in the manufacturing process (e.g., after packaging). As the demand for precision micromechanical parts increases, and as the complexity of micromechanical systems increases, developing better tools for characterizing the performance of MEMS becomes crucial.

We have investigated tools for in situ measurement of micromechanical motions based on the combination of light microscopy, video imaging, and machine vision. We have previously used such tools to measure cochlear micromechanics [3], and we have also demonstrated the feasibility of their application to MEMS [7]. In this paper, we describe practical applications of the tools — to calibrate motions of MEMS, to measure three-dimensional frequency responses of MEMS, and to obtain modal decompositions of motions.

METHODS

MEMS are viewed with a microscope and imaged with a CCD camera while being driven with a periodic electrical signal (Figure 1). An LED is strobed once per stimulus period at a chosen phase, to yield a snapshot of the device position at the specified phase. This process is repeated at several stimulus phases, and at several focal planes. Computer vision algorithms estimate the change in position of the device between successive images. From these estimates, the periodic motion of the device is determined. This process is repeated at other stimulus frequencies and/or amplitudes to characterize the device motion. Measured motions were decomposed into their predominant modes, and frequency responses of these modes were thereby obtained.

Video microscopy. Test structures were mounted on the stage of a light microscope (Zeiss Axioplan 2 Motorized Research Microscope, Oberkochen, Germany), resting on an active vibration isolation table (Integrated Dynamics Engineering, Woburn MA). The objective (Zeiss LD-Epiplan 20X, numerical aperture 0.4) has a 9.8 mm working distance, large enough to accommodate the use of external electrical probes. The magnified image was projected onto a scientific grade, 10-bit CCD camera (Kodak Megaplus 1.6i), which has 1534 × 1024 pixels with 9 μm spacing.

Stroboscopic illumination. The maximum frame rate of a scientific-grade video imager is typically on the order of tens of Hertz. To image faster motions, we use stroboscopic illumination. A green LED (Nichia NSPG500S, Tokushima 774, Japan) is pulsed so that the target is illuminated at a selected phase of its motion (see waveforms in Figure 1). Light from the LED was collected with a halogen lamp housing: the halogen lamp was removed, and the LED was mounted near the intended position of the tungsten filament. The plastic lens that originally covered the LED's die was milled away and the flat surface was polished, so that illumination was Köhler [11]. Since the intensity of the light emitted from an LED is more nearly proportional to current than voltage, the LED was driven by a computer-controlled D/A converter via a voltage-to-current converter. Because LEDs are fast, the shortest light pulse is limited in practice by the electronics driving the LED (roughly 1 μs for our circuit).

0-9640024-2-6/hh1998/$20©1998TRF
DOI 10.31438/trf.hh1998.33

Solid-State Sensors, Actuators, and Microsystems Workshop
Hilton Head Island, South Carolina, June 8-11, 1998

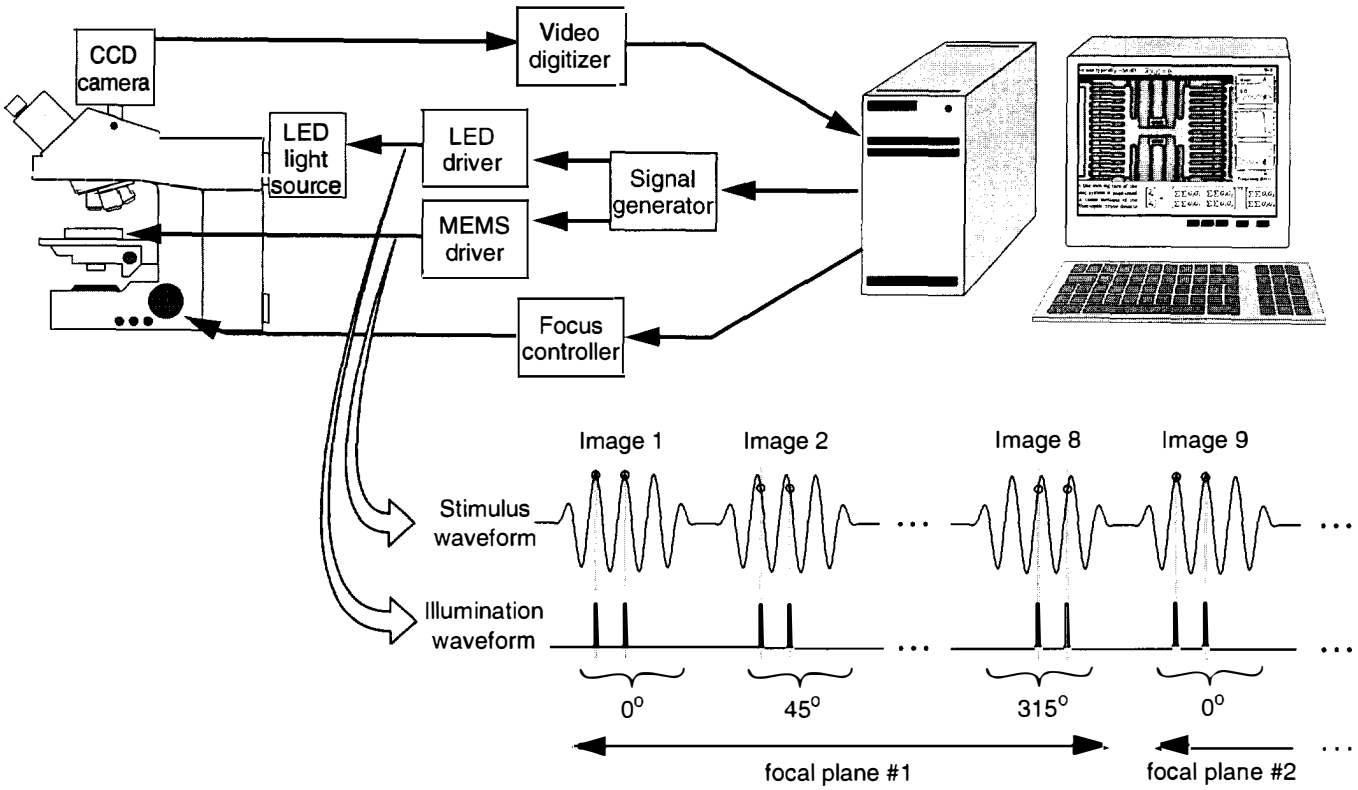

Figure 1. *Computer microvision measurement system. The test device is placed on the stage of the microscope (left). A Pentium-based computer controls a signal generator that provides two synchronized waveforms: one to drive motions of the test device and one to strobe the light source. Typical waveforms are shown. Motions are driven with a sinusoidal stimulus. The first image is acquired when light from the LED samples the image at times corresponding to peaks in the stimulus waveform. Successive images are acquired at different phases. This process is then repeated for different focal planes selected by a computer-controlled focus adjustment.*

Motion estimates from video images. To characterize sinusoidal motions, eight or sixteen images of the specimen were acquired at evenly-spaced phases of the stimulus cycle using stroboscopic illumination. The LED was gated so that the duty cycle was 1/8 period if eight images were collected or 1/16 period if 16 phases were collected.

Displacements between images acquired at successive phases were estimated directly from the video images. Although image resolution is limited by the optics [**8**] to distances on the order of the wavelength of light (typically 550 nm), displacements between two such images as small as nanometers can be reliably measured [**5**]. Algorithms for motion detection are described elsewhere [**4; 12**].

Translational and/or rotational displacement estimates at successive phases were used to reconstruct time waveforms of motion. The magnitude and phase of the fundamental component of that waveform were computed with an FFT. All magnitudes are reported as peak-to-peak values.

3D measurements. Silicon devices are opaque to green light. Nevertheless, information about axial motion can be obtained from images obtained from different focal planes. Images from above the best plane of focus of a structure are blurred. As the structure moves axially, the axial blurring pattern moves with the structure. Therefore, the algorithms that are used to track in-plane motions by computing in-plane gradients can equally track out-of-plane motions by computing out-of-plane gradients [**12**]. Images were acquired at different focal planes (50 nm resolution) to obtain information about 3D motion. In early experiments, focus was adjusted by translating the stage in the axial direction using an integrated stepper motor (part of the Zeiss Axioplan 2 Motorized Research Microscope). This method provided axial positioning with 0.05 μm resolution over large axial excursions — essentially limited only by the rack-and-pinion mechanism that supported the stage. However, axial motions were accompanied by submicrometer in-plane displacements. In later experiments, focus was controlled by translating the objective with a piezoelectric crystal (PIFOC, Polytec PI, Wandbronn, Germany). Although this device limited axial excursions to 100 μm, in-plane displacements were significantly smaller.

Modal analysis. MEMS were stimulated sinusoidally, and motions were measured as a function of frequency of the excitation. Frequency responses typically exhibited a small number of resonant peaks that suggest the importance of a small number of resonant modes of motion. When the resonant peaks were sharp, the spatial character of the mode could be determined simply by observing the pattern of motion at the resonant frequency. However, when the resonant peaks were not sharp, empirical methods for separating modes were employed.

One important empirical method takes advantage of common mode and difference mode decompositions of motion measurements at multiple sites. Consider, for example, out-of-plane motion measurements at two edges of a proof mass. The common-mode component of these measurements, which is simply the average of the two axial motions, provides a quantitative estimate of the amount

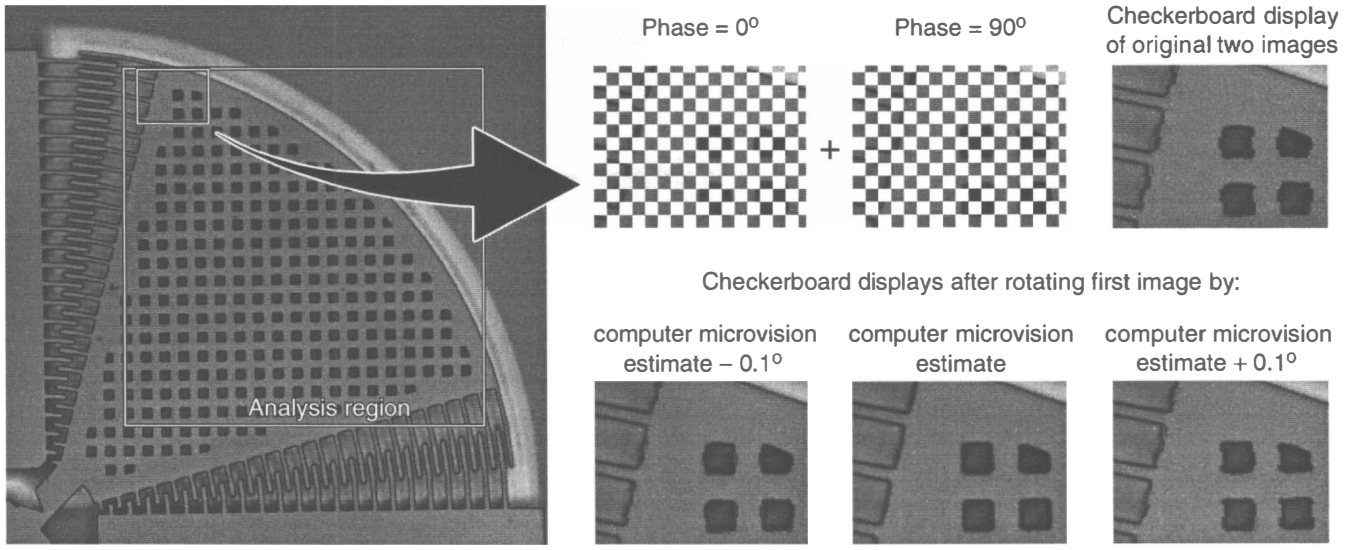

Figure 2. Accuracy of motion estimates using computer microvision. The left panel shows an image of a fatigue test structure designed by Failure Analysis Associates, Inc. One comb drive was stimulated sinusoidally at 20387.9 Hz to stimulate rotations at the mechanical resonance frequency of 40775.8 Hz. Images were acquired at 8 phases during each period of the electrical stimulus. Pixels in the analysis region indicated by the large white box were analyzed to determine the angular displacement. Portions from the upper right parts of the images taken at two phases were interleaved in a checkerboard fashion as shown in the upper right panel. The lower right panels illustrate similar checkerboard displays after the first image was rotated by the computer microvision estimate and by the estimate plus and minus 0.1°.

of the average levitation of the proof mass. The difference-mode component of these measurements, which is simply the difference of the two axial motions, provides an estimate of out-of-plane rocking. Thus, out-of-plane motions of a single proof mass can easily be decomposed into out-of-plane rocking and out-of-plane levitation modes using the common and difference mode decompositions.

A second important empirical method takes advantage of the fact that modes of motion are invariant to stimulus condition (provided that the stimulus amplitudes are small enough that nonlinearities are not important). Thus modes that are too small to measure under one stimulus condition can sometimes be measured using a different stimulus condition. Consider out-of-plane levitation as an example. Little out-of-plane levitation would be expected if two comb drives located on opposite sides of a proof mass provide push-pull excitations. Thus, motions in response to this stimulus condition would not provide much information about the resonant frequency or quality of tuning of the levitation mode. In this case, symmetrical electrical stimulation is useful to characterize out-of-plane levitation even if the normal stimulus condition is push-pull.

RESULTS

We have applied computer microvision to calibrate the motions of fatigue test structures, to measure in-plane and out-of-plane frequency responses of those structures, and to obtain modal decompositions of motions of microfabricated tuning fork gyroscopes.

Calibration of fatigue test structures from Failure Analysis Associates, Inc.

Failure Analysis Associates, Inc. has developed test structures to investigate effects of stimulus and environmental conditions, as well as manufacturing process conditions, on the performance, aging, and ultimate failure of MEMS [2]. The test structures consist of a proof mass that is rotated about its single point of attachment to the substrate (Figure 2, left panel). Motions are induced by electrical excitation of one comb drive and are sensed by the change in capacitance of the other comb. The goal is to control environmental conditions, to monitor changes in responses, and to formulate quantitative models of reliability for MEMS.

An important response property for development of quantitative reliability models is the angular displacement of the proof mass. However, direct measurements of angular displacement are difficult. By comparison, indirect measurements of angular displacement that are based on the change in capacitance of an integrated comb are relatively simple. These indirect measurements are especially important for long duration tests of a large number of devices. However, the same process variations and/or aging processes that can affect the mechanical properties of the fatigue test structure could, at least in principle, affect the relation between angular displacement and capacitance between the combs. Consider for example that out-of-plane bending of only a small fraction of a degree could significantly change the capacitance between the outermost teeth. To directly control for this possibility, we have applied computer microvision to calibrate motions of test structures developed by Failure Analysis Associates, Inc.

Test structures were excited with a variety of electrical stimuli and images were acquired and analyzed by computer microvision. Because the resulting motion estimates are derived directly from sequences of images, the quantitative results can be checked qualitatively by simply viewing the slow-motion video sequences. For example, to test that the rotation estimate between two images is qualitatively correct, the first image can be rotated by the estimate and then compared to the second. To the extent that the estimate is correct, the rotated first image should exactly align with the origi-

nal second image. Such a qualitative analysis is shown in Figure 2, where registration errors are emphasized in a checkerboard display. Jaggedness of the edges of structures in the checkerboard display indicates registration error between the images.

As shown in Figure 2, visual assessment of alignment can convincingly detect registration errors on the order of 0.1°. This is in good agreement with fundamental limitations of optics [8]. Visual assessments are diffraction limited, i.e., limited by blurring intrinsic to the optics, which is on the order of the wavelength of light for well-corrected optics. Blurring of images from our system, which uses green light (wavelength = 550 nm), is on the order of 0.5 μm. Thus, errors in alignment on the order of the blurring width translate to angular errors on the order of $\arctan(0.5/L)$, where L is the length of the structure in μm. For the test structure in Figure 2 $L \approx 400$ μm, suggesting blurring errors on the order of 0.07°.

Although images are blurred by diffraction, they can be accurately registered to within a small fraction of the blurring radius using algorithms from machine vision [9]. We use a gradient method [10] that relates changes in brightnesses across images to gradients in brightness within an image. For example, if a pixel is illuminated by a middle part of a target that is brighter to the right and dimmer to the left, then the pixel should get brighter if the target moves to the left and dimmer if the target moves to the right. The gradient algorithm combines changes in brightnesses of all pixels in a region of interest (large white box in left panel of Figure 2) using a least squares method [4; 5]. Figure 3 show results of this algorithm for 5 independent repetitions of the measurement at 15 different amplitudes of stimulation. The standard deviation for repeated trials is less than 4 milli-degrees p-p at all amplitudes.

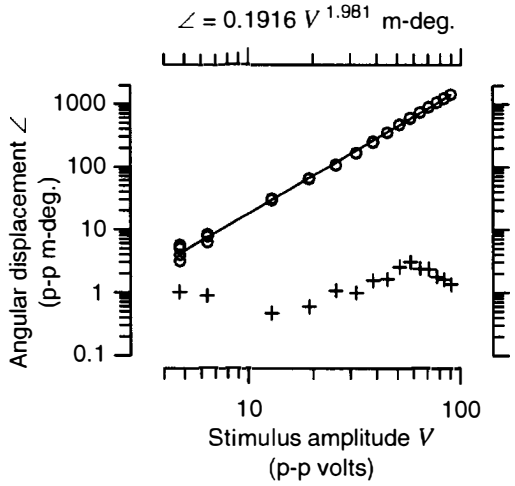

Figure 3. Calibration of fatigue test structure developed by Failure Analysis Associates, Inc. The device used in Figure 2 was stimulated at resonance with a sinusoidal voltage. Five independent measurements (circles) were made at each of 15 different amplitudes (abscissa) of stimulation. The line given by the equation at the top of the plot is a regression line fit by a least squares method. Pluses indicate the standard deviations of results at each amplitude.

Analysis of images at multiple planes of focus provides three-dimensional motion information (see Methods). Three-dimensional measurements at multiple points on the proof mass of the fatigue test structure allow determination of three-dimensional angular displacements. Figure 4 illustrates angular displacements as a function of stimulus frequency. These measurements exhibit high quality resonance for angular displacements in the plane of the proof mass and low-pass behaviors for out-of-plane levitation and rocking.

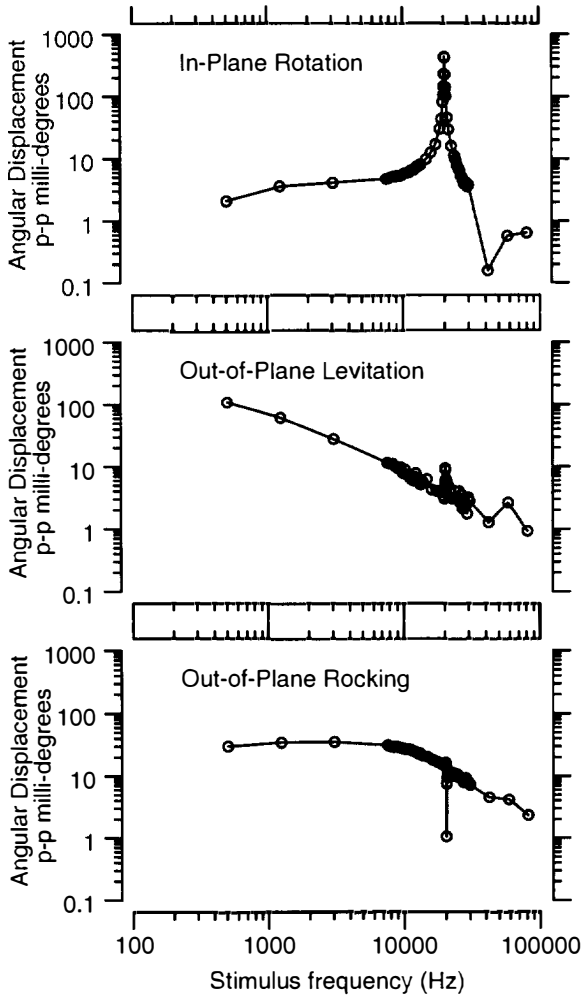

Figure 4. Three-dimensional rotations of fatigue test structure. Motions were excited with constant amplitude (60 V p-p) stimuli at 56 frequencies. Mechanical responses are at twice the stimulus frequency. Images at 12 focal planes (2 μm spacing) were analyzed to determine in-plane rotation, out-of-plane levitation, and out-of-plane rocking. Results are displayed as angular displacements. The outlier point in the out-of-plane rocking measurements falls exactly on the in-plane resonance frequency.

Modal analysis of the Draper gyroscope

The Charles Stark Draper Laboratory has developed a microfabricated gyroscope for sensing angular velocity [1]. The gyroscope consists of two proof masses suspended by cantilevers. The masses are driven by comb drives along one axis, so that angular rotation about the perpendicular in-plane axis induces a coriolis force in the out-of-plane direction. This force induces motion of the proof masses perpendicular to the substrate, and the motion is sensed as a change of capacitance between the proof mass and the substrate. The two masses are driven in opposite directions to facilitate separation of angular velocity from linear acceleration.

The gyroscope is structurally complex and supports many

modes of motion; the dominant modes of motion in the plane of the proof masses are a tuning-fork mode (the difference mode of the two proof masses), and a hula mode (the common mode of the two proof masses). The hula mode can complicate the sensing of angular velocity by adding unwanted sensitivity to linear acceleration. Draper Labs has applied design and simulation tools to analyze undesired modes of motion. We have extended these efforts by experimentally measuring displacements of the proof masses and determining the contribution of in-plane modes of motion to these displacements.

Motions of the proof masses were measured using computer microvision under three stimulus conditions. In stimulus condition A, the outer combs of both proof masses were driven with a 40V p-p sinusoid with 20V DC offset; this stimulus preferentially excites the tuning-fork mode. In stimulus condition B, the outer comb of the left-hand proof mass was driven; this stimulus preferentially excites the hula mode. In stimulus condition C, both combs of the left-hand proof mass were driven with the same voltage. This stimulus preferentially excites the out-of-plane levitation mode.

In all stimulus conditions, both tuning-fork and hula modes were induced. To estimate tuning properties of the tuning-fork mode, we computed half the difference in motion of the two proof masses in stimulus condition A. To estimate tuning properties of the hula mode, we computed half the sum of the motions of the two proof masses in stimulus condition B. The magnitude of the frequency response of each mode was fit with a low-pass second-order resonance. Each fit had three free parameters – DC gain, resonant frequency, and quality of tuning (Q). The measured and fitted phases were compared later to determine the goodness of the fit. Both modes were well fit by second-order resonances. The tuning-fork (difference mode) resonant frequency (in air) was 22.8 kHz with a Q of 202. The hula (common mode) resonant frequency was 20.9 kHz with a Q of 162. Figure 5 shows the measured modes and computed fits as a function of frequency.

Motions of any point on a structure can be described as a weighted sum of the dominant modes of motion of the structure [6]. For example, in-plane motions of one proof mass of the gyroscope can be fit with a weighted sum of the tuning-fork and hula modes. The weights are the DC gains of the modes, which vary with stimulus condition and level and determine the contribution of each mode to the overall motion. The sum of the tuning-fork and hula modes gives a four-pole, two-zero system where the relative weights of the modes determine the locations of the zeroes, but not of the poles. The magnitude of motion of one proof mass was fit by this four-pole, two-zero system with two free parameters: one (gain) affecting the overall level of the fit, and one (relative mode weights) affecting the shape by changing the frequency of the zeroes. The fit was performed for the left proof mass under stimulus condition A, and for the right proof mass under stimulus condition C. As with the modal fits, a post hoc comparison of phase was done to determine the goodness of the fit. Motion of the proof masses under both stimulus conditions was well fit by the weighted sum of the modes. In stimulus condition A, the tuning-fork mode had a DC gain of 0.0525 μm, and the hula mode had a DC gain of 0.00277 μm. In stimulus condition C, the tuning-fork mode had a DC gain of 0.00604 μm, and the hula mode had a DC gain of 0.00101 μm. Figure 6 shows the measured displacements and computed fits as a function of frequency.

DISCUSSION

We have demonstrated the use of computer microvision as a tool for in situ motion analysis of MEMS. We have employed this new tool to calibrate motions of a fatigue test structure and to perform a modal decomposition of motions of a microfabricated gyroscope.

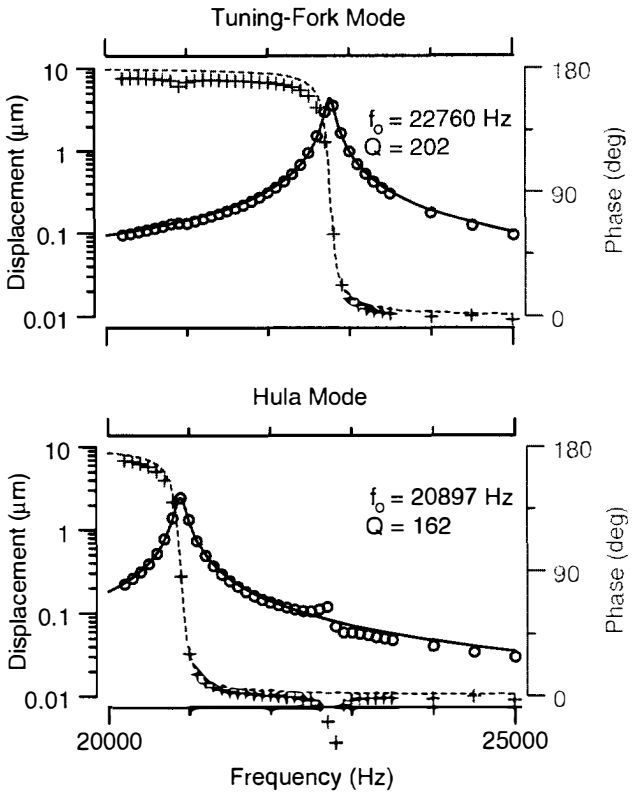

Figure 5. *Modes of motion of the Draper gyroscope. Proof masses were driven by 40V peak-to-peak sinusoid with 20V DC offset. Displacements of both proof masses in the direction of excitation were measured at each frequency using computer microvision. These displacements were subtracted and divided by 2 to estimate the tuning-fork component, and were summed and halved to estimate the hula component. The modes were then fit with low-pass second-order resonances. The plots show the measured (symbols) and fitted (lines) magnitude (black circles) and phase (gray pluses) of the two modes.* **A.** *Tuning-fork mode. This mode was preferentially excited by driving the outer combs of both proof masses (stimulus condition A). Resonant frequency = 22760 Hz; damping coefficient = 0.00247; mean squared error = 1.13 nm.* **B.** *Hula mode. This mode was preferentially excited by driving the outer comb of the left proof mass (stimulus condition B). Resonant frequency = 20897 Hz; damping coefficient = 0.03085; mean squared error = 0.660 nm.*

These results demonstrate several unique features of computer microvision. First, computer microvision provides estimates of translations and rotations in multiple dimensions. Measurements in multiple dimensions allow unambiguous characterization of complex motions. This contrasts with other measurement methods, such as laser interferometry or capacitive sensing, which provide an estimate of just one component of motion. Second, motion estimates with computer microvision are derived directly from sequences of images. Thus, all quantitative results can be checked qualitatively by simply viewing those images (Figure 2). This contrasts with other measurement systems, such as laser interferometry or capacitive sensing, which provide no internal consistency checks. Third, computer microvision provides concurrent measurements of all im-

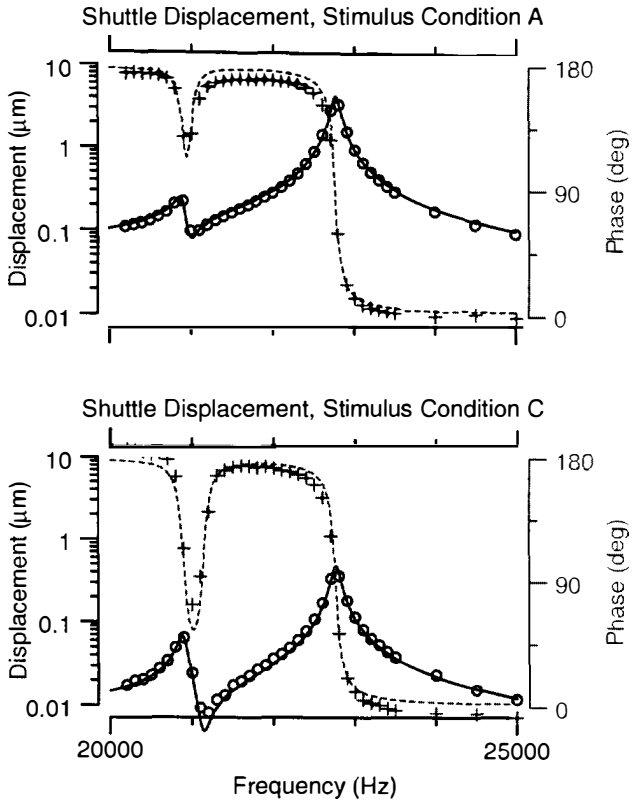

Figure 6. *Modal reconstruction of proof mass displacement. Both plots show the displacement of a proof mass as a function of frequency. These displacements were fit with a weighted sum of the two modes shown in Figure 5. Symbols are as in Figure 5.* **A.** *Displacement of the left proof mass, outer combs of both masses driven (stimulus condition A). The hula mode weight was 0.0528 relative to the tuning-fork mode. Mean squared error = 1.84 nm.* **B.** *Displacement of the right proof mass, both combs of left proof mass driven (stimulus condition C). The hula mode weight was 0.1673 relative to the tuning-fork mode. Mean squared error = 0.243 nm.*

aged structures. Motion measurements for different structures can be important for modal analysis (Figure 5). This contrasts with other measurement systems, such as laser interferometry or capacitive sensing, which measure motions of just one part of a structure.

Results in this paper demonstrate how computer microvision can be used to quantify motions of any imaged structure, and to relate motions of multiple structures to characterize complex modes of interaction. Modal analyses based on calibrated motion measurements provide important new opportunities for understanding the mechanical properties of MEMS.

ACKNOWLEDGMENTS

The authors acknowledge contributions to this project by previous colleages, including C. Quentin Davis, who developed the first computer microvision system, Zoher Z. Karu, who developed the three-dimensional algorithms, Laura K. Johnson, who first applied the method to analyze motions of the Draper gyroscope, and William W. Van Arsdell, who first applied the method to analyze motions of the fatigue test structure.

The authors gratefully acknowledge support of Failure Analysis Associates, Inc. and The Charles Stark Draper Laboratory. We especially thank Chris Muhlstein and Stuart Brown at Failure Analysis Associates, Inc. and Marc Weinberg, Jim Campbell, and John Bernstein for supplying test devices and for helping with measurements and interpretations. This work was supported by grants from DARPA (F30602-97-2-0106) and from The Charles Stark Draper Laboratory (E-96-414). This work builds on research in hearing supported by the NIH (2 R01 DC00238), which includes support for A. J. Aranyosi and D. M. Freeman. D. M. Freeman was supported in part by the W. M. Keck Career Development professorship.

REFERENCES

1. J. Bernstein, S. Cho, A. T. King, A. Kourepenis, P. Maciel, and M. Weinberg. A micromachined comb-drive tuning fork rate gyroscope. In *Solid-State Sensor and Actuator Workshop*, pages 143–148. Transducer Research Foundation, Inc., Cleveland, June 1993.

2. S. B. Brown, W. Van Arsdell, and C. L. Muhlstein. Materials reliability in MEMS devices. In *Transducers '97*, pages 591–593. 1997 International conference on Solid-State Sensors and Actuators, Chicago, June 1997.

3. C. Q. Davis and D. M. Freeman. Direct observations of sound-induced motions of the reticular lamina, tectorial membrane, hair bundles, and individual stereocilia. In *Abstracts of the Eighteenth Midwinter Research Meeting*, St. Petersburg Beach, Florida, February 1995. Association for Research in Otolaryngology.

4. C. Q. Davis and D. M. Freeman. Statistics of subpixel registration algorithms based on spatio-temporal gradients or block matching. *Optical Engineering*, 1998. (to appear in April).

5. C. Q. Davis and D. M. Freeman. Using a light microscope to measure motions with nanometer accuracy. *Optical Engineering*, 1998. (to appear in April).

6. D. G. Fertis. *Mechanical and Structural Vibrations.* John Wiley and Sons, Inc., New York, NY, 1995.

7. D. M. Freeman and C. Q. Davis. Using video microscopy to characterize micromechanics of biological and manmade micromachines. In *Solid-State Sensor and Actuator Workshop*, pages 161–167. Transducer Research Foundation, Inc., June 1996.

8. H. H. Hopkins and P. M. Barham. The influence of the condenser on microscopic resolution. *Proc. Phys. Soc.*, 63:737–744, 1950.

9. B. K. P. Horn. *Robot Vision.* MIT Press, Cambridge, MA, 1986.

10. B. K. P. Horn and E.J. Weldon, Jr. Direct methods for recovering motion. *Internatl. J. of Computer Vision*, 2:51–76, 1988.

11. Shinya Inoué. *Video Microscopy.* Plenum Press, New York, NY, 1986.

12. Z. Z. Karu. *Fast subpixel registration of 3-D images.* PhD thesis, Massachusetts Institute of Technology, 1997.

LUBRICATION OF POLYSILICON MICROMECHANISMS WITH SELF-ASSEMBLED MONOLAYERS

Uthara Srinivasan, Jonathan D. Foster, Usman Habib, Roger T. Howe, and Roya Maboudian
Berkeley Sensor & Actuator Center
University of California at Berkeley
Berkeley, CA 94720-1774

Donna Cowell Senft and Michael T. Dugger
Sandia National Laboratories
Albuquerque, NM 87185-0340

ABSTRACT

We have investigated the lubricating effects of self-assembled monolayers (SAMs) on microelectromechanical systems (MEMS) by measuring static and dynamic coefficients of friction with two polycrystalline silicon (polysilicon) surface-micromachined devices. The contacting elements in the first microstructure are as-deposited surfaces, and in the second device, they are etched sidewalls. Both devices are SAM-coated after the sacrificial layer etch following the procedures reported earlier [1,2]. The microstructures emerge released and dry from the final water rinse without requiring additional drying techniques. Using the first test structure, the coefficient of static friction, μ_s, between as-deposited surfaces was found to decrease from 2.0 ± 0.8 for the standard SiO_2 coating to 0.09 ± 0.01 and 0.10 ± 0.01 for films derived from octadecyltrichlorosilane (OTS) and 1H,1H,2H,2H-perfluorodecyltrichlorosilane (FDTS), respectively. OTS and FDTS SAM-coated structures exhibit kinetic coefficients of friction, μ_k, of 0.07 ± 0.01 and 0.08 ± 0.01, respectively. These values were found to be independent of the apparent contact area, and remain unchanged after 1 million impacts at an apparent pressure of 26 kPa, indicating that these SAMs continue to act as boundary lubricants despite repeated impacts. Measurements from a FDTS SAM-coated sidewall friction testing structure gave comparable μ_k values of 0.02 at an apparent contact pressure of 84 MPa. After 2100 cycles at this high pressure, μ_k was found to rise to 0.27, suggesting SAM wear. Despite this observation, results suggest the FDTS SAMs prolong device lifetime in comparison to oxide-coated counterparts.

INTRODUCTION

Due to their large surface area to volume ratios, adhesion and friction are critical issues for microactuators which contain contacting surfaces in relative motion [3-5]. High static friction is known to contribute to wear and can cause device seizure, and kinetic friction consumes a significant portion of the motive torque [6,7]. Investigations into the failure modes of electrostatic microengines, for example, indicate that the usual path to failure involves adhesion between rubbing surfaces [8]. In order to operate microactuators with sliding surfaces in high-reliability, long lifetime applications, a robust lubrication scheme which affords precise control of the friction forces is needed.

In MEMS, contacting surfaces are lightly loaded (~μN), placing friction in a regime where the contribution from adhesion dominates over that from asperity deformation [3,5,9]. While tribological studies have been conducted on untreated and chemically modified silicon surfaces at the nanoscale with atomic force microscopy (AFM) [10] and at the macroscale using pin-on-disc tribometers [11], there are difficulties in applying these results to surface-micromachined devices. For example, AFM work is generally conducted on smooth Si(100) and mica, whereas the surfaces in MEMS are relatively rough and hence, the real area of contact between them is not easily known. In pin-on-disc tribometer experiments, contact forces are typically on the order of mN over millimeter-sized areas, so that adhesion from capillary condensation – a critical problem in MEMS, is no longer significant. Therefore, in order to conduct friction studies with the contact pressures and surfaces topographies relevant to microactuators, it is desirable to use surface-micromachined test devices for *in situ* measurements.

Lim and coworkers investigated static friction in a micromachined device between polysilicon/polysilicon and polysilicon/Si_3N_4 interfaces, and reported μ_s values of 4.9 ± 1.2 and 2.5 ± 0.5, respectively [6]. Kinetic coefficients of friction have been measured by several groups using electrostatic micromotors and microbearings [3,12,13]. Bart *et al.* reported a μ_k range of 0.26-0.4 for polysilicon/polysilicon contacts, and similar ranges have been reported for polysilicon rubbing against Si(100) and Si_3N_4 [3,12,13]. Friction measurements between polysilicon/diamond-like carbon contacts have also been conducted, with reported μ_k of 0.38 ± 0.05 at an apparent contact pressure of 16.1 kPa [3].

Low surface energy organic films may be deposited on the contacting surfaces in microactuators to reduce adhesion and serve as boundary lubricants. SAMs formed from alkyltrichlorosilane precursors have been investigated in this regard [1,2,7,14,15]. The precursor molecules covalently bind to the substrate and each other through siloxane linkages (Si–O–Si) to form a dense monolayer. With thicknesses of 1-2 nm, these conformal coatings do not affect bulk material properties significantly, and are therefore well-suited to MEMS [15]. When applied to micromachined polysilicon surfaces, hydrocarbon- and fluorocarbon-based SAMs have been shown to reduce the adhesion energy by over three orders of magnitude [1,2]. In addition, these coatings show exceptional solvent and chemical resistance, wear and durability, and stability at the elevated temperatures encountered in MEMS packaging processes [1,2,7,16].

In microactuators, sliding friction can arise between etched sidewalls or laterally sliding as-deposited surfaces. These two types of surfaces have different topographies and possibly different chemical compositions due to their distinct processing histories. In this paper, we describe two surface-micromachined test structures designed to study friction between these types of contacts. Static and dynamic friction coefficients derived from OTS-, FDTS-, and oxide-coated test structures are presented. In addition, wear between FDTS SAM-coated surfaces in repetitive

0-9640024-2-6/hh1998/$20©1998TRF
DOI 10.31438/trf.hh1998.34

Solid-State Sensors, Actuators, and Microsystems Workshop
Hilton Head Island, South Carolina, June 8-11, 1998

normal impact and sliding situations is examined using friction measurements and SEM.

EXPERIMENTAL

Lateral Friction Test Structure. Fig. 1 shows SEM micrographs of the lateral friction test structure after the design of Lim *et al.* [6]. The microstructure consists of a shuttle with bumpers on its underside, maintained 2 μm above the ground plane by a folded beam suspension. The shuttle is attached to an electrostatic comb drive which is used to determine the spring constant of the folded beam suspension. An underlying electrode is used to pull on the shuttle and bring its bumpers into contact with an electrically separate, grounded landing pad.

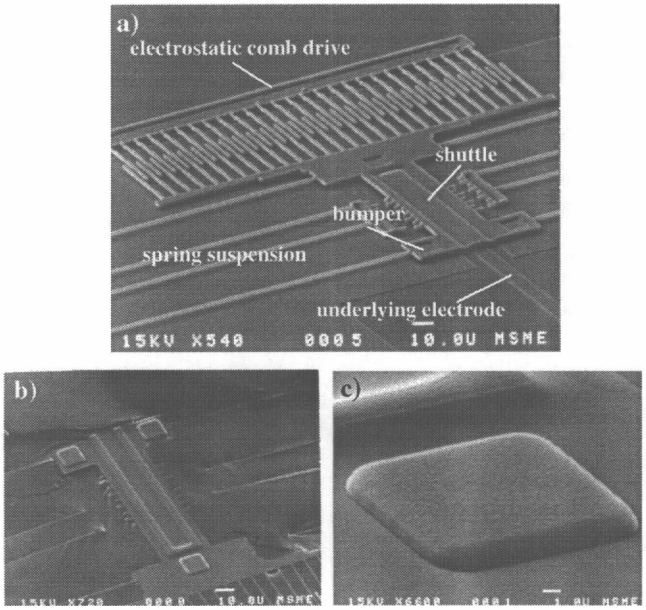

Figure 1. *SEM micrographs of* ***a)*** *the lateral friction testing microstructure, consisting of a spring-suspended shuttle attached to an electrostatic comb drive used for spring characterization,* ***b)*** *the underside of the shuttle, and* ***c)*** *a close-up of a 10×10×1 μm³ bumper.*

These test structures were fabricated at UC Berkeley using low-stress, low-strain gradient polysilicon films according to the deposition conditions in [17]. The 1 μm deep bumper molds are defined in the sacrificial oxide layer using a timed BHF wet etch. To assess frictional dependence on contact area, microstructures with varying numbers of bumpers and surface area per bumper were fabricated. A Topometrix atomic force microscope was used to image the contacting surfaces and study their textures.

Fig. 2 shows a schematic of the microstructure during the testing procedure [6]. First, the spring-suspended shuttle is laterally displaced a distance of Δx_1 using a tungsten probe tip. Then, the shuttle's bumpers are electrostatically brought into contact with the grounded landing pad by applying a voltage to the underlying electrode. (For the SAM-coated devices, this clamping voltage was 50 V; for the oxide-coated structures, 20 V was used since with higher voltages, the shuttle would often not move even after the clamping voltage was reduced to below the pull-in voltage, V_p.) When the lateral force is removed, static friction between the contacting surfaces maintains the displacement. The electrostatic clamping force is decreased slowly until the lateral suspension force can overcome the static frictional force, and the shuttle begins to move towards its equilibrium position. The shuttle slides a certain distance and stops at a residual displacement Δx_2.

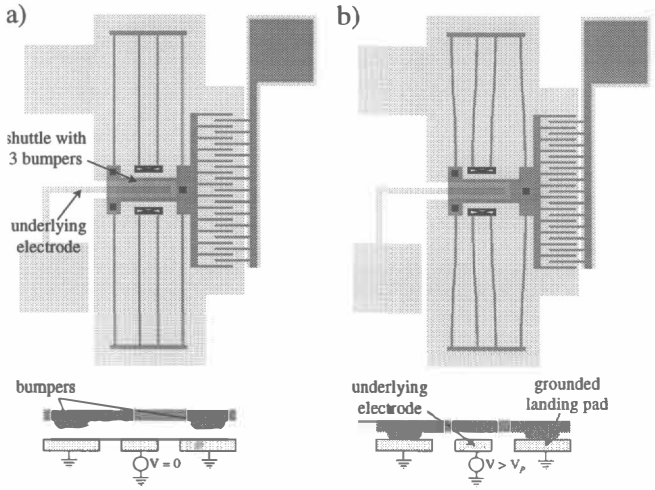

Figure 2. *Top and side views of the lateral friction testing microstructure in* ***a)*** *its equilibrium position and* ***b)*** *displaced and clamped.*

The coefficient of static friction, μ_s, is calculated using a force balance as in eq. 1 [6]:

$$\mu_s = \frac{F_t}{F_n} = \frac{k_x \Delta x_1}{F_n} \tag{1}$$

where F_t and F_n are the normal and tangential forces exerted on the shuttle at the point of slippage, respectively. F_n is composed of the electrostatic clamping force minus the spring suspension's restoring force in the z-direction, and can be calculated according to eq. 2, where α_z is a correction factor to account for fringing effects (taken as 1.1), l and w are the length and width of the underlying electrode, z is the gap distance, ε_o is the permittivity of air and V_s and V_p are the potentials at which the shuttle begins to slip and where it can overcome the spring's z-restoring force, respectively.

$$F_n = \frac{\alpha_z \varepsilon_o w l (V_s^2 - V_p^2)}{2z^2} \tag{2}$$

The lateral spring constant, k_x, used to calculate F_t is computed empirically by resonating the electrostatic comb drive and using Rayleigh's method [6,18]. With dimensions and masses substituted in, eq. 1 can be rewritten as follows:

$$\mu_s = \frac{0.2 f_o^{\,2} \Delta x}{V_s^2 - V_p^2} \tag{3}$$

where f_o is the resonant frequency of the spring suspension.

The difference in the shuttle's potential energy between its starting and stopping positions is due to dissipation to kinetic friction. Therefore, assuming μ_k is constant in this range, it can be derived from an energy balance and is given by:

$$\mu_k = \frac{1}{2}\mu_s \left(1 + \frac{\Delta x_2}{\Delta x_1}\right) \tag{4}$$

For the results reported here, testing is done in air ($RH \approx 30$-50%) at room temperature. For each test structure, f_o, Δx_1, Δx_2, V_s and V_p are measured and μ_s and μ_k are computed. The reported data is taken from chips from one wafer. For normal impact tests, 30 V square waves at a frequency of 10 Hz are applied to the electrode underneath the shuttle to repeatedly impact the bumpers with the grounded landing pad while the device is in the equilibrium position. FDTS SAM-coated devices are subject to 1 million impacts at an apparent contact pressure of 26 kPa. Coefficients of friction are monitored periodically.

Sidewall Friction Test Structure. The sidewall friction test device shown in Fig. 3 is driven by two sets of electrostatic comb drives, X and Y, which are used to reciprocate a beam back and forth against a rounded post. Each comb drive set can push and pull with a maximum force output of ≈10 μN. This microstructure was fabricated at Sandia National Laboratories using the SUMMiT process from four layers of polysilicon – one electrical and three structural layers [4, 19].

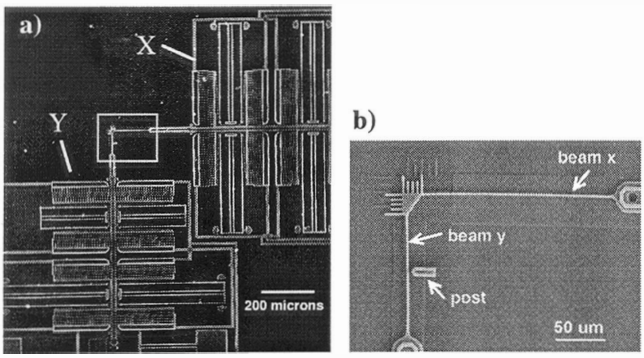

Figure 3. *a) An SEM of the sidewall friction testing device showing two sets of electrostatic comb drives 90° to each other b) close-up of the boxed area in a) showing the contacting elements.*

A high-magnification SEM of the contact geometry is given in Fig. 4. This geometry is used to maintain a constant contact area regardless of beam tilting. The beam is 2.5 μm high and 1.8 μm wide. The post is 4 μm high with a 2 μm thick cap, and sits on a grounded electrical polysilicon layer integral with the ground plane of the comb drives. As fabricated, there is a 3 μm clearance between the beam and the post.

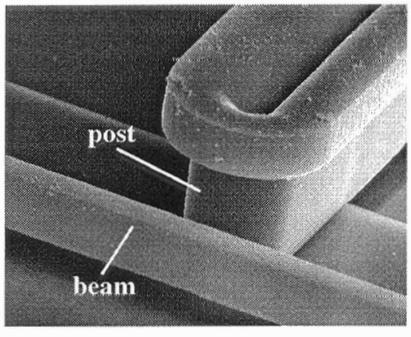

Figure 4. *SEM (6000× magnification) of contacting elements in the sidewall device. The beam rubs on the lower vertical sidewall of the post, and the cap on the post prevents the beam from sliding off.*

The testing procedure is as follows. First, the force exerted by comb drive Y is calibrated with the beam not in contact with the post. Square waves are used to drive the comb drive, and the resulting amplitude of the beam's motion, δ_o, is measured by capturing images using a strobe light synchronized with the drive signals. Since the moving parts have little inertia, the motion in response to the square wave occurs in less than 0.3 ms, leaving the part stationary for the remainder of the half-cycle [19]. The moving part advances until a force balance is achieved between the comb drive force (F_c) and the spring restoring forces of the comb drive's suspension ($k_c\delta_o$) and beam x ($k_b\delta_o$), as in eq. 5:

$$F_c = (k_c+k_b)(\delta_o) \tag{5}$$

Then, comb drive X is used in the pulling mode to bring the beam into contact with the post and exert a normal force between the two. Square waves are applied to comb drive Y to move the beam back and forth, and the amplitude of motion is measured. Due to frictional dissipation, this amplitude, δ, is less than δ_o. A force balance is achieved at the endpoints of motion, with the comb drive force balanced by the spring restoring forces and the kinetic friction force, F_k, yielding:

$$F_k = (k_c+k_b)(\delta-\delta_o) \tag{6}$$

where F_k is assumed to be constant.

The normal force exerted between the beam and post is calibrated in a separate step. Comb drive X is driven in the pushing mode to move beam y in the direction away from the post. This deflection is used with the spring constant of beam y to determine the force exerted by this comb drive. The dynamic coefficient of friction is then computed by dividing the frictional force, F_k, by the applied normal force.

In these experiments, a DC voltage of 70 V was applied to comb drive X resulting in a normal force of the beam on the post of 1.3 μN and a Hertzian contact pressure of 84 MPa [19]. Square waves 44 V in amplitude with a frequency of 100 Hz were applied to comb drive Y. The spring constants for beams x and y were calculated to be 0.087 N/m and 0.37 N/m, respectively, using dimensions measured with SEM and a value of 160 GPa for the Young's modulus. The spring constant for the comb drive suspension, derived by measuring beam deflection as a function of the comb drive voltage squared, was found to be 0.071 N/m, as confirmed by resonant methods [24].

SAM Coating Process. The structures were released in concentrated HF and then coated with SAMs. The procedure for SAM-coating microstructures is summarized in Table 1 [1]. The iso-octane, hexadecane, and chloroform used in the SAM coating are anhydrous (Aldrich), and the remaining chemicals are standard solvent grade.

Table 1. *SAM coating procedure for polysilicon microstructures. Solvent changes are accomplished by dilution rinses for the water soluble steps, and by quickly moving the wafer pieces to the next solvent for the organic solvent changes. The duration of each rinse step is ten minutes and the chips were immersed in H_2O_2 and the SAM solution for 15 minutes.*

1. Sacrificial Oxide Etch:	HF
2. Surface Oxidation:	H_2O rinse, H_2O_2 soak, H_2O rinse
3. Bulk Water Removal:	IPA rinse (×2), Iso-octane rinse (×2)
4. SAM Formation:	SAM solution
5. Excess Precursor Removal and Dry:	Iso-octane rinse (×2), IPA rinse (×2), H_2O rinse

The OTS SAM solution consists of 0.5 mM octadecyltrichlorosilane ($CH_3(CH_2)_{17}SiCl_3$, Aldrich, 95% purity) in a 4:1 vol. mixture of hexadecane and chloroform. This solution was prepared and used under a fume hood. The fluorinated SAM solution, 1 mM FDTS ($CF_3(CF_2)_8(CH_2)_2SiCl_3$, PCR Chemicals, 98% purity) in iso-octane was mixed and used in a glovebox (*RH* ≈ 10%) to prevent bulk polymerization caused by its highly water-sensitive headgroup. The oxide-coated microstructures used as a benchmark for the friction studies were released in HF, reoxidized with H_2O_2, and dried using supercritical CO_2. The surface treatments were done at UC Berkeley.

Contact angle measurements were taken with a Ramé-Hart goniometer with water and hexadecane as test liquids. Time-of-flight secondary ion mass spectroscopy (TOF-SIMS) using a PHI-TRIFT spectrometer was used to study the quality of the SAM coatings and confirm that the coverage is the same for both test devices.

RESULTS

Lateral Friction. Contact angle measurements on SAM-coated polysilicon with water (≈110° for both SAMs) and hexadecane (38° for OTS, 68° for FDTS) confirm that well-packed coatings were formed [1,16]. Atomic force microscopy of the ground plane polysilicon gives an rms roughness of 5 nm [1].

Table 2. *Average normal and tangential forces (F_n, F_t) and static and dynamic friction coefficients (μ_s, μ_k). The total bumper area is 300 μm^2 (three 10×10 μm^2 bumpers) and the shuttle displacement is 12 μm.*

	F_n (μN)	F_t (μN)	μ_s	μ_k
Oxide	*0.48*	*1.1*	*2.0 ±0.8*	-
OTS	*8.6*	*0.77*	*0.09 ±0.01*	*0.07 ±0.01*
FDTS	*7.6*	*0.76*	*0.10 ±0.01*	*0.08 ±0.01*

Table 2 shows μ_s and μ_k values and the normal and tangential forces at the onset of shuttle slippage for measurements taken with an initial displacement of 12 μm. Data from test structures with different total bumper areas (300 and 144 μm^2) is shown in Table 3. Each friction coefficient represents an average of at least 30 data points. Static friction measurements were also taken at different initial displacements between 4 and 12 μm corresponding to varying tangential forces. SAM-coated devices gave constant friction coefficient values at three different measurement positions. For oxide-coated structures, initial displacements of 9.5 and 12 μm gave similar μ_s values of 2.10 ± 0.8 and 2.0 ± 0.7, respectively. Tests using smaller initial displacements were unreliable due to stiction – often, the shuttle remained clamped to the substrate even when the applied normal force was reduced to zero.

Table 3. *Static coefficient of friction data taken from test structures with four 6×6 μm^2 and three 10×10 μm^2 bumpers (total areas of 144 μm^2 and 300 μm^2, respectively).*

	μ_s (A = 144 μm^2)	μ_s (A = 300 μm^2)
Oxide	*2.3 ±0.8*	*2.0 ±0.8*
OTS	*0.09 ±0.01*	*0.09 ±0.01*
FDTS	*0.11 ±0.01*	*0.10 ±0.01*

At a ramp-down speed of 1 V/s for the clamping force, the movement of SAM-coated structures was a mixture of continuous sliding and stick-slip motion. At higher ramp-down speeds (5 V/s), motion appeared continuous.

FDTS SAM-coated lateral friction testing devices subject to 1 million impact cycles at an apparent contact pressure of 26 kPa showed no degradation in μ_s and μ_k values.

Sidewall Friction. A plot of the sidewall friction coefficient as a function of the number of wear cycles at 84 MPa is shown in Fig. 5. For the first ~800 wear cycles, the friction coefficient is 0.02. Then, after ~2100 cycles μ_k is observed to increase to an average value of 0.23. After 3.7×10^5 cycles, stick-slip predominates, indicated in Fig. 5 by the oscillation between high and low friction coefficient values. Friction coefficient values of ~0.9 result when the force of the comb drive is insufficient to move the structure. In this case, the plotted value of 0.9 is a lower bound to the actual friction coefficient. The test was continued for 2.3×10^7 cycles with the number of sticking events reduced after 5 million cycles and μ_k slowly rising to 0.28.

Failure of the device is taken as the point where sticking first occurs, giving a lifetime of 3.7×10^5 cycles. In comparison, oxide-coated structures show a lower lifetime of 1.9×10^4 cycles [19]. The uncoated structure ceased moving altogether after 7.7×10^4 cycles, whereas the FDTS-coated sidewall device was still operating when the test was terminated at 2.3×10^7 cycles. The factor of 20 difference in cycles to onset of sticking, and factor of more than 350 before complete seizure, suggests that SAMs prolong lifetime even though the initial μ_k of 0.02 is only maintained for ~800 cycles.

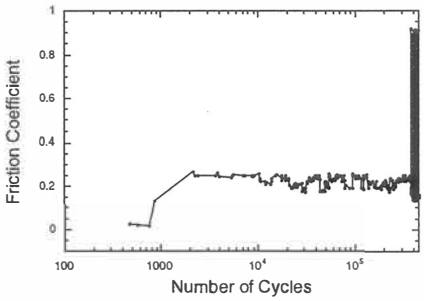

Figure 5. *The friction coefficient measured by the sidewall device during sliding friction. The large friction values intermittently measured after 3.7×10^5 cycles are due to sticking of the surfaces.*

After the wear test, the contacting surfaces were imaged by SEM as shown in Fig. 6. A buildup of material, presumably wear

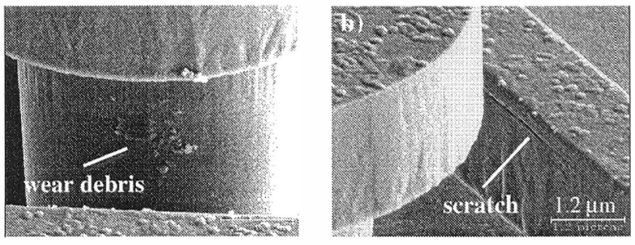

Figure 6. *SEM examination of the contacting surfaces of the sidewall device after 2×10^7 wear cycles shows a buildup of wear debris on the post and a horizontal scratch on the beam.*

debris, can be seen on the surface of the post. The surface of the beam shows a horizontal scratch and agglomerations of wear particles, each particle ~10 nm in size. SEM photos of unworn structures do not show evidence of particles or scratches.

DISCUSSION

Lateral Friction. Large differences in the static friction force are seen between structures coated with SAMs and SiO_2. The experiments performed on the lateral friction test structures give μ_s of 0.09 ± 0.01 and 0.10 ± 0.01 for OTS and FDTS films, respectively. These values are approximately 20 times lower than μ_s for the standard oxide coating, 2.0 ± 0.8. The results in Table 3 indicate that in this testing situation, these coefficients do not depend on apparent contact area, as expected from Amonton's law [6,20].

Since friction in MEMS arises from localized adhesion at the points of real contact, the high μ_s values for the oxide coating can be attributed to strong capillary forces between the surfaces. These attractions seem to be exerting a force between the contacting surfaces of comparable magnitude to the applied normal force. The dramatic reduction in μ_s with SAMs can be explained by the lack of capillary attractions between the hydrophobic SAM surfaces. Tests on cantilever beam arrays on the same chip support this– the apparent adhesive energy between the polysilicon surfaces is reduced by four orders of magnitude due to FDTS SAM films most likely through the elimination of capillary condensation [1].

The dynamic coefficients of friction ($\mu_{k,OTS}$ = 0.07 ± 0.01 and $\mu_{k,FDTS}$ = 0.09 ± 0.01) coincide well with literature results taken at the macroscale with pin-on-disc tribometers. Published values of μ_k for OTS SAM-coated Si(100) range from 0.07 [21] to 0.12 [11]. For the fluorinated monolayers, DePalma and Tillman report higher friction coefficients (μ_k = 0.16) despite their lower surface energies [21]. This has been attributed to greater adhesion hysteresis between the fluorinated films caused by the lower packing density of the fluoroalkyl chains [22]. The dynamic coefficients derived here are similar to those reported from Teflon-coated microengines (0.07) [23], and lower to those obtained for polysilicon/diamond-like carbon contacts under similar apparent pressures [3].

Using similar test structures, Lim and coworkers reported higher μ_s values of 4.9 ± 1.2 for oxide-coated polysilicon contacts [6]. The difference in μ_s may be due to the lower normal forces used (0.08 μN in [6] vs. 0.48 μN here), thus increasing the importance of adhesion between the surfaces. Also, different drying techniques were used, i.e., methanol rinse followed by air drying by Lim, *et al.* versus supercritical drying with ultrapure CO_2 in this paper. The high standard deviations in μ_{oxide} data given here as well as by Lim, *et al.* can be explained by considering that high surface energy oxide films favor the adsorption of polar contaminants from the ambient atmosphere, resulting in a highly variable surface layer. In contrast, low standard deviations in the friction data for the SAM films reflect improved reproducibility of these low energy surfaces.

With our test structures, the FDTS SAM film does not show degradation in friction coefficients after 1 million impacts at an apparent pressure of 26 kPa. Due to the rough nature of polysilicon surfaces, the real pressure between contacting asperities is expected to be significantly higher than the apparent pressure. An estimate for the real contact area between these surfaces can be made using an apparent adhesion energy of 23 $\mu J/m^2$, measured between OTS SAM-coated polysilicon surfaces [1]. (This value was obtained using surface-micromachined cantilever beam arrays fabricated on the same chip as the friction testers, and hence, with the same polysilicon topography.) Since the real adhesion energy between perfectly smooth, chemically identical surfaces is twice the surface energy, or ≈40 mJ/m^2 for OTS SAMs, the ratio of real to apparent area can be estimated as a ~0.001. Thus, the actual pressure between contacting asperties may be on the order of tens of MPa. In AFM experiments, OTS SAMs have been shown to be able to withstand local pressures in the tens of GPa [25].

Sidewall Friction. The initial μ_k value of 0.02 from the FDTS SAM-coated device is 7–10 times lower than that derived from an oxide-coated structure [19]. This friction coefficient is comparable to that measured using the lateral friction device. The factor of five difference may arise from the different surface topography encountered in the sidewall friction measurements.

The friction coefficient of 0.28 after ~2100 wear cycles at an apparent contact pressure of 84 MPa is consistent with prior measurements between oxide surfaces [19]. Due to the roughness of the reactive ion etched sidewall surfaces, the actual pressure at contacting asperities may be significantly larger than 84 MPa. SEM examination of the worn surfaces reveals wear debris and scratching at this pressure, possibly due to fracture of the underlying oxide and polysilicon surfaces [26]. The configuration of this test structure reproduces the sidewall contact found in some MEMS applications. The contact pressure is in the same range as the contact pressures calculated for Sandia microengine hub and pin joints, 27 and 140 MPa, respectively [27].

It is interesting to note that despite the increase in μ_k after ~800 cycles, the FDTS SAM-coated structure had a significantly longer operational lifetime than its oxide-coated counterpart [19]. The reason for this behavior is under investigation. Current work includes wear characterization of OTS coatings, which have shown superior wear properties to fluorocarbon SAMs [21,22].

CONCLUSIONS AND FUTURE WORK

Friction has been investigated between two types of contacts found in MEMS using surface-micromachined test devices. The results presented here show that nanometer-thick SAMs can serve as effective boundary lubricants of microactuators. Static friction coefficients between as-deposited contacts are reduced by a factor of 20 with respect to the standard oxide treatment. Dynamic friction coefficients are similarly low, and agree well with literature results taken at the macroscale. Measurements from the sidewall friction test device give a comparable μ_k, which is 7-10 times lower than that obtained with oxide-coated contacts. Impact tests indicate fluorocarbon SAMs can withstand 1 million cycles at an apparent pressure of 26 kPa without an increase in friction coefficients. Preliminary sliding wear experiments between FDTS-coated sidewall contacts at 84 MPa apparent pressure show increased friction after 800 cycles. Despite this observation, results suggest that these SAM coatings prolong device lifetime. Future work involves a systematic characterization of wear between SAM-treated surfaces, quantification of chemical and physical changes to the contacting surfaces during wear, and investigation into the effects of topography on friction.

ACKNOWLEDGMENTS

This research has been supported by Sandia National Laboratories. The authors acknowledge additional support from the National Science Foundation in the form of a graduate fellowship (US) and a young investigator award (RM).

Additional support from the William and Flora Hewlett Foundation in the form of a graduate fellowship (JDF) and from The Arnold and Mable Beckman Foundation in form of a young investigator award (RM) is gratefully acknowledged. The authors would like to thank Dr. Michael Houston for his work in fabricating the lateral friction test structures as well as the Berkeley Microfabrication Staff for their assistance. The work conducted at Sandia National Laboratories is supported by the United States Department of Energy under Contract DE-AC04-94AL85000. In addition, the authors would like to thank the staff of the Sandia National Laboratories Microelectronics Development Laboratory for fabricating the sidewall device.

REFERENCES

1. U. Srinivasan, M. R. Houston, R. T. Howe, and R. Maboudian, "Self-Assembled Fluorocarbon Films for Enhanced Stiction Reduction", *Proc. 1997 Int. Conf. on Solid-State Sensors and Actuators*, Chicago, IL, USA, June 16-19, 1997, Vol. 2, pp. 1399-1402.

2. M. R. Houston, R. Maboudian, and R. T. Howe, "Self-Assembled Monolayer Films as Durable Anti-Stiction Coatings for Polysilicon Microstructures", *Proc. IEEE Solid-State Sensor and Actuator Workshop*, Hilton Head, SC, USA, June 3-6, 1996, pp. 178-182.

3. U. Beerschwinger, R. L. Reuben, and S. J. Yang, "Frictional Study of Micromotor Bearings", *Sensors and Actuators A, 63*, 229-241 (1997).

4. E. J. Garcia and J. J. Sniegowski, "Surface Micromachined Microengine", *Sensors and Actuators A, 48*, 203 (1995).

5. K. Komvopoulos, "Surface Engineering and Microtribology for Microelectromechanical Systems", *Wear, 200*, 305-327 (1996).

6. M. G. Lim, J. C. Chang, D. P. Schultz, R. T. Howe, and R. M. White, "Polysilicon Microstructures to Characterize Static Friction", *Proc. IEEE MEMS Workshop*, Napa Valley, CA, USA, Feb. 11-14, 1990, pp. 82-88.

7. K. Deng, R. J. Collins, M. Mehregany, and C. N. Sukkenik, "Performance Impact of Monolayer Coating on Polysilicon Micromotors", *J. Electrochem. Soc., 142*, 1278-1285 (1995).

8. S. L. Miller, G. LaVigne, M. S. Rodgers, J. J. Sniegowski, J. P. Waters and P. J. McWhorter, "Routes to Failure in Rotaing MEMS Devices Experiencing Sliding Friction", *Proc. SPIE Micromachined Devices and Components III*, Vol. 3224, Austin, TX, USA, Sept. 29-30, 1997, pp. 24-30.

9. B. Bhushan, *Tribology and Mechanics of Magnetic Storage Devices*, Springer, New York (1990).

10. B. Bhushan, J. Israelachvili, and U. Landman, "Nano-tribology – Friction, Wear and Lubrication at the Atomic Scale", *Nature, 374*, 607-616 (1995).

11. P. Cléchet, C. Martelet, M. Belin, H. Zarrad, N. Jaffrezic-Renault, and S. Fayeulle, "Lubrication of Silicon Micromechanisms by Chemical Grafting of Long-Chain Molecules", *Sensors and Actuators A, 44*, 77-81 (1994).

12. Y-C. Tai and R. S. Muller, "Frictional Study of IC-Processed Micromotors", *Sensors and Actuators A*, 21, 180-183 (1990).

13. K. J. Gabriel, F. Behi, R. Mahadeven, and M. Mehregany, "*In situ* Friction and Wear Measurements in Integrated Polysilicon Mechanisms", *Sensors and Actuators A, 21*, 219-225 (1990).

14. R. L. Alley, R. T. Howe, and K. Komvopoulos, "Method of Applying a Monolayer Lubricant to Micromachines," US. Patent No. 5,403,665 (1995).

15. S. A. Henck, "Lubrication of Digital Micromirror Devices", *Tribology Letters, 3*, 239-247 (1997).

16. A. Ulman, *Introduction to Ultra-Thin Organic Films: From Langmuir Blodgett to Self-Assembly*, Academic Press, San Diego (1991).

17. M. Biebl, G. T. Mulhern, and R. T. Howe, "In situ Phosphorus-doped Polysilicon for Integrated MEMS", *Proc. 1995 Int. Conf. on Solid-State Sensors and Actuators*, Stockholm, Sweden, June 25-29, 1995, Vol. 1, pp. 198-201.

18. W. Tang, "Electrostatic Comb Drive for Resonant Sensor and Actuator Applications", Ph.D. Thesis, University of California at Berkeley, Berkeley, CA, 1990.

19. D. C. Senft and M. T. Dugger, "Friction and Wear in Surface Micromachined Tribological Test Devices", *Proc. SPIE Micromachined Devices and Components III*, Vol. 3224, Austin, TX, USA, Sept. 29-30, 1997, pp. 31-38.

20. F. P. Bowden and D. Tabor, *Friction and Lubrication*, Methuen & Co., 1967.

21. V. DePalma and N. Tillman, "Friction and Wear of Self-Assembled Trichlorosilane Monolayer Films on Silicon", *Langmuir, 5*, 868 (1989).

22. M. K. Chaudhury and M. J. Owen, "Adhesion Hysteresis and Friction", *Langmuir, 9*, 29 (1993).

23. B. K. Smith, J. J. Sniegowski, and G. J. LaVigne, "Thin Teflon-Like Films for Eliminating Adhesion in Released Polysilicon Microstructures", *Proc. of the 1997 Int. Conference on Solid-State Sensors and Actuators*, Chicago, IL, USA, June 16-19, 1997, Vol. 1, pp. 245-248.

24. S. L. Miller, J. J. Sniegowski, G. LaVigne, and P. J. McWhorter, "Friction in surface micromachined microengines", *Proc. SPIE Smart Electronics and MEMS*, San Diego, CA, USA, 1996, Vol. 2722, pp. 197-204.

25. V. T. Tsukruk, V. N. Bliznyuk, J. Hazel, and D. Visser, "Organic Molecular Films Under Shear Forces: Fluid and Solid Langmuir Monolayers", *Langmuir*, 12, 4840-4849 (1996).

26. U. Beershwinger, T. Albrecht, D. Mathiesson, R. L. Reuben, S. J. Yang and M. Taghizadeh, "Wear at Microscopic Scales and Light Loads for MEMS Applications", *Wear*, 181-183, 426-435 (1995).

27. D. M. Tanner, W. M. Miller *et al.*, "The Effect of Frequency on the Lifetime of a Surface Micromachined Microengine Driving a Load", *Proceedings of International Reliability Physics Symposium*, Reno, NV, USA, 1998.

PRESSURE-BASED MASS-FLOW CONTROL USING THERMOPNEUMATICALLY-ACTUATED MICROVALVES

John S. Fitch, Albert K. Henning, Errol B. Arkilic, James M. Harris
Redwood Microsystems, Inc., 959 Hamilton Avenue, Menlo Park, CA 94025

ABSTRACT

In this work, we demonstrate high-performance, pressure-based mass-flow control (PMFC). The microsystem is comprised of the following components: a thermopneumatically-actuated microvalve; an orifice; a temperature sensor; and two pressure sensors. The components are integrated using advanced packaging technologies, appropriate to and derived from the microelectronics industry. These PMFC devices have high accuracy and high resolution. They are targeted for gas and liquid control in the semiconductor process equipment industry, in such areas as chemical vapor deposition, plasma etch, liquid organic precursor control, and photoresist dispense. These applications require input pressures of up to several atmospheres, output pressures of a few Torr, and volumetric flow rates of between 0.2 and 1000 sccm.

INTRODUCTION

Previous MEMS work has demonstrated the performance of: thermopneumatically-actuated microvalves **[1]**; other micro-fabricated valves **[2]**; pressure and flow regulation using such valves **[3]**; microflow control using electrostatic valves **[4]**; and integrated, pressure-based mass-flow control **[5]**. Most mass-flow controllers (MFCs) today are thermal MFCs (TMFCs). They do not use MEMS-based components, but instead rely on the time-of-flight of a thermal pulse launched into a portion of the gas stream **[6]**. This work breaks new ground in several important areas. It demonstrates the high accuracy and repeatability available using pressure-based, as compared to thermal, mass-flow control. And, it demonstrates the integration of several micro-fabricated components, which (with an appropriate flow model) facilitates the realization of a PMFC having: high resolution; a wide range of flow control capability; relatively low power consumption; well-controlled materials in the wetted path; and adequate response time.

FLOW THEORY

The PMFC relies on analytical expressions for the flow through the fluidic elements of the device. These expressions are presented here.

As with TMFCs, the flow through the PMFC must be determined from sensor measurements. In this instance, however, the pressure upstream and downstream of a flow element (whether valve or orifice) is related to a calibrated flow model, in order to measure the flow. For gas flow, if there is no viscous loss, then the compressible flow model in the subsonic regime can be expressed as in Equation (1) **[7]**. δ is a parameter related solely to the ratio γ of specific heats (at constant pressure and volume) for the particular gas under control. R is the universal gas constant divided by the molecular weight of the gas. C_d is the coefficient of gas discharge for the flow element. P is the pressure either into, or out of, the flow element. T is the fluid temperature.

$$\dot{m} = \frac{P_{in}}{\sqrt{RT}} C_d A \left(\frac{P_{out}}{P_{in}}\right)^{\frac{1}{\gamma}} \delta(\gamma) \sqrt{\left(\frac{P_{in}}{P_{out}}\right)^{\frac{\gamma-1}{\gamma}} - 1} \qquad (1)$$

Sonic flow is given in Equation (2). α is a parameter similar to δ. Flow in the microvalve itself rarely enters the sonic regime. However, the flow area of the valve must be determined either using a loss coefficient model **[7]**, or some other means to relate the structural parameters (inlet area, and membrane-to-inlet gap) to the effective area. The valve and orifice have different values of C_d, between 0.7 and 0.9.

$$\dot{m} = P_{in} C_d A \frac{\alpha(\gamma)}{\sqrt{RT}} \qquad (2)$$

Liquid flow for the PMFC is given in Equation (3). C_l is the coefficient of liquid discharge for the flow element. β is the flow element inlet-to-plumbing diameter ratio.

$$\dot{m} = C_l A \sqrt{\frac{2\rho(P_{in} - P_{out})}{1 - \beta^4}} \qquad (3)$$

PRINCIPLE OF OPERATION

The PMFC is represented schematically in Figure 1. A ceramic package provides a modular foundation for the thermopneumatically-actuated microvalve, a flow orifice, two pressure sensors, and a temperature sensor. Specifications for the PMFCs are shown in Table I.

Figure 2 diagrams the system behavior, including feedback. In the following discussion, 'CO' refers to the flow orifice, and stands for 'critical orifice', even though the flow is not critical for liquids, and is occasionally sub-sonic for gases. 'NO' refers to the normally-open microvalve. The flow area of the CO is a constant. The effective flow area of the NO is proportional to the NO membrane stroke, which itself is governed by the power supplied to the microvalve. For gas flow through the CO in the sonic regime, the mass flow is linearly proportional to the absolute pressure upstream of the CO, as shown in Equation (2). The CO thus sets the flow range, consistent with the PMFC specification. Since the CO and NO devices are in series, the intersection of the flow models for each element determines both the sensed pressure P_x, and the mass flow. This principle is shown in Figure 3, where the PMFC module inlet pressure is 50 psia, and the module outlet pressure is 200 T. As the NO changes from 100 percent flow to lesser values of flow, the intersection of the NO and CO flow curves falls (the value of P_x falls), and the PMFC flow decreases.

The CO also sets the flow resolution, as shown in Figure 4 for sonic flow. Taking the derivative of Equation (2) with

0-9640024-2-6/hh1998/$20©1998TRF
DOI 10.31438/trf.hh1998.35

Solid-State Sensors, Actuators, and Microsystems Workshop
Hilton Head Island, South Carolina, June 8-11, 1998

respect to pressure upstream of the orifice creates the relationship between flow resolution and pressure resolution shown in this figure. For a given pressure sensor resolution and CO area, the minimum flow resolution becomes known. Thus, the CO determines not only the PMFC flow range, but also the minimum flow resolution.

PACKAGING AND SYSTEM INTEGRATION

Figure 5 shows the packaging associated with the PMFC. An on-board E^2PROM stores the flow calibration information which relates measured pressure to derived flow, using the appropriate flow equations shown earlier. The ceramic module is attached to a stainless steel manifold, for inclusion of the PMFC into the overall fluid control and distribution system. The feedback control electronics, and their incorporation into this package, are also depicted.

Figure 6 shows the natural extension of the PFMC's modular concept, into a complete, four-channel gas stick. Each channel consists of two vacuum leak-rate shut-off valves, a pressure regulator (derived from the PMFC), and a PMFC. A purge line for the channels is also included.

MEASUREMENTS

Figures 7-11 show measurements performed on a 10 sccm PMFC, as well as comparable TMFCs. The tests were performed under the SEMATECH specifications SEMASPEC #92071221 B-STD. The test system is based on a calibrated laminar flow element secondary standard, which is itself calibrated to a high-precision, rate-of-rise primary standard **[8]**. The figures demonstrate the PMFC has superior performance characteristics when juxtaposed with comparable TMFCs. It also has adequate response time for semiconductor process equipment applications.

DISCUSSION

The MEMS-based PMFC offers several benefits relative to the TMFC. *Small size:* For 'plug and play' applications, the PMFC with steel manifold is roughly one inch by 2 inches by 3 inches high, including electronics. In module form only, the size decreases by half. If remote electronics are utilized, the vertical dimension shrinks to one-half inch. *Higher resolution:* The use of 16 bit A/D for the pressure sensor, and 16 bit D/A for the valve driver, enables very high resolution, which exceeds the SEMATECH specifications. *Materials compatibility:* The wetted path in the PMFC is comprised of silicon, alumina (ceramic), and appropriate die attach materials. As such, it facilitates flow of all semiconductor processing fluids, save those which contain ionic fluorine, or other ionic elements which etch silicon. *Lowered defect generation:* MFC-generated particles are understood to derive from the number of sealing surfaces, the internal surface roughness, and the internal volume. Compared to TMFCs, the number of seals is reduced, and the internal dead volume is decreased by a factor of two to four.

Some liquids of interest in semiconductor processing must be maintained at a relatively low temperature to assure stability. A thermopneumatically actuated microvalve may require temperatures which, at the heater resistor, exceed this threshold temperature. However, proper valve design ensures the silicon membrane contact surface will remain well below this threshold temperature **[9]**.

CONCLUSIONS

We have demonstrated the science and technology required to design and fabricate flow distribution and control devices, specifically PFMCs, suitable for the semiconductor processing industry. These devices are comprised of normally-open microvalves, a microfabricated, passive flow restriction device, two microfabricated pressure sensors, and a temperature sensor. The valve actuation is based on previously developed thermopneumatic techniques. These components have been integrated using advanced packaging techniques, into a ceramic-based module. The MEMS-based PMFC has the benefit of small size, lower cost, higher resolution, materials compatibility, and lowered defect generation, when compared to its TMFC counterpart. The modular nature of the PMFC enables still higher levels of integration – when combined with MEMS-based pressure regulators, and vacuum leak-rate shut-off valves -- in the form of gas sticks, liquid distribution systems, and fully-integrated, multi-channel gas fluid control and distribution panels.

Acknowledgement

This work has been supported in part by DARPA, under Contract #DAAL01-94-C-3401.

REFERENCES

1. M. J. Zdeblick and J. B. Angell, In Proceedings, *Transducers '87 (1987 Int'l. Conf. Sol. State Sens. and Act.)*, pp. 827-829 [IEEE, Piscataway, NJ, 1987].
2. P. W. Barth, "Silicon microvalves for gas flow control." In Proceedings, *Transducers '95 (1995 Int'l. Conf. Sol. State Sens. and Act.)*, pp. 276-279 [IEEE, Piscataway, NJ, 1995].
3. M. Zdeblick, "Integrated, microminiature electric-to-fluidic valve and pressure/flow regulator." U.S. Patent 4,821,997 (1989).
4. J. Robertson, "An electrostatically-actuated integrated microflow controller." Ph.D. dissertation, U. Michigan, 1996.
5. M. Esashi, S. Eoh, T. Matsuo, and S. Choi, "The fabrication of integrated mass flow controllers." In Proceedings, *Transducers '87,* pp. 830-833 [Inst. Elec. Eng. Japan, 1987].
6. G. Chizinsky, "Recent advances in mass flow Control." *Solid State Technology*, p. 85 (September, 1994).
7. Frank M. White, Fluid Mechanics. McGraw-Hill (New York, 1979).
8. E. B. Arkilic, M. A. Schmidt, and K. S. Breuer, "A technique for high resolution mass flow measurements at atmospheric pressures." *Experiments in Fluids* (1997).
9. A. K. Henning, J. S. Fitch, D. J. Hopkins, Jr., L. Lilly, R. Faeth, E. Falsken, and M. J. Zdeblick, "A thermopneumatically actuated microvalve for liquid expansion and proportional control." In Proceedings, *Transducers '97 (1997 Int'l. Conf. Sol. State Sens. and Act.)*, pp. 825-828 [IEEE, Piscataway, NJ, 1997].

Fluid Media:	Gases/Liquids
Maximum Flow Rates:	1, 10, 100, 1000 sccm/ccm
Turndown Ratio:	5:1 (sonic); > 20:1 (subsonic)
Accuracy:	± 1% of F.S.
Repeatability:	± 0.1% of reading
Resolution:	± 0.1% of reading
Response Time:	500 ms typical
Inlet Pressure Range:	20 to 50 psig
Maximum Outlet Pressure:	200 Torr
Temperature Range:	0 to 50°C
Power Consumption:	1.5 W typical
Dimensions:	106 mm x 32 mm x 25 mm

Table I: *Specification for PMFC.*

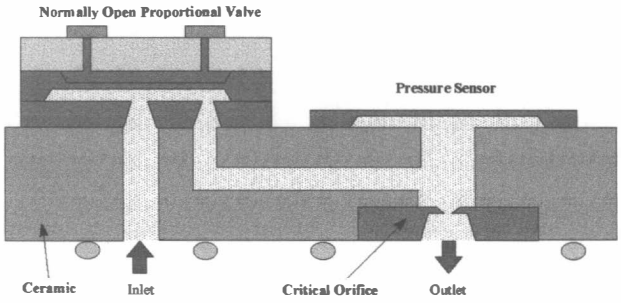

Figure 1: *Schematic representation of the PMFC.*

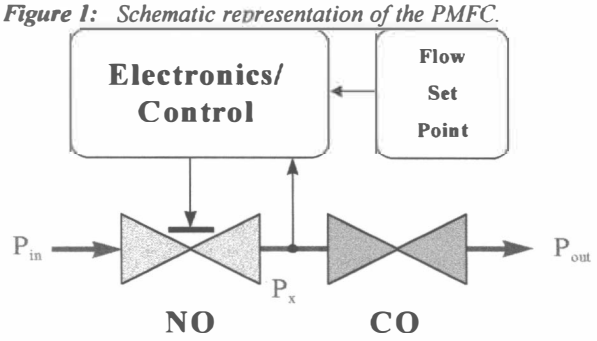

Figure 2: *Schematic representation of the compressible flow model for the series combination of a normally-open proportional valve, and a critical orifice.*

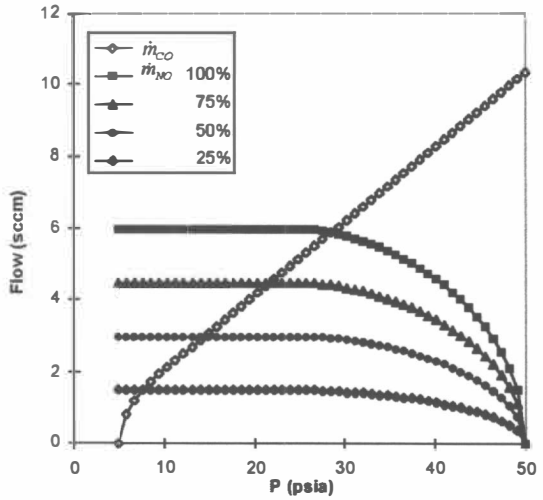

Figure 3: *Flow model for a 5 sccm gas PMFC.*

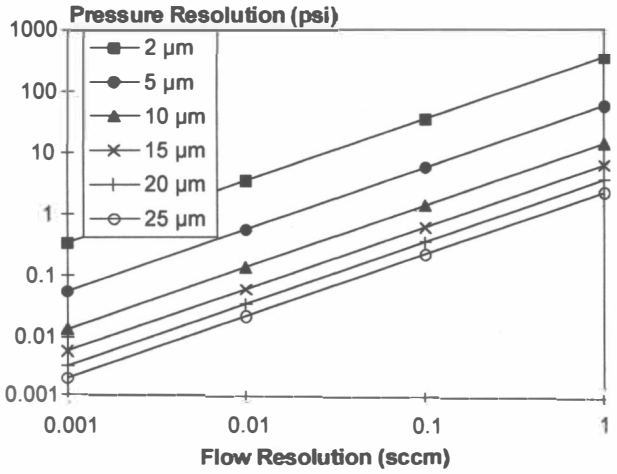

Figure 4: *Pressure resolution required to achieve a given flow resolution, versus CO hydraulic diameter.*

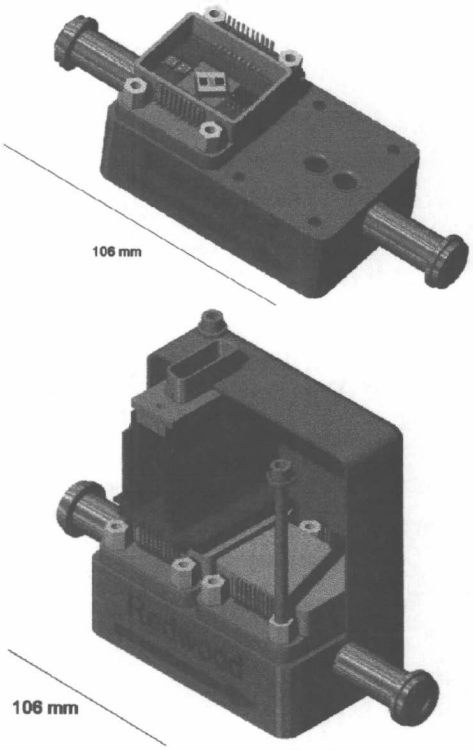

Figure 5: *(Top) A MEMS-based PMFC, showing a single module (with protective lid removed), mounted to a stainless steel manifold. The NO microvalve, two pressure sensors, and E^2PROM containing calibration coefficients, are visible. (Bottom) A two-module device, with a cut away enclosure revealing supporting electronics boards.*

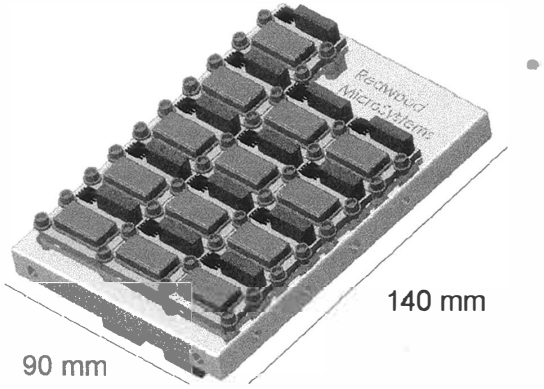

Figure 6: *A four-channel gas panel derived from PMFCs, as well as MEMS-based shut-off valves and pressure regulators.*

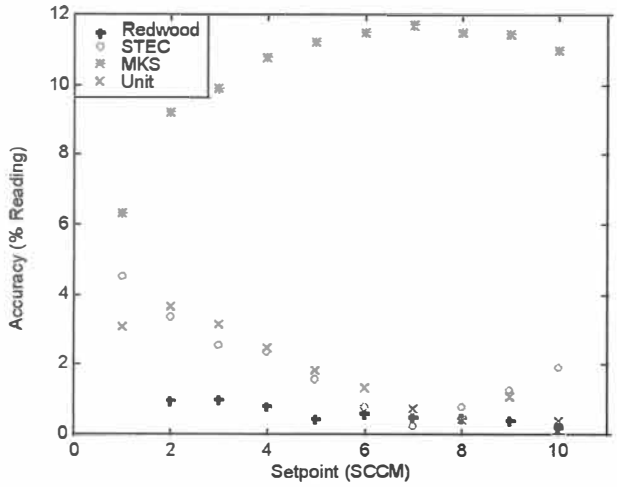

Figure 7: *MFC accuracy comparisons for PMFC (this work) and TMFCs (other units).*

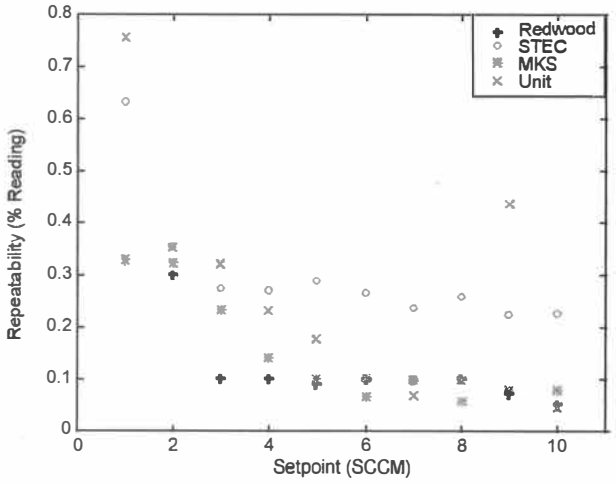

Figure 8: *MFC repeatability comparisons for PMFC (this work) and TMFCs (other units).*

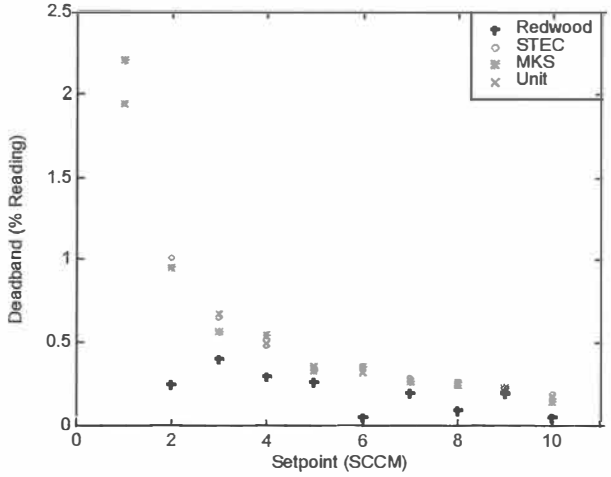

Figure 9: *MFC deadband (resolution) comparisons for PMFC (this work) and TMFCs (other units).*

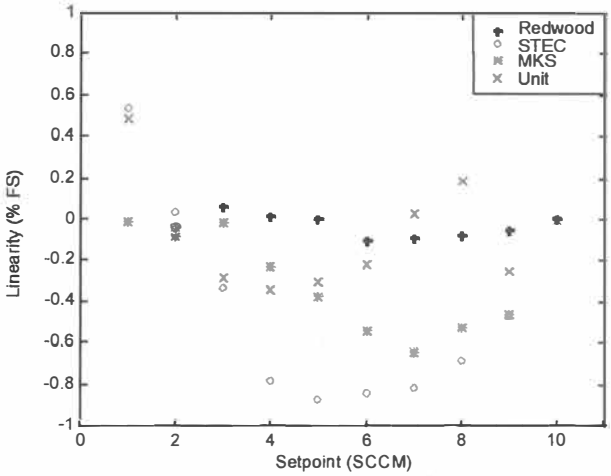

Figure 10: *MFC linearity comparisons for PMFC (this work) and TMFCs (other units).*

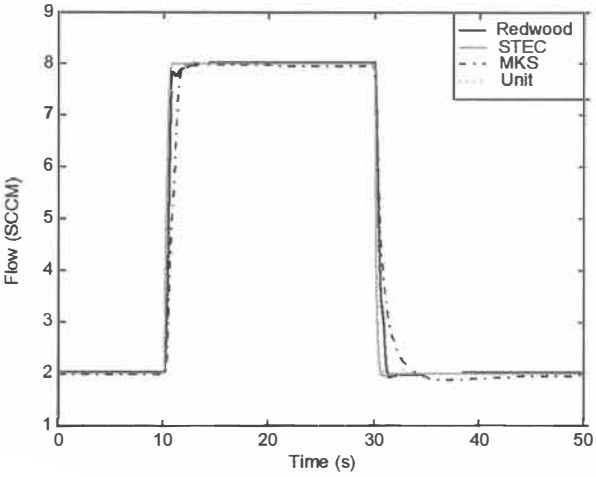

Figure 11: *MFC response time comparisons for PMFC (this work) and TMFCs (other units).*

A PARAMETRIC METHOD FOR LINKING MEMS PACKAGE AND DEVICE MODELS

Andrew C. McNeil
Motorola Sensors Division, Mail Stop Z-207
5005 E. McDowell Rd., Phoenix, AZ, 85008
e-mail: r16360@email.mot.com

ABSTRACT

Package stresses can significantly affect the performance of MEMS devices. This paper presents a method of modeling the effect of package stresses on MEMS device output. This method uses two separate FEA models, one for the MEMS device and one for the package. The results of the package model are approximated by several (1-6) parameters, and are used as inputs to the MEMS device model. This technique can efficiently model package stresses. It also provides parameters to quantify package effects, allowing communication between MEMS package and device designers. Model results are compared to experimental data, and are shown to be in good agreement.

INTRODUCTION

Many potential MEMS applications require low cost packaging to meet aggressive cost targets **[1]**, **[2]**, [3]. As these packages often use materials with coefficients of thermal expansion higher than silicon (e.g. polymers, metals) significant thermal stresses often develop during manufacture or operation. These stresses can affect MEMS device output. Thus a method is needed to efficiently simulate the effect of package stresses on MEMS devices during both package and MEMS device development.

Where some previous work has used one large, package-device FEA model **[4]**, it is often difficult to implement a single FEA model for both the package and the device. The device is usually much smaller than the package, and thus requires much higher mesh densities. Meshing the package with these high mesh densities would require an extremely large model (in some cases greater than a million nodes). Further, MEMS devices and packages are sometimes developed separately, and this makes it difficult to assemble a combined model.

The different scales of the package and device models can be accommodated by using two separate FEA models, a "fine mesh" model for the device and a "coarse mesh" model for the package. Because the package model is usually much more stiff (~ million X) than the device, the package model can be run independently of the device model, and displacements from the package model can then be passed to the device model, where they are imposed as boundary conditions. This method is available in several commercial FEA codes, and is sometimes called "sub-modeling" **[5]**. Although "sub-modeling" can accurately model package stress effects, it can be tedious to implement and does not provide a "figure of merit" (FOM) for package stress.

A method similar to "sub-modeling" is proposed in this paper. This method approximates the results (x, y, and z displacements) of the package model as functions of die location (x and y). These expressions have the form:

$$U_x = C_{xmn} x^m y^n \qquad U_y = C_{ymn} x^m y^n \qquad \text{Eqn. 2}$$

Where Ux, Uy, and Uz are displacements from the package model, and x, y are the coordinates in the package model. The parameters (coefficients) C_{xmn}, C_{ymn}, and C_{zmn} are found with curve fits of package model results. As an example C_{z20} is used to calculate the z-axis displacement proportional to the term x^2y^0. In many cases package model displacements can be approximated with a small number (1-6) of coefficients.

Parametric representation of package stress effects provides several advantages. It provides a method of linking package and device models so that package effects can be estimated. The parameters used to represent substrate deformation provide a relatively simple, quantitative way of evaluating both packages (how much substrate deformation a given package produces) and devices (how sensitive to a given package stress a device is). Finally, these parameters can provide a means of communication between package and device designers, facilitating parallel development of packages and devices.

MODELING PROCEDURE

The first step in modeling is to divide the system into device and package FEA models; this division is based on relative stiffness. The relatively small, movable MEMS structures form the MEMS device model, and the remainder of components form the package model (Figure 1). Note that the silicon die ("substrate") that the MEMS device is fabricated on is in the package model. This is counter to general convention, and is necessary because the substrate is comparable in scale (and hence stiffness) to the other package components.

The package FEA model is then run with the appropriate loading. Possible loadings include thermal stresses from manufacture at elevated temperatures, thermal stresses from specified operating temperature, or external stresses (e.g. mechanical stresses from mounting the device on a circuit board). As an example, if Temperature Coefficient of Sensitivity (TCS) was modeled, the package model would be

0-9640024-2-6/hh1998/$20©1998TRF
DOI 10.31438/trf.hh1998.36

Solid-State Sensors, Actuators, and Microsystems Workshop
Hilton Head Island, South Carolina, June 8-11, 1998

run at several different temperatures, to evaluate package stress vs. temperature.

Displacements from the package model are then fit with variations of Eqn. 1 and 2 (note: x, y, and z directions are defined in Figure 1, with the z direction defined as normal to the substrate die.). This fit should be performed over the region of interest, i.e. the region on the substrate where the device is anchored. Possible package displacement modes include:

Rigid Body Motion Modes:

These terms can be ignored as they represent a movement of the entire package-device combination. As an example, if the entire die moves upward 1 μ, the device will move identically, and no stress or relative displacements will result. Rigid body motion translation can be expressed by equations of the form:

$$U_x = C_{x00} \qquad \text{Eqn. 3}$$

Rigid body rotation about the x and y axes can be expressed by equations of the form:

$$U_z = C_{z10}\ x \qquad \text{Eqn. 4}$$

In-plane Displacement, "Stretching Modes":

This mode assumes a uniform strain in the substrate. This can be expressed by the equation:

$$U_x = C_{x10}\ x \qquad \text{Eqn. 5}$$
$$U_y = C_{y01}\ y \qquad \text{Eqn. 6}$$

In this case displacement is directly proportional to location. This is a constant strain with the coefficients C_{x10} and C_{y01} analogous to the x and y strains respectively. If the two constants are equal the substrate is subjected to isotropic strain with no shear strain [6]. The "Stretching mode" can cause axial stresses in tethers that support moving structures, and this can cause "stress stiffening", affecting spring constants [7].

"Bending Modes":

The following equation describes second order, "out of plane" displacements in the substrate. These are called "bending modes":

$$U_z = C_{z20}\,x^2 + C_{z02}\,y^2 \qquad \text{Eqn. 7}$$

This second order (parabolic) form approximates constant (circular) bending if the amount of displacement is small compared to the length of the surface (top of substrate). If the two constants are equal the substrate surface will have a spherical shape, with the radius of curvature approximated by $0.5/C_{z20}$. MEMS devices that rely on nanometer scale vertical displacements can be sensitive to this mode.

Other Modes:

Other modes may be required to accurately characterize substrate displacements in the package model. The following equation describes one form of "twisting":

$$U_z = C_{z11}\ xy \qquad \text{Eqn. 8}$$

Figures 2, 3, and 4 show actual examples of how package FEA model displacement data can be fit with equations 5, 6, and 7. Figures 2 and 3 show that a parabolic curvature provides a good approximation of substrate bending. Figure 4 shows a linear dependence between x-displacement x coordinate, indicating nearly constant value strain in this direction.

These parameters are then passed to the device model, where they are used to calculate boundary conditions. Several commercial FEA codes have features that allow automated input of boundary conditions, e.g. node displacements can be calculated as a function of location, as per eqn. 3 - 6. The device model is then run, and the effects of different package induced displacements can then be evaluated.

The MEMS device often has a significant Coefficient of Thermal Expansion (CTE). Polysilicon, for example has a CTE about that of single crystal silicon [8]. Thus it is important to also model thermal strains in the device model. Omitting thermal strains in the device model is equivalent to using a MEMS device material with a CTE of zero, and this will generate unrealistic stresses in the device model. In the case of polysilicon structures, the ideal package should have thermal strains identical to those of silicon.

The package and MEMS device models can also be run in isolation. Thus several package options can be run to see which produces the least substrate deformation. Conversely several MEMS device models can be compared with identical package stress parameters to see which device is least sensitive to package stress.

EXPERIMENTAL RESULTS

Several packaging configurations were tested for the production, z-axis, 50g accelerometer. The packaged sensor consisted of two dice (one capacitive device die and one control die) packaged in a PDIP package (see Figure 5). This package used an Alloy 42 leadframe, gold wire bonds, and was overmolded with a thermoset polymer. An elastomeric die bond and die coat were used to help isolate the device die from package stresses. The device die had a surface micromachined, polysilicon, z-axis accelerometer, and used a proof mass suspended by four tethers. The CMOS control die was used to produce a 0.5 to 4.5 V output [9], [10].

One package configuration caused accelerometer output to drift when stored at room temperature. Typically offset (zero acceleration reading) would shift upward, and sensitivity

would drift downward. Similar output shifts occurred when this package configuration was externally clamped.

Both package and device FEA models were generated using ANSYS 5.3. The package model indicated that separation of one of the polymeric interfaces could cause significant changes in substrate deformation, especially in the "stretching mode" [11] (see eqn. 5 and 6). These changes in substrate strain were then expressed in parametric form and passed to the device model of the accelerometer, and used as boundary conditions. The device model was used to evaluate z axis displacements, and these displacements were used to calculate accelerometer output. Figure 6 shows the two parameter shifts (offset and sensitivity) for two experimental cases, and for the model. The model was in reasonable agreement with experimental data [12]. Both experimental and model data indicated that for this package configuration a 1% decrease in sensitivity is accompanied by approximately an 18 mV increase in offset voltage. This modeling established that this interface separation was a possible cause of output shift in this package configuration.

CONCLUSIONS

Package stress effects can be efficiently modeled by using separate package and device FEA models. The package model can be run separately, and the resulting package stress (substrate deformation) data can be transferred to the device model in parametric form. These parameters provide a relatively simple way of quantifying package and device performance, and are suggested as a way of evaluating candidate package and device designs. This technique was used to model a package configuration for a capacitive, z-axis accelerometer, and model and experimental results were in approximate agreement.

ACKNOWLEDGMENTS

Many people provided help with this paper. These included Milena Vujosevic, Jonathan Hammond, Dan Koury, Gary O'Brien, Gary Li, Dave Monk, and Mike Saltmarsh.

REFERENCES

[1] G. Beardmore, "Packaging for Microengineered Devices. Lessons from the Real World," *IEEE Colloquium on Assembly and Connection in Microsystems*, pp. 2/1-8 (1997)

[2] T. Dickerson, M. Ward, "Low Deformation and Stress Packaging of Micro-Machined Devices," *IEEE Colloquium on Assembly and Connection in Microsystems*, (Ref. No.1997/004) pp. 7/1-3 (1997)

[3] A. D. Romig, P. V. Dressendorfer, D. W. Palmer, "High Performance Microsystem Packaging: A Perspective," *Microelectronic Reliability*, Vol. 37, No. 1011, pp. 1771-1781 (1997).

[4] F. Pourahmadi, K. Peterson, "Package Design of Silicon Micromachined Sensors Using Finite Element Modeling," *The 7th Annual Conference on Solid-State Sensors and Actuators*, (1993)

[5] ANSYS Procedure Manual, Revision 5.3., Swanson Analysis Systems, Inc. (1996)

[6] A. Higdon et al., "*Mechanics of Materials, third edition*," John Wiley and Sons (1976)

[7] W. C. Young, "Beam under simultaneous Axial and Transverse Loading," *Roarks Formulas for Stress and Strain, 6th Edition*, pp. 156-181, McGraw Hill (1989)

[8] D. W. Burns, "Micromechanics of Integrated Sensors and the Planar Processed Pressure Transducer," Phd. thesis, University of Wisconsin (1988)

[9] F. Shemansky, et al., "A Two-Chip Accelerometer System for Automotive Applications," *Microsystem Technologies*, Vol. 1, No. 3, p. 121 (1995).

[10] D. Dougherty, Q. Li, M. Shah, "Sensor Package Design Improvements Using Computer Simulation and Experimental Testing," *Sensors in Electronic Packaging* (ASME 1995 Congress), MED-Vol. 3, pp. 11-17 (1995).

[11] M. Vujosevic, M. Shah, "Mechanical Causes of the Shift in the Sensitivity and Offset of the Medium g Accelerometer in PDIP - Impact of Dome Coat Coverage," *Proceedings of the 1998 Winter Motorola AMT Symposium*, January 21&22, Phoenix, AZ, pp. 1.36 - 1.43 (1998)

[12] M. Saltmarsh, Motorola internal correspondence, Oct. 2 (1997)

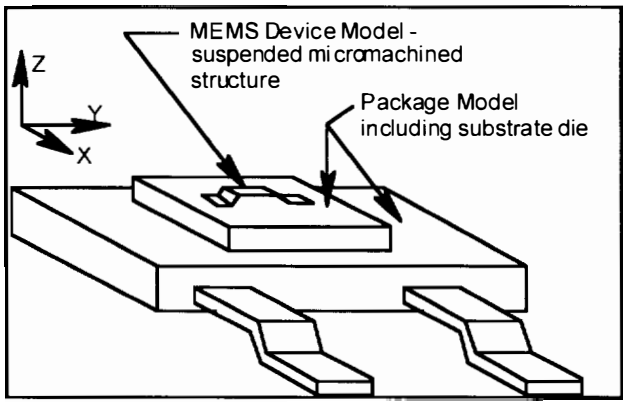

Figure 1: Schematic how a MEMS part is divided into two separate models. The package model includes conventional packaging plus the substrate die that MEMS device is fabricated on. The MEMS device model is comprised of the thin (micron range) micromachined structures.

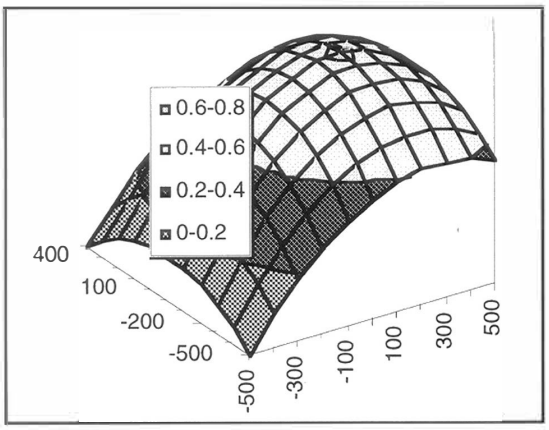

Figure 2: Z-displacement vs. die location (all units in microns) from package a FEA model, with Z-Displacement shown in the legend. This graph shows the curvature on the top surface of the device die.

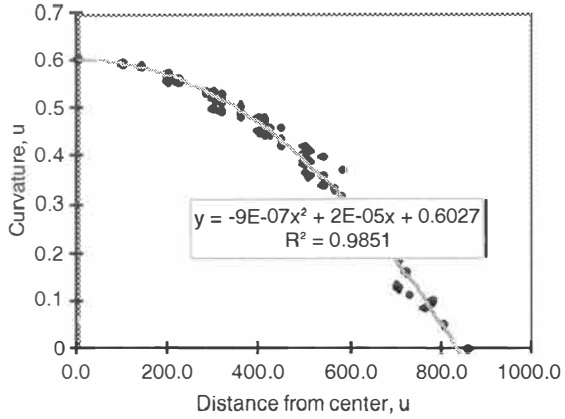

Figure 3: Z-displacements from Figure 2, plotted vs. radial distance from center of curvature. This data shows a good fit to a second order curve.

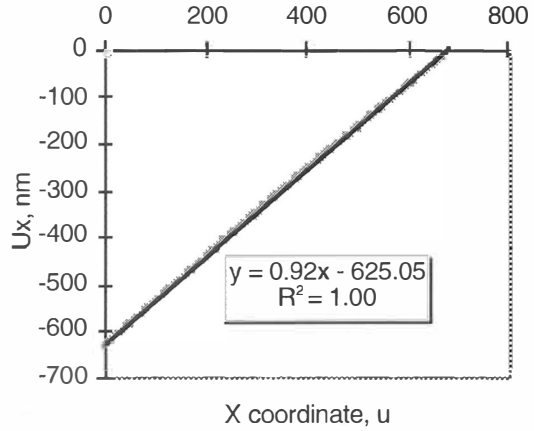

Figure 4: Package model, x-displacement as a function of die location, x-coordinate. The linear displacement function indicates constant strain, with the slope of the line equal to the strain.

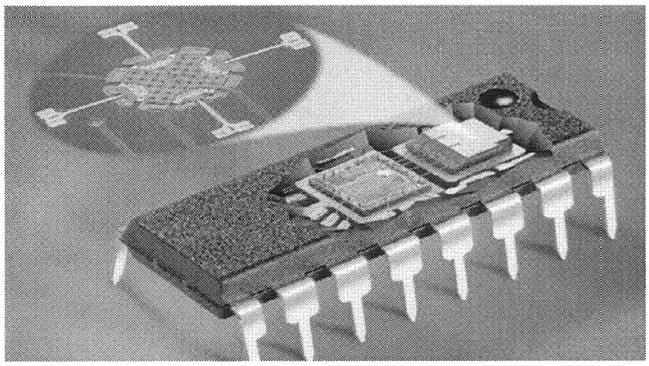

Figure 5: The z-axis accelerometer used for testing. Two dice (from left to right, control die and device die) are packaged in 16 pin, epoxy over-molded, PDIP package. A magnified view of the device die is shown. Note the proof mass suspended by four tethers.

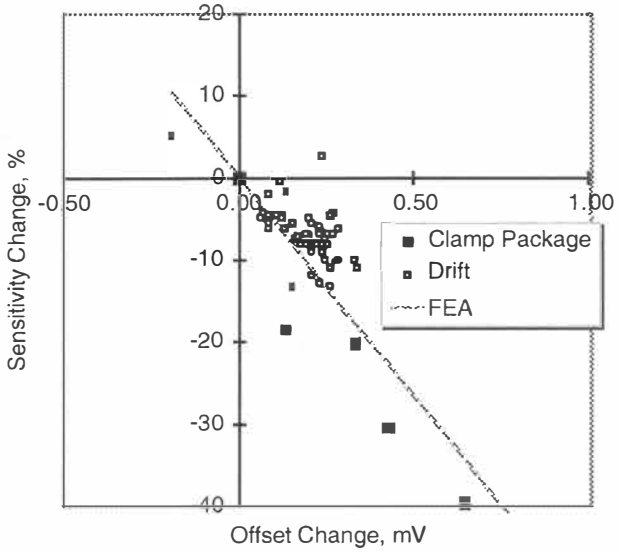

Figure 6: Comparison of FEA and Experimental Results, 40g z-axis accelerometer in a plastic PDIP package. This graph shows the relationship between two parametric shifts: Offset shift and sensitivity shift. "Drift" data shows changes in accelerometer output during room temperature storage. "Clamp" data shows changes in output that occur when the packaged device is externally clamped. Both experimental and modeling data show a similar relationship between these two parametric shifts.

DEVELOPMENT OF AN INNOVATIVE FLIP-CHIP BONDING TECHNIQUE USING MICROMACHINED CONDUCTIVE POLYMER BUMPS

Kwang W. Oh and Chong H. Ahn

University of Cincinnati
Center for Microelectronic Sensors and MEMS (CMSM)
Department of Electrical & Computer Engineering and Computer Science
P.O.Box 210030, Cincinnati, Ohio 45221-0030, USA

ABSTRACT

Using micromachining techniques with thick photoresists, an innovative conductive polymer flip-chip bonding technique that achieves both a low processing temperature and a high bumping alignment resolution has been developed and characterized in this work. By the use of UV-based photolithography with thick photoresists, molds for the flip-chip bumps have been patterned, filled with conductive polymers, and then removed, leaving molded conductive polymer bumps. After flip-chip bonding with the bumps, the contact resistances measured for 25 μm-high bumps with 300 μm x 300 μm area and 400 μm x 400 μm area were 35 mΩ and 12 mΩ, respectively. The conductive polymer flip-chip bonding technique developed in this work shows a very low contact resistance, simple processing steps, a high bumping alignment resolution (< ± 5 μm), and a lower bonding temperature (~170 °C). This new bonding technique has high potential to replace conventional flip-chip bonding technique for sensor and actuator systems, bio/chemical μ-TAS, optical MEMS, OE-MCMs, and electronic system applications.

INTRODUCTION

In recent years, the use of flip-chip bonding technology has grown in many packaging schemes. This is due to the advantages of improved reliability, lower costs, and higher I/O density in less packaging space. In developing flip-chip bonding techniques for sensor and actuator systems, optical MEMS, or optical interconnections, the most difficult problems usually come from precision bumping alignment and bonding temperature. Flip-chip bonding is preferred for the mounting or inverting of photonic devices on optical communication systems or recently emerging bio/chemical μ-TAS, where precise input/output coupling is required between photonic devices and optical waveguides or optic fibers, as shown in Figure 1 [1, 2]. Furthermore, low bonding process temperature is also required for compound semiconductor-based photonic devices. Although the conventional solder bump technology provides quite sufficient bumping alignment, it has several drawbacks due to high soldering temperature and multiple depositions of metal layers [3].

Nowadays, it is possible to buy conductive polymers tailored for specific electronic packaging applications from commercial suppliers. These conductive polymers are most often made using a silver flake fill in a polymer matrix. Since conductive polymer requires a low bonding temperature as well as fairly simple processing steps, the conventional solder bonding technique is being challenged by conductive polymer flip-chip bonding technique [4]. However, currently available screen printing techniques for the conductive polymer bumps have quite a crude bumping alignment resolution because the printer offers registration accuracies of ± 10 μm. This paper describes a new approach to address possible problems caused by the solder bump technique and the screen printing-based polymer bonding technique, such as high bonding temperature and poor bumping alignment.

TEST ASSEMBLY DESIGN

A conductive polymer bump sandwiched between the flip-chip and substrate has a certain amount of so-called contact resistance. This contact resistance is obviously an important parameter that impacts the behavior of devices, if flip-chip bonding is involved in their packaging. Quantitative determination of the contact resistance in ohms is very important and can be evaluated by using a four-terminal method [5].

Figure 2 shows test structures to characterize the electrical properties of the micromachined conductive polymer bumps. The first mask is used to define contact pad lines and terminal electrode pads for passing a current and reading a voltage drop through a conductive bump sandwiched between a flip-chip wafer and a

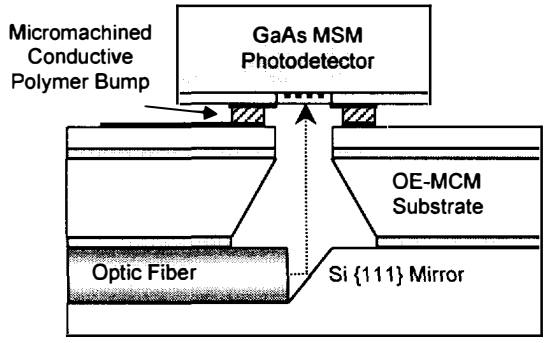

Figure 1. *Schematic diagram of an optical I/O coupler by the use of flip-chip bonding technique using micromachined conductive polymer bumps.*

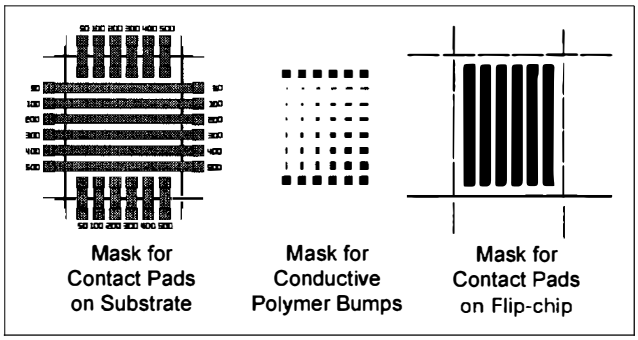

Figure 2. *Three-mask set of test structures to evaluate the electrical properties of the thermoplastic conductive polymer bumps by using a four-point terminal method.*

0-9640024-2-6/hh1998/$20©1998TRF
DOI 10.31438/trf.hh1998.37

substrate. To align with a diced flip-chip, a set of guidelines is included in the mask. The second mask contains the rectangular patterns with various sizes for thick photoresist bump-holes on the flip-chip wafer. The third mask is designed to define contact pad lines for bumps on the flip-chip wafer and guidelines for the dicing of the wafer.

FABRICATION

Figure 3 summarizes fabrication steps of the micromachined bumps by employing thick photoresist bump-holes as molding patterns. Initially Cr/Au contact metal pad lines and pads for the conductive polymer bumps were formed by lift-off on a silicon dioxide layer, which servers as the insulation layer (Figure 3(a)). Following this, the thick photoresist (AZ 4000 series) was patterned for bump-holes. High aspect ratio and straight side-wall patterns are very important as they are crucial for the molding of conductive polymer bumps (Figure 3(b)). After the lithography, thermoplastic conductive polymers were applied into the bump-hole patterns. Excess materials were immediately scraped off by a sharp blade or rubber pad (Figure 3(c)). The wafer was cured in a convection oven at 100 °C for 15 minutes. Due to the different curing conditions between the patterned thick photoresist and the conductive polymer filling in the bump-holes, the photoresist can be stripped away with a commercial photoresist stripper, leaving the conductive polymer bumps on the contact metal pads. After the removal of photoresist, the wafer was cured in a convection oven at 150 °C for 1 hour to achieve a better conductivity for conductive polymer bumps (Figure 3(d)). Figure 4 shows a micromachined thermoplastic conductive polymer bump with a thickness of 25 μm and an area of 400 μm x 400 μm on a 500 μm x 500 μm gold contact pad.

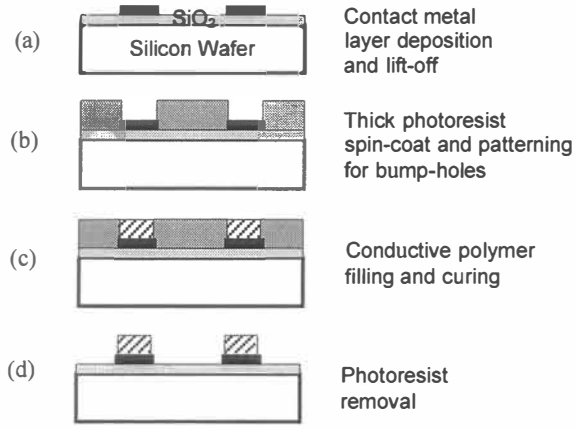

Figure 3. *Summarized fabrication steps for the formation of conductive polymer bumps on contact metal pads.*

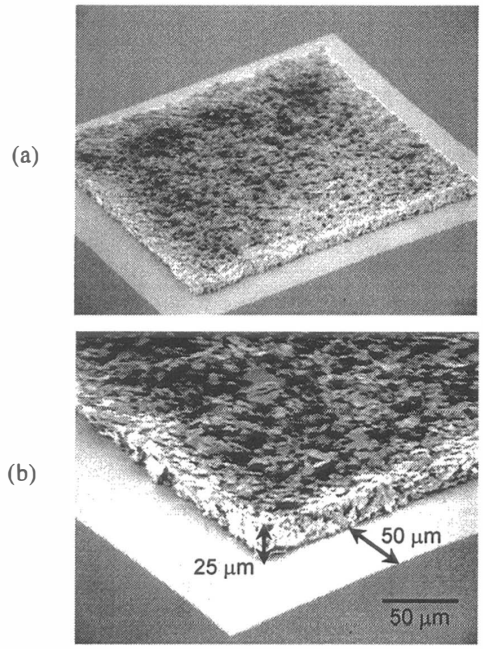

Figure 4. *SEM photographs: (a) a 25 μm high conductive polymer bump (400 μm x 400 μm) on gold contact pad (500 μm x 500 μm) and (b) close-up view of the corner of a 25 μm high bump.*

CONDUCTIVE POLYMER FLIP-CHIP BONDING

Figure 5 illustrates flip-chip bonding technique using thermoplastic conductive polymer bumps. Thermoplastic conductive polymers (Epo-Tek K/5022-115BE) used in this work possess the property of melting or re-wetting when heated to a specific temperature (150 °C). After substrate is pre-heated to approximately 20 °C above the thermoplastic polymer melting temperature, a diced flip-chip is flipped, aligned, and contacted onto it. The thermoplastic bumps then melt or re-wet onto the conductor pads of the substrate. The mechanical and electrical bonds are established as the substrate cools below the melting temperature of the thermoplastic materials. To enhance the mechanical bonding strength, a small amount of pressure is applied by placing a weight on the chip.

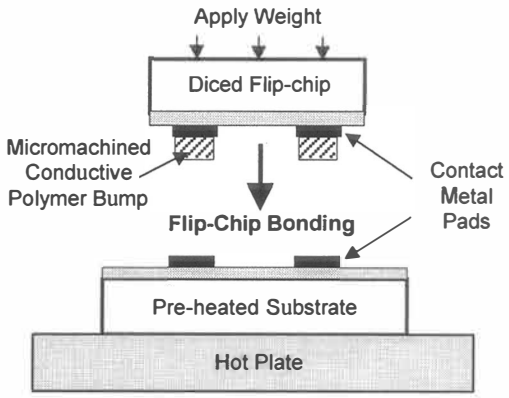

Figure 5. *Schematic illustration of an innovative flip-chip bonding technique using micromachined conductive polymer bumps.*

Figure 6(a) and (b) show a flip-chip wafer before and after the formation of bumps with 100 μm x 100 μm, 200 μm x 200 μm, and 300 μm x 300 μm squares on contact metal pads. The micromachined bumps have a *flat surface* morphology as shown in Figure 4 instead of a *mountain peak* morphology as when formed with the screen printing technique [4]. Each bump was uniformly micromachined on the contact pads with a thickness of 25 μm.

To test the thermoplastic conductive polymer flip-chip bonding arrangement, the flip-chip wafer with bumps and a substrate with a gold metal layer were used. During the bonding on a hot plate, the thermoplastic bumps melted onto the gold layer of the substrate. As the substrate cooled below the melting temperature of the thermoplastic materials, the mechanical and electrical bonds were established. To simply test the mechanical bonding strength and the bonding status, the flip-chip bonded

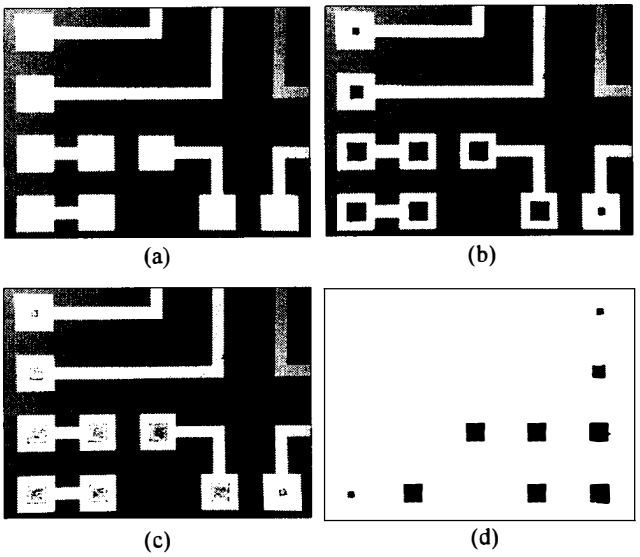

Figure 6. *Microphotographs: (a) a flip-chip wafer before formation of bumps on contact metal pads; (b) the wafer after formation of bumps with 100 μm x 100 μm, 200 μm x 200 μm, and 300 μm x 300 μm areas on contact metal pads; (c) the wafer with bumps left after separation of the testing assembly; and (d) a substrate with bumps left after separation of the testing assembly.*

assembly was separated into individual wafers. Separating the assembly, the bumps were left on the sides of both the substrate (Figure 6(c)) and the flip-chip wafer (Figure 6(d)), indicating a successful flip-chip bonding.

EXPERIMENTS

A schematic diagram of a flip-chip bonding for the contact resistance measurement using a four-terminal method is illustrated in Figure 7(a). In the four-terminal structure, a bump is sandwiched between two metal pad lines crossing each other. A constant direct current is made to flow through two of the contacts from each end of the metal pad lines, and the voltage across the other two contacts is measured with a high-impedance-voltmeter. An equivalent circuitry of the four-terminal method to measure the contact resistance of $Bump_2$ is shown in Figure 7(b). Current is forced between contact pads 1 and 2, and the voltage is measured between contact pads 3 and 4. There are two voltage drops between pad 1 and pad 2. The first is between pad 1 and upper pad B and the second is between upper pad B and pad 2. A high-impedance voltmeter used to measure the voltage, V_{34}, allows a negligibly small sensing current, I_{SENSE}, to flow between pads 3 and 4. Hence, the potential at the pad 3 is essentially identical to that in the upper pad B. V_{34} is solely due to the voltage drop across $Bump_2$, known as R_2. The contact resistance of $Bump_2$ is

$$R_2 = \frac{V_{34}}{I}, \qquad (1)$$

where it is simply the ratio of the voltage measured to the current applied. The contact resistance as defined here is the total resistance through $Bump_2$, which includes the bulk resistance of the bump and the two contact resistances between the metal pad B and bump.

Figure 8 shows the actual flip-chip, substrate, and their assembly used for the contact resistance measurement. White rectangles shown in Figure 8(a) are the micromachined thermoplastic conductive polymer bumps on the gold contact pad lines. The two bumps on each end of the individual contact pad

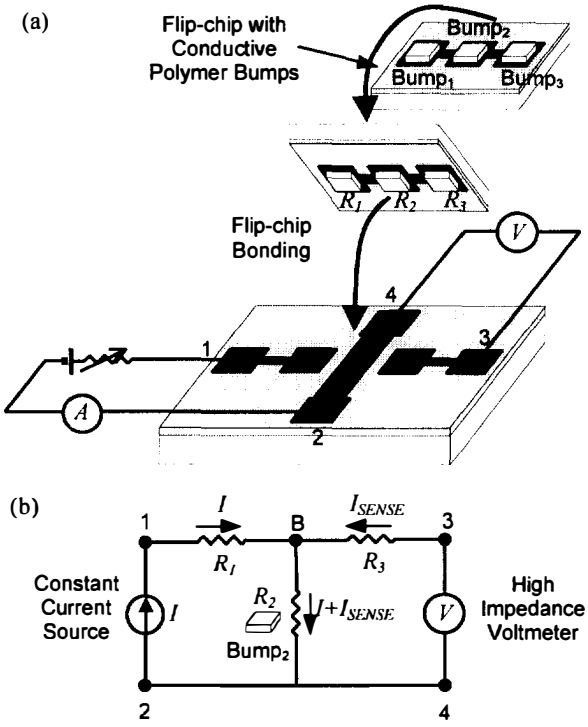

Figure 7. *Four-terminal method: (a) Schematic view of contact resistance measurement and (b) equivalent circuitry of a four-terminal method to measure the contact resistance of $Bump_2$.*

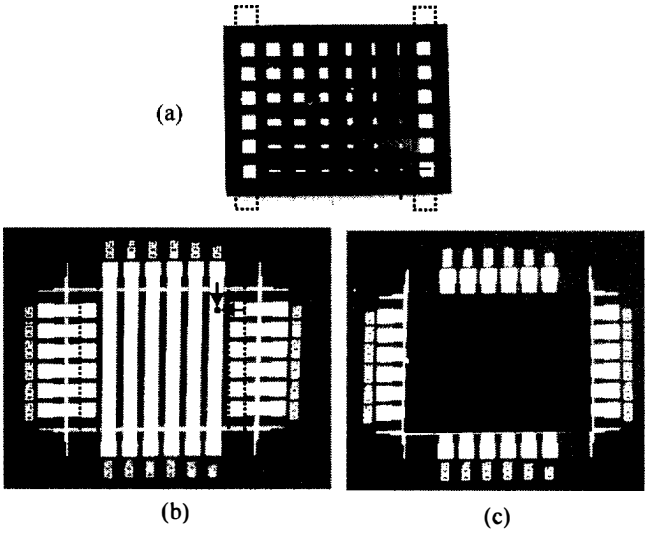

Figure 8. *Microphotographs of flip-chip assembly: (a) flip-chip; (b) substrate; and (c) their assembly used for the contact resistance measurement of the bumps.*

lines are used as conducting bumps, like R_1 and R_3 in Figure 7, to be connected with the probe pads on the substrate. Figure 8(b) shows the substrate with the other set of contact pad lines, guidelines to aid the alignment, and the numbers to indicate the dimensions of bumps sandwiched between metal pad lines on the flip-chip and substrate. For example, a 50 μm x 50 μm bump is in the lower right hand corner of Figure 8(a). This bump will be centered on the intersection of the arrows in Figure 8(b). Figure 8(c) shows their flip-chip assembly used for the contact resistance measurement.

RESULTS AND DISCUSSION

The I-V characteristics measured for 25 μm high bumps with various sizes are shown in Figure 9. The voltage drop was measured as the constant direct current was forced through the bumps up to 50 mA. The contact resistances measured for 25 μm high bumps with 400 μm x 400 μm, 300 μm x 300 μm, 200 μm x 200 μm, and 100 μm x 100 μm area were 12 mΩ, 35 mΩ, 75 mΩ, and 122 mΩ, respectively. The voltage drop obtained was proportional to the current with the contact resistance as simply the ratio of the voltage to the current. The slopes of the I-V graphs were linear with different driving currents. The linearity of I-V curves was not disturbed as the current was forced up to 50 mA.

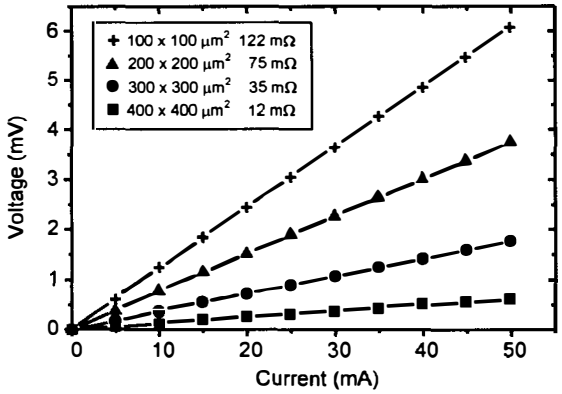

Figure 9. *I-V characteristics measured for 100 μm x 100 μm, 200 μm x 200 μm, 300 μm x 300 μm, and 400 μm x 400 μm bumps.*

In principle, the contact resistance decreases as a function of contact area for square contacts. Figure 10 (closed circles) shows the trend as a function of the contact area. The specific contact resistance, defined as the contact resistance multiplied by contact area, for the micromachined conductive polymer bumps was on the order of ~10^{-5} Ω-cm^2. In the case of metal-semiconductor ohmic contacts, typical ohmic contact with specific contact resistance of ~10^{-5} Ω-cm^2 has contact resistance of ~11 mΩ for an area of 300 μm x 300 μm and is considered a good quality contact [6]. The typical *flat surface* morphology shown in Figure 4 of the micromachined polymer bumps suggests that modeling the area as a simple rectangle may not suffice. The actual effective areas between the bumps and gold pad may not be the same as the calculated square areas due to the large grain size of the polymers.

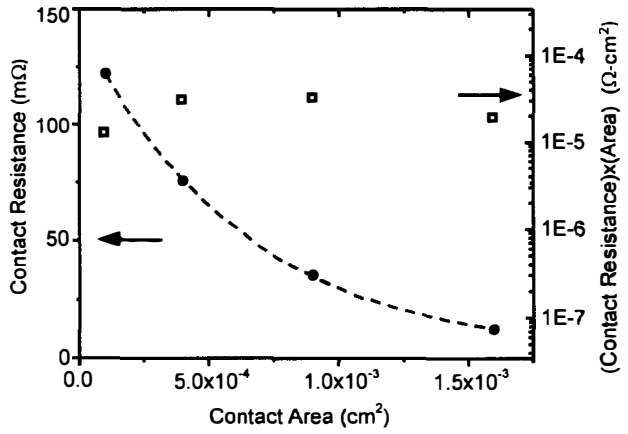

Figure 10. *Contact area dependence of contact resistance (closed circles) and area times contact resistance dependence of contact resistance (open squares).*

In addition, there may be variation from bump to bump with respect to the fraction of polymer matrixes used as adhesive and silver flakes used as conductive filler. Nevertheless, the contact resistance of the micromachined conductive polymer bumps measured here is comparable to the values achieved by solder metal bumps and shows satisfactory values over a wide range of bump sizes and applied currents.

CONCLUSION

Using micromachining techniques with thick photoresists, an innovative conductive polymer flip-chip bonding has been developed and characterized in this work. By the use of UV-based photolithography with thick photoresists, molds for the flip-chip bumps have been patterned, filled with conductive polymers, and then removed, leaving molded conductive polymer bumps. After flip-chip bonding with the bumps, the contact resistances measured by a four-terminal method were 35 mΩ and 12 mΩ for 25 μm-high bumps with 300 μm x 300 μm area and 400 μm x 400 μm area, respectively. The conductive polymer flip-chip bonding technique developed in this work shows a very low contact resistance, simple processing steps, a high bumping alignment resolution (< ± 5 μm), and a lower bonding temperature (~170 °C). This new bonding technique has high potential to replace conventional flip-chip bonding techniques for sensor and actuator systems, bio/chemical μ-TAS, optical MEMS, OE-MCMs, and electronic system applications.

ACKNOWLEDGMENT

This work was partially supported by a DARPA grant under contact number AF F30602-97-2-0102. The authors wish to thank Richard H. Estes in Epoxy Technology for donating conductive polymer materials and technical support.

REFERENCES

[1] C. H. Ahn, K. W. Oh, and K. P. Roenker, "Micromachined Optical I/O Couplers for Optoelectronic Multichip Modules (OE-MCMs)", Proc. Electronic and Photonic Packaging, EEP-Vol. 19-1, pp. 447-453 (1997).

[2] S. Koh, K. W. Oh, K. P. Roenker, and C. H. Ahn, "Design and Fabrication of Optoelectronic Multichip Module Prototypes using MEMS Fabrication Techniques", SPIE Proc., Miniaturized Systems with Micro Optics and Micromechanics II, Vol. 3008-05 (1997).

[3] A. F. J. Baggerman and M. J. Batenburg, "Reliable Au-Sn Flip-Chip Bonding on Flexible Prints", IEEE Trans. Comp., Packag., Manufact. Technol., Part B, Vol. 18, pp. 257-263 (1995).

[4] R. H. Estes, "Flip-Chip Packaging With Polymer Bumps", Semiconductor International, pp. 103-108 (Feb. 1997).

[5] K. Ishibashi and J. Kimura, "A New Anisotropic Conductive Film with Arrayed Conductive Particles", IEEE Trans. Comp., Packag., Manufact. Technol., Part B, Vol. 19, pp. 752-757 (1996).

[6] T. C. Shen, G. B. Gao, and H. Morkoc, "Recent Development in Ohmic Contacts for III-V Compound Semiconductors", J. Vac. Sci. Technol., B 10(5), pp. 2113-2132 (1992).

DENDRIMER-COATED SAW ARRAYS FOR VOLATILE ORGANIC DETECTION: ARRAY SIZE AND SIGNAL DEGRADATION EFFECTS

Gordon C. Osbourn, Antonio J. Ricco, John W. Bartholomew, and Rubel F. Martinez
Sandia National Laboratories, Albuquerque, New Mexico, 87185-1423

Maurie E. Garcia, Robert Peez, and Richard M. Crooks
Dept. of Chemistry, Texas A&M University
College Station, Texas, 77843-3255

Ralph Spindler and Mark E. Kaiser
Dendritech, Inc.
Midland, Michigan, 48642

ABSTRACT

Dendrimer film coatings for arrays of surface acoustic wave (SAW) devices were developed for the detection and recognition of volatile organic compounds (VOCs). Pattern recognition of array responses to 18 organic analytes was carried out, and correct identification with 99.5% accuracy, over wide concentration ranges, was obtained from arrays using six different coatings.

INTRODUCTION

Chemical microsensor arrays obviate the difficulty of developing a high-selectivity material for every analyte. The application of pattern recognition to the simultaneous responses of *different* microsensors enables the identification and quantification of multiple analytes with a single array. Maximum materials diversity is the surest means to create an effective array for many analytes [**1**], but using a single material "family" simplifies coating development.

Dendrimeric polymers, or dendrimers (Figure 1), are attractive for such arrays because they contain chemically tailorable endogenous and exogenous binding sites, in addition to tunable permeability and other physical properties [**2, 3**]. Dendrimers, prepared by repetitive branching, have three anatomical features: a central core, repetitive branch units, and terminal functional groups. Dendrimers are synthesized by adding repetitive branch units to the molecule one layer, or *generation*, at a time in iterative growth steps. Dendrimer size increases with generation number, leading to crowding of the surface functional groups, which causes the dendrimer to adopt a spherical or globular structure as of the fourth generation. In solution, these species recognize other molecules through both exo- and endoreception. Exoreception occurs when molecular species interact strongly with functional groups at the terminus of each dendrimer arm. Endoreception, a consequence of the dendrimer's globular molecular geometry, occurs when small species penetrate the interstices between the densely packed surface groups and are solvated in the large channels of the dendrimer's core.

In this paper, we report the successful combination of an array of dendrimer films with mass-sensitive SAW sensors to correctly identify 18 organic analytes over wide concentration ranges. We show, through a combinatorial comparison of VERI [**4, 5**] pattern recognition results, that six-sensor arrays are sufficient to give reliable recognition of these analytes.

EXPERIMENTAL DETAILS

The nine films we evaluated are described by Table 1 and Figure 1, which shows schematically the covalent attachment of dendrimers to the SAW device surface. The region of the SAW delay line between transducers is first modified by a 150 – 200 nm-thick Au film, followed by a self-assembled monolayer of mercaptoundecanoic acid (MUA) [**1 – 3**]. Chemical diversity is imparted to the dendrimers through bulk-phase coupling of appropriate terminal functional groups, elaborated in Table 1 and Figure 1, with the primary-amine-terminated dendrimer surface. Next, reaction of the dendrimers' few remaining unfunctionalized amines with the MUA monolayer yields amide-linked dendrimer films on the SAW devices.

Design and fabrication of SAW devices have been described elsewhere, as have measurement electronics and gas-flow system for our SAW array measurements [**4**], which we currently perform on 12 chemically functionalized SAW sensors simultaneously. The 97-MHz ST-quartz SAW delay lines, with accurate control of temperature (+/- 0.02°C), provide short-term frequency stability of ~ 0.3 Hz, yielding a surface mass/area detection limit of 100 pg/cm^2.

Table 2 shows 18 organic analytes that were examined in this work. This group of analytes contains multiple examples from several classes of VOCs, including simulants for nerve agents (the organophosphonates), as well as water. It also contains kerosene, which itself is a complex mixture of VOCs.

Table 1. Films used for SAW arrays.

No.	Terminal groups (see Figure 1)
1 *	OH (48%) and NH_2 (52%)
2 *	NH_2/NHR, R = C–6 (21%)[a]
3	NH_2/NHR/NR_2, R = C-6 (61%)[a]
4	NH_2/NHR, R = C2-phenyl (21%)[a]
5 *	NH_2/NHR, R = C–6 (2.5%)[a]
6 *	$CH_3(CH_2)_{15}SH$[b]
7 *	AEEA (45%) and NH_2 (55%)
8	NH_2
9 *	NH_2/NHR, R = C–12 (20%)[a]

*These films comprise the "best-6" set, for which isotherms are depicted in Figure 2.

[a]Indicates percentage of N—H bonds replaced by R to form NHR and NR_2 terminal groups (see Figure 1).

[b]This self-assembled alkanethiol-based monolayer is *not* depicted in Figure 1; all other films are dendrimers, as shown in the figure.

0-9640024-2-6/hh1998/$20©1998TRF
DOI 10.31438/trf.hh1998.38

SENSOR RESPONSES

The ability of an array to distinguish different analytes can be partially understood by viewing projections of the full array response, where the signal of each individual sensor is plotted along an orthogonal axis. Analytes can be distinguished if the clusters of points, associated with different concentrations of different analytes, are geometrically separate. Figure 2 shows a 2-D projection of 6-D response data for the best six-dendrimer array (films identified by "*" in Table 1); the 18 isotherms are displayed in two groups of nine for clarity. Sensor responses were preprocessed to provide equalized response ranges, and a constant-length vector was added to all responses to move the isotherms radially away from the origin.

To evaluate robustness of compound identification in the presence of signal degradation, each 6-D isotherm in Figure 2 includes mathematically calculated random film sensitivity losses of 0 to 8% in all dimensions (creating "clouds" of points at higher concentrations—the righthand regions of the isotherms). At low concentrations (lefthand regions of the isotherms), the responses range from moderately different (lower group of isotherms) to very different (upper group of isotherms): at submonolayer coverages, adsorption energy differences due to variation in film chemical functionalities are most pronounced. In contrast, the response curves are more nearly parallel for many of the 18 analytes at high concentrations (righthand regions of the isotherms), consistent with physical multilayer adsorption, a process which is dominated by analyte heat of condensation, not film/analyte interaction chemistry. Note that similar slopes does *not* imply that all analytes have the same heat of adsorption; rather, for each *individual* analyte, it implies that a change in its partial pressure evokes a comparable change in surface coverage for all the different sensor coating materials.

The data of Figure 2 illustrate that the responses from the different analytes are distinct, and the different analytes should be distinguishable using appropriate pattern-recognition techniques. However, the distributions of responses are quite complex, and are *not* easily converted into any of the simple forms needed for statistical-based pattern-recognition (PR) analysis.

DATA ANALYSIS

We analyzed the SAW/dendrimer array data using the VERI PR technique [**4**, **5**], a newly-developed multivariate analysis method based on an empirical model of human cluster perception. VERI analysis correctly treats arbitrarily complex sensor response distributions, and automatically determines the multivariate decision thresholds necessary to produce appropriate class volume shapes for the array responses to any chemical analyte. Appropriate class volume shapes are needed to obtain correct estimates of the chemical recognition performance of sensor arrays and to achieve the most effective discrimination against unknown analytes (i.e., those not in the training set). VERI leave-one-out analysis quantitatively compares the chemical recognition performance of alternative choices of SAW films, and thus finds the optimal subset of a group of films for a set of target analytes. These results enable quantitative array-element selection comparisons not possible with principal-component analysis [**5**, **6**]. Inclusion of modeled sensor response degradation into the VERI leave-one-out analysis provides a comparison of the robustness of array responses for different film combinations.

Figure 3 shows a subset of results from VERI leave-one-out analysis of all possible coated-SAW array combinations of the nine films of Table 1. Shown are best and worst array performance *vs.* array size, including the effects of film sensitivity changes over the array lifetime, using an ensemble-aging model [**5**, **6**]. The maximum sensitivity loss for any sensor is set at 8% or 16%, as indicated in the figure. Arrays of 5 or more sensors enable good chemical discrimination (99.5% accuracy with 6 films), with no improvement using more than six devices. Comparison of the 8% and 16% results also shows that there is no improvement in robustness against sensor response degradation by increasing the number of array sensors beyond six.

CONCLUSIONS

Dendrimer films have been shown to provide a range of chemical responses which make them useful in SAW array applications. Future work will explore the additional chemical recognition capability that results from combining selected dendrimer films with other classes of SAW coatings.

Sandia is a multiprogram laboratory operated by Sandia Corporation, a Lockheed Martin Company, for the United States Department of Energy under Contract DE-AC04-94AL85000. We gratefully acknowledge the excellent technical assistance of Alan W. Staton of Sandia Labs, and the financial support of DOE's Office of National Security and Nonproliferation, NN-20, as well as the National Science Foundation (CHE-9313441).

REFERENCES

1. A. J. Ricco, R. M. Crooks, and G. C. Osbourn, "SAW Chemical Sensor Arrays: New Chemically Sensitive Interfaces Combined with Novel Cluster Analysis to Detect Volatile Organic Compounds and Mixtures," *Accts. Chem. Res.*, *31*, xxxx (1998).
2. R. M. Crooks and A. J. Ricco, "New Organic Materials Suitable for Use in Chemical Sensor Arrays," *Accts. Chem. Res.*, *31*, xxxx (1998).
3. R. M. Crooks, H. Tokuhisa, A. J. Ricco, G. C. Osbourn, M. Kaiser, and R. Spindler, "Chemical Sensors Based on Surface-Confined Dendrimers," *Proc. Symp. Chem. and Biol. Sensors and Anal. Electrochem. Methods, 97-19*, The Electrochemical Society, Pennington (1997), pp. 134 – 140.
4. A. J. Ricco, G. C. Osbourn, J. W. Bartholomew, R. M. Crooks, C. Xu, and R. E. Allred, "New Materials and Multidimensional Cluster Analysis for SAW Chemical Sensor Arrays," *Technical Digest of the 1994 Solid-State Sensor and Actuator Workshop*, Transducers Research Foundation, Cleveland (1994), pp. 180 – 183.
5. G. C. Osbourn, J. W. Bartholomew, A. M. Bouchard, and R. F. Martinez, "Automated Pattern Recognition Based on the Visual Empirical Region of Influence (VERI) Method: A User's Guide", http://www.sandia.gov/1100/1155Web/1155home.htm
6. G. C. Osbourn, J. W. Bartholomew, A. J. Ricco, and G. C. Frye, "VERI Pattern Recognition Applied to Chemical Microsensor Array Selection and Chemical Analysis," *Accts. Chem. Res.*, *31*, xxxx (1998).

Table 2. Analytes arranged by chemical class.

Chemical class	Compounds studied	Number/symbol[a]
Aliphatic hydrocarbon	cyclohexane	1 +
	n-hexane	2 -
	i-octane	3 -
	kerosene[b]	4 -
Aromatic hydrocarbon	benzene	5 +
	toluene	6 -
Chlorinated hydrocarbon	carbon tetrachloride	7 +
	trichloroethylene	8 -
	chlorobenzene	9 +
Alcohol	methanol	10 -
	n-propanol	11 -
	pinacolyl alcohol[c]	12 -
Ketone	acetone	13 +
	methyl isobutyl ketone	14 -
Organophosphorous compound	dimethylmethylphosphonate	15 -
	diisopropylmethylphosphonate	16 +
	tributylphosphate	17 -
Water	H_2O	18 -

[a]Refers to isotherms of Figure 2.

[b]kerosene is typically a mixture of *n*-dodecane, several alkyl derivatives of benzene, naphthalene, and a pair of tetrahydronaphthalenes.

[c]*2, 2*-dimethyl-*3*-butanol

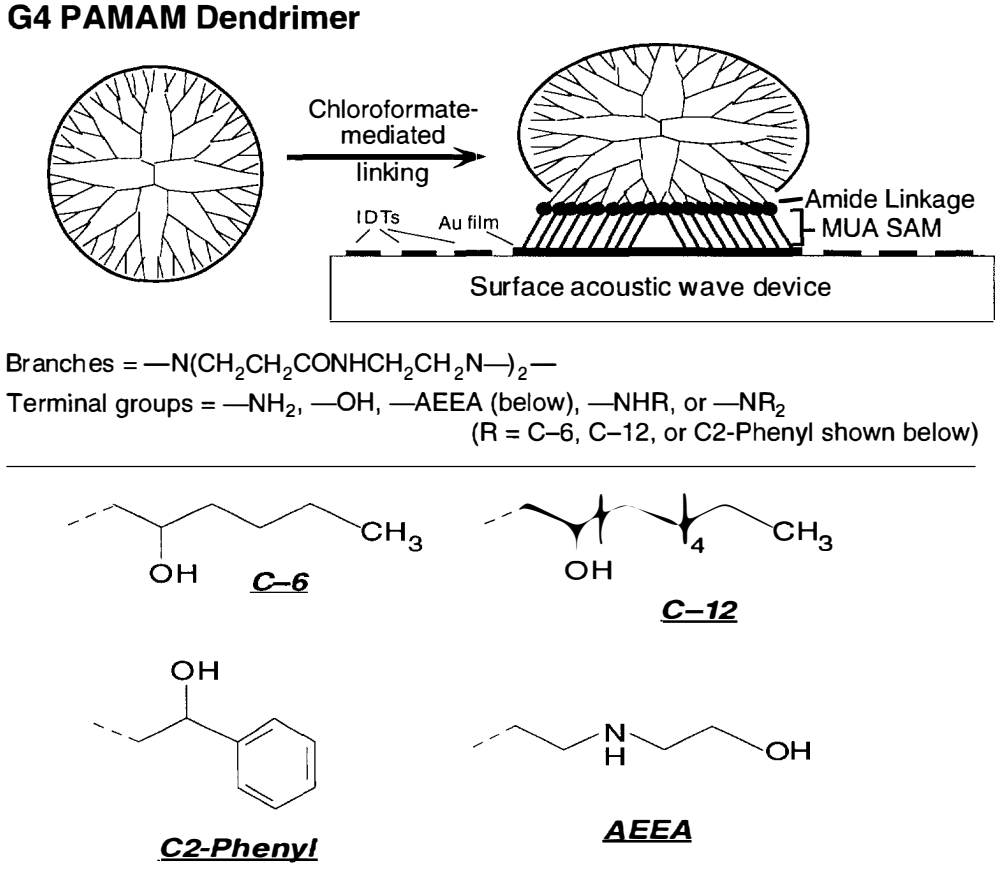

Figure 1. *Depiction of 4th-generation PAMAM (polyamidoamine) dendrimer and its attachment to an Au film on the SAW device surface (top). Each branch terminates either with —NH_2, —OH, AEEA, —NHR, or NR_2; R is given in the figure. Table 1 identifies film compositions used in SAW arrays.*

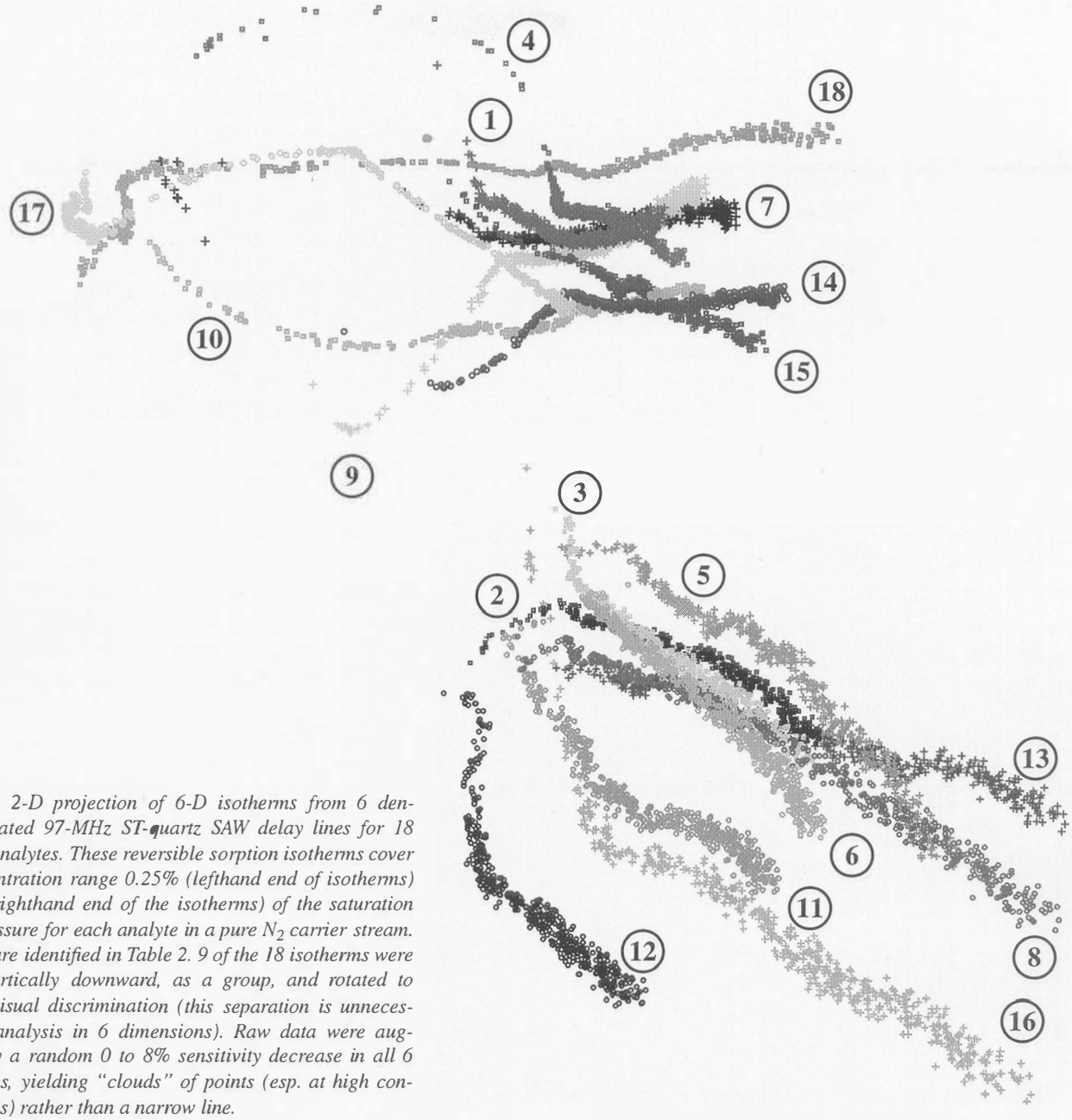

Figure 2. *2-D projection of 6-D isotherms from 6 dendrimer-coated 97-MHz ST-quartz SAW delay lines for 18 different analytes. These reversible sorption isotherms cover the concentration range 0.25% (lefthand end of isotherms) to 50% (righthand end of the isotherms) of the saturation vapor pressure for each analyte in a pure N_2 carrier stream. Analytes are identified in Table 2. 9 of the 18 isotherms were shifted vertically downward, as a group, and rotated to improve visual discrimination (this separation is unnecessary for analysis in 6 dimensions). Raw data were augmented by a random 0 to 8% sensitivity decrease in all 6 dimensions, yielding "clouds" of points (esp. at high concentrations) rather than a narrow line.*

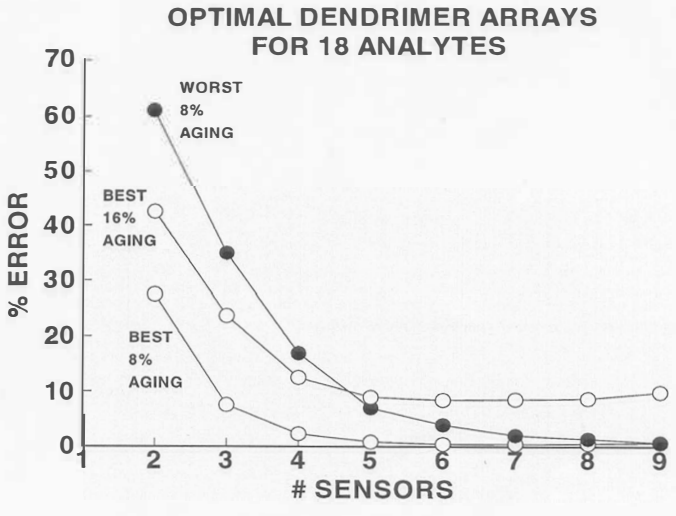

Figure 3. *Rate of error in identifying all concentrations of all 18 analytes (Table 2) as a function of the number of sensors selected for the array. Open circles show the situation when the best-performing array of* n *sensors* (n = 2 - 9) *is selected from the 9 dendrimer films evaluated, in the presence of either 8% (lowest curve) or 16% (middle curve) random degradation in signal fidelity. Solid circles show the worst-performing arrays of 2 - 9 sensors in the presence of 8% signal degradation. Note that the performance difference between best and worst arrays is more than a factor of 2 for the smallest array, converging to zero when all 9 materials are used.*

AN APPROACH TO THE CLASSIFICATION OF UNKNOWN BIOLOGICAL AGENTS WITH CELL BASED SENSORS

David A. Borkholder, B. Derek DeBusschere, and Gregory T.A. Kovacs
Electrical Engineering, Stanford University
Center for Integrated Systems, CISX 202X, Stanford, CA 94305-4075

ABSTRACT

The broad-spectrum sensitivity of cell based biosensors offers the capability for detecting previously unknown biological agents. One cellular parameter that is often measured is the action potential of electrically active cells. However, the complexity of this signal makes interpretation of the cellular response to a compound difficult to interpret. By analyzing shifts in the signal's power spectrum, it may be possible to classify the ionic channels modulated by the agent.

A system is described for the measurement of action potentials from cells cultured on a planar microelectrode array. Experimental results, simulations, and analyses are presented for three pharmaceuticals tested on chick myocardial cells. While the actual agents could readily be distinguished experimentally, the models used for simulation were a partial success, accurately predicting the response to one of the three agents tested.

INTRODUCTION

Cell based sensor technologies utilizing electrically active living cells cultured on extracellular electrode arrays have been a focus of research since 1972 [1]. However, most efforts have been directed towards pure neuroscience applications that require experienced interpretation of the signals. More recent work by some groups has attempted to expand the practical uses of action potential (AP) based systems to environmental and chemical monitoring and pharmaceutical screening [2-5]. However, there has been little work done on signal interpretation models for general classification of agents modulating cellular electrical characteristics. This work attempts to classify the type of ion channel (Na^+, K^+, Ca^{2+}) affected by an unknown, biologically active agent.

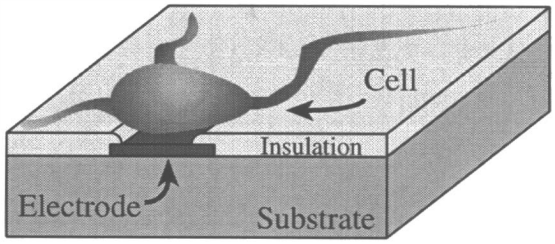

Figure 1. Conceptual drawing of a cultured cell coupled to a microelectrode.

Electrical activity in cells is generated by a complex interaction of both ligand and voltage gated ion channels. As a cell depolarizes (transmembrane potential changes), the voltage threshold for opening of different ion channels is reached, resulting in electrochemical gradient driven flow of ions through the cell membrane. Different channel classes open at different times and contribute to unique portions of this action potential. The cardiac AP studied in this work can be divided into several phases: an initial rapid depolarization due to increased Na^+ conductance; a plateau phase due to the slow opening of voltage-gated Ca^{2+} channels; and the final repolarization due to the closure of Ca^{2+} channels and the prolonged opening of K^+ channels [6]. The authors postulate that the frequency content of an AP may be correlated with specific ion channel classes. As the normal operation of these channels is altered by chemical or biological agents (toxins, pharmaceuticals, etc.), it is expected that the power spectral density (PSD) of the AP will change in a characteristic way for each channel type. Determination of a unique modulation function of a pharmaceutical on the AP may provide a useful method for rapid characterization of channel modulating agents.

MICROELECTRODE ARRAY

The microelectrodes used in this research consist of a 6×6 array of circular iridium, gold or platinum electrodes of varying areas (15 to 480 μm^2). The electrodes are fabricated on either glass or silicon substrates and have the basic structure shown in Figure 1. The dice are packaged in a ceramic 40 pin dual in-line package (DIP), and bond-wire connections are made between the die and package. The bond-wires are encapsulated in a biocompatible epoxy that is also used to attach a polystyrene petri dish to form a cell culture chamber as shown in Figure 2. Electrode impedances are reduced by electroplating platinum black on the electrode surface and using ultrasonic agitation to ensure adequate adhesion [7]. The fabrication, packaging and platinizing procedures have been described in detail elsewhere [8]. The packaged microelectrode arrays are used as a substrate for the culture of embryonic chick myocardial cells. These cells form a spontaneously beating syncytium which generates APs that travel through the cell layer. The electrical signals are monitored using the extracellular microelectrodes and low noise amplifiers.

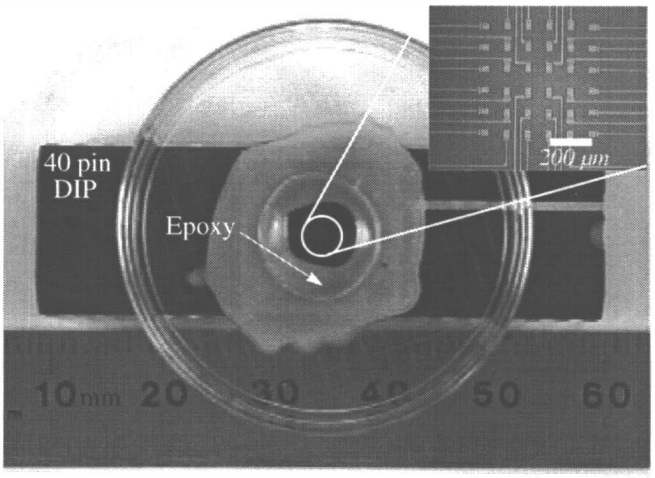

Figure 2. A microelectrode array is packaged in a ceramic 40 pin DIP. Bond-wires are encapsulated in epoxy and a 35 mm polystyrene cell culture dish (with hole drilled in the center) is attached to the top. Inset shows a close-up of the 6 × 6 element electrode array.

0-9640024-2-6/hh1998/$20©1998TRF
DOI 10.31438/trf.hh1998.39

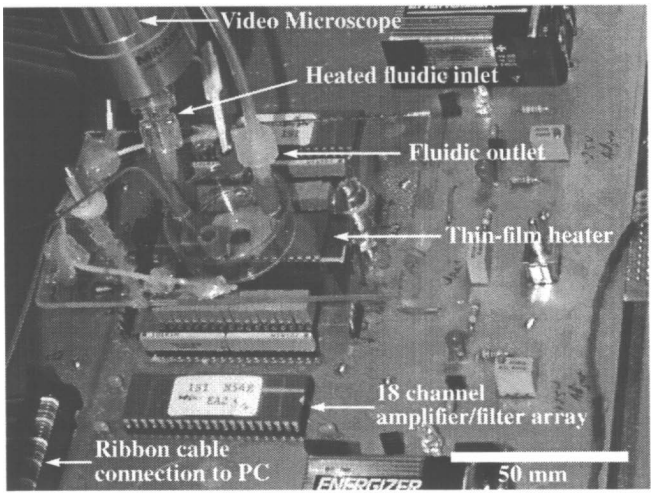

Figure 3. Measurement setup used for AP monitoring. The cell culture chamber is connected to the electronics via a ZIF socket. The amplified action potentials (through the custom 18 channel amplifier/filter arrays) are measured by direct connection to a PC via ribbon cables.

MEASUREMENT SYSTEM

Measurement of electrical activity from cultured cells *in vitro* requires a low noise amplification system coupled to data acquisition and storage equipment. As shown in Figure 3, the packaged microelectrode array is placed into the measurement system using a zero insertion force (ZIF) socket. Individual electrodes are AC coupled to a custom 18 channel amplifier/filter array (developed at Stanford University **[9-10]**). The amplifier has a midband gain of 45 dB, input referred noise of 8 μV_{rms} (10 Hz to 10 kHz), and an adjustable high pass filter (3 Hz to 10 kHz).

The amplified AP signals are routed via ribbon cable to a PC-based data acquisition system capable of simultaneously monitoring up to 32 channels and storing the digital, 12-bit data to disk (Experimenter's Workbench 32 by DataWave Technologies, Colorado). Off-line analysis of the AP waveforms was performed using additional software tools.

In addition to the AP electronics, the measurement system must also include fluidics for sample introduction and temperature regulation. As shown in Figure 3, an indium-tin oxide (ITO) coated glass plate is positioned over the cell culture chamber. Electrical current flowing through the resistive ITO heats the glass to assist in temperature control and reduce condensation (to allow for visual observation of the cells). Holes drilled through the plate allow for insertion of a teflon coated thermistor probe, fluidic inlet and outlet tubes, and a platinum wire to be used as a grounded electrode in the solution. Fluid is heated to 37°C prior to entering the dish using a resistive heater surrounding the inlet tube. The fluidic outlet consists of a 30 gauge needle connected to a vacuum source adjusted to match the inlet flow rate (2.0 ml/min). Die and package temperature is controlled by a thin-film heater positioned below the DIP. The combination of the heated glass plate, inlet fluid heating, and package heating result in a temperature at the electrode array of 37°C ± 0.3°C.

Media flow, controlled by both gravity and tubing resistance, was adjusted to 2.0 ml/min. Manual sample selection was accomplished via a teflon 8-way valve configured to allow up to four different solutions to be used in the same experiment. HEPES buffered recording media was prepared for experiments at

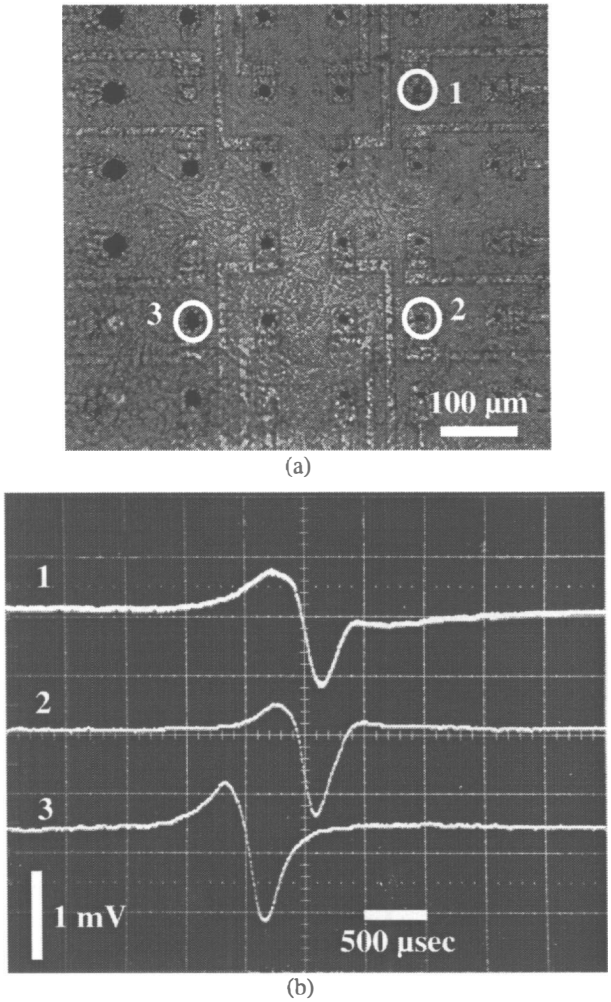

Figure 4. (a) Optical view of embryonic chick myocardial cells cultured on the microelectrode array. Spontaneous APs recorded extracellularly from the circled microelectrodes are shown in (b). The time delay observed between action potentials is due to the finite propagation velocity of the traveling action potential through the two dimensional sheet of cells.

atmospheric CO_2 levels, with both the pH and osmolality adjusted to physiologic levels (7.3 and 300mOsm/kg respectively). Where pharmaceuticals or toxins were to be tested, they were added directly to this recording media in concentrations which did not significantly alter the osmolality or pH of the solutions. Continuous flow was used to limit variations due to changing flow velocities and temperature which can be problematic with manual bolus injection systems.

ACTION POTENTIAL MEASUREMENT AND SIMULATION

Embryonic chick myocardial cells were explanted from 11 day old chicks and plated onto the microelectrode arrays described above at a density of 1,000 cells/mm^2 using the techniques of De Hann, Barry and Polinger **[11-13]**. APs were measured from the spontaneously beating, two-dimensional sheet of cells two to four days after plating. An optical image of cells cultured on the microelectrode array and typical action potential recordings are shown in Figure 4. Note the time delay between AP peaks, corresponding to the finite propagation velocity of the action potential wavefront through the tissue.

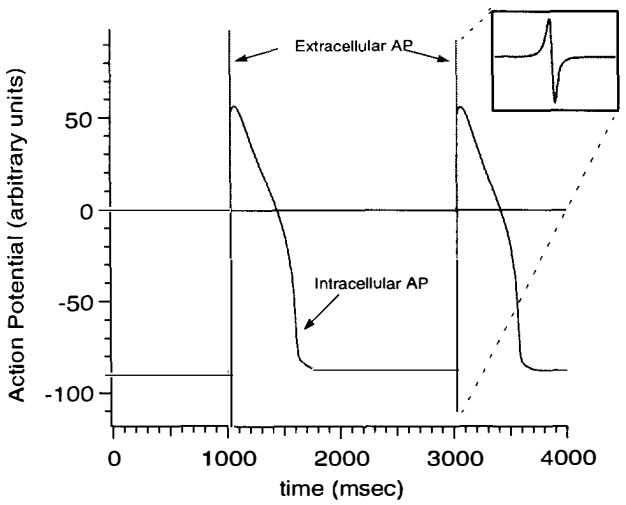

Figure 5. Simulated action potentials. Intracellular signals were calculated using SPICE and Hodgkin-Huxley type equations for the cellular membrane. The second time derivative of this intracellular signal was computed to estimate the expected extracellular signal to be recorded by a microelectrode. An expanded view of the 3 msec wide second derivative signal is shown in the inset.

Correlation of these extracellular signals to classical intracellular recordings (large literature base) is often difficult since they represent a temporal derivative of the intracellular signal dependent on the coupling of the cell to the microelectrode. For tightly coupled cells, the extracellular signal looks like the first derivative of the intracellular. As the coupling is reduced, higher order derivatives are observed [**14**]. For the data presented herein, second order derivative characteristics have been confirmed by comparison to the time derivative of intracellular action potentials from cultured embryonic chick myocardial cells taken from the literature [**15**]. This information is important for comparison of experimental data to simulations.

Simulation of spontaneous action potentials was carried out with the circuit simulator HSPICE using Hodgkin-Huxley type models developed for bullfrog atrial cells [**16**]. While differences between the chick and bullfrog are likely, the availability of suitable models was extremely limited. Additionally, the precise composition of the chick cardiac cell population in culture is not known (some combination of atrial, ventricular, and sinoatrial node cell types), making exact modeling difficult. In this system, the cell membrane was modeled as a capacitance connected in parallel to a number of conductive ionic channels. The model was modified to include two cells connected by a resistive gap junction to simulate the normal electrical connections between cardiac cells. One cell was stimulated using a current pulse, firing an AP which in turn elicited an AP in the second cell. Simulated results were obtained from this second action potential and compared to those obtained experimentally.

The simulation parameters were slightly modified to provide an intracellular signal similar in shape and duration to those published for embryonic chick myocardial cells in vitro [**15**]. The second time derivative was then taken resulting in the waveforms of Figure 5. Note the shape and duration are similar to the actual action potentials recorded in Figure 4.

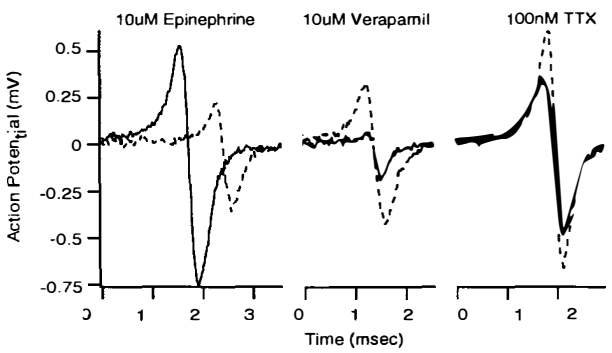

Figure 6. Action potential changes with pharmaceutical additions. Unmodulated APs are shown with dashed lines while post-agent APs are represented by solid lines. Epinephrine (Ca^{2+} channel agonist), Verapamil (Ca^{2+} channel blocker), and Tetrodotoxin (TTX) (Fast-Na^{+} channel blocker) effects are shown. The waveforms presented are extracellular recordings from a spontaneously beating culture of embryonic chick myocardial cells cultured on a planar microelectrode array. They represent the second temporal derivative of the intracellular signal. Note: the relative timing of each AP is not significant and can be altered by triggering during data acquisition.

PHARMACEUTICAL MODULATION

As mentioned previously, action potentials are the result of a complex coordination of ionic flows through the cellular membrane. The flow of specific ions is controlled by voltage or ligand gating of ion channels which exhibit specificity in ion transport. The biological effect of many toxins and pharmaceuticals is often coupled to specific binding of the agent to receptors on the cell membrane. This can result in enhanced or inhibited opening of channels or direct blockage of the ion transport region. Thus, the relative impact of the different ions on the action potential can be modulated, resulting in changes in AP shape.

Three different pharmaceuticals and toxins were examined in this study: tetrodotoxin, epinephrine, and verapamil. Tetrodotoxin (TTX) is a naturally occurring neurotoxin which binds specifically to voltage gated Na^{+} channels. It does not affect Ca^{2+} or K^{+} channels, nor the Na^{+} leakage that generally occurs through the

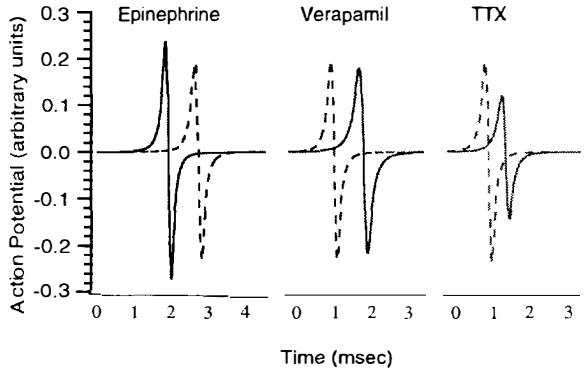

Figure 7. Simulated extracellular action potentials before and after pharmaceutical and toxin additions. Unmodulated APs are shown with dashed lines while post-agent APs are represented by solid lines. Note the responses to epinephrine and verapamil are significantly smaller than the physiological results shown in Figure 6. The response to TTX is a close approximation to that observed experimentally. Unlike Figure 6, the AP alignment offsets represent real delays rather than triggering during data acquisition.

non-gated channels and ion pumps of the resting cell membrane [**17**]. The action of TTX may be easily modeled by adjustment of a scaling factor on the fast sodium current (I_{Na}).

Epinephrine is a natural hormone released by the adrenal gland which acts on both α- and β-adrenergic receptors. In cardiac tissue, this agonist acts mainly on β-adrenergic receptors causing modulation of several ionic currents through second messenger pathways (cyclic adenosine 3',5'-monophosphate (cAMP) mediated). Both the inward, long-lasting (L-type) Ca^{2+} current ($I_{Ca,L}$) and the outward, delayed rectifier-type K^+ current (I_K) are enhanced [**18**].

Verapamil is a lipid-soluble compound which preferentially blocks L-type Ca^{2+} channels. It not only reduces the magnitude of the Ca^{2+} current, but also decreases the rate of recovery of the channel [**19**]. When applied at high enough doses (tens of μ**M**), verapamil can also affect voltage-gated K^+ channels resulting in enhanced inactivation of the rectifying I_K current [**20**].

From the actual data shown in Figure 6, it is clear that the compounds tested had a significant and distinct impact on the action potential shape. To simulate the effect of the pharmaceuticals and toxins, each ion channel current in the model was multiplied by a gating variable representing the percentage of channels which could open in response to an appropriate transmembrane voltage. For each agent examined, only the variable for the channel known to be affected was altered. This gating variable was adjusted to match the simulated waveforms as closely as possible to those measured experimentally. For tetrodotoxin this was achieved by blocking the fast Na^+ conductance by 25%, which resulted in an AP amplitude reduction similar to that observed experimentally. This can be seen by a comparison of the waveforms in Figures 6 and 7. The results for pharmaceuticals targeting calcium and potassium were not as convincing however. The effects of epinephrine could only be observed when the L-type Ca^{2+} and rectifying K^+ currents were increased by a factor of 10 (data shown in Figure 7). Even at this level, the AP amplitude was not increased as significantly as experimentally observed. Reduction of the L-type Ca^{2+} and rectifying K^+ currents by 50% to simulate the effects of verapamil resulted in only small changes in action potential amplitude. The width of the AP was modulated however, as can be seen from Figure 7.

It is important to note that both epinephrine and verapamil tend to affect the plateau phase of the action potential. Since this is not explicitly represented in the second-derivative signals obtained using extracellular microelectrodes in these experiments, the effects of pharmaceuticals acting on these channels were expected to be more difficult to observe than changes in the fast Na^+ conductance.

POWER SPECTRAL DENSITY ANALYSIS

To examine how the spectral characteristics of the action potentials change, the power spectral density (PSD) of each waveform was taken both before and after addition of the biologically active compound. This PSD was estimated by first taking the fast fourier transform (FFT) of the waveform, multiplying the FFT result by its complex conjugate and dividing by the frequency range. This was done for waveforms both before and after addition of the agent of interest (for simulation and experimental results). A modulation function for the pharmaceutical was then determined by dividing the PSD after agent addition by the PSD before agent addition. This ratio has been plotted for the experimental results in Figure 8 and the simulated results in Figure 9.

As can be seen from the experimental results of Figure 8,

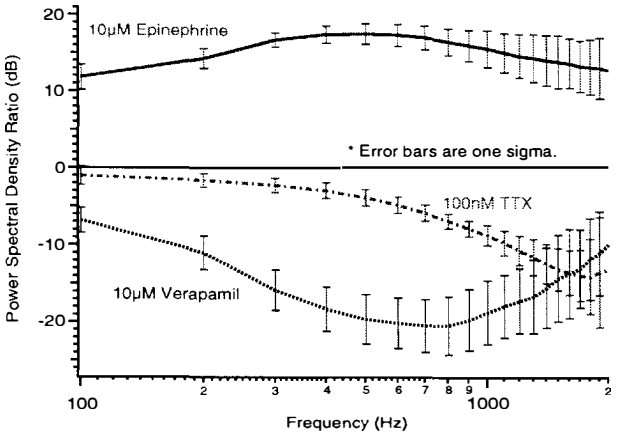

Figure 8. *Power spectral density (PSD) ratio plots ($PSD_{after\ agent} \div PSD_{before\ agent}$). Additions of 10 μm epinephrine (Ca^{2+} channel agonist), 100 nM tetrodotoxin (TTX) (Na^+ channel blocker), and 10 μM verapamil (Ca^{2+} channel blocker) are all shown to have different effects on the PSD of the measured action potential. Epinephrine and verapamil have opposite effects as expected. 8 channels of data were averaged with error bars of one sigma.*

there were characteristic modulation functions observed for each of the compounds tested. Epinephrine enhanced the power of the AP across a 2 kHz bandwidth with a slight bandpass effect observed. Verapamil had the opposite effect, reducing the overall AP power, again with a bandpass signature. Tetrodotoxin exhibited a low pass filter effect that clearly reduced the high frequency components of the AP. Additional data using a fast *and* slow Na^+ channel blocker (QX-314) resulted in a modulation function similar to that of TTX, but with additional attenuation at lower frequencies (data not shown). While extensive tests using multiple agents known to modulate similar channels have not been done, these results do show definite, unique characteristic responses for the agents tested. The similarity between the modulation functions for TTX and QX-

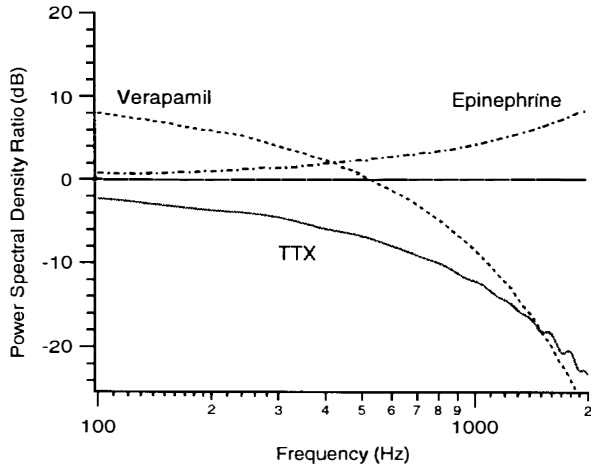

Figure 9: *Simulated power spectral density (PSD) ratio plots ($PSD_{after\ agent} \div PSD_{before\ agent}$). Shown are a 10× enhancement of L-type Ca^{2+} and rectifying K^+ currents for epinephrine, a 50% reduction in L-type Ca^{2+} and rectifying K^+ currents for verapamil, and a 25% reduction in Na^+ conductance for tetrodotoxin (TTX). The TTX simulation matches the experimental data in Figure 9 well, while those for epinephrine and verapamil were significantly different.*

314 is further evidence that unique response curves may exist for different classes of ionic channels. Further experimentation is required to verify this.

The simulated results matched extremely well for the case of tetrodotoxin, exhibiting the same lowpass response of approximately the same magnitude. However, the low frequency response of epinephrine was significantly lower than that observed experimentally, and the general shape of verapamil was completely wrong. This was most likely due to deficiencies in the empirically determined model [**16**] which does not accurately predict the behavior of second-messenger modulated effects, nor the subtle changes in the rising edge of the AP in response to changes in Ca^{2+} flux. As mentioned above, this was exacerbated by the fact that the second derivative does not represent the plateau phase of the AP, making it difficult to see effects not modeled precisely. Clearly from the experimental data of Figures 6 and 8 the pharmaceuticals tested do impact the shape and power spectrum of the extracellular action potential, but more detailed modeling is required to accurately predict these effects.

SUMMARY

The effects of three different biologically active agents (tetrodotoxin, verapamil and epinephrine) on the action potentials of spontaneously beating chick myocytes cultured on planar microelectrode arrays have been examined. The power spectral density of these APs revealed possibly unique modulation functions associated with action on specific classes of ion channels. Simulated action potential and PSD results matched those for tetrodotoxin well as expected given the second derivative nature of the measured signals. Simulation of the effects of verapamil and epinephrine resulted in modulation function shapes significantly different from those observed experimentally. This was attributed to deficiencies in the model.

While further simulation and experimental work are required to confirm the utility of the technique, the use of power spectral density analysis for classification of an unknown agent modulating ionic channels appears promising. A real-time version of such a technique could be implemented using simple analog/digital hardware, making its use in sensor applications and pharmaceutical screening more practical.

ACKNOWLEDGMENTS

The authors would like to thank Dr. Marco Bove and Dr. Joseph Pancrazio for their invaluable and greatly appreciated assistance with the action potential simulations, Dr. Nadim Maluf for his insights on data interpretation, and Dr. David Stenger for his continued support and guidance.

Funding for this project was provided by the DARPA MicroFlumes Program (Contract Number: N66001-96-C-8631).

REFERENCES

1. Thomas, C.A., Springer, P.A., Loeb, G.E., Berwald-Netter, Y. and Okun, L.M., "A miniature microelectrode array to monitor the bioelectric activity of cultured cells", *Experimental Cell Research*, 74:61-66 (1972).

2. Gross, G.W., Rhoades, B.K., Azzazy, H.M.E. and Wu, M.C., "The use of neuronal networks on multielectrode arrays as biosensors", *Biosensors and Bioelectronics*, 10:553-567 (1995).

3. Hickman, J.J., Foster, K.E., Kowtha, V., Bey, P. Jr. and Stenger, D.A., "Whole cell based biosensors", *Abstracts of Papers American Chemical Society*, 207(1-2):BTEC 76 (1994).

4. Stenger, D.A. and McKenna, T.M. (Eds.), *Enabling technologies for cultured neural networks*, Academic Press, San Diego, CA (1994).

5. Israel, D.A., Edell, D.J. and Mark, R.G., "Time delays in propagation of cardiac action potential", *American Journal of Physiology: Heart and Circulatory Physiology*, 27(6):H1906-H1917 (1990).

6. Ganong, W.F., *Review of medical physiology*, Prentice Hall, New Jersey (1993).

7. Marrese, C.A., "Preparation of strongly adherent platinum black coatings", *Analytical Chemistry*, 59:217-218 (1987).

8. Borkholder, D.A., Bao, J., Maluf, N.I., Perl, E.R. and Kovacs, G.T.A., "Microelectrode arrays for stimulation of neural slice preparations", *Journal of Neuroscience Methods*, 77:61-66 (1997).

9. Kewley, D.T., Hills, M.D., Borkholder, D.A., Opris, I.E., Maluf, N.I., Storment, C.W., Bower, J.M. and Kovacs, G.T.A., "Plasma-etched neural probes", *Sensors and Actuators: A Physical*, 58:27-35 (1997).

10. Borkholder, D.A., Opris, I.E., Maluf, N.I. and Kovacs, G.T.A., "Planar electrode array systems for neural recording and impedance measurements", *Conference Proceedings of the 1996 IEEE Engineering in Medicine and Biology*, Amsterdam, The Netherlands, 10/31-11/3, IEEE (1996).

11. De Hann, R.L., "Regulation of spontaneous activity and growth of embryonic chick heart cells in tissue culture", *Developmental Biology*, 16:216-249 (1967).

12. Barry, W.H., Pitzen, R., Protas, K. and Harrison, D.C., "Inotropic effects of different calcium ion concentrations on the embryonic chick ventricle", *Circulation Research*, 36:727-734 (1975).

13. Polinger, I.S., "Separation of Cell Types in Embryonic Heart Cell Cultures", *Experimental Cell Research*, 63:78-82 (1970).

14. Grattarola, M. and Martinoia, S., "Modeling the neuron-microtransducer junction: from extracellular to patch recording", *IEEE Transactions on Biomedical Engineering*, 40(1):35-41 (1993).

15. Connolly, P., Clark, P., Curtis, A.S.G., Dow, J.A.T. and Wilkinson, C.D.W., "An extracellular microelectrode array for monitoring electrogenic cells in culture", *Biosensors and Bioelectronics*, 5:223-234 (1990).

16. Rasmusson, R.L., Clark, J.W., Giles, W.R., Robinson, K., Clark, R.B., Shibata, E.F. and Campbell, D.L., "A mathematical model of electrophysiological activity in a bullfrog atrial cell", *American Journal of Physiology*, 259(2):H370-H389 (1990).

17. Hille, B., *Ionic channels of excitable membranes*, Second edition, Sinauer Associates, Inc., Sunderland, Massachusetts (1992).

18. Kandel, E.R., Schwartz, J.H. and Jessell, T.M. (Eds.), *Principles of neural science*, Third edition, Appleton and Lange, Norwalk, Connecticut (1991).

19. Hardman, J.G. and Limbird, L.E. (Eds), *Goodman & Gilman's The pharmacological basis of therapeutics*, Ninth edition, McGraw-Hill, New York (1996).

20. Pancrazio, J.J., Viglione, M.P., Kleiman, R.J. and Kim, Y.I. "Verapamil-induced blockade of voltage-activated potassium ion current in small-cell lung cancer cells" Journal Of Pharmacology And Experimental Therapeutics, 257(1):184-191 (1991).

A HIGH-SPEED CAPACITIVE HUMIDITY SENSOR

Uksong Kang and Kensall D. Wise
Center for Integrated Sensors and Circuits
Department of Electrical Engineering and Computer Science
University of Michigan, Ann Arbor, MI 48109-2122

ABSTRACT

This paper reports a high-speed capacitive humidity sensor with an integrated boron-diffused heater. A response time of 1.0sec and a sensitivity of 30.0fF/%RH have been obtained with the fabricated devices. High speed is achieved using multiple polyimide columns having diameters of a few microns and allowing moisture to diffuse into them circumferentially, altering the dielectric constant. A subsecond response time is expected when the geometry is further reduced. The purpose of the heater is to enable the sensor to recover from contamination and aging. It allows bake-out of the sensing film on demand and is useful in self-test protocols.

INTRODUCTION

Thin-film humidity sensors are widely used in many measurement and control applications, including those in automated process control, meteorology, domestic appliances, agriculture and medical equipment [1]. They can be categorized into different device types depending on the underlying sensing principle (capacitance, resistance, weight or stress changes in a thin film as a function of moisture absorption). Among these, capacitive devices are often preferred since they offer very low power consumption and a linear output response. Various ceramics, hygroscopic polymers, and electrolytes are used as humidity-sensitive materials.

In spite of a great deal of on-going research, thin-film humidity sensors continue to suffer from slow response (>30sec), low accuracy (<±2%RH) and substantial long-term drift. Slow speed is of particular concern in applications involving transient humidity changes or measurements that must be taken on the fly, including many in industrial process control and in the monitoring of atmospheric relative humidity using radiosonds, dropsonds or unmanned aerial vehicles [2]. Contamination and aging of the sensing film is also an important issue since it causes the sensor to drift, resulting in decreased accuracy [3]. The sensing film can be reset by integrating a heater underneath the sensor.

PRINCIPLE OF HIGH-SPEED HUMIDITY SENSING

Capacitive humidity sensors detect moisture-induced changes in the dielectric constant of a hygroscopic polymer or ceramic layer to measure the ambient relative humidity level. In conventional structures, the diffusion of moisture into the sensing film takes place from only one side of the film as in Fig. 1(a). In contrast, as shown in Fig. 1(b), the high-speed structure used here absorbs moisture circumferentially into cylindrical islands. A significant improvement in speed is achieved.

In order to compare the response times of the conventional and the high-speed (circumferential) structures,

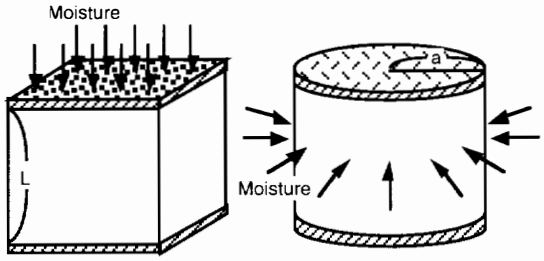

***Figure 1**. (a) Conventional structure (b) High-speed structure*

the equations governing the transient capacitance change as moisture diffuses into a thin film or into a cylindrical body have been derived [4]. In this analysis, it is assumed that no moisture is present inside the film in its initial state and that the diffusion constant is independent of moisture concentration. The normalized capacitance change after an abrupt change in the ambient relative humidity level for single-sided diffusion into a rectangular body is formulated as

$$C_{Norm,rec}(t) = \sum_{n=1}^{\infty} \frac{1-\exp\dfrac{-(2n-1)^2\pi^2 Dt}{4L^2}}{(2n-1)^2} \Bigg/ \sum_{n=1}^{\infty} \frac{1}{(2n-1)^2} \qquad (1)$$

where t is the time, D is the diffusion constant of moisture and L is the height of the block. Similarly, the normalized capacitance for diffusion into a cylindrical body is derived as

$$C_{Norm,cyl}(t) = \sum_{n=1}^{\infty} \frac{1-\exp(-Dk_n^2 t/a^2)}{k_n^2} \Bigg/ \sum_{n=1}^{\infty} \frac{1}{k_n^2} \qquad (2)$$

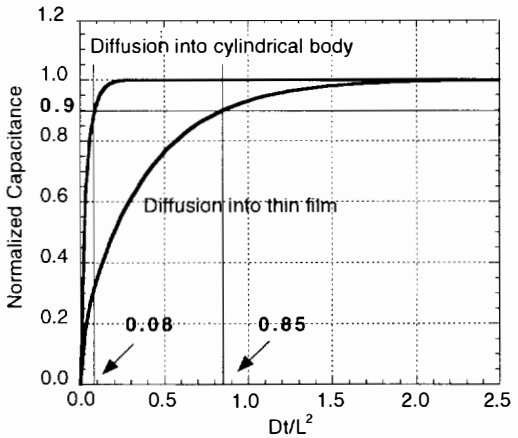

***Figure 2**. Analytical comparison of response times for diffusion into a thin film and into a cylindrical body. Improvement in the response time by a factor of 10 is obtained with the high-speed cylindrical structure. (t: time, L: thickness of film = diameter of cylinder, D: diffusion constant)*

0-9640024-2-6/hh1998/$20©1998TRF
DOI 10.31438/trf.hh1998.40

where a is the radius of the cylinder and the k_n's are roots of $J_o(k)=0$. J_o is the zeroth-order Bessel function. Note that the normalized capacitance is a function of Dt/a^2 from which it follows that the response time is proportional to the square of the radius and inversely proportional to the diffusion constant. Using equations (1) and (2), the normalized capacitance for both single-sided diffusion into a thin film and diffusion into a cylindrical body are plotted in Fig. 2. In this comparison, the hygroscopic film is of the same material for both cases and the thickness of the film is the same as the diameter of the cylinder. After an abrupt change in the ambient relative humidity level, it takes $0.85L^2/D$ and $0.08L^2/D$ seconds to reach the 90% point of the final steady state capacitance value for the conventional and the high-speed structure, respectively. Hence, an improvement in response time by about a factor of 10 is obtained with the high-speed structure.

DEVICE STRUCTURE AND DESIGN

A schematic diagram of the high-speed humidity sensor is shown in Fig. 3. The sensor is located on top of a boron-diffused heater and is electrically isolated from it by a thin dielectric layer. The sensor consists of thousands of polyimide columns, each of which has a diameter of a few microns. The columns are connected in parallel to form a capacitor. An upper electrode runs over the polyimide columns providing moisture free access to the sensing film. Besides serving as an electrode, this upper electrode also acts to filter out particles larger than the spacing between the adjacent conductors (a few microns). Contaminating gases can, in principle, be baked out of the polyimide using the integrated heater, enabling recovery of the sensing film from contamination, aging and hysteresis. A bulk-silicon boron-diffused heater has been chosen to maintain planarity over the device surface. The device is mounted on a thermal insulator to increase the efficiency of the heater.

A preimidized, photosensitive polyimide (ULTRADEL 7501 - Amoco Chemicals) has been used as the moisture sensing material due to its thermal stability, mechanical robustness, and compatibility with VLSI process technology [5]. A preimidized material has been chosen to reduce stress build-up between the upper electrode and the polyimide. Preimidized polyimide shrinks in thickness by only about 8% after curing, while the polyimide precursor shrinks by as much as 50%. Photosensitivity is necessary for forming the suspended top-electrode structure as will be described in the fabrication process sequence. ULTRADEL 7501 has a tensile modulus of

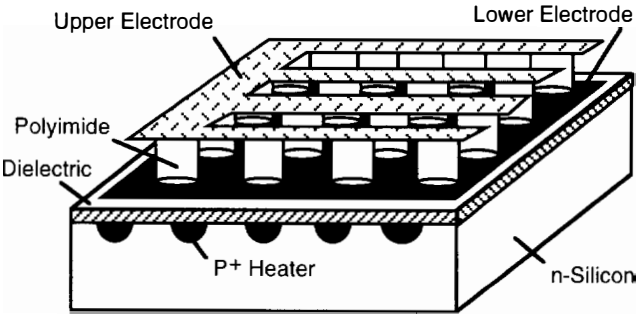

Figure 3. *Schematic diagram of the high-speed capacitive humidity sensor with a boron-diffused heater.*

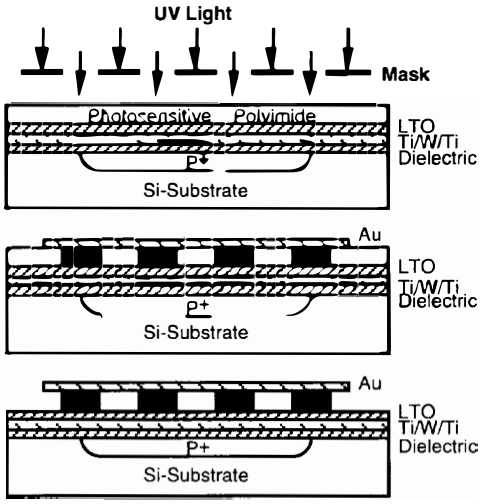

Figure 4. *Fabrication process sequence for the high-speed capacitive humidity sensor.*

510,000psi, a thermal expansion coefficient at 200°C of 24ppm/°C, and a moisture uptake at 100%RH of 3.4%.

The capacitance of the sensor originates from both the polyimide and the air-gap. The polyimide capacitance is the one to be measured while the air-gap capacitance is a parasitic by-product of the electrical interconnections needed to access the capacitance of polyimide columns. Although the air-gap contributes to the total sensor capacitance it does not affect the sensitivity of the device since the dielectric constant of air changes by only about 1.4ppm/%RH while that of polyimide changes by 3330ppm/%RH. The speed of the sensor is primarily determined by the diameter of polyimide columns. As noted above, the response time increases as the square of the column radius. The response time is not significantly influenced by the thickness of the polyimide film since diffusion takes place laterally. The sensitivity of the sensor for a given area, on the other hand, is determined by the thickness of the polyimide film as well as by its fill factor (the area that polyimide columns occupy per unit total area). The sensitivity becomes larger as the film thickness is reduced and the polyimide fill factor is increased.

DEVICE FABRICATION

The fabrication sequence is a 6 mask process. As shown in Fig. 4, fabrication starts with a deep boron diffusion into an n-type (100) wafer. A junction depth of 3µm forms the integrated heater. Then, a stress compensated LPCVD SiO_2/Si_3N_4/SiO_2 dielectric layer with a thickness of 0.5µm/0.25µm/0.5µm is deposited over the wafer. Contact holes to the heater are opened using RIE, followed by the deposition and lift-off of a Ti/W/Ti (30nm/800nm/30nm) layer to act as the lower electrode. A 0.5µm-thick low temperature oxide is now deposited over the wafer in order to eliminate the possibility of any conductive path between the upper and lower electrodes at high humidity or due to conductive particle trapping inside the air-gap. Vias are opened in the pad regions using BHF etching in order to enable wire bonding. After applying the adhesion promoter, a photosensitive polyimide (ULTRADEL 7501) is spun onto the wafer at 4500rpm for 60sec, resulting in a film thickness of 2µm. The polyimide columns are then defined

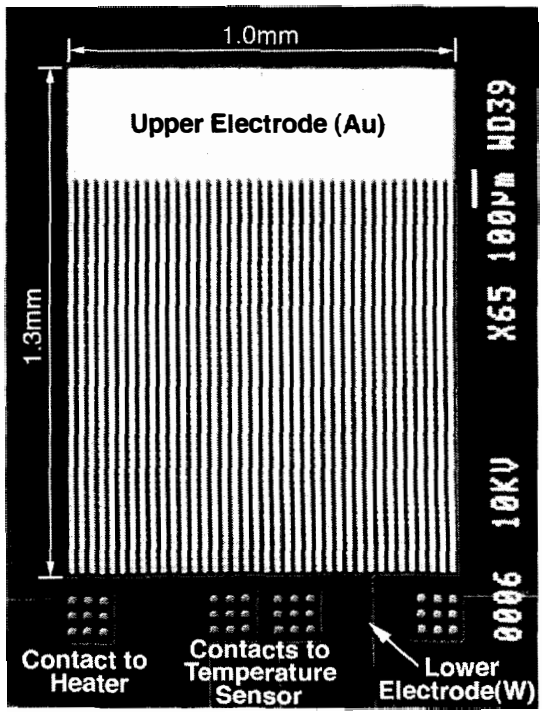

Figure 5. Top view of a fabricated type-B device. The overall size of the sensor is 1.3mm x 1.0mm

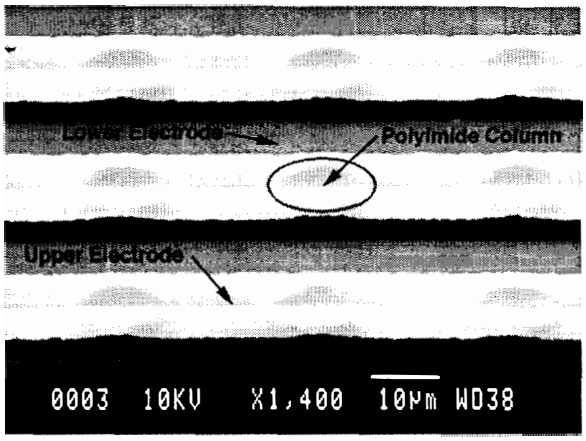

Figure 6. Close-up view of the upper electrode, lower electrode and polyimide columns.

lithographically followed by deposition of a Au layer with a thickness of 0.3µm. The Au layer is patterned by wet etching to form the upper electrode. The polyimide is now developed so that the unexposed regions are dissolved away to leave the polyimide columns supporting the suspended upper electrode. Finally, the polyimide is cured in a nitrogen-purged oven at 300°C for 5 hours.

Three different sensors (types A, B and C) have been fabricated having polyimide column diameters of 5µm, 10µm and 15µm, respectively. The total number of polyimide columns is 6138 for type A, 1900 for type B, and 891 for type C. An SEM picture of the type-B device is shown in Fig. 5. The overall size of the sensor is 1.3mm x 1.0mm. A serpentine boron-diffused heater and a boron-diffused temperature sensor are located underneath the sensor. The heater lines are 20µm

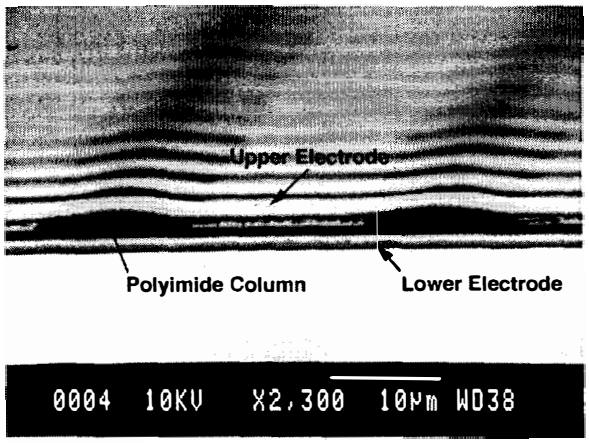

Figure 7. Side-view of the upper electrode supported by polyimide columns under which there is the lower electrode. The thickness of the upper electrode is 0.3µm and that of polyimide is 2µm.

wide and 3µm deep, and the measured heater resistance is 6.0kΩ. Contacts to the heater and temperature sensor are visible in the lower part of the picture. Electrical connection to the upper electrode is made directly to the Au rectangular pad by wire bonding. A close-up view of the upper metal strip lines supported by the polyimide columns is shown in Fig. 6, where the polyimide columns are visible as circles. A side-view is shown in Fig. 7.

TEST RESULTS

In Fig. 8, the measured output of the sensor is shown as a function of relative humidity at room temperature and a measurement frequency of 1MHz. The sensor output is linear with a sensitivity of 30.6fF/%RH, 25.8fF/%RH, and 31.3fF/%RH for types A, B, and C, respectively.

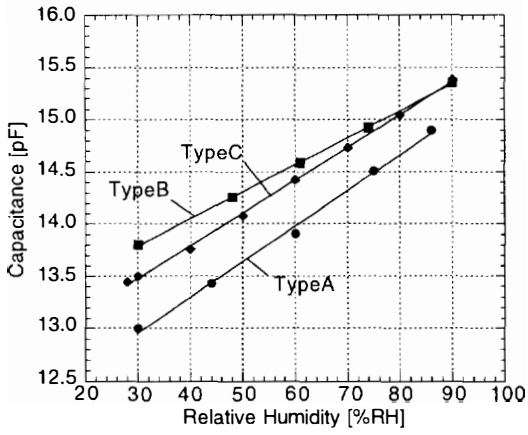

Figure 8. Sensor output as a function of relative humidity at room temperature for types A, B and C devices, which have polyimide column diameters of 5µm, 10µm and 15µm, respectively.

The response times of the fabricated devices have been measured and are shown in Fig. 9. A significant improvement

in speed has been obtained. The response times for types A, B and C sensors are 1.0sec, 1.9sec and 6.9sec, respectively. The response time is measured to the 90%-point of the final steady-state capacitance value after an abrupt change in the ambient relative humidity level from 33%RH to 90%RH.

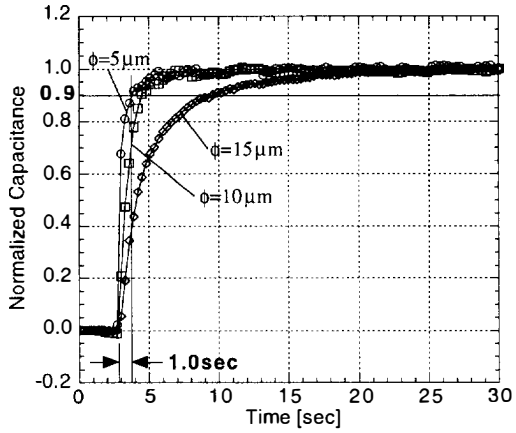

Figure 9. *Response of sensors having polyimide column diameters of 5μm, 10μm and 15μm to an abrupt change in ambient relative humidity from 33%RH to 90%RH at room temperature.*

The experimental set-up to expose the sensor to an abrupt change in relative humidity consists of a plastic container with a volume of 118ml located inside a temperature-humidity chamber. The humidity sensor is mounted on a platform the end of which is attached with a hinge to the wall of the container. A spring fixed underneath the platform enables the sensor to be transferred out of the container when the cap is opened. Two thirds of the container is filled with a saturated solution of $MgCl_2$, which maintains the trapped air at 33%RH when the container is sealed gas-tight and left for a sufficient amount of time. Using saturated salt solutions to calibrate humidity sensors is an inexpensive and practical method often used in industry **[6]**. After sealing the cap of the container with silicon rubber and waiting at least for 6 hours the chamber is set to 90%RH. When the chamber settles to this level, the cap is opened by pulling a wire attached to the cap. The spring action causes the sensor to be transferred out of container, resulting in an abrupt change from 33%RH to 90%RH. The container is positioned such that the sensor faces into air flow generated by a fan at the back of the chamber. The fan forces air at 90%RH onto the sensor.

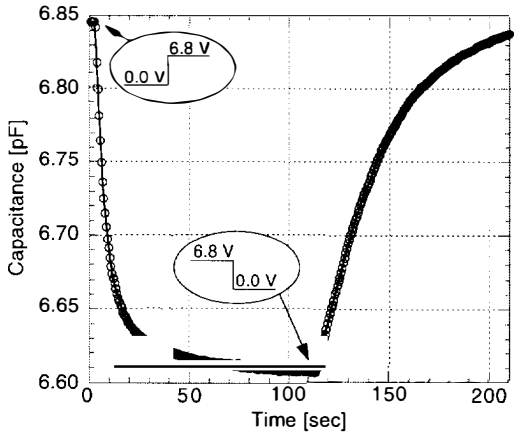

Figure 10. *Response of the type-C device to a 6.8V pulse applied to the heater (60%RH, 25°C).*

The sensor response to a 6.8V pulse applied to the heater is shown in Fig. 10. A type C device has been used here with the ambient set at 60%RH and 25°C. As the supply voltage across the heater is increased from 0.0V to 6.8V, the sensor capacitance decreases by about 250fF. As the heater is turned off, the sensor capacitance returns to its original value. The temperature sensor indicates a temperature rise on the chip of about 20°C due to this excitation. This decrease in capacitance with heating is believed to be primarily due to baking out moisture in the film rather than to any thermal expansion.

CONCLUSIONS

A high-speed humidity sensor has been designed, fabricated and tested. Three different device types have been fabricated having polyimide column diameters of 5μm, 10μm and 15μm. Response times of 1.0sec, 1.9sec, and 6.9sec have been measured for these devices, respectively. A subsecond response time is expected if the diameter of the polyimide columns is further reduced. The corresponding device sensitivities are 30.6fF/%RH, 25.8fF/%RH, and 31.3fF/%RH. The sensor outputs are highly linear with relative humidity. The response of the humidity sensor to heating has also been tested. The sensor capacitance decreases by about 250fF as the device temperature is increased from 25°C to 45°C and moisture is baked out of the sensing film.

ACKNOWLEDGMENTS

The authors would like to gratefully acknowledge the support provided by the Defense Advanced Research Projects Agency under contract DABT63-95-C-0111.

REFERENCES

1. N. Yamazoe, "Humidity Sensors: Principles and Applications", *Sensors and Actuators*, 10, 379 (1986).

2. A. Mason, N. Yazdi, K. Najafi, and K. D. Wise, "A Low-Power Wireless Microinstrumentation System for Environmental Monitoring", *Proc. Transducers'95,* Stockholm, Sweden, June (1995), pp. 107 - 110.

3. A.R.K. Ralston, M. C. Buncick and D. D. Denton, "Effects of Aging on Polyimide : a Model for Dielectric Behavior", *Technical Digest of the 1990 Solid-State Sensors and Actuators Workshop*, Hilton Head Isl., SC (1990), pp. 759 - 763.

4. J. Crank, *The Mathematics of Diffusion*, Chapter 5-6, Oxford University Press, London (1975).

5. T. Boltzhauser, L. Chandran, H. Baltes, and D. Steiner, "Humidity Sensing Properties and Electrical Permittivity of New Photosensitive Polyimides", *Sensors and Actuators B*, 5, 161 (1991).

6. A. Carotenuto, and M. Dell'Isola, "An Experimental Verification of Saturated Salt Solution-Based Humidity Fixed Points", *International Journal of Thermophysics*, 17, 1423 (1996).

INTEGRATED CHEMIRESISTOR AND WORK FUNCTION MICROSENSOR ARRAY WITH CARBON BLACK/POLYMER COMPOSITE MATERIALS

K. Domanský, V. S. Zapf, and J. W. Grate
Environmental Molecular Sciences Laboratory, Pacific Northwest National Laboratory
Richland, WA 99352

A. J. Ricco and W. G. Yelton
Microsensor R&D Department
Sandia National Laboratories
Albuquerque, NM 87185-1425

J. Janata
School of Chemistry and Biochemistry
Georgia Tech
Atlanta, GA 30332-0400

ABSTRACT

An array of chemically-sensitive field-effect transistors (CHEMFETs) that measure both work function and bulk resistance changes in thin films was used to detect volatile organic compounds. Carbon black/organic polymer composite films were deposited onto the CHEMFETs using an automated microdispensing method.

INTRODUCTION

Development of hybrid device arrays--those comprised of more than one sensor physical platform type--is an important technology for successful future applications of chemical sensors. Hybrid device arrays offer advantages over traditional sensor arrays because they introduce diversity by measuring different parameters of the sensing layers, as opposed to relying solely on the chemical diversity of the sensing elements. In theory, a low number of chemically diverse coatings deposited on different sensor platforms is sufficient to analyze a large number of chemical compounds.

In addition to increasing response information content, it is desirable to integrate different sensor platforms into a single device for cost and space efficiency reasons. We have fabricated chemically-sensitive field-effect transistors (CHEMFETs) which allow resistance and work function (WF) measurements on a single chemically sensitive layer [1]. In the work described here, carbon black/organic polymer composites were used as chemically sensitive coatings on these devices. Although carbon-loaded chemiresistors functioning via vapor-induced swelling have been previously demonstrated [2,3], the purpose of this work is to show the advantages of measuring both WF and electrical resistance.

We also show that composite materials can be successfully deposited onto the target sites of CHEMFETs by an automated microdispensing method [4]. In contrast to most traditional thin-film deposition techniques, microdispensing does not have to be combined with photolithographic or other patterning methods, because, typically, nanoliter volumes of materials are deposited only onto selected target locations.

EXPERIMENTAL DETAILS

The carbon black/polymer composite materials deposited on CHEMFETs are listed in Table 1. Graphitized carbon particles with a 27 - 30 nm diameter were used (Polysciences, Inc., Warrington, PA). Each polymer was dissolved in deionized water or toluene to yield a 2% weight/volume solution. To promote monodispersion of carbon particles, samples were agitated in an ultrasonic bath for several hours, followed by agitation with a point-source ultrasonic processor, resulting in samples that were kinetically stable for several weeks.

Table 1. Composite films deposited on CHEMFETs.

Coating Code	*Polymer*	*CL**	*Solvent*	*Resistivity*[†] [Ω-cm]
PVA-40-C	poly(vinyl-alcohol)	40	water	22 ± 4
PVA-50-C	poly(vinyl-alcohol)	50	water	1.0 ± 0.6
PVA-60-C	poly(vinyl-alcohol)	60	water	1.1 ± 0.3
PAAS-40-C	poly(acryl-amide-acrylic acid, Na^+ salt)	40	water	2.8 ± 0.8
EC-40-C	ethyl cellulose	40	toluene	3.1 ± 0.7

*CL - carbon loading of the solvent-free composite film, wt%.
[†]Measured at 21°C and 38% RH.

Resistivities of the samples deposited on an insulating substrate were calculated from the sheet resistance (4-point probe) and thickness (contact profilometer).

Carbon black/polymer composites were deposited on CHEMFETs using an automated dispensing system (Model A402B, Asymtek, Carlsbad, CA) equipped with AV-500 targeting offset camera and DV-01 syringe valve bracket [4], using 30-Gauge stainless-steel needles. Prior to film deposition, the top Si_3N_4 surface of each CHEMFET chip was etched in buffered HF. The materials were microdispensed as lines ~ 400 µm wide by 600 µm long. Typically, less than 30 µL of the solution was sufficient both for the deposition tests on Si wafers and on several CHEMFET chips. On each chip, the same material was deposited on two CHEMFET gates.

The dual-gate CHEMFETs with SiO_2/Si_3N_4 gate insulators were fabricated at the University of Utah [1]. On both sides of each CHEMFET channel, two parallel Au-plated Pt lines ~ 165 µm apart were formed to allow resistance measurement. Carbon black/polymer composites were deposited onto the Si_3N_4 surface over the channel area (20 x 400 µm) and on the Au-plated Pt lines, thereby forming the dual-use transistor gate/chemiresistor films (Fig. 1). Length of the electrode pair in contact with the coating was ~ 500 µm. CHEMFET chips with deposited films were attached to 16-pin TO-8 headers and wirebonded. Thickness profiles of carbon black/polymer composites were investigated with a Zygo NewView 200 non-contact profilometer. Headers with mounted CHEMFET chips were placed in a temperature-controlled stainless-steel flow cell [5]. Current-voltage

0-9640024-2-6/hh1998/$20©1998TRF
DOI 10.31438/trf.hh1998.41

characteristics of the composite films were measured with a Hewlett-Packard 4142 modular DC Source/Monitor.

An automated vapor-generating/mixing system provided dilutions of isooctane (IOC), acetonitrile (ACN), isopropyl alcohol (IPA), methyl isobutyl ketone (MIK), and water vapor in nitrogen at a flowrate of 100 sccm. Sensors were exposed for 20 min each to six concentrations of each organic vapor, separated by 20-minute N_2 exposures.

Both WF [5] and DC resistance measurements were obtained with multichannel instrumentation. WF changes were deduced by measuring the gate voltage (applied to the coating) necessary to maintain a preset drain-source current. The resistance changes of the films were measured across the width of the coating with HP 34401 multimeters in two-probe, constant-current mode (500 nA or 5 μA). Maximum voltage applied to coatings was ~ 2 V. The data-acquisition sampling period was 10 s. The sensors were maintained above the room temperature at 35°C during all measurements.

RESULTS AND DISCUSSION

A photograph of a carbon black/polymer composite microdispensed on a CHEMFET chip is shown in Fig. 2a. The composite film overlaps the gate electrodes and completely covers the channel area, critical for proper device operation. A significant advantage of automated microdispensing is that the deposition is localized, but a drawback is that the thickness uniformity across the film is difficult to control. Fig. 2b. shows a 3-D surface profile of one of the films. The thickness of PVA-60-C is greatest around the perimeter, a source of potential problems for resistance measurements: because the electrodes contact both the thick perimeter section and the thin middle area, the thick edge can adversely affect resistance response time. In contrast, WF response time is not affected because the thick edges are completely outside the transistor channel region. We note that edge effects can be eliminated by burying the electrodes under the perimeter in an electrically insulating film while leaving them exposed in the middle area, where the thickness of the composite material is relatively uniform.

Prior to vapor-exposure experiments, current-voltage characteristics of the composite films on CHEMFETs were measured, and all were found to be ohmic, justifying measurement of resistance changes in constant-current mode. We found resistances measured in N_2 and synthetic air to be very similar, indicating a minimal effect of oxygen. Comparison of the resistivity values in Table 1 with resistances measured on the coated CHEMFETs suggests that the average thickness of EC-40-C on a CHEMFET is approximately ten times less than that of PAAS-40-C.

When carbon black/polymer composites are exposed to a vapor, analyte molecules can adsorb on the surface of the composite material, absorb in the polymer, adsorb on the surface of carbon particles, and adsorb at the composite material/substrate interface. Vapor-induced polymer swelling and the resulting increase in the average spacing between conductive carbon particles is the predominant response mechanism for the resistance changes [2,3]. The effect of the composite material/vapor interaction on the transistor threshold voltage shift (ΔV_t) is more complex. We believe ΔV_t is controlled through chemical modulation of the WF by the adsorption of analyte molecules on the surface of carbon particles. However, other effects, such as the analyte-induced change of the polymer dielectric constant, or increased distance of the carbon particles from the Si_3N_4 surface, can also play a role.

Fig. 3 shows the resistance and WF responses of one of the composite materials, PVA-50-C, upon exposure to acetonitrile vapor. Two differences between the resistance and WF responses are notable. First, the WF response for this particular material and analyte is faster than the resistance response, perhaps a consequence of the thicker edge region of the film being probed by the resistance measurement but not by the WF. Second, the WF response is approximately logarithmic while the resistance response is linear. This trend is more clear in Fig. 4, which shows the response of PVA-50-C for acetonitrile as well as four other vapors. The linearity of the resistance effect is suggestive of a linear relationship between dissolved analyte and vapor concentrations, coupled with a linear dependence of resistance upon polymer swelling (over the range of concentrations examined). The logarithmic concentration dependence of the WF is likely a consequence of the dependence of the change in carbon-particle surface WF upon the number of adsorbate molecules, convoluted with the adsorption isotherm for the adsorbate on carbon particles.

The effect of carbon loading on the relative change of resistance for PVA is illustrated in Fig. 5. Since the resistance varies approximately linearly with concentration, each point represents a slope. The sensitivity for isooctane (a very nonpolar analyte) is independent of carbon loading, but for water and acetonitrile (the most polar, highest dielectric analytes), the sensitivity decreases with increasing carbon loading, while for isopropyl alcohol and methyl isobutyl ketone (moderate polarity/dielectric constant), the sensitivity increases. This interesting feature could be exploited to increase selectivity.

Figs. 6 and 7 show the resistance and WF response patterns of all five tested composite materials to five vapors. Resistance responses are either zero or positive, consistent with vapor-induced swelling. WF responses are mostly negative, consistent with the analytes being net electron donors to the carbon particles. For PVA, the responses decrease with increasing carbon loading for all vapors with the exception of isooctane.

CONCLUSIONS

The hybrid sensor array resolves all of the vapors at each of several concentrations reasonably well, which would not be possible using only the resistance or WF response alone. This demonstrates the advantage of the dual-mode measurement platform. Detail data analysis is necessary to quantitatively evaluate discrimination among vapors.

Work at PNNL, SNL, and GaTech was supported by the U.S. DOE Office of National Security and Nonproliferation. Sandia is a multiprogram laboratory operated by Sandia Corporation, a Lockheed Martin Company, for the United States Department of Energy under Contract DE-AC04-94AL85000.

REFERENCES

1. M. Liess, D. Chinn, D. Petelenz, and J. Janata, "Properties of Insulated Gate Field-Effect Transistor with a Polyaniline Gate Electrode", *Thin Solid Films*, *286*, 252 (1996).

2. B. Lundberg and B. Sundqvist, "Resistivity of a Composite Conducting Polymer as a Function of Temperature, Pressure, and Environment: Applications as a Pressure and Gas Concentration Transducer", *J. Appl. Phys., 60,* 1074 (1986).

3. M. C. Lonergan, E. J. Severin, B. J. Doleman, S. A. Beaber, R. H. Grubbs, and N. S. Lewis, "Array-Based Vapor Sensing using Chemically Sensitive, Carbon Black-Polymer Resistors" *Chem. Mater.*, 8, *2298* (1996).

4. K. Domansky and E. A. Watters, "A Technique for Depositing Sensing Layers in Integrated Microsensor Arrays by Automated Fluid Dispensing", *Proceedings of the Third International Symposium on Microstructures and Microfabricated Systems*, Electrochemical Proceedings Volume 97-5, The Electrochemical Society, Pennington (1997), pp. 144-151.

5. K. Domansky, D. L. Baldwin, J. W. Grate, T. B. Hall, J. Li. M. Josowicz, and J. Janata, "Development and Calibration of Field-Effect Transistor-Based Sensor Array for Measurement of Hydrogen and Ammonia Gas Mixtures in Humid Air", *Anal. Chem., 70,* 473 (1998).

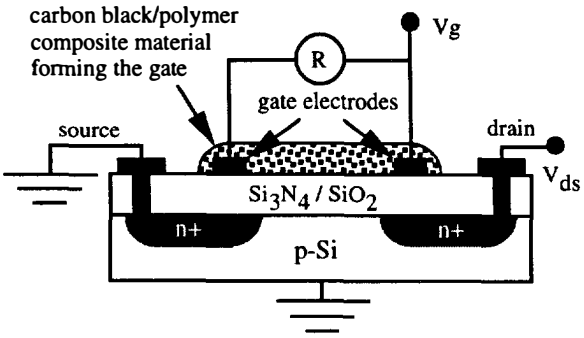

Fig. 1 Device cross section.

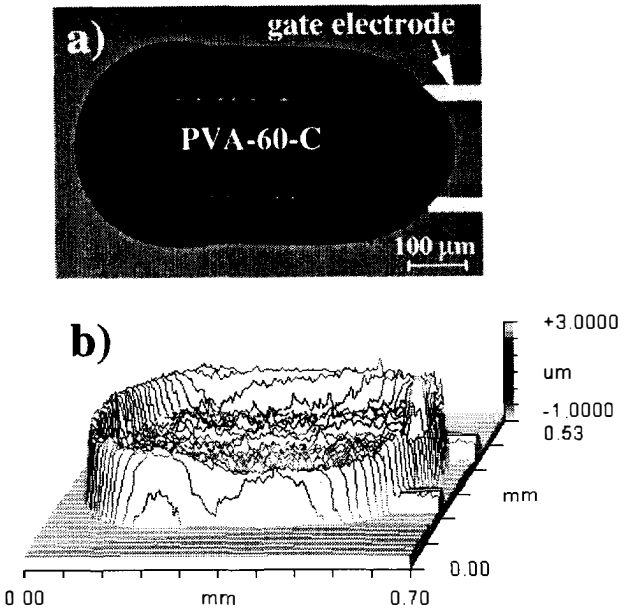

Figure 2. PVA-60-C microdispensed on a CHEMFET chip. a) Photograph of a gate. b) 3D surface profile of the same gate determined by non-contact profilometry.

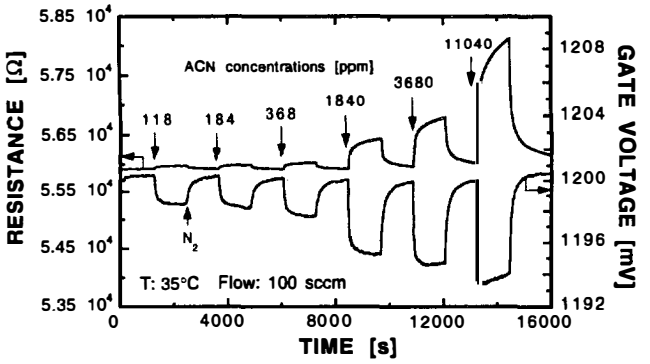

Figure 3. Resistance and work function responses of PVA-50-C to acetonitrile.

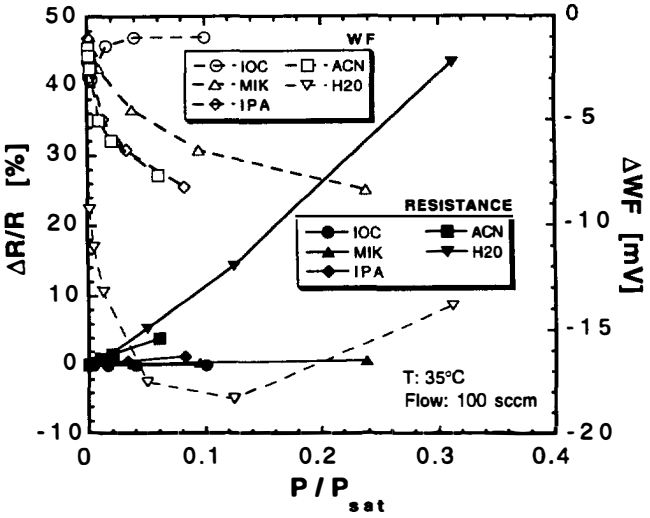

Figure 4. Calibration curves of PVA-50-C for isooctane, methyl isobutyl ketone, isopropyl alcohol, acetonitrile, and water.

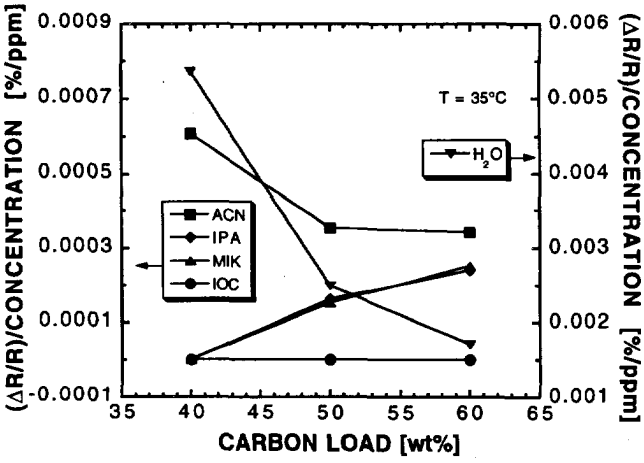

Figure 5. The effect of carbon load on the relative change of resistance for poly(vinyl alcohol).

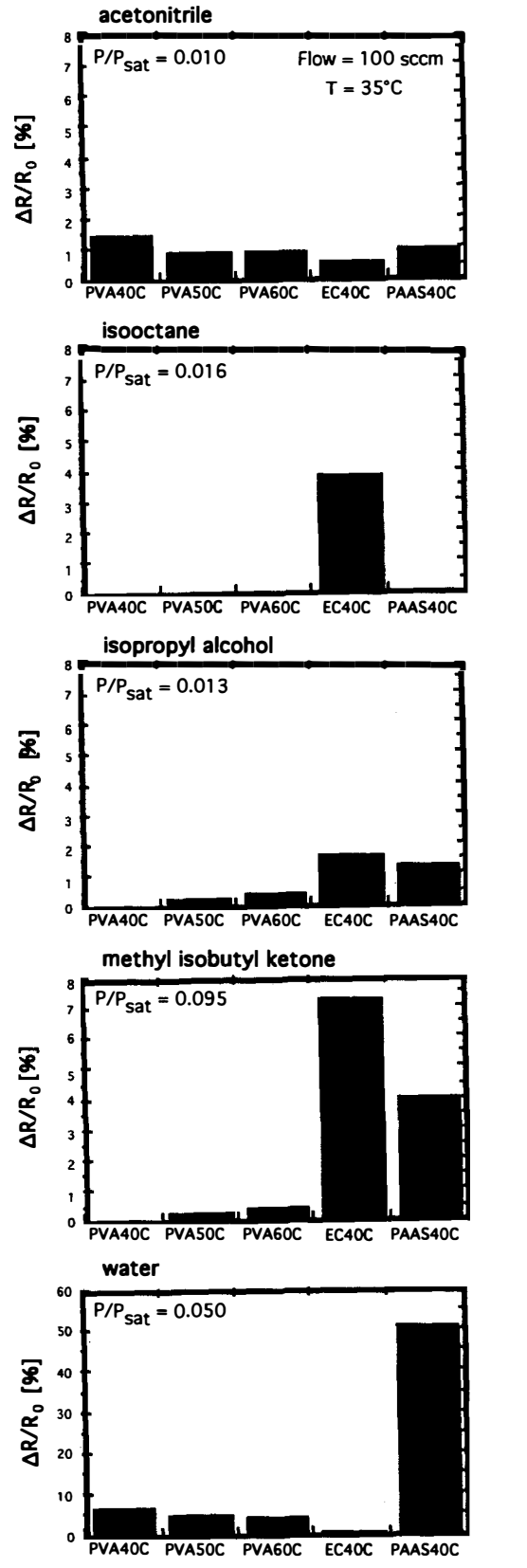

Figure 6. Resistance response patterns

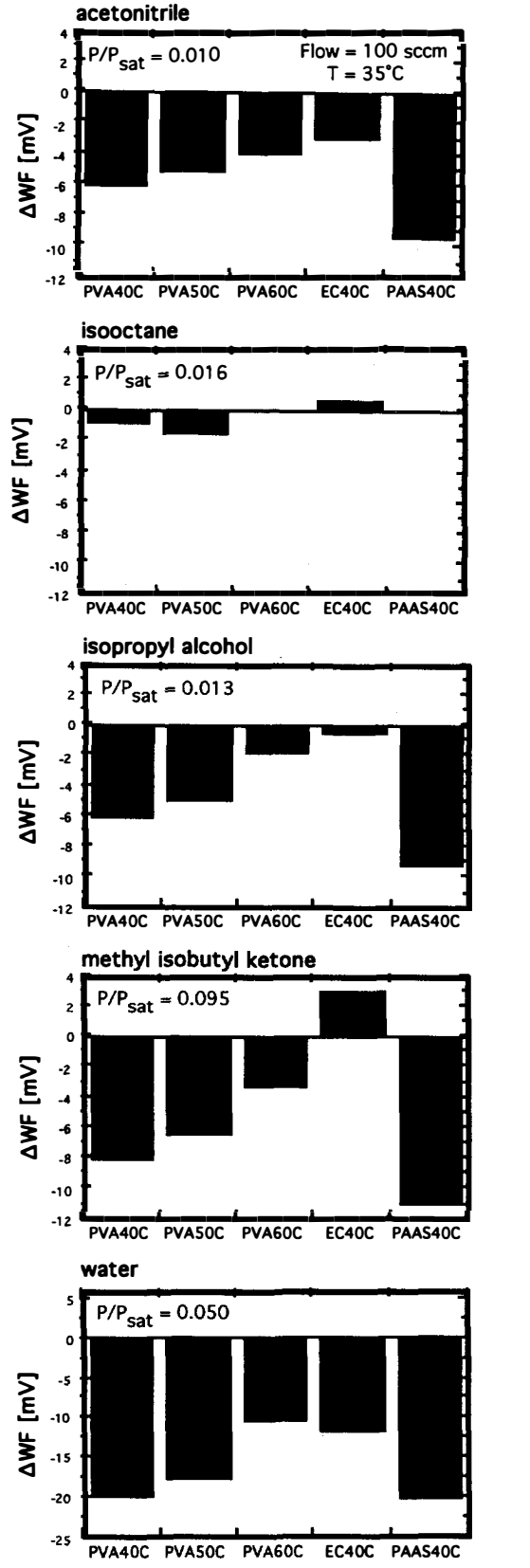

Figure 7. Work function response patterns

MEMS SIMULATION USING SUGAR v0.5

Jason Vaughn Clark, Ningning Zhou, and K. S. J. Pister
Berkeley Sensor and Actuator Center
University of California at Berkeley
497 Cory Hall, Berkeley, CA 94720

CONTEXT

Integrated Circuit (IC) fabrication technology development over the last few decades has been phenomenal. We have also seen the development of design and simulation tools which enable engineers to capture the full capabilities of the technology. MEMS fabrication technology has leveraged a huge fraction of the IC fabrication technology, but virtually none of the CAD support that goes with it. As a result, we can all envision MEMS which could be fabricated if they were designed, but which can not be designed due to the lack of support tools.

Rectifying this disparity in the design and fabrication technology is the subject of active research in the MEMS CAD community. To date, MEMS design tools have focussed mostly on process modeling **[1, 2]** and Finite Element and Boundary Element Analysis (FEA and BEA) for electromechanical functional modeling **[3, 4]**. This work has led to several products currently on the market **[5, 6, 7]**. These tools generally take as input a process flow and mask geometry from which they generate a solid model. The solid model is then meshed and simulated.

All of these approaches are geared toward process and device development, and they are generally analysis oriented rather than design oriented. While these activities will continue to be critical to the success of MEMS, there is a growing community of designers who need support at a higher level than device simulation. These users are designing systems with dozens or even thousands of components, far beyond the reach of FEA/BEA based tools.

In an attempt to leverage some of the CAD technology developed for the IC industry, several groups are now working toward a VLSI inspired approach to MEMS design, with an emphasis on hierarchical design, system simulation, and layout synthesis **[8, 9]**. Initial success in this area includes the synthesis of 1D resonators **[10]**, optimization-based synthesis of 2D resonators **[11]**, nodal analysis of multiple degree of freedom structures in Saber **[12]** and inertial sensors **[13]**. Some of this work has also become commercially available **[14]**.

The success of this approach is critically dependent on the ability to quickly and accurately simulate large numbers of interconnected MEMS devices. In the IC environment, this is done by abstracting the physical world in terms of N-terminal devices. Each device is modeled by ordinary differential equations (ODEs) with coefficients parameterized by device geometry, and material properties derived from measurements or process specifications. Devices are linked together at their terminals, or nodes, and the resulting coupled differential equations can be solved as a system of nonlinear ODEs using nodal analysis **[15]**.

A similar approach can also be used to abstract the behavior of MEMS devices so that MEMS can also be quickly and accurately simulated. This is a critical capability in the increasingly important framework of hierarchical design, simulation, and synthesis for MEMS.

OVERVIEW

SUGAR is a collection of Matlab **[24]** routines which implements a nodal analysis approach to MEMS simulation. A wide variety of planar electromechanical systems can be simulated. The user provides a text file describing the geometry and connectivity of the system, and then calls one or more analysis routines to determine static displacement, transient response, etc. Graphical results are displayed using Matlab function calls, and numerical results are available for additional Matlab processing if desired.

INPUT

The user provides a text file that describes the building blocks in terms of geometry, voltage, or applied force. The format for a typical input line is block type, node list, geometry list, and parameter list. Currently, block types for planar beams (b), anchors (a), electrostatic gaps (g), and force generators (f) have been defined. An example of a netlist is shown in Figure 1.

```
%Substrate anchor
a  1  2  5e-6   180   10e-6
%Horizontal beam: 34x2 microns
b  1  3  34e-6  0     2e-6
%Vertical beam: 70x2 microns
b  3  4  70e-6  -90   2e-6
%Electrostatic actuator, and the rest...
g  4  5  6  7  50e-6  0  4e-6  4e-6  10e-6  445
b  7  8  70e-6  0     2e-6
a  8  9  5e-6   0     10e-6
```

***Figure 1**. Input netlist. For example the fourth line describes a beam that extends from node 1 to 3 for a length of 34μm, at an angle of 0 degrees from the horizontal, and the beam's width is 2 μm.*

The layer thickness and Young's modulus are defined in a separate process file. Using the information provided by the netlist and process file, SUGAR creates individual stiffness $[k]_s$, mass $[m]_s$, and damping $[c]_s$ matrices for each structural block s. Since each structure in the netlist may have differing orientations, all local coordinates are transformed into global coordinates. The assemblage of the set of individual matrices into collective system matrices, [K], [M], and [C], where all structures are coupled at common nodes, is accomplished by superposition. Element indices in the system matrix directly correspond to nodal coordinate components. Structures with common nodes have additive contributions to that particular matrix element. Therefore the size of the entire system matrices only depend on the number of distinct nodes. The equation of motion describing the dynamics of the entire system can be expressed in a familiar form **[16]**

$$[M]\{\ddot{q}\} + [C]\{\dot{q}\} + [K]\{q\} = \{F\} \qquad (1)$$

where the nodal displacement $\{q\}=\{x_1\ y_1\ \theta_1 \ldots x_N\ y_N\ \theta_N\}$ is a $1x3N$ column vector and N is the number of nodes.

0-9640024-2-6/hh1998/$20©1998TRF
DOI 10.31438/trf.hh1998.42

ANALYSIS ROUTINES

The analysis of planar MEMS devices in SUGAR is accomplished by a collection of Matlab functions. This includes DC analysis, steady-state analysis, and transient analysis solvers.

Invoking the command *dq = cho_dc(netlist)*, where *netlist* is a string containing the name of the file, will solve for an equilibrium state for the system (not necessarily unique) and assign nodal displacements $\{\Delta x_n \ \Delta y_n \ \Delta\theta_n\}$ to $\{dq\}$ for each node n. The *cho_dc_display(netlist, dq)* function displays the resulting structure (Figure 2).

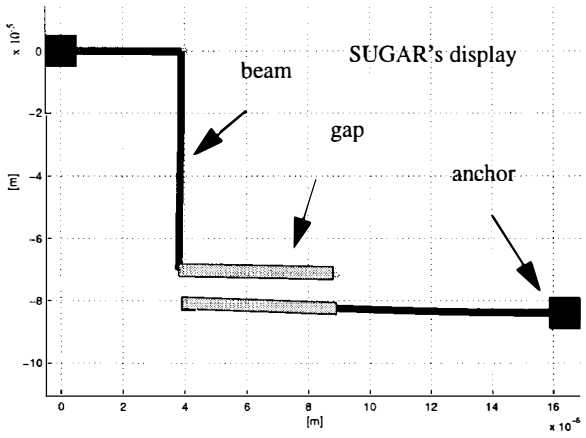

Figure 2. *Output display of a DC solution from the netlist in Figure 1. It shows bending due to a voltage applied across the electrostatic actuator (gap).*

Resonant mode calculation and display is accomplished using the *cho_mode(netlist,mode,scale)* function, where *mode* is the mode number and *scale* magnifies the amplitudes of the mode shapes in the display.

Xw = cho_ss_calc(netlist,W) computes the steady state response for an applied sinusoidal set of forces defined in *netlist.*

Animation of the steady state response is accomplished by the *cho_ss_animation(netlistfile,ω)* function, where ω is the angular frequency vector.

The *cho_bodeplot(ω,magnitude,phase)* function calculates and displays a Bode plot.

Transient analysis is provided by *cho_ta(time interval, initial conditions, netlist, parameter list)* function, which simulates the system dynamics for a system for a given initial condition and time varying force.

MODELS

The performance of many planar MEMS devices can be modeled with beams and electrostatic gaps. Linear and nonlinear beam models are implemented for small to large deflections, and the nonlinear behavior in the gap model is essential for accurate simulation of electrostatic actuation. As with SPICE, there are different model levels in SUGAR which allow the user to trade off accuracy and speed.

LINEAR BEAM MODEL

Any two coupled beams in SUGAR have common deflection and slope at shared nodal points. This condition satisfies the continuity of both the deflection and slope. The transverse deflection $v(x)$, axial displacement $u(x)$, and the angle of rotation $\theta(x)=(dv/dx)$ can be described by 3 degrees of freedom at each node (Figure 3).

In the region between nodes, the equation of equilibrium for a beam is

$$\frac{\partial^4}{\partial x^4} v(x) = 0 \qquad (2)$$

[17]. Solving this equation for $v(x)$ and imposing the boundary conditions at both end nodes yield 4 equations and 4 unknowns. By solving for the coefficients of $v(x)$ and $\theta(x)$ in terms of v_n and θ_n and grouping like-terms results in

$$v(x) = H_1(x)v_1 + H_2(x)\theta_1 + H_3(x)v_2 + H_4(x)\theta_2 \qquad (3)$$

where the cubic functions $H_i(x)$ are the Hermitian shape functions.

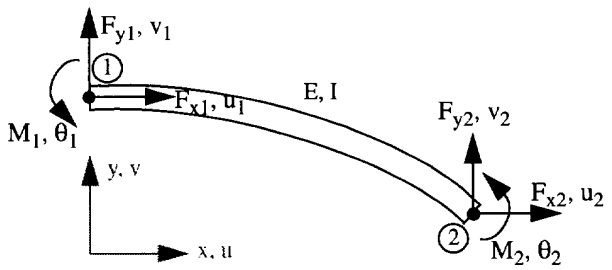

Figure 3. *A bent beam showing nodal forces, moments, and coordinates.*

The stiffness for this beam can be obtained by using Castigliano's theorem

$$F_i = \frac{\partial S}{\partial q_i} \qquad (4)$$

where F_i is the force or moment, and q_i is the displacement coordinate for degree of freedom $i = 1, 2, 3$ for $q = x, y, \theta$ respectively.

For the linear case, the strain energy S for a beam with uniform cross section is

$$S = \frac{EI}{2}\int_0^L \left(\frac{\partial^2}{\partial x^2} v(x)\right)^2 dx + \frac{EA}{2}\int_0^L \left(\frac{\partial}{\partial x} u(x)\right)^2 dx \qquad (5)$$

The substitution of Eq. (5) into Eq.(4) yields the stiffness

$$k_{ij} = EI\int_0^L H''_i(x)H''_j(x)dx + EA\int_0^L H'_i(x)H'_j(x)dx \qquad (6)$$

which gives

$$[k]_s = \frac{E}{L^3}\begin{bmatrix} AL^2 & 0 & 0 & -AL^2 & 0 & 0 \\ 0 & 12I & 12EI & 0 & -12I & 6IL \\ 0 & 6IL & 6EIL & 0 & -6IL & 2IL \\ -EAL^2 & 0 & 0 & AL^2 & 0 & 0 \\ 0 & -12I & -12EI & 0 & 12I & -6IL \\ 0 & 6IL & 6EIL & 0 & -6IL & 4IL \end{bmatrix} \qquad (7)$$

A mass matrix is found by equating internal and external work due to virtual displacements **[16]**. This results in

$$m_{ij} = \int_0^L \rho(x)A(x)H_i(x)H_j(x)dx \qquad (8)$$

where ρ(x) and A(x) are the density and cross sectional area at position x along the beam. If ρA is constant we have

$$[m]_s = \frac{\rho AL}{420}\begin{bmatrix} 140 & 0 & 0 & 70 & 0 & 0 \\ 0 & 156 & 22L & 0 & 54 & -13L \\ 0 & 22L & 4L^2 & 0 & 13L & -3L^2 \\ 70 & 0 & 0 & 140 & 0 & 0 \\ 0 & 54 & 13L & 0 & 156 & -22L \\ 0 & -13L & -3L^2 & 0 & -22L & 4L^2 \end{bmatrix} \quad (9)$$

where ρ is the density and A is the cross sectional area of the beam.

Using a simple Couette flow model we approximate the damping matrix (similar to Eq. (8)) as

$$[c]_s = \frac{\mu Lw}{420\Delta}\begin{bmatrix} 140 & 0 & 0 & 70 & 0 & 0 \\ 0 & 156 & 22L & 0 & 54 & -13L \\ 0 & 22L & 4L^2 & 0 & 13L & -3L^2 \\ 70 & 0 & 0 & 140 & 0 & 0 \\ 0 & 54 & 13L & 0 & 156 & -22L \\ 0 & -13L & -3L^2 & 0 & -22L & 4L^2 \end{bmatrix} \quad (10)$$

where μ is the viscosity of the fluid environment, and Δ is the distance from the device to the substrate. Both μ and Δ are defined in the process file.

NONLINEAR GAP MODEL

For a parallel electrostatic gap where the length of the beams L is much greater than the gap spacing d, and the layer thickness $h \sim d$, the total force on each beam is

$$F = \frac{-1}{2}\frac{\varepsilon_0 V^2 Lh\alpha(d/h)}{d^2} \quad (11)$$

where the factor $\alpha > 1$ is the fringing field contribution **[19]**.

As described previously, transverse displacements along the length of the beam can be described by nodal coordinates and Hermitian shape functions. Referring to Figure 4,

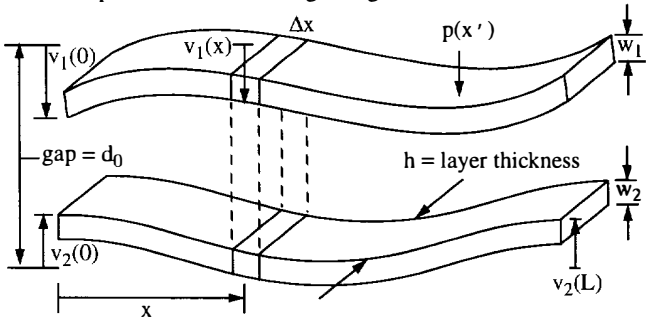

Figure 4*. The level-2 model of an electrostatic actuator. There is a distributed electrostatic force p(x) along the length of the beam which varies due to bending.*

the distance between the beams at position x is

$$d(x) = d_0 + v_1(x) - v_2(x) \quad (12)$$

where d_0 is the original gap spacing, and $v_1(x)$ and $v_2(x)$ are the transverse displacements Eq. (3) of the beams at position x. The nodal forces due to a distributed force per unit length are

$$F_i = \int_0^L p(x)H_i(x)dx \; . \quad (13)$$

For the electrostatic case, the force per unit length is approximated to be

$$p(x) = \frac{-1}{2}\frac{\varepsilon_0 V^2 h\alpha(d(x)/h)}{d(x)^2} \; . \quad (14)$$

In solving the integral in Eq. (13) for a general analytical expression the equivalent nodal forces and moments on each beam is obtained. This analytical expression is parameterized by voltage and nodal coordinates only, as required to fit the nodal analysis scheme of SUGAR. These nodal forces are added to the system force vector in Eq. (1) for further analysis. The level-1 gap model is similar to level-2 except the bending and fringing field contributions are not considered.

GAP MODEL WITH CONTACT FORCES

With the linear beam model and nonlinear electrostatic gap model, SUGAR can find the equilibrium position of the structure before and after pull-in. To simulate the contact behavior between the beams of an electrostatic gap, repulsive nodal forces are added to the interacting beams. The gap spacing and contact penetration depth of the beams are determined by Eq. (12). The equal and opposite contact forces prevent the absolute gap distance from approaching zero so that the electrostatic force model will not approach infinity.

A model for contact forces is chosen such that $|F_c| >> |F_e|$ when $d < d_c$ and $|F_c| << |F_e|$ when $d > d_c$, where F_c, F_e, and d_c are the contact force, electrostatic force, and critical gap distance respectively. Since the electrostatic forces are attractive and proportional to d^{-2}, we chose the contact force to be repulsive and proportional to d^{-3}. To avoid convergence problems, we made modifications for this function when d is very close to zero and less than zero.

An electrostatic gap (level-1) pull-in simulation is shown in Figure 5. The test structure is shown in Figure 5a. The pull-in voltage V as a function of beam length L is shown in Figure 5b. A good fit to the experimental data was obtained with a Young's modulus of 140 GPa.

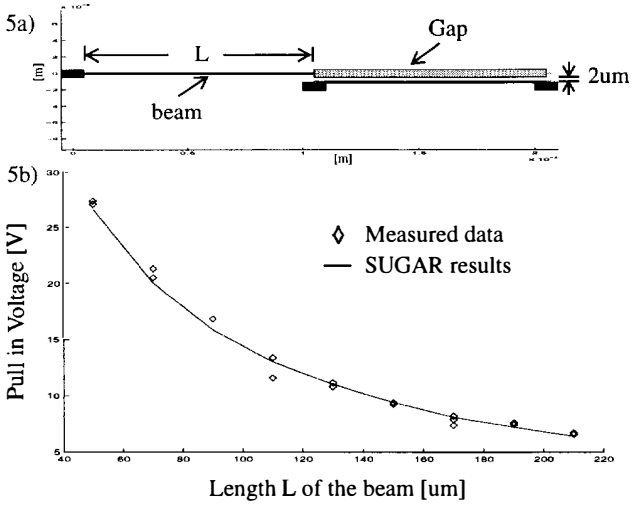

Figure 5: A comparison of simulated pull-in voltages with experimental data.

NONLINEAR BEAM MODEL

In the linear beam model, $\{q_i\}$ is proportional to $\{F_i\}$. This model is satisfactory for small deflections; however, there are nonlinear effects when deflections are large. For example, there may be changes in the projected length due to bending and changes in stiffness due to axial forces.

A level-2 (nonlinear) beam model was developed for the small rotation condition. Only the geometric nonlinearity is considered. This model starts from a linear interpolation for the longitudinal displacement and a cubic interpolation for the lateral displacement

$$u = u_1 + \frac{(u_2 - u_1)x}{L} \quad \textbf{(15)}$$

$$v = v_1 + \theta_1 x + \frac{(-2\theta_1 - \theta_2 + 3\theta_0)x^2}{L} + \frac{(\theta_1 + \theta_2 - 2\theta_0)x^3}{L^2} \quad \textbf{(16)}$$

where $\{u_1\ v_1\ q_1\}$ and $\{u_2\ v_2\ q_2\}$ are the nodal displacement vectors (Figure 3), and $\theta_0=(v_2-v_1)/L$.

The strain at every point on the beam can be calculated from the displacements **[25]**

$$\tilde{\varepsilon}(x,\eta) = \frac{du}{dx} + \frac{1}{L}\cdot\int_0^L\left(\frac{1}{2}\cdot\left(\frac{dv}{dx}\right)^2\right)dx + \eta\cdot\frac{d^2v}{dx^2} \quad \textbf{(17)}$$

where η is the distance from the neutral axis. The middle term in above equation is the average of $(dv/dx)^2/2$ along the beam.

Substituting Eq. (17) into the following gives the strain energy

$$S = \int_V \frac{1}{2}E\tilde{\varepsilon}^2 dV\,. \quad \textbf{(18)}$$

Then substituting Eq. (18) into Eq. (4) yields the nodal forces as a function of displacements. This model takes into account the contribution of the longitudinal displacement to the strain. Figure 6a shows a simulation of a clamped-clamped beam with a central concentrated load. Simulation of the load-deflection response (Figure 6b) is in close agreement with Abaqus **[18]** over a typical range of operation.

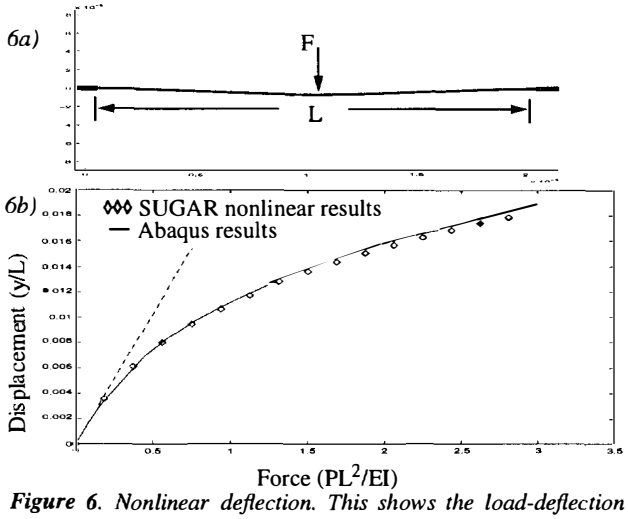

Figure 6. *Nonlinear deflection. This shows the load-deflection curve for the clamped-clamped beam with a concentrated load.*

ALGORITHMS AND RESULTS

This section describes the algorithms implemented in SUGAR. The DC algorithm deals with finding an the equilibrium state of a MEMS device when constant mechanical forces or voltages are applied. The steady state algorithm takes care of the response of a system subjected to damping and sinusoidal excitation forces. Finally the transient analysis algorithm uncovers the instantaneous state of a system as a function of time.

DC ALGORITHM

In DC analysis, the equilibrium position due to constant mechanical forces and voltages are calculated according to

$$[K]\{q\} - \{F\} = 0\,. \quad \textbf{(19)}$$

Since the electrostatic force and possibly the stiffness are nonlinear functions of displacement, numerical methods are needed to solve Eq. (19).

In general, there is no recognized "best" way for solving nonlinear equations. However, some methods are effective in finding the roots provided we know the approximate locations of those roots. SUGAR uses the Newton-Raphson Method.

Eq. (19) is a special case of the general form

$$f(\{q\}) = 0 \quad \textbf{(20)}$$

First, an initial guess $\{q_0\}$ is taken which is sufficiently near a root. In general, the Newton-Raphson method approaches the solution by the iteration

$$\{q_{n+1}\} = \{q_n\} - [f'(\{q_n\})]^{-1}\{f(\{q_n\})\} \quad \textbf{(21)}$$

where $[f'(\{q_n\})]$ is the system Jacobian matrix. The iteration will proceed until

$$\|\{q_{n+1}\} - \{q_n\}\| < \zeta \quad \textbf{(22)}$$

where ζ is the tolerance.

DC simulation of common flexural supports indicates that SUGAR can accurately model these structures. SUGAR analysis of a folded flexure suspension (Figure 7) agrees exactly with the Abaqus finite element simulations done by Judy **[20]**. Similarly, SUGAR analysis of serpentine suspensions (Figure 8) is identical to FEA simulations done by Fedder **[21]**. SUGAR also agrees with Fedder's analytical and measured data. Simulation of crab leg suspensions from **[21]** is equally accurate.

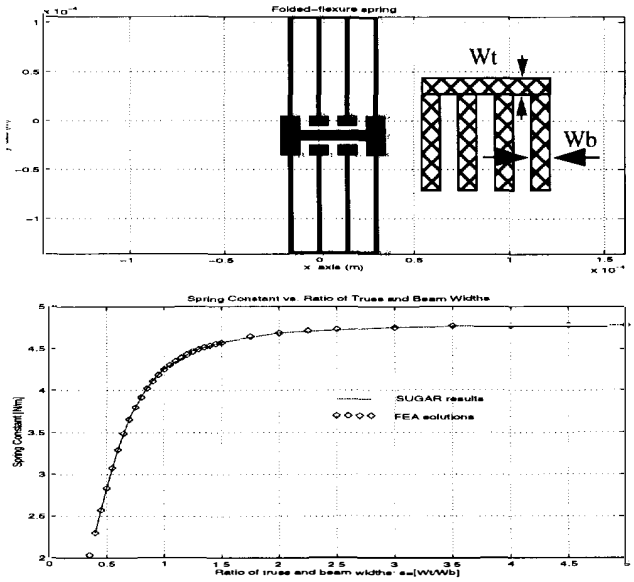

Figure 7*: Comparison of SUGAR results and FEA solution for the lateral spring constant of a folded-flexure (from Judy **[20]**) versus the ratio of the truss width Wt and beam width Wb.*

STEADY STATE ALGORITHM

In steady state analysis the following equation is solved

$$[M]\{\ddot{q}\} + [C]\{\dot{q}\} + [K]\{q\} = \{a_i\cos(\omega t + \beta_i)\} \quad \textbf{(23)}$$

where $\{a_i\cos(\omega t + \beta_i)\}$ is the sinusoidal external excitation.

The solution to this equation is the real part of the following complex equation:

$$[M]\cdot\{\ddot{z}\}+[C]\cdot\{\dot{z}\}+[K]\cdot\{z\}=\{B_i\}\cdot e^{j\omega t} \quad (24)$$

where $\{B_i\}=\{a_i(\cos\beta_i+j\sin\beta_i)\}$. A particular solution of equation (24) is of the following form

$$\{z\}=\{V\}\cdot e^{j\omega t} \quad (25)$$

where $\{V\}$, a complex vector, contains the magnitude and phase information of the system response. Substituting Eq. (25) into Eq. (24) gives

$$(-\omega^2[M]+j\omega[C]+[K])\cdot\{V\}=\{B\}. \quad (26)$$

Once Eq. (26) is solved, the magnitude and phase response for each node is evaluated. The steady state vibration of the structure can be animated.

SUGAR simulations of the multi-mode resonators reported by Brennan et al. **[22]** show the mode shapes and Bode plot of the semaphore mass displacement (Figure 9 and 10). These simulations use a simple Couette flow model for damping under all moving structures. Simulations of the first three modes agree with Brennen's experimental frequency data to within 5%.

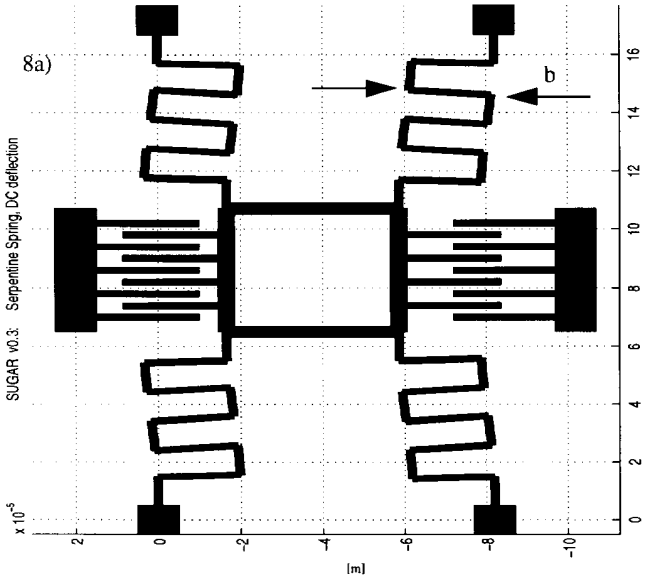

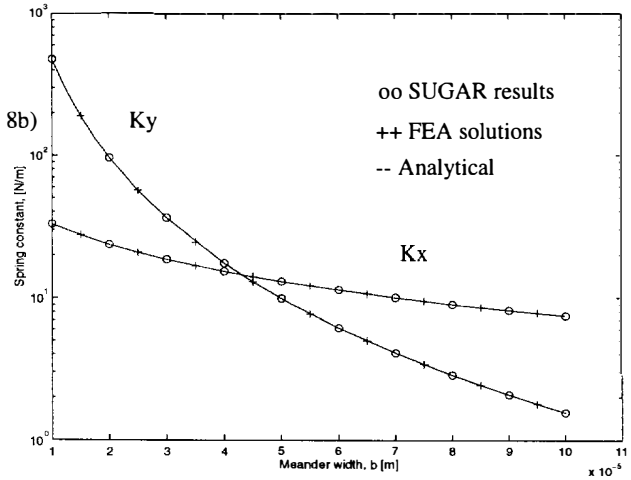

***Figure 8**: Horizontal and vertical spring constants for a serpentine spring structure (Fedder **[21]**). The graph shows stiffness in the x and y directions as a function of meander length b.*

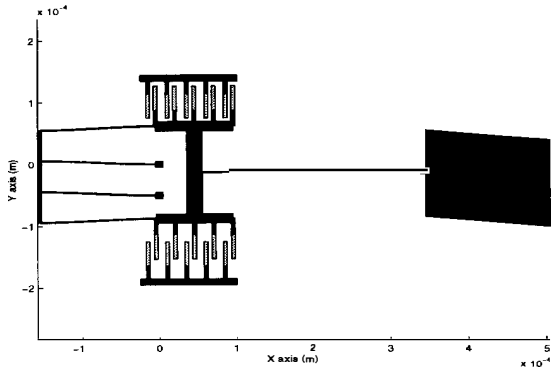

***Figure 9:** Simulations of the linear-drive multi-mode resonator structure of Brennen **[22]** shows the second resonant mode shape at 19.177 kHz.*

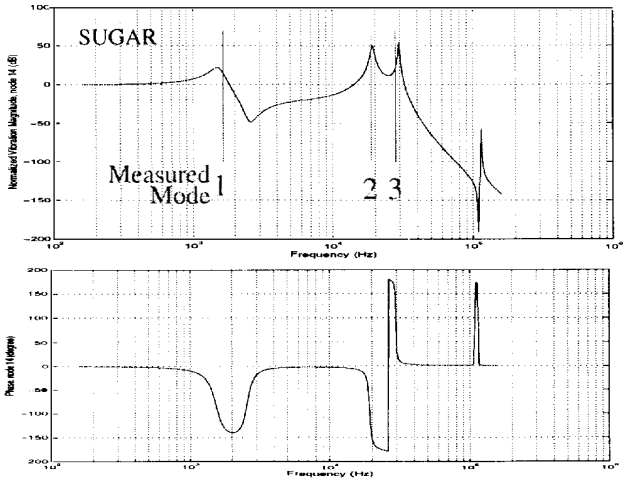

***Figure 10:** Simulations of the linear-drive multi-mode resonator showing the Bode magnitude and phase plot of the displacement at the base of the semaphore mass as a function of driving frequency. Experimental data from **[22]** match the predicted three modes to within 5%.*

TRANSIENT ANALYSIS

For transient behavior, we simulate nodal displacements of the system as functions of time by ordinary differential equation solvers such as (Runge-Kutta) ode45 **[24]** and central difference methods **[23, 16]** such as the summed form and Wilson-θ.

The dynamical equation of motion for a general system may be described by a form similar to Eq (1) where the matrices may be functions of position, velocity, and time.

The central difference method offers the least complexity. The crux of the main loop is similar to

$$\{\ddot{q}\}_t=[M]^{-1}(\{F(q,\dot{q},t)\}-[C]\{\dot{q}\}_t-[K(q)]\{q\}_t) \quad (27)$$

$$\{\dot{q}\}_{t+0.5\Delta t}=\{\dot{q}\}_{t-0.5\Delta t}+\Delta t\{\ddot{q}\}_t \quad (28)$$

$$\{q\}_{t+\Delta t}=\{q\}_t+\Delta t\{\dot{q}\}_{t+0.5\Delta t} \quad (29)$$

where $\Delta t < \Delta t_{crit}$ is the critical time step for stability **[23]**.

The instantaneous nodal positions for the entire system are calculated by integrating the displacements (solutions) of Eq. (1) from the given initial conditions at time t_i to a final time t_f where *{F}, [M], [C],* and *[K]* are continuously evaluated and updated

throughout the simulation. An example is shown in Figure 12.

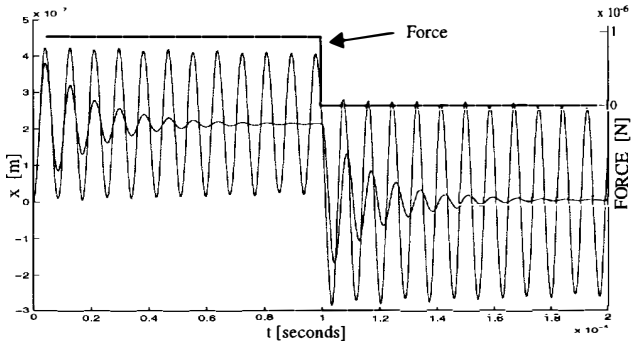

***Figure 12**: Transient simultions of the resonator from Figure 7. The top trace show the applied force (1 μN for 100 μs). The bottom trace shows the simulated response in air and water.*

CONCLUSION

A simulation program for the nodal analysis of many types planar MEMS devices has been demonstrated. SUGAR is simple to use, executes quickly, and gives results that are in agreement with traditional finite element simulation, analytical models, and experimental data. SUGAR is portable across all Unix, PC, and Macintosh platforms running Matlab (version 5 or greater). The free software is available on the web at http://www-bsac.eecs.berkeley.edu.

ACKNOWLEDGEMENTS

Thanks to A. Parameswaran for helpful review and thanks to E. Kruglick for electrostatic pull-in data.

This work is supported in part by the DARPA Composite CAD Program, the National Science Foundation, and a UC Berkeley GP4 Fellowship.

BIBLIOGRAPHY

1. G. M. Koppelman, "A Three-dimensional Structural Simulator for Microelectromechanical Design", *Sensors and Actuators, 20*, (1989), p179-185.

2. T. J. Hubbard, E. K. Antonsson, "Design of MEMS via Efficient Simulation of Fabrication", *Proc. of the 1996 ASME Design Engineering Conf.*, August 18-22, (1996), Irvine CA.

3. S. Crary, Y. Zhang, "Software Tools for Designers of Sensor and Actuator CAE Systems", *Solid-State Sensors and Actuators*, San Francisco, CA, June 23-27, (1991), pp. 498-501.

4. J. R. Gilbert, et. al., "Implementation of a MEMCAD System for Electrostatic and Mechanical Analysis of Complex Structures from Mask Descriptions", *IEEE Micro Electro Mechanical Systems Workshop,* (1993), Fort Lauderdale USA, p 207-212.

5. MEMCAD version 3., Microcosm, 201 Willesden Drive, Cary, NC 27513.

6. Y. He, R. Harris, G. Napadensky, and F. Maseeh, "IntelliCAD: A virtual prototype manufacturing software system for MEMS," *Proc. IEEE Micro Electro Mechanical Systems Workshop*, San Diego, CA, February (1996).

7. DRBEM, Coyote Systems, 2740 Van Ness Ave #210, San Francisco, CA 94109.

8. N. Lo, E. Berg, S. Quakkelaar, J. Simon, M. Tachiki, H. Lee, K. Pister, "Parameterized Layout Synthesis, Extraction, and SPICE Simulation for MEMS", *Intl. Symp. on Circuits and Systems*, Atlanta, GA, May (1996).

9. T. Mukherjee, and G. K. Fedder, "Structured Design of Microelectromechanical systems", *DAC '97*, Anaheim, CA, June 9-13, (1997).

10. E.C. Berg, N.R. Lo, J.N. Simon, H.J. Lee, K.S.J. Pister, "Synthesis and Simulation for MEMS Design", *ACM SIGDA Physical Design Workshop*, Reston, VA, April (1996), pp. 67-70.

11. S. Iyer, T. Mukherjee, and G. K. Fedder, "Automated Optimal Synthesis of Microresonators," *Solid-State Sensors and Actuators*, Chicago, IL, June 12-19, (1997).

12. J. Vandemeer, M. Kranz, G. Fedder, "Nodal Simulation of Suspended MEMS Multiple Degrees of Freedom", DSC-Vol.. 62 MEMS ASME (1997), pp 113-118.

13. J.E. Vandemeer, M. S. Kranz, and G. K. Fedder, "Hierarchical Representation and Simulation of Micromachined Inertial Sensors", *Modeling and Simulation of Microsystems*, Santa Clara, CA, April 6-8, (1998).

14. M. Maher and H. Lee, "MEMS Systems Design and Verification Tools", *SPIE 5th Annual Int. Symp. on Smart Structures and Materials*. March 1-5 (1998). San Diego, CA.

15. L. W. Nagel, "Computer analysis of nonlinear circuits excluding radiation", Ph. D. dissertation, UC Berkeley (1970).

16. M. Paz, "Structural Dynamics Theory and Computation", Litton Education Publishing, Inc (1980).

17. T. Y. Yang, "Finite Element Structural Analysis", Prentice-Hall, Inc (1985).

18. ABAQUS, Hibbitt, Karlsson & Sorensen, Inc. Pawtucket, IR, USA.

19. M. R. Boyd, S. B. Crary, M. D. Giles, "A Heuristic Approach to the Electromechanical Modeling of MEMS Beams", *Solid-State Sensor and Actuator Workshop*, Hilton Head, South Carolina, June 13-16, (1994), pp123-126.

20. M. Judy, "Micromechanisms Using Sidewall Beams", Ph.D. dissertation, UC Berkeley, (1994), p 62-67.

21. G. Fedder, "Simulations of Microelectromechanical Systems", Ph.D. dissertation, UC Berkeley, (1994), p 104-115.

22. R. Brennen, A. Pisano, Tang, "Multiple Mode Micromechanical Resonators", *Proc. IEEE Micro Electro Mechanical Systems Workshop* (1990).

23. R. R. Craig, Jr., Structural Dynamics: An Introduction to Computer Methods", John Wiley & Sons, Inc. New York (1981).

24. Matlab, *Matlab High-Performance Numeric Computation and Visualization Software Reference Guide*, The Math Works Inc., 24 Prime Park Way Natick, Mass, (1992).

25. R. Wen, J. Rahimzadeh, "Nonlinear Elastic Frame Analysis by Finite Element", *Journal of Structural Engineering*, Vol 109, No. 8, August (1983), pp 1952-1971.

AUTOMATIC GENERATION OF DYNAMIC MACRO-MODELS USING QUASI-STATIC SIMULATIONS IN COMBINATION WITH MODAL ANALYSIS

Lynn D. Gabbay and Stephen D. Senturia
Department of Electrical Engineering and Computer Science, Massachusetts Institute of Technology
Cambridge, MA 02139

ABSTRACT

Reduced-order macromodeling can be used to simplify the simulation problem in microelectromechanical systems. In this paper, we report the successful implementation of a methodology for automatically generating reduced-order macro-models for the conservative energy-domain behavior of electrostatically actuated MEMS devices from 3D simulations. These models are directly usable in circuit- and system-level simulators for complete MEMS system design. This method has been successfully applied to the electrostatic actuation of a suspended beam and an elastically supported plate with an eccentric electrode and unequal springs (producing tilting when actuated).

Keywords: Macromodel, Modal analysis

INTRODUCTION

While several CAD systems have begun to enable quasi-static simulation for MEMS devices, it has proven difficult to implement dynamics simulation **[1-2]**. Microelectromechanical structures obey a complex set of equations of motion that must account for the tight coupling of the multiple energy domains of the system. The determination of dynamic behavior via full three-dimensional simulation is computationally expensive. Furthermore, numerical dynamic simulation on fully meshed structures is too cumbersome to serve as the device model that can be part of a larger system of the designer's choosing, such as a black-box element controlled by a feedback circuit.

In this paper, we present a means by which a three-dimensional model of a two conductor electromechanical device without dissipation can be converted into a reduced-order macromodel that can readily be inserted as a black-box circuit element into an analog circuit simulator. This process is based upon the energy method approach **[3]**, in that we shall construct analytical models for each of the conservative energy domains of the system and determine all forces as gradients of the energy. The energy method approach has the advantage of making this process modular, enabling us to incorporate other energy domains into our models in the future. Another benefit of energy methods is that the models we shall construct are guaranteed to be energy conserving, because the stored energies in each domain shall each be constructed as an analytical function, and all forces shall be computed directly from analytically computed gradients. This process also has the advantage of being able to be performed almost entirely automatically, requiring the designer only to construct the model, run a few full three-dimensional numerical computations, and set a few preferences a priori. Above all, this process has the ultimate benefit of constructing models that are computationally efficient, allowing their use in a dynamical system-level simulator.

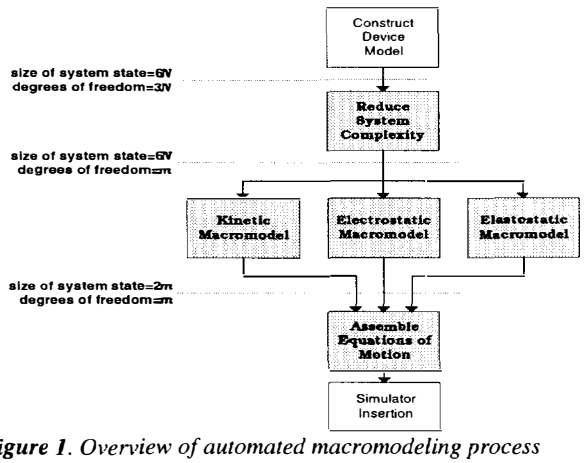

***Figure 1**. Overview of automated macromodeling process*

THEORY

A high level description of our approach is depicted in Figure 1. Our first task is to reduce the degrees of freedom of the system. Rather than allow each node in a finite element model to be free to move in any direction, we constrain the motion of the system to a linear superposition of a select set of deformation shapes. This set will act as our basis set of motion. The positional state of the system will hence be reduced to a set of generalized coordinates, each coordinate being the scaling factor by which its corresponding basis shape will contribute. Next, we must construct analytical macromodels of each of the energy domains of the system. In the case of conservative capacitive electromechanical systems, these consist of the electrostatic, elastostatic, and kinetic energy domains. These macromodels will be analytical functions of the generalized coordinates. We can then use Lagrangian mechanics in order to construct the equations of motion of the system in terms of its generalized coordinates. Finally, we can translate these equations of motion into an analog hardware description language, thereby constructing a black-box model of the electromechanical system that can be inserted into an analog circuit simulator.

MODEL COMPLEXITY REDUCTION

The MEMS device is first constructed as a finite element model with N free nodes. Neglecting node rotations, this system has $3N$ degrees of freedom. The dynamical state of the system requires $6N$ terms, where $3N$ terms record the node positions, and an additional $3N$ terms record the node velocities. For $6N$ state terms, $6N$ first order differential equations are needed to represent the equations of motion of the system. If N is large, it is computationally expensive to integrate the equations in time.

To solve this problem, we restrict the motion of the system. Let us define ψ to be a $3N$ element vector representing the positional state of the system. We constrain the degrees of freedom of the system by declaring that ψ is a linear superposition of m linearly independent basis shapes φ_i offset from an equilibrium state ψ_{eqm}. Note that this equilibrium state is the shape of the structure *after* any initial stress relaxation take place; naturally, if there are no initial stresses or the structure is constrained so as to prevent stress relaxation, the basic shape is already at its

0-9640024-2-6/hh1998/$20©1998TRF
DOI 10.31438/trf.hh1998.43

equilibrium position. Thus, we rewrite our representation of the state of the system as

$$\psi = \psi_{eqm} + \sum_{i=1}^{m} q_i \varphi_i$$

where q_i are the coefficients of the basis shapes of the linear superposition. Henceforth, we refer to the q_i as the generalized coordinates of the system. In effect, this constrains the description of the system from $3N$ to m spatial degrees of freedom. Correspondingly, this reduces the number of terms needed to represent the dynamical state of the system, and thus the number of first order differential equations in the equations of motion, to $2m$. When $m << N$, this constitutes a significant computational advantage over the full $6N$ representation.

When choosing the basis shapes, the designer is faced with two questions. The first is how to find candidate basis shapes. Because any complete basis set of a $3N$ element vector can have $3N$ linearly independent basis shapes, the second question is which shapes from the complete set should be used. There are numerous sources to construct the shapes among which we will choose. Ananthasuresh **[4]** demonstrated the use of mechanical harmonic mode shapes for use with MEMS device complexity reduction. Hung **[5]** presented a technique for using actual system motion to construct a set of representative basis shapes. Any or all of these methods are valid.

For this research, we use mechanical harmonic mode shapes for our basis shapes. Numerical modal analysis yields the eigenvalues φ_i of the mechanical system, being the N element vectors that describe the shapes of the modes of vibration, as well as the associated generalized frequencies ω_i and masses m_i. There are several advantages to choosing mode shapes for the basis set. For one, Ananthasuresh demonstrated that only a few mechanical mode shapes are necessary to accurately capture the motion of simple MEMS devices. Also, the mode shapes constitute a linearly independent set of basis shapes; thus it is not necessary to perform a back orthogonalization to confirm the independence of each additional mode shape. Furthermore, the modal formulation readily provides a representation for the kinetic energy of the system $T(\dot{q})$, given by

$$T(\dot{q}) = \sum_i \frac{1}{2} m_i \dot{q}_i^2 \qquad (1)$$

and a linear representation for the elastostatic strain energy of the system $U_{\text{linear strain}}(q)$, given by

$$U_{\text{linear strain}}(q) = \sum_i \frac{1}{2} m_i \omega_i^2 q_i^2 \qquad (2)$$

Once a set of M basis shapes is chosen, we must choose the minimum number m of those shapes necessary to characterize typical motion behavior of the structure. Our approach begins with a single coupled-energy-domain three-dimensional quasistatic simulation for the system under a typical example of actuation. Let us define ψ_{ex} to be the positional state calculated by a single quasistatic simulation. It is possible to determine the coefficients c_i such that

$$\psi_{ex} = \psi_{eqm} + \sum_{i=1}^{M} c_i \varphi_i$$

If we assume that ψ_{ex} is an example of typical motion, then by sorting the shapes in decreasing order of contribution toward our example motion, we construct a prioritized list of which basis shapes will have the greatest significance on general overall motion. The designer can now decide which and how many shapes to use in the reduced model of the system. Furthermore, the magnitudes of the coefficients c_i can be used to understand the relative expected magnitudes of the generalized coordinates during dynamics simulation. By providing c_i, we enable the designers to make an educated selection for the system operating range.

MACROMODEL CONSTRUCTION

The next step is to construct macromodels that replace the full 3D simulation for each of the system's energy domains. As mentioned above, the use of mode shapes automatically creates macromodels for the kinetic energy and linearized elastostatic energy domains. Here, we shall present how we construct macromodels for any function that would normally require full 3D simulation and then apply this technique to create macromodels for the electrostatic energy domain.

The requirements for a macromodel are that it must be an analytical function of the generalized coordinates and compare accurately to full three-dimensional simulation. The process by which we create such a macromodel is depicted in Figure 2. Full 3D simulation in the energy domain of interest is run several times for values of the generalized coordinates that adequately span the predetermined operating range for the system. Then, we select a generalized functional form, on which we then use the Levenberg-Marquardt non-linear function fitting scheme **[6]** in order to determine the parameters that fit this generalized form to the appropriate stored energy function. This algorithm remains the same, regardless of the nature of the 3D simulation.

In order to construct the electrostatic macromodel, recall that electrostatic forces are produced by the charges that accumulate on the conductor surfaces of the MEMS device under an applied voltage. The force $\mathbf{F}_e$ that stores energy into the electrostatic domain of the system is given by the gradient of the electrostatic energy U_e:

$$\mathbf{F}_e = \nabla U_e \qquad (3)$$

The electrostatic energy U_e and co-energy U_e^* are given by

$$U_e = \frac{1}{2}\frac{Q^2}{C} \quad U_e^* = \frac{1}{2} C V^2$$

where Q is the charge on the conductors, C is the capacitance between the conductors, and V is the applied voltage. It is generally advantageous for us to consider the co-energy, as we prefer to work in terms of voltage rather than charge. In this case, the gradient of the electrostatic co-energy U_e^* is the force that draws energy out of the electrostatic domain. Thus, the force $\mathbf{F}_e$

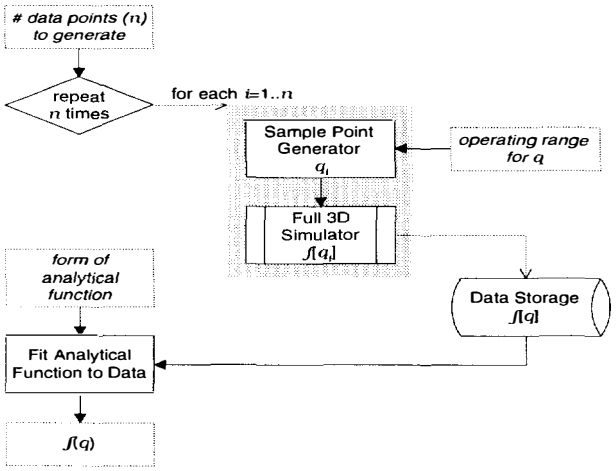

Figure 2. *Macromodeling algorithm for full 3D simulation domain*

that puts energy into the electrostatic domain is given by

$$\mathbf{F}_e = -\nabla U_e^* \quad (4)$$

When comparing Equations 3 and 4, we note the sign change. Because we choose to determine our electrostatic forces from the electrostatic co-energy rather than energy, a sign change must be taken into account.

Let us return to determining the electrostatic forces. Because the applied voltage is independent of motion, the gradient need only be applied to the capacitance, thus:

$$\mathbf{F}_e = -\left(\frac{1}{2}V^2\right)\nabla C \quad (5)$$

In order to construct a macromodel of the electrostatic domain, we must construct an analytical model of the *capacitance* of the system. We shall use an arbitrary multivariate form to represent the capacitance, but it should be designed such that it can capture the non-linearities that can be expected from a capacitance function. Recall that the capacitance of a large parallel-plate capacitor neglecting fringe field effects is given by $\varepsilon_0 A/d$, where A is the area of the plate, and d is the distance between the plates. Our generalized coordinates would most correspond to the gap d. Thus, it makes sense that our analytical form should have denominator terms. In this research, we use the form of a rational fraction of multivariate Taylor polynomials to represent the capacitance function. This form is given by:

$$\frac{\sum_{i_1=0}^{R_1}\sum_{i_2=0}^{R_2}\cdots\sum_{i_m=0}^{R_m} a_{i_1 i_2 \cdots i_m} q_1^{i_1} q_2^{i_2}\cdots q_m^{i_m}}{\sum_{i_1=0}^{S_1}\sum_{i_2=0}^{S_2}\cdots\sum_{i_m=0}^{S_m} b_{i_1 i_2 \cdots i_m} q_1^{i_1} q_2^{i_2}\cdots q_m^{i_m}}$$

Henceforth, we shall refer to this as a $[R_1 \;\; R_2 \;\; \cdots \;\; R_m / S_1 \;\; S_2 \;\; \cdots \;\; S_m]$ model.

ASSEMBLING THE EQUATIONS OF MOTION

Given representations for the kinetic and potential energy domains of a system, we can use Lagrangian mechanics to construct the equations of motion **[7]**. Recall that the Lagrangian $L(q,\dot{q},t)$ is a function of the general coordinates q, their first time derivatives $\dot{q}$, and time t. $L(q,\dot{q},t)$ is defined by

$$L(q,\dot{q},t) = T(q,\dot{q},t) - U(q,\dot{q},t)$$

where $T(q,\dot{q},t)$ is the kinetic energy and $U(q,\dot{q},t)$ is the potential energy of the system. The equations of motion come directly from Lagrange's equations, given by

$$\frac{d}{dt}\left(\frac{\partial L}{\partial \dot{q}_i}\right) - \frac{\partial L}{\partial q_i} = 0$$

representing a set of m equations, one for each generalized coordinate q_i. By incorporating the macromodels for the kinetic, elastostatic, and electrostatic energy domains, given by Equations 1, 2, and 5 respectively, and correctly accounting for the use of electrostatic co-energy instead of energy, our equations of motion become:

$$m_i \ddot{q}_i = +\frac{1}{2}V(t)^2 \frac{\partial C(q)}{\partial q_i} - m_i \omega_i^2 q_i \quad (6)$$

Because our representation of the capacitance is an analytical function, we can compute the gradients of these functions analytically rather than numerically. This averts the possibility of numerical error creating hidden energy sources or sinks, thereby creating or destroying energy arbitrarily within our equations of motion.

Finally, the resulting equations of motion are written to an analog hardware description language input file for the SABER simulation suite **[8]**. Note that all data extraction, macromodel generation, equation of motion assembly, and input file exportation are done automatically by computer. The initial investment of time to generate the circuit simulator input file need only be made once. The input file may then be used repeatedly for any number of dynamics simulations.

RESULTS

Here, we present the results of this process for the case of a simple fixed-fixed beam suspended above a fixed electrode strip. Both the beam and the electrode are assumed to be unstressed polysilicon conductors with a Young's modulus of 165 GPa and a Poisson ratio of 0.23, have dimensions of 100x20x0.5μm, and are separated by a 2μm gap. Modal analysis is then performed to determine the first three modes. For our single quasistatic solution, we apply a voltage of 80 volts. By projecting the resulting actuated motion onto the mode shapes, we note that the first mode dominates the overall motion, with a contribution of -0.809704. Thus, our single generalized coordinate shall be the first mode shape, depicted in Figure 3.

Table 1 summarizes the reduction in model complexity from the fully meshed model to the macro-model. Full 3D simulation of the capacitance of the system is performed 20 times, and this data is then fit to a [4 / 4] rational polynomial as described above. The macromodels for each of the energy domains are then automatically exported to a SABER input file, and a black-box circuit element that represents this fixed-fixed beam structure is then simulated when driven by a variety of voltage profiles. Figure 4 depicts the response of our example device when actuated by a 100 volt saw wave with a rise time of 15μs, a hold time of 10μs, and a total period of 40μs. Figure 5 depicts the response of our example device when actuated by an 80 volt saw wave with a rise time of 5μs, a hold time of 10μs, a fall time of 10μs, and a total period of 40μs.

This process has been applied to more complex structures,

# nodes *N*	534
# modes *m*	1
# data points for *C[q]*	20
form of *C(q)*	[4 / 4]
# terms *C(q)*	9
chi-squared	3.59E-24
measure of %error	4.2E-04

***Table 1**. Summary of macromodel*

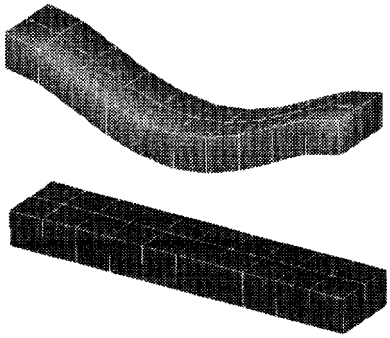

***Figure 3**. First mode shape for fixed-fixed beam example. Vertical scale expanded by factor of 20. This image connotes a negative value for the generalized coordinate, which is typical for this device under electrostatic actuation.*

such as a suspended plate supported by four beams of unequal thickness and actuated by an eccentric electrode. We have macromodeled this device using 5 mode shapes. A sample of simulation is given in Figure 6. We have also implemented this process to include non-linear strain-energy representations, but have discovered that large displacements result in excessively high strain energy calculations. This is because the system state determined from a superposition of node displacement vectors does not necessarily result in the minimum mechanical energy state of the system. This problem remains unsolved.

CONCLUSIONS

We have presented a method for macromodeling two conductor electromechanical devices without dissipation, and we have successfully applied this to the electrostatic actuation of a suspended beam and an elastically supported plate with an eccentric electrode and unequal springs. Furthermore, this technique is extendable to systems with other conservative energy domains.

An important benefit of this automated macromodeling approach is that it minimizes the number of iterative self-consistent coupled simulations that must be performed. A single such simulation is used to get estimates of the size of the modal workspace, but all simulations thereafter are single-energy-domain, hence fast. Further, the resulting dynamical nonlinear macromodel is *automatically* exported to a SABER network element.

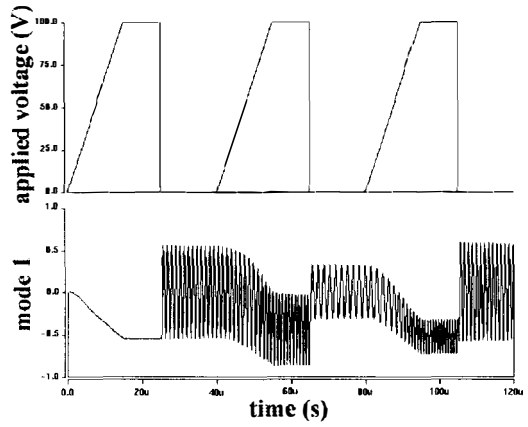

***Figure 4**. Response to a 100v saw wave with 15μs rise, 10μs hold, and 40μs period*

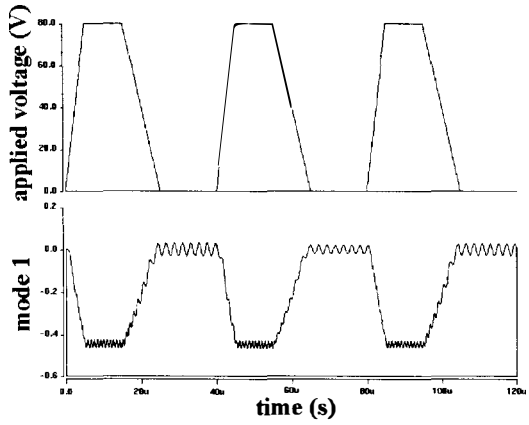

***Figure 5.** Response to an 80v saw wave with 5μs rise, 10μs hold, 10μs fall, and 40μs period*

ACKNOWLEDGMENTS

This project was sponsored by the DARPA ETO MEMS program under contract J-FBI-95-215. The authors wish to thank Microcosm Technologies **[9]** for extensive cooperation in interfacing MEMCAD 3.2 with the macromodeling tools developed here.

REFERENCES

1. S. D. Senturia, "CAD for Microelectromechanical Systems", *Proc. Transducers '95*, Stockholm, Sweden; 25-29 June 1995, vol. 2, pp. 5-8.

2. S. D. Senturia, N. Aluru, and J. White, "Simulating the Behavior of MEMS Devices: Computational Methods and Needs", IEEE Computational Science and Engineering, vol. 4, no. 1, 1997, pp. 30-43.

3. H. A. Haus and J. R. Melcher, *Electromagnetic Fields and Energy*, Prentice Hall, 1989.

4. G. K. Ananthasuresh, R. K. Gupta, and S. D. Senturia, "An Approach to Macromodeling of MEMS for Nonlinear Dynamic Simulation", in *Microelectromechanical Systems (MEMS)*, ASME Dynamic Systems & Control (DSC) ser. Vol. 59, part of *Proc. 1996 ASM Int'l Mechanical Engineering Congress and Exposition*, Am. Soc. Of Mechanical Engineers, New York, 1996.

5. E. S. Hung, Y.-J. Yang, and S. D. Senturia, "Low-Order Models For Fast Dynamical Simulation of MEMS Microstructures," *Transducers '97*, pp. 1101-1104.

6. W. H. Press, S. A. Teukolsky, et al., *Numerical Recipes in C: The Art of Scientific Computing*, 2nd edition, Cambridge University Press, 1995, pp. 681-688.

7. H. Goldstein, *Classical Mechanics*, 2nd edition, Addison-Wesley Publishing Company, 1981, pp. 16-21.

8. SABER, Analogy Inc., Beaverton, Oregon, http://www.analogy.com

9. Microcosm Technologies, Cambridge, Massachusetts, http://www.memcad.com

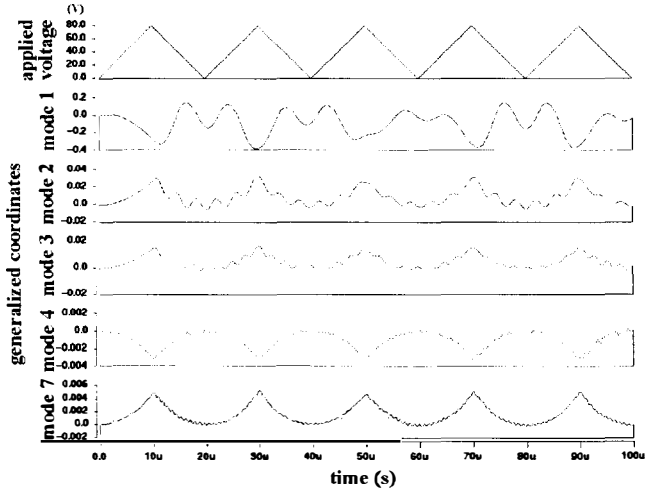

***Figure 6.** Response of asymmetrically supported plate 5-mode macromodel to an 80v saw wave with 20μs period*

THE CONSTRAINED BOUNDARY ELEMENT METHOD, A TECHNIQUE ALLOWING GENERAL SURFACE MESHES IN MEMS SIMULATIONS

M. Bächtold and P. Ljung

Coyote Systems Inc., 2740 Van Ness Ave., San Francisco, USA
Phone: (415) 346-4223, Fax: (415) 346-6282, email: martinb@coyotesystems.com

ABSTRACT

The meshing of the device geometry is of critical importance in the numerical analysis of MEMS, since MEMS typically exhibit high geometric complexity and accurate simulation results require a well-chosen mesh. Most numerical methods for device simulation impose severe restrictions during the meshing process, accepting only very specific discretizations as legal computational meshes. For MEMS simulation models generated by an automated process [1], robust meshing and simulation tools are needed, capable of handling the generated geometries without user intervention. This work presents the Constrained Boundary Element Method (CBEM), an extension to the Boundary Element Method (BEM) [2], [3] which enables the robust analysis of 3D geometries by operating on general surface meshes.

INTRODUCTION

The meshing of a general 3D geometry for numerical analysis is a formidable task: numerical methods such as the finite elements (FEM), finite differences (FDM), boundary elements (BEM) or the box method (BM) impose a number of restrictions on the shape of the elements used and the geometric configurations allowed between neighboring elements. If these meshing restrictions are not satisfied valid results cannot be expected from a numerical analysis. Moreover, the discretization of a device geometry has a major impact on the accuracy and the computational cost of a simulation. A legal computational mesh can produce inaccurate results or cause prohibitive computational effort if the distribution of the elements does not conform to the distribution of the calculated solution. Ideally, a computational mesh should be anisotropically refined and should employ elements of different size, shape and polynomial order to optimally resolve the distribution of the computed solution fields [4]. Constructing such a mesh manually is a time-consuming task, requiring experience in numerical simulation to be able to estimate the accuracy of an obtained solution. MEMS designers want to be able to numerically analyze device designs quickly and accurately, without having to focus on meshing issues. This requires robust, sophisticated automated meshing tools and numerical methods which support very general mesh configurations.

Boundary integral methods such as the BEM only discretize material interfaces and contact surfaces [2], whereas volume-based methods like the FEM require a volumetric mesh of the entire device geometry. The ability of the BEM to operate on surface meshes is an important advantage for automated meshing, because it significantly simplifies the task of generating a valid computational mesh. However, manually constructing an optimal mesh is non-trivial and time-consuming, even when using boundary elements. This is especially true when dealing with anisotropic local mesh refinement and when mixing elements of various polynomial orders.

Local anisotropic mesh refinement, also known as h-type refinement, dramatically increases the accuracy of a simulation by introducing new elements exactly at those locations, where they are most needed to decrease the error in the computed solution distribution. However, anisotropic mesh refinement, as shown in Figure 1,

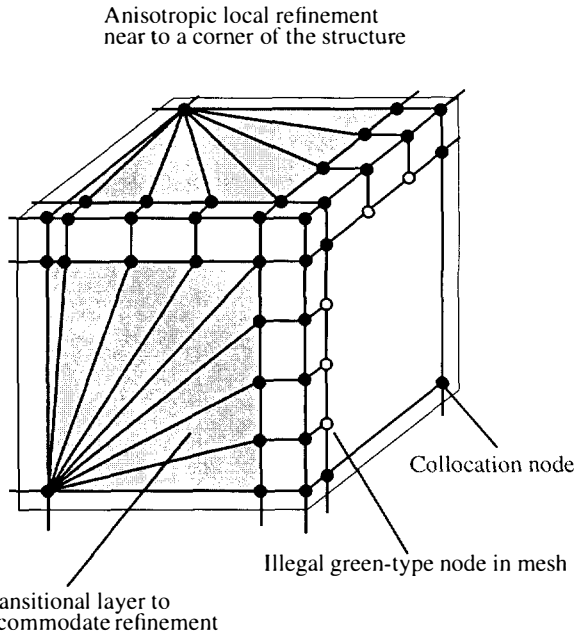

Figure 1. *Meshing problems involved with h-type refinement and green-type nodes.*

can introduce green-type nodes into the mesh, i.e., nodes which do not coincide an element vertex, but are located on the edge of another element. Such green-type nodes raise a number of meshing problems:

- Green-type nodes are illegal in most numerical methods, including FEM, and continuous BEM.
- Local refinement requires a transitional layer of elements to avoid green-type nodes (see Figure 1).
- The transitional elements cause large computational overhead.
- The transitional elements are often of bad shape (high aspect ratio) thereby affecting the overall solution accuracy

Other discretization problems arise when combining elements of different polynomial orders. As in the case of h-type refinement the solution accuracy can be significantly improved by using higher order elements in critical areas, a strategy also known

0-9640024-2-6/hh1998/$20©1998TRF
DOI 10.31438/trf.hh1998.44

TABLE 1: THE CONSTRAINED BOUNDARY ELEMENT METHOD

Boundary integral equation			$u(\xi) = \frac{1}{c(\xi)}\int_{\Gamma} q(x) \cdot u^*(\xi, x) \cdot d\Gamma(x) - \frac{1}{c(\xi)}\int_{\Gamma} u(x) \cdot q^*(\xi, x) \cdot d\Gamma(x)$ (1)
Symbols:	Γ	:	Simulation domain boundary.
	$c(\xi)$	:	Boundary integration singularity factor at position ξ.
	$u^*(\xi, x)$	:	Fundamental solution: The potential at x generated by a unit-sized charge at ξ.
	$q^*(\xi, x)$	:	The flux through the boundary position x generated by a unit-sized charge at ξ.
	$u(\xi)$, $q(\xi)$	:	Potential and flux at the boundary position ξ.
Constrained global system of equations			$u_j = \frac{1}{c(\xi_j)}\int_{\Gamma}\left(\left(\sum_i q_i N_i(x) + \sum_k q_k' N_k(x)\right)u^*(\xi_j, x) - \left(\sum_i u_i N_i(x) + \sum_k u'_k N_k(x)\right)q^*(\xi_j, x)\right)dx$ (2)
			$\boldsymbol{u}' = \boldsymbol{P}(\boldsymbol{u})$ and $\boldsymbol{q}' = \boldsymbol{F}(\boldsymbol{q})$ (3)
Symbols:	ξ_j, $N_j(x)$	:	Position and boundary shape function of the collocation node j
	$\boldsymbol{u}$, $\boldsymbol{q}$	:	The vector of potential value and flux at the unconstrained boundary collocation nodes.
	u_i, q_i	:	Potential value and flux of the unconstrained boundary collocation node i.
	$\boldsymbol{u}'$, $\boldsymbol{q}'$	:	The vector of potential value and flux at the constrained boundary collocation nodes.
	u_k', q_k'	:	Potential value and flux of the constrained boundary collocation node k.
	$\boldsymbol{P}(\boldsymbol{u})$	:	Constraining functions for the potential values
	$\boldsymbol{F}(\boldsymbol{q})$	:	Constraining function for the flux values

as p-type refinement (see Figure 2). The problems with p-type refinement in the meshing process include:

- To be able to apply local p-type refinement, various order elements must be able to mix freely in the mesh.
- Refining an element by increasing its order should not cause refinement in all its neighbor elements.
- Traditional numerical methods require many different element types to accommodate transitions between neighboring elements of varying order.

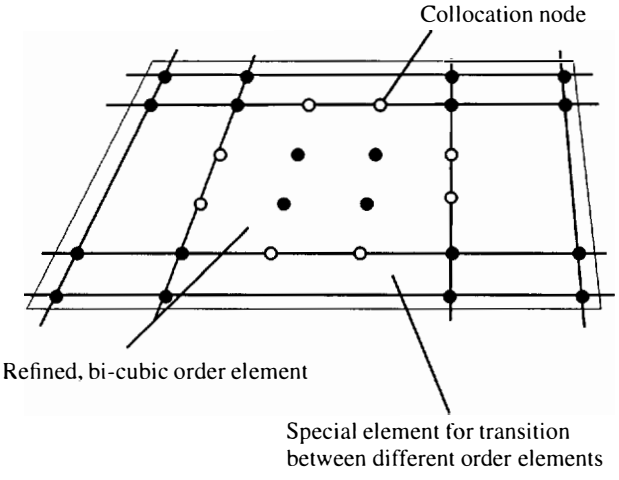

Figure 2. *Meshing issues involved with p-type refinement when mixing elements of varying order.*

This work presents the Constrained Boundary Element Method (CBEM), an approach which enables the robust analysis of 3D geometries while operating on general surface meshes. The CBEM facilitates the discretization process in two ways: being a boundary integral method, only interfaces instead of volumes are meshed, and general geometrical configurations of the elements are allowed by using constrained nodes. The CBEM is an enabling technology for automated device simulation, allowing numerical analysis directly from the mask layout of a device **[1]**. Further, the CBEM supports robust adaptive and anisotropic mesh refinement to construct an optimal mesh that delivers high solution accuracy with minimal computational effort **[4]**.

THE CONSTRAINED BOUNDARY ELEMENT METHOD

The Boundary Element Method (BEM) solves the partial differential equation (PDE) that governs the device behavior by solving a discretized boundary integral formulation see equation (1) in Table 1. The BEM for continuous fields requires that the boundaries and material interfaces are meshed such that no green-type nodes occur and that neighboring elements are of the same order. This makes the construction of an initial mesh for an arbitrary geometry very difficult and also complicates subsequent mesh improvement using h-type or p-type refinement. In contrast, the CBEM handles green-type nodes and mixed order element edges by treating them as constrained. At such constrained nodes, the solution value is not found using the BEM's boundary integral formulation (equation (1)). The constrained node uses a constraint equation, as shown in equation (3), to compute its solution by interpolating the node's value from the solution values at the unconstrained nodes. The constrained node and the corresponding constraint equation at a green-type node are shown in Figure 3. Similarly, Figure 4 shows the constraint situation that arises when two neighboring elements are of different order.

The CBEM automatically identifies constrained nodes by checking for overlapping element edges at node positions. If overlapping edges are detected, the CBEM will determine for each node whether it should be marked as free or as constrained and supply

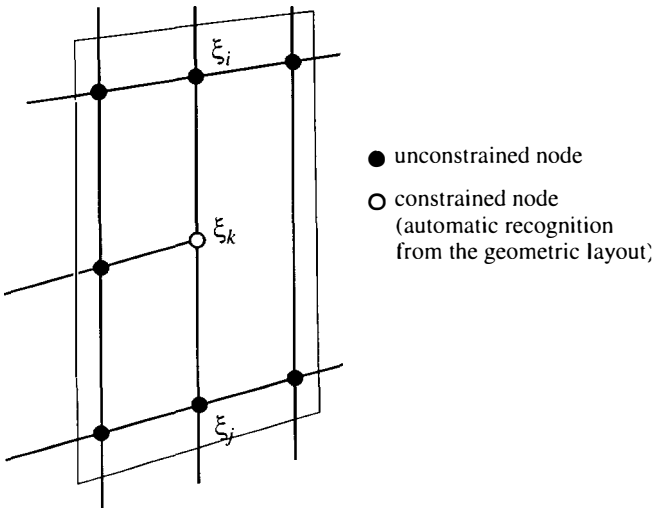

Figure 3. *Legal CBEM mesh containing h-type refinement using a constrained green-type node*

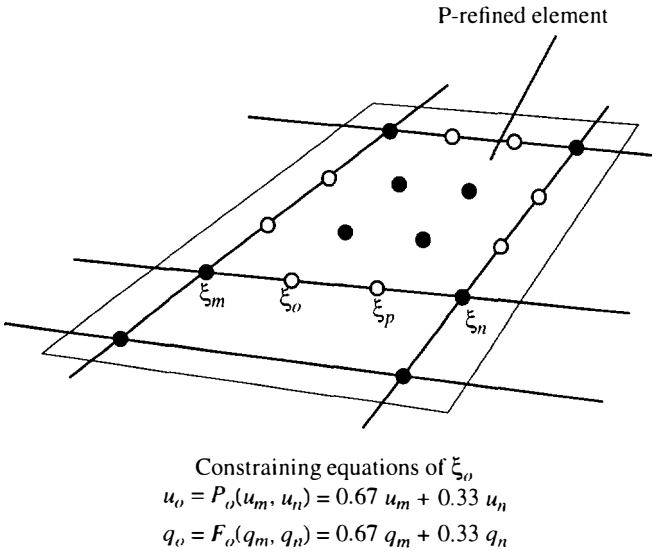

Figure 4. *Legal CBEM mesh containing a p-refined bi-cubic element, embedded in bi-linear elements*

the corresponding constraining equation for each constrained node. The computational cost of recognizing constrained nodes in an arbitrary mesh is significantly reduced by using domain decomposition methods. Due to the linear nature of interpolation functions used in the constraint equations, it is possible to rewrite the set of constraint equations (3) as linear equation systems that allow determining the values at the constrained nodes from the solution at the unconstrained nodes:

$$\boldsymbol{P}' \cdot \boldsymbol{u}' = \boldsymbol{P} \cdot \boldsymbol{u} \text{ and } \boldsymbol{F}' \cdot \boldsymbol{q}' = \boldsymbol{F} \cdot \boldsymbol{q}\,. \tag{4}$$

Here, the matrices $\boldsymbol{P}$, $\boldsymbol{P}'$, $\boldsymbol{F}$, and $\boldsymbol{F}'$ are extremely sparse matrices that contain the interpolation coefficients of the constraint equations shown in the Figures 3 and 4. It is possible to sort the constraint variables such that the value with index k depends only on the values at the unconstrained nodes and the constrained values with the indices $0...k\text{-}1$:

$$u_k' = P_k(u_{1\ldots N}, u'_{1\ldots k-1})\,, \tag{5}$$

with a similar formulation for the constrained flux variables q_k'. This implies that the matrices $\boldsymbol{P}'$ and $\boldsymbol{F}'$ contain non-zero entries only on or below the main diagonal, thereby allowing us to efficiently solve for $\boldsymbol{u}'$ and $\boldsymbol{q}'$ in equation (4) by simple backsubstitution. Together, the BEM equations (equation (2) in Table 1) and the set of constraint equations (4) uniquely define the solution at all boundary nodes. This system of equations is solved efficiently using a matrix-free, iterative solver **[5]**, shown in Figure 5. This keeps the computational cost of a constrained node constant, both in terms of run-time and memory consumption, regardless of the overall size of a simulation.

A finite element approach using constrained green-type nodes must carefully maintain flux conservation with the neighboring elements in order to converge to a valid solution of the governing PDE **[6]**. In contrast, the CBEM solution will always satisfy the PDE exactly, due to the fact that it is a superposition of Green's functions, so constrained nodes can easily be used.

RESULTS

The CBEM can robustly discretize any geometry generated using CAD tools, fabrication process emulation or imported from other sources. In Figure 6, the geometry of a MEMS accelerometer is imported and automatically discretized into a valid computational mesh for the CBEM. The initial mesh is then adaptively refined in several iterations, creating a highly optimized mesh to achieve high solution accuracy with minimal computational effort, as shown in Figure 7. The CBEM method readily integrates with BEM multipole acceleration techniques **[7]**, **[8]** which require the matrix-free iterative solver shown in Figure 5. The flexibility of CBEM meshes and the efficiency of the multipole accelerated BEM allow MEMS

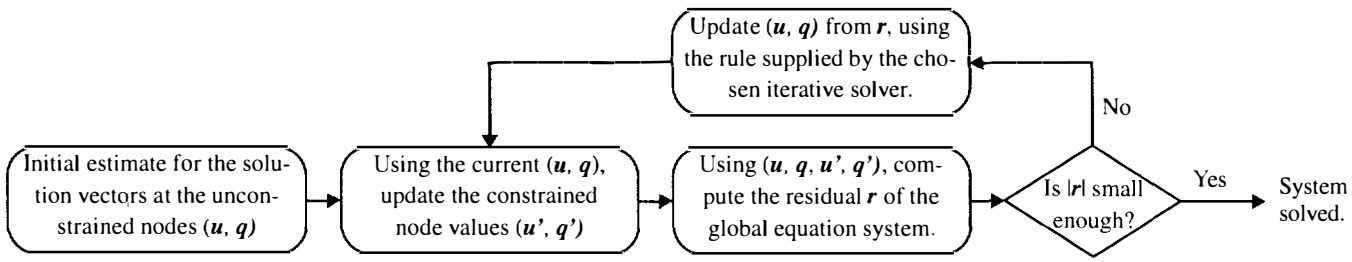

Figure 5. *Solving the CBEM global system of equations using a matrix-free iterative method. Applicable are all Krylov subspace solvers, including the GMRES, CG, BiCG, CGS or Bi-CGSTAB methods [5].*

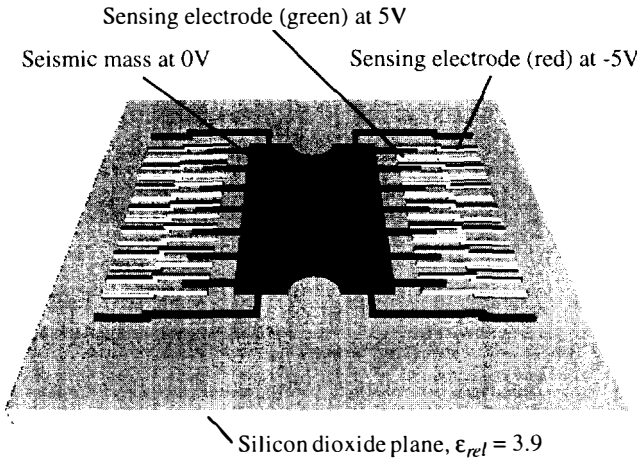

Figure 6. *Automatically generated geometry of an electrostatic MEMS accelerometer*

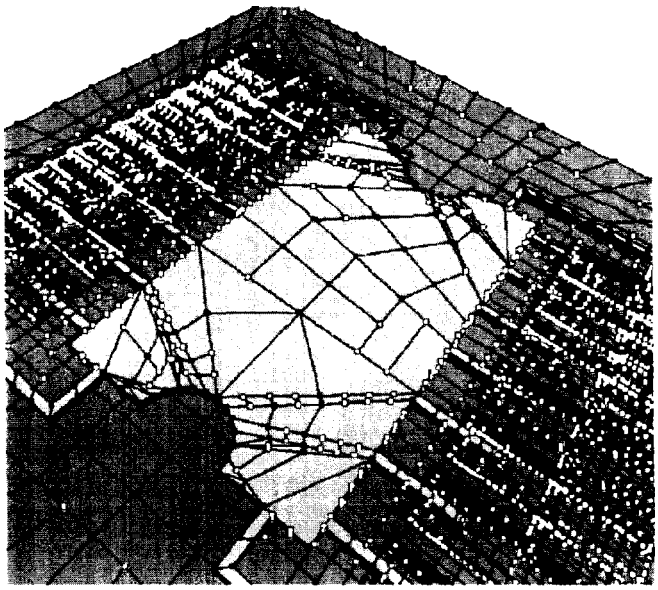

The adaptive CBEM mesh:	
• 6 levels of refinement	• 2990 constrained nodes (white)
• 7125 elements	• 4663 unconstrained nodes (black)

Figure 7. *CBEM mesh created from an automatically generated initial mesh using iterative adaptive refinement [4]*

developers to simulate the behavior of an entire device instead of being limited to small portions of a complex system.

This CBEM model now has 4663 degrees of freedom (DOFs) and is solved in 10 minutes on an engineering workstation (233MHz Pentium II), using a multipole accelerated BEM engine **[3]**. The traditional BEM approach using discontinuous boundary elements **[9]** to handle the same general mesh and provide comparable accuracy requires 7,125 linear elements, resulting in 28,500 DOFs, and takes two hours to solve, when applying the same advanced multipole acceleration techniques.

ACKNOWLEDGMENT

This work is supported by DARPA under contract F30602-96-2-0305.

REFERENCES

1. M. Bächtold, S. Taschini, J.G. Korvink, H Baltes, "Automated Extraction of Capacitances and Electrostatic Forces in MEMS and ULSI Interconnects from the Mask Layout", *Proc. IEDM*, IEEE, 1997, pp. 129-132.

2. P. Ljung, R. Howe, A. Pisano, "Sequential Solutions of Field Equations Using a Single BEM Model", *Tech. Digest Solid State Sensor and Actuator Workshop*, Hiltonhead, 1996, pp. 117-122.

3. M. Bächtold, *Efficient 3D Computation of Electrostatic Fields and Forces in Microsystems*, Ph. D. Thesis, ETH Zurich, Physical Electronics Laboratory, 1997.

4. M. Bächtold, J.G. Korvink, H Baltes, "An Error Indicator and Automatic Adaptive Meshing for 3D Electrostatic Boundary Element Simulations", *Boundary Elements XIX*, Comput. Mechanics Publ., Southampton, 1997, pp. 709-718.

5. R. Barrett et al., *Templates for the Solution of Linear Systems: Building Blocks for Iterative Methods*, SIAM, Philadelphia PA, 1994.

6. J.G. Korvink, *An Implementation of the Adaptive Finite Element Method for Semiconductor Sensor Simulation*, Ph.D. thesis, ETH Zurich, Verlag der Fachvereine, Zurich, 1993.

7. K. Nabors, *Efficient Three-Dimensional Capacitance Calculation*, Ph.D. thesis, M.I.T., Cambridge MA, 1993.

8. M. Bächtold, J.G. Korvink, H Baltes, "Enhanced Multipole Acceleration Technique for the Solution of large Poisson Computations", *IEEE Trans. on CAD of Integrated Circuits and Systems*, vol. 15(12), 1996, pp. 1541-1546.

9. C.A. Brebbia, J.C.F. Telles, L.C. Wrobel, *Boundary Element Techniques, Theory and Applications in Engineering*, Springer Verlag Berlin, 1984.

Micropower High-Detectivity Infrared Sensor System

David T. Chang, Gladney C. Asada, William J. Kaiser, Oscar M. Stafsudd
Electrical Engineering Department, University of California, Los Angeles
Los Angeles, CA 90095-1594

Abstract

In this paper we report a thermal infrared detector system for wireless integrated network sensors (WINS). This detector system includes a high sensitivity thin-film radiation thermopile and a micropower analog-to-digital converter (ADC) optimized for this unique system. The thermopile has an excellent responsivity of 100 V/W and a normalized detectivity of 1.1×10^9 cm*Hz$^{1/2}$/W in vacuum. The ADC includes a chopper for low noise measurement of the low frequency infrared sensor output. The ADC provides greater than 9-bit resolution and DC stability at a micropower level of 30μW.

Introduction

The development and deployment of tactical sensors and distributed monitoring and control systems have been hindered in the past by the requirements of complex installation and communication network requirements. Conventional distributed sensors have required cable interface, and therefore, extensive modification to structures for sensor installation. The wireless integrated network sensor (WINS) technology, reported here, provides new product opportunities and new system capabilities.

Low power systems offer a new approach for distributed sensors based on a wireless sensor infrastructure. A wireless microsensor network may be distributed rapidly and without modification to large structures and systems. Also, wireless sensors may be applied in areas where volume and mass constraints limit the application of conventional wireline interface sensors. The wireless network architecture allows microsensor nodes to be deployed in a broad spectrum of commercial and military applications ranging from clinical medicine, precision manufacturing, and transportation to battlefield perimeter security and shoreline reconnaissance. Wireless microsensor nodes may also be applied to rotating machinery without the complex slip-ring systems that would normally be required for a conventional sensor electrical interface.

A large class of WINS applications will operate with battery energy sources at micropower levels **[1]**. For example, typical low duty cycle, low peak data rate (1kbps) and short range (10 - 30 m) communication can permit 30 μA average current for a WINS node operating at 3V. A conventional, (2.5 cm diameter, 0.7 cm thickness) Li coin cell provides this current and bias level for greater than three years of unattended operating life.

WINS applications in manufacturing, medical, and tactical areas bring new requirements for infrared pyrometry and imaging. The stringent power consumption requirement of 100 μW dissipation and three-year operation with lithium coin cell places restriction on the selection of infrared sensors to be used in wireless applications. Since they require no bias current for operation, thermopiles and pyroelectric **[2]** infrared detectors are favored over bolometer detectors. Now, pyroelectric sensors provide the required high frequency performance. However, battlefield and commercial applications demand operation at low frequency. Further, due to the poor detector gain at low frequency, pyroelectric sensors due not provide adequate DC response capability. Thus, for new WINS applications, thermopile technology has been selected for the thermal infrared detector.

Thermal infrared sensor design is constrained by the limitations induced by electronic and thermal noise sources. Thermal noise power, determined by thermal conductance of the supports for the infrared absorbing element, increases with increasing conductance of the sensor structure. The ideal thermopile detector would be supported by mechanical structures with thermal conductances no greater than that of the thermopile itself. Now, electronic Johnson noise increases with increasing electrical resistance of the structure. The optimal combination of materials for thermopile applications, therefore, depends on thermoelectric coefficient, and electronic and thermal conductances. The figure of merit of the material of choice is, $Z = \alpha^2/(\rho * \kappa)$ where α is the thermoelectric power, ρ the electrical resistivity, and κ the thermal conductivity.

Element	α (μV/K)	ρ (μΩ m)	κ (W/m*K)	Z (10^{-6}/K)
Antimony	32	0.417	18.9	130
Bismuth	-72.8	1.1	8.38	574
Iron	13.4	0.086	79	26
Nickel	-20.4	0.0614	90	75
p-poly Si	400	10	84	190
n-poly Si	-400	10	84	190

It is seen that the antimony-to-bismuth thermocouple junction system is ideal for this application.

In addition to requirements on sensor sensitivity and stability, the WINS system requires a micropower data converter interface for the thermopile sensor. Design challenges for this data converter include the increase in input referred noise resulting from power reduction. In addition, WINS infrared detector applications require low noise performance at low frequency (less than 10 Hz) for surveillance and condition based maintenance. This creates additional challenges since CMOS interface circuits display large "1/f" noise, yielding unacceptable low frequency performance. The Σ-Δ converter described here, designed for operation with the thermopile infrared sensor, incorporates an input chopper, providing DC stability in micropower CMOS.

Thermopile Fabrication

Thermal infrared sensors rely on a temperature sensitive element that may absorb incident radiation and is thermally isolated from its fixed temperature support. Sensitivity, limited by thermal noise contributed by the finite thermal conductance of the support, is optimized by reducing thermal conductance of the structure. For this sensor, a thin film insulating membrane

0-9640024-2-6/hh1998/$20©1998TRF
DOI 10.31438/trf.hh1998.45

supports the thermopile structure. The thin-film radiation thermopile infrared detector is created by the conventional bulk micromachining method. The device is fabricated as follows (figure 1). First, a 0.5 μm thickness of LPCVD low-stress nitride is deposited onto an n-type silicon substrate to form the structural layer. By using front and backside wafer photolithography and reactive ion etching, etch windows and alignment marks are created. Anisotropic etching of the silicon substrate in 30% potassium hydroxide (KOH) solution at 80°C for 4 hours leaves a 30μm thick silicon layer behind the silicon nitride membrane for simplification of the subsequent processing. The detector element consists of 30 pairs of bismuth to antimony measurement junctions on the silicon nitride membrane and an equal number of reference junctions on the silicon frame. The 24μm wide, 0.3μm thick bismuth and antimony lines are deposited by a single-step optical photolithographic lift-off process with chlorobenzene treatment.

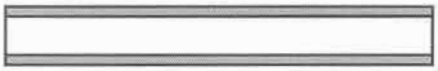

(a) *Deposition of 0.5μm LPCVD low-stress silicon nitride on n-Si.*

(b) *Front and back lithography and RIE backside etch windows.*

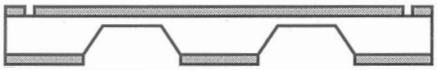

(c) *KOH deep etch @ 80°C for 4 hours, leave ~30μm Si.*

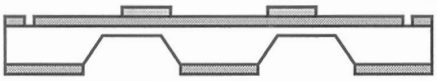

(d) *E-beam evaporate bismuth thin film, acetone lift-off.*

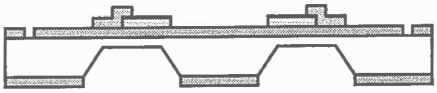

(e) *E-beam evaporate antimony thin film, acetone lift-off.*

(f) *E-beam evaporate titanium/gold thin films, acetone lift-off.*

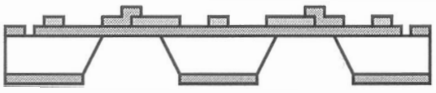

(g) *Protect top side with wax, remove the last 30μm of Si.*

Figure 1. Bismuth/Antimony thermopile fabrication process flow.

Titanium and gold bonding pads are then evaporated to complete the thermopile. After all steps involving photolithography are completed, the wafer is protected by wax on the device side and put back into KOH to remove the last 30μm of silicon behind the nitride membrane. In order to improve infrared absorption, a layer

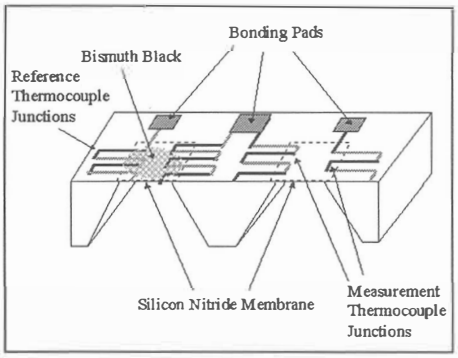

Figure 2. A simplified cross-section view of the dual-element 30-thermocouple bismuth- antimony radiation thermopile.

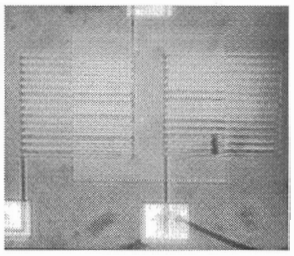

Figure 3. Top view of the bismuth-antimony radiation thermopile.

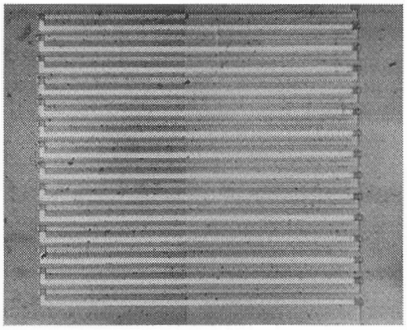

Figure 4. Top view of one half of the detector element. Reference junctions are on the silicon frame (left half) and the measurement junctions on the 0.5μm thick silicon nitride membrane (right half.)

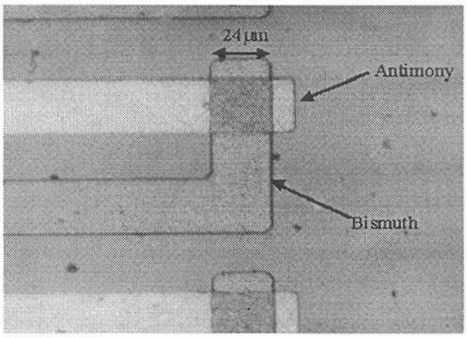

Figure 5. The bismuth-antimony thermocouple junction.

of metal black [2] is deposited at the center of the active area to complete the fabrication. A 3-D drawing and several top views of the detector are shown in figures 2-5.

Micropower Analog-to-Digital Converter

A micropower analog-to-digital converter (ADC) is required to enable digital signal processing of infrared signals for event detection. A first order Sigma-Delta (Σ-Δ) converter is chosen over other architectures because of power constraints. Architectures including parallel or pipelined ADCs provide high throughput at high power. Further, sequential approximation converters require multibit digital-to-analog converter (DAC) systems which also require large power dissipation. In contrast, the first order Σ-Δ converter uses a single integrator, a comparator, and a one bit DAC (figure 6).

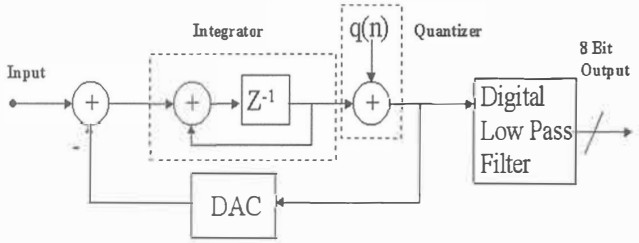

Figure 6. A block diagram of a first order Sigma-Delta analog-to- digital converter loop.

Additional benefits appear as a result of the Σ-Δ oversampled architecture. Specifically, by comparison, all other ADCs sample at the Nyquist rate of the input signal. Ensuring Nyquist rate signals requires the use of input anti-aliasing filters. However, the oversampled converter samples at a frequency 2^N times greater than the Nyquist rate, where N is the resolution (word length) of the converter [3]. This characteristic translates the aliased input signal to a much higher frequency than in other architectures thus minimizing or eliminating the filter before the ADC.

A further benefit of the Σ-Δ architecture for micropower circuits is the ability to trade component requirements for the over sampling ratio (the sampling frequency divided by the Nyquist frequency). The analog components of the ADC operate in deep subthreshold to meet the goal of low current micropower operation [4]. This imposes severe restrictions on the performance of the circuits within the loop. A high oversampling ratio of 1024 is thus chosen to overcome the problems associated with low performance circuits. The possible increased power consumption of digital components in the signal path including the low pass filter is prevented with the use of low power cell libraries and architecture.

WINS infrared sensor applications present an additional challenge for ADC design. Specifically, the WINS infrared detector system must measure variations of infrared signals at low frequencies (less than 1 Hz). This is required for continuous monitoring of a slowly moving threat object or monitoring of temperature variation in condition based maintenance applications

However, implementation of low noise ADC systems in CMOS encounters the severe "1/f" input noise. Noise rejection and DC stability in these CMOS ADC systems is achieved here by signal "chopping" methods. The chopper ADC mixes the input signal to an intermediate frequency (IF) before delivery to the Σ-Δ loop. Another mixing stage, to bring the signal back into the band of interest, is done before the pulse code modulated signal is fed into the digital low pass filter (figure 7). This approach requires only the use of a commutating switch at the analog input (where no charge injection will occur) and a second commutating switch at the digital output, again where no charge injection error may occur.

Because of the low frequencies of the input signal, the main source of noise in the analog components of the ADC is 1/f noise. Moving the input signal to an IF minimizes the noise allowed to corrupt conversion [5]. The input of the Σ-Δ at an IF ensures that the loop will not saturate with a large DC output from the infrared sensor. Additional power consumption is avoided by the use of a passive mixer to chop the input to an IF of $1/8^{th}$ of the sampling frequency.

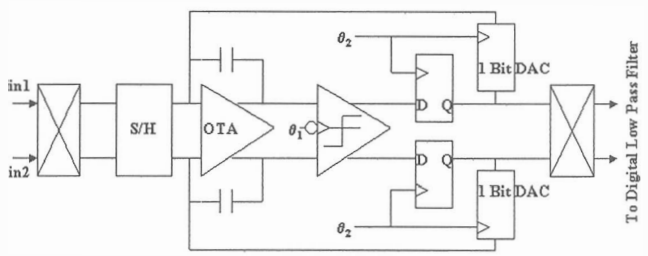

Figure 7. A block diagram of the pulse code modulator part of the Σ-Δ ADC showing the location of the chopping blocks.

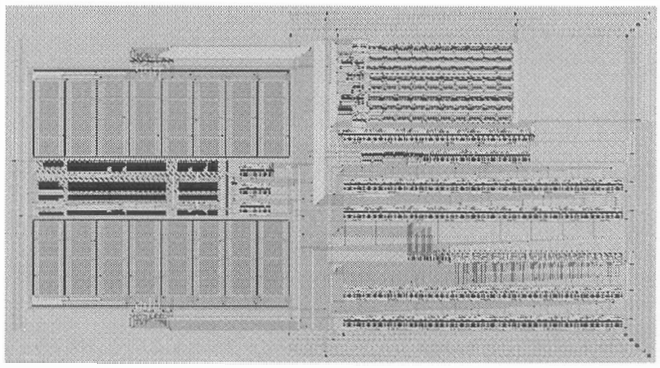

Figure 8. Layout of the core of the chopped Σ-Δ ADC showing the analog components (on the left), the digital low pass filter (bottom right), and the clock generation circuit (top middle).

The first order Σ-Δ ADC has been fabricated in the HPCMOS 0.8μm process (figure 8). Direct measurement shows that the converter achieve greater than 9 bit resolution for a 100 Hz band limited signal with a power consumption of only 30μW on a single 3V rail. This chopper ADC has been demonstrated to have a frequency-independent SNR from 0.1 – 100Hz. This resolution is adequate for the infrared sensor tactical motion detection application.

Measurement Results

The infrared detector characterization apparatus is shown in figure 9. A 1.55μm wavelength diode laser modulated by a function generator serves as the coherent infrared source.

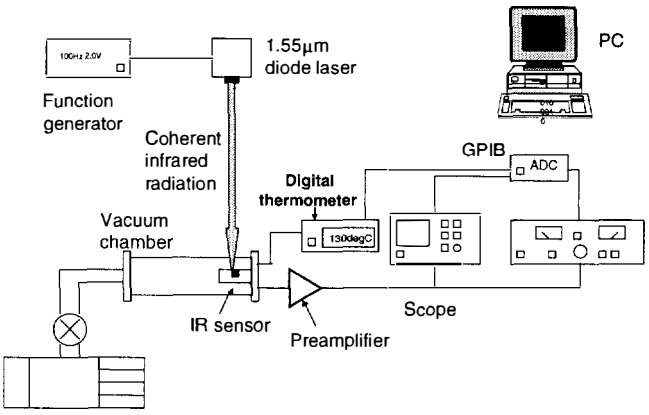

Figure 9. Infrared measurement setup for the thermopile detector.

The sensor can be tested in an evacuated environment to reduce thermal conduction loss to air. A scan of the infrared detector response is shown in figure 10.

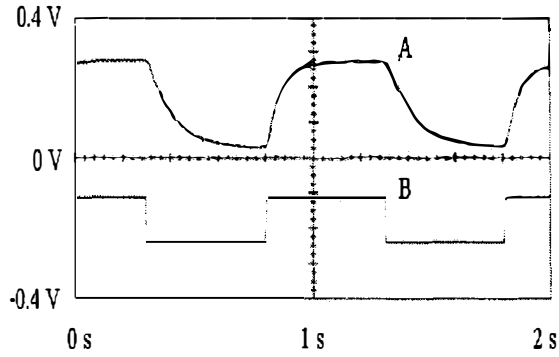

Figure 10. A scan of the infrared detector response in vacuum (trace A) to a 1 Hz, 1.55μm wavelength, square-wave modulated radiation (trace B).

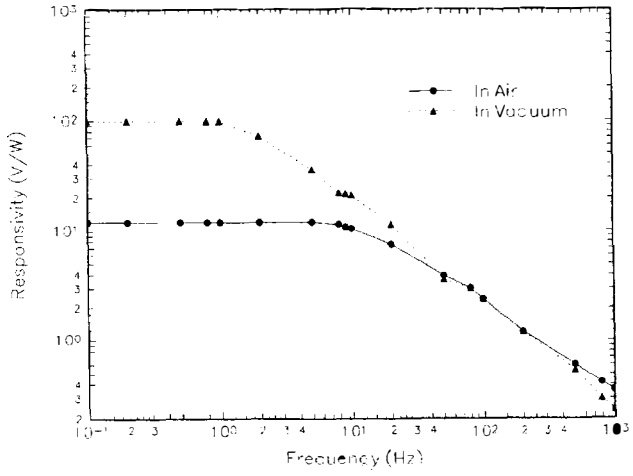

Figure 11. Responsivity vs. frequency plot of the thermopile measured in air and vacuum. The influence of thermal conductance of the atmosphere is seen in the magnitude and frequency response.

In addition, the responsivity of the thermopile is measured as a function of frequency in both air and vacuum. Figure 10 shows that the response of the sensor in vacuum increases by almost an order of magnitude over that in air. The detector has a peak responsivity of 100 V/W in vacuum and 12.5 V/W in air. The noise-equivalent-power was measured by an HP35660A dynamic signal analyzer to be 1.8 nW/ $Hz^{1/2}$ at 1Hz. The normalized detectivity D* of this sensor is $1.1x10^9$ cm*$Hz^{1/2}$/W in vacuum and $1.38x10^8$ cm*$Hz^{1/2}$/W in air. This result compared favorably with a previously reported 60-thermocouple polysilicon infrared sensor **[6]**. This sensitivity is ideally suited for many of the applications listed above.

CONCLUSIONS

A micropower thermal infrared sensor based on suspended metal thermopile structures has been developed with a micropower CMOS data converter system. The thermopile sensor element is compatible with a range of integration technologies including flip-chip technology methods. The development of a chopper Σ-Δ data converter provides DC stability. The detectivity of this detector is $1.1x10^9$ cm*$Hz^{1/2}$/W in a vacuum package. Early applications of these devices will be with the WINS node platform for situational awareness. However, additional applications will follow in condition based maintenance.

ACKNOWLEDGMENTS

This research is supported by the Defense Advanced Research Projects Agency (DARPA). The authors would like to thank Pamela Patterson for valuable discussions.

REFERENCES

[1] K. Bult, A. Burstein, D. Chang, M. Dong, M. Fielding, E. Kruglick, J. Ho, F. Lin, T. H. Lin, W. J. Kaiser, H. Marcy, R. Mukai, P. Nelson, F. Newburg, K. S. J. Pister, G. Pottie, H. Sanchez, O. M Stafsudd, K. B. Tan, C. M. Ward, S. Xue, J. Yao," *Technical Digest of the 1996 Solid-State Sensor and Actuator Workshop,* pp. 205-210, 1996.

[2] D. T. Chang, D. M. Chen, F. H. Lin, W. J. Kaiser, O. M. Stafsudd, "CMOS Integrated Infrared Sensor," *Proceedings of the 1997 International Conference on Solid-State Sensors and Actuators (Transducers '97)*, vol. 2, pp. 1259-1262, 1997.

[3] E. Vittoz, *Design of Analog-Digital VLSI Circuits for Telecommunications & Signal Processing*. ed. J. E. Franca and Y. Tsividis, New York, Prentice Hall, 1994.

[4] P. Aziz, H. Sorensen, J. Spiegel, *IEEE Signal Processing Magazine*, vol. 13, pp. 61-70, 1996.

[5] Y. Chang, C. Wu, T. Yu, "Chopper-Stabilized Sigma-Delta Modulator," *Proceedings of the 1993 IEEE International Symposium on Circuits and Systems*, pp. 1286-1289, 1993.

[6] M. Muller, W. Budde, R. Gottfried-Gottfried, "A Thermoelectric Infrared Radiation Sensor," *Proceedings of the 1995 International Conference on Solid-State Sensors and Actuators (Transducers '95)*, pp 640-3, 1995.

A MICRO-MACHINED PYROELECTRIC DETECTOR ARRAY

Paul M. Zavracky, Keith Warner, and Gregory Jenkins
Northeastern University, Department of Electrical and Computer Engineering
360 Huntington Ave., Boston, MA 02115

Steve Etienne
CRL Ltd., Hayes, Middlesex, UK

Charles Logan
Ohmeda Inc., Louisville, CO 80027

Roger Grace
Roger Grace Associates,
San Francisco, CA

ABSTRACT

Using a novel bulk silicon micro-machining technique, an infrared detector has been fabricated for use in medical monitoring products. The device employs a thin (<5um) free-standing membrane of poly(vinylidene flouride-trifluoroethylene) (P(VDF/TrFE)) co-polymer supported by a silicon frame. IR light incident upon a semi-transparent Cr lower electrode is absorbed by the membrane, producing a voltage between this electrode and a series of Cr/Au electrodes on the top. In this configuration, 74 electrodes provide spatial resolution that corresponds to spectral resolution when the device is mated to a linearly-graded IR filter.

INTRODUCTION

During certain medical procedures it is desirable to monitor the concentration of gases within various media. The ability to provide this information on a real-time basis with minimal signal conditioning is a key requirement, along with low cost and reliable operation. Absorption spectroscopy using a near-infrared source can meet these constraints, provided that a suitable detector is available. Photoconductive and photovoltaic semiconductor devices can be used, but these usually require external cooling from a Peltier junction in order to increase the signal-to-noise ratio. As an alternative, the incident radiation can be coupled into a ferroelectric material. The highly anisotropic crystalline structure of a ferroelectric will produce an electric field when the lattice is strained; when strain is induced by localized heating, the effect is known as pyroelectricity.

Recently, a number of researchers have investigated the use of poly(vinylidene flouride-trifluoroethylene) (P(VDF/TrFE)) co-polymer thin-films as pyroelectric sensing agents [1-7]. This material system is particularly well-suited for integration into microfabrication processes, since it can be applied to a substrate by spin-on from a solvent-based precursor. CMOS devices fabricated in the substrate can be used for amplification and signal processing. However, thermal conduction from the sensing film to the substrate can limit sensitivity. To circumvent this problem, Kohler, et.al. [8] and Setiadi, et.al. [9] describe devices where the co-polymer film is supported by a silicon nitride membrane formed by anisotropic etching of the silicon substrate.

The device presented here employs a completely free-standing co-polymer film, supported by a silicon frame. As shown in Figure 1, 74 electrodes are fabricated along the top of the device, and a thin layer of Cr is used for the bottom electrode. The thickness of the co-polymer membrane is adjusted to provide optimal absorption at the wavelengths of interest. The resistivity of the bottom electrode is targeted to be 377Ω/sq., matching the impedance of free-space.

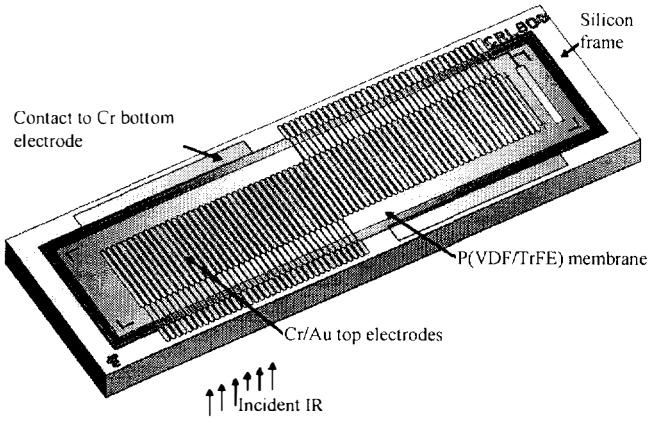

Figure 1. *Isometric view of sensing array.*

FABRICATION

Figure 2 shows the fabrication sequence. A 75mm silicon wafer that has been back-lapped and polished to a thickness of 285um is cleaned and thermally oxidized to 1 μm. A chromium film 1000A thick is sputter deposited onto the back of the wafer. The Cr and oxide layers are patterned and etched and used as a mask for a backside silicon etch in 25% TMAH at 80°C to form the frame for the device. The TMAH etch is carefully timed and monitored to obtain 50 μm thick Si diaphragms. Each wafer contains 19 diaphragms measuring approximately 4mm x 11mm. The separation webs for the devices are also formed during this step, eliminating the need for a potentially damaging dicing operation. The diaphragms are quite robust and can be subjected to moderate vacuum (2-3") during lithographic operations. (Spin coating is performed with a vacuum-less chuck).

A window is patterned in the oxide on the front of the device (using IR alignment), and a thin (~100A) layer of Cr is deposited to form the bottom electrode. As noted above, the sheet resistivity of this layer is controlled to 377 ± 50 Ω/sq. to match the impedance of free-space. Simulations of the absorbance vs. wavelength indicate that a variation of 200-500 Ω/sq. has little effect on the overall performance of the device. After patterning the Cr, a solution of 70%/30% P(VDF/TrFE) copolymer dissolved in butanone is applied to the substrate by spin-on at 4KRPM. The co-polymer is baked at 105°C for 1 min. on a hot plate. A 1000A thick layer of copper is sputter deposited to act as a mask for etching the co-polymer in an O_2 plasma, which also strips the photoresist. The copper is removed in a solution of ferric chloride after the co-polymer etch. A layer of 200A Cr/3000A Au/300A Ti-W is then deposited and patterned to form the top electrodes. The PR

0-9640024-2-6/hh1998/$20©1998TRF
DOI 10.31438/trf.hh1998.46

Solid-State Sensors, Actuators, and Microsystems Workshop
Hilton Head Island, South Carolina, June 8-11, 1998

from this mask is stripped by flood exposure and development, which does not affect the co-polymer film. The Ti-W is stripped in H_2O_2 to remove any remaining PR residue.

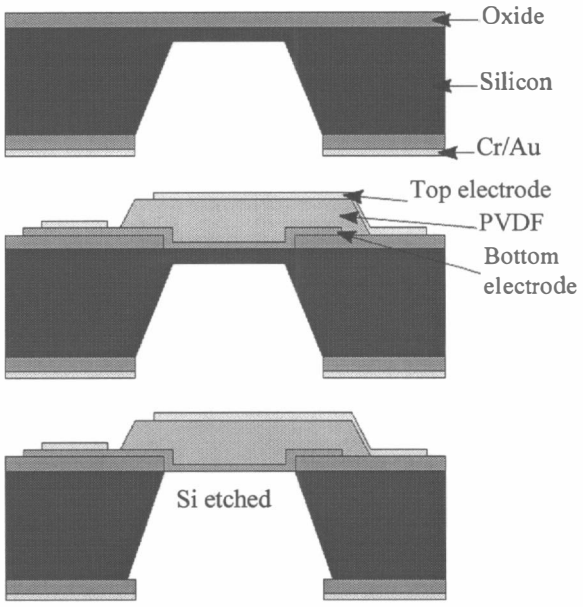

Figure 2. Fabrication sequence.

The front of the wafer is coated with Ti-W/Cu to protect the gold electrodes during the release etch. (We have observed that Au is attacked by XeF_2, as reported by others [12]). After a 50:1 HF dip and a 95°C dehydration bake, the wafer is placed face-down on a Teflon holder in a home-built XeF_2 pulse etcher (Figure 3). This etching method was chosen for its extreme selectivity to oxide and other materials and its gentle characteristics [10,11]. This step also releases the die from the wafer. The die etch at slightly different rates, requiring an overetch that does not affect any of the devices. For a etch/pump cycle of 7s/5s it takes about 3 hours to completely remove the diaphragms. The chamber pressure during the etch interval is about 2.2T. None of the membranes are damaged by the etching process. A SEM photo of the released film (Figure 4) also shows rounding of the TMAH-etched corners from the XeF_2 etch.

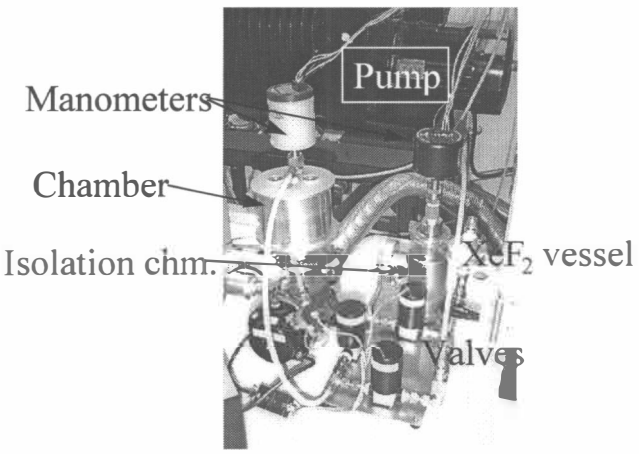

Figure 3. Photograph of XeF_2 etching system.

After release, the individual die are transferred to a polypropylene holder to facilitate handling. The holder is arranged in a radial configuration to allow the die to be processed by placing the holder into a standard wafer carrier. The Cu and Ti-W protection layers are then removed in $FeCl_3$ and H_2O_2, respectively. The co-polymer is then annealed at 140°C for 6 hrs., followed by a 12 hr. cooling ramp to room temperature. A photograph of a completed device is shown in Figure 5.

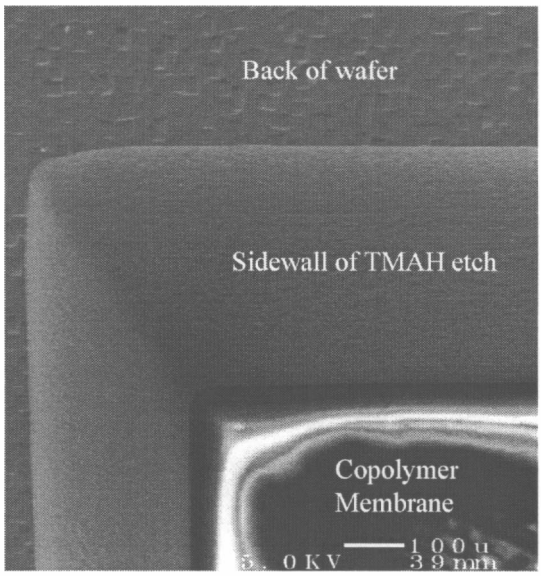

Figure 4. SEM of released membrane.

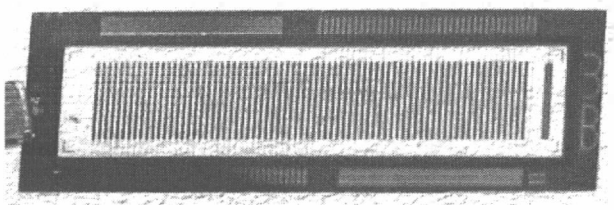

Figure 5. Photograph of completed die.

RESULTS

The individual devices are poled by applying 180V across the electrodes in three cycles of 10 seconds duration. After each cycle the polarity is reversed. Characteristics obtained from devices fabricated at CRL using a precursor process are shown in Figure 6. Room temperature response is measured at over 1400 V/W, with a signal-to-noise ratio of 43.1 dB. The device is used in an application which requires a 40 Hz response rate.

REFERENCES

1. P.E. Bloomfield, F. Castro, and R.M. Goeller, "The Design, Processing, Evaluation and Characterization of Pyroelectric PVDF Copolymer/Silicon MOSFET Detector Arrays", *Proc. of the Ninth IEEE ISAF* (1994), IEEE 94CH3416-5, 1/95, 725.
2. W. von Munch, M. Nagele, G. Wohl, B. Ploss, and W. Ruppel, "A 3x3 Pyroelectric Detector Array with Improved

Sensor Technology", *Sensors and Actuators A*, 41-42(1994), 156-160.
3. E. Yamaka, "Pyroelectric IR Sensor using Vinylidene Flouride-Trifluoroethylene Copolymer Film", *Ferroelectrics*, 57, 337-342 (1984).
4. D. Setiadi, A. Armitage, T.D. Binnie, P.P.L. Regtien, and P.M. Sarro, "An Integrated Charge Amplifier for a Pyroelectric Sensor", *Sensors and Actuators A*, 61(1997), 421-426.
5. A. Mahrane, M. Djafari-Rouhani, A. Najmi, D. Franques, and D. Esteve, "P(VDF-TrFE) Copolymer Sensor for Passive IR Detection in Automotives", *Sensors and Actuators A*, 46-47(1995), 399-402.
6. D. Setiadi and P.P.L. Regtien, "A VDF/TrFE Copolymer on Silicon Pyroelectric Sensor: Design Considerations and Experiments", *Sensors and Actuators A*, 46-47(1995), 408-412.
7. M. Levesque, M. Cote, S. Lelievre, and P. Galarneau, "P(VDF-TrFE) Infrared Detectors and Array", *SPIE Proceedings* vol. 2269, Infrared Technology XX(1994), 125-130.
8. R. Kohler, N. Neumann, and G. Hofmann, "Pyroelectric Single-element and Linear-array Sensors based on P(VDF/TrFE) Thin Films", *Sensors and Actuators A*, 45(1994), 209-218.
9. D. Setiadi, P.M. Sarro, and P.P.L. Regtien, "A 3x1 Integrated Pyroelectric Sensor based on VDF/TrFE Copolymer", *Proc. Transducers '95*, vol. 2, 644-647.
10. P.B. Chu, J.T. Chen, R. Yeh, G. Lin, J.C.P. Huang, B.A. Warneke, and K.S.J. Pister, "Controlled Pulse-etching with Xenon Difluoride", *Proc. Transducers '97*, vol. 1, 665-668.
11. M. Hecht, R.P. Vasquez, F.J. Grunthaner, N. Zamani, and J. Maserjian, "A Novel X-ray Photoelectron Spectroscopy Study of the Al/SiO2 Interface", *J. Appl. Phys.*, 57(12), 5256-5261 (1985).
12. N.H. Tea, V. Milanovic, C.A. Zincke, J.S. Suehle, M. Gaitan, M.E. Zaghloul, and J. Geist, "Hybrid Postprocessing Etching for CMOS-Compatible MEMS", *Jour. of Microelectromechanical Systems*, 6(4), 363-372 (1997).

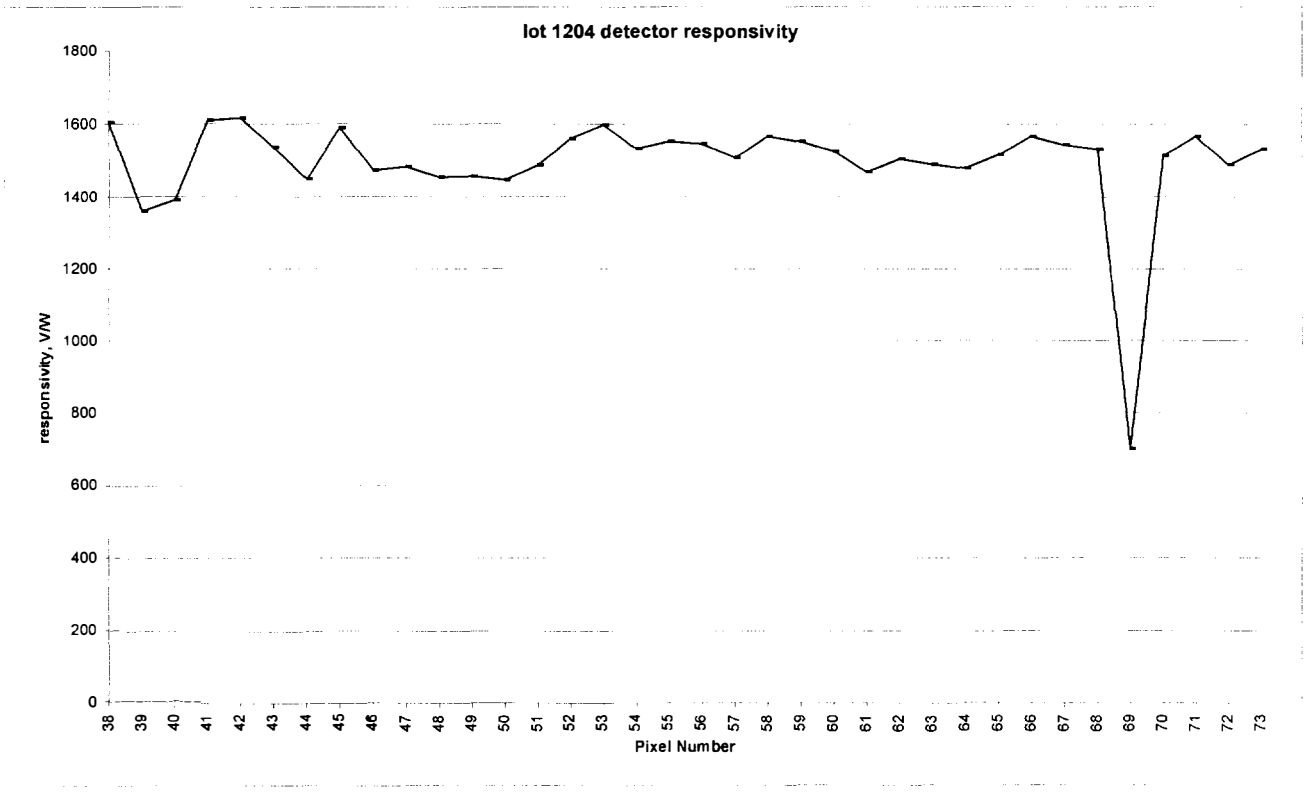

Figure 6. *Device response.*

A MULTI-LEAD VACUUM-SEALED CAPACITIVE PRESSURE SENSOR

Abhijeet V. Chavan and Kensall D. Wise

Center for Integrated Sensors and Circuits
Department of Electrical Engineering and Computer Science
The University of Michigan, Ann Arbor, MI 48109-2122

ABSTRACT

To improve the sensitivity, dynamic range and resolution of capacitive pressure sensors, it is necessary to eliminate the effects of environmental factors such as trapped gas and material thermal mismatches in addition to reducing parasitics. If the desired sensor signal can be amplified in the sealed transducer cavity itself, then the effects of externally-induced noise will be eliminated almost entirely. This work reports a new multi-lead absolute capacitive pressure sensor which lends itself to achieving these goals. The sensor has a resolution of 25mTorr over a pressure range from 500 to 800 Torr with a TCO at 750Torr of <1000ppm/°C and a TCS of 1350ppm/°C. The parasitic capacitance on individual leads is 500fF, which is an order of magnitude lower than a previously-reported vacuum-sealed device [1]. The new device structure also eliminates the need to protect the outer silicon body when operating in high humidity. The resistances of the lead transfers accessing the sealed cavity are of the order of 50 ohms. The device is completely batch fabricated and provides a general purpose MEMS process for future circuit integration within sealed cavities where moving micromechanical structures are enclosed.

INTRODUCTION

Silicon-based capacitive pressure sensors are increasingly being used in a variety of applications to achieve high resolution and low temperature sensitivity. As compared to piezoresistive pressure sensors, capacitive pressure sensors also have greatly reduced power consumption. Capacitive devices in general are more susceptible to noise coupling from the environment, however, which requires the readout circuit to be in close proximity to the actual transducer. The development of a lead transfer process having low parasitics between the vacuum-sealed cavity and the outside world is a challenging problem. The sensor described here is a second-generation multi-transducer device suitable for use over the barometric pressure range from 500 to 800 Torr with a resolution of 25mTorr. This high resolution is maintained in the face of atmospheric offset pressure over a temperature range from 25°C to 85°C. Parasitic capacitance in parallel with the sensor capacitance has a different thermal behavior than the actual sensing element and thus complicates temperature compensation. This device significantly reduces such parasitics and eliminates any leakage paths which may occur along the leads.

STRUCTURAL DESIGN AND OPERATION

A new device structure with multiple stacked polysilicon and dielectric layers is employed. Each transducer can have several lead transfers from the internal reference cavity to the outside world and provides additional Ti/Pt electrodes to block the electric field across the entire cavity and getter any outdiffusing oxygen ions. To achieve this, two levels of polysilicon are used. Polysilicon-glass seals are known to be hermetic [2]. The sensor cross-section is diagrammed in Fig. 1 and consists of vacuum-sealed capacitors realized in a silicon-on-glass dissolved-wafer process. In the structure shown in Fig. 1, the polysilicon-1 layer near the glass forms a continuous sealing ring while the polysilicon-2 layer forms a bridge for the individual lead transfers. Using this approach, wafer-level bonds can be made to 7740 glass. As is evident, the need for glass drilling, epoxy seals, or special metal seals [3,4] is eliminated. In addition since the vacuum seal is done at wafer level before etch-back, the cavity is never exposed to the etch, and stiction problems are avoided. A significant practical advantage is that a metal or polysilicon electrode which is on the p++ silicon diaphragm inside the cavity, but is isolated from it electrically, can be transferred outside of the cavity. This eliminates the need to passivate the exposed p++ silicon surface in case of operation under moist and dirty conditions because the p++ housing forms only the physical transducer but is electrically isolated from the electrode. Fig. 1(c) shows a cross-section of this scheme.

The overall pressure range is divided among different transducers having diaphragm diameters ranging from 920 to 1100µm with a gap separation of 9.8µm and a diaphragm thickness of 2.4µm. The diaphragm has a centrally stiffened area to obtain first-order linearization of the output characteristics. One of the transducers is used for coarse pressure sub-range selection and then the appropriate segment tranducers is read-out for obtaining higher resolution. The high atmospheric offset keeps the diaphragms heavily deflected and results in an operational gap between 0.8 and 0.2µm, which in turn provides high sensitivity for the device. The device is designed to operate with a resultant diaphragm tensile stress of ~25 Mpa. In Fig. 1a, the internal sensing lead on the glass is transferred to poly1 and then through a contact opening to poly2 , back again to poly1, and then back to metal externally using Pt-Pt compression bonds formed during the electrostatic bonding operation. Since the potential of the polysilicon must be connected to the silicon bulk during bonding, but must be well isolated later, lateral polysilicon tabs are used to contact the lightly-doped portion of the bulk. This area is automatically removed during the etch-back process to provide the required isolation. Permanent contacts to the top silicon electrode are made via similar transfers to the p+ body region as shown in Fig. 1b. In the case of a multi-lead device, the majority of the anchor formed by the polysilicon ring is electrically isolated from the leads themselves. Thus, it is important to be able to do probe (batch) testing to verify this isolation. Special contacts are provided to the rim to test for this isolation. Figure 2(a) shows a complete five transducer sensor with an on-chip reference capacitor in the center of the lower row. This pressure-

0-9640024-2-6/hh1998/$20©1998TRF
DOI 10.31438/trf.hh1998.47

independent reference capacitor tracks the pressure dependent transducers over temperature and is used differentially with a switched-capacitor readout circuit. Fig. 2(b) views a single transducer, showing all lead transfers as seen through the glass.

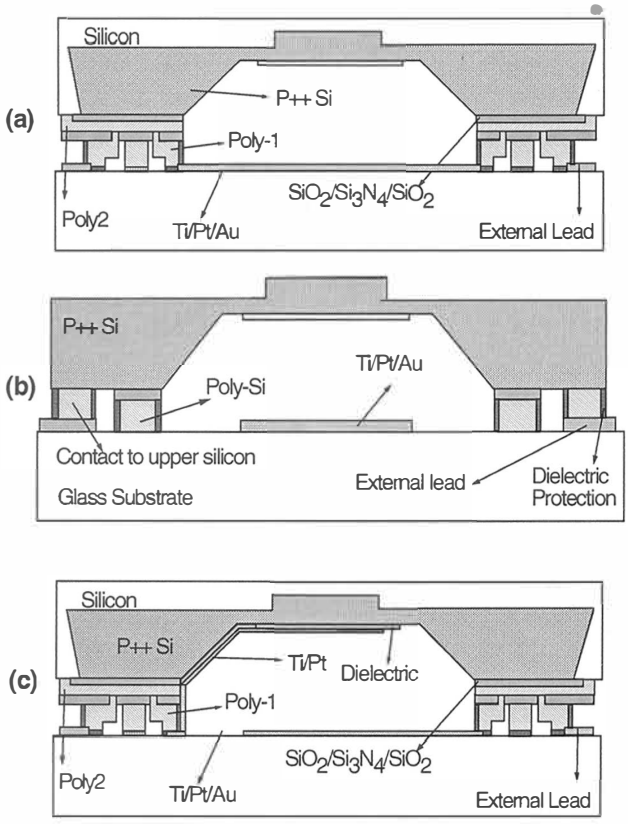

Fig. 1: Cross-sections of the capacitive sensor. In (a) the cut is shown through the lead transfer that brings the glass electrode out of the cavity. A tab used to contact the wafer bulk during bonding is also shown. In (b) the cut is shown along a device diagonal. The inner ring forms the vacuum seal; the outer ring provides a permanent contact to the silicon electrode. (c) Scheme showing the lead transfers with both electrodes isolated from the silicon bulk.

FABRICATION PROCESS

A compressed process flow is shown in Fig. 3. The device is fabricated using a ten-mask bulk-micromachined dissolved wafer process. As shown in Fig. 3(a), the silicon process starts with a KOH recess etch of about 7µm. Subsequently deposited layers can compensate for any variation in this etch depth. A patterned masking oxide (Fig 3b) is used to define the anchor area using a solid-source deep boron diffusion at 1175°C. A nominal etch-stop depth of 15µm is obtained. This is followed by a shallow boron diffusion step to define the diaphragm, which is approximately 2.4µm thick. The next step involves the deposition of an LPCVD $SiO_2/Si_3N_4/SiO_2$ layer having a total thickness of 0.75µm. A short boron diffusion at 1000°C is done to reduce the resistance of the polysilicon. In addition, p+ doping reduces the rate of attack from EDP if the protective dielectric coating on the polysilicon is broken. It is adequate to dope the polysilicon at low temperatures due to the ease of boron diffusion through the grain boundaries. The polysilicon is patterned using SF_6 plasma etching. This etch step is done using a two-step lithography. In the first step, the individual leads are patterned. This is done on the polysilicon which is on top of the anchor area. The isolation formed must have straight sidewalls because of the subsequent isolation refill using $SiO_2/Si_3N_4/SiO_2$. In the second etch step, the polysilicon from the recesses is etched. The need for two steps is due to the substantial difference in height for patterns on the anchor and patterns in the recess. After etching, the polysilicon and the dielectric layer on the diaphragm area are removed using wet etching. This is followed by a second LPCVD $SiO_2/Si_3N_4/SiO_2$ layer with a total thickness of 0.75µm. Contact openings are made for the subsequent polysilicon-1 layer to make contact to the: a) silicon bulk along the periphery to form the tabs useful in bonding, and b) along the leads to form the electrical bridges for lead transfer. This is followed by the deposition of a 1.2µm-thick layer of polysilicon-1, which is p++ doped at 1000°C. A CMP (chemical mechanical polishing) step is used to achieve a surface roughness of <500Å-rms and to overcome any non-planarities due to wafer bowing [7]. For polishing polysilicon, it has been observed that

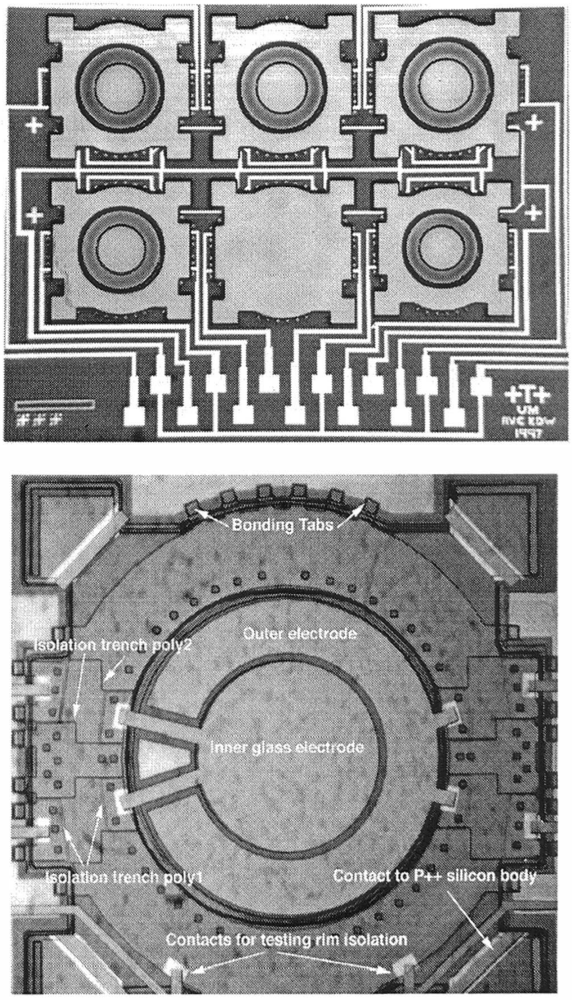

Fig. 2: Top views of the fabricated devices. In (a) five transducers are formed per die having staggered diameters and pressure ranges. A reference capacitor can be seen in the center of the lower row. In (b) the view is through the glass side of a completed transducer.

colloidal silica-based slurries give a good surface finish devoid of any scratches and other CMP related defects [5]. It is important to immediately clean the wafers after CMP to avoid any residues. which are difficult to remove once the wafers are dry This is followed by another Si_3N_4 layer of 800Å thickness, which provides protection to the polysilicon from attack by EDP. Another thin dielectric layer is now deposited on the diaphragm area to provide isolation for the two electrodes of the capacitor and provide stress compensation. The dielectric layer on the anchor areas is patterned so as to cover only the anchor area and permit contact openings. Ti-Pt is evaporated so as to contact the polysilicon and produce a total height of about 500Å. At this point, the polysilicon is completely covered by a dielectric layer and has two metal contact areas. Due to the loss of some polysilicon during boron diffusion and CMP, the total height of the dielectric layer and polysilicon stack is about 2.8µm. Thus, we have a total recess depth of 9.8µm. This forms the working gap distance for the capacitor.

The glass processing consists of depositing approximately 250/350/1000Å of a composite Ti-Pt-Au layer. The Au is then etched back in the contact areas. The glass is partially diced at this point so that the devices can be easily separated after the wafer dissolution step. After this step, we perform wafer-level anodic bonding to 7740 glass in vacuum ($1x10^{-6}$ Torr); the structure is as shown in Fig. 3(g). Due to poor heat transfer in vacuum, it is important to first heat the wafers to 400°C in rough vacuum and then pump down the bonding chamber to higher vacuum levels. Also, pre-heating the wafers for 30 minutes helps out-diffusion of gases from the inner-walls of the sealed cavity, which is subsequently evacuated via the recessed areas between cavities when high vacuum is applied. While trying to bond wafers which have disjointed bond surfaces, a continuous bond front which can pull in the non-uniform parts of a wafer cannot be formed, and it is imperative that the surface flatness of the silicon wafer be uniform to obtain a high yield. Use of a graphite disk which covers the entire glass surface and an electrode pressure of at least 2500mbar also contribute significantly to a better bond yield. The next step is to dissolve the wafer in EDP to obtain the final structure as shown in Fig. 3(h). As can be seen, the diaphragm is heavily deflected under normal atmospheric conditions.

TEST RESULTS

The device was characterized for both dynamic behavior and DC parameters such as lead resistance and parasitic capacitance. The device was also tested after interfacing it to a switched-capacitor readout circuit. Calibration/compensation is done in software to achieve the resolution of 25mTorr. Each transducer has two redundant parallel lead transfers for each electrode with a nominal resistance of about 50 ohms and a TCO of 1000 ppm/°C. As mentioned earlier, the high parasitic capacitance observed with the first-generation device has been reduced to 500fF, which is about 5% of the nominal sensor capacitance. The parasitic capacitance is primarily dependent on the width of the rim, the thickness of the dielectric layer between the p++ silicon and the polysilicon, and the width of the polysilicon bridge formed in the poly-2 layer. An additional ring of Ti/Pt metal is used on the glass to reduce the open glass surface exposed to the cavity. The Ti is effective in gettering any O_2 ions outdiffusing from the glass. The gas pressure in the cavity has been characterized earlier [1] to be in the 200mTorr range. The additional Ti/Pt ring as seen in Fig. 2(b) along with the main metal electrode on glass effectively blocks the high electric field during bonding from the entire cavity. This is a necessary feature if future circuitry is to be placed inside the cavity [8,9,10]. The multi-lead structure also makes it feasible to have an independent metal electrode on the silicon isolated from the silicon body, thereby eliminating the need to protect the etched back silicon bulk during operation in humid environments. Fig. 4(a) shows the behavior of a typical device.

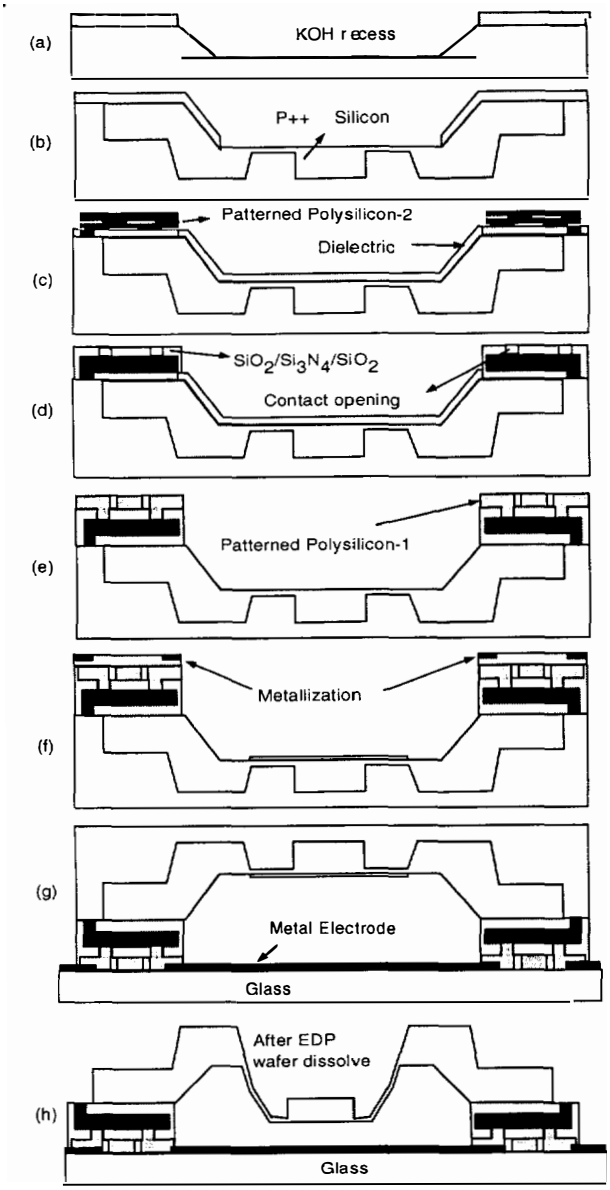

Fig. 3: Process flow for the multi-lead vacuum-sealed capacitive pressure sensor.

The nominal sensitivity for the segment devices is 24fF/Torr (2450 ppm/Torr). The TCO at 750 Torr is 1350ppm/°C and is primarily due to the mismatch of expansion coefficients of the anchor materials and the glass. The TCS is about 1000ppm/°C. The resolution of 25mTorr is achieved after interfacing to a programmable gain switched-capacitor readout circuit and doing digital compensation in software. In the case of this sensor, each transducer in the device has a range of about 50 Torr. The maximum pressure sensitivity after interfacing to a switched-capacitor circuit, while still covering the entire 50 Torr range, is

0.06mV/mTorr. In a 5V system, 25mTorr resolution is obtained using a 12b A/D after allowing some margin for noise. In this case, since we have software-programmable gain, we can use different transducers with higher gain to achieve a resolution of 25 mTorr.

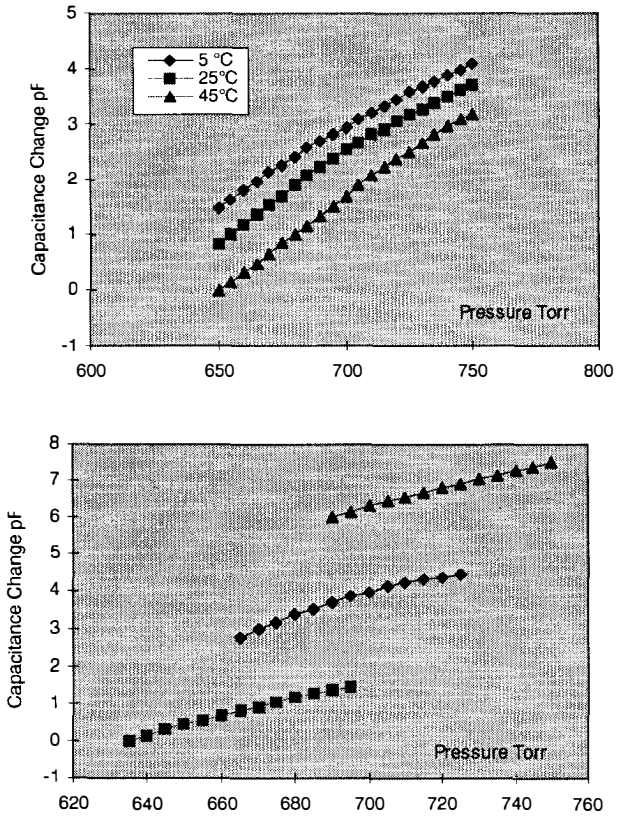

Fig. 4: (a) Typical pressure response for a single transducer over temperature. (b) Response of three different segment transducers.

In order to evaluate the long-term stability of the highly deflected boron-diffused membranes and the integrity of the polysilicon vacuum seals, we have been monitoring a number of of devices for over a year. The total observed variation in sensitivity of the global transducer was less than ±30ppm/mmHg for a baseline sensitivity of 1050ppm/mmHg. At room temperature, the variations in C_0 (the 760Torr, 25°C baseline capacitance) for the global transducer were less than ±12fF for a baseline C_0 of 12.050pF, measured using a HP4284A LCR meter. Some of these changes are likely due to present measurement accuracy. We see no significant unidirectional shift in baseline capacitance or in the sensitivity of these membranes. Long-term detailed testing of the devices is continuing using DH Instruments PPC2 calibrator.

CONCLUSIONS

A vacuum-sealed multi-lead/multi-transducer capacitive barometric pressure sensor employing a robust batch process has been fabricated. Two polysilicon layers are used to achieve lead transfers from the inside of the cavity and form a continuous sealing ring. A completely-isolated metal electrode on the silicon side can be used to eliminate need for passivation of the dissolved bulk silicon. Elimination of stiction problems, higher bandwidth capability, and adaptability to other glass-Si MEMS devices make this a suitable process for a variety of integrated MEMS applications. By operating at a gap spacing of between 0.3μm and 0.8μm, the sensor achieves a resolution of 25 mTorr under atmospheric offset pressures and has been stable for over one year.

ACKNOWLEDGMENTS

The authors would like to express their thanks to Mr. Larry Jordan of Delphi Delco Electronics Corporation and Jeff Kempinsky of the GM Research Laboratories for their assistance with the anodic bonding of the wafers. We would also like to thank Chuck Geyer of Logitech, Inc., for assistance with the CMP process. This project is supported by DARPA contract DABT63-95-C-0111. Abhi Chavan is supported by a fellowship from the Delphi Delco Electronics Corporation.

REFERENCES

[1]. A. V. Chavan and K. D. Wise, "A Batch-Processed Vacuum-Sealed Capacitive Pressure Sensor," *Digest IEEE Int. Conf. on Solid-State Sensors and Actuators (Transducers '97),* Chicago, pp. 1449-1452, June 1997.

[2]. J. Von Arx, B. Ziaie, M. Dokmeci, and K. Najafi, "Hermeticity Testing of Glass-Silicon Packages with On-Chip Feedthroughs," *Digest Int. Conf. on Solid-State Sensors and Actuators,* Stockholm, pp. 244-247, June 1995.

[3]. J. M. Giachino, et al., US Patents 4261086 (4/1981) and 4386453 (6/1983) and Peters, et al., US Patent 4586109 (4/1986).

[4]. M. Esashi, Y. Matsumoto and S. Shoji, " Absolute Pressure Sensors by Air-Tight Electrical Feedthrough Structure", *Sensors and Actuators,* A21-A23, 1990, pp. 1048-1052.

[5]. DeJule Ruth, "CMP Challenges below a Quarter Micron," *Semiconductor International*, November 1997, pp 55-60.

[6]. B. Puers, E. Peeters, A. Van Den Bossche and W. Sansen, "A Capacitive Pressure Sensor with Low Impedance Output and Active Suppression of Parasitic Effects", *Sensors and Actuators*, A21-A23, 1990 pp 108-114.

[7]. J. Sniegowski, "Chemical Mechanical Polishing: Enhancing the Manufacturability of MEMS," *SPIE Vol. 2879*, 1996, pp. 104-115.

[8]. C. Sander, J. Knutti and J. Meindl, "A Monolithic Capacitive Pressure Sensor with Pulse-Period Output," *IEEE Tran on Electron Devices,* Vol. ED-27, No. 5 May 1980, pp 927-930.

[9] Y. Gianchandani, K. J. Ma and K. Najafi, "A CMOS Dissolved-Wafer Process for Integrated p++ Microelectro-mechanical Systems", *Digest IEEE Int Conf on Solid-State Sensors and Actuators,* (Stockholm) pp. 79-82, June 1995.

[10]. T. Kudoh, Shuichi Shoji and Masayoshi Esashi, "An Integrated miniature Capacitive Pressure Sensor,"Sensors and Actuators, A-29, 1991, pp 185-193.

AN IMPLANTABLE PRESSURE SENSOR CUFF FOR TONOMETRIC BLOOD PRESSURE MEASUREMENT

Babak Ziaie, Tzu-Wen Wu, Namik Kocaman, Khalil Najafi, and David J. Anderson

Center for Integrated Sensors and Circuits
Department of Electrical Engineering and Computer Science
University of Michigan, 1301 Beal Avenue, Ann Arbor, Michigan 48109-2122
e-mail: babak@engin.umich.edu, Tel: (734) 936-1413, Fax: (734) 647-1781

ABSTRACT

This paper presents an implantable capacitive pressure sensor cuff for tonometric blood pressure measurement in unrestrained animals. A new structure and fabrication process have been developed which produce a flat surface necessary for tonometric pressure measurement. An array of three capacitive sensors is used to increase signal output and improve stability. A custom switched-capacitor CMOS interface circuit is used to measure changes in capacitance. *In-vitro* calibration tests have been performed on the complete cuff using a fluid-filled silastic tube to mimic a pliable blood vessel. A sensitivity of 2mV/mmHg @ 100mmHg and a resolution of 0.5mmHg (based on 1mV RMS interface chip noise floor) has been obtained. The cuff system measures 10mm×6.5mm×3mm.

INTRODUCTION

Chronic measurement of arterial blood pressure in small mammals is a cornerstone of basic research in hypertension and cardiovascular physiology **[1]**. Long-term baseline stability has been a major requirement, and still poses many challenges to the successful deployment of implantable pressure sensors. Most available implantable sensors are piezoresistive devices (e.g., Data Sciences International, Roseville, Minnesota, and Konigsberg Instruments Inc., Pasadena, California), and either penetrate the vessel (Konigsberg), or connect to the vessel via an indwelling catheter (Data Sciences Int.). Both methods are very invasive and carry the risk of creating blood clots. These sensors have a long-term baseline drift of > 5mmHg/month **[2,3]** which is excessive for applications in low pressure systems (e.g., venous and urogenital system) or experiments that require a few months of continuos monitoring. To overcome these shortcomings, we have developed a miniature capacitive pressure sensor cuff for tonometric blood pressure measurement **[4,5]**. Capacitive sensors have high sensitivity, low power consumption, and are less prone to package stress which is the main source of baseline drift **[6]**. This paper reports a new sensor structure based on the dissolved-wafer process, which produces a flat surface necessary for tonometric pressure measurement, and presents the development of a complete system consisting of a custom switched-capacitor CMOS interface circuit for sensor readout, as well as a custom designed package for use in eventual animal studies.

TONOMETRIC MEASUREMENT PRINCIPLE

Tonometry is a non-invasive technique for the continuos measurement of pressure in closed vessels (blood vessels, uterus, bladder, brain pressure). Figure 1 illustrates the principle of tonometric blood pressure measurement. The blood vessel is pressed flush against the sensor surface until appropriate flattening is achieved. According to Laplace's law, the pressure gradient across the vessel wall is given by:

$$P_{out} - P_{in} = \frac{T}{r} \qquad (1)$$

where *Pout* and *Pin* are the pressures outside and inside the vessel, respectively. *T* is the vessel wall tension, and *r* is the vessel radius. As can be seen, if the vessel wall is completely flattened against a smooth sensor surface ($r \rightarrow \infty$), the measured pressure will be equal to the intra-luminal blood pressure ($\Delta P \rightarrow 0$). Two important requirements regarding this measurement technique are: 1) the hold down force should flatten the vessel wall without creating occlusion, and 2) the pressure sensor diaphragm should be stiffer than the vessel wall. The second requirement is to ensure appropriate flattening and prevent any excessive bending of the vessel wall during the measurement.

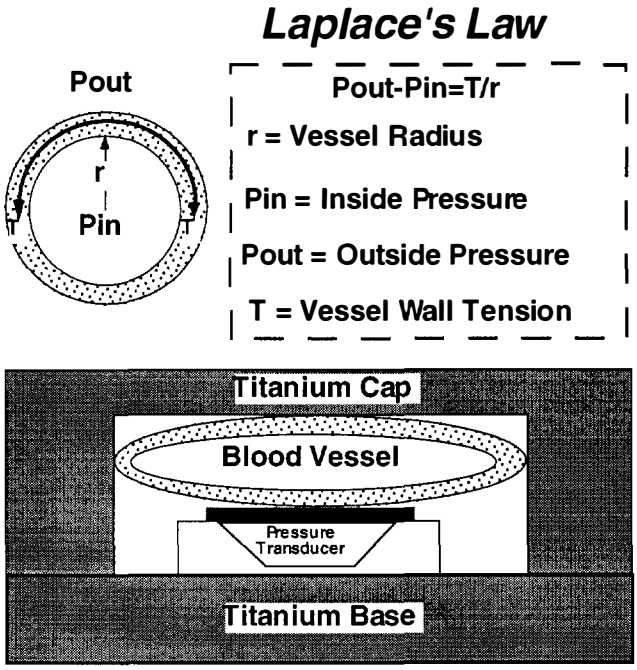

***Figure 1**: Basic principle of tonometric blood pressure measurement.*

MICROSYSTEM STRUCTURE AND DESIGN

Figure 2 shows the pressure sensor cuff microsystem for blood pressure measurement. The microsystem consists of four

0-9640024-2-6/hh1998/$20©1998TRF
DOI 10.31438/trf.hh1998.48

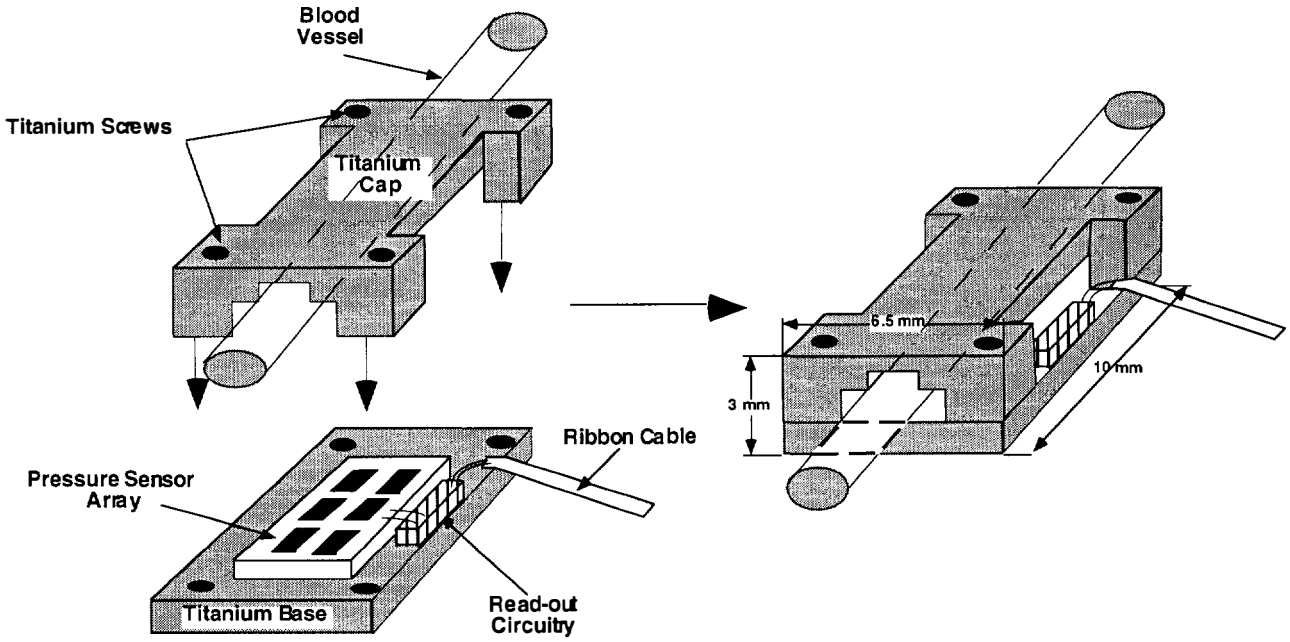

***Figure 2**: Pressure sensor cuff microsystem for tonometric blood pressure measurement.*

major components: 1) a titanium base for supporting the pressure sensor and interface chip, 2) a capacitive pressure sensor array, 3) a switched-capacitor interface chip, and 4) a titanium cap.

The assembly and packaging of the complete system is critical in reducing drift. The sensor and interface chips are mounted on a titanium base with medical grade silicone rubber (NuSil Silicone Technologies, Carpinteria, CA). The blood vessel is subsequently laid on top of the sensor, and a titanium cap is then clamped to the base using four miniature screws (Walter Lorenz Surgical, Jacksonville, Fl.), thus pressing the blood vessel flat against the silicon diaphragm. This assembly technique isolates the pressure sensor from package stress by preventing any direct contact between the transducer and the rest of the package except through the highly compliant silicone rubber adhesive.

The capacitive pressure sensor was designed to measure arterial blood pressure in small mammals. The measurement site was chosen to be rat's descending aorta (1.5-2mm in diameter, 0.1mm wall thickness). This location provides sufficient space to fit the pressure sensor cuff without exerting pressure on vital organs. Table 1 summarizes the design parameters for the pressure transducer. An array of three pressure sensors (1.5mm spacing) is located underneath the vessel to increase signal output and improve stability. In order to increase the sensitivity, a long rectangular diaphragm ($0.4 \times 1.4 mm^2$) was designed. The central deflection of a rectangular diaphragm under applied pressure is greater than a circular or an square diaphragm (assuming a width equal to the diameter or side of the circular or square diaphragm), and under large deflections is given by:

$$\frac{Pa^4}{Eh^4} = \frac{1}{\alpha(1-\upsilon^2)}\left(\frac{y}{h}\right) + \frac{1}{A^3}\left(\frac{y}{h}\right)^3 + \frac{\sigma a^2}{\beta E h^2}\left(\frac{y}{h}\right) \qquad (2)$$

where P is the applied pressure, y is the central deflection, a and h are the diaphragm width and thickness, E and υ are Young's modulus and Poisson's ratio of the diaphragm material, σ is the internal stress, and finally, α, β, and A are geometrical constants depending on the length to width ratio [7]. For the designed diaphragm a pressure of 100mmHg yields a central deflection of ~ 2μm. An initial (zero differential pressure) gap of 4μm was chosen for the pressure sensor to achieve enough sensitivity (~ 3fF/mmHg @ 100mmHg) while providing the required bandwidth (~ 50Hz).

***Table 1**: Design parameters for the pressure transducer.*

Pressure Range	0-300mmHg
Resolution	1mmHg
Base-line Drift	< 1mmHg/month
Frequency Response	0-50Hz

A custom-made switched-capacitor interface chip was designed to readout the sensor output. Figure 3 shows the block diagram of the interface chip. It consists of a charge integrator stage followed by a gain stage. The gain and the offset can be adjusted by laser trimming on-chip capacitors. Figure 4 shows the photograph of the interface capacitive readout chip. Table 2 summarizes important characteristics of the interface chip.

***Table 2**: Important characteristics of the interface chip.*

Clock Frequency	1kHz
Supply Voltage	3V
Power Consumption	120μW
Trimmable Offset Cap.	6.6 pF in 1,10,100,500fF Steps
Trimmable Gain	1-7
Resolution	1.4fF
Die Area	3.3mmx0.64mm

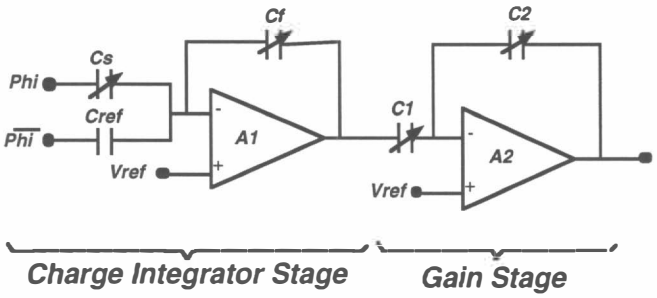

Figure 3: Block diagram of the interface readout circuitry.

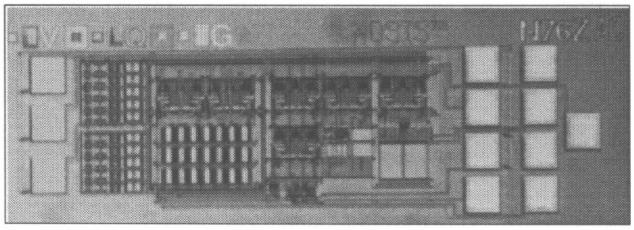

Figure 4: Photograph of an interface capacitive readout chip.

PRESSURE SENSOR FABRICATION

To form a flat sensor surface, we have developed a new structure and fabrication process (Figure 5), based on the dissolved-wafer process [6]. The capacitive air gap (~4μm) is formed by etching a recess in a glass substrate using $HF/HNO_3/DI$ (7:3:10, etch rate ~2.2μm/min). The glass substrate also supports Ti/Pt/Au (200Å/200Å/1000Å) lines to form the bottom capacitor plate and interconnect lines. A silicon wafer is patterned for a shallow boron diffusion step using an oxide mask (7500Å). A 2.5μm p++ diffusion is performed to create the pressure sensor diaphragms and bonding areas. This is followed by a thin oxide isolation layer (1000Å) deposition and patterning over the diaphragm areas. The silicon wafer is then electrostatically bonded to the glass wafer and the undoped silicon is dissolved away in EDP to form pressure sensors wherever there is a recess. This technique creates a perfect flat surface, and sealed cavities to prevent fluid accumulation and stiction during the silicon etch. Openings are formed in the silicon using a dry etch (NF_3=10sccm, O_2=15sccm, 200mT, 100W, etch rate ~3000Å/min) to provide access to bonding pads. Figure 6 shows a fabricated sensor array (dimensions ~ 4.8mmx5.7mm).

TEST RESULTS

In-vitro tests have been performed on the complete cuff using a fluid-filled silastic tube (Scientific Products, Deerfield, Ill.) to mimic a pliable blood vessel. The cavity of the pressure sensor was sealed using a high viscosity, low outgassing epoxy (Master Bond, EP51ND) at atmospheric pressure. It was then attached to the titanium base. A silastic tube was subsequently laid on top of the diaphragm and the titanium cap was screwed to the base. The silastic tube was subsequently pressurized with air using a handheld manometer pump. Figure 7 shows the photograph of an assembled unit, which measures 10mmx6.5mmx3mm. Figure 8 shows the measured output

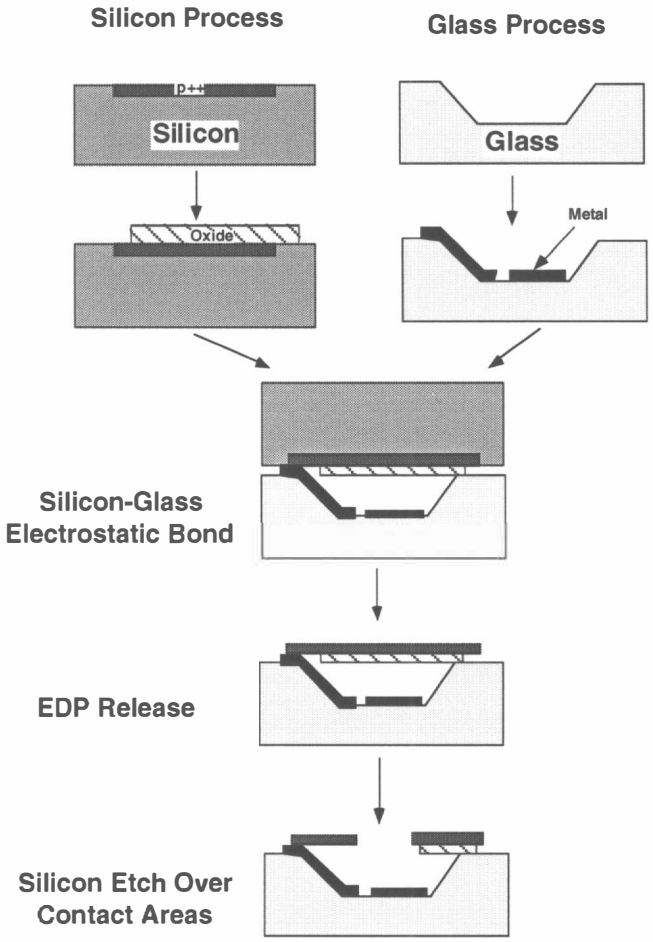

Figure 5: Fabrication process flow for tonometric blood pressure transducer.

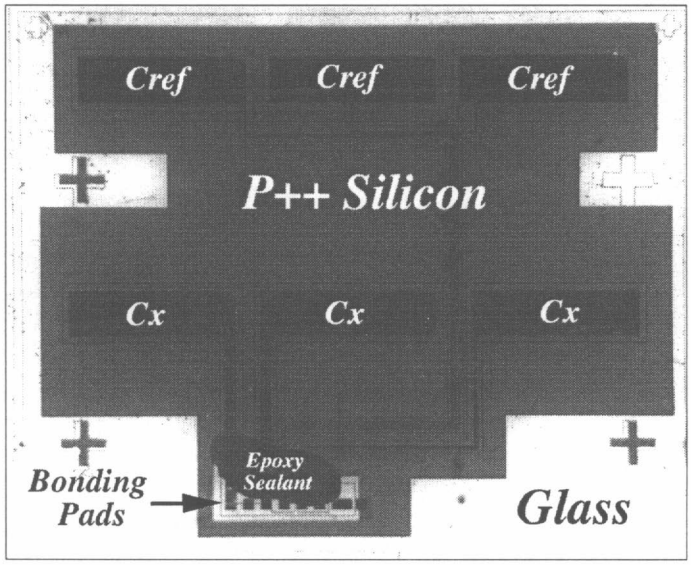

Figure 6: Photograph of a fabricated pressure sensor array.

voltage as a function of pressure in the silastic tube. A sensitivity of 2.0mV/mmHg @100mmHg and a resolution of 0.5mmHg has been obtained, as summarized in Table 3. The RMS value of output noise was measured to be ~ 0.5mV (peak-peak ~ 4mV). The major source of base-line drift in implantable pressure transducers is the package induced stress, which can be transferred to the transducer diaphragm. By using a compliant silicone rubber to attach the sensor to the package and isolating the sensor from the rest of the assembly, we anticipate to achieve a rather low base-line drift. To test the base-line stability, the pressure sensor output has to be monitored at a fixed temperature and pressure. This requires a controlled test setup to ensure a minimum interference from these variables. We are planning a controlled long term stability test and will report on our results in the future.

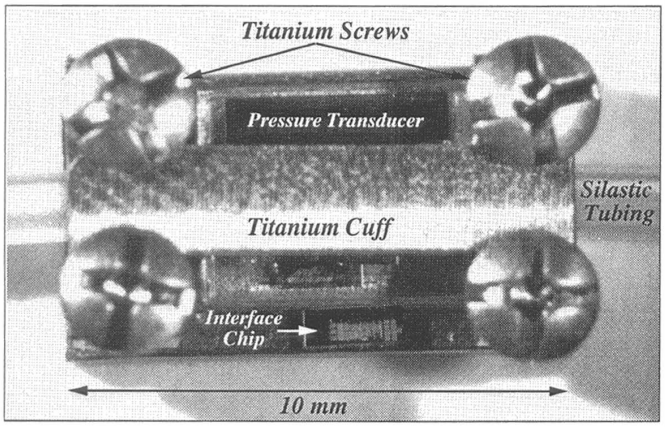

***Figure 7**: Photograph of an assembled unit showing various components of the microsystem.*

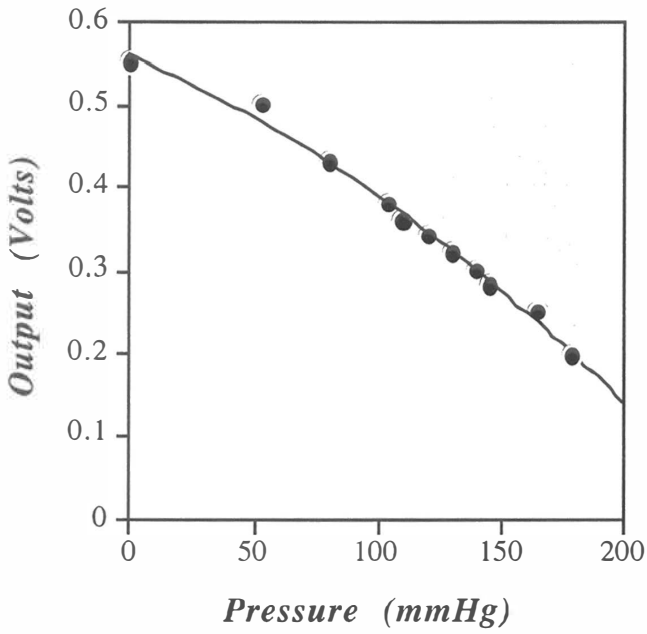

***Figure 8**: Pressure sensor calibration curve in the arterial blood pressure range with lowest gain setting.*

***Table 3**: Important characteristics of the pressure sensor cuff.*

Co	1.5pF
ΔC/ΔP @ 100mmHg	2.8fF/mmHg
ΔV/ΔP @ 100mmHg	2.0mV/mmHg
Interface Chip Noise	1mV, RMS
Resolution	0.5mmHg
Sensor Chip Dimensions	4.8mmx5.7mm
Ti Cuff Dimensions (H x W x L)	3mmx6.5mmx10mm

CONCLUSION

A biomedical microsystem for tonometric blood pressure measurement using micromachining techniques has been developed. This system is the smallest implantable pressure cuff that includes an integrated package, a completely planar capacitive sensor, and an on-board interface circuit (dimensions ~ 3mmx6.5mmx10mm).. A titanium base supports a planar pressure transducer and a custom-made switched-capacitor interface chip. The blood vessel is positioned on top of the sensor and a titanium cap is screwed to the base to clamp the vessel. *In-vitro* tests have shown a sensitivity and resolution of 2.0mV/mmHg and 0.5mmHg at 100mmHg, respectively. The interface chip has a noise floor of 1mV RMS. Long term base-line stability tests under controlled environment are planed.

ACKNOWLEDGMENTS

The authors wish to thank Mr. John W. Hines and Dr. Chris. J. Somps of the NASA Ames research center for their support and encouragement. We would also like to thank Walter Lorenz Surgical for their generous help in providing miniature titanium screws. This work is supported by the National Aeronautics and Space Administration (NASA), under grant NAWG-4494.

REFERENCES

[1] T. P. Broten *et al.*, "Techniques for the Measurement of Arterial Blood Pressure," in *Measurement of Cardiovascular Function*, J. H. McNeil Ed., CRC Press, 1997.

[2] B. Brockway, *et al*, "A New Method for Chronic Measurement and Recording of Blood Pressure, Heart Rate and Activity in the Rat via Radio-Telemeter," in *Clin. and Exper. Hyper.-Theory and Practice*, A13(5), pp. 885-895, 1991.

[3] Konigsberg Instrument, Inc., *Biomedical Product Cathalog*, April 1994.

[4] G. M. Drzeweicki, J. Melbin, and A. Noordergraaf, "Arterial Tonometry: Review and Analysis," *J. Biomechanics*, Vol. 16, No. 2, pp. 141-152, 1983.

[5] S. Terry *et al.*, "Silicon Pressure Transducer Arrays for Blood Pressure Measurement," *Sensors and Actuators*, A21-A23, pp. 1070-1079, 1990.

[6] H. L. Chau, and K. D. Wise, "An Ultraminiature Solid-State Pressure Sensor for a Cardiovascular Catheter," *IEEE Trans. Electron Devices*, Vol. ED-235, pp. 2355-2362, Dec. 1988.

[7] M. Di Giovanni, *Flat and Corrugated Diaphragm Design Handbook*, Marcel Dekker, New York, 1982.

FABRICATION OF HIGH-DENSITY CANTILEVER ARRAYS AND THROUGH-WAFER INTERCONNECTS

Eugene M. Chow, Hyongsok T. Soh, Aaron Partridge, Jonah A. Harley, Thomas W. Kenny, and Calvin F. Quate
E. L. Ginzton Laboratory, Stanford University
Stanford, CA 94305-4085

Shahram Abdollahi-Alibeik and James P. McVittie
Center for Integrated Systems, Stanford University
Stanford, CA 94305

Anthony McCarthy
Lawrence Livermore National Laboratory
Livermore, CA 94551

ABSTRACT

Processes to fabricate dense, dry released microstructures with electrical connections on the opposite side of the wafer are described. A 10 × 10 array of silicon and polysilicon cantilevers with high packing density (5 tips/mm^2) and high uniformity (<10 μm length variation across the wafer) are demonstrated. The cantilever release process uses a deep SF_6/C_4F_8 plasma etch followed by a HBr plasma etch to accurately release cantilevers. A process for fabricating electrical contacts through the backside of the wafer is also described. Electrodeposited resist, conformal CVD metal deposition, and deep SF_6/C_4F_8 plasma etching are used to make 30 μm/side square vias each of which has a resistance of 50 mΩ.

INTRODUCTION

Since the invention of the atomic force microscope [**1**], micromachined cantilevers have found applications in surface science [**2**], lithography [**3,4**], data storage [**5**], and biological sensors [**6,7**]. While scanning probe devices have proven their importance in many areas of science and engineering, they suffer from slow speeds and long scan times, because the scanning probe is inherently a serial device. Parallel operation of an array of scanning probes will address this problem as system bandwidth, scan area, and reliability (through redundancy) are increased.

Specific requirements for an array of scanning probe devices vary with application, but generally include: 1) fabrication of cantilevers with high yield and density and, 2) a method of addressing each cantilever electrically for sensing and/or actuation. Also, if circuitry is to be integrated on the same chip, the fabrication process must conform to standard CMOS processing techniques.

High densities and yields, however, are not easily achievable with conventional processing. Cantilevers are typically released by etching through the entire wafer from the backside. Because etch profiles are restricted to crystallographic planes, potential cantilever density is severely limited, as demonstrated in Fig. 1. Also, process yields are often low because of front side protection. Protecting a front-side metal layer, which is necessary for a one-sided etch in liquid, is difficult for the long durations and elevated temperatures needed for etchants such as TMAH and KOH. Stiction, especially for thin and long cantilevers, is another source of yield reduction for wet processes.

The requirement for electrical connections is particularly challenging for two-dimensional arrays. Interconnects for each cantilever are needed when piezoresistive or piezoelectric effects are utilized. Addressing all of these elements is complicated by the need to keep bonding wires out of the scanning region, which could be only a few microns above the sample. Hence, it is important to be able to place the array element on the front side of the wafer, while electrically connecting them to the bond pads on the backside of the wafer. Such through-wafer contacts have been demonstrated with wet etching, but this exacerbates the density problem depicted in Fig. 1 [**8**].

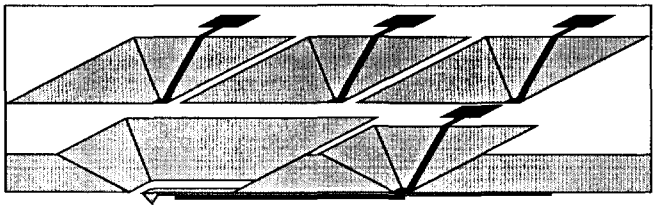

Figure 1. *Drawing of a wet released cantilever and its through wafer electrical contacts (with four leads.) For a 100 μm × 500 μm release region with one cantilever per release region, using a 500 μm thick wafer, tip densities are limited to < 0.3 tips/mm^2.*

To address these issues, we have developed high-yield fabrication processes to release dense cantilever arrays, and create small, through-wafer interconnects. A key advance is to replace wet etches with deep, anisotropic etching with high density low pressure (HDLP) plasmas [**9**]. Cantilever densities more than an order of magnitude greater than that possible with wet etching are achieved, implying that significantly shorter scan times (Fig. 2) are now possible.

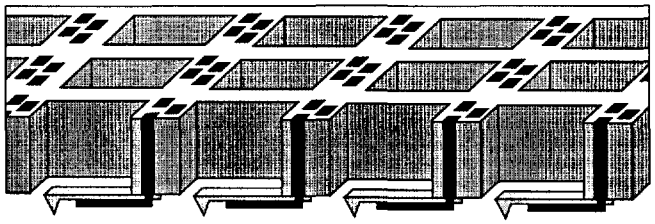

Figure 2. *Cross section drawing of anisotropic released cantilevers with through wafer electrical contacts. For a 100 μm × 500 μm release region with one cantilever per release region, and using a 500 μm thick wafer, tip densities of >20 tips/mm^2 are achievable.*

0-9640024-2-6/hh1998/$20©1998TRF
DOI 10.31438/trf.hh1998.49

The cantilever release process uses a two part etch, a deep SF_6/C_4F_8 plasma etch followed by a well controlled HBr plasma etch. The process is uniform and capable of releasing thin cantilevers which are CMOS compatible and applicable to other structures. Dense arrays of cantilevers (5 tips/mm^2) with high yields and uniform mechanical properties (< 10 μm length variation) across the wafer are demonstrated.

Through-wafer vias (TWV) which are 30 μm/side and with a resistance of 50 mΩ/via have also been fabricated. This resistance is significantly less than that of typical piezoresistor sensors used in cantilevers (~1 kΩ.) In addition to benefiting cantilever technology, this process can be applied to circuits (i.e., ground connections in mixed signal circuits), packaging (i.e., multi-chip stacking) and MEMS (i.e., 3D structures.) Critical steps include HDLP etching, conformal metallization by CVD, and patterning of high-aspect ratio holes using electrodeposited resists.

CANTILEVER ARRAYS

The cantilever dry release process, summarized in Fig. 3, starts with a 4" silicon-on-insulator (SOI) wafer or a layer of polysilicon on silicon dioxide. First the cantilevers are patterned into the device layer. At this time piezoresistive sensors and/or on-chip CMOS circuitry can be integrated. For the process demonstrated, simple optical detection cantilevers (200-400 μm long, 5-50 μm wide and 1-3 μm thick) without integrated sensors were fabricated.

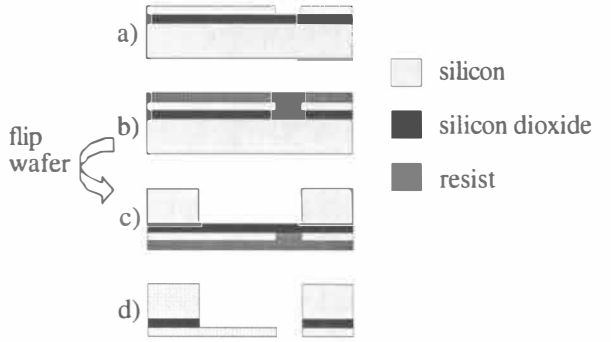

Figure 3. Cantilever Process. a) Pattern cantilevers into device layer. b) Coat with support resist. c) Pattern backside and HDLP etch through wafer stopping on buried oxide layer. d) HF vapor etch oxide and plasma etch the resist for final release.

The cantilevers are then coated with photoresist which will be used as a sacrificial support layer for the final release. Next, the backside of the wafer, polished or unpolished, is patterned with a backside release mask of 8 μm photoresist (Shipley AZ4620). A two part anisotropic HDLP etch is then performed to release the underside of the cantilevers. An aggressive SF_6/C_4F_8 based plasma etch is used to etch through the entire wafer (~500 μm) until the buried oxide layer is reached. Another HDLP etch is then performed using an HBr dominated chemistry to complete the etch in a controlled manner. These HDLP etches will be discussed in detail later.

Then the buried oxide layer is etched in a concentrated hydrofluoric acid (HF) vapor, performed at room temperature and pressure. With the absence of surface tension effects, vapor reaches the bottom of high aspect ratio holes easier than wet etchants. Brief heating of the wafer prior to etching reduces water condensation on the wafer, making more exotic HF vapor etching techniques unnecessary [10]. The thick support resist above the cantilevers enabled a water rinse, which was necessary to remove silicon shards left from the backside etch. Finally the top layer photoresist is stripped in an oxygen plasma to free the cantilevers.

The deep part of the two part etch is performed in a commercial high density low pressure (HDLP) plasma etcher, which uses separate RF sources for the plasma generation (coil) and ion acceleration (substrate platen) [11]. The anisotropy is obtained by alternating between etching and passivating processes. The etch part employs a 600 watt coil, 120 watt platen, 130 sccm SF_6 flow, and 15 mTorr chamber pressure. The passivation is performed at identical plasma power and pressure, but uses 85 sccm of C_4F_8 with no platen power. A repeating cycle of etching for 11 seconds alternating with passivation for 8 seconds resulted in near vertical walls and an etch rate of 4.5 μm/min.

The cantilever release pattern consists of a die with a 10 × 10 array of 100 μm × 500 μm areas. Carefully measuring the etch rate for this pattern enabled consistent stopping on the oxide without overetching. Figure 4 shows a completed deep etch through the wafer, which has stopped on the buried oxide layer. The etch was uniform and selective enough to fully etch die throughout the wafer with only 3800Å of thermally grown silicon dioxide (a common SOI thickness) as an etch stop layer.

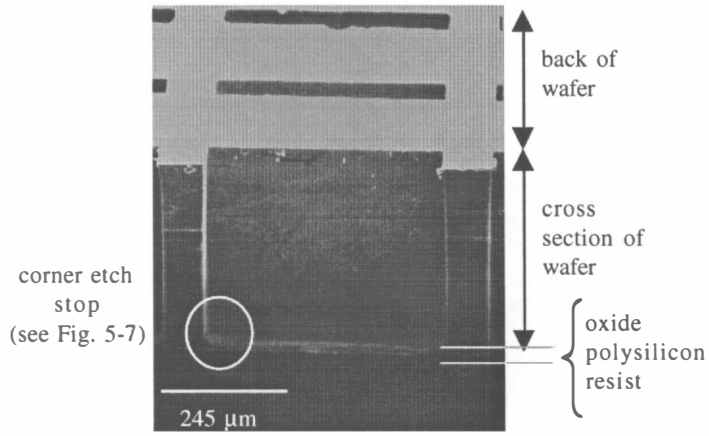

Figure 4. Cross section of a cantilever release region after a deep SF_6 etch through the backside of the wafer. The etch proceeded downward in the picture until reaching the oxide and device layer. The oxide and device layers are supported by thick photoresist. The cantilever is not in the picture.

Critical to the effective length of the cantilevers is the accuracy of the backside etch. The definition of the cantilever base needs to be consistent over a die so that the mechanical characteristics of the cantilevers are uniform throughout the array, facilitating plans for individual cantilever controller and sensor design [4]. Wafer scale uniformity is important for increasing functional device yields. Unfortunately, the uniformity of the etch is such that overetching on the order of minutes is required to clear die throughout the wafer. Using the fluorine based HDLP etch, however, causes extreme lateral silicon etching at the oxide interface, as depicted in Fig. 5.

This can be minimized at a certain radius of the wafer by near perfect timing, but neighboring die will exhibit lateral etching. This is likely because fluorine has the ability to etch silicon spontaneously, without ion bombardment [12]. When the etch reaches the oxide there is a sudden increase in fluorine radicals as the vertical silicon etching has stopped. This increased fluorine etches through the sidewall passivation at the base of the hole, and etches into the silicon. Thus the aggressive SF_6/C_4F_8 works well for etching anisotropically and quickly, but does not consistently define the cantilever base throughout the wafer.

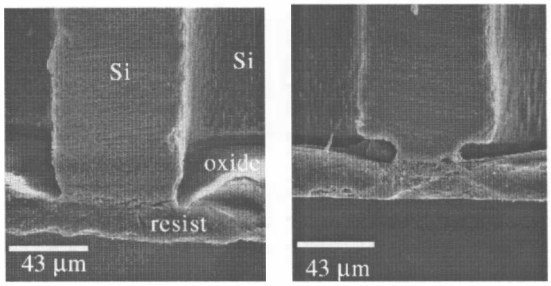

a) b)

Figure 5. *The aggressive SF_6/C_4F_8 based HDLP etch can be carefully timed for a well defined stop in the middle of the wafer (a), but the edge of the wafer still experiences severe lateral silicon etching. These views have the same orientation as figure 4, with the device layer beneath the oxide.*

To control the oxide stop, an HBr based HDLP etch is used to finish the backside etch. First the deep etch is stopped early so that silicon feet, shown in figure 6, are left at the cantilever bases throughout the wafer. Then another commercial HDLP etcher, also with separate coil and platen RF sources, but without the sequential etch/passivate ability, is used [13]. Operating at 10 mTorr, with an RF coil power of 250 watts and platen power of 60 watts, HBr (150 sccm flow) and O_2 (15 sccm flow) are simultaneously used to etch the remnant silicon feet. The chemistry of this etch does not permit rapid lateral silicon etching at the oxide interface, as ion bombardment is necessary for activation of the silicon etch [12]. Combined with a high silicon-to-oxide etch selectivity (>200:1), controllable rates (3000 Å/min for Si), and high anisotropy, this etch is ideal for clearing out the remnant silicon feet in a controlled manner. Since overetching can be tolerated, the cantilever bases can be well defined throughout the wafer (Fig. 7).

A completed cantilever array is shown in Fig. 8. A density of 5 tips/mm^2 is demonstrated here, though higher densities are possible with this process. Near perfect yields were obtained, as out of 45 die per wafer, typically 2-3 of the die had single defects. As shown in Fig. 7, the two part etch results in a silicon foot length deviation of 5 µm or less, which is a significant improvement over the 20 µm variations typical of the SF_6/C_4F_8 etch stop. With longer HBr etching, this variation between the center and edge of the wafer could be reduced, especially since the chemistry of the etch tolerates overetching.

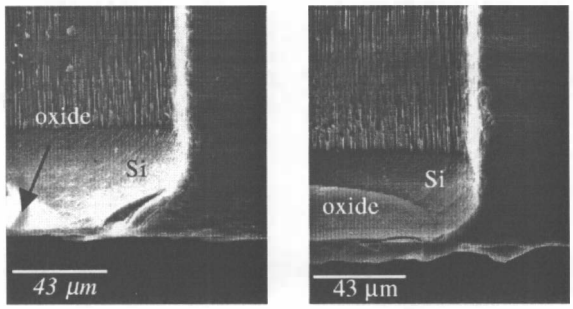

b)

Figure 6. *The deep etch is timed to leave a silicon foot in the center (1) and edge (b) of the wafer. The oxide and device layer is supported by thick photoresist.*

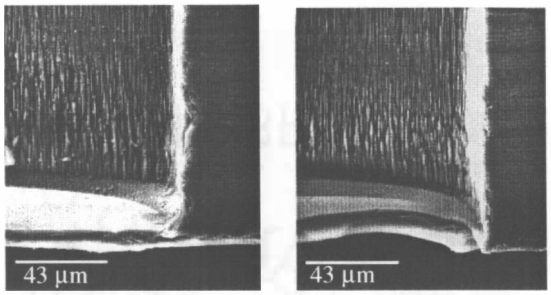

a)

Figure 7. *The HBr based HDLP etch clears out the remnant silicon foot in a controlled manner in the middle (a), and edge (b) of the wafer.*

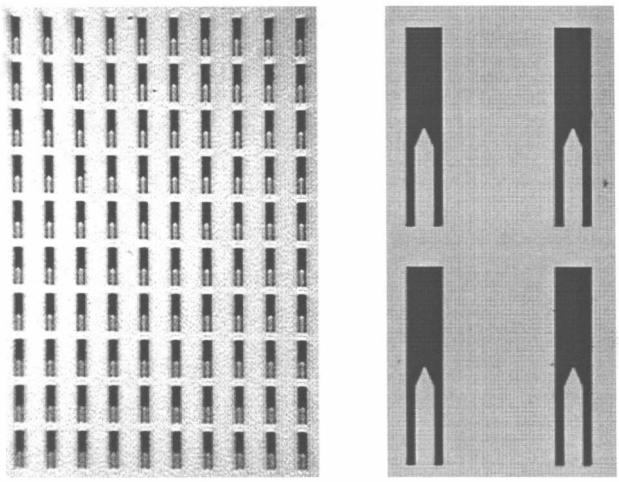

a)

Figure 8. *a) Optical photographs of a finished 10 × 10 array of cantilevers, with release regions of 100 µm × 500 µm each. b) Close up of the same array. These cantilevers are made of polysilicon, and are 50 µm wide, 200 µm long, and 1.6 µm wide.*

More work needs to be done to improve the absolute accuracy of the etch profile, which is important for this application. The etch profiles are currently slanted out (getting larger as they proceed down) by 1 to 1.5 degrees. Over the thickness of the wafer this generates about a 10 μm absolute error in effective opening area, with a variation of 5 μm. Thus the profile and lateral etch effects combined give less than 10 μm variation in effective cantilever length over the wafer. Further tuning of the etch to passivation time ratio should help rectify the deep profiles.

Another issue is the observation of severe lateral silicon etching at the oxide interface along the longer side (500 μm side) of the cantilever release region. The current uniformity of the deep SF_6/C_4F_8 etch make this unavoidable because the etch rate is slower along the short side of a release region (100 μm side.) This lateral etching on the long side, similar to that pictured in Fig. 5b, does not effect these cantilevers because the cantilever base is only along the short side. However, unless it can be controlled, this phenomena suggests that architectures with multiple cantilevers along the same side in a release region will be difficult to release with the precision demonstrated in this work.

THROUGH-WAFER INTERCONNECTS

In addition to fabricating a high-density array, we have developed techniques to create electrical connections through the wafer. We report here on the fabrication of through-wafer vias (TWV) with small size, ultra-low resistance, and CMOS processing compatibility.

The TWV process consists of three main steps: 1) etching of a high-aspect ratio trench through the wafer, 2) electrical isolation and conformal metallization of the high aspect ratio trench, and 3) patterning of the top and bottom sides of the wafer while protecting the metallized via. The process is outlined in Fig. 9. The substrate is a p-type, 4-inch, 525 μm thick, 10 Ω-cm, double-polished silicon wafer. First, the square vias are patterned using 16-um thick photoresist (Shipley AZ4620). Then vias are etched with the same deep HDLP etcher described in the previous section. Since the vias are 30 μm/side and their depths are 525 um, the aspect ratio of the vias is 17.5:1 (Fig. 9a). The etch rate of the vias is 2.2 μm/min.

To isolate each via electrically, a 1 μm thick thermal oxide is grown at 1100°C. Then, a 1.5 μm thick undoped polysilicon layer is deposited using low pressure chemical vapor deposition (LPCVD) (Fig. 9b). Both the thermal oxide and LPCVD polysilicon are completely conformal on the sidewalls of the vias. The polysilicon serves as the sticking layer for the 250 nm thick CVD copper since the adhesion of the CVD copper is poor on thermal oxides. To decrease the resistance of the vias, a 6 μm thick copper layer is electroplated on top of the CVD copper (Fig. 9c). The resulting sheet resistance is 2.8 mΩ/□. The electroplated copper has good sidewall coverage on the high aspect-ratio vias as shown by the low resistance.

Photolithography over widely varying topography is difficult using a conventional spin-on type photoresist, unless the surface is planarized. Direct application of a spin-on resist over deep trenches or tall mesas creates streaks which cause serous problems during exposure. In addition, it does not coat the inside of the vias where the metal must be protected. To overcome this problem, we used an electrodeposited photoresist (Shipley PEPR 2400)[**14**]. The resist was 7 μm thick on both the top and the bottom sides of the wafer, and it coated the walls of the vias so that the metal is protected. The resist was then exposed on a standard mask aligner (Fig. 9d). Finally, the copper layer is wet etched in (Fig. 9e) and the polysilicon is dry etched in a conventional SF_6 plasma (Fig. 9f). A finished TWV, depicted in Fig. 10, had a resistance of 50 mΩ.

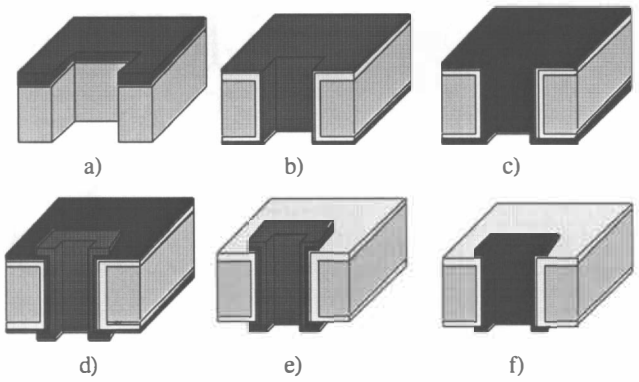

Figure 9. *Through wafer via process. a) Etch via through the wafer. b) Isolate vias with thermal oxide and deposit LPCVD polysilicon sticking layer. c) CVD and then electroplate copper. d) Electrodeposit and pattern resist. e) Wet etch copper and f) plasma etch polysilicon to complete TWV.*

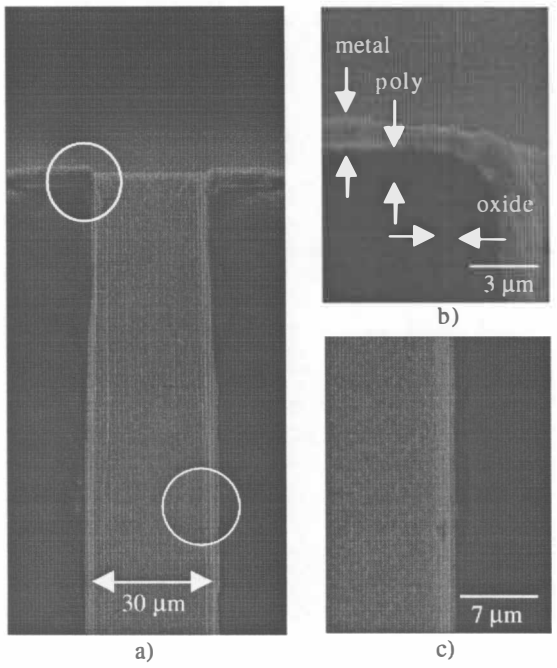

Figure 10. *Cross sectional SEM micrographs of a through wafer via. a) The via is 30 μm wide and 525 μm deep. Deposited films have good step coverage at b) the corners and at c) the sidewalls.*

CONCLUSION

The ability to fabricate high density, two-dimensional arrays of micromachined cantilevers with backside contacts is critical to the continued advancement of scanning probe technologies. We have reported here on CMOS compatible fabrication techniques which accurately release structures throughout an entire wafer, and form small, ultra-low resistance electrical contacts between the front and back side of the wafer.

Precise HDLP etching with SF_6/C_4F_8 and then HBr are key steps in the cantilever release process, which produces cantilevers with good uniformity (< 10 µm length variation) and high yields throughout the wafer. Probe densities of 5 tips/mm^2 are demonstrated with a 10 x 10 array of cantilevers, though higher densities are possible with this process. Small (30 µm/side), through wafer vias with ultra-low resistance (50 mΩ/via) have also been demonstrated. HDLP etching, CVD copper, and electrodeposited resist result in interconnects with a resistance well below that necessary for piezoresistive cantilever sensing.

Current work includes integrating the two processes and adding integrated piezoresistive cantilevers and tips. Further profile optimization of the deep HDLP etch is also ongoing.

ACKNOWLEDGEMENTS

This work was supported by the National Science Foundation (NSF), Defense Advanced Research Projects Agency (DARPA)/ U.S. Air Force (contract no. 30602-97-2-0103), and the U. S. Department of Energy at Lawrence Livermore National Laboratory (LLNL) (contract no. W-7405-ENG-48.) The authors thank V. Malba and C. Harvey at LLNL, Bill Martin, Marnel King, Karl Brandt and the rest of the staff at the Stanford Nanofabrication Facility.

REFERENCES

1. Binning, G, Quate, C. F., Gerber, C., "Atomic force microscope," *Physical Review Letters*, *56* (9), 930-933 (1986).

2. Quate, C.F., "The AFM as a tool for surface imaging", *Surface Science*, *299-300*, (1-3), 980-95 (1994).

3. Soh, Hyongsok T., *et al.*, "Fabrication of 100 nm pMOSFETs with hybrid AFM/STM lithography", *Proceedings of the 1997 Symposium on VLSI Technology*, Kyoto, Japan. Digest of Technical Papers - Symposium on VLSI Technology 1997. IEEE, Piscataway, NJ, USA, pp 129-130.

4. Minne, S.C., *et al.*, "Parallel atomic force microscopy using cantilevers with integrated piezoresistive sensors and integrated piezoelectric actuators", *Applied Physics Letters*, *67* (26), 3918-20 (1995).

5. Chui, B. W., *et al.*, "Improved cantilevers for AFM thermomechanical data storage", *Technical Digest of the 1996 Solid-State Sensor and Actuator Workshop,* Hilton Head Isl., SC, 6/2-6/96, Transducer Research Foundation, Cleveland (1996), pp.219-224.

6. Shao, Z., *et al.*, "Biological atomic force microscopy: what is achieved and what is needed", *Advances in Physics, 45* (1) 1-86 (1996).

7. Baselt, D. R., *et al.*, "A high-sensitivity micromachined biosensor", *Proceedings of the IEEE*, *85* (4), 672-680 (1997).

8. S. Linder, *et al.*, "Fabrication Technology for wafer Through-Hole Interconnections and Three-Dimensional Stacks of Chips and Wafers", *Proceedings IEEE Micro Electro Mechanical Systems An Investigation of Micro Structures, Sensors, Actuators, Machines and Robotic Systems*, Oiso, Jap. (1994), pp. 349-54.

9. M. Lutwyche, *et al.*, "Microfabrication and parallel operation of 5x5 2D AFM cantilever arrays for data storage and imaging", *Proceedings IEEE International Workshop on Micro Electro Mechanical Systems"*, Heidelberg, Germany (1998), pp. 8-11.

10. Y. I. Lee, *et al.*, "Dry release for surface micromachining with HF vapor-phase etching", *Journal of Microelectromechanical Systems*, *6* (3), 226-233 (1997).

11. Bhardwaj, J, *et al.*, "Advanced silicon anisotropic processes", *European Semiconductor, 19* (7), 35-6, 39 (1997).

12. G. S. Oehrlein, in *Handbook of plasma processing technology,* edited by S.M. Rossnagel, J.J. Cuomo, and W.D. (Westwood, Noyes Publications, New Jersey, 1990).

13. J. B. Carter, *et al.*, "Transformer coupled plasma etch technology for the fabrication of subhalf micron structures", *Journal of Vacuum Science Technology A, 11* (4), 1301-06 (1993).

14. P. Kersten *et al.*, "Photolithography on a micromachined 3d surface using electrodeposited photoresists", *Sensors and Actuators, Physical A*, *51*, 51-4 (1995).

POST-PACKAGING RELEASE
A NEW CONCEPT FOR SURFACE- MICROMACHINED DEVICES.

Balaji Sridharan, Chang-Jin "CJ" Kim and Long-Sun Huang
Mechanical and Aerospace Engineering Department
University of California, Los Angeles, CA 90095-1597

ABSTRACT

A novel procedure of post-packaging release, i.e., releasing surface-micromachined elements "after" packaging has been performed, is presented in this paper. This new concept of "post-packaging release" makes MEMS packaging considerably less demanding and thus much cheaper by completing most of the packaging steps "before" the delicate microstructures are released (freed). The concept has been successfully demonstrated with two types of test chips (MCNC MUMPs processed) by sublimation release after packaging. The concept of post-packaging release is even more attractive if the sacrificial layer can be removed by vapor-phase etchants such as HF vapor (for oxide) or XeF_2 or BrF_3 (for silicon), since a full spectrum of bonding methods are compatible.

INTRODUCTION

Packaging of MEMS devices starts usually after micromachining is complete, i.e., after microstructures are released (freed). During packaging the microstructures are free to move and are susceptible to damage as a result of improper handling. This paper presents a unique concept which makes devices more rugged during packaging and hence less susceptible to damage. This concept coined "post-packaging release" refers to releasing microelements on the chip after it is housed by a cap and protected. Two methods of post-packaging release are discussed, and the concept has been successfully verified using one of the methods.

Concept

Post-packaging release using sublimation release technique: In this method, the sacrificial layer is removed in wet chemicals but, without ever being dried, the microstructures are embedded in a coating that can be sublimated after packaging has been performed. Release holes are provided on the cap wafer for this purpose. This concept is schematically illustrated in Figure 1(a) and will be experimentally verified in this paper.

Post-packaging release using vapor-phase release technique: In this method of performing post- packaging release, the sacrificial layer is not removed until packaging has been performed. Examples are removing oxide with HF vapor **[1]** or removing silicon with XeF_2 **[2]** or BrF_3 **[3]**. This concept is being proposed as schematically shown in Figure 1(b) but yet to be experimentally tested. The advantage is that a whole spectrum of bonding methods can be employed, whereas the sublimation technique is restricted by the melting point of the sublimation solid.

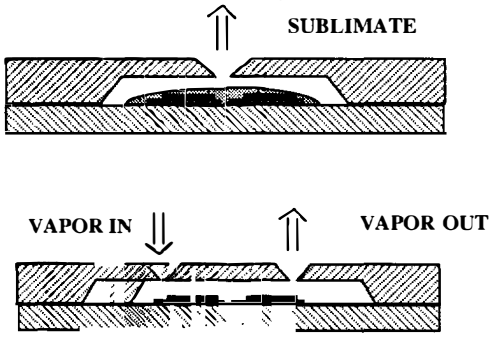

Figure 1. *Post- packaging release: concept (a) Sublimation release, (b) Vapor- phase release*

Sublimation

Sublimation release procedure was initially developed in MEMS community as a method to prevent stiction of microelements during the process of releasing surface-micromachined devices (e.g. **[4]**). While freeing microstructures by drying, the devices are pulled down to the substrate as a result of surface tension. If the devices contact the substrate, permanent sticking of the devices to the substrate may be brought about by molecular range interactions (e.g. hydrogen bonding and van der Waals forces). One method of preventing this phenomenon of stiction is to avoid the formation of liquid-air interface between the microstructures and the substrate. The sublimation release procedure avoids the formation of liquid-air interface by forming a solid-air interface and thus completely avoids the pull down force and thereby prevents stiction during release. Two convenient sublimation materials are p-dichlorobenzene **[4]** and t-butyl alcohol **[5]**.

EXPERIMENT

Fabrication of base and cap wafer

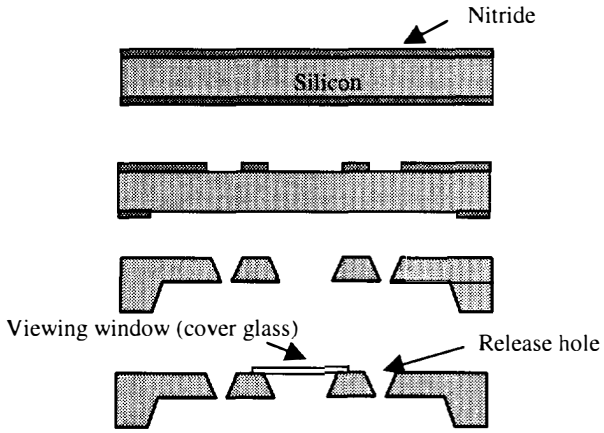

Figure 2. *Fabrication of cap wafer*

The cap wafer for post-packaging release has to be fabricated to provide release holes for sublimating the solid substance and also to provide a transparent window on the top for demonstration purposes to observe the released microstructures after packaging has been performed. The fabrication of the cap wafer starts by growing a thermal oxide on a (100) silicon wafer and deposition of a silicon nitride by LPCVD as an etch mask for KOH. The mask for the release holes is then patterned on the top side of the cap wafer, and the mask for the cavity to enclose the microdevices is

0-9640024-2-6/hh1998/$20©1998TRF
DOI 10.31438/trf.hh1998.50

Solid-State Sensors, Actuators, and Microsystems Workshop
Hilton Head Island, South Carolina, June 8-11, 1998

patterned on the bottom side using a front-to-back side aligner (Karl Suss). After this process of double side alignment and patterning, the cap wafer is sculptured by etching in KOH to complete the formation of release holes and the cavity. If a viewing window is used, a large extra hole is made on the cap wafer and covered with a thin cover glass as shown in Figure 2.

The base wafer has to be fabricated in a way to accommodate a typical surface-micromachined chip. Hence, the base wafer is made by bonding two silicon wafers, one of which is etched through (before bonding) using KOH. The wafer with the through hole is then patterned with gold bonding pads to provide electrical connection through wire bonding to activate the devices on the test chip after packaging has been completed. The bond pads are fabricated by doing a Ti/Au lift-off process. The Ti serves as an adhesion promoter for gold on silicon. This bulk-etched wafer is then bonded to another bare silicon wafer to complete the base wafer assembly.

Procedure

After the completion of the base and cap wafer as outlined in the earlier section, a test chip (MCNC's Multi-User MEMS Processes) is released using HF (49%) for 2-2.5 minutes. This time is usually more than sufficient to completely etch away the sacrificial PSG (phosphosilicate glass) and release the microstructures. After two successive rinses are carried out in DI water for 10 minutes each, the chip is then transferred to a methanol bath. The reason for this rinse step is that the p-dichlorobenzene is soluble in methanol and it is necessary to replace the DI water from the previous step with methanol before introducing p-dichlorobenzene. After this the chip is transferred to another bath with methanol maintained at around 60°C as the elevation in temperature helps the solubility of methanol in p-dichlorobenzene. For the purpose of post-packaging release it is necessary that only a thin coating of sublimation solid remains on the surface. Thin coating is necessary to ensure that the chip with the coating can be accommodated in the cavity provided in the cap wafer. This thin coating is achieved by the following process. After the final rinse in liquid p-dichlorobenzene, the chip with a thick coating of p-dichlorobenzene is placed on a Peltier chip **[6]** maintained at 50°C. This causes the liquid dichlorobenzene to evaporate at a rapid rate, and after a few seconds only a thin film remains on the surface. This liquid film is solidified by cooling the chip down to the room temperature, leaving a thin film of solid p-dichlorobenzene on the chip surface (100-200 µm thick). After this process the chip with the p-dichlorbenzene coating is placed in the cavity provided in the base wafer, and if an external connection is to be made wire bonding is done with the corresponding bond pads on the base wafer at this stage. The cap wafer is then bonded to the base wafer using an adhesive bonding technique such as epoxy bonding. It is desirable to limit the temperature in the bonding process to a temperature much below the melting point of p-dichlorobenzene (56°C at atmospheric pressure). After packaging the chip, the base-cap wafer assembly with the chip coated with p-dichlorobenzene is placed inside a vacuum chamber and the p-dichlorobenzene is sublimated under vacuum to complete the release procedure. The released chip is then observed through the cover glass window provided in the cap wafer for this purpose to observe the results of the release and packaging procedure.

Need for new sublimation setup

The release of packaged chip, through the release holes located in the cap wafer, took much longer (10 hours) than the regular sublimation release of open chips (30 minutes) **[6]**. Sublimation was limited by diffusion through these small release

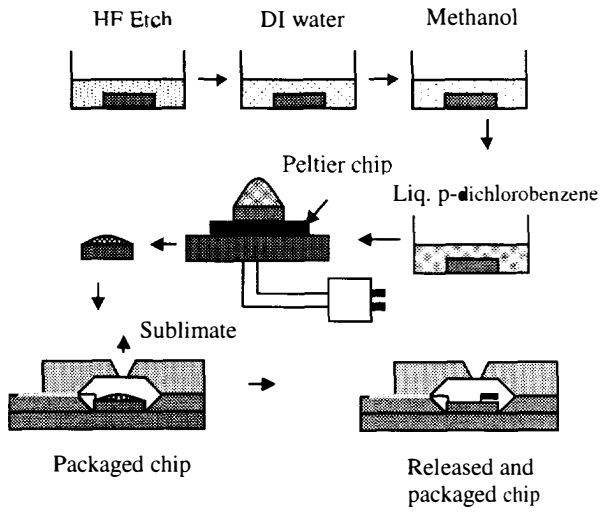

Figure 3. *Post packaging release procedure*

holes (200 µm x 200 µm). This called for us to investigate the sublimation of the chemical used (p-dichlorobenzene) and propose a method of overcoming this limitation.

The rate of sublimation of a solid can be determined by the following equation,

$$\dot{r} = g_m(m_s - m_e) \quad (1)$$

where g_m = *mass transfer conductance*
m_s = *mass fraction of p-dichlorobenzene*
m_e = *mass fraction of p-dichlorobenzene at* ∞

$$m_s = \left(\frac{P_s}{P}\right) \times \left(\frac{Md}{M_{air}}\right) \quad (2)$$

while P_s = *sublimation pressure of p-dichlorobenzene*
P = *Total pressure in the vacuum chamber*
M_d = *molecular mass of p-dichlorobenzene*
M_{air} = *molecular mass of air.*

Combining Eq. (1) and Eq. (2) and since m_e=0.

$$\dot{r} = \left(\frac{P_s}{P}\right) \times \left(\frac{Md}{M_{air}}\right) \times g_m \quad (3)$$

In the above equation, g_m is a factor dependent on the physical properties of the material, temperature, airflow etc. and can be assumed to be a constant as there is not much of a variation in these factors in our experiments:

$$\dot{r} = const \times \left(\frac{P_s}{P}\right) \quad (4)$$

From the Equation (4), it is clear that the sublimation rate is a strong function of the ratio of sublimation pressure to the total pressure of the system. This indicates that the sublimation rate can be increased by either increasing the sublimation pressure or by lowering the total pressure of the system. The sublimation pressure

of p-dichlorobenzene has been experimentally determined by Polednick et al. and fitted according to Antonine equation [7].

$$P = \exp\{28.4986 - 6272.86/(T - 32.2741)\} \quad (5)$$

where P is the sublimation pressure of p-dichlorobenzene in Pascals and T is the temperature in Kelvin. The graph of the variation of sublimation pressure with temperature is shown in Figure 4.

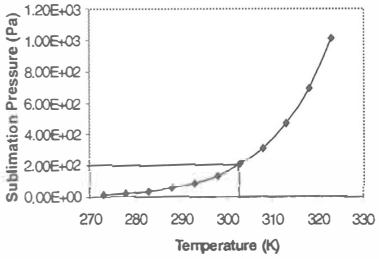

Figure 4. Sublimation pressure of p-dichlorobenzene as function of temperature [7]

As seen from the graph, the sublimation pressure of p-dichlorobenzene increases with the temperature. The sublimation rate can thus be improved by raising the temperature. This method of increasing the temperature can be easily performed using the Peltier chip design in the sublimation setup described in [6]. The sublimation rate was observed to increase if the temperature of the substrate was raised to ~40°C (still below the melting point of dichlorobenzene). However the dichlorbenzene sublimated from the chip surface tends to deposit on the inside cavity wall of the cap wafer as the temperature is lower on the cap than the base wafer.

Another method of increasing the sublimation rate is by decreasing the total pressure of the system. This decrease in total pressure was achieved by an improved sublimation setup described below.

New sublimation setup

The new sublimation setup incorporates a high vacuum pump capable of going down to the sublimation pressure of p-dichlorobenzene. A Speedivac 2 rotary vacuum pump which has an ultimate vacuum of 10 Pa was used for this purpose. A foreline trap was installed between the vacuum chamber and the vacuum pump. The vacuum chamber is also fitted with a pressure indicator and valve for regulating the vacuum. The valve serves the purpose of breaking the vacuum in the chamber before shutting off the pump and preventing seeping of the oil from the pump to the vacuum chamber. A cooling tower is also included in the setup to prevent the p-dichlorobenzene vapor from escaping into the atmosphere. The schematic layout of various components of the vacuum setup along with a picture of the setup is shown below.

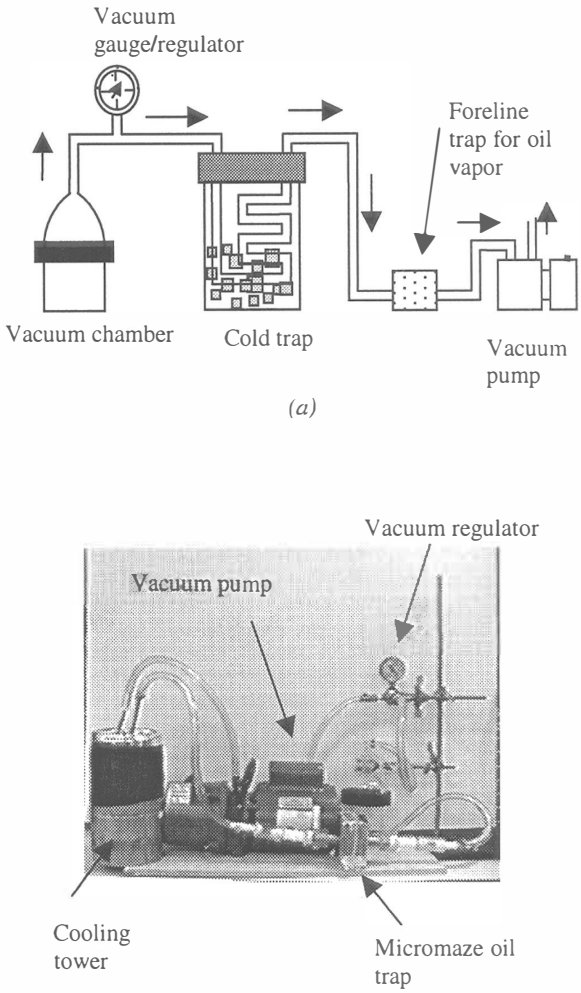

Figure 5. Sublimation setup (a) schematic, (b) picture

TEST STRUCTURE AND RESULTS

The test structures used for demonstrating the post-packaging release concept were fabricated using MCNC's MUMPs. One set of test structures for verifying the results of post-packaging release consists of a set of polysilicon beam structures. The beams are 2 μm thick and are suspended at a distance of 2 μm from the substrate. The width of the beam structures vary from 2 μm to 12 μm. This varying beam width enables us to compare the data obtained for release length vs. thickness with those previously obtained using the unpackaged chips [6]. In order to further verify the success of this unique method of post-packaging release, another set of structures were fabricated using the MUMPs process. This set incorporated different sets of comb drives, which can be actuated through actuation pads on the chip, which in turn are wire bonded to corresponding bonding pads on the base wafer. The purpose of designing these devices was to drive the packaged comb actuators from outside the package and observe the performance through the viewing window provided on the cap

wafer. The layout of the test chip and picture of the packaged device are shown in Figures 6 and 7 respectively. The results obtained on the chip containing beams of varying width is plotted as a function of detachment length vs. beam width in Figure 8. The data obtained with open (unpackaged) chips [6] is plotted alongside for reference. As seen from the data, there is little difference between the post-packaging release procedure and the sublimation release procedure, implying the success of this method. The comb drive structures released using this method were also actuated to test this method and were found to function without any difficulties.

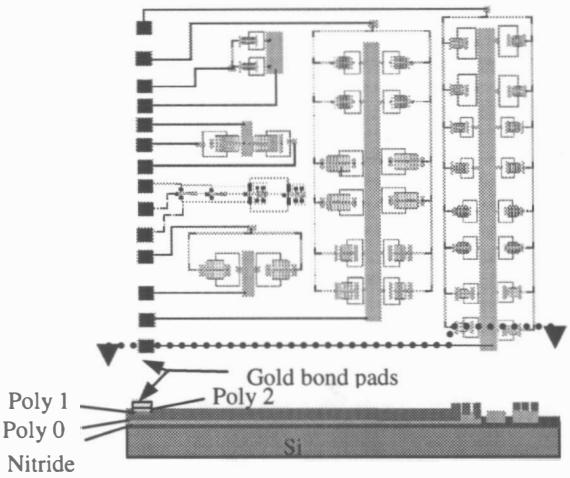

Figure 6. Layout of a test chip

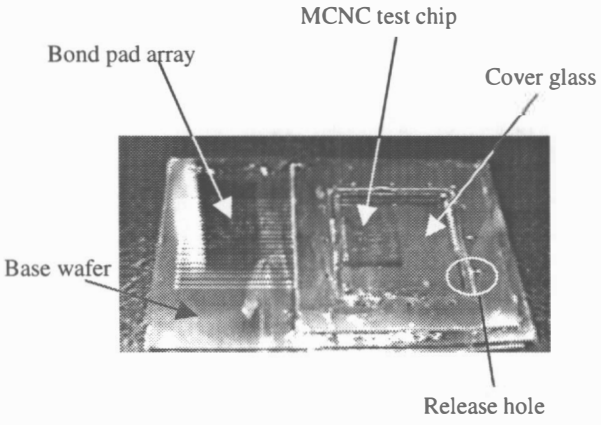

Figure 7. Picture of a post- packaging release chip

CONCLUSION

In this paper, we have demonstrated a method of releasing the surface-micromachined devices after packaging has been performed, thereby making the overall production procedure much more rugged and economical. An improved setup for sublimation release was also developed during the course of this work, which improves the sublimation rate considerably. Experiments showed no apparent ill effect of packaging to surface-micromachined elements. With the introduction of new room temperature wafer bonding procedures like the microriveting [8], this method of post-packaging release is believed to improve production of MEMS devices. A method of post- packaging release using vapor-phase etchants was also proposed.

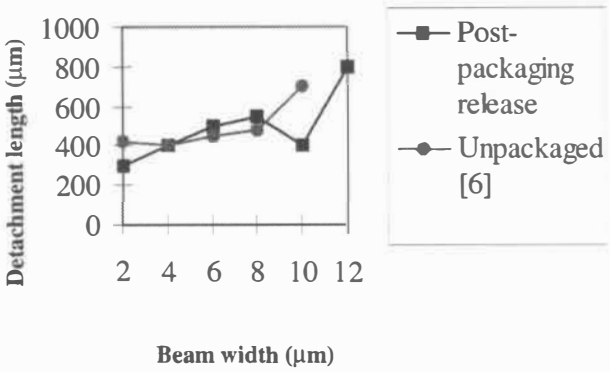

Figure 8. Results of post packaging release

ACKNOWLEDGEMENT

This project was supported by the Defense Advanced Research Projects Agency (DARPA) MEMS program.

REFERENCES

1. Y. -I. Lee, K.-H. Park, J. Lee, C.-S. Lee, H.J. Yoo, C.-J. Kim and Y.-S. Yoon, "Dry Release for Surface Micromachining with HF Vapor-Phase Etching", *J. Microelectromechanical System,* Vol. 6, No. 3, Sept. 1997, pp. 226-234.

2. P. Chu, J. Chen, R. Yueh, G .Lin, J. Huang, B. Warneke and K. Pister, "Controlled pulse etching using xenon di flouride", *Transducers 97,* Chicago, Illinois, June 1997, pp. 665-668.

3. X. Wang, X. Yang, K. Walsh and Y.-C. Tai, "Gas-phase etching with bromine triflouride", *Transducers 97*, Chicago, Illinois, June 1997, pp. 1505-1508.

4. G. Lin, C.-J. Kim, S. Konishi and H. Fujita, "Design, fabrication and testing of C-shaped actuator", *Transducers 95,* Stockholm, Sweden, June 1995, pp. 416-419.

5. N. Takeshima, K. Gabriel, M. Ozaki, H. Horiguchi and H. Fujita, "Electrostatic parallelogram actuator", *Transducers 91*, San Francisco, California, June 1991, pp. 63-66.

6. C.-J. Kim, J. Kim and B. Sridharan, "Comparative evaluation of drying techniques for surface micromachining", *Sensors and Actuators A 64 (1998)*, pp. 17-26.

7. M. Polednick, T. Guetachew, J. Jose, V. Ruzicka, V. Rohac and M. Zabransky, "Vapor pressures and sublimation pressures of dichlorobenzenes (1,2-, 1,3- and 1,4-), trichlorobenzenes (1,2,3- and 1,3,5-) and pentachlorobenzene", *ELDATA: International Electronic Journal of Physical Chemistry Data 1996*, 2, pp.41-50.

8. B. Shivkumar and C.-J. Kim, "Microrivets for MEMS Packaging: Concept, Fabrication and Strength Testing", *J. Microelectromechanical Systems*, Vol. 6, No. 3, Sept. 1997, pp. 217-225.

AN ON-CHIP HERMETIC PACKAGING TECHNOLOGY FOR MICROMECHANICAL DEVICES

Steve T. Cho[1] and Francis M. Erdmann[2]

[1]The Charles Stark Draper Laboratory, 555 Technology Sq, Cambridge, MA 02139
currently with: Abbott Laboratories, 755 Jarvis Dr, Morgan Hill, CA 95037

[2] Boeing North American, Inc., 3370 Miraloma Ave, Anaheim, CA 92803

ABSTRACT

A novel on-chip hermetic packaging technology utilizing electrostatic bonding and eutectic sealing is presented. Planarization of the lead transfers is not required since the leads conform to the interfacial layer by forming a eutectic seal with the bonding layer (amorphous polysilicon). The leads also have an isolation resistance of >4GΩ/sq. This approach requires only one masking step and exhibits low induced stress, high thermal shock resistance, and a leak rate of $<10^{-16}$ SCCM.

INTRODUCTION

In many applications related to biological, physical, and inertial sensors, there is a need to hermetically seal the sensor on-chip. Encasing the sensor in a miniature shell has several advantages, including small size, low packaging cost, and great robustness. For manufacturing applications, an inherent problem with suspended micromechanical structures is protecting the die during assembly. By encapsulating the device in a low cost shell, standard processes such as wafer sawing can be performed without yield loss.

Some of the key performance challenges in developing this technology include: i) low leak rate, ii) transferring leads from inside the package to external connections (i.e., lead transfer), iii) low temperature sealing, iv) small package size, v) induced package stress, and vi) low cost. Current approaches include anodic bonding, glass frit seals, deposited plug seals, deposited lead transfers, and thin film seals [1-4]. Although each of these techniques is adequate for sealing transducers, each approach has a significant drawback. Vacuum frit seals require large areas (>1mm width) and the choice of metals is limited due to potential dissolution during sealing. Deposited plug seal structures have limited strength over large areas and there is the potential to deposit material inside the package during sealing. Metal seals (e.g., Au-Si, In) require dielectric isolation for the lead transfers and these isolation layers require planarization; the strength of these seals is also typically less than electrostatic or frit seals. Polysilicon-to-glass anodic seals with planarized polysilicon lead transfers have demonstrated hermetic seals with great robustness. However, this process also requires planarization, and for applications which require long lead transfers (e.g., flat panel displays), the resistance of the polysilicon (10Ω/sq) can be an issue.

This paper presents a novel hermetic sealing technology that meets the performance goals of on-chip packaging. By integrating the techniques of anodic bonding and eutectic sealing, an on-chip seal with a leak rate of $<10^{-16}$ SCCM has been demonstrated. This seal is formed by electrostatically bonding amorphous polysilicon over gold. The anodic bond forms an atomic scale seal over the glass regions, while the gold migrates into the polysilicon to form a eutectic seal. During the sealing process, the gold flows into any microvoids that may exist; the compression due to the anodic bonding also forms a planar boundary layer. The shell material is made out of glass, which offers several advantages over silicon shells, including low stray capacitance and transparency for inspection (Fig. 1). Electrically isolating the metal leads is achieved by the high resistance of the undoped amorphous polysilicon. The process temperature can be biased far below the eutectic temperature (363°C) due to localized joule heating around the metal areas. This process is simple and only requires 1 masking step. Packaged devices utilizing resonant comb drive structures have been fabricated and tested. The packages were characterized for leak rate (change in Q or pressure over time), lead isolation, seal strength, and thermal shock.

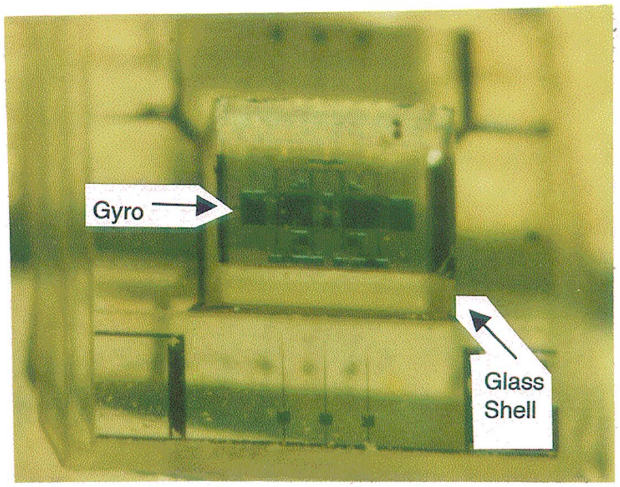

Fig. 1: Packaged Micro-Gyroscope.

In applying this approach to vacuum packaging, the key issue is outgassing. It was previously reported that the evolution of oxygen-based gases during electrostatic sealing prevented vacuum sealing and the presence of a getter was required [1]. However, by preconditioning and electrostatically outgassing the parts before bonding, vacuum seals were achieved. A proof-of-concept test was run on membrane test structures; if the membranes collapsed, then the vacuum was maintained inside the cavity. This technique can potentially reduce outgassing to low enough levels that package lifetime can be extended over 10 years.

0-9640024-2-6/hh1998/$20©1998TRF
DOI 10.31438/trf.hh1998.51

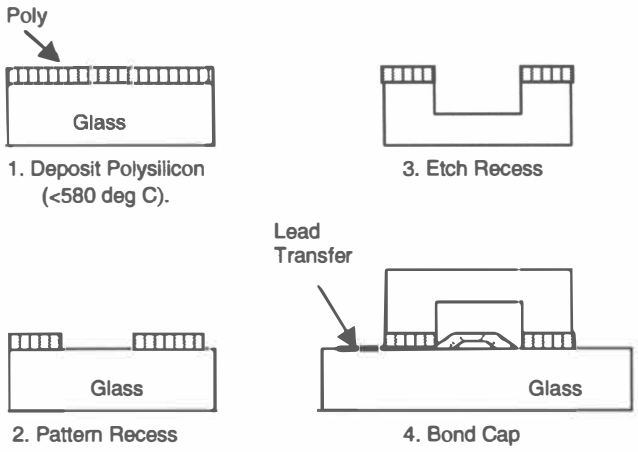

Fig. 2: Process Flow for an On-Chip Glass Shell.

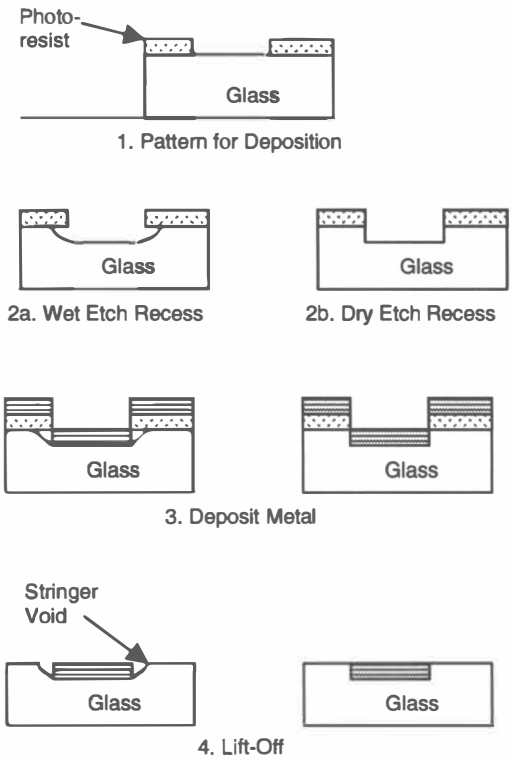

Fig. 3: Self-Aligned Metallization Process.

PROCESS DEVELOPMENT

The ideal on-chip package should have the following characteristics: low cost, simple batch processing, high seal strength, low induced stress, low temperature sealing, and isolated lead transfers. Figure 2 shows the process flow for the shell. An amorphous structured polysilicon film is deposited on a pyrex 7740 glass wafer (far below the softening point of 821°C). The amorphous structure is important for two reasons: high electrical resistance and low surface roughness. The poly is then patterned and etched in a plasma reactor. Using the poly as a mask, a deep recess is etched into the glass using an HF-based solution.

The lead transfers are run on the transducer substrate. A self-aligned lift-off process is used (Fig. 3) to define the metal. A photoresist pattern is defined on the glass and shallow recess is etched into the glass by RIE [5]. A Ti-Pt-Au layer is then deposited and lifted off. The cap is anodically bonded to the surface of the transducer. During bonding, the gold migrates into the silicon and also flows into any microvoids that exist at the Si-glass-Au interface. The RIE step is important for the lead transfer structure; wet etched recesses generated "stringer" voids at the gold-glass interface (Fig. 2a, 4). The gold migration did not consistently fill these voids. The bias temperature of the process is below the Si-Au eutectic (363°C); localized joule heating raises the bond temperature above the diffusion point.

Figure 5 shows a cross-section of the bond. During glass breaking, the interface most likely to shear was the glass-Ti area. Smooth and planar bond interfaces are evident, and the gold migration extends through the polysilicon film. The gold also fills in any potential interfacial voids that may exist.

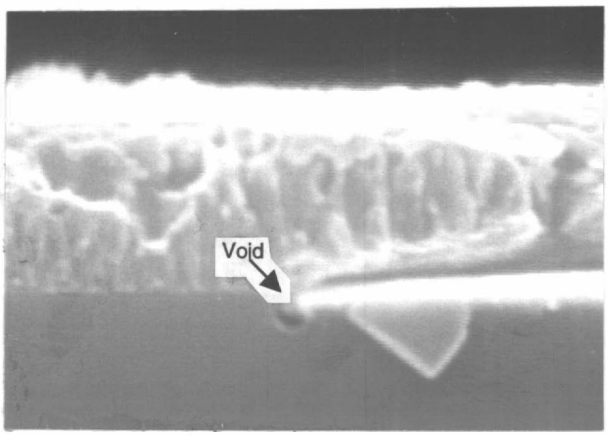

Fig. 4: Stringer Void Generated by Wet Etching.

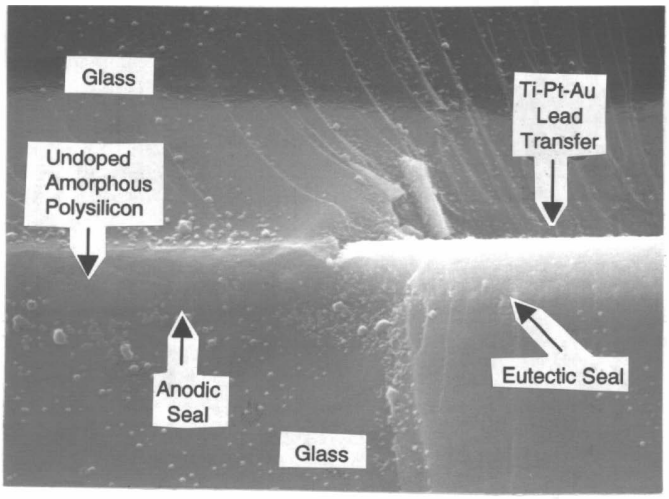

Fig. 5: Cross-Section of Bond Region.

CHARACTERIZATION

1. *Induced Stress*

In order to measure any induced stress by the package, micromechanical resonant gyroscopes were sealed in on-chip shells. The resonant frequency before sealing was >25,000 Hz; the change in frequency after sealing was <200Hz. Since all the materials (poly, silicon, 7740 glass) have close thermal expansion coefficient matches, the small shift was expected. For this application, the shift does not affect performance.

2. *Hermeticity*

Leak rates are defined by the pressure loss multiplied by the package volume per unit time. Atmospherically sealed shells were placed in a vacuum vessel (1uTorr) and monitored for 2 weeks for changes in quality factor (Q). Since Q is a function of pressure, the change in pressure can be measured (Fig. 6). The measured Q was 210 which corresponds to pressure of about 370 Torr (the part was sealed under atmosphere; however, subsequent cooling dropped the pressure to about half the bond ambient pressure).

After two weeks, the change in Q was 1 (this is within the noise of the measurement); a ΔQ of 1 corresponds to a pressure change of about 1uTorr. Therefore, for a package volume of 2.4×10^{-4} cm^3, the total leak rate is 1.6×10^{-17} SCCM. However, at this low level, helium permeation, ambient outgassing, and other factors will dominate the vacuum level.

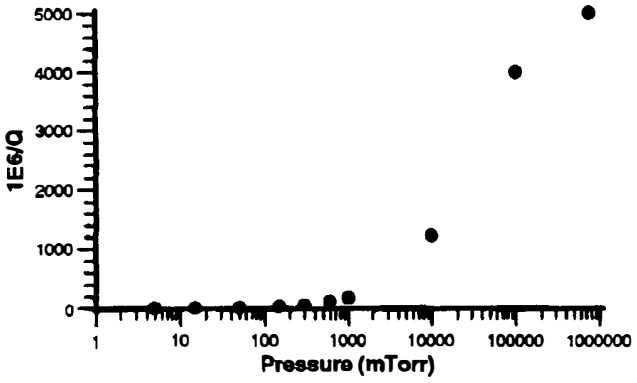

Fig. 6: Quality Factor (Q) versus Pressure.

3. *Lead Transfer*

The isolation between the lead transfers was characterized. Using resistance structures of different length, the resistance of the amorphous poly was measured at 4.5±0.5 GΩ/sq. Higher temperature polysilicon films (625°C) that are undoped typically have 1-2 GΩ/sq of resistance. Figure 7 shows an I-V plot of a resistance measurement; the response is linear, indicating that the gold has made good ohmic contact to the poly.

This resistance can be increased by more than an order of magnitude. By reducing the thickness of the poly and narrowing the width of the seal, the isolation resistance can be raised to >50GΩ/sq. Whether this is adequate depends on the noise level that can be tolerated by the application and the density of the lead transfers. However, it should be noted that typical printed circuit board resistance is 100MΩ-1GΩ/sq.

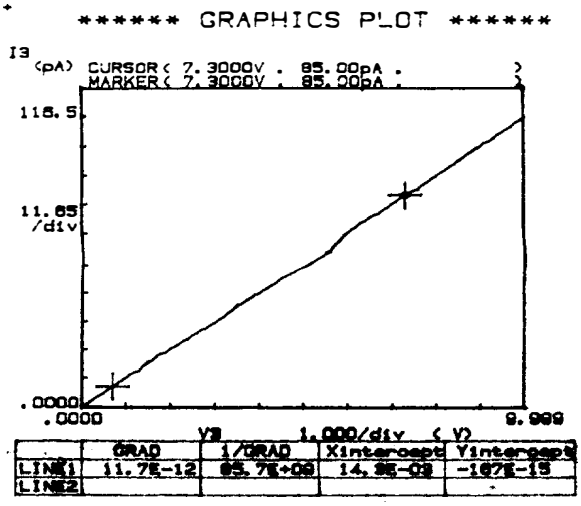

Fig. 7: I-V Plot Measuring Lead Isolation. Resistance is 4.3 GΩ/sq (85.7 GΩ/20 sq).

4. *Mechanical Robustness and Area*

The mechanical and thermal stability of the package was tested. In pull tests of the glass, the fractured or the Ti layer pulled off, but the interfacial bonds remained intact. This is consistent with traditional Si-glass anodic bonds; the bond interface is stronger than the bulk materials. The shell adhesion was also sufficiently strong enough to withstand wafer sawing. Due to the high seal strength, the bond width can be made much less than most technologies, such a frit seals.

A thermal shock test was also performed. The samples were first cooled in liquid nitrogen, then immediately placed in a convection oven operating at 150°C. The samples maintained their mechanical integrity and hermeticity. The equivalent thermal shock is 4152°K/min.

5. *Vacuum Hermetic Sealing*

When vacuum sealing a vessel, there are several factors that determine the vacuum level, including virtual leaks, gettering, outgassing during sealing, and outgassing over the lifetime of the package. Virtual leaks are normally not a critical issue with micromechanical devices since non-porous, high vacuum materials are being used. Although lithographic getters have been developed for micro-applications [7], getter process compatability, size, and activation are primary concerns. Furthermore, the small volumes inside micromechanical packages limit the getter volume and the getter capacity. Non-getter vacuum sealing has been achieved by low temperature sealing (e.g., indium at <150°C); this low temperature is critical since outgassing rates are logarithmic.

The key issue in on-chip non-getter vacuum sealing is outgassing. Outgassing during sealing determines the initial pressure of the package and outgassing within the package determines the package lifetime. Given a package with a surface area of 1.2mm x 2.0mm, a 100um high cap, a bond time of 20 minutes, an outgas rate of 10^{-7} liter-Torr/cm^2-sec, and a sealing pressure ambient of <1uTorr, this would give an initial pressure which is marginally acceptable for most resonant applications. The outgas rate is dependent on how the parts are preconditioned before sealing; the rate of 10^{-7} liter- Torr/cm^2-sec is considered to be nominal. Glasses typically have a room temperature outgas rate of 10^{-10} liter-Torr/cm^2-sec; pyrex has a peak outgas rate at about 315°C

[8]. If the lifetime of the package is considered to be double the initial pressure and assuming that the outgas rate does not decrease over time, then the room temperature lifetime of this package is 15 days. However, if the outgas rate could be decreased by 3 orders of magnitude, then lifetimes of up to 40 years can be achieved.

Outgassing of parts is typically performed under high vacuum (uTorr-nTorr) conditions at elevated temperatures for several hours. For high volume, high throughput applications, these practices may not be acceptable. Electrostatics offer the potential of accelerating the outgas process by liberating surface species under the influence of high electric fields. During electrostatic bonding, the depletion of oxygen-based species extends far beyond the surface of the glass.

A proof of concept test was run using membrane structures (Fig. 8) with small volumes (2mm x 2mm, 1.0um gap) which would be sensitive to outgassing. The first set of parts was not outgassed and bonded at 315°C for 1h at 1uTorr. The membranes buckled slightly away from glass substrate. The second set of parts were electrostatically outgassed. A spacer separated the silicon and glass to prevent bonding. The parts had several kV's applied for one hour, then bonded at the same 315°C in a 1uTorr ambient. The membrane pressed against the bottom substrate, indicating vacuum. More research is being performed to understand and quantify the electrostatic outgassing behavior. The performance of this technology is summarized in Table 1.

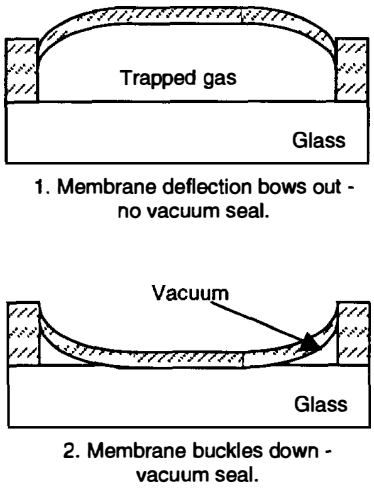

Fig. 8: Vacuum Sealing Test Structures.

Table 1: Hermetic Sealing Performance Summary

Parameter	*Performance*
Pressure Change (2 weeks) - Leak Rate	<1uT <10^{-16} SCCM
Seal Strength	>20MPa
Lead Isolation Resistance	4-5 GΩ/sq
Thermal Shock	4152°K/min.

CONCLUSIONS

In many micromechanical applications related to transducers and manufacturing, there is a need to hermetically package devices on-chip. Although several approaches have been proposed, there are significant trade-offs with regards to size, cost, process complexity, and robustness. A novel sealing technology based on anodic and eutectic bonding has been presented which offers a simple, low cost approach to batch hermetic packaging. The packages are robust (mechanical strength, thermal shock) and can support vacuum sealing. Lead transfers are isolated by an amorphous polysilicon thin film with a resistance of 4.5 GΩ/sq. An electrostatic outgas approach has been presented which can potentially eliminate the use of getters in a 10 year lifetime package.

ACKNOWLEDGEMENTS

The authors would like to thank Dave Warren of Boeing, Connie Cardoso and James Cousens of Draper Labs; Paul Maciel of US Incorp., George Hopple of Candescent Technologies, and Dr. Khalil Najafi of the University of Michigan.

REFERENCES

[1] K. Minami, T. Moriuchi, and M. Esashi, "Cavity Pressure Control for Critical Damping or Packaged Micromechanical Devices", Transducers '95, pp. 240-243.

[2] S.A. Audet and K.M. Endfeld, "Integrated Sensor Level Packaging", *Transducers '97*, pp. 287-289.

[3] B. Ziaie, J. Von Arx, M. Dokmeci, and K. Najafi, "A Hermetic Glass-Silicon Micropackage with High Density On-Chip Feedthroughs for Sensors and Actuators", *JMEMS*, pp. 166-179, Vol. 5, No. 3, Sept 1996.

[4] L. Lin et al, "Vacuum Encapsulated Micro-resonators" *Transducers '93*, p. 270, 1993.

[5] S.T. Cho, "A Batch Dissolved Wafer Process for Low Cost Sensor Applications", *Meeting of the SPIE*, Vol. 2639, pp. 10-15, October 1995.

[6] S.T. Cho, K. Najafi, and K.D. Wise, "Internal Stress Compensation and Scaling of Ultrasensitive Boron-Doped Silicon Membranes", *IEEE Trans Electron Devices*, Vol. 39, No. 4, pp. 836-842, April 1992.

[7] Private Communication, SAES Getters, Milan, Italy.

[8] A. Roth, *Vacuum Sealing Techniques*, Pergamon Press, 1968.

Localized Silicon Fusion and Eutectic Bonding for MEMS Fabrication and Packaging

Y. T. Cheng, Liwei Lin*, and Khalil Najafi

Department of Electrical Engineering and Computer Science.
*Department of Mechanical Engineering and Applied Mechanics,
The University of Michigan, Ann Arbor, MI. 48109-2122, USA.
E-mail: ytcheng@engin.umich.edu

ABSTRACT

Localized silicon fusion and eutectic bonding processes based on the technique of *localized heating* are demonstrated and reported for the first time. Phosphorus-doped polysilicon is applied in the localized, silicon-to-glass fusion bonding experiments. Gold is used in the silicon-to-gold eutectic bonding tests. Polysilicon and gold films are patterned as line-shape resistive heaters and they react as the bonding materials. It is found that both processes can be accomplished in 5 minutes and the high temperature bonding region can be confined in a small area. This new class of bonding scheme has potential applications for MEMS fabrication and packaging that require low temperature processing at the wafer level, excellent bonding strength and hermetic sealing characteristics.

INTRODUCTION

Bonding techniques, including fusion, eutectic, and anodic bonding, have been used in IC and MEMS manufacturing for many years **[1,2]**. Although still an emerging technology, silicon bonding is already producing such commercial devices as pressure sensors and accelerometers. All of these bonding processes require two basic elements. First, two bonding surfaces must be flat to have intimate contact for bonding. Second, proper processing temperatures are required to provide the bonding energy. For example, the conventional silicon-to-silicon fusion bonding process occurs at a bonding temperature of above 1000°C **[3]**. Anodic bonding, on the other hand, is performed at a much lower temperature of about 450°C with the aid of a high electrostatic field **[4]**. The silicon-gold eutectic state occurs at a temperature of 363°C that is the theoretical bonding temperature **[5]**. Among these bonding processes, one common drawback is the high temperature requirement that may damage and degrade temperature-sensitive materials and integrated circuits. Therefore, they are not generally applicable in fabrication or packaging devices when temperature-sensitive materials exist. For the past few years, many efforts have been undertaken to find a reliable bonding process that can be conducted at a low temperature. Unfortunately, these new bonding processes depend highly on the bonding material **[6]**, surface treatment **[7]**, and surface flatness **[8]**.

This paper presents a new bonding process based on the concept of localized heating. High temperature, localized bonding processes are performed while the whole wafer is maintained at a low temperature. Moreover, localized high temperature is able to cause softening of the bonding material and alleviate the surface roughness problem. Two types of localized bonding processes have been investigated: (1) silicon-to-glass fusion bonding, and (2) silicon-to-gold eutectic bonding. Technical issues in bonding conditions, strength and procedures for both fusion and eutectic bonding are discussed. It is our belief that this technique can greatly simplify MEMS fabrication and packaging at both the wafer and chip levels.

PRINCIPLE OF LOCALIZED HEATING AND BONDING

Figure 1 shows the experimental setup for the bonding tests: (a) cross sectional view, (b) the design of microheater and (c) the design of a temperature sensor. Figure 1(a) shows the cross sectional view where a silicon or glass cap is to be bonded to the device substrate. A silicon dioxide layer is grown on the device substrate for electrical and thermal insulation. In the fusion bonding experiments, polysilicon is grown and patterned as the heating and bonding material. In the eutectic bonding experiment, gold resistive heaters are used as the heating and bonding materials. A proper pressure (about 1 MPa) is then applied to put the cap substrate in contact with the bonding resistors as shown in Fig. 1(a). Figure 1 (b) shows the design of the enclosed-shape microheater that can be used to encapsulate MEMS devices. In order to measure the temperature surrounding the microheater, a temperature sensor made of polysilicon or gold is placed 15 μm away from the bonding area as shown in Fig. 1(c). The temperature is characterized by monitoring the change in resistance

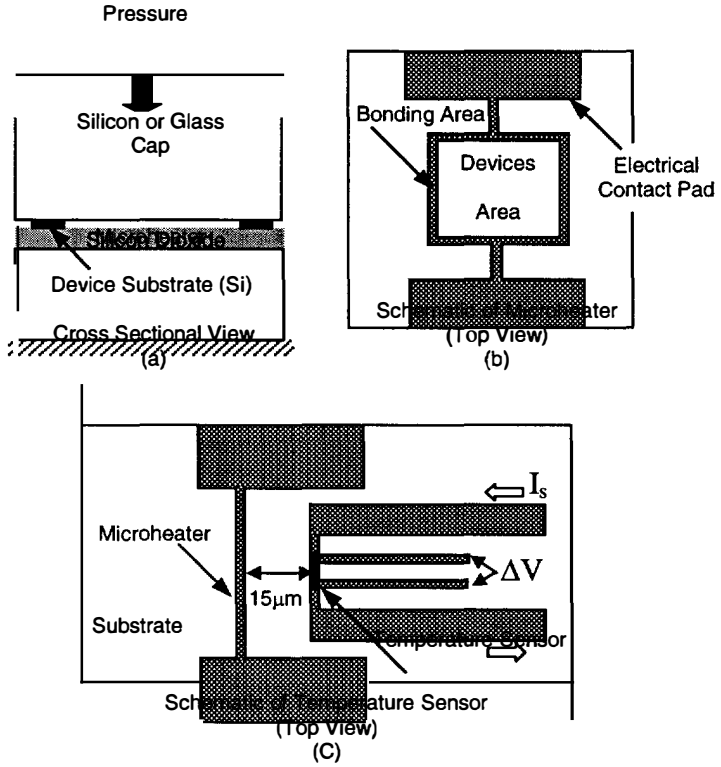

FIG 1. The schematic of the localized bonding experiments. (a) cross sectional view, (b) schematic of microheater, (c) a temperature sensor.

0-9640024-2-6/hh1998/$20©1998TRF
DOI 10.31438/trf.hh1998.52

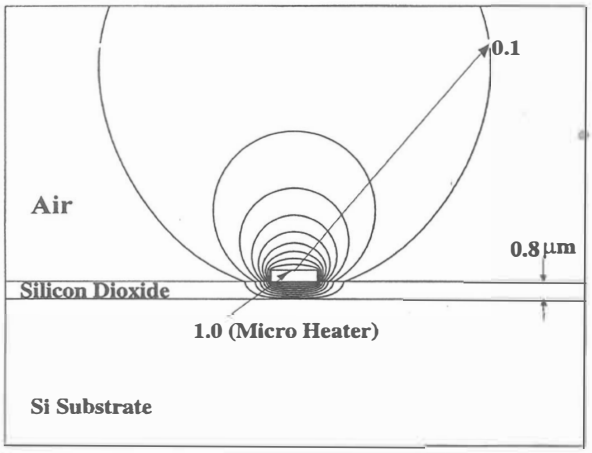

FIG 2. Isotherms around a 2 μm wide microheater **[9].**

Which can be achieved by dividing ΔV by the input current I_s. In a recent heat transfer study **[9]**, high temperature region is found to be confined in a very small region. Figure 2 shows the isotherm of such a system. If the microheater is at a high temperature of 1000°C, the temperature drops to 100°C less than 2 μm away from the heater as shown. Therefore, localized heating can be achieved by the proper arrangement of microheaters and insulation layers.

Two widths, 5 or 7 μm, of the microheaters are designed and tested with a square bonding area of 500 μm^2. A pressure of 1 MPa is applied on top of two wafers and a current, which depends on the design of the microheaters, is passed through the heater to provide the bonding temperature. An electro-thermal model that was previously established based on the conservation of energy **[9]** was used here to estimate the temperature. Figure 3 shows the simulation results (solid lines) and experiments (symbols) of polysilicon microheaters under different input currents without the cap substrate. The experimental data is calculated by assuming a linear dependence of resistivity with respect to temperature:

$$\rho(T) = \rho_o (1 + \xi(T-T_o)) \qquad (1)$$

where ρ_o is the resistivity at room temperature and ξ is the temperature coefficient of resistivity. For N-type polysilicon with dopant concentration of 7.5 x $10^{19}/cm^3$, this temperature coefficient is about 1.2 x 10^{-3}/°K **[10,11]**.

The same principle is used in the temperature sensor to determine the temperature changes at a short distance, 15 μm, away from the microheater. It is found that when an electric current of 30 mA is passed through the 5 μm polysilicon resistive heater, the temperature reaches the melting point of polysilicon (~1415°C). At the same time, the temperature sensor indicates a temperature increase of less than 40°C. Apparently, the high temperature region is well confined in a very small region in the device substrate

LOCALIZED FUSION BONDING

Based on the concept of localized heating, localized silicon-to-glass bonding is demonstrated in this paper. First, a Pyrex glass cap substrate (7740 from Dow Corning) is placed and pressed on the top of polysilicon microheaters as shown in Fig. 1(a). A 31mA input current which is very close to cause melting of polysilicon is then applied to the 5 μm wide, 1.1 μm thick polysilicon microheater for about 5 minutes. This input current generates a temperature of about 1300°C based on the current-temperature simulation that includes the effect of the glass cap on top of the micro-

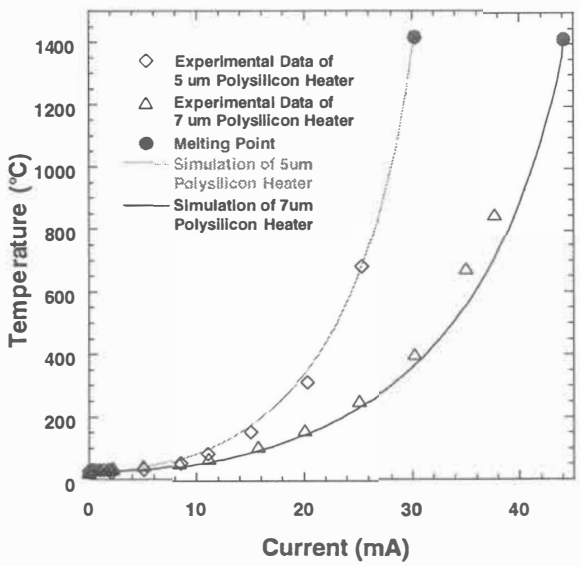

FIG. 3. Experimental and simulation results of 5 and 7 μm wide polysilicon microheaters under different current inputs

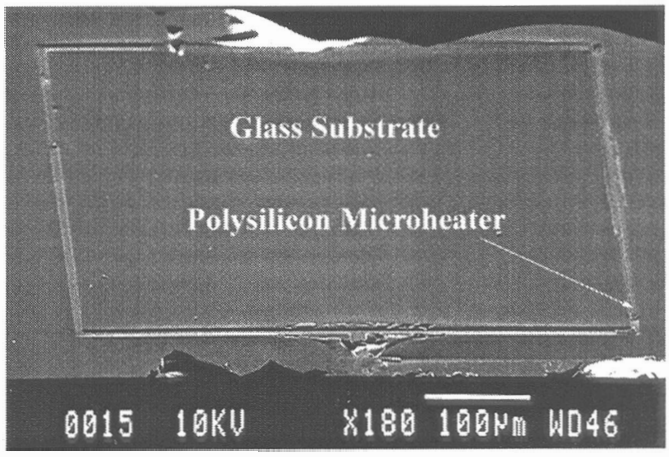

FIG. 4 A SEM micrograph showing the glass cap substrate is softened and has the shape of the polysilicon microheater.

-heater. This temperature is slightly lower than the data shown in Fig. 3 under the same input current because of heat losses to the glass cap.

Figure 4 shows the SEM micrograph of a forcefully broken fusion bond on the glass cap. It is observed that the square shape microheater is reflected on the originally flat glass substrate. Moreover, part of the polysilicon was attached to the glass cap. This microphoto demonstrates two very important features for the localized fusion bonding experiment. First, it is very easy to raise the microheater temperature to be above the glass soften point of ~820°C such that the glass cap is locally softened. Second, the applied pressure is high enough to cause intimate contact of the glass cap and the microheaters. Since intimate contact has been made, a good and reliable fusion bond can be expected with proper temperature and reaction time.

In order to determine the bonding strength, a close-up SEM microphoto was taken as shown in Fig. 5. For this particular sample, the breakage was along one of the microheater. Polysilicon heater, underneath silicon dioxide layer and the top glass cap can be clearly identified. The morphology of glass near the heater line shows the glass has been softened locally. After dipping the sample into HF solution, the polysilicon heater is clearly

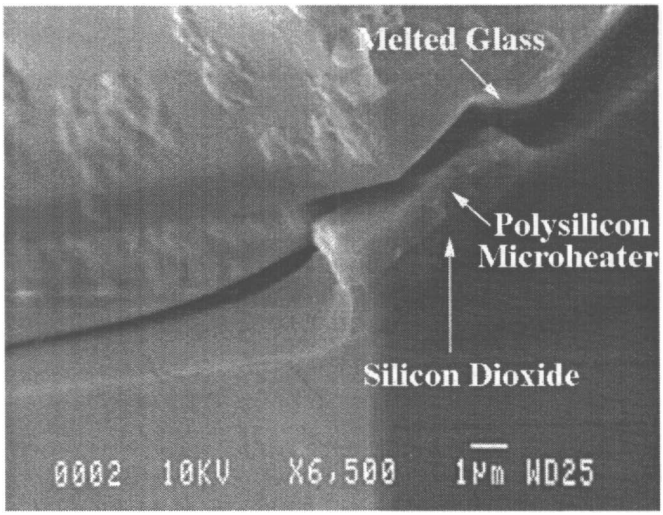

FIG. 5. A SEM micrograph shows the localized silicon-glass fusion bonding. After the bond is forcefully broken, microheater, silicon dioxide and glass cover are clearly observed.

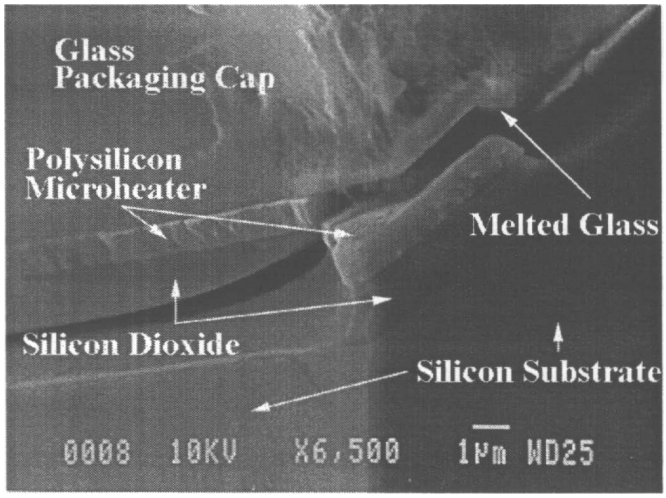

FIG. 6. Polysilicon microheater appears after dipping into HF

delineated as shown in Figure 6. In this case, the polysilicon-glass bond seems to be stronger than the bottom polysilicon-oxide adhesion where the broken trace can be clearly observed. Therefore, these results strongly suggest that an excellent silicon-to-glass fusion bonding is achieved.

According to the fusion bonding principle [3], flat surfaces, hydrophilic surface treatment, sufficient high bonding temperature and reasonable bonding time will result in successful bonding. The typical conventional bonding temperature is above 1000°C for about 2 hours. In the experiments presented in this paper, microheaters are cleaned by SPM (sulfuric peroxide mixture, i.e., a mixture of $H SO_4$ and H_2O clean followed by HF dip and water rinse for hydrophilic surface treatment [12]. Bright red light emits from microheaters during the bonding process. It is found that when the bonding temperature is raised to very close to the melting temperature of polysilicon, the silicon-to-glass fusion bonding occurs in less than 2 minutes. In another experiment, a lower bonding current of 29 mA which corresponds to a temperature of about 1000°C is applied continuously for 30 minutes. The result shows poor bonding strength and uniformity. According to these experimental results, it is believed that excellent, hermetic bonding

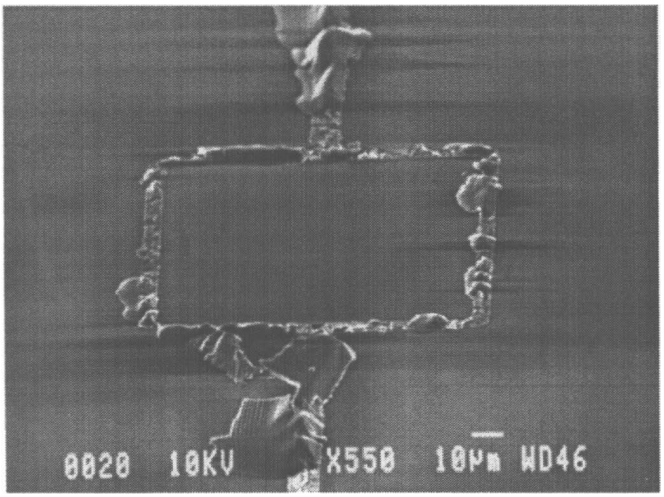

FIG. 7. A SEM micrograph showing localized silicon-to-gold eutectic bonding. After the bond is forcefully broken, silicon is attached to the gold line.

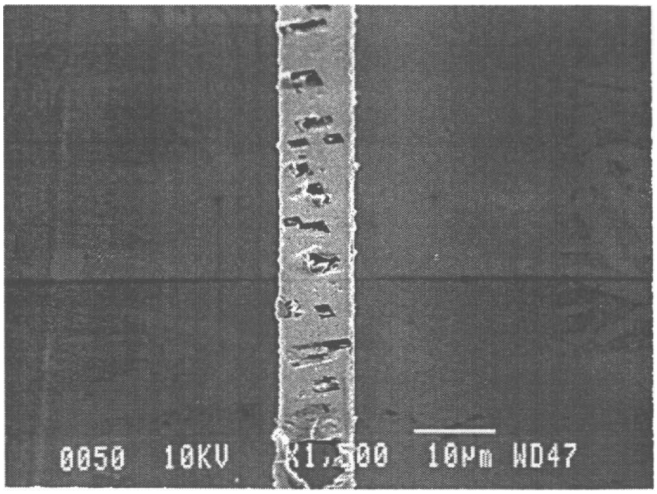

FIG. 8. Non-uniformity is found in a conventional eutectic bonding process.

can be achieved when the bonding temperature is controlled to be very close to the melting point of the polysilion material. At a lower bonding temperature, a longer bonding period is expected to achieve excellent bonding.

LOCALIZED EUTECTIC BONDING

In the silicon-to-gold eutectic bonding experiments, gold microheaters are used as the heating and bonding materials. A silicon cap substrate is placed on top of the gold microheater as shown in Fig. 1(a). A 0.27 A electric current is then applied to the 5 μm wide, 0.5 μm thick gold microheater for about 5 minutes. The bonding temperature is estimated to be about 800°C. During the bonding process, gold diffuses into silicon and the resistivity of gold line increases. It is necessary to increase the current density to maintain a high bonding temperature during the bonding process. Figure 7 shows the result of silicon-to-gold eutectic bonding by the technique of localized heating. It appears that silicon is broken and attached to the gold microheater when the eutectic bond is forcefully broken. Moreover, uniform eutectic bonds can be observed around the square shape microheater.

For comparison purposes, the same eutectic bonding experiment is also performed by using the conventional eutectic bonding technique **[5,13]**. The process is conducted in an oven that provides global heating and bonding. The processing temperature is first ramped to 410°C in 10 minutes and is kept at 410°C for 10 minutes before cooling down to room temperature in 10 minutes. Figure 8 shows the bonding result in a SEM microphoto. Nonuniform eutectic bonding can be clearly observed in this photo. This is probably the reason that hermetic sealing was not achieved in a previous report **[13]**. It is well-known that the diffusivity **[14]** and solubility **[15]** of gold into silicon substrate increase when the processing temperature increases. At higher bonding temperatures as those used in the localized bonding process, more gold atoms can diffuse into silicon. Therefore, a thicker layer of gold-silicon alloy can form at a higher bonding temperature **[16]** and a stronger eutectic bond is expected **[17]**.

DISCUSSION

Temperature and processing time are the two key factors for both fusion and eutectic bonding if intimate contact has been achieved. In the silicon-to-glass fusion bonding system, atoms obtain thermal energy provided by temperature to overcome reaction barrier to form chemical bonds. In the silicon-to-gold eutectic eutectic
bonding system, diffusion is activated under high temperature environment when atoms overcome the diffusion barrier to from eutectic bonds. It is desirable to have high processing temperatures in both fusion and eutectic bonding processes for higher diffusion constant
and reaction rates. Localized heating provides an excellent way to accomplish the high temperature requirement while maintaining low temperature at the wafer level. Therefore, fast reaction and strong bonding are expected to occur locally. There are many ways to achieve localized heating, including using microheaters or focused micro laser **[18]**. The key structural design is to prevent the heat losses to the environment or substrate. An insulation layer underneath the heating element serves well for this purpose as illustrated in Fig. 2. Design optimizations can be conducted based on the principle of heat transfer to improve the effectiveness of localized heating.

This paper presents *direct* silicon fusion and eutectic bonding techniques where the heating elements are also serving as the bonding materials. One drawback for the direct bonding technique is that the bonding materials may diffuse or melt during the process. Therefore, the resistance of the microheater changes and it is very difficult to control the bonding temperature and process. We are currently pursuing the same localized heating idea but adding soldering materials for *indirect* bonding. Since the microheaters can be preserved during the indirect bonding process, good temperature and process control are expected. Furthermore, encapsulation of microresonators in vacuum environment is underway. We expect to quantitatively analyze the hermetic sealing characteristics of this new technique by monitoring the performance of packaged microresonators.

CONCLUSION

Localized fusion and eutectic bonding processes have been successfully demonstrated. Phosphorus doped polysilicon and gold resistive heaters are used in silicon-to-glass fusion and silicon-to-gold eutectic bonding processes, respectively. It is found that both processes can be accomplished in less than 5 minutes with excellent bonding strength and uniformity. In the silicon-to-glass fusion bonding process, an input current of about 31 mA is necessary to reach a bonding temperature of about 1300°C. In the silicon-to-gold eutectic bonding process, an input current of about 0.27 A is needed to reach a bonding temperature of about 800°C. We believe these techniques can greatly simplify MEMS fabrication and packaging at both the wafer and chip levels.

ACKNOWLEDGEMENTS

The authors would like to thank Prof. Nugyen at the University of Michigan for valuable discussions. Prof. Liwei Lin is supported by the National Science Foundation CAREER award. The project is supported by DARPA.

REFERENCES

[1] W. H. Ko, J. T. Suminto, and G. J. Yeh, "Bonding Techniques for Microsensors", Micromachining and Micropackaging for Transducers, Elsevier Science Publishers, 1985.

[2] P. W. Barth, "Silicon Fusion for Fabrication of Sensors, Actuators and Microstructures", Sensors and Actuators, **A 23**, pp. 919~926, 1990.

[3] C. Harendt, H. -G. Graf, B. HÖfflinger, and E. Penteker, J. "Silicon Fusion Bonding and Its Characterization", J. Micromech. Microeng, **2**, pp. 113~116, 1992.

[4] G. D. Wallis, and D. I. Pomerantz, "Field Assisted Glass-Metal Sealing", J. Appl. Phys. **40**, pp. 3946~3948. 1969

[5] L. Valero, "The Fundamentals of Eutectic Die Attach", Semiconductor Int., **7**, pp. 236~241, 1984.

[6] H. Reichl, "Packaging and Interconnection of Sensors", Sensors and Actuators, A, **25**, pp. 63~71, 1990.

[7] Q. Y. Tong, and G. Cha, R. Gafiteanu, and U. Gösele, " Low Temperature Wafer Direct Bonding", J. MEMS, **3**, pp. 29~35.1994.

[8] B. Ziaie, J. Von Arx, M. Dokmeci, and K. Najafi, "A Hermetic Glass-silicon Micropackages with High Density On-Chip feedthroughs for Sensors and Actuators", J. MEMS, **5**, pp. 166~179, 1996.

[9] Liwei Lin, "Selective Encapsulations of MEMS: Micro Channels, Needles, Resonators, and Electromechanical Filters", Ph.D. Thesis, UC Berkeley, 21, 1993.

[10] N. C. C. Lu, L. Gerzberg, and J. D. Meindl, " A Quantitative Model of The Effect of Grain Sizeon the resistivity of polycrystalline silicon films", IEEE Electron Device Letter, **EDL-1**, pp. 38~41, 1980.

[11] J. Y. W. Seto, "The Electrical Propertiesof Polycrytalline Silicon" J. Appl. Phys. , **46**, pp. 5247~5254, 1975.

[12] K. Ljungberg, Ulf Jansson, S. Bengtsson, and A. Söderbärg, " Modification of Silicon Surface with H_2SO_4:H_2O:HF and HNO_3:HF for Wafer Bonding Applications", J. Electrochem. Soc., **143**, pp.1709~1714, 1996.

[13] M. B. Cohn, Y. Liang, R. Howe, and A. P. Pisano, "Wafer to Wafer Transfer OF Microstructures for Vacuum Package", Technical Digest of the 1996 Solid State Sensor and Actuator Workshop, Hilton Head, pp. 32~35, 1996.

[14] CRC Materias Science and Engineering Handbook, pp. 255, 1997.

[15] H. Okamoto, and T. B. Massalaski, Binary Phase Diagram, pp. 312, 1986.

[16] P. –H, Chang, G. Berman, C. C. Chen, "Transmission electron microscopy of gold-silicon interactions on the backside of wafers", J. Appl. Phys., **63**, pp. 1473~1477, 1988.

[17] A. L. Tiensuu, M. Bexwell, J.-Schweitz, L. Smith, and S. Johansson, "Assembling three-diamensional microstructures using gold-silicon eutectic bonding", Sensors and Actuators A , **45**, pp. 227~236, 1994.

[18] C. L. Rambin, and R. O. Warrington, "Micro-assembly with A Focused Laser Beam", Proceeding of the IEEE Micro Electro Mechanical System, pp. 285~290, 1994.

SUBSTRATE AND ANNEALING INFLUENCES ON THE RESIDUAL STRESS OF POLYSILICON

Thomas W. Kim, Bishnu Gogoi, Ken G. Goldman, Andrew C. McNeil, Nicholas J. Rivette, Stephen E. Garling, and Daniel J. Koch
Motorola, Semiconductor Products Sector, Transportation Systems Group, MEMS1
Phoenix, AZ 85008

ABSTRACT

Our study reports the compressive and tensile residual stresses of LPCVD undoped polysilicon (poly-Si) deposited over three different substrates—silicon oxide (SiO_2), densified phosphosilicate glass (PSG), and silicon nitride (Si_3N_4). Using the design of experiment methodology, the thickness of the polysilicon film was varied from 0.1 μm to 3.2 μm and the as-deposited stress values (as well as the residual stresses after annealing at four different conditions) were recorded. Stress profiles as a function of poly-Si thickness for each poly-substrate group and for each anneal condition were obtained. SEM images were also taken to reveal the texture of each poly-Si film surface, enabling a qualitative discussion of the different crystallographic states and the various mechanisms of island and void formation for poly-Si. Our results have direct engineering applications for MEMS surface micromachined devices by providing residual stress values of poly-Si in conjunction with widely used substrates such as stoichiometric silicon nitride, thermal oxide, and PSG, before and after annealing. It assists endeavors to create more accurate micromechanical models and to construct yet unrealized micromachined devices.

INTRODUCTION

Polysilicon (Poly-Si) is commonly used as a mechanical structure or a sacrificial layer in various surface micromachined MEMS applications [**1**]. Because the film is isotropic and has superior material properties compared to metal films, polysilicon is the structural material of choice when designing surface micromachined sensors and actuators [**2**]. Numerous deposition and processing techniques have been documented for both thin (< 2 μm) and thick (up to 10 μm) polysilicon [**3**,**4**] but material characterization of thin film polysilicon (especially in the thickness range of 0.1 μm to 1 μm) is still required. Oftentimes, thin film polysilicon is employed in devices where the parametric electrical behavior of the sensor is dependent on the film's mechanical properties. Also, polysilicon is used in conjunction with other MEMS-application films such as thermal silicon oxide (SiO_2), densified phosphosilicate glass (PSG), and silicon nitride (Si_3N_4).

Deposited thin films can produce stress on a micromachined structure. In order to study the effects of poly on various substrates, radius of curvature, R, measurements were made using a wafer bowing system. Stress was calculated using Stoney's equation:

$$\sigma = \frac{E_s t_s^{\,2}}{6(1-\nu_s)Rt_f} \qquad (1)$$

where $E_s/1-\nu_s$ is the biaxial modulus of the silicon substrate, t_s is the thickness of the substrate, t_f is the thickness of the deposited film, and σ is the calculated film stress. The equation assumes that stress is equi-biaxial and homogeneous over the entire substrate.

Thin films have different material properties than their bulk material counterparts. Residual stresses of thin films often depend on deposition parameters. Polysilicon initially forms an amorphous solid that subsequently may crystallize during the deposition process. Highly columnar poly-Si films arise from a seed layer of random, small polysilicon grains formed by the bombardment of adatoms on the substrate. During thin film nucleation, intrinsic stresses caused by lattice mismatch, interstitial effects, and/or unequal growth mechanisms change the material properties of the thin film. Extrinsic stresses, such as non-uniform plastic deformation and thermal expansion (expressed quantitatively by the thermal expansion coefficient, CTE) may also change the behavior of the thin film.

In our study, the stress measurement of the resulting thin deposits are confounded with the type of substrate deposited beneath the polysilicon. Thermal SiO_2 is readily employed as a sacrificial layer or dielectric film for passivation in surface micromachining. It is a compressive film. Stoichiometric LPCVD Si_3N_4 is tensile and is used mainly as an isolation and buffer layer. Designers tend to shy away from using thermal oxide and/or nitride as mechanical components because of their high residual stress. Phosphosilicate glass (PSG) etches rapidly in HF and is used as a sacrificial layer. Due to its low melting temperature (approximately 950°C), PSG softens and flows under standard anneal conditions. The residual stress profiles for poly-Si on PSG can be expected to behave differently than poly-Si on nitride or thermal oxide.

Annealing and doping are popular techniques employed in MEMS applications to reduce the residual compressive and tensile stresses of as-deposited polysilicon [**5**]. Not only does annealing reduce residual stresses caused by the differences in the thermal expansion coefficient of the film-substrate interface and the non-uniform growth of the film, it also provides a means to increase the surface roughness of the film preventing stiction/delamination of further deposited films. SEM images of the poly-Si film surface before anneal provides qualitative information on the rate of island and void formation.

EXPERIMENTAL METHODS

A screening experiment was run following a set design of experiment (DOE) (Table 1). Low thicknesses of poly-Si on LPCVD silicon nitride were not sought because rarely are the two combined with the given film thicknesses in sensor applications. A Tencor™ FLX-2320 system monitored the radius of curvature on 100 mm dia., p-type <100> silicon test wafers. Bare silicon test wafers were baselined *after* deposition of the three different substrates—nitride, oxide, and PSG. Each

0-9640024-2-6/hh1998/$20©1998TRF
DOI 10.31438/trf.hh1998.53

Solid-State Sensors, Actuators, and Microsystems Workshop
Hilton Head Island, South Carolina, June 8-11, 1998

wafer was annealed for further stress analysis to 900°C (1hr), 950°C (1hr), 1000°C (1hr), or 1100°C (RTA, 1min).

Table 1. *Design of Experiment. The table indicates the number of test wafers in each cell deposited to the set compressive (-) or tensile (+) poly-Si thickness with a corresponding substrate.*

Poly-Si	w/SiO_2	w/PSG	w/Si_3N_4
0.1 μm	8	8	--
0.2 μm	8	8	--
0.4 μm	8	8	--
0.8 μm	8	8	8
1.6 μm	8	8	8
3.2 μm	8	8	8

LPCVD undoped poly-Si was deposited using a vertical thermal reactor with silane (SiH_4) as the main gas component at approximately 600°C. (Note that only the deposition time was altered to achieve greater thicknesses. All other deposition conditions were held constant.) With some adjustments in silane flow rate, pressure, and deposition temperature, both compressive and tensile poly-Si films were produced. A wet KOH bath system was used for subsequent backside etching. A Prometrix™ FT-750 system with film specific algorithms was used to measure the thickness of all the films. Only one poly-Si film (in compression at 3.2 μm) could not be read due to the "hazy" quality of the film's refraction.

Standard procedures were used to deposit the three substrates. A dry oxidation process was employed to deposit 0.04 μm of thermal oxide. Phosphite was used as the phosphorous dopant for 1 μm of PSG and the glass was densified at 950°C. A vertical LPCVD furnace was employed for 0.14 μm thick stoichiometric nitride deposition with dichlorosilane (DCS) and ammonia (NH_3) as the main gaseous components. All anneals occurred in a horizontal furnace with nitrogen gas save the rapid thermal anneal process.

RESULTS AND DISCUSSION

Figure 1 shows the stress profile for compressive poly-Si films deposited over three different substrates. As the thickness of the poly-Si film increases, the absolute stress values decrease. The profiles for poly on nitride and poly on oxide are similar at thicknesses greater than 0.8 μm. Although at room temperature thermal oxide is compressive and nitride is tensile, very thin films were used as substrates in this experiment (0.14 μm for nitride and 0.04 μm for oxide). At high poly film thicknesses, there is perhaps enough poly to mask the effect of the substrate on the film. The trend is linear at these greater thicknesses with the stress value approaching 200 MPa at 3.2 μm. Nevertheless, a difference is perceived through the entire DOE space for poly on 1 μm PSG. PSG tends to be "inelastic," becoming viscous at high temperatures. At low poly thicknesses, poly on PSG has higher compressive stress values than the other two film-substrate groups. In turn, at high poly-Si thicknesses, poly on PSG has lower compressive stress values. For low thicknesses of poly-Si, the higher stress values could be the result of more severe lattice mismatch between the polysilicon and PSG as well as misfit stresses caused by interstitial impurities.

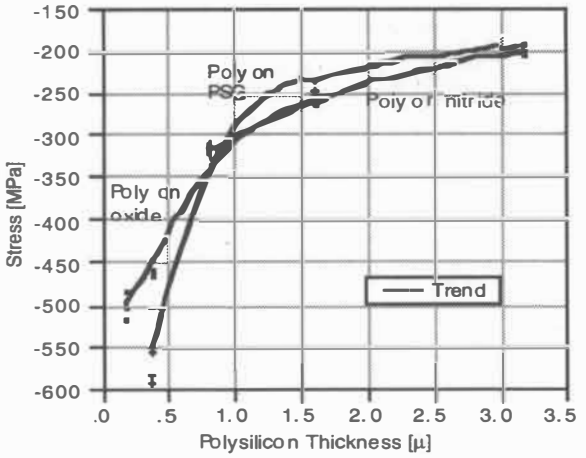

Figure 1. *As-deposited compressive stress vs. poly-Si thickness for poly on three different substrates: 0.04 μm thermal oxide, 0.14 μm LPCVD nitride, and 1 μm densified PSG.*

Krulevitch has suggested that low thickness compressive polysilicon films are made up of small grains that are misoriented [6]. The adatoms do not have enough surface mobility to find the lowest energy levels; that is, the film is amorphous at first. As-deposited compressive stress values for very thin polysilicon films tend to be high as seen in Figure 1. As the deposition time is increased, however, polysilicon film thickness increases by favoring those grains preferentially oriented in the z-direction. Polysilicon films begin to grow vertically in a columnar fashion, and distinct islands arise changing the initially amorphous film into a crystalline structure. This competitive grain growth mechanism explains the crystallographic structure of compressive thin film polysilicon at higher thicknesses. As-deposited stresses decrease as poly-Si thickness increases. Figure 2a shows the evolution of polysilicon into a highly crystalline film. Note the rise of the columnar structure with islands approximately 0.75 μm to 4.5 μm across.

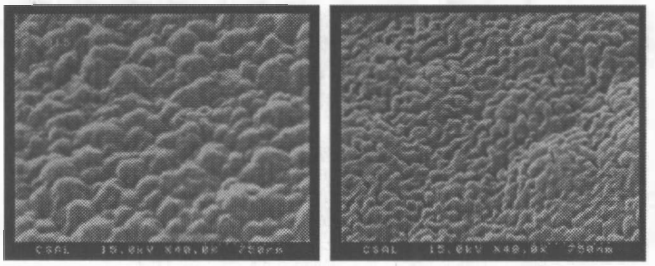

Figure 2. *Pre-anneal SEM images of (a) 1.6 μm compressive and (b) 1.3 μm tensile poly-Si deposited on 0.04 μm thermal oxide. Images were magnified 40k times and were taken at a 52° tilt.*

Tensile polysilicon films behaved differently. As poly-Si thickness increased to 2.5 μm, the as-deposited tensile stress values continued to increase, leveling off at approximately 275 to 300 MPa (see Figure 3). As expected, poly on PSG had greater tensile stress values by about 40 MPa throughout the DOE space and the profiles for poly on nitride and poly on thermal oxide are similar. There appears to be little dependence

on poly-Si thickness for stress values at film thicknesses greater than 1.3 μm.

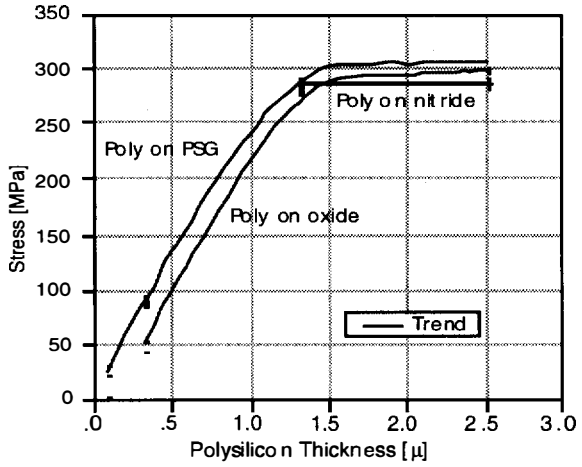

Figure 3. *As-deposited tensile stress vs. poly-Si thickness for poly on three different substrates: 0.04 μm thermal oxide, 0.14 μm LPCVD nitride, and 1 μm densified PSG.*

Tensile films are created when intermediate gases are driven off during deposition, leaving gaps within the film's microstructure. (Tensile films tend to contract.) Microvoids are expected since lateral diffusion of atoms evolves too slowly to fill all these gaps. A SEM image of tensile polysilicon revealed its amorphous structure (see Figure 2b). As poly-Si thickness increases, microvoids become more apparent. The "cobblestone" texture of 1.3 μm thick poly was present for 0.4 μm and 2.5 μm samples as well. The 1.3 μm sample shows unequal vertical growth most likely due to interstitial impurities.

Thermal stresses are the highest contributors to the overall stress value. Annealing reduces stresses caused by thermal mismatch expansions and non-uniform nucleation of the film. For polysilicon, annealing at temperatures well above its deposition temperature (which is approx. 600°C) should allow the atoms to find the lowest energy level, changing amorphous structures into crystalline forms. Figure 4 displays the residual stress profiles of compressive polysilicon (deposited on three different substrates) after being processed to four different anneal conditions. In general, as the anneal temperature increased, the film had lower compressive stress values. Also, the residual stress was independent of film thickness. (At film thicknesses less than approx. 1 μm though, compressive stress values did have a dependence on poly-Si thickness. At higher thicknesses, however, it was mainly the temperature that drove the relaxation.) The rapid thermal anneal process (RTA) had promising results, bringing the residual compressive stress values for poly on oxide to less than 25 MPa and to less than 50 MPa for compressive poly on PSG. RTA did, however, push the compressive poly on nitride into the tensile regime, but this may be an indication of the set temperature [7]. A hot temperature excursion should be run with these samples to further understand the changes in thermal expansion.

Figure 5 shows residual stress plots of tensile polysilicon films (deposited on three different substrates) after annealing. Similar conclusions may be drawn about the effect of annealing on these tensile samples as with the compressive samples. Temperature seems to drive the different levels of relaxation and there is little dependence on poly-Si thickness (above 1 μm). Again, higher temperatures produced lower residual stress films.

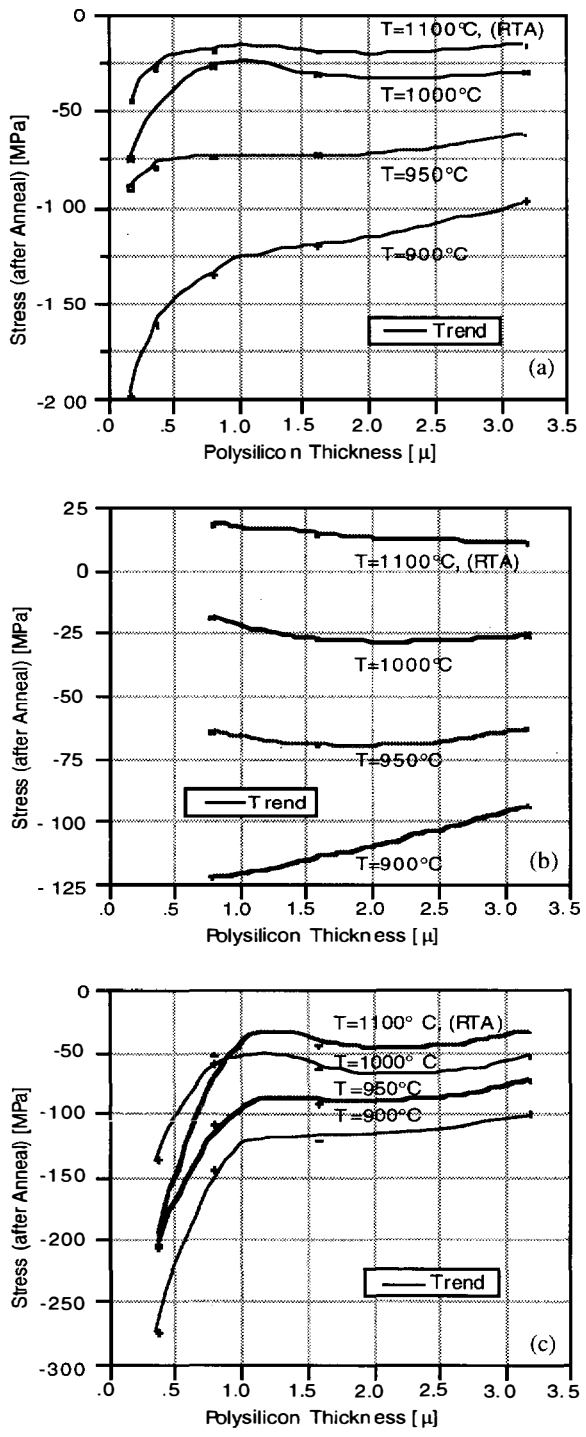

Figure 4. *Residual stress profiles of compressive polysilicon as a function of the film's thickness. The poly-Si film is deposited on (a) 0.04 μm thermal oxide, (b) 0.14 μm LPCVD nitride, and (c) 1 μm densified PSG. Samples at 900°C, 950°C and 1000°C were annealed for one hour while samples at 1100°C were annealed for one minute using a rapid thermal anneal (RTA) process.*

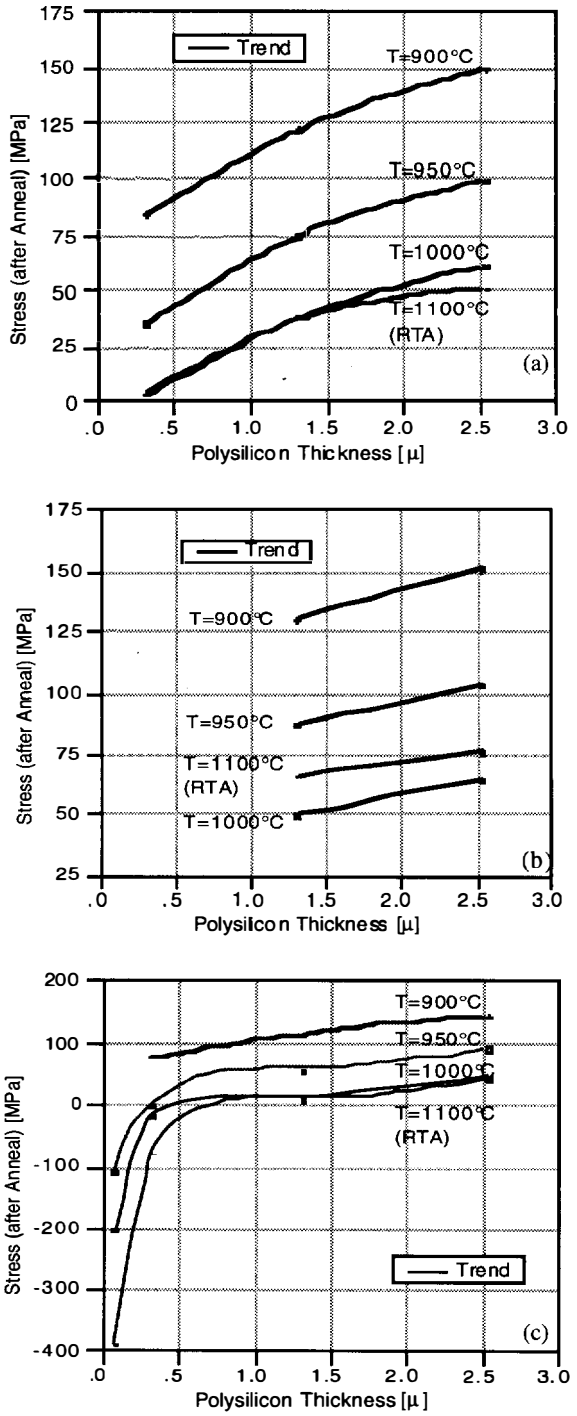

Figure 5. *Residual stress profiles of tensile polysilicon as a function of the film's thickness. The poly-Si film is deposited on (a) 0.04 μm thermal oxide, (b) 0.14 μm LPCVD nitride, and (c) 1 μm densified PSG. Samples at 900°C, 950°C and 1000°C were annealed for one hour while samples at 1100°C were annealed for one minute using a rapid thermal anneal (RTA) process.*

SUMMARY AND CONCLUSIONS

Using the design of experiment (DOE) methodology, we examined compressive and tensile LPCVD polysilicon films (of 0.1 to 3.2 μm thickness) deposited over three different substrates—silicon oxide (SiO_2), densified phosphosilicate glass (PSG), and silicon nitride (Si_3N_4). Stress measurements were made of as-deposited polysilicon films and stress profiles are provided for each poly-substrate group. Compressive polysilicon films had stress values ranging from 600 to 200 MPa as poly thickness increased from 0.1 to 3.2 μm. The profiles of stress vs. poly thickness for each different substrate revealed that poly on PSG has the lowest (most negative) stress values and that poly on oxide and poly on nitride have similar stress profiles. Tensile polysilicon films had stress values ranging from 5 to 300 MPa as poly film thickness increased from 0.1 to 2.5 μm. Poly on PSG had higher stress values than poly on nitride and poly on oxide (indicating the "inelastic" nature of PSG).

Characterization of LPCVD polysilicon also included determining the stress of the film after four different anneal procedures: 900°C for 60 min; 950°C for 60 min; 1000°C for 60 min; and 1100°C for 1 min (rapid thermal anneal, RTA). Generally, as the set anneal temperature increased, both compressive and tensile stresses approached 0, independent of film thickness. This study contributes to the growing material analysis of polysilicon thin films and it provides new stress profiles (before and after anneal) of polysilicon used in MEMS manufacturing (i.e. in conjunction with nitride, oxide, or PSG).

REFERENCES

1. R. T. Howe, "Applications of Polysilicon Films in Micro-sensors and Microactuators", *Materials Research Society Symposium Proceedings, 106*, 213 (1988).

2. M. J. Madou, *Fundamentals of Microfabrication*, CRC Press, Boca Raton, 1997.

3. T. I. Kamins, *Polycrystalline Silicon for Integrated Circuit Applications*, Kluwer Academic Publishers, Boston, 1988.

4. M. Kirsten, B. Wenk, F. Ericson, J. A. Schweitz, W. Riethmüller, and P. Lange, "Deposition of Thick Doped Polysilicon Films with Low Stress in an Epitaxial Reactor for Surface Micromachining Applications," *Thin Solid Films, 259*, 181 (1995).

5. L. Ristic, M. L. Kniffin, R. Gutteridge, and H. G. Hughes, "Properties of Polysilicon Films Annealed by a Rapid Thermal Expansion Annealing Process," *Thin Solid Films, 220*, 106 (1992).

6. P. Krulevitch, G. C. Johnson, and R. T. Howe, "Stress and Microstructure in Phosphorous Doped Polycrystalline Silicon", *Materials Research Society Symposium Proceedings, 276*, 79 (1992).

7. H. Guckel, D. W. Burns, C. C. G. Visser, H. A. C. Tilmans, and D. Deroo, "Fine-Grained Polysilicon Films with Built-In Tensile Strain", *IEEE Transactions on Electronic Devices, 35*, 800 (1988).

ULTRA-THIN P^{++} MONOCRYSTALLINE SILICON MICROSTRUCTURES

Chunchieh Huang and Khalil Najafi
Center for Integrated Sensors and Circuits, University of Michigan
1301 Beal Avenue, Ann Arbor, Michigan 48109-2122

ABSTRACT

This paper discusses the fabrication of submicron p^{++} microstructures for a number of MEMS applications using boron ion implantation, rapid thermal annealing, and boron etch-stop. To form these thin structures, the silicon is implanted with boron at an energy of 40keV and doses of $5\times10^{15}cm^{-2}$ and $7\times10^{15}cm^{-2}$, which produce a peak concentration of more than $10^{20}cm^{-3}$, sufficient for achieving an effective etch-stop in EDP. The thickness of the p^{++} layer varies from 0.2 to 0.3μm depending on the annealing time and temperature. A number of microstructures, including thin silicon diaphragms as large as 2mm on a side and 0.2μm thick, hot wire anemometers with a TCR of ~1600ppm/°C, and piezoresistive sound detectors, have been fabricated with high reproducibility, uniformity, and yield.

INTRODUCTION

Operation of many physical sensors is based on thin membranes or beams which deflect in response to an external parameter. Generally, the sensitivity of the sensor is strongly dependent on the thickness of these microstructures. One common technique for fabricating thin microstructures is based on high-temperature boron diffusion and boron etch-stop [**1**]. Forming microstructures from p^{++} silicon has been a powerful technique for fabricating a variety of high-performance sensors [**2**]. This technology offers several features, including the ability to form single-crystalline silicon microstructures which possess reliable and reproducible material properties, process simplicity, and reproducibility. However, thermal diffusion limits the minimum thickness of a p^{++} film to >2-3μm due to the high temperature process which is necessary to create a high boron concentration ($>9\times10^{19}cm^{-3}$) for achieving an effective etch-stop. The ability to form submicron p^{++} membranes is instrumental to many emerging applications which require a wide dynamic range and high sensitivity. This paper presents the fabrication of submicron p^{++} microstructures using boron ion implantation and EDP etching. Extensive simulation and experimental results are presented to define the limits and capabilities of this process, and examples of various devices fabricated using this technology are discussed.

FABRICATION PROCESS

The most critical step in the fabrication of submicron p^{++} silicon microstructures is determining the most appropriate implant and annealing parameters, and choosing an appropriate etchant for achieving a reliable and uniform etch-stop. The etch-stop characteristics of boron-doped silicon in KOH and EDP as a function of boron concentration have been studied and characterized by other researchers [**3**]. In order to achieve an effective etch-stop, the ratio of the etch rates between undoped and highly-doped silicon should be generally higher than 100. As a result, for an effective boron etch-stop in EDP, the boron concentration has to be $>9\times10^{19}cm^{-3}$. In order to obtain a thin microstructure, this region of high concentration has to be confined to a narrow region, which is possible using ion implantation. SUPREM simulation has been used to determine the range of implantation energies, doses, and annealing steps. Table I shows the simulated thickness of a p^{++} layer for various implant conditions (annealed at 1100°C for 30sec.). As can be seen, the thickness varies from 0.3μm to 0.5μm by changing the dose and the energy; higher energies and doses produce thicker layers. Since the final thickness is a strong function of boron concentration, it can also be altered by either implanting the boron through an oxide mask, or by post-implant annealing under different conditions. Figure 1 shows the simulated boron concentration profiles for four different annealing temperatures and times after an implantation dose of $7\times10^{15}cm^{-2}$ and energy of 40keV. The maximum doping concentration is about $2.1\times10^{20}cm^{-3}$ after rapid thermal annealing (RTA) at 1100°C for 30sec. Such a high concentration is sufficient for achieving an effective etch-stop.

The determination of the most suitable annealing step is dependent on the device structure. As can be seen form Figure 1, the surface concentration of the implanted silicon after a 1000°C anneal is much lower than that after an 1100°C anneal. Therefore, if the ion implantation layer is protected from EDP from the front side, then either of these annealing steps can be used depending on the required thickness. Otherwise, an 1100°C anneal should be used to produce a high boron concentration for an effective etch-stop. As will be presented later, these simulated results nicely match our experimental results.

Another important and critical element in the formation of thin p^{++} layers is the silicon etchant used for dissolving the undoped layer and stopping on the p^{++} film. Typically two wet etchants are used in bulk silicon micromachining, KOH and EDP. Although Folkmer *et al.* did successfully fabricate p^{++} silicon structures using KOH [**4**], the temperature and concentration of the KOH bath needed to be well controlled to prevent p^{++} silicon overetching. This is primarily because KOH has a lower etch-stop selectivity than EDP [**3**]. In the experiments reported here we have used EDP as the silicon etchant with a composition of: 150ml ethylenediamine, 48g catechol, 48ml water, and 0.9g pyrazine. The EDP temperature is 104°C which provides a better etch rate control. The total EDP time is between 90min. up to three hours. For an EDP etch at a higher temperature or much longer period than described above, the thin implanted p^{++} layer could be attacked by EDP. Although the surface concentration of the implanted silicon wafers after anneal is higher than $9\times10^{19}cm^{-3}$, there is still a finite etch rate for the implanted region. From [**3**], the ratio of the etch rates in EDP between undoped and highly-doped silicon ($C_B=2.1\times10^{20}cm^{-3}$) is about $1:4\times10^{-4}$. As a result, the EDP etch will consume ~800Å of the highly-doped silicon in the same time it will take EDP to dissolve away 200μm of undoped silicon (this assumes that the p^{++} silicon is not protected from the EDP during this etch). The silicon sample has to be removed from EDP as soon as the undoped silicon is etched away to prevent overetching the implanted layer.

Determining the most appropriate implant energy and dose is dependent on the particular application and the corresponding fabrication sequences. On the one hand, because of the finite etch

0-9640024-2-6/hh1998/$20©1998TRF
DOI 10.31438/trf.hh1998.54

Solid-State Sensors, Actuators, and Microsystems Workshop
Hilton Head Island, South Carolina, June 8-11, 1998

rate of highly-doped silicon in EDP, a low-energy, low-dose implant is not favorable. On the other hand, to fabricate extremely thin structures and to reduce production costs, a high-energy, high-dose implant is not desirable. As indicated by the data in Table **I**, the designer has fairly wide latitude in choosing the best energy and dose to suit a particular application. For all of the devices reported in this paper, we used an implant energy of 40keV, and doses of $5\times10^{15}cm^{-2}$ and $7\times10^{15}cm^{-2}$.

***Table I:** SUPREM simulation results**

Dose (cm^{-2})	Energy (keV)	Etch-stop (μm)
5×10^{15}	30	0.28
5×10^{15}	40	0.31
5×10^{15}	50	0.33
5×10^{15}	60	0.36
7×10^{15}	30	0.33
7×10^{15}	40	0.36
7×10^{15}	50	0.38
7×10^{15}	60	0.41
1×10^{16}	30	0.37
1×10^{16}	40	0.40
1×10^{16}	50	0.42
1×10^{16}	60	0.45

* Etch-stop layer thickness is based on the silicon thickness at a boron concentration of $9\times10^{19}cm^{-3}$.

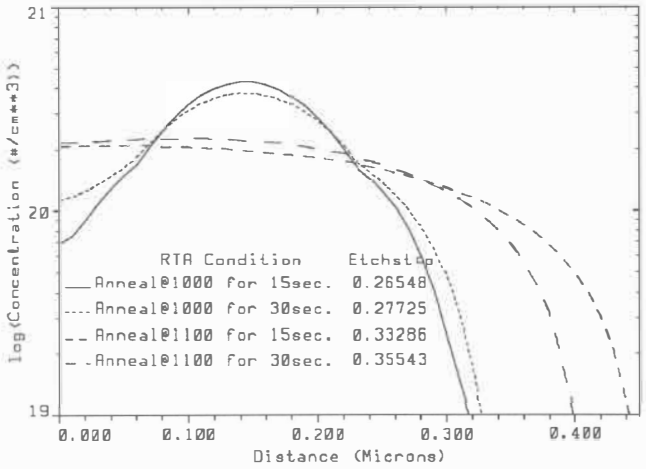

***Figure 1:** Boron concentration profile after various annealing temperatures and times.*

EXAMPLES

The above technology has been applied to fabricate a number of devices, including thin silicon membranes for capacitive pressure sensors, p^{++} silicon wires for flow sensors, and p^{++} resistors for piezoresistive pressure sensors and sound detectors. Thin membrane fabrication is performed in standard bulk micromachining, while the silicon wires and piezoresistive sensors are fabricated using the dissolved wafer process [**5**]. The fabrication of each of these devices will be briefly described below.

To fabricate the ultra-thin silicon membranes, the front side of a silicon wafer was first implanted with boron at 40keV at a dose of $7\times10^{15}cm^{-2}$. After implantation, the wafer is thinned down to 200μm to reduce the EDP etch time. Note that EDP still etches highly-doped silicon at a slow rate because the front side of the wafer is exposed to the EDP etch during the entire etch period. Next, the backside of the silicon wafer is covered with a 2000Å layer of PECVD nitride, which is deposited at a temperature of 400°C for 10 minutes. Low temperature dielectric deposition is important for obtaining thin p^{++} layers because high temperature processes will drive the boron deeper into the silicon substrate and lower the dopant concentration. The PECVD dielectric layer is now patterned to create windows for the EDP etch, which etches through the entire thickness of the wafer and stops on the p^{++} film. Figure 2 shows a silicon membrane formed using EDP etching following an RTA at 1000°C for 20sec. The diaphragm is buckled due to non-uniform stress distribution. This is easily corrected by performing a second RTA at 1100°C for 30sec. after the EDP etch, as shown in Figure 3. The diaphragm thickness is about ~2000Å which is very close to the simulation result taking the finite etch rate of highly-doped silicon into consideration.

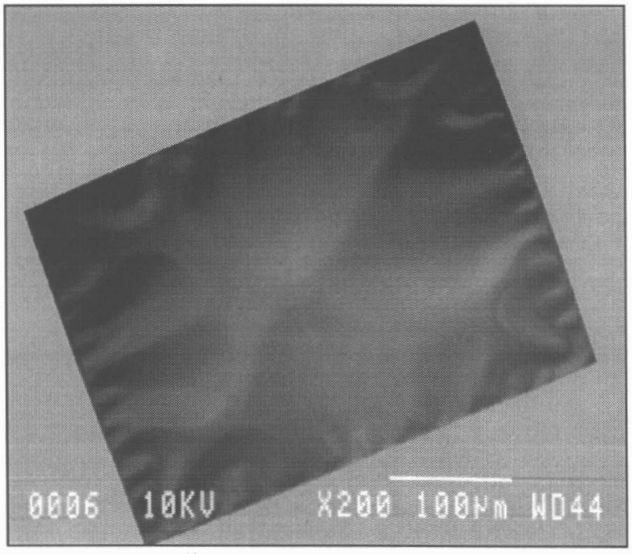

***Figure 2:** Thin p^{++} silicon membrane after 3 hours EDP etch. The membrane is buckled after release.*

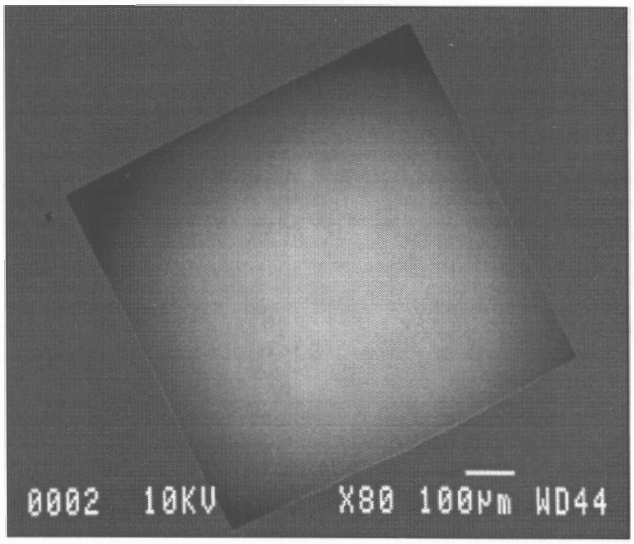

***Figure 3:** The 800μm-square silicon membrane is flat after RTA at 1100°C for 30sec.*

In order to obtain a flat diaphragm, one can also perform the RTA anneal at 1100°C before EDP. Note that since the anneal time is very short and since the anneal is performed using an RTA, one can easily perform the annealing step after the diaphragms are released since there is no need for any additional wet processing or

cleaning of the wafer. The above diaphragms can be uniformly and reliably fabricated. Thickness uniformity is mainly dependent on the temperature uniformity of the EDP etch bath. In all of our experiments we etched only pieces of a 4" wafer, but in all of these experiments we obtained intact and flat diaphragms ranging in size from 300μm-square to 2mm×4mm. Figure 4 shows the cross section and a close-up view of one of these ultra-thin membranes.

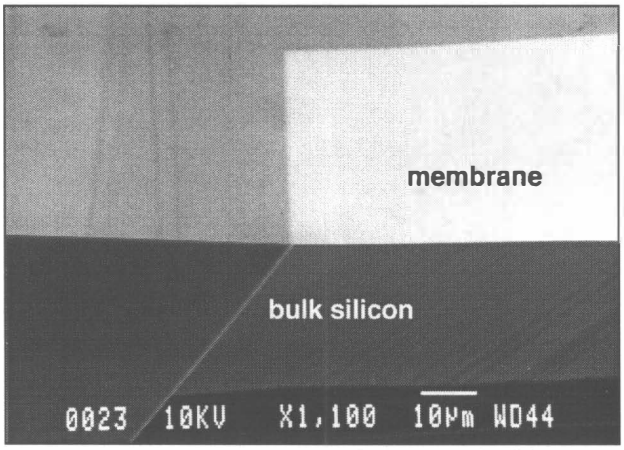

(a)

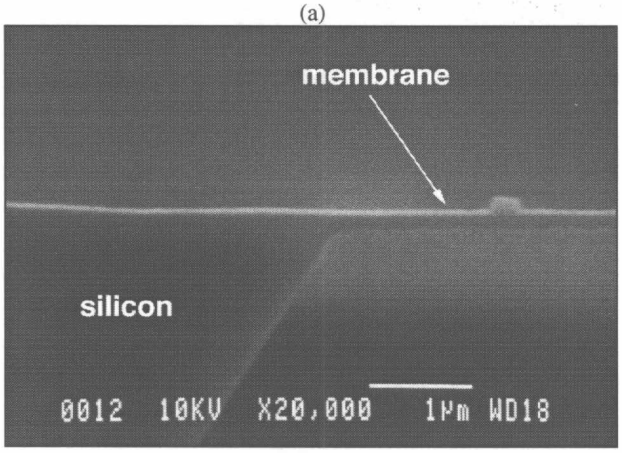

(b)

***Figure 4**: (a) SEM cross-section at one corner of the silicon membrane; (b) close-up view.*

To fabricate the ultra-thin silicon bridge, the front side of the silicon wafer is implanted with boron at 40keV at a dose of $7\times10^{15}cm^{-2}$. After implantation, the wafer is patterned using RIE to etch through the implanted layer leaving behind only those regions that include the bridges and bonding anchors. The silicon wafer is then thinned down to 200μm, and is subsequently bonded to a glass wafer. The glass substrate is patterned and recessed to a depth of ~7μm using a mixture of HF/HNO_3 to create the bonding anchors. Glass processing is completed after patterning Ti/Pt/Au interconnect lines on it. Finally, the silicon wafer is electrostatically bonded to the glass wafer, and the sandwich is then immersed in EDP to dissolve away the undoped silicon, leaving the p^{++} silicon structures mounted on the glass substrate. Figure 5 shows a thin p^{++} silicon bridge bonded to glass. The thickness of the silicon bridge after EDP is about 2400Å and 2200Å for devices annealed at 1100°C for 30sec. and for 15sec., respectively. This measured thickness matches simulation results if one takes into account the finite etch rate of highly-doped silicon in EDP. Figure 6 shows the change in resistance of the bridge as a function of temperature. To eliminate the piezoresistive effect of silicon due to the thermal expansion of glass, the change of the resistance due to piezoresistive effect is calculated from:

$$\frac{\Delta R}{R}=\frac{\Delta L}{L}G=\frac{\Delta L}{L}Y_l\pi_l \qquad (1)$$

where $\Delta L/L$ is the strain of the resistor and G the gauge factor which is equal to the product of Young's modulus and piezoresistive coefficient. The strain of the resistor is equal to the strain of the glass because the p^{++} resistor is very thin and will not affect the overall strain. The thermal expansion coefficient of Corning 7740 glass is 32.5×10^{-7}cm/cm/°C [6]. The Young's modulus of p^{++} silicon is ~175GPa, and the piezoresistive coefficient is dominant by $\pi_{44}/2$, which is 21.5×10^{12} (cm^2/dyn) [7]. As a result, $\Delta R/R$ is equal to 122ppm/°C, which is much smaller than the measured temperature coefficient of resistance (TCR) of the silicon bridges. Therefore, the resistance changes due to the piezoresistive effect can be neglected. The measured TCR varies from 1584ppm/°C to 1864ppm/°C based on six devices. These values closely match those reported by other researchers [8].

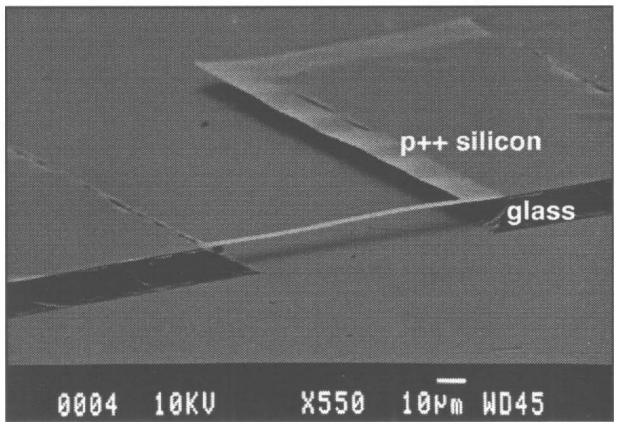

***Figure 5**: The p^{++} silicon bridge is 100μm long, 5μm wide, 0.24μm thick, and is bonded to glass anchors.*

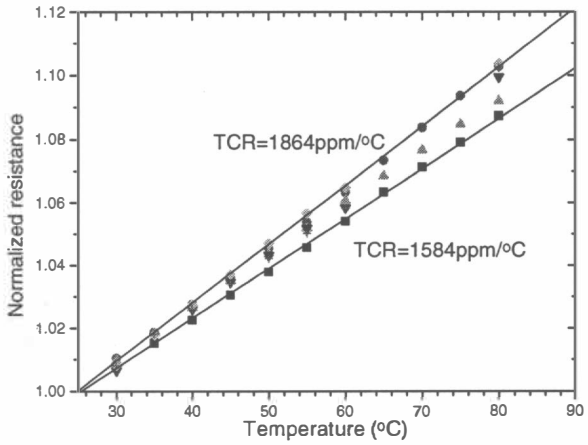

***Figure 6**: Measured temperature coefficient of resistance of a p^{++} silicon resistor.*

Combined with a dielectric diaphragm, the p^{++} silicon resistors can be used in a piezoresistive sound detector fabricated using the dissolved wafer process [5]. Fabrication starts by recessing the silicon wafer with RIE to a depth of 1μm, except in those areas that will later be bonded to the glass substrate. This recess is also used to create air ducts to equalize the pressure inside the cavity of the sound detector. Next a selective deep boron diffusion (~15μm) is performed at 1175°C for 15 hours, which

defines the rims of the sound detectors. A selective boron ion implantation at 40keV and a dose of $5\times10^{15}cm^{-2}$ is followed to define the piezoresistors. In order to activate the boron atoms, the wafer is annealed at 1000°C for 30sec. After annealing, a 2260Å low temperature oxide layer is deposited at 420°C followed by the deposition of a 1900Å PECVD nitride layer to form the diaphragm. The initial stress of the diaphragm can be reduced by varying the relative thickness of the nitride and oxide films, thus improving the sensitivity. The wafer is metallized with a Ti/Pt layer to form lead transfers to metal lines on the glass substrate and is then thinned down to ~100μm. The glass wafer is patterned and recessed to a depth of ~20μm to create the bonding anchors. This recess allows the formation of a large air gap under the silicon structure to reduce the possibility of clamping and the damping effect on the diaphragm. Glass processing is completed after patterning Ti/Pt/Au interconnect lines on it. Finally, the silicon wafer is electrostatically bonded to the glass wafer, and the sandwich is then immersed in EDP to dissolve away the undoped silicon, leaving the p^{++} silicon devices mounted on the glass substrate.

Figure 7 shows the structure of this piezoresistive pressure sensor. It consists of a 0.4μm-thick dielectric diaphragm suspended over a large air gap, and four 0.2μm-thick p^{++} ion-implanted piezoresistors. One of the advantage in using monocrystalline silicon instead of polysilicon is the high piezoresistive coefficient of single crystal silicon. The coefficient, π_{44}, is 43×10^{12} (cm^2/dyn) for p^{++}-type monocrystalline silicon [7], which is ~4 times higher than that of p-type polysilicon piezoresistors [9]. Figure 8 shows the measured pressure sensitivity of the detector, which is 1.1μV/V·Pa, with a nonlinearity of 2% over the full scale range of 10kPa.

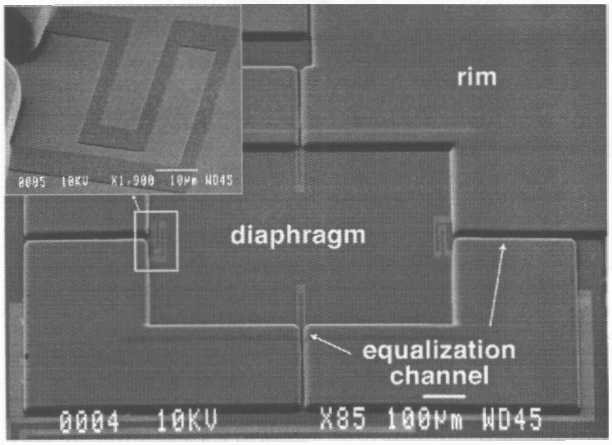

Figure 7: *SEM view of a 710μm-square silicon sound detector and a close-up view of one of the piezoresistors.*

CONCLUSIONS

We have successfully utilized ion implantation, rapid thermal annealing, and EDP etch-stop to form submicron p^{++} microstructures. Boron implantation at an energy of 40keV and doses of $5\times10^{15}cm^{-2}$ and $7\times10^{15}cm^{-2}$ have been used. The thickness of the p^{++} layer varies from 0.2 to 0.3μm depending on the annealing time and temperature. Since the highly-doped silicon layer is very thin, high temperature processes are eliminated to achieve a high boron concentration for an effective etch-stop. Boron ion implantation and etch-stop is a powerful technique because it allows the formation of a p^{++} microstructure on a standard CMOS wafer since ion implantation and annealing can be easily performed at the end of the process. In addition, it is simply possible to use the resident p^{++} layers in a standard CMOS process that are used for forming source/drain junctions of pMOS transistors. Finally, ion implantation provides flexibility in controlling the thickness and uniformity of the microstructure layer. We have reliably fabricated p^{++} microstructures as thin as 0.2μm.

Acknowledgments

The authors would like to thank Mr. Brendan Casey for wire bonding the devices. This work was sponsored by the Air Force Office of Scientific Research under contracts #F49620-94-0184 and F49620-96-0293. The views and conclusions contained herein are those of the authors and should not be interpreted as necessarily representing the official policies or endorsements, either expressed or implied, of the Air Force Office of Science Research or the U.S. Government.

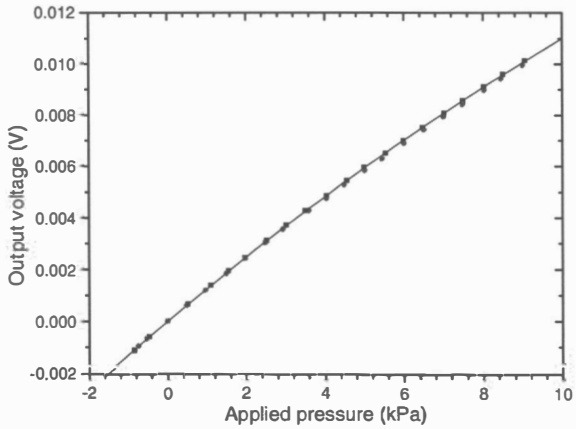

Figure 8: *Measured pressure sensitivity of the sound detector is 1.1μV/V·Pa with a nonlinearity of 2%.*

REFERENCES

1. A. Bohg, "Ethylene Diaminie-Pyrocatechol-Water Mixture Shows etching Anomaly in Boron-Doped Silicon", *J. Electrochem. Soc.*, 118, 1971, pp.401-402.

2. Y. Gianchandani and K. Najafi, "A Bulk Silicon Dissolved Wafer Process for Microelectromechanical Devices", *J-MEMS*, Vol. 1, No. 2, 1992, pp. 77-85.

3. C. H. Mastrangelo, W. C. Tang, "Semiconductor Sensor Technologies", in *Semiconductor Sensors*, Ed. S. M. Sze, 1994.

4. B. Folkmer, P. Steiner, and W. Lang, "Silicon Nitride Membrane Sensors with Monocrystalline Transducers", *Sensors and Actuators A* 51, 1995, pp. 71-75.

5. C. Huang, K. Najafi, E. Alnajjar, C. Christophorou, A. Naguib, and H. Nagib, "Operation and Testing of Electrostatic Microactuators and Micromachined Sound Detectors for Active Control of High Speed Flows", *Proc. Eleventh Annual Int. Workshop on MEMS*, 1998, pp. 81-86.

6. *ASM Engineering Materials Reference Book*, Second Edition, 1994, p. 320.

7. Y. Kanda, "Piezoresistance Effect of Silicon", *Sensors and Actuators A* 28, 1991, pp. 83-91.

8 P. W. Chapman, O. N. Tufte, J. D. Zook, and D. Long, "Electrical Properties of Heavily Doped Silicon", *J. Applied Physics*, V. 34, No. 11, 1963, pp.3291-3295.

9. H. Guckel, "Fine Grained Film and Its Application to Planar Pressure Transducers", *Proc. 4th Int. Conf. Solid-State Sensors and Actuators*, Tokyo, Japan, 1987, pp. 277-282.

DEVELOPMENT OF AN ELECTROPLATING PROCESS FOR HIGH THROUGHPUT, HIGH YIELD MANUFACTURING OF MAGNETIC COMPONENTS

Steven D. Leith and Daniel T. Schwartz[1]
Department of Chemical Engineering, Box 351750
University of Washington, Seattle, WA 98195

Keren Deng[2]
MEMStek Products LLC.
Vancouver, WA 98661

ABSTRACT

Geometrically complex NiFe components are deposited from a well characterized electrolyte using a custom designed plating apparatus. Structural and compositional features of plated parts are investigated using scanning electron microscopy (SEM) and energy dispersive x-ray spectroscopy (EDS). Results show that high rate, high yield electroplating of magnetic NiFe parts is possible through optimization of fundamental LIGA manufacturing principles.

INTRODUCTION

Many LIGA manufactured MEMS incorporate soft magnetic materials such as electroplated NiFe as mechanical microactuators [1,2]. The magnetic properties of electroplated NiFe are dictated by the composition and structure of the deposit which, in turn, are primarily determined by electrolyte mixing at the cathode surface and the applied current density during plating. Control of these processing variables on three length scales (*i.e.* workpiece, pattern and feature) is essential for successful plating of geometrically complex NiFe components with uniform magnetic properties. While much work has been devoted to optimization of through-mask plating of uniform NiFe deposits for use in magnetic data storage devices [2], this previous research has generally focused on plating through relatively thin photoresist masks (< 5 μm). With the increased interest in fabrication of much thicker, high aspect ratio magnetic components there exists a clear need for development of a manufacturing process for these types of materials. In this study, we report on the development and continual optimization of a high rate, efficient LIGA manufacturing process for fabrication of soft magnetic NiFe components. To achieve this goal, we have addressed three fundamental issues : 1. Formulation and characterization of a NiFe plating bath; 2. Design and fabrication of a wafer-scale plating apparatus and 3. Design and fabrication of a well conceived PMMA pattern.

To assess and optimize the LIGA manufacturing process, NiFe microgears ~200 μm thick and 1200 μm in diameter were galvanostatically plated onto a Si/Ti/Cu substrate through a patterned PMMA mask using a custom designed plating device developed in our lab. These microgear components serve as a process test bed for proprietary magnetic actuator designs. Growth and composition uniformity within individual parts and across the wafer were studied using scanning electron microscopy (SEM) in conjunction with energy dispersive x-ray spectroscopy (EDS). Results from the composition and deposit growth analysis are used to probe the effects of local mixing and current distribution during plating and to investigate effects of process modifications. Based on our studies, a LIGA manufacturing process has been developed capable of plating NiFe components at least 200 μm thick at rates exceeding 50 μm/hr with minimal yield loss due to deposit defects.

EXPERIMENTAL DETAILS

A nickel sulfamate/iron chloride plating bath capable of high rate NiFe plating was developed to operate at room temperature and pH = 3.00 [3]. The bath was comprised of nickel and iron salts (Ni:Fe molar ratio = 20:1), boric acid, sodium saccharin, sodium dodecyl

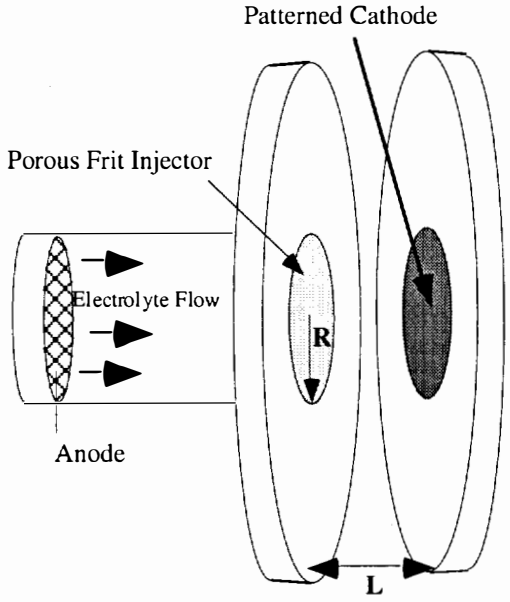

Figure 1. *Schematic representation of the electroplating device. Operation with L/2R<<1 results in uniform convective mass transfer to and a uniform current distribution on the patterned cathode.*

1. Author to whom correspondence should be addressed.
2. Current Address : CMRC, Semiconductor Research and Development, Texas Instruments Incorporated, PO 655012, MS 921, Dallas, TX 75265

0-9640024-2-6/hh1998/$20©1998TRF
DOI 10.31438/trf.hh1998.55

sulfate and ascorbic acid. To determine the effects of electrolyte agitation and applied current density on alloy composition, NiFe films were electroplated onto a platinum rotating ring-disk electrode using a range of current densities and electrolyte mixing rates. Composition of the resulting deposits was determined using potentiostatic stripping voltammetry, a well known electroanalytic technique commonly used to determine the composition of electroplated alloys **[4]**. Relationships between electrolyte agitation rate, applied current density and deposit composition for the plating bath were determined for alloys plated at current densities ranging from -20 to -100 mA/cm^2 and convective mass transfer coefficients ranging from 0.0015 to 0.013 cm/s (*i.e.* from weak to very strong agitation).

A wafer-scale electroplating apparatus was fabricated based on the design of the uniform injection cell (UIC) and is shown schematically in Fig. 1 **[5, 6]**. Proper operation of the UIC ensures uniform current distribution and electrolyte mixing at the workpiece length scale. NiFe microgears were electrodeposited from the nickel sulfamate/iron chloride plating bath onto a Si/Ti/Cu substrate through a patterned PMMA mask. To minimize the effects of current crowding at the edges of the patterned features, PMMA masks were designed such that individual patterned parts were closely packed **[7]**. A typical masked pattern measured 1.1 x 1.6 cm and contained nearly 150 individual microgear parts. Plating gears to a thickness in excess of 200 μm typically required between four and seven hours, depending on the current density used. After plating, the microgears were first planarized (while still confined within the mask) and then the PMMA was removed from the wafer. While still attached to the wafer, structural and compositional features of the plated microgears were studied using SEM and EDS.

RESULTS AND DISCUSSION

Figure 2 illustrates the relationships between plating current density (j), electrolyte mixing strength (k) and deposit composition (X_{Fe}) as determined from characterization of the plating bath. The figure shows that deposit composition is quite sensitive to variations in applied current density and electrolyte agitation. These data illustrate that through proper control of j and k, engineered NiFe alloys of various compositions can be electroplated from the bath. Additionally, the figure shows that there are a number of different sets of plating conditions that can be employed to deposit any one desired alloy composition. For example, to deposit an alloy that is 28 mol% Fe, one can electroplate at either -20, -60 or -100 mA/cm^2, as long as adequate and well controlled electrolyte mixing is provided. While the results in Fig. 2 were determined using an unmasked, planar electrode, the same $X_{Fe}(j, k)$ relationships are applicable to plating composition controlled, 3-dimensional MEMS components.

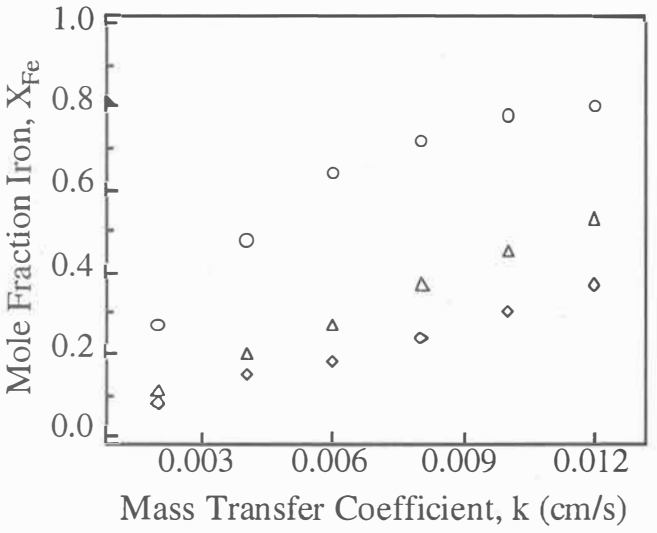

Figure 2. *Effect of electrolyte mixing strength on the composition of NiFe electroplated at -20 (O), -60 (Δ) and -100 (◇) mA/cm^2. Plating at high current densities and/or with weak electrolyte mixing (i.e. small k) produces deposits with a high nickel concentration.*

Figure 3 is an SEM micrograph showing electroplated permalloy (nominally $Ni_{81}Fe_{19}$) microgears 240 μm thick and 1200 μm in diameter before release from the wafer. Microgears shown in this figure were plated at -60 mA/cm^2, corresponding to a deposit growth rate of *ca.* 65 μm/hr. In many gears plated using an early

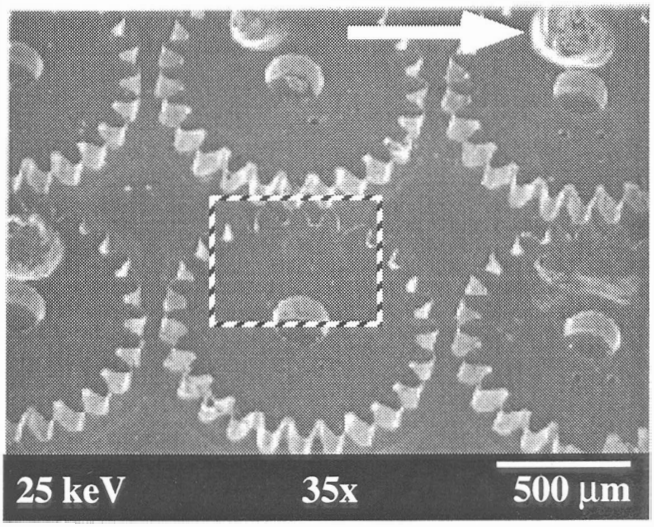

Figure 3. *Scanning electron micrograph of electroplated permalloy microgears before release from the Si/Ti/Cu substrate. A plating rate of 65 μm/hr has been achieved using the plating apparatus shown in Fig. 1. The arrow points to a pit defect caused by gas evolution and entrapment during plating.*

version of the UIC, gas evolution and entrapment resulted in creation of pit defects as indicated by the arrow in Fig. 3. This gas entrapment led to poor product yield in initial studies. Subsequent UIC design modifications have all but eliminated the problem and part yields are now close to 90%.

Even though the UIC provides uniform mixing and current distribution at the workpiece, composition uniformity in plated microgears is affected by non-uniformities in electrolyte mixing and current density on the feature length scale. Figure 4 is an EDS composition map of a typical plated microgear in which dark shading represents relatively higher concentration of nickel. The figure shows subtle composition variation across the entire gear. Since current crowding at the tip of the gear teeth and near the hub of the gear results in relatively higher local current densities in these areas, such non-uniformity should lead to an overall higher (and roughly uniform) nickel concentration in these regions, as can be deduced from Fig. 2. However, it appears that local variations in electrolyte agitation within the gear (in the form of strong eddy mixing) results in bands of low nickel concentration as illustrated

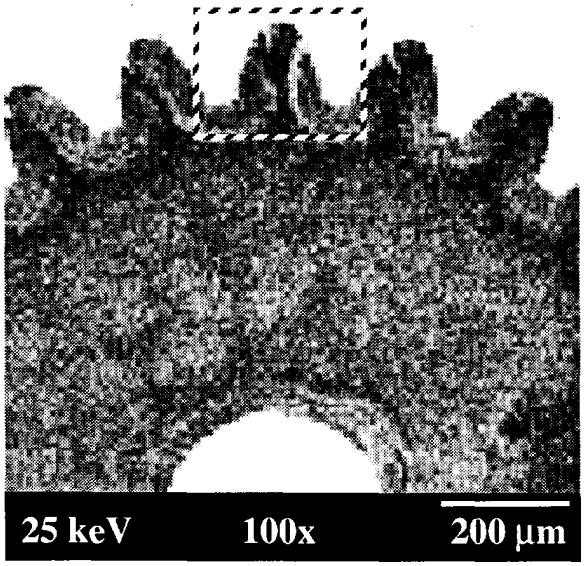

Figure 4. Composition map of the microgear shown in the boxed region of Fig. 3. Darker shading represents areas of relatively higher nickel concentrations. The map was created using energy dispersive x-ray spectroscopy.

by the light regions in Figs. 4 and 5. To minimize compositionvariation within plated gears, we have modified the UIC to improve current density uniformity at the pattern scale and are currently developing a plating bath that is less sensitive to the electrolyte agitation conditions.

CONCLUSIONS

By addressing and optimizing the fundamental aspects of LIGA manufacturing, we have made significant progress toward development of an electroplating process for high throughput, high yield manufacturing of MEMS magnetic components. Through careful formulation and characterization of a plating bath and the design and fabrication of a wafer scale plating device, we have realized a 10-fold increase in NiFe part throughput. Current studies are focusing on minimization of composition variation within plated parts through the systematic investigation of local current distribution and electrolyte mixing characteristics on the feature length scale.

ACKNOWLEDGMENTS

Support for this research was provided by MEMStek Products, the Washington Technology Center, and the National Science Foundation through a Young Investigator Award to D.T. S..

REFERENCES

1. Tabat, N., Klein, J. and Guckel, H., "Single Flux-Path Bi-directional Linear Actuators", *Transducers 97 Technical Digest,* Vol. 2, pp. 789-792, 1997.
2. Romankiw, L.T., "A path : from electroplating through lithographic masks in electronics to LIGA in MEMS", *Electrochim. Acta*, Vol. 42, pp. 2985-3005, 1997.
3. Leith, S.D. and Schwartz, D.T., "Electrodeposition of NiFe Thin Films from a Sulfamate/Chloride Bath", *Electrochim. Acta*, submitted April, 1998.
4. Andricacos, P.C., Arana, C., Tabib, J., Dukovic, J. and Romankiw, L.T., "Electrodeposition of Nickel-Iron Alloys I. Effect of Agitation", *J. Electrochem. Soc.*, Vol. 136, pp. 1336-1340, 1989.
5. Medina, J.A. and Schwartz, D.T., "Steady-State Characterization of the Uniform-Injection Cell I. Theoretical Analysis", *J. Electrochem. Soc.*, Vol. 142, pp. 451-456, 1995.
6. Medina, J.A., Sexton, D.L. and Schwartz, D.T., "Steady-State Characterization of the Uniform-Injection Cell II. Experimental Analysis", *J. Electrochem. Soc.*, Vol. 142, pp. 457-462, 1995.
7. DeBecker, B. and West, A.C., "Workpiece, Pattern, and Feature Scale Current Distributions", *J. Electrochem. Soc.*, Vol. 143, pp. 486-492, 1996.

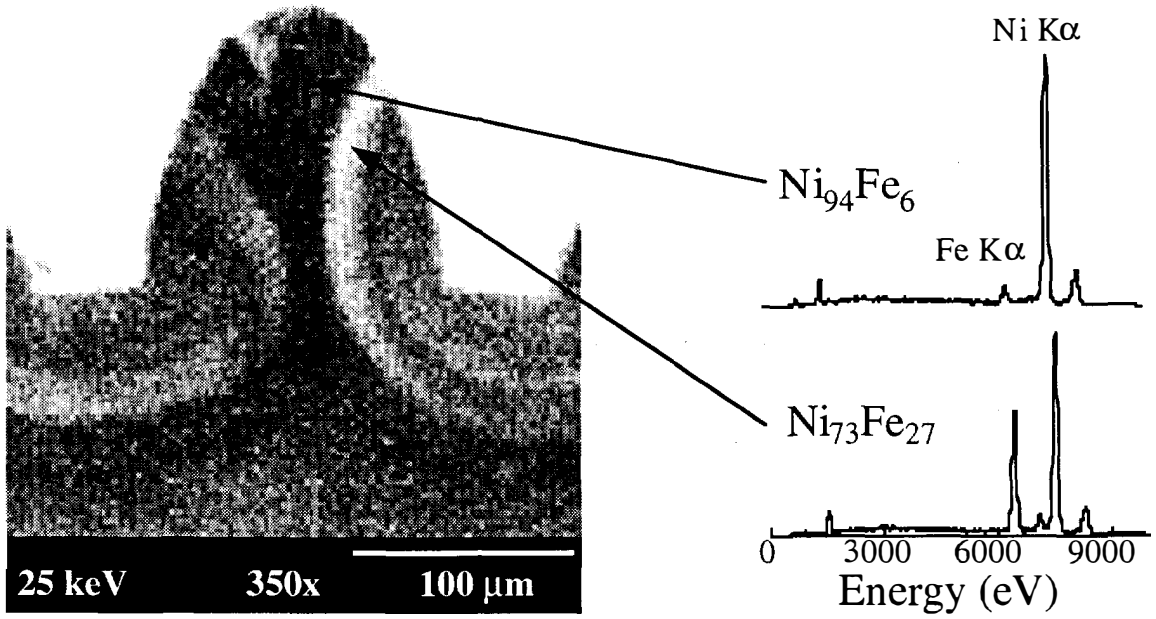

Figure 5. Composition map and x-ray energy spectra of the microgear tooth shown in the boxed area of Fig. 4. Local variation in composition results from feature-scale current density non-uniformities and flow effects within the pattern.

Selective Copper Plating of Polysilicon Surface Micromachined Structures

Jer-Liang Andrew Yeh, Jia-Ming Chen, Tom Kudrle, Hercules P. Neves, and Norman C. Tien
School of Electrical Engineering, Cornell University
401 Philips Hall, Ithaca, NY 14853

ABSTRACT

Selective electroless copper plating of polysilicon surface micromachined structures has been demonstrated. The encapsulation of free-standing polysilicon structures with copper will allow polysilicon to be used in MEMS applications requiring high conductivity. This copper deposition technique has the advantages of simplifying the metallization process, high deposition rate, low thermal stress, low bending stress, and backside metal coating. Palladium is used as the activated base metal for copper plating. Resisitivity and surface roughness characteristics of the copper are presented.

INTRODUCTION

Many microelectromechanical systems (MEMS) applications need metal structures for their electrical or optical properties. In wireless communication systems, components such as mechanical switches or high-Q passive elements require the high conductivity only available with metals. For instance, aluminum surface micromachining was used recently to fabricate a variable air-gap capacitor [1]. For optical systems, elements such as mirrors use metal because of their high reflectivity. Texas Instruments' Digital Mirror Device for projection displays [2] also uses aluminum structures.

There are, however, manufacturing challenges in using metal structures. One major difficulty is controlling the stress in metal films which causes bending of the structure. This leads to a restriction on the size of the element sometimes to less than 200 μm in any dimension [1]. Warping in these structures can be caused by the thermal mismatch between the metal and the sacrificial layer, which is usually photoresist or polyimide. Polysilicon surface micromachining, on the other hand, is a more mature technology that has demonstrated the ability to create not only larger-size low-stress structures, but also complex multi-level components. The drawback is that the electrical resistivity is higher and the optical reflectivity is lower for polysilicon when compared to most metals. Metallization of the polysilicon improves the electrical and optical characteristics. The typical procedure involves metal deposition (evaporation or sputtering) on the top of the polysilicon. This, however, results in a bimorph structure that could lead to warpage. Another metallization technique is electroless metal deposition [3,4]. Copper deposition on single-crystal silicon micromachined structures using an electroless plating technique [5] has been recently demonstrated.

Using this technique, we have selectively encapsulated polysilicon structures with copper, intended for use in wireless communication systems and in silicon micro-optical benches. Copper has a higher conductivity than aluminum which makes it attractive for high–Q RF elements. This method is compatible with silicon integrated circuit fabrication as copper will likely be used in future generations of integrated-circuit interconnects.

The copper deposition is a low-temperature process that minimizes the thermal stresses between itself and the polysilicon. Furthermore, copper deposited on both the top and backside of a structure is apt to balance the bending stress caused by copper plating the topside only. The encapsulation of a polysilicon cantilever has been demonstrated, shown in Figure 1.

The method has also been used to deposit copper on both sides of a hinged plate that can be used in silicon micro-optical systems, shown in Figure 2. A reflective surface on the backside of structures would allow more design flexibility, particularly for the hinged or folded-up optical elements used in the free-space micro-optical bench on silicon [6,7]. For instance, system design may require a hinged diffraction grating [8], with only topside metallization to be rotated to angles greater than 90°, which presents a difficult challenge for many actuators.

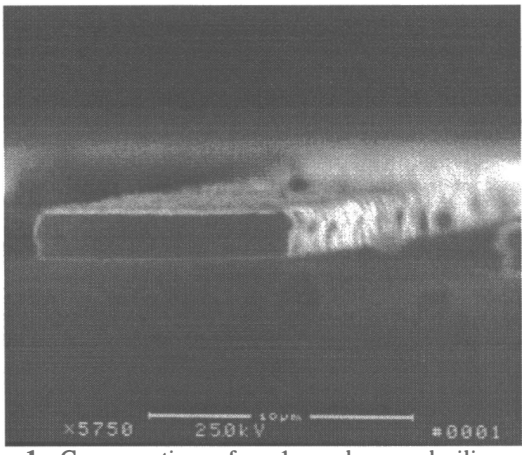

Figure 1: Cross section of a 1mm long polysilicon beam. Approximately 0.2μm of copper is deposited on the whole surface of polysilicon.

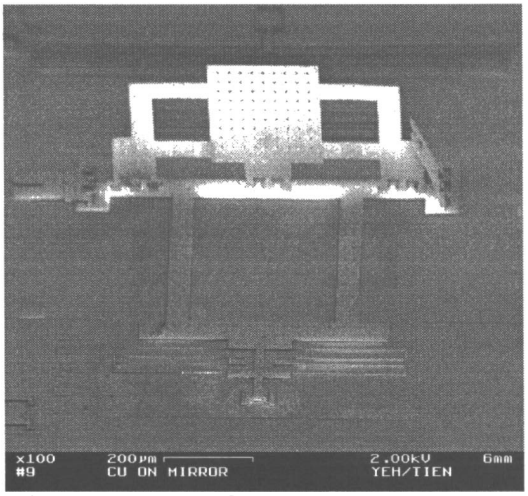

Figure 2: Backside of a flipped-up hinged polysilicon plate encapsulated in copper.

0-9640024-2-6/hh1998/$20©1998TRF
DOI 10.31438/trf.hh1998.56

Solid-State Sensors, Actuators, and Microsystems Workshop
Hilton Head Island, South Carolina, June 8-11, 1998

This metallization method also simplifies the polysilicon surface micromachining fabrication process. Etching or lift-off of the metal is not required because the copper only deposits on the layers that are activated which in this case is polysilicon and not isolation layers such as nitride and oxide. The need for a metal photolithography step over the large topography commonly in three or four layer polysilicon surface micromachining is avoided.

Copper is not the only metal that can be used for selective electroless plating of polysilicon surface micromachined structures. Some ferretic metals such as iron (Fe), nickle (Ni), cobalt (Co) are also can be selectively deposited on polysilicon through palladium activation. In this paper, copper is used to demonstrated how this electroless plating process is applied to polysilicon surface micromachined structures.

BASICS OF SELECTIVE ELECTROLESS COPPER PLATING

Selective copper deposition **[4]** starts with wet activation on the surface of polysilicon. Through the mechanism of contact displacement between a catalytic metal and silicon, catalytic metal (palladium) is used to form an activated film on the silicon surface and not on the isolation layers such as silicon dioxide or silicon nitride. The native oxide on silicon surface is removed by diluted HF. For our work, palladium plays the role of a base metal for copper deposition, while silicon dioxide and silicon nitride stay inactive to either catalytic metal or copper during the deposition.

The electroless copper plating occurs in the temperature range of 55°C to 80°C and at a pH value ranging from 12 to 13. The deposition process in a formaldehyde-based plating solution is well documented **[3,4].** Our solution contains a cupric salt, a reducing agent (formadelhyde), and a complexing agent (Ethylenediaminetetraacetic acid, EDTA) to keep the cupric ions in solution. The basic reaction can be expressed as

$$Cu^{2+} + 2HCHO + 4OH^- = Cu + H_2 + 2H_2O + 2HCOO^-$$

Additives to electroless Cu deposition solutions are surfactant RE610, surfactant/stabilizer Triton® X-100, and stabilizer 2,2'-dipyridyl. The surfactant RE610 is added to make copper surface smooth and give it a shining appearance. Triton® reduces defect density and enhances the electrical uniformity of Cu films. On the other hand, stabilizers decrease the deposition rate. A more detailed description of this technique will be published by Neves, H. P. et al. **[9]**.

EXPERIMENTAL PROCESS AND RESULT

The test devices fabricated at the Cornell Nanofabrication Facility (CNF) follow a conventional three-layer polysilicon surface micromachining process. At CNF, we use a p-type LPCVD (low pressure chemical vapor deposition) polysilicon deposited at the temperature of 610°C as the structural material and a LPCVD low-temperature oxide deposited at the temperature of 400°C as the sacrificial layer. The p-type polysilicon is in-situ doped using B_2H_6 (diborane) as the boron source. This polysilicon surface micromachining process begins with the passivation layer including 0.5μm-thick thermal oxide and 0.2μm-thick LPCVD nitride.

The next steps involve deposition and definition of the ground polysilicon layer of thickness of 0.5μm. This layer is lithographically patterned and then etched by a chlorine-based reactive-ion etch (RIE). A 2μm-thick low-temperature oxide (LTO) is deposited as the first sacrificial layer and followed by lithographic patterning and a CHF_3-based plasma etch of dimples and anchor openings. Another 2μm-thick in-situ boron-doped polysilicon layer that acts as the first structural material is deposited and patterned. An annealing step is performed at 1000°C for one hour in N_2. The second LPCVD LTO sacrificial layer of a thickness of 1.2μm is patterned and etched for the formation of anchor openings and poly1-poly2-vias. The last step of fabrication is to deposit and to pattern the 2μm-thick second structural polysilicon layer.

Post-process primarily includes a hydrofluoric acid (HF) release, copper metallization, and self-assembly monolayer (SAM) coating to reduce stiction. First, the polysilicon structures are released by removing the sacrificial oxide with 49% hydrofluoric acid, HF, and then followed by deionized (DI) water rinse. The samples are kept in DI to prevent the stiction of the structures on to the substrate or with each other which commonly occurs when they are dried. Then, the samples are transferred to a palladium solution that selectively activates the polysilicon structures (on all sides) and initiates the autocatalytic electroless copper deposition. During the activation, both the sacrificial layer (oxide) and the passivation layer (nitride) remain inactive to palladium ions. Right after the activation on the surface of polysilicon, samples are immersed in a copper plating solution. At a temperature between 55-80°C, the copper nuclei are initially formed on the Pd^+-activated polysilicon surface. After the formation of a thin-layer copper, copper starts to deposit on this thin initiated copper film. Upon completion of the deposition, samples are coated with a self-assembled monolayer of octadecyltrichlorosilane (C^{18} OTS) in a process developed by Houston et al. to prevent stiction **[10]**.

Alternatively, copper may also be selectively deposited in only certain regions on the chip. Before the HF release, photoresist is applied to the wafer. A photolithography step is used to open the areas where copper is to be deposited. After the buffered HF release of these areas, the photoresist is removed and is followed by the copper deposition. The sacrificial oxide prevents copper from depositing anywhere but released polysilicon regions (Figures 3 and 4).

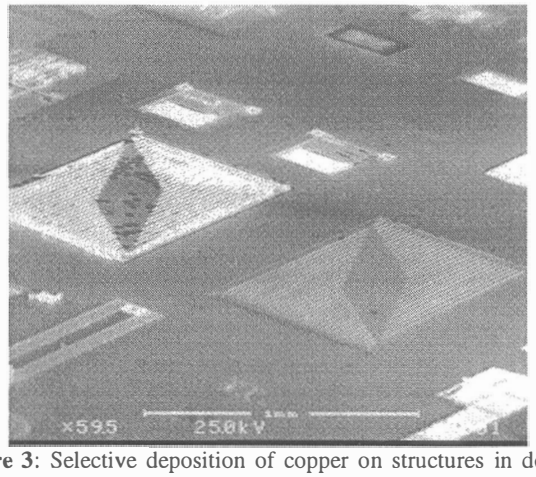

Figure 3: Selective deposition of copper on structures in desired areas on the chip. The bright structures imply copper deposited on polysilicon.

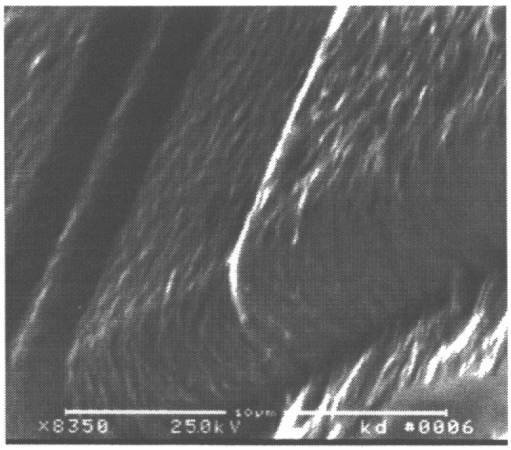

Figure 4: Selective deposition of copper on polysilicon. The oxide on the left-hand side of the polysilicon was protected during release. The right-hand side shows copper deposition. The copper is conformal to the polysilicon topography.

CHARACTERISTICS OF COPPER

For our work, the characteristics measurements we have performed include resistivity, deposition rate, grain size, roughness, and backside observation. The resistivity of electroless copper is measured by a Prometrix four-point probe instrument and is found to be 2.3μΩ-cm when deposited at the temperature of 66°C. As the deposition temperature increases, the resistivity decreases and approaches 1.8μΩ-cm. The deposition rate is found to be 55nm/min at the temperature of 66°C. The deposition rate goes up to 120nm/min as the deposition temperature increases to 80°C.

The surface morphology of the copper can be seen from a scanning electron microscope image of a sample with 400nm of copper deposited (Figure 5). The rms surface roughness of the copper was measured to be approximately 20nm over an area of 100 x 100 μm^2 using the contact mode of atomic force microscope (AFM). The rms surface roughness of the in-situ boron-doped polysilicon underneath the copper was found to be about 10nm. Scanning over an area of 1 x 1 μm^2, (Figure 6) we estimate that the average grain size of the copper to be 60nm.

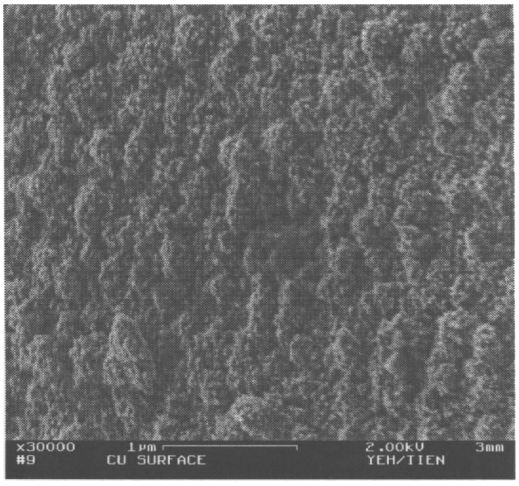

Figure 5: A SEM image of 0.4μm-thick copper on the top of polysilicon.

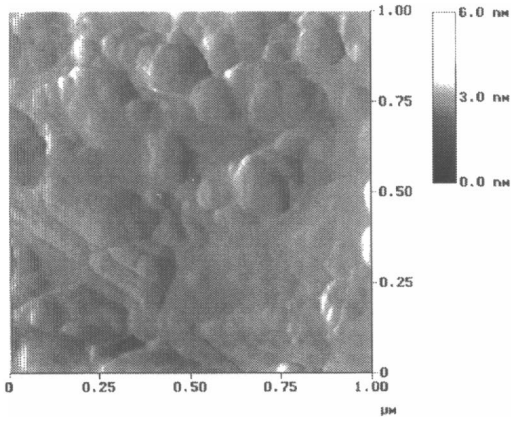

Figure 6: AFM surface scan of a sample with 0.4μm-thick copper on it.

The electroless copper was conformally deposited on the sidewalls of polysilicon structures and exhibited the same microstructure as that on the topside surface (Figure 7). It was also found that the edges of etch holes or structures have higher deposition rate than other places. In particular, the edges on the topside surface tend to attract more and larger particles which may eventually block the transportation of copper ions and by-products in and out through etch holes.

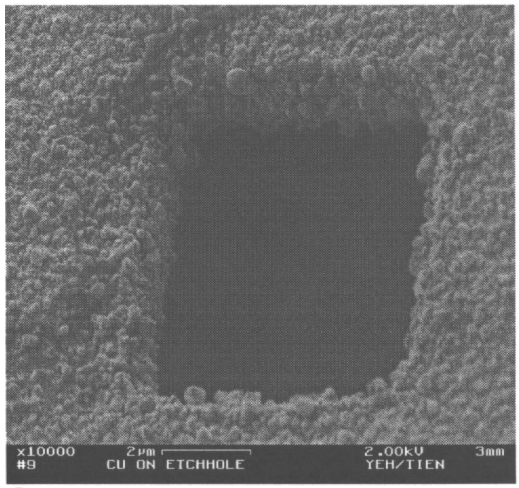

Figure 7: Electroless deposited copper around an etchhole.

We observed the copper deposition on the backside of polysilicon membrane with different size of etch holes and different spacing between the etch holes. At a deposition rate of 100nm/min for 2 minutes, copper aggregates form randomly within 5μm around etch holes. At a deposition rate of 30nm/min, scattered copper aggregates start to link with each other as time progresses. There are three primary factors in the quality of the backside deposition: palladium contact displacement on backside; the ratio between the diffusion length and the gap between the backside and substrate; and the degree in which the edge deposition blocks the copper ion diffusion.

FUTURE WORK

Selective electroless copper plating has been used to encapsulate free-standing polysilicon structures. This method allows polysilicon surface micromachining to be used for applications which require high conductivity, particularly on all

sides of low-stress structures. Using this technique, we will develop high-Q RF passive elements such as airgap capacitors, three-dimensional inductors, and mechanical switches for wireless communication applications. Cantilever beams encapsulated by copper can be employed to make an electrical switch which has copper-to-copper contact interface. This switch may have better performance than polysilicon switches without backside metal coating due to lower contact resistance and lower stiction.

For all these copper-coated devices, oxidation is an extremely critical issue. To prevent copper from oxidation, thin metal protective layers can be electroless deposited with a palladium activation right after the copper plating. Adhesion is also a critical issue in this process which will be studied further. For example, bubbling of the copper foil occurs occasionally because of low palladium activation concentration and no emission holes for hydrogen gas. The amount of activation can be optimized by controlling the palladium and HF concentration, and the activation time. Techniques such as a 400°C vacuum annealing can also enhance adhesion and uniformity.

The method has been used to deposit copper on both sides of a hinged plate that can be used in silicon micro-optical systems. Refinement of the deposition process parameters may improve the surface quality in terms of reflectivity and other metals may need to be considered. For instance, a micromirror reflective on both sides can be used in a bi-directional optical switch with two input fibers and two output fibers. The switching output of two input signals is controlled by the on/off position of the mirror.

ACKNOWLEDGMENT

The authors would like to thank the entire Cornell Nanofabrication Facility (CNF) staff for their support, Jocelyn Nee for her fabrication assistance, and Daryl Dagel and Hongrui Jiang for characteristic measurements.

REFERENCES

1. D. J. Young and B. E. Boser, "A micromachined variable capacitor for monolithic low-noise VCOs," Proc. IEEE Solid-State Sensor and Actuator Workshop, Hilton Head, SC (1996), pp. 86-89.
2. L. J. Hornbeck, "Digital Light Processing$_{TM}$ for high-brightness, high-resolution applications," Proceedings of the SPIE - The International Society for Optical Engineering, vol.3013, pp. 27-40 (1997).
3. M. H. Kiang, et al., "Planarized copper interconnects by selective electroless plating," MRS Symposium, Vol. 260, pp. 745-755 (1992).
4. Y. Shacham-Diamand, et al., "Copper electroless deposition technology for ultra-large-scale-integration (ULSI) metallization," Microelectronic Engineering, vol.33, no.1-4, pp. 47-58 (1997).
5. T. Kudrle, H. P. Neves, and N. C. MacDonald, "Microfabricated single crystal silicon transmission lines," to be published
6. M. C. Wu, et al., "Micromachined free space integrated micro-optics," Sensor and Actuators A, Phys., Vol. 50, pp. 127-134 (1995).
7. N. C. Tien, et al., "Surface-micromachined mirrors for laser-beam positioning," 8th International Conference on Solid-State Sensors and Actuators and Eurosensors IX. Digest of Technical Papers, Sweden (1995), Vol. 2, pp. 352-355
8. M. -H. Kiang, et al., "Actuated polysilicon micromirrors for Raster-scanning display," Transducers 1997 Digest of Technical Papers, Vol. 1, pp. 343-345.
9. H. P. Neves, T. Kudrle, J.-M. Chen, and N. C. MacDonald, "Characterization of electroless copper deposition for MEMS applications," to be published.
10. M. R. Houston, et al., "Self-assembly monolayer films as durable anit-stiction coatings for polysilicon microstructures," Proc. IEEE Solid-State Sensor and Actuators Workshop, Hilton Head, SC (1996), pp. 42-47.

ANODIC SACRIFICIAL LAYER ETCH (ASLE) FOR LARGE AREA AND BLIND CAVITY RELEASE OF METALLIC STRUCTURES

John C. Selby and Mark A. Shannon
University of Illinois at Urbana-Champaign
Urbana, IL 61801
email: **mas1@uiuc.edu** *voice:* **217-244-1545** *fax:* **217-244-6534**

ABSTRACT

A method to release metallic structures without the addition of diffusion etch holes is presented. The method employs an anodic sacrificial layer etch (ASLE) process which allows micro-structures with large surface area substrate coverage and/or structures with sacrificial areas that are not directly exposed to etchant from the surface (blind cavities) to be released in very short times. In addition, the thickness of the sacrificial etch layer can be arbitrarily set from about 200 Å to as thick as needed for controlling the tolerances between mating surfaces. One-dimensional etch rate experiments were conducted to directly compare ASLE with standard etching. The specific system tested was nickel electroplated on a copper seed layer, which is sacrificially released in a copper (II) nitrate-based etchant. The results show that the combination of fast etching of large areas with ultra-thin sacrificial layer is achievable with the ASLE process.

INTRODUCTION

Sacrificial layer etching is an integral step in the fabrication of many sensors and actuators [1,2]. When an electroplated metal serves as the principle structural material, release techniques often rely on various sacrificial layer etches in common wet etchants [3]. In these applications, designs for large area structures of the order of millimeters are limited by the necessity of etch ports [4] and relatively thick (1 µm and greater) sacrificial layers. Manufacturing throughput is limited by the times required for the various sacrificial layer etch procedures, as is the minimum selectivity ratio between the sacrificial layer and the structure. In addition, the release from cavities or structures with irregularly shaped interfaces is impeded where etchant flow is severely restricted. A main motivation for developing the anodic sacrificial layer etch (ASLE) process is to improve on these limitations, in order to release very large, arbitrarily shaped structures on the order of centimeters, with tight, controllable tolerances. The purpose of this article is to demonstrate that the ASLE process can dramatically enhance sacrificial layer etching, by removing the limitation that diffusion of chemical species normally imposes on standard wet etching.

THEORY

The concept underlying the ASLE process is shown in Fig. 1. In the ASLE process, the sacrificial layer is made into an anode, with respect to the etchant. By applying a voltage bias (both DC and a AC voltage with DC offset can be used), an additional driving force is supplied to the reactants at the interface of the sacrificial layer and etchant. This anodically driven etch process differs fundamentally from the usual wet etch process, in that it is not inherently diffusion limited. As depicted in the inset, the etch rate is determined by the normalized concentration (C*) gradient of the ions being removed. For very small layer thickness and large etch depth L, the normal etching process quickly becomes diffusion limited, since the gradient at the interface goes to zero. For the ASLE process, the gradient at the interface is governed by the applied field at the interface, and the concentration gradient does not tend to zero. The electrochemical process occurring at the interface and in the channel is in general very complicated and is in need of further study. However, the concept underlying ASLE is fairly general and a number of different etchant and sacrificial layer systems can be developed to exploit the process. Depending on the chemistry of the materials and

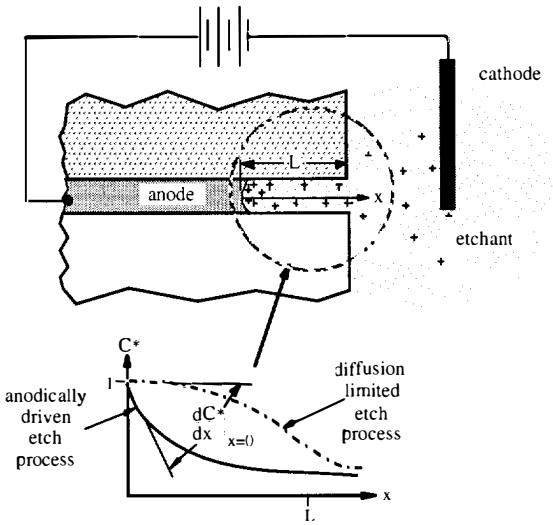

Figure 1 Concept of anodic sacrificial layer etch (ASLE) release.

etchant to be used, the anodic potential may act to increase the etch rate of the sacrificial layer with respect to the principle materials, or may drive a reaction forward that would not normally occur. Etch rate selectivity depends on both bath chemistry and applied potential. This dual dependency enables the ASLE process to independently or simultaneously etch sacrificial layers of different composition.

The sacrificial etching of a copper (Cu) layer in a bath of copper (II) nitrate and ammonium hydroxide electroplated with nickel (Ni) or permalloy ($Ni_{80}Fe_{20}$) demonstrates each of these aspects: (i) standard etching of the Cu sacrificial layer in a cupric nitrate bath can occur without any applied potential; (ii) applying an anodic AC and/or DC potential can dramatically increase the etch rate of Cu; and (iii) increasing the potential beyond a specific over-voltage initiates the etching of Ni or $Ni_{80}Fe_{20}$, the principle structural materials used in this study. Table I indicates the compositions of the etchant baths used. Standard and anodic etch rates are directly compared to demonstrate two fundamentally different limits of sacrificial layer etching: diffusion vs. reaction limited.

Normal sacrificial etching of the Cu layer with the standard etchant in Table I is primarily governed by diffusion of the reacting species. For release of thin sacrificial layers, the oxidizing species, copper (II) nitrate, must come into contact with the solid Cu, which is at the end of the effective etch channel, as shown in Fig. 1. Since two moles of copper (I) nitrate are produced for each depleted copper (II) nitrate, a net outflow occurs opposing the depletion gradient of Cu^{2+}. As the etch front recedes from the etchant bath of essentially constant concentration in Cu^{2+}, the depletion gradient decreases. Since it is this depletion gradient of Cu^{2+} that is driving the etch process, the etch rate will slow until it become diffusion limited, and the etching essentially stops. This process is complicated by subsequent thermodynamically-favored oxidation of Cu^{+} to Cu^{2+} in the channel; however, the basic concept remains.

The etching reaction changes considerably from the standard process when an electric potential is applied to the Cu. A net outflow of Cu cations from the surface occurs, as with the non-anodic etching reaction. However, unlike the case where

0-9640024-2-6/hh1998/$20©1998TRF
DOI 10.31438/trf.hh1998.57

Solid-State Sensors, Actuators, and Microsystems Workshop
Hilton Head Island, South Carolina, June 8-11, 1998

Table I: Copper Bath Etchant Compositions

Component	Standard Bath*	Reduced Bath
$Cu(NO_3)_2 \cdot 2.5\ H_2O$	7.5 g	0.15 g
NH_4OH (commercial 14.8 N)	36 mL	16 mL
DI H_2O	498 mL	24 mL

**Recipe for Standard Bath from H. Guckel's U. Wisconsin web page at* http://mems.engr.wisc.edu/products.html

the reacting specie must overcome the outflow driven only by a depletion gradient, the anodic potential also acts as a body force very near the etch front, driving the anions to the Cu surface for reaction. Conversely, the positive potential also drives the cations away from the front, creating an observably higher fluid velocity away from the front, helping to bring unreacted fluid nearer to the front due to conservation of mass. The higher the applied positive potential, the stronger the body forces act near the solid, which drives the reaction harder producing accelerated etch rates.

As with standard etching, the anodic reaction becomes more complicated when the principle metals are present in the etchant. With an applied potential, the principle metals electroplated on to the Cu also assume an anodic character, and can react with the etchant directly. Depending on the concentration of the copper (II) nitrate in the bath, we observed two competing reactions: passivation of the principle metal surface, and oxidation and etching of the metals. For the standard etchant, passivation of a pure Ni wire acting as the anode occurred for potentials below 3 V. Passivation increased with added potential: less with AC than for DC of the same mean voltage. In the standard bath, bubble formation initiates at the Ni anode above 3 V, starting the removal of the passivation layer. Higher nitrate concentration appears to increase both the passivation and bubble formation rates. Above approximately 5 V, bubble formation appears to completely remove the passivation layer and etching of the Ni began. Our working assumption is that principle metal etching begins with bubble formation, since no etching is observable or measurable below the initiation potential. The formation of a passivation layer on the principle layer is, in general, undesirable, since the thickness of the layer increases with time if no bubble formation is present. As the thickness increases, the etchant channel narrows, slowing the etch process and decreasing the desired clearance. The strongest effect on passivation layer formation is the concentration of the nitrite in the etchant bath. For low concentrations, no passivation layer was observed to occur at any applied positive potential.

The limit in the ASLE reaction rate in very small channels depends on several factors: passivation layer and bubble formation, Cu precipitate formation, viscous flow, and reaction kinetics. At a high enough potential, the fluid begins to form gas bubbles in the etchant, presumably at the Ni anode surface since bubbles did not form with Cu alone. As the formation of gas bubbles increases, the etchant is forced out of the channel, and the bubbles shield the etchant reaching the Cu surface. The bubble flow dynamics can become quite complex, at times enhancing etchant flow and other times shielding, with corresponding increases and decreases observed in the etch rate. Another limit in the anodic etch rate was observed when the voltage was increased high enough in the high copper (II) nitrate etchant to form a soluble, light-blue, Cu precipitate. Our working assumption is that the Cu ion compound forms as the Cu^+ ion is oxidized further to Cu^{2+}, forming a coordinated compound with water. This precipitate could then impede the flow of ions to and from the etch front, thereby creating essentially a new diffusion limit. Several species of copper nitrates and/or hydroxides can be formed by such a process. While soluble in NH_4OH, if the reaction rate is high enough, the local formation of such compounds can exceed the local solubility, and the precipitate forms. This precipitate dissolves when left in the bulk bath for a short time, but persists inside the channel. Another possible rate limit is viscous drag imposed on the outgoing and incoming ions by the walls of the channel. We would expect that as the gap narrows and lengthens, viscous drag on the ions increases and the etch rate decreases. More work will be needed to definitively find the viscous limit for ASLE, if it exists. The final limiting case considered here is the kinetic reaction limit. The reaction limit is the desired limit, since for the ASLE process the kinetic rate is determined by the electron flow and reacting ion concentration. Thus, the etch rate can be controlled for a given concentration by adjusting the voltage, as long as one of the other limits does not occur first. Our preliminary data shows that for samples where one of the other limits was not reached, the etch rate was only a weak function of depth of etch, and depended only on the current density. Therefore, it appears that it may be possible to optimize a given ASLE process to be rate limited, to etch extremely high aspect ratio sacrificial layers.

EXPERIMENT

To determine the effectiveness of the ASLE process, one-dimensional etch rate experiments were conducted using the copper etchant described above to directly compare ASLE to standard sacrificial layer etching. A Cu sacrificial layer and the copper (II) nitrate-based etchant were chosen since the etchant can be used for both standard and anodic etching for direct comparison. Other potential anodic etchants would not etch Cu without an applied potential. Two sets of samples with Ni electroplated on a Cu sacrificial seed layer were fabricated. The samples varied in copper sacrificial layer thicknesses, with each sample having an identical counterpart in the other set.

In order to quantify our comparison, the etch front of the sacrificial layer was monitored *in situ* [5], through an ordinary pre-cleaned Pyrex microscope slide as depicted in Fig. 2. Sequential metal films of titanium (Ti) and Cu were evaporated on the slide. Ti was used as an adhesion layer to the glass and as an oxidation shield for the Cu seed/sacrificial layer. Four thicknesses of Ti/Cu/Ti were used in each set: 150/300/150 Å, 150/3000/150 Å, 300/500/150 Å, and 300/2000/150 Å. The thicker 300 Å Ti adhesion layer was used on the last two due to concerns that the roughness of the glass substrate prevented full coverage. However, no large differences were observed, save difficulties seeing through the thicker Ti layer. A rectangular photoresist mask 2 by 3.25 cm was used as the electroplating mold. Prior to electroplating, the upper layer of Ti was removed in a 1:50 HF:DI acid bath, exposing the copper layer. A standard nickel sulfamate bath was used to electroplate Ni on Cu

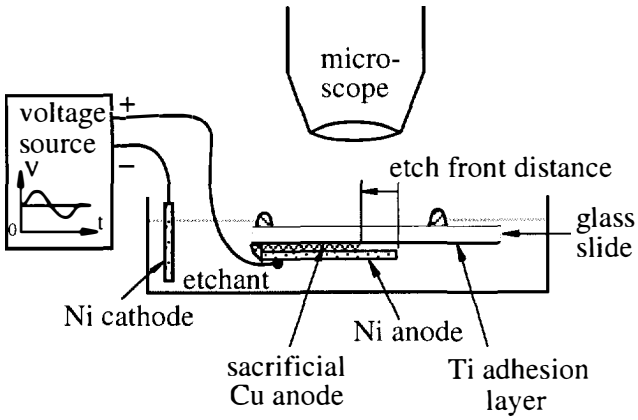

Figure 2 Experimental set-up of 1-D etch rate monitoring.

at a conventional current density of 50 mA/cm^2 for one hour. Following electrodeposition, the photoresist and the exposed upper layer of Ti was removed, and a silicone sealant was applied to three of the four sides of the nickel rectangle in order to form a one-dimensional rectilinear etch port [6]. On the back surface of each slide, additional silicone was applied to form an embankment mirroring the location of the nickel structure in order to keep etchant from flowing over this surface. The 150-300 Å Ti adhesion layer was translucent: thus we monitored the movement of the etch front of the Cu layer through the back of the glass slide using an ordinary optical microscope.

One set of 4 slides was immersed in the standard etchant and monitored at various time intervals to track the distance that the etch front moved from the edge of the Ni. The other set had electrical leads attached with conductive epoxy to one corner of the nickel structure, and then sealed with silicone. After immersion in the etchant, a DC potential was applied, with a coil of Ni wire serving as the cathode. Progression of the etch front was monitored to about 500 μm at which point the potential was removed. One sample was then used to determine the characteristics of an applied AC potential, while another was used to evaluate etch rate characteristics of a different bath chemistry.

RESULTS AND DISCUSSION

Prior to the controlled etch studies, metallic structures of large planar area and others with blind cavities were fabricated on silicon wafer substrates and released using an earlier form of the ASLE process. Chronologically, the first attempts of anodic sacrificial layer etching were performed on nickel structures using a Ti adhesion layer as the anodic layer. Buffered oxide etch (BOE) was used to etch the Ti, and a potential of 10 VDC was applied to accelerate the process. Although the nickel structure was released quickly with negligible attack on the Ni, the combination of the potential and the BOE actually etched large holes (300 μm) through the silicon! Subsequently, different metal systems and/or selective etchants [7] were investigated to find more suitable systems to anodically release over Si. The copper (II) nitrate/ammonium hydroxide bath listed in Table I, and its peculiar selectivity of copper over titanium, is one such system. To test this etchant with Ni and Fe, permalloy structures were electroplated using various well known electroplating baths and methods [8,9]. These structures were fabricated on planar silicon substrates as well as in cavities created in the silicon substrate using KOH anisotropic etch procedures. These early ASLE experiments were designed to find out how fast the etch process could go, how much area could be released without the addition of etch holes, how thin the sacrificial layer could be, and if structures plated into cavities could be released. Consequently, we used relatively high potentials (> 10 V), and we were not excessively concerned with selectivity with respect to the principle metal material, or their cosmetic appearance. Two examples of early experimental large area release samples can be viewed in Fig. 3. For both Ni and $Ni_{80}Fe_{20}$, solid plated areas of over 1 cm^2 were released in approximately 1 hr. In addition, the thickness of the seed layer could be taken down to as little as 200 Å, and release would still occur. Each aspect of high speed, large size, and ultra-thin sacrificial layer exceeded the standard methods of release we are aware of by several orders of magnitude.

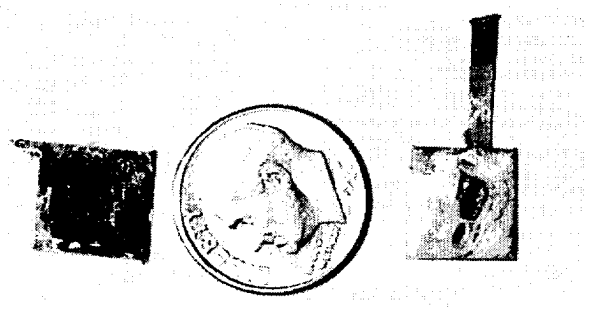

Figure 3 - Inelegant, but effective, examples of large area (~ 1 cm^2) release in about 1 hr. from an ultra-thin (< 500 Å) sacrificial layer using ASLE, without any etch holes added to enhance diffusion. On the left is permalloy approximately 25 μm thick, and the right is nickel about 80 μm thick. Both layers were plated on Ti(150 Å)/Cu(300 Å) with adhesion to the wafer stronger than the fracture strength of the underlying Si.

To quantify the results, one-dimensional etch experiments were conducted with the Cu/copper (II) etchant system. Figure 4 shows the etch front distance vs. time for Cu layers of 300 and 3000 Å thickness. In (a), the diffusion limit for the normal etch case is clearly seen as the rate goes to zero at times over 2000 min. at about 1 mm depth. The ASLE using a DC potential at 3 V for the same case shows no such limit to the same depth. In (b), the results for the 3000 Å case are plotted in log-log form to show the order of magnitude higher initial etch rate in the ASLE before the standard case becomes diffusion limited, with little drop-off in rate. The nearly constant rate is indicative of a reaction limited etch. Similar results were found for all the other samples tested. However, we did note that using the standard bath for ASLE that a Cu precipitate formed in the channels. The precipitate often clogged the channels, causing uneven etching and some rate fluctuation with distance.

(a)

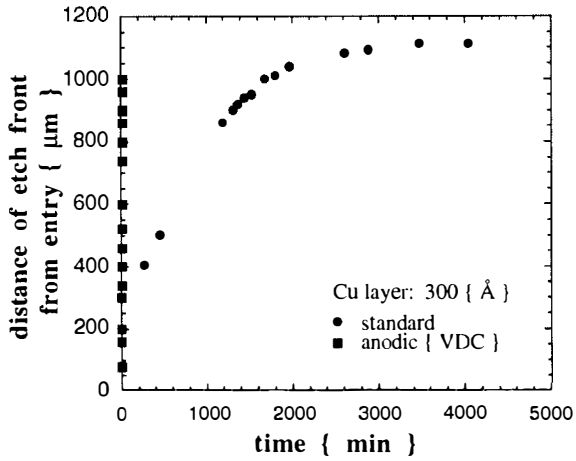

(b)

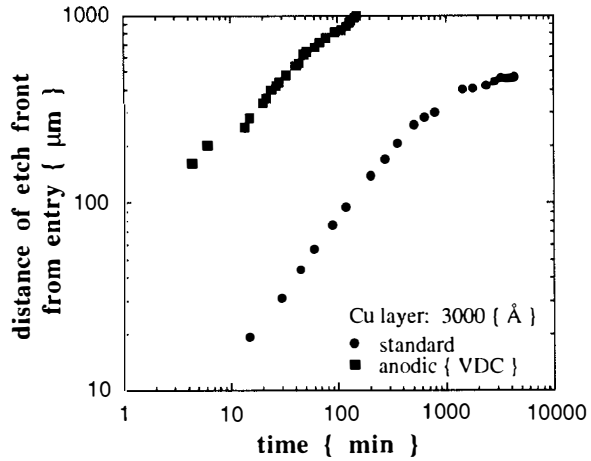

Figure 4 - Observed 1-D etch depth vs. time for (a) 300 and (b) 3000 Å thick Cu sacrificial layer. Fig. (a) shows diffusion limited behavior vs. time of standard etch, and (b) in log-log shows the initial order of magnitude higher etch rate of the anodic vs. standard before standard becomes diffusion limited.

Although the precipitate which exited the channel due to the induced flow during the anodic etch dissolved in the bulk fluid, the precipitate persisted in the channels as the depth increased, presumably due to local changes in NH_4OH concentration. In separate tests, the formation of precipitate was found to be a strong function of nitrate concentration. By dropping the nitrate concentration in the bath, the precipitation could be completely suppressed. However, the etch rate exhibited nearly a step function with respect to a minimum in copper (II) nitrate concentration. Etching proceeded extremely slowly at no to very low concentrations in copper (II). Once a minimum value, slightly below that given in Table I for the reduced bath, was reached, etching continued at the same rate as for the standard case, but without the fluctuations observed earlier, as shown in Fig. 5 for a 2000 Å thick Cu layer. The etch rate is essentially linear in this regime, and thus appears to be limited only by the reaction due to the applied voltage and thus current density. It should be noted that for the reduced concentration, no observed etching occurred without an applied potential. Therefore, the anodic potential is essential for the reaction to proceed.

In separate tests to investigate the formation of the passivation layer and bubbles on the Ni anode, we observed that applying an AC potential with a mean at the previously tested DC voltage, reduced both the passivation layer and large bubble formation, particularly at frequencies over 1 KHz, though no further changes were easily observed at higher frequencies (to 10 MHz). If the passivation layer grows too large, the channel may close off, slowing the rate. Also, if bubble formation is excessive, the etch rate may fall. Therefore, we tested a 1 KHz AC potential, where the minimum is above 0 V to avoid redeposition of Cu. As seen in Fig. 6, applying an AC potential more than doubled the etch rate over the DC case. The diffusion-limited standard etch case is included for comparison. Clearly, AC excitation and its enhancement mechanisms require further investigation.

CONCLUSION

This study is an initial investigation of the anodic sacrificial layer etch process for achieving orders of magnitude improvement in release of micro-structures. The process has yet to be optimized, but the results so far are promising and suggest several areas of future study, including: different ASLE systems, DC vs. AC, etchant concentrations, binary anodes, and limiting mechanisms. In addition, the Cu process described here can be can be integrated with an ammonium fluoride and CO_2 supercritical drying process to prevent stiction of moveable structures [10], potentially enhancing ASLE's use for releasing blind structures in-place: research currently underway at UIUC.

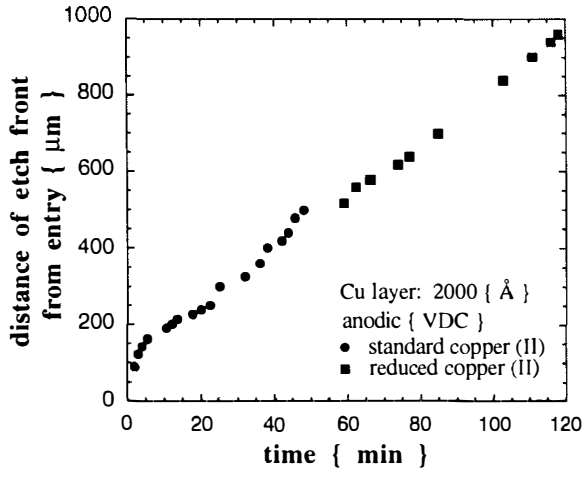

Figure 5 - Anodic etch using with the standard and reduced copper (II) nitrate etchants. Linear behavior of reduced bath suggests reaction limited etch is occurring.

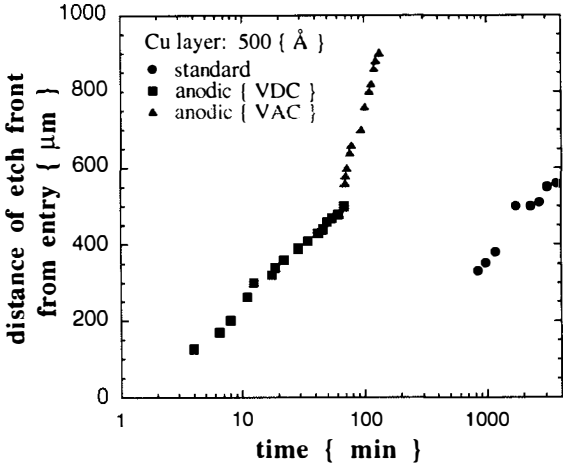

Figure 6 - Shows DC and 1 KHz AC anodic etch compared to standard etch for 500 Å Cu layer. Enhanced affect of AC excitation over DC is clearly seen for this sample.

REFERENCES

[1] C.H. Ahn, Y. J. Kim, and M. G. Allen, "A Planar Variable Reluctance Magnetic Micromotor with Fully Integrated Stator and Coils", *Journal of Microelectromechanical Systems 2*, (4), December 1993, pp. 165-173.

[2] J.W. Judy and R.S. Muller, "Batch Fabricated, Addressable, Magnetically Actuated Microstructures", *Technical Digest of the 1996 Solid-State Sensor and Actuator Workshop*, pp. 187-190.

[3] A.B. Frazier and M.G. Allen, "Metallic Microstructures Fabricated Using Photosensitive Polyimide Electroplating Molds", *Journal of Microelectromechanical Systems 2*, (2), June 1993, pp. 87-94.

[4] C. Liu, T. Tsao, Y-C Tai, T-S. Leu, C-M Ho, W-L Tang, and D. Miu, "Out-of-Plane Permalloy Magnetic Actuators for Delta-Wing Control", *Proceedings of the IEEE Workshop on Micro-Electro-Mechanical Systems*, 1995, pp. 7-12.

[5] W.P. Eaton, J.H. Smith, and R.L. Jarecki, "Release-Etch Modeling for Complex Surface Micromachined Structures", *Proceedings of SPIE on Micromachining and Microfabrication Process Technology II*, October 1996, pp. 80-93.

[6] J. Liu, Y-C Tai, J. Lee, K-C. Pong, Y. Zohar, and C-M. Ho, "*In Situ* Monitoring and Universal Modeling of Sacrificial PSG Etching using Hydrofluoric Acid", *Proceedings of the IEEE Workshop on Micro Electro Mechanical Systems*, February 1993, pp. 71-76.

[7] K.R. Williams and R.S. Muller, "Etch Rates for Micromachining Processing", *Journal of Microelectromechanical Systems 5*, (4), December 1996, pp. 256-269.

[8] I.W. Wolf, "Electrodeposition of Magnetic Materials", *Journal of Applied Physics 33*, (3), March 1962, pp. 1152-1159.

[9] M.E. Henstock and E.S. Spencer-Timms, "The Composition of Thin Electrodeposited Alloy Films with Special Reference to Nickel-Iron", *Transactions of the Institute of Metal Finishing 40*, 1963, pp. 179-185.

[10] M.R. Houston, R. Maboudian, and R.T. Howe, "Ammonium Fluoride Anti-Stiction Treatments for Polysilicon Microstructures," *Transducers 95 Technical Digest*, pp. 210-213.

CARBONIZED PARYLENE AS A CONFORMAL SACRIFICIAL LAYER

Elliot E. Hui[*], Chris G. Keller[+], and Roger T. Howe[*#]
Depts. of EECS[*], MSME[+], and ME[#]
Berkeley Sensor & Actuator Center
University of California at Berkeley
Berkeley, CA 94720-1774

ABSTRACT

This paper describes a conformal carbon sacrificial layer process with application to molded polysilicon structures. Molded structures 25 μm tall have been fabricated and released using a sacrificial layer only 0.3 μm thick. Parylene is deposited from the vapor phase as a conformal film. After a pre-treatment in a plasma of CHF_3 and He to cross link its surface, the parylene is pre-baked at 400 °C and then heated in an N_2 ambient at 700 – 1000 °C to form a conformal layer of carbon. Following conventional deposition, annealing, and patterning of the polysilicon structural film, the carbon sacrificial layer is removed by oxidation. At 700°C, the oxidation rate is as high as 50 μm/min for the first 2000 μm of undercut.

INTRODUCTION

Surface micromachining is dependent on highly selective removal of sacrificial layers with minimal attack of either the structural layers or the isolation films used to protect the substrate [1]. Silicon dioxide is a common sacrificial layer for polysilicon and silicon nitride microstructures, with hydrofluoric acid being used as the selective etch for oxide. There are several drawbacks with deposited oxide sacrificial layers for molded polysilicon processes (Hexsil) [2], which demand highly conformal film coverage and can involve very long etches in concentrated HF to remove oxide films coating a complex, deep-etched mold.

In order to achieve a precision replication of the mold, a thin, uniform sacrificial layer is needed. Conformal SiO_2 films can be deposited using tetraethylorthosilicate (TEOS) as a precursor [3]. For faster etching, phosphorus-rich sacrificial layers are desirable, however, such PSG films tend to deposit less conformally [4]. In order to ensure that the mold is adequately coated by a less conformal sacrificial layer, thicker depositions are required.

The wet etching of SiO_2 sacrificial layers has been extensively studied [5]. Lengthy undercuts, such as those needed for releasing Hexsil molded parts, translate into very long etch times due to the slow etch rate and ultimately, due to diffusion effects. Wet release processes are also prone to stiction of the released structures after drying due to capillary forces [6]. Hexsil molded structures, with their large surface areas, are especially vulnerable to this phenomenon. Finally, it has been conjectured that long exposure to HF during the sacrificial oxide etch can damage polysilicon structural films, through attack at the grain boundaries or other mechanisms [7-9]. A recent study suggests pitting from HF attack as one cause of the large spread in polysilicon fracture stress [10].

Carbon as an alternative sacrificial layer was pioneered by J. Bernstein over a decade ago and applied to sheet polysilicon fabrication for solar cells [11]. A principal advantage of carbon is that it can be etched with extremely high selectivity with respect to inorganic materials such as silicon, oxides, or nitrides by simple oxidation – a dry process. Oxidation of carbon can be a very rapid process at moderate temperatures, which, together with the near-infinite selectivity, implies that large areas of polysilicon can be undercut. Polysilicon nucleation on carbon films was also found to be superior to that on oxide films [11].

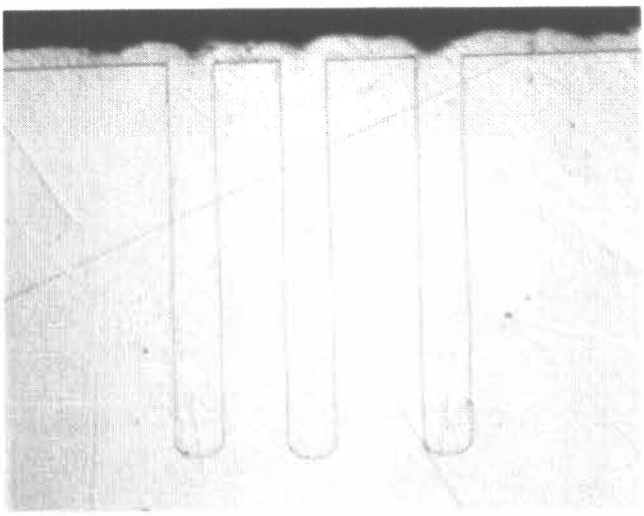

Figure 1. *50* μm *x* 8 μm trenches lined with a 0.3 μm carbon sacrificial layer and filled with molded LPCVD polysilicon.

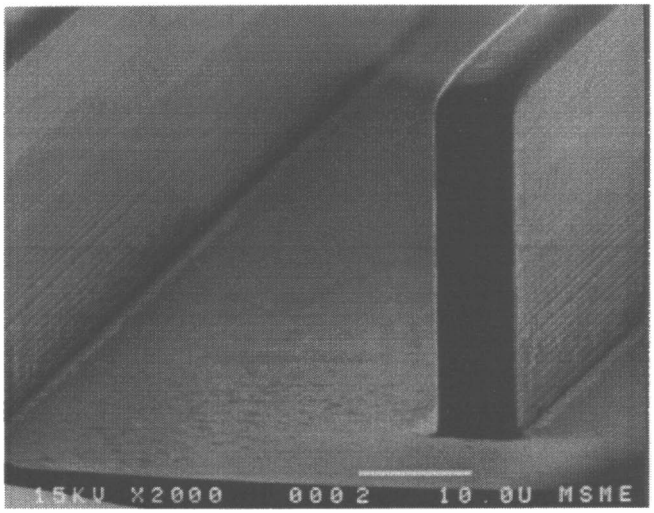

Figure 2. *A 25-μm tall polysilicon fin, molded and released using a 0.3-μm carbon sacrificial layer. The lines on the sidewalls are an accurate representation of the mold, which has scalloping on walls caused by the deep RIE etcher.*

In order to extend the carbon process to the conformal sacrificial layers needed for molded polysilicon microstructures, this paper characterizes processes for carbonizing a conformally deposited parylene film. A critical step is the stabilization of the parylene against flow while heating to temperatures of 700-1000°C

0-9640024-2-6/hh1998/$20©1998TRF
DOI 10.31438/trf.hh1998.58

Solid-State Sensors, Actuators, and Microsystems Workshop
Hilton Head Island, South Carolina, June 8-11, 1998

in N_2 during carbonization, which we have achieved to a large degree using a plasma treatment and pre-bake. After describing the formation of the carbon sacrificial layer, its initial application to the fabrication of Hexsil test structures is outlined

As can be seen from the lapped cross section in Fig. 1 and the SEM of a released polysilicon fin in Fig. 2, carbonized parylene approaches the ideal thin and conformal sacrificial layer. Sidewall features on the released polysilicon fin replicate the scalloped surface of the silicon mold with good fidelity, owing to the 0.3 um-thick conformal carbon sacrificial layer. Oxidation at 700°C was used to etch the carbon and release the polysilicon part.

BASIC PROCESS

Carbon Preparation

Formation of the carbon film involves deposition of parylene, hardening of the parylene surface, and finally carbonization of the parylene by heating in the absence of O_2. Parylene polymers are vapor deposited at low pressure at room temperature. Prior to deposition, an adhesion layer of A-174 Silane is applied to the silicon mold wafer. 2-μm coatings of Parylene C (poly 2-chloro-paraxylene) were used in this work.

Hardening of the parylene surface is needed in order to prevent flow of the parylene during the high temperature carbonization step. Currently, the most effective hardening step consists of a 1-minute exposure to a 100-W plasma of CHF_3 and He, followed by a pre-bake in N_2. For the pre-bake, the furnace temperature is ramped from room temperature up to 400 °C and then immediately turned off and allowed to cool back down to room temperature.

Heating to 700 – 1000 °C completes carbonization. Care must be taken not to expose parylene or carbon to oxygen while at high temperature. Samples are inserted into a furnace tube at room temperature. After sealing and purging the tube with nitrogen gas, the furnace is ramped up to the desired temperature. One hour at the elevated temperature has been found to be sufficient for carbonization. The furnace tube is then allowed to cool to room temperature before the samples are removed. The thickness of the resulting carbon layer is reduced by factor of four from that of the originally deposited parylene.

The polysilicon structural layer is deposited and annealed conventionally. Inserting samples into the LPCVD tube at around 600 °C has not been found to adversely affect the carbon even though oxygen is present to some extent during insertion. Piranha and HF cleaning also do not harm the carbon. Patterning of the structural layer should be straightforward, although we have not attempted this yet.

Oxidation burnout for release is performed with dry O_2 in a furnace tube. The oxidation temperature currently used is 700 °C.

Process Characterization

To examine the application of the carbon sacrificial layer to Hexsil technology, high aspect ratio trench structures were fabricated using anisotropic KOH etching of (110) silicon. Trenches were 200 μm deep and 4 - 16 μm wide, as shown in Fig. 3(a). Hexsil molds were also prepared using deep RIE.

In order to observe the conformality of the parylene deposition, coated trench structures were dipped in liquid nitrogen to freeze the parylene film and then immediately cleaved for cross-sectional SEM imaging.

Coated test structures were carbonized following a variety of pre-treatments in order to characterize the effect of various pre-bake temperatures as well as the presence or absence of different

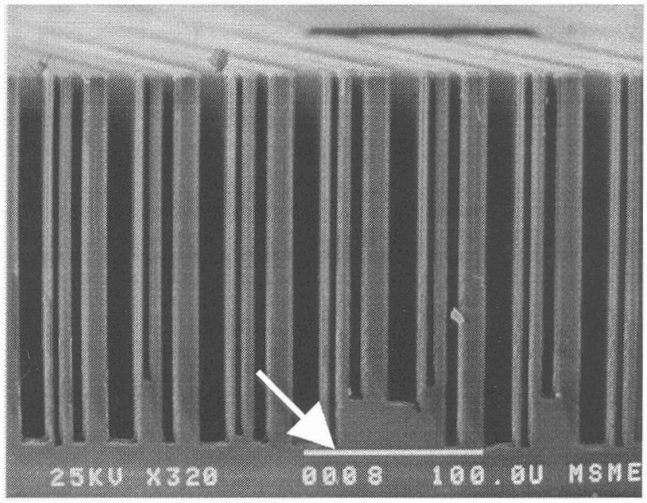

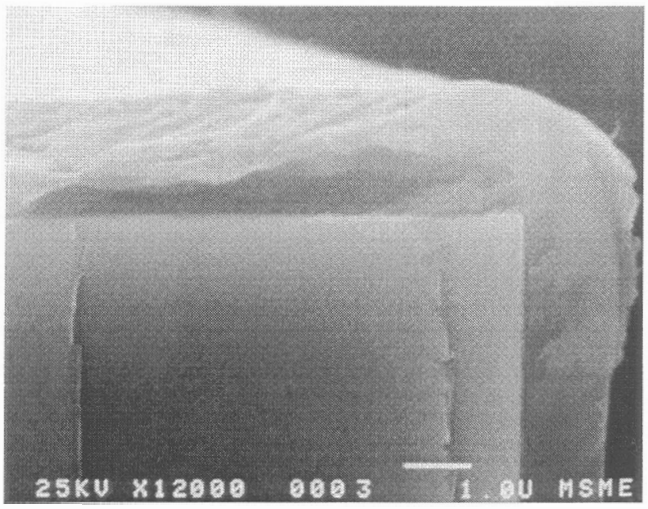

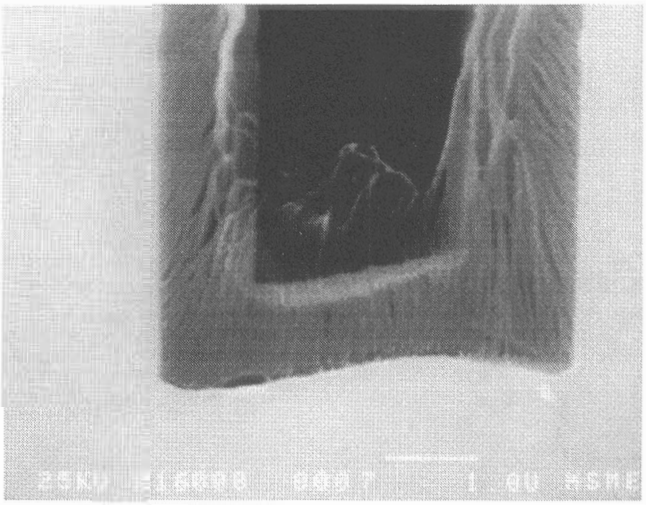

Figure 3. (a) Cross-sectional view of high aspect ratio test structures, 200 μm deep and 4 – 16 μm wide, coated with parylene. The arrow indicates the location of 3(c). (b) Close-up view of a corner shows that the parylene step coverage is excellent. (c) Coverage is also very good at the bottom of a trench. The wispy strings are an artifact of sample preparation, in which the ductile parylene was frozen in liquid nitrogen prior to cleaving the wafer.

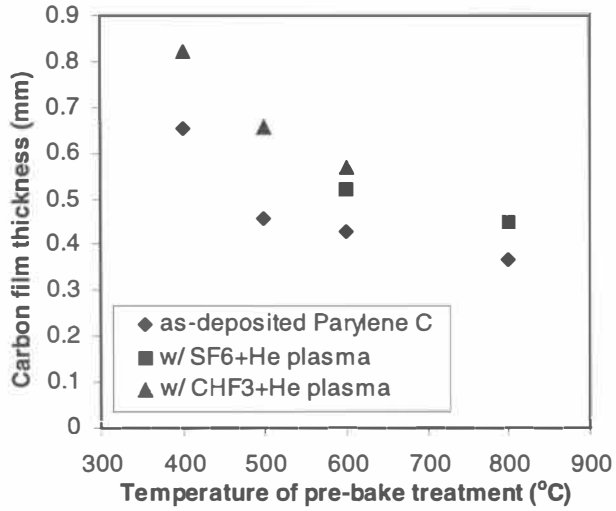

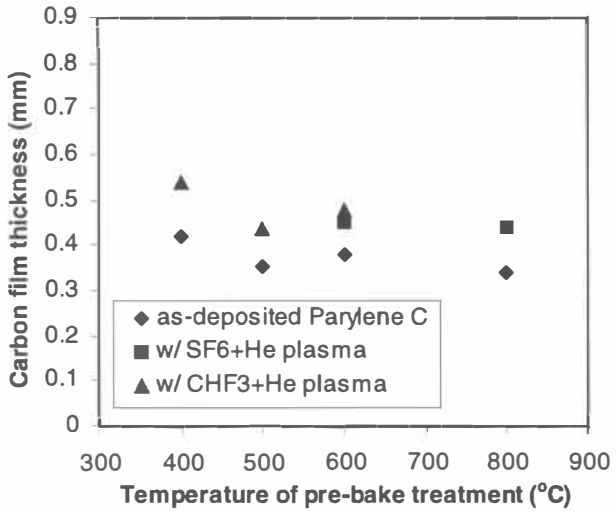

Figure 4. (a) Thicknesses of parylene/carbon films following various combinations of plasma and pre-bake pre-treatments before carbonization, and (b) after carbonization. The 400°C pre-bake and CHF_3 and He plasma give the greatest carbon yield.

plasmas. Changes in film thickness were monitored by measuring the step height at an edge of the film with a profilometer. The film edge was created by scratching off a portion of the deposited parylene using a razor blade. Carbon coatings on trench structures were examined by cleaving the wafer and examining the cross section by a SEM.

To measure the oxidation-undercut rate, a carbon film on a plain wafer was coated with polysilicon, and then part of the wafer was cleaved to expose the carbon at one edge. Samples were inserted directly into the oxidation furnace tube at 700 °C. At the end of the desired oxidation period, the samples were directly removed from the hot furnace and the undercut distance was measured with an optical microscope.

The etch rate of carbon in an O_2 plasma was also measured. In this case, the carbon was directly exposed to the plasma instead of being burned out from underneath a polysilicon layer. Film thickness was measured with a profilometer as described above.

Finally, AFM and water contact angle measurements were performed on released polysilicon. The surface of interest was that which had previously been in contact with the carbon.

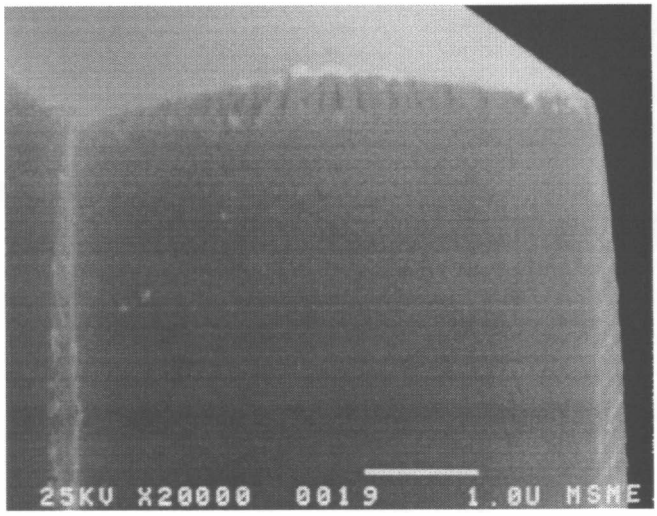

Figure 5. As-deposited parylene flows during the carbonization process, leading to poor corner coverage.

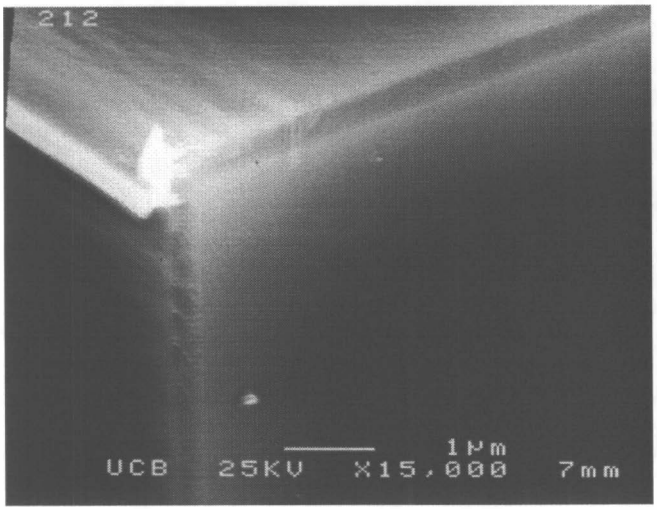

Figure 6. Pre-treating the parylene with a plasma-hardening step and a low-temperature pre-bake results in a much more conformal film at convex corners after carbonization

RESULTS AND DISCUSSION

Parylene was found to deposit extremely conformally, as shown in Fig. 3. Corner coverage is very good. However, the coating is not perfectly uniform but instead becomes slightly thinner going down deep and narrow trenches. This may be a result of loading.

Carbonization reduces the polymer film thickness by roughly a factor of four, which is not unusual in the carbonization of polymers [12]. Fig. 4 shows that proper pre-treatment can significantly increase the total carbon yield. The best result found was the use of a CHF_3 and He plasma combined with a 400 °C pre-bake, resulting in a final carbon thickness of 0.54 μm.

Significant reflow was found to occur during carbonization of as-deposited parylene. Fig. 5 shows the poor corner coverage that results. The film in Fig. 6 was carbonized after receiving the pre-treatment described above and shows much better conformality. A side-effect of the plasma treatment is that the crosslinked crust wrinkles slightly as the film volume decreases during carbonization. Sometimes a lip can even develop at

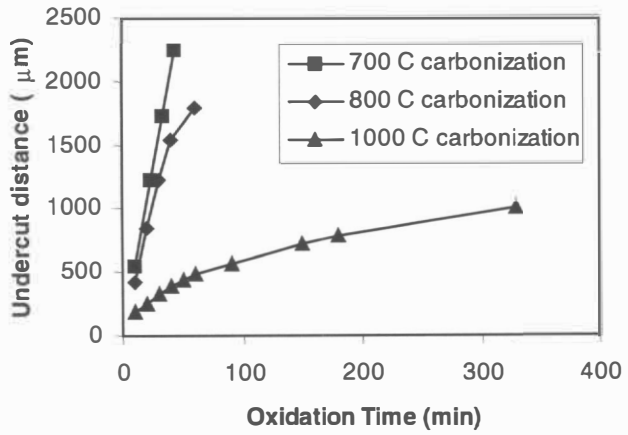

Figure 7. Distance of undercut as a function of time as carbon is being oxidized out from underneath a sheet of polysilicon at a temperature of 700 °C. Note that carbon prepared at lower carbonization temperatures oxidizes faster.

corners. The lip should be easy to remove with a light O_2 plasma etch.

Fig. 7 shows the oxidation-undercut rate of carbon at an oxidation temperature of 700 °C. The oxidation rate is very rapid – as high as 50 μm/min for the carbon prepared at a carbonization temperature of 700 °C. The oxidation rate slows significantly for films carbonized at higher temperatures, indicating that some change in carbon structure occurs at higher temperatures of carbonization. It is interesting to note that all three samples were annealed at 1000 °C for 1 hour following the polysilicon deposition, and yet the carbon prepared at lower temperatures still oxidized more easily. Note also that there were other variations besides carbonization temperature in the preparation of the three samples and so the ratios of etch rates for the three types of carbon cannot be determined exactly from this data.

The etch rate of carbon in an O_2 plasma was found to be 0.1 μm/min at 100 W and 0.2 μm/min at 300 W.

The underside surface was found to be hydrophilic, with a water contact angle of 16°. Underside roughness measurements of the released polysilicon (580 °C, 300 mT deposition), obtained using an AFM, showed a surface roughness of 1.4 nm rms. This is much lower than the 12-nm-rms underside roughness of HF-released poly (585 °C, 500 mT deposition) deposited on PSG [13].

We have successfully applied a carbon sacrificial layer to mold and release high aspect ratio polysilicon structures. As shown in Fig. 1, the carbon provides an extremely thin and conformal sacrificial layer, and consequently, the molded parts very closely resemble their molds, as shown in Figs. 2 and 9.

A couple of the failure modes encountered in our initial runs are shown in Fig. 8. Fig. 8(a) shows the effect of micropores in the carbon, through which polysilicon deposited, attaching the part to the mold. Most of these pores are around 0.1 μm in diameter and do not result in enough force to actually bind the part into the mold, but larger ones may be a cause for our currently low yield.

A more significant problem lay in our molds, where accelerated undercut at convex corners led to a footing effect, making the mold larger at the bottom than at the neck constriction. With a thick sacrificial layer, the part might still have been able to be pulled out, but with the thin carbon layer, the footing was enough to prevent mold extraction. This problem can be solved by retuning the deep RIE etcher to eliminate the foot.

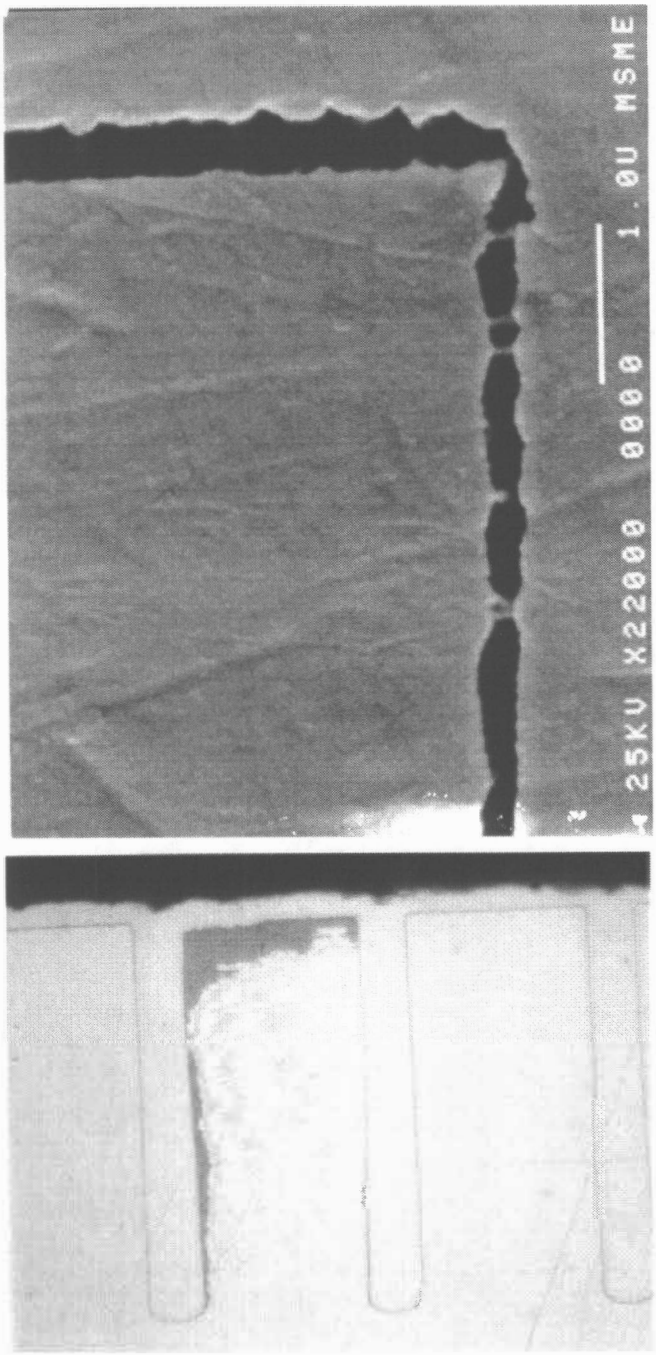

Figure 8. Failure modes in our recent Hexsil run. (a) Strands of polysilicon connect the part to the mold. These deposited through micropores in the carbon film. To prepare the sample for the SEM, the carbon was been etched back about a micron to make the interface more visible. (b) This cross section cuts right at the edge of a trench intersection. The convex corner presented by the intersection is undercut more rapidly, leading to the footing effect where the bottom of the trench is wider than the top.

CONCLUSIONS

Carbonized parylene has been demonstrated as a highly conformal, quickly etching sacrificial layer for Hexsil molding. Work remains to be done to optimize the process to minimize film shrinkage, reflow, and porosity.

In Bernstein's earlier work with carbon sacrificial layers, it is claimed that a layer of silicon carbide remains on the polysilicon surface following oxidation [11]. We will investigate whether the polysilicon from our parylene process also leaves a silicon carbide coating, and if so, whether this coating is effective for reducing friction and wear.

We will also study the fracture strength of polysilicon fabricated and released in this process to see if any improvements result from elimination of the HF release. Finally, carbon does not necessarily have to be used as a replacement for oxide, but can be used as a complementary sacrificial layer alongside oxide since the methods used to etch one material do not affect the other. We are beginning investigation of microfabricated structures involving multiple sacrificial layers for progressive release of parts.

ACKNOWLEDGEMENTS

The authors thank Mike Smith at Specialty Coating Systems, Ontario, CA; and Xuan-Qi Wang and Prof. Y.C. Tai at the California Institute of Technology, Pasadena, CA, for providing parylene coatings.

In addition we wish to thank Jim Bustillo for deep-trench processing assistance; Ron Wilson and Sharon Tackaberry for help in obtaining SEM pictures; as well as Dr. Jonathon Kluth, Dr. Carlo Carrero, and Prof. Roya Maboudian for assistance in obtaining AFM and water surface contact angle measurements.

This material is based upon work supported under a National Science Foundation Graduate Fellowship.

REFERENCES

1. J. M. Bustillo, R. T. Howe, and R. S. Muller, "Surface micromachining for micro-electro-mechanical systems", to be published in *Proc. IEEE*, 1998.

2. C. G. Keller, Ph.D. Thesis, Dept. of Materials Science and Mineral Engineering, University of California at Berkeley, May 1998.

3. S. M. Sze, *VLSI Technology,* 2nd ed. McGraw-Hill, 1988.

4. C. G. Keller, R. T. Howe, *Transducers '95, The 8th International Conference on Solid-State Sensors and Actuators, Vol. 1*, June 1995, Stockholm, Sweden, pp. 99-102.

5. D. J. Monk, D. S. Soane, and R. T. Howe, *J. Electrochem. Soc., 141*, 1, 264-269 (1994).

6. R. Maboudian and R. T. Howe, *J. Vac. Science and Tech. B, 15*, 1-19, (1997).

7. T. A. Lober and R. T. Howe, *IEEE Solid-State Sensors and Actuators Workshop*, Hilton Head, S.C., June 6-9, 1988, pp. 59-62.

8. J. A. Walker, K. J. Gabriel, M. Mehregany, *Proceedings IEEE MEMS-90*, Napa Valley, Feb 11-14, 1990, pp. 56-59.

9. P. T. Jones, G. C. Johnson, R. T. Howe, *Microelectromechanical Systems (MEMS) ASME 1996*, DSC-Vol. 59, pp. 325-330.

10. T. Tsuchiya, O. Tabata, J. Sakata, Y. Taga, *IEEE/ASME J. Micro Electro Mech. Systems*, March, 1998, pp.106-113.

11. J. Bernstein, T.B. Kroger, *J. of the Electrochemical Society: Solid-State Science and Technology*, Aug, 1988, pp. 2086-2090.

12. G. M. Jenkins and K. Kawamura, *Polymeric carbons – carbon fibre, glass and char*, 1976, pp.11-17.

13. M. R. Houston, Ph.D. thesis, Dept. of Chemical Engineering, University of California at Berkeley, 1996.

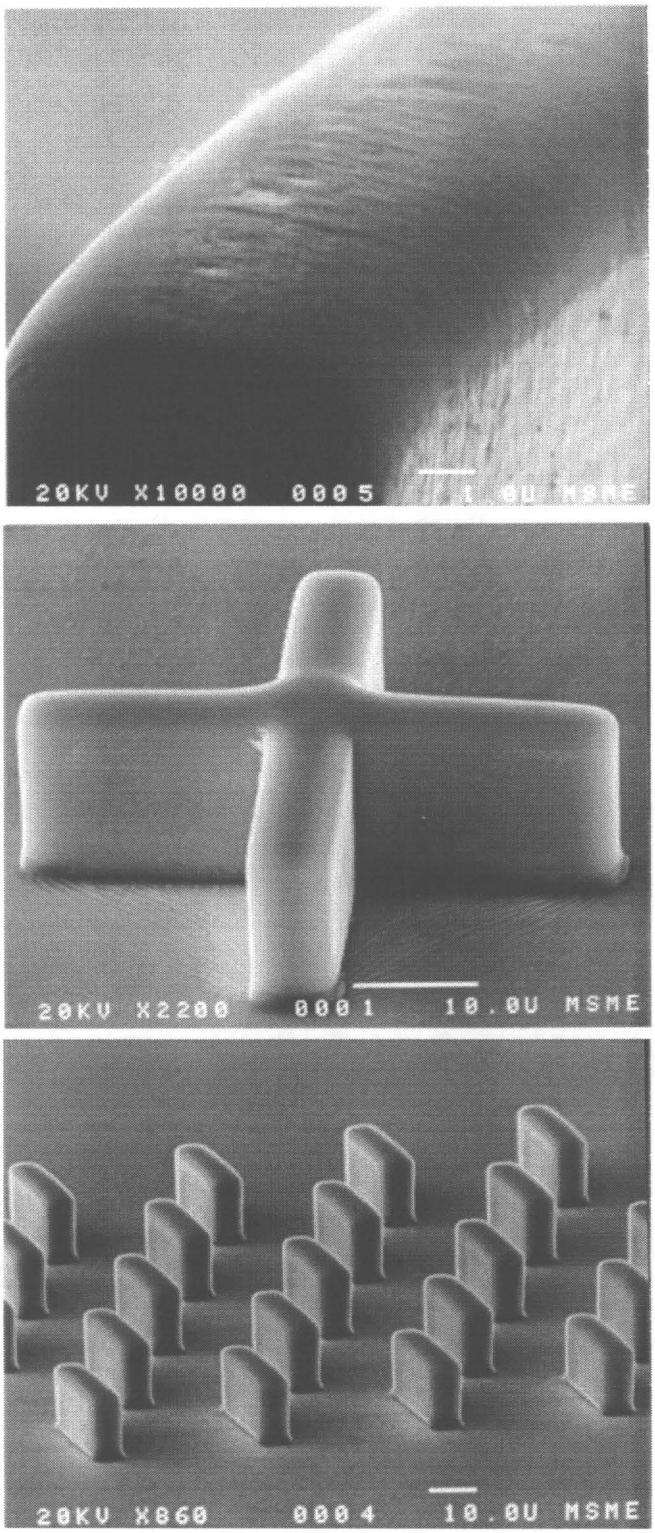

Figure 9. *(a) A close-up view of the tip of a molded fin. This is formed at the bottom of the mold trench. (b) A molded Hexsil cross. (c) An array of molded fins. Note that the surface poly is intact and that no etch holes were used to release this entire sheet.*

HIGH ASPECT RATIO STRUCTURES ACHIEVED BY SACRIFICIAL CONFORMAL COATING

Florent Cros and Mark G. Allen
School of Electrical and Computer Engineering
Georgia Institute of Technology
Atlanta GA 30332-0250

ABSTRACT

This paper reports on advances in the use of conformal scarificial layers to produce small gaps in high aspect ratio electroplated structures. The processes developed are based on the deposition and subsequent sacrificial removal of poly-(para-xylylene), or parylene, layers. Two processes are presented: one which allows released devices normal to the substrate surface and one which allows released devices parallel to the wafer surface. The two processes presented use conventional techniques of surface micromachining such as LIGA-like UV techniques, micromolding, and electroplating. Since the gaps between plated structures are defined not lithographically but instead by the thickness of the deposited parylene layer, and since the microstructures are fabricated in parylene-coated micromolds in a self-aligned fashion, extremely narrow gaps without the corresponding need for precise alignment and lithography through thick layers can be achieved. Examples of both processes, demonstrating 1:9 aspect ratios, are given.

INTRODUCTION

Thick metallic high aspect ratio microstructures present many advantages for both electrostatic and magnetic applications. For example, the driving voltages of electrostatic comb drives can be reduced by increasing the surface area (e.g., height) of the electrodes while decreasing the gap between electrodes. However, the level of processing difficulty increases with the above requirements. In addition to conventional thick photoresist processes, several different fabrication technologies have already been developed to realize high aspect ratio microstructures: LIGA (lithography, galvanoforming, and molding) [1], photosensitive polyimide [2] or epoxy [3] processes, and an electroplated aluminum sacrificial layer process [4]. Each of these processes has advantages and disadvantages which dictate their use in certain applications. The purpose of this paper is to describe the advantages which can be obtained by the combination of epoxy-based plating molds with a conformal parylene sacrificial layer. The idea is similar to that presented in the aluminum electroplating approach [4], but replaces the aluminum deposition with a parylene deposition. Since electrodeposited aluminum has the drawback that it should be electrodeposited from an ethereal solution (which is both water sensitive and highly flammable), and since parylene is a commonly used large area manufacturing deposition process without these drawbacks, it is anticipated that a parylene-based process will be able to be more widely implemented than an aluminum process, especially on larger area substrates.

Parylene (poly-(para-xylylene)) deposition provides an excellent conformal film with thickness ranging from 2 to 50 microns [5]. Moreover, it has excellent chemical resistance and can be deposited at low temperature (25 °C) so that thermal damage to any previous structure is unlikely to occur [5-6]. These desirable features have been exploited in the past by other MEMS researchers who have incorporated parylene into various devices; for example, the use of parylene in a micromachined capillary electrophoresis stage is described in [7].

Thick resist structuring using an SU-8-epoxy-based resin originally developed by IBM and subsequently optimized for MEMS applications has been demonstrated in [3]. This epoxy resist is exposed using conventional UV lithography techniques and can easily provide high aspect ratio micromolds compatible with eletroplating techniques.. In the present work, parylene is used as a sacrificial layer between a first (primary) electroplated structure (originally created using a micromold of thick photoresist), and a second (secondary) electroplated structure, created around the primary in a self-aligned, self-molding process. After the parylene is removed, an air-gap, corresponding to the original parylene thickness, is created between the primary and secondary electroplated structures.

This basic process can be implemented in two different ways, depending on the desired relative motion between the first and second structures once the parylene is removed. The first process introduces a generic method to create overlapped structures able to move normal to the substrate; these are designated in this paper as *vertical structures* (Fig 1/a). The second demonstrates the possibility to create two structures electroplated on the same substrate, leading to motion parallel to the plane of the substrate, resulting in motion similar to that of micromechanical comb actuators; these are designated in this paper as *horizontal structures* (Fig 1/b).

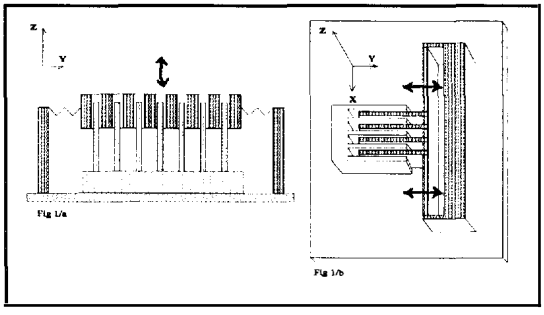

Figure 1: *Examples of the two types of structures produced using this process. Fig. 1/a; side view of device capable of motion normal to the substrate (vertical device). Fig. 1/b; perspective view of device capable of motion parallel to the plane of the substrate (horizontal device). Both structures are formed using a self-aligned, self-molding process.*

0-9640024-2-6/hh1998/$20©1998TRF
DOI 10.31438/trf.hh1998.59

Solid-State Sensors, Actuators, and Microsystems Workshop
Hilton Head Island, South Carolina, June 8-11, 1998

VERTICAL DEVICE FABRICATION

The fabrication process for vertical devices consists of deposition of a primary structure through an epoxy mold, followed by conformal parylene coating, deposition of the secondary metal structure, and isotropic removal of the parylene mold. A description of the fabrication process is presented in Figure 2.

A. Ni-Fe electroplated structures into SU-8 micro-molds

A metal seed layer system consisting of 50 nm of Ti, an overlying electroplating seed layer of 150 nm of Cu, and a final 50 nm of Ti is evaporated onto oxidized 3 inch <111> silicon wafer substrates. Next, 40 microns of thick photosensitive epoxy Epon SU-8 prepared as described in [3] is spin-cast onto the metal system.. Using exposure and development guidelines described in [3], the resist is photolithographically patterned to create a mold through which the primary NiFe structures are then electroplated as described in [2] (Figure 2/a). A long O2/CHF4 plasma etch is used to remove the mold (Figure 2/b). A short ultrasonic cleaning step can be performed so that any residue still remaining at the bottom of each structure is removed.

B. Conformal coating and second electroplating

At this point, the sample is conformally coated with 5 microns of Parylene-C (Figure 2/c). An overlying Ti/Cu/Ti seed layer system similar to that described above is then deposited (Figure 2/d); it is destined to provide a base onto which a second structure will be electroplated. This second structure is electrically isolated from the first one, due to the conformal coat of parylene. The secondary metallic structure is then electrodeposited in a self-aligned fashion, using the bottom and sidewalls of the primary structure as a mold (Figure 2/e). The parylene is removed by a long isotropic plasma etch (Figure 2f). Figure 3/a shows a scanning electron micrograph of a released vertical structure, along with a schematic drawing (Figure 3/b) of the structures to better illustrate the micrograph.

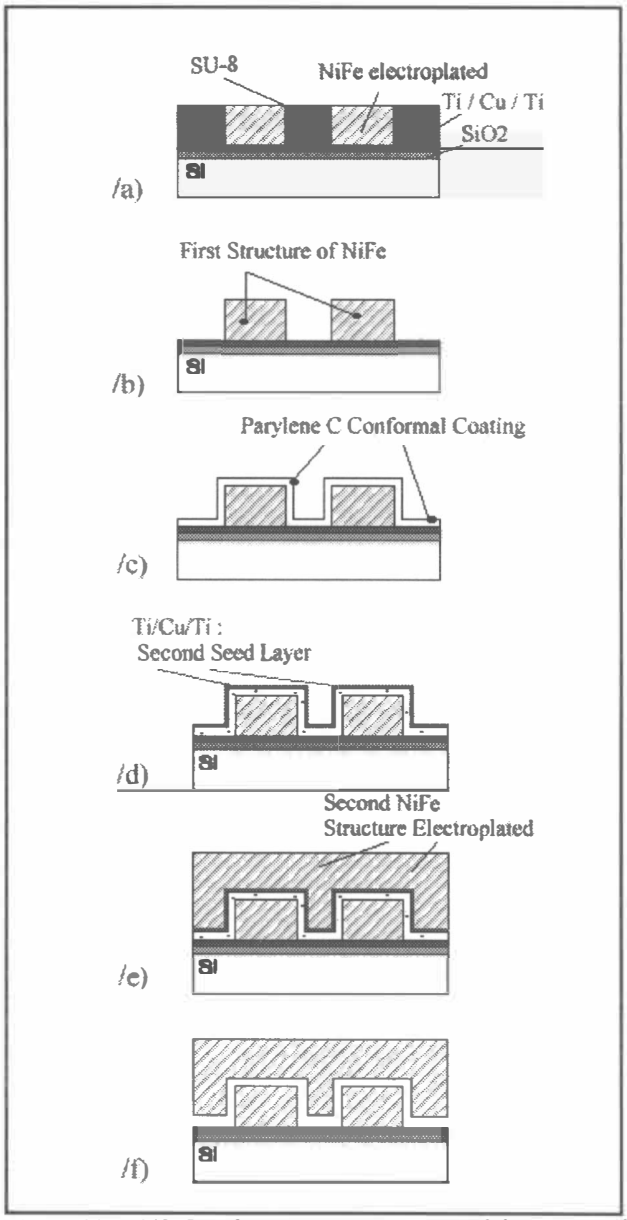

***Figure 2/a - 2/f**: Step-by-step representation of the process for fabrication of vertical devices.*

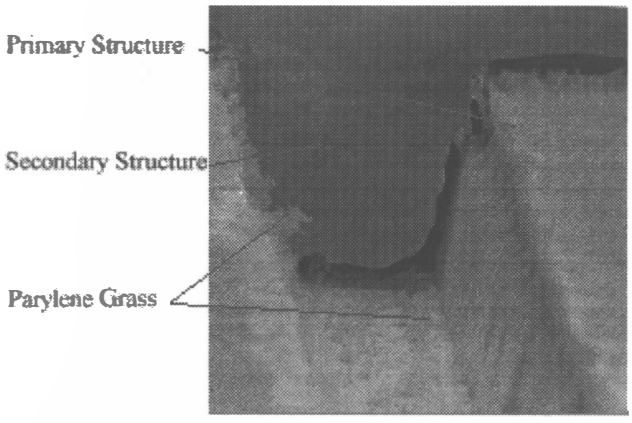

***Figure 3a:** Scanning electron micrograph (3/a) and schematic drawing (3/b) of a released vertical structure.*

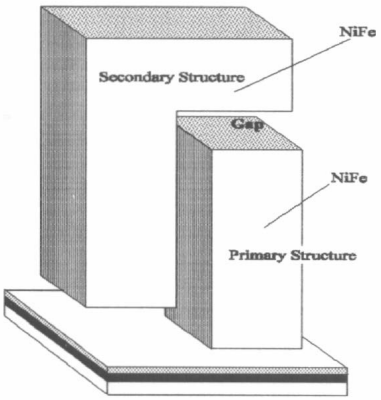

***Figure 3b** : Schematic drawing (3/b) of a released vertical structure.*

HORIZONTAL DEVICE FABRICATION

A. Ni-Fe electroplated structures into SU-8 micro-molds

The same technique for the realization of NiFe electroplated structures into SU-8 micromolds presented in the vertical device fabrication section is utilized, with some change in process parameters since thicker epoxy films were utilized. An epoxy layer 230 microns in thickness is spin-cast, pre-baked, patterned, post-baked, and developed as described in [3]. The first electroplating step is performed (Fig 2/a). In order to reduce the surface tension of the bath and to avoid any bubbles remaining in these higher aspect ratio micromolds, 0.1 g/l of a surfactant (sodium dodecyl sulfate) is added to the conventional NiFe galvanic bath. The surrounding epoxy is then removed using a dry etch similar to that used for the vertical structure fabrication described above.

B. Conformal coating and second electroplating

At this point, 28 microns of parylene C are deposited (Figure 4/a). An overlying 100 nm thick aluminum layer is sputter-deposited and patterned using conventional positive photoresist.. The aluminum mask must be wider than the previous NiFe structure by at least the thickness of the deposited parylene C itself (Figure 4/b). The role of this Al mask is to protect the parylene on the upper surface of each of the primary structures, as well as the regions near the tops of each of the parylene-C-coated sidewalls. Poor alignment during this step can result in etching of the parylene at the top corners of the primary structure, as shown in Figure 5, which would result in additional 'mushroom-like' plating on this exposed region when the secondary structure is electrodeposited. In some applications, this additional plating may be desirable; for example, to act as a retainer for the horizontal structures. A highly anisotropic reactive ion etching (RIE) step then removes the parylene exclusively at the bottom of each NiFe structure (Figure 4/c). The etch must be sufficiently anisotropic in order to not etch the side walls; this is achieved by performing the etch in a low pressure, high power environment. In some cases, small amounts of fluorine-containing species were added to the etch environment to reduce the problem of parylene 'grass' formation. The RIE step usually removes the Ti layer of the underlying seed layer Ti/Cu/Ti system deposited in part (A). The exposed copper is used as a base for the next electroplating step, but it also can provide a useful visual test to determine when the parylene etch is complete.

The parylene still present on the side walls of each structure will act as a spacer between the primary structure and the about-to-be-electrodeposited secondary NiFe structure. A second electroplating step is now performed (Figure 4/d) using the original seed layer, resulting in a secondary metal structure formed in a self-aligned fashion between the walls of the primary structure, but insulated from it by the parylene layer. A long isotropic plasma etch then removes the parylene sacrificial layer (Figure 4/e).

Figure 6/a shows a scanning electron micrograph of a released horizontal structure, along with a schematic drawing (Figure 6/b) of the structure to better illustrate the micrograph. There is some parylene still remaining between the primary and secondary microstructures, indicating that some further plasma etching is needed. The gap between the two structures is 24 microns and the final aspect ratio achieved in a first attempt is already better that 1 to 8 for the central secondary structure and better than 1 to 9 for the air gaps surrounding the second structure. It should be re-emphasized that the secondary structure is self-aligned with the primary since the primary structure has been used as a mold for forming the secondary structure.

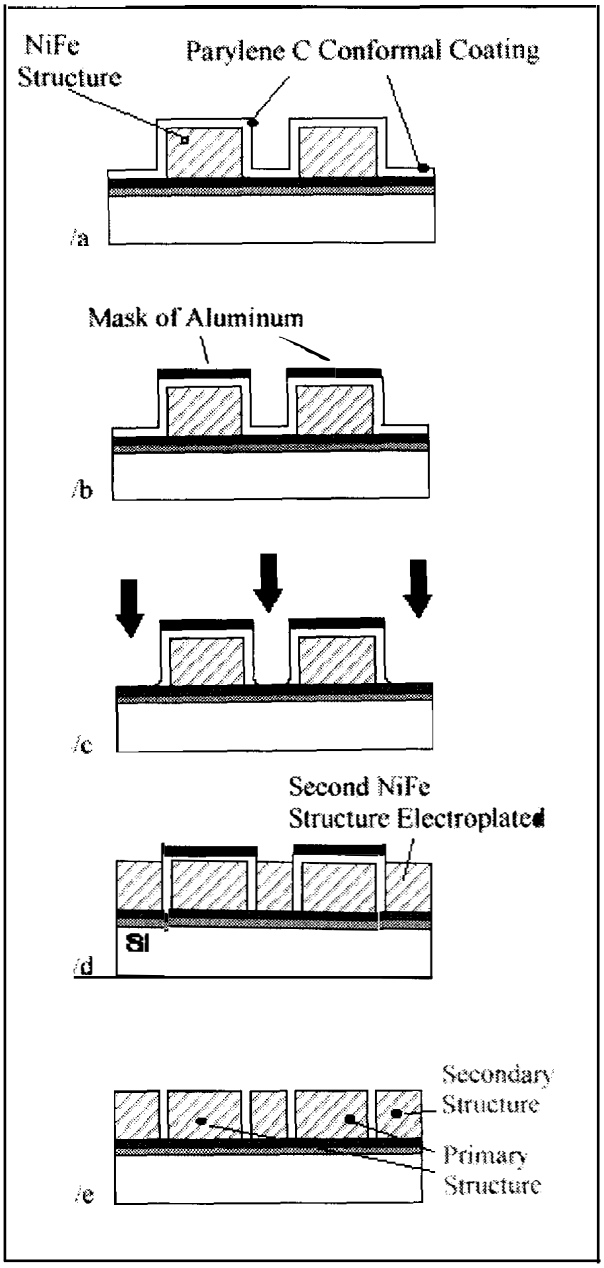

Figure 4/a - 4/e: *Step-by-step representation of the process for fabrication of horizontal structures.*

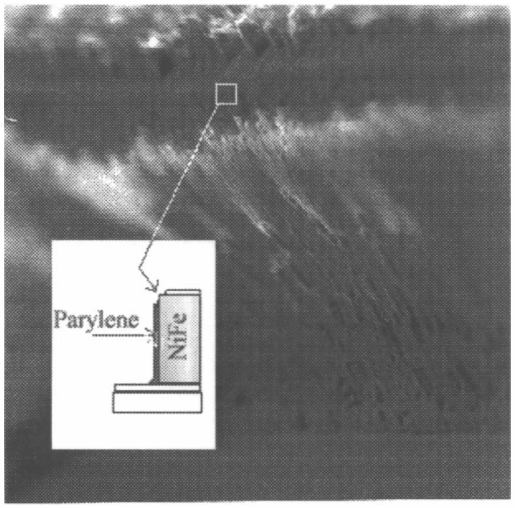

Figure 5: Scanning electron micrograph of a poorly-aligned structure, illustrating a gap between the parylene coated on the sidewalls and on the top of the primary structure.

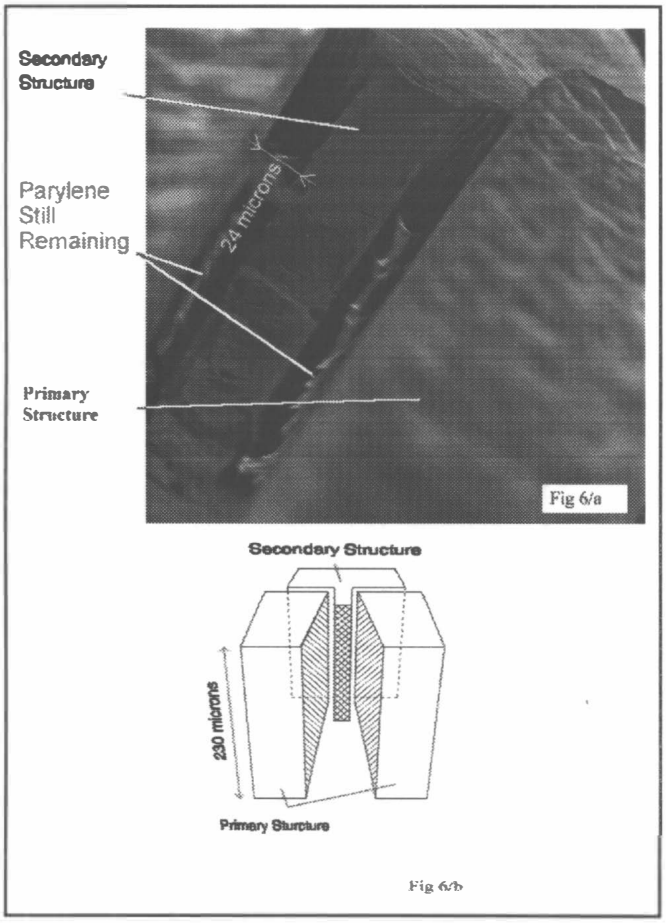

Figure 6: Scanning electron micrograph (6/a) and schematic drawing (6/b) of a released horizontal structure.

CONCLUSIONS

Two processes based on parylene conformal sacrificial layers have been presented for the realization of self-aligned and molded, vertical and horizontal released devices. Used in conjunction with high-aspect-ratio processing such as SU-8-based electroplating of metallic structures, these parylene-based processes offer the potential to create extremely narrow gap structures with a variety of pertinent MEMS applications.

REFERENCES

[1] E.W. Becker, W. Ehrfeld, P. Hagmann, A. Maner, and D. Munchmeyer, "Fabrication of Microstructures with High Aspect Ratios and Great Structural Heights by Synchrotron Radiation, Lithography, Galvanoforming, and Plastic Moulding (LIGA process)", *Microelectronic Eng.*, vol. 4, p. 35-56 (1986)

[2] A.B. Frazier and M.G. Allen, "Metallic Microstructures Fabricated Using Photosensitive Polyimide Electroplating Molds", *Journal of Microelectromechanical Systems*, vol. 2, no. 2, p. 87-94 (1993)

[3] M. Despont, H.Lorenz, N. Fahrni, P. Renaud and P. Vettiger, "High-Aspect-Ratio, Ultrathick, Negative-Tone Near-UV Photoresist For MEMS Applications", *Sensors and Actuators A (Physical),* 1 Jan. 1998, vol.A64, n°.1, pp.33-9

[4] A.B. Frazier and M.G Allen, "Uses of Electroplated Aluminum for the Development of Microstructures and Micro-machining Processes", *Journal of Microelectromechanical Systems*, June 1997 vol.6, n°2, pp.91-8

[5] L. You, G.-R. Yang, C.I. Lang, P. Wu, J.A. Moore, J.F. McDonald, and T.M. Lu, "Vapor Deposition Of Parylene Films From Precursors", *Mat. Res. Soc. Symp. Proc.* vol. 282, 1993, pp 593-598

[6] "Parylene For Electronics", available from Paratronix, Inc., Attleboro, MA

[7] J.R. Webster and C.H. Mastrangelo, "Large-Volume Integrated Capillary Electrophoresis Stage Fabricated Using Micromachining of Plastics on Silicon Substrates", *Proc. Transducers '97*, vol. 1, p. 503-506 (1997)

POLYMOLDING: TWO WAFER POLYSILICON MICROMOLDING OF CLOSED-FLOW PASSAGES FOR MICRONEEDLES AND MICROFLUIDIC DEVICES

Neil H. Talbot and Albert P. Pisano
Department of Mechanical Engineering
University of California at Berkeley
Berkeley, CA 94720

Abstract

A two wafer polysilicon micromolding process we call Polymolding has been developed that permits the fabrication of hollow tubes and other structures useful for fluidic systems and relatively large mechanical structures. A related process known as HexSil, developed by Chris Keller at UC Berkeley, involves the deposition of an oxide release layer and polysilicon on a single mold wafer from which polysilicon structures are subsequently released [1]. In contrast, this new process uses two mold wafers that are temporarily bonded together after the deposition of the oxide release layer. The two wafers form a complete mold with internal chambers. Then amorphous polysilicon is vapor deposited and coats the internal chambers of the mold via access holes in the top mold wafer. After some further processing, the wafers are separated and the structures are released. This process is particularly useful for fluidic applications because complex closed flow passages, such as microfilters, interconnected chambers, fluid manifolds etc. can be easily be created. Polysilicon microneedles from 100 to 200 microns in diameter and 1 mm to 7 mm in length and sub-micron tip radii have been fabricated using this process. These microneedles are valuable for small volume drug injection where minimal tissue damage and/or minimal pain are desired. In addition, the Polymolding process does not damage the mold wafers, so they can be reused many times at a huge cost savings.

INTRODUCTION

The primary motivation for the development of Polymolding and Polymolded microneedles is the need for very small hypodermic injection needles that are economical to fabricate. Small needles are very desirable because they reduce insertion pain and tissue damage in the patient. This is particularly important for Type I diabetics who typically have to inject themselves with insulin 3 times a day. Currently the smallest needles available for diabetics are 30 gauge needles which are 305 microns in diameter with a wall thickness of 76 microns. Traditional machining techniques are unable to produce a viable needle with a significantly smaller diameter than 300 microns. The typical needle material, medical grade stainless steel, is simply too ductile when the wall thickness is only tens of microns. In addition, there are various designs of small needles that are impossible or impractical to fabricate with traditional machining techniques. For example sharp, 90^{o} bends are impossible to machine out of drawn steel tubes because they always crimp at the bend and close the fluid flow passage. Needles with multiple fluid channels are also very difficult to machine. However, with silicon micromachining, microneedles with these, and other useful features are easily fabricated. Extreme sharpness can also be achieved with Polymolded microneedles (Fig. 1) while stainless steel needles can be comparatively rough (Fig. 2).

The early research on microfabricated microneedles was done by Liwei Lin at the University of California at Berkeley [2] and Kensall Wise at the University of Michigan [3]. In both of these approaches the microneedles were made of single crystal silicon. The device wafer was sacrificed or dissolved away in a silicon etchant leaving the microneedles behind. Wise' approach took advantage of the slow etch rate of heavily boron doped silicon in EDP. Lin's approached used both the differential etch rate of EDP and a timed etch to produce the desired needle shape. The main contrast and key advantage of Polymolding in that the mold wafers are not sacrificed during the fabrication process. Since the process is a molding process, the mold wafers can be re-used many times at a huge cost savings as compared to sacrificial processing techniques.

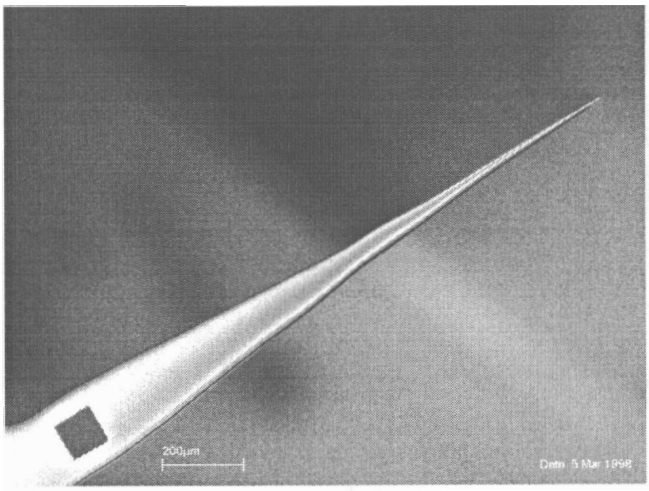

Figure 1. *SEM of the tip of a Polymolded microneedle with sub-micron tip radii.*

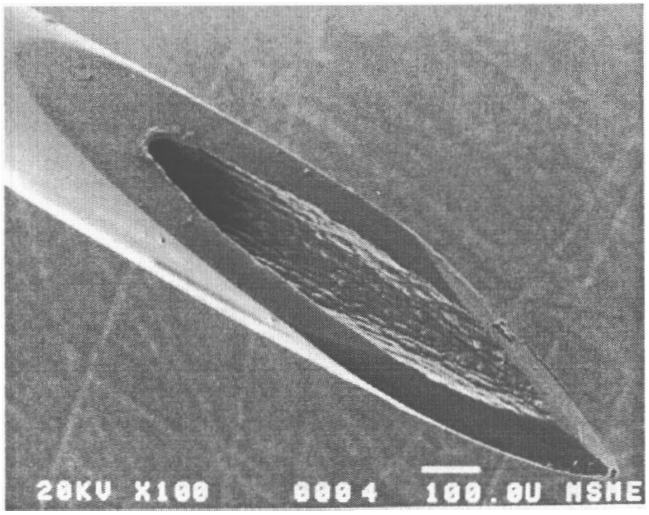

Figure 2. *SEM of the tip of a 30 gauge stainless steel needle.*

0-9640024-2-6/hh1998/$20©1998TRF
DOI 10.31438/trf.hh1998.60

Solid-State Sensors, Actuators, and Microsystems Workshop
Hilton Head Island, South Carolina, June 8-11, 1998

FABRICATION

Polymolding is a two wafer molding process (Fig. 3). Polysilicon is used as the structural material for the parts, which in this case were microneedles. The molds were made from lightly doped, p-type, (100), single-crystal silicon wafers. Up to this point 100 mm wafers have been used, but this process is easily scalable to larger wafers. Double-sided polished wafers were used for the top mold wafers. The top mold wafer was coated with 0.3 microns of LPCVD low-stress silicon nitride that was then patterned with a dark field mask to expose through-hole regions. After the nitride was etched away in these regions, the photoresist was stripped and the through-holes were etched with KOH. The remaining silicon nitride was removed with concentrated HF.

The bottom mold wafers were masked with about 2 microns of photoresist and then patterned. They were then deep-trench etched in a Surface Technology Systems (STS) silicon etcher to define the microneedle body shapes and features. Typical etch depths were 100 to 130 microns. The etch recipe required careful tuning for each die design to obtain a desirable etch profile. Unoptimized recipes produced re-entrant (undercut) etch profiles which required very thick release layers to ensure that the microneedles could be removed from the mold. A thick release layer means that the minimum feature size ends up being much larger than normal, which was naturally undesirable for intricate designs. Typically both top and bottom mold wafers were coated with 2 microns of PSG (Fig. 4B). After the PSG was densified, bottom mold wafers requiring a thicker release layer were coated with 0.5 microns of 580°C polysilicon which was then oxidized to form 1 micron of oxide. Then wafers were aligned and pressure bonded in nitrogen at 1000°C (Fig. 4C).

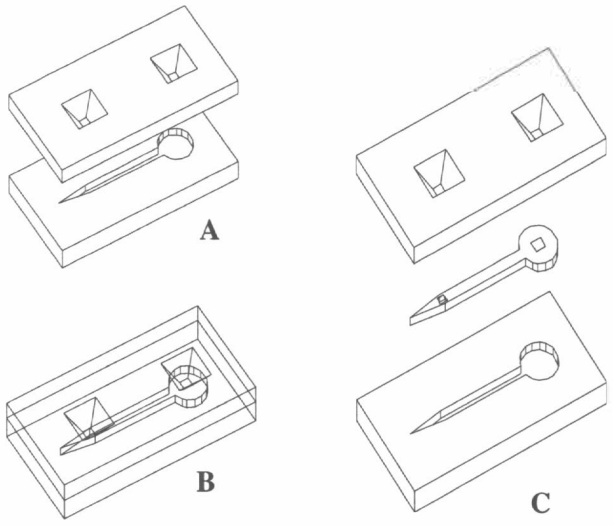

Figure 3. Oblique view of the mold wafers prior to bonding (A), after bonding (B), and after the final release step (C).

After bonding, 3 microns of LPCVD polysilicon were deposited on the mold wafers at 580°C (Fig. 6A). This low deposition temperature was used in order to produce amorphous polysilicon that has desirable mechanical properties when annealed and deposits extremely conformally. The molds were then annealed in nitrogen for 1 hour at 1000°C. Then the next layer of polysilicon was deposited and annealed. These deposition and annealing steps were repeated until the desired thickness of polysilicon was achieved -- typically 12 to 18 microns.

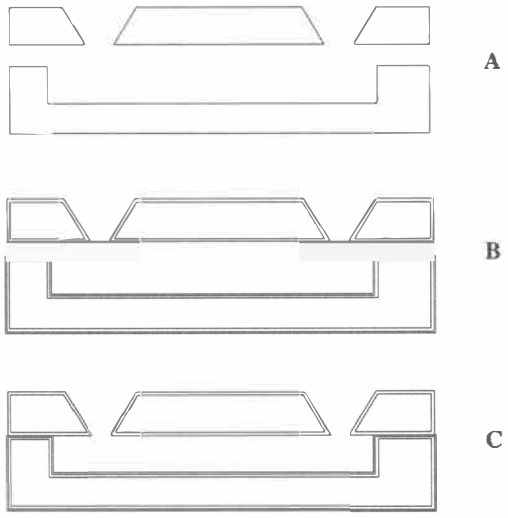

Figure 4. Mold wafers as fabricated (A); after application of the release layer (B); after bonding (C).

The next step was to anisotropically remove the polysilicon on the top of the mold using the STS etcher. A Lam polysilicon etcher has also been used for this step. The surface polysilicon was etched until it cleared and then over-etched by 25% to 100%. Some batches were over-etched only 25%, so there was still a thin polysilicon "funnel" structurally attaching the microneedles to the top mold wafer. After the final release etch these microneedles remained loosely attached to the top mold wafer for greater ease of handling and/or post processing (Fig. 5).

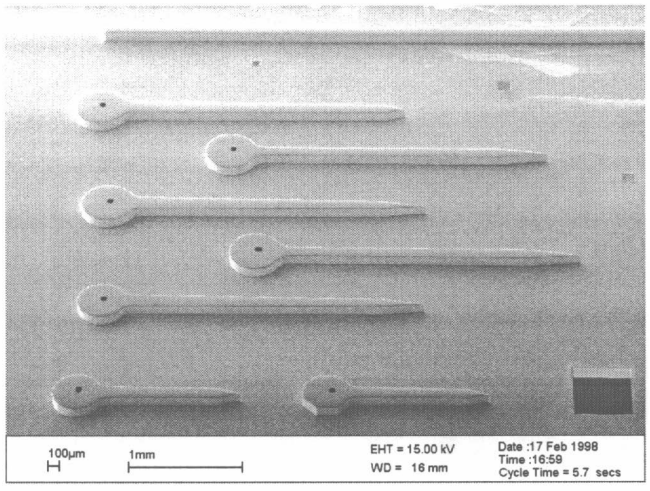

Figure 5. SEM of a group of released microneedles loosely attached to the top mold wafer for ease of handling

During the final release etch in concentrated HF, the wafers were separated and the microneedles were liberated from the mold with a release etch. Release times varied from a few hours to overnight depending on the mold geometry and the separation of the etch holes.

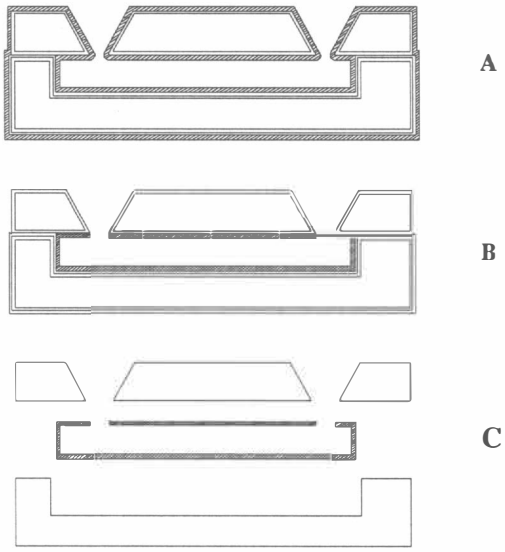

Figure 6. Mold wafers after polysilicon deposition (A); after external polysilicon removed (B); after the release step (C).

RESULTS AND DISCUSSION

Four batches of microneedles have been fabricated with minor variations in the described process flow. The first two batches had release layers for the bottom mold wafer that were composed of 2 microns of PSG and two subsequent layers of oxidized polysilicon each 1 micron thick. The top mold wafer simply had 2 microns of PSG. The microneedle designs of these first two batches were fairly simple due to the thickness of the release layer. The most intricate design was a dual channel microneedle. The thick release layer was necessary because of the poor quality of the out-sourced deep-trench etching of the bottom mold wafer. The first batch had a polysilicon wall thickness of 12 microns (Fig. 7) and their cross-section was 100 microns square with a slight taper. These microneedles were too weak to be handled easily. The second batch had a polysilicon wall thickness of 18 microns (Fig. 5 and was much stronger, being able withstand bending moments of up to 0.53 mNm. Some of these microneedles were also electroplated or sputtered with metals such as nickel (Fig. 7) and could withstand bending moments of up to 0.71 mNm.

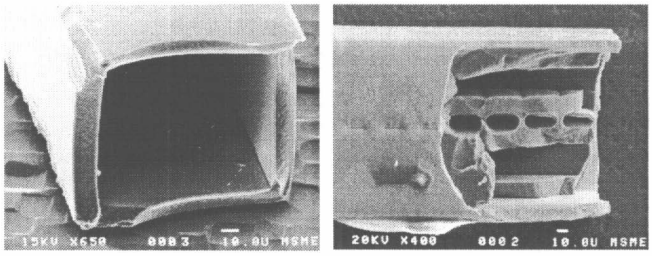

Figure 7. SEM of the cross-section of a microneedle from batch one (left). SEM of the internal structure of a metal plated dual channel microneedle (right).

In order to make the microneedles stronger the molds for batches 3 and 4 were redesigned. The principal design changes were that the diameter of the microneedles was increase to 200 microns in the plane of the wafer and 110 microns out of plane and also internal wall reinforcement features were added (Fig. 8). These detailed features demonstrate the remarkable flexibility of this process.

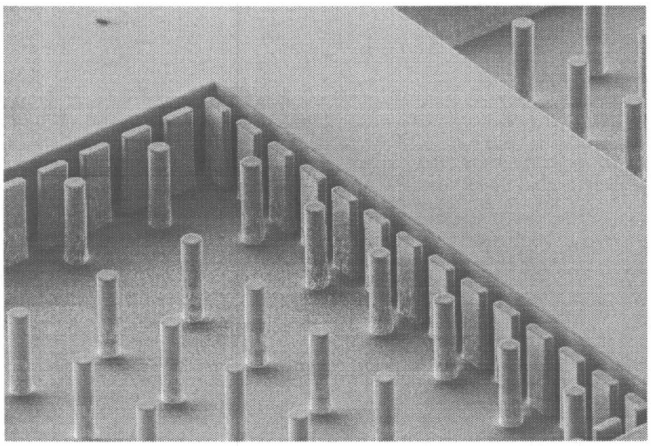

Figure 8. SEM of a mold showing strength enhancement features.

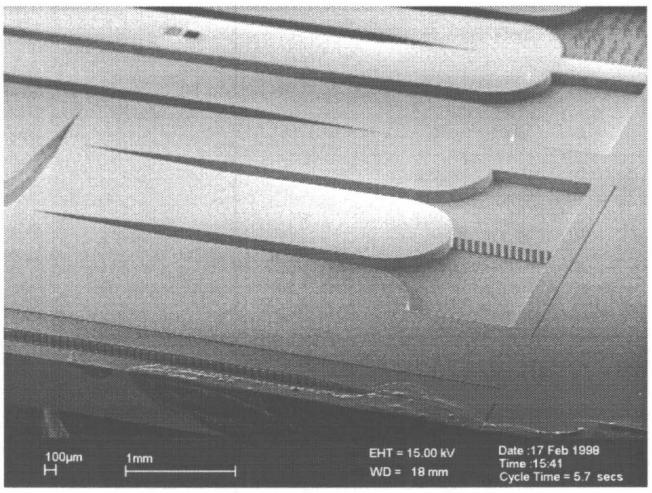

Figure 9. SEM of a dual shaft microneedle mold.

The third batch of microneedles had a release layer of 3 microns of PSG. After the bonding step, 0.3 micron of polysilicon was deposited and then oxidized in order to reduce or eliminate the thin layer of polysilicon that tends to form where the halves of the mold meet. This thin layer of extraneous polysilicon, known as mold flash, was not significantly reduced by the oxidized polysilicon, so other solutions are being investigated. These microneedles were not very strong because of separation of the layers of polysilicon in the needles. Due to improvements in the deep-trench etching recipe the release layer for the fourth batch was reduced to only 1.5 microns of PSG and 0.6 microns of oxidized polysilicon. Several unique microneedle designs were included in the last two batches such as a dual shaft microneedle (Fig. 9, Fig. 10) and a microneedle with filter in the base (Fig. 11, Fig. 12).

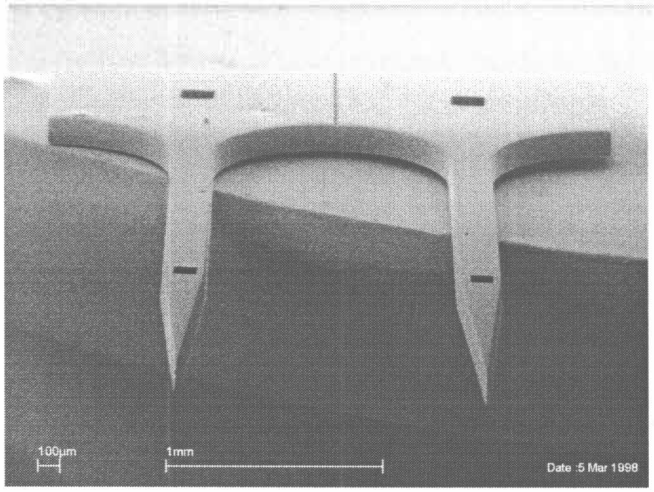

Figure 10. SEM of a 4 mm long dual shaft microneedle.

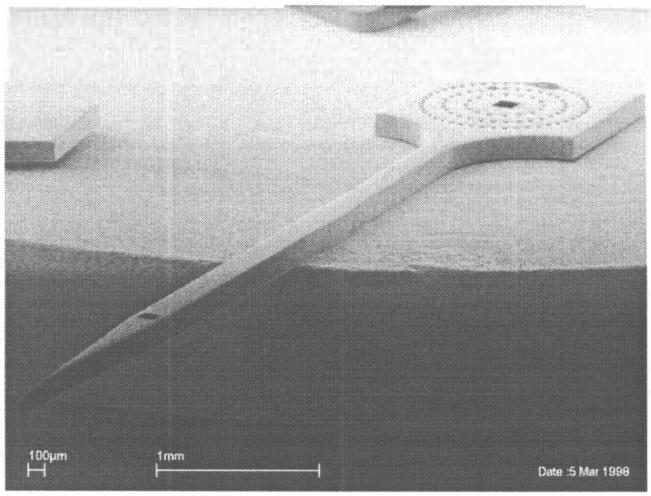

Figure 11. SEM of a microneedle with a 6 mm shaft and a microfilter in its base.

CONCLUSIONS

Polymolding, a versatile process for the fabrication of microneedles and other microfluidic and mechanical devices has been developed and demonstrated. Polysilicon microneedles 100 to 200 microns in outer diameter have been fabricated that are capable of supporting bending moments of up to 0.71 mNm. This new process is extremely flexible especially when compared to traditional machining techniques because detailed structures can be fabricated such as microfilters, interconnected chambers, fluid manifolds etc. In addition, for the fabrication of microneedles, this process is more economical than other microfabrication processes because the device wafer (or mold) is re-usable.

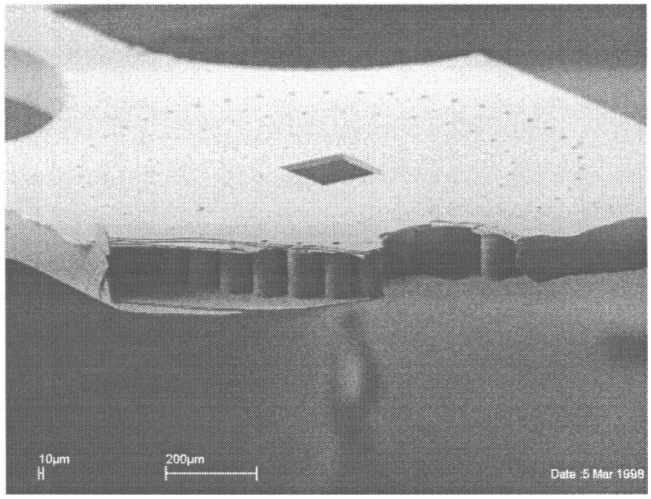

Figure 12. Close-up of the base of microneedle with a built-in filter that has been cleaved.

ACKNOWLEGEMENTS

This research was supported by the Becton Dickinson Research Center. Contact: Burton Sage

REFERENCES

1. C.G. Keller, R.T. Howe, "Nickel-filled hexsil thermally actuated tweezer," International Solid-State Sensors and Actuators Conference, Transducers '95, Stockholm, Sweden, pp.376-379

2. L. Lin, A.P. Pisano, R.S Muller, "Silicon processed microneedles," International Solid-State Sensors and Actuators Conference, Transducers '93, Japan, pp. 237-240

3. J. Chen, K.D. Wise, "A multichannel neural probe for selective chemical delivery at the cellular level," Solid State Sensor and Actuator Workshop, Hilton Head, S.C., (1994), pp. 256-259

Parallel Assembly of Hinged Microstructures Using Magnetic Actuation

Yong Yi and Chang Liu
Microelectronics Laboratory
University of Illinois at Urbana-Champaign
Urbana, IL 61801

ABSTRACT

We have developed a new surface-micromachining process for realizing three-dimensional MEMS devices from hinged planar structures. Magnetic actuation, which is provided by Permalloy material attached to hinged plates, provides efficient and high-yield out-of-plane actuation. Parallel actuation of large arrays of hinged microstructures is achieved under a globally applied external magnetic field. The magnitude of the actuation can be controlled by either the volume of the magnetic piece or the stiffness of a flexural-beam loading spring. Asynchronous displacement of hinged structures allow these devices to lock into three dimensional assemblies that remain stable after the activation magnetic field is removed.

INTRODUCTION

It has been demonstrated that three-dimensional MEMS devices can be attained through assembly of hinged microstructures **[1]**, which are capable of rotation about their base. Potential applications of assembled 3-D devices include micro opto-electro-mechanical components and fluidic turbulators, to name a few. Existing techniques for achieving displacements include water rinse, scratch drive actuation **[2]**, and thermal actuation **[3]**. However, these methods do not offer sufficient reliability and efficiency. In most developed methods using active actuation, one actuator is connected to only a single hinged plate; the efficiency is low for deploying large arrays of devices. These actuators also occupy significant chip area. In order to accomplish mass fabrication of array 3-D MEMS, a high yield and efficient process for activating and assembling hinged structures must be developed.

In this paper, we present a new process for actuation and assembly of hinged structures based on magnetic actuation. Detailed mechanisms are described in the following section. Parallel assembly using magnetic forces offers the following unique advantages: (1) high yield; (2) low chip-area requirements and high device density; (3) efficient wafer-scale assembly. A globally applied external magnetic field (H_{ext}) can address a large number of devices simultaneously. A linear sweep of the magnitude of H_{ext} induces the formation of three-dimensional structures, which remain stable even after H_{ext} has been removed. The actuation mechanism is relatively simple and exhibits higher efficiency and yield compared with other afore-mentioned methods.

DESIGN AND THEORY

A piece of magnetic material (Permalloy) is attached to each hinged microstructure (so called flap) by an electroplating process to provide a means of actuation (Fig. 1). Each flap is capable of rotation about its base. The electroplating step follows established hinge-fabrication processes (such as MUMPS) and has no influence on existing designs and recipes. If an external magnetic field is applied perpendicular to the substrate (Fig. 1c), the Permalloy material develops a magnetization, M. It subsequently interacts with H_{ext} to induce a torque, T, on the hinged structure and causes it to deflect away from the substrate plane. The magnitude of T is given by:

$$T = MAH_{ext}l_{mag}\cos\theta \qquad (1)$$

where A and l_{mag} are the cross-sectional area and the length of the Permalloy piece, respectively, and θ represents the angle between the flap and the substrate.

In order for hinged flaps to assemble into a predetermined 3-D shape, it is important to control the speed of actuation of each individual flap component, so that they exhibit different displacement under a global magnetic field. In our work, this has been realized using two methods. First, the volume and orientation of the electroplated magnetic piece determine the magnitude of the magnetic torque and, subsequently, the displacement angle, under a given H_{ext}. In the second method, a cantilever-beam spring loading mechanism is developed to provide a resistive force to the otherwise free flap as it rotates out of plane. By using these two methods, individual hinged components can be lifted in a predetermined asynchronous order.

Two types of hinged structures have been designed, based on the control methods described earlier. Type I structures consist of a flap which is hinged at the base and may rotate without restriction (except for friction) about the y-axis (Fig. 1).

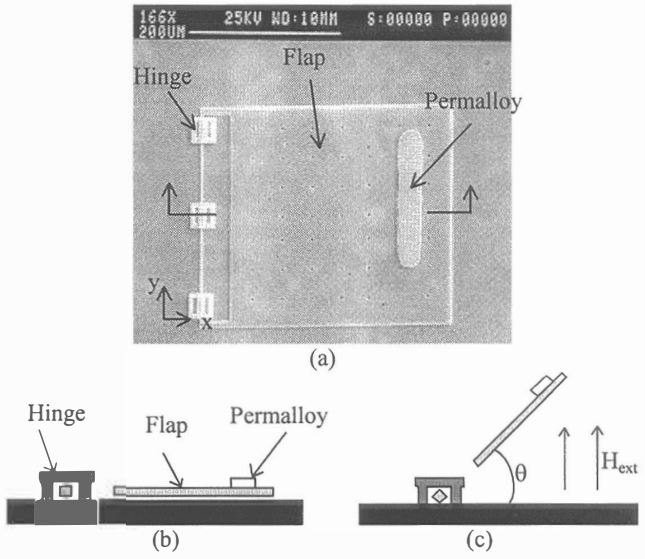

Figure 1. *(a) An SEM micrograph of a Type I structure. The flap is allowed to rotate about the y-axis. (b) Schematic cross-sectional view of the structure at rest; (c) schematic cross-sectional view of the flap as H_{ext} is increased.*

0-9640024-2-6/hh1998/$20©1998TRF
DOI 10.31438/trf.hh1998.61

Solid-State Sensors, Actuators, and Microsystems Workshop
Hilton Head Island, South Carolina, June 8-11, 1998

A Type II structure, on the other hand (Fig. 2), consists of an offset slab and a fixed cantilever-beam loading spring. When the flap is at rest (θ=0°), the offset slab and the cantilever beam are not in contact. As the flap is rotated away from plane, the offset slab, which is wider than average hinge pins, comes into contact with the loading spring and experiences a reactive force due to the bent cantilever beam. The vertical deflection of the cantilever beam at its free end, y_{max}, is related to the reactive force, F, using small-bending assumptions **[4]**:

$$y_{\max} = \frac{Fl^3}{3EI} \tag{2}$$

where l is the effective length of the beam, E is the modulus of elasticity, and I is the moment of inertia of the cantilever beam. I equals $wh^3/12$, where w is the base width and h is the thickness of beam

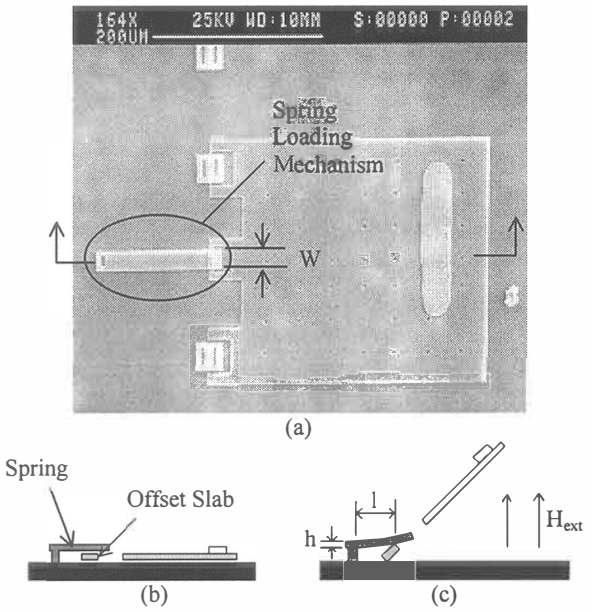

Figure 2. *(a) SEM micrograph of the Type II structure; (b) schematic cross-sectional view of the structure at rest; (c) schematic cross-sectional view of the structure when H_{ext} is increased.*

The geometry of the cantilever beam, therefore, determines the spring constant and the magnitude of the resistance to the flap displacement. Tests were conducted for cantilever beams with lengths of 75, 100, and 125 μm and widths of 15, 25, and 35 μm. Dimensions of the flaps for both types are 300x300x2 μm^3. The dimensions of the Permalloy pieces are 200x40x2.1 μm^3.

Assemblies of 3-D devices using Type I structures have been accomplished based on asynchronous actuation. One mechanism involves two flaps and requires a precise sequence of actuation to assemble. The second mechanism involves three flaps; the order of actuation is not critical in this assembly process. Detailed mechanisms for locking and assembly will be discussed in the results section.

FABRICATION

Hinged flaps and assemblies can be fabricated based on established surface micromachining processes such as the MCNC MUMPS. The major steps in the process are shown in Figure 3. To form the flap, a layer of polysilicon is deposited and patterned on top of a sacrificial oxide. A second oxide layer is grown and vias are etched so that hinges can anchor to the substrate. The final step in structure fabrication is to deposit and pattern a second polysilicon layer, forming the hinge.

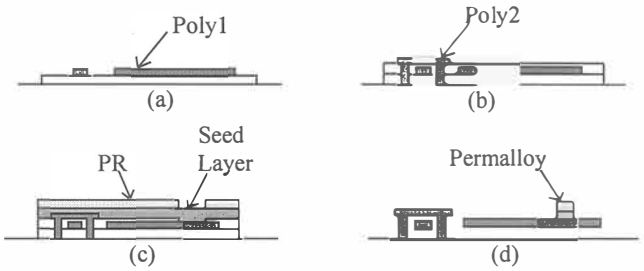

Figure 3. *Major steps in the fabrication process for the hinged microstructures (not to scale). (a) Deposition of polysilicon as the structural layer of the flap; (b) deposition of polysilicon for the hinge; (c) deposit seed layers and pattern PR to prepare for electroplating; (d) electroplate Permalloy and release structure.*

A piece of magnetic material (Permalloy, $Ni_{80}Fe_{20}$) is then attached to the flap **[5]**. The first step is to expose the first polysilicon layer by selectively opening the second oxide. Layers of Cr and Cu are then deposited as the seed layer for the electroplating process. Because Cu does not adhere well to the substrate, an initial 200 Å-thick Cr layer is sputtered to act as an adhesion promoter between polysilicon and Cu. A layer of Cu (4000Å) is evaporated to provide adequate electrical continuity for the electroplating process. A 6.2 μm layer of photoresist is patterned on the seed layer and the chip is mold electroplated to the desired thickness.

After the magnetic material has been electroplated, the PR and the exposed seed layer materials are removed. The structures are then released in HF (49% wt.) and rinsed in DI water. The patterned Permalloy is unaffected throughout this process as it is resistive to HF, Cu, and Cr etchants. The final step is to place the chip in isopropyl alcohol and allow the solution to dry in air. As the isopropyl alcohol evaporates, surface tensions of the liquid can force the flaps to come into contact with the substrate and cause stiction. To remedy this, a magnetic field ($8.1x10^4$ A/m) is applied to the chip so that the flaps are rotated by 90° during the liquid evaporation; the magnetic field is maintained until the isopropyl alcohol is completely evaporated. This method, also used in **[6]**, significantly increases the yield.

EXPERIMENTAL SETUP

Measurements of flap angular displacement vs. H_{ext} are obtained using a video-microscopy setup illustrated in Fig. 4. The camera is placed at an angle, α, with respect to the wafer substrate. The estimated error for the measurements in the angular displacement is ±5°. The tests are conducted with the structures immersed in isopropyl alcohol and placed on top of an electromagnet. The purpose of isopropyl alcohol is to minimize frictional effects at the base and potential stiction between the flap and substrate.

The tilted viewing angle and the refraction at the liquid-air interface causes the perceived displacement angle, β, to be different from the actual displacement angle, denoted θ. The relationship between β and θ can be expressed by:

$$\tan\theta = \frac{\tan\beta \tan\left[\cos^{-1}\left(\frac{n_1}{n_2}\cos\alpha\right)\right]}{\sin\alpha} \quad (3)$$

where n_1 and n_2 are the refractive indices for air and isopropyl alcohol, respectively.

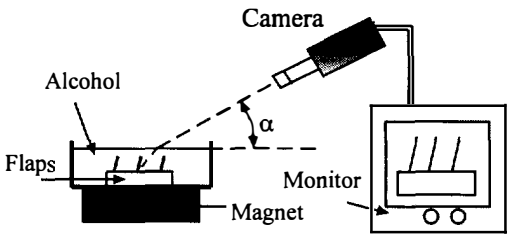

Figure 4. *Experimental setup. The chip is immersed in alcohol. The CCD camera views the structures at an inclined angle α. A magnified image of the structures is displayed on an external monitor. Angular displacement measurements are taken from the monitor.*

RESULTS AND DISCUSSION

Within an external magnetic field, Type I structures behave in a binary fashion; they can assume only two stable positions, 0° or 90°. The flaps are initially in plane, θ=0°, when no H_{ext} is applied. As H_{ext} increases, the flap remains at 0° until a threshold magnetic field strength (H_t) is reached. At H_t, the flap makes a direct transition to 90°. Figure 5 shows the measured H_t values for three separate Type I structures of identical geometries within ten trials. The average H_t is 7.1x10^3 A/m with a standard deviation of 484 A/m.

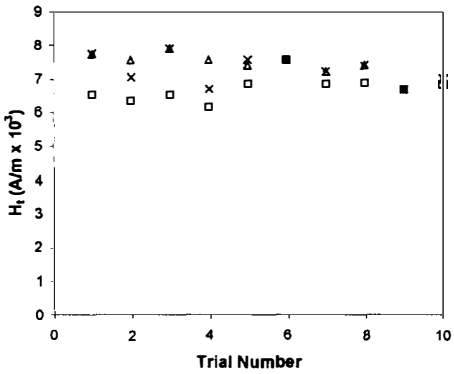

Figure 5. *Threshold H_{ext} for the Type I structures. The Type I structure has two stable positions. Tests were conducted on 3 identical Type I structures for 10 trials each.*

The H_t is found to be dependant on an initial angular displacement. Some flaps have an initial angle, θ≈8°; for these, the average H_t is 3.8x10^3 A/m with the standard deviation being 324 A/m for 30 trials. We conjecture that such a behavior is related to the fluid. At θ=0, it is assumed that there is no fluid between the flap and the substrate. As the flap rotates, the space underneath it must be replaced with fluid. If θ is originally greater than 0°, fluid can fill the same space with less effort. As a result, less energy and a lower H_t is required when the flap is initially deflected.

Unlike Type I structures, Type II structures can achieve a continuous range of angular displacements due to the counteracting spring loading created by the cantilever beam. Figure 6 shows the actuation behavior of three Type II structures with different cantilever-beam geometries and spring constants. The offset slab will not contact the cantilever-beam loading spring until the flap has been deflected by nearly 35°, as defined by slacks caused by removed sacrificial material. After the contact has been made, flap displacement increases continuously as H_{ext} is increased. The behavior of the Type II structures appear to have three regimes after the offset slab and the cantilever beam have made contact. For small values of θ, increases in H_{ext} result in slow linear increment of θ. This could be attributed to partial magnetization of the Permalloy. Near θ=50°, the rate of change in θ with respect to H_{ext} begins to increase, indicating the Permalloy has become fully magnetized. The curve then begins to saturate again as the flap approaches 90°. This behavior can be explained by Eq. 1, which predicts that the magnitude of the magnetic torque will decrease with increased θ. The general trends are the same for all other cantilever beam dimensions we have tested. As predicted by linear beam theory, flaps with stiffer cantilever beams require a stronger H_{ext} to achieve 90° displacements.

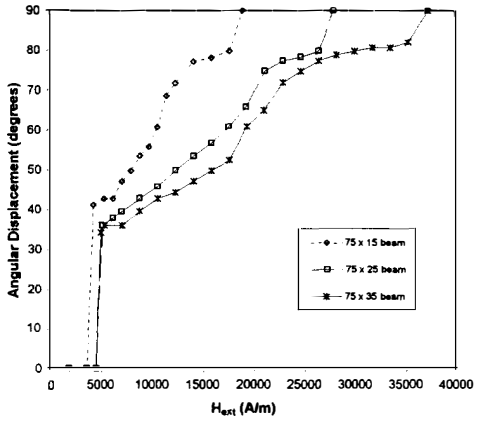

Figure 6. *Behavior of the Type II structures. Type II structures are able to acheive a range of stable angular displacements. The data is for cantilever beams of length 75 μm and widths of 15,25, and 35 μm.*

Type II structures with no added locking mechanisms can remain stable at 90° after H_{ext} has been removed. When the flap is at 90°, a flat portion of the offset slab is in contact with the cantilever beam. The applied restoring force provided by the cantilever beam to the slab is large enough to maintain the flap at 90°. We conjecture that the intrinsic stability of such an assembly is low as environmental factors (e.g. vibrations, fluid forces) can cause the flap to collapse.

Combinations of two or three Type I flaps were used to construct stable 3-D assemblies. An assembled device which uses two structures is shown in Figure 7. This device consists of a primary flap and a secondary flap. The secondary flap contains a slot used to lock the primary flap and maintain a stable position utilizing frictional forces between flaps. These two flaps are lifted in a predetermined order (Fig. 8). Under a uniform magnetic field, the displacement of flaps is controlled by using different volumes of the magnetic pieces. The volume of Permalloy is 200x40x2.1 μm^3 on the primary flap and 100x40x2.1 μm^3 on the secondary flap. Both flaps are initially in plane (Fig. 8a) when there is no external magnetic field. As H_{ext} is gradually increased, the primary flap will rise to 90° (Fig. 8b) first. A further increase of H_{ext} causes the secondary flap to rise to 90° and lock the primary flap into a fixed position (Fig. 8c).

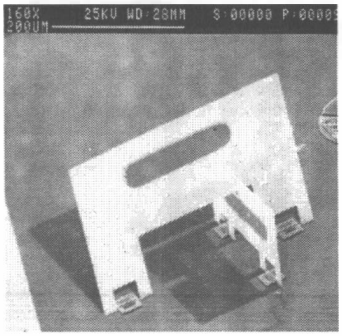

Figure 7. *SEM micrograph of a 3-D device using two Type I structures. The sequence of actuation was controlled by the use of different Permalloy volumes.*

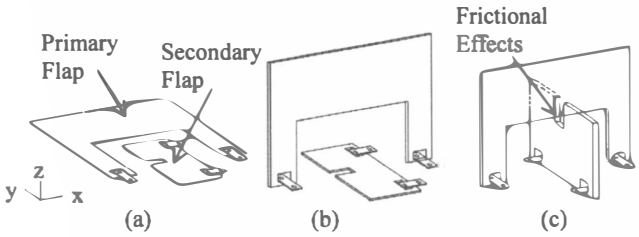

Figure 8. *Schematic of the assembly process for the flap 3-D devices. (a) Both flaps in the resting position; (b) primary flap raised to 90° at $H_{ext}=H_1$; (c) full 3-D assembly is achieved at $H_{ext}=H_2$ ($H_2>H_1$).*

3-D assemblies utilizing three flaps, one primary and two secondary, have also been designed (Fig. 9). The primary flap has a tapered area and the secondary flaps contain locking slots. The advantage of this design is that the order of actuation is not critical to the assembly of the device. The device will assemble if all three flaps rise to 90°, regardless of the order of actuation. If the primary hinge rises to 90° first, then the secondary hinges rise 90° to lock the primary hinge into place. On the other hand, secondary hinges may rise to 90° first. As the primary hinge rises to 90°, it pushes the secondary hinges outward and then locks into place when it reaches the slots. Both the two and three hinge assemblies are capable of remaining assembled after H_{ext} is removed.

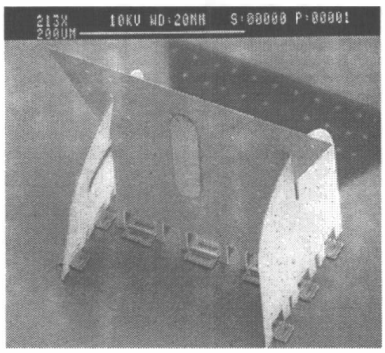

Figure 9. *An SEM micrograph of a 3-D device using three Type I flaps. The sequence of actuation is not critical to the assembly of this device.*

A primary advantage that magnetostatic actuation offers is the ability to control an array of devices in parallel with a uniform magnetic field. Figures 10 and 11 show examples of hinged microstructures that have been actuated with a linear sweep of H_{ext}.

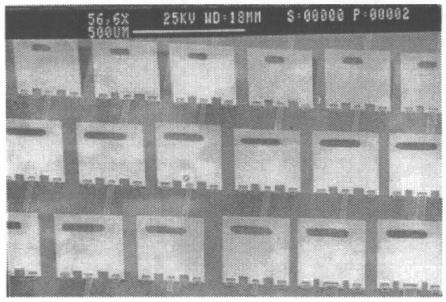

Figure 10. *SEM micrograph of an array of Type II structures. The flaps are rotated 90° and there is no H_{ext} applied.*

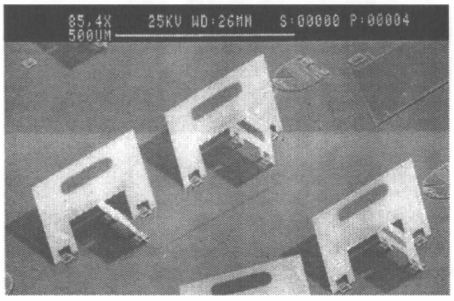

Figure 11. *SEM micrograph of an array of 3-D devices. H_{ext} has been removed.*

CONCLUSIONS

Sequential and parallel actuation of hinged microstructures has been demonstrated through the use of magnetic actuation. The angular displacement of the structures can be controlled by varying the volume of magnetic material or the stiffness of a cantilever-beam loading device. The behavior of two types of hinged microstructures, using these principles, have been characterized. It was observed that Type I structures have two stable positions, while the inclusion of a cantilever spring in Type II structures allow them to achieve a range of stable angular displacements. The ability to control the angular displacement of individual hinged flaps under a global magnetic field has enabled us to assemble three dimensional devices.

REFERENCES

1. K. S. J Pister, M. W. Judy, S.R. Burgett, and R. S. Fearing. "Microfabricated hinges," *Sensors and Actuators* A, 33 (1992).
2. J.H. Comtois and V.M. Bright. "Surface micromachined polysilicon thermal actuator arrays and applications," Proceedings, IEEE Solid-State Sensors&Actuators Workship, Hilton Head, SC, p. 174, 1996.
3. L. Fan, M.C. Wu, et al.. "Self-assembled microactuated XYZ stages for optical scanning and alignment," *Transducer '97*, Vol. 1, p. 319, 1997.
4. J. Shigley and C. Mischke, Mechanical Engineering Design, McGraw-Hill. NewYork, 1989.
5. C. Liu, T. Tsao, and Y. Tai. "Out-of-Plane Permalloy Magnetic Actuators for Delta-Wing Control." *MEMS '95*, p. 7,1995.
6. C. Liu, T. Tsao, Y.C. Tai. "A High Yield Drying/Release Process for Surface Micromachined Polysilicon Structures," *Transducers '97*, June 1997.

MAGNETICALLY ACTUATED MICROMIRRORS for FIBER-OPTIC SWITCHING

Behrang Behin, Kam Y. Lau, and Richard S. Muller
Berkeley Sensor & Actuator Center (BSAC)
Department of EECS, University of California
Berkeley, CA 94720-1770

ABSTRACT

We describe the design, fabrication, and operation of magnetically actuated micromirrors with electrostatic clamping in dual positions for fiber-optic switching applications. The mirrors are actuated by an off-chip electromagnet and can be individually addressed by electrostatic clamping either to the substrate surface or to the vertically etched sidewalls formed on a top-mounted (110)-silicon chip. We show that the positioning accuracy inherent in our approach makes it suitable for NxM optical switches.

INTRODUCTION

The growth of fiber-optic communications networks and the increased use of fiber-optics in sensing applications has created demand for low-loss, low-cost, reliable, and mass-producible fiber-optic switches. Free-space optical switches are needed for multi-mode fiber switching and for applications that require lower crosstalk than that provided by waveguide-based electro-optical switches. A significant opportunity exists for MEMS in the realization of low-cost free-space optical switches [1,2]. Batch-processing and –assembly make MEMS especially suitable for large-scale switching applications such as NxM fiber-optic non-blocking switches. A number of authors have described NxM switches based on silicon surface- and bulk-micromachining [3-6].

A MEMS design for an NxM switch is a matrix of micromirrors arranged in a crossbar configuration, as shown in Fig. 1 [3]. The mirrors are positioned at 45° relative to the fiber/collimator arrays. Once flipped vertically, a mirror reflects the collimated output from an input fiber into an output fiber. Accuracy of the mirror angle in the vertical position is a major challenge to the efficacy of this design. Assuming that the fiber/collimator arrays are perfectly orthogonal, all mirrors must have the same vertical angle to achieve a low insertion loss. Reproducibly accurate positioning of the mirrors requires either the use of active positioning control or of mechanical stops. The latter design can be accomplished with less complexity, but may require several precise alignment steps during system assembly. We describe a design that only demands a single alignment step of the MEMS mirror assembly to the fiber/collimator arrays.

OPTICAL DESIGN CONSIDERATIONS

A major parameter describing an optical switch is its insertion loss. For the NxM crossbar switch shown in Fig. 1, separation between the fiber/collimator assemblies and misalignment of the mirrors both result in coupling losses. Fiber collimators (lenses) are used to expand the beam radius to *fN.A.*, where *f* is the lens focal length and *N.A.* is the numerical aperture of the fiber. Use of these collimators reduces sensitivity to lateral misalignment of the fibers, so we can model coupling sensitivity as resulting only from separation and angular mismatch.

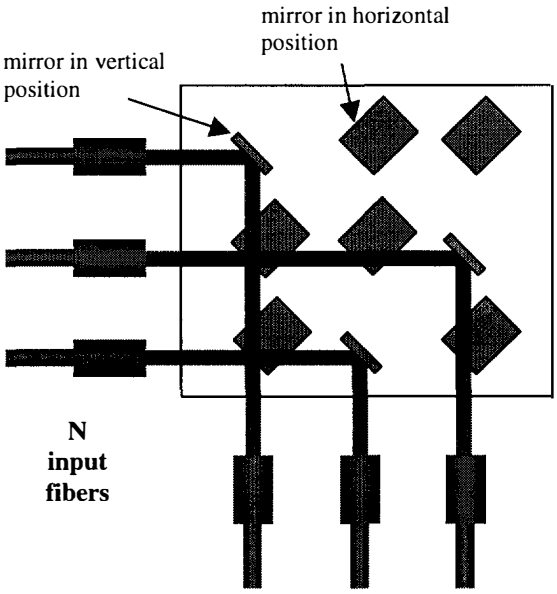

Figure 1. *MEMS design concept for a 3x3 crossbar optical switching network.*

For a fiber placed at the focal plane of a lens, as shown in Fig. 2(a), the output beam has angular divergence *a/f*, where *a* is the fiber core radius. As the beam traverses a distance *s* to another fiber/collimator assembly, the spot radius increases from (*fN.A.*) to (*fN.A.* + *as/f*), resulting in coupling loss between the two fibers. Loss due to angular misalignment is illustrated in Fig. 2(b). The image of a beam incident on the collimator at an angle θ is projected onto the fiber end-face with a lateral translation relative to the fiber core. Note that for reflection from a mirror, θ is twice the angular misalignment of that mirror. Coupling loss due to angular mismatch is higher for fibers having smaller core radii because the lateral translation of the projected image is larger relative to the core radius.

Detailed treatments of coupling loss between fibers due to separation, lateral misalignments, and angular mismatches have been used to model coupling in free-space optical interconnects [7,8]. The data in Fig. 3 were generated for typical parameters expected in a MEMS 3x3 switch array using analytical approximations developed by di Vita *et. al.* and Rossi in references 7 and 8. Although our analysis is based upon expressions derived for multi-mode fibers, we also generate data for single-mode fibers to establish rough guidelines and evaluate tradeoffs for the design of a MEMS crossbar switch. The plots in Fig. 3 show coupling efficiency η *vs.* θ for two fibers with different core radii, each with two lenses of differing focal lengths. For the single-mode case, a

0-9640024-2-6/hh1998/$20©1998TRF
DOI 10.31438/trf.hh1998.62

smaller core radius results in less beam spreading and higher maximum efficiency. However, a smaller core radius also makes η more sensitive to angular misalignments. For both fibers, a shorter focal length results in lower sensitivity to angular mismatch; however, the coupling loss at θ = 0 is higher for shorter focal lengths because of beam spreading. To use a longer focal length

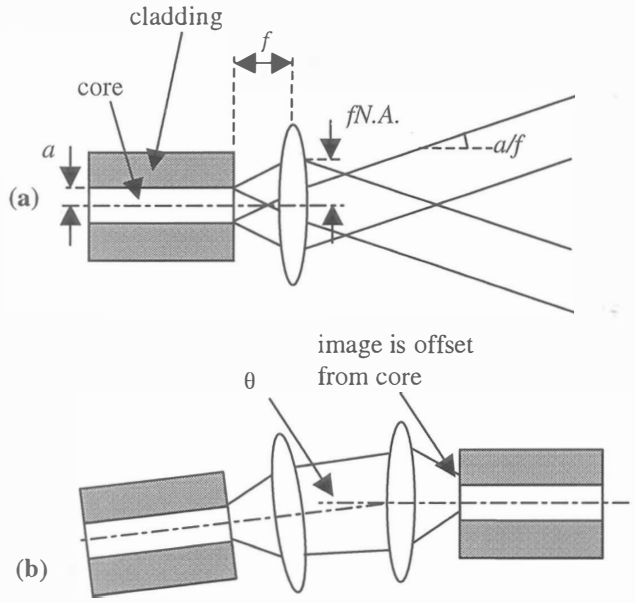

Figure 2. **(a)** *Beam divergence for fiber/collimator assembly.* **(b)** *Beam image projection is offset from core owing to angular mismatch.*

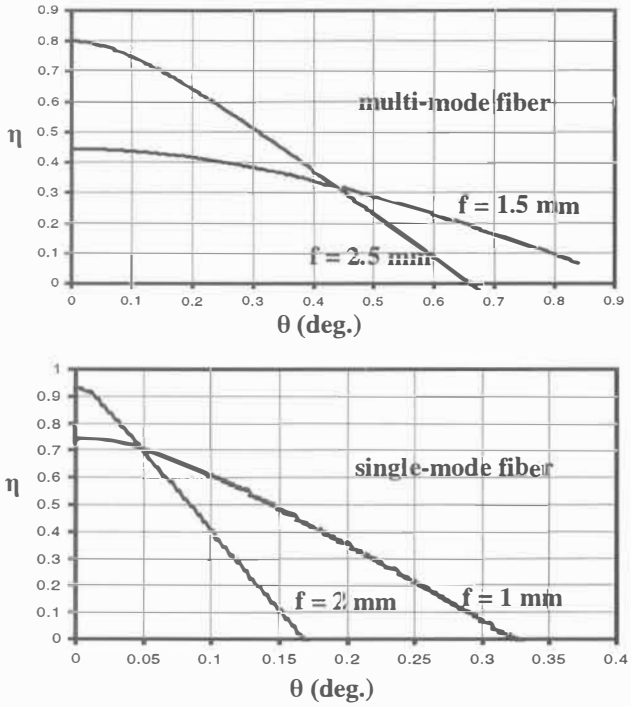

Figure 3. *Simulated approximate coupling efficiency vs. angular mismatch for different fiber/collimator assemblies. θ is twice the angular misalignment of the mirror. In all cases, N.A. = 0.1, and s = 1 cm. The fiber core radius is 25 μm in the top graph and 5 μm in the bottom graph.*

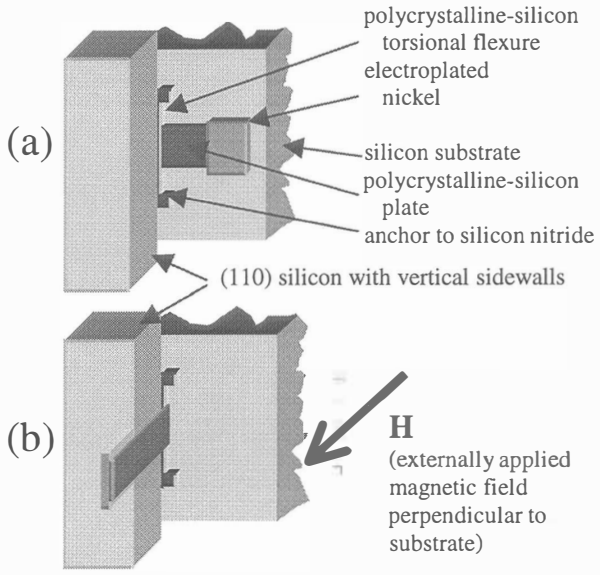

Figure 4. *Torsion-bar-mounted magnetic mirror with (110)-oriented silicon chip bonded on the base chip, shown in its horizontal and vertical position.*

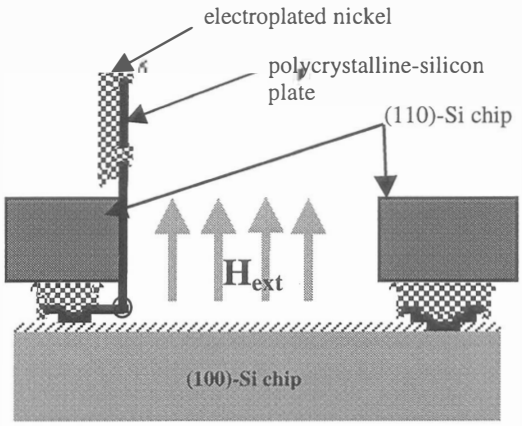

Figure 5. *Cross section of mirror assembly.*

(for improved coupling efficiency), a tighter angular tolerance must be maintained. From the analysis summarized in Fig. 3, we conclude that coupling is extremely sensitive to the beam angular incidence. For example, for an insertion loss of 3 dB, the mirrors in a typical MEMS 3x3 switch must be positioned with ~0.15° accuracy for multi-mode fibers and ~0.08° accuracy for single-mode fibers.

DESIGN

To control the vertical mirror angle precisely, we employ electrostatic clamping of magnetically actuated torsion-bar-mounted mirrors to vertical sidewalls of an anisotropically etched (110)-silicon top-mounted structure. Previous work has established that magnetically actuated mirrors can be clamped electrostatically to the substrate [11,12]. In references 11 and 12, mirrors were either torqued out of the substrate plane by an external electromagnet or selectively kept in the horizontal position by applying a voltage between the mirrors and the substrate. In this work, we introduce a vertical clamping structure, as shown in Fig. 4, to fix the "mirror-up" position. We insure uniformity of the vertical-mirror angle over the entire device by employing selective

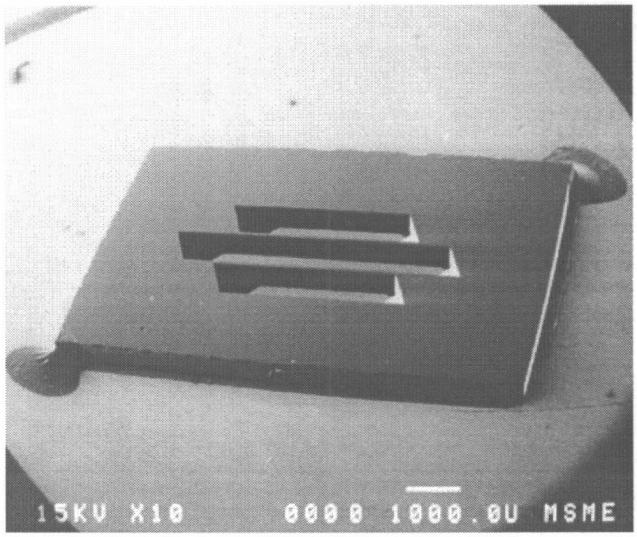

Figure 6. *SEM image of KOH-etched (110)-silicon chip for electrostatic clamping of magnetic torsion mirrors.*

etching along the <110> crystal axis [9,10] to define the precise orientation of the vertical clamping electrodes.

Vertical clamping also allows us to address individual mirrors in an NxM mirror matrix independently. Figure 4 shows the mirror in its two positions. A field (typically ~300 Gauss) applied from an external magnet actuates the mirror between these two positions by applying a force on the magnetized nickel plate situated on the top portion of the mirror structure. An applied voltage (typically 15 to 25 V) can be used to clamp the mirror by electrostatic forces that exceed those from the magnetic field. Hence, every mirror can be individually switched between its two positions without disturbing any of the other mirrors.

FABRICATION

The mirror assembly is built up of two silicon chips: a (100)-silicon chip on which the surface-micromachined mirrors are fabricated, and a (110)-silicon chip containing via-holes with vertically etched sidewalls. The surface-micromachined mirrors consist of polycrystalline-silicon plates that are anchored to the substrate by two torsion flexures. The top parts of the plates are electroplated with nickel to interact with the magnetic field. Low-stress silicon nitride electrically isolates the mirrors from the substrate. A more detailed description of mirror fabrication and actuation is provided by Judy *et. al.* [11,12].

The top-mounted (110)-silicon structure is formed by KOH anisotropic etching. First, a radial pattern of rectangular openings at 0.05° increments along the wafer perimeter is defined in a 0.12 μm-thick silicon nitride etch mask. The exposed silicon is etched 200 μm deep using KOH to produce a series of pits along the wafer perimeter. Those openings having edges parallel to the (111) planes give rise to pits having the minimum mask undercut [13]. A second mask is aligned to the pits with minimal mask undercut (and hence to the (111) planes) and used to define larger openings in the silicon nitride. A subsequent KOH etch forms via holes having vertical sidewalls. The etch is carried out using a mixture of 30% KOH and water at 80 °C, resulting in an etch rate of ~2.4 μm/min for the (110) planes and 100:1 selectivity to the perpendicular (111) planes. The bath is stirred and the wafers are rotated 90° every 30 minutes to insure uniform etching across the wafer. The degree of undercut below the silicon nitride etch mask (due to etching of the (111) planes) is used to infer the uniformity of the vertical-sidewall-angle (average deviation ≈ 0.015° across wafer). Finally, the silicon nitride mask is removed and 160 nm of thermal oxide is grown on the wafer. Figure 6 is an SEM of a chip designed for a 2x2 switch. A stylus scan along the length of the sidewall reveals 300 nm irregularities that repeat every 0.5 mm. These steps are due to slight misalignment of the second mask to the crystal [13].

To address the individual mirrors independently, mirrors in the vertical position must be unaffected by the switching of other mirrors. A problem arises when the field is not perfectly parallel

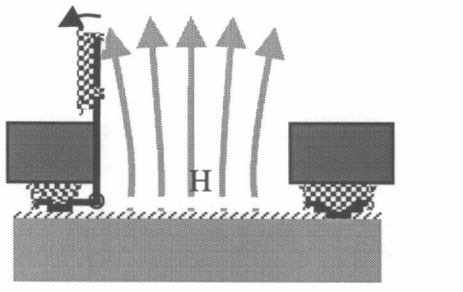

Figure 7. *A magnetic field that is not perfectly vertical can induce bending in vertically clamped mirrors.*

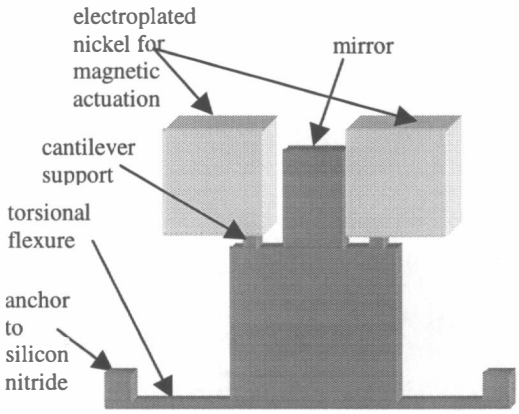

(a)

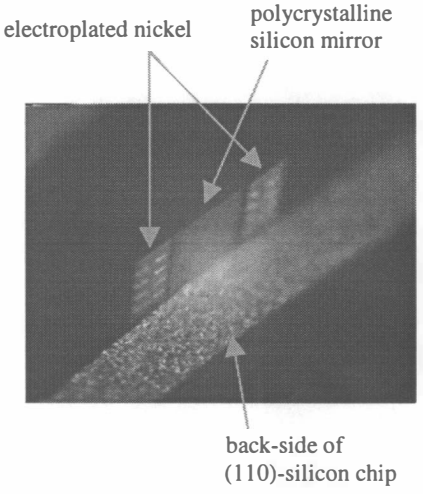

(b)

Figure 8. **(a)** *Design to reduce effect of magnetic torque on vertically clamped mirrors. The electrodeposited nickel thickness has been exaggerated.* **(b)** *Mirror clamped vertically to (110)-silicon structure.*

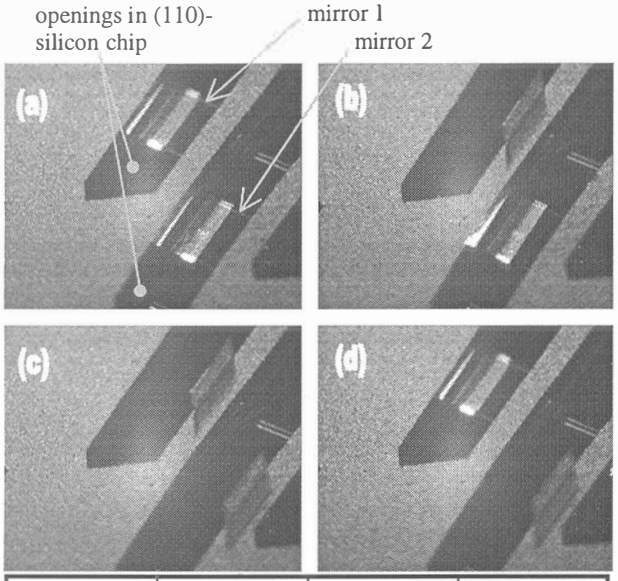

Figure 9	Mirror 1 Voltage	Mirror 2 Voltage	Magnetic Field
(a)	on	on	off
not shown	off	on	on
(b)	on	on	off
not shown	on	off	on
(c)	on	on	off
(d)	off	on	off

Figure 9 and Table 1. *Mirror operation and individual addressing.*

to the vertical mirror position. In Fig. 7, the divergence of the external field is exaggerated to illustrate this effect. A non-parallel magnetic field induces a slight torque and resultant bending in vertically clamped mirrors, causing misalignment of the reflected beams.

The design shown in Fig. 8(a) reduces bending effects on optical performance by mechanically isolating the reflecting surface from the nickel plates. The magnetically active portion of the mirror is connected to the rest of the structure by narrow support arms that isolate the mirror surface from the forces on the nickel plates when the mirror is clamped vertically. Mirrors of the design shown in Fig. 8(a) are shown clamped vertically in Fig. 8(b). These mirrors show significantly smaller bending effects in response to non-vertical magnetic fields. For these prototype mirrors, reflection was taken directly from the silicon surface.

MIRROR OPERATION

Mirror switching, as shown in Fig. 9, is implemented by an off-chip electromagnet. Both substrates are kept at electrical ground and clamping voltages are applied to individual mirrors to hold them either in vertical or horizontal positions. We have found that ac voltages (typically square waves above 250 Hz) result in more reliable operation than does pure dc clamping. The nature of this effect is under study.

The mirrors are approximately 1 mm^2, with 1100 x 400 x 10 μm nickel plates and 15 x 500 x 1.9 μm torsion flexures. They are actuated by a ~320 Gauss magnetic field and clamped with a 15 V amplitude 1 kHz square-wave. The vertical mirror angle (with the electromagnet off) for a single mirror was measured by monitoring the reflected beam with a position-sensitive photodetector and was found to be reproducible to within ~0.04°. Switching rates are presently under study.

In Fig. 9(a), both mirrors are clamped horizontally. The clamping voltage for mirror 1 is turned off and the electromagnet is turned on to swing it vertically. Next, the clamping voltage for mirror 1 is turned on and the electromagnet turned off (Fig. 9(b)). With mirror 1 clamped vertically, mirror 2 is flipped vertically and clamped (Fig. 9(c)). In Fig. 9(d), the voltage on mirror 1 is turned off and the torsion flexures force the mirror to the horizontal position.

CONCLUSIONS

We have demonstrated magnetically actuated micromirrors with electrostatic clamping in dual positions. Rough calculations show that fiber-optic switching applications require precise control of the mirror angle ($\lesssim$0.15° for multi-mode fibers and $\lesssim$0.08° for single-mode fibers to achieve 3 dB insertion loss). We have shown that employing vertically etched sidewalls of a top-mounted (110)-silicon chip to electrostatically clamp the mirrors can achieve the positioning accuracy necessary for fiber-optic switching applications. The top-mounted bulk-machined chip also allows single-step parallel assembly of all mirrors in an NxM matrix.

ACKNOWLEDGMENTS

The fabrication was carried out at the U.C. Berkeley Microlab, and we thank Microlab staff, especially Jim Bustillo, for technical assistance. Carl Chang provided help with nickel electroplating, and Kris Pister and Chris Keller gave helpful technical discussions.

REFERENCES

1. K. Y. Lau, "MEM's the word for optical beam manipulation," *IEEE Circuits and Devices*, vol. 13, no. 4, 11-8, July 1997.
2. M. C. Wu, "Micromachining for optical and optoelectronic systems," *Proc. IEEE*, vol. 85, no. 11, 1833-56, Nov. 1997.
3. H. Toshiyoshi and H. Fujita, "Electrostatic micro torsion mirrors for an optical switch matrix," *J. Microelectromech. Syst.*, vol. 5, no. 4, 231-7, Dec. 1996.
4. S.-S. Lee and M. C. Wu, "Surface-micromachined vertical torsion mirror switches," *Tech. Dig. MOEMS97*, 115-8, 1997.
5. C. Marxer, C. Thio, N. F. de Rooij, O. Anthamatten, R. Battig, B. Valk, P. Vogel, "Micro-opto-mechanical 2x2 switch for single mode fibers based on plasma-etched silicon mirror and electrostatic actuation," *Tech. Dig. MOEMS97*, 233-7, 1997.
6. W. H. Juan and S. W. Pang, "Batch-micromachined, high aspect ratio Si mirror arrays for optical switching applications," *Transducers '97*, 93-6, 1997.
7. P. di Vita and U. Rossi, "Theory of power coupling between multimode optical fibers," *Opt. Quantum Electron.*, vol. 10, 107, 1978.
8. A. Nicia, "Lens coupling in fiber-optic devices: efficiency limits," *Applied Optics*, vol. 20, no. 18, 3136-45 Sep. 1981.
9. Y. Uenishi, M. Tsugai and M. Mehregany, "Micro-opto-mechanical devices fabricated by anisotropic etching of (110) silicon," *J. Micromech. Microeng.* 5, 305-12, 1995.
10. R. A. Miller, Y.-C. Tai, G. Xu, J. Bartha, and F. Lin, "An electromagnetic MEMS 2x2 fiber optic bypass switch," *Transducers'97*, 89-92, 1997.
11. J. W. Judy and R. S. Muller, "Batch-fabricated, addressable, magnetically actuated microstructures," *Tech. Dig. Solid-State Sensor and Actuator Workshop*, 187-90, 1996.
12. J. W. Judy and R. S. Muller, "Magnetically Actuated, Addressable Microstructures" *J. Microelectromech. Syst.*, vol. 6, no.3, pp. 249-56, 1997.
13. D. L. Kendall, "On etching very narrow grooves in silicon," *Appl. Phys. Lett.*, vol. 26, no. 4, 195-8, Feb. 1975.

Microsystems for Three Axis Active Fiber Alignment

Vijay R. Dhuler, Robert L. Wood, John M. Haake*, Allen B. Cowen

MEMS Technology Application Center, MCNC
3021 Cornwallis Road, RTP, NC 27709

*The Boeing Company
PO Box 516, St. Louis, MO 63166

ABSTRACT

This paper reports the development of novel microsystems capable of three-axis active in-package alignment of fiber optic and micro-optic components with submicron tolerances. Three competing designs have been successfully fabricated and tested. These devices are batch fabricated using a combination of silicon micromachining and LIGA. A novel thermal in-plane actuation mechanism has been developed and used to generate high force and large displacement. High force is necessary to overcome friction, fiber bending, counter force springs, and wire bonds. Displacements exceeding 20 microns have been demonstrated in all three axes in an in-package configuration. Devices were subjected to over 10 million cycles of operation and showed no failure or fatigue.

INTRODUCTION

Single mode optical fibers are expected to bring rapid advancements in a wide array of photonic applications. High bandwidth handling capabilities of single mode fibers is key to enabling high power and high data rate applications such as video links, fiber laser and fiber amplifier systems, and direct-write laser printing. Principle reason for lack of implementation of all optical and single mode opto-electronics in the consumer and military marketplace is the lack of reliable and cost-effective single mode fiber optic alignment and bonding to discrete opto-electronic and photonic devices. The extremely small apertures of single mode fibers make the fiber-to-fiber and fiber-to-photonic connections an exacting and expensive process. Existing procedures for aligning fiber optics and micro-optics are very labor-intensive and require expensive capital equipment. The packaging of individual single mode opto-electronic components currently dominates the product cost in excess of 50%, limiting their implementation in the market place.

Two fundamental approaches are employed in fiber alignment: Active and passive. In active alignment, the operator or the machine manipulates the fiber relative to the coupled device and seeks active feedback, such as the output from a photodiode, to optimize the alignment. Once optimized, the fiber is cemented in place using adhesive or eutectic bonding. The existing procedures for active alignment are very expensive. Passive alignment relies on precision fixturing of the fiber relative to coupled device. A typical example is the use of a micromachined V-groove in a silicon substrate for precision placement of the fiber followed by bonding. Silicon micromachining permits very precise definition of the V-groove with respect to the fiber dimensions and to the silicon surface, which in turn can provide accurate one-dimensional fixturing of fibers. The passive alignment approach is potentially much more cost effective than active alignment, yet it has not measured up to the demands for 3-axis alignment. Researchers [1, 2] have reported microfabricated active alignment strategies that are either not fully integrated, or do not provide alignment in all three axes.

DESIGN AND FABRICATION

Three different microsystem designs [3] (Figs. 1-3) have been fabricated and tested. Each design provides a platform for holding the fiber using either a V-Groove or a LIGA defined channel. The platform is moved in three axes with respect to a fixed reference provided either internally or externally to the silicon chip. Novel in-plane thermal actuators located either on the movable platform or on the fixed base move the platform and hence the fiber in two axes. A thermal bimorph actuator lifts the platform out-of-plane. The forces generated by the actuators are large enough to overcome the friction between the moving and the fixed surfaces, the restoring force provided by the fiber and the wire bonds, and the counter force springs. These actuators provide displacements in excess of twenty microns, which significantly reduces the required pre-alignment accuracy. Also, note that the designs presented here have not yet been optimized for the size. We believe that the sizes could be reduced significantly.

Design 1

Figure 1 shows the plan and cross-sectional schematic of design 1. The end of the fiber to be aligned is glued in the V-groove provided on the silicon platform. The silicon platform is mounted onto an external base using two fixed mounts on the external base and the LIGA frame provided on the platform. The LIGA frame has two sets of four arms that fit onto the mounts. The mounts pass through the holes fabricated in the silicon platform. The LIGA frame is supported on the silicon platform by four LIGA springs and two anchors. This arrangement allows for three axis motion of the silicon platform with respect to the fixed mounts and the external base. The fixed mounts and the external base serve as the reference for alignment. This first generation design as depicted does not support out-of-plane (third axis) motion. X and Y actuators for in-plane motion are attached to the silicon platform and push against the LIGA frame to move the silicon platform in two axes. The photonic device to be aligned to the fiber would be mounted on the external base.

Design 2

Figure 2 shows a three dimensional schematic of design 2. The end of the fiber to be aligned is glued in the V-groove provided on the silicon platform. The silicon platform is housed in an external housing. Two LIGA counter force springs are provided on two sides of the platform and fixed LIGA bearings on the other two sides. They extend beyond the edge of the silicon platform and define the periphery of the platform accurately. This allows for accurate pre-alignment of the fiber with respect to the external housing. X and Y

0-9640024-2-6/hh1998/$20©1998TRF
DOI 10.31438/trf.hh1998.63

actuators for in-plane motion are attached to the silicon platform and have arms extending beyond the edge of the platform. These arms push against the reference wall of the external housing and move the platform in two axes against the counter force springs.

In addition to the in-plane actuators an out-of-plane actuator is fabricated on the silicon platform. This actuator is a thermal bimorph of single crystal silicon and LIGA-defined Nickel. When actuated it lifts the silicon platform out-of-plane by acting against the base of the external housing. The photonic device that needs to be aligned is mounted into the external housing.

Design 3

Figure 3 shows a three dimensional schematic of design 3. In this design the silicon platform is divided into two sections: a fixed mounting base and a movable base. The end of the fiber to be aligned is glued in the LIGA-defined fiber optic channel provided on the movable base, which is free to move both in plane and out-of-plane. The movable base is supported by four LIGA fabricated counter force and retainer springs, which are anchored to the fixed mounting base. X and Y actuators for in-plane motion are attached to the fixed mounting base. When actuated they push against the fixed LIGA surfaces on the movable base moving it in two axes.

In this case, the out-of-plane actuator, which is a thermal bimorph similar to that used in design 2, is fabricated on the movable base. When actuated it lifts the movable base by acting against the surface on which the platform is supported. The photonic device that needs to be aligned is mounted on the same surface on which the silicon platform is mounted.

Design 3 is the most compact of the three designs and requires the least amount of assembly and pre-alignment. It is also the least expensive of the three designs.

Fabrication

The silicon platforms in all the three designs are fabricated using a similar process. Fabrication starts with a single crystal silicon substrate. Surface micromachining and LIGA techniques are used to define the actuators and the various springs. Anisotropic etching is used to define the V-groove, out-of-plane actuator, separation channel for design 3 and holes for design 1.

RESULTS AND DISCUSSION

To characterize the performance of these actuators and microsystems, an inexpensive but accurate method of measuring force and displacement by using a calibrated, cantilevered fiber optic beam as a force probe has been developed. This method has a large dynamic range from 10 μN to 100's of mN with accuracies of a few percent [**4**, **5**].

Displacement Measurement

Displacement measurements are done using a high power microscope with a translation stage and a graduated microscope eyepiece. The translation stage is equipped with an electronic vernier for x,y,z motion with an accuracy of +/- 1 micron.

As shown in figure 4 the displacement is fairly linear as a function of the applied power. Displacements of up to 30 microns are realized for an applied power of 0.45 W. Qualitative characterization of the out-of-plane actuator indicates platform displacements in excess of 100 microns for powers less than 0.5 watts.

Force Measurement

The measurement of force involves the accurate measurement of the fiber optic force probe base deflection and the movement of the actuator to which the fiber optic force probe is being applied [**4**, **5**]. By measuring the fiber optic probe tip deflection the applied force to the actuators is calculated. There is a limit to how much force could be applied to the actuator before buckling occurs. Therefore, a small displacement on the actuator of 5 microns in the direction opposite to that of the actuator movement was used to measure the force that an actuator can exert at different power levels. Figure 5 shows a plot of force as a function of power applied to the actuator. The plot indicates that the actuators can supply a force of ~20 mN at 0.3 watts.

Dynamic Characterization

A laser vibrometer was used to measure the rate at which the platform could move axially. Figure 6 shows the plot of the laser vibrometer output as a function of the frequency of oscillation. The plot indicates a 3dB point at 60 Hz.

In Package Demonstration

Figure 7 shows the experimental setup and demonstration for two-axis active alignment for design1 in an in-package configuration. The lateral actuator is used to bring the actuated fiber in alignment with the fixed fiber. The second in-plane actuator is used for focusing. Sinusoidal actuation signals are applied to the actuators. Oscilloscope display of the drive and the detected signals indicates the alignment of the fibers. Design 3 has been successfully tested for three axis motion of the platform.

CONCLUSIONS

The design, fabrication, and operation of microsystems for active three axis fiber alignment have been demonstrated. Thermal actuator technology capable of large force (>20 mN) and displacements (>20 μM) has been implemented. Operation cycles in excess of 10 million cycles have been demonstrated.

ACKNOWLEDGMENT

This work was performed under Army Research Office contract funded by the DARPA-Defense Sciences Office. The authors wish to thank Dr. Robert Crowe of DARPA-DSO and Dr. John Prater of ARO for their support.

REFERENCES

1. Li Fan, *et al.*, "Self-Assembled Microactuated XYZ stages for Optical Scanning and Alignment", Transducers 97 Technical Digest, Vol. 1, p. 319.

2. R. Jebens, *et al.*, "Microactuators for Aligning Optical Fibers", Sensors and Actuators, 20 1989, p. 65.

3. Patenting in progress

4. J. Haake, *et al.*, "In-Package Active Fiber Optic Micro-Aligner", Photonics West 98 Technical Digest.

5. J. Haake *et al.*, "Direct Measurement of Force and Displacement of LIGA Micro Springs and Actuators", Technical Digest, SPIE 1997 Conference on Micromachining and Microfabrication.

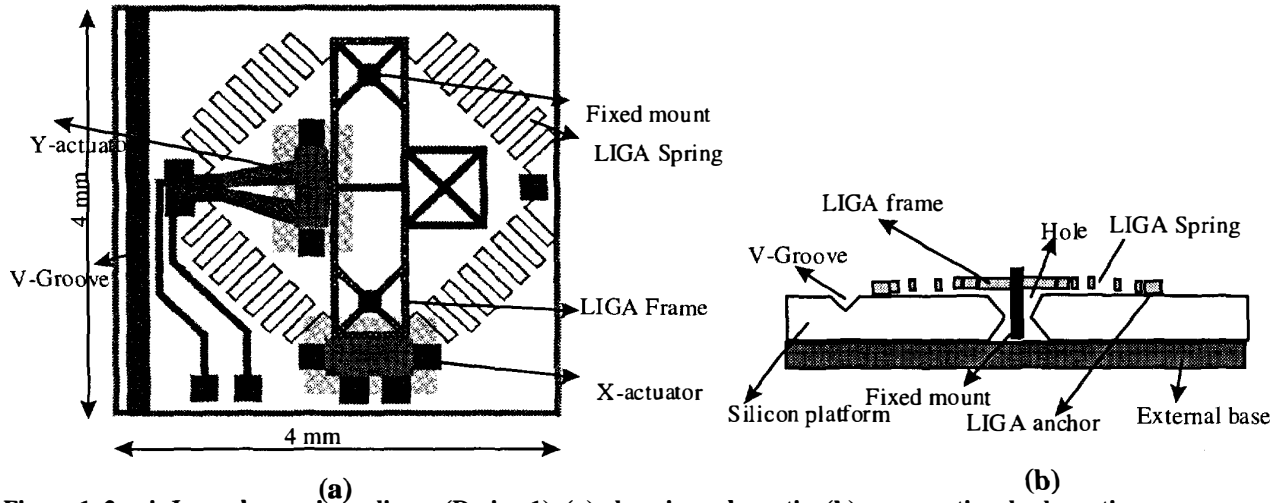

Figure 1. 2-axis In-package micro aligner (Design 1): (a) plan view schematic; (b) cross-sectional schematic

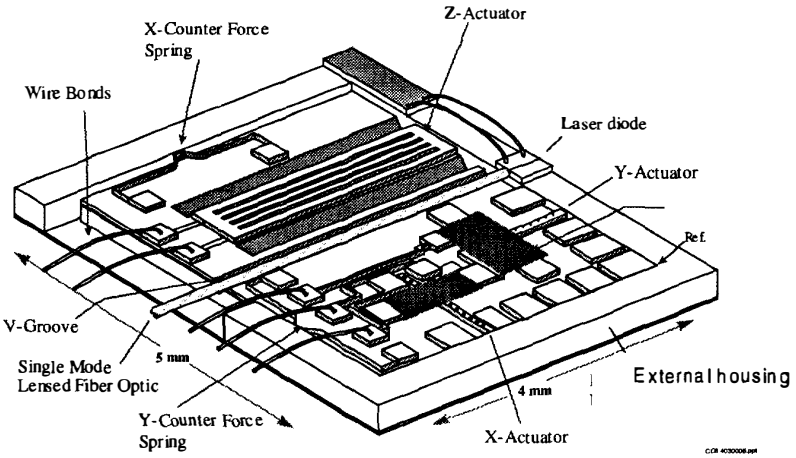

Figure 2. 3-axis In-package micro aligner (Design 2)

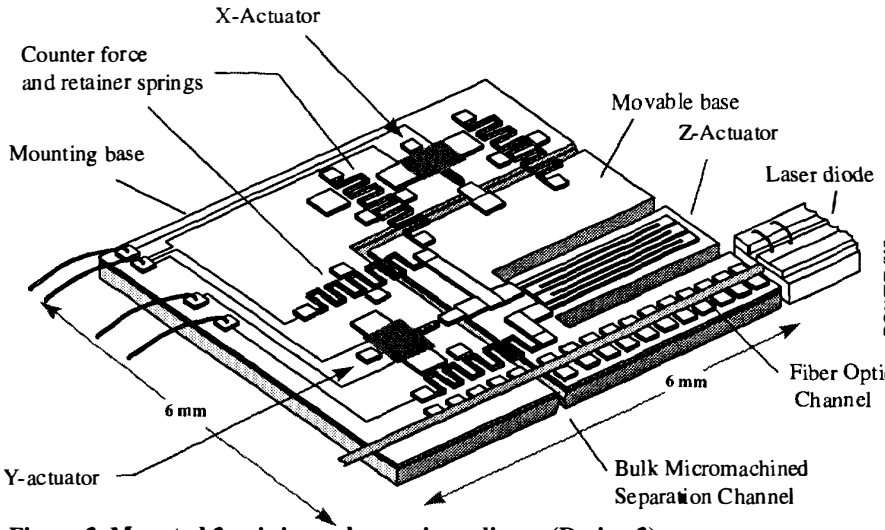

Figure 3. Mounted 3-axis in-package micro aligner (Design 3)

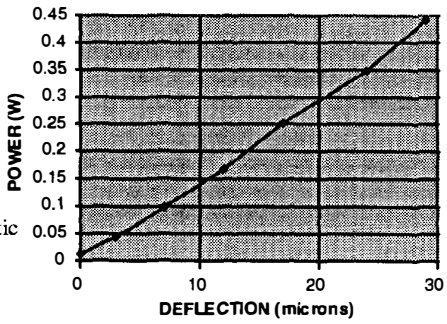

Figure 4. In-plane thermal actuation

* 240 micron Diameter Polyimide Coated fiberoptic
* Fiber optic Length = 11mm
* Forced measured at 5μm back deflection of actuator at each power level

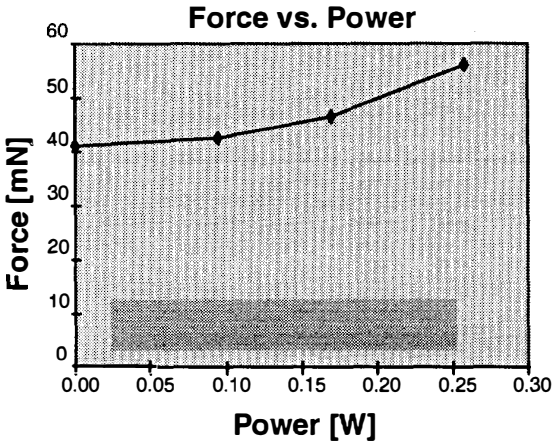

Figure 5. In-plane actuation: force versus power

- 3 dB @ 60 Hz

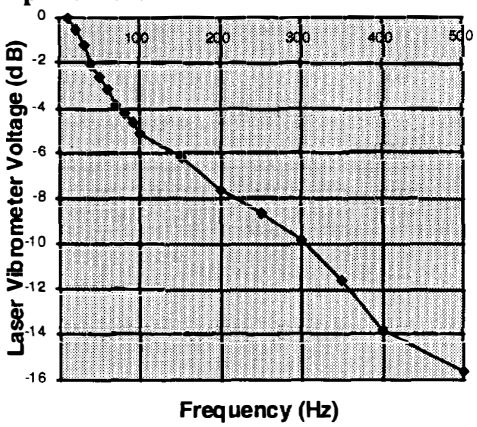

Figure 6. Mechanical frequency of in-plane actuation (design 1)

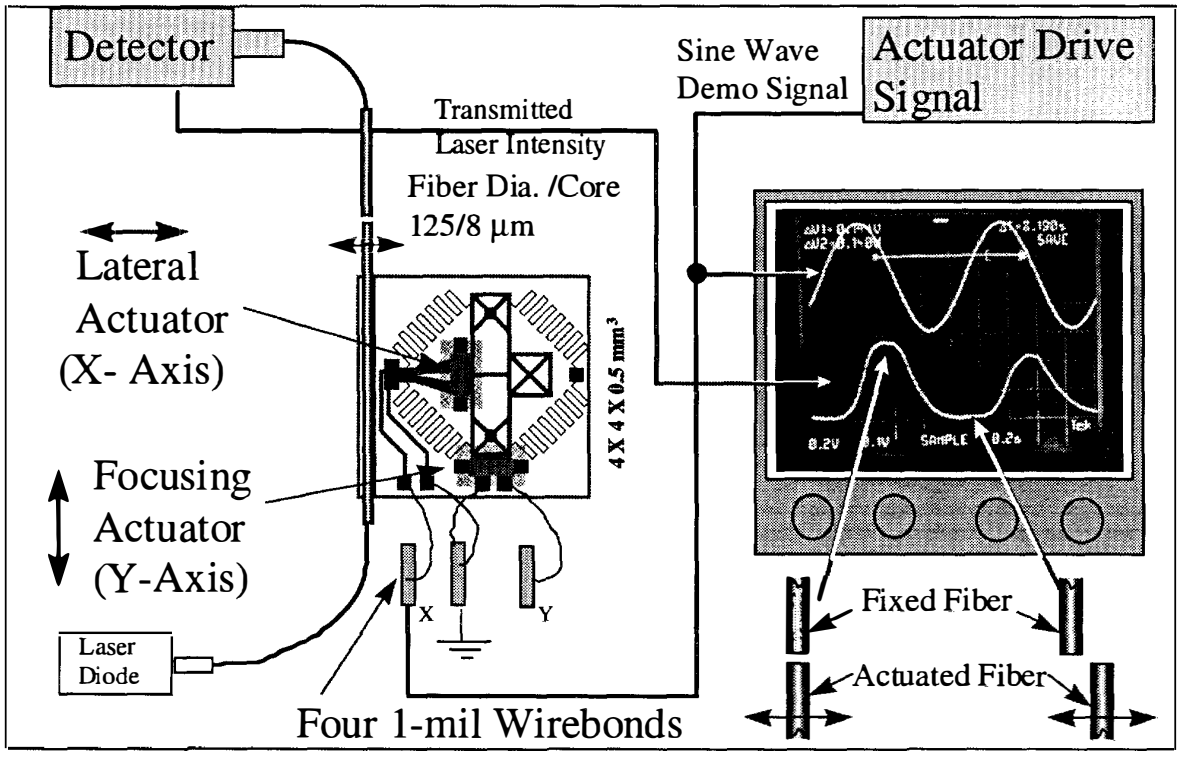

Figure 7. Two-Axis active fiber aligner experimental set-up and demonstration

2x2 MEMS FIBER OPTIC SWITCHES WITH SILICON SUB-MOUNT FOR LOW-COST PACKAGING

Shi-Sheng Lee, Long-Sun Huang*, Chang-Jin "CJ" Kim* and Ming C. Wu

Electrical Engineering Department, UCLA
63-128, Engineering IV Building, Los Angeles, California 90095-1594
*Mechanical and Aerospace Engineering Department

ABSTRACT

We report on a novel 2x2 MEMS fiber optic switch. The switch is implemented by ganging up multiple vertical torsion mirror devices that are fabricated using silicon surface micromachining process. Bulk-micromachined silicon submount has been developed for the switch. The submount is designed to accommodate the surface-micromachined vertical torsion mirrors (mirror chip), micro lenses and optical fibers. This new hybrid-packaging method is used to minimize active optical alignment between the mirror chip and optical fibers, thus reduce the packaging cost of the switch. Sub-millisecond switching times have been achieved. With this hybrid-packaging scheme, the size, weight, and potentially the cost of current fiber optic switches can be dramatically reduced.

INTRODUCTION

There has been a significant growth of optical fiber networks due to the need of fast, broadband local area networks. The rapid growth of fiber-based local area networks has created a large demand for low-cost fiber optic switches. Fiber optic switches are used to reconfigure the network and/or increase its reliability. For example, the FDDI (Fiber Data Distribution Interface) fiber optic ring network employs optional 2x2 fiber optic switches, called optical bypass switches, to bypass the failed nodes thus preserve the network reliability.

There has been a growing interest in applying MEMS (Micro-Electro-Mechanical System) technology to reduce the size, weight, and cost of the opto-mechanical switches **[1-3]**. Micromachined torsion mirrors are very attractive for implementing optical switches because of their fast switching time and proven reliability **[4]**. However, conventional torsion mirrors with in-plane torsion beams present a great challenge for packaging since the optical beams are scanned in the out-of-plane direction. Recently, we have reported a novel vertical torsion mirror switching device **[5]** whose torsion beam is perpendicular to the substrate. Such vertical torsion mirror is particularly suitable for implementing fiber optic switches since the mirror remains perpendicular to the substrate at all scanning angles.

In this paper, we report a novel 2x2 MEMS fiber optic switch that consists of four vertical torsion mirror devices. In addition, a new hybrid packaging scheme has been developed using bulk-micromachined silicon submount for low cost manufacturing of the switches. The torsion mirror has a pull-in voltage of 83.5 V. Sub-millisecond switching times have been achieved. The detail design and fabrication of the switch will be presented in the following sections.

DESIGN AND FABRICATION

Scanning electron micrograph (SEM) of the switch is shown in Fig. 1. The switch consists of a mirror chip and a silicon submount. The mirror chip comprising four surface-micromachined vertical torsion mirror devices is passively integrated with the silicon submount. The principle of switch operation is illustrated in Fig. 2. The four vertical torsion mirror devices are arranged such that in the REFLECTION mode, the input beams are reflected by two 45-degree vertical torsion mirrors and coupled into the output fibers located on the same side of the chip. In the TRANSMISSION mode, the vertical torsion mirrors are rotated out of the optical paths, and the input beams are coupled into the opposite output fibers.

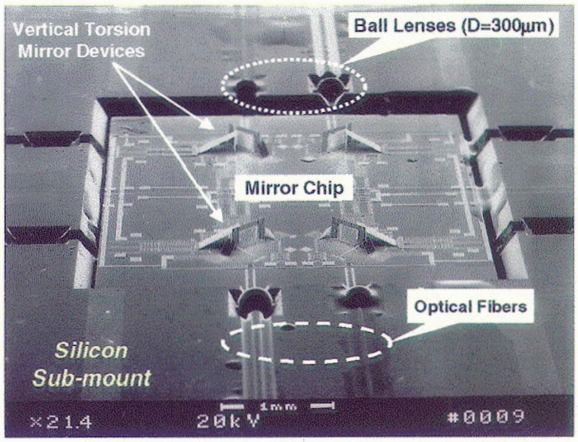

***Figure 1**. SEM of the 2x2 MEMS fiber optic switch.*

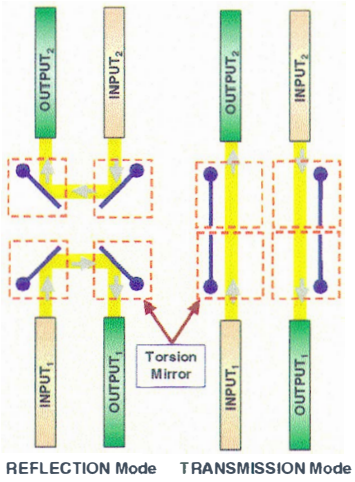

***Figure 2.** Schematic illustrations of the principle of operation.*

The basic microstructures of the mirror chip is fabricated by the three-layer polysilicon surface-micromachining process at MEMS Technology Application Center at North Carolina (MCNC) under the Multi-User MEMS Processes (MUMPs) service. Additional in-house processes have been done in order to improve

0-9640024-2-6/hh1998/$20©1998TRF
DOI 10.31438/trf.hh1998.64

both mechanical and optical characteristics of the switch. The submount is fully designed and fabricated at UCLA.

Mirror Chip

The mirror chip is made of four vertical torsion mirror switches. A torsion mirror device consists of a vertical torsion mirror and a vertical back electrode plate. The vertical back electrode is employed to electrostatically bias the mirror plate. Both the vertical torsion mirror and the back electrode are realized by the micro-hinge technology **[6]**. The angle between the vertical torsion mirror and the back electrode is designed to be 45°. Figure 3 shows SEM of a torsion mirror device. The back electrode plate is integrated with a scratch drive actuator (SDA) **[7]** array for self-assembly purpose. This self-assembly approach could dramatically reduce total assembly time of the switch. It is particularly important when multiple vertical torsion devices are used to implement more sophisticated functions. In principle, the vertical torsion mirror can also be self-assembled.

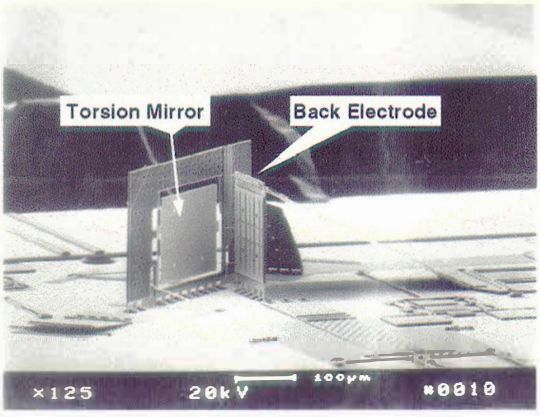

Figure 3. *SEM of the torsion mirror device.*

Vertical torsion mirror consists of a torsion mirror and a vertical-supporting frame. SEM of the vertical torsion mirror is shown in Fig. 4. The mirror is connected to a fixed vertical frame through a torsion beam. A 6 µm-wide and 2 µm-thick polysilicon stopper beam is integrated with the supporting frame to prevent overshoot of the mirror plate when it is restored by the torsion beam. The mirror plate is 200 µm-wide, 160 µm-tall and 1.5 µm-thick. The torsion beam is 2.0 µm-wide, 78 µm long and 0.8 µm thick. The surface of the mirror is coated with 0.1 µm-thick gold layer to improve the optical reflectivity. The micro-hinge allows

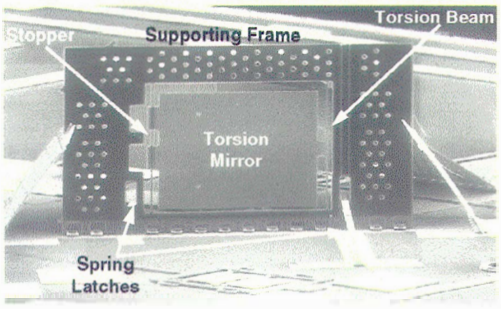

Figure 4. *SEM of the vertical torsion mirror.*

the supporting frame to rotate out of the Si substrate and stand perpendicular to the substrate. The frame is fixed by two side support plates and a pair of spring latches. The two spring latches are anchored to the opposite sides of the frame to cancel out possible excess free movement of the plate and to minimize the separation between the assembled mirror and the back electrode. The side support plates minimize the motion of the frame during the switch operation. Many large etching holes are used on the frame to reduce the electrostatic interaction between back electrode and the frame.

Vertical back electrode is made of three polysilicon plates (a back electrode plate, a support plate, and an actuator plate for self-assembly) that are jointed together by micro-hinges as shown in Fig. 5. When the electrode is assembled by the SDA, it forms a triangular shape from the side view. This configuration strengthens the stability of the back electrode during the switch operation. The total displacement of SDA array is designed such that the back electrode will be perpendicular to the wafer when SDA array is fully actuated. To prevent direct contact with the mirror during switch operation, a micro-stopper has been employed.

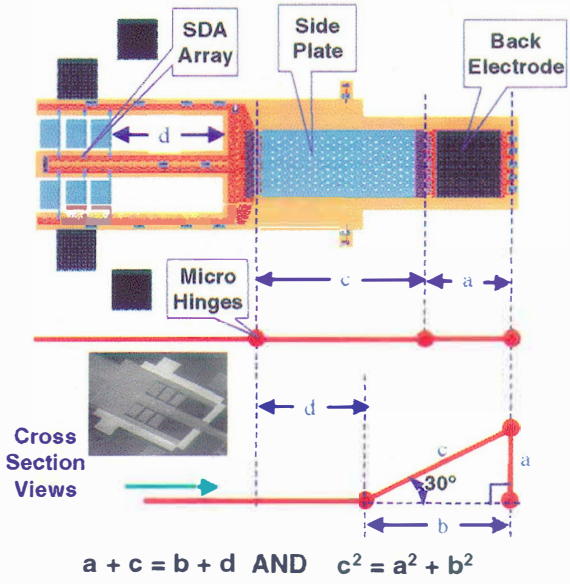

Figure 5. *Schematic drawing of the back electrode.*

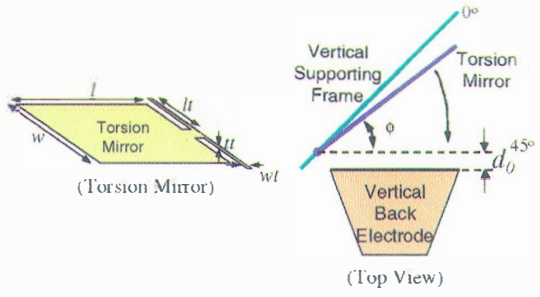

Figure 6. *Geometrical relations between the mirror and back electrode.*

The switch is designed to have a switching voltage of less than 100 V. Figure 6 shows the geometrical relation between the mirror and the back electrode. The electrostatic torque (Te) exerted by the applied voltage and the restoring torque (Tr) of the torsion beam can be expressed as functions of the rotation angle ϕ (ϕ can vary from 0° to 45°) **[1]**, where G is the shear modulus of polysilicon.

$$Tr = \frac{2}{3}\cdot\frac{G\cdot wt\cdot tt^{3}\cdot\varphi}{lt}\cdot\left(1-\frac{192}{\pi^{5}}\cdot\frac{tt}{wt}\cdot\tanh\left(\frac{\pi\cdot wt}{2\cdot tt}\right)\right) \quad (1)$$

$$Te = \frac{\varepsilon\cdot w\cdot V^{2}}{2}\cdot\int_{0}^{l}\frac{x}{\left[\left(\frac{\pi}{4}-\varphi\right)\cdot x+do\right]^{2}}\,dx \quad (2)$$

Since the restoring torque is roughly proportional to the third power of the torsion beam thickness, reducing the thickness is the most effective way to reduce the operating voltage without increasing the size of the switch. Here, the thickness of the torsion beam is reduced from 1.5 μm to 0.6 μm by reactive ion etching (RIE) with SF_6 gas, which yields a pull-in voltage of 83.5 V. No change of the mechanical strength of the torsion mirror plate is observed after etching.

Silicon Submount

The packaging scheme of the switch using silicon submount is to achieve a pick-and-drop type of hybrid packaging. Figure 7 shows the cross-section view of the package – a free-space micro mirror chip placed in the silicon submount. The submount consists of two bulk-micromachined silicon substrates bonded together.

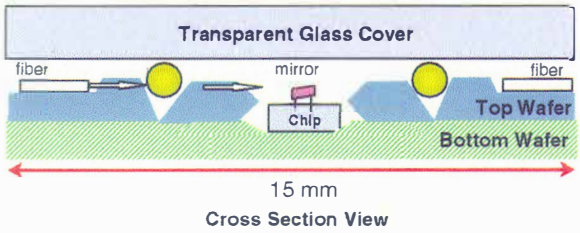

Figure 7. Cross-section view of the package: a mirror chip placed on Si submount and covered.

The top wafer of the Si submount has a central opening for the mirror chip, V-grooves for optical fibers, and micropits for micro ball lenses. The bottom substrate has a central recess area and is bonded to the top substrate. With two-substrate approach, free-space MOEMS (Micro-Optical-Electro-Mechanical Systems) devices of different designs can be accommodated with only minor modification. With this hybrid packaging scheme, the mirror chip and the silicon submount can be fabricated and optimized separately, thus avoiding the complexity associated with fabricating all the features on a single chip. The packaged mirror chip can then be easily packaged into a final product.

For the switch, light emitted from the input fiber is transmitted to the opposite fiber or redirected by the mirror to the fiber on the same side. Micro ball lenses are used to enhance optical coupling efficiency and increase working distance. In order to assemble optical elements, the silicon submount is required to have proper mechanical structures to hold the optical components. The silicon structures required for optical elements on the submount are V-grooves for fibers, micropits for ball lenses, and a central recess for a mirror chip. The V-grooves, micropits and central recess can be realized by anisotropic wet etching of (100) silicon wafer. However, it is known that convex corner on a (100) silicon wafer is attacked during an anisotropic wet etch process making formation of convex corners difficut. Therefore, carefully designed corner compensation structures [8] are used to preserve convex corners during the wet etching process.

Figure 8 shows the fabrication procedures. Two (100) silicon wafers are used for the top (double polished) and the bottom substrates. First, a 1000Å-thick silicon dioxide is thermally grown, followed by a 1500Å-thick LPCVD (low-pressure chemical-vapor-deposition) silicon nitride layer as a silicon-etching mask during the anisotropic wet etching. To minimize the effect of silicon crystal lattice-to-mask misalignment during the etching, determination of the true crystal direction within 0.1° accruacy [9] is desirable for the top wafer. Reference marks are etched to reveal the true crystal direction at the beginning of the process. After using reactive ion etching (RIE) (CF_4/O_2) to open up all etch windows on the both sides of the top wafer, the top wafer is etched in KOH. Once the central hole is opened, the wafer is taken out of the etching solution. All the features are fabricated in a single anisotropic wet etching step. Then a 5000Å-thick aluminum pad is deposited for wire bonding by the lift-off process. The bottom silicon substrate is prepared by a simpler process to create the recess for the switch chip.

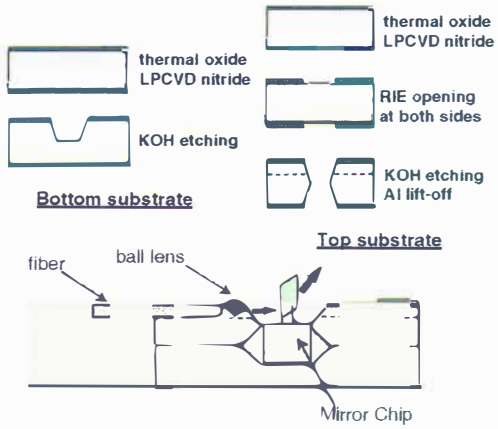

Figure 8. Process flow of Si submount.

Assembly

Figure 9 shows the schematic drawing of the silicon submount with optical fibers and micro ball lenses in place. First, the top and bottom wafers are diced to the size of 15 mm x 15 mm. In order to align top and bottom substrates, dummy optical fibers with diameter of 125 μm are used. These optical fibers are placed in the channels that are formed by two V-grooves in the interface of top and bottom substrates. Thermally cured adhesive applied along the perimeter of the bottom surface bonds the two substrates together. Orthogonally arranged dummy fibers lock the two substrates against translational and rotational sliding during the curing step when pressure is applied to the two mating substrates. Then, the mirror chip is dropped in the center opening and 300 μm-diameter ball lenses are picked and dropped into the micropits. Finally, four optical fibers are placed in V-grooves and glued using UV epoxy. Figure 10 shows the assembly of the fiber and ball lens on the V-groove and micropit.

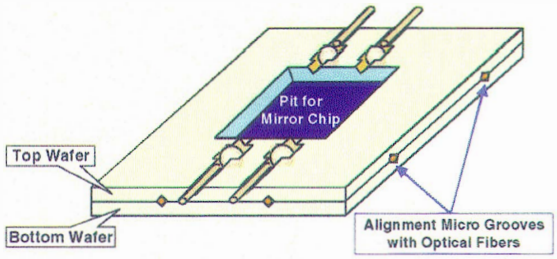

Figure 9. Schematic illustration of the silicon submount.

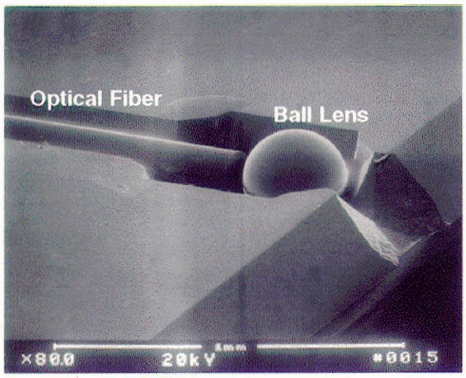

Figure 10. SEM of the fiber and ball lens assembly.

EXPERIMENTAL RESULTS

The dc switching characteristics is plotted in Fig. 11, which shows the measured angle of the mirror versus the applied DC voltage. A pull-in voltage of 83.5 V and a releasing voltage of 53 V have been achieved. The plot clearly shows the hysteresis that is characteristic of an electrostatic gap-closing actuator. The pull-in voltage and releasing voltage can be optimized further by adjusting the thickness of the torsion beam and the area of the back electrode. Electrical insulation between the mirror and the back electrode after pull-in is achieved by a mechanical stopper.

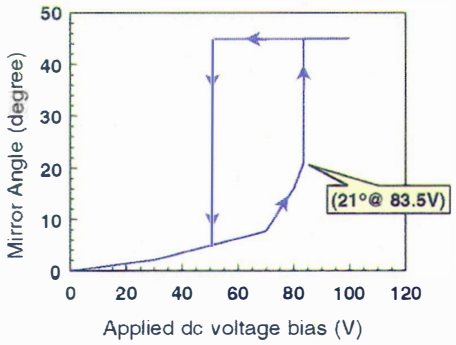

Figure 11. DC switching characteristic.

The dynamic response of the switch is plotted in Fig. 12. TRACE 1 corresponds to the 0°-to-45° switching by the electrostatic torque, and TRACE 2 corresponds to the 45°-to-0° switching by the restoring torque of torsion beam. Switching time (including the settling time) of less than 1 ms has been achieved. We have observed some oscillations after the initial switching. We believe the oscillations are due to bending of the torsion beam and overshoot during impact with the micro-stopper. This effect can be minimized by modifying mirror structure or using a programmed voltage to slow down the impact speed of the mirror during the switching thus reduce the mechanical oscillation. Eliminating the oscillations can further reduce the switching time.

Before mounting the switch on the silicon submount, the optical insertion loss is measured to be 1 dB with active optical alignment and a working distance of 600 μm. With passive optical alignment on the silicon submount, due to a relatively large mirror chip size, optical coupling loss is on the order of 10 dB (includes Fresnel loss and spherical aberration loss). It is possible to achieve an optical coupling loss of less than 2 dB (includes Fresnel loss and spherical aberration loss) by reducing the mirror chip to less than 1 mm in size. The crosstalk of the switch is less than –60 dB (measurement limit).

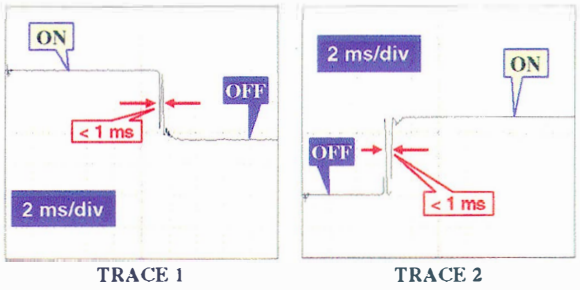

Figure 12. Dynamic response of the switch.

CONCLUSION

We have demonstrated a 2x2 MEMS fiber optic switch based on vertical torsion mirrors fabricated by the surface micromachining process. A new bulk micromachined silicon submount has been developed for optical packaging of the switch. The submount is used to minimize active optical alignment between the mirror chip and optical fibers, thus reduce the packaging cost of the switch. Optical coupling loss is relatively high for the current device, however, the coupling loss can be further reduced by reducing the size of the mirror chips. Sub-millisecond switching times have been achieved. With this hybrid-packaging scheme, the size, weight, and potentially the cost of current fiber optic switches can be dramatically reduced.

REFERENCE

1. H. Toshiyoshi and H. Fujita, "Optical crossconnection by silicon micromachined torsion mirrors", *Digest of IEEE/LEOS 1996 Summer Topical Meetings*, pp. 63-64, Keystone, CO, August, 5-9, 1996.

2. C. Marser, M.-A. Gretillat, N. F. de Rooji, *et al*, "Vertical mirrors fabricated by reactive ion etching for fiber optical switching applications", *Proc. 10th IEEE International MEMS Workshop*, pp. 349-54, Nagoya, Japan, January 26-30, 1997.

3. S. S. Lee and M. C. Wu, "Surface-micromachined free-space fiber optic switches with integrated microactuators for optical fiber communication", *International Solid-State Sensors and Actuators Conference - TRANSDUCERS '97*, pp. 85-88, Chicago, IL, June 16-19, 1997.

4. L. J. Hornbeck, "Digital light processing and MEMS: an overview", *Digest. IEEE/LEOS 1996 Summer Topical Meetings*, pp. 7-8, Keystone, CO, August 5-9, 1996.

5. S. S. Lee and M. C. Wu, "Surface-micromachined vertical torsion mirror switches", *International Conference on Optical MEMS and Their Applications- MOEMS'97*, pp. 115-118, Nara, Japan, Nov. 18-21, 1997.

6. K. S. J. Pister, M. W. Judy, S. R. Burgett, and R. S. Fearing, "Microfabricated hinges", *Sensors and Actuators A-Physical*, Vol. 33, no. 3, pp. 249-256, 1992.

7. T. Akiyama and H. Fujita, "A quantitative analysis of scratch drive actuator using buckling motion", *Proc. 8th IEEE International MEMS Workshop*, pp. 310-315, Amsterdam, Netherlands, January 29-February 2, 1995.

8. L.-S. Huang, S. S. Lee, E. Motamedi, M. C. Wu and C.-J. Kim, "MEMS packaging for micro mirror switch", *48th IEEE Electronic Components & Technology Conference*, Seattle, WA, May 25-28, 1998 (to be appeared).

9. G. Ensell, "Alignment of mask patterns to crystal orientation", *Proc. 8th International Conference on Solid-State Sensors and Actuators – TRANSDUCERS'95, Eurosensors IX*, pp. 186-189,vol. 1, Stockholm, Sweden, June 25 – 29, 1995.

MICROMIRROR PIXEL ADDRESSING USING ELECTROMECHANICAL BISTABILITY

Brian T. Cunningham, Jonathan J. Bernstein, Don Seltzer, and David Hom
The Charles Stark Draper Laboratory
555 Technology Square, Cambridge, MA 02139

ABSTRACT

In this work, a novel bistable array of micromirrors (BAMM) has been designed, fabricated, and tested which utilizes the electromechanical properties of the flexural hinged mirror elements to store the desired individual mirror states. Using the mirror structures as electromechanically bistable storage devices, pixels can be addressed individually without the use of integrated static random access memory (SRAM) cells beneath each element. Through the elimination of integrated RAM circuitry, the mirror array fabrication sequence is greatly simplified, and decreased yielded die costs are expected compared to fabrication which relies upon the combined yield of the memory and mirror processes.

INTRODUCTION

The commercialization of MEMS spatial light modulator (SLM) arrays has been pioneered by Texas Instruments and others through the development of the Digital Micromirror Device (DMD) and deformable grating light valve arrays for use in digital high resolution color projection displays **[1-4]**. The DMD pixel elements consist of reflective aluminum platforms which can be rotated about a torsion hinge into one of two bistable states using electrostatic electrodes beneath the platform. The MEMS structure is typically fabricated monolithically over a CMOS SRAM cell which is used to address the pixel by digitally storing the desired state of the mirror for the subsequent video frame.

While integration of the CMOS process with the MEMS process may be the most economically advantageous fabrication method for applications where high sales volume and large capital equipment resources permit, many applications with smaller expected markets require arrays of SLMs which can be individually addressed. For such applications, simplification of the fabrication process and the ability to utilize commercially available electronic components is key to providing SLM arrays with low cost and high yield. The impact of fabrication yield is especially important for video display applications where a defect within a single pixel during the SRAM or MEMS portion of the process will result in rejection of an entire large area array.

In this work, a bistable array of micromirrors (BAMM) is presented which enables individual pixel row/column addressing without the use of an SRAM cell beneath each pixel. The addressing method allows one to set the desired state of every mirror in a selected row simultaneously while holding all other rows fixed. The on/off state of every pixel in the array is set by addressing the rows in sequence. 10x10 and 100x100 mirror arrays were fabricated using the MCNC MUMPs process to demonstrate the BAMM addressing approach. In principle, the BAMM addressing method is applicable to bistable mirror arrays fabricated by any process. Using the BAMM addressing approach, mirror arrays can be fabricated with only 6 photomask steps, eliminating the need for a special CMOS SRAM wafer and processes associated with interfacing CMOS with MEMS such as surface planarization and interconnect vias. Through the use of a stand-alone MEMS process, high temperature materials such as polysilicon can be considered which would otherwise not be compatible with finished CMOS circuitry. The use of polysilicon hinges may result in longer pixel lifetime compared to aluminum hinges which can show plastic and fatigue behavior. A simple, inexpensive switch relay network was designed and built to operate the 10x10 array which can easily be scaled to address larger arrays.

THEORY

A schematic drawing of a BAMM pixel element is shown in Figure 1. The reflective platform pivots around a thin torsion hinge when a voltage applied to either the "left" or "right" electrode breaks the symmetry while an electrostatic snapdown voltage is applied with the "hold" electrode. Once the platform is deflected to its desired state, the "hold" electrode maintains the pixel's position until it is released for a subsequent write cycle. Using this method, a row of pixels in an x-y array can be addressed by writing to one row while all other rows are "held" as shown in Figure 2. A timing sequence for the addressing process is shown in Figure 3.

The rotational snapdown voltage of the pixel is given by

$$V_{SD} = \sqrt{\frac{k_\theta x_0^3}{2\varepsilon A_c L_c^2}}$$

where k_θ is the rotational spring constant of the torsion hinge (N-m/rad), x_0 is the quiescent capacitor gap, ε is the dielectric constant of air, A_c is the left or right side area, and L_c is the distance from the center line to the center of the electrode. The design goal, within the constraints of the MUMPs fabrication process design rules, was to produce pixels with $V_{SD} < 15V$. Because x_0 is fixed by the MUMPs process at $x_0 \sim 2$ μm, devices were fabricated with various pixel sizes to affect A_c and L_c and various flexure widths to affect k_θ.

EXPERIMENTAL RESULTS

For demonstration of the BAMM concept, 50x50 μm and 100x100 μm pixels were designed with flexure widths of 1.0, 1.5, and 2.0 μm. 1.0 μm was the smallest linewidth allowed by MUMPs. Two types of pixels were fabricated: exposed flexures and hidden flexures. While both types of pixels use flexures and a rotational platform built from the 2.0 μm thick Poly1 layer, the hidden flexure designs incorporate an additional upper metalized (Cr/Au) 1.5 μm Poly3 layer to increase optical fill factor and to provide a more reflective top surface. A 100x100 μm pixel element with a 1 μm wide hidden hinge is shown in Figure 4. Selected pixel designs were incorporated into 10x10 and 100x100 element arrays. A

0-9640024-2-6/hh1998/$20©1998TRF
DOI 10.31438/trf.hh1998.65

Solid-State Sensors, Actuators, and Microsystems Workshop
Hilton Head Island, South Carolina, June 8-11, 1998

portion of a 100x100 element array with 1.5 μm exposed flexures is shown in Figure 5.

Pixel snapdown voltage was characterized for the various designs and flexure widths. As shown in Figure 6, 50x50 μm pixels were found to require excessive V_{SD} for all flexure widths while 100x100 μm pixels using the hidden flexure design with 1.0 μm wide flexures required a V_{SD} of only 9V. Due to chip area constraints, 10x10 element arrays with the hidden flexure design were only fabricated using 1.5 μm wide flexures, with V_{SD} = 18V. Therefore, demonstration of the BAMM addressing approach was performed with this design. As shown in Figure 6, device-to-device snapdown voltage repeatability was excellent.

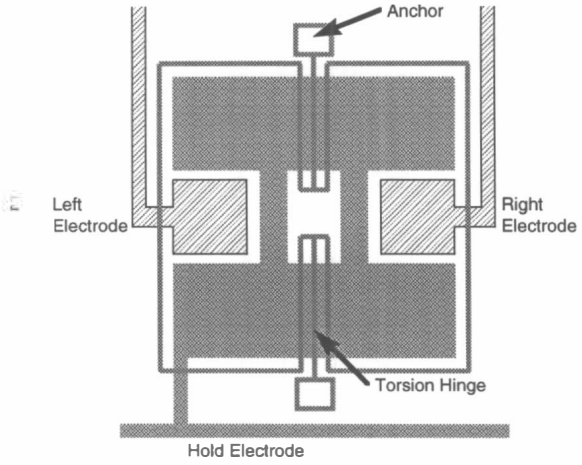

Figure 1. *Schematic drawing of a BAMM pixel element. The mirror platform is supported by a central thin torsion hinge. The "Left" and "Right" electrodes are used to break the symmetry when an electrostatic snapdown voltage is applied with the "Hold" electrode. The "Hold" electrode extends across the center of the pixel to keep the pixel in its intended state until it is released for the next write cycle.*

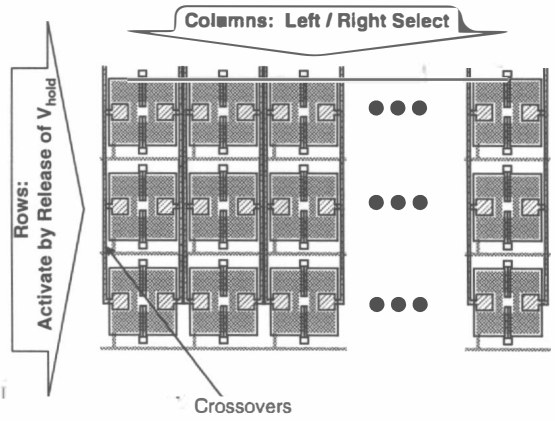

Figure 2. *The left/right state is selected for every column simultaneously. By releasing the "Hold" voltage from a single row, only one row is affected by the selected left/right state. Array pixel addressing is achieved by sequentially releasing V_{hold} for each row, synchronized with the application of desired left/right state from the column lines.*

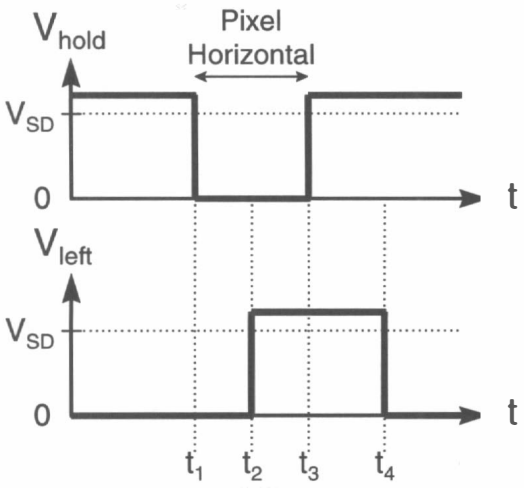

Figure 3. *Example timing sequence for directing a pixel to rotate to its "left" state. After V_{hold} is released for a row at t_1, either V_{left} or V_{right} is activated at t_2 to direct the pixel. When V_{hold} is reapplied, the pixel snaps to the desired state, and V_{left} is reset at t_4 to address the state of the next row. The pixel is up for $t_1 < t < t_3$ while V_{hold} is released.*

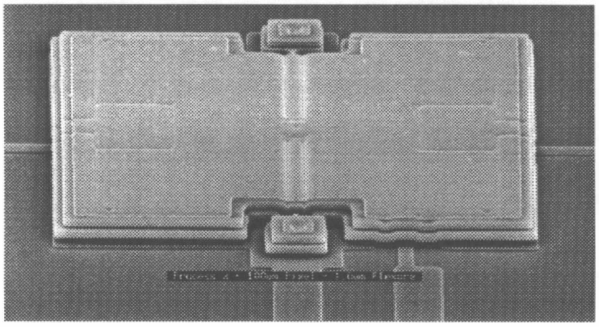

Figure 4. *SEM photo of 100x100 μm pixel with 1.0 μm wide hidden flexure.*

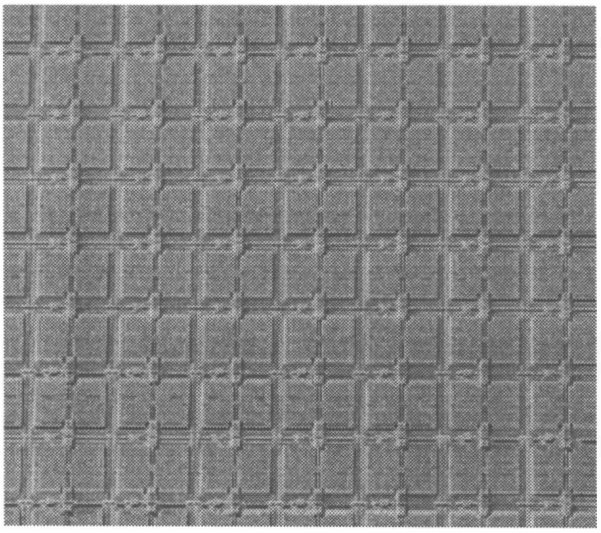

Figure 5. *SEM photo of portion of a 100x100 element BAMM array with 100x100 μm pixels and 1.5 μm wide exposed flexures.*

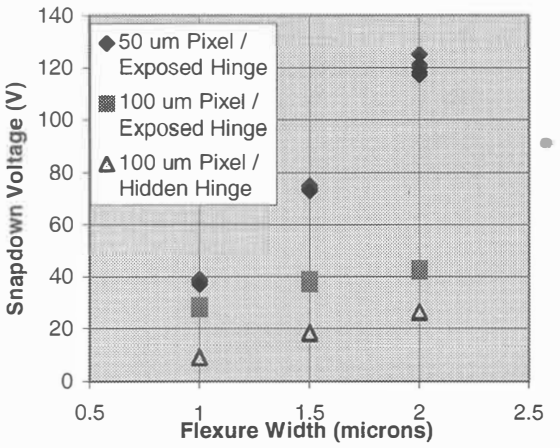

Figure 6. *Snapdown voltage as a function of flexure width for three BAMM pixel designs. Five pixels are sampled for each design and flexure width.*

Mirror control electronics were built to demonstrate functionality of the 10x10 element hidden 1.5 μm flexure array. Because V_{SD} = 18V for this design, high voltage components were required for switching the "hold" and "left/right" select electrodes. As shown in Figure 7, a computer is used to control the high voltage relay network which sequentially writes column data to rows which are activated by removal of the "hold" voltage. Using computer control, sequences of programmed pixel patterns can be displayed by the mirror array. For this work, equal voltages were applied to the "hold" and "left/right" electrodes. For pixels with a measured V_{SD} = 18V, an applied voltage of V = 20V was found to give the most reliable operation. Operation with V > 30V was found to result in a small percentage of "sticky" pixels which would remain fixed in one state for several cycles, but which would eventually release. No effort was made to apply anti-stiction coatings, although the pixels incorporate small dimples on the bottom sides of the mirror elements to minimize surface contact area during snapdown.

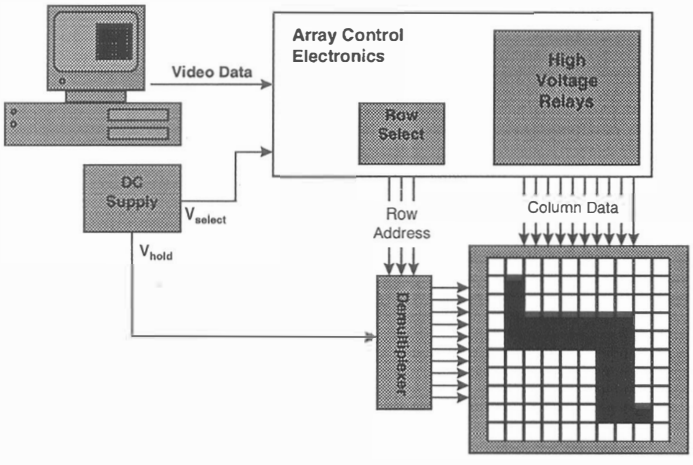

Figure 7. *Mirror array control electronics for operation of a 10x10 element BAMM array.*

CONCLUSION

A bistable mirror array addressing approach has been demonstrated which enables individual pixel addressing without the use of an integrated SRAM memory cell. The approach relies upon the electromechanical bistability of the mirror pixel's torsional hinge to maintain the position of the array elements while a single row is addressed. The method was demonstrated using 10x10 polysilicon mirror arrays fabricated with the MCNC MUMPs process. The BAMM approach is broadly applicable to SLM arrays of mirrors or deformable gratings fabricated by any method.

Further optimization work would focus on using chemical-mechanical polishing (CMP) to provide a smoother top surface, as well as addition of an upper aluminum metalization layer for increased reflectivity. The use of thinner and narrower flexures will allow reduction of the applied voltages to <5V for compatibility with standard CMOS electronics.

ACKNOWLEDGEMENTS

The authors would like to acknowledge the Draper Laboratory MEMS Center of Excellence for providing the funding for this project, and to Dr. Marc Weinberg and Dr. Byong Ahn for their management interest and support.

REFERENCES

1. L. Hornbeck, *Proc. of Micromachining and Microfabrication '95*, Plenary Session, Austin, TX, October 23-24.
2. V.P. Jaecklin, *Sensors and Actuators A, 43*, p. 269 (1994).
3. E. Chiu, *1995 Intl. Symp. On VLSI Technology, Systems, and Applications*, p. 137.
4. R. Apte, *Technical Digest of the1994 Sensor and Actuator Workshop*, Hilton Head Isl., SC, p 1-6.

Squeeze Film Damping of Doubly Supported Ribbons in Noble Gas Atmospheres

C. S. Gudeman, B. Staker, and M. Daneman
Silicon Light Machines
385 Moffett Park Drive, Suite 115
Sunnyvale, CA 94089-1208

ABSTRACT

Doubly supported MEMS ribbons of a Grating Light Valve device have been characterized for damping time when excited by an impulse in noble gas atmospheres. A simple linear relationship is found between the damping time of the ribbons and the gas viscosity when corrected for rarefaction effects.

INTRODUCTION

The Grating Light Valve (GLV™) modulator is an emerging technology employing doubly supported beams (ribbons) as elements of a projection display array **[1]**. The low effective mass and high tension in these ribbons permit operation at speeds of up to 20 MHz, which is the highest operational speed of all MEMS ribbons or cantilevers to date. The geometry and speed of the GLV ribbons are such that viscous forces in atmospheric gas phase environments play a vital role in damping the mechanical response of ribbons when actuated by an electrical impulse. To understand this viscous damping a detailed study of GLV ribbon ring down characteristics has been made in inert atmospheres of He, Ne, Ar, Kr, and N_2 at 1 atm pressure and in N_2 at 0.5 and 1.5 atm. The results are reported in this article. From these data we analytically relate damping time to the viscosity and Knudsen Number of the gas and the geometry of the ribbon. In the current case solution of the Reynolds Equation is unnecessary. A simple closed form expression of the gas viscosity, corrected for slip flow according to Burgdorfer **[2]**, is sufficient to accurately predict the effect of gas viscosity for all gases and pressures studied.

GRATING LIGHT VALVE TECHNOLOGY

Measurements of MEMS ribbons reported here are based on the grating light valve structure, which is depicted in Fig. 1. The device is built up of thin films and processes that are common in the fabrication of CMOS electronic devices, with the major difference being that, like most MEMS devices, a layer of sacrificial material is required for the release of the device from the underlying layers. For the GLV structure this sacrificial layer is polycrystalline silicon that is isotropically etched out from under the ribbons. The thickness of this sacrificial layer determines the air gap spacing y_o that, as will be seen below, is the nominal thickness of the gas squeeze film.

Referring to Fig. 1, the ribbon arrays are built up on silicon substrates. The substrate itself is used as the bottom electrode. The sacrificial layer is deposited, followed by an etch step to create post vias for ribbon support and electrical connections. The Si_3N_4 ribbon layer of nominally 100 nm thickness is deposited, followed by the top aluminum electrode layer. The ribbons are patterned, thus exposing a path to the sacrificial layer for the release etch, which is the final step. The dimensions of the ribbon can be varied over a very broad range. Experimentally lengths of 15 - 300 μm and widths of 2.0 - 7.75 μm have been fabricated, and have shown predicted resonant frequencies and actuation voltages. The air gap, defined by the sacrificial layer, has been varied from 150 nm to 750 nm, again yielding predictable behavior in the GLV dynamics.

The GLV device is ideal for the study of ribbon dynamics, since the defracted light of the GLV grating provides a means of sensing the ribbon deflection. Because it is the diffraction of light that is used in this study to sense the dynamic response of the ribbon, a brief description of GLV diffraction will be presented next.

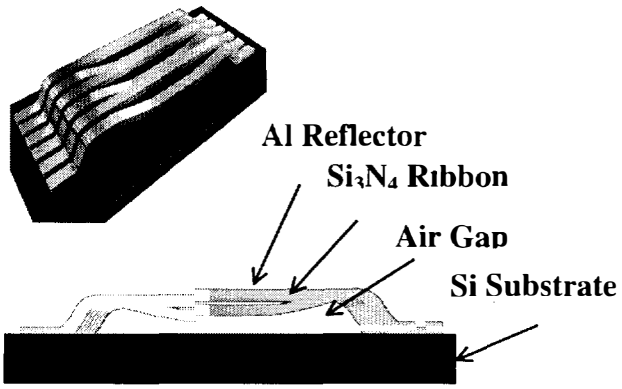

Figure 1. Diagram of the GLV structure. Upper left relief drawing depicts a pixel in the bright state.

Consider normal incidence illumination of the device with collimated monochromatic light (cf. Fig. 2). The light will be reflected back to the source as shown in Fig. 2a when the ribbons lie in a single plane. This is the case when no potential difference is applied between the ribbon aluminum and the bottom electrode. If a non-zero potential is applied to alternate ribbons in the array (Fig. 2b), these ribbons will be electrostatically attracted to the bottom electrode, causing them to deflect. A phase grating is created, and light is diffracted at angles θ, where

$$\theta = \arcsin(m\Lambda/d). \quad (1)$$

0-9640024-2-6/hh1998/$20©1998TRF
DOI 10.31438/trf.hh1998.66

Solid-State Sensors, Actuators, and Microsystems Workshop
Hilton Head Island, South Carolina, June 8-11, 1998

Here Λ is the wavelength of light, d is the period between deflected ribbons, and m is a signed integer representing the order of diffraction. Note that the defraction angle is independent of the ribbon deflection δy. For the current case first order light is diffracted at roughly four degrees. The intensity of light that is diffracted into first order does vary with the magnitude of the deflection, with the following dependence:

$$I = I_o \sin^2(2\pi\delta y/\Lambda). \quad (2)$$

Here I_o is the maximum intensity defracted into 1st order. Thus the ribbon response to an applied voltage impulse can be sensed as a function of time from the intensity of light diffracted into first order. $\delta y(t)$ can then be determined from the ratio I/I_o, given the wavelength of incident light Λ.

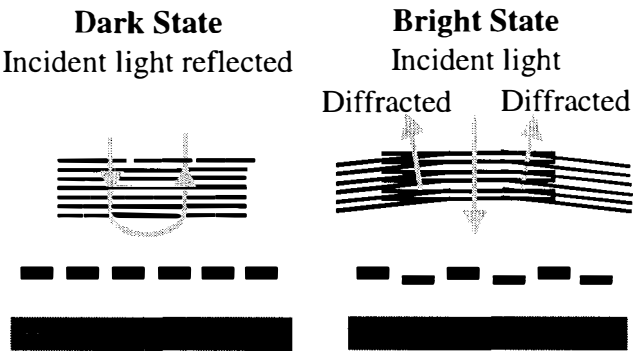

Figure 2. *Diagram of the GLV pixel operation. The dark state occurs when the all six ribbons are coplanar and light is specularly reflected back to the source. The bright state occurs when alternate ribbons are deflected a distance of $\Lambda/4$ and the light is diffracted.*

EXPERIMENTAL

The diffracted light from a damped device is monitored in an environmental chamber as shown in Fig. 3. The light from a 680 nm diode laser is directed through a large (6 inch diameter) window in a vacuum chamber onto the ribbon array with an incidence angle of 30 degrees and a focus of 25 μm. In the undeflected state the ribbons reflect the incident light specularly back though the window. When the ribbons are deflected, light is lost from of the specular beam and transferred into the diffraction orders, which also pass back through the chamber window. The 1st order beams are the most intense and are well separated from the specular beam. A photodetector is placed in the path of one of the 1st order lobes, and the output from the photodetector is displayed on a digitizing oscilloscope and finally captured by a computer. Noise in the system is dominated by laser noise in the 50 MHz passband of the photodetector.

The impulse applied to the GLV aluminum layer is a 100 kHz square wave that is offset to be unipolar with an adjustable amplitude of 10 - 30 V. The rise and fall times of the impulse are approximately 100 nsec. The amplitude is adjusted to deflect the ribbons roughly 50% of $\Lambda_{eff}/4$ or ~ 100 nm. (Note that here $\Lambda_{eff} = \Lambda/\cos\theta$, where θ = angle of incidence with respect to the normal. This factor permits the simple treatment above to be applied to the more general case of non-normal incidence.) This provides large intensity modulation (as can be inferred from Eq. 2), but avoids close approach to the bottom electrode, where complications of small separations (snap down and the surface roughness contribution to the effective air gap separation) arise.

Prior to a series of ring down measurements, consisting of ring down curve acquisition of both rising and falling impulse edges for a range of ribbon arrays spanning 70 - 100 μm in length, the vacuum chamber is evacuated to a base pressure of ~ 10^{-6} Torr. The chamber is then back filled with the chosen gas to the desired pressure (generally 1 atmosphere), as measured by a Bourdon gauge. The measurements are made in a static gas system, and the level of outgassing contamination during the ~30 minute measurement series is less than 100 ppm. The gases studied were He, Ne, Ar, Kr, and N_2 at 1 atm. Additionally ring down data is reported here in N_2 at 0.5 and 1.5 atm.

DATA ANALYSIS

Fig. 4 shows the 1st order optical response following both rising and falling edges of an applied impulse. Note that the rising edge of the impulse induces a ringing response characteristic of a simple damped harmonic oscillator. The optical response following the falling edge, on the other hand, appears doubled in frequency and the intensity for each cycle returns to a common

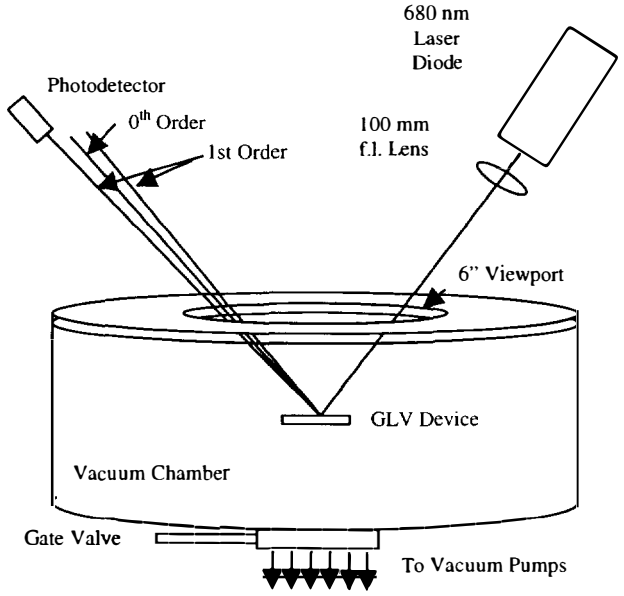

Figure 3. *Diagram of the test apparatus, including the environmental chamber optics probe.*

base line. This "rectification" following the falling edge occurs because the ribbons ring about the undeflected plane, where the optical response function is even, as inspection of Eq. 2 shows when δy is nominally zero. Following the rising edge the ribbons

ring about a steady state deflection of ~100 nm, where the optical response function is approximately linear.

Although the rising and falling edges have seemingly different character, a single function describing both has fairly simple form:

$$I = D + I_o \sin^2(2\pi/\Lambda)(B + Ae^{-t/\tau}\sin(2\pi\nu t + \phi), \quad (3)$$

where δy in Eq. 2 has been replaced by $B + Ae^{-t/\tau}\sin(2\pi\nu t + \phi)$. This expression provides terms for the steady state position B of the ribbons following the impulse edge, the undamped ringing amplitude A, exponential damping with time constant τ, harmonic oscillation at frequency ν, and a phase factor ϕ. The additive constant D is included to accommodate the photodetector dark current and all other DC offset contributions of the detection system.

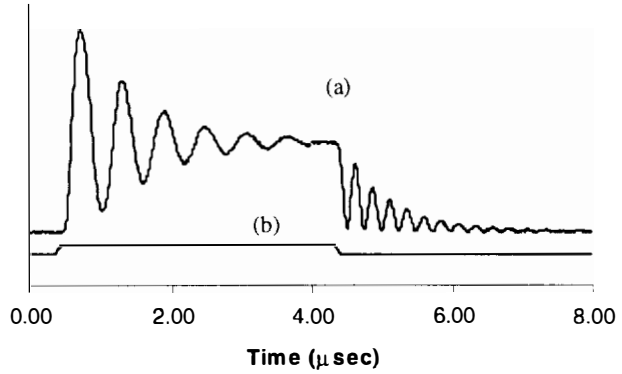

Figure 4. *Optical response of a GLV pixel (a) following impulse excitation (b) of the ribbons in He gas at 1 atm.*

A typical ring down data set, such as the one shown in Fig. 4, consists of 1000 points sampled at a rate of 125 - 250 MHz. This intensity vs. time data set is then fitted to Eq. 3 using the Levenberg - Marquardt nonlinear least squares algorithm **[3]**. Prior to fitting, the constants D and I_o are determined by direct measurement of the dark response at zero applied ribbon voltage and the peak response occurring when the ribbons are deflected by $\Lambda/4$. The fit then determines the parameters A, B, ν, τ, and ϕ. Generally convergence occurs in 15 - 25 iterations, requiring ~10 seconds of computation time on a 133 MHz P5 computer in either of two interpreted languages (APL2PC for DOS and LABVIEW 4.0). Stable convergence is particularly sensitive to the initial guess of the phase factor ϕ. Thus it is convenient to code the fit such that initial guess of ϕ is easily adjustable. Residuals (not shown here to avoid congestion in the plot) are typically < 5% of the peak signal response.

The responses to rising and falling edges must be fitted separately since all 5 fitting parameters are in general different in the two states. A brief qualitative description of these differences for ν and τ is germane to this analysis, since the ringing behavior in the deflected state (following the rising edge) is encumbered by two factors that make it a less accurate measure of viscous effects than that of the undeflected state. Briefly, these differences can be described as follows. First, spring softening, an effective reduction in the spring constant and therefore the natural frequency of the ribbon, occurs because the mechanical restoring force $-k_{mech}\delta y$ is opposite in direction to the electrostatic force $k_{elec}V^2/(y_o-\delta y)^2$ that deflects the ribbon. Here V is the deflecting potential and the k's are positive proportionality constants. Thus in all cases, the natural frequency ν is observed to be lower in the deflected state. Second, in the deflected state the ribbon takes on a half-sine profile, and thus on average the air gap is non-uniform along the length of the ribbon, with the air gap at the center of the ribbon considerably less than the nominal value y_o. As a result, the damping time τ is experimentally observed to be lower in the deflected state. Because of these effects, only ringing behavior data from the undeflected state is reported in this article.

RESULTS

Fig. 5 shows extracted values of ν and τ for all ribbon lengths studied. In all five of these cases in this figure, the gas pressure is 1 atm. Several observations are evident.

First, ν shows little dependence on damping gas, but falls off with inverse ribbon length, as expected. Conversely, τ shows a very marked dependence on damping gas, but is essentially independent of ribbon length. It is the dependence of τ on damping gas that is examined next.

Table 1 summarizes several properties of the damping gases including viscosity η and mean free path λ at the specified pressures for ambient temperature (297 K). Note that although Ne

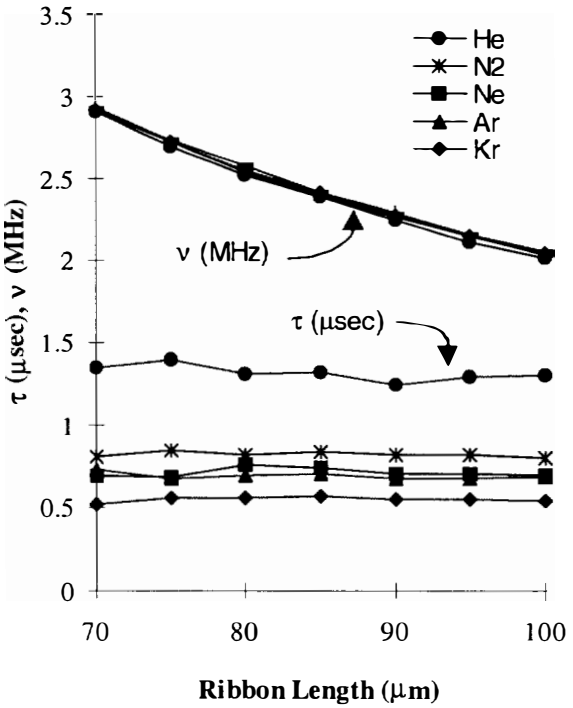

Figure 5. *Values of natural frequency ν and damping time τ extracted from fits of GLV optical response in the undeflected state. Note that the curves for ν fall nearly on top of one another.*

possesses the highest viscosity of the series, Kr provides the most

efficient damping. Thus viscosity alone is insufficient to accurately describe the damping behavior. For the case reported here, where the nominal air gap (650 nm) is comparable in length to the mean free path λ of these gases, rarefaction effects occur, even at atmospheric pressure. Veijola, et al **[4]**. have summarized the various correction factors to gaseous viscosity accounting for rarefaction in the gas. In general these corrections vary with the Knudsen number $K_n = \lambda/y$. For low K_n (<1) the various correction factors generally converge to the expression derived by Burgdorfer **[2]**:

$$\eta_{eff} = \eta/(1 + 6K_n). \quad \textbf{(4)}$$

The effective viscosity values thus calculated are also given in Table 1, where y is assumed to be 650 nm and λ is calculated using

$$\lambda = \frac{1}{\sqrt{2}\pi d_o^2 n}, \quad \textbf{(5)}$$

a result of the simple kinetic theory of gases **[5]**.

If it is now assumed that τ is inversely proportional to η_{eff}, this simple correction factor can easily be tested. Fig. 5 shows a plot of τ vs. $(\eta_{eff})^{-1}$ for the five noble gases at 1 atm. Additionally, this plot includes data for N_2 damping at 0.5 and 1.5 atm pressure. The R^2 correlation value for a straight line of 0.995 indicates the effectiveness of this correction factor.

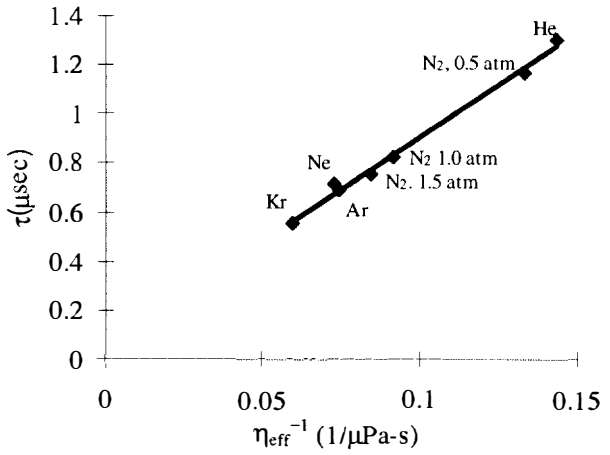

Figure 6. *Damping time vs. the effective viscosity of the damping atmosphere at 1 atm pressure (unless otherwise noted).*

Further testing of this model can be made by again assuming $\tau = k/\eta_{eff}$ and rearrangement Eq. 4, yielding

$$\tau\eta = k + (6k\lambda/y). \quad \textbf{(6)}$$

A plot of $\tau\eta$ vs. λ then gives a line with slope of 6k/y and intercept k. Note that y in this case is the nominal air gap y_o, yielding y_o = 624 nm. This is in very good agreement with the process target of 650 nm.

Table 1. *Summary of viscosity, mean free path (nm), effective viscosity, and damping time at 20°C for the gas atmospheres used in this study.*

Gas	*Viscosity[a] (μPa-s)*	*Mean free path[b] (nm)*	*Effective Viscosity (μPa-s)*	*τ (μsec)*
He	19.41	194	6.96	1.3
Ne	31.11	138	13.73	0.71
N_2	17.49	67	10.91	0.82
Ar	22.17	70	13.51	0.69
Kr	25.04	53	16.80	0.55
N_2 (0.5 atm)	17.49	134	7.51	1.16
N_2 (1.5 atm)	17.49	44	11.82	0.75

a) Ref. 6.
b) From Eq. (5).

CONCLUSIONS

A simple slip flow model that accurately describes the squeeze film damping of doubly supported MEMS ribbons when actuated by an electrical impulse has been demonstrated. The viscosity of five different gases was shown to be correctable for rarefaction effects in the damping gas by a scaling factor that depends only on the Knudsen number of the gas in the air gap under the ribbon.

REFERENCES

1. R. Apte, F. Sandejas, W. Banyai, and D. Bloom, "Grating Light Valves for High Resolution Displays," Solid State Sensors and Actuators Workshop, June 1994. D. Bloom, "The Grating Light Valve: Revolutionizing Display Technology," Projection Displays III Symposium, SPIE Proceedings Volume 3013, February 1997.

2. A. Burgdorfer, "The Influence of the Molecular Mean Free Path on the Performance of Hydrodynamic Gas Lubricated Bearings," J. Basic Eng., ASME, 81 (1959) 94-99.

3. W. H Press, B. P. Flannery, S. A. Teukolsky, and W. T. Vetterling, *Numerical Recipes in C*, Cambridge Press, Cambridge, 1988.

4. T. Veijola, H. Kuisma, J. Lahdenpera, and T. Ryhanen, "Equivalent-circuit Model of the Squeezed Gas Film in a Silicon Accelerometer," Sensors and Actuators A, 48 (1995) 239-248.

5. J. F. O'Hanlon, *A User's Guide to Vacuum Technology*, John Wiley and Sons, New York, 1980.

6. *Handbook of Chemistry and Physics*, 51st edition. Ed. Robert C. Weast, TheChemical Rubber Company, Cleveland, OH (1971)

TUNABLE CAPACITORS WITH PROGRAMMABLE CAPACITANCE-VOLTAGE CHARACTERISTIC

Elmer S. Hung and Stephen D. Senturia
Massachusetts Institute of Technology
Cambridge, MA 02139

ABSTRACT

We report the design and fabrication of a micromechanical tunable capacitance device with a lithographically-programmable capacitance-voltage (C-V) characteristic. Device prototypes utilizing a contact "zipping" actuator achieve a 25% tuning range with a linear C-V characteristic. Three significant results are described: (1) realization of a device with a large capacitive tuning range and programmable C-V device characteristics, (2) development of a stable zipping actuator using flat structures, and (3) development of an automated meshed simulation/optimization technique used to design the device.

INTRODUCTION

Recent growth in the wireless communications industry has spawned tremendous interest in the development of highly-integrated transceiver solutions. Microelectromechanical (MEMS) tuning elements have received increasing attention for integrating off-chip components in order to reduce the fabrication cost, size, and complexity and increase the power efficiency of wireless devices.

For example, voltage-controlled oscillators (VCOs) traditionally require an off-chip LC tank using a tunable capacitor (a varactor) for frequency tuning. Fabricating the LC tank on chip requires the development of low-loss monolithic inductors and varactors in order to meet phase noise requirements. VCOs have been constructed by Young and Boser [1,2] using micromechanical varactors consisting of an electrostatically-actuated aluminum plate suspended over a fixed bottom plate fabricated in a CMOS-compatible process. The two plates are not allowed to contact each other, so the tuning range is limited to the top 1/3 of the gap, due to the electrostatic pull-in instability.

Other variable capacitance MEMS devices for RF systems include RF switches [3–5] for use in phase shifters and steerable antenna arrays. Although these switches are not designed for analog capacitance tuning, large on/off capacitance changes can be obtained by electrostatically pulling down one conductive diaphragm electrode onto a thin insulating layer deposited on top of the second electrode of a two-plate capacitor [5].

In this paper, we report the design and fabrication of analog-tuned micromechanical varactors based on a contact electrostatic "zipper" actuator. Zipper actuators are attractive for varactor applications for several reasons.

First, like MEMS RF switches, a large ratio of available gap sizes is used to obtain increased capacitive tuning ranges and large capacitances per unit area. However, unlike previous RF switches or analog-tuned varactors, the zipper varactors are designed to always operate in a contact "zipping" mode, providing analog capacitance tuning without significant limitations from electrostatic pull-in instabilities.

In addition, the specific capacitance-voltage (C-V) characteristic of the device can be tailored by lithographically programming the geometry of an electrode. The specific geometry that is necessary to achieve a desired C-V characteristic is determined by an optimization requiring meshed simulations of a coupled electromechanical problem involving contact mechanics.

DEVICE DESCRIPTION

The zipping actuator varactor (Fig. 1) consists of a conductive cantilever beam over a shaped bottom electrode. The capacitance between the beam and the bottom electrode is controlled by an applied DC voltage, and the C-V characteristic of the device is determined by the geometry of the bottom electrode.

When an increasing voltage is applied between the beam and the bottom electrode, the beam first bends downward, then collapses toward the substrate due to the electrostatic pull-in effect. Dimples in the cantilever hold the beam a small distance off the bottom electrode. At first, only the beam tip contacts the substrate, but as additional voltage is applied, the tip flattens and the beam "zips" along the substrate toward the cantilever support, increasing the area of the beam close to the bottom electrode, thus changing the device capacitance (see Fig. 2).

The device is designed to operate in the "zipping" regime (Fig. 2(c)) with the actuator in contact with the substrate. Electrostatic zipper actuators are attractive for a variety of applications because they provide large, stable displacements. Actuation force can be comparatively small due to small gaps and the zipping action of electrodes that are curved during operation. Previous efforts to fabricate zippers relied on the fabrication of curved electrodes [6–8]. Gilbert and Senturia [9] proposed a zipper actuator for use in torsional mirrors involving flat electrodes separated by a dielectric; however, no devices were fabricated.

As in previous work on zippers [6–9], the first versions of the varactors were fabricated using a dielectric to isolate the two electrodes. However, hysteresis was observed in these devices, which we attribute to trapped charge on the surfaces of the dielectric. In order to eliminate this effect, the dielectric between the electrodes was removed and replaced by an air gap defined by dimple spacers. The dimples also help reduce any other adhesion effects due to surface contact. In addition, the cantilever and substrate are DC grounds, minimizing the potential difference across the dielectric between the beam and the substrate. The device is actuated by applying a DC bias to the bottom electrode.

Prototype devices were fabricated using the MUMPs process from MCNC [10]. With the MUMPs process,

0-9640024-2-6/hh1998/$20©1998TRF
DOI 10.31438/trf.hh1998.67

Solid-State Sensors, Actuators, and Microsystems Workshop
Hilton Head Island, South Carolina, June 8-11, 1998

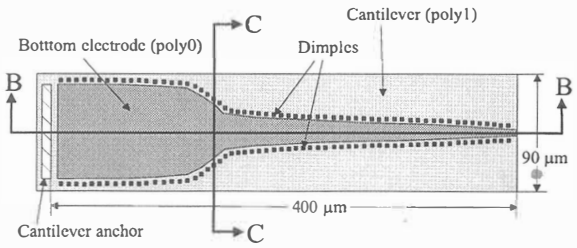

(a) Top View

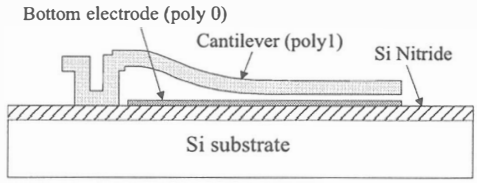

(b) Cross-section B (under actuation)

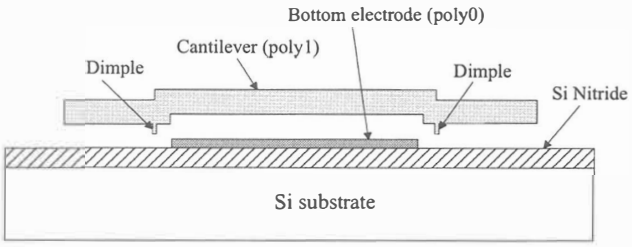

(c) Cross-section C

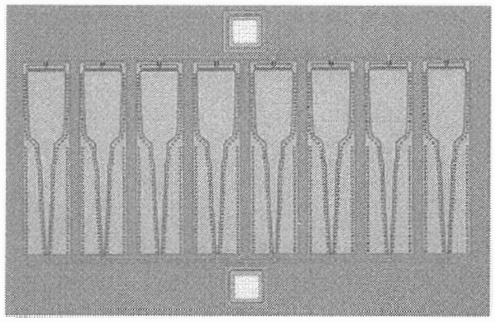

(d)

Figure 1. *Tunable capacitance device. (a) Top view showing a shaped bottom electrode underneath a rectangular cantilever beam. (b) Lengthwise cross-section of beam under actuation in the zipping regime. The air gap under the end of the beam is defined by dimple spacers. (c) Width cross-section showing the dimple spacers. (d) Photograph of device.*

the cantilever and bottom electrode are both polysilicon. The nominal beam thickness and gap size are $2\,\mu m$ and the dimple depth is $0.75\,\mu m$. The MUMPs process is not optimal for varactor fabrication. The default thickness values and dimple depth severely limits the design space. Also, metalized structures will ultimately be necessary to minimize resistive losses for many RF applications. However, MUMPs was chosen for prototyping convenience in order to test the basic actuation principle and verify the capacitance-voltage characteristics of the varactors.

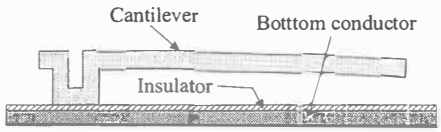

(a) Cantilever bending (before pull-in)

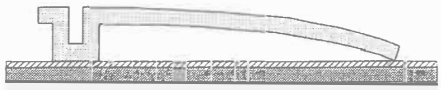

(b) Cantilever tip pull-in

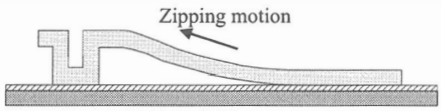

(c) Zipping regime

Figure 2. *Zipper actuator operation with increasing voltage applied between the cantilever and bottom conductor. (a) At first, the beam bends stably. (b) The beam suddenly crashes to the substrate, supported by the beam tip. (c) The tip flattens and the beam "zips" along in contact with the substrate. In the varactors, the insulating layer is replaced by an air gap defined by dimple spacers in order to reduce hysteretic effects of dielectric charging and stiction.*

SIMULATION

Because of the computational demands of optimization, it is important to be able to simulate the device quickly as well as accurately. The deflection of the cantilever is modeled by an elastic beam equation with electrostatic force and a contact force when the beam touches the substrate:

$$EI\frac{\partial^4 z}{\partial x^4} = F_{elec} + F_{bot} \tag{1}$$

where $z(x)$ is the height of the lower beam above the bottom electrode, x is the distance along the length of the beam, E is the elastic modulus of polysilicon, $I = wh^3/12$ is the moment of inertia of the beam, w is the width of the beam, h is the thickness of the beam, F_{bot} is the force exerted on the beam by the substrate once the beam touches down, and F_{elec} is the electrostatic force per unit length. If fringing fields are neglected we can approximate:

$$F_{elec} = -\frac{\epsilon_0 w(x) V^2}{2z^2} \tag{2}$$

where $w(x)$ represents the shape of the bottom electrode and V is the applied voltage. The cantilever support is assumed to have perfectly clamped boundary conditions. Eq. (1) is simulated using finite differences. Full $3D$ simulations [11] would produce greater accuracy, but the computation time would be prohibitive, since hundreds or thousands of beam deflection profiles must be computed for each design.

The contact condition (F_{bot}) adds significant complexity to the simulation. It requires solving both for the contact area and force simultaneously with the beam equation. This is accomplished by using a time-based relaxation technique. A hard contact condition is assumed

constraining $z(x) \geq d$ for all x where d is the dimple depth. No sliding is allowed. Note that an air gap remains between the beam and bottom electrode when the dimples are in contact, so there is some unmodeled deflection of the beam along the width of the beam. Varactors must be designed so that the deflection along the width does not cause the beam to contact the bottom electrode.

The C-V characteristic of the device is computed by simulating the deflection profile of the beam at several different voltages and calculating the capacitance at each voltage according to the parallel-plate formula (i.e., neglecting fringing):

$$C(V) = \int \frac{\epsilon_0 w(x)}{z(x,V)} dx.$$

OPTIMIZATION

Previous efforts to automate the design of micromechanical devices have focused on the optimization of a few parameters of lumped-element models [12]. Electrode shaping and optimization techniques for comb drives have also recently been reported [13].

The design of the varactor requires meshed simulation and optimization of the continuous shape of an electrode. For the varactor, it would be quite difficult to design the device without the use of a significant simulation and optimization effort, since the resulting electrode shapes are not trivial.

The inputs to the optimization routine consist of geometric specifications including the length L and width W of the cantilever device as well as the optimization merit function to use. The merit function $M : E \rightarrow \mathrm{R}$ takes a bottom electrode geometry representation, $e \in E$, and returns a scalar evaluation of how good the design is, where E is the space representing possible bottom electrode widths $w(x)$. In defining the merit function, there is a choice in how to represent electrode geometry. For example, $w(x)$ could be represented by a parameterized family of functions [13], or a discretized approximation. In addition, one can also choose the range of operating voltages that should be targeted for device operation.

For example, for the first prototype varactors, we attempt to design devices with a linear C-V characteristic while maximizing the capacitive tuning range. Electrode geometry $e \in E = \mathrm{R^N}$ is represented by a simple N-point discretization of the width function $w(x)$. A specific voltage range is input as the target voltage range for linear C-V behavior. This voltage range is chosen so that it is possible for the device to reach the zipping regime with the given geometrical constraints.

The merit function for this design is computed as follows: First, a C-V curve is sampled in the target voltage range $V \in [V_1, V_2]$ using the given electrode geometry, e. A linear regression is then performed to approximate the capacitance as $C = a + bV$ in this voltage range, where a and b are fitting constants. Let $\Delta V = |V_2 - V_1|$. We then set M to be the product of three factors:

$$M = p\,(\frac{b\Delta V}{a + bV_1})\,(\frac{(b\Delta V)^2}{\chi^2}) \qquad (3)$$

where χ^2 is the least squares regression residual, and p is a penalty factor which incorporates design rule constraints and verifies that the device is in the zipping regime. Note that the second factor in Eq. (3) is a measure of the capacitive tuning range, while the third factor is a measure of how closely the C-V curve approximates a straight line. Clearly, this is not the only choice, and one can use different functions to emphasize different characteristics.

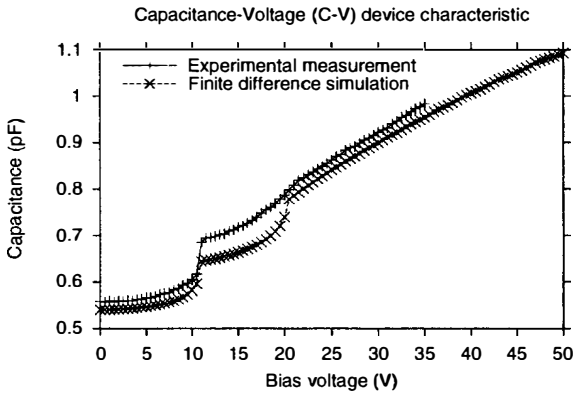

Figure 3. *Comparison of measured and simulated C-V characteristic for a MUMPs device with 8 cantilevers in parallel. Jumps in each curve around* $10V$ *and* $20V$ *demark transitions between pull-in regimes (Fig. 2). The discrepancy in the data between* $10V$ *and* $20V$ *may be due to unmodeled slippage of the cantilever tip. Model and measurement agree well in the linear zipping regime (20-35V) in which the device is designed to operate.*

Since the merit function, M, is quite complicated, it is difficult to compute the gradient of M. Thus gradient-based optimization routines are not used. Instead a downhill-simplex [14] optimization routine is used to minimize $1/M$.

RESULTS

The C-V characteristics of prototype MUMPs varactors were measured using an HP4192A. Fig. 3 shows a comparison of measured and simulated C-V characteristics for a device with 8 cantilevers in parallel (Fig. 1(d)). The cantilevers are $400\,\mu m$ long and $90\,\mu m$ wide. The device is optimized to obtain a linear C-V characteristic in the zipping regime voltage range, 20-35V.

The simulation uses film thickness data measured using a WYKO interferometer. Experimental data is only available up to $35V$ due to test setup limitations. Jumps in each curve around $10V$ and $20V$ demark transitions between the regimes depicted in Fig. 2. Initial beam pull-in occurs around $10V$. From $10V$ to $20V$, only the tip of the beam contacts the substrate. Above $20V$, the device is in the zipping regime. The discrepancy in the data between $10V$ and $20V$ may be due to unmodeled slippage of the cantilever tip in the real device. The measured C-V characteristic is quite linear in the zipping regime (20-35V) and agrees well with simulation in this voltage range. The offset between the measured and simulated C-V characteristic may be due to unmodeled fringing fields and parasitics.

Since experimental data from MUMPs devices verify basic actuator function and modeling accuracy, it is interesting to explore simulated varactor designs with

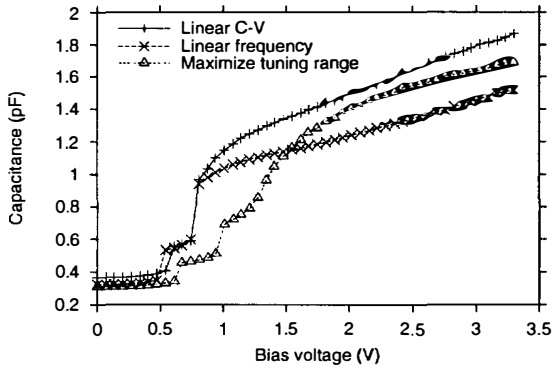

(a)

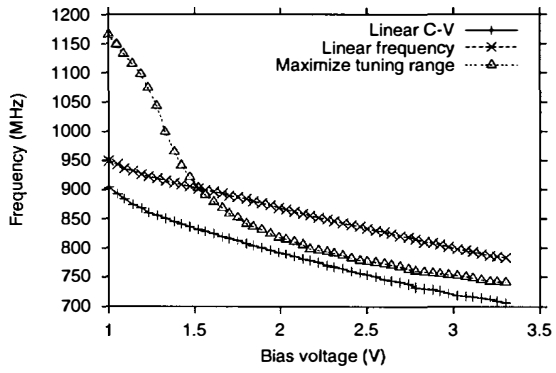

(b)

Figure 4. *Simulation of aluminum varactor with 8 parallel cantilevers (0.5 μm thickness, 0.25 μm dimple). (a) C-V characteristic. (b) Frequency, $\frac{1}{2\pi\sqrt{LC}}$, with $L = 20.4nH$. The three different curves represent optimizations for linear C-V, linear frequency dependence on V, and maximal tuning range. The operational voltage range is* 1-3.3V.

high conductivity material and different geometric constraints. There are two geometric parameters to consider, the cantilever thickness and the dimple depth. The cantilever thickness controls the actuation voltage and the dimple depth controls the capacitive tuning range.

Consider an aluminum varactor similar to the baseline MUMPs design except with a 0.5 μm beam thickness, 0.25 μm dimple depth, and 70 μm beam width (width is reduced to prevent electrode contact due to deflection across the width of the beam). We optimize for three different objectives using actuation voltages (1.0-3.3V) consistent with CMOS: (1) linear C-V characteristic, (2) linear $1/\sqrt{C(V)}$, for linear frequency tuning of an LC tank, and (3) maximum tuning range.

The results are depicted in Fig. 4. The simulations show that it should be possible to actuate varactors with 3.3 V while optimizing for the three different objectives. Note that an analog tuning range greater than 150% (2.5:1 ratio) can be achieved if one allows a highly nonlinear C-V characteristic.

CONCLUSIONS

This paper reports results in three areas. First, successful development and fabrication of a stable zipping actuator is reported using flat structures. Second, this actuator is used to implement a tunable capacitance with a programmable C-V characteristic determined by the geometry of a shaped electrode. Third, the automated meshed simulation, optimization, and layout procedure used to design the electrode geometry shape is implemented and verified with experimental data.

Prototype devices were fabricated using the MUMPs process from MCNC. A numerical study shows that this approach can be applied to metalized structures, as will be required for integrated RF applications.

ACKNOWLEDGMENTS

Support for this research was provided by the Defense Advanced Research Project Agency under contract N66001-97-C-8620. The authors wish to thank Darrin Young, Vladimir Rabinovich, and John Gilbert for many useful discussions.

REFERENCES

[1] D. J. Young and B. E. Boser, "A micromachined variable capacitor for monolithic low-noise VCOS," *Proc. Solid State Sensor and Actuator Workshop,* Hilton Head, SC, 1996, pp. 86-89.

[2] D. J. Young and B. E. Boser, "A micromachined-based RF low-noise voltage-controlled oscillator," *IEEE Custom Integrated Circuits Conference*, 1997, pp. 431-434.

[3] L. E. Larson, R. H. Hackett, and R. F. Lohr, "Microactuators for GaAs-based microwave integrated circuits," *Transducers '91*, pp. 743-746.

[4] J. J. Yao and F. M. Chang, "A surface micromachined miniature switch for telecommunications applications with signal frequencies from DC up to 4 GHz," *Transducers '95*, pp. 384-387.

[5] J. N. Randall, C. Goldsmith, D. Denniston, and T.-H. Lin, "Fabrication of micromechanical switches for routing radio frequency signals," *J. Vac. Sci. Technol. B*, **14** 6, 1996, pp. 3692-3696.

[6] K. Sato and M. Shikida, "Electrostatic film actuator with a large vertical displacement," *Proc. MEMS 1992*, pp. 1-5.

[7] J. Branebjerg and P. Gravesen, "A new electrostatic actuator providing improved stroke length and force," *Proc. MEMS 1992*, pp. 6-11.

[8] R. Legtenberg, E. Berenschot, M. Elwenspoek, and J. Fluitman, "Electrostatic curved electrode actuators," *Proc. MEMS 1995*, pp. 37-42.

[9] J. R. Gilbert and S. D. Senturia, "Two phase actuators: stable zipping devices without fabrication of curved structures," *Proc. Solid State Sensor and Actuator Workshop,* Hilton Head, SC, 1996, pp. 98-100.

[10] D. A. Koester, R. Mahadevan, and K. W. Markus, *MUMPs Introduction and Design Rules*, MCNC MEMS Technology Applications Center, 1994.

[11] J. R. Gilbert, G. K. Ananthasuresh, and S. D. Senturia, "3D modeling of contact problems and hysteresis in coupled electro-mechanics," *Proc. MEMS 1996*, pp. 127-132.

[12] G. K. Fedder, S. Iyer, and T. Mukherjee, "Automated optimal synthesis of microresonators," *Transducers '97*, pp. 1109-1112.

[13] W. Ye, S. Mukherjee, and N. C. MacDonald, "Optimal shape design of an electrostatic comb drive in microelectromechanical systems," *J. Microelectromech. Syst.*, **7** 1, March 1998, pp. 16-26.

[14] W. H. Press, et al., *Numerical Recipes in C: The Art of Scientific Computing*, 2nd edition, Cambridge UP, 1992.

HIGH RELIABILITY TOUCH-MODE ELECTROSTATIC ACTUATORS (TMEA)

C. Cabuz, E. I. Cabuz, T. R. Ohnstein, J. Neus
Honeywell Inc., Honeywell Technology Center
12001 State Hwy. 55
Plymouth, Minnesota 55441-4799

R. Maboudian
Department of Chemical Engineering
University of California
Berkeley, California 94720

ABSTRACT

This paper discusses the failure modes frequently encountered in TMEA and reports on practical ways of increasing the time to failure. Humidity is identified as the main source of anomalies in the behavior of TMEA and charge trapping in the dielectric as the main cause of stiction. A method for direct charge measurement is derived and the measurements show good agreement with the calculated data. A new driving scheme is proposed that together with surface treatments desensitizes the actuator to environmental conditions. Actuators working without failure for over 40 millions cycles are reported.

INTRODUCTION

Electrostatic actuation is an efficient actuation method in terms of power consumption and structural complexity, being probably the only one that can be used to build large 3D arrays of actuators. In electrostatic actuators, the displacement is induced by the attractive force between a distribution of opposite sign charges placed on two electrodes. The electrodes are embedded in the constituent parts of the actuator (hereinafter called plates) of which at least one is movable. The charge is generated by a power supply connected to the electrodes. The actuators can be designed such as to allow or to prevent the direct contact of the plates.

In non-touch electrostatic actuators such as the comb drives[**1**], the plates are not coming in contact with each other during normal operation. These actuators are made out of conductive materials and can be regarded as single capacitors with spring loaded plates and a variable air gap. They can work reliably in a wide range of environmental conditions and for indefinitely long periods of time. However, the forces/pressures generated by such actuators are very small (fractions of an atmosphere), limiting their use.

In the touch-mode electrostatic actuators (TMEA), the two plates are allowed to come in touch. A thin (few thousands angstroms) insulating layer covers one or both electrodes to prevent current flow during the touch phase of the actuation cycle. In such actuators electrostatic pressures above ten atmospheres can be generated and held with relatively low voltages (<100V) and with very low power (μW).

A particular type of TMEA is the rolling-contact actuator (Fig.1, [**2**]). In these actuators the plates are configured to create a variable gap: extremely narrow (close to zero) at one location (hinge) and very large (hundreds of microns) at another location (tip). Such actuators offer a unique solution to the conflicting relation displacement/driving voltage, allowing large forces and large displacements to be obtained with the same actuator.

The force/displacement benefits of TMEA are penalized by the practical problems associated with the ill-defined state of the dielectric surfaces and with the contacting surfaces. The literature records numerous reports of erratic behavior and failures of such actuators [**3-5**].

This paper will provide a brief overview of the failure modes frequently encountered in TMEA, will identify the causes behind the failures and will offer practical solutions for high reliability touch-mode electrostatic actuators.

FAILURE MODES IN TMEA

Figure 1 shows the schematic structure of the rolling-contact TMEA used in our experiment. Listed below are the observed operational anomalies and failures:

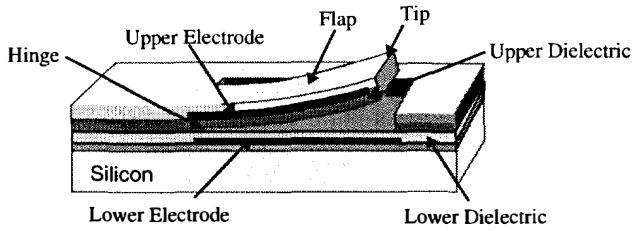

***Figure 1**. Schematic structure of the rolling-contact TMEA used as test device .*

a) The DC voltage required to produce the actuation is significantly higher than the theoretical value;

b) The generated electrostatic pressure in the closed state is much lower than predicted;

c) The actuator closes and opens as expected at the first applied DC pulse; it does not close at the second pulse unless a higher voltage is applied; the voltage required to close increases with every cycle and eventually breakdown occurs;

d) Under a stable DC voltage the actuator closes and then opens; in some cases it starts to vibrate between short closed and open states;

e) The hysteresis associated with the non-linearity of the electrostatic force is reversed (the voltage to open is higher than the voltage to close) ;

f) The actuator remains closed for many seconds after applying 0V; it opens immediately if the original DC voltage is slightly reduced;

g) When kept closed under high electric field (>2MV/cm), permanent stiction occurs;

h) After a certain number of actuation cycles (>x10^6 cycles), permanent stiction occurs;

It is obvious that the field responsible for the actuation is not related to the driving voltage through the simple formula ***E=V/d.***

THEORETICAL CONSIDERATIONS

Most of the anomalies and failure modes observed in the rolling contact actuator are related to the closed state. In this state the actuator has the structure of a parallel plate capacitor. The force between the actuator plates can be written as:

$$F_{el} = \underset{\text{(i)}}{\frac{Q^2}{2A\varepsilon}} = \underset{\text{(ii)}}{\frac{QE}{2}} = \underset{\text{(iii)}}{\frac{\varepsilon A E^2}{2}} = \underset{\text{(iv)}}{\frac{\varepsilon A V^2}{2d^2}} \qquad (1)$$

0-9640024-2-6/hh1998/$20©1998TRF
DOI 10.31438/trf.hh1998.68

where $|Q|$ is the total charge on each actuator plate, E is the field between the two plates, A the area of each plate, V is the voltage applied to the electrodes, ε_d is the dielectric constant of the dielectric covering the electrodes and d the total thickness of the dielectric layers (the dielectric layers on the two electrodes are supposed identical).

The formula connecting the force to the driving voltage (iv) is the most used but also the most misleading. It holds true only when between the electrodes there is a uniform dielectric. In the real structures, the surface of the dielectric represent a discontinuity that can affect the charge distribution, the field at the interface and the voltage to be used in (iv). The discontinuity can be in the resistivity of the surface layer, in its dielectric constant or can be associated with the surface roughness.

A solid dielectric is a complex material, being characterized by a large number of parameters. The most important ones are: the dielectric constant (ε_d); the dielectric strength (E_{max}); the bulk resistivity (ρ); the surface resistivity (ρ_s); the fixed charge (Q_f); the density and properties of interface traps (D_{it}); the density and properties of bulk traps (D_B); the chemical stability of the surface (water affinity); the mechanical properties of the surface (roughness). All these parameters have a strong dependence on the deposition method. Some of them (ρ_s, E_{max}) depend on the environmental conditions, while others (the charge injected and trapped in the bulk and surface traps) depend on the applied electric field, the number of actuation cycles, the geometry and the material properties of the electrodes.

During this study we tried to understand whether the observed anomalies are associated with a particular dielectric or are general to this type of actuators. Special attention was paid to the effect of the environmental conditions (mainly humidity) and the driving voltage on the reliability of the actuation process.

TEST STRUCTURES

In a previous study, the high frequency C-V characteristics of the thermal and PECVD silicon oxides and of the sputtered, LPCVD and PECVD silicon nitrides were compared using as test vehicles silicon-insulator-metal capacitors [7]. Except for the thermal oxide, the characteristics were indicative of significant amounts of fixed charge as well as charge injection and retention in the dielectrics. The measured dielectric strength for the thermal oxide and the LPCVD nitride was of about 5MV/cm while for the other dielectrics was of about 2.5 MV/cm. The dielectric constant of the oxides was close to 4 while for the nitrides it ranged between 7 in the LPCVD nitride to 12 in some types of sputtered nitride. In TMEA, the quantity $\varepsilon_d E_{max}^2/2$ is very important as it gives the maximum electrostatic pressure that can be obtained with a certain dielectric. Materials with high dielectric constants and high dielectric strength are highly desirable.

Rolling-contact actuators with different configurations of the electrode/dielectric stack were fabricated and tested (Fig.1, Table 1). The fabricated flaps were 400μm long by 360μm wide and about 1μm thick. The devices were designed to have similar spring constants. Each actuator device consisted of an array of 5x5 flaps working in parallel.

Fabrication Process

In the structures type #1 and type #2, a thin dielectric layer was used to isolate the lower metal electrodes from the silicon wafer. In structure #1, 1000Å of sputtered nitride was deposited to form the lower dielectric; 500Å of Al was used as the sacrificial layer; 1000Å (type #1) and 2000Å (type#2) sputtered nitride were deposited as the upper dielectric, followed by a chromium upper electrode and about 0.9 μ of sputtered nitride as the flap body. The upward bending of the flaps was controlled through the stress in the layers. Contacts were opened to both electrodes by dry etching. Cr/Au was deposited and patterned to define the contact pads. The lateral definition of the flaps was done by dry etching the nitrides down to the sacrificial layer. The sacrificial aluminum was etched in KOH and the flaps released. After the final rinse the wafers were dried by using the freeze—drying technique [6].

Structures #4 started with <100> silicon wafers followed by 500Å thermal oxide, blanket implant and anneal, 2000Å LPCVD nitride, deposition and patterning of 500Å Al sacrificial layer, deposition and patterning of 500Å Cr for the upper electrode, deposition of 1μm sputtered nitride, continued to completion as for structures #1 and #2.

Table 1

Structure Type	Lower Dielectric		Upper Dielectric		Electrodes	
	type	d_1 [Å]	type	d_2 [Å]	#1	#2
#1	Si_3N_4 Sputtered	1000	Si_3N_4 Sputtered	1000	Cr	Cr
#2	No Dielectric		Si_3N_4 Sputtered	2000	Cr	Cr
#3	SiO_2 Thermal	1000	SiO_2 Thermal	1000	Si*	Cr
#4	Si_3N_4 LPCVD	2000	No Dielectric		Si*	Cr

*Highly doped

For structure #3 polysilicon was used as a sacrificial layer and oxidized polysilicon was used as the upper dielectric.

EXPERIMENTAL RESULTS

The effects of the dielectric material, of the environmental humidity, the type of driving voltage (DC vs. AC), the type of hydrophobic coating and the magnitude of the electric field on the operation of the test structures were studied. A method for the measurement of the accumulated charge in TMEA was developed and measurements were performed. Long term cycling was performed on different type of devices.

Humidity Effect

Measurements were performed on all the fabricated structures at relative humidity ranging from zero (nitrogen dry box) to 95% and for DC and AC driving voltages.

DC Driving. When driving the actuators with DC voltages at humidity levels above 35%, the effects (a-e) were observed in *all types* of test structures. Humidity proved to be the most important cause of anomalies and failure, much more important than the charging characteristics of the dielectric. When environmental humidity is reduced below 30% or the samples are heated at around 90°C, the effects (a-e) are very much reduced or completely eliminated.

On the other side, when the devices are operated in dry air or nitrogen and driven with DC voltages, the effects (f-h) appear. It was observed that the time scale of the experiments (duration of the closed cycle) and the magnitude of the driving field were strongly related to the time to open and with the occurrence of stiction.

AC Driving. By using a square wave, AC driving voltage with a frequency of a few hundred Hertz, the actuator could be operated (controllably closed and opened) at higher humidity levels (up to 55%). However, the generated electrostatic pressure was significantly reduced by increasing the humidity. At higher humidity levels the actuator could not be maintained in the closed position.

When the AC driving is used in dry air or nitrogen, the effects (f-h) are significantly reduced. The actuator opens promptly when the actuation voltage is brought to zero and it can be kept closed for long periods of time without inducing stiction. It was concluded that AC driving is effective in fighting the RC effects but it cannot fully overcome humidity effects. For reliable operation, the hydration of the dielectric surface has to be eliminated.

The above observation helped us in developing a refined electro-mechanical model of the TMEA which, except for the permanent stiction, is able to explain all the other experimental observations [**11**].

The Hydrophobic Coatings

All the silicon based dielectrics (nitrides and oxides) have on the exposed surfaces a thin native oxide which is highly hydrophilic (work of adhesion 20mJ/m^2, [**8,9**]) . Such surfaces become easily hydrated, with the density of water molecules attached to the surface being strongly dependent on the relative humidity in the environment. In humidity levels above 60%, multiple layers of water are formed on the surface. To completely avoid the formation of hydrated layers on the dielectric surface, hydrophobic self assembled monolayers (SAM) having as precursors the octa-decyl-trichloro-silane (OTS) **[8]** and the per-fluoro-decyl-trichloro-silane (PFTS) [**9**] were used.

The Coating Procedure. Following the final sacrificial etch, the wafers were freeze-dried, tested and evaluated at a wafer level and stored as needed prior to the SAM coating. The coating process started with a thorough cleaning and oxidation using piranha (H_2SO_4:H_2O_2 4:1) at 115° for 1 min. This step was found to be very critical to the quality of the wafer-level coating. The rest of the process was performed essentially as reported in [**9**]. At the end the wafer was pulled vertically from water and let dry in an oven at 100°. Generally the wafer level yield of the coating process was higher than 95%.

The Properties of the Self Assembled Monolayers. The water contact angle measured on the OTS and the PFTS coated samples are of about 112° and 115° respectively [**9**]. The evaluated work of adhesion is 23μJ/m^2 for the OTS and about 2 to 5 μJ/m^2 for the PFTS [**9**]. The thickness of the resulted SAM is about 15 Å for the PFTS and about 28Å for the OTS. The dielectric constant of the layer is supposed to be between 3 and 4, as in other similar organic compounds. The resistivity of the monolayers is important for their application in TMEA but very difficult to evaluate. The simulation of the devices showed that the time constants observed in the DC operation of the actuators are strongly related to the electrical characteristics of the surface layers. From the comparison of the simulated and measured data, an equivalent resistivity of about 10^{15} ohm-cm was estimated for the OTS coated surfaces and of about $2x10^{14}$ohm-cm for the PFTS coated surfaces.

The Effect of Coatings on the Actuation Process. Test devices were coated with OTS (devices type #1) and with PFTS (devices type #1 and #3) and tested in humidity levels ranging from zero to 95%. The OTS coating completely removed the humidity effects, both for DC and AC driving. Fig 3 shows the dependence of the generated electrostatic pressure on the relative humidity for an OTS coated sample and a non-coated sample, both driven with a square wave AC voltage with peak value of 25V and a frequency of 200Hz. In order to evaluate the generated electrostatic pressure, a back-pressure was applied through a hole etched in some of the test devices. The magnitude of the pressure required to open the actuator was used as a direct indication of the generated electrostatic pressure. The OTS coated sample operated properly in humidity levels up to 95% while the non-coated samples stopped generating any useful electrostatic force at humidity levels higher than about 35%. The AC driven PFTS coated devices could work in up to 95% humidity; the DC drive could be used up to about 70% humidity, becoming unreliable afterwards.

Even though the OTS coatings posses a work of adhesion significantly lower than that of the silicon dioxide, the OTS coated devices driven both in the DC and the AC mode showed enhanced in-use stiction as compared to the non-coated devices. We considered that as an indication of the fact that capillarity is not the primary cause for in -use stiction in our actuators. We speculate that the permanent stiction in the OTS coated devices can be caused by enhanced surface charging associated with the higher resistivity of the layer and/or by surface interactions taking place between the hydrophobic layers. On the other side, in the PFTS coated devices driven in the AC mode the stiction was virtually eliminated. Such devices were used for long term testing.

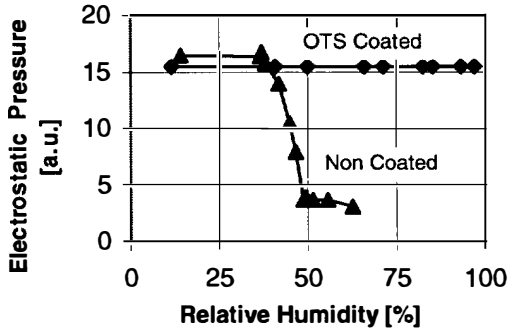

Fig. 3 *The dependence of the generated electrostatic pressure on the relative humidity for coated and non coated TMEA.*

The Charge Measurement Method

Strong experimental evidence supports the idea that in the TMEA the nature of in-use stiction is mainly electrostatic. The charge producing stiction should be mainly accumulated at the interfaces between the dielectric and the coating layer (in interface traps) and/or on the outer surface of the actuator plates, in the areas where surface roughness prevents the intimate contact between the two surfaces. A rough estimation of the charge required to produce stiction is given by the formula:

$$Q = \frac{A_c}{A} V_{\min} \sqrt{\frac{\varepsilon_c}{\varepsilon_d}} C_{ac} + \frac{A_g}{A} V_{\min} \sqrt{\frac{1}{\varepsilon_d}} C_{ac} \qquad (2)$$

where A_c is the contacting area, A_g is the non-contacting area, ε_c is the dielectric constant of the coating (3 to 4), ε_d is the dielectric constant of the insulator (9), C_{ac} is the capacitance of the actuator in the closed state (0.8nF) and V_{min} is the minimum voltage required to hold the actuator in the closed position (5V). From the above equation, the charge required to produce stiction is about 1.4nC, with possible values between 1nC and 2nC for different values of the involved parameters.

To measure the accumulated charge, a Keithley 617 Programmable Electrometer was used in the setup presented in Fig. 4. The measurement method is based on the fact that (i) in the closed state the distance between charges is much smaller than the thickness of the dielectric (about 20 times smaller) allowing the field to close on the accumulated charges and (ii) the thickness of the dielectric is very small, ensuring the induction of an equal charge in the electrode, once the accumulated charges are separated [**10**].

In the first step (Fig. 4, a) both electrodes are grounded, the electrometer being connected in series with the lower electrode.

After the null condition is realized, the top plate of the actuator is removed (Fig. 4,b) by using tape. The charge remaining on the lower plate of the actuator induces an equal and opposite charge on the lower electrode. The electrometer connected in series with the electrode integrates the current and gives the total charge. The measurements were done in dry air.

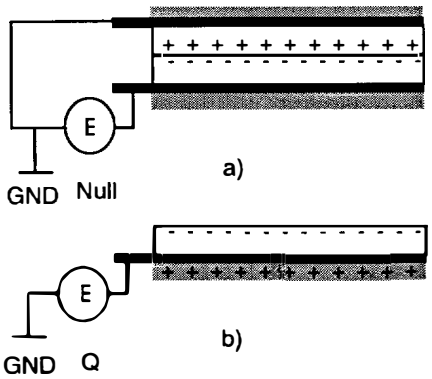

Fig. 4 Experimental setup for the direct evaluation of the accumulated charge in TMEA by using an electrometer E and by mechanically separating the charges [10].

The measurements performed on different structures indicated a *positive charge* between 0.8 and 1.2 nC on the lower plate of the stuck actuators, in good agreement with the estimated values. Measurements were also performed on new devices that did not show stiction and no charge could be measured.

The Long Term Tests

Non-coated devices as well as OTS coated and PFTS coated devices were subjected to long term cycling tests, in nitrogen for non- coated devices and in clean room air with variable humidity (from 14% to about 65%) for coated devices. The frequency of the actuation was between 0.3 and 20Hz. Only AC driving voltages were used. Testing of non-packaged as well as of packaged (but not sealed) devices were performed. The results are given in Table 2.

Table 2

Structure type	Driving Voltage	Env.	Cycles
#1-not coated	+/-16V, triangular	N_2	$1x10^8$
#1-not coated	+/-25V, square wave	N_2	10^6
#1-OTS	+/-30V, square wave	clean air	$2.5x10^5$
#1-PFTS	+/-30V, square wave	clean air	$1.8x10^6$
#1-PFTS	+/-30V, square wave	clean air	$4x10^7$ *

* 8 months test; packaged;

CONCLUSIONS

The relative effects of the dielectric material, the environment, the surface properties and the amplitude and shape of the driving voltage on the operation and life time of a TMEA were examined.

It was determined that charge injection and trapping in the dielectric have little impact on the short term behavior of TMEA when moderate electric fields are used (<2MV/cm). The anomalies in the short term behavior of the TMEA are considered to be produced by the altered electrical properties of the dielectric surface and by the surface roughness. The variations in resistivity and dielectric constant associated with the surface of the dielectric generate charge and voltage redistribution in the stack. All these effects are reduced when AC driving is used.

Humidity, through the hydration of the dielectric surface was identified as the major source of anomalies in the DC and AC operation. For the first time the humidity was clearly associated with the failure to close and hold the actuator in the touch-mode rather than with stiction.

Hydrophobic self assembled monolayer coatings were used in order to control electrical effects in TMEA rather than to prevent stiction. It was found that some hydrophobic coatings can actually enhance the in-use stiction.

We believe that in our actuators the residual in-use stiction is related to permanently trapped charges. A method for charge measurement was devised and the results found in good agreement with the estimations. The exact mechanism of charge injection is not clear and will be further investigated.

By using dielectrics with hydrophobic surfaces and AC driving voltage reliable long term operation could be obtained.

ACKNOWLEDGMENTS

Jim Bustillo, Michael Houston and Uthara Srinivasan from U.C. Berkeley are gratefully acknowledged for assisting with the coating process. We also want to thank Bill Herb and Dave Zook from HTC for their much appreciated contributions with the simulation and the overall understanding of the actuators.

REFERENCES

1. W. A.Clark, R.T.Howe, R.Horowitz, *Proc. of Solid-State Sensor and Actuator Workshop, Hilton Head, SC,* June 2-6, 283, (1996)
2. T. Ohnstein, T.Fukiura, J.Ridley, U.Bonne, *Proc. of IEEE Microelectro Mechanical Systems, Napa Valley, CA, Feb. 11-14,* 95, (1990)
3. A.P.Lee, J.Hamilton, J. Trevino, *DSC-Vol.59, Micro-electromechanical Systems (MEMS) ASME,* 345 (1996)
4. Y-C.Tai, R.S.Muller, *Sensors & Actuators, 20,* 49, (1989);
5. J.K.Robertson, K.D.Wise *Solid-State Sensor and Actuator Workshop, Hilton Head, SC,* June 2-6, 148, (1996)
6. H. Guckel, J.J. Sniegowski, T.R.Christenson, F.Raissi, *Sensors and Actuators A21-23,* 346, (1990)
7. C. Cabuz, *Optical Engineering, 36,* 1298, (1997)
8. M.R.Houston, R. Maboudian, R.T. Howe, *Proc. of IEEE Solid-State Sensor and Actuator Workshop,* Hilton Head '96, Hilton Head Island, SC, 42 (1996)
9. U. Srinivasan, M. R. Houston, R. T. Howe, and R. Maboudian, *Proc. of 1997 International Conference on Solid-State Sensors and Actuators, Transducers'97,* Chicago, IL, 1399-1402 (1997).
10. D. T. Smith, *Journal of Electrostatics, 26,* 291 (1991)
11. C.Cabuz, M. Yoneda, E.Cabuz, *To be published.*

THIN FILM METALLIZATION FOR MICRO-BIMETALLIC ACTUATORS

Jonathan Gorrell
Motorola, 5005 E. McDowel Road, Phoenix, AZ 85008

Paul Holloway and Kenneth Shannon, III
University of Florida, Department of Materials Science and Engineering
Gainesville, FL 32611

ABSTRACT

In this study, eleven different thin film metallization systems were evaluated for use in micro-bimetallic actuators for microelectromechanical structures. These films were evaporated or sputtered onto silicon wafers. The film stress and stress relaxation were determined by measuring changes in the wafer curvature.

Bimetallic actuator may be operated to generate either force or displacement. A figure of merit was developed to aid in the selection for either mode of operation. The displacement mode is dominated by the coefficient of thermal expansion, while the force mode is dependent on both the Young's modulus and the coefficient of thermal expansion of the active layer material. In both modes the maximum displacement or force is limited by the material's yield strength.

Three aluminum alloy thin films were studied. The 5052 aluminum alloy films showed that solid solution strengthening can double the yield strength of a thin film. The T201 aluminum alloy films showed that precipitates can increase yield strength by 2.5 times. The 2090 alloy film oxidized during the first heating and is not of interest for bimetallic actuators..

Nickel, copper, titanium, and manganese films all oxidized on their first heating to 350°C. The copper film also oxidized at 50°C over 48 hours and changed the stress state versus time. Thus oxidation resistance is a significant requirement for materials in thermal actuators.

Al_3Ti intermetallic films were also evaluated and showed no stress relaxation at 450°C, plastically deformed only above 500°C, had limited oxidation up to 800°C and had a room temperature residual stress of 950 MPa, nearly 5 time greater than the Al-Si-Cu alloy film. Thus Al_3Ti is a very promising high temperature bimetallic metallization.

INTRODUCTION

Micro-Bimetallic actuators have been shown to be an effective actuation mechanism for MEMS devices [1,2,3]. They can produce a large force over a large displacement, are easily manufactured, and can potentially operate in severe environments. The performance of a bimetallic actuator is determined, to a large degree, by the mechanical properties of the materials of which they are constructed. The reason for this dependence on the mechanical properties of the materials is that the force or displacement generated in a bimetallic actuator is caused by the interaction of the materials in the device. The principle of actuation using a bimetallic element is shown in Fig. 1 for a cantilevered strip. In this example, the active layer, Al with a high coefficient of thermal expansion (CTE = 25 ppm/°C), is deposited or bonded to the passive layer, Si with a low coefficient of thermal expansion (2.3 ppm/°C). When the temperature of the couple is increased the Al layer expands more than the Si layer, changing the shear stress between these two layers which cases the couple to deflect down. Conversely, for a temperature reduction the Al layer contracts more than the Si layer causing the couple to deflect upwards.

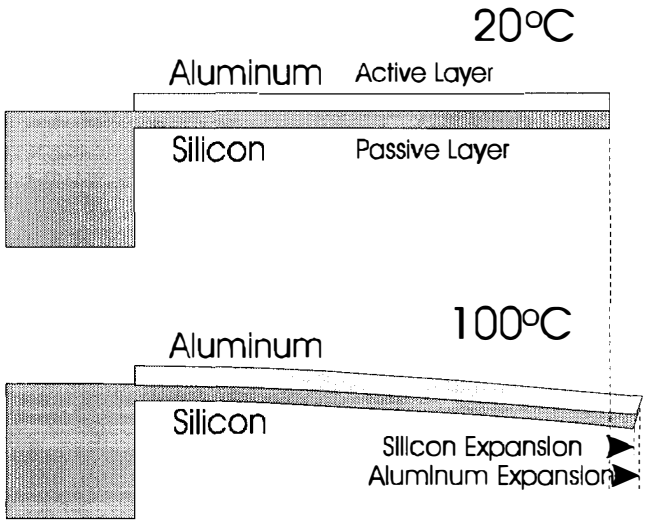

Figure 1. *Diagram of a bimetallic couple showing the curvature at 20°C in the absence of stress and the curvature at 100°C due to the extrinsic stress generated from the differences in the CTEs.*

By examining the equations that describe the performance of a bimetallic actuator, developed by Timoshenko [4], the effects of materials properties can be evaluated. For a bimetallic strip the curvature k, which is equivalent to displacement, is given by:

$$k = \frac{3}{2} \cdot \frac{(\alpha_1 - \alpha_2)}{h} \cdot \Delta T. \quad (1)$$

where ΔT is the change in temperature, α_1 and α_2 are the CTE's of the active and passive layers and h is the thickness of the strip. As can be seen from this equation it is the difference in the thermal expansion of the two layers that determines the curvature for a given temperature change and strip thickness. Given that the passive layer will be silicon for most MEMS bimetallic actuators the active layer material should have the largest CTE possible. For the case of force generation, equation 2 gives the restraining force R needed to stop a bimetallic strip from bending, which is the maximum force generated by the strip where L is the length of the device and E_1 and E_2 are the Young's moduli for the active and passive layers. As can be seen, the restraining force is now proportional to the product of the active layers Young's modulus and CTE. Thus for maximum force a

$$R = \frac{9}{4} \cdot \frac{\left(\frac{E_1 + E_2}{2}\right) \cdot \frac{h^3}{12}}{h \cdot L} \cdot (\alpha_1 - \alpha_2) \cdot \Delta T. \quad (2)$$

0-9640024-2-6/hh1998/$20©1998TRF
DOI 10.31438/trf.hh1998.69

material with a high modulus and CTE is desired for the active layers. It has also been shown by Jerman [5] that these same trends hold for a bimetallic disk.

In both equation it is assumed that the materials behave elastically. Any plastic deformation of either layer would result in a reduction of force and or displacement of and actuator and has been seen in bimetallic actuators of pure aluminum or Al-Si-Cu on silicon [5]. In addition, Draper and Hill [6] have shown that the biaxial stress in bimetallic couples can relax at near room temperature. Thus, while not included in the equation the describe the performance of a bimetallic strip, a materials yield strength determines the operating range of an actuator.

It can be shown that to a first approximation a material's thermal expansion is inversely proportional to its Young's modulus which is in turn proportional to its yield strength [7]. For an actuator design to produce force this does not create a problem as a material with a moderate CTE, high Young's modulus and high yield strength can be selected (ie Nickel, Stainless Steal). However, for an actuator designed for displacement, material selection is more difficult. Materials with high CTE's generally have lower yield strength and are more susceptible to plastic deformation, creep and stress relaxation [8]. Materials with high CTE's (Al, Mg) can be strengthen by a number of techniques [9,10]. However, the effectiveness of these strengthening techniques have not been extensively studied in thin films. Therefore, this studies examines the effectiveness of two bulk strengthening mechanism in thin films.

In addition to the stresses that are generated due to the difference in thermal expansion, called extrinsic stress, stress can also develop during the deposition process, called the intrinsic stress. Intrinsic stress from deposition has been discussed by Thorton and Hoffman [11,12] and Dorner and Nix [13]. These stresses may be varied by changing the conditions of deposition of the thin films [11-13]. For the deposition of high Young's modulus materials the intrinsic stresses must be controlled during the deposition process to limit the stresses between the active and passive layers. Intrinsic stresses in high modulus materials can be high enough to damage MEMS devices. However, for high CTE material such as aluminum the extrinsic stresses tend to dominate over the temperatures that the actuators operate in.

There is also a desire for actuators to work at elevated temperatures and in severe environments. For these requirements a number of other elemental metals and intermetallics were evaluated. Intermetallics constitute a class of material that is a cross between metals and ceramics [14] and may have very high strength and resistant to oxidation at elevated temperature.

EXPERIMENTAL PROCEDURES

Thin films ~ 1 μm thick were deposited onto (100) oriented 4" diameter Si wafers with a 100 nm thermally grown SiO_2 layer on the surface. The wafers were cleaned using the RCA procedure prior to deposition. The samples were loaded into a vacuum system and pumped to less than 3 x 10^{-7} Torr, followed by deposition from an 8" DC planar magnetron source at 5KW in 8 mTorr of Ar with the wafers at 100°C. Films of commercial alloys designated T201, 5052 and 2090 were deposited (see table 1 for chemical composition). The sputter targets were cut from sheet stock. Copper gold intermetallic thin films were sputter deposited by alternating layers of pure gold and copper. The other elemental metals and the Al_3Ti intermetallic were deposited by electron beam evaporation using 99.999% pure material. The Al_3Ti intermetallic thin films were grown by alternating depositions of pure Al and Ti. The electron beam evaporation was performed in a diffusion pumped, liquid nitrogen trapped vacuum system operated at a base pressure of 5 x10^{-7} Torr. During deposition the pressure typically rose to 5 x 10^{-6} Torr and the substrate was heated to 150°C.

The stress and stress relaxation in the bimetallic couples was determined by using a Tencor FleXus model 2320. This instrument uses an optical lever to measure the curvature of the sample before and after deposition of the film and during temperature cycles ranging from -60°C to 500°C. The stress in the film is then calculated using Stoney's equation [18]. Unless otherwise stated, all temperature cycles were performed a 1°C/minute. For the isothermal stress relaxation test, the samples were first taken to 300°C, held at this temperature for 30 minutes, returned to 20°C, then heated to the testing temperature. The samples were held at temperature for 48 hours with measurements being taken every 15 minutes. Environmental stability studies of the metallizations were limited to studies of the oxidation resistance [15].

RESULTS AND DISCUSSION

For a general discussion of the aluminum alloy, and those used in this study, see reference [16]. The Al-Si-Cu alloy was developed for VLSI interconnect metallization [17]. This alloy was designed to reduce "spiking of the aluminum into the silicon" cause by silicon diffusion into the aluminum, and to reduce electromigration. The Al-Si-Cu alloy was not developed for strength in contrast to the other aluminum alloys examined in this study. The 5052 alloy used Mg to solid solution strengthen the alloy. Solid solution strengthening is stable over a wide temperature range and is a homogenous alloy. The T201 alloy is strengthen with Cu to form θ Al_2Cu precipitates that are stabilized to higher temperatures by the addition of the Ag. The Mg and Mn alloying elements provide solid solution strengthen to the T201 alloy. The 2090 alloy is strengthen by the formation of Al_2Li-Cu precipitates. In the commercial alloys, Zr, Ti and Cr are added to stabilize grain structure.

The stress versus temperature plot for pure aluminum and the Al-Si-Cu alloy are shown in figure 2. Of interest in this plot is the linear dependence of stress versus temperature during the heating cycle. When stress is linearly dependent upon temperature, plas-

TABLE 1

Materials tested, deposition thickness and composition/purity

Material	Deposited Thickness μm	Composition or Purity, (wt. %)
T201 Aluminum	1.3	Al - 4.6Cu - 0.57Ag - 0.36Mn - 0.2Mg - 0.27Ti
5052 Aluminum	1.3	Al - 2.5Mg - 0.25Cr
2090 Aluminum	1.3	Al - 2.57Cu - 2.1Li - 0.12Zr
Nickel	0.8	99.98
Titanium	0.55	99.99
Manganese	0.4	99.9
Copper	0.9	99.9
Al_3Ti	0.4	Al-99.99, Ti-99.99
Cu_3Au	1.3	Cu-99.99 Au-99.99
CuAu	1.3	Cu-99.99 Au-99.99
$CuAu_3$	1.3	Cu-99.99 Au-99.99

tic deformation is not occurring and the film could be used in a bimetallic actuator. For pure aluminum, this linear region goes from 150 MPa at room temperature to near -25 MPa (compression) at 125°C. The linear region is only slightly larger for the Al-Si-Cu alloy, going from 200 MPa at room temperature to -25 MPa at 175°C, a 225 MPa region. In contrast figures 3 and 4 show the stress temperature curves for the 5052 alloy and the T201 alloy. Both of these alloys show a much larger linear region with the 5052 alloy being linear from 300 MPa at room temperature to near -25 MPa at 225 °C, and the T201 alloy going from 400MPa to -50MPa. The 5052 and T201 alloys would increase the operation range of a bimetallic actuator as compare with pure aluminum and Al-Si-Cu alloy. The 2090 alloy oxidized on the first temperature cycle and is therefore not useful for thermal actuation.

In addition to plastic deformation, stress relaxation is also a concern for thermal actuation. Figure 5 show the isothermal stress relaxation cure for a T201 alloy film at 100°C over 48 hours. These data were collected for the T201 and 5052 alloy films at 50, 75, 100, 125 and150 °C, and for the pure aluminum and Al-Si-Cu films at 50°C. These data showed that the percentage of the total stress which relaxed in T201 and 5052 alloy films was much less than that for the pure aluminum and Al-Si-Cu alloy [7]. In addition, the room temperature stress in the 5052 alloy could be reduced to 125 MPa by cooling a sample to -196°C [19]. At this lower stress the films showed no isothermal stress relaxation. However, if the film was heated again to 350°C the residual stresses returned to the same value as before cooling with liquid nitrogen. This cooling procedure has been shown

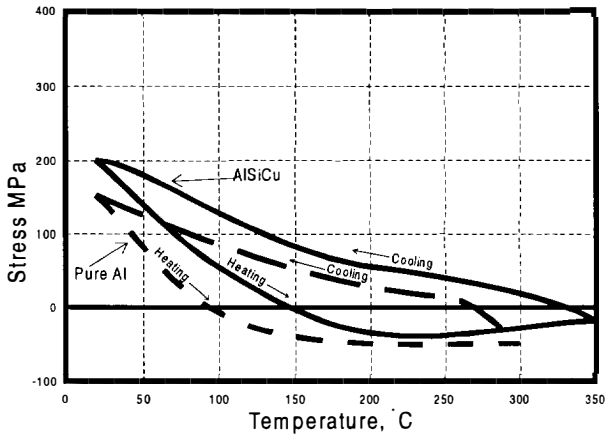

Figure 2. *Stress temperature plot for pure aluminum and Al-Si-Cu alloy films.*

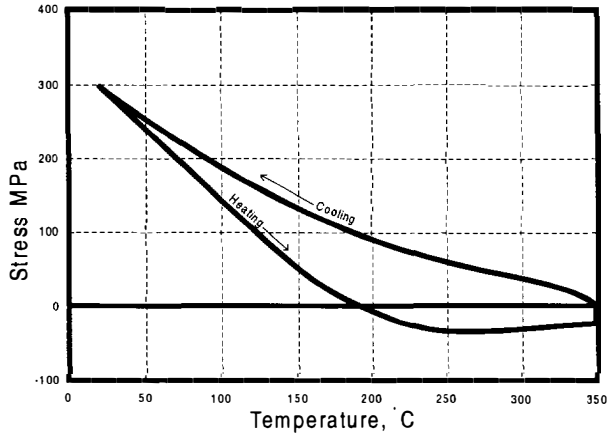

Figure 3. *Stress temperature plot for 5052 aluminum alloy films.*

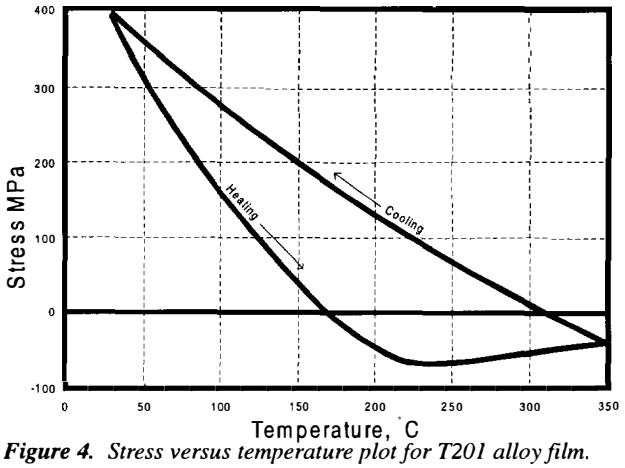

Figure 4. *Stress versus temperature plot for T201 alloy film.*

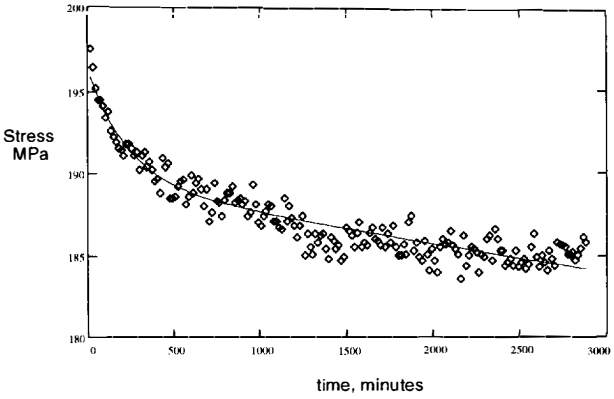

Figure 5. *Isothermal stress relaxation for T201 alloy film at 100°C.*

to reduce biaxial stress in pure aluminum and Al-Si-Cu alloy films [19], but did not change the stress in the T201 samples.

The stress versus temperature plot for the Al_3Ti intermetallic film is shown in figure 6. This film was deposited in layers. On the first heating, the layers began to interdiffuse at 350°C, resulting in a less compressive stress. On subsequent heating to 500°C the stress temperature curve was linear and without hysteresis. Samples were then heated to 800 °C, and they plastically deformed above 550°C. There was also a slight increase in the oxide thickness after this temperature, but the Al_3Ti intermetallic films are remarkably stable. The copper gold intermetallic films were not as stable. These films oxidized upon there first heating and are not useful for this application.

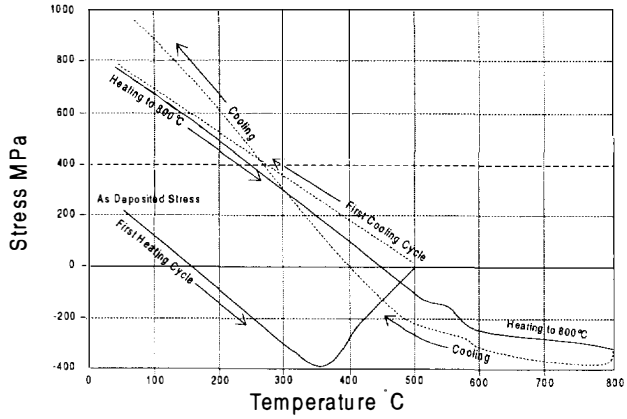

Figure 6. *Stress versus temperature plot of Al3Ti intermetallic thin film.*

In addition to the aluminum alloys and intermetallics four other metals were evaluated: copper, nickel, titanium and manganese. Figure 7 shows the initial stress temperature plot for a titanium film. At 350°C the film oxidized, causing the large change from tensile to compressive stress. All the other elemental metals had similar results [7]. A copper film was tested at 50°C for 48 hours. As shown in figure 8, it showed significant stress relaxation and oxidized severely, changing from compressive to tensile stress during the relaxation test.

FIGURE OF MERIT

Given the complexity of selecting a material for the active layer to satisfy a number of different requirement, a figure of merit was develop to assist in materials selection. Equation 3 gives the formulation of the figure of merit, FOM, where MHT is a constant based on the type of material (0.4 of most metals, 0.65 for intermetallics), MOT is maximum operating temperate, MP is the melting point of the material in degrees Kelvin, CTE is the coefficient of thermal expansion, E is the Young's modulus, and FD is a constant

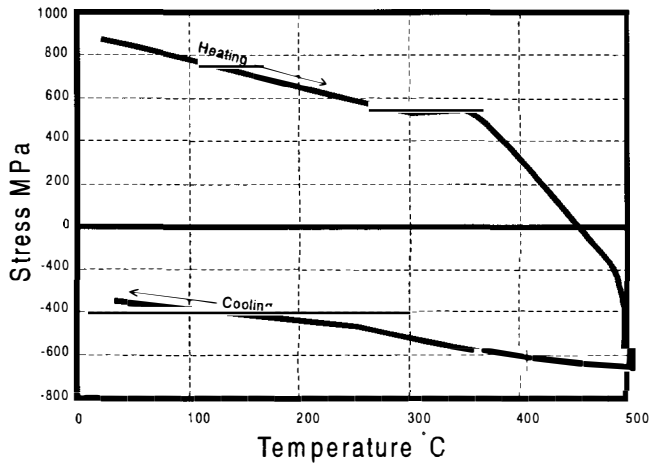

Figure 7. *Stress versus temperatue plot for a titamium thin film.*

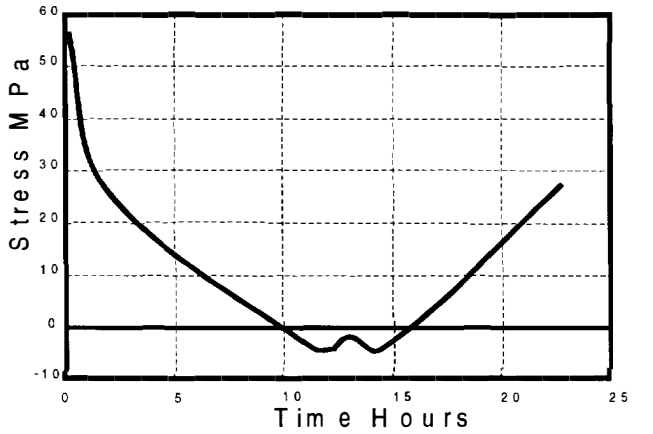

Figure 8. *Isothermal stress plot for copper film at 50°C*

$$FOM = \left(MHT - \frac{MOT}{MP}\right)^{1} \cdot YS^{.5} \cdot \left[\left(FD \cdot CTE \cdot 10^{6}\,^{\circ}C\right) + \left(E \cdot 10^{10}\,Pa^{1} \cdot (1 - FD)\right)\right]^{4} \quad (3)$$

Temperature compensated yield strength — Displacement mode — Force mode

varying from 0 to 1 (zero to maximize force, and one to maximizing displacement). Based on this FOM, Al_3Ti is the most attractive material for force and T201 is the most attractive for displacement (maximum temperature of 200°C).

CONCLUSIONS

This study has shown that the strengthening mechanism used in bulk metals can be effective at increasing the yield strength of thin films. Strengthened thin films can significantly increase the performance of a bimetallic actuator. Intermetallic Al_3Ti films were found to perform well at elevated temperatures and showed little or no stress relaxation. Oxidation was found significantly affect the other elemental metals and the copper gold intermetallics reducing there usefulness for this application.

ACKNOWLEDGEMENTS

This work was supported by DARPA contract DABT63-95-C-0038 through ICSensors. Contributions from Hal Jerman (formerly at ICSensors), Vladimir Vaganov, and Nicolai Belov are gratefully acknowledged.

REFERENCES

1. M.Madou, *Fundamentals of Microfabrication* (CRC Press LLC, New York, 1997).
2. H. Jerman, Micromach Microeng, **4** ,210 (1994).
3. P.W. Barth, C.C. Beatty, L.A. Field, J.W Baker and G.B. Gordin, Solid-State Sensor and Actuator Workshop Hilton Head, SC, June 13-16, P.248 (1994).
4. S. Timoshenko, J. Opt. Soc. AM., **11**, 23 (1925).
5. H. Jerman, personal communications (1995).
6. B.L. Draper and T.A. Hill, J. Vac. Sci. Technol., B9,1956 (1991).
7. J.F. Gorrell, " Thin Film Metallization for Micro-Bimetallic Actuators". Ph.D. Dissertation, University of Florida, June, 1997.
8. R.W. Cahn and P. Haasen, *Physical Metallurgy 3rd edition* (North-Holland Physics Publishing, New York, 1983).
9. C.R. Brooks, *Heat Treatment, Structure and Properties of Nonferrous Alloys* (American Society for Metals, Metals Park Ohio, 1982).
10. R.E. Reed-Hill and R. Abbaschien, *Physical Metallurgy Principles* (PWS-Kent Publishing Company, Boston, 1992).
11. J.A. Thorton and D.W. Hoffman, Thin Solid Films, **171**, 5 (1989).
12. R.W. Hoffman, Thin Solid Films, **34**, 185 (1975).
13. M.F. Dorner and W.D Nix, Crit Rev. Solid State Materials Science, **14**, 225 (1988).
14. D.P. Pope, *Mat. Res. Symp. Proc.*, **81**, 4 (1987).
15. J.H. Westbrook and R.L. Fleischer, *Intermetallic Compounds Principles and Proctice* (John Wiley & Son, New York, 1995).
16. Metals Handbook, Volume 2: *Properties and Selection: Nonferrous Alloys and Special Purpose Materials*, Tenth Edition (American Society for Metals, Metals Park Ohio, 1982).
17. J. W. Mayer and S.S. Lau, *Electronic Materials Science: For Integrated Circuits in Si and GaAs* (Macmillan Publishing Company, New York, 1990).
18. G.G. Stoney, Proc. Roy. Soc. London, **82**, 172 (1909).
19. F. Baldwin, P.H. Holloway, M. Bordelon and T.R. Watkins, *Mat. Res. Soc. Symp. Proc.*, **309**, 261 (1994).

A MAGNETOSTATIC MEMS SWITCH FOR DC BRUSHLESS MOTOR COMMUTATION

John A. Wright and Yu-Chong Tai
California Institute of Technology
Division of Engineering and Applied Science
Pasadena, California 91125

Gerald Lilienthal
Jet Propulsion Laboratory
Pasadena, California 91109

ABSTRACT

A magnetostatic micromachined switch for commutation of DC brushless motors has been developed. Large contact closure forces (> 5 mN) are generated on a permalloy plate by strong permanent magnets attached to the rotating motor shaft. Four point measurements of the switch show a contact resistance of less than 35 milliohms. Commutation of a three-phase, four-pole DC brushless motor by three of the MEMS switches has been successfully demonstrated. In hot-switched, resistive load lifetime testing, no failure is seen after greater than 500 million cycles at low currents (< 1 mA) but at much higher currents (0.45 A), lifetime is reduced to less than 1 million cycles.

INTRODUCTION

DC brushless motors are widely used in applications ranging from spacecraft to the video players. As is prevalent in many industries, demand for miniaturization is driving motors to much smaller sizes and at the same time requiring improved performance. While reduction of motor size is advancing (non-micromachined motors as small as 3-mm-diameter are commercially available **[1]**), miniaturizing the size of commutation electronics is not keeping pace. Figure 1 shows a miniature DC brushless motor that is about an inch in diameter. It sits on top of its commutation electronics package which is nearly four times the motor's volume.

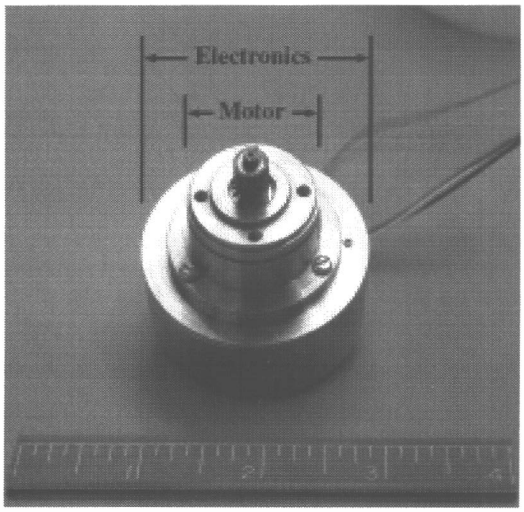

Figure 1. *Miniature DC brushless motor mounted to its commutation electronics. The volume of the electronics if four times that of the motor.*

Control of DC brushless motors is achieved by a complex package of position sensing and power electronics. To properly operate, a given winding of the motor must be energized only for a portion of the rotor's rotation. If the winding is active otherwise, it retards the motor rotation, decreasing efficiency and increasing torque ripple. For this reason, shaft position must be accurately sensed, usually by either hall sensors or an encoder. The signals from the sensor are used by the commutation electronics to generate the appropriate waveforms for each motor winding. The end result is a complex controller consisting of a hundred or more components occupying a relatively large volume and consuming a notable amount of power. To keep pace with motor miniaturization, reduction of part count and complexity is needed.

Replacement of both position sensor and commutation electronics can be achieved using a single micromachined magnetostatic switch for each motor phase. Utilization of magnetostatic actuation forces has been previously used **[2-5]** to produce large, out-of-plane deflection devices. Micromachining permits the switches to have nearly negligible size and weight which will allow them to be mounted inside the motor. Mounting the devices inside the motor provides two very attractive benefits. First, the distance of the wires run between the motor and the switches is minimized. Second, and most importantly, actuation and control of the switches can be provided by the motor itself. The magnetic fields produced by the magnets within the motor fluctuates as the motor turns. By proper design and placement of the magnetostatic switches, these fields can act as both the control and the actuating force to open and close the switches while providing perfect synchronization of switching time versus rotor position. By eliminating the need for the sensing and control circuits, system complexity is reduced while reliability is greatly enhanced. No external power source is needed to actuate the switches, saving energy, while reliability is further improved by minimizing the number of wiring connections in the system.

DESIGN

The proposed micromachined magnetostatic switches, actuated by an external magnetic field consist of three main components: a cantilever-beam spring, a magnetic actuation plate and two electrical contact points. When the switch is inactive, the cantilever beam holds the contact points apart. To activate the switch, an external magnetic field is applied perpendicular to the magnetic actuation plate. Forces are generated that attempt to align the plate with the

0-9640024-2-6/hh1998/$20©1998TRF
DOI 10.31438/trf.hh1998.70

magnetic field, causing the cantilever beam to bend. If the external magnetic field exceeds the design threshold of the switch, the bending of the beam will bring the two electrical contacts together and complete a circuit. The circuit is broken when the external magnetic field is removed and the restoring force in the cantilever beam pulls the electrical contacts apart.

To create a suitable switch, a number of physical design parameters must be considered. Large actuation forces are desirable for the proposed application of the microswitch. The larger the force generated, the stiffer the cantilever beam that can be employed. A stiffer beam makes for a device with faster switching time, higher g-force tolerance and greater contact breaking force. Published research **[6]** has shown that for common contact materials such as gold and silver, contact forces between 100 μN and 1 mN are necessary to minimize contact resistance. Large actuation forces can be used to produce large deflections allowing contact gap distances to be large. The larger the gap, the higher the device breakdown voltage **[6]**. Switching lifetime is also found to increase with high contact breaking force as stronger contact-to-contact welding points, which can occur during closure, can be broken.

The forces and deflections that can be generated with external magnetic fields are quite large and have been well characterized by Liu and Tai **[7]**. It can be shown (see figure 3) that the external magnetic field generates a large bending force on the magnetic plate which is described by equation (1). To maximize the force generated on the end of the plate, equation (1) shows that M_S, W, T and H should be maximized and that θ should be minimized. In the case of the magnetostatic switch, H and θ are dictated by the target motor and the desired contact gap. In a typical DC brushless motor, $H \approx 2500$ gauss is a reasonable available magnetic field. The small contact gap, relative to the overall size of the switch, effectively eliminates the plate rotation so that $\theta \approx 0$.

To maximize M_S, W and T, permalloy ($Ni_{80}Fe_{20}$) is chosen to form the plate. Using this soft magnetic material eliminates the need to align the M_S field of the switches with the applied external field of motor magnets. The permalloy automatically magnetizes with the proper magnetization orientation during actuation. With a high M_S value (> 0.8 Tesla) and thick plating capability (tens of microns), the permalloy makes large forces possible. Based on the performance constraints for the switch, magnetic plate dimensions of $W = 3$ mm and $T = 10$ μm were chosen to produce actuation forces in excess of 5 mN.

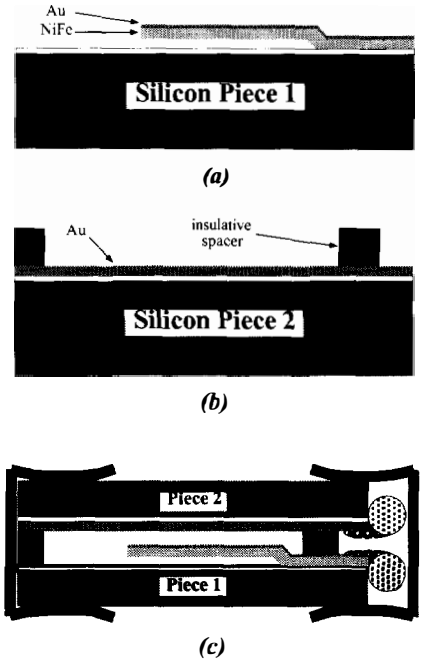

Figure 2. *Switch Fabrication: (a) Create a free-standing, permalloy plate on a rigid substrate. (b) Coat an second substrate with contact material then deposit and pattern spacer. (c) Attach bond wires to pieces. Flip piece 2 over and bond with piece 1 to complete switch.*

FABRICATION

Fabrication may be achieved with either a single substrate or dual substrate design. Because implementation as a dual substrate makes analyzing switch performance and contact wear much easier, the first generation of devices are fabricated using this approach. The first half of the switch is the permalloy plate which acts as the moving element in the switch. Its mating part is simply a substrate coated with a contact material with a spacer layer.

Processing of the first of the two pieces begins on an insulated substrate. A sacrificial spacer layer is deposited to a thickness ranging from 2 to 20 μm and patterned to provide anchor holes to the substrate. Over the spacer, an electroplating seedlayer is deposited and a photoresist plating mold is laid down and patterned. Permalloy is plated to a thickness of 10 to 20 μm. The permalloy is then coated with contact material which, in the case of the data presented in this paper, is gold. The last step is the removal of the sacrificial spacer producing a free-standing permalloy plate anchored to the substrate.

The second piece of the dual substrate design is very simple. Contact material is laid down on a rigid substrate followed by the deposition and patterning of a permanent spacer layer ranging in thickness from 10 to 200 μm. This approach permits experiments with a wide range of contact materials to be conducted. As with the first substrate, this paper present data for a contact substrate of gold.

As the last step in the process, the two substrate are assembled into the final device as shown schematically in figure 2. Note that the two pieces are not permanently bonded together permitting the switch to be non-destructively disassembled. This facilitates easy access to the contact regions so that wear and failure analysis can be conducted via microscope and SEM.

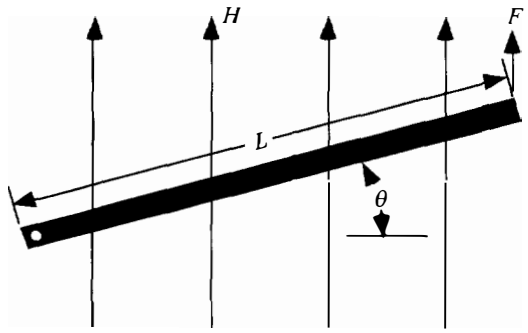

$$F = \text{Bending Force} = M_S\,(WT)\,H\cos\theta \qquad (1)$$

T = *plate thickness* W = *plate width*
L = *plate length* θ = *plate deflection angle*
H = *external magnetic field strength*
M_S = *saturation magnetization*

Figure 3. *Schematic showing theoretical forces generated on a plate of soft magnetic material by an externally applied magnetic field.*

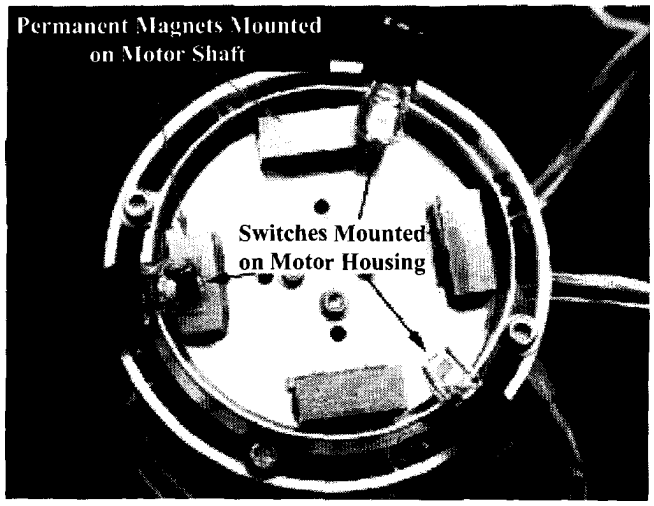

Figure 5. *Photo of three switches mounted to the housing of a 3-phase, DC brushless motor. Attached to the shaft of the motor are four permanent magnets mounted on a disk. Applying a single DC voltage to the motor makes it to turn without any external controlling electronics.*

EXPERIMENTAL SECTION

Characterization

Static beam deflection and mechanically-simulated switch testing has been used to examine contact resistance ($R_{contact}$) vs. contact force ($F_{contact}$). Testing was performed on a setup capable of monitoring force as a function of deflection. During loading, four-point-resistance data were collected from the switch generating the graphs shown in figure 4. This shows that a contact force of 3-5 mN is required to achieve an $R_{contact}$ of less than 25 milliohms and that the minimum $R_{contact}$ achievable is 1-2 milliohms. It can also be seen that the $R_{contact}$ maintains slightly lower values for decreasing $F_{contact}$ as compared to increasing $F_{contact}$. For the beams tested and with a contact gap of 100 μm, the data show that approximately 1 mN of the total bending force is required for plate deflection producing a switch with a significant break force.

Magnetic switch actuation testing has been performed on a target 3 phase, four pole DC brushless motor. The motor with three mounted switches is shown in figure 5. To simplify mounting, switches were not installed inside the motor as they will be in the final implementation. As such, the motor magnets could not be used as the source of the actuating external magnetic field. Instead, four

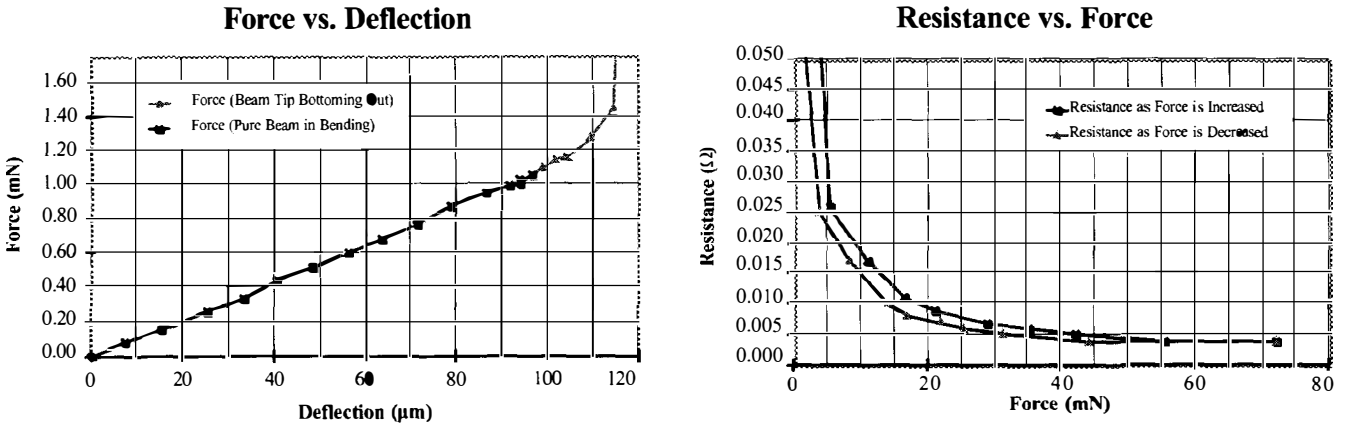

Figure 4. *Graphs showing the linear beam-in-bending and contact resistance vs. contact force behavior of a MEMS magnetostatic switch.*

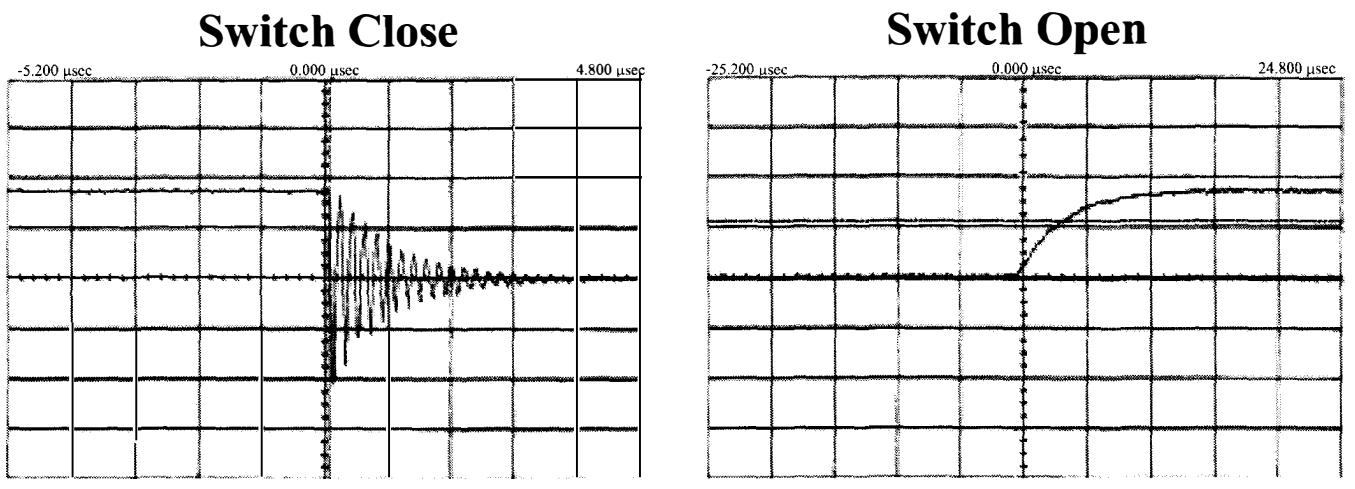

Figure 6. *Oscilloscope traces of the voltage across switch as it opens and closes. The non-ideal response is due to test circuit RC parasitics. The ringing exponential decay occurs as the switch closure adds an inductance to the testing circuit.*

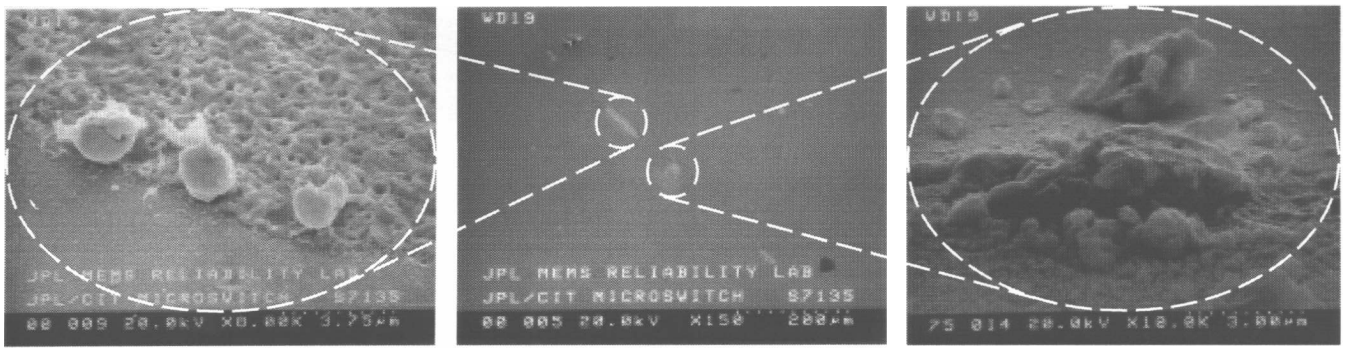

Figure 7. Center SEM shows the contact points ablated in the solid contact plate of a switch used to commutate a DC brushless motor. The contact points fall along a straight line defined by the end of the permalloy flap (not shown). The left SEM shows damage due to melting of the contact material. The right SEM shows contact material that has been ablated from the plate and redeposited on the contact plate.

permanent magnets that generated field comparable to the motor magnets (≈ 2500 gauss) were attached to an aluminum plate which was mounted to the motor's external shaft. Mounted to the motor housing, three switches are positioned at 120° intervals around the motor so that they extend over the magnets. With the motor turning, fine alignment is performed to precisely position each switch to minimize torque ripple. Winding currents for this motor range from 100 to 200 mA at DC voltages ranging from 5 to 36 volts at up to 2000 RPM.

Characterization of the switching performance has been conducted using this motor setup. Switches mounted on this motor have $R_{contact} < 35$ milliohms when closed. Oscilloscope traces of switch opening and closure are shown in figure 6. Switch bounce on closure is not seen. The resonance on closure and exponential rise on opening are caused by circuits parasitics and are not due to the switch itself. The traces indicate that contact make and break times are less than 2 μsec, however this is not the switching frequency of the devices. The rise and fall of the external magnetic field seen by the switches is not a sharp transition. Instead, the field ramps gradually from zero to 2500 gauss as the motor rotation brings the permanent magnets beneath the switches. This produces "soft-switching" as the contact points on the permalloy plate "slowly" make and break eliminating contact bounce. A maximum switching speed, limited by the capability of the motor testing setup, of up to 120 Hz has been measured.

Lifetime Testing and Contact Failure

Extensive experimental hot-switched testing has been completed at 100 Hz with an on-duty-cycle of 37%. The external magnetic field of ≈ 2500 gauss translates into a switch contact force > 5 mN. Under low switching currents (1 mA) with a resistive load, no failure is seen after more than 5 x 10^8 cycles. Reduced lifetimes of 10^5 - 10^6 cycles are seen under high current (0.45A). As expected, switching of inductive loads also limits switch lifetimes. Hot switching 0.25 amps through a 4.2 mH inductive load results in switch failure after 10^5 - 10^6 cycles. Significant contact arcing is observed in this case. On the whole, the performance of the MEMS switch is comparable to commercial reed relays.

Installed on the testing motor, commutation using three magnetostatic switches has been realized. To maximize operation time, zener diodes were placed across the switches to provide arc suppression. While this does reduce electric discharge, arcing still occurs. Even so, the test motor has been successfully commutated for several hours at several hundred RPM without failure. Additionally, motor operation in vacuum, necessary for space applications, has been realized.

Study of the failure mechanism under hot cycle testing has been performed. Evidence of metal melt, splatter and redeposition from one contact onto its opposing contact is seen. The SEMs in figure 7 show the damage to two contact areas. It should be noted that as fabricated, the contact "points" were designed as the entire width of the edge of the bending plate. They are not distinct, predefined areas. As such, the melting and redeposition occurs along an intermittent line spanning the width of the plate. Failure is predominately characterized by a drastic rise in $R_{contact}$ on the order of 10^6 ohms although welding of the contacts resulting in permanent shorting of the switch is occasionally seen.

CONCLUSIONS

Design, characterization and successful application of a magnetostatic switch is presented. Using several of these devices, the relatively large and complex electronics packages used to commutate miniature DC brushless motors can be eliminated. This results in a substantial reduction of size, weight and complexity of the final motor system. The present design, employing gold-to-gold contacts, has produced devices capable of commutating motors at up to 36 volts and 200 mA for at least several hours. With proper selection of contact materials, lifetimes should be able to be significantly extended and switching of larger currents made possible.

ACKNOWLEDGMENTS

This work is supported by NASA-JPL through JPL task, number RF295. Special thanks to Michael R. Johnson for his work in designing and building the test setup and providing insight into integrating the switches with the DC brushless motor.

REFERENCES

[1] M. A. Gottschalk, "Miniature Motors Deliver Big Performance," *Design* News, v52, n9, p 67, May 5, 1997.

[2] C. Liu, T. Tsao, Y.C. Tai, *et al.*, "A Micromachined Permalloy Magnetic Actuator Array for Micro Robotics Assembly Systems," Tech. Digest, 8th Int'l Conf. Solid-State Sensors and Actuators (Transducers '95/ Eurosensors IX), Stockholm, Sweden, Vol. 1, pp. 328-331, Jun. 25-29 (1995).

[3] R. A. Miller, G. W. Burr, Y. C. Tai, *et al.*, "Electromagnetic MEMS Scanning Mirrors For Holographic Data Storage," Tech. Digest, Solid-State Sensor and Actuator Workshop, Hilton Head Island, SC, pp. 183-186, June 3-6 (1996).

[4] R. Miller, G. Burr, Y.C. Tai and D. Psaltis, "A Magnetically Actuated MEMS Scanning Mirror," Proc. SPIE, Miniaturized Systems With Micro-Optics and Micromachining, Vol. 2687, pp. 47-52, Jan. 1996.

[5] R. Miller, G. Burr, Y.C. Tai and D. Psaltis, "Magnetically Actuated Micromirrors For Use As Optical Deflectors," Proc ElectroChem Soc, Vol. 95-18, pp. 474-480, Oct. 1995.

[6] H. Hosaka, H Kuwano and K. Yanagisawa, "Electromagnetic Microrelays: Concepts and Fundamental Characteristics," Proc. IEEE Microelectromechanical Sys. Conf., pp. 12-17, 1993.

[7] C. Liu, T. Tsao and Y. C. Tai, "Out of Plane Permalloy Magnetic Actuators for Delta-Wing Control," Proc, 1995 IEEE Micro Electro Mech. Sys. Workshop (MEMS '95), Amsterdam, The Netherlands, pp. 7-12, Jan. 29-Feb. 2 (1995).

A MONOLITHIC POLYIMIDE NOZZLE ARRAY FOR INKJET PRINTING

Jingkuang Chen, Wenhan Juan*, Joel Kubby, and Biay-Cheng Hseih

Xerox Wilson Research Center
800 Phillips Road/Bldg. 114-41D, Webster, NY 14580

**Center for Integrated Sensors and Circuits, The University of Michigan*
Ann Arbor, MI 48109-2122

ABSTRACT

A monolithic polyimide nozzle array for thermal inkjet printing has been developed. This print head was realized by molding polyimide nozzles on top of a silicon wafer with a micro heater array. On this print head, closely spaced nozzles and 22μm high micro cavities/channels are formed using a direct photolithographic process on a photosensitive polyimide and a sacrificial etch on a thick photoresist using a low temperature (<300°C) process. The micro cavities under each nozzle are separated from each other by polyimide columns which in this design have a minimum width of 6μm. All the micro cavities connect to a common ink reservoir which is formed during the same sacrificial etch used to build the ink cavities. Ink is supplied to the reservoir through a hole in the silicon substrate. Nozzle arrays with densities ranging from 300 dots per inch (dpi) to 800 dpi have been designed and fabricated. Different geometrical configurations of the ink cavity-reservoir connection have also been designed and tested for optimizing the ink supply efficiency.

INTRODUCTION

The rapid advance of inkjet printing [1] technology has changed the nature of the consumer printer market as well as brought significant impact on many areas which are related to images/text production. Inkjet printers produce images/texts by ejecting ink drops onto paper/medium through a uniformly spaced nozzle array. Because of its low cost, lightweight, compactness, and capability of producing high quality color images/text, inkjet printing has become the technology of choice for personal computers over the past decade. With a continuous R&D effort which improve the the image quality of inkjet printing, the inkjet printers market is expanding from low-end marking to high-end printing and even to areas that traditionally did not belong to direct marking, for example, printing of photograph and color inkjet copying.

The key factors that support the success of the inkjet market include the high image quality and the low device cost. Over the past twenty years, much effort has been made to improve the image quality of inkjet printing. For example, different nozzle structures have been designed for increasing the printing resolution, different actuators have been explored to enhance the gray scale and the energy efficiency, and different inks have been developed for producing more vivid images and for reducing ink smearing. The advance of inkjet printing is remarkable: twenty years ago, the images it produced were not much better than that of a dot matrix printer, however, today an inkjet printer can print images comparable to that of a laser printer.

Printer cost is the other important factor that drives the rapid growth of the inkjet market. With its comparatively simple structure, the cost of an inkjet system is significantly lower than other printing technologies that can produce high quality color images. The major component of an inkjet system is the printhead. It is composed of a nozzle array, an ink reservoir that supplies ink to the nozzles, micro actuators for ejecting an ink droplet, and control circuitry. Currently, many commercial inkjet nozzle heads are realized using bonding technology to assemble the fluidic and microelectronic components together. Each component is built separately using different processes. These approaches typically require relatively complicated fabrication processes and therefore increase product cost.

In this paper, a monolithic approach is used to fabricate an inkjet nozzle. This print head was realized by molding polyimide nozzles on top of a silicon wafer with a micro heater array using a low temperature (<300°C) process. The process was designed to be IC compatible such that it can be mass produced in a foundry. Compared with metal micro structures realized using electroplating [2], micro structures made of polyimide introduce less thermal crosstalk and provide more process flexibility for inkjet applications. Polyimide is mechanically strong and has been widely studied in various micro sensor/actuator applications [3]. Polyimide is stable in inks which are free of the OH^- ion, and has been broadly used in inkjet nozzle head fabrication either as the passivation layer for protecting circuitry or as a part of the nozzle structure. Polyimide can be shaped to various micro structures, either through a direct photolithographic process or a dry etch. While most photoresists dissolve in acetone, polyimide does not and therefore photoresist can be used as a sacrificial layer for undercutting a polyimide microstructure. The construction of polyimide micro structures is a low temperature process and compatible with MOS circuitry integration as well as some wet etch processes for surface and/or bulk micromachining. Because of these merits, polyimide was chosen to fabricate the nozzle array. The design, fabrication and testing of such a monolithic polyimide nozzle head will be described in the following sections.

PRINTHEAD DESIGN

Figure 1 shows a perspective view of this polyimide nozzle head. The substrate of this printhead is a (100) silicon wafer, which supports the heater array and provides via holes for ink supply. On top of the silicon substrate, a polyimide manifold which includes nozzles, ink cavities, and part of the front-end ink reservoir is monolithically molded on the silicon substrate. The polyimide nozzles, which sit on 22μm high micro cavities, are used

0-9640024-2-6/hh1998/$20©1998TRF
DOI 10.31438/trf.hh1998.71

for guiding ink ejection. These micro cavities are separated from each other by polyimide columns which in this design have a minimum width of 6μm and a height of approximately 22μm. Under each micro cavity is a thin-film heater, which is used for heating ink to generate the actuation force to expel an ink droplet. All the micro cavities connect to a common ink reservoir which is formed during the same sacrificial etch used to build the ink cavities. Ink is supplied to the reservoir through a hole etched from the back side of the silicon substrate. Nozzle arrays with densities ranging from 300 dots per inch (dpi) to 800 dpi have been designed and fabricated.

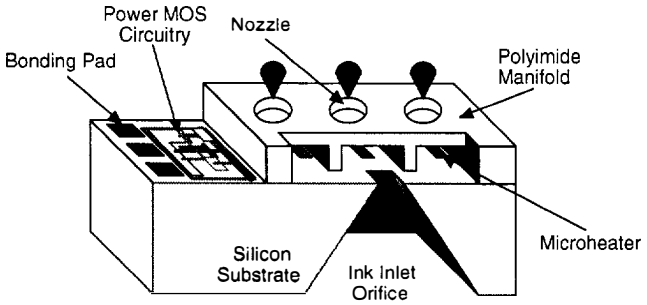

Figure 1: Perspective view of a monolithic inkjet printhead which is composed of a polyimide manifold on top of a silicon substrate.

In this design, the thin film resistors are used as heaters for drop ejection as well as temperature sensors for monitoring the heater temperature variation during the ejection process. The temperature resolution of such thin film resistors can be as high as 0.1°C if appropriate material and doping concentration are used [4].

The ink refilling process is one of the major factors that limits the printing speed of an inkjet system. After a drop of ink is ejected out of a nozzle, the nozzle cannot be fired again until after it is refilled from the reservoir. Typically, the major driving force for the refilling process is capillary action. For a circular tube of internal radius r, the movement of liquid inside this tube due to capillary action can be described by [5]

$$\frac{d(\rho ALV)}{dt} = 2\pi r\sigma(\cos\Theta) - f \qquad (1)$$

Where ρ is the density of the liquid, A is the internal cross sectional area of the tube, L is the length of the tube that is filled with the liquid, V is the velocity of the fluid driven by the capillary force, σ is the surface tension force, Θ is the contact angle of the liquid to the internal wall of the tube, and f is the friction force. The behavior of fluid in a pipe with a non-circular cross section can be described by a similar formula in which the term 2πr is replaced by the internal perimeter length of the tube. With a given boundary condition this equation can be solved using a numerical method and the transient behavior of the ink in the chamber can be predicted.

In order to reduce the ink refill time, either the cross-sectional area or the number of supply channels needs to be increased. However, these approaches generally degrade the ejector efficiency, which is defined as the ratio of the volume of ink expelled out of the nozzle to the total volume change of the cavity [6]. This is because in this case, a significant portion of the actuation momentum is used to push the ink back into the ink supply. In order to achieve an optimal design, different geometrical configurations of the ink cavity-reservoir connection have been designed and verified using numerical analysis. It was found that it is possible to achieve increased refilling speed with an acceptable ejection efficiency by using some multiple channel-supply arrangements.

DEVICE FABRICATION

The fabrication of this inkjet nozzle head started with the formation of a thin film micro heater array on a (100) silicon wafer. On top of the heater, dielectrics composed of stress balanced oxide/nitride/oxide triple layers were deposited using Low Pressure Chemical Vapor Deposition (LPCVD). Via holes for ink supply were then etched through the wafer using a wet etch, as shown in Figure 2(a). In order to protect the heaters from mechanical bombardment which occurs when an ink bubble collapses on the heater surface, the heaters are covered by metal shields which were defined by using a sputtering and a lift-off process. Next were the steps for the formation of the polyimide manifold. A 22μm thick photoresist (AZ4620) was first spun and patterned to form the ink cavities, fluid channels and front-end ink reservoirs. In order to define closely-spaced cavities and microchannels, which are typically 22μm high and have a minimum separation of 5μm, contrast enhancement material (CEM) [7] was used in the lithographic process. The cavities and reservoirs were formed after the final sacrificial layer removal, as shown in Fig. 2(d). Before spinning coating of polyimide, the sacrificial photoresist was encapsulated with a thin film which was deposited at low temperature. This film separates the sacrificial photoresist from the polyimide to prevent the solvent in the polyimide from mixing with the photoresist.

The next step was the deposition and patterning of polyimide. A photo-sensitive polyimide and a CEM were spin coated and patterned to define the nozzle structure. The application of CEM is important in this processing step because it significantly enhances the accuracy of nozzle definition. The separation film in the nozzle areas were then selectively dislodged using a dry etch, and the sacrificial photoresist was removed using a wet etch in acetone. The polyimide manifold was then cured. Finally, each nozzle head was separated using a dicing saw.

Figure 3 shows the top view photograph of a 16 nozzle array. The circular part represents the polyimide manifold, in which the nozzles are aligned in the center with two semicircular ink supply reservoirs. The thin film electrical interconnect leads and their bonding pads can be clearly seen. Figure 4 is a close-up of this nozzle array. The diameter of each nozzle is 28μm while the nozzle-to-nozzle separation is 10μm, resulting in a 668 dots per inch resolution.

TESTING RESULTS

The polyimide manifold is transparent. After the cavity is filled with ink, the movement of the ink in the manifold can be clearly seen during the printing process. The temperature coefficient of resistance (TCR) of the micro heater is about 1100ppm/°C, providing a 0.3°C resolution when working as a

temperature sensor. A series of life tests and ink refill efficiency measurements are now being undertaken to assess the performance of this nozzle head.

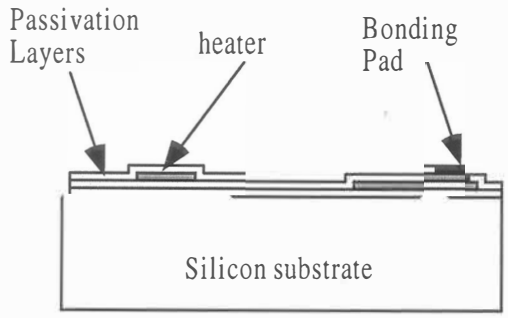

(a) Formation of a micro heater array.

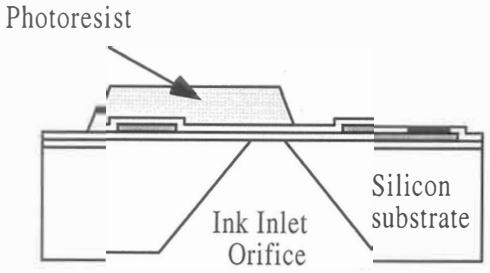

(b) Etch via holes for ink supply, formation of a thick photoresist sacrificial layer.

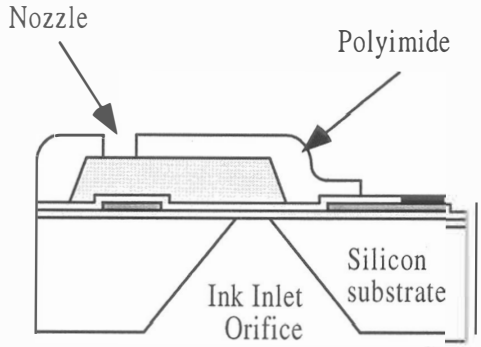

(c) Spin coating and patterning of polyimide

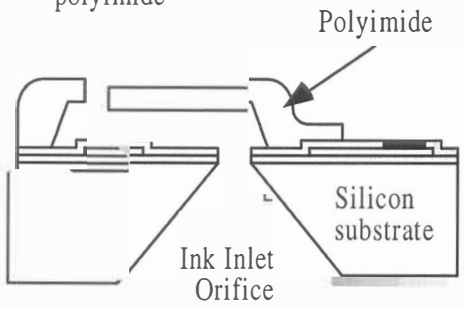

(d) Removal of sacrificial photoresist, completely opening of via holes.

Figure 2: Process sequence for the fabrication of a monolithic polyimide nozzle array for inkjet printing.

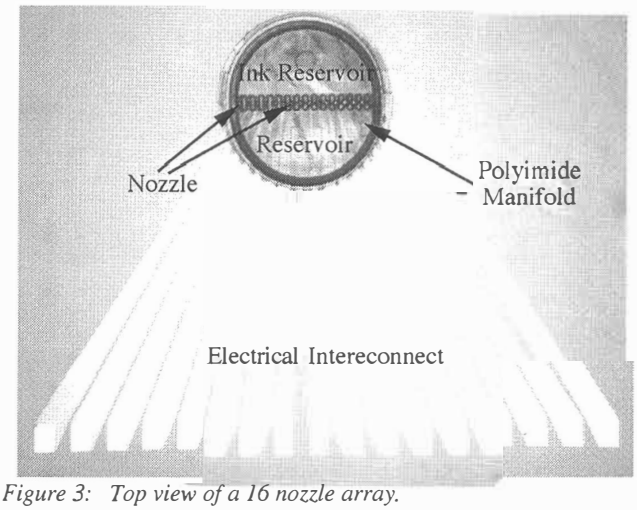

Figure 3: Top view of a 16 nozzle array.

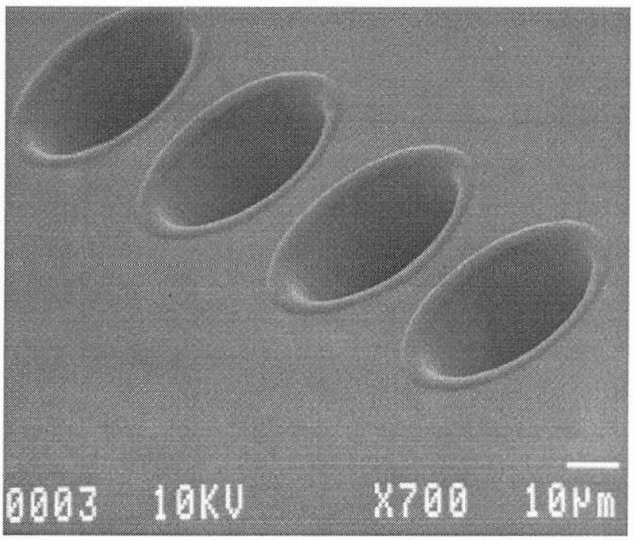

Figure 4: SEM photograph of a polyimide nozzle array defined using a direct photolithographic process on a photosensitive polyimide.

CONCLUSIONS

A fully monolithic polyimide nozzle array for inkjet printing has been developed. This print head was realized by molding polyimide nozzles on top of a silicon wafer with micro actuators. On this thermal inkjet print head, closely spaced nozzles and 22µm high micro cavities/channels are formed using a direct photolithographic process on a photosensitive polyimide and a sacrificial etch on a thick photoresist. The formation of these polyimide microfluidic structures is a low temperature (<300°C) process, allowing integration of polyimide microfluidic elements with thin-film electrical interconnects, micro heaters, CMOS circuitry, and/or other micro-electro-mechanical components on silicon for fluid manipulation. The integration of these electrical and fluidic elements into a microfluidic system allows for the fabrication of a low-cost monolithic ink jet printhead.

Nozzle arrays with densities ranging from 300 dots per inch (dpi) to 800 dpi have been designed and fabricated. Different geometrical configurations of ink cavity-reservoir connection have also been designed and are currently being tested for optimizing the

ink supply efficiency. The key step of this printhead fabrication process is the protection of the structural polyimide from mixing with the sacrificial photoresist underneath. Various separation materials have been tried and optimal candidates have been identified for inkjet applications. This novel fabrication approach improves upon existing technology which uses bonding to assemble parts into a printhead by using a simpler and more cost-effective fabrication process that produces improved resolution. The technology can also be combined with an implementation of multi-polysilicon-layer surface micromachined structures to realize various microfluidic systems for chemical analysis and for biomedical applications.

REFERENCES

1. G. L. Siewell, W. R. Boucher, and P. H. McClelland, "The ThinkJet Orifice Plate: A Part with Many Function," HP Journal, pp. 33-37, May 1985.

2. J. Lee, H. D. Lee, H. J. Lee, J. Yoon, K. Han, J. Kim, C. Kim, and C. Han, "A Monolithic Thermal Inkjet Printhead Utilizing Electrochemical Etching and Two-Step Electroplating Techniques," 1995 IEDM, pp. 601-604.

3. Y. Lin, P. Hesketh, and J. Boyd, "Characteristics of a Polyimide Microvalve," 1996 IEEE Solid-State Sensor and Actuator Workshop, Hilton Head, S.C., pp. 113-116.

4. J. Chen and K. D. Wise, "A Silicon Probe with Integrated Microheater for Thermal Marking and Monitoring of Neural Tissue," IEEE Trans. Biomd. Eng., vol. 44, pp. 770-774, August 1997.

5. Frank M. White., "Fluid Mechanics," 2nd Ed. McGraw-Hill, 1986.

6. S. Pond, "Drop-On-Demand Ink Jet Transducer Effective-ness," IS&T's Tenth International Congress on Advances in Non-Impact Printing Technologies, 1994, pp. 414-417.

7. H. Miyajima and M. Mehregany, "High-Aspect-Ratio Photolithography for MEMS Applications," Journal of Microelectromechanical Systems, vol. 4, pp.220-229, Dec. 1995.

DRIE-Fabricated Nozzles for Generating Supersonic Flows in Micropropulsion Systems

Robert L. Bayt, Kenneth S. Breuer*, and Arturo A. Ayón
Massachusetts Institute of Technology/School of Aeronautics and Astronautics
77 Massachusetts Ave 37-401
Cambridge, MA 02139 USA

ABSTRACT

A contoured converging-diverging nozzle has been created for the acceleration of gas flows to supersonic velocities. Extruded two-dimensional devices, with minimum feature sizes averaging 19 microns and 35 microns, are etched using deep reactive ion etching. Mass flow efficiencies through the nozzles range from 88% to 98% and are within experimental error to those predicted by a 2-D Navier-Stokes fluid simulation for Reynolds numbers 500 to 4500. The thrust of a 17.1 to 1 expansion ratio nozzle was measured to be 11.3 mN at 97 psia chamber pressure. This corresponds to an exit velocity of 590 m/s, which is Mach 3.8 at a chamber temperature of 300 K.

INTRODUCTION

Various trends in the spacecraft industry are driving the development of low-thrust propulsion systems. These may be needed for fine attitude control, or to reduce the mass of the propulsion system through the use of small lightweight components. The nozzle converts the stored energy in the pressurized gas into kinetic energy through an expansion. The nozzle efficiency is characterized by the amount of kinetic energy leaving the nozzle, and is governed by the exit Mach number. In an isentropic nozzle, the exit Mach number is set solely by the ratio of exit area to throat.

Prior to micromachining, low thrust was achieved by fabricating the smallest nozzle possible through conventional machining (~600 μm throat [1]), and then running the device at a low chamber pressure to reduce thrust. However, the device Reynolds number scales with both the nozzle throat width as well as the chamber pressure (or chamber density):

$$\mathrm{Re} = \frac{\rho a D}{\mu} = \frac{4\dot{m}}{\pi \mu D} \qquad (1)$$

where ρ is density a is speed of sound, D is width and μ is viscosity all defined at the throat condition. Mass flow rate (mdot) can be substituted into this expression to yield the term on the right hand side, which is true for an axisymmetric nozzle or a 2-D nozzle of constant aspect ratio. The thrust of a nozzle is approximately equivalent to the momentum flux from the nozzle and can be written as

$$T \propto \dot{m} u_e \propto D \,\mathrm{Re}\, u_e \qquad [2]$$

where u_e is the average exit velocity of the gas. The exit velocity is set by the expansion ratio and remains constant for constant geometries. Thus, if thrust is held constant, Reynolds number increases as feature size decreases for a constant mass flow. Therefore, micromachining can be used to improve nozzle performance over its low-thrust conventionally-machined counterpart by allowing them to be operated at higher Reynolds numbers.

Previous attempts at micromachining supersonic nozzles have been through the anisotropic etching of silicon along crystalline planes using KOH [2]. This results in symmetric nozzles with a 35.3° expansion. This is the angle of the flow exiting the nozzle relative to the centerline. This large angle combined with the sharp edge at the throat results in probable flow separation and thus lower mass flow efficiencies than might be achieved in a smoothly varying converging-diverging nozzle. Typical nozzle designs maintain a 15-20 degree expansion and a throat radius of curvature twice that of the throat width. In addition, there is thrust lost to the component of the fluid momentum that is not along the thruster axis, which is larger for high exit divergence angles.

Deep Reactive Ion Etching (DRIE) allows arbitrary geometries to be etched in the plane of the wafer. This affords flexibility in the nozzle geometry that can be used to design against flow separation and minimize divergence losses. By fabricating the nozzle in the wafer plane, the expansion ratio can be made arbitrarily large, where as the KOH nozzles are limited by the thickness of the wafer. Finally, there is flexibility in the nozzle thrust by adjusting the depth of the etch or the thickness of the wafer. This changes the exit area without changing the expansion ratio and the exit Mach number. However, the nozzle aspect ratio (the ratio of nozzle depth to local width) must be large enough to minimize the influence of the sidewall boundary layers.

DEVICE CONCEPT

The nozzle-plenum system is illustrated in Figure 1. This isometric view shows the silicon die which has the nozzle pattern etched completely through the chip. The flow channel is encapsulated by anodically bonding Pyrex to the upper and lower surfaces. In order to achieve high device performance, the gas must be injected into the nozzle with as low an entrance velocity as possible. To accomplish this, a settling chamber (or plenum chamber) is fabricated in parallel with the nozzle. This chamber is a region of large volume that is pressurized and remains at nearly constant pressure for the duration of the nozzle firing. The upper surface has been ultransonically drilled with a 1 mm hole to allow gas injection into the chamber. The nozzle is etched through the wafer in order to maintain a constant feature depth. Partial etches will cause narrow features to etch slower, and result in an uneven nozzle floor. This is further described in the Fabrication section.

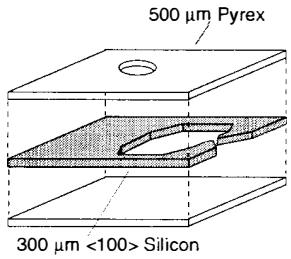

***Figure 1**: Expanded isometric view of nozzle assembly*

FLOW MODELING

In order to assess the performance of the nozzles, a viscous fluid model is developed that establishes a benchmark to which the experimental work is compared. Due to the nature of the problem,

*Corresponding Author

0-9640024-2-6/hh1998/$20©1998TRF
DOI 10.31438/trf.hh1998.72

flow through a high aspect ratio extruded nozzle, a two-dimensional model should adequately simulate the core viscous nozzle flow. The model calculates the steady state conditions through a finite volume simulation of the Navier-Stokes equations. The geometry is non-dimensionalized by the throat width, and the Reynolds number from equation (1) is used to scale the influence of viscosity [3].

The inlet conditions are set by the total pressure in the nozzle chamber, which is assumed to have only an axial component of velocity when entering the nozzle. Since the exit conditions are supersonic except in the boundary layer, the entire exit condition is extrapolated from the interior flow. The sidewalls are considered at a constant temperature consistent with the plenum temperature. Since the thermal mass of the silicon is much larger than that of the gas, the nozzle walls maintain their temperature. Also, the walls are modeled with velocity slip, which is a function of the Knudsen number, the ratio of the mean free path of the fluid to the local feature size. For these runs, the mean free path is sufficiently small that the velocity slip is only important near the region of greatest expansion, and has only a slight effect on the performance of the system (1% variation of thrust at the lowest pressures). Finally, the pressure gradient normal to the wall is a function of the ratio of slip velocity to wall curvature. In regions where curvature is finite, the slip velocity is negligible, and where slip velocity is important the wall is flat. Thus, the wall normal pressure gradient can be neglected, which allows the density to be computed, completing the state vector at the boundaries.

Figure 2 depicts the Mach number distribution through a 5.6:1 area ratio nozzle. This run was performed at a Reynolds number of 1255 that corresponds to a nozzle with a 19-micron throat width at a chamber pressure of 44 psia. The exit Mach number in the simulation is 3.13, which deviates from the inviscid value of 3.29. The coefficient of discharge, or mass flow efficiency, is the ratio of the actually mass flow to the theoretical mass flow for a given throat condition. This quantifies the blockage associated with the boundary layers. For this case, the C_d is 94.7%.

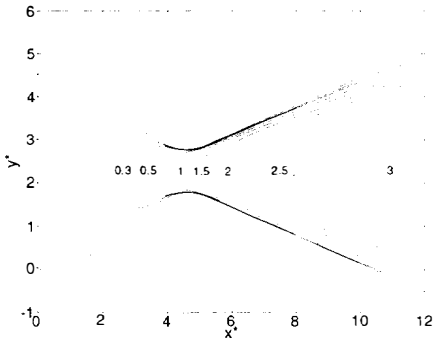

***Figure 2**: Mach contours for a Reynolds number of 1255 in a nozzle with 5.6:1 expansion ratio. The nozzle axes are not equally dimensioned to ease plot readability.*

The model is used to verify the ability of these flow channels to achieve supersonic flow and to determine the performance for various chamber conditions. Three-dimensional effects will reduce the mass flow due to the sidewall boundary layers. A first order calculation predicts a sidewall boundary layer of the same order as those found on the nozzle surfaces in the simulation. This is about 20 microns at the nozzle exit. For a 300-micron deep etch, this is 15% of the total cross section, which justifies performance estimations made with the 2-D model. The comparison of the simulation's predictions with experimental data is detailed in the Results section.

FABRICATION

The micronozzle process flow is straightforward in principle. The challenge lies in attaining a highly variable geometry that maintains anisotropy over the full height of the structure. Large features etch faster than small features, which causes the smaller features to distort when performing a deep etch. If small features of a constant geometry are etched, wall roughness becomes accentuated.

At the heart of this research program is a Surface Technology Systems (STS) deep reactive ion etcher [4]. The Multiplex ICP is an etcher that maintains tight control on ion directionality by using an inductively coupled plasma which allows anisotropy to be maintained to great depths.

The process flow is shown in Figure 3. A clean wafer is protected with photoresist that can be applied with thicknesses up to 12 microns. The resist is patterned and developed and the resulting features are etched through the wafer. Typical etch rates are measured between 2-3 µm/min depending on feature size and recipe. The silicon wafers are mounted to quartz wafers with photoresist to prevent any problems when the features etch through the wafer, and allow the cleared features to be detected by inspection.

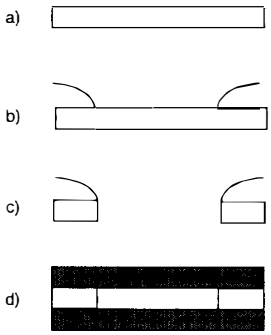

***Figure 3**: Fabrication sequence for the micronozzle. a) begin with a clean <100> wafer b) coat in photoresist c) DRIE through nozzle 4) Strip resist and anodically bond to glass*

The upper surface is anodically bonded [5] to Pyrex at 500° C with 1000 Volts and 2400 mbars of pressure applied across the stack. This task is accomplished with an Electronic Visions/Aligner Bonder. The bonder enables the silicon wafer to be aligned with alignment holes in the glass permitting the gas injection holes to line up with the chambers. The Pyrex wafer has an auxiliary hole drilled in it so that electrical contact can be made, through a brass spring, with the silicon when the second Pyrex wafer is bonded to the stack. This contact allows a voltage to be applied only relative to the second Pyrex wafer and the silicon while maintaining the integrity of the first bond. Finally, the wafer is diced along lanes which intersect the nozzle, but prevent the nozzle geometry from being distorted by inaccurate blade alignment. The dicing exposes the flow channel permitting the gas to discharge from the nozzle through the edge of the die. The dicing is accomplished with a resin-bonded blade.

Micrographs of the first attempt at fabrication are depicted in Figure 4a. This process was reported previously by Bayt et al [3]. This process etches the full nozzle-plenum geometry simultaneously. The DRIE performs well for about 200 microns depth with the full geometry. There is noticeable loading effect at the throat, which is designed to have a width of 8 microns. The etch rate is 0.3 µm/minute less than the larger features. Ultimately, the throat region becomes distorted through the over etching that is necessary to clear the throat region. This distortion is obvious near the bottom of the throat in Figure 4b. This process results in functioning nozzles, but the geometry is distorted and prevents adequate comparison to the fluid model.

a)

b)

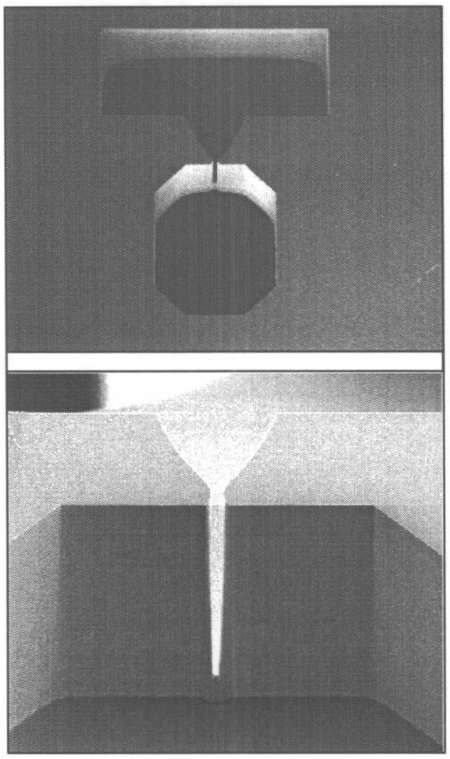

Figure 4: a) Micrograph of a nozzle-plenum system with associated dicing box attached to the nozzle b) close-up of nozzle throat revealing distortion in geometry near bottom of etch

One attempt at reducing the loading effect was to use a nested mask set that allows the nozzles to be etched initially to a depth of about 40 microns before the larger features are exposed. An oxide layer is patterned with the nozzles, and then coated with photoresist, which is patterned with the settling chamber. The STS etcher begins the etch in the nozzle region, and then the oxide is stripped in the settling chamber region with a buffered oxide etch. The wafer then goes back into the STS to complete the etch. The success of this scheme is too constrained by the etch timing, and once again leads to overetching and feature distortion. It is apparent from these results that success would only be possible through etching a constant feature size.

The optimal geometry was eventually achieved by etching a feature of similar size to maintain constant loading. A halo mask accomplishes this. The nozzle outline is defined by a 10-micron trench outlining the feature of interest. This allows the centerbody to fall out after the etch is completely through the wafer. Because of small feature distortion, best results are obtained for etches 300 microns in depth. Figure 5 is a micrograph of a nozzle for which this process was used. The anisotropy of this nozzle is striking. There is only a 1-micron variation in feature size from the top to the bottom of the wafer. The wall roughness is larger for this type of mask due to the small halo trench. The roughness is on the order of 1 micron, where it had been about 0.3 microns with the previous processes.

This etch process results in feature enlargement from the photoresist mask which breaks down over time. The features are 10 microns on the mask and become 18 microns by the completion of the etch. It may be possible to mitigate this affect with an oxide mask. In addition to feature enlargement, there is a variation in etch rate across the wafer due to asymmetric etchant delivery to the chamber. Further characteristics of the STS etcher can be found in Ayon et al [6].

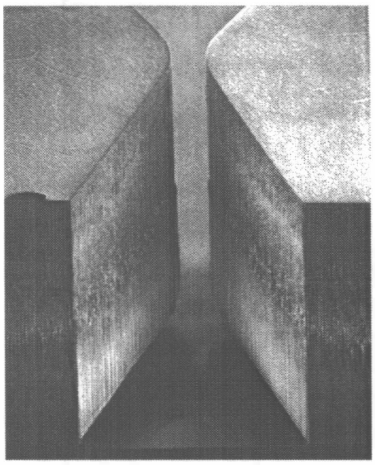

***Figure 5**: Micrograph of nozzle etched using a halo mask. Throat diameter is 20 micron with and expansion ratio of 5.4:1*

Once the die has been fabricated, it must be packaged to interface with the macroscopic world. Figure 6 depicts the gas injection manifold that allows the die to interface with a standard high-pressure source. The manifold consists of an o-ring gland that runs to a ¼" pipe fitting that is interconnected with stainless steel tubing. The die is clamped against the o-ring to prevent fluid leakage. A valve and regulator are present upstream to allow flow control to the nozzle. Pressure in the chamber is read from a transducer that is integrated into the manifold. The pressure drop in the flow channels leading to the die is less than 0.1 psi at these low flow rates.

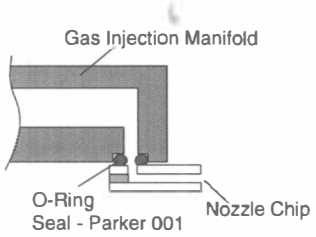

***Figure 6:** Nozzle Packaging Concept*

EXPERIMENTAL RESULTS

The test set-up utilizes grade 5.0 nitrogen regulated to chamber pressures ranging from 5 to 300 psia. A 0.5-micron filter is in line to prevent contamination from entering the nozzle. The flow rate is measured using a Teledyne-Hastings HFM-200 0-1000 sccm flow meter which is accurate to 0.5% of full scale, and the system is verified to be free of leaks before tests are run. The results reported in Bayt et al [3] verifies that sonic flow is achieved in nozzles. Since these results, the more recent mass flow measurements with improved accuracy have produced data that can be compared against the flow model data.

Figure 7 compares the mass flow test data with the model data. At the highest Reynolds number the test data is higher than the model data, but to within experimental uncertainty. In addition to the error in the mass flow meter, the feature geometry can only be measured in plane to within 0.5 microns, which results in a 2.5% uncertainty in the theoretical mass flow. As the pressure is reduced, and hence the Reynolds number is reduced, the experimental C_d falls off much faster than the model data. This is due to the influence of the sidewall boundary layers not modeled in the 2-D simulation.

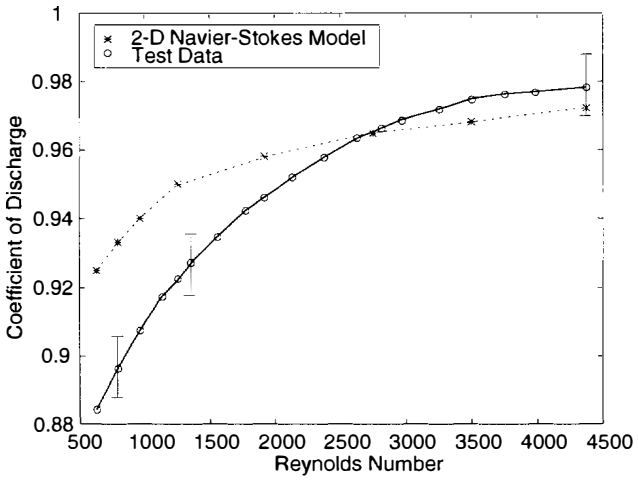

Figure 7: *Mass flow results for both the fluid model and the experimental testing for a nozzle with a 19-micron throat and a 5.4:1 expansion ratio*

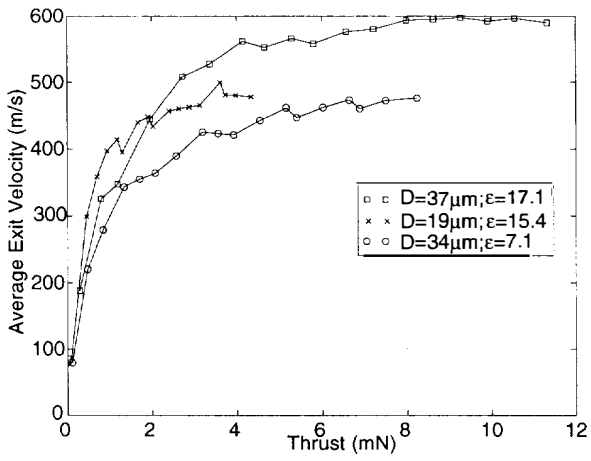

Figure 8: *Variation of Exit Velocity with Thrust for several nozzle geometries*

This trend is consistent for the different nozzle geometries tested with similar lengths and throat Reynolds numbers. For nozzles with similar throat Reynolds number but with different expansion ratios (and therefore lengths) the C_d is degraded due to the additional boundary layer growth incurred.

Finally, tests were performed with the devices to determine the thrust level. The thrust stand is accurate to 1 milliNewton of thrust over the range of 1-20 mN. For a nozzle with a 37-micron throat and a 17.1:1 expansion ratio, 11.3 mN of thrust was generated at a chamber pressure of 97.2 psia. The mass flow of this device was 924 sccm, which results in an exit velocity of 590 m/s. This is approximately Mach 3.8 as compared to the isentropic value of 4.5. Thus, the thrust tests verify that supersonic flow has been achieved.

The thrust tests, which are detailed in [7], are shown in Figure 8. The exit velocity is a direct indication of the momentum exchange for this device, thus it is a direct indication of the nozzle performance. The exit velocity should remain insensitive to chamber pressure and thrust for high Reynolds numbers. The decrease in exit velocity (hence performance) is due to the low Reynolds number viscous effects which are present at the low chamber pressures.

CONCLUSIONS

Supersonic flow can be achieved in micron-scale contoured devices to be used in micropropulsion systems. This is possible because of the anisotropy afforded during nozzle fabrication by deep reactive ion etching. This allows features to be etched which are of a constant geometry between the upper and lower surfaces where the geometric measurements are quantified. Feature distortion occurs when objects of variable geometry are etched. This can be overcome by etching a trench of constant width about the feature of interest. Thrust measurements indicate that Mach 3.8 flow is achieved for 17:1 expansion ratios, which is degraded from the 4.5 predicted by isentropic theory. The mass flow rates of these devices can be measured and produce similar repeatable results for nozzles of similar lengths and Reynolds numbers. The experimental results indicate a reduction in mass flow efficiency with Reynolds numbers. This efficiency compares well with the numerical model at high Reynolds numbers, and deviates at low Reynolds number due to the three-dimensional effects of the flow.

ACKNOWLEDGEMENTS

The authors would like to thank the JPL Microdevices Laboratory by whom this program was funded. In addition, we would like to thank Siegfried Janson at the Aerospace Corporation for the use of their thrust stand for measurements presented here. Also, our gratitude is extended to Professor Martin A. Schmidt of the Microsystems Technology Laboratory for his assistance and insight in the development of the process flow.

REFERENCES

1. S.P. Grisnik, T.A. Smith, L.E. Salz, 'Experimental Study of Low Reynolds Number Nozzles", AIAA Paper 87-0092, May 1987.

2. S.W. Janson, and H. Helvajian, "Batch-Fabricated Microthrusters: Initial Results", 32nd AIAA Joint Propulsion Conference AIAA Paper 96-2988, July 1996.

3. R.L. Bayt, A.A. Ayon, and K.S. Breuer, "A Performance Evaluation of MEMS-based Micronozzles", 33rd AIAA Joint Propulsion Conference AIAA Paper 97-3169, July 1997.

4. R. Bosch, "Method for anisotropically etching silicon", US Patents 4855017, 4789720, Germany Patent 4241045C1.

5. G. Wallis and D.I. Pomerantz, "Field Assisted Glass-Metal Sealing", *Journal of Applied Physics, 40,* 10, September 1969, pp. 3945-3949.

6. A. Ayon, B. Braff, C. Lin, H. Sawin, M. Schmidt, "Characterization of an Inductively Coupled Plasma Etcher", submitted to the *Journal of the Electrochemical Society.*

7. R.L. Bayt and K.S. Breuer, "Performance Enhancement to MEMS-Based Mircopropulsion Systems", 34th AIAA Joint Propulsion Conference AIAA Paper 98-3921, July 1998.

A Low Power MEMS Silicone/Parylene Valve

Xing Yang, Charles Grosjean, and Yu-Chong Tai
Caltech Micromachining Laboratory
Electrical Engineering, 136-93
California Institute of Technology
Pasadena, CA 91125

ABSTRACT

A low power thermopneumatic MEMS valve utilizing several novel components has been developed. 61 mW of power is sufficient to control a nitrogen flow of 1.1 lpm with an inlet pressure of 24 psi. Previous work **[1,3]** has shown that silicone rubber has a low Young's modulus (~1 MPa) and exhibits good sealing properties. Thermopneumatic actuation **[1,2]** has the potential for large forces through long displacements. By using a "soft" membrane with a large gap, and thermopneumatic actuation, high flow rates are achievable while still keeping power consumption low. However, silicone has been shown to be permeable to a wide range of liquids including Fluorinert™ which necessitates the addition of a barrier layer, in this case Parylene C. This paper presents a low power valve constructed with a composite silicone/Parylene membrane, a suspended heater for low heat loss through conduction, and a valve seat designed for improved sealing and particle resistance.

INTRODUCTION

Several MEMS silicone rubber membrane valves **[1,3,5]** have been developed in the past. Silicone rubber has a low Young's modulus (~1 MPa), good compatibility with IC processes, high elongation (100% – 1,000%) and good sealing properties on rough surfaces. Previously, we reported **[1]** a MEMS silicone membrane valve. The valve consisted of a cavity filled with a working fluid and sealed with a glass substrate heater on one side and a silicone membrane on the other. Using thermopneumatic actuation, large deflections were obtained compared to devices using silicon membranes **[2]**. Although good performance was achieved, the working fluid would leak through the permeable silicone membrane in a matter of days rendering the valves unusable. The solution was a composite membrane with a vapor barrier for keeping the working fluid in the cavity and a layer of silicone for sealing purposes. Most IC compatible materials that are impermeable to our chosen working liquids have very high modulus which defeats the purpose of a silicone membrane valve, but Parylene C is an effective barrier and has a fairly low modulus. The power consumption of the valve was high, and in part due to the design of the heater as a gold resistor on a glass substrate. A large portion of the input power would go into heating the substrate rather than the working fluid and computer simulation shows that 98% of the heat generated by a heater can be lost through the glass substrate **[4]**. To remedy this, we have designed a heater with the resistive element suspended on a thin silicon nitride membrane. Because of the small cross section of the membrane and the inherent low thermal conductivity of Si_xN_y, the heat lost to the substrate and environment is minimized. Finally, we have developed a corrugated valve seat optimized for the compliant silicone membrane. The outlet hole is surrounded by concentric grooves to create redundant seals and reduce the chance of a leak due to particles.

DESIGN AND FABRICATION

Load deflection tests **[6]** were used to determine the Young's modulus of MRTV1 silicone rubber (0.51 MPa) and Parylene C (4.5 GPa) which are both orders of magnitude lower than silicon. To keep the membranes fairly soft, a very thin layer of Parylene was used compared to the silicone thickness when fabricating the composite membranes. As it was suspected that silicone absorbs Fluorinert™, the Parylene layer was kept next to the liquid. The process flow for the composite membrane is shown in Fig. 1. A <100> wafer is oxidized and patterned on both sides prior to KOH etching to form two cavities. The top cavity is 5 mm x 5 mm and

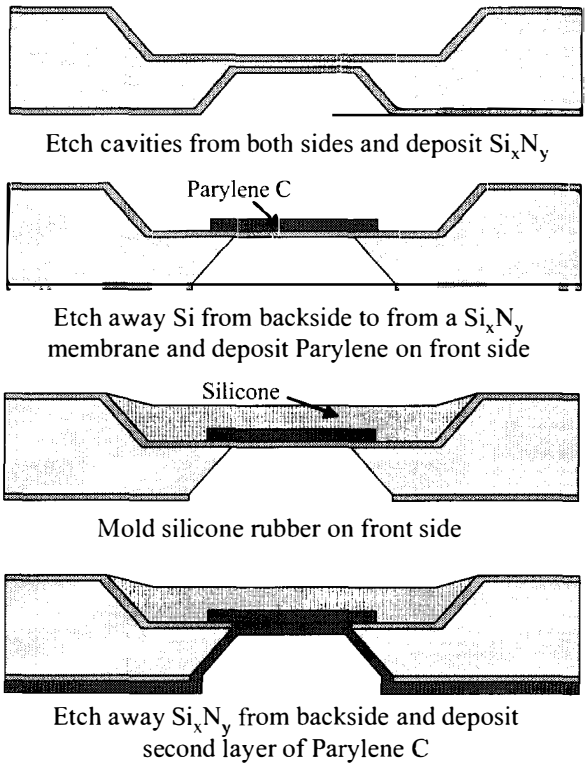

Figure 1. *Composite membrane fabrication process*

0-9640024-2-6/hh1998/$20©1998TRF
DOI 10.31438/trf.hh1998.73

Solid-State Sensors, Actuators, and Microsystems Workshop
Hilton Head Island, South Carolina, June 8-11, 1998

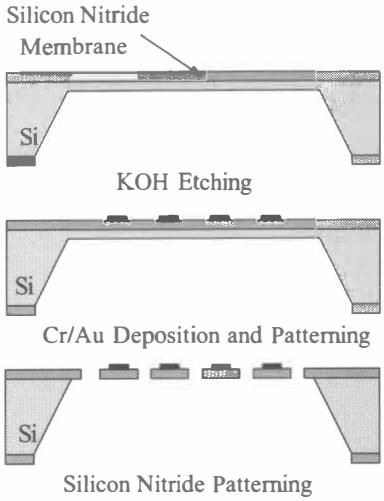

Figure 2. *Si_xN_y membrane heater fabrication process*

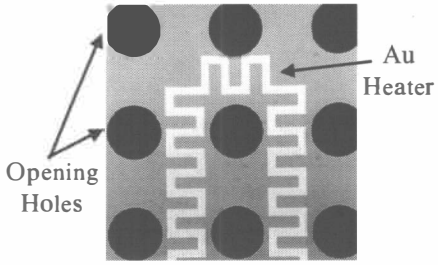

Figure 3. *Fabricated Si_xN_y membrane heater showing the holes that equalize the pressure across the membrane during valve operation.*

serves as a mold for the silicone rubber. The bottom cavity serves as the reservoir for the working fluid and defines the dimensions of the final composite membrane which is 2.7 mm x 2.7 mm. The 520 μm thick wafer is etched 235 μm on each side in KOH leaving a 50 μm thick silicon membrane. A 0.5 μm low-stress Si_xN_y film is deposited on both sides and the Si_xN_y on the backside is removed using SF_6/O_2 plasma. The wafer is put back into KOH to etch away the silicon layer and a Si_xN_y membrane is formed. Then, 2 μm of Parylene C is deposited and patterned at the bottom of the top cavity, followed by the molding of MRTV1 silicone rubber into the top cavity. The backside nitride is patterned using SF_6/O_2 plasma to free the membrane. Finally, another layer of 2 μm thick Parylene C is deposited on the backside to strengthen the edge of the membrane.

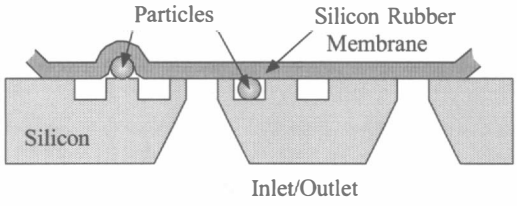

Figure 4. *New Valve Seat Design ,the corrugated valve seat creates redundant seals and reduce the chance of a leak due to particles.*

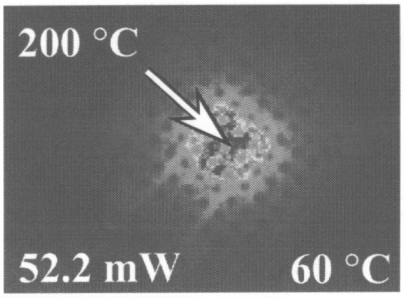

(a) Si_xN_y membrane heater

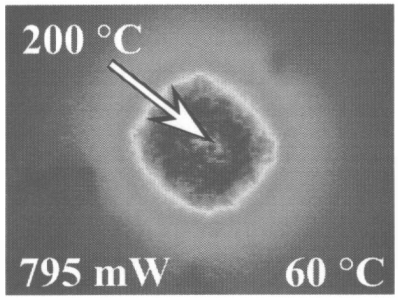

(b) Glass Susbstrate Heater

Figure 5. *2-D temperature profile of heater surface; to reach the same temperature on the surface, the Si_xN_y membrane heater requires much less power than the glass substrate heater.*

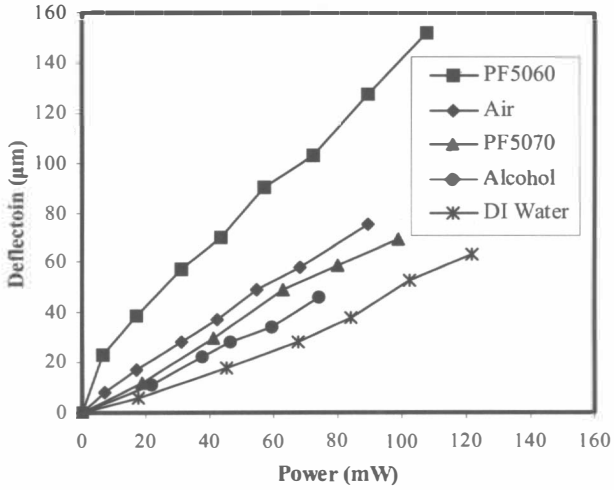

Figure 6. *Thermopneumatic actuation, Fluorinert™ PF-5060 gives the best thermopneumatic actuation performance.*

For improved thermal isolation, the gold heater is patterned on a suspended Si_xN_y membrane formed by KOH etching. As shown in Fig. 2, KOH etching is used to form a silicon frame with a free standing Si_xN_y membrane. Then a layer of 100 Å Cr/5000 Å Au is evaporated and patterned to define the heater. Finally, an array of 200 μm diameter holes is etched in the Si_xN_y membrane using SF_6/O_2 plasma. These holes equalize the pressure across the heater membrane during valve operation. Fig. 3 shows a fabricated heater.

The new valve seat is designed to form redundant sealing rings so that poor seals due to particles don't compromise the

performance of the valve. Instead of two simple holes for the inlet/outlet, 30 μm wide grooves are etched into the silicon substrate by RIE. As shown in Fig. 4, these grooves reduce the chance of the particles sticking near the inlet/outlet.

THERMOPNEUMATIC ACTUATION

The thermal performance of the Si_xN_y membrane heater and glass substrate heater is studied using an infrared thermal imager. The results are shown in Fig. 5. The Si_xN_y membrane heater surface reaches 200 °C with only 52.2 mW power input while the glass heater requires 795 mW power input for the same temperature. This confirms that the Si_xN_y membrane provides better thermal insulation.

To test the thermopneumatic actuation efficiency of various working liquids, a variety of actuators were assembled (valves without valve seats). Actuation was observed by applying a fixed amount of power to the cavity and measuring deflection of the membrane from its rest position under a microscope. Fig. 6 shows the results for DI water, Fluorinert™ (PF-5060, PF-5070), isopropanol, and air. With the same power input to the heater, the actuator sealed with PF-5060 achieved the highest deflection among all the liquids. Because of the high temperatures achievable with the Si_xN_y membrane heaters, it is necessary to use a fully filled liquid cavity to prevent bubble formation on the heater. Tests with an air-filled cavity resulted in heater damage at high power and plastic deformation in the silicone/Parylene membrane.

By using the method of laser interferometry, the transient response of the thermopneumatic actuator was studied. By applying a square wave to the heater of the actuator, the deflection of the actuator as a function of time was measured using a laser interferometer. In most cases, the response has two time constants, a short one which is associated with heating the working liquid in the cavity and a long one which is associated with heating the whole chip package. A heater with good thermal insulation consumes less power, but it also takes longer for the heat to dissipate. There is a trade-off between the power consumption and operation speed. Experimentally, it was found that for actuators with a fixed volume, thermal properties (specific heat, density, and thermal conductivity) of the working fluids change the transient response of thermopneumatic actuators. The actuators with air as the working fluid has the shortest time constant among all the fluids. The reason is although air has a very low thermal conductivity, its density is dramatically lower than all the liquids.

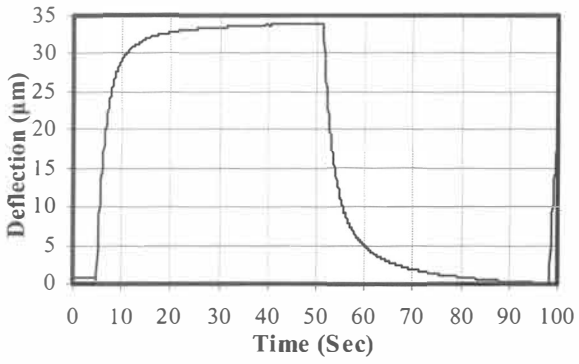

Figure 7. *Transient response of thermopneumatic actuation as measured with a laser interferometer for an actuator filled with PF56060 with a glass backing plate on a metal heat sink*

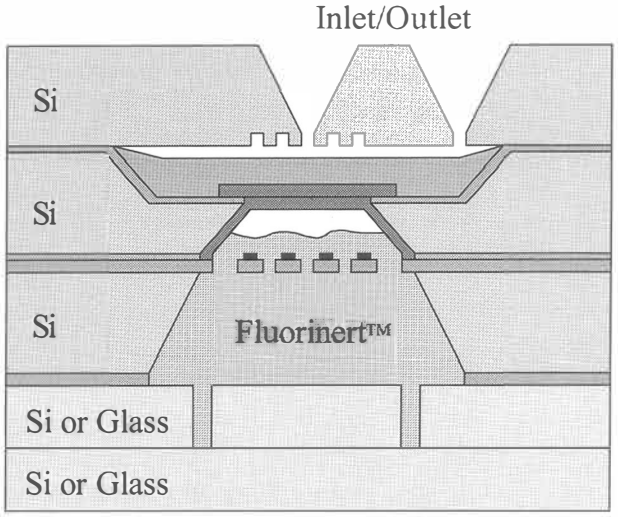

Figure 8.*Cross-Section of the Valve*

The package design of the actuators will also change the response. By using a silicon backing plate for the actuator or attaching a metal heat sink underneath the actuator, the response of the actuator will be faster while the power consumption will be higher. For example, an actuator with PF-5060 as the working fluid has heating time constants of 1.7 sec and 38.2 sec, cooling time constants of 2.1 sec and 37.0 sec. As shown in Fig. 7, when a metal heat sink is attached, the heating time constants become 1.5 sec and 7.1 sec and cooling time constants become 1.8 sec and 9.4 sec, which agrees with theoretical calculations.

VALVE PERFORMANCE

Valves are made by assembling a valve seat die, membrane chip die, heater die and backing plate. Fig. 8 shows the cross-sectional view of the valve. Fig. 9 is the picture of a fully packaged valve. It should be noticed that the 50 to 60 μm recess of the cured silicone rubber film defines the gap between the membrane and valve seat, which simplifies the fabrication of the valve seat. The inlet and outlet of the valve seat are 500 by 500 μm^2. As suggested by the thermopneumatic actuation results, all the valves are fully filled with Fluorinert™ PF-5060. The valves were tested and the results are shown in Fig. 10. Under inlet

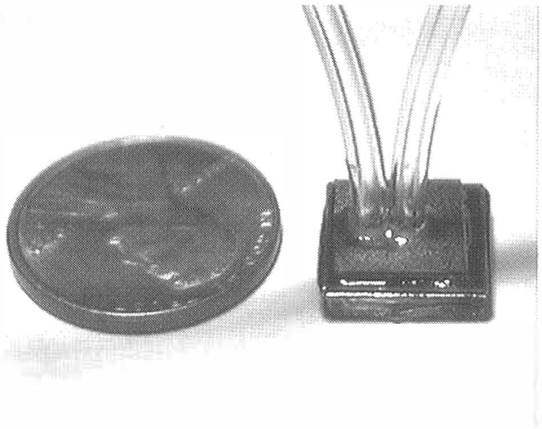

Figure 9. *Picture of a fully packaged valve*

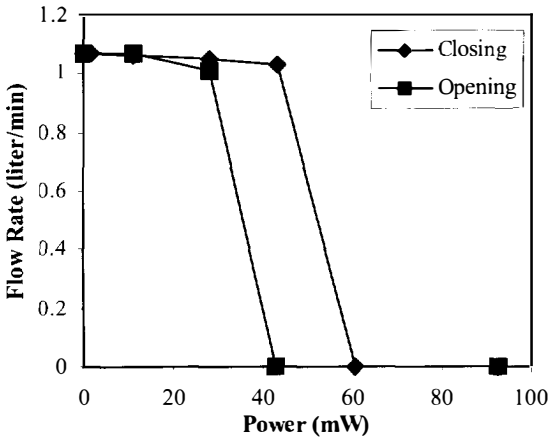

(a) *Inlet Pressure = 24 psi*

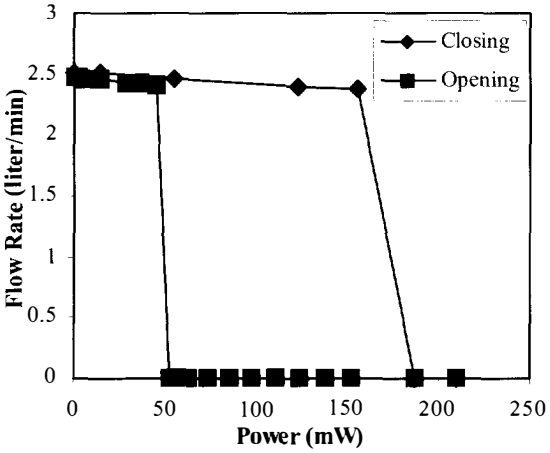

(b)

Inlet Pressure = 54 psi

Figure 10. *Valve performance using nitrogen showing low power operation and hysterisis due to good thermal insulation.*

pressure of 24 psi, a power input of 61 mW is enough to shut off a nitrogen flow of 1.1 liter/min. The valve has been tested up to 70 psi without any damage. Fig. 10 (b) shows the valve performance under high pressure input. Under inlet pressure of 55 psi, 187 mW is sufficient to control a nitrogen flow of 2.5 liter/min. It can be seen that the valve shows serious hysteresis. It takes a lot of power to heat up the liquid to the working temperature and deflect the membrane. Once up to the temperature, it takes less power to keep the membrane deflected. The good thermal insulation of the valve package makes the problem worse by keeping the heat from dissipating away. The valve hysteresis can be decreased by attaching a metal heat sink to the valve package with the tradeoff that power consumption is increased.

CONCLUSION

A normally open low power thermopneumatic MEMS valve utilizing a composite silicone rubber/Parylene membrane has been designed, fabricated and tested. A novel suspended heater has been developed to reduce heat loss. By using a "soft" membrane with a large gap, and thermopneumatic actuation, high flow rates are achievable while still keeping power consumption low. A new valve seat has been developed to reduce the leak rate of the valve when the valve is closed. The steady state and transient response of the thermopneumatic action have been studied. The valve shows very low power consumption. 61 mW of power is sufficient to control a nitrogen flow of 1.1 lpm with an inlet pressure of 24 psi.

ACKNOWLEDGMENTS

This work is supported by the DARPA MICROFLUMES program under Naval Ocean Systems Center Contract N66001-96-C-83632. The authors would like to thank Ms. Ellis Meng for help with testing and Mr. Trevor Roper for help with processing.

REFERENCES

1. X. Yang, C. Grosjean, Y.-C. Tai, and C.-M. Ho, "A MEMS Thermopneumatic Silicone Membrane Valve", *Proceedings of IEEE the 10th Annual International Workshop on Mciro Electro Mechanical Systems*, Jan 26-30, 1997, Nagoya, Japan, pp.114-118.

2. M. Zdeblick, R. Anderson, J. Janskowski, B. Kline-Schoder, L. Christel, R. Miles and W. Weber, "Thermopneumatically Actuated Microvalves and Integrated Electro-fluidic Circuits", *Technical Digest of the 1994 Solid State Sensor and Actuator Workshop*, Hilton Head Island, SC, June 13-16, 1994, pp. 251-255.

3. L. Bousse, E. Dijkstra and O. Guenat, "High Density Array of Valves and Interconnects for Liquid Switching", *Technical Digest of the 1996 Solid State Sensor and Actuator Workshop*, Hilton Head Island, SC, June 3-6, 1996, pp. 272-275.

4. P. L. Bergstrom, J. Ji, Y.-N. Liu, M. Kaviany, and K. D. Wise, "Thermally Driven Phase-Change Microactuation", *Journal of Microelectromechanical Systems*, Vol. 4, No.1, 1995, pp. 10-17.

5. C. Vieider, O. Ohman and H. Elderstig, "A Pneumatically Actuated Microvalve with a Silicone Rubber Membrane for Integration with Fluid Handling Systems", *Technical Digest of the 8th International Conference on Solid-State Sensors and Actuators*, Vol. 2, June, 1995, pp. 284-286.

6. O. Tabata, K. Kawahata, S. Sugiyama and I. Igarashi, "Mechanical Property Measurements of Thin Films Using Load Deflection of Composite Rectangular Membranes", *Sensors and Actuators*, 20 (1989) pp. 135-141.

A NEW PULSED-MODE MICROMACHINED FLOW SENSOR FOR AN INTEGRATED MICROFLUIDIC SYSTEM

Nihat Okulan, H. Thurman Henderson and Chong H. Ahn
Center for Microelectronic Sensors and MEMS
University of Cincinnati
Department of Electrical and Computer Engineering
P.O. Box 210030, Cincinnati, Ohio 45221-0030

Abstract

A new pulsed-mode micromachined flow sensor for an integrated microfluidic system has been designed, fabricated and characterized. This micro flow sensor has several unique physical and operational characteristics, as a part of the complex of components constituting a generic fully integrated microfluidic system [1,2] for autonomous bio-chemical analysis. Companion elements include microvalves, micropumps, microreservoirs, microchannels, etc., whose liquid (or gaseous) fluid dynamics must be characterized by these micromachined sensors.

1. Introduction

In contrast to other thermally-based flow sensors [3], here the sensing elements are located in the microchannel walls. This novel design prevents clogging by virtue of dead volume or other interference which may cause nucleation of particle deposition. Nevertheless, the single crystalline silicon elements are thermally isolated from the bulk by unique low stress, low temperature-deposited (<150 °C) PECVD SiO_2 [4], which is considerably superior to other electrical and thermal isolation schemes. In essence, the sensor measures liquid flow through the integrated channel sidewall.

In order to minimize possible thermally induced effects in the fluid, the elements are pulsed at a fixed current level (typically 2.5mA) for 50 to 100 ms intervals at a low duty cycle, typically 2-4 per second. High resistivity (50 Ohm-cm) silicon results in a highly sensitive element, which easily achieves full operation during the on-cycle, because of the fast time response resulting from miniature size and thermal isolation.

Unamplified sensitivities up to 25mV at 10ul/min are achieved. However, a novel negative differential resistance (NDR) modality is also possible by (stable) transient operation in thermal run-away. Depending on the several modalities made possible, the sensitivity can be enhanced by taking advantage of the onset of intrinsic operation or by deep impurity operation (not covered here in detail).

In contrast to earlier in-flow immersion, the electrodes are located outside the channel and thus do not need further electrical passivation. The thermal field can be made to variously penetrate the boundary layer appropriately. A numerical simulation of the liquid flow field [6] and thermal distribution has been realized using ANSYS 53 and the FLOTRAM CFD option.

Other members of our research team have also developed effective electronics for integrating the digital sampling to achieve high resolution measurement of total flow volume, however this will be reported separately elsewhere.

2. Design and Fabrication

Since thermal devices are dependent on differential temperatures, it was essential to make use of an effective thermal isolation structure. Figure 1 shows an SEM micrograph of the top view of the fabricated flow sensor. Thermal isolation was achieved by constructing a physical isolation channel between the

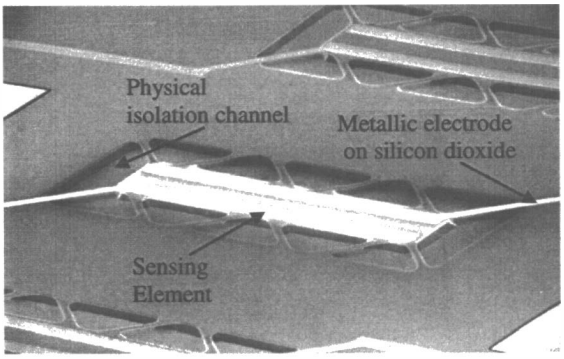

Figure 1. SEM micrograph of the top of a linear array of three fabricated flow sensors

sensing element and the surrounding bulk silicon using the low stress silicon dioxide bridges [4], which are approximately an order of magnitude better than silicon nitride for thermal isolation. Electrically conducting layers from the bulk to the sensing element where formed over two of the bridges in order to access the electrodes on the sensing element. The physical channel was generated by aligning the edges of windows to the {111} crystallographic planes of the underlying (100) silicon, opening these windows in the SiO_2 and etching away the silicon during a KOH anisotropic etching process [3].

Compared to other thermally based flow sensors a significant advantage of this micro flow sensor is its detailed design. Complex electrical passivation procedures are not necessary since the sensing elements are integrated in the microchannel walls. As can be seen in Fig.2, the electrodes are located outside the flow channel. Furthermore, having the sensing elements not immersed in the flow

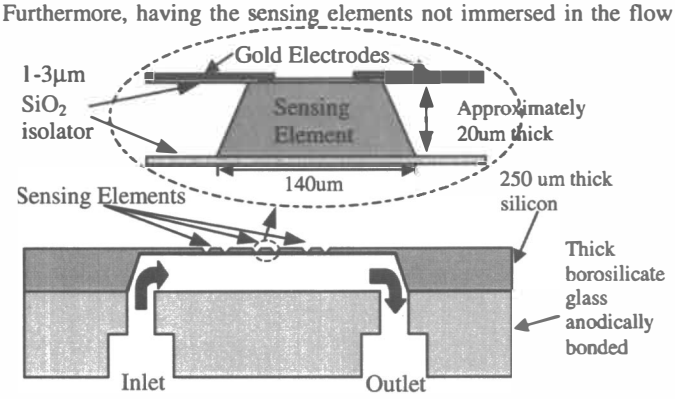

Figure 2: Physical structure of the three-sensor array. The array allows the alternative method of upstream and downstream temperature measurement.

stream prevents possible clogging and dead spaces. The shape of the etched channel allows a convenient packaging scheme for a multi-

0-9640024-2-6/hh1998/$20©1998TRF
DOI 10.31438/trf.hh1998.74

level bonded package in an integrated biochemical "lab-on-a-chip" [2]. These very novel arrangements specifically add reliability and simplicity for this specific application.

3. Operating Principle

The sensing element is pulsed at a fixed current level in time intervals of 50 to 100ms at a relatively low duty cycle at 2-4 times per second. This measuring scheme results in high sensitivity and repeatability. At the same time this scheme is simple and economical; and it allows a simple driving circuitry, consequently saving chip space and battery lifetime.

Choosing the appropriate duty cycle is of importance, since a high duty cycle could lead to an elevated fluid temperature that could alter the properties of the biochemistry being performed. On the other hand, a to low duty cycle could degrade the accuracy (e.g. an unacceptable low sample rate).

During the operational mode, the sensor is typically pulsed with 2.5mA for 100ms with a duty cycle of 25%. The temperature of the sensing element, T_s, will be elevated to a value above the fluid temperature, T_f, depending on the flow rate of the fluid. The increase in T_s leads to an increase in sensing element resistance and thus to an increase in voltage drop across the resistor.

The behavior of the voltage drop across the sensing element due to electrical current flow during the pulsing period is shown in Fig. 3. The output voltage is plotted as a function of time for various flow rates. The output voltage increases in a

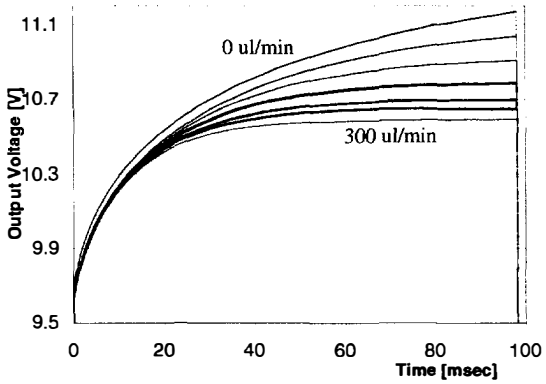

***Figure 3:** Output voltage versus time at a family of flow rates from 0 to 300ul/min separated in 50ul/min steps*

saturation curve with a time constant $\tau=R_{th}C_{th}$, where R_{th} is the system thermal resistance and C_{th} the thermal capacitance, related to sensor size.

When there is no flow, the power dissipated by the sensing element causes a conductive heat flow into the fluid and the surrounding bulk silicon. If liquid passes, a forced convective heat flow is added, which drops the temperature of the sensing element and decreases the thermal resistance. The drop of temperature leads to a decreased electrical resistance of the sensing element and thus to a drop in output voltage. In addition, the decrease in thermal resistance leads to a smaller τ because of the added (shorting) thermal conductance. The output voltage or the time constant can alternatively be used as an indicator for the flow rate.

To determine the fluid temperature for on-line temperature correction to a changing ambient, the resistance of the sensing element was measured by using a very low current pulse of 100uA just before pulsing the sensor. The low current ambient temperature-measuring pulse avoids any significant heating and thus does not interfere with the flow rate measurement.

The basic operation is not unlike the classical "hot-wire anemometer." To understand the relationship between sensing element resistance and temperature, and to understand the relationship between the sensing element temperature and the flow rate, a brief theory is presented.

3.1 Sensing Element Temperature Versus Flow Rate

The heat flux from the sensing element increases with the flow rate. In addition to the heat conveyed away by the flow, Q_{conv} (forced heat convection), heat is conducted, Q_{cond}, to the fluid and carrier substrate in which the sensor is imbedded. The radiated heat is negligible. In steady state, the heat transfer is balanced by the power dissipation P in the sensor:

$$P = Q_{cond} + Q_{conv} \quad (1)$$

The flow measurement depends on the relationship between Q_{conv} and the flow (other secondary heat transfer effects, such as radiation and natural convection, can be included in Q_{cond}). The amount of heat Q_{conv} transferred to the fluid is proportional to the temperature difference between the hot sensing element, T_s, and the fluid temperature, T_f:

$$Q_{conv} = G_{conv}(T_s - T_f) \quad (2)$$

where G_{conv} is the heat conductance due to forced convection and is a function of the flow velocity.

Considering laminar flow and the decreasing thermal boundary layer with increasing velocity, the heat transfer increases in relation with the flow velocity U. The surface heat flux per unit area Q'_{conv} is given by

$$Q'_{conv} = 0.332 k_f (T_s - T_f)\sqrt[3]{P_r}\sqrt{U/(xv)} \quad (3)$$

where k_f and v are the thermal conductivity and kinematic viscosity, respectively, of the fluid and P_r is the Prandtl number; position x is measured from the upstream edge of the sensing element.

Integrating Q'_{conv} over the entire surface (which is determined by the length and width of the sensing element) and dividing by (T_s-T_f) results in G_{conv}. Thus, G_{conf} increases in proportion to $U^{1/2}$ for laminar flow. The relation between power dissipation, the flow velocity and the temperature difference between T_s and T_f can be written as

$$P/(T_s - T_f) = G_0 + K\sqrt{U} \quad (4)$$

where K is the flow sensitivity (a geometrical term), and the zero-flow thermal conductance is G_o. These are parameters which for a simple sensor geometry can be estimated from theoretical analysis. Solving equation (4) for the sensing element temperature results in:

$$T_s = T_f + P/\left(G_0 + K\sqrt{U}\right) \quad (5)$$

Figure 4 illustrates the relationship between sensing element temperature and flow velocity.

3.2 Sensing Element Resistivity Versus Temperature

Since the sensitivity of the micro flow sensor depends primarily on the change in electrical resistivity with temperature, it is important to review the relevant classical device physics of the micro flow sensor. The relationship for electrical resistivity ρ is a function of temperature T and is given as

$$\rho^{-1}(T) = q[n(T)\mu_n(T) + p(T)\mu_p(T)] \quad (5)$$

where q is the magnitude of electronic charge , $n_{(T)}$ and $p_{(T)}$ are free electron and hole concentrations, respectively, and $\mu_{n(T)}$ and $\mu_{p(T)}$ are electron and hole mobilities, respectively. The

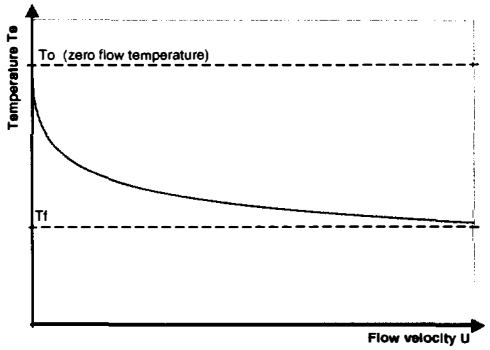

Figure 4: *Element temperature versus velocity (proportional to flow rate)*

temperature dependence of the mobility in the range of interest is approximately proportional to $T^{2/3}$ (a more detailed relationship was used in the calculation). To determine the free carrier concentrations the charge neutrality equation must be solved. The micro flow sensors where fabricated using 50 Ohm-cm, n-type silicon, which corresponds to a phosphorus concentration, N_d, of 8.5E13cm^{-3}. Hence, the charge neutrality equation reduces to

$$n = p + N_d \tag{7}$$

and

$$p(T, E_f) = N_v \exp[\frac{-(E_f - E_v)}{kT}] \tag{8}$$

$$n(T, E_f) = N_c(T) \exp[\frac{-(E_c - E_f)}{kT}] \tag{9}$$

where $N_c(T)$ and $N_v(T)$ are conduction and valence band effective densities of states, E_c and E_v are conduction and valence band edges, k is the Boltzman constant and E_f is the Fermi level.

Solving the charge neutrality equation transcendentally for E_f, and using E_f to solve for the electron and hole concentration, the resistivity at any temperature T can be calculated. Figure 5 shows the calculated resistivity over the range from 0-300 °C.

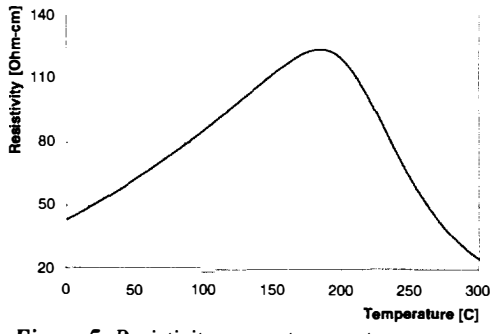

Figure 5: *Resistivity versus temperature*

The current is constant during each heating pulse, and the heating is thus proportional to the resistivity, resistance or voltage. Thus, it can be seen that the sensor can be operated in two modalities. In the lower temperature ranges, one can take advantage of the positive differential resistance (PDR) modality.

However, a novel negative differential (NDR) modality is also possible by (stable) transient operation in "thermal run-away". This would lead to an increase in sensitivity but as a trade-off would have to be operated in higher temperature ranges. An alternative modality, not covered here but to be later published, is to achieve an even higher sensitivity using a deep impurity such as gold, with a relatively low operating temperature.

4. Finite Element Analysis

The numerical simulation of the liquid flow field and thermal distribution has been realized using ANSYS 53 and the FLOTRAN CFD option. The CFD program solves the coupled fields of temperature and flow. A simple two-dimensional model was calculated where the channel was reduced to a rectangular configuration with the dimensions of the real sensor. Three sensing elements were located in the middle of the flow field and a constant heat source was applied to the sensing element in the center. (Of course an alternative flow measurement scheme [5] is to use the center element merely as a heater then measure flow by virtue of the incremental resistance of the up and downstream sensor.)

The liquid flow was measured by its influence on the temperature distribution in the channel resulting from the heat generated from the center element. The analysis showed that the temperature change of the center sensing element with respect to the flow rate was much larger than the upstream and downstream located sensing elements. Figure 6 indicates the temperature of the center sensing element as a function of flow rate.

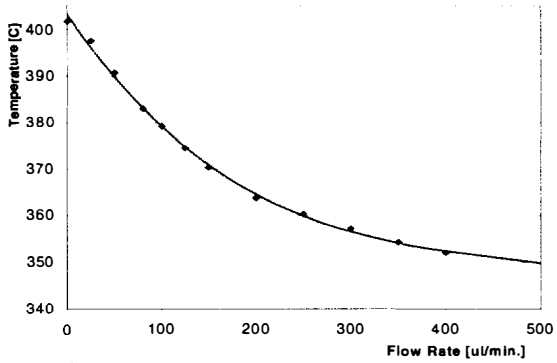

Figure 6: *Sensing element temperature versus flow rate*

As expected, the temperature consistently decreases with the flow. As a conclusion, one achieves more sensitivity using only a singular "heating-sensing" element, which can also be used to sample ambient temperature, as noted earlier.

However, at these MEMS dimensions such traditional modeling tools have limited validity but can still be used for proof of concept.

5. Experimental Results and Discussion

The measuring system consists of a LC-pump (which will be replaced with an integrated pump in the eventual microfluidic system) with adjustable flowrates from 10ul/min to 10ml/min, a data acquisition module that can record data up to 100K samples/s with a 12 bit resolution, a voltage controllable current source and a control computer. It allowed automatic measuring and recording of experimental results. Water was used for testing the sensor.

Figure 8 shows that the measured temperature dependence of the sensing element resistance agrees rather well with the calculated theoretical temperature dependence. The resistance was calculated by multiplying the above determined resistivity with the dimensional factor of the sensor.

Measurements of the flow rates were performed by arbitrarily adjusting a specific flow rate at the pump and gathering data during

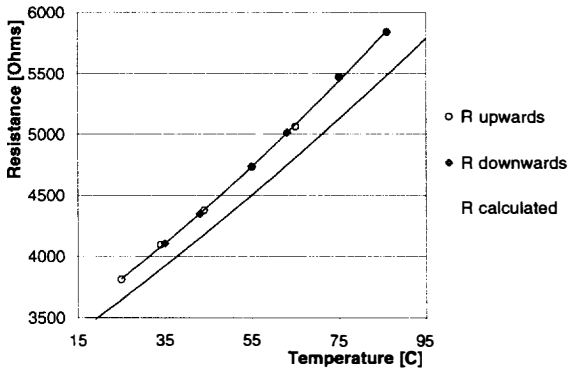

Figure 8: *Resistance versus temperature*

50 duty cycles. For simplicity, an average value of the last 20milliseconds (1500 measurements) of each output voltage pulse was evaluated and used as an indicator for the flow rate. Figure 9 shows the output voltage versus flow rate. The output

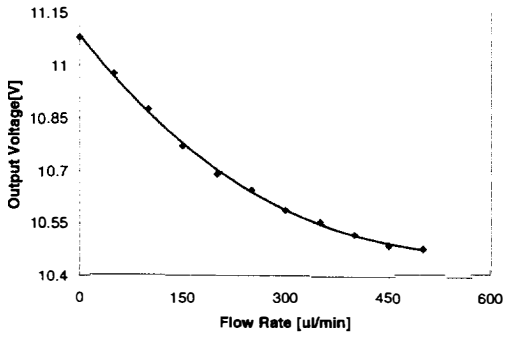

Figure 9: *Output voltage versus flow rate*

voltage drops with increasing flow rates, because of cooling, and has the experimental shape as was analytically derived. Unamplified sensitivities up to 25mV per 10ul/min were achieved.

Flow measurements for three selected fluid temperatures were taken. The output voltage as a function of fluid temperature and flow rate is shown in Fig. 10. As one can see,

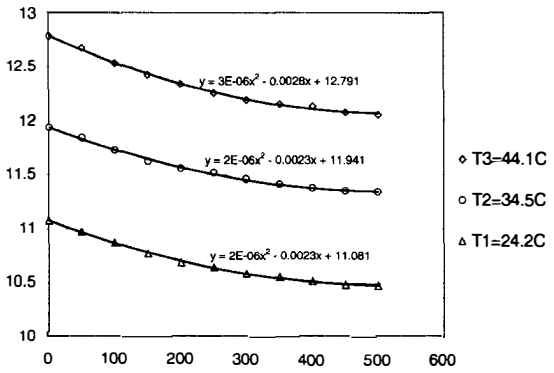

Figure 10: *Output voltage versus temperature and flow rate*

the behavior of the output voltage versus flow rate can be described with similar curve fitted relationships where each fit begins at a different zero flow rate offset voltage V_0. The offset voltage is tied to the fluid temperature. As the fluid temperature increases, V_0 increases. Temperature compensation circuitry is being designed to allow a high degree of accuracy in the full range of operational temperatures for the associated generic microfluidic system.

6. Conclusions

A micro flow-sensor, which has also been rendered in smaller versions than herein reported, has been fabricated and dedicated to the measurement of small liquid flows for autonomous bio-chemical analysis. Due to well defined arrangements of the sensing elements integrated into the microchannel walls, clogging and dead spaces are minimized. Further, the complex electrical passivation of electrodes is eliminated. Thermal insulation is achieved by implementing a physical isolation channel between sensing elements and the bulk silicon, leading to a fast time response due to the small mass of the elements. Experimental data show promising results with fast and highly sensitive signals for regulation of microflow in the range of 0.001-10ml/min.

A pulsing modality minimizes thermally induced effects in the fluid and also allows minimization of potential drift. Further, this mode of operation saves valuable battery lifetime.

Acknowledgements

This research has been funded in part by DARPA contract P9619-80 under the Microflumes/ETO program directed by Dr. Rose Ritts, for use in a generic integrated microfluidic system. We acknowledge the associated flow sensor contributions of colleagues Gerd Berger and Karsten Klein. Also we wish to thank Dr. Thomas Mantei and his group, including F. Li and C.-T. Lin, for development of the special technique for deposition of the low stress silicon dioxide.

References

1. M. Elwenspoek, "Toward integrating microliquid handling system", *J. Micromech. Microeng.*, 1994, Vol.4, p.227.

2. DARPA BBA96-19 No. P9619-80, "Generic microfluidic system for remote sensors", *Unversity of Cincinnati*, 1997.

3. Timothy M. Betzner, "Structural design and characteristics of a thermal isolated, sensitivity-enhanced, bulk-michromachined, silicon flow sensor", *J. Micromech. Microeng.*,1996, Vol.6, p.217.

4. J.Pilchowski, F. Li, C.-T. Lin, T. D. Mantei, H. T. Henderson, "Silicon dioxide deposition in high density plasma for packaging application", Proc. of *The Electrochemical Society, 193rd meeting, San Diego*, Calif., May 3-8, 1998.

5. R.G.Johnson, R.E. Higashi, "A highly sensitive silicon chip microtransducer for air flow and differential pressure sensing applications", *Sens. Actuators 11*, 1987, p.63.

6. R. Zengerle, M. Richter, "Simulation of microfluidic systems", *J. Micromech. Microeng.*, 1994, Vol.4, p.192

PULSED-SOURCE INTERFEROMETRY FOR CHARACTERIZATION OF RESONANT MICROMACHINED STRUCTURES

Roman C. Gutierrez, Kirill V. Shcheglov, and Tony K. Tang
Jet Propulsion Laboratory, California Institute of Technology
Pasadena, CA 91109-8099

ABSTRACT

We present a new microscopy tool for quantitative measurement of the resonant motion of microstructures. The new instrument uses optical interferometry to generate a three-dimensional surface topographic map of a vibrating micromachined resonator in vacuum. By strobing the light source, the image of the moving device is frozen at an arbitrary position in its vibration cycle. By varying the phase between the excitation signal and the pulsing of the light source, the out of plane motion of the resonant device can be measured with a resolution of less than 0.5 nm.

INTRODUCTION

Resonant micromachined structures are used for many applications in which the frequency, the damping and the coupling of the resonant modes of the structure is used to measure acceleration, pressure, rotation rate, and other physical and chemical phenomena. To characterize these devices it is necessary to understand the dynamic properties of the micromachined structures. Conventional microscopy tools accurately measure the static properties of MEMS devices, but dynamic properties are not available with these techniques. This paper describes a new instrument that measures dynamic properties of MEMS structures.

PRINCIPLE OF OPERATION

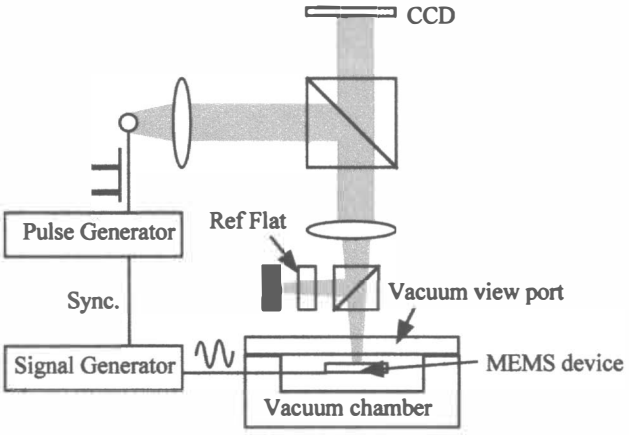

Figure 1. *Schematic of the modified instrument.*

Optical interferometry uses the interference of light to accurately measure distances. When two light beams of equal intensity are superimposed, the intensity of the light in the overlapping region varies between zero and twice the total intensity of the two beams. The pattern generated is usually referred to as a fringe pattern. The intensity at any point of the fringe pattern is a measure of the relative phase shift between the two beams. For metrology, the path that one of the beams travels is fixed, and the fringe pattern is a measure of the distance that the other beam traversed. The WYKO RST Plus optical profiler, a commercially available instrument, utilizes this principle to accurately measure surface topography of static structures [1, 2]. This instrument was modified to enable measurement of resonating structures. A diagram of the new instrument is shown in Figure 1. The halogen light bulb used in the original instrument has been replaced with an LED to enable rapid pulsing of the light source. The LED is driven by a variable-width pulse generator synchronized to a signal generator which excites the structure. Since many micromachined structures do not vibrate at atmospheric pressure, the structure is placed in a small vacuum chamber. A matched optical flat is used in the reference arm of the interferometer to allow interferometry through the viewport glass using a broad spectrum source.

Figure 2(a) shows an interferogram of a micromachined cloverleaf structure resonance mode at 7.767 kHz using continuous LED illumination. A significant blurring of fringes is observed, and the node-lines, where the motion is much less than the wavelength of the source, are clearly visible as areas with high-contrast fringes. Upon switching to pulsed-source illumination, high-contrast interference fringes are recovered over the whole structure as seen in Fig. 2(b). Figure 2(c) shows the structure under the same conditions as 2(b), except it has been tilted to accentuate the symmetry of the mode.

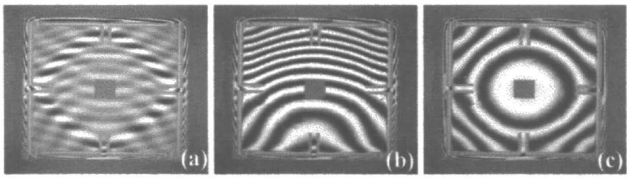

Figure 2. *Fringe pattern of the vibrating cloverleaf structure with (a) continuous illumination, (b), (c) pulsed illumination.*

The WYKO instrument uses a piezo vertical translation stage and a software package called WYKO Vision™ to interpret the fringe patterns and generate a high resolution surface profile. Figure 3 shows a three dimensional rendering of the cloverleaf structure modeshape corresponding to the fringe patterns in figure 2.

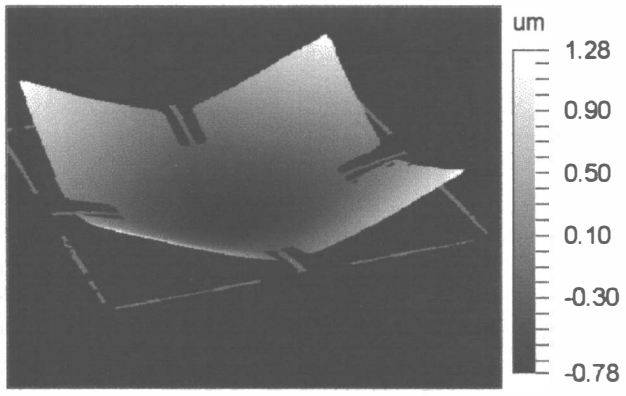

Figure 3. *Modeshape of the 7.767 kHz mode.*

0-9640024-2-6/hh1998/$20©1998TRF
DOI 10.31438/trf.hh1998.75

The modeshape is obtained by subtracting the two surface profiles at the maximum deflection points. (Note that one modeshape is insufficient when measuring the motion due to two nearly degenerate modes.)

EXPERIMENTAL RESULTS

This instrument has been used to characterize a number of micromachined devices. Here, we will show the results for a clover leaf structure used for a microgyro [3] and a vacuum sensor [4], and a deformable mirror for adaptive optics [5].

Using this instrument, we can determine all resonance modeshapes and frequencies, as well as Q's. These measurements are used to determine mechanical parameters such as membrane tension (in the case of the deformable mirror) and spring constants, characterize asymmetry, determine location of cracks and defects, and to aid analytical modeling.

The resonance frequencies are found by tuning the excitation frequency with the LED in pulsed mode. As the frequency approaches resonance the fringe pattern changes. The Q is then measured by measuring the width of the resonance peak.

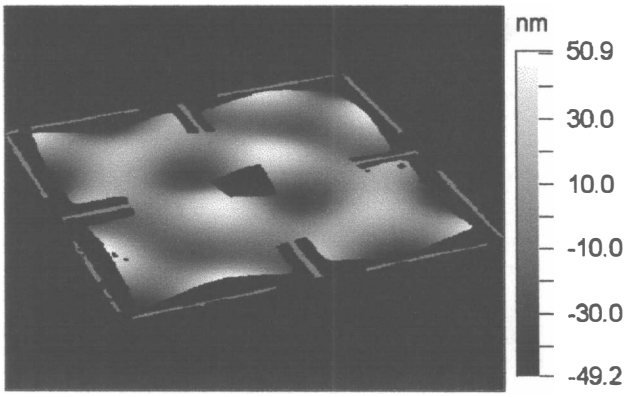

Figure 4. *Modeshape of the 102.270 kHz resonance.*

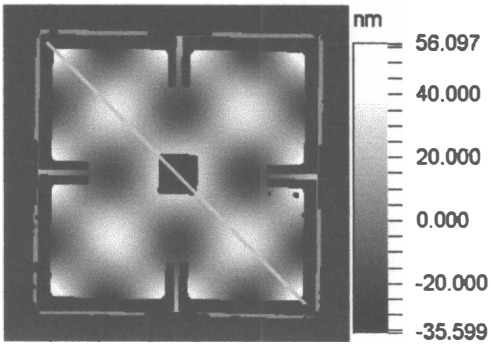

Figure 5. *Modeshape of the 105.615 kHz resonance.*

For the cloverleaf structure, we measured all modeshapes and frequencies for resonances up to 200 kHz. Each clover leaf in this structure is 2 mm on each side and 26 microns thick. The springs are about 100 microns wide. Figure 4 shows the modeshape of a resonance found at 102.270 kHz. The amplitude of the mode is only 50 nm peak-peak, but the instrument can easily resolve the motion. Quantitative information can be obtained as well, which is particularly useful when comparing identical devices. Figure 5 shows a different modeshape at 105.615 kHz. Figure 6 shows a cross-sectional profile along the diagonal of the cloverleaf. This plot reveals slight asymmetries in the mode which are probably related to variations in the thickness of the epilayer used in the bulk micromachining process.

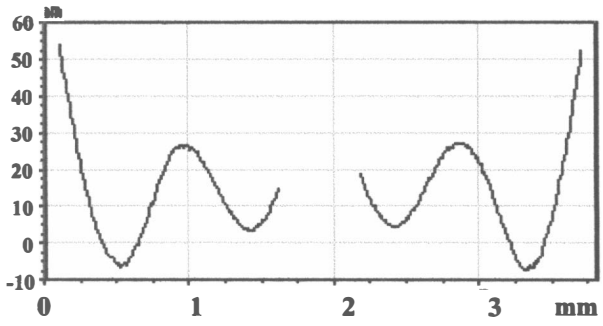

Figure 6. *Cross-sectional profile of the 105.615 kHz mode along the diagonal shown in Figure 5. Vertical scale is in nanometers.*

For the deformable mirror structure, modeshapes were measured up to 200 kHz as well. The mirror is made out of a 1 cm diameter Silicon Nitride membrane 0.5 microns thick with metal deposited on both sides. Table 1 shows several representative modeshapes that demonstrate the capability of the intrument. For the lower frequency modes, these measurements match theory relatively well. The surface is defined by circle polynomials where the radial variations are given by Bessel functions and the circumferential variations are sinusoidal functions. But as the fequency increases, the asymmetry in the membrane is more evident. This asymmetry is thought to come from a variation in the membrane tension. Note that all modes seem to be "locked" along the diagonal from the upper left corner to the lower right.

INSTRUMENT PERFORMANCE

The minimum resolvable out-of-plane motion was determined by taking a difference of measurements at the same position in the vibration cycle. The resulting RMS value integrated over the whole surface was 0.5 nm. This is the same as the resolution of the unmodified instrument for stationary structures.

When the motion of the structure is large, a small illumination duty cycle is required to maintain high contrast fringes. To maintain reasonable contrast, we have found that the motion in the duration of the illumination pulse should not exceed 50 nm or 10 % of the maximum structure motion, whichever is less. The LED's we used have a modulation bandwidth of 3 MHz. This puts a limit of about 300 kHz on the maximum frequency of motion that the instrument can measure. The maximum amplitude of motion resolvable at 300 kHz is about 600 nm for the LED presently used. These limitations can be overcome by using a semiconductor laser diode. The large modulation bandwidth of laser diodes would allow imaging of moving structures at frequencies up to about 100 MHz, which should be sufficient for any micromachined structure.

Presently, the lateral resolution is limited to 10 microns, since the lowest magnification objective was the only one that we fitted with the compensation optical flat required to measure inside the vacuum chamber. In principle, a higher magnification objective can be modified to match the latteral resolution of commercial optical microscopes (<1 micron). Since the structure is in vacuum, an important consideration is the working distance of the objective. With the current vacuum system, which has a 6 mm thick viewport, the working distance of the objective must be larger than 1 cm.

13230 Hz	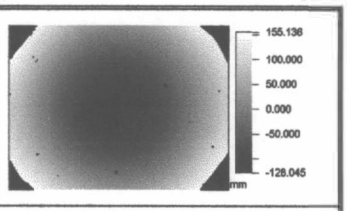
19568 Hz	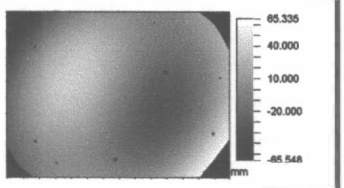
27043 Hz	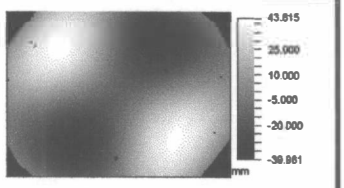
32648 Hz	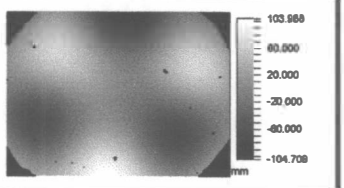
35888 Hz	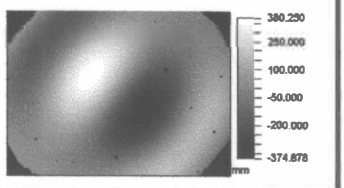
38901 Hz	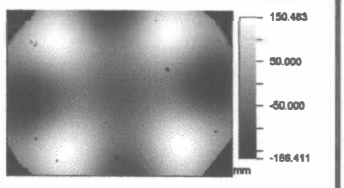
45062 Hz	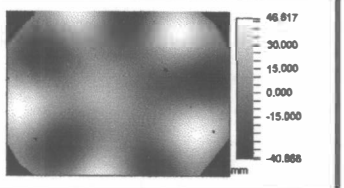
60590.2 Hz	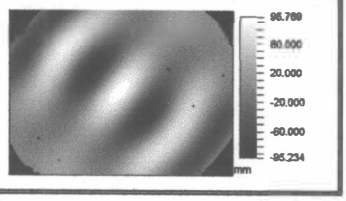

68637.2 Hz	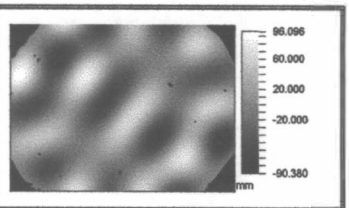
69047 Hz	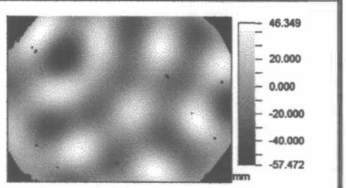
73032.5 Hz	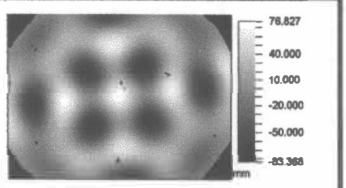
100656 Hz	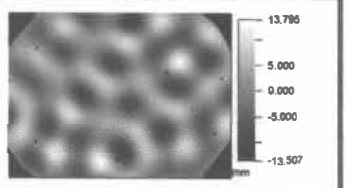
139441 Hz	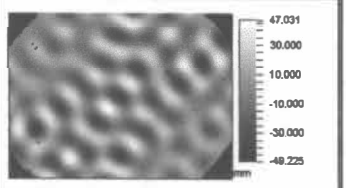
150811 Hz	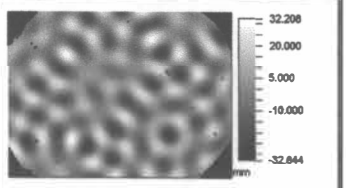
193148 Hz	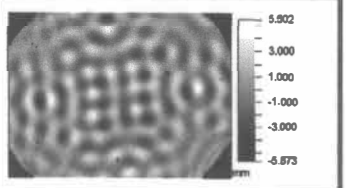
195782 Hz	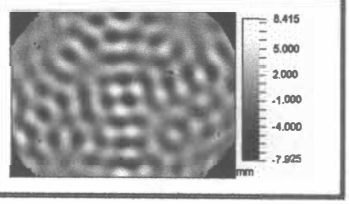

Table 1. *Selected modeshapes of the deformable mirror membrane*

APPLICATIONS

Potential applications of the pulsed-source imaging interferometer are very broad. While it was initially used to characterize the motion of microgyroscopes, the information this instrument provides is critical to characterizing mechanical properties for a wide array of MEMS devices. In the study of MEMS reliability, for instance, an accurate knowledge of the motion of the structure over long periods of time can help solve some of the most fundamental questions related to the lifetime and failure mechanisms of micromachined devices.

With a solid state laser light source the pulsed-source imaging interferometer should enable measurements of high frequency micro-mechanical resonators, such as acousto-optic modulators, SAW filters, quartz crystal oscillators, and micromachined RF resonators.

The inventors envision an eventual marriage of the instrument with FEA modeling software. Numerical modeling generates a prediction of resonance frequencies and modeshapes from three dimensional structural data. Comparing the predictions with the experimental data, an iterative process to match the two should result in a more accurate model of real micromachined structures. This will enable a much faster device development cycle.

CONCLUSION

This paper describes a pulsed-source imaging interferometer which was constructed by modifying a commercial optical profiler manufactured by the WYKO corporation. The instrument is used to measure resonance frequencies, modeshapes, and Q's of MEMS structures. The instrument measures motion with a resolution of 0.5 nm RMS which is the same as the profile resolution of the unmodified instrument for stationary structures. This instrument can be used to characterize a broad spectrum of MEMS devices adding important new capabilities to the MEMS research community.

A patent for this new technology has been filed by the California Institute of Technology.

ACKNOWLEDGMENTS

The work described in this paper was performed by the Center for Space Microelectronics Technology, Jet Propulsion Laboratory, California Institute of Technology, under contract with the National Aeronautics and Space Administration.

REFERENCES

1. P.J. Caber, "Interferometric profiler for rough surfaces", Appl. Opt. **32**, 3438-3441 (1993).

2. D.K. Cohen, P.J. Caber, and C.P. Brophy, "Rough Surface Profiler and Method", United States Patent No. 5,133,601 (1992).

3. T.K.Tang, R.C.Gutierrez, J. Wilcox, C. Stell, V. Vorperian, R. Calvet, W. Li, I. Charkaborty, R. Bartman, W. Kaiser, "Silicon Bulk Micromachined Vibratory Gyroscope", Tech Digest, Solid-State Sensor and Actuator Workshop, Hilton Head, S.C. pp.288-293, June 1996.

4. Roman C. Gutierrez, Tony K. Tang, Christopher B. Stell, Vatche Vorperian, and Kirill V. Shcheglov, " Bulk Micromachined Vacuum Sensor", the Ninth International Conference on Solid-State Sensors and Actuators, Transducers '97 , Chicago, IL, 1997.

5. L.M. Miller, M.A. Agronin, R.K. Bartman, W.J. Kaiser, T.W. Kenny, and E.C. Vote, "A Micromachined Deformable Mirror for Adaptive Optics Applications", 40th National Symposium of the American Vacuum Society, Orlando, FL, 1993.

SURFACE-MICROMACHINED 1MHz OSCILLATOR WITH LOW-NOISE PIERCE CONFIGURATION

Trey A. Roessig, Roger T. Howe, and Albert P. Pisano
University of California, Berkeley
Berkeley, CA 94720

James H. Smith
Sandia National Laboratories
Albuquerque, NM 87185

ABSTRACT

A prototype high-frequency tuning fork oscillator has been fabricated and tested in an integrated surface micromachining technology. The amplifier circuitry uses a capacitive current detection method, which offers superior noise performance over previous resistive methods. The prototype device has an output frequency of 1.022 MHz and exhibits a noise floor of –88 dBc/Hz at a distance of 500 Hz from the carrier. The dominant source of frequency instability is the nonlinearity introduced by the use of parallel-plate actuation.

INTRODUCTION

Oscillators appear in a wide variety of modern applications. They are used extensively in communication systems, both as frequency references and voltage-controlled oscillators. With the current trend towards smaller and more integrated systems, these applications would benefit greatly from the ability to integrate low-noise micromachined oscillators or arrays of oscillators onto the chip [1]. Oscillators are also used in number of sensors, including resonant sensors [2] and vibratory rate gyroscopes [3]. An improvement in the oscillator noise in one of these sensors results in an improvement in the noise floor of the sensor itself.

Previous surface-micromachined oscillators [2-5] have used resistive methods to detect motional current, introducing a relatively high noise floor into the system. This noise floor, in addition to causing its own phase noise far from the output frequency, forces the mechanical structure to vibrate at a high amplitude so the carrier can be seen. This causes nonlinearity in the vibration, which has been shown to be the dominant source of phase noise near the carrier [6].

This paper describes a prototype surface-micromachined oscillator based on a capacitive current detection method. Because of the large impedance at the sense node, the capacitive method introduces smaller amounts of input-referred current noise than the resistive method. This method of detection integrates the current at the input node, so it requires a second integration to properly complete the oscillation loop. This double integration loop is known in the oscillator literature as the Pierce configuration [7].

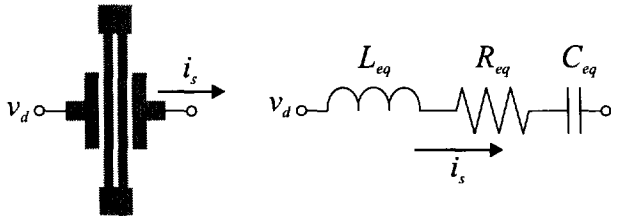

Figure 1. *Electrical behavior of micromachined tuning fork. The motion of the tines translates to current on the output node.*

This paper compares the various analog current-sensing methods and demonstrates that for low-noise applications, the capacitive method is superior. Next, the implementation of the oscillation amplifier is presented. Following this, the mechanical structure and electrostatic actuation are discussed. Finally, the experimental results from the system are presented.

CURRENT DETECTION

Surface-micromachined resonators, like quartz resonators, can be modeled as a series LCR circuit, as shown in Figure 1 [8]. A voltage is applied to the drive electrode of the resonator, and the response is a motional current on the sense node. So the problem of detecting resonator motion reduces to one of detecting current.

In CMOS technology, there are only a few ways of detecting

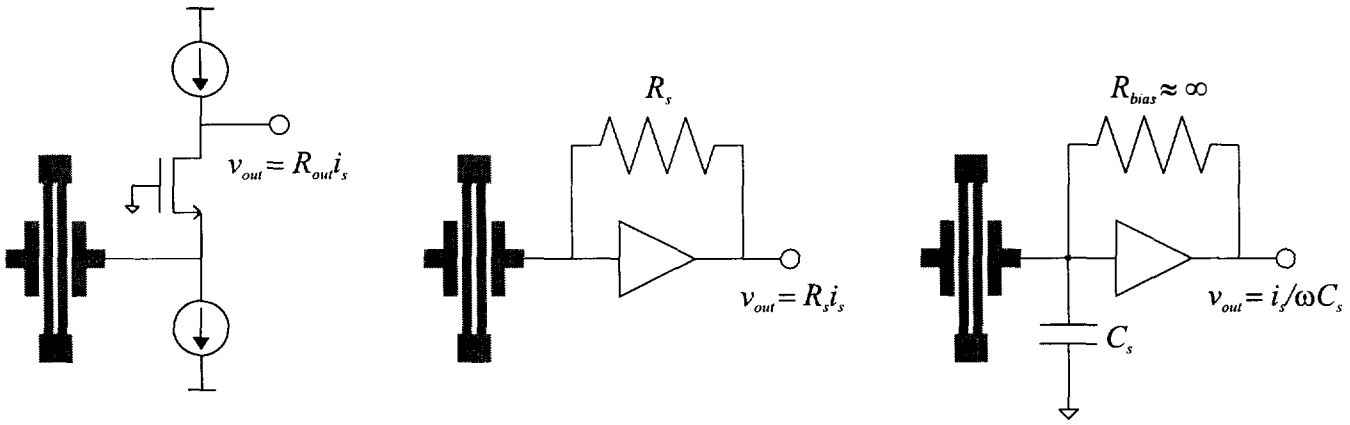

Figure 2. *Three potential methods of sensing motional current. From left to right, they are: common base detection, resistive detection, and capacitive detection. Each method introduces an equivalent current noise at the input node to the circuit.*

0-9640024-2-6/hh1998/$20©1998TRF
DOI 10.31438/trf.hh1998.76

Solid-State Sensors, Actuators, and Microsystems Workshop
Hilton Head Island, South Carolina, June 8-11, 1998

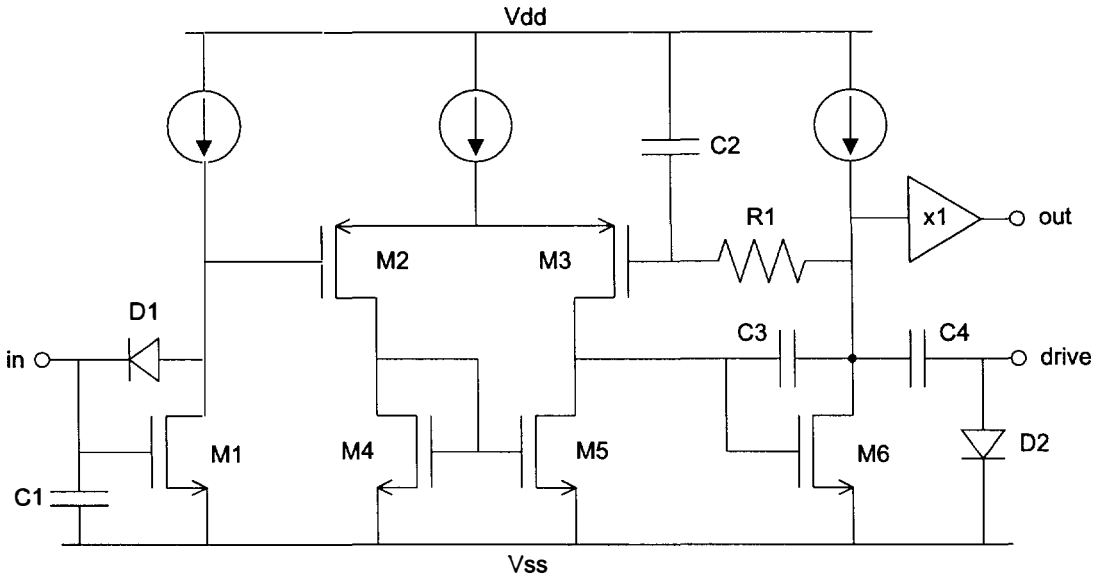

Figure 3. *Simplified schematic of Pierce amplifier implementation. Motional current is integrated at the input node. The M2-M3 differential pair serves as the input to the two-stage operational amplifier used both in the bias loop and as the second integration. The R1-C2 pair serves as the bias pole, and the compensation capacitor C3 serves as the integration pole. The output signal is AC-coupled to the resonator through C4-D2.*

current using non-sampled techniques. Three of these methods are shown in Figure 2. The first of these is the common base configuration, but the analysis holds for any other feedback configuration where the sense electrode is directly connected to the source or drain of a MOS transistor. In these cases, assuming the transistor is in saturation, the current noise introduced by the MOS is:

$$\bar{i}_n^2 = 4kT(\frac{2}{3}g_m) \tag{1}$$

where i_n^2 is the equivalent current on the sense node, and g_m is the transconductance of the transistor. Note that this equation does not include the effects of the bias and load current sources, which add additional noise.

The second method shown in Figure 2 is the resistive method. A resistor in series with the resonator can be used to create a voltage proportional to the motional current. This voltage can then be measured with a MOS gate without directly adding to the current noise on the node. With this detection method, the current noise at the sense node (ignoring the equivalent input noise of the amplifier) is:

$$\bar{i}_n^2 = \frac{4kT}{R_s} \tag{2}$$

The third method shown in Figure 2 is the capacitive detection method. This method involves integrating the output current by putting a capacitor in series with the resonator and measuring the resulting voltage. A resistor is still required for biasing purposes, but is large enough that the impedance at the sense node is dominated by the capacitor. In this method, the input-referred current noise is simply:

$$\bar{i}_n^2 = \frac{4kT}{R_{bias}} \tag{3}$$

It can be seen, then, that the lowest noise is achieved with the capacitive method. In the source/drain case, the g_m of the input transistor would have to be very small to lower the noise to a level comparable to the other methods. Unless the MOS is biased with an extremely small current, it is difficult to get a low enough g_m to do this. The resistive method is better, but as the sense resistor is increased to reduce the noise, the bandwidth of the input stage becomes unacceptably small. The capacitive pickoff method deliberately operates past the bandwidth of the input stage, so that it will integrate the current. This allows R_{bias} to be arbitrarily large, giving the capacitive method the lowest noise of the three.

Operating past the RC constant also has advantages in terms of resonator loading. The impedance at the input node for a given frequency can be shown to be [7]:

$$Z_{in} = \frac{R_{bias}}{R_{bias}^2 C_s^2 \omega^2 + 1} - j\frac{R_{bias}^2 C_s \omega}{R_{bias}^2 C_s^2 \omega^2 + 1} \tag{4}$$

where ω is the frequency in question.

Maintaining a high Q (low energy loss) in the system is important in sustaining oscillation and reducing phase noise [8]. Resistive impedances in series with the structure increase the damping and reduce the Q of the resonator. Reactive impedances change the frequency of the resonator itself, but have no effect on

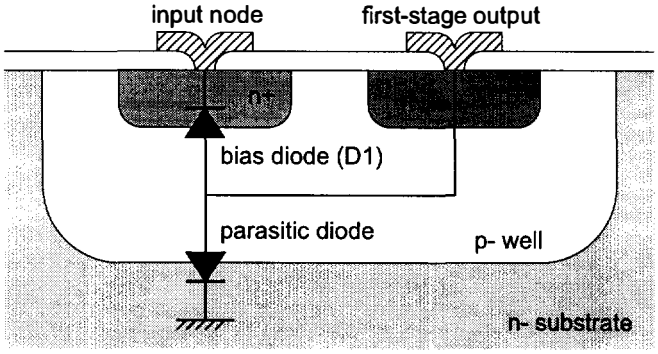

Figure 4. *Illustration of the parasitic diode. Layout is arranged so that the parasitic diode is on the lower-impedance output node.*

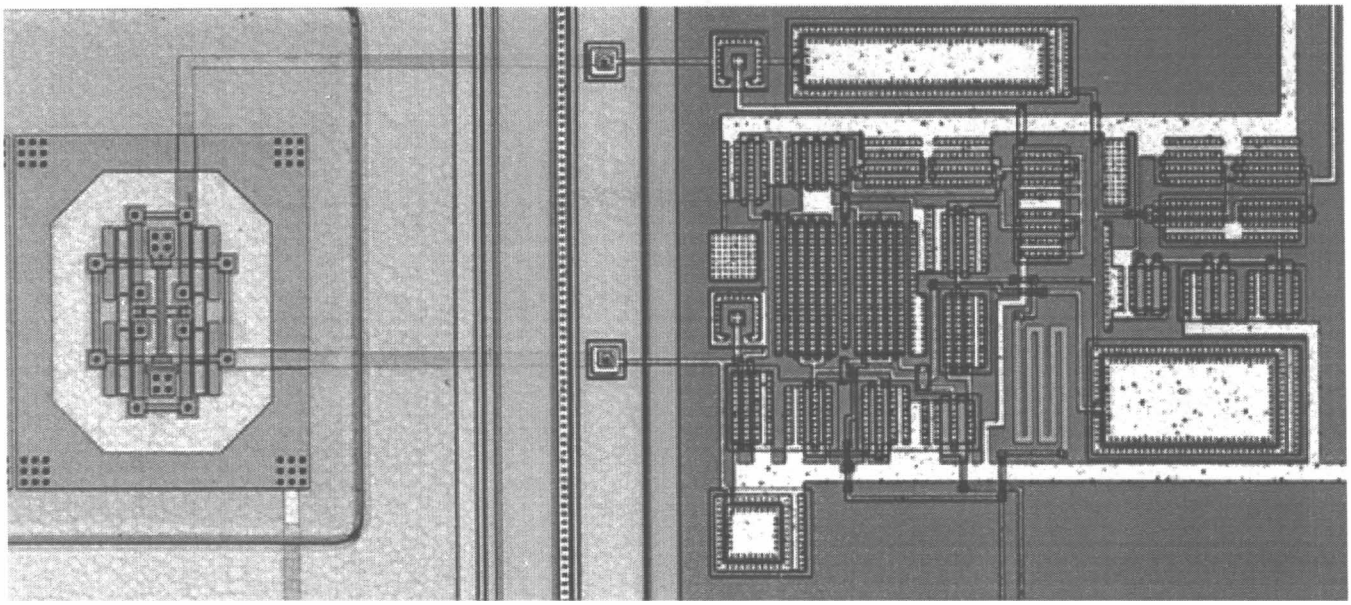

Figure 5. Die photo of fabricated oscillator. The resonator structure is fabricated in a bulk-etched well before CMOS processing. The die area shown here is approximately 450μm by 750μm.

the Q. Since the oscillator is designed to operate at a frequency well above $(R_{bias}C_s)^{-1}$, Equation 4 shows that the impedance at the input node is primarily reactive. This implies that, despite the presence of a large DC resistance, the input impedance does not reduce the Q of the resonator appreciably. What it will do is change the resonator frequency slightly. Fortunately, because of the stiffness of surface micromachined structures, this frequency pulling effect is minor [9].

AMPLIFIER IMPLEMENTATION

While the arbitrarily large resistors described above result in good noise performance for the amplifier, they can be difficult to realize. A few possible solutions are subthreshold MOS devices [3] or zero-biased diodes [10]. The latter is used here.

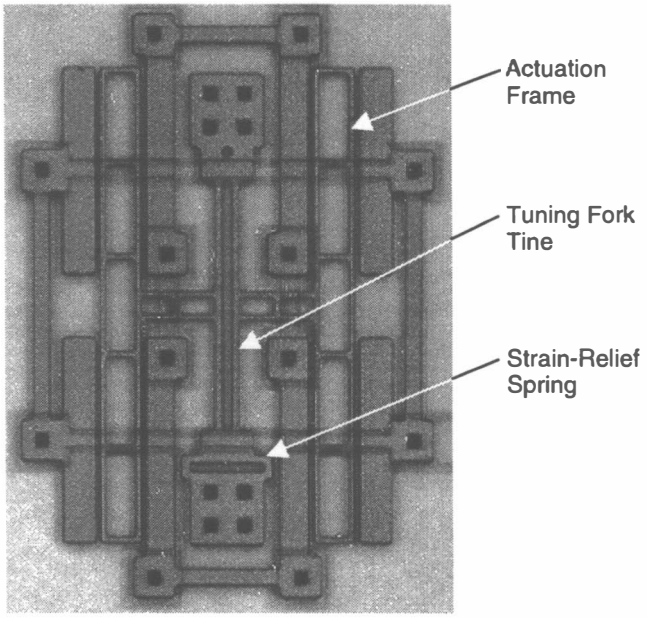

Figure 6. Close-up view of the resonator structure. The tines are 2μm wide, 60μm long, and 2μm thick.

Another issue with the Pierce implementation is the requirement of a second integration. It is difficult to get a pole low enough to be sufficient with a simple RC filter. In addition, because of the high impedance input node, small leakage currents can have a large effect on the bias point. The second stage must not only integrate the signal, but must be able to bias correctly for a large range of input voltages.

The circuit implementation chosen for the prototype device is shown in Figure 3. The first stage is a single common-source stage biased by a diode placed across the drain and gate. Since there is no DC current flow across the diode, ignoring leakage currents, the bias voltage across the diode is near zero. This results in a high small-signal impedance. A capacitor on the input node guarantees that the front end of the circuit is an integrator at the frequency of interest. It also reduces the effect of the parasitic feedback capacitance across the diode.

The layout of the bias diode (D1 in Figure 3) is important. The diode is placed in a p-type well, as shown in Figure 4. The device is laid out so that the parasitic well-substrate diode does not shunt the high-impedance input node. This prevents the leakage currents from the parasitic diode from affecting the input bias of the amplifier, which could render the circuit inoperable. This arrangement also removes the well depletion capacitance from the input node.

The remainder of the circuit is a simple two-stage op-amp with a Miller-compensated pole. The bias network around the amplifier forces the DC bias to be whatever the output voltage of the first stage is. In this case, the pole of the bias network was set with an off-chip capacitor. The bias network has no effect at the oscillation frequency, so the amplifier runs open-loop. The Miller pole serves as the second integration, completing the loop with the correct phase necessary for oscillation.

RESONATOR STRUCTURE

The resonator structure is a simple double-ended tuning fork. The reason for the use of this structure is the availability of high frequencies while maintaining a reasonable aspect ratio for the beams. One disadvantage of this structure, however, is its sensitivity to axial strains. This drawback has been reduced

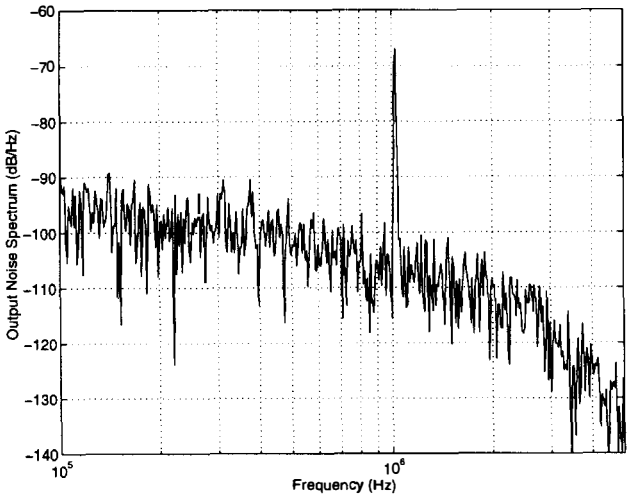

Figure 7. Far-field output noise spectrum of integrated oscillator. No higher harmonics of the oscillation are visible.

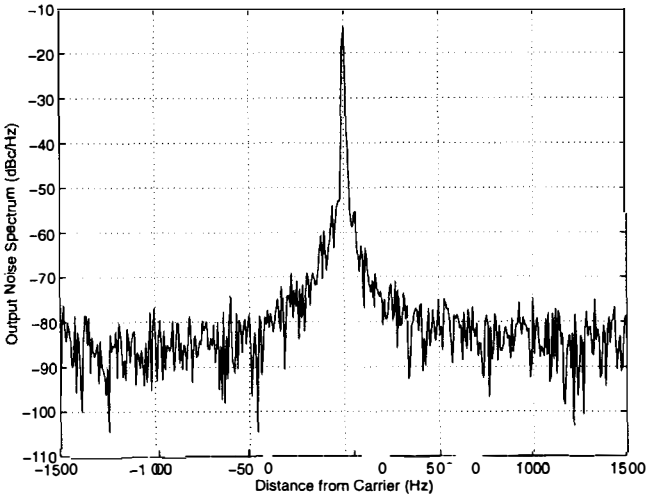

Figure 8. Near-carrier output noise spectrum of oscillator. The sidebands fall behind the noise floor at 500 Hz from the carrier.

somewhat by placing a strain relief spring at one end of the tuning fork.

The tuning fork tines are actuated with a balanced parallel plate structure. Each tine has equal sets of drive and sense plates, and the two tines are wired in parallel. This rejects the symmetric vibration mode of the structure, exciting only the high-Q antisymmetric mode.

The choice of parallel-plate actuation was made to lower the series resistance of the structure, but comes at a price. Parallel-plate actuators provide more transduction and add less mass to the structure than their comb-drive counterparts. This greatly reduces the series resistance of the structure, making it easier to sustain oscillation. The drawback to these actuators, however, is the nonlinearity associated with them. The force-displacement curve for the movable portion has a non-zero slope at the center, implying that the electrostatic forces impart a "negative electrical spring" to the structure [3]. This directly changes its natural frequency. Since the frequency change is a function of the DC voltage across the plates, the frequency of the oscillator becomes a function of that voltage. This implies the increased transduction has come at the price of reduced oscillator stability.

The structure itself is made of 2μm-thick polysilicon and consists of two parallel tines, each 2μm wide by 60μm long. Each actuation frame has stiffening bars to keep it from developing its own parasitic oscillation. All area underneath the structure that is not used for interconnect is covered with a polysilicon shield and shorted to the resonator to reduce feedthrough currents and eliminate pulldown of the structure itself.

The prototype oscillator described above was fabricated in Sandia National Lab's embedded MEMS/CMOS surface micromachining process [11]. A die photo of the resonator and oscillator are shown in Figure 5, and a close-up of the structure itself is shown in Figure 6.

EXPERIMENTAL RESULTS

The amplifier behavior can be tested by applying an input signal on the structural node of the resonator while the chip is held at atmospheric pressure. The amplifier input node sees a voltage capacitively divided between the resonator static capacitance and the input capacitor. This signal can be used to characterize the amplifier while the ambient pressure suppresses the oscillation. The behavior of the circuit is in line with expectations, with the integration pole appearing at about 350 kHz.

Mechanical oscillation is sustained when the chip is held in vacuum. The nominal output frequency of the device is 1.022 MHz. The far-field output spectrum from the oscillator is shown in **Figure 7**, as taken by a HP 4195A Spectrum Analyzer. Note the integrating nature of the circuit can be inferred from the downward-sloping noise. The 350 kHz pole can be seen in the noise shape, along with the 3 MHz bandwidth of the buffer used to drive the analyzer. There are no other peaks visible, implying the second and third harmonics are at least 45 dB below the carrier.

Oscillation is sustained for a surprisingly narrow range of structural polarization voltages, between 6.5V and 7.5V. For polarization voltages less than that, no oscillation begins, implying a large series resistance in the structure. For voltages higher than

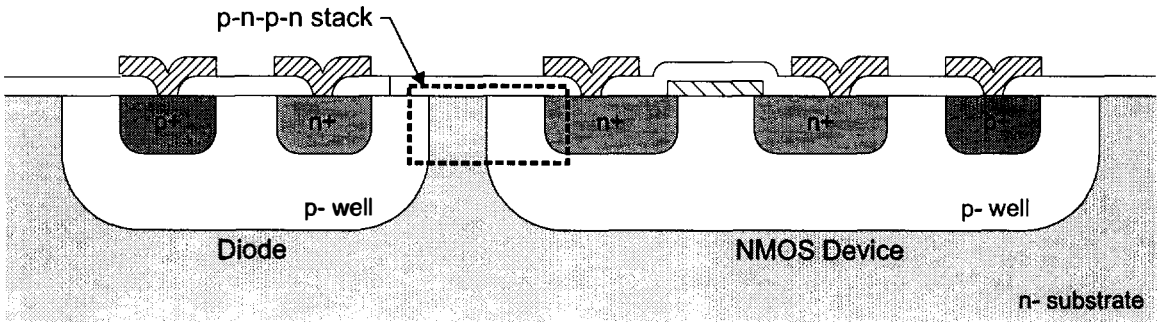

Figure 9. Illustration of the pnpn *stack that causes latchup in the front end of the circuit. Future layouts will include substrate contacts between the input devices and the bias diode.*

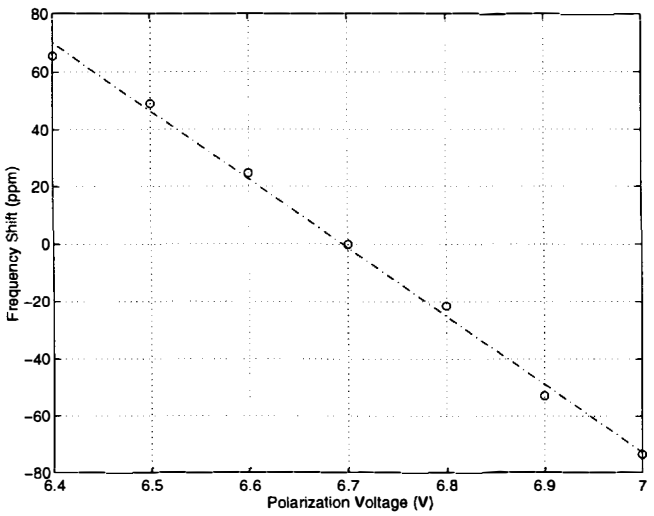

Figure 10. *Polarization voltage effect on natural frequency. The downward trend and linearity imply a direct effect on the natural frequency.*

7V, a large distortion can be seen in the waveform. For voltages higher than 7.5V, the input stage of the amplifier latches up. The layout of the bias diode next to the input NMOS, a cross-section of which is shown in Figure 9, creates a *pnpn* layer stack which results in latchup for large signals [12]. While a substrate contact was placed near the diode, it apparently was not enough to prevent this phenomenon. Future designs will include substrate contacts between the diode and input transistor.

The near-carrier output spectrum is shown in Figure 8. The noise floor of the circuit near the carrier is –106 dB/Hz and the carrier power varies between –18 and –29 dB, depending on the polarization voltage in use. This results in a best-case noise floor of –88 dBc/Hz at a distance of 500 Hz from the carrier. This number would have dropped even further, if not for limitation on the output power caused by the latchup problem. Nevertheless, this is more than a 20 dBc/Hz improvement over previous surface-micromachined tuning fork oscillators [2].

The oscillator does not suffer from the mechanical stiffening nonlinearity seen in previous tuning fork structures [6], or at least it is too small to be detectable. The dominant source of voltage-frequency dependence present is that of the electrostatic nonlinearity introduced by the parallel-plate actuation. Figure 10 shows the variation in frequency with changes in the polarization voltage. This plot shows a linear downward slope, indicative of direct natural frequency shifts. The slope of the curve, 250 Hz/V, is in good agreement with the model prediction of the nonlinearity.

CONCLUSIONS

A prototype high-frequency surface-micromachined oscillator has been fabricated and tested. Despite some difficulty with latchup phenomena in the input stage, the oscillator is still a large improvement over previous implementations from a background noise perspective. The dominant source of frequency shifts is the electrostatic nonlinearity present in the actuation. Future designs will incorporate extra protection against latchup, and will minimize electrostatic effects on natural frequency.

ACKNOWLEDGEMENTS

The authors would like to acknowledge the students of the Berkeley Sensor & Actuator Center for their help and support, Sandia National Labs for fabrication of the oscillators, and the DARPA MEMS program for financial support of this research.

Sandia is a multi-program laboratory operated by the Sandia Corporation, a Lockheed-Martin company, for the US Department of Energy under contract DE-AC04-94AL85000.

REFERENCES

1. C. T.-C. Nguyen, "Microelectromechanical devices for wireless communications", *Eleventh IEEE International Workshop on Microelectromechanical Systems (MEMS '98)*, Heidelberg, Germany, 1998, pp. 1-7

2. T. A. Roessig, R. T. Howe, A. P. Pisano, and J. H. Smith, "Surface-micromachined resonant accelerometer", *Ninth International Conference on Solid-State Sensors and Actuators (Transducers '97)*, Chicago, IL, 1997, pp. 859-862

3. W. A. Clark, R. T. Howe, and R. Horowitz, "Surface-micromachined vibratory rate gyroscope", *Solid State Sensor and Actuator Workshop*, Hilton Head, SC, 1996, pp. 283-287

4. C. T.-C. Nguyen and R. T. Howe, "CMOS micromechanical resonator oscillator", *IEEE International Electron Devices Meeting*, Washington, DC, 1993, pp. 127-134

5. T. A. Roessig, A. P. Pisano, and R. T. Howe, "Surface micromachined resonant force sensor", *Proceedings of the ASME Dynamic Systems and Control Division*, DSC-Vol. 57-2, 1995 ASME IMECE, San Francisco, CA, 1995, pp. 871-876

6. T. A. Roessig, R. T. Howe, A. P. Pisano, and J. H. Smith, "Nonlinear mixing in surface micromachined tuning fork oscillators", *IEEE Frequency Control Symposium*, Orlando FL, 1997, pp. 778-782

7. Robins, W. P., Phase Noise in Signal Sources, London, Peter Peregrinus, Ltd., 1982

8. C. T.-C. Nguyen, "Micromechanical signal processors", Ph.D. Dissertation, UC Berkeley, 1994

9. T. A. Roessig, "Integrated MEMS tuning fork oscillators for sensor applications", Ph.D. Dissertation, UC Berkeley, 1998

10. G. K. Fedder and R. T. Howe, "Multimode digital control of a suspended polysilicon microstructure", Journal of Microelectromechanical Systems, Vol. 5, No.4, 1996, pp. 283-297

11. J. H. Smith, et al., "Embedded Micromechanical Devices for the Monolithic Integration of MEMS and CMOS", *IEEE International Solid-State Circuits Conference*, San Francisco, CA, 1995, pp. 609-612

12. P. R. Gray and R. G. Meyer, Analysis and Design of Analog Integrated Circuits, 3rd Ed., New York, John Wiley & Sons, Inc., 1993

BISTABLE MEMS RELAYS AND CONTACT CHARACTERIZATION

Ezekiel J.J. Kruglick, Kristofer S. J. Pister
University of California Berkeley Sensors and Actuators Center
497 Cory Hall; Berkeley, CA 94720-1770, USA

ABSTRACT

A bistable switching relay structure for DC signals has been developed which provides a self-holding double gold contact with as low as 2.4 Ω measured contact resistance, 80mA current carrying ability, 7-12V actuation, and air gap isolation when open. The bistable frame structure can be used to design the holding force of the contact with minimal impact on actuator requirements. The frame also allows control over the necessary force and displacement of actuation almost independent of relay requirements. A lateral contact geometry was designed to allow fabrication of the relays in the MCNC MUMPs dual polysilicon foundry process with no assembly. The contact design was characterized using a polysilicon vernier structure to develop force/current/conductance curves and reliability information. The characterization data has been used to develop design information for microcontacts.

INTRODUCTION

MEMS relays have numerous potential applications. The North American relay market alone is US$1.4 billion, and the recent explosive market share of surface mount relays (from 1.2% in 1993 to 19.6% in 1997) demonstrates the value of miniaturization[1]. Additionally, new applications become available as it becomes feasible to integrate large numbers of relays onto smaller substrates. Some of our target applications are voltage generation in the hundreds of volts and similarly high voltage driver switching which cannot be realized reasonably with solid-state devices due to limited breakdown voltages. The low parasitic feedthrough can also be taken advantage of in certain high fidelity applications such as RF and sensor switching.

For our target applications the most important performance requirements are low drive voltages, truly "micro" size so that large scale integration is possible, and zero assembly. Impressive previous work has been done using electrostatic[2][3][5][6], magnetic[4], fluid flow[7], and thermal actuation[8] but none meet all three of our requirements. For large scale analog integration it is also important that a relay be bistable such as [9] to minimize power dissipation during non-transition periods.

Here we present a bistable MEMS frame which allows a relay to be realized which is bistable and can be actuated by a range of methods. Appropriate electrodes have been developed and tested, and the importance of force and current levels have been measured to define a functional design space for designing microrelays. The device has been fabricated in the commercial foundry MUMPs process [10] using a design which does not require assembly.

THE BISTABLE RELAY FRAME

The principle of the bistable frame is shown schematically in figure 1. The frame is fabricated in the open position. The rotary beams ride on fixed pin joints which allow them to rotate in a circular path. This circular path deflects parallel support springs inward as the structure transitions from one stable state to the other (figure 1b). In figure 1c the bistable action has been stopped as the crossbar runs into the electrodes. The remaining spring force from the bistable action holds the con-

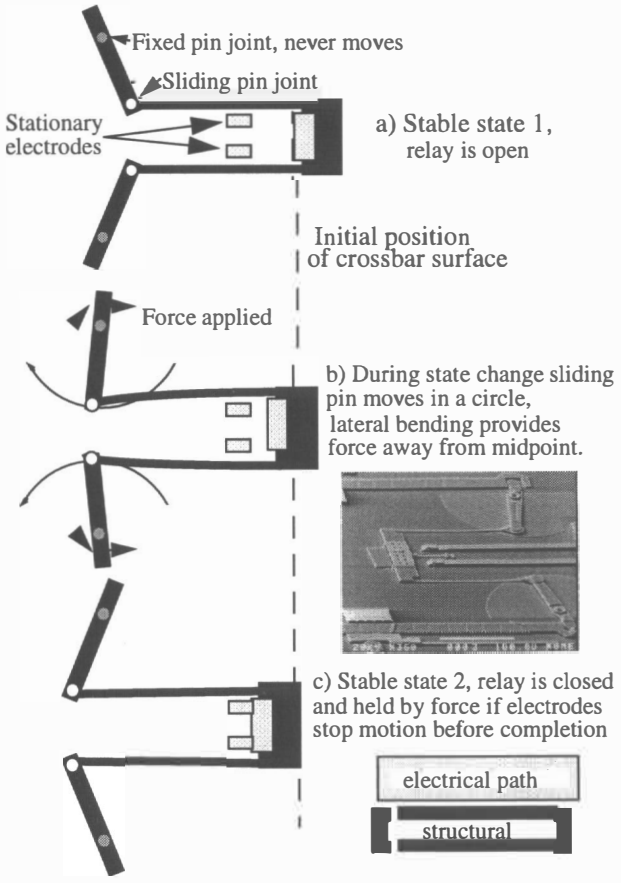

Figure 1. *Bistable action in the relay frame holds the device in an open or closed state without actuation. Inset SEM shows a bistable frame with pin & joint interface for use with a thermal stepper motor.*

0-9640024-2-6/hh1998/$20©1998TRF
DOI 10.31438/trf.hh1998.77

Solid-State Sensors, Actuators, and Microsystems Workshop
Hilton Head Island, South Carolina, June 8-11, 1998

tact shut. By changing the position of the electrodes the contact closure force can be changed.

Electrode placement controls the proportion of the spring force which is applied as contact force. The magnitude of the spring force can be controlled separately by design of the lateral flexing beams. Once the frame has been designed to set the contact force a particular moment around the fixed pin becomes necessary to actuate the bistable relay. The design of the rotating beam provides leverage between the actuator and the required moment, increasing design flexibility by allowing force/distance trade-offs. The minimum moment arm is currently set by fabrication requirements and play in the pin joints to about 4μm. Some improvement is possible.

Many designs were tried for the sliding pin joint. The most reliable we found is a circle of second poly over a toroid of first poly with a circle of contact from second poly to first poly within, but not touching, the geometry of the first poly. The overetch does not reach the substrate and the results is a strong and reliable sliding pin made with only two polysilicon layers.

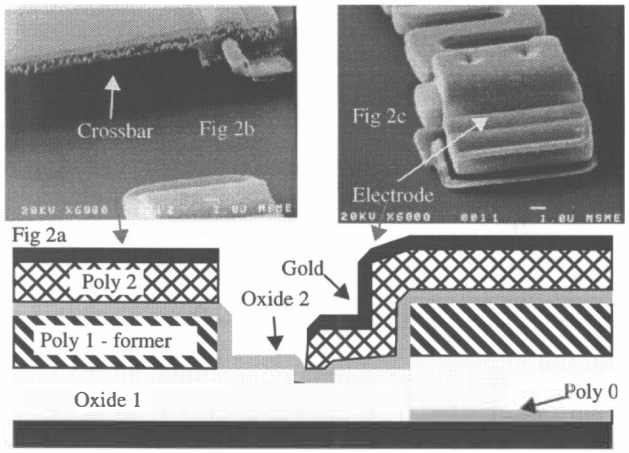

Figure 2. *Electrode and crossbar cross-sections. The crossbar (top polysilicon on the left) moves to the right during relay actuation, the first poly underneath it is a forming piece and is left behind. SEMs shows that some gold is deposited on the face of the crossbar where it will hit the gold face of the electrodes.*

CONTACT GEOMETRY

The process has two structural polysilicon layers and we want to allow a lateral relay contact design using final metallization (gold in the MUMPs process). Several lateral contact geometries were designed and a successful one is shown in figure 2. The crossbar (shown in figure 2b) provides contact by sliding into and

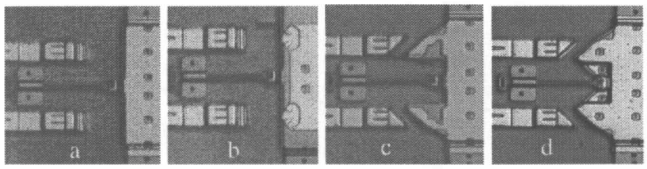

Figure 3. *Several different contact shapes using the cross section of figure 2. A and B have contact perpendicular to the applied force. C and D have contact at an angle to the applied force. A is the structure from the SEMs of figure 2. B has convolutions to reshape the gold. C has flexible angled contact arms on the crossbar. D is rigid, and has the best reliability and lowest contact resistance.*

bridging across two electrodes (figure 2c). The SEMs show an arrangement in which the contact and crossbar meet perpendicular to the forces being applied, this is equivalent to figure 3 a and b. Structures using the cross-section from figure 2 and the geometry shown in figure 3d had the lowest contact resistance and best reliability. The device shown in figure 3d exhibited a contact resistance below 9Ω when cycled over 80 times with a 5V open circuit, 400μA load and forces near 500μN. Fatigue testing of this sort has been limited by the inevitable eventual mistakes made at a manual probe station. Automatic test structures and SEM investigation of reliability are planned.

A direct thermally actuated [11] relay (non-bistable) using the structure in figure 3a achieved 2.4Ω contact resistance (for a total relay resistance of 4.8Ω) and 80mA current maximum when actuated at 7-12V. Cyclic testing was limited by a design flaw in the thermal actuators which required running them beyond elasticity to achieve contact.

A functional device with both frame and contact is shown in figure 4. These structures were also fabricated with vernier springs to measure the force required to actuate the bistable frame and

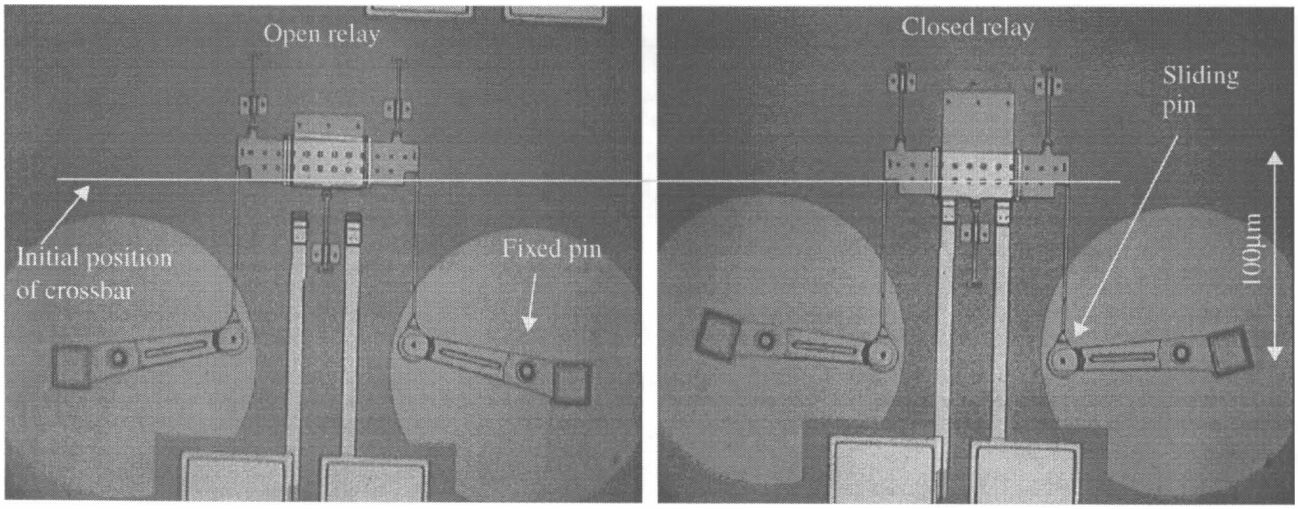

Figure 4. *Micrographs showing the bistable frame used to put the crossbar across the electrodes to form a bistable relay. Positions in between these are not stable and snap to one of these. The photo on the left corresponds to figure 1a and the photo on the right corresponds to figure 1c.*

achieve contact. On structures without stiction problems the snapthrough using geometries shown in figure 4 required less than 7μN (on a throw of 100μm) and achieved electrical contact consistent with the results in figure 6 when held by the force from the bistable frame. Thermal stepper motors have been demonstrated with arbitrary throw and greater force (50-100μN) than this[11]. One interesting point is that this force is best applied in a circle tangent to the rotating path of the actuating arm, leading us to a ball-in-slot actuating design to couple the motors and bistable frames. The ball in slot interface was designed by simulation in the Working Model software package[12].

CONTACT MATERIAL ISSUES

The primary consideration for microrelay contact design is contact area. Higher contact area corresponds to lower constriction resistance and lower contact temperature (with correspondingly longer contact lifetime and higher current levels). True contact area and quality at this scale is determined primarily by the hardness of the contact material and its resistance to forming surface layers, not by the apparent surface areas brought into contact. Thus the ideal contact material should be both soft and relatively corrosion resistant. Gold, the available metal in the foundry MUMPs process, fits these design criteria quite well.

A second consideration is the adherence force in the relay. The adherence force must be overcome to separate the electrodes and crossbar once contact has been made and depends greatly on the mode of operation. As the two contact surfaces come close the first interactions take place at asperities which project above the average surface of the contacts. Initial contact is elastic in nature and has fundamentally derivable electromechanical behavior. As the temperatures increase (softening the material) and the force increases the surface asperities begin to yield and deform progressively and contact becomes "weak" plastic behavior. Weak plastic behavior is more complicated than elastic and is typically characterized by empirical models[13]. As temperature and current densities continue to increase the contact material begins to liquefy and deform destructively and nonrepeatably. This is sometimes referred to as "strong" plastic deformation and is bad for reliability if the contact layers are microscopic, as here. We do not consider strong plastic deformation to be a viable operating regime for micro relays and have attempted to avoid it.

The elastic behavior adherence forces measured in [15] and elsewhere are different for different materials. There are significant differences between hard and soft metals.

The weak plastic behavior adherence force derived in [13] is approximately 40% of the closure force if the separation motion is perpendicular to the surface. This number is independent of contact material because it stems from clean metal-metal adhesion in areas where plastic deformation has broken away any surface film. The plastically deformed contact area is inversely related to the material hardness and the tensile strength to pull the contact area apart again is proportional to the hardness [14] so, to first order, the material hardness properties cancel if we assume plastic deformation is reached. It has been noted that harder materials such as rhodium show less adherence than gold at comparable force levels [15]. We are not interested in constant force contact design here, but rather comparable contact performance. Rhodium, a typical "hard" contact material, exhibits a higher resistance in the tests where it exhibits low adherence, and theory predicts that it will exhibit similar adherence once it deforms enough to match the lower resistance of gold contacts. Interestingly, the 40% adherence estimate means that for comparable performance with softer and harder metals the harder metal will have a higher adherence force because it takes more force to reach plastic deformation and low contact resistance. This implies that if large actuation forces are available, such as in macro relays, the hard and soft metal issue must be entirely reconsidered. One of the primary considerations in force limited design, then, is what regime of operation we wish to use in the contact: plastic or elastic deformation. If we run in plastic deformation, the design favors soft metals. Optimal design thus requires extensive contact characterization.

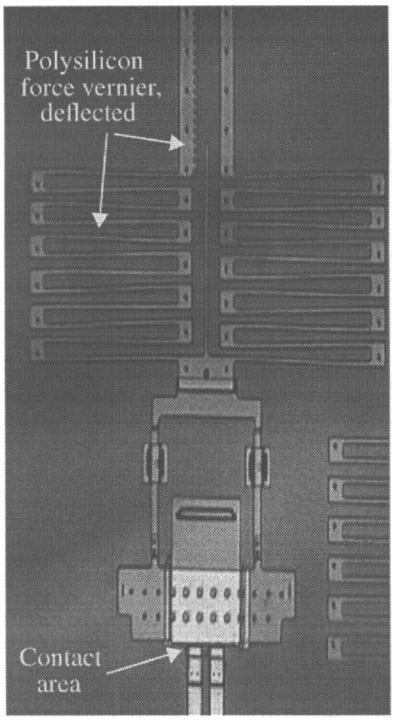

Figure 5. *Crossbar on polysilicon vernier to allow measurement of force during I-V contact characterization. Deflection of vernier is converted to force through linear beam theory.*

We expect designs such as the one in figure 3d with contact surfaces oblique to the applied force to exhibit lower adherence forces due to the occurance of shear rather than tensile separation. We have no quantitative estimate for this yet.

CONTACT CHARACTERIZATION

To characterize the contacts shown in figure 2 we designed structures supporting a crossbar on a vernier support with a predictable spring constant as in [16] (figure 5). The structure was pushed into contact using probes and the force was measured by measuring the displacement of the vernier springs on a video screen. The resolution of the system is 0.1μN after magnification, measurement, and calculation. Great care must be taken not to let stiction interfere with the measurements -- the vernier is only accurate when all the rovings are deflecting together in a coordinated fashion and the crossbar is sliding freely.

In order to characterize the mechanical mechanisms occurring at various current levels, I-V characteristics were taken at multiple forces and the data was fit to the established relation

$$G \propto aF^b . \qquad \textbf{(EQ 1)}$$

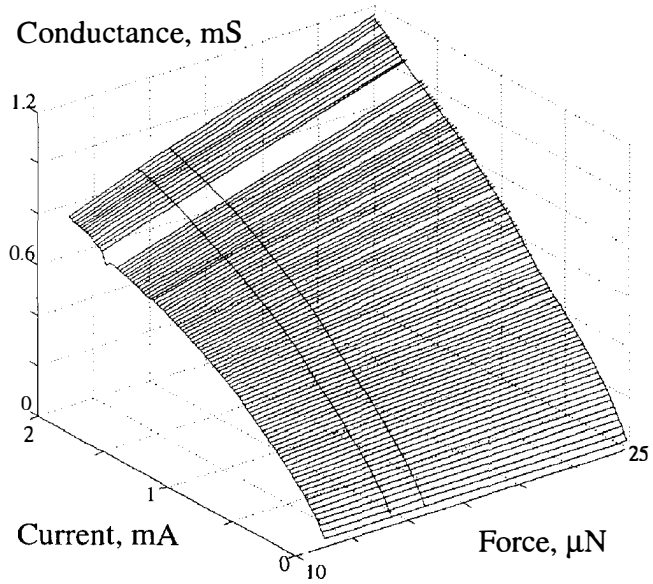

Figure 6. *Conductance versus force and current. Current is a factor because of temperature. Equicurrent lines represent model fits to equation 1. Data was not fitted for a group of four points where the data at the lowest force had bad values.*

Where G is the conductance, a is an offset, and b is the exponential relation between force and conductance. As surface asperities are forced against each other and electrical contact is made it can be calculated from basic principles that the conduction area goes as force to the 1/3 power during elastic behavior[17]. This means that we expect b to remain at 1/3 during the entire elastic regime. The exponent b has been approximated [13] as 0.5 during weak plastic deformation and unity during strong plastic deformation. Current, Conductance, and Force data is shown in figure 6. We expect the equicurrent fits to show different values of b as the gold contact asperities soften with temperature.

The resulting values of b from these fits are shown in figure 7. The expected elastic region (region I, b = 1/3) is clearly visible. At a certain current (and associated temperature) the value of b begins to increase again, signalling a transition into weak plastic

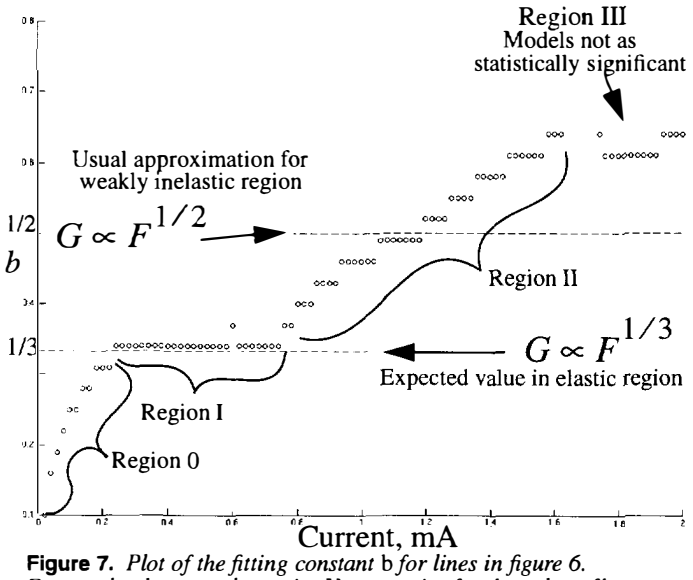

Figure 7. *Plot of the fitting constant* b *for lines in figure 6. Expected values are drawn in. Uncertanties for the value of* b *are 0.015. The data here shows experimental confimation of the predicted behavior.*

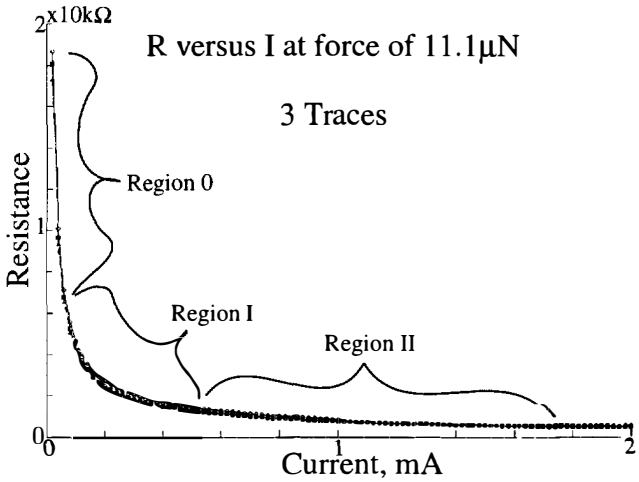

Figure 8. *3 successive traces of contact resistance versus current show the practical effects of the trends in figure 7 on contact performance. The similarity of the 3 traces show that the contact is not being degraded at these current levels.*

yielding (region II). As the current continues to increase the value of b begins to change more slowly and the statistical accuracy of the models degrade. The initial rise to 1/3 in figure 7 contains statistically very significant models but is not well understood. Previous work has indicated that at extremely small deformation levels the elastic behavior of gold increases by a factor of 10 and approaches the ideal crystalline strength[18]. It is possible that region 0 represents transition from this much higher modulus to bulk behavior, but this is still speculation. Currents beyond those shown here caused nonrepeatable degradation in contact behavior for this particular contact geometry and were therefore excluded from this test so that all data could be verified on the same structures. All I-V data sets were taken 100 times and any that did not prove consistent within our error bounds were discarded as unstable. Very good vibration isolation was required. Lifetime tests at different currents are underway.

Since the current carrying capability of a contact run in plastic deformation is significantly higher than during elastic deformation we want to design relays that run in the safe region of small scale plastic deformation (region II). Given our previous discussion of contact and adhesion force this design preference reinforces our decision to use the softest appropriate material.

IMPLICATIONS FOR DESIGN

The R-I curve in figure 8 shows 3 traces of data from the contacts being characterized. This data is from the same structure as produced the data in figure 6, but none of these traces were used to generate figure 6 or the models. The regions marked correspond to those in figure 7. The poorly understood initial rise to elastic behavior has been labelled as "region 0". This resistance to current relation shows that there are many regimes of operation which work in a repeatable fashion. If we design relays which operate in region II, the weak plastic deformation region, in a given application we can maximize performance and reliability while also optimizing materials for low force.

During data collection for figure 6 no current was applied to the relay during mechanical switching. The results show the regions of operation and predict behavior, but will not necessarily predict absolute resistances when switching under load.

CONCLUSIONS

We have designed a bistable frame for actuating a relay which provides a repeatable closure force, lever interface to actuators, and no force input requirement to hold the relay in place. Relays have been designed, fabricated and tested using this frame. The lateral contact design has been fabricated and tested to further explore design variables, and acceptable regions of operation have been established. The test data also provides insight into the behavior of microcontacts and allows for some materials considerations. Additional characterization will be needed for higher frequency performance.

Further research will explore the possibilities of single step actuation and further explore the physics of relays to advance design. The bistable relays presented here typically have a higher resistance than is desirable for our target applications but new contact shapes have demonstrated higher reliability and lower resistances.

Layout and additional information can be found online at www-bsac.eecs.berkeley.edu.

ACKNOWLEDGMENTS

We would like to thank Ron Wilson for his excellent SEM work and the Hertz Foundation for graduate student support. We gratefully acknowledge beneficial interaction with Dr. Joachim Schimkat of Berlin.

REFERENCES

[1] *Semiconductor Business News*, Monday, April 14, 1997 Vol. 5, No. 43

[2] Gretillat, M.-A.; Yang, Y.-J.; Hung, E.S.; Rabinovich, V.; Ananthasuresh, G.K.; De Rooij, N.F.; Senturia, S.D. "Nonlinear electromechanical behaviour of an electrostatic microrelay"1997 International Conference on Solid-State Sensors and Actuators. (Transducers 97), Chicago, June . p.1141-4 vol.2.

[3] Majumder, S.; McGruer, N.E.; Zavracky, P.M.; Adams, G.G.; Morrison, R.H.; Krim, J. "Measurement and modelling of surface micromachined, electrostatically actuated microswitches" 1997 International Conference on Solid-State Sensors and Actuators. (Transducers 97) Chicago June 1997. p.1145-8 vol.2

[4] Taylor, W.P.; Allen, M.G. "Integrated magnetic microrelays: normally open, normally closed, and multi-pole devices" 1997 International Conference on Solid-State Sensors and Actuators. (Transducers 97) Chicago, June p.1149-52 vol.2.

[5] Schiele, I.; Hillerich, B.; Kozlowski, F.; Evers, C. "Micromechanical relay with electrostatic actuation" 1997 International Conference on Solid-State Sensors and Actuators (Transducers 97) Chicago, June p.1165-8 vol.2

[6] Schlaak, H.; Arndt, F.; Hanke, M. "Silicon-Microrelay - a small signal relay with electrostatic actuator" Proceedings 45th Annual International Relay Conference, April 21-23 1997, Lake Buena FL, USA paper 10

[7] Simon, J.; Saffer, S.; Kim, C.-J. "A micromechanical relay with a thermally-driven mercury micro-drop" IEEE, The Ninth Annual International Workshop on Micro Electro Mechanical Systems, San Diego, CA, USA, 11-15 Feb. 1996. p.515-20

[8] Shifang Zhou; Xi-Qing Sun; Carr, W.N. "A micro variable inductor chip using MEMS relays" 1997 International Conference on Solid-State Sensors and Actuators. (Transducers 97) Chicago, June . p.1137-40 vol.2

[9] Sun, X-Q.; Farmer, K. R.; Carr, W.N. "A Bistable Microrelay based on two-segment multimorph cantilever actuators" 11th Annual Workshop on Micro Electrical Mechanical Systems, Heidelberg, Germany; January 25-29, 1998 p 154-159

[10] MEMS Technology Applications Center; 3021 Cornwallis Road; P.O. Box 12889; Research Triangle Park, NC 27709-2889

[11] J. H. Comtois, V. M. Bright; "Surface Micromachined Polysilicon Thermal Actuator Arrays and Applications," Solid-State Sensor and Actuator Workshop, Hilton Head South Carolina, 1996, pp 174-177

[12] Working Model 2D software, version 4.0; Knowledge Revolution 66 Bovet Road, San Mateo CA 94402

[13] R. Holm; "Electric Contacts" Almquist & Wiksells, Uppsala, 1946

[14] T.H. Courtney; "Mechanical Behavior of Materials" McGraw Hill, New York, 1990

[15] Schimkat, J. "Contact Materials for Microrelays" 11th Annual Workshop on Micro Electrical Mechanical Systems, Heidelberg, Germany; January 25-29, 1998 p 190-194

[16] Yeh, R.; Pister, K.S.J. "Measurement of static friction in mechanical couplings of articulated microrobots" SPIE, vol.2642, Micromachined Devices and Components, Austin, TX, USA, 23-24 Oct. 1995. p.40-50.

[17] Landau, L.D.; Lifshitz, E.M. "Theory of Elasticity" Pergamon Press, New York, 1986 p 31

[18] Oliver, W.C.; Hutchings, R.; Pethica, J.B. "Measurements of hardnes at indentation depths as low as 20 nanometers", Microindentation Techniques in Materials Science and Engineering, ASTM STP 889, 1986, p.7637-42

DEVELOPMENT OF RECHARGEABLE MICROBATTERIES FOR AUTONOMOUS MEMS APPLICATIONS

L.G. Salmon, R.A. Barksdale, B. R. Beachem
Electrical and Computer Engineering, Brigham Young University
Provo, Utah 84602-4101

R. M. LaFollette
Bipolar Technologies Incorporated
Provo, Utah 84604

J.N. Harb, J. D. Holladay, P.H. Humble
Chemical Engineering, Brigham Young University
Provo, Utah 84602-4101

ABSTRACT

This paper outlines fabrication and evaluation of a thin-film, rechargeable microbattery that provides sufficient power for many autonomous MEMS applications. Initial prototype microbattery cells achieved current densities greater than 12mA/cm^2 and were recharged for more than 260 cycles at an operating voltage of ~1.5volts. Other prototype microbattery cells produced current densities greater than 18mA/cm^2 and successfully recharged more than 35 times. The microbattery reported here was fabricated using high-volume, thin-film processes that produce microbattery cells with thicknesses of less than 100μm (excluding the inert substrate)and a form factor consistent with high-volume electronic assembly methods.

MEMS REQUIREMENTS FOR MICROBATTERIES

MEMS devices have the potential to revolutionize the way computational capability connects with the world of our experience. The paradigm of fabrication for MEMS provides the promise of inexpensive, capable sensing/actuation systems that will permeate our lives in the future. MEMS promise to greatly enhance the gathering, evaluation, and communication of information in future applications.

The great strength of MEMS as a technology frequently depends on 1) the ability that MEMS provides to combine great functionality in a single, integrated system solution, 2) the low-cost, high-volume nature of MEMS fabrication, and 3) the overall reduction in size and mass of sensor/actuator systems. Most existing technology emphasizes development of the technology necessary to fabricate MEMS and electronic devices that meet these three goals. The overall goals of many applications will not be met, however, unless an appropriate power source solution is developed as well. For many applications a thin-film microbattery is such a power source solution.

Table 1 compares the characteristics of several power source options with respect to size, weight, energy supply capability, and difficulty of assembling the battery into a low-cost, high-volume system. The characteristics of each of these power sources determines the area of application for which they can be used. As can be seen from the table, the microbattery provides a small, rechargeable, easily integrable power solution that no other power option provides. Of particular interest is the capability of microbatteries to be integrated into complete MEMS systems using automated assembly techniques developed for electronic systems. Use of these assembly techniques sharply decreases the cost and increases the obtainable complexity of integrated MEMS systems.

Power Source	Size	Weight	Energy Capability	Assembly Difficulty
From the Wall	Very Large	N/A	High	N/A
Battery Brick	Large	Heavy	Moderate	Very Difficult
Coin Type Battery	Small	Light	Low	Difficult
Micro-battery	Micro	Very Light	Low	Simple

Table 1 - Qualitative comparison of power source characteristics

Table 2 lists several potential high-volume applications for MEMS together with an indication of the power source requirements for the majority of applications in the given application area. As shown in the table, many of the application areas require an integrable microbattery power solution. In general, systems that require mobile, autonomous, extensively integrated sensors require a microbattery solution. A requirement for mobility excludes standard wired power sources. A requirement for autonomy excludes primary battery systems that cannot power integrated systems for extended periods. A requirement for small size, extensive integration, and large numbers of units excludes the use of coin or standard format batteries because of the difficulty of automated mounting such batteries into integrated system formats.

Microbatteries also have performance advantages that can be critical to specific system applications such as: multiple, definable voltage levels, high level of integrability, and better power distribution.

0-9640024-2-6/hh1998/$20©1998TRF
DOI 10.31438/trf.hh1998.78

Applica-ton/ Require-ment	Remote Sensing Arrays	Integrated Fluidic Systems	Low-power Displays	Embedde d Sensors	Optical MEMS
Size	Micro	Small	Small/ Large	Micro/ Small	Micro/ Small
Weight	Very Light	Light/ Heavy	Light/ Heavy	Light/ Very Light	Light/ Very Light
Energy	Low	Moderate	Moderate	Low	Low/ Moderate
Assembly Difficulty	Simple	Moderate	Moderate	Simple	Simple/ Moderate
Extemal Recharge	Required	Not Always Required	Required	Required	Not Always Required
Required Power Solution	µBattery	Coin/ µBattery	Brick/ µBattery	µBattery	Coin/ µBattery

Table 2 - MEMS applications and associated power source requirements

BACKGROUND

Thin-film rechargeable batteries (batteries with active layers on the order of 1-10µm) have been a topic of research since at least the early 1980s. Thin-film microbatteries using a metallic lithium electrode layer have been reported.[1] These batteries have lateral dimensions greater than a centimeter and produced relatively low current densities.

Bates *et al.* built on this work and reported a thin-film, microbattery with electrodes of metallic lithium and $LiMn_2O_4$ and with a solid, Li_3PO_4 electrolyte. [1,2] The authors also reported development of a multi-layer coating that protected the highly reactive lithium electrode from reaction with the microbattery environment.

The $Li/LiMn_2O_4$ electrochemical system produced an output voltage between 3.8 and 4.5 volts and were able to be cycled from charge to discharge more than 600 times. The microbattery cells described in these papers were fully solid state and were processed using evaporation and sputtering deposition techniques. The microbattery cells reported in reference 1 exhibited an energy capacity of 34.2mC/cm^2 (9.50µA-hr/cm^2) at a current density of 8.3µA/cm^2 and an output voltage of ~4.1volts.

Due to diffusion limits in the $LiMn_2O_4$ cathode, current densities for the reported $Li/LiMn_2O_4$ cells were limited to less than 1mA/cm^2 and battery output current densities above 0.2mA/cm^2 resulted in reduced energy capacity. For example, the microbattery reported in reference 1 produced a maximum current density of 0.83mA/cm^2 but with an energy capacity of 20.8mC/cm^2 at an output voltage of ~3.9volts.

The low current density and energy capacity of the microbatteries reported by Bates *et al.* limits their use in many MEMS applications, even those with low-power requirements. The reactivity of metallic lithium also limits the integration of the microbattery process with integrated circuit and MEMS processes.

The goal of the work reported in this paper is to produce a microbattery that can produce current densities greater than 10mA/cm^2, with an associate energy capacity ofgreater than 250mC/cm^2. Battery output voltage must also be greater than 1.0volt. Higher system voltages can be easily obtained using these 1.0volt cells due to the ease with which the microbattery cells can be placed in series to produce higher output voltages.

The Ni/Zn system using a KOH electrolyte was selected because it met these requirements. The open circuit voltage of this electrochemical system is 1.73 volts and high current densities are possible. The promise of this system was born out by the measured results reported here for microbattery cells fabricated using the NiO-OH/KOH/Zn system. Fabricated prototype microbattery cells produced current densities as high as 12mA/cm^2 with an associated energy capacity of 290mC/cm^2 at an output voltage of ~1.5volts.

FABRICATION

The microbatteries developed in this work are based on a Ni/Zn electrochemical couple and an aqueous KOH electrolyte. The processes used to fabricate the microbatteries are all traditional integrated circuit processes and were fabricated in the class-10 cleanroom facility of the Integrated Microelectronics Laboratory at Brigham Young University. The completed microbattery structure has a thickness of less than 100µm, excluding the thickness of the base silicon substrate. Figure 1 illustrates the process flow using schematic profiles of the process during fabrication.

The process begins with growth of a global, thermal SiO_2 layer on the silicon substrate. The purpose of the SiO_2 layer is to electrically isolate the first battery electrode from the substrate and from other microbattery cells. The only function of the silicon wafer is to act as a substrate for subsequent fabrication and it does not participate electrically in the function of the microbattery.

Following SiO_2 growth, a 0.7µm Ti/Ni plating base is deposited by e-beam evaporation and the first electrode is globally elecro-deposited. The electro-deposited material is 5µm of NiO-OH that reacts with Zn and H_2O to form $Ni(OH)_2$during discharge of the microbattery cell. At this point of the process, no patterning of the wafer has occurred and figure 1-a) represents the wafer profile.

A photosensitive layer is then spin-deposited on the wafer and the first electrode material is patterned using an aqueous etch of the NiO-OH and Ni layers. The patterned etch is required in order to separate individual microbattery cells as shown in figure 1-b).

Following the deposition and patterning of the first electrode, a 10µm layer of Dupont Pyralin 2611D polyimide is spin-deposited on the wafer and cured at 210C. Following cure of the polyimide, a 1µm layer of Zn is thermally evaporated onto the wafer to form the top electrode of the microbattery. A photoresist layer is then deposited and a pattern is developed. The Zn layer is then etched with HCl using the resist as a mask. The structure profile at this point of the process is illustrated in figure 1-c).

The patterned Zn then serves as a mask for subsequent O_2 etching of the well for the electrolyte in the polyimide. The etching is performed using a plasma etcher that provides an isotropic etch of the polyimide. The polyimide is thus etched underneath the Zn

mask and the resulting structure profile is shown in figure 1-d). The amount of underetch is critical to proper operation of the microbattery since the cavity volume determines the current output of the cell. During the development phase of the process, test wafers were fabricated that replaced the Zn layer with an evaporated layer of SiO_x. The SiO_x layer is transparent and when test wafers and microbattery wafers were etched in the same etch run, the test wafer could be used to visually evaluate the cavity volume.

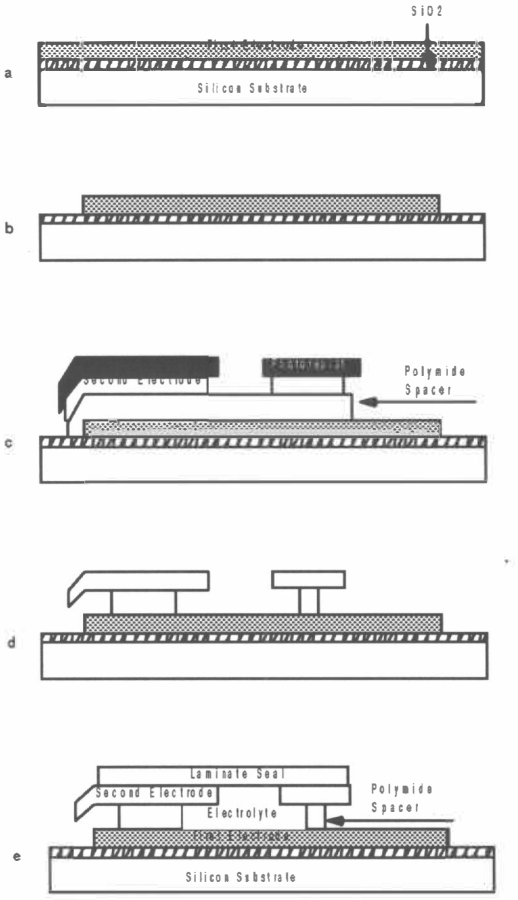

Figure 1 - Outline of the microbattery process

After etching of the cavity, the cavity is filled with the liquid, 5 Molar KOH electrolyte. During the development of this technology the microbattery cavities were filled individually using a teflon coated syringe needle that was manipulated into position using a probe station and an adapted probe manipulator. Eventually filling will be performed using a batch process. After completion of cell formation, the cells can be sealed using a laminated polymer film. Contact to the Zn and NiO-OH layers is then made through contact holes etched in the polymeric overlayer. The final microbattery profile is shown in Figure 1-e).

Figure 2 is a micrograph of a completed microbattery prototype that was $(200\mu m)^2$. The rough surface of the lower microbattery electrode is critical to the high-capacity of the cell. Also note the etch/fill hole in the top Zn electrode layer. This hole is the opening in the electrolyte cavity. During prototype fabrication, a teflon coated needle was used to introduce the small volumes of KOH required for operation of the cell. This opening can be sealed using an inert polymeric laminate after filling of the electrolyte cavity.

Microbattery cells were fabricated in the Integrated Microelectronics Laboratory at Brigham Young University using the process discussed above. Microbattery cells were fabricated with various geometries from a minimum size of $(100\mu m)^2$ to a maximum size of $(1000\mu m)^2$. All of the cells had a thickness of less than $100\mu m$, excluding the thickness of the substrate. A variety of microbattery geometries were fabricated and the current density results were found to scale with area except for the minimum size microbatteries, $(100\mu m)^2$, where processing limitations significantly degraded microbattery performance.

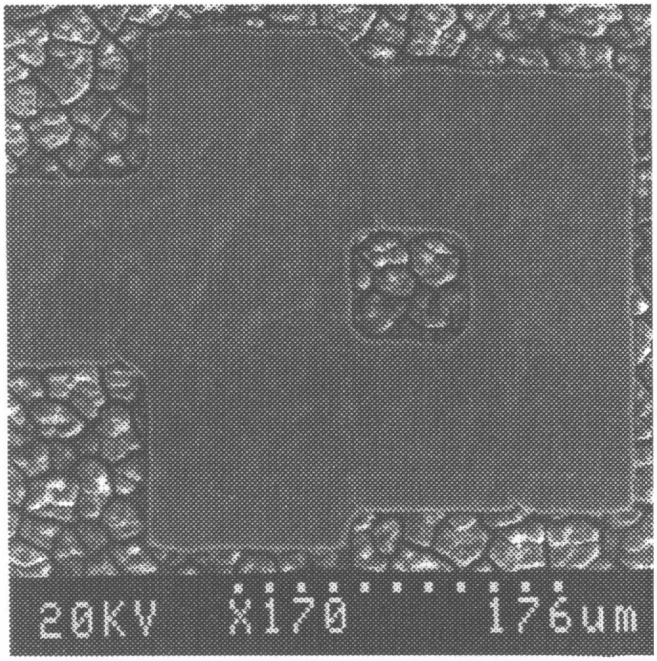

Figure 2 - SEM micrograph of microbattery cell

MEASUREMENT RESULTS

Initial prototype microbatteries fabricated using this process provided capacities of 200-300mC/cm² at current densities of 10 to 20mA/cm². Given an operating voltage of approximately 1.5 volts, these cells produced power densities from 15mW/cm² to 30mW/cm². The results from this work are much higher than current density results reported by Bates *et al.* for $Li/LiMn_2O_4$ microbatteries and were within the original design targets for the Ni/Zn microbattery cell.

Figure 3 shows discharge data for a set of six microscopic Ni/Zn, $(300\mu m)^2$ cells connected in parallel. These cells produced an average current density of 12.2mA/cm² and showed an adequate cycle life of 265 cycles. It is believed that the cycle life of these cells was limited by loss of electrolyte from the cells and will be improved by sealing the cells prior to testing. Greater detail of the measurement of these cells is provided in the paper by LaFollette *et al.*[4]

Although the current densities reported for these cells is high enough for many MEMS devices, the energy capacity is lower than needed for many autonomous applications. As part of this work, the

authors have developed an improved procedure for plating of the NiO-OH electrode that has resulted in energy capacities of greater than 2C/cm^2 in patterned microscopic electrodes. Work is continuing whose goal is to incorporate this high capacity electrode material in a complete microbattery cell. If this improved electrode material is successfully implemented into the microbattery structure described in this paper, a microbattery system consisting of a set of (200μm)^2 microbattery cells with a total area of 2cm^2 will provide for the period of an hour between recharging: a peak current of 20mA, an average current output of 1mA, and an output voltage of 1.5volts. Applications requiring longer time between charges can be accommodated in a straightforward manner by decreasing average power consumption, increasing the microbattery area, or by stacking the microbattery cells to decrease the system area required to obtain the required energy density.

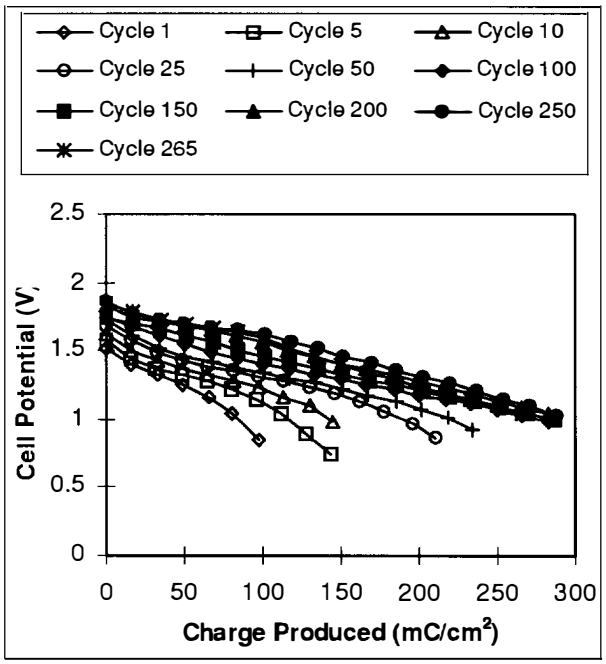

Figure 3 - Performance of a set of parallel microbattery cells

CONCLUSIONS

This work reports fabrication and testing of a thin-film, microscopic Ni/Zn battery that can provide the power requirements for a number of MEMS applications. The fabricated microbattery cells were measured and provided current densities as high as 12mA/cm^2 at an output voltage of ~1.5volts and were cycled through the charge/discharge cycle more than 260 times. The energy capacity of these same cells was 290mC/cm^2. A new electrode deposition process tested using macroscopic thin-film batteries was measured to have an energy capacity of 2C/cm^2. Future work incorporating this electrode material into a thin-film microbattery promises to produce microbattery cells that provide current densities as high as 10mA/cm^2 for extended periods.

ACKNOWLEDGMENTS

This work was sponsored in part by the Ballistic Missile Defense Organization (Contracts F33615-96-C-2674 and F33615-97-C-2785) and the U. S. Air Force (Contract F29601-96-C-0078). Their support is gratefully acknowledged.

REFERENCES

[1] J. Bates, G. Gruzalski, N. Dudney, C. Luck, X.-H. Yu, and S. D. Jones, "Rechargeable Thin-Film Lithium Microbatteries," *Solid State Technology*. (July 1993) pp. 59-64.

[2] J. Bates, D. Lubben, and N. Dudney, "Thin Film Li-LiMn2O4 Batteries," *Proceedings of the 10th Annual Battery Conference on Applications and Advances*. (1995) pp. 319-321.

[3] R. LaFollette, J. Harb, J. Holladay, P. Humble, L. Salmon, R. Barksdale, B. Beachem and D. Ryan, "The Peformance of Microscopic Batteries Developed for MEMS Applications," *Proceedings of the IECEC'98 Conference*. (August 1998) to be published

CHARACTERIZATION OF A MICROMACHINED ELECTRICAL FIELD-FLOW FRACTIONATION (μ-EFFF) SYSTEM

[1]Bruce K. Gale, [1,3]Karin D. Caldwell, [1,2]A. Bruno Frazier
[1]Department of Bioengineering, [2]Department of Electrical Engineering, [3]Department of Chemistry
University of Utah, Salt Lake City, UT 84112

ABSTRACT

This work introduces a μ-EFFF system with an integrated conductivity detection scheme. Critical parameters in the μ-EFFF system are examined including the steric transition point, system time constants, time to equilibrium, and the effects of flow rate and applied voltage on band broadening and resolution. In addition, the design, fabrication, and testing of an on-chip conductivity detector is described. The critical parameters for the on-chip conductivity detector are compared to an off-chip detector. System improvements including a streamlined channel geometry and a refined interface technique are demonstrated. Electrical time constants were reduced to the point where alternating fields may be possible. Plate heights reduced significantly with miniaturization of the system, especially with the addition of an on-chip detector. Resolution using the off-chip detector was comparable to that for macro-systems but the analysis time is one-third that of macro systems. Resolution using the on-chip detector was five times better than for the off-chip detector with an additional 50% reduction in analysis times.

INTRODUCTION

Electrical Field- Flow Fractionation (EFFF) was first described in the mid-60's, but a functional system was not built until 1991 [1]. The system was found to be excellent for the separation of colloids and other suspensions. Recently, our lab announced the development of a miniaturized EFFF system fabricated using micromachining technologies [2]. EFFF theory suggests that miniaturization of the system will improve the resolution and separation capabilities of the system by increasing the effective field realized in the channel.

Electrical Field-Flow Fractionation relies on an electric field perpendicular to the direction of separation as shown in Figure 1. The separations are performed in a low-viscosity liquid (typically an aqueous buffer solution) which is pumped through the separation channel. EFFF controls the relative velocity of particles by forcing particles towards the wall of the channel. Particles with high charge density pack closer to the wall while particles of lower charge density form a more diffuse cloud. Since flow in the channel is laminar and therefore parabolic, the particles move through the channel at differential rates based on charge and particle size. Since particle size can be determined using other techniques, the effect of the EFFF process is to separate particles by charge.

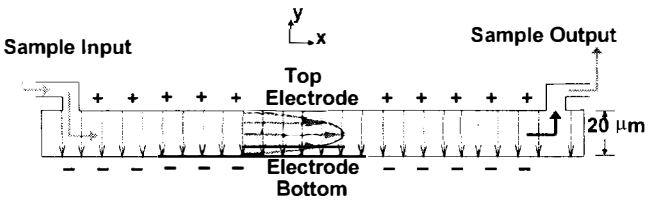

Figure 1. *Schematic diagram of the operation of an EFFF system.*

EFFF allows collection of fractions and has the ability to perform separations on cells, large molecules, colloids, emulsions, and delicate structures such as liposomes: separations that may be difficult or impossible in other separation systems. Applications of EFFF include cell and organelle separations, characterization of emulsions, liposomes, and other particulate vehicles, quick and accurate separations of macromolecules, environmental water monitoring, and tests for sample contamination. EFFF systems also find application in sample pretreatment.

In the last several years, great progress has been made in the fabrication of micro-scale separation systems. A myriad of successful micromachined systems of all types have been demonstrated. These publications detail several advantages found in miniaturized separation systems including increased resolution, reduced separation time, smaller sample size, and increased manufacturing precision. EFFF systems also improve when scaled into the micromachining domain.

Current macro EFFF systems are constructed using slab conductors with a thin, patterned mylar sheet between them [1]. The mylar acts as a dielectric spacer and defines the separation channel. Typical macro systems have a length of 30 to 60 cm, a height of 127 μm or greater and a height of about 2 cm. Some experimentation was done with smaller channels, but very little has been published on the subject. Our recently published development of micromachined channels produced systems that were 6 cm in length, 8 mm in breadth, and 20 μm in height [2].

THEORY

The EFFF channel, as shown in figure 1, is a thin channel of rectangular cross-section with an aspect ratio over 80. (The high aspect ratio is required to approximate infinite parallel plates.) In general, the theory behind FFF systems is well developed [3]. Understanding the theory behind EFFF is critical in understanding the operation and applications of EFFF systems and in determining the advantages created by miniaturizing the system. Several parameters of the EFFF system are expected to change with the channel height including plate height, steric transition point, the time for samples to equilibrate in the channel, electrical time constants, and effective fields in the channel.

In EFFF, an electric field is used to control the average velocity of the particles in the channel by controlling the average distance an exponentially distributed cloud of particles protrudes into the flow stream with respect to the top and bottom surfaces of the channel. If the electric field is applied as shown in figure 1, particles with higher charge will reside closer to the wall of the channel than particles with a lower charge. The particle cloud protrudes less into the flow stream and therefore has a lower velocity than particles in the middle of the stream. The difference in average velocity produces the separation. The equation for the resolution, R_s, of an EFFF system is shown in equation 1, where

0-9640024-2-6/hh1998/$20©1998TRF
DOI 10.31438/trf.hh1998.79

Solid-State Sensors, Actuators, and Microsystems Workshop
Hilton Head Island, South Carolina, June 8-11, 1998

$$R_S = \frac{\frac{\Delta d}{d}}{8Dw}\sqrt{\frac{L\mu^3 V_{eff}^3}{6 < v >}} \qquad (1)$$

Δd is the difference between the diameters of the two particles, d is the average diameter of the particles, D is the average diffusion coefficient of the particles, w is the plate separation or channel height, μ is the electrophoretic mobility of the particles, V_{eff}, is the effective voltage across the channel, L is the channel length, and $<v>$ is the average buffer velocity. Examination of the equation reveals why miniaturization of the system is expected to be advantageous. The channel height, w, is inversely proportional to the resolution indicating that the channel dimension should be minimized. Since all the other parameters are either impossible to change or give undesirable consequences (longer run times or electrolysis), channel height reduction seems the only answer to improving EFFF systems. The question then becomes whether reducing w will have the desired effect on operation of the EFFF system.

The effective voltage, V_{eff}, is a critical term that is unfortunately difficult to measure. The typical estimate of field strength made by dividing the applied voltage by the electrode separation distance, w, has been shown to be inconsistent with actual EFFF operation. Previous results have shown that the effective voltage is typically about 0.5 to 1% of the applied voltage depending on the makeup of the buffer [1,4]. This loss of effective voltage is caused by a double layer of ions that build up at the interface of the buffer and the electrode. If the double layer grows so large as to fill the separation channel, no retention occurs, the effective voltage essentially falls to zero, and the separations are destroyed. This phenomenon thus limits the ionic strength of the buffering solutions employed in the channel. A concern with miniaturizing the EFFF system is that the double layer will fill the channel even at low ionic strengths. In this case there is no advantage gained by reducing the dimensions of the channel. In our initial report of the μ-EFFF system, examples of separations were given indicating that the effective voltage does not go to zero, but the changes in effective voltage were not characterized. The effective voltage in the channel during a separation can be found using calibration techniques in which known particles are retained in the system and the required effective voltage for the observed level of retention can be calculated.

Another effect encountered in EFFF systems is the steric transition point where particle elution times begin to reverse once the radius of the particles being separated exceeds a certain length. In normal EFFF modes, smaller particles will elute before larger particles. Beyond the steric transition point, the larger particles will elute before the smaller ones. Since the steric transition point is related to the channel thickness we expect miniaturization of the system to impact the steric transition point and that determination of the steric transition points will give us information regarding the effective field in the channel. The steric inversion diameter, d_i, is given in equation 2 where k is the Boltzmann constant, T is the absolute temperature, and η is the fluid viscosity [5].

$$d_i = \sqrt{\frac{2kTw}{3\pi\eta\mu V_{eff}}} \qquad (2)$$

Important characteristics of any separation system are the peak broadening and resolution of the system, which are both measured in terms of plate heights. The plate height, H, is a measure of variance created by the system while the particles move through the channel. The total plate height is the sum of several contributing factors. One group of factors, known as instrumental factors, H_i, can be minimized by good instrument design and operation procedures. A second group of factors are the non-equilibrium effects, H_n. These non-equilibrium effects are caused by the natural distribution of the sample over volume elements and the slow movement of particles between volumes. The plate height, H, is then given in equation 3. H_n can be found using equation 4 if non-polar samples are used [3].

$$H = H_n + H_i \qquad (3)$$

$$H_n = \frac{1}{105}\frac{w^2\langle v\rangle}{D} \qquad (4)$$

Experimentally, plate heights, H, can be measured and estimates of H_n and H_i can be made. Combining equations 3 and 4, we find that plate heights should increase linearly with flow rate and the y-intercept on the plot is equivalent to the instrumental broadening, H_i, which we are seeking to minimize.

One area in which miniaturization is expected to improve the EFFF system is the area of sample equilibration and the need for stop flow. The establishment of equilibrium in the channel is not instantaneous and requires a relaxation time, τ, equal to the time required for a particle to migrate from one electrode to the other in the presence of the applied electric field. The relaxation time, τ, can be found using equation 5.

$$\tau = \frac{w^2}{2\mu V_{eff}} \qquad (5)$$

EXPERIMENTAL METHODS

Several prototype μ-EFFF systems whose fabrication was similar to that described in earlier communications, were used in this study [2]. Most of the changes in fabrication were designed to reduce peak broadening in the system. First, the input ports were reduced in size to 200 μm on a side. Second, the electrical connection was not made through the input and output ports, but rather the metallization that comprised the electrodes was extended to the edge of the silicon wafer where the connection was then made. Third, angled input and output flow regions were added to the channel. Fourth, a conductive adhesive was used to bond a wire directly to the wafer in the area of the electrode metallization to allow electrical contact. Fifth, the interface between the macro and micro fluid regimes was altered. A plastic ferrule from Upchurch Scientific was bonded using a UV adhesive to the surface of the silicon wafer directly over the input and output ports. The ferrule was used to localize the 125 μm inner diameter steel tubing bonded in place over the input and output ports. The μ-EFFF devices were 5.4 cm in length, 6 mm in width, and with a plate separation distance of 28 μm. These dimensions give a void volume of 9.072 μL. The layout of the channel is shown in figure 2.

Two detectors, an on-chip and an off-chip, were demonstrated and compared with respect to the EFFF system performance. The off-chip detector was a UV detector monitoring at a wavelength of 254 nm. The on-chip detector was a conductivity detector that was fabricated directly in the channel for detection of particles before they exit the EFFF channel. The detector consists of two parallel wires on the glass and silicon wafer surfaces that were fabricated in the exact same manner as the

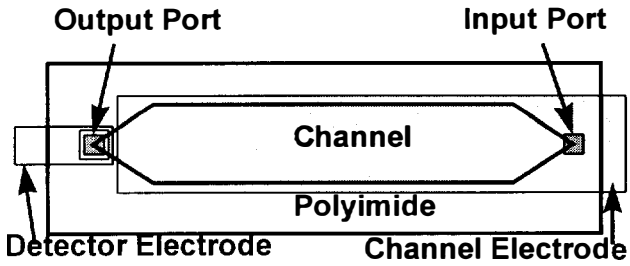

Figure 2. *Configuration of channel and detector electrodes in relation to channel.*

EFFF channel electrodes. Electrical connection to the detector was made as described above for the electrodes. The relationship between the detector and the channel is shown in Figure 2. The conductivity detector operated by applying a constant 5 V across the channel then measuring the current in the circuit.

RESULTS

Several of the earlier problems with micromachined systems were solved by the changes mentioned earlier. The dead volume in the connections to the channel was reduced to 7.7 μL from the earlier systems 55 μL. At a flow rate of 1 mL/hr (0.174 cm/s in the channel) this reduces the delay to 27 sec in our channel.

The time constant for changes in the electric current in the channel and by association the internal electric field was measured using a voltage step test as shown in Figure 3. The data from this test indicates that the time constant for the channel is about 4 seconds, or an order of magnitude less than that reported for a macro system [4]. Though this may still be too slow for a quickly changing field, the possibility of using a variable field is now much closer to reality.

To perform the plate height measurements, 100 nL samples of acetone were injected into the system for a series of flow rates. The band broadening calculations were performed using equations 3-4 and the results plotted to determine the instrumental component of the plate height. Of particular interest is the difference in band broadening between the system with the on-chip detector and the off-chip detector. The results of band broadening calculations for the μ-EFFF system are shown in figure 4. For comparison, the results are shown with typical band broadening calculations for current macro FFF systems and earlier reported results for a micromachined system [2]. Figure 4 shows that thinner channels produce smaller peak broadening only if the instrumental band broadening is small. The instrumental band broadening is indicated by the y-intercept on the graph. Note the great improvements made in band broadening by improving the macro-to-micro interfaces and switching to an on-chip detector. One effect not shown here is the influence that diffusion has on peak broadening in the off-chip detector. Figure 5 shows the peak broadening measurements with the off-chip detector. The increasing values for low flow rates indicate that diffusion is beginning to dominate at the low flow rates. Since this effect disappears with the on-chip detector, it is apparent that the diffusion must occur in the detector itself. The reason for the change in the relative importance of diffusion is due to the large dimensions found in the detector compared to the channel itself. Thus in miniaturized separation systems it appears that a requirement of the system will be on-chip detection.

The necessary relaxation time for the polystyrene particles used in these tests is less than two seconds for channels up to 30

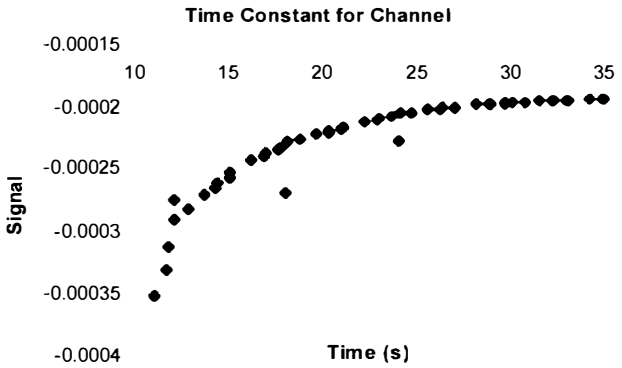

Figure 3. *Step test for channel giving time constant of 4 seconds*

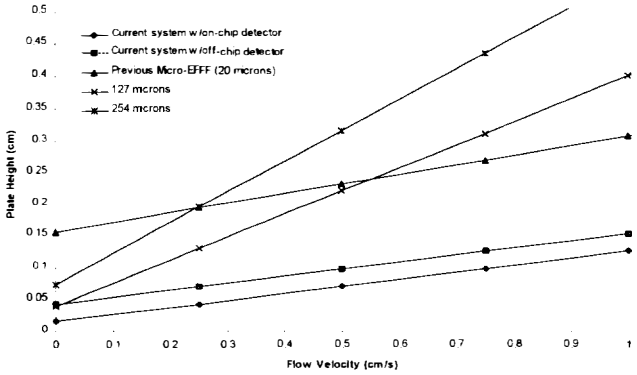

Figure 4. *Plate height comparison between systems described here with both on and off chip detection, previously reported micromachined EFFF systems and two sizes of macro systems, 127 μm and 254 μm channel. Note three-fold improvement over the previously reported values for a micromachined system when using the off chip detector and the five-fold improvement for the on-chip detector.*

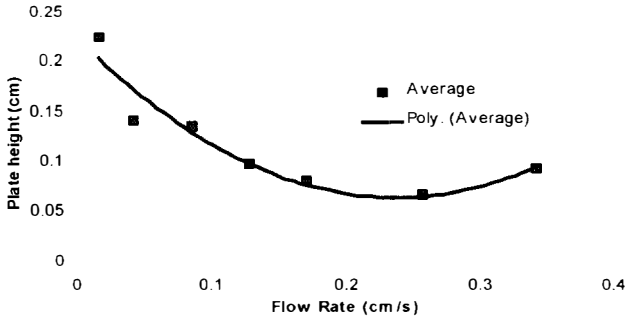

Figure 5. *Plate heights for channel using off-chip detector for a series of flow rates.*

μm in height. This value compares to the relaxation time in the macro systems of 45 seconds and up. Our results indicate that separations can be performed without any stop time with little loss of resolution or they can be performed with a short stop time (~10 s) to allow equilibration and an improvement in separation. This time is much less than the 5-10 min typical of macro systems.

Figure 6 shows the change in elution time as particle size increases. Note the transition from increasing elution times to decreasing elution times as a function of particle size that indicates

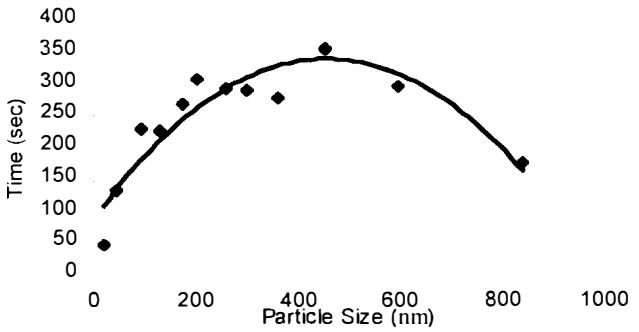

***Figure 6**. Graph of elution time for increasing particle diameter showing steric transition at about 450 nm. Flow rate was 0.6 mL/hr with a current of about 145 μA*

the steric transition. The steric transition appears to occur at about 450 nm for this low field strength. The transition point gives a measure of the thickness of the particle cloud and which is important for determining the optimum separation conditions. Also, the data indicates that the fields are comparable to those for macro systems indicating little danger of finding effective fields too small to perform separations.

●f great importance in determining the value of a miniaturized EFFF system is an understanding of changes that occur in the effective field as the channel dimensions decrease. The effective field measurements were made as described in the theory section. A separation with the off-chip detector is shown in Figure 7. Initial measurements indicate that the effective field is from 0.38% to 0.55% of the applied field, depending on flow rate, indicating that during the scale down, some loss in effective field occurs. Reported effective field values for macro systems are generally about 1 % of the applied field. Even with the apparent reduction in effective field with miniaturization, the resolution should still increase 5-fold at these values for effective field. For example, the resolution shown in figure 7 is similar to that achievable by a macro system, but the analysis time for the macro systems is at least 3 times as long. A possible explanation for loss in the measured effective field not related to miniaturization is the change in electrode materials. Gold was used for these electrodes while most macro systems use graphite. Further study of possible material effects will be studied in the future.

Figure 8 shows a separation performed using the on-chip detector. Notice the 50 % reduction in run time compared to the off-chip detector. While there is significant noise in the unfiltered signal, notice the sharp peaks indicating the void peak and the various particles. The cause of the double peaks is unknown, but may be an artifact of the injection system. The resolution of the system using the double peaks as one peak is still 5 times that of the separation in figure 7 with the off-chip detector. If the double peak is eliminated, then resolution will be 10 times higher than with the off-chip detector. With some additional filtering and improvement in the measurement system, we anticipate that the on-chip detector will provide a higher performance, lower cost replacement for the bulky and expensive off-chip detectors.

CONCLUSION

A μ-EFFF system was characterized with regard to changes in electric field and plate height with channel height. The steric transition point, system time constants, time to equilibrium, and dead volumes were also measured. In addition, the design, fabrication, and testing of an on-chip conductivity detector was

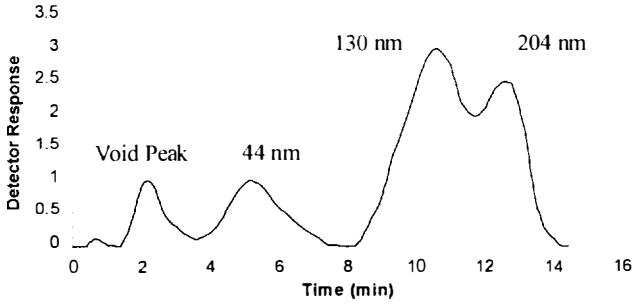

***Figure 7**. Separation with off-chip detector showing separation of 44, 130, and 204 nm particles. Flow rate was 0.6 mL/hr with a current of 170 μA.*

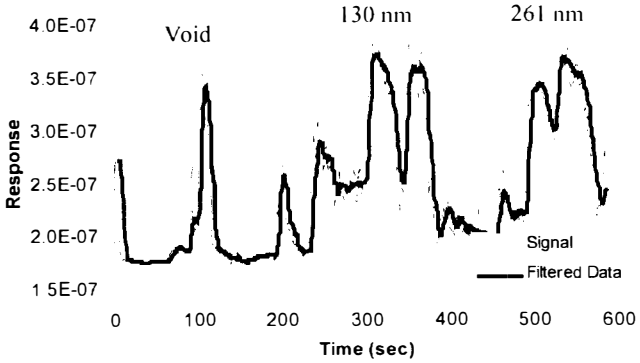

***Figure 8**. Separation using on-chip detector with 130 and 261 nm particles. The flow rate was 0.6 mL/hr with a current of 145 μA.*

described. Comparison was made between on and off chip detectors and the on-chip detector was shown to be superior in terms of plate heights.

ACKNOWLEDGMENTS

The authors would like to acknowledge support from Amoco Chemical Corp., a National Science Foundation Graduate Research Fellowship, and the Whitaker Foundation.

REFERENCES

1. K. D. Caldwell and Y. S. Gao, "Electrical field-flow fractionation in particle separation. Monodisperse standards," *Anal. Chem.*, *65*, 1764-1772, (1993).

2. B. K. Gale, K. D. Caldwell, and A. B. Frazier, "A Micromachined Electrical Field- Flow Fractionation System" *IEEE-TBE*, accepted.

3. J. C. Giddings, and K. D. Caldwell, "Field Flow Fractionation" In *Physical Methods of Chemistry, Vol IIIB*, B. W. Rossiter, J. F. Hamilton, Eds, New York: John Wiley & Sons, (1989).

4. S. A. Palkar and M. R. Schure, "Mechanistic Study of Electrical Field Flow Fractionation. I. Nature of the Internal Field," *Anal. Chem.*, *69*, 3223-29, (1997).

5. M. N. Meyers and J. C. Giddings, "Properties of the Transition from Normal to Steric Field-Flow Fractionation," *Anal. Chem.*, *54*, 2284-89, (1982).

NANOLITER-VOLUME DISCRETE DROP INJECTION AND PUMPING IN MICROFABRICATED CHEMICAL ANALYSIS SYSTEMS

Kalyan Handique[1], David T. Burke[2], Carlos H.Mastrangelo[3] and Mark A.Burns[1*]

[1]Department of Chemical Engineering
[2]Department of Human Genetics
[3]Department of Electrical Engineering and Computer Science
The University of Michigan,
2300 Hayward Street, Rm. 3029, Ann Arbor, MI 48109
Phone: (313) 763 3078, Fax: (313) 763 0459
*Email: maburns@umich.edu

ABSTRACT

This paper presents the combined use of selective hydrophobic patterns and on-chip pressure generation for injection, pumping, mixing, and positioning of discrete sample drops in a microfabricated chemical analysis device. The device consisting of a glass substrate bonded to a silicon/quartz substrate has been fabricated and tested. Specfic regions of the etched microchannel network are selectively patterned to be hydrophobic. These hydrophobic regions are used to control the location of liquid inside the microchannel network. Precise nanoliter-volume liquid samples are split-off and moved by heating air trapped in microfabricated chambers. Discrete sample drops of the order of 35 nl have been injected, moved, mixed and positioned in the device. This device demonstrates a simple valveless technique for performing microfluidic operations without the use of mechanical moving parts.

Keywords: Discrete Drop, Injection, Pumping, Hydrophobic Patterns, On-chip Pressure.

INTRODUCTION

Injection, motion, and positioning of discrete drops is crucial in microfabricated chemical analysis systems [1,2]. The mixing, reaction, and separation steps performed in these systems require precise volumes of liquid samples to be accurately moved and positioned in the micro-channel network [1,2]. Although mechanical valves and pumps have been reported in literature [3,4], combinations of these have been mostly used for pumping continuous liquid samples. Discrete pumping of liquid samples has been shown using thermocapillary pumping [2] and using air pressure regulated by external pneumatic valves [1,5]. In our earlier work, we have shown splitting of a nanoliter-volume discrete drop using external air pressures and selective hydrophobic patches in microchannels [5]. We also demonstrated the on-chip generation of air pressure required for drop splitting [5]. In this paper, we will show the use of selective hydrophobic patterns and on-chip pressure generation to perform the microfluidic operations of discrete drop injection, motion, mixing and positioning.

Typical microfluidic operations in microfabricated chemical analysis systems involve injection of liquid samples and reagents into microchannels. The liquid samples are mixed and moved to the "reaction" stage of the device. After performing a reaction, the liquid sample drop is then moved to the next stage of the device for detection and analysis of the reaction products. Figure 1 shows the schematic of such a device which consists of a microchannel network with specific regions selectively patterned hydrophobic. The device comprises two main channels merging into one with appropriate overflow channels and vents intersecting the main channel. During operation, liquid placed at the inlet gets drawn into the channel by capillary action and stops at the hydrophobic patch. After positioning the liquid samples, definite-sized discrete drops are split-off by use of external pressure supplied through hydrophobic air lines. The volume of each drop is defined by the channel cross-sectional area and the distance from the splitting air line to the hydrophobic interface. The two drops merge at the y-intersection and are positioned beyond the hydrophobic vent. The drop may be moved again by use of air pressures after closing the vent.

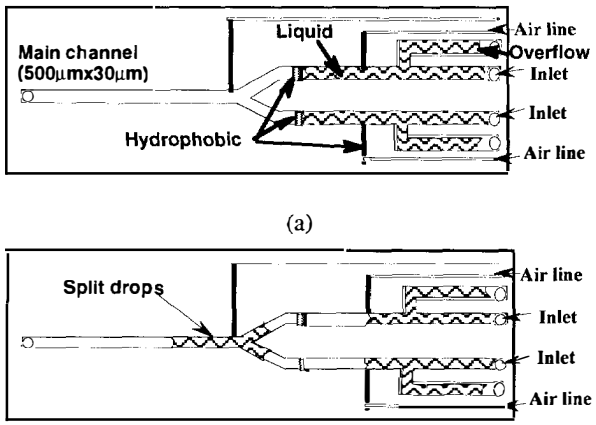

Figure 1. Schematic of a device to perform injection, mixing and positioning of discrete liquid samples. The microchannel network contains hydrophobic patches for stopping the liquid. Hydrophobic air lines are also used for pumping discrete drops and the vents are used for positioning the drops. (a): Water placed at the inlet gets drawn into the microchannel and is stopped at the hydrophobic interface. (b): Pressurizing the air lines splits off two discrete sample drops, merges them and positions them beyond the hydrophobic vent.

The pressure required for splitting and moving of discrete drops can also be generated by heating air trapped in

0-9640024-2-6/hh1998/$20©1998TRF
DOI 10.31438/trf.hh1998.80

strategically located microfabricated chambers. We have demonstrated the use of on-chip pressure generation for the injection of a single drop [5]. Figure 2 shows the schematic of a device similar to Figure 1 with an added ability to generate the required air pressure on-chip. Air chambers are connected to the main channel through the splitting channel and heaters placed beneath the chamber heat the air inside the chamber to increase the air pressure. This heating, in effect, splits off two discrete sample drops and moves them. The two drops are then mixed at the y-intersection and positioned beyond the hydrophobic vent. Cooling the air chamber slowly allows air to flow from outside and re-establish atmospheric pressure inside the chamber. The discrete drop may then be moved again by reheating the air chambers after having closed the vent line.

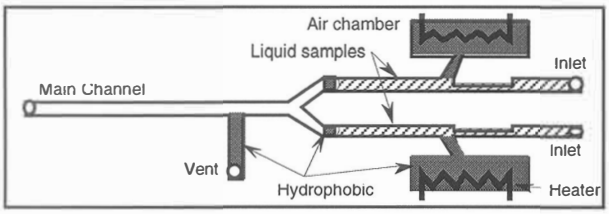

(a)

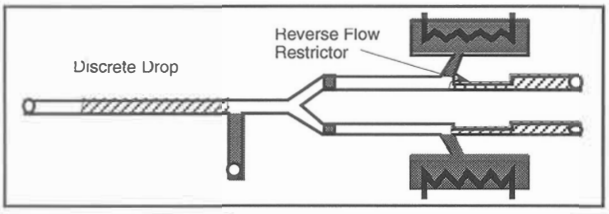

(b)

Figure 2. *Schematic of a device to perform microfluidic operations using air chambers for on-chip pressure generation.* ***(a)****: Liquid samples placed at the inlet stop at the hydrophobic patches.* ***(b)****: Actuation of the heaters increases the temperature, and hence pressure, inside the chamber. The subsequent air expansion splits off two discrete sample drops, mixes them at the y-intersection and positions the combined drop beyond the hydrophobic vent.*

MODELING

The ability of an air chamber to maintain a certain gauge pressure will depend on the chamber volume. The air chamber volume and the heat required to achieve specific pressures can be estimated by modeling the dynamics of the air flowing out of a heated air chamber (Figure 3a). The chamber is maintained at room temperature initially. At time t = 0, heat is supplied to raise the temperature (and pressure) of air in the chamber and induce convective air flow out of the chamber.

The heat and mass balance equations are solved after making some simplifying assumptions that include [6]: the gas is assumed to be ideal; the power supplied heats only the air inside the chamber; there are no entrance and exit effects in the flow of gas; the pressure and temperature is uniform inside the chamber; and, the flow rate of air maintained in the channel is proportional to the pressure drop. Chambers should be able to generate a few inches of water and maintain this pressure during the time of operation (a few seconds) in order to move a drop. From the modeling results (Figure 3), chamber volumes of the order of 0.1 mm^3 should be sufficient.

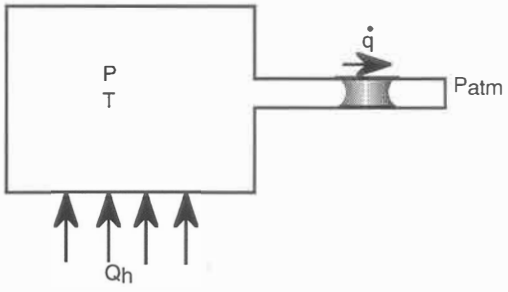

(a)

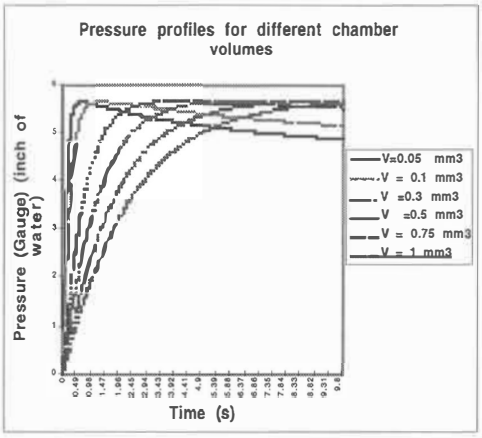

(b)

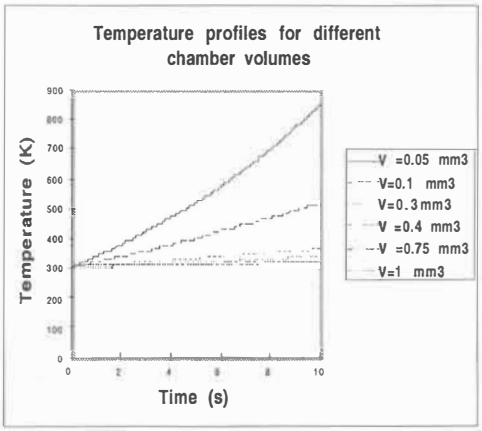

(c)

Figure 3.(a). *Diagram of a chamber connected to a channel. Heat supplied to the chamber causes the air inside to expand and thus provide the pressure drop required for discrete drop motion;* ***(b)****: Gauge pressure versus time for different chamber volumes for constant power (2 μW) and flow proportionality constant (1000 inch water.s/(mm³)); (c):Temperature profiles obtained inside the chamber under the same conditions as 3(b).*

DEVICE FABRICATION

The device consists of a glass top containing etched chambers bonded to a silicon or quartz substrate containing metal resistive heaters and resistive temperature detectors. The fabrication steps have been described earlier [5]. For these experiments, the device has been patterned hydrophobic using a self assembled monolayer of 1H,1H,2H,2H-perfluorodecyltri-chlorosilane (FDTS) [7]. Figure 4 and 5 shows the diagram and cross section of the device respectively.

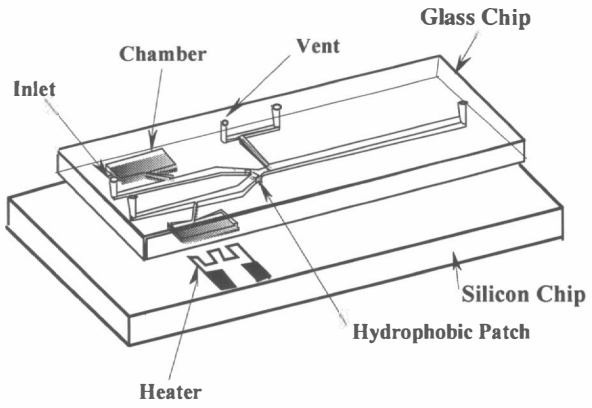

Figure 4. Diagram of the fabricated device which consists of a glass chip bonded to a Silicon/Quartz chip. Channels and chambers are etched onto the glass side. The heaters and Resistive Temperature Detectors (RTD) are fabricated on the silicon/quartz chip.

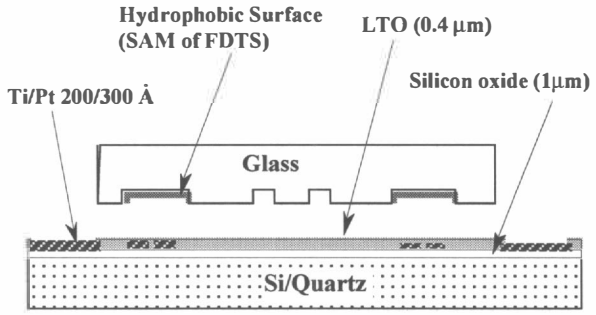

Figure 5. Cross-section of the fabricated device shown in Figure 4.

RESULTS AND DISCUSSIONS

Use of External Air Pressure

Figure 6 shows photographs of the device described earlier in Figure 1. It has a glass cap bonded to a silicon chip. The microchannels etched onto glass have a cross-section of 500 μm by 30 μm. Water placed at the inlet by a sequencing pipet (Sigma, least count 0.5 μl) was drawn in and stopped at the hydrophobic patches. The excess water filled the overflow channel but avoided the hydrophobic air lines. The air lines were then pressurized (a few inches of water) causing two discrete-sized drops (~100 nl each) to split off and merge at the y-intersection and get positioned beyond the air vent. The discrete drop could be moved further by closing the air vent.

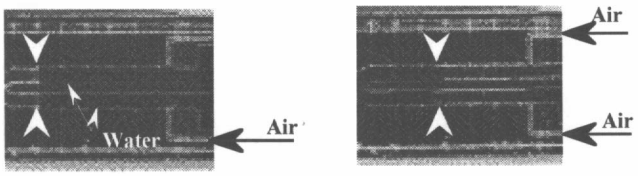

(a) (b)

Figure 6. Demonstration of injection, motion mixing, and positinoning of discrete drops by the use of external air pressure. (a): Water placed at the inlets stops at the hydrophobic interfaces. (b): Two discrete sized drops (~100 nl each) split off and mix at the channel intersection.

On-Chip Air Pressure Generation

Figure 7 shows the device fabricated to perform microfluidic operations by generating the air pressures on-chip. We have performed experiments with chamber volumes ranging from 0.1 mm^3 to 0.4 mm^3. The main channel has a dimension of 300 μm by 30 μm. The channels between the splitting channel and the inlet holes is narrowed down to a cross-section of 100 μm by 30 μm so that the pressure generated by the air chamber is directed towards the left of the chamber.

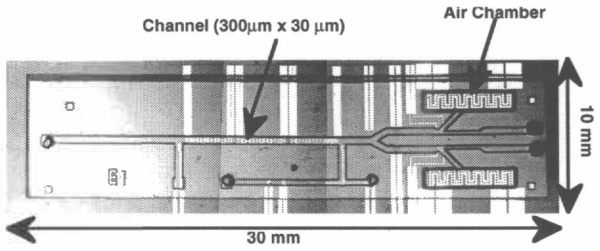

Figure 7. Photograph of the fabricated device. the chamber has a volume of 0.4 mm^3.

Figure 8 shows photographs and schematics of the microfluidic operations performed. Water placed at the inlet holes stop at the hydrophobic patches. The metal heaters beneath the air chambers have a resistance of 50-56 ohms. Actuating the heaters with 4 volts causes the temperature and hence the pressure inside the chambers to rise. As a result, two drops (~ 35 nl each) are split off and moved beyond the hydrophobic patches. The drops merge and stop just beyond the hydrophobic vent. The air flowing out of the chambers flows out through the vent and ceases to push the drops further. The two drops moved a distance of 5 mm each in 8 seconds. The voltage applied to the heaters is then gradually reduced to zero in 4 seconds. This causes the temperature inside the chamber to

gradually reach room temperature and thereby avoiding a sharp drop in the pressure inside the chamber. Some microfluidic operations such as a thermal reaction may be performed before the discrete drop is moved again in the micro-channel. The vent channel is then filled with water and the heaters actuated again to push the discrete drop further down the channel.

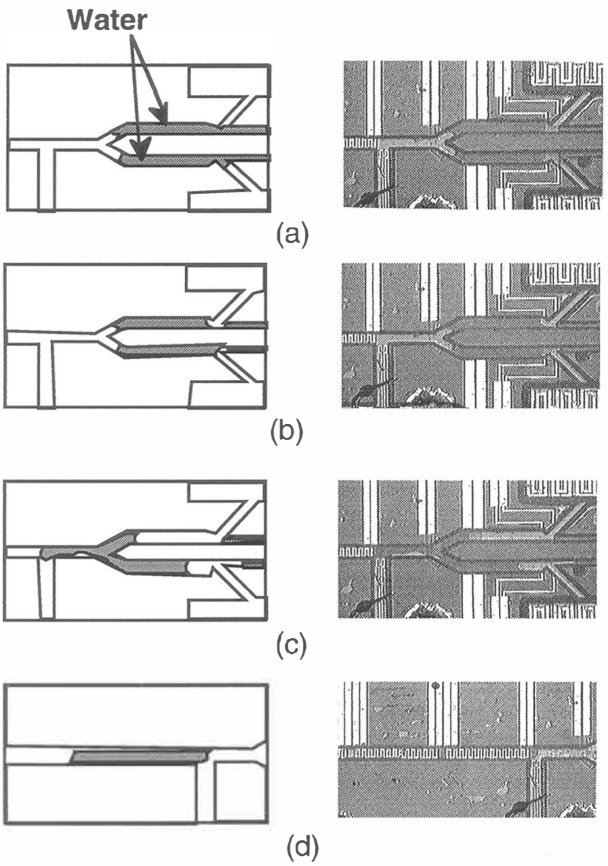

Figure 8. Schematic and photograph of the device in operation. (a): Water placed at the inlet holes are stopped at the hydrophobic patches; (b) On actuating the heaters beneath the air chambers, two discrete liquid drops (~35 nl each) split off; (c). 4 seconds after the heaters are turned on; (d). The mixed drop is positioned beyond the hydrophobic vent.

SUMMARY

We have demonstrated the use of selective hydrophobic patterns inside microfabrifcated channel networks to control the movement of liquid samples. The air pressure required for drop splitting and motion has been generated by heating air trapped in chambers. A device has been fabricated which is used to split precisely-controlled nanoliter-volumes of different liquid samples, mix them and stop at a predetermined location. The mixed sample drop is further moved to another location by reheating the chambers after closing the vent with water.

ACKNOWLEDGMENTS

This work was supported by the National Institutes of Health under grants NIH-R01-HG01044 and NIH-R01-HG01406. We are indebted to Tim Sammarco, Brian Johnson, Sundaresh Brahmasandra and Madhavi Krishnan for their help.

REFERENCES

1. Anderson, R.C.; Bogdan, G.J.; Barniv, Z.; T.D. Dawes, J. Winkler and K. Roy, "Microfluidic Biochemical Analysis System",*Tranducers'97,* pp. 477-480, 1997.

2. Burns, M.A.; Mastrangelo, C.H.; T. S. Sammarco, F.P. Man, J.R. Webster, B.N. Johnson, B. Poerster, D. Jones, Y. Fields, A.R. Kaiser and D.T. Burke, "Microfabricated Structures for Integrated DNA Analysis", *Proc. Natl. Acad. Sci., USA,* vol.**93**, pp 5556-5561, 1996.

3. M. Koch, N. Harris, A.G.R. Evans, N.M. White and A Brunnschweiler, "A Novel Micromachined Pump Based on Thick-Film Piezoelectric Actuation", *Transducers'97*, pp 353 - 356, 1997.

4. M. Stehr, S. Messner, H. Sandmaier, R. Zengerle; " A New Micropump with Bidirectional Fluid Transport and Selfblocking Effect", *Proc. MEMS '96*; pp 485-490, 1996.

5. K. Handique; B.P. Gogoi, D.T. Burke, C.H. Mastrangelo, and M.A. Burns, Microfluidic Flow Control using Selective Hydrophobic Patterning, *Proceedings of SPIE Conference on Micromachined Devices and Components*, Vol. 3224, pp185-195, 1997.

6. K.Handique amd Mark A. Burns, unpublished work ,1998.

7. U.Srinivasan, M.R. Houston, R.T. Howe, and R. Maboudian,"Self-Assembled Fluorocarbon Films For Enhanced Stiction Reduction", *Transducers'97,*pp. 1399-1402, 1997.

BIOLOGY LAB-ON-A-CHIP FOR DRUG SCREENING

Hossein Salimi-Moosavi[1], Rod Szarka[2], Per Andersson[1], Richard Smith[2], D. Jed Harrison[1]
1) Department of Chemistry, University of Alberta, Edmonton, Alberta, Canada, T6G 2G2
2) Carbohydrate Chemistry, Alberta Research Council, P.O. Box 8330, Edmonton, Alberta, Canada, T6H 5X2

ABSTRACT

Integrated microfluidic systems for the evaluation of cell-drug interactions are described. Within a network of flow channels cells can be mxied and reacted with activators and inhibitors of cell functions in a highly controlled fashion, allowing evaluation of a chemical's potency as a potential drug with minimal consumption of the reagent. Assays for reagents that prevent calcium ion uptake in human lymphocytes are described. Measurements of cell adhesion were evaluated on-chip using a cell rolling method, which can be used to screen the ability of candidate drugs to prevent the activation of the human neutrophil cell response during the early stages of inflamatory response.

INTRODUCTION

Microfluidic chips used to study cellular events can provide the same high level of integration of reagent addition, reaction, separation and observation steps that have been demonstrated for integrated chemical and biochemical analysis systems [1-9]. The results presented here illustrate the integration of several reagent delivery steps in a biological study of cell-drug interactions, providing a biological example of the lab-on-a-chip concept. Because a microchip consumes between 0.1 nL and a few µL per experiment, such device volumes could provide a cost-saving advantage for work involving expensive or supply limited reagents, especially candidate compounds tested in drug-screening [9].

In the first part of this report, we demonstrate the manipulation and transport of single non-adherent cells using pressure driven flow, followed by cell reactions with agonists or antagonists, all within an integrated network of microfluidic channels. The important cellular process of activation of Ca^{2+} influx [10-12] within human lymphocytes was chosen to illustrate the ability of microfluidic chips to deliver cells, inhibitors and activators to confined, well defined locations, mix them, then follow the kinetics of the interactions at the single cell level with high precision. This procedure can be extended to nearly any analytical problem for which cell stains that indicate activity exist, and could ultimately serve either for drug screening or for clinical diagnostic purposes.

Another microfluidic system was developed to study cell adhesion phenomenon [12-14]. Adhesion of leukocytes is a primary step in the inflammatory response [12]. Screening tests for drugs that might reduce such responses in arthritis or other autoimmune diseases require the use of cell and animal models for accurate results, but these consume large amounts of compound. Cell rolling along a surface subject to a shear stress induced by solvent flow is an indicator that adhesion forces have been activated [13]. As an alternative, a microfluidic chip for the study of cell rolling that uses much less material per assay has been designed and tested. When a cell bearing stream flows through the test bed and is viewed under a microscope, cells that do not adhere move by too fast to be captured at video rates, while adhering cells appear to roll slowly along the surface as they stick and release, indicating adhesion and the onset of inflammatory response, as suggested by the cartoon in Figure 1. Compounds which reduce or eliminate this rolling effect are potential drug candidates [12,13].

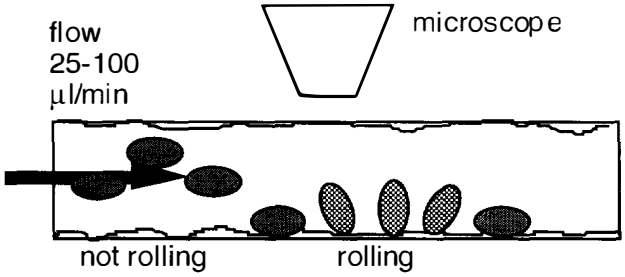

Figure 1 *Cell rolling arises from a cycle of temporary adhesion and release of cells on a surface once they are activated by a biochemical signal, as illustrated in the cartoon. Non-adhering cells stream by in the solvent flow.*

RESULTS AND DISCUSSION

Single Cell Flux Assays

Figure 2 shows the schematic layout of a post-column reaction device (PCRD1) microchip, utilized previously by Fluri et al. [15] for chemical reactions and separations. For our present work with non-adherent cells, solvent flow was driven by suction applied to the waste outlet, drawing solution from all four inlet reservoirs. The flow rates were designed to be controlled by the relative resistance to flow of each channel, which was a function of each channel segment length and cross section. Based on dimensions, the two side positioned inlet channels at point "t" each contribute 37.5% of the flow into the incubation channel, while the middle inlet channel contributes 25%. A microscope positioned

0-9640024-2-6/hh1998/$20©1998TRF
DOI 10.31438/trf.hh1998.81

Solid-State Sensors, Actuators, and Microsystems Workshop
Hilton Head Island, South Carolina, June 8-11, 1998

over the mixing and detection zone, point "m", allowed observation of cells as they passed into the zone. The device was operated in a stopped flow mode, in which flow was stopped when a cell entered the detection zone. Stopped flow allowed the two unmixed zones at the intersection to diffuse into each other, initiating cell reaction with the added reagent at a well identified time and concentration. When required, cells could be stopped just before entry into the mixing zone then moved into the mixing region, so that both before and after images were easily obtained. Video images, obtained at about 16 ms/frame, showed that cells entered the observation zone at about 8.7 mm/s. Stopping the flow with a hand controlled syringe resulted in backward cell motion of about 5 μm over the first frame, then the cell was stationary to the maximum resolution for all remaining frames over many seconds.

Numerous fluorogenic stains for the identification and quantitation of intracellular events are now available [16, 17], and are ideally suited for fluorescent detection of single cell events within these microfluidic devices. To illustrate the utility of the device we investigated the manipulation of cytostolic calcium ion levels in lymphocytes with several different activators and inhibitors. Observations of fluorescence changes downstream of mixing point m, at which an activator can be introduced, provide a means to determine dose-response profiles and the kinetics of activation. Inhibitors can be readily introduced into the cell feedstream at point t, and the incubation time controlled with the flow velocity along the incubation channel. In this way the dose-response curves and the incubation kinetics can be readily evaluated, with the consumption of less than a μl of inhibitor solution.

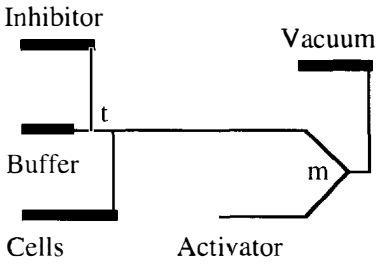

Figure 2 *Flow channel layout of the Single Cell Ca^{2+} flux chip.*

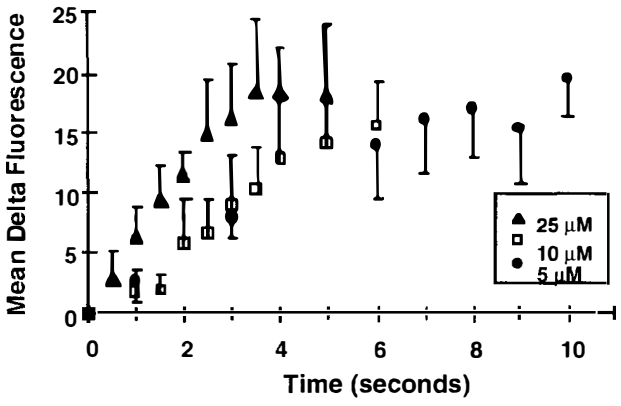

Figure 3 *Dose-response curve obtained with the Ca^{2+}-flux chip for the activation of human lymphocytes by the ionophore A23187, delivered at mixing point "m" and evaluated in stopped-flow mode. Time is measured from when flow stops and mixing begins. The average change in fluorescence is shown for 6 cells at each A23187 concentration.*

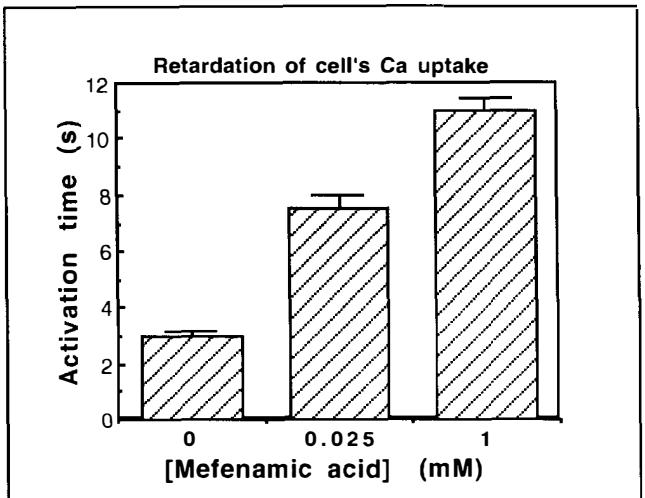

Figure 4 *Bar graph showing the increase in incubation time required for fMLP activation of Ca^{2+}-uptake by human lymphocytes, as a result of exposure to increasing amounts of the inhibitor Mefenamic acid. Mefenamic acid was introduced at point "t", incubated for 10 s with the cells as they were transported towards the mixing point "m", where the activator was added.*

Isolated Human lymphocytes were first loaded with the fluorescent Ca^{2+} indicator fluo-3, introduced into the chip reservoir marked cells, then transported downstream to the mixing point. To inhibit cell activation and adhesion on the glass channels 5% fetal calf serum (FCS) was introduced to the RPMI media used to prepare all solutions introduced into the chip. Figure 3 illustrates the kinetics and the dose-response characteristics for the reaction of human T- and B- lymphocytes with the Ca^{2+} ionophore, A23187, which is a membrane transport agent. Typically, we see a 5 to 10-fold increase in fluorescence over background after reaction with the activator. This is consistent with reports of increases of 2 to 40-fold upon Ca^{2+} activation, depending on the cell type.

An activator/inhibitor pair was also investigated. The tri-peptide, formyl-Met-Leu-Phe (fMLP) activates lymphocytes through a cascade that activates a Ca^{2+} ion channel , and thus shows different kinetics than A23187. During the activation step there is a concentration dependent incubation period, followed by a rapid rise in fluorescence. These kinetics are consistent with a Ca^{2+} channel activator. The inhibitor, mefenamic acid (MA), an anti-inflammatory drug, was used to inhibit lymphocytes activated with fMLP. MA did not permanently inhibit Ca^{2+} uptake, rather activation was delayed by a period of seconds. Figure 4 shows how the inhibitory period increased with increasing MA dose. These pharmacokinetics of MA inhibition are readily observed with the microchip-based stop flow format, but would be missed entirely using a method such as flow cytometry that does not include on-line mixing of reagents and cells.

Cell Rolling and Adhesion Devices.

A microfluidic chip for the study of cell rolling that consumes much less reagent than conventional methods do has been designed and tested [12-14]. It consists of a simple y-mixer port, with a flow region downstream to allow observation of cell adhesion, Figure 5. However, for the studies reported here, the inhibitors were added to the cell suspension prior to loading on the chip, and the second part of the Y-channel was used to introduce a selectin [18] to the microchannels, in order to coat the surfaces with a material that induces rolling. Cell rolling in a glass device with 400 μm wide, 100 μm deep channels can be observed with a microscope and video camera, Figure 1, when the surfaces are treated first with a selectin, and then with other appropriate coatings (see below). Experiments were performed at a flow rate of 50-60 μl/min, which ensures a high enough shear rate (about 800 min^{-1} at this flow) to mimic blood flow in a vascular capillary. An example of the rolling images is shown in Figure 6. The streaks seen are in fact non-rolling cells traveling through the field of view too fast to resolve. The cells frozen in the image are slowly rolling across the field of view, and are readily captured on video. Figures 7 and 8 illustrate quantitative analysis of the images, in terms of the number of cells rolling within the visual field (200 μm long in the direction of flow) and the average time a rolling cell stays within the visual field.

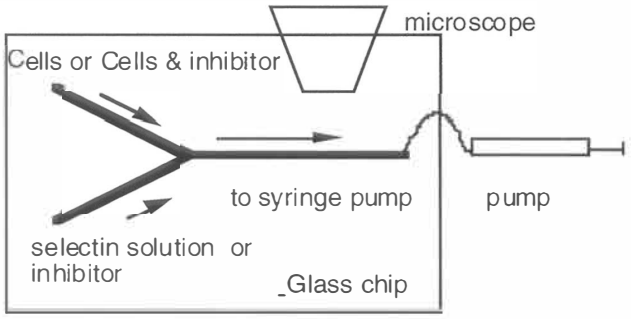

Figure 5 Flow chip design for cell rolling studies.

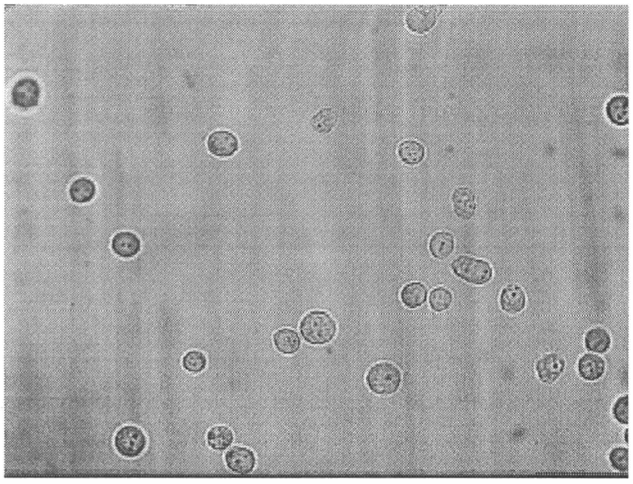

Figure 6 Rolling lymphocytes on an E-selectin coated surface. flow is from the top to bottom of the figure, a distance of 200 μm. Non-rolling cells move by too fast to observe.

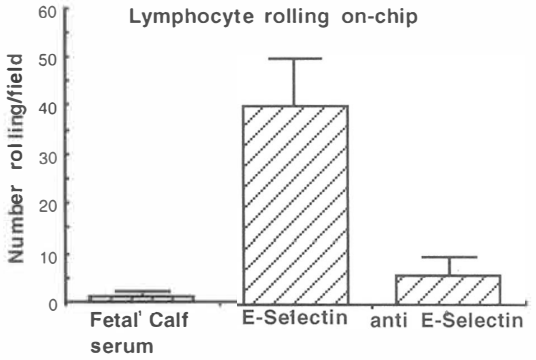

Figure 7 The number of cells rolling per field of view on a control surface (fetal calf serum coated), an active, E-selectin coated surface, and a surface subsequently treated with the antibody to E-selectin to reduce the surface activity for adhesion by binding the antibody.

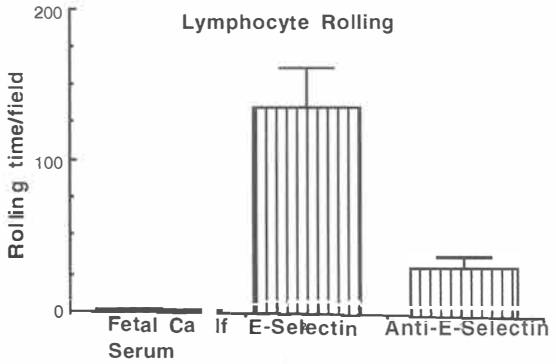

Figure 8 The time required for cells to roll across the field of view on different surfaces, for the same data as analyzed in Figure 7.

Coating the chip walls with fetal calf serum (FCS) induced no cell rolling for human neutrophils and lymphocytes. Coating the chip walls with P or E-Selectin (by exposure to a selectin solution for a 2 h period, then flushing out the solution) allowed the study of induced cell rolling for human lymphocytes, neutrophils and the immortalized human cell lines HL-60 and Jurkat. The induced rolling depended on the cell and the selectin type. For example, Jurkats did not roll on the E-selectin surface that induced HL-60 rolling,. Human lymphocytes and neutrophils rolled on both P and E-Selectin surfaces.

An adhesion inhibitor was mixed with the cells off-chip and introduced into one of the channels to determine whether cell rolling could be prevented. The antibodies to P- or E-Selectin stopped cell rolling on these surfaces, providing a control experiment to demonstrate that masking the selectin could prevent rolling. Exposure of the selectin coated surface to a flow of Sialyl-lewis^x or to a proprietary drug designed to prevent rolling eliminated or nearly eliminated cell rolling.

CONCLUSION

The drug screening process requires large numbers of test be performed on a limited amount of sample. Both types of cell assay devices described here require minimal volumes of reagent per assay, on the order of 1000-fold less than macroscopic systems demand. This feature alone is a highly desirable aspect of these microchip systems. These devices are particularly important for screening in cell rolling studies, where conventional screening methods with receptor or enzyme binding assays have proved uninformative, necessitating cell rolling studies in systems that consume far too much of an untried, expensive-to-synthesize reagent. Additionally, the ability to study cell kinetics for cell-drug interactions on a single cell level should prove valuable both in screening of new compounds and for advancing the science of cell biology.

ACKNOWLEDGMENTS

We thank the Natural Sciences and Engineering Research Council of Canada for funding, and the Albert Microelectronic Centre for device fabrication.

REFERENCES

1. D.J. Harrison, K. Fluri, K. Seiler, Z. Fan, C.S. Effenhauser, A. Manz *Science 261*, 895 (1993).
2. S. Effenhauser, A. Manz, H.M. Widmer *Anal. Chem. 65,* 2637 (1993) .
3. S.C. Jacobson, R. Hergenröder, L.B. Koutny, J.M. Ramsey *Anal. Chem. 66,* 1118 (1994).
4. A.T. Woolley, D. Hadley, P. Landre, A.J. Demello, R.A. Mathies, M.A. Northrup *Anal. Chem. 68,* 4081 (1996).
5. N. Chiem, D.J. Harrison, *Clin. Chem., 44*, 591 (1998).
6. L.J. Kricka, O. Nozaki, S. Heyner, W.T. Gorside, P. Wilding *Clin. Chem. 39,* 1944 (1993).
7. P. Wilding, J. Pfahler, H.H. Bau, J.N. Zemel, L.J. Kricka *Clin. Chem. 40,* 43 (1994).
8. D. Sobek, A.M. Young, M.L. Gray, S.D. Senturia Proc. IEEE MEMS Workshop, FL, Feb 7-10, pp 214 (1993).
9. P.E. Andersson, P.C.H. Li, R. Smith, R.J. Szarka, D.J. Harrison, *Technical Digest: 1997 International Conference on Solid-State Sensors and Actuators, Transducers 97*, June 16-19, 1311 (1997).
10. P. Vandenberghe, J. Ceuppens, *J. Immunolog. Meth. 127,* 197 (1990).
11. M.B. Hallett, E.V. Davies, A.K. Campbell *Cell Calcium 11,* 655 (1990).
12. T. Springer *Cell*76, 301 (1994).
13. S.D. Rosen, C.R. Bertossi *Curr. Opin. Cell Biol. 6,* 663 (1994)
14. M. Lawrence, T. Springer *J. Immunol. 151,* 6338 (1993).
15. K. Fluri, G. Fitzpatrick, D.J. Harrison, *Anal. Chem., 68,* 4285 (1996).
16. S.D. Rosen, C.R. Bertossi *Curr. Opin. Cell Biol. 6,* 663 (1994).
17. V.A. Golovina, M.P. Blaustein *Science 275,* 1643 (1997).
18. M. Lawrence, T. Springer *J. Immunol. 151,* 6338 (1993).

BIOLUMINESCENT BIOREPORTER INTEGRATED CIRCUITS (BBICs): WHOLE-CELL CHEMICAL BIOSENSORS[1]

Michael Simpson, Michael Paulus, and Gerald Jellison
Oak Ridge National Laboratory
P.O. Box 2008, MS 6006 Oak Ridge, TN 37831

Gary Sayler, Bruce Applegate, Steve Ripp, and David Nivens,
University of Tennessee Center for Environmental Biotechnology
Knoxville, TN 37996

ABSTRACT

We report a chemical sensing technology composed of engineered bioluminescent bacteria placed on an optical application specific integrated circuit (OASIC). The bacteria have been engineered to luminesce when the targeted compound is metabolized, while the OAISC detects, processes, and then reports the magnitude of this optical signal. In this work we report a toluene sensing device that uses the bioreporter *P. putida* TVA8, and a naphthalene sensing device that uses the bioreporter *P. fluorescens* HK44. These sensors are capable of detecting low parts per billion concentrations of the targeted substance.

INTRODUCTION

Biosensors are hybrid devices combining a biological component with an analytical measuring element. The biological component typically reacts and/or interacts with an analyte of interest producing a response that can be quantified by an electronic, optical, or mechanical transducer. The most common configuration uses immobilized biomolecules such as enzymes or antibodies as the biological component providing the needed selectivity. Another less utilized approach uses living microorganisms or sections of organs or tissues as the biological element. Originally these biosensors, sometimes referred to as whole-cell biosensors **[1]**, used electrochemical transducers to detect the activity of growing cells **[2]**. Whole-cell biosensors have functioned in controlled environments but are not widely applicable, largely because of interference caused by growth on nutrients other than the target analyte.

Alternatively, molecular biological techniques have been used to produce cells or bioreporter strains that have much greater selectivity. Typically, DNA sequences that code for a specific promoter sequence are fused with gene(s) coding for reporter enzyme(s) and introduced into a host cell. When the target molecule is present, the reporter genes are expressed to produce the enzyme(s) responsible for the production of the measured signal. Thus, gene regulation and not consequences of microbial activity provides selectivity.

Some commonly used reporter enzymes are beta-galactosidase (*lacZ*) and catechol 2,3-dioxygenase (*xylE*). Both of these systems use colorimetric detection methods, requiring cell destruction to produce the signal. In the past decade, bioluminescent bioreporters have become popular since the bioluminescent response is easily detected and the assay need not be destructive to the cells. Thus, the bioreporter can be continuously monitored in real time. Genetically engineered bioluminescent bioreporters using both eukaryotic and prokaryotic bioluminescence enzymes have been developed for detecting toxins and pollutants in water and soil and to assess the bioavailability and functional processes of pollutant biodegradation.

Bioluminescence of bioreporters has been detected by a number of different types of optical transducers, including photomultiplier tubes, photodiodes, microchannel plates, photographic films, and charge-coupled devices. In many of these applications, light is collected and transferred to the transducer using lenses, fiber optic cables, or liquid light guides. However, applications requiring small volumes, remote detection, or multiple parallel sensing necessitate a new type of instrumentation that is small and portable, yet maintains a high degree of sensitivity.

We report here a novel approach that eliminates the need for bulky and expensive optical transfer and detection devices. A bioluminescent bioreporter integrated circuit (BBIC) is formed by placing whole-cell bioreporters engineered to bioluminesce in the presence of a particular substance on an integrated circuit (IC) designed to detect light, process this signal, and then report the results. In this concept, the bioreporters can be thought of as another component (analogous to a transistor, resistor, or capacitor) available to the IC designer. The chief advantage to this approach is that the entire sensor, including all signal processing and communication functions, can be realized in a single-chip, low-power, rugged, inexpensive device. While other transducers only detect the light and require other components to make a complete system, the IC provides the analog, digital, and radio frequency (RF) circuit capabilities required to make a complete stand-alone sensor. Additionally, as there are inexpensive, prototype quantity, IC fabrication facilities, BBICs can be individually crafted to fit particular applications. Thus, a feature such as global position sensing could be included in a BBIC designed for a distributed sensing application.

BIOLUMINESCENT BIOREPORTERS

In prokaryotes, the system, designated *lux*, consists of a luciferase composed of two different subunits coded by the genes *luxA* and *luxB* that oxidize a long chain fatty aldehyde to the corresponding fatty acid resulting in a blue-green light emission near 490 nm **[3-5]**. The system also contains a multienzyme fatty acid reductase consisting of three proteins (a reductase encoded by *luxC*, a transferase encoded by *luxD*, and a synthetase encoded by *luxE*) which both initially converts and recycles the fatty acid to the aldehyde substrate. Thus, no exogenous addition of substrate is required to induce luminescence. The genes are contained on a

[1] Research partially sponsored by the U.S. Department of Energy and partially performed at Oak Ridge National Laboratory, managed by Lockheed Martin Energy Research Corp. for the U.S. Department of Energy under Contract No. DE-AC05-96OR22464.

0-9640024-2-6/hh1998/$20©1998TRF
DOI 10.31438/trf.hh1998.82

single continuous operon. This genetic configuration allows the cloning of the complete *lux* gene cassette (reporter genes) downstream from different promoters for the utilization of bioluminescence to monitor gene expression.

Implicit in the use of a bioreporter strain for a BBIC is that the bioluminescent signal generated is directly related to the concentration of the target substance, most desirably in a selective and quantitative manner. In general, the *lux* reporter genes are placed under the regulatory control of inducible operons maintained in native plasmids, broad host range plasmids, or chromosomally integrated into the host strain. In these genetic systems, the target analyte or its degradation products act as the inducer of the bioluminescence genes, and are responsible for selectivity and the resultant response. For example, *P. fluorescens* HK44 is a bioreporter that produces light in the presence of naphthalene. This strain has two genetic operons positively regulated by a LysR protein. One of the operons contains the *lux* bioluminescence genes and the other the genes responsible for the degradation of naphthalene to salicylate, the metabolic intermediate of naphthalene degradation. Both operons are induced when salicylate interacts with the regulatory protein NahR. Therefore, exposure of HK44 to either naphthalene or salicylate results in increased naphthalene gene expression and increased bioluminescence.

Initial studies in continuous cultures of *P. fluorescens* HK44 have demonstrated that the magnitude of the bioluminescence response correlated with the aqueous phase concentration of naphthalene under dynamic pulsed perturbation conditions **[6]**. Reproducible bioluminescence was observed not only in aqueous naphthalene samples but also in soil slurry samples which were spiked with naphthalene, complex soil leachates, and the water soluble components of jet fuel **[7]**. *P. fluorescens* HK44 can be applied in environmental use for either quantitative analysis of contaminant presence or bioavailability. However, for such applications both the chemical complexity of the environment and the physiological conditions of the organisms must be considered in interpreting the bioluminescence response.

Many types of bioluminescent (*lux*) transcriptional gene fusions have been used to develop light emitting bioreporter bacterial strains to sense the presence, bioavailability, and biodegradation of other pollutants including toluene **[8]**, and isopropylbenzene **[9]**. Analogous genetic approaches have also been reported for inducible heavy metal detoxification and resistance systems including mercury **[10]**, as well as the heat shock response **[11]** and response to oxidative stress **[12]**. In addition, genetically engineered Gram positive bioreporters have been used to examine the efficacy of antimicrobial agents (decreased light equates to greater efficacy) **[13,14]**. Eukaryotic bioreporters have also been generated to detect toxic compounds **[15,16]**, oxygen **[17]**, ultraviolet light **[18]**, and estrogenic and antiestrogenic compounds **[19]**. Environmental applications involving bioluminescence measurements have been reviewed **[20]**.

PROTOTYPE BBIC AND EXPERIMENTAL RESULTS

A prototype BBIC was constructed by placing the toluene sensitive bioreporter, *P. putida* TVA8, above a custom optical application specific integrated circuit (OASIC) shown in Fig. 1. This device employed the p-diffusion (source and drain diffusions of p-channel MOSFETs) as a photodiode. The shallow p-diffusion has a strong response to the 490-nm bioluminescent signal **[21]**, and the p-diffusion/n-well junction can be operated

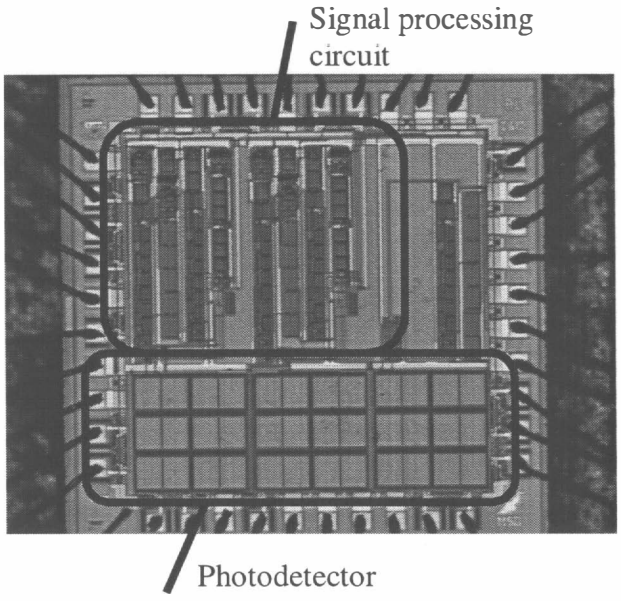

Figure 1. *The OASIC used in the BBIC prototype. This device measures 2.2 mm X 2.2 mm and was fabricated in a standard CMOS IC process.*

with a zero reverse bias without being set to either power supply rail. Thus, the leakage and noise of the photodiode can be minimized.

The front-end signal conditioning circuit (Fig. 2) was a current-to-frequency converter (CFC). When compared to conventional electrometer circuits, this signal conditioning circuit provided lower noise (no resistor in the feedback path), faster recovery from overloads (no long time constants), and larger dynamic range. A digital signal proportional to the sum of the leakage and photo- current was generated by counting pulses from the CFC for a specified time (i.e. the integration time). The entire OASIC, including photodetector and CFC measured 2.2 mm X 2.2 mm, and was fabricated in a standard 1.2-μm, n-well, CMOS process. Fig. 3 shows the BBIC (including the bioreporter enclosure) as used in the characterization experiments.

With no luminescent signal coming from the cells, multiple measurements were taken with the integration time set to 1-minute. Leakage currents produced a signal of ~ 6 counts/minute with a standard deviation (σ) of 0.22 counts/minute. As expected, the σ decreased with the square root of the integration time. Longer integration times were produced off-line by summing 1-minute measurements.

Bioluminescence was induced in the BBIC cells and a control sample of cells by exposure to toluene vapor. From the control sample measurements, we estimate that the toluene concentration was no more than 1 ppm. A signal of 12 counts/minute (6 counts/minute above background) was measured. From previous measurements, *P. putida* TVA8 is known to have a linear response to toluene concentration until saturating when the concentration reaches a level of approximately 10 ppm **[8]**. Assuming that a minimum detectable signal is 2σ above background, then the minimum detectable concentration (MDC) of toluene for this BBIC (in parts per billion (ppb)) is given by

$$MDC = \frac{20{,}000\sigma}{\sqrt{T_{\text{int}}}\,S_{sat}} \qquad (1)$$

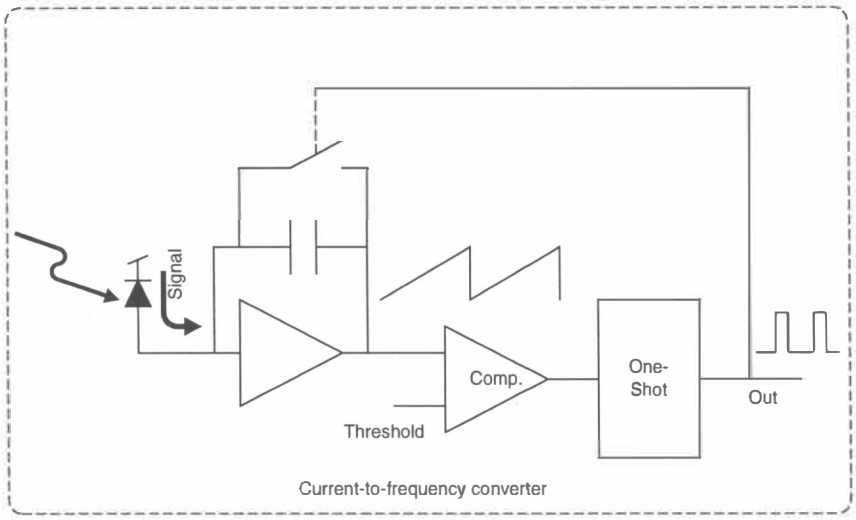

Figure 2. *Front-end signal processing circuit for the prototype BBIC.*

where *Ssat* is the signal in counts/minute at a concentration of 10 ppm, and T_{int} is the integration time in minutes. The minimum detectable toluene concentration for this BBIC as a function of integration time is shown in Fig. 4. In general, the minimum detectable concentration is also a function of the number of bioreporter cells and the area of the photodiode.

A naphthalene-sensitive BBIC was produced using the OASIC described above and the bioreporter *P. fluorescens* 5RL. Using the same experimental procedure described above, this BBIC was exposed to napthalene vapor with a concentration of approximately 10 ppm. A signal of 240 counts/minute was recorded. The minimum detectable concentration of naphthalene as a function of integration time for this BBIC is shown in Fig. 5.

CONCLUSIONS

This paper presents early results from efforts to produce chemical sensors by combining engineered bioluminescent bioreporters and integrated circuit technology. The experimental results we have presented show that very good sensitivity can be

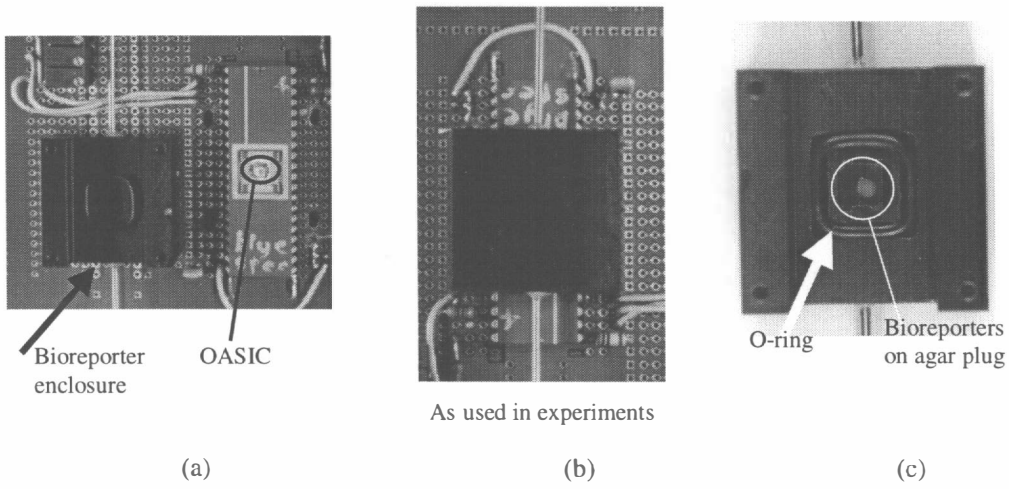

Figure 3. *The prototype BBIC showing: (a) the OASIC mounted in a 40-pin ceramic chip carrier and the enclosure for the cells; (b) the enclosure mounted on the chip as configured for experiments; and (c) the enclosure with bioreporters on an agar plug. The o-ring is used to make a light-tight seal between the ceramic chip carrier and the bioreporter enclosure.*

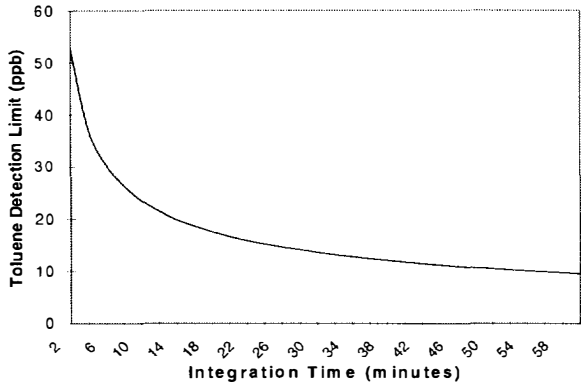

Figure 4. *Minimum detectable concentration of toluene as a function of integration time for the prototype BBIC employing the bioreporter Pseudomonas putida TVA8.*

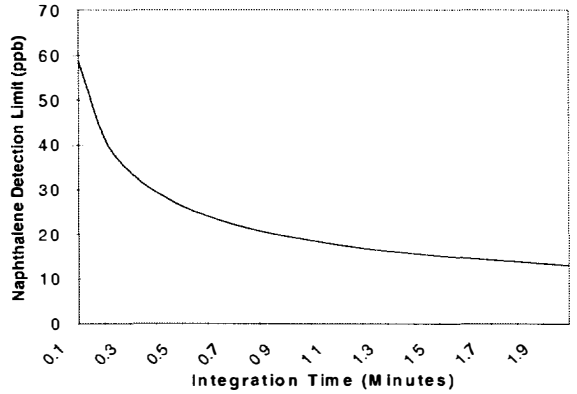

Figure 5. *Minimum detectable concentration of naphthalene as a function of integration time for the prototype BBIC employing the bioreporter P. fluorescens 5RL.*

obtained using the BBIC concept. In addition, the bioreporters can provide exceptional specificity. However, to this point, our experiments have been conducted in well-controlled laboratory environments.

At present we have on-going work to develop bioreporter entrapment techniques and bioresistant/biocompatible thin-film deposition techniques that promise to produce rugged, long-lived BBICs that can be deployed in useful sensing applications **[22]**. In addition, we are adding signal processing and communications functionality to the OASIC to increase the flexibility of the BBIC. With the successful development of these technologies, we envision BBICs being used in applications such as environmental sensing/assessment, medical diagnostics, and drug discovery.

ACKNOWLEDGEMENTS

Portions of this report are supported by U.S. DOE grant # DE-FG05-94ER61870 from the Office of Biological and Environmental Research.

REFERENCES

1. Bousse, L. (1996) *Sens. Actuat.* 34, 270-275
2. Buerk, D. G. (1993) in *Biosensors, Theory and Applications* pp. 1179-1193, Technomic Publications, Lancaster, PA, USA
3. Tu, S. and Mager, H. I. X. (1995) *Photochem. Photobiol.* 62, 615-624
4. Meighen, E. A. (1991) *Microbiol. Rev.* 55, 123-142
5. O'Kane, D. J. and Prasher, D. C. (1992) *Mol. Microbiol.* 6, 443-449
6. King, J. M. H. (1990) *et al. Science* 249, 778-781
7. Heitzer, A. *et al.* (1992) *Appl. Environ. Microbiol.* 60, 1487-1494
8. Applegate, B. *et al.* (1997) *J. Ind. Microbiol.* 18, 4-9
9. Selifonova, O. V. and Eaton, R. W. (1996) *Appl. Environ. Microbiol.* 62, 778-783
10. Selifonova, O., Burlage, R. S. and Barkay, T. (1993) *Appl. Environ. Microbiol.* 59, 3083-3090
11. Van Dyk *et al.* (1994) *Appl. Environ. Microbiol.* 60, 1414-1420
12. Belkin, S. *et al.* (1996) *Appl. Environ. Microbiol.* 62, 2252-2256
13. Andrew, P. W. and Roberts, I. S. (1993) *J. Clin. Microbiol.* 31, 2251-2254
14. Cooksey, R. C., Crawford, J. T., Jacobs, W. R. Jr. and Shinnick, T. M. (1993) *Antimicrob. Agents Chemother.* 37, 1348-1352
15. Anderson, J. W., Rossi, S. S., Tukey, R. H. and Quattrochi, L. C. (1995) *Environ. Toxicol. Chem.* 14, 1159-1169
16. Gupta, M. and Goldwasser, E. (1996) *Nucleic Acids Res.* 24, 4768-4774
17. Filatov, D., Björklund, S., Johansson, E. and Thelander, L. (1996) *J. Biol. Chem.* 271, 23698-23704
18. Biberger, C. and Angerer, E. V. (1996) *J. Steroid Biochem. Mol. Biol.* 58, 31-43
19. Pons, M., Gagne, D., Nicolas, J. C. and Mehtali, M. (1990) *BioTechniques* 9, 450-459
20. Steinberg, S. M. and Poziomek, E. J. (1995) *Chemosphere* 11, 2155-2197
21. Simpson, M. L. et al. (1997) *Rev. of Sci. Instr.* 69, No. 2, Feb. 1998, pp. 377-383
22. Simpson, M. L., et al. (1998) *Trends in Biotech.*, to be published

DESIGN OF AN INTEGRATED SILICON-PDMS CELL CARTRIDGE

B. Derek DeBusschere, David A. Borkholder, and Gregory T.A. Kovacs
Electrical Engineering, Stanford University
Center for Integrated Systems, CISX 202X, Stanford, CA 94305-4075

ABSTRACT

The use of cell based biosensors for applications outside of the laboratory has been limited in part due to packaging issues. A design for an integrated cell cartridge that addresses the requirements of sterile fluidic interconnect and environmental regulation is presented. The device consists of a PDMS (polydimethylsiloxane) part, a glass cover, and a silicon sensing die mounted on a printed circuit board. The PDMS part forms the fluidic channels, interconnect ports, septa, and two 10 µl chambers over the active sensing area. The silicon die will include integrated biological sensors and a temperature regulation system, and the glass cover seals the chambers. Electrical and fluidic connections are made simultaneously as needles pierce septa on the cartridge when it is plugged into a zero-insertion force (ZIF) socket.

The viability of injecting suspended cells into a 10 µl volume chamber and culturing them for greater than one week using a continuous flow perfusion system has been demonstrated. Initial prototypes of the cell cartridges have been assembled and cells have been cultured in the 10 µl PDMS chambers.

INTRODUCTION

The potential uses of cell based biosensors range from high-throughput drug discovery to environmental monitoring [**1**]. Although there has been significant progress toward producing practically useful biosensors [**1-5**], there has been limited effort devoted to creating packaging that would enable their use outside of the laboratory. Current packaging designs range from petri dishes with patterned electrodes that are placed in an incubator [**3**] to elaborate sealed chambers that allow culture outside of an incubator but require laboratory facilities [**6**]. However, none of these address the critical issues of cell life support and reliable interconnect required in a portable system. In order to explore and overcome these issues, the development of an integrated silicon-PDMS cell cartridge has been undertaken.

The special requirements of a cell-based biosensor lead to a segregation of the system design into three components: sample fluidics, computer interface electronics, and a cell cartridge that integrates the cells, sensors, and environmental control. The fluidics and computer interface form the permanent base for the system while the cell cartridges are exchangeable. This paper will present a brief system overview and then provide more details on issues involved in the cell cartridge design.

SYSTEM OVERVIEW

A simplified fluid flow diagram of the system is shown in Figure 1(a) and the physical implementation in Figure 1(b). A pump is used to continuously perfuse culture media into two separate chambers on a cell cartridge. The sample under test is mixed with the input stream of one of the chambers, while the other chamber acts as a control. Both the control and test chambers experience

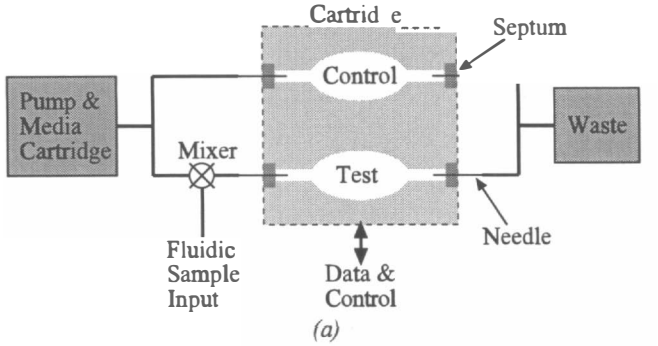

(a)

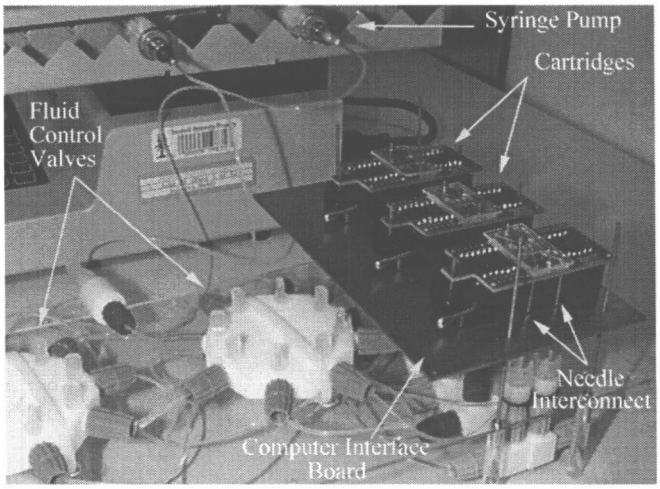

(b)

Figure 1. *(a) Simplified diagram of system showing fluid flow paths. The two chambers of the cartridge are labeled "Test" and "Control." (b) The current implementation uses a syringe pump and supports three cartridges in parallel. The computer interface board is removeable, allowing the entire fluidics system to be sterilized by autoclaving.*

the same temperature and base media, allowing for the removal of those variables from the sensor's output. The cartridge design has an integrated temperature regulation system and integrated sensors that monitor cellular activity.

Fluidic interconnect is one of the more difficult challenges for a cell based biosensor used outside of the laboratory since sterility must be maintained and the introduction of air bubbles must be avoided. Contamination of the culture by fast growing microorganisms, such as bacteria, will overwhelm the sensing cells. Excessive mechanical forces due to air bubbles moving through a microchamber can physically damage cells and overcome cell to substrate adhesion. The interconnect approach used in this design are needles that pierce septa (resealable membranes) on the cartridge. Needles and septa proved to be a simple and effective way to create a bubble-free fluidic connection that has a high probability of remaining sterile. Electrical and fluidic connections are made simultaneously

0-9640024-2-6/hh1998/$20©1998TRF
DOI 10.31438/trf.hh1998.83

as the cartridge is inserted into a ZIF socket, simplifying use and handling and allowing the cell cartridges to be easily exchanged.

Cells will be seeded into the assembled and sterilized cartridge chambers by injection through the septa. This approach allows for the possibility of chamber seeding to occur outside of a sterile hood. For remote applications, cells could be transported and stored while in suspension using hibernation media or cryogenic means [7,8]. At the location of use, the cells could be revived and injected into the cartridges without requiring a sterile hood. After the cells are given time to attach, spread, and stabilize, the cartridges would be ready to plug into the sensing system and sample flow could begin.

CELLULAR REQUIREMENTS

The cell cartridge must provide a hospitable environment for the cells. The major environmental properties that must be controlled for cell culture are the incubation temperature, the substrate material, the media, and the gas phase mixture [9]. The optimal incubation temperature for a cell culture varies according to cell type and origin, but most mammalian cell lines will grow satisfactorily at 37 °C. Cells can withstand considerable temperature drops for short periods of times and can be stored for up to a month at 4 °C using hibernation media [7] or for years at cryogenic temperatures [8]. Although temperatures a few degrees below optimal do not affect viability, cells can not tolerate higher temperatures and will die rapidly at temperatures above 40 °C. Thus, it is important to regulate the temperature in a manner that avoids overheating the cells at local hot spots. Since both the metabolism and growth rate of cells are dependent on temperature, consistency is more important than accuracy, and regulation should be maintained within ± 0.5 °C [9]. Temperature uniformity is particularly important in biosensor systems that rely on cellular metabolism as the transducer mechanism.

Most mammalian cells are anchorage dependent, that is, they require attachment to a substrate in order to survive and grow. Cells do not attach to the substrate directly but to extracellular matrix proteins that are either contained in the culture media or excreted by the cells themselves. Surfaces that do not bind well with these proteins, such as uncharged hydrophobic ones, will not support anchorage dependent cells. An additional important requirement of the substrate and of all materials that contact the culture media is biocompatibility. Biocompatible materials do not leech or vent significant amounts of toxins over the duration of the sensor's lifetime.

The two most significant constituents of the gas phase are oxygen and carbon dioxide. Oxygen is necessary for the oxidative metabolism of eukaryotic cells and is utilized at the rate of approximately 2 to 10 pg/cell/hr [10]. Since the solubility of oxygen in culture media is approximately 8 ng/µl at 37 °C, a cell culture of 1,000 cells will consume all of the dissolved oxygen in 1 µl of culture media in approximately 1 hour. Carbon dioxide is necessary only indirectly as it is involved in the bicarbonate buffer system. A lack of carbon dioxide results in a depletion of HCO_3^- in the media which is detrimental to cellular health. Most cell cultures are incubated in an atmosphere of 5 to 10% CO_2 in air that equilibrates with the bicarbonate buffer in the media at the proper pH for the cells.

The culture medium provides the nutrients (inorganic salts, amino acids, glucose, and in many cell lines, serum) necessary for cell growth and survival. In addition to the nutrients, two important properties of the media are its pH and osmolality. The CO_2 gas phase regulates the pH through the bicarbonate buffer system as described above to a typical value of approximately 7.4. The importance of osmolality arises in sample injection, as care must be taken to adjust the osmotic strength of the sample to limit osmotic stresses across the cell membrane. Although cells are tolerant of osmolalities in the range of 260 to 320 mOsm/kg, consistency to within ± 10 mOsm/kg should be maintained to avoid interfering with cellular function [9].

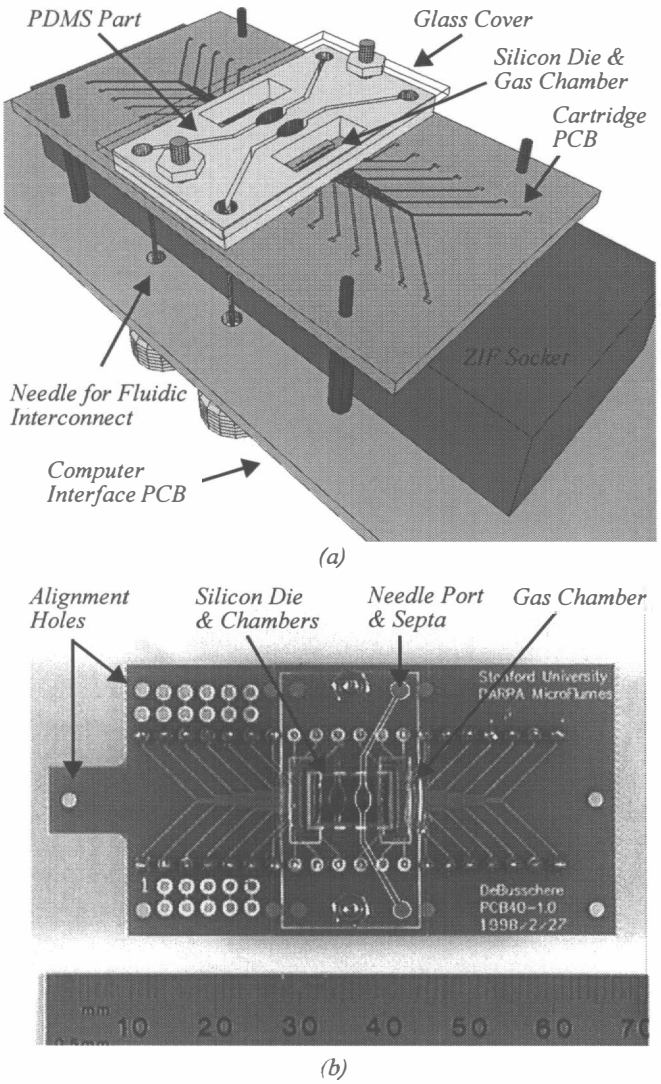

Figure 2. *(a) CAD design of the cell cartridge. The silicon die is mounted directly on the PCB and enclosed on the top and sides (except for exposed bond pad areas) by the PDMS part. As the cartridge is lowered into the ZIF socket, the needles pierce septa to form the fluidic interconnect. (b) Top view of cell cartridge prototype. The 6x9 mm silicon die can be seen as the dark rectangle beneath the two oval chambers. The 0.5 mm wide fluid channels on the right side have been highlighted in white.*

CARTRIDGE DESIGN.

Important design issues for the cell cartridge are satisfying the cellular requirements, creating reliable electrical and fluidic connections, and integrating useful biological sensors to monitor cellular activity. The cartridge design consists of a PDMS part, a glass cover, and a silicon sensing die mounted on a printed circuit

board (Figure 2). The PDMS part forms the fluidic channels, interconnect ports, septa, and two 10 µl chambers over the active sensing area. The silicon die contains microelectrodes for action potential and impedance measurements, temperature sensors, thin-film pH sensors, and a temperature regulator. The glass cover seals the chambers and allows the additional use of visual and fluorescence microscopy to monitor cellular activity.

The printed circuit board acts as rigid mounting structure and forms the electrical interconnect from the silicon die to the ZIF socket. Soft gold was used for the traces in order to allow bond pad wire connections to be made to them. The PCB also contains alignment holes for guide posts that ensure that the fluidic system needles contact only the septa during cartridge removal and insertion.

The properties of PDMS (Dow Corning Sylgard 184 Silicone Elastomer) make it a nearly ideal material for this application. PDMS is biocompatible and its strong hydrophobicity prevents cellular material from easily adhering to it **[11]**. It can withstand a broad temperature range (-55 °C to 130 °C) while maintaining its soft, elastomeric properties which are useful in both acting as a gasket to form a seal with the silicon die and glass cover and acting as septa for the fluidic connections. Unlike most silicones, PDMS absorbs less than 0.1% water, and sterilization can be accomplished using Cobalt 60 or autoclaving. As can be seen in Figure 2, PDMS is very transparent even at thicknesses greater than one millimeter. Another very important property is its high gas permeability to oxygen and carbon dioxide (7 and 35 x 10^{-15} $m^3(STP)\cdot m/(m^2\cdot s\cdot Pa)$, respectively) **[12]**. Thus, with only one material, PDMS can be used to form the fluidic channels and chambers, the septa, the gasket seal, and the permeable membrane while providing optical access.

The standard cell substrates used in traditional cell culture are glass and single-use plastics such as polystyrene which have good optical properties and favorable surface charges. In the application of silicon based biological sensors, the variety of possible cell substrates is constrained by the thin films available in the integrated circuit process. Potential candidates are silicon dioxide, silicon nitride, silicon carbide, and organics such as photoresist and polyimide. The most important properties of the thin film are biocompatibility and a favorable surface charge that promotes cellular adherence. Other factors, such as the ability to block mobile ions in the culture media from the integrated circuits below, low dielectric constant to minimize electrical parasitics to the wafer substrate below, and ease of cleaning and sterilization, are also important to consider. With the exception of a low dielectric constant, silicon nitride has all of these favorable properties and has been used successfully in earlier designs **[5]**.

Calculations predict heater power consumption will be less than 50 mW, with the majority of the power loss due to conduction through the PCB and the bond wires and not due to heating the media. This power consumption level should not create a temperature gradient of more than 0.15 °C across the die beneath the chambers, and these calculations were used to justify the assumption of an isothermal silicon die for the computer simulation shown in Figure 3(a). This simulation was performed to verify that room temperature media will reach the proper temperature before it contacts the cells. All simulations assume a flow rate of 10 µl/min. Although this rate is approximately 10 to 100 times the required rate to supply sufficient oxygen to the cells, these rates may be desirable during testing for biological agents. Assumptions made in the simulation include an isothermal silicon die at 37 °C, room temperature media at 20 °C, and a power loss of 25 $W/(m^2\cdot K)$ from the materials to the surrounding air. The simulated worst case required power consumption to maintain the cells at the proper temperature was less than 100 mW. It is important to remember that the incoming media needs to have been equilibrated at 37 °C with the proper gas phase in order to prevent the formation of air bubbles when the media is heated in the chambers.

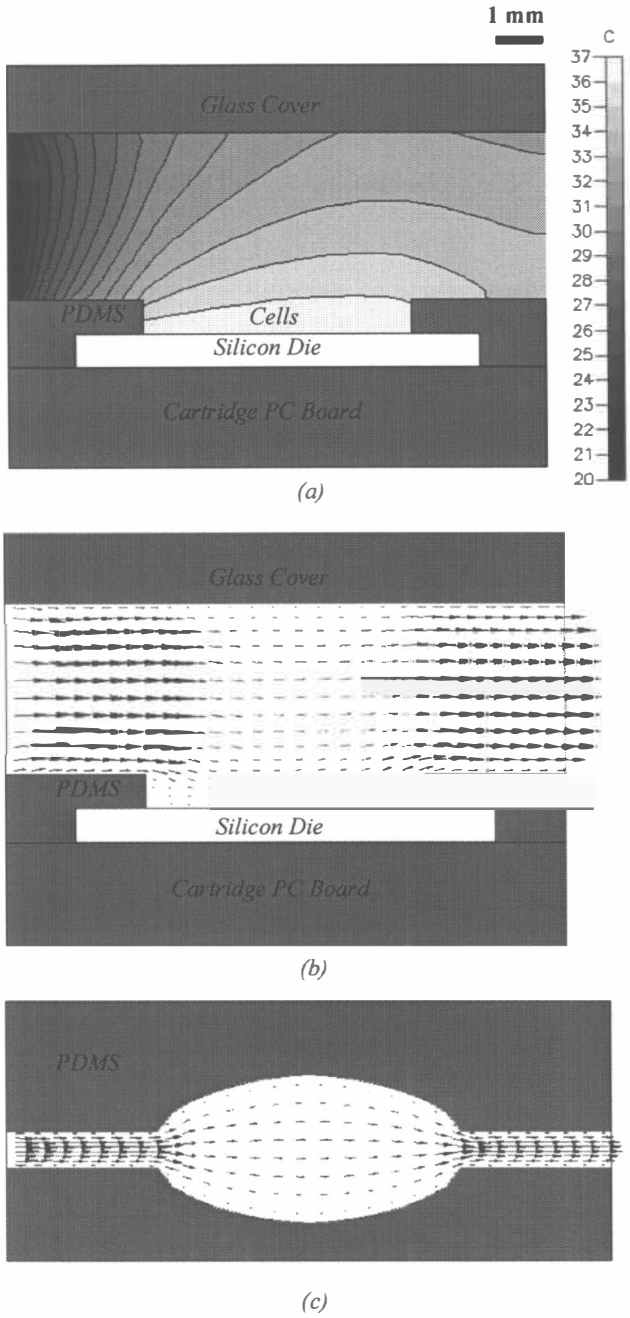

Figure 3. *Computer simulations (software tool from the CFD Research Company) of temperature distribution and fluid flow through the microincubator. All assume a flow rate of 10 µL/min from left to right. (a) The side view of the temperature profile shows that room temperature media is heated to the required 37 °C above the cells. Side view (b) and top view (c) of fluid flow velocity. Larger arrows indicate higher fluid velocity.*

The simulations shown in Figures 3(b) and 3(c) were performed in order to visualize the fluid flow. The simulations indicate that the 0.5 mm high protective shelf formed by the PDMS overlapping the silicon die will provide some protection from shear forces

due to strong currents. Even without flow mixing, the shelf is thin enough that diffusion should allow samples to reach the cells.

Although the nutrient supply in the chamber is sufficient to last a week without replenishment, the oxygen supply in a sealed chamber will typically last less than a day. The substrate area of the 10 µl chamber is approximately 6.5 mm^2 which will typically support a cell density of up to about 5,000 cells (typical plating densities range from 100 to 1,000 cells/mm^2). The amount of dissolved oxygen in 10 µl of chamber will support these cells for less than two hours; thus, either a gas permeable membrane must exist or media must be continuously perfused to provide oxygen. The oxygen requirement does not pose a problem during testing since a flow perfusion system is required for sample introduction. However, for incubation periods, it would be preferable to not require an active fluidics system. Fortunately, with the proper chamber design, the high gas permeability of PDMS will provide sufficient oxygen to the cells, but the high permeability to carbon dioxide can also disrupt the CO_2 gas phase and alter the pH of the media. In order to take advantage of the gas permeability, a gas reservoir with the proper gas mixture must be in contact with the membrane; so, the design incorporates two gas chambers (Figure 2(a)) over the silicon die's bond pads. These chambers will be filled (by injection) with the proper CO_2 in air mixture to control the pH and provide enough oxygen for the cells to survive several days. The sides of the PDMS exterior need to be coated with a CO_2 impermeable material in order to preserve the injected gas mixture.

Several experiments have been performed in order to test the cartridge design. Cell adhesion properties have been tested on silicon oxide, silicon nitride, silicon carbide, and on a LPCVD PTFE-like thin film. Silicon nitride and silicon carbide both support cell culture quite well, and the hydrophobic PTFE-like surface inhibits cellular adhesion allowing for the possibility for photolithographic patterning of cell location. The viability of injecting suspended cells into a gas impermeable 10 µl volume chamber and culturing them for greater than one week using a continuous flow perfusion system has been demonstrated with NG-108 (neuroblastoma x glioma hybrid) cells. The needle and septa interconnect system worked well outside of a sterile hood, allowing multiple connections as media sources were exchanged. Cells have been cultured in the PDMS chamber discussed in this paper, but since the integrated circuit die has not yet been fabricated, an external heater was necessary.

INTEGRATED CIRCUITS AND SENSORS

The 6 x 9 mm floorplan for the silicon die is shown in Figure 4. A smaller 2.5 x 2.5 mm test die with the identical subcircuits is in fabrication, and upon verification of correct circuit functionality, devices with this larger floorplan will be fabricated. The black outline of the PDMS part shows the chamber locations and that the bondpads are uncovered to allow for wire bonding to the PCB. Each chamber has three large pseudo-reference electrodes, four arrays of sixteen microelectrodes each, multiple pH and temperature sensors, and nine sixteen channel multiplexers. Digital logic, which uses a three wire serial interface, controls the multiplexers.

The temperature regulation system is located in the center of the die. The system consists of a diode temperature sensor, a control amplifier, and a MOSFET heater connected in a closed loop system (Figure 5(a)). The temperature control reference voltage will be set with an off-chip resistor, and the control loop will be compensated with an off-chip capacitor. The heater surrounds the temperature

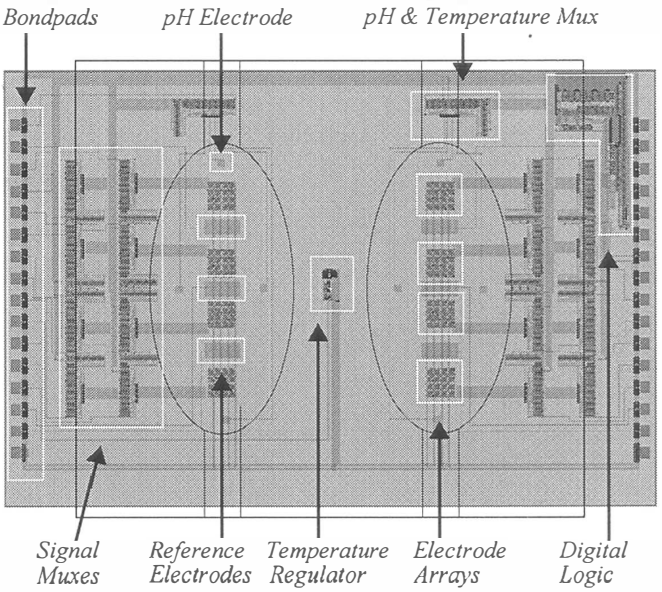

Figure 4. *Circuit layout with analog amplifiers, temperature regulator, and digital logic. The PDMS part is outlined in black above the layout to indicate chamber positions.*

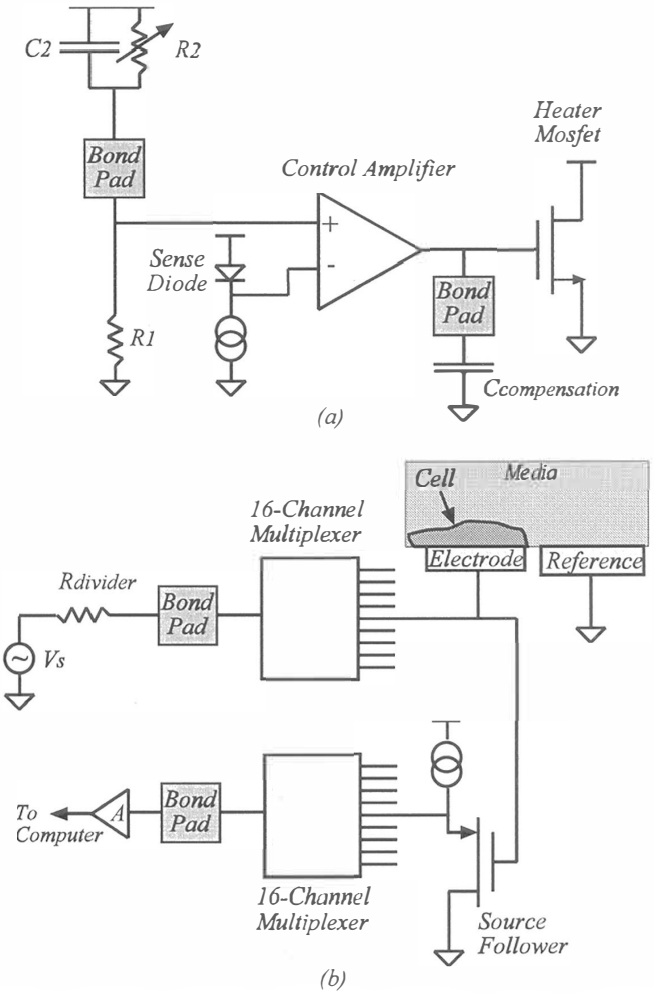

Figure 5. *Block diagrams of circuits planned for cartridge chip. (a) The temperature regulation system. (b) The analog signal paths for the microelectrode arrays.*

sensor at a distance of less than 20 microns in order to maximize the bandwidth of the thermal pole. The close proximity of the sensor should also prevent any local overheating due to temperature gradients from the heater to the sensor.

The primary sensors for the cell cartridge are platinized gold microelectrodes. Each microelectrode has a connection to two separate multiplexers (Figure 5(b)). One connection is direct to a multiplexer (for platinization, impedance measurements, and unbuffered action potential measurements), while the other connection goes to a low-noise source follower whose output is routed through the second multiplexer (for buffered action potential measurements). This allows simultaneous action potential recordings from four buffered and four unbuffered microelectrodes per chamber. The impedance of the cell-electrode interface has also been shown to be an indicator of biological activity [**3**]. During impedance measurements, the AC signal V_s is voltage divided by the combination of $R_{divider}$ and the impedance of the cell-electrode interface. The pseudo-reference electrodes, approximately 1,000 times the area of the sensing microelectrodes, will be used to hold the solution at a near constant potential during the impedance and action potential measurements.

Two additional multiplexers provide analog channels for monitoring temperature and pH across the chambers. Diode temperature sensors will be distributed across the die to monitor any temperature gradients due to heating losses. A pH sensor will allow the detection of shifts in pH due to incorrect gas phase, improper sample preparation, or contamination. When continuous perfusion is not used, the pH will also indicate when the gas mixture in the gas chambers needs to be replenished. The lack of a true reference electrode in the microchamber requires the use of differential sensing between three electrodes to measure pH [**13**]. In this method, two pH sensitive thin-film electrodes (or potentially ISFETs) with different output slopes are measured differentially against a noble metal pseudo-reference electrode. The output of this method eliminates the requirement of measuring the actual potential of the electrolyte. The anticipated method of forming the pH sensitive electrodes will be by electrochemical deposition of thin films, such as iridium oxide, onto gold microelectrodes [**14**].

SUMMARY

The requirements to create a fieldable cell based sensor are discussed and the current design solution outlined. Prototypes have been constructed, materials have been tested, signals have been recorded from electrodes, and cells have been cultured in small volumes. Circuit designs, including amplifiers, source followers, digital control circuits, analog multiplexers, and a temperature regulation system, have been completed and are in fabrication.

ACKNOWLEDGMENTS

Dr. Dominik Jaeggi provided invaluable and greatly appreciated assistance with the modeling simulations.

DeBusschere is supported by a NDSEG Research Fellowship and project funding was provided by the DARPA MicroFlumes Program (Contract Number: N66001-96-C-8631).

REFERENCES

1. L. Bousse, "Whole Cell Biosensors", *Sensors and Actuators B (Chemical), vol. B34(1-3),* 270-5 (1996).

2. G. W. Gross, B. K. Rhoades, H. M. E. Azzazy, and M. Wu, "The Use of Neuronal Networks on Multielectrode Arrays as Biosensors", *Biosensors & Bioelectronics, vol. 10(6-7),* 553-67 (1995).

3. C. R. Keese and I. Giaever, "A Biosensor that Monitors Cell Morphology with Electric Fields", *IEEE Engineering in Medicine and Biology, vol. 13(3),* 402-8 (June/July 1994).

4. H. M. McConnell, J. C. Owicki, J. W. Parce, D. L. Miller, G. T. Baxter, H. G. Wada, and S. Pitchford, "The Cytosensor Microphysiometer: Biological Applications of Silicon Technology", *Science, vol. 257(5078),* 1906-12 (25 September 1992).

5. D. A. Borkholder, B. D. DeBusschere, and G. T. A. Kovacs, "An Approach to the Classification of Unknown Biological Agents With Cell Based Sensors", *Technical digest of the 1998 Solid-State Sensor and Actuator Workshop*, Hilton Head Island, SC, 6/7-6/11, Transducer Research Foundation, Cleveland (1998).

6. G. W. Gross and F. U. Schwalm, "A Closed Flow Chamber for Long-term Multichannel Recording and Optical Monitoring", *Journal of Neuroscience Methods, vol. 52,* 73-85 (1994).

7. G. J. Brewer and P. J. Price, "Viable Cultured Neurons in Ambient Carbon Dioxide and Hibernation Storage for a Month", *Neuroreport, vol. 7(9),* 1509-1512 (1996).

8. J. Hornung, T. Muller, and G. Fuhr, "Cryopreservation of Anchorage-Dependent Mammalian Cells Fixed to Structured Glass and Silicon Substrates", *Cryobiology, vol. 33(2),* 260-270 (1996).

9. R. I. Freshney, "Culture of Animal Cells: A Manual of Basic Technique", 3rd ed., Wiley-Liss, Inc., New York, NY (1994).

10. R. E. Spier and B. Griffiths, "An Examination of the Concepts Germane to the Oxygenation of Cultured Animal Cells", *Developments in Biological Standards, vol. 55,* 81-92 (1982).

11. A. J. You, R. J. Jackman, G. M. Whitesides, and S. L. Schreiber, "A Miniaturized Arrayed Assay Format for Detecting Small Molecule-Protein Interactions in Cells", Chemistry & Biology, vol. 4(12), 969-975 (1997).

12. S. A. Stern, V. M. Shah, and B. J. Hardy, "Structure-Permeability Relationships in Silicone Polymers", *Journal of Polymer Science, Polymer Physics Edition, vol. 25,* 1263-1298 (1987).

13. H. Wong and M. H. White, "A CMOS-Integrated 'ISFET-Operational Amplifier' Chemical Sensor Employing Differential Sensing". *IEEE Transactions on Electron Devices, vol. 36(3),* 479-487 (1989).

14. K. Pasztor, A. Sekiguchi, N. Shimo, N. Kitamura, and H. Masuhara, "Iridium Oxide-based Microelectrochemical Transistors for pH Sensing", *Sensors and Actuators B (Chemical), vol. B12(3),* 225-230 (1993).

HIGH ASPECT RATIO SILICON MICROSTRUCTURES FOR NUCLEIC ACID EXTRACTION

Lee A. Christel, Kurt Petersen, William McMillan, Gregory T. A. Kovacs
Cepheid
1190 Borregas Ave
Sunnyvale, CA 94089

ABSTRACT

Silicon fluidic microchips with high surface area to volume ratios have been fabricated using deep reactive ion etching (DRIE) technology **[1,2]**. These microchips have been used as capture surfaces for nucleic acids (NA). Short (500 bp) and medium size (48,000 bp) DNA have been captured, washed, and eluted with these chips using glass binding chemistries. DNA quantities approaching 40 ng/cm^2 of binding area were captured from input solutions in the 100-1000 ng/mL concentration range, and detected using fluorescence techniques. For low concentration studies, PCR and gel electrophoresis were used as the detection method. Extraction efficiencies of about 50%, and concentration factors of about 10 have been demonstrated using bacteriophage lambda DNA as the target. From an input volume of 500 µL containing 5 x 10^4 DNA molecules, 2-3 x 10^4 DNA molecules were extracted and eluted into a 25 µL volume. These results demonstrate the viability of utilizing such microchips as an element in a compact, disposable cartridge format for the detection of DNA in applications such as clinical diagnostics, biowarfare agent detection, food quality control, and environmental monitoring.

INTRODUCTION

Important diagnostic tests such as HIV viral load in the blood of clinical AIDS patients depend on the detection of small quantities of DNA or RNA. Such tests utilize polymerase chain reaction (PCR) **[3]** to amplify (multiply) the number of copies of a target sequence to a detectable level. The PCR technique requires a relatively pure DNA sample in aqueous solution, free of contaminants that inhibit the PCR process. Such inhibitors include heavy metals, such as the iron in hemoglobin, nucleases, certain proteins and enzymes found in raw biological samples. There is thus a need for methods to extract and purify DNA from a variety of samples.

Many DNA purification kits are available commercially **[4]**, each for a particular DNA or RNA and input sample. Typically, these kits utilize some form of silica gel, glass matrix, or membrane as the capture medium since it is known that NA will bind to glass or other silica-type surfaces under the proper chemical conditions **[5]**. A typical protocol for DNA purification involves a number a steps whereby various reagents are added to the sample and the sample is centrifuged to separate precipitated components from the solution. Such a procedure is quite involved, and in many cases is still done manually. Although such a procedure can be automated using robotics, integrating such a protocol into a low cost, disposable analysis format requires a reexamination of the entire process.

As the broad application of the PCR technique continues to be refined and recognized, there is enormous market pressure to improve the cost and throughput of DNA/RNA tests. There are many applications where a small DNA analysis tool utilizing disposable cartridges would expand markets if the costs and throughputs can be improved. Such cartridges would likely combine low-cost plastics technology with selected micromachined components for critical functions such as DNA extraction. The motivation for this work is the broader goal of developing an automated analysis system which takes raw sample inputs and gives a PCR result in a few minutes. Flow-through cartridge designs capable of reagent containment, mixing and delivery for the processing of significant clinical sample volumes, while maintaining small internal volumes of critical components, appear promising. DNA extraction chips are an important component of this strategy.

We have fabricated high surface area DNA capture surfaces of oxidized silicon using deep reactive ion etching (DRIE) and are investigating the ability of these structures to controllably capture and release DNA from test solutions. Several parameters are of primary importance if such a chip is to be commercially viable. The chip must have sufficient binding capacity to retain the quantity of DNA required for the subsequent assay. It must extract the DNA efficiently, i.e. the ratio of target DNA captured to target DNA input must be high (exceed 50%). It must be able to complete the extraction in a reasonable amount of time, i.e. the capture must occur at reasonable flow rates, so that clinically realistic volumes (sometimes several mL) can be processed expeditiously. The chip must also concentrate the input DNA, allowing the DNA to be eluted (released) into a small volume for PCR amplification. These volumes are typically 100 µL or less to conserve expensive PCR reagents. The chip must allow wash solutions to be efficiently passed through while retaining the DNA, so that contaminants, such as PCR inhibitors, can be excluded from the final elution without requiring large volumes of wash solution typically associated with commercial kits. Finally, the chip must have a reasonable cost, preferably less than one dollar, in order to be used in a disposable format. If the above conditions can be met, there is a large market opportunity for DNA assays in a wide range of markets, including clinical and veterinary diagnostics, food and environmental monitoring, forensics, and biowarfare detection.

CHIP FABRICATION

The process used to produce the DNA capture chips is shown in Fig. 1. This process is simpler than competing technologies such as LIGA **[6]**. Fabrication starts with 100mm (100) silicon, double-side polished, approximately 400 µm thick. The wafer is first oxidized to produce a thin pad oxide, and then coated with silicon nitride. The backside is patterned and etched in KOH to produce fluidic ports that are 200 µm deep. The frontside is next patterned with the DRIE mask, and etched for approximately one hour in an STS DRIE plasma etcher to produce a field of up to 5,000 pillars, each being 200 µm high. At the end of this etch, the frontside pattern meets the backside ports. The wafer is further oxidized to coat the internal surfaces with silicon dioxide. The silicon nitride prevents additional oxidation of the top surface. The nitride and underlying pad oxide are now removed by plasma and wet etching to produce a bare silicon upper surface. A cover of pyrex™ is anodically bonded to the wafer to finish the process. The wafer is then ready for sawing to produce the finished square die, which are 3.85 mm on a side.

0-9640024-2-6/hh1998/$20©1998TRF
DOI 10.31438/trf.hh1998.84

Solid-State Sensors, Actuators, and Microsystems Workshop
Hilton Head Island, South Carolina, June 8-11, 1998

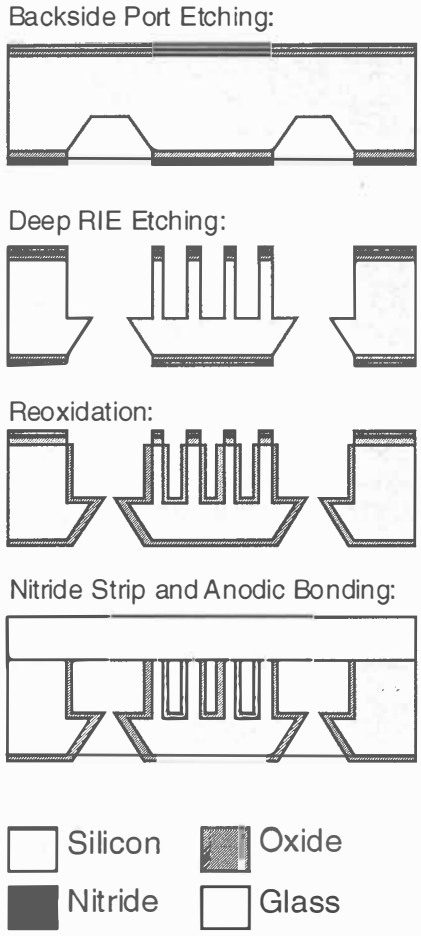

Figure 1. *Process flow for the fabrication of high aspect ratio DNA capture surfaces in silicon*

Figure 2 shows an SEM of one chip surface consisting of 200 μm high columns, each about 20 μm in diameter, with a pitch of 34 μm. Chips with pillar diameters of 10 μm and a pitch of 18 μm have also been made. After anodic bonding to the glass top cover, the chip has a total internal surface area of 36 mm^2 in an 'active' area of 3.5 mm^2.

EXPERIMENTAL DETAILS

The DNA capture studies reported here can be divided into two types: high concentration inputs (on the order of 100-1,000 ng/mL) and low concentration inputs (at or below 10^5 copies of target DNA). These two regimes have relevance to different clinical situations. Samples involving genomic DNA, such as might be present in a sample containing lysed white blood cells, typically have large concentrations of DNA. On the other hand, samples used for diagnosis of infectious diseases often contain only very small amount of pathogenic DNA of interest. Serum, plasma, and urine are examples of the latter situation. For high concentration studies, the quantities of DNA are large enough that fluorescence techniques can be used to detect the DNA. For low concentrations however, PCR must be used to first amplify a target sequence, and only then can the presence of the target DNA be verified usually by gel electrophoresis. Quantitation of the PCR product is more difficult, and the use of calibration standards run through PCR in parallel is mandatory.

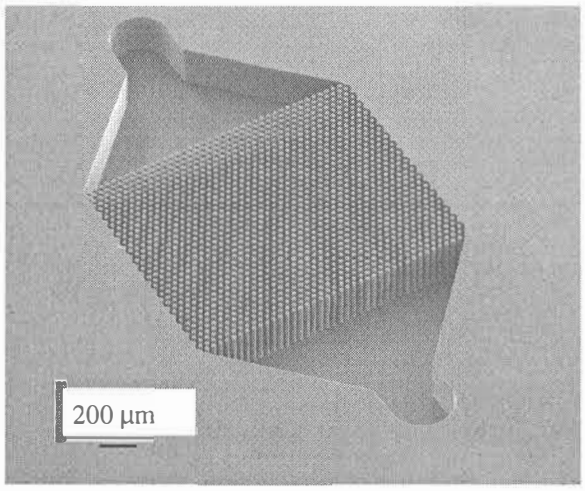

Figure 2. *SEM of DNA Capture Chip Surface. These pillars are 200 μm high with a pitch of 34 μm.*

For DNA capture studies, a fluidic test system has been constructed. It consists of a chip holder, and several computer controlled syringe pumps and valves. A schematic representation of the fluidic system is shown in Fig. 3. An acrylic chip holder allows multiple fluidic connections to be made to the backside of the chip via 0.01" ports and an elastomeric gasket between the chip and fixture. Two syringe pumps allow fluids to be aspirated from source reservoirs into storage loops, and dispensed either to the chip or to waste. Several distribution valves are used to control fluid routing. All valve and pump motions are controlled via the RS-232 interface of an IBM-compatible PC. Protocols are written and stored as stand-alone programs, insuring that the experimental conditions are consistent from run to run.

Starting solutions were obtained by diluting high concentration DNA stock solutions with a glass binding solution from a commercially available DNA purification kit **[4]**. This binding solution is a chaotropic salt solution, intended to both denature proteins that might be present in a real clinical sample, and to produce conditions that allow binding to glass. Such a solution is a good representation of the chemical environment that would be presented to the chip in a real clinical sample. Wash and elution reagents were also taken from the same commercial kit. The wash solution is typically an ethanol-based solution, with several other ionic components. Elution solutions are either TE (10 mM Tris-HCl and 1 mM EDTA), or water.

A typical experimental protocol is as follows. The chaotropic DNA starting solution is first passed through the chip, during which DNA present in the solution binds to the silicon dioxide-coated microstructure. This is then followed by the ethanol-based wash solution. The wash solution is intended to wash away the salts and other PCR inhibitors that might be present in the sample. Finally an elution reagent is passed through the chip, releasing the DNA back into the fluid stream. This elution is collected in small aliquots for analysis.

For detection of elutions of high concentration DNA, a Carl Zeiss fluorescence microscope was used in conjunction with a photon-counting photomultiplier tube (PMT) and software from Photon Technologies, Inc (Monmouth Junction, NJ). The microscope was fitted with a filter set designed for fluorescein. This filter set allows excitation of the sample at 490 nm, and detection at 515 nm and beyond. This setup is suitable for fluorescein-labeled DNA, as well as for several other DNA dyes, such as YOYO-1 and PicoGreen **[7]**.

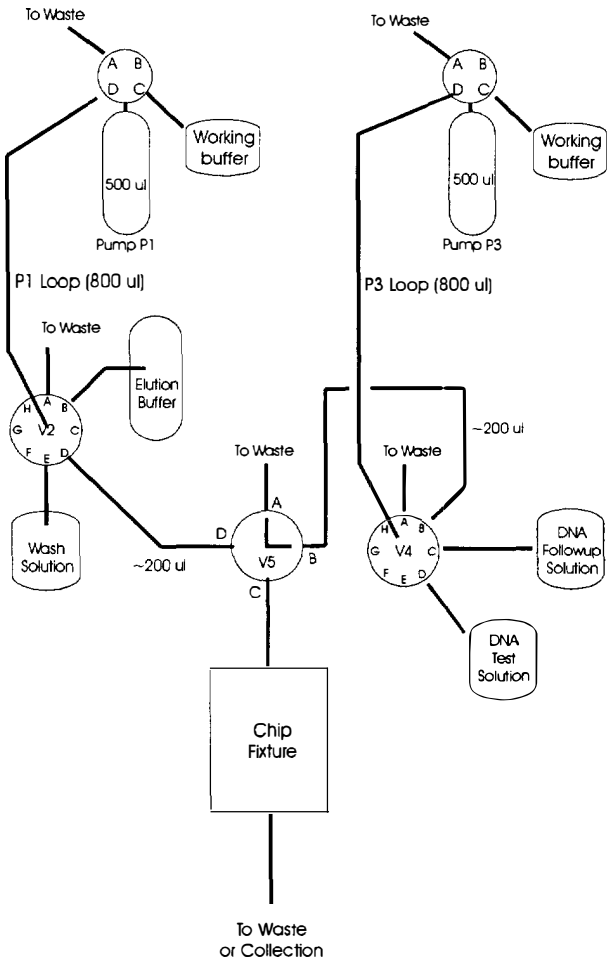

Figure 3. Schematic of Fluidic Test System.

For low concentration studies, chip output was processed through a standard PCR protocol using a Perkin Elmer 9700 thermal cycler. Reference samples spanning several orders of magnitude in target starting copy number were run in parallel. PCR product was then processed through gel electrophoresis, typically with 1% agarose gels and ethidium bromide staining. Photographs of the resulting gel bands were compared visually to the reference standards to estimate the starting copy number in the chip elutions. Work in progress is aimed at improving further the quantitation of the PCR product.

HIGH CONCENTRATION RESULTS

For high concentration studies, a solution of plasmid digest DNA from Bio-Rad was used as the starting material **[8]**. This solution consists of a mix of DNA with an average length of about 500 bp. The material is tagged with fluorescein, a fluorescent marker, allowing in-situ observation of the DNA during sample processing.

The chip elutions were collected into a Delrin fixture consisting of a number of small wells, each with a volume of approximately 25 µL. A number of 20 µL elution droplets were captured into the wells. In parallel, a series of standards of known concentration were dispensed into separate wells. 5 µL of 1.0 µM YOYO-1 dye **[7]** were then added to each well. This dye further enhances the fluorescence of the samples. After a short incubation period, the wells were measured for signal using the fluorescence microscope/PMT system.

The above protocol was performed under several experimental conditions. The ranges of experimental parameters are given in Table 1. Note that the internal volume of the chip is about 0.2 µL, leading to a residence time of 200 msec at a flow rate of 1.0 µL/s.

Table 1. *Experimental Conditions for High Concentration DNA Capture Experiments.*

Parameter	Range
DNA Conc.	100 - 1000 ng/mL
DNA Volume	400 µL
DNA Total Dose	40 - 400 ng
DNA Flow Rate	0.1 - 5.0 µL/s
Wash Volume	400 µL
Wash Flow Rate	0.5 - 5.0 µL/s
Elution Flow Rate	0.5 µL/s

The total binding capacity of high aspect ratio chips was investigated using an input of 400 ng of DNA (400 µL of a 1,000 ng/mL solution) followed by 400 µL of wash and then elution. All flow rates were 0.5 µL/s. The fluorescence signals from the sample wells, as well as those of the reference standards are shown in Fig. 4. By comparing each elution signal to the standards, and summing them, we conclude that 11-12 ng of DNA has been captured, then eluted from the chip. It has been reported **[9]** that the maximum binding capacity of glass is $\approx$ 40 ng/cm^2. Since the internal surface area of the chip is $\approx$ 0.36 cm^2, it is evident that in this experiment, an amount of DNA consistent with the maximum binding capacity of glass has been captured.

As a comparison, the same protocol was run utilizing a 'flat' chip without the enhanced surface area. This chip had an internal surface area of about 0.06 cm^2. In this case, about 2.5 ng of DNA was captured and eluted, very nearly 1/6 of that captured on the DRIE chip. This is also consistent with binding at the capacity limit of glass.

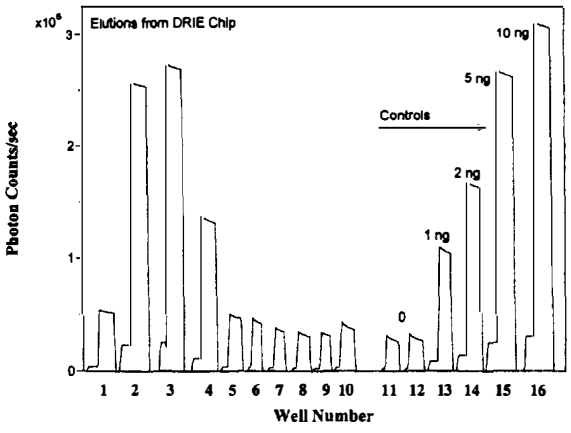

Figure. 4. *Fluorescent signals from DNA chip elutions, with reference samples. The total DNA captured is about 12 ng.*

Several other experimental conditions were examined. It was found that DNA flow rates higher than 0.5 µL/s led to reduced capture efficiency, but wash flow rates could be increased up to 5.0 µL/s without loss of efficiency. These results are summarized in Table 2.

Table 2. *Experimental Conditions for High Concentration DNA Capture Experiments. All input volumes were 400 µL.*

DNA Conc (ng/mL)	DNA Flow Rate (µL/s)	Wash Flow Rate (µL/s)	Capture Efficiency (%)
1000	0.5	5.0	2.8[1]
100	0.1	0.5	10
100	0.5	0.5	10
100	0.5	5.0	10
100	5.0	5.0	5

[1] DNA capture is at the binding limit of the structure.

LOW CONCENTRATION RESULTS

For the low concentration studies, lambda DNA (48,000 bp) **[10]** was used as a bacteria simulant. Starting solutions were again prepared by dilution of lambda stock with chaotropic salt solutions. Starting copy number for the first set of experiments was 5 x 10^4 copies in 500 µL of solution. As a control, the experimental protocol was first run using a chaotropic solution without DNA. Standards of known copy number (10^4 and 5 x 10^4) were also prepared using both water that had passed through the chip test system, and pure water.

The protocol was similar to that of the high concentration studies. Typically, 500 µL of the input test solution was passed through the chip at 0.5 µL/s, followed by 250 µL of wash solution. Following the wash, an air gap was introduced to delineate the wash/elution boundary. Elution agent was introduced into the chip, and allowed to stand for several minutes. Elution droplets were then collected directly into PCR reaction tubes. Four elution samples were taken from the chip, consisting of three samples of 25 µL followed by an additional sample of 50 µL. The 25 µL samples were diluted up to 50 µL after collection so that all samples submitted to PCR were 50 µL. The 500 bp PCR products were run through gel electrophoresis and photographs of the gel (under UV illuminuation) were taken and used to compare the chip elution samples to the standards of known copy number.

Fig. 5 shows the gel photograph from one such experiment. The standards prepared with system water are shown first, followed by the run with blank solution, the run with DNA solution, and standards prepared with pure water. By comparing the first 25 µL chip elution to the 10^4 and 5 x 10^4 standards in system water, it is estimated that the first chip elution contains about 2.5 x 10^4 copies. This implies a 10X concentration effect, and a 50% capture efficiency. There is a small amount of PCR inhibition evidenced by the fact that the 5 x 10^4 standard prepared using system water is not as intensely stained as the 5 x 10^4 standard prepared using pure water.

CONCLUSIONS

DNA analysis technology is playing an increasing role in many health-related areas. Laborious, manual procedures introduce human variability, possible cross contamination and high cost. By replacing such procedures with automated, disposable assays, the cost and applicability of this exciting new technology will gain the widest possible market. Automated bench-top and hand-held DNA analysis tools utilizing disposable cartridge formats are being developed to serve this need. As a component of such systems, the use of silicon microstructures for the extraction and concentration of target DNA can play an important role.

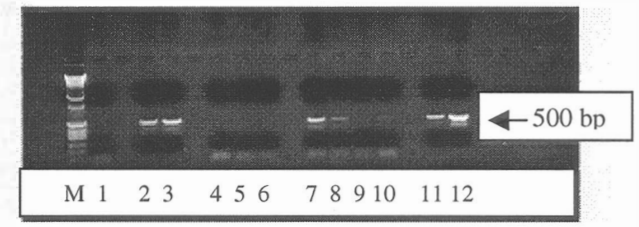

Figure 5. *Photograph of electrophoretic gel showing DNA chip capture. Lanes: M: Molecular weight standard, 1: Neg Ctl, 2: 10^4 standard in system water, 3: 5 x 10^4 standard in system water, 4-6: control run with no DNA, 7 – 10: Chip Elutions from DNA run, 11: 10^4 standard in pure water, 12: 5 x 10^4 standard in pure water. By comparing lane 7, obtained from the first 25 µL chip elution, to standard lanes 2 and 3, it is estimated that a capture efficiency of 50% was achieved, with a concentration factor of about 10X in the first elution.*

We have shown that deep reactive ion etching can be used to produce high surface area structures suitable for use as DNA capture elements. With proper design of structure and protocol, we believe such devices will be critical, cost effective components in future DNA analysis systems.

ACKNOWLEDGMENTS

The authors would like to thank Rick Faeth for wafer fabrication, and Linda Western and Sandy Zaner for PCR processing. This work was supported in part by funds from the United States Army Medical Research Institute of Infectious Diseases (USAMRIID).

REFERENCES

1. J.K. Bhardwaj, H. Ashraf, "Advanced Silicon Etching using High Density Plasmas", *SPIE Micromachining and Fabrication Technology Proc. 2639*, pp. 224-233 (1995).
2. B. P. van Drieënhuizen, N. I. Maluf, I. E. Opris, and G. T. A. Kovacs, "Force-Balanced Accelerometer with mG Resolution, Fabricated using Silicon Fusion Bonding and Deep Reactive Ion Etching", Technical Digest of the 1997 International Conference on Solid-State Sensors and Actuators, Transducers '97, Chicago, IL, pp. 1229-1230 (1997).
3. R.K. Saiki, S. Scharf, F. Faloona, K.B. Mullis, G.T. Horn, H.A. Erlick and N. Arnheim, "Enzymatic amplification of β-globin genomic sequences and restriction site analysis for diagnosis of sickle cell anemia", *Science 230*, pp 1350-1354 (1985).
4. Biorad Labs, Hercules CA, Promega, Madison WI, and Qiagen Inc., Santa Clarita, CA.
5. Willem R. Boom et al, US Patent 5,234,809 (Aug 1993).
6. Christophe Marques, Yohannes M. Desta, James Rogers, Michael C. Murphy, and Kevin Kelly, "Fabrication of High-Aspect-Ratio Microstructures on Planar and Nonplanar Surfaces Using a Modified LIGA Process", *JMEMS 6(4)*, pp. 329-336 (1997).
7. Molecular Probes, Eugene OR. YOYO-1: P/N Y-3601, PicoGreen: P/N P7581.
8. Bio-Rad Low Range Fluorescein Standard P/N 170-3123.
9. Bert Vogelstein and David Gillespie, "Preparative and analytical purification of DNA from agarose", *Proc. Natl. Acad. Sci., 76(2)*, pp. 615-619 (1979).
10. Pharmacia, Bridgewater, NJ.

CHEMICAL SENSORS BASED ON PULSED LASER DEPOSITED MOLECULAR SIEVES

Mary E. Gimon-Kinsel and Kenneth J. Balkus, Jr.
Department of Chemistry, The University of Texas at Dallas
Richardson, Texas 75083-0688 USA

ABSTRACT

Films of microporous and mesoporous molecular sieves were generated using pulsed laser deposition followed by a brief post hydrothermal treatment. Specifically, films of MeAPO-5 such as CoAPO-5 and Nb-TMS1 were made and subsequently used as the dielectric phase in capacitive-type chemical sensors. The capacitance change of mesoporous Nb-TMS1 based devices to the relative moisture in their environment makes them useful as potential humidity sensors. The CoAPO-5 based chemical sensors were evaluated for the detection of N_2, CO and CO_2.

INTRODUCTION

Molecular sieves comprise a class of low density metal oxides which possess highly organized one-, two- or three-dimensional pores and/or cage-like structures. The size and shape of the pores allow molecules to be discriminated based on steric properties; molecules of similar size can be differentiated based on polarity and acid/base properties. Numerous applications for these selective absorbents as sensors can be envisioned ranging from optical to mass sensitive and capacitive-type devices. These devices would benefit from the fabrication of thin films of molecular sieves.

We have developed a method for molecular sieve thin film generation which utilizes pulsed laser deposition (PLD) and a brief post hydrothermal treatment. This technique has been applied to a variety of porous metal oxide compositions some of which require a sensitizer. We refer to this modification as guest assisted laser ablation (GALA) [1]. We have demonstrated that PLD can be employed to generate thin films of microporous molecular sieves such as UTD-1 [2] and aluminophosphate molecular sieves including $AlPO_4$-5 and MeAPO (Me = V, Mn and Mg) [3, 4] . Thin films have been deposited on a variety of substrates including silicon, platinum, titanium nitride (TiN), indium-doped tin oxide (ITO), Mylar and glass. Parallel plate capacitors have been fabricated from these molecular sieve films. The absorption of small molecules (eg., CO, N_2, H_2O, CO_2 and NH_3) result in large changes in capacitance which readily allow for the discrimination and detection of such gases at the ppm level.

Recent results for PLD of the microporous molecular sieve CoAPO-5 (pore size 7 Å) and the mesoporous molecular sieve Nb-TMS1 (pore sizes 22-33 Å) will be presented. The CoAPO-5 molecular sieves has an AFI framework topology, and the Nb-TMS1 consists of a hexagonal mesostructure (see Figure 1). This is the first time mesoporous films have been made using this laser deposition technique. The Nb-TMS1 is interesting because it possesses semiconductor properties which might be exploited in electronic devices. Results for the capacitance change of Nb-TMS1 response indicate that they are potential humidity sensors. Preliminary results using CoAPO-5 devices will also be presented.

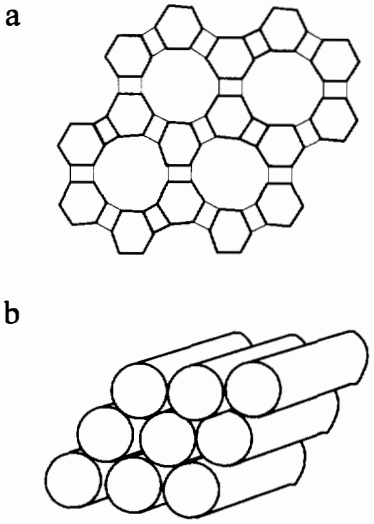

Figure 1. *(a) AFI framework structure of CoAPO-5 viewed along the 001 direction (b) hexagonal mesostructure of Nb-TMS1.*

EXPERIMENTAL DETAILS

Molecular Sieve Synthesis. The transition metal oxide mesoporous molecular sieve Nb-TMS1 (pore size 22 Å) was synthesized according to the published procedure. [5] A typical preparation of the synthesis gel involved the mixing of niobium (V) ethoxide (CHEMAT Technology, Inc.) and dodecylamine (Aldrich) with a molar ratio 1:1.25. The resulting mixture was heated at 50°C for approximately 1 minute, then 10 mL ethanol followed by 10 mL deionized water were added which resulted in the precipitation of a white solid. The solid was aged in the supernatant for 72 hours. The white solid and supernatant were loaded into a 23 mL Teflon lined stainless steel autoclave and heated for 24 hours at 80°C, 24 hours 100°C, followed by 7 days at 180°C. The white product was isolated by suction filtration, washed with deionized water, ethanol and diethylether and dried overnight at room temperature.

0-9640024-2-6/hh1998/$20©1998TRF
DOI 10.31438/trf.hh1998.85

The microporous metal substituted molecular sieve CoAPO-5 was synthesized according to the published procedure. [6] Briefly, the initial synthesis gel was made by combining 1.56 g of $CoSO_4$ with 1.8 mL of 85% phosphoric acid in 10 mL of deionized water. 2.08 g of $Al(OH)_3$ (83.34%) was added to the cobalt phosphoric acid solution and stirred until homogeneous. 2.9 mL of triethylammine (TEA) was added to the cobalt phosphoric acid gel and stirred for 1 hour and had a reactant molar ratio of 1.5 TEA:0.8 Al_2O_3:1 P_2O_5: 40H_2O:0.4CoO. The gel was transferred to a Teflon lined stainless steel autoclave and heated under static conditions at 200°C for 20 hours. The deep blue CoAPO-5 crystals were centrifuged, washed with deionized water and dried at room temperature.

Pulsed Laser Ablation and Post Hydrothermal Treatment of Films. An illustration of the PLD and post hydrothermal treatment of laser deposited molecular sieve films is shown in Figure 2. A pressed pellet of the molecular sieve was placed in a controlled-atmosphere chamber and irradiated using a Lumonics HyperEx-400 excimer laser (248 nm (KrF*), pulse length 14 ns, repetition rate 10 Hz). The laser energy was measured using a Scientech pyroelectric head (model 380402) and found to range from 90 to 100 mJ/pulse. A computer controlled rastoring mirror (Oriel) was used to turn the laser beam 90° and move the beam across the pellet surface. A focusing lens was employed to decrease the laser beam to a spot size of ca. 0.001 cm^2. Films were deposited by placing a substrate such as TiN (500Å) coated silicon on the heated substrate holder locate approximately 2.5 cm in front of the pellet. Typical film deposition conditions was as follows: laser power density, 100 MW/cm^2; substrate temperature, 150-300°; background oxygen pressure, 250-300 mTorr; deposition time, 10-20 min. Scanning electron microscopy (SEM) was used to examine the morphology and determine the thickness of the deposited films.

The laser deposited Nb-TMS1 and CoAPO-5 films were determined by XRD to be amorphous and partially crystalline, respectively. Both the Nb-TMS1 and CoAPO-5 films were then subjected to solution phase hydrothermal treatment. The solution phase treatment of the Nb-TMS1 has been described previously [7]. Briefly, the Nb-TMS1 coated substrate was positioned in the Teflon lined stainless steel autoclave at approximately 60° angle with the film side facing down. The melted niobium (V) ethoxide and dodecyl amine (molar ratio 1: 1.25) mixture was added to the Teflon liner followed by 20 mL ethanol. The resulting mixture was allowed to age for 72 hours at room temperature, 4 hours at 90°C, 4 hours at 140°C and 24 hours to 3 days at 180°C. The film was washed with deionized water, ethanol and diethylether and dried at room temperature. Because solution phase hydrothermal treatment of the CoAPO-5 films resulted in the reorganization of the laser deposited material to yield mixed molecular sieve phases (CoAPO-5 and CoAPO-34) and rapid growth in film thickness, the partially crystalline CoAPO-5 films were used as deposited.

Chemical Sensor Fabrication. A capacitive-type sensor was prepared from a hydrothermally treated/template-free Nb-TMS1 film coating a TiN/silicon substrate. The organic template was removed by washing in a solution of 3:1 isopropanol: water acidified with nitric acid to pH 1.75 for 3 hours followed by washing in ethanol. A Au/Pd alloy was patterned onto the film surface using a shadow mask. The device was then heated to 200°C to desorb water and immediately transferred to an environmental chamber under a positive pressure of high purity nitrogen where it was allowed to cool to room temperature (24°C).

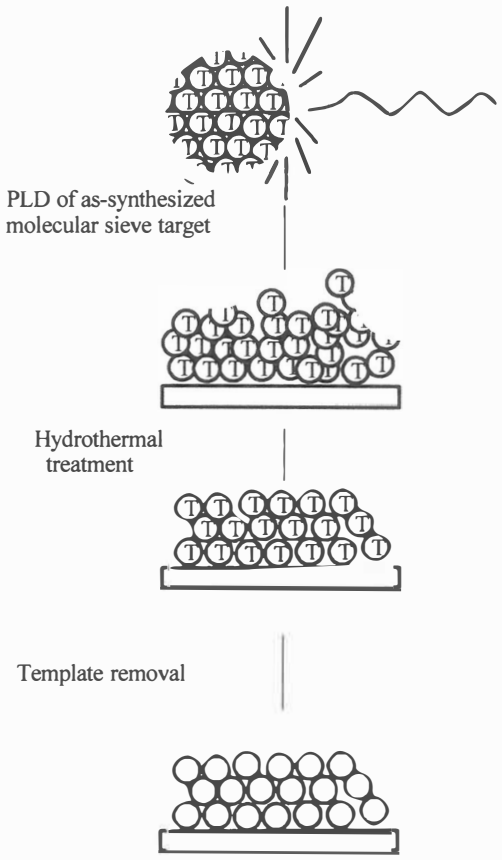

Figure 2. *Experimental methodology for pulsed laser deposition and post hydrothermal treatment of molecular sieve films.*

The environmental chamber was equipped with two probes by which film plus adsorbate capacitance was measured. One probe made electrical contact with the bare TiN surface and the other probe made contact with a 0.184 mm^2 Au/Pd electrode. A voltage was applied and the capacitance signal was received by a WayneKerr Precision Component Analyzer 6425. A virtual instrument program written in house LabView for Windows 3.0.1 allowed the applied voltage to be stepped from 0V to 0.300V and the measured capacitance plotted as a function of applied voltage.

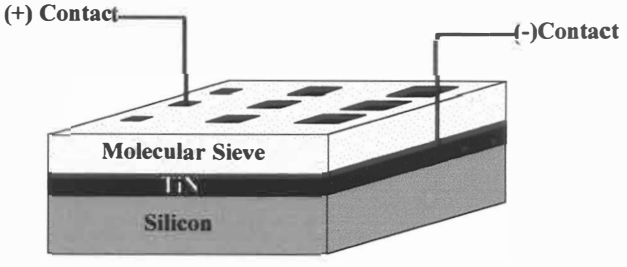

Figure 3. *Schematic of molecular sieve thin film based sensor.*

RESULTS AND DISCUSSION

SEM and Transmission electron microscopy (TEM) were used to characterize the laser deposited Nb-TMS1 films. In general, SEM images show a continuous, uniform films composed

of 30-50 nm particulates. The laser deposited film cross-section is shown in Figure 4. This film is on the order of 200 nm thick which is in the range needed to minimize leakage current while still maintaining significant capacitance changes.

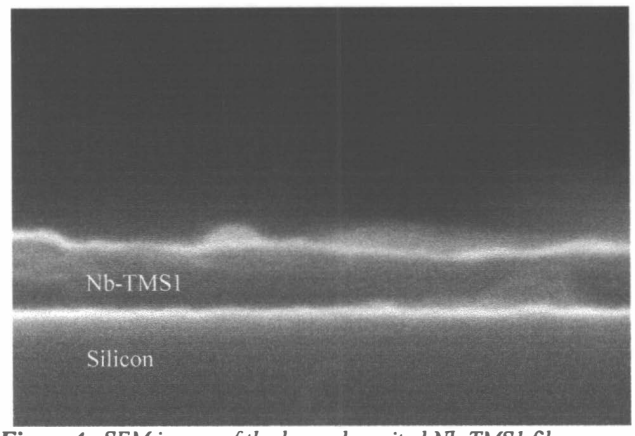

Figure 4. *SEM image of the laser deposited Nb-TMS1 films cross-section.*

The laser deposited Nb-TMS1 appeared to be largely X-ray amorphous by powder XRD. However, further examination by TEM revealed areas of crystalline molecular sieve dispersed in an amorphous matrix (see Figure 5).

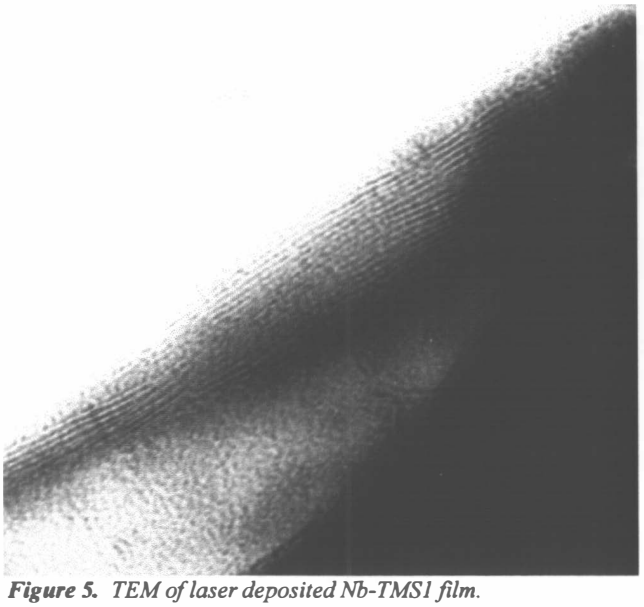

Figure 5. *TEM of laser deposited Nb-TMS1 film.*

We have found that the laser deposited films can be reorganized using a post hydrothermal treatment. Figure 6 illustrates the change in the TEM images that occur following a hydrothermal treatment that was heated at 180°C for 24 hours. Larger regions of crystallinity are observed which can be described as having a "worm-like" motif [8]. The XRD pattern also reflects the increase in crystallinity with the appearance of a low angle peak between 2-3 two-theta. (data not shown).

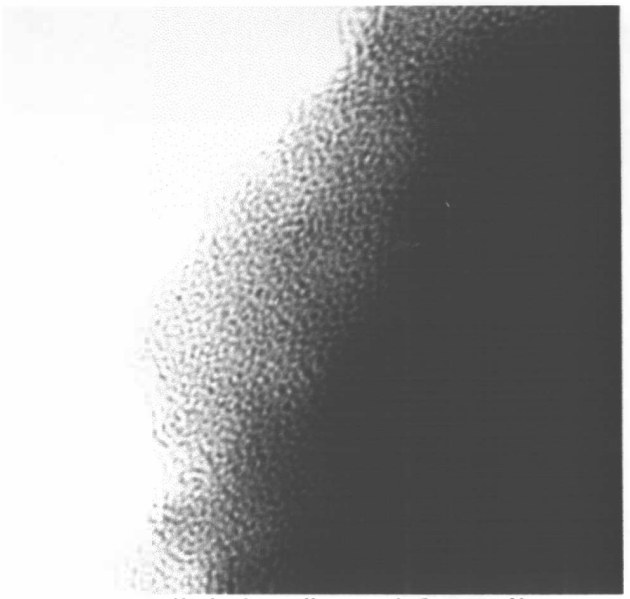

Figure 6. *TEM of hydrothermally treated Nb-TMS1 film.*

The crystallinity of the laser deposited CoAPO-5 films were shown to range from X-ray amorphous to partially crystalline by powder XRD. The morphology of the laser deposited CoAPO-5 films were very similar to that observed by SEM of the laser deposited Nb-TMS1 films.

Capacitive-type chemical sensors were fabricated using the hydrothermally treated/template-free Nb-TMS1 and/or calcined (template-free) CoAPO-5 films as the dielectric phase, the TiN substrate as an electrode and patterned Au\Pd as the other electrode. By applying a potential between the electrodes, changes in the capacitance were recorded upon adsorption of analyte molecules into the molecular sieve film. We found that the Nb-TMS1 films were particularly sensitive to the relative level of moisture in the environmental chamber. When the Nb-TMS1 based sensor was subjected to a flow of nitrogen containing water vapor, the capacitance measured across the hydrothermally treated film increased as the water was adsorbed. The background capacitance/area measured in flowing high purity nitrogen was on the order of 0.30 nF/mm^2. The capacitance/area increased to 5.2 nF/mm^2 when water was introduced into the flowing nitrogen. Because water can moved freely into and out of the pores of the hydrothermally treated film, the capacitance response can be monitored as a function of time. For example, Figure 5 illustrates the reversible response to water of sensors based on mesoporous Nb-TMS1 films which are approximately 300 nm thick. A repeat cycle (X3) of 90% humidity followed by a flush of high purity nitrogen was used to determined the reproducibility of the sensor response. During each 10 minute flush with nitrogen, the capacitance returned to its baseline within 1 minute. The average capacitance change varied no more than +/- 2.5% for the three sequential cycles.

The specificity of the Nb-TMS1 based chemical sensors to water was tested on a variety of gaseous and volatile organics including CO_2, methanol and acetone. No measurable response was recorded when the sensor was exposed to CO_2. Both methanol and acetone produced a minimal capacitance change (< 1 nF/mm^2) and therefore would be expected to interfere in the detection of water. The effect of other potential analytes is currently under investigation.

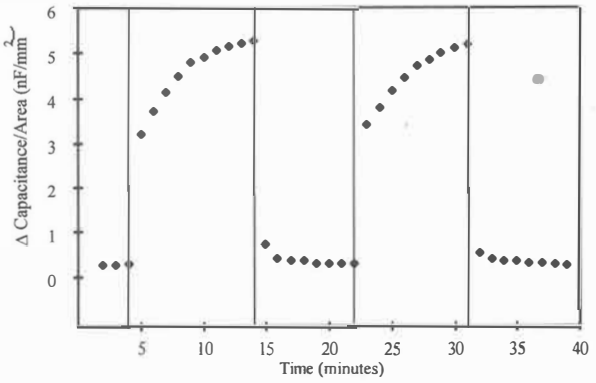

Figure 7. *Average reversible response for a capacitive-type Nb-TMS1 chemical sensor to the presence of water vapor in flowing nitrogen (average film thickness 300 nm).*

A comparison with sensors fabricated from dense Nb_2O_5 films indicates that the accessible mesoporosity of the Nb-TMS1 results in capacitance changes which are at least 3X that observed with the dense phase devices.

The response of the CoAPO-5 based chemical sensors was measured in the presence of a number of analytes including N_2, CO_2 and CO. The CoAPO-5 based devices were found to be selective and sensitive to CO and CO_2 (see Figure 8). The background capacitance measured in the presence of high purity nitrogen was on the order of 10^{-14} F/mm^2. When CO_2 is added to the nitrogen flow, the capacitance increases to 10^{-9} F/mm^2. A change in capacitance of >3 orders of magnitude is observed when the sensor is exposed to CO indicating CoAPO-5 is a viable sensor for CO even in the presence of CO_2. The difference in the sensor response is dramatic for molecules of similar size and shape. The kinetic diameter of CO (3.8Å) is larger than CO_2 (3.3Å).

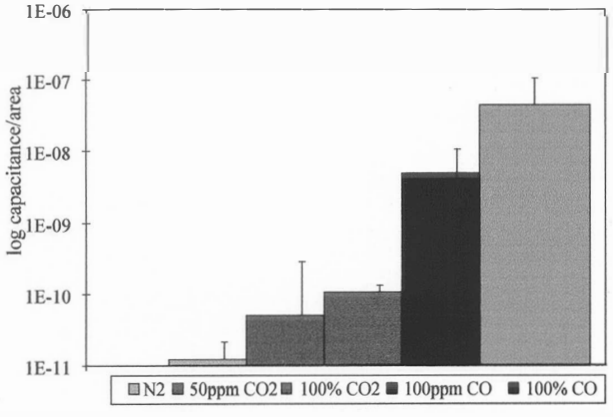

Figure 8. *Capacitance response of CoAPO-5 based sensor to CO_2 and CO (film 227 nm thick).*

CONCLUSIONS

Continuous films of mesoporous and microporous molecular sieves have been prepared using pulsed laser deposition. PLD followed by a solution phase or vapor phase post hydrothermal treatment can be used to generate crystalline Nb-TMS1 and CoAPO-5 films, respectively. Capacitance-type chemical sensors can then be fabricated using these films as the dielectric phase. It was shown that chemical sensors based on Nb-TMS1 films are sensitive to the relative level of moisture in the environment which makes such sensors useful as potential humidity sensors. In contrast, CoAPO-5 is not sensitive to water but exhibits large capacitance changes upon exposure to CO. The thermal stability of the molecular sieves (>400°C) suggest that sensors based on these materials may be particularly useful for the detection of combustion gases. We anticipate that the compositional variances available for both mesoporous and microporous molecular sieves will lead to more selective sensors as well as other applications for these thin films.

ACKNOWLEGMENTS

We wish to thank the Texas Advancd Technology Program and Kenneth Hoffman for assistance with the TEM.

REFERENCES

1. M. E. Gimon-Kinsel, T. Muñoz, Jr., A. Ayala, and K. J. Balkus, Jr. (manuscript in preparation).
2. K. J. Balkus, Jr., T. Muñoz, Jr., and M. E. Gimon-Kinsel "Pulsed Laser Deposition of Zeolite UTD-1: Evidence for Oriented Film Growth", *Chem. Mater., 10,* 464 (1998).
3. K. J. Balkus, Jr., L. J. Ball, M. E. Gimon-Kinsel, J. M. Anthony, and B. E. Gnade "A capactivite -type chemical sensor that employs VAPO-5, MnAPO-5 and MAPO-36 molecular sieves as the dielectric phase", *Sensors & Actuators B, 42,* 67 (1997).
4. K. J. Balkus, Jr., L. J. Sottile, B. E. Gnade, and J. M. Anthony " A capacitance type chemical sensor based on $AlPO_4$-5 molecular sieves", *Chem. Mater., 9,* 380 (1997) and unpublished results.
5. D. M. Antonelli, A. Nakahira, and J. Ying "Ligand-assisted liquid crystal templating in mesoporous niobium oxide molecular sieves" *Inorg. Chem.,35,* 3126 (1996).
6. K. J. Chao, S. P. Sheu, S. H. Chen, J. C. Lin, and J. Lievens "*Molecular Sieves: Synthesis of Microporous Materials,*" M. L. Occelli and H. Ratson (Eds) (1992), p.317.
7. M. E. Gimon-Kinsel and K. J. Balkus, Jr. " Mesoporous molecular sieve thin films", to be presented at the *First International Symposium on Mesoporous Molecular Sieves.*, Baltimore, MD (1998).
8. S. A. Bagshaw and T. J. Pinnavaia, " Mesoporous Molecular Sieves," *Angew. Chem. Int. Ed. Engl., 35,* 1102 (1996).

IN-SITU MONITORING OF MICRO-CHEMICAL VAPOR DEPOSITION (μ-CVD): EXPERIMENTAL RESULTS AND SPICE MODELING

Ronald P. Manginell, James H. Smith, Antonio J. Ricco,
Robert C. Hughes, and Daniel J. Moreno
Sandia National Laboratories
Albuquerque, New Mexico, 87185-1425

Robert J. Huber
University of Utah
Salt Lake City, Utah, 84112

ABSTRACT

Two new methods of monitoring the thickness of metallic films *as deposited* on microfabricated bridge structures *via* micro-chemical vapor deposition (μ-CVD) are described. These methods require no additional fabrication to produce four-point resistance-based thickness probes. Instead, the relatively large increase in (a) the heat conductance and (b) the heat capacity of the microbridge/metal system as a result of deposited metal are detected as variations in the heating power provided to the microbridge by the control circuitry.

Experimental results demonstrating these effects are given for a microbridge controlled with a novel constant-resistance circuit. The heat-transfer equations for the microbridge/metal system and the circuit model for the control circuit are then solved using SPICE. This coupled model predicts within 10% the measured thickness of μ–CVD platinum.

INTRODUCTION

Recently, μ–CVD of metals on micromachined devices has been reported [1,2,3,4]. In this technique the self heating of microhotplates and microbridges is used to thermally decompose precursors directly on their surface (Figures 1 and 2). The high degree of thermal isolation of these structures confines deposition only to their active regions, and is therefore highly selective. In the absence of this technique, one additional deposition and patterning step would be required in a conventional microfabrication sequence to fabricate such a film [5], and coverage of the underside of suspended structures would be difficult to achieve. Applications of μ–CVD include noble-metal catalyst deposition for calorimetric gas sensors [3] and metal deposition for conductometric gas sensors [1,2,4].

In-situ thickness monitoring *via* measurement of the thin-film resistance of μ–CVD metal on microhotplates has been demonstrated [1,2]; for this purpose, four-point probes were fabricated. We show that the sensitive heat-transfer properties of microheater platforms such as microhotplates and microbridges can be utilized instead. Given their relatively small values prior to metal deposition, the (a) heat conductance and (b) heat capacity of the microheater/metal system increase significantly with deposited metal quantity and can be detected *in situ* with appropriate control circuitry. While (a) alters the steady-state heating power requirements of the system, (b) introduces a delay in its transient response to a heating pulse.

These effects are demonstrated experimentally for μ–CVD of Pt on CMOS-compatible, silicon-nitride-encapsulated, polysilicon microbridges. A constant-resistance control circuit used for microbridge heating during μ–CVD is presented (Figure 3). This circuit provides both steady-state (CW) and pulsed resistance set points so that both heat conductance and capacity changes can be probed. It should be stressed that the techniques described here are applicable to microhotplates as well, and that no additional microfabrication is required, in contrast to four-point resistance probes. Furthermore, *in-situ* monitoring of the μ–CVD of *dielectrics* should also be achievable in a pulsed-bias mode, since this technique only requires changes in heat capacity.

An electro-thermal model of the microbridge/metal system is coupled with the circuit model of the control circuit and solved in SPICE. Boundary conditions, implementations of temperature-variable resistors, and the conductivity and heat capacity of the deposited metal are described. Simulations predict metal thickness within 10% of measured values for both CW and pulsed heating bias.

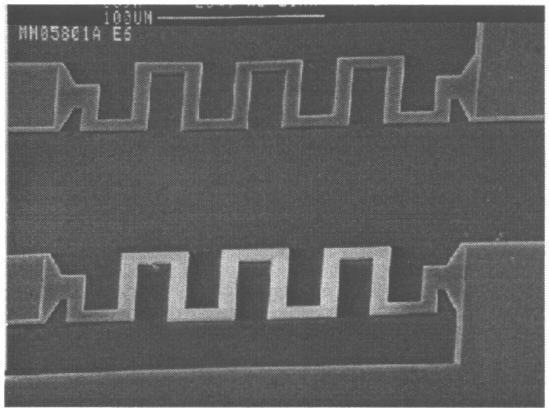

Figure 1. *Scanning electron micrograph of two meandered microbridges. The lower bridge appears brighter due to a smooth layer of Pt approximately 0.1 μm in thickness, which was deposited by μ-CVD from the precursor* $Pt(acac)_2$.

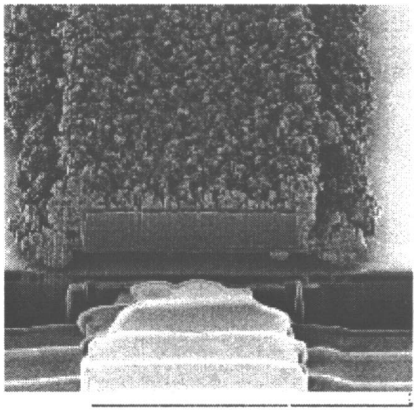

Figure 2. *Focused ion beam cross section of a silicon-nitride-encapsulated, polysilicon microbridge with a rough coating of μ-CVD platinum. The microbridge is 2 μm thick and 10 μm wide.*

0-9640024-2-6/hh1998/$20©1998TRF
DOI 10.31438/trf.hh1998.86

THEORY

As the thickness of metal deposited on a microbridge increases, so does its ability to conduct heat along the device. This means that the power, $P(t)$, required to maintain the bridge/metal system at constant resistance, R, increases with deposition time. The relative power provided to the bridge can be written

$$P(t)/P_O = 1 + P_m(t)/P_O, \qquad (1)$$

where P_m is the increasing power conducted by the catalyst and P_o is the power required prior deposition. By the chain rule, the rate of increase of P_m with metal thickness, z_m, at constant resistance is

$$\left.\frac{dP_m}{dt}\right|_R = \left.\frac{dP_m}{dz_m}\right|_R \cdot \left.\frac{dz_m}{dt}\right|_R . \qquad (2)$$

The growth rate of the film is then

$$\left.\frac{dz_m}{dt}\right|_R = \left.\frac{dP_m}{dt}\right|_R \cdot \left(\left.\frac{dP_m}{dz_m}\right|_R\right)^{-1} . \qquad (3)$$

The composite thermal conductivity K of the microbridge with deposited metal is

$$K(z_m) = K_b + \left[\frac{(2z + w)z_m}{wz}\right] \cdot K_m \cdot f , \qquad (4)$$

where K_b, z and w are the conductivity, thickness, and width, respectively of the bridge. The factor f accounts for the fact that the deposited film has less than bulk density (Figure 2), so its actual conductance is less than that implied by the bulk conductivity K_m of the metal. Finally, the term in brackets is the ratio of cross-sectional area of the deposited film, to that of the bridge, as shown in Figure 4.

The heat capacity of a differential element of the bridge/metal system is the parallel combination of the capacity of the bridge, and the capacity of the metal. For a bridge of length L divided into N elements, the latter term is

$$C_m = f \cdot c_m \cdot (2z + w) \cdot z_m \cdot (L / N), \qquad (5)$$

where c_m is the bulk specific heat of the metal. The factor f is the same as in Eq. (4).

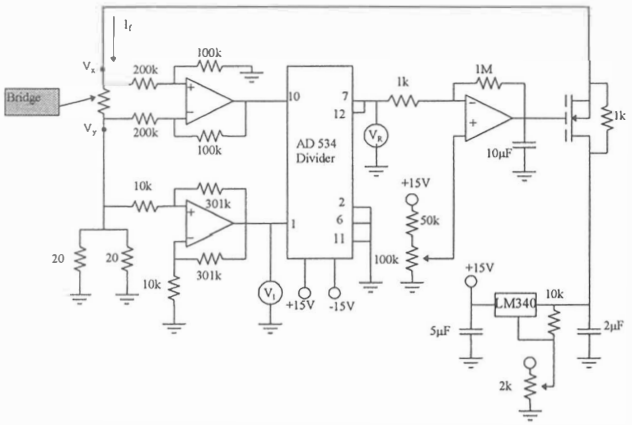

Figure 3. *Constant-resistance control circuit. A CW set point is shown, but pulsed operation is also possible.*

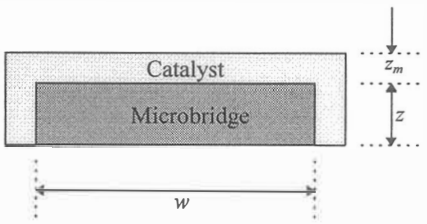

Figure 4. *A cross section of the microbridge with deposited metal catalyst. Dimensions of the bridge and assumed average thickness of the catalyst are shown*

EXPERIMENTAL DETAILS

The μ-CVD apparatus is described elsewhere **[3,6]**. During μ-CVD of Pt, the microbridge was heated with a constant-resistance control circuit (Figure 3) and the power provided to the device was monitored. Referring to Figure 3, the resistance and current of the bridge (for the feedback resistor values shown) are

$$R = 60.2 \cdot V_R \quad \text{and} \quad I = V_I / 0.31 , \qquad (6)$$

and the power is obtained by the relation $P = I^2R$. For CW biasing, the voltages V_R and V_I of Eq. (6) were recorded with a digital multimeter; for pulsed biasing, an 8-bit digitizing oscilloscope was used. Note that the polysilicon bridge material is electrically insulated from the deposited metal by a 0.25 μm layer of LPCVD silicon nitride.

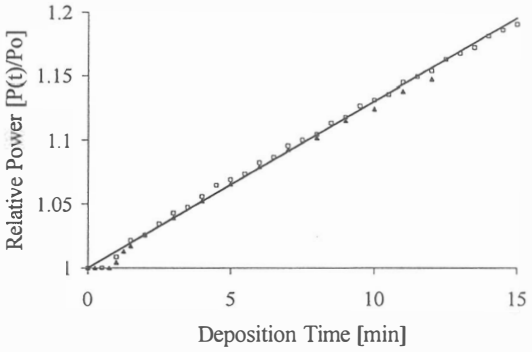

Figure 5. *Relative power provided to a microbridge by the control circuit in a CW bias-mode μ-CVD experiment. P_o is the power required prior to metal deposition. Depositions for 12 min (filled triangles), and 15 min (open squares) are shown, along with a linear fit to the latter data. For both depositions, the bridge resistance was maintained at $1.4R_o$, where R_o is its room-temperature resistance.*

EXPERIMENTAL RESULTS AND DISCUSSION

The relative power provided by the control circuit to maintain constant (CW) resistance during Pt deposition is shown in Figure 5. Two depositions of 12 and 15 min total time on two separate devices are shown. These data can be described by Eq. (1). Initially, the power does not increase due to the fact that although Pt is being deposited, the film is not yet continuous and carries no additional heat to the bridge ends. With increasing deposition time, however, the Pt nucleation sites connect and the film begins to conduct heat; this change is evident at 0.75 min into the deposition. Subsequently, growth is nearly linear in time and the slope is precisely that given by the left-hand side of Eq. (2).

Following deposition, the device with a 12 min deposition was cross-sectioned in four places along its length using a focused ion beam (FIB). A metal thickness distribution was thereby

obtained, and from this an average metal thickness of 0.67 μm was derived. One such FIB cross section is shown in Figure 2.

Deposited Pt significantly increases the heat capacity of the microbridge/metal system, introducing a measurable delay in the transient response of the system to a heating pulse. The two curves shown at the top of Figure 6 are the measured response of a microbridge to a square heating pulse (a) before and (b) after a 12 min CW deposition. (Note that this deposition was performed at a bridge resistance of 1.4 times the room-temperature value for the bridge, the same conditions under which the CW depositions of Figure 5 were performed.) The system's response *after* metal deposition is delayed with respect to that *before*. Furthermore, in the steady state, the power required after deposition is greater than that before; this is the same effect as that already described for the CW depositions above.

SIMULATION DETAILS

The basic electro-thermal model of a microbridge is based on the work of Mastrangelo **[7]**, where the temperature of an element of the bridge is determined by Joule heat gain, and losses due to (a) conduction along the bridge, (b) conduction through the air gap from the hot bridge to the underlying substrate, (c) convection, and (d) radiation. The length of an element is L/N for a bridge of length L divided into N elements.

Using electrical analogues of thermal parameters, components representing the various heat-loss mechanisms and Joule heating gains were implemented in PSPICE™, as diagrammed in Figure 7. Voltage-controlled current sources (VCCS) were used to make the magnitude of convective and radiative losses and Joule heat gains in a given element dependent on the temperature (voltage) of the node. In this way, complex functional dependencies, such as the fourth-order temperature dependence of radiation, were easily implemented. Secondly, temperature-variable thermal and electrical resistors were constructed from a series combination of a voltage-controlled voltage source and an ammeter (a 0-V independent source in PSPICE™). This is possible since, by Ohm's Law, resistance and voltage are proportional. The output of a VCVS for a given element (the element resistance) is directly proportional to the heating current into that element, as measured by the ammeter. The thermal resistance of an element is also inversely proportional to the thermal conductivity defined in Eq. (4).

Mastrangelo's model assumed that the temperature of the silicon substrate below the device remains constant, regardless of device temperature. In fact, since the substrate is not an ideal heat sink, the temperature in the vicinity of the microbridge increases as the microbridge is heated. This effect is greatest at the microbridge ends, as most of the heat generated within the device is conducted along its length and deposited at its extremities. This leads to localized heating at the ends of a microbridge and increased resistance to heat flow there. By analogy to electrical spreading resistance **[8]**, this effect has been called "thermal spreading resistance", and can be modeled in SPICE by placing additional thermal resistance between the bridge ends and the substrate **[5,6]**.

With measured values of the thermal conductivity, K_b, and heat capacity, C_b, of polysilicon inserted, the SPICE model just described accurately predicts the temperature profile, current-voltage characteristics, and transient response of microbridges without deposited metal **[5,6]**. To simulate the effects of deposited metal on the steady-state heating characteristics of the bridge/metal system, a thermal conductivity given by Eq. (4) is required. For transient analysis of the system, the elemental heat capacity, C_m, of the deposited metal, given by Eq. (5), is also required and was added in parallel to C_b. Finally, to simulate the coupled response of the system and control circuit, a circuit model for the control circuit of Figure 3 was constructed and connected to the electro-thermal model of the system.

SIMULATION RESULTS

Simulation results for the coupled model consisting of the control circuit and bridge/metal system are described in this section. The growth rate, as defined by Eq. (3), was first predicted. The first factor there is given experimentally by the slope of the line in Figure 5. The second factor, the rate of change of P_m with z_m, is easily determined with the SPICE model, since the composite thermal conductivity described by Eq. (4) introduces the effects of z_m and f on the steady-state behavior of the system. With this in place, one simply selects values of f, R, and z_m and the model calculates the corresponding power. From the 15 min deposition at $R = 1.4R_o$ in Figure 5, $dP_m/dt = 0.82$ mW/min. For this same set point and $f = 1/3$, SPICE calculations yield $dP_m/dz_m = 14$ mW/μm. From Eq. (3), then, a Pt growth rate of 59 nm/min is obtained. By way of comparison, this rate implies a thickness of 0.7 μm for a 12 min deposition, in agreement with the measured value of 0.67 μm obtained by FIB cross sections.

The transient response of the system to a heating pulse was next simulated, and a comparison with experiment is given in Figure 6. The two curves in each graph of Figure 6 represent the transient response (a) *before*, and (b) *after* a 12 min CW deposition at $1.4R_o$. Note that this was the same deposition used to evaluate the CW results above. One would expect, then, that the value of f obtained here should be close to 1/3. In fact, in the simulation of Figure 6 values of $f = 1/3$ and $z_m = 0.7$ μm were used for comparison with the CW results. The simulated heating delay (measured at 40 mW) was 0.29 ms, a value 15% smaller than the measured value of 0.35 ms. Using $f = 0.37$, however, yields the correct heating delay of 0.35 ms. This value of f is within 10% of that used in the continuous set-point simulation. Finally, it should be noted that the simulated and measured steady-state heating difference before and after deposition (shown as P_c in Figure 6), agree within 10%.

SUMMARY AND CONCLUSIONS

The relatively large increase in the heat conductance and heat capacity of a microbridge due to μ-CVD metal can be detected in real time *as the metal is being deposited* through a variation in the heating power provided to the microbridge/metal system. A novel constant-resistance control circuit was presented that can provide either a continuous or pulsed heating bias to the microbridge during deposition. During steady-state operation, the change in heat conductance with the deposited metal is obtained, and can be used to determine the film thickness *in situ*. On the other hand, during pulsed biasing, the increase in heat capacity with film deposition is extracted and can also be used for *in-situ* determination of the film thickness.

The techniques described here are applicable to *in-situ* monitoring of μ-CVD on microhotplates as well, and do not require any additional microfabrication to produce four-point resistance-based thickness probes on the device. Finally, *in-situ* detection of the μ-CVD of dielectrics on microheater platforms should also be possible using pulsed biasing, since this technique only requires changes in the heat capacity of the system for detection.

The principal advantage of SPICE modeling over other numerical methods is the ability to simultaneously simulate the electro-thermal behavior of a device and its control/sense electronics. Such a coupled model was presented for a microbridge with deposited metal and its constant resistance control circuit. Simulations predicted within 10% the measured values of the thickness of μ-CVD metal in both pulsed- and CW-deposition bias modes.

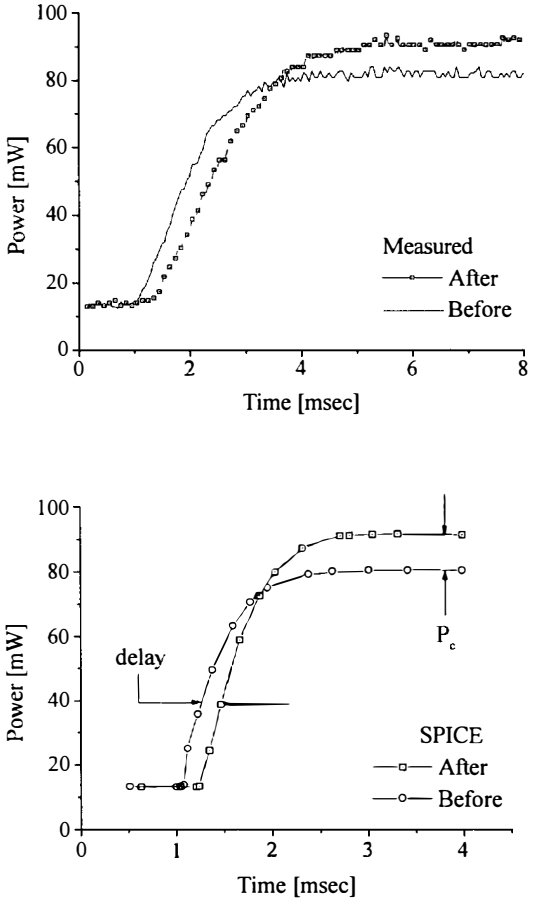

Figure 6. *The measured (top) and simulated (bottom) response of a 100-μm bridge to a $1.3R_o$ square heating pulse, where R_o is the room-temperature resistance of the bridge. The power indicated is that required to maintain $1.3R_o$. Time response both "before" and "after" a 0.7 μm thick Pt deposition are shown. Note that heating was initiated at the same time both before and after deposition. Simulation results are for $f = 0.33$.*

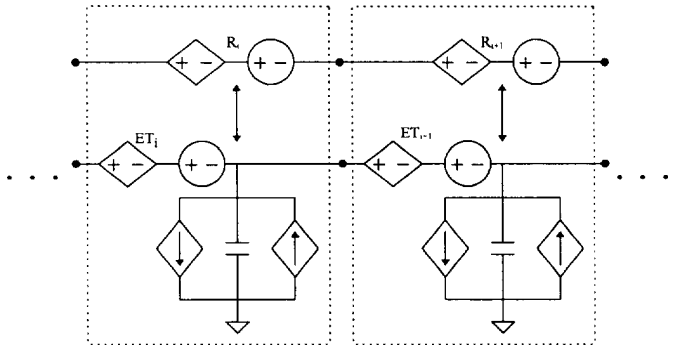

Figure 7. *Elements 'i' and 'i+1' of the bridge in SPICE. The electrical resistors, 'R', are coupled to the thermal model at the points indicated by double arrows. The series combination of a VCVS and 0-V independent source functions as a temperature-dependent resistor. Joule heating (upward-pointing arrow) and losses (downward-pointing arrow) are modeled with VCCSs. The heat capacity of an element is represented by a capacitor.*

ACKNOWLEDGMENTS

Sandia is a multiprogram laboratory operated by Sandia Corporation, a Lockheed Martin Company, for the United States Department of Energy under contract DE-AC04-94AL85000. The microbridges shown herein were produced at Sandia's Microelectronics Development Laboratory. The excellent technical assistance of the engineers and operators of the MDL is gratefully acknowledged. (Information on the MDL can be found at http://www.mdl.sandia.gov/Micromachine.) Finally, special thanks goes to Alan W. Staton for assistance with catalyst deposition.

REFERENCES

1. Semancik, R. E. Cavicchi, K. G. Kreider, J. S. Suehle, P. Chaparala, "Selected-Area Deposition of Multiple Active Films for Conductometric Microsensor Arrays", *8th International Conference on Solid-State Sensors and Actuators and Eurosensors IX, Digest of Technical Papers, 1*, 831 (1995).

2. S. Majoo, J. W. Schwank, J. L. Gland, and K. D. Wise, "A Selected-Area CVD Method for Deposition of Sensing Films on Monolithically Integrated Gas Detectors", *IEEE Electron Device Letters, 16*, 217 (1995).

3. R. P. Manginell, J. H. Smith, A. J. Ricco, D. J.Moreno, R. C. Hughes, R. J. Huber, S. D. Senturia, "Selective, Pulsed CVD of Platinum on Microfilament Gas Sensors", *Tech. Digest 1996 Sol.-State Sensor and Actuator Workshop*, Transducers Research Foundation, Cleveland (1996), pp. 53 - 56.

4. S. Majoo, J. L. Gland, K. D. Wise, and J. W. Schwank, "A Silicon Micromachined Conductometric Gas Sensor with a Maskless Pt Sensing Film Deposited by Selected-Area CVD", *Sensors and Actuators B, 35 - 36*, 312 (1996).

5. R. P. Manginell, J. H. Smith, and A. J. Ricco, "An Overview of Micromachined Platforms for Thermal Sensing and Gas Detection", *SPIE's 4th Annual Symposium on Smart Structures and Materials*, San Diego, 3/3-6/97.

6. R. P. Manginell, "Polycrystalline-Silicon Microbridge Combustible Gas Sensor", Ph.D. Dissertation, University of New Mexico, 1997.

7. C. H. Mastrangelo, "Thermal Applications of Microbridges", Ph.D. Dissertation, U. C. Berkeley, 1991.

8. S. M. Sze, "Physics of Semiconductor Devices" 2nd Ed., John Wiley & Sons, New York (1981), p. 217.

HIGH-TEMPERATURE HYDROCARBON GAS SENSING WITH MESOPOROUS SiO_2 THIN FILMS ON TSM RESONATORS*

R. W. Cernosek and J. R. Bigbie
Microsensor Research and Development Department, Sandia National Laboratories
P. O. Box 5800, MS 1425, Albuquerque, NM 87185-1425

M. T. Anderson
3M Industrial and Consumer Sector Res. Laboratory
Ceramic Technology Center, St. Paul, MN 55144

J. H. Small and P. S. Sawyer
Encapsulants and Foams Department
Sandia National Laboratories, Albuquerque, NM

ABSTRACT

A new type of sensor has been developed for the detection of hydrocarbon gases at high temperatures. The sensor consists of a thickness shear mode (TSM) quartz resonator coated with a thin mesoporous silica layer ion-exchanged with palladium ions. When operated at temperatures above 300 °C, the high surface area film catalyzes the combustion of hydrocarbon vapors in the presence of oxygen. The sensor acts as a calorimeter as the exothermic reaction slightly increases the temperature, stressing the sensor surface and producing a measurable deviation in the resonator frequency. Sensitivities as high as 0.44 (ppm-Δf)/(ppm-gas) have been measured for propylene gas, with minimum detectable levels of < 50 ppm of propylene at 500 °C. One potential sensor application is on-line monitoring in vehicle exhaust streams for catalytic converter efficiency or regulatory compliance.

INTRODUCTION

In recent years, acoustic wave devices with specific surface affinity layers have been developed for gas phase chemical sensing **[1]**. Most of their applicability has been in low-temperature sensing due to the large temperature coefficients of the piezoelectric crystals and limited access to coating materials for high-temperature use. Only a few attempts have been made to adapt acoustic wave sensors to the high temperature region **[2,3]**. In this paper, we describe a new acoustic wave-based sensing device for high-temperature detection of gaseous hydrocarbons. Many of the previous limitations to high-temperature operation have been overcome or harnessed for specific applications.

A hydrocarbon gas sensor has potential application as an exhaust monitor for internal-combustion (IC) engine vehicles. Residual hydrocarbons, along with nitrogen oxides (NO_x) and carbon monoxide (CO), are present in the vehicle exhaust stream as a result of incomplete fuel combustion. Specifications for on-board hydrocarbon sensors require a measurement range from 25 ppm to 1000 ppm (0.1%) with a detection resolution of 25 ppm. The new acoustic sensor described in this paper shows a capacity to meet these requirements.

The sensor utilizes AT-cut quartz resonators operating in the thickness shear mode (TSM) and coated with a thin layer of surfactant-templated periodic mesoporous silica **[4,5]** ion-changed with metals. AT-cut resonators are commonly used as mass deposition monitors **[6]** and usually are operated near room ambient where the resonant frequency deviates little with temperature fluctuations. At much higher temperatures, the frequency response exhibits a nonlinear temperature dependence (see Fig. 1) **[7]**. Coefficients are > 100 (ppm Δf)/°C above 385 °C and have approximately a quadratic variation with temperature. As seen in Fig. 1, the presence of the thin films has no significant effect on the frequency-temperature curve. The large temperature dependence along with the strain sensitivity of the quartz resonator sensors make them useful for detecting exothermic or endothermic gas reactions as long as the operating temperature is stable and does not exceed the quartz Curie point (α to β phase transition) of 573 °C. At even higher temperatures, other piezoelectric materials such as lithium niobate ($LiNbO_3$) or gallium orthophosphate ($GaPO_4$) **[8]** could be used in a similar fashion since they maintain their piezoelectric properties.

MESOPOROUS SILICA THIN FILMS

Sensitivity and selectivity of chemical sensors is determined by the properties of thin film surface layers. The high-temperature hydrocarbon sensor utilizes a sol-gel deposited surfactant-templated SiO_2 film. An alcoholic acid catalyzed silica sol is prepared with a pH near the isoelectric point of silica **[5]**. Cetyltrimethylammonium bromide (CTAB) surfactant is added to the sol in concentrations of 1.5 to 4.2 % by weight. After proper masking of the quartz resonator electrodes, the sol is spin-deposited on one surface. The films are then calcined at 400 °C for one hour (using a 1 °C/min ramp up and down) to burn out the organic template and access the porosity. Calcined films resemble

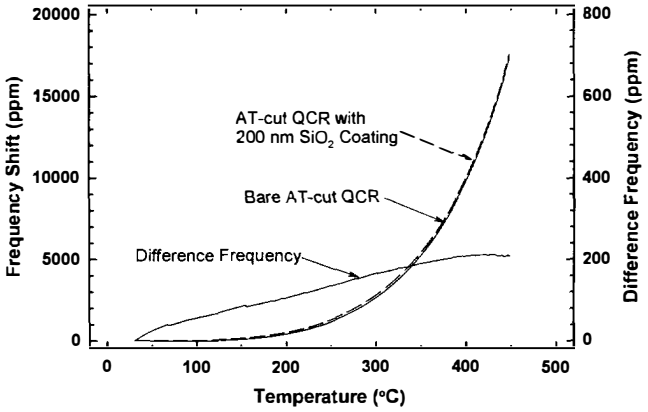

Figure 1. *Measured frequency shift vs. temperature for a bare and an SiO_2-coated TSM resonator. Temperature coefficients exceed 100 ppm/°C above 385 °C, but thermal noise reduction is possible using reference sensors and frequency mixing.*

* This work was performed at Sandia National Laboratories supported by the United States Department of Energy under Contract DE-AC04-94AL85000. Sandia is a multiprogram laboratory operated by Sandia Corporation, a Lockheed Martin Company, for the United States Department of Energy.

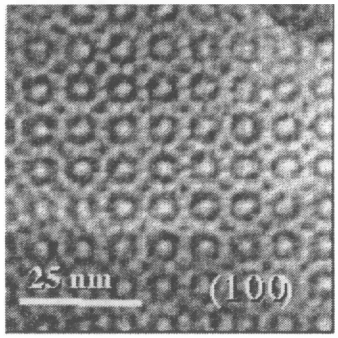

Figure 2. *A TEM image of the [100]-zone of a calcined fragment from a surfactant-templated mesoporous thin film. In this image, the pores have a diameter of ~ 3 nm and a spacing of ~ 8 nm. Choice of surfactant type and concentration determines pore modality and size. Typical film thicknesses are 150 to 200 nm.*

the structure shown in Fig. 2. Films prepared using this technique have extremely high surface area (> 700 m^2/g), tunable pore diameters between ~ 2.0 and 3.5 nm, and 40-50% porosity. Spin-deposition is controlled to give film thicknesses between 150 to 200 nm. These thicknesses represent a good compromise between needed detection sensitivity and minimal loading and surface stress on the quartz resonator (see Fig. 1).

Gas selectivity is improved by ion-exchanging transition metals into the SiO_2 matrix to catalyze specific interactions. Sensors were prepared with Cu, Pd, Fe, V, Mo, and Cr ions by submersion in low-molarity metal-salt solutions for 5 to 30 minutes. Electron paramagnetic resonance (EPR) spectroscopy was performed on one of the Cu:SiO_2 devices which revealed a density of Cu^{2+} sites of approximately 0.1 atom percent. After a 400 °C anneal, the ion density was slightly reduced. None of the other ion-exchanged sensors were characterized for ion density, however, they are expected to be on the same order as the Cu:SiO_2 device. Full optimization of the ion-exchange process for selective detection is now being performed.

EXPERIMENTAL CONFIGURATIONS

High-temperature evaluations of the metal:SiO_2-coated resonator sensors were performed in a specially-designed test cell. A photo of this test cell is shown in Fig. 3. The cell uses resistance heaters embedded in a metal housing above and below a flow cavity to control temperature. Maximum test temperatures were 500 °C with a control stability of ± 0.1°C. The resonators are wire-bonded to gold-plated alumina substrates which are configured as RF striplines for carrying electrical signals to the devices. The heated structure around the resonators forms a gas cavity of ~ 2.4 ml volume; an 8 cm long serpentine channel in the test cell cover preheats the gas before introduction into the cavity.

A vapor flow system provided the appropriate mixtures and flow rates for the target gases. Multi-component mixtures (up to three gases) along with a diluent and purge stream (nitrogen or air) were delivered by an array of mass-flow controllers and valves. Source gases were provided from calibrated bottles with desired concentrations or controlled flow through a bubbler (only water was mixed from a bubbler). Gas mixture concentrations using the flow system ranged from 10 ppm to 100%, while flow rates were controlled over the range 0.005 to 0.3 liters/min.

The quartz resonator sensors were configured as part of the Sandia-patented "lever" oscillator circuits that provide two signal outputs: the device resonance frequency (approximately 6 MHz)

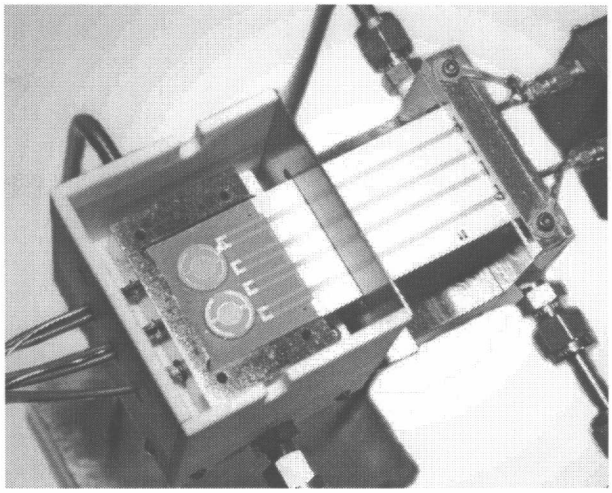

Figure 3. *Interior view of the high-temperature test cell used for gas exposure of the mesoporous SiO_2-coated resonators. Two TSM resonators — one coated device, one uncoated reference device — are wire-bonded to ceramic striplines. Resistance heater control to 500 °C with ± 0.1 °C stability is possible using the fixture.*

and a voltage proportional to the resonant resistance (related to the device quality factor or Q) **[9]**. Two resonators were mounted in the test cell: one coated device acting as the sensor, and an uncoated device acting as the reference. The frequency outputs from the two devices were mixed, providing a low frequency for measurement and a noise-rejection mechanism for operating in the difficult high-temperature environment (see difference frequency in Fig. 1).

A Windows-based computing system running code written in HPVEE and Visual Basic handled all sensor data acquisition, test cell temperature control, and vapor flow system control.

RESULTS AND DISCUSSIONS

Several resonators coated with metal ion-exchanged, mesoporous SiO_2 thin films were evaluated for response to hydrocarbon vapors and cross-sensitivity to other gases present in the vehicle exhaust stream. To date, only one type of sensor — a resonator coated with a Pd:SiO_2 film — has shown good sensitivity for hydrocarbon detection. Figure 4 shows the measured frequency shift (in ppm) when this sensor is exposed to repeated intervals of 1 % by volume propylene gas in an oxygen-

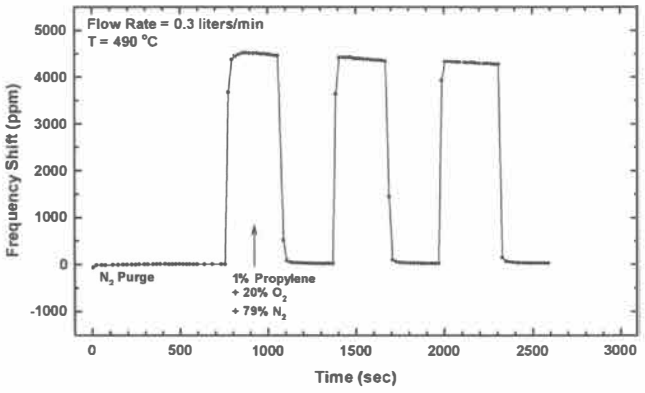

Figure 4. *Measured frequency shift vs. time for one Pd:SiO_2-coated TSM resonator when exposed to repeated intervals of 1% propylene gas mixed with 20 % oxygen.*

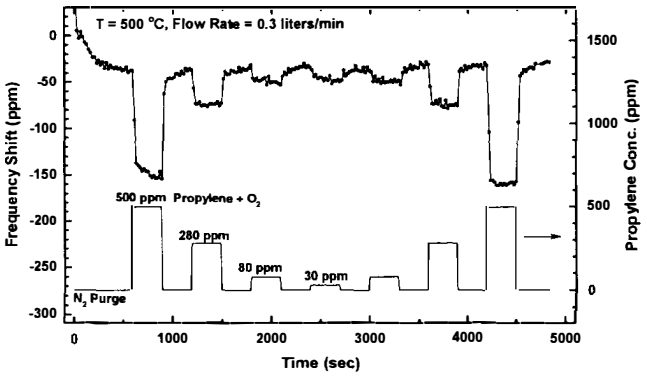

Figure 5. *Measured frequency shift vs. time for a Pd:SiO_2-coated sensor when exposed to low concentrations of propylene in an oxygen-rich atmosphere. Signal detection is possible below 50 ppm. Negative frequency shifts are seen in this figure (compared to Fig. 4) due to frequency mixing with a reference device.*

rich atmosphere at 490 °C. (Propylene gas is used as one simulant for hydrocarbons in vehicle exhaust since it exists in a higher concentration than other non-methane organic gases and has one of the highest reactivity factors.) Maximum sensitivity at 490 °C to propylene vapors is ~ 0.44 (ppm-Δf)/(ppm-gas). Sensor response is rapid, < 20 sec., however, full evaluations of this feature were limited by the 10 sec. data acquisition interval of the measurement system. The minimum detection capability for the Pd:SiO_2 sensor is < 50 ppm propylene at 500 °C as shown in Fig. 5. Smaller propylene concentrations produce noticeable deviations in the frequency response, but it is not certain what fraction of this response is thermal noise created by slight flow rate changes as the vapor delivery system toggles between the target and purge gases.

This sensor functions much like a typical calorimeter or combustible gas detector **[10-12]**. Figure 6 shows that measured responses increase with higher temperature for all the test gases: propylene, ethylene, propane, methane, and hydrogen. This is due to increases in both the gas enthalpy and the quartz resonator response coefficient as the temperature rises. The response magnitude also increases with the number of carbon atoms in each target gas molecule as evidenced by the propylene (C3) and ethylene (C2) responses. In Fig. 7, the measured response to propylene gas is shown to decrease as the oxygen atmosphere becomes leaner and saturate in high concentrations of oxygen.

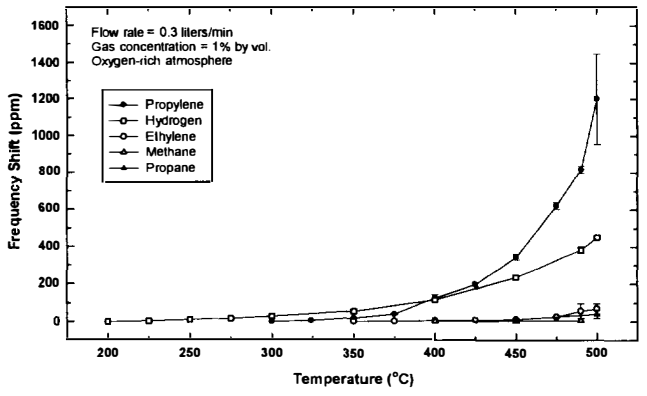

Figure 6. *Measured frequency shift vs. temperature for a Pd:SiO_2-coated sensor exposed to 1% concentrations of propylene, ethylene, propane, methane, and hydrogen gases mixed with oxygen.*

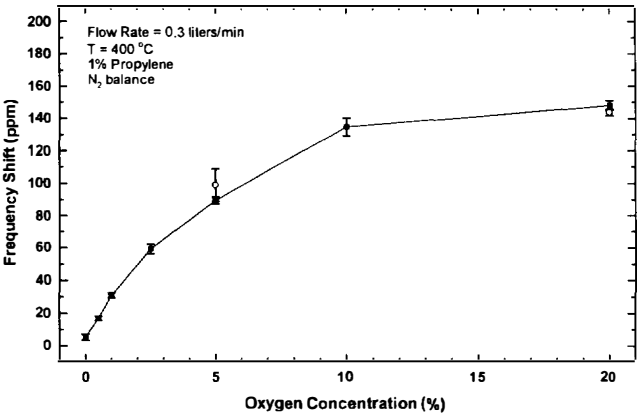

Figure 7. *Measured frequency shift vs. oxygen concentration for 1% propylene gas flowing across a Pd:SiO_2-coated sensor. No response occurs for hydrocarbons in an oxygen-deficient atmosphere. The different plotted points (open circles and filled squares) represent values from two separate tests.*

Again, this behavior is typical of calorimetric sensors.

However, based on the limited sensor measurements for these few test gases, the Pd:SiO_2 sensor response is somewhat atypical for a calorimeter. The olefins (represented by propylene) produce significantly larger frequency shifts than the paraffins (propane), ~ 20 times greater as seen in Fig. 6, and hydrogen sensitivity is relatively large compared to several of the hydrocarbons. Combustible gas detectors will also show some response to carbon monoxide in the presence of oxygen. But this sensor shows no reaction (although in an oxygen-deficient atmosphere at the highest temperatures, CO strips oxygen from the SiO_2 matrix, producing a small, but measurable, mass shift).

The palladium in the matrix obviously modifies the gas sensitivity and selectivity giving it an enhanced catalytic activity. Figure 8 shows the response of two sensors, one having only a surfactant-templated mesoporous SiO_2 thin film and the other with an identical SiO_2 film with palladium introduced in the matrix, exposed to a 1% propylene gas mixture. The virgin SiO_2 device shows a small reaction at the highest temperatures due to the large surface area of the porous film, but its response is much lower than that of the Pd:SiO_2-coated sensor. The exact dependence on the metal ions exchanged in the SiO_2 films is still under investigation; some limited work to date has shown that sensors with V, Cu, or Fe in the matrix exhibit no favorable hydrocarbon or hydrogen

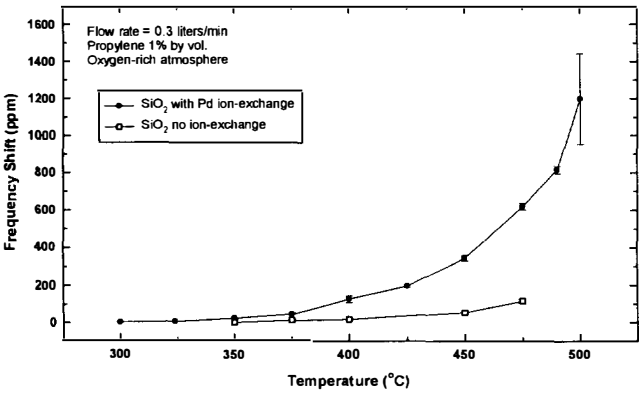

Figure 8. *Measured frequency shift vs. temperature for a propylene-oxygen mixture comparing the sensitivity enhancement due to Pd ion-exchange in the mesoporous SiO_2 thin film coatings.*

catalytic reactivity and often have responses no larger than those for the SiO_2 film alone.

From measurements using the Pd:SiO_2-coated resonators, it appears that sensitivity to hydrocarbon detection may be greater than for other types of calorimeters. It is postulated that catalyzed combustion (and the associated temperature increase) in the porous films stress the resonator surface, producing a frequency shift much greater than that for an equivalent temperature shift in the bulk quartz (as illustrated in Fig. 1).

Utility of the surfactant-templated mesoporous silica sensors for vehicle exhaust monitoring depends on discrimination in the presence of other gas constituents. The Pd:SiO_2 devices exhibit no measurable response to NO or NO_2 at concentrations up to 9000 ppm, levels several times higher than expected in the exhaust stream. CO_2 illicits a small response (~ 20 ppm-Δf at 15% by volume concentration at 450 °C) due to a much larger heat capacity than the other test gases. Since CO_2 concentration in vehicle exhaust is usually near the values tested, it could interfere with detection of low levels of hydrocarbons. Water vapor, when exposed individually to the sensors, does not illicit a response. However, when water vapor is mixed into a propylene-oxygen stream at high temperatures (> 300 °C), a significant reduction in measured frequency shift (approx. a factor of two for 3 % H_2O) occurs. This reaction is unexpected as the difference in gas thermal conductivity alone does not account for such a large shift in response from a small concentration of water. Some of the shift in response magnitude could be an anomaly of the measurement system, and the phenomenon is still being studied. If proved real, the interference from water vapor would be detrimental to eventual sensor implementation.

A comparison of responses for the Pd:SiO_2-coated resonators when exposed to all the test gases is given in Table 1. Sensitivities are listed for only one specified temperature and gas concentration.

CONCLUSIONS

TSM quartz resonators coated with thin films of mesoporous silica and ion-exchanged with palladium ions have shown good sensitivity and selectivity for high-temperature detection of hydrocarbon gases in the presence of oxygen. The sensors act much like calorimeters responding to slight temperature increases produced by catalyzed combustion in the high surface area films. Additional investigations are in progress to determine catalytic specificity provided by different metal ions in the silica matrix and to further understand interference effects from water vapor.

REFERENCES

1. S. J. Martin, G. C. Frye, J. J. Spates, and M. A. Butler, "Gas Sensing with Acoustic Wave Devices," *Proc. IEEE Ultrasonics Symp.*, pp. 423-434 (1996).

2. N. Miura, H. Minamoto, G. Sakai, and N. Yamazoe, "New-type Calorimetric Gas Sensor Using Temperature Characteristics of Piezoelectric Quartz Crystal Fitted with Noble Metal Catalyst Film," *Sensors and Actuators B*, **5**, pp. 211-217 (1991).

3. V. I. Anisimkin, M. Penza, V. A. Osipenko, and L. Vasanelli, "Gas Thermal Conductivity Sensor Based on SAW," *IEEE Trans. UFFC*, **42**, pp. 978-980 (1995).

4. J. E. Martin, M. T. Anderson, J. Odinek, and P. Newcomer, "Synthesis of Periodic Mesoporous Silica Thin Films," *Langmuir*, **13** (15), pp. 4133 -4141 (1997).

5. Y. Lu, R. Ganguli, M. T. Anderson, C. A. Drewien, C. J. Brinker, W. Gong, Y. Guo, H. Soyez, B. Dunn, M. H. Huang, and J. I. Zink, "Continuous Formation of Supported Cubic and Hexagonal Mesoporous Films by Sol-gel Dip-coating," *Nature*, **389**, pp. 364-368 (1997).

6. G. Sauerbrey, "Verwendung von Schwingquarzen zur Wägung dünner Schechten and zur Mikrowägung," *Z. Phys.*, **155**, pp. 206-222 (1959).

7. see for example R. Bechmann, "Frequency-Temperature-Angle Characteristics of AT- and BT-Type Quartz Oscillators in an Extended Temperature Range," *Proc. IRE*, **48**, p. 1494 (1960).

8. P. Krempl, G. Schleinzer, W. Wallnofer, and J. Glaser, "Gallium Phosphate, $GaPO_4$: A New Piezoelectric Crystal Material for High Temperature Sensorics," *Proc. Eurosensors X*, pp. 1093-1096, Leuven, Belgium (1996).

9. K. O. Wessendorf, "The Lever Oscillator for Use in High Resistance Resonator Applications," *Proc. IEEE Intl. Frequency Control Symp.*, pp. 711-717 (1993).

10. A. W. van Herwaarden, P. M. Sarro, J. W. Gardner, and P. Bataillard, "Micro-Calorimeters for (Bio)chemical Measurements in Gases and Liquids," *Tech. Digest, 7th Int'l. Conf. On Solid-State Sensors and Actuators (Transducers '93)*, pp. 411-414 (1993).

11. Visser, M. Zanini, L. Rimai, R. E. Soltis, A. Kovalchuk, D. W. Hoffman, E. M. Logothetis, U. Bonne, L. T. Brewer, O. W. Bynum, and M. A. Richard, "Catalytic Calorimetric Gas Sensors," *Digest, 5th Int'l Mtg. On Chemical Sensors*, Rome, Italy, pp. 468-471 (1994).

12. B. Makovos, F. W. Montague, L. Dudik, and C. C. Liu, "A Calorimetric Combustible Gas Detector Employing Platinum Film Heaters," *Sensors and Actuators B*, **12**, pp. 91-94 (1993).

Table 1. *Comparison of Pd:SiO_2-coated resonator response for various gases at specified temperatures and concentrations.*

Gas	Temp (°C) / Conc. (%)	Sensitivity (ppm-Δf)/(ppm-gas)	Comments
Propylene (C_3H_6)	450 / 1	5.4×10^{-2}	due to catalytic combustion in O_2
Ethylene (C_2H_4)	450 / 1	2.4×10^{-3}	"
Propane (C_3H_8)	450 / 1	2.1×10^{-3}	"
Methane (CH_4)	450 / 1	$< 5 \times 10^{-4}$	too small to quantify
Hydrogen (H_2)	450 / 1	3.8×10^{-2}	due to catalytic combustion in O_2
Carbon Monoxide (CO)	450 / 1	$\sim 1 \times 10^{-3}$	only in oxygen-deficient atmosphere
Carbon Dioxide (CO_2)	450 / 15	2.7×10^{-4}	due to higher specific heat
Nitric Oxide (NO)	450 / 0.5	none	
Nitrogen Dioxide (NO_2)	500 / 0.9	none	
Water Vapor (H_2O)	400 / 3	$< 5 \times 10^{-5}$	anomalous response in mixtures

APPLICATION OF THE SOLUBILITY PARAMETER CONCEPT TO THE DESIGN OF CHEMIRESISTOR ARRAYS

R. C. Hughes, M. P. Eastman,* W. G. Yelton, A. J. Ricco, S. V. Patel, and M. W. Jenkins
Sandia National Laboratories, Albuquerque, New Mexico, 87185-1425
*Department of Chemistry, Northern Arizona University, Flagstaff, Arizona, 86011

ABSTRACT

Arrays of unheated chemically sensitive resistors (chemiresistors) can serve as extremely small, low-power-consumption sensors with simple read-out electronics. Most work has focused on the exotic polymeric organic metals, but here we report new results on carbon-loaded polymer composites, as well as polymeric ionic conductors. We use the solubility parameter concept to understand and categorize the chemiresistor responses and, in particular, we compare chemiresistors fabricated from polyisobutylene (PIB) to results from PIB-coated acoustic wave sensors.

INTRODUCTION

Microsensor development for sensing vapors has often focused on creating single devices or arrays with the maximum selectivity to specific vapors **[1-4]**. Applications include systems for environmental monitoring, industrial process control, contraband detection, and the like. A problem having different constraints is the detection of solvent spills in areas containing electrical equipment: many different solvents may attack the insulators used in cables, connectors, wire bundles, and encapsulation, and the identity of the solvent is less important than its effect. Since the nature of this challenge depends on a range of unpredictable factors, good design dictates the development of a system using the minimum number of sensors capable of responding to all possible solvents. In addressing this problem, we sought to design a series of chemiresistors, whose responses span "all solvent space," that would be planar, extremely small, and compatible with silicon microelectronics. With today's miniaturized communications technology, it is possible to envisage extremely small packages that include the sensors, analog electronics, and telemetry for transmission of sensor data.

In discussing "solvent space," it is important to have at least a semi-quantitative measure of solvent-polymer interactions. The solubility parameter, δ, introduced by Hildebrand **[5],** has been widely used as a tool to find the best solvent for a particular polymer. For a given solvent (or polymer), δ is loosely related to its cohesive energy and, thus, the energy of interaction among the molecules of the substance. Large tables compile measured solubility parameters for both solvents and polymers **[6]**.

The majority of the results reported here are for carbon particle/insulating organic polymer composites. There is a long history of these composites being applied as conductive, flexible films; commercial products include self-regulating heating tape and resettable fuses, both of which exploit these materials' positive temperature coefficient of resistance (PTC) **[7]**. A number of papers have also reported the chemical sensing properties of these films **[2, 8, 9]**. The temperature, pressure, and chemical response of these films all depend on the same physics: the film resistance is a strong function of the volume fraction occupied by the conductive particles. If the polymer host increases its volume by thermal expansion or swelling due to absorption of analyte molecules, the resistance increases due to breakage of some of the conductive pathways through the film. The magnitude of the response of such chemical sensors appears to depend almost entirely on the solvent-polymer interactions, with the conductive particles serving to report the degree of swelling of the host polymer matrix.

We also examined a second class of chemiresistor material, those relying upon the mobility of ions in an ionically conductive matrix to report the presence of an analyte. It is well documented that the ionic conductivity of such films is enhanced by solvents, particularly water **[2]**. The increased mobility can result from reduced viscosity of the polymer matrix when plasticized by the analyte, dielectric screening of the charged polymer backbone by the analytes **[10]**, or solvation of the mobile ions.

EXPERIMENTAL DETAILS

Planar interdigitated electrodes (IDEs), fabricated at Sandia, consist of quartz platforms (5 x 8 mm) supporting 50 pairs of photolithographically defined interdigitated electrodes (1.6 mm^2 overall) comprised of 2000 Å of gold on a 150-Å chrome adhesion layer (both metals thermally evaporated). The 1.6 mm x 8-μm-wide electrodes are separated by 8 μm. A widely spaced (3 mm) pair of 6-mm-long electrodes was also fabricated on the same chip, providing higher resistance for those materials having exceptionally low resistance across the IDEs.

Insulating polymer/conductive particle composites were prepared by co-dissolving a nonconductive organic polymer and 40%-by-weight (relative to the polymer) of 30-nm graphitized carbon particles in an appropriate solvent, then coating the IDEs by spin-coating or deposition from a pipette. The polymer matrix materials include polyisobutylene (PIB); polydiphenoxyphosphazine (DPPZ); syndiotactic polybutadiene (PBS); polyvinylalcohol (PVA); and polyethylene/vinylacetate copolymer (PEVA). These were selected to cover a wide range of solubility parameters.

Two types of ionically conductive composites were prepared. An organic polymer/liquid crystal composite device was made by dispersing 0.3 g of the nematic liquid crystal "K21" in 0.24 g of PVA (MW = 25,000) dissolved in 2 - 3 ml of water; 3 mg of tetraethylammonium bromide was added to provide mobile ions. A second material was based upon hectorite clay, which includes mobile cations intercalated between sheets of fixed anionic sites. A gold colloid/hectorite coating was prepared by suspending sodium hectorite (NL Industries, as-received) in a solution of colloidal gold (Unconjugated Polygold, 40 nm; Polysciences, Inc.). Sensors were prepared by spin coating or smearing a thin film on the IDE. Impedance spectroscopy was used to characterize the response of the ionically conductive films; the optimal frequency range was found to be 2 Hz - 1 kHz.

Analytes included isooctane, cyclohexane, toluene, trichloroethylene, xylene, DIMP (diisopropylmethylphosphonate), ethanol, methanol, and water. Solvents and analytes were commercially available (Fisher Chemical) and used as received, except ethanol, which was distilled to remove water.

IDE devices were placed in a stainless-steel fixture housed in a constant-temperature oven. Nitrogen gas from a cryogenic source was passed through gas bubblers filled with the analyte and maintained at room temperature. Flow rates were controlled by mass-flow controllers. Resistance measurements were made using a Keithley Model 2001 Multimeter or, in the case of high-impedance ($> 10^7$ ohms) devices requiring AC measurement at

0-9640024-2-6/hh1998/$20©1998TRF
DOI 10.31438/trf.hh1998.88

Solid-State Sensors, Actuators, and Microsystems Workshop
Hilton Head Island, South Carolina, June 8-11, 1998

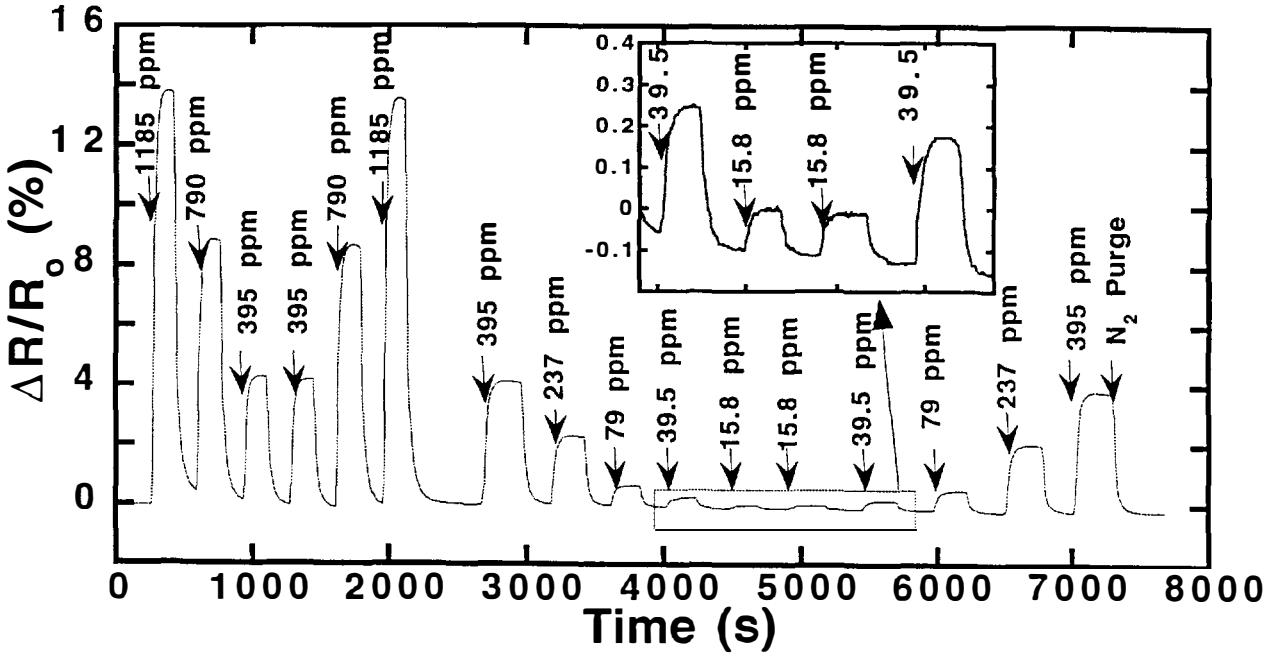

Figure 1. *Response of a chemiresistor to pulses of different concentrations of* m-*xylene in* N_2. *The sensor is a carbon particle-loaded (40% by weight) film of PIB held at 32°C. The inset expands the response at low partial pressures of xylene.*

specific frequencies, a Stanford Research Systems SR 830 DSP Lock-In Amplifier interfaced to a Keithley Model 427 current amplifier. LabVIEW was used to set flow controllers and acquire data from the multimeters.

RESULTS AND DISCUSSION

We studied two important polymers not previously reported in the literature of carbon/polymer composite sensors. The first of these. PIB, is a rubbery polymer that has been utilized extensively as a chemically sensitive coating on surface acoustic wave devices **[3,11]**. As a consequence, there is a large body of information on the interaction of organic vapors with thin films of this polymer, including the isotherms (sensor response vs. vapor partial pressure), speed of response for both absorption and desorption, and response to mixtures of vapors.

Figure 1 shows the response of a carbon-loaded PIB film to pulses of various concentrations of *m*-xylene vapor.The sensor temperature was maintained at 32°C in the oven; the bubbler temperature was 23°C. The equilibrium vapor pressure of *m*-xylene at 21°C is 7900 ppm. The partial pressures in the pulses of vapor are given in Figure 1. Response and recovery are rapid, and reproducibility is good. The inset in Figure 1 expands the responses at the lowest partial pressures.

The responses in Figure 1 are similar to those reported for PIB films on acoustic wave devices, consistent with the notion that the concentration of analyte in the film determines both the magnitude of the acoustic wave device response, and the swelling of the polymer matrix, which in turn affects the volume fraction occupied by the carbon particles and hence film resistance.

The PIB chemiresistor responds to a variety of organic vapors. Figure 2 shows the relative response to seven different solvents as a function of solubility parameter. Plotted for comparison are the relative responses of a PIB-coated acoustic wave device **[11]**. The PIB has a δ value of 15.5 **[6]**, and the peak responses of both the chemiresistor and SAW data are nearby, at 17 - 18. Obtaining a large sensor response for matching δ values holds, but not with high accuracy.

The second important polymer system is PVA. This polymer is readily prepared as a thin film and is expected to interact especially strongly with polar molecules (δ = 25.8 **[6]**); as a consequence, it should respond to analytes that might not produce a strong response in a PIB-based sensor. We have incorporated PVA into our sensors in two distinct ways. The first is in the form of the carbon-loaded polymer composite: the second is in the form of an ionically conductive mixture of PVA-dispersed liquid crystal, doped with an organic salt to confer conductivity.

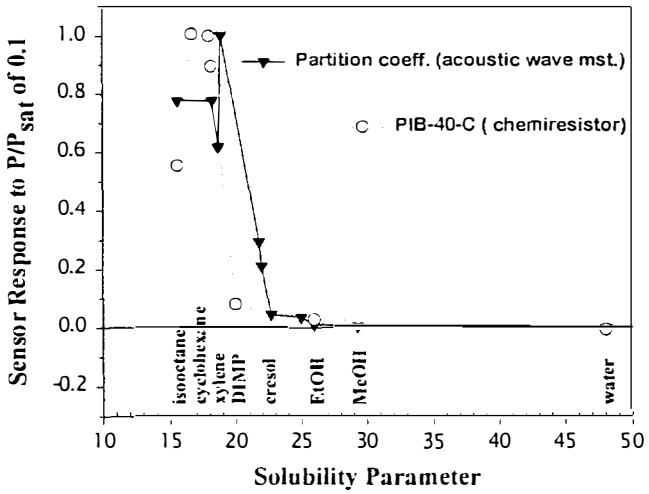

Figure 2. *Normalized response of the PIB chemiresistor to a variety of solvents with the maximum signal at 10% P/P$_{sat}$ set to 1. These data are compared with the SAW-measured partition coefficients* **[6]** *for the same solvents (plus some additional ones) and plotted* vs. *the solubility parameters of the solvents. A number of the solvents are labeled on the figure. This suggests that the chemiresistor response is closely related to the swelling of the polymer phase.*

The PVA/liquid crystal system is reminiscent of the multicomponent polymer electrolyte sensors recently reported by Cammann *et al.* **[12]**; however, it is important to recognize that the

liquid crystal imparts some important properties to the sensor. First, the liquid crystal segregates into microdroplets as the film forms on the sensor; thus, the films are two-phase materials, and each phase can respond differently to various vapors. Thus, the potential exists for polymer-dispersed microdroplet materials to respond to a broad range of analytes and concentrations.

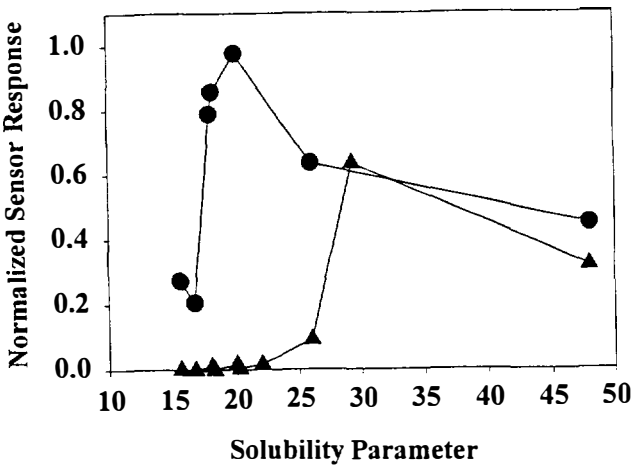

Figure 3. *Normalized response of the two types of PVA-based sensors, plotted* vs. *solubility parameter as in Figure 2. The two-phase PVA/K21 has a broader response than the single-phase PVA, but requires AC voltages for measurement.*

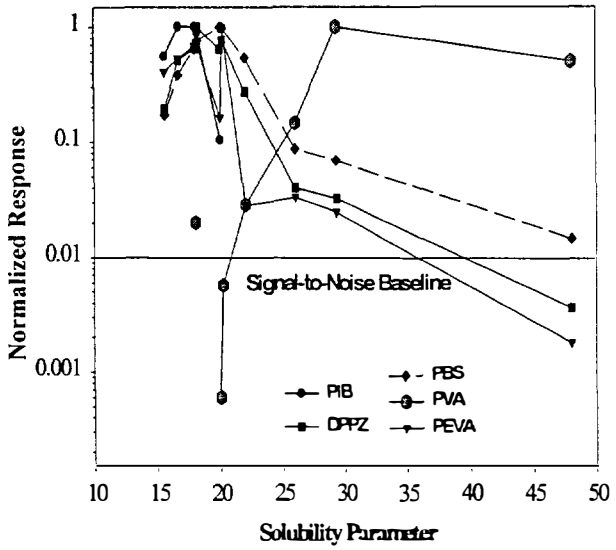

Figure 4. *Responses of five carbon/polymer composite sensors* vs. *solvent solubility parameter. The log scale helps to separate the responses; the "Signal-to-Noise Baseline" gives an indication of the size of signal below which data are generally unreliable due to drift and noise. The symbols identify the polymers, which are defined in the Experimental section.*

Figure 3 shows the response curves for PVA/K21 and carbon-loaded PVA *vs.* solubility parameter. The PVA/carbon film shows a peak response for methanol ($\delta = 29.3$) and good response to relative humidity; it responds weakly at lower δ values. In contrast, the two-phase PVA/K21 responds at both high and low δ values. The responses for PVA/K21 were measured at 2 Hz and 0.5 V using the lock-in amplifier setup. Impedance *vs.* frequency curves were similar to poly(hexane viologen) responses we reported elsewhere **[10]**.

Figure 4 uses the format of Figs. 2 and 3 to plot the responses of three other carbon/polymer composites: DPPZ, PEVA, and PBS, plus PVA. There are some unpredicted features in these responses, such as the low response for DIMP compared with trichloroethylene for PEVA, but no solvent goes unmeasured by at least one of the sensors.

PATTERN RECOGNITION

Having an array of sensors not only provides responses to a wide variety of solvents, it also presents an opportunity to identify particular solvents using pattern-recognition (PR) techniques. VERI PR, developed at Sandia, has been used extensively by us to interpret data from acoustic wave and catalytic gate sensors **[4, 13]**. Application of VERI PR is illustrated in Figure 5, showing the responses of three chemiresistors to four solvents in a 3-D plot. Each point represents a different concentration of the indicated solvent. The responses have been equalized and normalized so that each response is a vector ending on the surface of a unit sphere (outlined by the solid curves). The readers' vision allows her/him to see that classification of the signals from each of the four solvents is unambiguous at all tested concentrations. VERI PR can be used for large arrays (higher dimensions than three); it reports whether the response to an unknown sample clusters with any previously tested classes, or must be treated as a previously untested chemical.

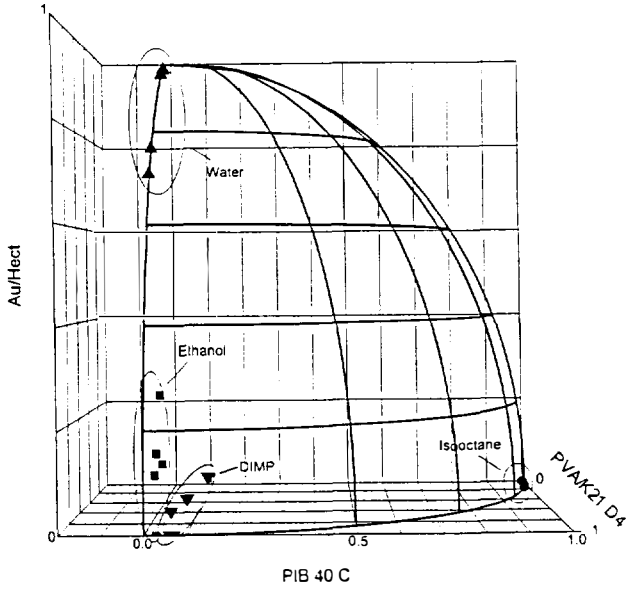

Figure 5. *Pattern recognition plot to identify individual solvents from the response to three sensors. Each point represents a different concentration of the labeled solvent; each axis represents the normalized response of one of the sensors.*

THE CHEMICAL FUSE

An interesting and valuable property of the carbon-loaded polymer/composite chemiresistors is that very high concentrations of solvent cause orders-of-magnitude increase in their resistance. In cases where the polymer can completely dissolve in the solvent, and with sufficient mechanical agitation, the sensor will permanently remain at high (or infinite) resistance; the sensor is destroyed. In some cases, however, the solvent will eventually evaporate in much the same way that the sensor was originally fabricated, restoring the sensor.

An example is given in Figure 6, where a drop of liquid isooctane was placed on a horizontal PIB-based sensor. The sampling period was 100 ms; in less than one second, the resistance

increased over three orders of magnitude. As long as liquid isooctane remained visible on the sensor, the resistance remained very high (300 MΩ), but measurable. As the isooctane evaporated, a sharp drop in resistance was observed. The sensor was still functional for sensing lower concentrations, but the baseline resistance had decreased permanently. Subsequent doses of liquid isooctane always produced large increases in resistance, but the "under-liquid" and baseline resistances changed by smaller amounts. Further engineering is required to make a reproducible fuse similar to the commercially available PTC electrical fuse [7].

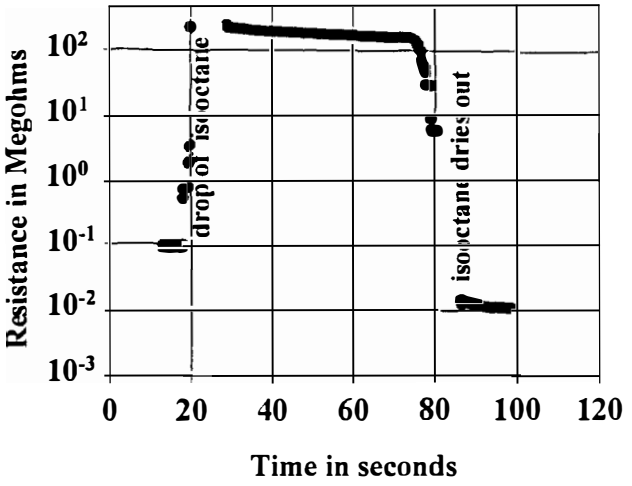

Figure 6. *Resistance of a PIB sensor acting as a (resettable) chemical fuse to liquid isooctane. A rapid increase in resistance results from a small drop of isooctane (0.1 seconds per data point from a 16-bit digitizer) and recovery occurs when the isooctane evaporates.*

SUMMARY AND CONCLUSIONS

We believe the data in this paper demonstrate that an extremely small, low-power-consumption array of chemiresistors can identify almost any kind of solvent spill. This preliminary report builds the framework for further efforts to develop the "universal solvent sensor."

Solubility parameters were used to characterize sensor films and as an aid in selecting sensors for use in arrays to discriminate between members of similar or dissimilar solvent classes. Chemiresistors based on several carbon-loaded polymers were studied, along with an ionically conductive, polymer-dispersed liquid crystal system. The various sensors show differing sensitivities in different regions of "solvent space." PIB shows maximum sensitivity to analytes characterized by small δ values, while PVA responds best to solvents with large δ values. The PVA/K21 two-phase film has the broadest response range of the materials evaluated. Additional data must be acquired to provide adequate training sets for determining a range of unknowns in the field.

Figure 4 illustrates the feasibility of selecting 3 or 4 sensors, at least one of which responds to every possible solvent above some threshold concentration. Although some solvent might produce too small a response to be detected, our logic in protecting electronic components and packaging is to select polymers representative of those used in such applications. Figure 6 shows how chemiresistors can act as resettable chemical fuses to give rapid, unambiguous warning of a solvent spill. The chemical fuse failure mode is high resistance, so other hazards such as fire, physical destruction, or strong oxidizing agents (e.g., nitric acid) will yield a similar failure response.

Conductive particle/polymer composite sensors can be fabricated in an extremely small (< 1 mm^2) planar format and consume almost no power to measure DC resistance. Sensor arrays are readily fabricated using fluid-dispensing techniques. Ionic conductivity-based sensors are equally small, but require more complex circuitry for AC measurement; unique selectivity or sensitivity can make these materials attractive nonetheless.

ACKNOWLEDGMENTS

Sandia is a multiprogram laboratory operated by Sandia Corporation, a Lockheed Martin Company, for the United States Department of Energy under Contract DE-AC04-94AL85000. MPE acknowledges sabbatical support by Northern Arizona University and supplementary financial support by Sandia National Laboratories.

REFERENCES

1. *Techniques and Mechanisms in Gas Sensing*, P. T. Moseley, J. O. W. Norris, and D. E. Williams, Eds., IOP Publishing (Adam Hilger Series on Sensors), Bristol, England (1991).
2. G. Harsanyi, *Polymer Films in Sensor Applications*, Technomic Publishing, Lancaster (1995).
3. D. S. Ballantine, Jr., *et al. Acoustic Wave Sensors: Theory, Design and Physico-Chemical Applications*, Academic Press, Inc., San Diego (1997), Ch. 5.
4. A. J. Ricco, R. M. Crooks, and G. C. Osbourn, "SAW Chemical Sensor Arrays: New Chemically Sensitive Interfaces Combined with Novel Cluster Analysis to Detect Volatile Organic Compounds and Mixtures," *Accts. Chem. Res.*, *31*, xxxx (1998).
5. D. W. Van Krevelen, *Properties of Polymers*, Elsevier, New York (1976), Ch. 7.
6. E. A. Grulke, in *Polymer Handbook, 3rd Edition*, J. Brandrup and E. H. Immergut, Eds., Wiley and Sons, New York, (1989), p. VII/519.
7. M. B. Heaney, "Resistance-Expansion Temperature Behavior of a Disordered Conductor-Insulator Composite," *Appl. Phys. Lett.*, *69*, 2602 (1996).
8. M. C. Lonergan, E. J. Severin, B. J. Doleman, S. A. Beaber, R. H. Grubbs, and N. S. Lewis, "Array-Based Vapor Sensing using Chemically Sensitive Carbon Black-Polymer Resistors," *Chem. Mater.*, *8*, 2298 (1996).
9. B. Lundberg and B. Sundqvist, "Resistivity of a Composite Conducting Polymer as a Function of Temperature, Pressure and Environment: Applications as a Pressure and Gas Concentration Transducer," *J. Appl. Phys.*, *60*, 1074 (1986).
10. K. B. Pfeifer, R. C. Hughes, M. W. Jenkins, and T. W. Schneider, "Viologen Polymer-Coated Impedance Sensors for Midrange Moisture Sensing," *J. Electrochem. Soc.*, submitted for publication.
11. R. A. McGill, M. H. Abraham, and J. W. Grate, "Choosing Polymer Coatings for Chemical Sensors," *Chemtech*, *Sept.* (1994), p. 27.
12. K. Cammann, K. Buhlmann, B. Schlatt, H. Muller, and A. Choulga, "Multicomponent Polymer Electrolytes: New Extremely Versatile Receptor Materials for Gas Sensor and Electronic Noses," *Technical Digest, Transducers '97*, IEEE, New York (1997), p. 1395.
13. G. C. Osbourn, J. W. Bartholomew, G. C. Frye, and A. J. Ricco, "Clustering-Based Pattern Recognition Applied to Chemical Recognition Using SAW Array Signals", *Technical Digest, Solid-State Sensor and Actuator Workshop*, Transducers Research Foundation, Cleveland (1994), p. 193.

AUTHOR INDEX

KEYWORD INDEX